Springer Series in Optical Sciences 111

Junji Ohtsubo

Semiconductor Lasers

Stability, Instability and Chaos

Fourth Edition

Springer

Springer Series in Optical Sciences

Volume 111

Founded by

H.K.V. Lotsch

Editor-in-Chief

William T. Rhodes, Georgia Institute of Technology, Atlanta, USA

Editorial Board

Ali Adibi, Georgia Institute of Technology, Atlanta, USA
Theodor W. Hänsch, Max-Planck-Institut für Quantenoptik, Garching, Germany
Ferenc Krausz, Ludwig-Maximilians-Universität München, Garching, Germany
Barry R. Masters, Cambridge, USA
Katsumi Midorikawa, Saitama, Japan
Herbert Venghaus, Fraunhofer Institut für Nachrichtentechnik, Berlin, Germany
Horst Weber, Technische Universität Berlin, Berlin, Germany
Harald Weinfurter, Ludwig-Maximilians-Universität München, Munchen, Germany

Springer Series in Optical Sciences

The Springer Series in Optical Sciences, under the leadership of Editor-in-Chief William T. Rhodes, Georgia Institute of Technology, USA, provides an expanding selection of research monographs in all major areas of optics: lasers and quantum optics, ultrafast phenomena, optical spectroscopy techniques, optoelectronics, quantum information, information optics, applied laser technology, industrial applications, and other topics of contemporary interest.

With this broad coverage of topics, the series is of use to all research scientists and engineers who need up-to-date reference books.

The editors encourage prospective authors to correspond with them in advance of submitting a manuscript. Submission of manuscripts should be made to the Editor-in-Chief or one of the Editors. See also www.springer.com/series/624

Editor-in-Chief

William T. Rhodes
School of Electrical and Computer Engineering
Georgia Institute of Technology
Atlanta, GA 30332-0250
USA
e-mail: bill.rhodes@ece.gatech.edu

Editorial Board

Ali Adibi
School of Electrical and Computer Engineering
Georgia Institute of Technology
Atlanta, GA 30332-0250
USA
e-mail: adibi@ee.gatech.edu

Theodor W. Hänsch
Max-Planck-Institut für Quantenoptik
Hans-Kopfermann-Straße 1
85748 Garching, Germany
e-mail: t.w.haensch@physik.uni-muenchen.de

Ferenc Krausz
Ludwig-Maximilians-Universität München
Lehrstuhl für Experimentelle Physik
Am Coulombwall 1
85748 Garching, Germany *and*

Max-Planck-Institut für Quantenoptik
Hans-Kopfermann-Straße 1
85748 Garching, Germany
e-mail: ferenc.krausz@mpq.mpg.de

Barry R. Masters
Cambridge
USA

Katsumi Midorikawa
Saitama
Japan

Herbert Venghaus
Fraunhofer Institut für Nachrichtentechnik
Heinrich-Hertz-Institut
Einsteinufer 37
10587 Berlin, Germany
e-mail: venghaus@hhi.de

Horst Weber
Optisches Institut
Technische Universität Berlin
Straße des 17. Juni 135
10623 Berlin, Germany
e-mail: weber@physik.tu-berlin.de

Harald Weinfurter
Sektion Physik
Ludwig-Maximilians-Universität München
Schellingstraße 4/III
80799 München, Germany
e-mail: harald.weinfurter@physik.uni-muenchen.de

More information about this series at http://www.springer.com/series/624

Junji Ohtsubo

Semiconductor Lasers

Stability, Instability and Chaos

Fourth Edition

Springer

Junji Ohtsubo
Shizuoka University
Shizuoka
Japan

ISSN 0342-4111 ISSN 1556-1534 (electronic)
Springer Series in Optical Sciences
ISBN 978-3-319-56137-0 ISBN 978-3-319-56138-7 (eBook)
DOI 10.1007/978-3-319-56138-7

Library of Congress Control Number: 2017934868

1st–3th edition: © Springer-Verlag Berlin Heidelberg 2006, 2008, 2013
4th edition: © Springer International Publishing AG 2017
This work is subject to copyright. All rights are reserved by the Publisher, whether the whole or part of the material is concerned, specifically the rights of translation, reprinting, reuse of illustrations, recitation, broadcasting, reproduction on microfilms or in any other physical way, and transmission or information storage and retrieval, electronic adaptation, computer software, or by similar or dissimilar methodology now known or hereafter developed.
The use of general descriptive names, registered names, trademarks, service marks, etc. in this publication does not imply, even in the absence of a specific statement, that such names are exempt from the relevant protective laws and regulations and therefore free for general use.
The publisher, the authors and the editors are safe to assume that the advice and information in this book are believed to be true and accurate at the date of publication. Neither the publisher nor the authors or the editors give a warranty, express or implied, with respect to the material contained herein or for any errors or omissions that may have been made. The publisher remains neutral with regard to jurisdictional claims in published maps and institutional affiliations.

Printed on acid-free paper

This Springer imprint is published by Springer Nature
The registered company is Springer International Publishing AG
The registered company address is: Gewerbestrasse 11, 6330 Cham, Switzerland

Preface to the Fourth Edition

In the fourth edition, I include further progress of the recent study of fundamental dynamics and applications in chaotic semiconductor lasers. Semiconductor lasers with extra device structures are essentially unstable lasers that exhibit chaos even without external perturbations as discussed in the previous editions. The new results for the stability and instability in such devices, e.g., vertical-cavity surface-emitting lasers, broad-area semiconductor lasers, quantum-dot semiconductor lasers, and quantum-cascade lasers, are treated. New developments are also achieved in the control and applications of instability and chaos in semiconductor lasers. For example, the method of self-mixing interferometry in quantum-cascade lasers treated in the current edition is indispensable in practical applications, since fast external photodetector is not available in those THz optical wavelength regions. One of the new topics in this edition is the consistency and synchronization property of many coupled semiconductor lasers in connection with the analogy of the dynamics in synaptic neurons. In particular, zero-lag synchronization is very important in nonlinear networks, since zero-lag synchronization between distant neurons plays a crucial role for the information processing in the human brain. The consistency and synchronization properties in chaotic networks consisting of many coupled semiconductor lasers are discussed as a new chapter in this edition. Also, as an application of the consistency and synchronization in chaotic semiconductor lasers, neuro-inspired information processing, which is called reservoir computing, is presented.

Shizuoka, Japan — Junji Ohtsubo

Preface to the Third Edition

After the publication of the second edition of this book in 2008, further significant advance has been made in chaos research in semiconductor lasers. One of the topics that is worth treating in this book is the method of ultrafast physical random number generations using chaotic semiconductor lasers, which is suitable for random key distributions in modern cryptographic applications. Based on the method, we can generate true physical random numbers that are hundred times or even thousand times faster than those in existing methods. In conjunction with the method, photonic integrated circuits for chaotic light generators have recently been developed. Thus, chaos, especially chaos in semiconductor lasers, is now not only an interesting issue from the viewpoint of fundamental research, but also an important tool for engineering applications. These topics are treated as a new chapter in this book. In parallel with these topics, great advance has been made for the study of the dynamics in various types of semiconductor lasers with new device structures. I have already treated the dynamics in vertical-cavity surface-emitting lasers and broad-area semiconductor lasers in the first and second editions. Further advance has been brought in the dynamics of these lasers and they have been added in the third edition. Other examples of newly developed lasers are quantum-dot and quantum-cascade semiconductor lasers and they show interesting dynamics. I also discuss these new topics in Chap. 8. At the same time, several subjects are appropriately revised and a number of misprints in the second edition have been corrected. For the second edition, I have received several advices and comments for the improvements of the book, although I would not mention each of them. I have taken some of them into account for the new edition. I would like to thank those persons.

Junji Ohtsubo

Preface to the Second Edition

Chaos research in laser physics, especially in semiconductor lasers, has developed further even after completion of the first edition of this book in the late summer of 2004, and it is still growing rapidly. For example, various forms of chaotic dynamics have been applied in newly developed semiconductor lasers, such as in vertical-cavity surface-emitting semiconductor lasers and broad-area semiconductor lasers. Chaotic dynamics plays an important role in these new lasers, even for their solitary oscillations, and control of the dynamics is currently an important issue for practical applications. Another significant advance has been made in the area of chaotic optical secure communications. Chaotic secure communications using existing public optical communications links have been tested, and successful results have been obtained. In this second edition, I have filled in the gaps in the explanation of chaotic laser dynamics in the previous edition, and I have also added several important topics that have been developed recently. In particular, a new chapter on laser stabilizations has been added, and a number of misprints in the first edition have been corrected. I believe this book will be of interest not only to researchers in the field of laser chaos, but also to those working in nonlinear science and technology.

Hamamatsu
Spring 2007

Junji Ohtsubo

Preface to the First Edition

The aim of this book is the description of the state of the art of chaos research in semiconductor lasers and their applications, and the future perspective of this field. However, for the beginner, including graduates who intend to participate newly in this field, the book starts with an introduction and explanation of chaos in laser systems and the derivation of semiconductor laser rate equations assuming two-level systems. I discuss stabilities, instabilities, and various chaotic dynamics in semiconductor lasers induced by optical and optoelectronic feedback, optical injection, and injection current modulation. As optical feedback, the effects of the conventional reflector, the grating feedback mirror, and the phase-conjugate mirror are considered. Recent results both for theoretical and experimental investigations are presented. Instabilities and chaotic dynamics for novel laser structures (self-pulsating semiconductor lasers, vertical-cavity surface-emitting semiconductor lasers (VCSELs), broad-area semiconductor lasers, and semiconductor laser arrays) are also discussed not only for solitary operations but also in the presence of external perturbations.

As applications of semiconductor laser chaos, control and noise suppression of lasers based on chaos control algorithm are presented. Externally controlled lasers are also interesting for applications of new laser systems with high coherent light sources or tunable light sources. The self-mixing interferometer in semiconductor lasers is an attractive application based on dynamic properties using bistable states in optical feedback effects. I also discuss these subjects. As another application of chaos, several methods of data encryption into the chaotic carrier and its decryption are introduced for secure data transmissions and communications based on chaos synchronization in semiconductor laser systems. This book is focused on the dynamic characteristics of semiconductor lasers and their applications. Therefore, the detailed descriptions for materials and structures of semiconductor lasers are beyond the scope of this book. Of course, such characteristics are closely related to chaotic phenomena in semiconductor lasers. The interested reader is referred to the related books. For those who are interested in optics but not familiar with nonlinear systems and chaos, I have attached an appendix to describe the phenomena of chaotic dynamics and to accustom the reader to the common tools for chaos

analyses in nonlinear systems. Chaos research, especially in semiconductor laser systems, is still developing rapidly and is expected to produce fruitful results not only for the fundamental research of chaos but also for applications as dynamic engineering.

Chapters 1, 2, 3 and 4 are devoted to the basics and the introduction of laser chaos and chaotic dynamics in semiconductor lasers, so that readers who want to know what laser chaos is and how it behaves in semiconductor lasers can follow them. Chapters 5, 6, 7, 8, 9, 10, 11 and 12 discuss the topics of chaos in semiconductor lasers and readers may skip to each topic according to their interest. Expected readers of this book are as follows; first, I assume those researchers who have already been involved in this field to gain an overview of the state of the art of their research. The next group is the graduate students and researchers who intend to participate in this field. For them, I have derived and explained most equations in the text from first principles as far as possible. Those readers who are familiar with electromagnetic theory and have some fundamental knowledge of optics and lasers will be able to follow the book. Finally, this book is devoted to all other researchers and engineers who are interested in dynamics in nonlinear systems and laser instabilities and applications. Since the laser is a very excellent model of a nonlinear system that shows chaotic dynamics, I believe that this book will provide useful information for readers not only in the field of optics but also in other related areas. Moreover, I hope that the ideas and techniques discussed here will give rise to a new paradigm of nonlinear systems such as chaos engineering or dynamic engineering.

For the publication of this book, I am indebted to many people. Here, I will not be able to express thanks to all those people, but, at first, I would like to thank colleagues and some previous students in my laboratory, Drs. Yun Liu, Atsushi Murakami, Keizo Nakayama, Yoshiro Takiguchi, Shuying Ye, Hong Yu, for their many discussions and support. I also extend my thanks to many other researchers at various institutions and universities who gave me fruitful discussions and advice. They are Prof. Wolfgang Elsäßer, Dr. Peter Davis, Dr. Ingo Fischer, Prof. Jia-Ming Liu, Dr. Cristina Masoller, Dr. Claudio Mirasso, Prof. Rajarshi Roy, Prof. Kevin Alan Shore, and Dr. Atsuhi Uchida. I also owe thanks to many other people with whom I had useful discussions. Finally, I express sincere thanks to Prof. Toshimitsu Asakura who gave me the opportunity to write this book and also encouraged me in various stages of the research.

Hamamatsu Junji Ohtsubo
April 2005

Contents

1 Introduction 1
1.1 Chaos and Lasers 1
1.2 Historical Perspectives of Chaos in Semiconductor Lasers 3
1.3 Outline of This Book 7
References 11

2 Chaos in Laser Systems 15
2.1 Laser Model and Bloch Equations 15
2.1.1 Laser Model in a Ring Resonator 15
2.1.2 Light Emission and Absorption in Two-Level Atoms 17
2.1.3 Maxwell–Bloch Equations 18
2.2 Lorenz–Haken Equations and Laser Thresholds 19
2.2.1 Lorenz–Haken Equations 19
2.2.2 First Laser Threshold 22
2.2.3 Second Laser Threshold 23
2.3 Classifications of Lasers 25
2.3.1 Classes of Lasers 25
2.3.2 Class C Lasers 26
2.3.3 Class B Lasers 27
2.3.4 Class A Lasers 30
References 30

3 Semiconductor Lasers and Theory 33
3.1 Semiconductor Lasers 33
3.2 Oscillation Conditions of Semiconductor Lasers 35
3.2.1 Laser Oscillation Conditions 35
3.2.2 Laser Oscillation Frequency 36
3.2.3 Dependence of Oscillation Frequency on Carrier Density 37

3.3 Derivation of Rate Equations . . . 38
3.3.1 Gain at Laser Oscillation . . . 38
3.3.2 Rate Equation for the Field . . . 39
3.3.3 Linewidth Enhancement Factor . . . 41
3.3.4 Laser Rate Equations . . . 43
3.4 Optical Gain . . . 47
3.5 Linear Stability Analysis and Relaxation Oscillation . . . 51
3.5.1 Linear Stability Analysis . . . 51
3.5.2 Relaxation Oscillation . . . 53
3.6 Langevin Noises . . . 56
3.6.1 Rate Equations Including Langevin Noises . . . 56
3.6.2 Langevin Noises . . . 56
3.6.3 Implementation of Noise Terms for Numerical Calculations . . . 58
3.6.4 Noise Spectrum . . . 60
3.6.5 Relative Intensity Noise . . . 61
3.6.6 Phase Noise and Spectral Linewidth . . . 62
3.7 Modulation Characteristics . . . 65
3.7.1 Injection Current Modulation . . . 65
3.7.2 Intensity Modulation Characteristics . . . 67
3.7.3 Phase Modulation Characteristics . . . 68
3.8 Waveguide Models of Semiconductor Lasers . . . 70
3.8.1 Index- and Gain-Guided Structures . . . 70
3.8.2 Waveguide Models . . . 71
3.8.3 Spatial Modes of Gain- and Index-Guided Lasers . . . 73
3.8.4 Effects of Spontaneous Emission in Gain- and Index-Guided Lasers . . . 75
3.8.5 Laser Types . . . 76
References . . . 80

4 Theory of Optical Feedback in Semiconductor Lasers . . . 83
4.1 Theory of Optical Feedback . . . 83
4.1.1 Optical Feedback Effects and Classifications of Optical Feedback Phenomena . . . 83
4.1.2 Theoretical Model . . . 86
4.2 Linear Stability Analysis for Optical Feedback Systems . . . 88
4.2.1 Steady-State Solutions . . . 88
4.2.2 Linear Stability Analysis . . . 91
4.2.3 Linear Mode, and Stability and Instability in Semiconductor Lasers . . . 93
4.2.4 Gain Reduction Due to Optical Feedback . . . 95
4.2.5 Linewidth in the Presence of Optical Feedback . . . 96

4.3 Feedback from a Grating Mirror 97
4.3.1 Plane Grating Optical Feedback 97
4.3.2 Fiber Bragg Grating Optical Feedback 100
4.4 Phase-Conjugate Feedback 101
4.5 Incoherent Feedback 105
4.6 Polarization-Rotated Optical Feedback 106
4.7 Filtered Feedback 107
References 109

5 Dynamics of Semiconductor Lasers with Optical Feedback 113
5.1 Optical Feedback from a Conventional Reflector 113
5.1.1 Optical Feedback Effects 113
5.1.2 Potential Model in Feedback-Induced Instability 115
5.1.3 Optical Spectrum in Stable and Unstable Feedback Regimes 117
5.1.4 Chaos in Semiconductor Lasers with Optical Feedback 119
5.1.5 Chaotic Bifurcations 121
5.1.6 Dynamics for Injection Current Variations 124
5.2 Dependence of Chaotic Dynamics on the External Mirror Position 128
5.2.1 Periodic Stability Enhancement for Variations of the External Cavity Length 128
5.2.2 Origin of Periodic Stability Enhancement 132
5.2.3 Effects of Linewidth Enhancement Factor 134
5.2.4 Sensitivity of the Optical Phase 136
5.2.5 Chaotic Dynamics for a Small Change of the External Cavity Length 137
5.3 Low-Frequency Fluctuations 140
5.3.1 Low-Frequency Fluctuation Phenomena 140
5.3.2 Low-Frequency Fluctuation Characteristics 143
5.3.3 Origin of Low-Frequency Fluctuations 144
5.4 Chaotic Dynamics in Short External Cavity Limit 150
5.4.1 Stable and Unstable Conditions in Short External Cavity 150
5.4.2 Regular Pulse Package Oscillations in Short External Cavity 152
5.4.3 Bifurcations of Regular Pulse Package 154
5.5 Dynamics in Semiconductor Lasers with Grating Mirror Feedback 156
5.6 Dynamics in Semiconductor Lasers with Phase-Conjugate Mirror Feedback 159
5.6.1 Linear Stability Analysis 159
5.6.2 Dynamics Induced by Phase-Conjugate Feedback . . . 160

5.6.3 Dynamics in the Presence of Frequency Detuning . . . 161
5.6.4 Finite and Slow Response Phase-Conjugate Feedback . . . 162
5.7 Dynamics of Incoherent Optical Feedback . . . 164
5.8 Dynamics of Polarization-Rotated Optical Feedback . . . 167
5.8.1 TE–TM Mode Dynamics in Polarization-Rotated Optical Feedback . . . 167
5.8.2 Square-Wave Generation in Polarization-Rotated Optical Feedback . . . 170
5.9 Dynamics of Filtered Optical Feedback . . . 172
5.9.1 Filtered Optical Feedback . . . 172
5.9.2 External Cavity Modes . . . 174
5.9.3 Frequency Oscillations and Chaotic Dynamics . . . 176
References . . . 178

6 Dynamics in Semiconductor Lasers with Optical Injection . . . 183
6.1 Optical Injection . . . 183
6.1.1 Optical Injection Locking . . . 183
6.1.2 Injection Locking Condition . . . 186
6.2 Stability and Instability in Optical Injection Systems . . . 192
6.2.1 Rate Equations . . . 192
6.2.2 Chaotic Bifurcations by Optical Injection . . . 194
6.2.3 Chaos Map in the Phase Space of Frequency Detuning and Injection . . . 199
6.2.4 Coexistence of Chaotic Attractors in Optically Injected Semiconductor Lasers . . . 201
6.3 Enhancement of Modulation Bandwidth and Generation of High Frequency Chaotic Oscillation by Strong Optical Injection . . . 204
6.3.1 Enhancement of Modulation Bandwidth by Strong Optical Injection . . . 204
6.3.2 Origin of Modulation Bandwidth Enhancement . . . 210
6.3.3 Visual Solution for Resonance Frequency . . . 214
6.3.4 Modulation Response by Strong Optical Injection . . . 217
6.3.5 Suppression of Frequency Chirping by Strong Optical Injection . . . 218
6.3.6 Generation of High-Frequency Chaotic Oscillation by Strong Optical Injection . . . 220
References . . . 223

7 Dynamics of Semiconductor Lasers with Optoelectronic Feedback and Modulation 227
7.1 Theory of Optoelectronic Feedback 227
7.1.1 Optoelectronic Feedback Systems 227
7.1.2 Pulsation Oscillations in Optoelectronic Feedback Systems 229
7.2 Linear Stability Analysis for Optoelectronic Feedback Systems 232
7.2.1 Linear Stability Analysis 232
7.2.2 Characteristics of Semiconductor Lasers with Optoelectronic Feedback 235
7.3 Dynamics and Chaos in Semiconductor Lasers with Optoelectronic Feedback 237
7.3.1 Chaotic Dynamics in Negative Optoelectronic Feedback 237
7.3.2 Chaotic Dynamics in Positive Optoelectronic Feedback 240
7.4 Optoelectronic Feedback with Wavelength Filter 244
7.4.1 System of Optoelectronic Feedback with Wavelength Filter 244
7.4.2 Dynamics of Optoelectronic Feedback with Wavelength Filter 246
7.5 Chaotic Dynamics of Semiconductor Lasers Induced by Injection Current Modulation 248
7.5.1 Instabilities of a Modulated Semiconductor Laser . . . 248
7.5.2 Linear Stability Analysis 250
7.5.3 Chaotic Dynamics in Modulated Semiconductor Lasers 252
7.6 Nonlinear Dynamics of Various Combinations of External Perturbations 254
7.6.1 Optically Injected Semiconductor Laser Subject to Optoelectronic Feedback 254
7.6.2 Semiconductor Lasers with Optical Feedback and Modulation 257
References 259

8 Instability and Chaos in Various Laser Structures 263
8.1 Multimode Lasers 263
8.1.1 Multimode Operation of Semiconductor Lasers 263
8.1.2 Theoretical Model of Multimode Lasers 265
8.1.3 Dynamics of Multimode Semiconductor Lasers with Optical Feedback 268

8.2 Self-Pulsating Lasers 270
8.2.1 Theory of Self-Pulsating Lasers 270
8.2.2 Instabilities at Solitary Oscillations 273
8.2.3 Instability and Chaos by Optical Feedback 277
8.2.4 Instability and Chaos by Injection Current Modulation 280
8.3 Vertical-Cavity Surface-Emitting Lasers 282
8.3.1 Structure of Vertical-Cavity Surface-Emitting Lasers 282
8.3.2 Spatial-Mode Expansion Model 284
8.3.3 Spin-Flip Model 286
8.3.4 Two-Gain Model 291
8.3.5 Characteristics of VCSELs in Solitary Oscillations 293
8.3.6 Spatio-Temporal Dynamics in VCSELs 297
8.3.7 Optical Feedback Effects in VCSELs 300
8.3.8 Square-Wave Generation in VCSELs 304
8.3.9 Short Optical Feedback in VCSELs 305
8.3.10 Optical Injection Dynamics in VCSEL 307
8.4 Broad-Area Semiconductor Lasers 311
8.4.1 Theoretical Model of Broad-Area Semiconductor Lasers 311
8.4.2 Dynamics of Broad-Area Semiconductor Lasers at Solitary Oscillations 316
8.4.3 Optical Feedback Effects in Broad-Area Semiconductor Lasers 324
8.4.4 Effects of Optical Injection in Broad-Area Semiconductor Lasers 327
8.5 Laser Arrays 329
8.6 Quantum-Dot Semiconductor Lasers 331
8.6.1 Theory of Quantum-Dot Semiconductor Lasers 331
8.6.2 Quantum-Dot Semiconductor Lasers in Solitary Oscillations 336
8.6.3 Optical Feedback Effects in Quantum-Dot Semiconductor Lasers 338
8.6.4 Optical Injection Effects in Quantum-Dot Semiconductor Lasers 339
8.6.5 Bandwidth Enhancement in Optically Injected Quantum-Dot Semiconductor Lasers 342
8.7 Quantum-Cascade Semiconductor Lasers 344
8.7.1 Principle of Quantum-Cascade Semiconductor Lasers 344
8.7.2 Linewidth Enhancement Factor of Quantum-Cascade Semiconductor Lasers 346

8.7.3 Rate Equations of Quantum Cascade Semiconductor Lasers . . . 348
8.7.4 Nonlinear Interactions in Quantum-Cascade Semiconductor Lasers . . . 350
8.7.5 Effects of Optical Feedback in Quantum-Cascade Semiconductor Lasers . . . 352
8.7.6 Enhancement of Modulation Bandwidth in Quantum-Cascade Semiconductor Lasers . . . 353
References . . . 356

9 Chaos Control and Applications . . . 363
9.1 General Methods of Chaos Control . . . 363
9.1.1 OGY Method . . . 363
9.1.2 Continuous Control Method . . . 364
9.1.3 Occasional Proportional Method . . . 365
9.1.4 Sinusoidal Modulation Method . . . 366
9.2 Chaos Control in Semiconductor Lasers . . . 367
9.2.1 Continuous Control . . . 367
9.2.2 Occasional Proportional Feedback Control . . . 369
9.2.3 Sinusoidal Modulation Control . . . 370
9.2.4 Optical Control . . . 372
9.3 Controlling Chaos and Noise Suppression . . . 376
9.3.1 Noise Suppression by Sinusoidal Modulation . . . 376
9.3.2 Stability and Instability of LFFs by Injection Current Modulation . . . 380
9.3.3 Chaos Targeting . . . 382
References . . . 383

10 Stabilization of Semiconductor Lasers . . . 385
10.1 Linewidth Narrowing by Optical Feedback . . . 385
10.1.1 Linewidth Narrowing by Strong Optical Feedback . . . 385
10.1.2 Linewidth Narrowing by Grating Feedback . . . 388
10.1.3 Linewidth Narrowing by Phase-Conjugate Optical Feedback . . . 389
10.1.4 Linewidth Narrowing by Resonant Optical Feedback . . . 393
10.2 Linewidth Narrowing by Optoelectronic Feedback . . . 396
10.3 Stabilization in Lasers with Various Structures . . . 398
10.3.1 Noise Suppression in Self-pulsation Semiconductor Laser . . . 398
10.3.2 Stabilization of VCSELs . . . 399
10.3.3 Stabilization of Broad-Area Semiconductor Lasers . . . 402
10.3.4 Stabilization of Laser Arrays . . . 407

10.4 Controls in Nobel Structure Lasers . . . 408
10.4.1 Photonic VCSELs . . . 408
10.4.2 Control of Mode Distribution Through Etched Microstructure in Broad-Area Semiconductor Lasers . . . 410
10.4.3 Quantum-Dot Broad-Area Semiconductor Lasers . . . 411
References . . . 413

11 Metrology Based on Chaotic Semiconductor Lasers . . . 419
11.1 Optical Feedback Interferometers . . . 419
11.1.1 Bistability and Multistability in Feedback Interferometers . . . 419
11.1.2 Interferometric Measurement in Self-mixing Semiconductor Lasers . . . 423
11.2 Applications in Feedback Interferometer . . . 425
11.2.1 Displacement and Vibration Measurement . . . 425
11.2.2 Absolute Position Measurement . . . 428
11.2.3 Angle Measurement . . . 429
11.2.4 Measurement of the Linewidth Enhancement Factor . . . 431
11.3 Sensing of Self-mixing Signal Across Laser Diode Voltage . . . 433
11.3.1 Detection Principles . . . 433
11.3.2 Self-mixing Interferometry in VCSELs . . . 435
11.3.3 Self-mixing Interferometry in QCLs . . . 438
11.4 Self-mixing Doppler Velocimetry . . . 441
11.4.1 Velocity Measurement . . . 441
11.4.2 Rigorous Rate Equations of Self-mixing Doppler Effects . . . 442
11.5 Chaotic Lidar . . . 445
11.6 Active Feedback Interferometer and Applications . . . 448
11.6.1 Stability and Bistability in Active Feedback Interferometer . . . 448
11.6.2 Chaos Control in Active Feedback Interferometers . . . 452
References . . . 455

12 Chaos Synchronization in Semiconductor Lasers . . . 459
12.1 Concept of Chaos Synchronization . . . 459
12.1.1 Chaos Synchronization . . . 459
12.1.2 Generalized and Complete Chaos Synchronization . . . 463
12.2 Theory of Chaos Synchronization in Semiconductor Lasers with Optical Feedback . . . 466
12.2.1 Model of Synchronization Systems . . . 466

12.2.2 Rate Equations in Unidirectional Coupling Systems . . . 468
12.2.3 Generalized Chaos Synchronization . . . 469
12.2.4 Complete Chaos Synchronization . . . 469
12.2.5 Mutual Coupling Systems . . . 470
12.3 Chaos Synchronization in Semiconductor Lasers with an Optical Feedback System . . . 472
12.3.1 Chaos Synchronization—Numerical Examples . . . 472
12.3.2 Chaos Synchronization—Experimental Examples . . . 476
12.3.3 Anticipating Chaos Synchronization . . . 478
12.3.4 Bandwidth Enhanced Chaos Synchronization . . . 480
12.3.5 Incoherent Synchronization Systems . . . 481
12.3.6 Polarization Rotated Chaos Synchronization . . . 483
12.3.7 Synchronization in Broad-Area Semiconductor Lasers . . . 487
12.4 Chaos Synchronization in Optically Injected Lasers . . . 490
12.4.1 Theory of Chaos Synchronization in Optically Injected Lasers . . . 490
12.4.2 Examples of Chaos Synchronization in Optically Injected Lasers . . . 492
12.5 Chaos Synchronization in Optoelectronic Feedback Systems . . . 494
12.5.1 Theory of Chaos Synchronization in Optoelectronic Feedback Systems . . . 494
12.5.2 Examples of Chaos Synchronization in Optoelectronic Feedback Systems . . . 495
12.6 Chaos Synchronization in Injection Current Modulated Systems . . . 496
12.7 Chaos Synchronization in Mutually Coupled Lasers . . . 497
12.7.1 Mutually Coupled Edge-Emitting Semiconductor Lasers . . . 497
12.7.2 Mutually Coupled VCSELs . . . 500
12.7.3 Optoelectronic Mutually Coupled Semiconductor Lasers . . . 501
12.8 Common-Chaotic-Signal Induced Synchronization in Semiconductor Lasers . . . 504
References . . . 507

13 Chaotic Communications in Semiconductor Lasers . . . 511
13.1 Message Encryption in a Chaotic Carrier and Its Decryption . . . 511
13.1.1 Chaotic Communications . . . 511
13.1.2 Chaos Masking . . . 513
13.1.3 Chaos Modulation . . . 515

13.1.4 Chaos Shift Keying . . . 515
13.1.5 Chaotic Data Communications in Laser Systems . . . 516
13.2 Cryptographic Applications in Optical Feedback Systems . . . 517
13.2.1 Chaotic Communications in Optical Feedback Systems . . . 517
13.2.2 Chaos Masking in Optical Feedback Systems . . . 520
13.2.3 Chaos Modulation in Optical Feedback Systems . . . 525
13.2.4 Chaos Shift Keying in Optical Feedback Systems . . . 527
13.2.5 Chaotic Communications in Incoherent Optical Feedback Systems . . . 528
13.2.6 Chaos Pass Filtering Effects . . . 529
13.3 Cryptographic Applications in Optical Injection Systems . . . 532
13.4 Cryptographic Applications in Optoelectronic Systems . . . 534
13.5 Chaotic Communications in Mutually Coupled Semiconductor Lasers . . . 535
13.5.1 Communications in Mutually Coupled Semiconductor Lasers . . . 535
13.5.2 Chaos-Pass Filtering Effects in Mutually Coupled Systems . . . 538
13.6 Chaotic Communications in Drive-Response Systems . . . 539
13.7 Performance of Chaotic Communications . . . 541
13.8 Security of Chaotic Communications . . . 544
13.9 Chaotic Carrier and Bandwidth of Communications . . . 548
13.10 Chaos Communications in the Real World . . . 549
13.10.1 Chaos Masking Video Signal Transmissions . . . 549
13.10.2 Chaotic Signal Transmissions Through Public Data Link . . . 552
References . . . 555

14 Semiconductor Laser Networks: Synchrony, Consistency, and Analogy of Synaptic Neurons . . . 559
14.1 Nonlinear Networks and Coupled Semiconductor Lasers . . . 559
14.1.1 Coupled Nonlinear Networks . . . 559
14.1.2 Chaotic Semiconductor Lasers and Neurons . . . 560
14.1.3 Semiconductor Lasers as Chaotic Elements . . . 561
14.2 Two Coupled Semiconductor Lasers . . . 563
14.2.1 Two Unidirectionally Coupled Semiconductor Lasers . . . 563
14.2.2 Two Mutually Coupled Semiconductor Lasers . . . 563
14.3 Three Coupled Semiconductor Lasers . . . 566
14.3.1 Three Coupled Lasers . . . 566
14.3.2 Three Chain-Coupled Semiconductor Lasers . . . 567
14.3.3 Three Ring-Coupled Semiconductor Lasers . . . 570

14.4 Four Coupled Semiconductor Lasers 572
14.4.1 Four Chain-Coupled Semiconductor Lasers 572
14.4.2 Four Ring-Coupled Semiconductor Lasers 572
14.5 Star-Coupled Semiconductor Lasers 575
14.5.1 Unidirectional Coupled Hub-Star Systems 575
14.5.2 Mutually Coupled Hub-Star Systems 576
14.5.3 Group Synchrony in Hub-Star Laser Systems 579
14.6 Many Coupled Semiconductor Lasers 580
14.6.1 Examples of Many Coupled Semiconductor Lasers 580
14.6.2 Synchronization Properties Depending on Topological Configurations 582
14.6.3 Greatest Common Divisor Rule in Coupled Semiconductor Laser Networks 584
14.7 Reservoir Computing and Application 585
14.7.1 Neuro-Inspired Information Processing 585
14.7.2 Neural Networks and Reservoir Computing 587
14.7.3 Reservoir Computing and Implementation 589
14.7.4 Application of Reservoir Computing to Time Series Perdition 591
References 594

15 Physical Random Number Generations and Photonic Integrated Circuits for Chaotic Generators 597
15.1 Introduction to Physical Random Number Generations 597
15.2 Signatures in Optical Feedback Induced Chaos 599
15.3 Probability Distributions of Chaotic Signals 604
15.4 Chaotic Physical Random Number Generations 606
15.4.1 Principles of Chaotic Physical Random Number Generations 606
15.4.2 Fast Chaotic Random Number Generators 611
15.4.3 All Optical Chaotic Random Number Generators . . . 615
15.5 Photonic Integrated Circuit for Chaotic Generators 618
15.6 Application for Random Number Key Distribution with Chaotic Semiconductor Lasers 622
References 624

Appendix: Chaos 627

Index 653

About the Author

Junji Ohtsubo received the B.S. degree in Electronics from the Kyushu Institute of Technology in 1973, and the M.S. and Ph.D. degrees in Electronics from Hokkaido University in 1975 and 1978, respectively. In 1978, he joined the Mechanical Engineering Laboratory, MITI, Japan. During 1981–1982, he was a Research Associate at the Institute of Optics, University of Rochester. He joined Shizuoka University, Shizuoka, Japan, as Associate Professor in 1985 and was Professor at the Department of Systems Engineering from 1993. He is now Professor Emeritus of Shizuoka Univeristy. His current research interests are nonlinear dynamics in optics, chaos in semiconductor lasers, optical information processing and computing, optical security systems, statistical optics, speckle, and optical metrology.

Professor Ohtsubo is a Fellow of the Optical Society of America and a member of IEEE, SPIE, ASP, the Japanese Society of Applied Physics, the Optical Society of Japan, and the Laser Society of Japan.

Chapter 1
Introduction

Abstract Irregularity induced by chaotic dynamics is essentially different from random fluctuation based on a stochastic process, since the chaotic system can be described by a set of rigorous equations, namely deterministic equations. Lasers are essentially chaotic systems described by nonlinear differential equations with three variables and they show a rich variety of chaotic dynamics. In this chapter, we briefly discuss laser chaos in relation to ordinary nonlinear systems and present a historical perspective of chaos research in semiconductor lasers. Then, the outline of this book will be presented.

1.1 Chaos and Lasers

It was in 1963 that Lorenz (1963) investigated the behaviors of convective fluids as a model for the atmospheric flow and showed that nonlinear systems described by three variables could exhibit chaotic dynamics. Of course, many researchers were aware of the existence of complex dynamics in well-defined systems from the beginning of the early 1900s. Poincaré (1913), a prominent French mathematician, at first noted the "sensitivity to initial condition" in dynamical systems. In his book, he wrote that "it may happen that small differences in the initial conditions produce very great ones in the final phenomena. A small error in the former will produce an enormous error in the latter. Prediction becomes impossible, and we have the fortuitous phenomenon."

However, modern research of chaos started from the study of irregular and complex dynamics of a nonlinear system developed by Lorenz (Motter and Campbell 2013). In actual, in 1961 ahead of the study by Lorenz, Ueda showed a strange attractor in the output power from an electrical circuit of a van der Pol/Duffing oscillator, which is now known as Ueda attractor or Japanese attractor (Ueda et al. 1992). Chaos is not only a description of a different viewpoint of nonlinear phenomena but also in itself a new physics. Chaos is a phenomenon of irregular variations of systems' outputs derived from models that are described by a set of deterministic equations. We must distinguish "chaos" from the observation of

© Springer International Publishing AG 2017

J. Ohtsubo, *Semiconductor Lasers*, Springer Series in Optical Sciences 111,
DOI 10.1007/978-3-319-56138-7_1

"random" events, such as the flipping of a coin, since chaos is generated in accordance with the deterministic order, namely, chaotic dynamics refers to deterministic development with chaotic outcome (Appendix A.1). The system evolves in a deterministic way and the current state of the system depends on the previous state in a rigidly deterministic way, although the systems' output shows random variations. This is in contrast to a random system where the present observation has no causal connection to the previous one. In spite of the deterministic models, we cannot foresee the future of the output, since chaos is very sensitive to the initial conditions, as Poincaré pointed out, and each system behaves completely different from each other even if the difference of the initial state is very small.

Chaos is always accompanied by nonlinearity. Nonlinearity in a system simply means that the measured values of the properties in the system depend in a complicated way on the conditions in the earlier state. Nonlinear property in a system does not always guarantee the occurrence of chaos, but some form of nonlinearity is required for the realization of chaotic dynamics. Chaos can be observed in various fields of engineering, physics, chemistry, biology, and economics. Even our cardiac rhythms are proved to be chaotic (Elbert et al. 1994). Though the fields are different, some of the chaotic systems can be characterized by similar differential equations. They show similar chaotic dynamics and the same mathematical tools can be applied for the analysis of their chaotic dynamics.

Nonlinear systems can be also found in optics. Many optical materials and devices show nonlinear response to the optical field and, therefore, they are candidates for nonlinear elements in chaotic systems. One such device is the laser. Since lasers themselves are nonlinear systems and are typically characterized by three variables; field, polarization of matter, and population inversion, they are also candidates for chaotic systems. Indeed, it was proved in the mid-1970s by Haken (1975) that lasers are nonlinear systems similar to the Lorenz model and show chaotic dynamics in their output powers. He assumed a ring laser model and considered two-level atoms in the laser medium. Though lasers are not always described by his model, the approximations are reasonable for most lasers. Thereafter, the laser rate equations that are described by the nonlinear equations with three variables, are called Lorenz–Haken equations after their contributor (Haken 1985). However, ordinary lasers do not exhibit chaotic behavior and only a few of the lasers with bad cavity conditions show chaotic dynamics. In the meantime, chaotic behaviors were theoretically demonstrated in a ring laser system (Ikeda 1979). Chaotic oscillations of infrared gas lasers in experiments were reported for Xe lasers, He–Ne lasers, and NH_3 lasers (Casperson 1978; Weiss and King 1982; Weiss et al. 1985). Weiss and Brock (1986) experimentally observed Lorenz–Haken-type chaos in infrared NH_3 lasers.

Contrary to the prediction of Haken, ordinary lasers are stable systems and only a few systems of infrared gas lasers show chaotic behaviors in their output powers. Arecchi et al. (1984) investigated laser systems from the viewpoint of the characteristic relaxation times of the three variables and categorized lasers into three classes. According to their classifications, one or two of the relaxation times are in

general very fast compared with the other timescales and most lasers are described by the rate equations with one or two variables. Therefore, they are stable systems that are categorized into class A and B lasers. Only class C lasers have the full description of the rate equations with three variables and can show chaotic dynamics. However, class A and B lasers can show chaotic dynamics when one or more degrees of freedom are introduced to the laser systems.

Class B lasers are characterized by the rate equations for field and population inversion, and they are easily destabilized by an additional degree of freedom as an external perturbation. For example, solid-state lasers, fiber lasers, and CO_2 lasers that are categorized as class B lasers, show unstable oscillations by external optical injection or modulation for accessible laser parameters. Semiconductor lasers, which are also classified into class B lasers and are the main topic of this book, are also very sensitive to self-induced optical feedback, optical injection from different lasers, optoelectronic feedback, and injection current modulation. A review of the earlier study of laser instabilities and chaos has been given by Abraham et al. (1988).

1.2 Historical Perspectives of Chaos in Semiconductor Lasers

Chaos in semiconductor lasers is of particular importance in practical applications, since chaos induced by semiconductor lasers is very fast and the main frequency of irregular oscillations is usually over giga hertz, which is much faster than those of chaos such as in electronic circuits. Indeed, chaos in semiconductor lasers is usually two digits or more faster than that attained by fast electronic circuits. Also, light is a carrier of modern communications and such chaotic oscillations match well with fast data transmissions in the existing optical network channels. Semiconductor lasers (edge-emitting and narrow-stripe types), which are the main topics of this book, are intrinsically stable lasers. However, semiconductor lasers, which are described by the field and the carrier density (equivalently the population inversion) equations, can be easily destabilized by the introduction of external perturbations such as external optical feedback, optical injection, or modulation for accessible laser parameters. Since the early 1980s, feedback-induced instabilities and chaos in semiconductor lasers have been extensively examined (Lang and Kobayashi 1980). In a semiconductor laser, the laser oscillation is affected considerably when the light reflected back from an external reflector couples with the original field in the laser cavity. A variety of dynamics can be observed in semiconductor lasers with optical feedback and they have been investigated by many researchers for the past two decades.

One of the main differences between semiconductor lasers and other lasers is the low reflectivity of the internal mirrors in the laser cavity. It ranges typically only from 10 to 30% of the intensity in edge-emitting semiconductor lasers. This makes

the self-feedback effects significant in semiconductor lasers. Another difference is a large absolute value of the linewidth enhancement factor α of the laser media. The value of the linewidth enhancement factor α = 2–7 was reported depending on the laser materials, while this value is almost zero for other lasers. Then, the coupling between the phase and the carrier density is encountered in the laser dynamics. These factors lead to a variety of dynamics quite different from any other lasers. At weak to moderate external optical feedback reflectivity, the laser output shows interesting dynamical behaviors such as stable state, periodic and quasi-periodic oscillations, and chaos for the variations of the system parameters. These ranges of external reflectivity are not only interesting from the viewpoint of fundamental physics, but also very important in practical applications of semiconductor lasers, such as in optical data storage systems and optical communications. Extensive lists of the recent literature for the dynamic characteristics in semiconductor lasers with optical feedback can be found in the following references (van Tartwijk and Agrawal 1998; Otsuka 1999; Ohtsubo 1999, 2002a, 2005, 2008, 2012; Uchida 2012).

Optical injection-locking phenomena are a universal feature in lasers. Since the internal reflectivity of the facet in a semiconductor laser is very low compared with other lasers, one can easily realize injection locking from a different laser. Moreover, the effects of injection locking stand out due to the nonzero value of the linewidth enhancement factor α and one can observe not only stable injection locking but also various dynamics of unstable optical injection phenomena depending on the injection parameters. Semiconductor lasers usually have different laser oscillations characteristics for the same product number or even for the same wafer, but the oscillation frequency can be easily tuned on the order of GHz by changing the injection current. Therefore, a light source for injection locking to different lasers with appropriate frequency detuning is easily available. Thus, optical injection-locking phenomena have been extensively studied in semiconductor lasers. However, earlier work was limited to stable injection-locking phenomena for amplification of signals and laser stabilization. In these applications, the laser is locked to the external laser, which means that it almost copies the spectrum of the injected light. On the other hand, unstable injection locking, instabilities, and mixing of detuned frequencies occur outside the region of stable injection locking in the phase space of the frequency detuning and the injection ratio. From the viewpoint of chaos, optical injection is an addition of an extra degree of freedom to semiconductor lasers and it may induce chaotic oscillations in the laser output. It was numerically predicted (Sacher et al. 1992; Annovazzi-Lodi et al. 1994) and experimentally demonstrated (Simpson et al. 1994, 1995) that an optically injected semiconductor laser follows a period-doubling route to chaos.

Direct modulation for accessible parameters is not an easy task in most lasers, however, the output power of a semiconductor laser is easily controlled through the injection current and, at the same time, the laser frequency can be changed by the injection current modulation. Small amplitude injection current modulation or even large modulation under appropriate conditions for laser oscillations may produce faithful copies of the modulation amplitude for the output power in a semiconductor

laser. However, modulation for the injection current is a perturbation to the laser and also the introduction of an extra degree of freedom to it. Indeed, instablities and chaotic oscillations have been observed by the injection current modulation in semiconductor lasers under the conditions of high frequency modulation with a large modulation index close to the relaxation oscillation frequency of the laser (Hori et al. 1988).

Optoelectronic feedback systems in which the emitted light from a semiconductor laser is once detected and fed back through the injection current are also studied to stabilize the laser oscillations. For a certain range of optoelectronic feedback, the laser may indeed be stabilized and the method is applied to obtain an ultra-high coherent light source. However, optoelectronic feedback has a similar effect to the above perturbations on the dynamics in semiconductor lasers. We can also observe unstable pulsation oscillations in the output of a semiconductor laser for certain conditions (Olesen et al. 1986). With the availability of high-speed electronic circuits, optoelectronic feedback systems having a time response of the same order as the relaxation oscillation frequency (on the order of GHz) have been studied and useful applications of chaos dynamics have been proposed based on high-speed optoelectronic feedback (Tang and Liu 2001a, b).

A variety of novel semiconductor laser devices with different structures has been proposed and fabricated beside narrow-stripe edge-emitting semiconductor lasers, for example, self-pulsating semiconductor lasers, vertical-cavity surface-emitting semiconductor lasers (VSCELs), broad-area semiconductor lasers, quantum-dot semiconductor lasers, quantum-cascade semiconductor lasers, and so on. These lasers themselves have extra degrees of freedom in addition to the characteristics of ordinary narrow-stripe edge-emitting semiconductor lasers. For example, space-dependent differential terms due to a wide stripe width are introduced in the rate equations for broad-area lasers and these terms play an important role in the laser dynamics. Therefore, these newly developed lasers themselves are unstable and exhibit chaotic dynamics without any external perturbations (Yamada 1993; Law et al. 1997; Gehrig and Hess 2000). The studies of chaotic dynamics in semiconductor lasers including new structure devices are excellent models for nonlinear chaotic systems and are very interesting from the viewpoint of basic chaotic research. Instabilities and chaotic behaviors are also greatly enhanced by additional external perturbations to these lasers in the same manner as narrow-stripe edge-emitting semiconductor lasers.

In the case of the vertical-cavity surface-emitting lasers (VCSELs), the reflectivity of the internal mirrors is very high at more than 99%, however, they are also sensitive to external optical feedback due to a small number of photons in the internal cavity. Therefore, semiconductor lasers of all types are essentially very sensitive to external optical feedback. In spite of the differences in device structures, the dynamics of semiconductor lasers are the same as long as the laser rate equations are written in the same or similar forms. The dynamics of narrow-stripe edge-emitting single-mode semiconductor lasers have been extensively studied for a long time and a lot of fruitful results have been obtained. However, they are still important issues for the fundamental physics of optical chaos and also for practical

applications. On the other hand, a little investigation into the dynamics of newly developed laser structures has been carried out.

Through external perturbations, semiconductor lasers are either stabilized or destabilized. The effects of such perturbations on laser dynamics, stability and instability, are two sides of the same coin. Examples include optical feedback, optical injection, and optoelectronic feedback. To stabilize laser oscillations, the disturbances may be weak or strong. The lasers can then be strongly stabilized under appropriate conditions of external parameters and operating conditions of the lasers. Stabilization of semiconductor lasers is very important with regard to their application. For example, frequency stabilization, linewidth narrowing, power stabilization, polarization fixing, and beam shaping are very important in optical communications, optical data storage systems, and optical measurements. In particular, ultra-stabilized semiconductor lasers are expected in broadband optical communications, high precision optical measurements, and standard light sources. Semiconductor lasers are rather unstable compared with other lasers, and their stabilization has been an important issue from the beginning of their development. For newly developed semiconductor lasers, such as VCSELs and broad-area semiconductor lasers, we can apply the same techniques of laser stabilization as those for narrow-stripe edge-emitting semiconductor lasers. However, these lasers themselves demonstrate instabilities in their solitary oscillations. In VCSELs, controls for polarization and spatial mode instabilities are essential in applications. In broad-area semiconductor lasers, filament suppression of the oscillation pattern can greatly improve beam quality, producing a high-density beam. Such unstable oscillations are also stabilized using similar techniques through external controls, as discussed above. Semiconductor lasers are still developing, and stabilization both by the device structure and through external controls is currently an important research area.

In the meantime, important breakthroughs for applications of chaos were made in the early 1990s. The ideas of chaos control and chaos synchronization were proposed and developed in this decade as common interests in various fields of nonlinear and chaos research. The ideas of chaos control (Ott et al. 1990) and chaos synchronization (Pecora and Carroll 1990) were proposed and developed in this decade. Noise suppression of feedback-induced chaotic oscillations in semiconductor lasers has been proposed based on chaos control (Liu et al. 1995). Also, fixed point or periodic oscillations, precursor to the onset of chaos in semiconductor lasers with optical feedback, can be used for laser control and optical measurements (Donati et al. 1995). In optical feedback interferometry, which is called self-mixing interferometry, the feedback light from a target to be measured is usually detected by a photodetector installed within a package of a semiconductor laser and a very compact sensor for the interferometric measurements can be constructed. However, in some types of semiconductor lasers, it is not easy to install a photodetector within a laser package. For example, it is difficult to fabricate a photodetector in quantum-cascade semiconductor lasers, which emit THz optical light. More than that, a stand-alone and fast response photodetector is not available in THz wavelength. Instead of using a photodetector in self-mixing interferometry, the voltage

variations across the laser diode induced by self-mixing effects can be employed for the detection of mixing signals. This provides an effective tool for interferometric measurements based on self-mixing interferometry in THz optical wave region, which cannot be obtained by conventional technology (Lim et al. 2011).

As another application, the possibility of chaotic communications has been discussed based on chaos synchronization in two chaotic solid-state laser systems (Colet and Roy 1994). After their pioneering work, the study of secure data transmissions and communications has also been discussed based on synchronization in two chaotic semiconductor laser systems (Chen and Wornell 2001; Feature Section IEEE J Quantum Electron 2002; Ohtsubo 2002b; Uchida 2012). Further, chaos synchronization occurs among many coupled semiconductor lasers. Zero-lag or cluster synchronization among semiconductor lasers appears depending on the topological structure of coupling networks (Nixon et al. 2011; Ohtsubo et al. 2015). The phenomena are strongly related to crowd synchrony in many coupled nonlinear elements (Strogatz et al. 2005). The keys of the dynamics in those networks are synchronization among nonlinear elements and consistent responses as drive-response systems, which are a typical feature appeared in neural networks, such as in neurons in the human brain. Depending on the phenomenon, bio-inspired information processing called reservoir computing is proposed, in which a single semiconductor laser subjected to optical feedback is used as a reservoir in the neural networks (Appeltant et al. 2011). Irregular chaotic oscillations in semiconductor lasers have also provided a new method of ultrafast physical random number generations, which is the key technology in modern cryptographic applications (Uchida et al. 2008; Uchida 2012). Also for those applications, photonic integrated circuits to generate chaotic light have been proposed (Argyris et al. 2008). Harnessing chaotic lasers is very attractive from the viewpoint of applications, since optics is very fast and contains parallelism as a nature of light. Applications of chaotic lasers are still growing and developing. Thus, chaotic lasers are not only important for basic research but also for engineering applications.

1.3 Outline of This Book

In this book, we focus on the dynamics and applications in semiconductor lasers subjected to external perturbations. In Chap. 2, we first introduce general forms of laser rate equations, which are equivalent to the Lorenz equations, and the classifications of lasers are given. The instabilities intrinsically involved in the rate equations are studied. Next, semiconductor lasers as class B lasers are described. The possibility of unstable oscillations in semiconductor lasers by the introduction of external perturbations is discussed. A solitary semiconductor laser is characterized by two equations for the field and the carrier density (population inversion). We then derive the forms of the rate equations for edge-emitting semiconductor lasers with a narrow stripe width in Chap. 3. Linear stability analysis used as a common tool for investigating the stability and instability conditions of nonlinear

chaotic systems is introduced and the laser relaxation oscillation frequency, which plays an important role in the chaotic dynamics, is derived. Several fundamental characteristics of semiconductor lasers are also introduced.

In Chap. 4, the theory of optical feedback in semiconductor lasers is presented. The effects of feedback in various external reflectors, including grating mirrors and phase-conjugate mirrors, are taken into account and the formulations of their systems are presented by introducing rate equations with optical feedback effects. In Chap. 5, substantial feedback effects and chaotic dynamics in semiconductor lasers are discussed and both numerical and experimental results are given under variations of the system parameters. Feedback-induced chaos depending on the external cavity length and the feedback fraction is investigated. Chaos induced by external optical injection with frequency detuning is also an important issue in semiconductor laser systems. The theory of optical injection and their instabilities are discussed in Chap. 6. Unstable and chaotic oscillations are observed in the region outside the stable injection locking in the phase space of the frequency detuning and the injection fraction. The coexistence state of chaotic attractors, which is known as one of the characteristics in nonlinear systems, is demonstrated in the injection-locking systems. The effects for the modulation bandwidth in optically injection-locked semiconductor lasers are discussed in this chapter. Also, enhancement of chaotic frequency by strong optical injection locking is demonstrated. In Chap. 7, dynamic characteristics of optoelectronic feedback and injection current modulations are presented. Unstable chaotic pulsations induced by feedback and modulation to the injection current are investigated in relation to the characteristics of optoelectronic feedback circuits.

The rate equations of semiconductor lasers with various laser structures are introduced in Chap. 8. We assume a single mode oscillation for a semiconductor laser in the preceding chapters, however, the effects of the multimode oscillations in narrow-stripe edge-emitting semiconductor lasers are considered and dynamic properties of multimode lasers are discussed in this chapter. Stable and unstable periodic oscillations, and chaotic pulsations of self-pulsating semiconductor lasers, which are developed as light sources for optical data storage systems, are studied. VCSELs have quite different structure from other semiconductor lasers, since the laser has a circular aperture with very short cavity length compatible with the optical wavelength. Such lasers show spatial and polarization dynamics and their control is an important issue for applications. Broad-area lasers and laser arrays are also interesting future devices in engineering applications as high power lasers. They show unique spatio-temporal dynamics and the controls of instabilities are important in applications. Quantum-dot semiconductor lasers have been developed for stable and highly coherent light sources in optical communications. However, they still exhibit instabilities for external perturbations. Quantum-cascade semiconductor lasers are expected as new THz light sources. They have a mechanism of light emission different from other semiconductor lasers, namely, the carriers are only electrons and the laser oscillations are based on inter-subband optical transition through multi-stage quantum-cascade band structures. They also show interesting dynamics. These new types of semiconductor lasers themselves contain instability

arising from their structures and show chaotic behaviors even in the absence of external perturbations.

We cannot foresee the future of chaotic oscillations for time evolution, since chaos has a strong dependence on the initial condition of a system. However, chaos can be controlled. In Chap. 9, methods of chaos control are introduced. Control of chaotic oscillations in semiconductor lasers with optical feedback is discussed and the reduction of the feedback-induced relative intensity noise (RIN) is demonstrated based on the method of chaos control. These methods can also be applied not only to ordinary narrow-stripe edge-emitting semiconductor lasers but also to other semiconductor lasers with newly developed structures. Either stabilities or instabilities are enhanced by external perturbations in semiconductor lasers, and their dynamics are discussed in Chap. 10. In this chapter, methods of stabilization and control of semiconductor lasers are presented. Some of these are closely related to chaos control, as discussed in Chap. 9, and others involve forced control of stable oscillations. Stabilization for laser oscillations such as linewidth, frequency, spatial modes, polarization, and so on, are introduced in narrow-stripe edge-emitting semiconductor lasers. Similar control techniques are also applied to newly developed semiconductor lasers. In semiconductor lasers with optical and optoelectronic feedback systems, periodic oscillations of the outputs preceding the onset of chaos are observed for the variations of chaotic parameters. These properties can be applied to various measurements, such as interferometric displacement and vibration measurements. In Chap. 11, applications of self-mixing interferometers and active interferometers are discussed, in which bistable states of the systems before the onset of chaotic bifurcations are used. In particular, self-mixing interferometry using quantum-cascade semiconductor lasers provides an effective interferometric measurement in THz optical wave region, which cannot be obtain by conventional technology. Other interferometric and correlation techniques of chaotic semiconductor lasers for various measurements are discussed in this chapter.

Synchronization of two chaotic nonlinear systems is interesting not only from the viewpoint of fundamental physics but also from applications. It is not self-evident that two chaotic nonlinear systems show synchronization and the theoretical background for chaos synchronization has not yet been fully established. However, synchronization of chaotic oscillations has been observed by experiments and numerical simulations. Chaos synchronization can be also observed in systems of chaotic semiconductor lasers. The systems and conditions for synchronization in chaotic semiconductor lasers are discussed in Chap. 12. Chapter 13 follows the applications of chaos synchronization. Since strict conditions must be satisfied for chaos synchronization in nonlinear systems, one can construct a secure communication channel in the sense of hardware levels. The possibility of chaos communications is presented based on chaos synchronization in semiconductor laser systems. Also, chaotic communications through the existing public communication channel is demonstrated. Chaos communications in Chap. 13 are based on analog techniques of hiding messages behind irregular chaotic undulations. Laser chaos, especially chaos induced by semiconductor lasers is fast and is suitable for data transmissions in current optical communication channels.

Chaos synchronization is not only appeared in two coupled semiconductor lasers but also more than two coupled systems. Chapter 14 discusses phenomena of zero-lag and cluster synchronization in many coupled semiconductor lasers with different topological structures. The dynamics of these systems have an analogy with those of neuron networks in the human brain. In this chapter, we also present a new type of information process and its application based on reservoir computing, in which a single semiconductor laser subjected to optical feedback is used as a reservoir in the neural network. The keys for common dynamics of such systems are the consistency in drive-response nonlinear systems and the synchronization properties between distant nonlinear elements. On the other hand, digital techniques of chaotic semiconductor lasers for cryptographic applications have been developed. For distributions of random keys in cryptography, the method of ultrafast physical random number generations over the rate of giga-bit-per-second has been proposed. In Chap. 15, the principle and practice of fast physical random number generations using chaotic semiconductor lasers are discussed. For the purpose of communication applications of chaotic semiconductor lasers, compact and stable light sources as chaotic generators are expected. Monolithic and optically integrated circuits for chaotic light generators are presented in this chapter.

The origins of chaos are unique for each nonlinear system, but there are common tools for the analyses of chaotic dynamics. For detailed descriptions of chaos and their analyses, the reader is referred to appropriate books. However, for readers not familiar with chaos and its analyses, I finally attached an appendix on the origins of chaos in nonlinear systems and some of their common tools for chaotic data analyses. In this book, I treat the main topics of chaos dynamics and applications in semiconductor lasers, however, they are not the entirety of the research. Other related topics are dynamics in new types of semiconductor lasers, such as micro-cavity semiconductor lasers (Lee et al. 2002; Cao and Wiersig 2015), random lasers (Cao 2003), flared broad-area lasers (Levy and Hardy 1997), and others. Also, optoelectronic chaotic oscillator, in which chaos is not generated from the nonlinearity of a semiconductor laser itself but from the nonlinear delayed response of light due to delayed optoelectronic hybrid feedback through EO modulator (an integrated EO Mach–Zehnder interferometer), is an attractive system, and widely used as a useful chaotic source for various applications (Argyris et al. 2005; Larger and Dudley 2010). The systems are also important and interesting with relation to the study of stabilities, instabilities, and chaos in nonlinear systems. But, we here limit the discussion for the fundamentals and applications of the dynamics intrinsically induced by the nonlinearity in semiconductor lasers themselves. Research into chaos in semiconductor lasers is still ongoing, and we can expect fruitful results both for basic physics and practical applications.

References

N.B. Abraham, P. Mandel, L.M. Narducci, Dynamical instabilities and pulsations in lasers (Chap. 1), in *Progress in Optics*, vol. 25, ed. by E. Wolf (North-Holland, Amsterdam, 1988)

V. Annovazzi-Lodi, S. Donati, M. Manna, Chaos and locking in a semiconductor laser due to external injection. IEEE J. Quantum Electron. **30**, 1537–1541 (1994)

L. Appeltant, M.C. Soriano, V. Van der Sande, J. Danckaert, S. Massa, J. Dambre, B. Schrauwen, C.R. Mirasso, I. Fischer, Information processing using a single dynamical node as complex system. Nat. Commun. **2**, 468–474 (2011)

F.T. Arecchi, G.L. Lippi, G.P. Puccioni, J.R. Tredicce, Deterministic chaos in laser with injected signal. Opt. Commun. **51**, 308–314 (1984)

A. Argyris, D. Syvridis, L. Larger, V. Annovazzi-Lodi, P. Colet, I. Fischer, J. Garcia-Ojalvo, C.R. Mirasso, L. Pesquera, A.K. Shore, Chaos-based communications at high bit rates using commercial fibre-optic links. Nature **438**, 343–346 (2005)

A. Argyris, M. Hamacher, K.E. Chlouverakis, A. Bogris, D. Syvridis, Photonic integrated device for chaos applications in communications. Phys. Rev. Lett. **100**, 14101-1–14101-4 (2008)

H. Cao, Lasing in disordered media (Chap. 6), in *Progress in Optics*, vol. 45, ed. by E. Wolf (North-Holland, Amsterdam, 2003)

H. Cao, J. Wiersig, Dielectric microcavities: model systems for wave chaos and non-Hermitian physics. Rev. Mod. Phys. **87**, 61–111 (2015)

L.W. Casperson, Spontaneous coherent pulsations in laser oscillators. IEEE J. Quantum Electron. **14**, 756–761 (1978)

B. Chen, G.W. Wornell, Special issue on applications of chaos in modern communication systems. IEEE Trans. Circuits Syst. I **48**(12) (2001)

P. Colet, R. Roy, Digital communication with synchronized chaotic lasers. Opt. Lett. **19**, 2056–2058 (1994)

S. Donati, G. Giuliani, S. Merlo, Laser diode feedback interferometer for measurement of displacements without ambiguity. IEEE J. Quantum Electron. **31**, 113–119 (1995)

T. Elbert, W.J. Ray, Z.J. Kowalik, J.E. Skinner, K.E. Graf, N. Birbaumer, Chaos and physiology: deterministic chaos in excitable cell assemblies. Physiol. Rev. **74**, 1–47 (1994)

Feature section on optical chaos and applications to cryptography, IEEE J. Quantum Electron. **38** (9) (2002)

E. Gehrig, O. Hess, Dynamics of high-power diode lasers, in *High-Power Diode Lasers-Fundamentals, Technology, Applications*, ed. by R. Diehl (Springer, Berlin, 2000)

H. Haken, Analogy between higher instabilities in fluids and lasers. Phys. Lett. **53A**, 77–78 (1975)

H. Haken, *Light*, vol. 2 (North-Holland, Amsterdam, 1985)

Y. Hori, H. Serizawa, H. Sato, Chaos in directly modulated semiconductor lasers. J. Opt. Soc. Am. B **5**, 1128–1133 (1988)

K. Ikeda, Multiple-valued stationary state and its instability of the transmitted light by a ring cavity system. Opt. Commun. **30**, 257–261 (1979)

R. Lang, K. Kobayashi, External optical feedback effects on semiconductor injection properties. IEEE J. Quantum Electron. **16**, 347–355 (1980)

L. Larger, J.M. Dudley, Nonlinear dynamics: optoelectronic chaos. Nature **465**, 41–42 (2010)

J.Y. Law, G.H.M. van Tartwijk, G.P. Agrawal, Effects of transverse-mode competition on the injection dynamics of vertical-cavity surface-emitting lasers. Quantum Semiclass. Opt. **9**, 737–747 (1997)

S.B. Lee, J.H. Lee, J.S. Chang, Observation of scarred modes in asymmetrically deformed microcylinder lasers. Phys. Rev. Lett. **88**, 033903-1–033903-4 (2002)

G. Levy, A.A. Hardy, Chaotic effects in flared lasers: a numerical analysis. IEEE J. Quantum Electron. **33**, 26–32 (1997)

Y.L. Lim, P. Dean, M. Nikolić, R. Kliese, S.P. Khanna, M. Lachab, A. Valavanis, D. Indjin, Z. Ikonić, P. Harrison, E.H. Linfield, A.G. Davies, S.J. Wilson, A.D. Rakić, Demonstration of a

self-mixing displacement sensor based on terahertz quantum cascade lasers. Appl. Phys. Lett. **99**, 081108–1–081108-3 (2011)
Y. Liu, N. Kikuchi, J. Ohtsubo, Controlling of dynamical behavior of semiconductor lasers with external optical feedback. Phys. Rev. E **51**, 2697–2700 (1995)
E.N. Lorenz, Deterministic nonperiodic flow. J. Atmos. Sci. **20**, 130–148 (1963)
A.E. Motter, D.K. Campbell, Chaos at fifty. Phys. Today **66**, 27–33 (2013)
M. Nixon, M. Friedman, E. Ronen, A.A. Friesem, N. Davidson, I. Kanter, Synchronized cluster formation in coupled laser networks. Phys. Rev. Lett. **106**, 223901–1–223901-4 (2011)
J. Ohtsubo, Feedback induced instability and chaos in semiconductor lasers and their applications. Opt. Rev. **6**, 1–15 (1999)
J. Ohtsubo, Chaotic dynamics in semiconductor lasers with optical feedback (Chap. 1), in *Progress in Optics*, vol. 44, ed. by E. Wolf (North-Holland, Amsterdam, 2002a)
J. Ohtsubo, Chaos synchronization and chaotic signal masking in semiconductor lasers with optical feedback. IEEE J. Quantum Electron. **38**, 1141–1154 (2002b)
J. Ohtsubo, *Semiconductor Lasers; Stability, Instability and Chaos* (Springer, Berlin, 2005)
J. Ohtsubo, *Semiconductor Lasers; Stability, Instability and Chaos*, 2nd edn. (Springer, Berlin, 2008)
J. Ohtsubo, *Semiconductor Lasers; Stability, Instability and Chaos*, 3rd edn. (Springer, Berlin, 2012)
J. Ohtsubo, R. Ozawa, M. Nanbu, Synchronization of small nonlinear networks in chaotic semiconductor lasers. Jpn. J. App. Phys. **54**, 072702-1–072702-6 (2015)
H. Olesen, J.H. Osmundsen, B. Tromborg, Nonlinear dynamics and spectral behavior for an external cavity laser. IEEE J. Quantum Electron. **22**, 726–773 (1986)
K. Otsuka, *Nonlinear Dynamics in Optical Complex Systems* (KTK Scientific Publishers, Tokyo, 1999)
E. Ott, C. Grebogi, J.A. Yorke, Controlling chaos. Phys. Rev. Lett. **64**, 1196–1199 (1990)
L.M. Pecora, T.L. Carroll, Synchronization in chaotic systems. Phys. Rev. Lett. **64**, 821–824 (1990)
H. Poincaré, *The Foundation Of Science: Science and Method* (The Science Press, Lancaster, 1913)
J. Sacher, D. Baums, P. Panknin, W. Elsäßer, E.O. Göbel, Intensity instabilities of semiconductor lasers under current modulation, external light injection, and delayed feedback. Phys. Rev. A **45**, 1893–1905 (1992)
T.B. Simpson, J.M. Liu, A. Gavrielides, V. Kovanis, P.M. Alsing, Period-doubling route to chaos in a semiconductor laser subject to optical injection. Appl. Phys. Lett. **64**, 3539–3541 (1994)
T.B. Simpson, J.M. Liu, A. Gavrielides, V. Kovanis, P.M. Alsing, Period-doubling cascades and chaos in a semiconductor laser with optical injection. Phys. Rev. A **51**, 418–4185 (1995)
S.H. Strogatz, D.M. Abrams, A. McRobie, B. Eckhardt, E. Ott, Crowd synchrony on the Millennium Bridge. Nature **438**, 43–44 (2005)
S. Tang, J.M. Liu, Message encoding/decoding at 2.5 Gbits/s through synchronization of chaotic pulsing semiconductor lasers. Opt. Lett. **26**, 1843–1845 (2001a)
S. Tang, J.M. Liu, Synchronization of high-frequency chaotic optical pulses. Opt. Lett. **26**, 596–598 (2001b)
A. Uchida, K. Amano, M. Inoue, K. Hirano, S. Naito, H. Someya, I. Oowada, T. Kurashige, M. Shiki, S. Yoshimori, K. Yoshimura, P. Davis, Fast physical random bit generation with chaotic semiconductor lasers. Nat. Photonics **2**, 728–732 (2008)
A. Uchida, *Optical Communication with Chaotic Lasers* (Wiley-VCH, Weinheim, 2012)
Y. Ueda, R.H. Abraham, H.B. Stewart, The Road to Chaos (1. Some Problems in the Theory of Nonlinear Oscillations). (Aerial Press 1992)
G.H.M. van Tartwijk, G.P. Agrawal, Laser instabilities: a modern perspective. Prog. Quantum Electron. **22**, 43–122 (1998)
C.O. Weiss, H. King, Oscillation period doubling chaos in a laser. Opt. Commun. **44**, 59–61 (1982)

C.O. Weiss, W. Klische, P.S. Ering, M. Cooper, Instabilities and chaos of a single mode NH_3 ring laser. Opt. Commun. **44**, 405–408 (1985)

C.O. Weiss, J. Brock, Evidence for Lorenz-type chaos in a laser. Phys. Rev. Lett. **57**, 2804–2806 (1986)

M. Yamada, A theoretical analysis of self-sustained pulsation phenomena in narrow-stripe semiconductor lasers. IEEE J. Quantum Electron. **29**, 1330–1336 (1993)

Chapter 2
Chaos in Laser Systems

Abstract Starting from the Maxwell equation in a laser medium based on the model of two-level atoms, we derive the time-dependent Maxwell–Bloch equations for field, polarization of matter, and population inversion. Then, we prove that the three differential equations are the same as those of Lorenz chaos. Well above the laser threshold, the laser reaches an unstable point at certain pump level, which is called second laser threshold. However, only a few real lasers show chaotic dynamics with a second threshold and most other lasers do not have the second threshold, resulting in stable oscillations for the increase of the pump. Stable and unstable oscillations of lasers are related to the scales of the relaxation times for the laser variables. We discuss stability and instability of lasers based on the rate equations and present their classifications from the stability point of view.

2.1 Laser Model and Bloch Equations

2.1.1 Laser Model in a Ring Resonator

The theory of lasers should be treated by the interaction between matter and electromagnetic field based on quantum mechanics. However, we employ here the semi-classical treatment followed by Haken (1985) and van Tartwijk and Agrawal (1998), which is very easy to understand. Figure 2.1 shows a ring resonator for a laser model with two-level atoms. The model treats only unidirectional wave propagation without considering the backward propagation of light, therefore the development of the equations for the model is very easy. Actual lasers are composed of a Fabry–Perot resonator and have forward and backward waves of light propagations in the laser medium. A few contain a unidirectional ring resonator. The semiconductor laser, which is the main issue of this book, is also basically a Fabry–Perot laser (Abraham et al. 1988). Although the model is not always applicable to real lasers, the description for a unidirectional traveling-wave ring resonator is very simple and the theory can be easily extended to ordinary Fabry–Perot lasers.

© Springer International Publishing AG 2017

J. Ohtsubo, *Semiconductor Lasers*, Springer Series in Optical Sciences 111,
DOI 10.1007/978-3-319-56138-7_2

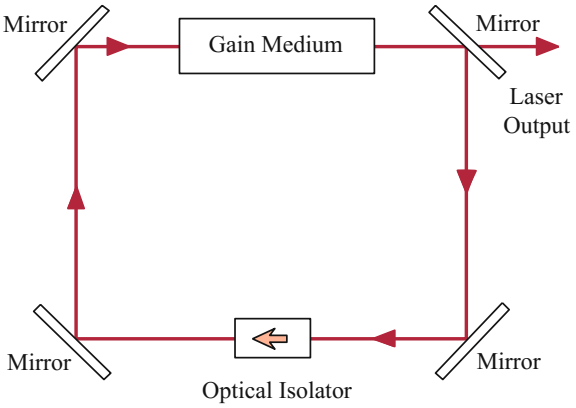

Fig. 2.1 Laser model with a ring resonator

The light propagation equation in the laser medium is derived first. The electric field $\boldsymbol{\mathcal{E}}$ (vector field) is written by a time-dependent Maxwell equation as

$$\nabla^2 \boldsymbol{\mathcal{E}}(z,t) - \frac{1}{c^2}\frac{\partial^2 \varepsilon \boldsymbol{\mathcal{E}}(z,t)}{\partial t^2} = \mu_0 \frac{\partial^2 \boldsymbol{\mathcal{P}}(z,t)}{\partial t^2} \tag{2.1}$$

where $\boldsymbol{\mathcal{P}}$ is the polarization vector of matter, $\boldsymbol{\varepsilon}$ is the electric permittivity tensor, c is the speed of light in vacuum, and μ_0 is the magnetic permeability in vacuum. We assume that the conductance of the medium is negligibly small, however we can add term $-\sigma/(\varepsilon_0 c^2) \cdot (\partial \boldsymbol{\mathcal{E}}/\partial t)$ (σ is the conductance of the medium) in the left-hand side of the equation in (2.1) when necessary. Indeed, $\sigma \approx 0$ for most lasers. Also assuming a uniform refractive index of the laser medium and linearly polarized spatial modes for the x and y directions with the propagation for the z axis, the field and the polarization of matter reduce to scalar quantities propagating only to the z direction and (2.1) can be reduced to the following scalar equation:

$$\frac{\partial^2 \boldsymbol{\mathcal{E}}(z,t)}{\partial z^2} - \frac{\eta^2}{c^2}\frac{\partial^2 \boldsymbol{\mathcal{E}}(z,t)}{\partial t^2} = \mu_0 \frac{\partial^2 \boldsymbol{\mathcal{P}}(z,t)}{\partial t^2} \tag{2.2}$$

where η is the refractive index of the laser medium.

The field and the polarization propagate for the z direction with the wavenumber $k = \eta\omega_0/c$ and the angular oscillation frequency ω_0, are then written as

$$\boldsymbol{\mathcal{E}}(z,t) = \frac{1}{2}E(z,t)\exp\{i(kz - \omega_0 t)\} + c.c. \tag{2.3}$$

$$\boldsymbol{\mathcal{P}}(z,t) = \frac{1}{2}P(z,t)\exp\{i(kz - \omega_0 t)\} + c.c. \tag{2.4}$$

Here, *c.c.* represents the complex conjugate of the preceding terms. $E(z, t)$ and $P(z, t)$ are the amplitudes of the respective variables and are assumed to vary slowly

compared with the optical frequency (Slowly Varying Envelope Approximation: SVEA). Neglecting the second order small infinities and substituting (2.3) and (2.4) into (2.2), we obtain an equation for the amplitudes

$$\frac{\partial E(z,t)}{\partial z} + \frac{\eta}{c}\frac{\partial E(z,t)}{\partial t} = i\frac{k}{2\varepsilon_0\eta^2}P(z,t) \tag{2.5}$$

2.1.2 Light Emission and Absorption in Two-Level Atoms

Before deriving the complete form of the propagation equation, we discuss absorption and emission of light from two-level atoms based on the semi-classical quantum theory and, then, derive the Bloch equation. Using the Hamiltonian $\mathcal{H}_0$ without perturbation for the electric field $\boldsymbol{\mathcal{E}}$, the Hamiltonian $\mathcal{H}$ of the two-level atom is given by

$$\mathcal{H} = \mathcal{H}_0 - \boldsymbol{\mu}\cdot\boldsymbol{\mathcal{E}} \tag{2.6}$$

where $\boldsymbol{\mu} = e\mathbf{r}$ is the moment of the transition between the two levels ($\mathbf{r}$ and e are the position vector and the fundamental electric charge). For the eigenstates ϕ_j (j = 1, 2) of the two levels and the energy of each level as $\hbar\omega_j$ ($\hbar$ being the Planck constant), the interaction between the two levels is written by

$$\langle\varphi_j|\mathcal{H}_0|\varphi_k\rangle = \hbar\omega_j\delta_{jk} \tag{2.7}$$

where δ_{ik} represents the Kronecker delta. The angular frequency of light emitted or absorbed in the two-level atoms is given by $\omega_\mathrm{A} = \omega_2 - \omega_1$. In the presence of the optical field, the quantum state $|\psi\rangle$ of the two-level atoms is written by the linear addition of the two states as

$$|\psi\rangle = c_1(t)\exp(-i\omega_1 t)|\varphi_1\rangle + c_2(t)\exp(-i\omega_2 t)|\varphi_2\rangle \tag{2.8}$$

Substituting the above equation into the Schrödinger equation, the coefficients c_1 and c_2 for the two states are calculated by solving the following coupled equations:

$$\frac{\mathrm{d}c_1(t)}{\mathrm{d}t} = \frac{c_2(t)}{i\hbar}\exp(-i\omega_\mathrm{A}t)\langle\varphi_1|\boldsymbol{\mu}\cdot\boldsymbol{\mathcal{E}}|\varphi_2\rangle \tag{2.9}$$

$$\frac{\mathrm{d}c_2(t)}{\mathrm{d}t} = \frac{c_1(t)}{i\hbar}\exp(i\omega_\mathrm{A}t)\langle\varphi_2|\boldsymbol{\mu}\cdot\boldsymbol{\mathcal{E}}|\varphi_1\rangle \tag{2.10}$$

These are known as the Bloch equations (1946).

Using the number N_A of atoms in the unit volume, the macroscopic polarization of the medium is defined by

$$\boldsymbol{\mathcal{P}} = N_{\mathrm{A}}\langle\psi|\boldsymbol{\mu}|\psi\rangle \tag{2.11}$$

From (2.8), the above equation reads as

$$\boldsymbol{\mathcal{P}} = N_{\mathrm{A}}\{p(t)\mu_{12} + p^{*}(t)\mu_{21}\} \tag{2.12}$$

Then, the microscopic polarization $p(t)$ for each atom is given by

$$p(t) = c_1^{*}(t)c_2(t)\exp(-i\omega_A t) \tag{2.13}$$

$$\mu_{ij} = \langle\varphi_j|\boldsymbol{\mu}|\varphi_i\rangle \tag{2.14}$$

where μ_{ij} $(i, j = 1, 2)$ is the moment of the transition from the lower to the upper state or vice versa. Finally, substituting the above equations into (2.9) and (2.10), we obtain the equation for the polarization of atoms

$$\frac{\mathrm{d}p(t)}{\mathrm{d}t} = -i\omega_{\mathrm{A}}p(t) + \frac{i}{\hbar}E(t)\mu_{21}w(t) \tag{2.15}$$

and the distribution $w(t) = |c_2(t)|^2 - |c_1(t)|^2$ for the population inversion of the two-level atoms

$$\frac{\mathrm{d}w(t)}{\mathrm{d}t} = \frac{2}{i\hbar}E(t)\{p^{*}(t)\mu_{21} - p(t)\mu_{12}\} \tag{2.16}$$

2.1.3 Maxwell–Bloch Equations

Rearranging the equations obtained for the field and the polarization and considering the time development of the population inversion in the laser medium, we derive the complete set of laser rate equations, which are the same expressions as those of Lorenz chaos. Differentiating (2.4) with time and using the relations of (2.12) and (2.15), the macroscopic polarization equation is calculated as

$$\begin{aligned}\frac{\mathrm{d}P(z,t)}{\mathrm{d}t} =& -i(\omega_{\mathrm{A}} - \omega_0)P(z,t) \\ &+ \frac{i\mu^2}{2\hbar}W(z,t)[E(z,t) + E^{*}(z,t)\exp\{-2i(kz - \omega_0 t)\}]\end{aligned} \tag{2.17}$$

where $W = N_{\mathrm{A}}w$ is the macroscopic population inversion and $\mu = |\mu_{12}|$. From (2.16), the equation for the population inversion is given by

$$\frac{dW(z,t)}{dt} = \frac{1}{i\hbar}[E(z,t)P^*(z,t) - E(z,t)P(z,t) \exp\{2i(kz - \omega_0 t)\} - c.c.] \tag{2.18}$$

Since we are concerned with slowly varying variables compared with optical frequency (Rotating-Wave Approximation: RWA), we can omit the terms related to fast oscillation terms of the angular frequency $2\omega_0$ in (2.17) and (2.18) (Milloni and Eberly 1988).

We need the external pump to lase, so that we add an extra term to (2.18) for lasing in the actual laser. Further, we add the phenomenological terms for the damping oscillations to (2.5), (2.17), and (2.18). The resulting equations, the Maxwell–Bloch equations, for field E, polarization P, and population inversion W are given by

$$\frac{\partial E(z,t)}{\partial z} + \frac{\eta}{c}\frac{\partial E(z,t)}{\partial t} = i\frac{k}{2\varepsilon_0 \eta^2}P(z,t) - \frac{\eta}{2T_{\rm ph}c}E(z,t) \tag{2.19}$$

$$\frac{\partial P(z,t)}{\partial t} = -i(\omega_{\rm A} - \omega_0)P(z,t) + \frac{i\mu^2}{2\hbar}E(z,t)W(z,t) - \frac{P(z,t)}{T_2} \tag{2.20}$$

$$\frac{\partial W(z,t)}{\partial t} = \frac{1}{i\hbar}\{E(z,t)P^*(z,t) - E^*(z,t)P(z,t)\} + \frac{W_0 - W(z,t)}{T_1} \tag{2.21}$$

where W_0 is the population inversion induced by the pump at the laser threshold. $T_{\rm ph}$, T_2, and T_1 are the relaxation times of the photons (photon lifetime), the polarization (transverse relaxation), and the population inversion (longitudinal relaxation), respectively. The actual laser exhibits spontaneous emission and, then, statistical Langevin noise terms are added to each equation to explain the noise effects (Petermann 1988; Risken 1996). However, statistical noises and irregular chaotic oscillations are of different origins and they can be discussed separately. Chaos is a phenomenon described by deterministic equations, so that such terms are excluded for investigating the pure laser dynamics. Noises are only introduced to account for the effects of laser oscillations when necessary. The Langevin noises will be briefly discussed in Chap. 3.

2.2 Lorenz–Haken Equations and Laser Thresholds

2.2.1 Lorenz–Haken Equations

We have derived the laser equations for field amplitudes and polarization, and population inversion. In the following, we show that these equations are equivalent to Lorenz equations, which describe a model of the convective fluid flow for the

atmosphere. Scaling the field E, the polarization P, and the population inversion W in (2.19), (2.20), and (2.21) as $\bar{E} = \sqrt{\varepsilon_0 c\eta/2}E$, $\bar{P} = k/\varepsilon_0\eta^2\sqrt{\varepsilon_0 c\eta/2}P$, and $w = \sigma_s W$ (with $\sigma_s = \mu^2\omega_0 T_2/2\varepsilon_0\hbar c\eta$), and neglecting the term $\partial E/\partial z$ as a small mean field that propagates in the z direction, the Maxwell–Bloch equations are written as follows (Haken 1975):

$$\frac{\mathrm{d}\bar{E}(t)}{\mathrm{d}t} = i\frac{c}{2\eta}\bar{P}(t) - \frac{1}{2T_{\mathrm{ph}}}\bar{E}(t) \tag{2.22}$$

$$T_2\frac{\mathrm{d}\bar{P}(t)}{\mathrm{d}t} = -(1 - i\delta)\bar{P}(t) + i\bar{E}(t)w(t) \tag{2.23}$$

$$T_1\frac{\mathrm{d}w(t)}{\mathrm{d}t} = w_0 - w(t) + \frac{\mathrm{Im}[\bar{E}^*(\mathrm{t})\bar{P}(t)]}{I_{\mathrm{sat}}} \tag{2.24}$$

where $\delta = (\omega_0 - \omega_{\mathrm{A}})T_2$ is the scaled atomic detuning and $I_{\mathrm{sat}} = \hbar^2 c\eta\varepsilon_0/2\mu^2 T_1 T_2$ is the saturation intensity.

In the meantime, Lorenz proposed the differential equations for three variables X, Y, and Z as a model of atmospheric flow (Rayleigh–Bénard configuration) and proved the existence of chaos in the system (Lorenz 1963). Here, variables X, Y, and Z represent circulatory fluid flow velocity, temperature difference between rising and falling fluid regions, and distortion of vertical temperature profile, respectively. Using chaotic parameters Σ (Prandtl number), R (Raleigh number), and β (a parameter related to the geometrical boundary of the flow), the Lorenz equations are written as

$$\frac{\mathrm{d}X(t)}{\mathrm{d}t} = -\Sigma\{X(t) - Y(t)\} \tag{2.25}$$

$$\frac{\mathrm{d}Y(t)}{\mathrm{d}t} = RX(t) - Y(t) - X(t)Z(t) \tag{2.26}$$

$$\frac{\mathrm{d}Z(t)}{\mathrm{d}t} = -\beta Z(t) + X(t)Y(t) \tag{2.27}$$

Lorenz suggested that systems described by nonlinearly coupled differential equations with three variables are candidates for chaotic systems (Li and Yorke 1975).

For the Maxwell–Bloch equations in laser model, using normalized variables as $x = \sqrt{b/I_{\mathrm{sat}}}\,\bar{E}$, $y = i(cT_{\mathrm{ph}}/\eta)\sqrt{b/I_{\mathrm{sat}}}\,\bar{P}$, and $z = (w_0 - w)cT_{\mathrm{ph}}/\eta$, and replacing time by $t/T_2 \rightarrow t$, the equations in (2.22)–(2.24) are written as

$$\frac{\mathrm{d}x(t)}{\mathrm{d}t} = -\sigma\{x(t) - y(t)\} \tag{2.28}$$

$$\frac{\mathrm{d}y(t)}{\mathrm{d}t} = -(1 - i\delta)y(t) + \{r - z(t)\}x(t) \tag{2.29}$$

$$\frac{\mathrm{d}z(t)}{\mathrm{d}t} = -bz(t) + \mathrm{Re}[x^*(t)y(t)] \tag{2.30}$$

where $\sigma = T_2/2T_{\mathrm{ph}}$, $b = T_2/T_1$, and $r = w_0 cT_{\mathrm{ph}}/\eta$. The above three equations are almost the same as those of the Lorenz model and lasers described by two-level atoms are essentially the same chaotic system as convective fluid in the atmospheric flow. Therefore, (2.28)–(2.30) are called Lorenz–Haken equations. Figure 2.2 shows an example of chaotic oscillations calculated from (2.28)–(2.30) for a parameter set of $\sigma = 3$, $\delta = 0$, $r = 28$, and $b = 1$. The normalized pump parameter r is well above the second laser threshold and these parameters correspond to a bad cavity condition for class C laser that is discussed in Sect. 2.2.3. Figure 2.2a, b are time series of chaotic oscillation of the laser output and its chaotic attractor in the phase space of the real parts of the field and the polarization, respectively. Under the condition, the laser becomes unstable and shows chaotic oscillations. In the figure, one can see pulsating and irregular oscillations of chaos in the laser intensity. The double scroll trajectory is sometimes called butterfly attractor, which is commonly observed in Lorenz-like chaos (see Appendix A.2). Thus, laser is in general categorized into a chaotic system like Lorenz system.

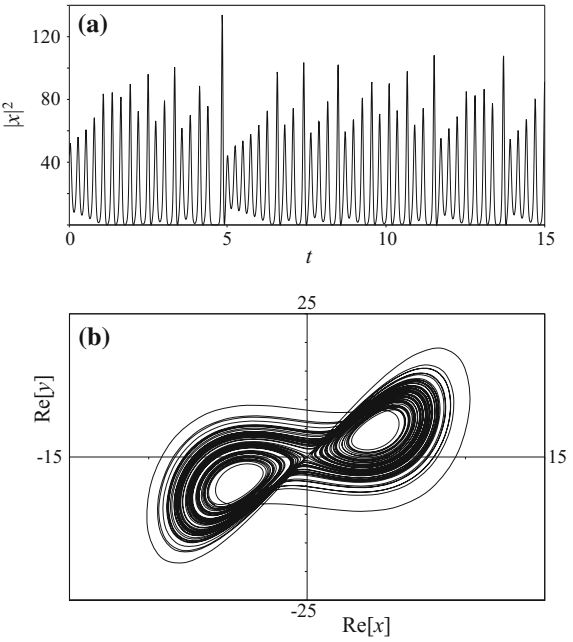

Fig. 2.2 Lorenz–Haken chaos of laser oscillation. **a** Time evolution of the laser intensity for $\sigma = 3$, $\delta = 0$, $r = 28$, and $b = 1$, and **b** its attractor in the phase space of the real parts of the field and the polarization

2.2.2 First Laser Threshold

A laser oscillation starts when the population inversion exceeds a certain level, namely the pumping threshold. The laser threshold can be calculated from (2.28)–(2.30) based on the linear stability analysis. The linear stability analysis, which applies small perturbations on the steady states of the laser variables, is frequently used for obtaining the stability conditions. Assuming the stable solutions in (2.28)–(2.30) as x_s, y_s, and z_s, and applying small perturbations on the steady-state values, we write the time developments of the variables as $x(t) = x_s + \delta x(t)$, $y(t) = y_s + \delta y(t)$, and $z(t) = z_s + \delta z(t)$, where $\delta x(t)$, $\delta y(t)$, $\delta z(t)$ are small perturbations. Substituting these values into (2.28)–(2.30), we obtain the following differential equations for the perturbations:

$$\frac{\mathrm{d}\delta x(t)}{\mathrm{d}t} = -\sigma\{\delta x(t) - \delta y(t)\} \tag{2.31}$$

$$\frac{\mathrm{d}\delta y(t)}{\mathrm{d}t} = -(1 - i\delta)\delta y(t) - \{r - \delta z(t)\}\delta x(t) \tag{2.32}$$

$$\frac{\mathrm{d}\delta z(t)}{\mathrm{d}t} = -b\delta z(t) + \mathrm{Re}[\delta x^*(t)\delta y(t)] \tag{2.33}$$

We can neglect the second small infinities such as $\delta z \delta x$ and $\delta x^* \delta y$, thus the equations are linearized.

When we put the time developments of the variables as $\delta h = \delta h_0 \exp(\gamma t)$ ($h = x$, y, z), the laser is stable for solutions of negative real parts of γ. On the other hand, it is unstable for solutions of positive real parts and the solutions diverge to infinities for the time development. Substituting the time developments $\delta h = \delta h_0 \exp(\gamma t)$ into (2.31)–(2.33), we obtain the following characteristic relation for the non-trivial solutions:

$$\begin{vmatrix} \gamma + \sigma & -\sigma & 0 \\ -r & \gamma + 1 - i\delta & 0 \\ 0 & 0 & \gamma + b \end{vmatrix} = 0 \tag{2.34}$$

The real parts of the solutions in the above equations represent the measure for stability or instability of the solutions and the imaginary parts denote the oscillation frequencies of the corresponding solutions. Since $b = T_2/T_1$ is positive, one of the solutions $\gamma = -b$ is a stable solution with uniform convergence. The other solutions are calculated by solving the following equations:

$$\gamma^2 + (\sigma + 1 - i\delta)\gamma - \sigma(r - 1 + i\delta) = 0 \tag{2.35}$$

When the pumping r reaches a certain value, the laser exceeds the threshold and laser oscillation starts. Above the threshold, the solutions of the imaginary parts are

enough to take into account. Putting the form of the solutions as $\gamma = i\Omega$ and substituting it into (2.35), we obtain the laser threshold from the conditions having zero values for the real and imaginary parts of (2.35) as

$$r_{\mathrm{th}}^{(1)} = 1 + \frac{\delta^2}{(\sigma+1)^2} \tag{2.36}$$

For the laser oscillation, there is an accompanying frequency $\nu = \Omega/2\pi$ that corresponds to the solution of the imaginary part for the characteristic equation. Using the threshold, the frequency is given by

$$\nu_{\mathrm{R}} = \frac{\sigma}{2\pi}\sqrt{r_{\mathrm{th}}^{(1)} - 1} \tag{2.37}$$

The frequency ν_{R} is known as the relaxation oscillation frequency. When the detuning δ is zero, the threshold is $r_{\mathrm{th}}^{(1)} = 1$ or $w_0 = \eta/cT_{\mathrm{ph}}$, as expected. The extra term in the threshold in (2.36) is the increase of the threshold, which compensates the loss due to the detuning. As we discuss in the following section, there is another threshold that is called second laser threshold. Therefore, $r_{\mathrm{th}}^{(1)}$ is called first laser threshold.

2.2.3 Second Laser Threshold

Laser oscillation starts above the first threshold and shows a stable output power at a certain pump. Here, we again apply linear stability analysis for the laser operation. As we are considering the oscillation above the threshold, the field and the polarization vary with time at the same optical frequency for the steady-state values of x_{s}, y_{s}, and z_{s}. Assuming the difference of the angular detuning frequency $\Delta\omega$ between the laser oscillation and the internal cavity frequencies, and the phase fluctuation ϕ_{s} of the complex field, we put the forms of the steady-state solutions as

$$x_{\mathrm{s}} = x_0 \exp\{-i(\Delta\omega_{\mathrm{s}} t + \phi_{\mathrm{s}})\} \tag{2.38}$$

$$y_{\mathrm{s}} = y_0 \exp(-i\Delta\omega_{\mathrm{s}} t) \tag{2.39}$$

$$z_{\mathrm{s}} = z_0 \tag{2.40}$$

where $x_0 = \sqrt{bz_0}$, $y_0 = \sqrt{r_{\mathrm{th}}^{(1)} bz_0}$, $z_0 = r - r_{\mathrm{th}}^{(1)}$, $\Delta\omega_{\mathrm{s}} = -\delta\sigma/(\sigma + 1)$, and $\tan \phi_{\mathrm{s}} = \delta/(\sigma + 1)$. The laser output power is given by the square of x_0 and reads

$$x_0^2 = b(r - r_{\text{th}}^{(1)}) \tag{2.41}$$

This is the well-known result that the laser output power linearly increases with the increase of the pump r well above the threshold $r_{\text{th}}^{(1)}$.

For a pump below the laser threshold, the laser does not reach laser oscillation and it only exhibits a faint light output due to spontaneous emission, thus the laser is also under another stable condition. For the increase of the pump r over the threshold, whether the laser output power increases with the increase of the pump or not? In actual fact, there are nonlinear effects, such as saturation of gains of the laser material, to limit the optical output power. The effects also induce the change of laser parameter values describing the laser rate equations. Of course, what we are considering is not such effects, but the nonlinear effects intrinsically involved in the laser rate equations in (2.28)–(2.30). Here, consider the unstable phenomena induced by the increase of the pump r for these equations. For this purpose, we again employ the linear stability analysis for (2.38)–(2.40) near the steady-state values for the variables. The procedure is almost the same as the previous calculations. For simplicity, we calculate the stability solutions for the condition $\delta = 0$ (zero detuning condition). After some calculations, the same as the derivation for (2.35), the characteristic equation reads as

$$\gamma^3 + a_2\gamma^2 + a_1\gamma + a_0 = 0 \tag{2.42}$$

where $a_2 = \sigma + b + 1$, $a_1 = b(\sigma + r)$, and $a_0 = 2b\sigma(r - 1)$. The stability solutions are calculated by solving the above equation.

At the threshold of the stable solution, the variable γ is purely imaginary, and it is assumed as $\gamma = i\Omega$. From the comparison between the real and imaginary parts for the solution, we obtain the threshold as

$$r_{\text{th}}^{(2)} = \frac{\sigma(\sigma + b + 3)}{\sigma - b - 1} \tag{2.43}$$

Over the pump r exceeding the threshold $r_{\text{th}}^{(2)}$, the laser gets unstable states and exhibits irregular oscillations of chaos via Hopf bifurcations (see Appendix A.1). In actual evolution processes for bifurcations, there are various routes to chaos, for example, chaos follows immediately after period-1 oscillation (quasi-period doubling bifurcation). The other example is that instability to chaos follows after intermittent oscillations like spiky irregular oscillations. The details of routes to chaos in semiconductor lasers will be demonstrated in the following chapters. The threshold $r_{\text{th}}^{(2)}$ is called second threshold to distinguish it from the first laser threshold $r_{\text{th}}^{(1)}$. For example, for the conditions of $T_2 \ll T_1$, $b \approx 0$, and $\sigma = 2$ ($T_2 = 4T_{\text{ph}}$), the threshold value is equal to $r_{\text{th}}^{(2)} = 10$ and it is much higher than the first threshold $r_{\text{th}}^{(1)} = 1$ without detuning. Actual unstable lasers have the second

threshold values around tens to one hundred. We already presented such an example in Fig. 2.2.

The typical frequency of the irregular pulsing can also be calculated from the characteristic equation for the pure imaginary part value of the variable γ, and it is given by

$$\nu_{R2} = \frac{1}{2\pi}\sqrt{b(\sigma + r_{th}^{(2)})} \tag{2.44}$$

For the existence of the second threshold, the condition of $\sigma > b + 1$ must be satisfied from (2.43). This is known as the bad-cavity condition of a laser that gives rise to unstable laser oscillations. The bad-cavity condition is rewritten by using the actual time constants as follows:

$$\frac{1}{2T_{ph}} > \frac{1}{T_2} + \frac{1}{T_1} \tag{2.45}$$

Namely, the bad-cavity of a laser oscillation is a lossy and dissipative system for photons having a low quality factor Q of the resonator. Further discussion of the bad-cavity conditions and instabilities above the second laser threshold can be found in van Tartwijk and Agrawal (1998). Equations (2.43) and (2.44) were derived for the condition of zero frequency detuning $\delta = 0$. For nonzero detuning $\delta \neq 0$, the analysis becomes much more complex, but the expression for this case has been given and almost the same order of the second laser threshold $r_{th}^{(2)}$ has been obtained (Mandel and Zeghlache 1983; Zeghlache and Mandel 1985; Ning and Haken 1990).

2.3 Classifications of Lasers

2.3.1 Classes of Lasers

We have taken into consideration all of the time constants for the field, the polarization of matter, and the population inversion in the laser rate equations. The second laser threshold has been calculated for the inclusions of these parameters. However, lasers do not always show instabilities and chaotic behaviors with increased pumping, and most lasers are indeed stable. Only few lasers emitting infrared lines exhibit chaotic oscillations. For stability and instability of lasers, we have assumed the model of a ring laser with two-level atoms. On the other hand, most lasers in practical use are modeled by three- or four-level atoms. Therefore, lasers must be modeled by these in a strict sense and some modifications may be required for the above derivations. However, the results derived for the two-level atoms can here be extended to three or four-level atoms and still be applicable for the discussion of the stability and instability for practical lasers.

Even for the same material, the laser may have several oscillation lines. In such a case, the laser has a different gain for each line and has different time constants for the relaxation oscillations depending on the oscillation frequency. Therefore, a laser with a certain material may be stable for a certain oscillation line and have no second threshold, while it may be unstable and have the second threshold for another line. The stability and instability of lasers intrinsically involved in laser rate equations are classified according to the scales of time constants for the relaxation oscillations T_{ph}, T_2, and T_1 introduced in Sect. 2.2.1. Namely, one or two of the time constants among the three in the differential equations may be adiabatically eliminated and one or two of the laser rate equations are enough to describe actual laser operations. Depending on the scales of the time constants, the stabilities of lasers are classified into the following three classes; class A, B, and C lasers (Arecchi et al. 1984; Tredicce et al. 1985).

2.3.2 Class C Lasers

When the time constants of the relaxations are of the same order, we must consider all of the Lorenz–Haken differential equations. As already discussed, the laser oscillation starts at the first threshold with stable light output for a certain pump and it reaches the second laser threshold for the increase of the pump. Over pumping above the second threshold in the bad-cavity condition with low Q factor, the laser shows unstable oscillation like irregular pulsations and chaotic oscillations. According to the classifications of laser operations by Arecchi et al. (1984), these lasers are called class C lasers. Class C lasers are generally infrared gas lasers and far-infrared lasers are almost classified into class C. This is originated from the fact that the three time constants of the relaxation oscillations for the field, the polarization of matter, and the population inversion tend to be of the same order. Examples of class C lasers are NH_3 lasers (Weiss et al. 1985; Hogenboom et al. 1985), Ne–Xe lasers (3.51 μm line) (Casperson 1978; Abraham et al. 1985), and He–Ne lasers at 3.39 μm line (Weiss and King 1982; Weiss et al. 1983). Though He–Ne lasers operating at infrared lines are class C lasers, He–Ne lasers at visible oscillations are categorized into a different class because the constants of the polarization and the population inversion have different timescales from those of the infrared operations. In general, these class C lasers do not have any commercial application.

Figure 2.3 is an example of experimentally observed chaotic waveforms in an infrared He–Ne laser at 3.39 μm oscillation (Weiss et al. 1983). The bad-cavity condition was realized by tilting the angle of one of the mirrors in the laser resonator. A stable laser state (Fig. 2.3a) evolves into unstable oscillations (Fig. 2.3b–d) to chaotic state (Fig. 2.3e) with the increase of the mirror tilting angle. Figure 2.4 shows the oscillation spectra of the laser corresponding to period doubling

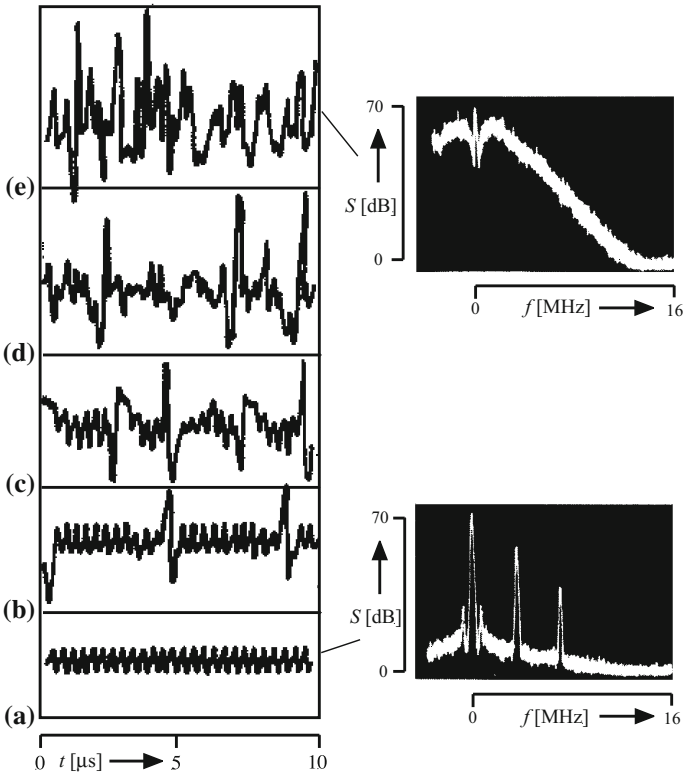

Fig. 2.3 Experimentally observed chaotic time series in an infrared He–Ne laser. Stable oscillation state **a** to chaotic state **e**. One of the mirrors in the laser cavity is tilted and the bad-cavity condition is realized [after Weiss et al. (1983); © 1983 APS]

bifurcations to chaos for the increase of the mirror tilting angle. Figure 2.5 is another experimental example of chaos showing pulsation instability in a Xe laser at 3.51 μm oscillation (Casperson 1978). With increasing pump, period-1 pulsation at first appears in Fig. 2.5a and the laser switches to period-2 pulsation in Fig. 2.5b. Thus, routes to chaos are not unique and depend on systems and parameters.

2.3.3 Class B Lasers

If the time constant T_2 of the polarization of matter (transverse relaxation) is small enough compared with the other time constants, i.e., T_{ph}, $T_1 \gg T_2$, the differential equation for the polarization is adiabatically eliminated and we obtain for the representation of the polarization in (2.29) (Haken 1985)

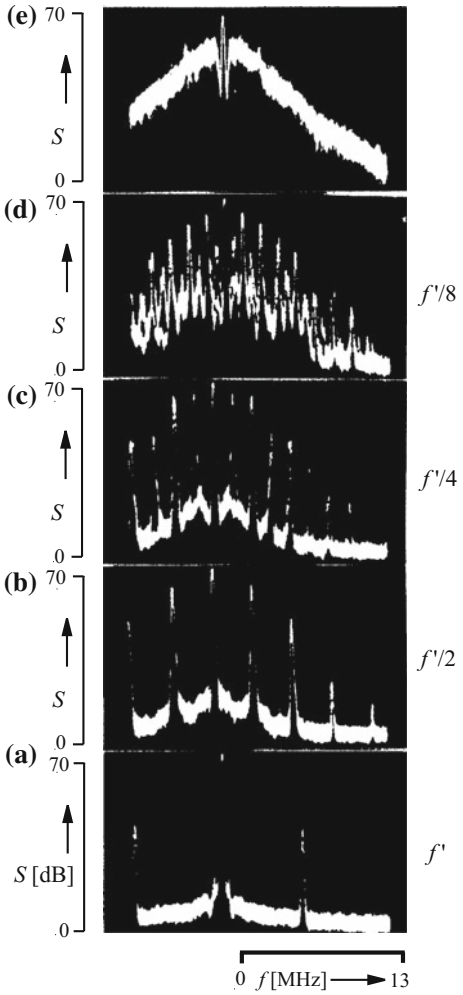

Fig. 2.4 Experimentally observed optical power spectra in an infrared He–Ne laser for period-doubling route to chaos. Tilting of one of the resonator mirrors leads to oscillations to **a** period-1, **b** period-2, **c** period-4, **d** period- 8, and **e** chaos [after Weiss et al. (1983); © 1983 APS]

$$y = \frac{r - z}{1 - i\delta} x \tag{2.46}$$

Then, the laser rate equations can be described by the two differential equations for the field x and the population inversion z. These lasers are called class B lasers and they are stable in nature, since the lasers have the first threshold but do not have the second threshold. The electric field is complex and the complex field equation can be split into two differential equations, the amplitude and phase equations. However, the phase equation has no effect on other variables, so that these systems can still be characterized by two differential equations. Therefore, class B lasers are intrinsically stable.

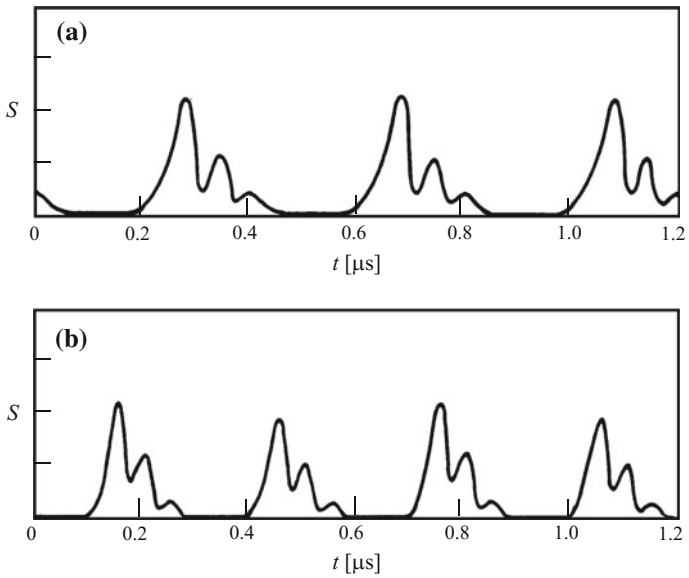

Fig. 2.5 Experimental plots of pulsation instabilities in a Xe laser at 3.51 μm oscillation for **a** period-1 pulsation at a discharge current of 40 mA and **b** period-2 pulsations at a discharge current of 50 mA [after Casperson (1978); © 1978 IEEE]

However, they are easily destabilized by the introduction of external perturbations, resulting in the addition of extra degrees of freedom. If the equations for the field amplitude and the phase couple with each other through a perturbation, the laser must be described by the rate equations coupled with three variables. A laser coupled with three variables becomes a chaotic system and shows instabilities. Examples of external perturbations are modulation for the accessible laser parameters, external optical injection, and optical self-feedback from external optical components. Semiconductor laser, which is the main topic of this book, is classified into class B laser, as discussed later. Indeed, semiconductor lasers are easily destabilized and show chaotic behaviors by external perturbations, such as external optical feedback (van Tartwijk and Agrawal 1998; Ohtsubo 2002). One of the typical features of class B lasers is a relaxation oscillation of the laser output that is observed for a step-time response when the population inversion does not follow the photon decay rate, i.e., $T_1 > T_{ph}$. Many lasers are classified into class B lasers and other examples are CO_2 lasers and solid-state lasers including fiber lasers. It is noted that CO_2 lasers are gas lasers and have oscillation lines in infrared region of wavelength around 9.4–10.6 μm. However they are stable class B lasers since the oscillation mechanism is different from those of common class C lasers. The oscillations of CO_2 lasers are performed through the excitations of molecular vibrations, which is different from the mechanism of two-level atoms for class C lasers discussed in the previous subsection. Class B lasers are important and widely used in practical applications.

2.3.4 Class A Lasers

When the lifetime of photons in a laser medium is large enough compared with the other time constants of the relaxations, i.e., $T_{\mathrm{ph}} \gg T_1, T_2$, the differential equations for the polarization of matter and the population inversion are adiabatically eliminated. In the same manner as class B lasers, the adiabatical relation for the polarization in (2.46) also holds and, in addition, the steady-state population inversion is given by (Haken 1985)

$$z = \frac{1}{b}\mathrm{Re}[x^* y] \tag{2.47}$$

Then, the laser oscillation is only described by the differential equation for the field. Lasers satisfying the relations are called class A lasers and they are the most stable lasers with a high Q factor among the three classes. Even for class A lasers, they may be destabilized and show chaotic behaviors by external perturbations with two or more extra degrees of freedom as discussed in class B lasers. Visible He–Ne lasers, Ar-ion lasers, and dye lasers are examples of class A lasers.

References

N.B. Abraham, L.A. Lugiato, L.M. Narducci (eds.) Special issue: instability in active optical media. J. Opt. Soc. Am. B **2** (1985)
N.B. Abraham, P. Mandel, L.M. Narducci, Dynamical instabilities and pulsations in lasers (Chap. 1), in *Progress in Optics, vol. 25,*, ed. by E. Wolf (North-Holland, Amsterdam, 1988)
F.T. Arecchi, G.L. Lippi, G.P. Puccioni, J.R. Tredicce, Deterministic chaos in laser with injected signal. Opt. Commun. **51**, 308–314 (1984)
F. Bloch, Nuclear induction. Phys. Rev. **70**, 460–474 (1946)
L.W. Casperson, Spontaneous coherent pulsations in laser oscillators. IEEE J. Quantum Electron. **14**, 756–761 (1978)
H. Haken, Analogy between higher instabilities in fluids and lasers. Phys. Lett. **53A**, 77–78 (1975)
H. Haken, *Light.* vol. 2 (North-Holland, Amsterdam, 1985)
E.H.M. Hogenboom, W. Klische, C.O. Weiss, A. Godone, Instabilities of a homogeneously broadened laser. Phys. Rev. Lett. **55**, 2571–2574 (1985)
T.Y. Li, J.A. Yorke, Period three implies chaos. Am. Math. Mon. **82**, 985–992 (1975)
E.N. Lorenz, Deterministic nonperiodic flow. J. Atmos. Sci. **20**, 130–148 (1963)
P. Mandel, H. Zeghlache, Stability of a detuned single mode homogeneously broadened ring laser. Opt. Commun. **47**, 146–150 (1983)
P.W. Milloni, J.H. Eberly, *Laser* (Wiley, New York, 1988)
C. Ning, H. Haken, Detuned lasers and the complex Lorenz equations: subcritical and supercritical Hopf bifurcations. Phys. Rev. A **41**, 3826–3837 (1990)
J. Ohtsubo, Chaotic dynamics in semiconductor lasers with optical feedback (Chap. 1), in *Progress in Optics, vol. 44,*, ed. by E. Wolf (North-Holland, Amsterdam, 2002)
K. Petermann, *Laser Diode Modulation and Noise* (Kluwer Academic, Dordrecht, 1988)
H. Risken, *The Fokker-Planck Equation: Methods of Solution and Applications*, 2nd edn. (Springer, Berlin, 1996)

J.R. Tredicce, F.T. Arecchi, G.L. Lippi, P. Puccioni, Instabilities in lasers with an injected signal. J. Opt. Soc. Am. B **2**, 173–183 (1985)
G.H.M. van Tartwijk, G.P. Agrawal, Laser instabilities: a modern perspective. Prog. Quantum Electron. **22**, 43–122 (1998)
C.O. Weiss, H. King, Oscillation period doubling chaos in a laser. Opt. Commun. **44**, 59–61 (1982)
C.O. Weiss, A. Godone, A. Olafsson, Routes to chaotic emission in a cw He-Ne laser. Phys. Rev. A **28**, 892–895 (1983)
C.O. Weiss, W. Klische, P.S. Ering, M. Cooper, Instabilities and chaos of a single mode NH_3 ring laser. Opt. Commun. **44**, 405–408 (1985)
H. Zeghlache, P. Mandel, Influence of detuning on the properties of laser equations. J. Opt. Soc. Am. B **2**, 18–22 (1985)

Chapter 3
Semiconductor Lasers and Theory

Abstract In this chapter, we discuss the oscillation conditions for semiconductor lasers and, then, derive the rate equations, which are the starting points of the study of chaotic dynamics in semiconductor lasers. The semiconductor laser described here is a Fabry-Perot type with a mono-layer of the active region, however other narrow-stripe edge-emitting lasers such as multi-quantum well (MQW) lasers and distributed feedback (DFB) lasers can be theoretically treated in the same manner as Fabry-Perot lasers. Therefore, the macroscopic features of these lasers show the same behaviors from the viewpoint of chaotic dynamics, although the detailed characteristics strongly depend on the laser structure and the particular values of the device parameters. The relaxation oscillation frequency, which is calculated from the rate equations, plays an important role for the dynamics of semiconductor lasers. The Langevin terms, which are stochastic noise effects induced by spontaneous emission of light in the laser medium, are introduced in the rate equations. Some other fundamental characteristics of semiconductor lasers are also discussed.

3.1 Semiconductor Lasers

We assume that the readers of this book are familiar with semiconductor lasers and how they operate. An extensive review for the characteristics of semiconductor lasers and the details of their operations can be found, for example, in the books of Agrawal and Dutta (1993), and Petermann (1988). We treat here the dynamics of narrow-stripe edge-emitting semiconductor lasers, which have stripe widths of less than a few microns, namely, the stripe width is the same order as that of the laser wavelength. Indeed, almost semiconductor lasers under commercial use are these types. For such structures, the laser can only be described by time-dependent differential equations as a class B laser, since we can assume uniform intensity distribution inside the laser cavity at a certain time instance and we can neglect carrier diffusion and diffraction of light along the direction of the stripe width. As far as the laser oscillations are described by the same forms of the rate equations, they show the same or similar dynamics independent of the laser types. In the meantime,

© Springer International Publishing AG 2017

J. Ohtsubo, *Semiconductor Lasers*, Springer Series in Optical Sciences 111,
DOI 10.1007/978-3-319-56138-7_3

newly developed structures of semiconductor lasers, for example, vertical-cavity surface-emitting semiconductor lasers (VCSELs), show unique characteristics that are different from conventional edge-emitting semiconductor lasers. We need some modifications of the rate equations for such newly developed lasers. These new lasers still show the same or similar dynamics as those of narrow-stripe edge-emitting lasers. However, they have extra device structures compared with narrow-stripe edge-emitting semiconductor lasers. Extra structures for semiconductor lasers mean the introductions of extra degree of freedoms in the viewpoint of nonlinear dynamics. Therefore, they are essentially unstable lasers even in their solitary oscillations and exhibit additional complex dynamics. We will derive the rate equations for these lasers and discuss their dynamics in Chap. 8.

The structure of semiconductor lasers is based on the p–n junction of the semiconductor materials and the laser oscillation is realized by the emission of light due to carrier recombination between the conduction and valence bands, namely, inter-band optical transitions. The band structure of actual lasers is not modeled by a simple two-level system. Therefore, we cannot straightforwardly apply the results of Chap. 2 and we need some modification of the model and of the strict theoretical treatment. However, the intra-band relaxation within the medium of the semiconductor laser is fast enough of the order of 10^{-13} s compared with the carrier recombination rate of 10^{-9} s (Petermann 1988). This fact makes it possible to use approximately the model of two-level atoms for the theoretical investigation of the dynamics of semiconductor lasers (Agrawal and Dutta 1993). The rigorous treatment of semiconductor lasers can be found in the reference (Chow et al. 1993), but here we employ the approximate model of laser oscillations based on two-level atoms.

As discussed in the previous chapter, the relaxation time of the polarization in the semiconductor laser material is as small as $T_2 < 0.1$ ps, which is much smaller than the other timescales of the relaxations, T_{ph}—several picoseconds and T_1—several nanoseconds, and the laser is classified into class B. Therefore, the polarization term is adiabatically eliminated and the effect is simply replaced by the linear relation between the field and the polarization. The population inversion for semiconductor lasers is replaced by the carrier density produced by electron-hole recombination. The photon number (which is equivalent to the absolute square of the field amplitude) and the carrier density are frequently used as the variables of the rate equations. However, for the general descriptions of the dynamics in semiconductor lasers, we must employ the complex amplitude of the field (the amplitude and the phase of the field) instead of the photon number. In particular, coherent descriptions of rate equations are essential when we treat the dynamics in semiconductor lasers, such as effects of optical feedback and optical injection. There are several ways to derive the complex field equation, however they reach the same result. Here, we follow the derivation of the complex field equation by Petermann (1988).

3.2 Oscillation Conditions of Semiconductor Lasers

3.2.1 Laser Oscillation Conditions

In this chapter, we derive the rate equations for edge-emitting semiconductor lasers with a narrow-stripe width. Even for edge-emitting lasers, there are several kinds of device structures, for example, Fabry-Perot, MQW, and DFB structures. Also, there are two main structures for the guiding of light in the active layer, i.e., gain- and index-guiding structures. Even for these different device structures, the derivation of the rate equations for laser operations is similarly given and almost the same equations are obtained, although the parameters appearing in the rate equations may vary from one laser to the other. Before deriving the rate equations in semiconductor lasers, we consider several conditions and relations for laser oscillations. At first, we discuss the conditions for laser oscillations (Yariv and Yeh 2007). The model of a Fabry-Perot resonator is shown in Fig. 3.1. Assuming a cavity length l, and reflectivities of the front and back facts r_1 and r_2, the fields E_f and E_b propagating forward and backward directions are written by

$$E_f(z) = E_{0f} \exp\left\{ ikz + \frac{1}{2}(g-a)z \right\} \tag{3.1}$$

$$E_b(z) = E_{0b} \exp\left\{ ik(l-z) + \frac{1}{2}(g-a)(l-z) \right\} \tag{3.2}$$

where g is the gain in the laser medium and a is the total loss due to absorption and scattering in the medium. All the parameters are defined for the laser intensity, so that a factor of 1/2 is introduced in the above equations.

From the boundary conditions at the facets, $E_f(0) = r_1 E_b(0)$ and $E_b(l) = r_2 E_f(l)$, the steady-state condition for the laser oscillation is given by

$$r_1 r_2 \exp\{2ikl + (g-a)l\} = 1 \tag{3.3}$$

From the real part of the above equation, the amplitude condition of the laser oscillation for the threshold gain g_{th} is given by

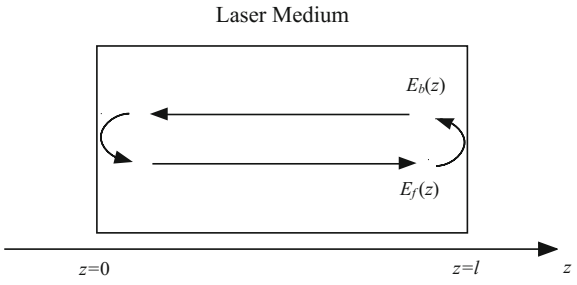

Fig. 3.1 Model of a Fabry-Perot laser

$$g_{\text{th}} = a + \frac{1}{l}\ln\left(\frac{1}{r_1 r_2}\right) \tag{3.4}$$

Since there is spontaneous emission of light within the active region in the laser, the actual gain is slightly less than g_{th}. Also, the phase condition is calculated from the imaginary part and reads as

$$kl = m\pi \tag{3.5}$$

where m is an integer. Equation (3.4) is the condition for the laser threshold and is interpreted as the balance of the gain with the losses of the internal absorption and reflection in the laser medium. For example, when we consider a InGaAsP semiconductor laser oscillating at a near-infrared line of 1.3–1.5 μm with cleaved facets as a laser resonator, the threshold gain is calculated as $g_{\text{th}} \approx 75\ \text{cm}^{-1}$ for the facet intensity reflectivities of $R_1 = R_2 \approx 0.32$ (where $R_1 = r_1^2$ and $R_2 = r_2^2$, and the refractive index of the medium of 3.6) and the internal losses of $a \approx 30\ \text{cm}^{-1}$ (Buss and Adams 1979). In actual fact, we roughly require double of this amount for lasing (about $g'_{\text{th}} \approx 150\ \text{cm}^{-1}$), since the laser light is not only confined within the active region and the confinement factor is about 0.5 or less of the calculated gain.

3.2.2 *Laser Oscillation Frequency*

From (3.5), the possible frequency of laser oscillations is given by

$$\nu_m = m\frac{c}{2\eta l} \tag{3.6}$$

where m is again an integer. The laser will be oscillated at one of these possible frequencies or a few lines of them. ν_m is called the mode frequency and it corresponds to the m-th longitudinal mode of the laser oscillations. Usually, a laser oscillates at or near the maximum gain mode, which is very close to one of the resonator frequencies. Therefore, the actual frequency of laser oscillations deviates from the value calculated from (3.6), though the deviation is very small.

The refractive index η in the semiconductor laser is a function of the optical oscillation frequency ν due to the presence of the dispersion of laser materials. Using the notation of a small quantity such as Δ, we have the relation

$$\Delta(\eta\nu) = \eta\Delta\nu + \nu\Delta\eta \tag{3.7}$$

Here, we define the effective refractive index as

$$\eta_e = \eta + v\frac{\partial \eta}{\partial v} \tag{3.8}$$

With the above relation and the equality for the successive modes m and $m + 1$, $\Delta(\eta v) = c/2l$, we obtain the mode separation between the m and $m + 1$ modes

$$\Delta v = \frac{c}{2\eta_e l} \tag{3.9}$$

This corresponds to the round trip time of light within the internal cavity of lasers and the time is given by

$$\tau_{\text{in}} = \frac{2\eta_e l}{c} \tag{3.10}$$

As an example, we consider the same InGaAsP lasers as in the previous subsection. We obtain a frequency separation of $\Delta v = 150$ GHz for $l = 250$ μm, $\eta \approx 3.6$, and $\eta_e \approx 4$. The corresponding separation of the wavelengths in the laser oscillation is $\Delta\lambda = \lambda^2 \Delta v/c = 1$ nm. Also, the round trip time of light is calculated to be $\tau_{\text{in}} = 6.7$ ps (Petermann 1988).

3.2.3 Dependence of Oscillation Frequency on Carrier Density

In this subsection, we derive the dependence of the oscillation frequency on the carrier density, which plays an important role in laser operations. The refractive index of the active layer is a function of the carrier density n_{th} and the optical frequency v_{th} at the laser threshold, and is written by

$$\eta = \eta_0 + \frac{\partial \eta}{\partial v}(v - v_{\text{th}}) + \frac{\partial \eta}{\partial n}(n - n_{\text{th}}) \tag{3.11}$$

where n is the carrier density at the laser oscillation and η_0 is the refractive index at the threshold. Then, the threshold gain g_{th} and the oscillation frequency v_{th} at the laser threshold is given by

$$g_{\text{th}} = g(n_{\text{th}}) \tag{3.12}$$

$$v_{\text{th}} = m\frac{c}{2\eta_0 l} \tag{3.13}$$

Substituting (3.6) and (3.13) into (3.11), and using the relation of (3.8), we obtain an important relation between the laser oscillation frequency and the carrier density as

$$(v - v_{\text{th}}) = -\frac{v_{\text{th}}}{\eta_e}\frac{\partial \eta}{\partial n}(n - n_{\text{th}}) \tag{3.14}$$

To derive above equation, we assume $\frac{v}{v_{\text{th}}} \approx \frac{v_m}{v_{\text{th}}} = \frac{\eta_0}{\eta} \approx 1$ from the relations of $v_m = m\frac{c}{2\eta l}$ and $v_{\text{th}} = m\frac{c}{2\eta_0 l}$. Since the oscillation frequency has a linear relation to the carrier density as given by (3.14), the laser power is proportional to the frequency through the linear relation between the carrier density and the optical power.

3.3 Derivation of Rate Equations

3.3.1 Gain at Laser Oscillation

To derive the rate equations of semiconductor lasers, we at first consider the gain at the lasing condition. The gain of light after the round trip within the cavity is given by the same equation for the steady-state laser oscillation condition as

$$G = r_1 r_2 \exp\{2ikl + (g - a)l\} \tag{3.15}$$

The wavenumber k depends on the refractive index of the laser medium and is a function of the optical frequency v (or the angular frequency $\omega = 2\pi v$) and also the carrier density n. From (3.14), $\omega = \omega_{\text{th}} - \frac{\omega_{\text{th}}}{\eta_e}\frac{\partial \eta}{\partial n}(n - n_{\text{th}})$. Using this, (3.8), and (3.11), the wavenumber can be expanded by the threshold values of those parameters as

$$k = \eta\frac{\omega}{c} = \frac{\omega_{\text{th}}}{c}\left\{\eta_0 + \frac{\partial \eta}{\partial n}(n - n_{\text{th}}) + \frac{\eta_e}{\omega_{\text{th}}}(\omega - \omega_{\text{th}})\right\} \tag{3.16}$$

Using (3.16), the gain G is written by the product of the frequency dependent and non-dependent terms, G_1 and G_2, as

$$G = G_1 G_2 \tag{3.17}$$

$$G_1 = r_1 r_2 \exp\{(g - a)l + i\phi_0\} \tag{3.18}$$

$$G_2 = \exp\left[i\frac{2\omega_{\text{th}} l}{c}\left\{\eta_0 + \frac{\eta_e}{\omega_{\text{th}}}(\omega - \omega_{\text{th}})\right\}\right] \tag{3.19}$$

The phase ϕ_0 of the above equation is given by

$$\phi_0 = \frac{2\omega_{\text{th}} l}{c}\frac{\partial \eta}{\partial n}(n - n_{\text{th}}) = -\tau_{\text{in}}(\omega - \omega_{\text{th}}) \tag{3.20}$$

In (3.19), we have used the condition for the laser oscillation that the phase $2\omega_{\text{th}}\eta_0 L/c$ must be equal to integer multiples of 2π. Then, replacing the quantity $-i\omega$ as the equivalent to the operator d/dt, (3.19) reads as

$$G_2 = \exp\{i\tau_{\text{in}}(\omega - \omega_{\text{th}})\} = \exp(-i\omega_{\text{th}}\tau_{\text{in}})\exp\left(-\tau_{\text{in}}\frac{\text{d}}{\text{d}t}\right) \tag{3.21}$$

Since frequency and time are a Fourier transform pair, (3.21) is derived from the equivalence of the equation in the frequency domain with that in the time domain.

3.3.2 *Rate Equation for the Field*

To attain the laser oscillations, the complex field after the round trip within the laser cavity must coincide exactly with the previous field. Assuming the gain in between (3.17), (3.18) and (3.21) as a kind of an operator, we can obtain the following relation:

$$E_f(t) = GE_f(t) \tag{3.22}$$

Then, using (3.21), the field after the round trip in the cavity is written as

$$E_f(t) = G_1 exp(-i\omega_{\text{th}}\tau_{\text{in}})\exp\left(-\tau_{\text{in}}\frac{\text{d}}{\text{d}t}\right)E_f(t) \tag{3.23}$$

We divide the laser field $E_f(t)$ into two terms, the term changing with angular frequency ω_{th} and the term $\hat{E}_f(t)$ that varies slowly compared with the angular frequency. Then, the field is given by

$$E_f(t) = \hat{E}_f(t)\exp(-i\omega_{\text{th}}t) \tag{3.24}$$

With this expression and the fact that the operator $\exp(-\tau_{\text{in}}\text{d}/\text{d}t)$ is equivalent to the time delay effect of τ_{in}, (3.23) yields

$$\begin{aligned}\hat{E}_f(t)\exp(-i\omega_{\text{th}}t) = {} & G_1\exp(-i\omega_{\text{th}}\tau_{\text{in}}) \\ & \times \hat{E}_f(t-\tau_{\text{in}})\exp\{-i\omega_{\text{th}}(t-\tau_{\text{in}})\}\end{aligned} \tag{3.25}$$

Therefore, we can write the field $\hat{E}_f(t)$ as

$$\hat{E}_f(t) = G_1 \hat{E}_f(t - \tau_{\text{in}}) \tag{3.26}$$

This equation means that the field $\hat{E}_f(t)$ after the round trip time of τ_{in} with SVEA approximation returns as the same form of the field with gain G_1. We have discussed the field propagation for the positive direction. Similarly, we obtain the same results for the field propagation for the negative direction and the same relation as that of (3.26) is derived for the field. Then, the total field $E(t)$ can be written as the same form as $\hat{E}_f(t)$ in (3.26).

For simplicity, we again use the notation for the field $\hat{E}(t)$ as $E(t)$ in the following. When the round trip time τ_{in} is small enough, we can expand the total field around the delay time τ_{in} as

$$E(t - \tau_{\text{in}}) = E(t) - \tau_{\text{in}} \frac{\mathrm{d}E(t)}{\mathrm{d}t} \tag{3.27}$$

Then, we obtain the differential form for the field as follows:

$$\frac{\mathrm{d}E(t)}{\mathrm{d}t} = \frac{1}{\tau_{\text{in}}} \left(1 - \frac{1}{G_1}\right) E(t) \tag{3.28}$$

Since the gain G_1 is very close to unity for laser oscillation, we approximate the gain from (3.18) as

$$\begin{aligned} \frac{1}{G_1} &= \exp\{-\ln(r_1 r_2) - (g - a)l - i\phi_0\} \\ &\approx 1 + \ln \frac{1}{r_1 r_2} - gl + al - i\phi_0 \end{aligned} \tag{3.29}$$

Substituting the above equation into (3.28) and using the relation of (3.20), we finally obtain the rate equation for the field as

$$\frac{\mathrm{d}E(t)}{\mathrm{d}t} = \left\{-i(\omega_0 - \omega_{\text{th}}) + \frac{1}{2}\left(g v_g - \frac{1}{\tau_{\text{ph}}}\right)\right\} E(t) \tag{3.30}$$

where $v_g = c/\eta_e$ is the group velocity of light in vacuum and the laser is assumed to operate at the angular optical frequency of $\omega = \omega_0$. Here, τ_{ph} (which is the same as T_{ph} in the previous notation) is the photon lifetime describing the loss due to absorption and scattering of light in the cavity and it is written by

$$\frac{1}{\tau_{\text{ph}}} = v_g \left\{a + \frac{1}{l} \ln\left(\frac{1}{r_1 r_2}\right)\right\} \tag{3.31}$$

where the relation $c/\eta_e = v_g = 2\ l/\tau_{\text{in}}$ holds for the group velocity of light within the laser resonator.

3.3.3 Linewidth Enhancement Factor

For the derived rate equation of (3.30), we rewrite the field equation in a different form, which is frequently used in the following discussion. At the same time, we derive the equation for the carrier density. Before formulating them, we discuss the complex susceptibility of the medium at laser oscillation and derive the important parameter of semiconductor lasers known as the linewidth enhancement factor. We can define the susceptibility under laser oscillation in the same manner as that below the laser threshold. We consider the extra complex susceptibility $\chi_l = \chi_l' + i\chi_l''$ due to the laser oscillation and add it to that below threshold, $\chi_0 = \chi_0' + i\chi_0''$ The complex susceptibility is a function of the laser frequency, therefore we write the total susceptibility $\chi(\omega)$ as

$$\chi(\omega) = \chi_0(\omega) + \chi_l(\omega) = \chi_0'(\omega) + \chi_l'(\omega) + i\{\chi_0''(\omega) + \chi_l''(\omega)\} \tag{3.32}$$

In the following, we will explicitly write susceptibilities as a function of the laser frequency only when necessary. Otherwise, the equivalent quantity of the complex electric permittivity has the following form:

$$\varepsilon = \varepsilon_b + \chi_l' + i\left(\chi_0'' + \chi_l'' + \frac{\sigma}{\varepsilon_0\omega}\right) \tag{3.33}$$

where $\sqrt{\varepsilon_b} = \eta_b$ is the refractive index below the laser threshold. We here add the conductivity, σ, of the laser medium introduced in Chap. 2.

Assuming the propagation of light toward z direction along the laser resonator, the spatial field to that direction is given by

$$E(z) = |E(z)| \exp(ikz) \tag{3.34}$$

The propagation constant is written by

$$k = \eta_c k_0 = \eta k_0 + i\frac{a_{abs}}{2} \tag{3.35}$$

where k_0 is the propagation constant in vacuum, η_c is the complex refractivity, and a_{abs} is the intensity absorption coefficient in the medium. Since the relation of $a_{\text{abs}} \ll \eta k_0$ usually holds, the refractive index η and the absorption coefficient a_{abs} are given by

$$\eta = \sqrt{\varepsilon_b + \chi_l{}'} \approx \eta_b + \frac{\chi_l{}'}{2\eta_b} \tag{3.36}$$

$$a_{abs} = \frac{k_0}{\eta}\left(\chi_0{}'' + \chi_l{}'' + \frac{\sigma}{\varepsilon_0\omega}\right) \approx \frac{k_0}{\eta_b}\left(\chi_0{}'' + \chi_l{}'' + \frac{\sigma}{\varepsilon_0\omega}\right) \tag{3.37}$$

where $\sigma/\varepsilon_0\omega$ corresponds to the optical loss induced by non-zero conductivity of the semiconductor medium and the rests in (3.37) are other losses of light in the medium. The increment of the refractive index η for laser oscillation is equal to $n\partial\eta/\partial n$, so that $\chi_l{}'$ is expressed by $\chi_l' = 2\eta_b n\partial\eta/\partial n$. Also using the gain for starting the laser oscillation, $g = a_{\text{abs}}$ (actually, this is the gain of the laser oscillation at transparency), the increment of the absorption (negative sign of g) is $-n\partial g/\partial n$. Then, $\chi_l{}''$ is represented by $\chi_l'' = -(\eta_b n/k_0)(\partial g/\partial n)$. The addition of the complex susceptibility due to laser oscillation is given by

$$\chi_l = 2\eta_b n\left(\frac{\partial\eta}{\partial n} - \frac{i}{2k_0}\frac{\partial g}{\partial n}\right) \tag{3.38}$$

The macroscopic complex refractive index at laser oscillation is written by

$$\eta_e = \eta - i\eta' \tag{3.39}$$

where η' is the imaginary part of the refractive index. The imaginary part of the refractive index has the relation with the gain g as

$$\eta' = -\frac{1}{2k_0}g \tag{3.40}$$

Then, with this relation together with (3.14), we have

$$(\omega - \omega_{\text{th}}) = -\frac{\omega_{\text{th}}}{\eta_e}\frac{\partial\eta}{\partial n}(n - n_{\text{th}}) = \frac{1}{2}\alpha v_g\frac{\partial g}{\partial n}(n - n_{\text{th}}) \tag{3.41}$$

The parameter α in (3.41) is an important parameter in semiconductor lasers, known as linewidth enhancement factor or α parameter, and plays a crucial role for laser oscillations. Easily understood from the above equation and the relation of (3.38), the α parameter is defined by

$$\alpha = \frac{\text{Re}[\chi_l]}{\text{Im}[\chi_l]} = -2\frac{\omega}{c}\frac{\frac{\partial\eta}{\partial n}}{\frac{\partial g}{\partial n}} \tag{3.42}$$

where χ_l is the complex electric susceptibility defined in (3.32). The value of linewidth enhancement factor for ordinary lasers, such as gas lasers, is almost equal to zero, while it has a nonzero value for semiconductor lasers and usual

semiconductor lasers have positive values from 3 to 7 (Cook and Nash 1975; Osinski and Buss 1987). This nonzero value of the α parameter gives rise to complex dynamics of semiconductor lasers. The typical feature of semiconductor lasers is a broad linewidth of laser oscillations due to a nonzero α parameter. Therefore, the parameter is also called the linewidth enhancement factor. Indeed, the oscillation linewidth of semiconductor lasers is $1 + \alpha^2$ times larger than those of ordinary lasers (Henry 1982). We will return to this subject in Sect. 3.6.6.

3.3.4 *Laser Rate Equations*

Under operations close to laser threshold, the gain g is linearized for the carrier density

$$g = g_{\text{th}} + \frac{\partial g}{\partial n}(n - n_{\text{th}}) \tag{3.43}$$

where g_{th} is the gain of the medium at the threshold and it has a relation through the carrier density n_0 at the transparency as

$$g_{\text{th}} = \frac{\partial g}{\partial n}(n_{\text{th}} - n_0) \tag{3.44}$$

Under this condition, the gain balances with the loss and $g_0 = a$, where g_0 is the gain at transparency. The gain must exceed this value for laser oscillations. However, the actual gain required for laser oscillations is slightly larger than this value, since photons dissipate from the laser facets. At a laser oscillation well above the threshold, the effect of gain saturation must be taken into account (Nakamura et al. 1978; Lang 1979; Henry 1982). In that case, we use the coefficient of gain saturation ε_s and obtain the relation

$$g = \frac{g_{\text{th}}}{1 + \varepsilon_s |E|^2} \tag{3.45}$$

When the saturation effect is very small (as is often the case and, indeed, the saturation intensity is usually attained at well above the laser threshold), we can approximate the gain as

$$g \approx g_{\text{th}}(1 - \varepsilon_s |E|^2) \tag{3.46}$$

This expression is frequently used in theoretical treatments.

In the following discussion, we use the linearized gain for the formulation of equations assuming that the laser operation is not so far from the laser threshold. If this is not the case, we take into account the gain saturation term of (3.45). From

(3.41) to (3.43), the field equation is a function of the time-dependent carrier density and it is rewritten as

$$\frac{\mathrm{d}E(t)}{\mathrm{d}t} = \frac{1}{2}(1 - i\alpha)G_n\{n(t) - n_{\mathrm{th}}\}E(t) + E_{\mathrm{sp}}(t) \tag{3.47}$$

where we define the linear gain $G_n = v_g \partial g / \partial n$. We must consider the effect of spontaneous emissions of light in laser oscillations. $E_{\mathrm{sp}}(t)$ (dimension of 1/time) is the stochastic function corresponding to the random field for spontaneous emissions. The ensemble average of the product $E^* E_{\mathrm{sp}}$ has the relation as $2\mathrm{Re}\left[\left\langle E^*(t)E_{\mathrm{sp}}(t)\right\rangle\right] = R_{\mathrm{sp}}$. The term R_{sp} is generally used for the effect of spontaneous emission in the photon number equation and is given by Petermann (1988)

$$R_{\mathrm{sp}}(t) = \beta_{\mathrm{sp}}\xi_{\mathrm{sp}}\frac{n(t)}{\tau_s} \tag{3.48}$$

where β_{sp} is the coefficient of spontaneous emissions, ξ_{sp} is the internal quantum efficiency for spontaneous emissions, and τ_s is the carrier lifetime in the laser cavity. An alternative expression for R_{sp} can be obtained by using the Einstein relation that relates the gain spectrum to the spontaneous emission spectrum and, as a result, the $R_{\mathrm{sp}}(\omega)$ is proportional to the mode gain $G_n(\omega)$ (Henry 1986). In fact, E_{sp} contains statistical components and we must take into account the terms in numerical calculations for optical field. The forms of the noise terms suitable for practical numerical calculations will be discussed in Sect. 3.6.3. However, we frequently omitted the term unless necessary since it is usually as small as $\beta_{\mathrm{sp}} \approx 10^{-5}$ (Thompson 1980). Furthermore, when we investigate the fundamental dynamics of instability and chaos in nonlinear systems, we can treat only the deterministic terms without considering statistical noises. Noise is essentially considered as a separate effect from chaotic oscillations in as far as it is small.

Using the notation of the complex field $E(t) = A(t)\exp\{-i\phi(t)\}$, the amplitude $A(t)$ and the phase $\phi(t)$ of the field equation are separately given by

$$\frac{\mathrm{d}A(t)}{\mathrm{d}t} = \frac{1}{2}G_n\{n(t) - n_{\mathrm{th}}\}A(t) \tag{3.49}$$

$$\frac{\mathrm{d}\phi(t)}{\mathrm{d}t} = \frac{1}{2}\alpha G_n\{n(t) - n_{\mathrm{th}}\} \tag{3.50}$$

It should be noted that in this text, the time-dependent harmonic term of the propagating electromagnetic field is defined as $\exp(-i\omega_0 t)$. However, some papers and texts use the notation of $\exp(i\omega_0 t)$ for the propagating term. In that case, the coefficient of the term related to the α parameter in the right-hand side of (3.47) is written by $(1 + i\alpha)$ instead of $(1 - i\alpha)$. Although starting from the different sign of

the equation for the complex field, the amplitude and phase equations result in the same forms as between (3.49) and (3.50).

From the physical model of two-level atoms in semiconductor lasers, the differential equation for the carrier density n, which is equivalent to the population inversion in common lasers is given by Agrawal and Dutta (1993)

$$\frac{\mathrm{d}n(t)}{\mathrm{d}t} = \frac{J}{ed} - \frac{n(t)}{\tau_s} - G_n\{n(t) - n_0\}A^2(t) \tag{3.51}$$

where J is the injection current density and d is the thickness of the active layer. The first term on the right side of the equation is the pumping by the injection current. The second term is the carrier recombination due to spontaneous emissions. In actual, the carrier life time τ_s in the carrier density equation is a function of the carrier density, which is written by

$$\frac{1}{\tau_s} = A_{nr} + Bn + Cn^2 \tag{3.52}$$

where A_{nr} is the nonradiative carrier recombination rate induced by defect and trap, B is the recombination coefficient for spontaneous radiation, and C is the Auger coefficient, which plays an important role for long-wavelength (infrared oscillations) semiconductor lasers. However, we here assume a constant carrier lifetime and the approximation well holds for most case of the dynamic analysis in semiconductor lasers. The third term in (3.51) represents the carrier recombination induced by the laser emission. The photon lifetime and the carrier densities at threshold and transparency have the relation

$$v_g \frac{\partial g}{\partial n}(n_{\mathrm{th}} - n_0) = \frac{1}{\tau_{\mathrm{ph}}} \tag{3.53}$$

In general, Langevin noise should be considered for the carrier density equation, however, it is usually less effect for the laser dynamics due to slower response of carriers compared to that of photons. Therefore, the term is sometimes ignored. The Langevin noise for carriers will also be discussed in Sect. 3.6.

The photon number S inside the laser cavity is derived by the internal optical energy U and defined by the following relation:

$$S = \frac{U}{\hbar\omega} = \frac{\varepsilon_0 \bar{\eta} \eta_e}{2\hbar\omega} \int_{\mathrm{cavity}} \mathrm{d}^3\mathbf{r} |E_{\mathrm{real}}(\mathbf{r})|^2 \tag{3.54}$$

where $\bar{\eta}$ is the refractive index for the mode, $\mathbf{r}$ is the three-dimensional coordinate, and E_{real} is the real optical field inside the cavity. In the derivations of between (3.47) and (3.51), we assume that the field is normalized by the square root of the photon numbers. Assuming that the field inside the laser cavity is constant over the

coordinate at a fixed time, the relation of the photon number S and the real optical field E_{real} is approximated by

$$S = |E|^2 = \frac{\varepsilon_0 \bar{\eta} \eta_e}{2\hbar\omega} |E_{\text{real}}|^2 V \tag{3.55}$$

where V is the volume of the active layer (Agrawal and Dutta 1993). When we write the field amplitude A, it is given by $A = \sqrt{S} = \sqrt{\varepsilon_0 \bar{\eta} \eta_e V / 2\hbar\omega} |E_{\text{real}}|$. Using the internal photon number, the output power outside the laser cavity reads as (Petermann 1988)

$$S_{\text{ext}} = \frac{\xi_{\text{ext}}}{\xi_{\text{int}}} \frac{1}{\tau_{\text{ph}}} S \tag{3.56}$$

where $\xi_{\text{ext}}/\xi_{\text{int}}$ is the ratio between the external and internal differential quantum efficiencies. Normally, a semiconductor laser is fabricated to take different facet reflectivities to obtain a maximum laser power. Assuming the different facet intensity reflectivities R_1 and R_2, the photon number emitted from the facet with the reflectivity R_1 is calculated as follows (Petermann 1988):

$$S_{R_1}^{\text{out}} = \frac{(1 - R_1)\sqrt{R_2}}{(\sqrt{R_1} + \sqrt{R_2})(1 - \sqrt{R_1 R_2})} S_{\text{ext}} \tag{3.57}$$

If the two facets have the same reflectivity, i.e., $R_1 = R_2$, the photon numbers emitted from the facets are $S_{R1}^{\text{out}} = S_{R2}^{\text{out}} = S_{\text{ext}}/2$.

For the sake of easiness of asymptotic studies of the dynamics, the variables and parameters in the rate equations are normalized and the dimensionless equations corresponding to between (3.47) and (3.51) are frequently employed. Using the normalized field and the carrier density as $\tilde{E} = \sqrt{\frac{1}{2}\tau_s G_n} E$ and $\tilde{n} = \frac{\tau_{\text{ph}}}{2} G_n (n - n_{\text{th}})$, with also the normalized time of $\tilde{t} = \frac{t}{\tau_{\text{ph}}}$, the non-dimensional field equation reads as

$$\frac{\mathrm{d}\tilde{E}}{\mathrm{d}\tilde{t}} = (1 - i\alpha)\tilde{n}\tilde{E} \tag{3.58}$$

For the carrier density equation, using a new time constant of $T = \frac{\tau_s}{\tau_{\text{ph}}}$ and a pumping parameter of $P = \frac{\tau_s \tau_{\text{ph}} G_n}{2ed} (J - J_{\text{th}})$, it is given by

$$T \frac{\mathrm{d}\tilde{n}}{\mathrm{d}\tilde{t}} = P - \tilde{n} - (2\tilde{n} + 1)|\tilde{E}|^2 \tag{3.59}$$

When the condition of $n_{\text{th}} \gg n_0$ holds for the carrier densities (which corresponds to a case of large mirror losses), the pump parameter is approximated as $P = \frac{\tau_{\text{ph}} G_n n_{\text{th}}}{2} \frac{J - J_{\text{th}}}{J_{\text{th}}} = \frac{1 + \tau_{\text{ph}} G_n n_0}{2} \frac{J - J_{\text{th}}}{J_{\text{th}}} \approx \frac{J - J_{\text{th}}}{2J_{\text{th}}}$. The notations of the above two equations are sometimes used for studying the dynamics and analyzing theoretically stability and instability conditions for laser operations.

As described in Sect. 3.2.1, the gain in actual lasers must be multiplied by a factor less than unity (confinement factor Γ_T) and the effect must be taken into consideration for numerical simulations of semiconductor lasers (Botez 1981). The detailed discussion of the confinement factor can be found in the book by Agrawal and Dutta (1993). When the effects of statistical noises induced by spontaneous emission of light are important for laser oscillations, the Langevin terms are generally added not only to (3.47) but also to (3.51). Since semiconductor laser is a class B laser, we need not consider the differential equation for the polarization of matter. The polarization is included through the relation $P = \varepsilon_0 \chi E$ in (3.47). However, the laser is described by the three equations for the field amplitude in (3.49), the phase in (3.50), and the population inversion (the carrier density) in (3.51). A nonlinear system described by three coupled differential equations is a candidate for a chaotic system. The semiconductor laser is described by three equations, but the phase does not affect the other rate equations. Therefore, the two equations, the field and carrier density equations, are enough to describe the operation of narrow-stripe edge-emitting semiconductor lasers and, thus, they are stable lasers at solitary oscillation. We did not consider the carrier diffusion from the active layer in the carrier density equation. We need not take into account this effect for ordinary narrow-stripe edge-emitting semiconductor lasers, because the stripe width of the active region is small enough (~ 3 μm). However, it plays an important role for the dynamics in VCSELs and broad-area lasers. For those lasers, the terms for carrier diffusion are included in the laser rate equations and the laser dynamics are greatly affected by the non-negligible finite stripe size. The effects will be discussed in Chap. 8.

3.4 Optical Gain

Semiconductor laser has a broad gain compared to other lasers. Further, the dynamics are strongly affected by the coupling between the real and imaginary parts of the complex susceptibility of the medium as already discussed in the previous section. Also the variation of the refractive index of the medium brings the change of the gain. As a result, the laser has a high gain at higher optical frequency after the lasing oscillation. However, with the increase of injection current below threshold, the oscillation frequency tends to decrease and it is red-shifted due to the increase of the carrier number and the increase of the temperature (free plasma effects) in the medium. After the lasing, the carrier is saturated and the effect of the temperature becomes dominant. Therefore, the gain profile become constant and the oscillation frequency is governed by the temperature. The gain profile as a function of the oscillation frequency is very important to understand the physical background of the dynamics of semiconductor lasers, since the shape of the gain profile is not symmetric viewing from the frequency at the maximum gain. In the following, we will formulate the optical gain in semiconductor lasers in relation to the laser oscillation frequency.

The optical gain can be derived from the theory for the density matrices of electrons based on the quantum electronics (Agrawal and Dutta 1993). However, we here derive the form from the semi-classical theory, which is easy to understand intuitively (Yariv and Poch 2007). The imaginary part of the susceptibility χ'' of semiconductor materials is related to the optical gain in laser oscillations. Assuming Lorentzian spectrum for emission of light, the susceptibility χ'' is calculated from transition of electrons in the medium and is given by (Yariv and Poch 2007)

$$\chi''(\omega) = \frac{\lambda_0^3}{8\pi^2 \eta_b \tau_{\mathrm{sp}}} \frac{T_2}{1 + (\omega - \omega_0)^2 T_2^2} (n_1 - n_2) \tag{3.60}$$

where τ_{sp} is the lifetime of spontaneous emission of light, η_b is the refractive index of the medium defined in (3.33), η_0 is the center oscillation angular frequency of radiation, T_2 is the mean lifetime for coherent interaction of electrons with a monochromatic field, and n_2 and n_1 are the densities of electron populations in upper and lower states. T_2 is very fast and is usually the order of $\sim 10^{12}$ ps. Then, from (3.37), the optical gain under laser oscillation is written as

$$g(\omega) = -\frac{k_0}{\eta_b} \chi''(\omega) = \frac{\lambda_0^2}{4\eta_b^2 \tau_{\mathrm{sp}}} \frac{T_2}{\pi \left\{ 1 + (\omega - \omega_0)^2 T_2^2 \right\}} (n_2 - n_1) \tag{3.61}$$

Next, we consider a transition of electron from level "a" in the conduction band to "b" in the valence band. Concerning to a transition of electron states (either induced or spontaneous) interested in ordinary semiconductor lasers, the two states must have the same **k** vector. The transition probability $R_{\mathrm{a}\to\mathrm{b}}$ is related to the probability functions $f_{\mathrm{c}}(E_{\mathrm{a}})$ and $f_{\mathrm{v}}(E_{\mathrm{b}})$ as $R_{\mathrm{a}\to\mathrm{b}} \propto f_{\mathrm{c}}(E_{\mathrm{a}})\{1 - f_{\mathrm{v}}(E_{\mathrm{b}})\}$, where $f_{\mathrm{c}}(E_{\mathrm{a}})$ is an probability that the upper state (conduction band) is occupied by an electron, while $f_{\mathrm{v}}(E_{\mathrm{b}})$ is that for the lower state (valence band). Note that we use "*E*" for an energy in this section and it is not for optical field according to the traditional notation. The transition probabilities are given by

$$f_{\mathrm{c}}(E_{\mathrm{a}}) = \frac{1}{\exp\left(\frac{E_{\mathrm{a}} - E_{\mathrm{Fc}}}{k_{\mathrm{B}} T}\right) + 1} \tag{3.62a}$$

$$f_{\mathrm{v}}(E_{\mathrm{b}}) = \frac{1}{\exp\left(\frac{E_{\mathrm{b}} - E_{\mathrm{Fv}}}{k_{\mathrm{B}} T}\right) + 1} \tag{3.62b}$$

where E_{Fc} and E_{Fv} are the conduction-band and valence-band quasi-Fermi levels, respectively, k_{B} is the Boltzmann constant, and T is the temperature. In very highly doped semiconductor lasers, quasi-Fermi levels E_{Fc} and E_{Fv} are not equal and the Fermi level is forced either into the conduction band or into the valence band. Also the quasi-Fermi level is a function of the carrier density.

To obtain the optical gain, we need to calculate the densities of electrons in the upper and lower states. For the number of quantum state, $\rho(k)$, within a spherical shell of radial thickness dk and radius k in k space, the number state is given by the following relation:

$$\rho(k)\mathrm{d}k = 2 \cdot \frac{2\pi k^2 \mathrm{d}k}{\Delta V_k} = \frac{kV}{\pi^2}\mathrm{d}k \tag{3.63}$$

where $\Delta V_k = (2\pi)^3/V$ and V is the volume of the medium. A factor 2 for spin is introduced to account for the fact that each given electron can accommodate up- or down-spin state. As for the electron density n, we obtain the following relation between the numbers of the electron states in k and E spaces:

$$n = \frac{1}{V}\rho(k)\mathrm{d}k = \rho(E)\mathrm{d}E \tag{3.64}$$

Then, the population inversion density $n_2 - n_1$ is replaced by the effective inversion due to electrons and holes within dk as

$$\begin{aligned} n_2 - n_1 &= \frac{1}{V}\rho(r)\mathrm{d}k[f_\mathrm{c}(E_\mathrm{a})\{1 - f_\mathrm{v}(E_\mathrm{b})\} - f_\mathrm{v}(E_\mathrm{b})\{1 - f_\mathrm{c}(E_\mathrm{a})\}] \\ &= \frac{1}{V}\rho(r)\mathrm{d}k\{f_\mathrm{c}(E_\mathrm{a}) - f_\mathrm{v}(E_\mathrm{b})\} \end{aligned} \tag{3.65}$$

Form (3.61) to (3.62), the optical gain d$g(\omega_0)$ of stimulated emission due to electrons and holes within range [k, k + dk] is written by

$$\mathrm{d}g(\omega_0) = \frac{\lambda_0^2}{4\eta_b^2\tau_\mathrm{sp}} \frac{T_2}{\pi\left\{1 + (\omega - \omega_0)^2 T_2^2\right\}} \frac{f_\mathrm{c} - f_\mathrm{v}}{V}\rho(k)\mathrm{d}k \tag{3.66}$$

Then, the net gain is given by the integral over the whole k space. The energy of electron is given by

$$E(k) = \frac{\hbar^2 k^2}{2m} \tag{3.67}$$

where m is the reduced effective mass of an electron. Defining the transition energy from a to b as $E_\mathrm{a} - E_\mathrm{b} = \hbar\omega$, we obtain

$$\hbar\omega = E_\mathrm{g} + \frac{\hbar^2 k^2}{2m_\mathrm{c}} + \frac{\hbar^2 k^2}{2m_\mathrm{v}} = E_\mathrm{g} + \frac{\hbar^2 k^2}{2m_r} \tag{3.68}$$

where E_g is the gap energy between the conduction and valence bands, and m_c and m_v are the effective masses in the conduction and valence bands, respectively.

$1/m_r = 1/m_v + 1/m_c$ is the reduced effective mass. Using these results, we obtain the transform relations from k to ω space as

$$d\omega = \frac{\hbar}{m_r} k dk \tag{3.69a}$$

$$k = \sqrt{\hbar\omega - E_g}\left(\frac{2m_r}{\hbar^2}\right) \tag{3.69b}$$

As a result, integrating over ω in (3.66), we finally obtain the optical gain as

$$g(\omega_0) = \frac{m_r \lambda_0^2}{4\eta_b^2 \pi^2 \hbar \tau_{sp}} \sqrt{\frac{2m_r}{\hbar}} \int_0^\infty \sqrt{\hbar\omega - E_g}\{f_c(\omega) - f_v(\omega)\} \frac{T_2}{\pi\{1 + (\omega - \omega_0)^2 T_2^2\}} d\omega \tag{3.70}$$

Since quasi-Fermi levels E_{Fc} and E_{Fv} are functions of the carrier injection rate (injection current), one need to obtain the relation between the Fermi level and the carrier injection rate for the numerical calculation in (3.70). Electrons are excited by injection current I to the conduction band and relax to the valence band with a lifetime of τ_s. At that time, the electron density n_c has the relation as

$$\frac{n_c}{\tau_s} = \frac{I}{eV} \tag{3.71}$$

where V is the confined volume of electrons. Using the relations of between (3.62a) and (3.64), and substituting them into (3.70), the carrier density is given by

$$n_c = \frac{I\tau_s}{eV} = \int_0^\infty \rho_c(E) f_c(E) dE = \frac{1}{2\pi^2}\left(\frac{2m_c}{\hbar^2}\right)^2 \int_0^\infty \frac{\sqrt{E}}{\exp\left(\frac{E - E_{Fc}}{k_B T}\right) + 1} dE \tag{3.72}$$

The density $\rho_c(E)$ was calculated from (3.64) to (3.67) to be

$$\rho_c(E) = \frac{1}{2\pi^2}\left(\frac{2m_c}{\hbar^2}\right)^{3/2} \sqrt{E} \tag{3.73}$$

For a given value of carrier density n_c, the quasi-Fermi level E_{Fc} can be numerically calculated form (3.72). For example, when $T \to 0$, the integral is replaced by $(2/3)E_F^{3/2}$ and E_{Fc} is explicitly given by a function of n_c as

$$E_{Fc} = (3\pi^2)^{2/3} \frac{\hbar^2}{2m_c} n_c^{2/3} \tag{3.74}$$

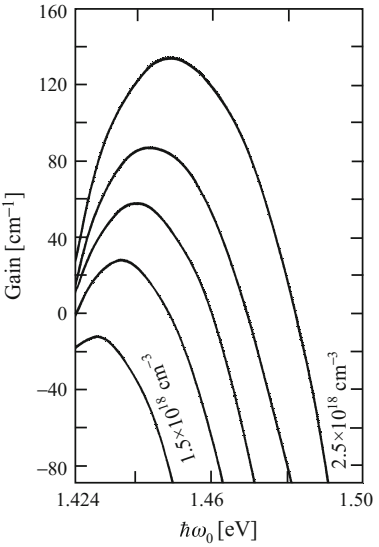

Fig. 3.2 Calculated gain spectrum for a GaAs medium at several excitations of the carrier density from 1.50×10^{18} cm^{-3} to 2.50×10^{18} cm^{-3} at $m_c = 0.67\ m_e$ (m_e is electron mass), $m_v = 0.48\ m_e$, $T_2 = 0.5$ ps, $\tau_s = 3 \times 10^{-9}$ s, and $E_g = 1.43$ eV. Note that the minimum density to achieve transparency is $N_0 \sim 1.55 \times 10^{18}$ cm^{-3} [after Vahala et al. 1983; ©1983 AIP]

For highly injected carrier, the density of holes in the valence band is almost equal to that of electrons in the conduction band. Then, the quasi-Fermi level E_{Fv} is calculated from the same equation by replacing the effective mass from m_c to m_v. Form the calculated quasi-Fermi levels E_{Fc} and E_{Fv}, the optical gain in (3.70) can be numerically calculated for the change of the injection current (carrier density). Figure 3.2 is an example of the optical gain calculated from (3.70) for different values of the carrier injection (Vahala et al. 1983b). It is important to note that the gain profile has an asymmetric profile for the optical frequency (or optical wavelength), which produces a rich variety of dynamics like chaos in semiconductor lasers.

3.5 Linear Stability Analysis and Relaxation Oscillation

3.5.1 Linear Stability Analysis

We have already introduced linear stability analysis for a steady-state laser operation in Sect. 2.2.2 and discussed the stability of laser for small perturbations. Here, we apply the method to semiconductor lasers (Ikegami and Suematsu 1967; Paoli and Ripper 1970; Arnold et al. 1982; Tucker 1985). From (3.49) to (3.51), we summarize the rate equations for the field amplitude, the phase, and the carrier density as follows:

$$\frac{\mathrm{d}A(t)}{\mathrm{d}t} = \frac{1}{2} G_n \{n(t) - n_{\mathrm{th}}\} A(t) \tag{3.75}$$

$$\frac{\mathrm{d}\phi(t)}{\mathrm{d}t} = \frac{1}{2} \alpha G_n \{n(t) - n_{\mathrm{th}}\} \tag{3.76}$$

$$\frac{\mathrm{d}n(t)}{\mathrm{d}t} = \frac{J}{ed} - \frac{n(t)}{\tau_s} - G_n \{n(t) - n_0\} A^2(t) \tag{3.77}$$

Setting the differential terms of the above equations to zero, we obtain the steady-state solutions for the field amplitude A_s, the phase ϕ_s, and the carrier density n_s

$$A_s^2 = \tau_{\mathrm{ph}} \left(\frac{J}{ed} - \frac{n_{\mathrm{th}}}{\tau_s} \right) \tag{3.78}$$

$$\phi_s = 0 \tag{3.79}$$

$$n_s = n_{\mathrm{th}} \tag{3.80}$$

For a small perturbation δx, we write the variable as $x(t) = x_s + \delta x(t)$ ($x = A$, ϕ, n), then, we can calculate the differential equations for the perturbations as

$$\frac{\mathrm{d}\delta A(t)}{\mathrm{d}t} = \frac{1}{2} G_n A_s \delta n(t) \tag{3.81}$$

$$\frac{\mathrm{d}\delta \phi(t)}{\mathrm{d}t} = \frac{1}{2} \alpha G_n \delta n(t) \tag{3.82}$$

$$\frac{\mathrm{d}\delta n(t)}{\mathrm{d}t} = -\frac{2A_s}{\tau_{\mathrm{ph}}} \delta A(t) - \left(\frac{1}{\tau_s} + G_n A_s^2 \right) \delta n(t) \tag{3.83}$$

where we neglect the second order small infinities in the same manner as in Sect. 2.2.2. As the condition for non-trivial solutions of the above equations, the determinant of the coefficient matrix in the differential equations must have the following equality:

$$\begin{vmatrix} \gamma & 0 & -\frac{1}{2} G_n A_s \\ 0 & \gamma & -\frac{1}{2} \alpha G_n \\ \frac{2A_s}{\tau_{\mathrm{ph}}} & 0 & \gamma + \frac{1}{\tau_s} + G_n A_s^2 \end{vmatrix} = 0 \tag{3.84}$$

γ is the solution of the following characteristic equation:

$$\gamma \left\{ \gamma^2 + \left(\frac{1}{\tau_s} + G_n A_s^2 \right) \gamma + \frac{G_n A_s^2}{\tau_{\mathrm{ph}}} \right\} = 0 \tag{3.85}$$

By solving the equation, we can discuss stability and instability of semiconductor lasers.

3.5.2 Relaxation Oscillation

We do not consider the trivial solution $\gamma = 0$ in (3.85). The other two solutions are easily calculated by putting the real and imaginary parts of the solutions as $\gamma = \Gamma_R + i\omega_R$. Then, we obtain a solution which satisfies the physical condition.

$$\Gamma_R = -\frac{1}{2}\left(G_n A_s^2 + \frac{1}{\tau_s}\right) \tag{3.86}$$

$$\omega_R = \sqrt{\frac{G_n A_s^2}{\tau_{ph}} - \Gamma_R^2} \tag{3.87}$$

Since the value of the real part Γ_R is negative, the laser oscillation corresponding to this solution quickly decays out even once it is excited. Therefore, the laser does not become unstable even in the presence of relaxation oscillation. This oscillation is called relaxation oscillation and the frequency $\nu_R = \omega_R/2\pi$ is known as the relaxation oscillation frequency. For a low laser output power, the relation $\Gamma_R^2 \ll G_n A_s^2/\tau_{ph}$ holds, and then the relaxation oscillation frequency is approximated as $\nu_R = \sqrt{G_n A_s^2/\tau_{ph}}/2\pi$.

Relaxation oscillation in a semiconductor laser occurs because the carrier cannot follow the photon decay rate. A relaxation oscillation is easily excited by a step input to the injection current, a shot noise originating from the driving circuit, or perturbations such as small external optical feedback. These relaxation oscillations smoothly decay out as long as the disturbances are small enough. The relaxation oscillation frequency of ordinary semiconductor lasers is of the order of 1–10 GHz. Only a few specific lasers have a relaxation oscillation frequency over 10 GHz. The relaxation oscillation frequency is a measure of the maximum modulation ability in semiconductor lasers through the injection current. Above the relaxation oscillation, the modulation efficiency is greatly degraded and intensity modulation through the injection current becomes difficult. Therefore, an external intensity modulator, such as an electro-optic (EO) modulator is usually used for a high-speed signal modulation over 10 GHz.

When the laser oscillates not so far from the threshold, the photon number at the steady state is calculated from (3.78) and is given by

$$S = \frac{\tau_{ph}}{ed}(J - J_{th}) \tag{3.88}$$

where $J_{th} = edn_{th}/\tau_s$ is the threshold current. The relaxation oscillation frequency is also written by

$$\nu_R = \frac{1}{2\pi}\sqrt{\frac{G_n}{ed}(J - J_{th})} \tag{3.89}$$

The presence of the relaxation oscillation in semiconductor lasers gives rise to complex dynamics when the laser is constantly perturbed by external disturbances as discussed in the following chapters. For example, for a moderate amount of optical feedback from an external mirror to a semiconductor laser, the relaxation oscillation does not damp out and the laser shows various dynamic behaviors, not only simple sinusoidal oscillations but also chaotic oscillations. Figure 3.3 shows the example of calculated relaxation oscillations for a step input to the injection current. The actual laser oscillates at multimode lines close to the threshold but it recovers single mode oscillation well above the threshold (Marcuse and Lee 1983). We discuss single mode semiconductor lasers in this chapter, but the model used in Fig. 3.3 is a multimode operation, which will be discussed in Chap. 8. The numerical simulation reflects the fact and the relaxation oscillations for the main and sub-modes start when the carrier density exceeds the threshold. However, for a big enough pump, the relaxation oscillations rapidly decay out and the constant laser oscillation is achieved.

In the following, we derive a useful expression to understand the origin of the relaxation oscillation frequency. We introduce here an injection current at carrier

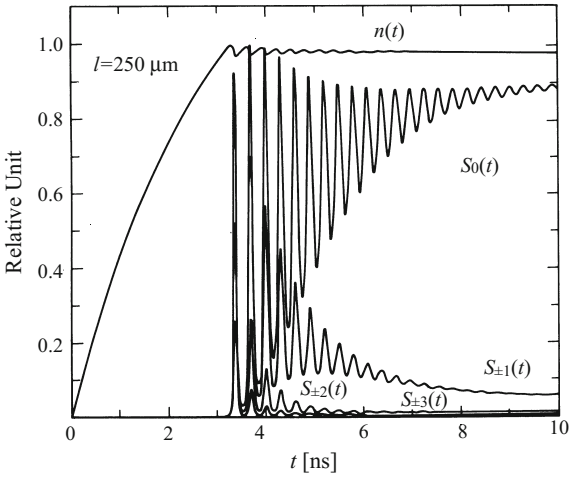

Fig. 3.3 Time evolution of the carrier density n and the photon population S under relaxation oscillations [after Marcuse and Lee (1983); © (1983) IEEE]

transparency as $J_0 = edn_0/\tau_s$. From the relation of equation in (3.53) together with the relation of $J_{\text{th}} = edn_{\text{th}}/\tau_s$, the gain coefficient can be expressed as

$$G_n = \frac{ed}{\tau_s \tau_{\text{ph}} (J_{\text{th}} - J_0)} \tag{3.90}$$

Substituting the above equation into (3.89), one obtains the relaxation oscillation frequency using carrier and photon lifetimes as

$$\nu_{\text{R}} = \frac{1}{2\pi} \sqrt{\frac{1}{\tau_s \tau_{\text{ph}}} \frac{J - J_{\text{th}}}{J_{\text{th}} - J_0}} \tag{3.91}$$

Namely, the relaxation oscillation frequency can be determined by only the carrier and photon lifetimes once the bias injection current is given. The above equation shows that the relaxation oscillation frequency ν_{R} is proportional to $\tau_{\text{ph}}^{-1}(\tau_s/\tau_{\text{ph}})^{-1/2}$. Thus, a laser with a faster time constant of the carrier relaxation has a higher modulation bandwidth, which is quite consistent with the physical meaning of the origin of the relaxation oscillation frequency in semiconductor lasers. Similarly, substituting between (3.88) and (3.90) into (3.91), the damping factor is written by

$$\Gamma_{\text{R}} = -\frac{1}{2\tau_s} \frac{J - J_0}{J_{\text{th}} - J_0} \tag{3.92}$$

Namely, the damping factor is only given by the carrier lifetime for a fixed bias injection current.

In real lasers, we could not ignore the effects of spontaneous emissions. Further, gain saturation effects are encountered in laser oscillations. In such a case, the relaxation oscillation angular frequency is given by almost the same form as (3.87), but we need some modifications for the damping factor (Yoon et al. 1989). In that case, instead of (3.86), the damping factor is given by

$$\Gamma'_{\text{R}} = -\frac{1}{2} \left\{ \frac{1}{\tau_s} + G_n A_s^2 + \frac{1}{\tau_{\text{ph}}} \left(\varepsilon_s G_n \tau_s A_s^2 + \beta_{\text{sp}} \frac{G_n \tau_{\text{ph}} n_0 + 1}{G_n \tau_s A_s^2} \right) \right\} \tag{3.93}$$

Both the gain saturation and the spontaneous emission increase the damping rate. The effect of gain saturation is usually small and it is only remarkable at very high laser power. As for the effect of spontaneous emission, the damping rate is much enhanced at lower laser power and, thus, it is remarkable for a lower injection current close to the laser threshold. At a higher pump, the effect of spontaneous emission noise on the damping oscillation becomes small and the intrinsic effect of the power dependence (the term $G_n A_s^2$) prevails.

3.6 Langevin Noises

3.6.1 Rate Equations Including Langevin Noises

Langevin noises are defined for the photon number in laser oscillations. Since the differential equation for the field in (3.49) is obtained from an approximation of SVEA and the field amplitude is equivalent to the square root of the photon number $A(t) \propto \sqrt{S(t)}$, we can write the rate equations for the photon number S, the phase ϕ, and the carrier density n. The rate equations including the effects of spontaneous emission and statistical Langevin noises are given by

$$\frac{\mathrm{d}S(t)}{\mathrm{d}t} = [G_n\{n(t) - n_{\mathrm{th}}\}]S(t) + R_{\mathrm{sp}}(t) + F_S(t) \tag{3.94}$$

$$\frac{\mathrm{d}\varphi(t)}{\mathrm{d}t} = \frac{1}{2}\alpha G_n\{n(t) - n_{\mathrm{th}}\} + F_\varphi(t) \tag{3.95}$$

$$\frac{\mathrm{d}n(t)}{\mathrm{d}t} = \frac{J(t)}{ed} - \frac{n(t)}{\tau_s} - G_n\{n(t) - n_0\}S(t) + F_n(t) \tag{3.96}$$

where R_{sp} is the spontaneous emission term introduced in (3.48). The injection current may be a function of time through, e.g., a direct injection current modulation, therefore it is explicitly written by a time-dependent function. The final term of each equation, $F_S(t)$, $F_\phi(t)$, and $F_n(t)$, is the effect of statistical Langevin noises (Risken 1996). As already mentioned, the terms may be omitted to calculate pure dynamics of chaos in semiconductor lasers. Again, note that the phase equation is not coupled with the other equations and the system still behaves stably even though it is described by three differential equations. Namely, the time development of phase does not affect the field amplitude and the carrier density. On the other hand, the field and the carrier density couples with each other. The effects of Langevin noises have been discussed in relation to AM and FM noises in laser modulations (McCmber 1966; Haug 1969; Henry 1982, 1983; Yamamoto 1983; Vahala and Yariv 1983a, b).

3.6.2 Langevin Noises

Real lasers include statistical Langevin noises and they are important to evaluate the performance of practical systems using semiconductor lasers as light sources. Langevin noises have common features observed not only in semiconductor lasers but also in all other lasers and they are formulated as the same equations (Risken 1996). Noises also sometimes trigger unstable oscillations in semiconductor lasers. In this subsection, we discuss the performance of semiconductor lasers induced by

Langevin noises. The Langevin terms $F_S(t)$ and $F_\phi(t)$ are random noises induced by the quantum effects of spontaneous emission of light and the term $F_n(t)$ is induced by a noise originated by random carrier generation and recombination. They all originate from random shot noise effects. Since the effect of the carrier noise, $F_n(t)$, is negligible compared with that of $F_S(t)$, the term is sometimes omitted even when we consider the effects induced by Langevin noises in semiconductor lasers. Langevin noises have been extensively studied in detail (Lax 1960; McCmber 1966; Lax and Louisell 1969; Haug 1969; Saleh 1978; Yamamoto 1983; Henry 1986). We need statistical methods to investigate the characteristics and effects of Langevin noises. We consider Langevin noises obeying the Markov process and assume that the correlation times of the noises are much less than the photon lifetime τ_{ph} and the carrier lifetime τ_s. We briefly show the derivations of the statistical noises and summarize them. In the rate equations from (3.84) to (3.86), denoting each Langevin noise term by $F_i(t)$ ($i = S$, ϕ, and n), the noise is a zero mean and the average is written by

$$\langle F_i(t) \rangle = 0 \tag{3.97}$$

We assume that the noise is like a shot noise and the correlation time is short enough, then, we obtain the correlation between the two Langevin noises

$$\left\langle F_i(t) F_j(t') \right\rangle = 2D_{ij}\delta(t - t') \tag{3.98}$$

where D_{ij} is the diffusion coefficient for the differential diffusion equation in the presence of the Langevin force.

Since the explicit form of the diffusion coefficient D_{ij} is not easy to derive, we only show the procedure for the derivations. At first, we use the fact that the power spectrum is calculated by the Fourier transform relation with the correlation function and that it is equivalent to the correlation. For a differential equation of a variable $v(t)$ with a time-dependent statistical force $F(t)$ (Langevin force)

$$\frac{\mathrm{d}v(t)}{\mathrm{d}t} + \gamma v(t) = F(t) \tag{3.99}$$

the average of the power spectrum $\Phi(\omega)$ is calculated from the Fourier transform of its correlation function of $F(t)$ as

$$\Phi(\omega) = \int_{-\infty}^{\infty} \langle F(t)F(t') \rangle \exp\{-i\omega(t - t')\} \mathrm{d}(t - t') = 2D \tag{3.100}$$

where D is the diffusion coefficient of the correlation function. To derive the power spectra for the Langevin noises, we first calculate the Fourier transforms of the rate (3.94)–(3.96). Then, we take the ensemble averages for the equations to obtain the averaged power spectra. The detailed statistical processes of the photon number and

the carrier are different from each other and obey non-correlated quantum processes like shot noises. However, we assume Poisson random processes for them and calculate the averages, i.e., the statistical average is equal to the squared average. Calculating the correlation coefficient around the steady-state solution in each differential equation, we obtain the following relations for the coefficients (Henry 1986):

$$D_{SS} = R_{\mathrm{sp}} S \tag{3.101a}$$

$$D_{\phi\phi} = \frac{R_{\mathrm{sp}}}{4S} \tag{3.101b}$$

$$D_{nn} = R_{\mathrm{sp}} S + \frac{n}{\tau_s} \tag{3.101c}$$

$$D_{S\phi} = 0 \tag{3.101d}$$

$$D_{Sn} = -R_{\mathrm{sp}} S \tag{3.101e}$$

$$D_{n\phi} = 0 \tag{3.101f}$$

The effects of Langevin noises are mainly generated by spontaneous emission and the effect of noise originating from carrier recombination is much smaller than that from spontaneous emission. Therefore, the noise due to carrier recombination is sometimes neglected in numerical simulations for the effects of noises in semiconductor lasers.

3.6.3 *Implementation of Noise Terms for Numerical Calculations*

In order to numerically investigate the effects of noises on the chaotic dynamics in semiconductor lasers, the spontaneous noise must be generated within a computer. Furthermore, numerical calculation without the terms sometimes fails when the calculation is trapped into an infinitely small value of the field amplitude. Since the Langevin noises are defined for photon number as discussed in the preceding subsections, we need the forms of the terms suitable for the numerical calculations in the field equation. In the following, we derive noise terms, which can be applied to the field equation, however, it is noted that the derivation is mathematically not precise and the obtained results are fairly rough estimates. From (3.47) to (3.94), the spontaneous noise in the photon number equation is given by

$$R_{\mathrm{sp}}(t) + F_S(t) = 2\mathrm{Re}[E^*(t) E_{\mathrm{sp}}(t)] \tag{3.102}$$

where R_{sp} is a DC term of spontaneous emissions given by (3.48) and F_S corresponds to a statistical AC term with zero-mean variable. E_{sp} is considered as a white

noise process with a Gaussian probability distribution. For numerical modeling, E_{sp} is considered as constant for a short time slot $\Delta t = t_{i+1} - t_i$. Δt corresponds to a time step for numerical calculations for solving the differential equations on a computer. With such a time slot, the product of $E^* E_{sp}$ is written as (Schunk and Petermann 1986; Petermann 1988)

$$\begin{aligned} E^*(t)E_{sp}(t) &= \{E^*(t) - E^*(t_i)\}E_{sp}(t) + E^*(t_i)E_{sp}(t) \\ &= \Delta E^*(t)E_{sp}(t) + E^*(t_i)E_{sp}(t) \\ &\approx \langle \Delta E^*(t)E_{sp}(t)\rangle + E^*(t_i)E_{sp}(t) \end{aligned} \tag{3.103}$$

Since E_{sp} is approximated as a zero-mean variable and is independent from the preceding time slot, the second term in (3.103) is a zero-mean value, whereas the first term exhibits a mean value different from zero. The first DC term is small enough compared to the second term, so that the term for $\Delta E^* E_{sp}$ can be replaced by its mean value with good approximation.

In fact, the field E_{sp} contains a DC component, however, this term has a very small quantity. So, for the moment, we consider the dominant AC component of the field. Noting that the starting differential equations are all defined for the photon number and E_{sp} is expressed by white Gaussian random process, the stochastic field, E_{sp}, can be approximately defined by

$$E_{sp}(t) \approx \sqrt{\frac{A}{\Delta t}}(x_r + ix_i) \tag{3.104}$$

where x_r and x_i are independent Gaussian random variables with unit variance for any time slot of width Δt and A is a certain real constant for a given time slot. Meanwhile, the following relation is held from (3.102) to (3.103) as

$$R_{sp}(t) = 2\,\mathrm{Re}[\langle \Delta E^*(t)E_{sp}(t)\rangle] \tag{3.105}$$

For a sufficiently short time Δt, the increment or decrement of ΔE is almost equal to E_{sp}, namely $\mathrm{d}(\Delta E)/\mathrm{d}t \approx E_{sp}$, then we obtain $\Delta E(t) \approx tE_{sp}$. Using this result and (3.105), the ensemble average of $\Delta E^* E_{sp}$ is calculated to be

$$\langle \Delta E^*(t)E_{sp}(t)\rangle = \frac{1}{\Delta t}\int_0^{\Delta t} \Delta E^*(t)E_{sp}(t)\mathrm{d}t = A = \frac{R_{sp}}{2} \tag{3.106}$$

Expressing the field by the photon number S and the phase ϕ as $E = \sqrt{S}\exp(-i\phi)$, (3.103) is finally given by

$$E^*(t)E_{sp}(t) = \frac{R_{sp}(t)}{2} + \sqrt{\frac{S(t_i)R_{sp}(t)}{2\Delta t}}(\xi_E + i\xi_\varphi) \tag{3.107}$$

where ξ_E and ξ_ϕ represent Gaussian random variables defined by x_r, x_i, and ϕ, and they are still uncorrelated zero-mean and unit-variance variables.

From the above discussion, we obtain a useful expression for the noise terms to calculate the field equation (Kallimani and O'Mahony 1998)

$$E_{sp}(t) = \frac{1}{2}\frac{E(t)}{S(t)}R_{sp}(t) + \frac{E(t)}{\sqrt{S(t)}}\sqrt{\frac{R_{sp}(t)}{2\Delta t}}(\xi_E + i\xi_\phi) \tag{3.108}$$

In the above equation, the second term excepting for the statistical variables is very large compared to the first term as expected. It is again noted that the noise term E_{sp} for the field equation has a unit of 1/time. Using (3.108), the statistical noise terms for the photon number and optical phase are given by

$$F_S(t) = \sqrt{\frac{2S(t)R_{sp}(t)}{\Delta t}}\xi_E \tag{3.109a}$$

$$F_\phi(t) = \frac{1}{S(t)}\sqrt{\frac{2R_{sp}(t)}{\Delta t}}\xi_\phi \tag{3.109b}$$

Taking into account (3.101c) and the fact that spontaneous emission is induced by carrier transition, the statistical term F_n of the carrier density equation in (3.96) is given by

$$F_n(t) = -\sqrt{\frac{2S(t)R_{sp}(t)}{\Delta t}}\xi_E + \sqrt{\frac{2n(t)}{\tau_s \Delta t}}\xi_n \tag{3.110}$$

Again, ξ_n is a zero-mean, unit-variance Gaussian distribution. As already discussed, the noises play important roles in the dynamics of semiconductor lasers. Particularly, noises for the field or the photon number are very important, since the timescale of the photon decay is very fast compared with that of the carrier decay and the laser is very sensitive to photon noises.

3.6.4 Noise Spectrum

Statistical noise characteristics of semiconductor lasers are investigated from the rate equations with Langevin noises. Here, we calculate the characteristics of intensity and phase noises from the rate equations by applying linear stability analysis. For the steady-state variables, we introduce small perturbations and linearize the rate equations. Then, we obtain the differential equations for the perturbations in the presence of Langevin noises

$$\frac{\mathrm{d}\delta S(t)}{\mathrm{d}t} = G_n A_s^2 \delta n(t) + F_S(t) \tag{3.111}$$

$$\frac{\mathrm{d}\delta \phi(t)}{\mathrm{d}t} = \frac{1}{2}\alpha G_n \delta n(t) + F_\phi(t) \tag{3.112}$$

$$\frac{\mathrm{d}\delta n(t)}{\mathrm{d}t} = -\left(\frac{1}{\tau_s} + G_n A_s^2\right)\delta n(t) - \frac{1}{\tau_{\mathrm{ph}}}\delta S(t) + F_n(t) \tag{3.113}$$

Due to the noises, the phase is not constant for the time development, which gives rise to unstable oscillations and sometimes induces instability and chaos in semiconductor lasers. We neglected the gain saturation and photons generated by spontaneous emissions such as small quantities. The noise characteristics are represented by using the Fourier components of the perturbations S, $\delta\phi$, and δn, then the corresponding Fourier components $\delta\tilde{S}$, $\delta\tilde{\phi}$, and $\delta\tilde{n}$ are calculated to be

$$\delta\tilde{S}(\omega) = \frac{(1/\tau_s + G_n A_s^2 + i\omega)\tilde{F}_S(\omega) + G_n A_s^2 \tilde{F}_n(\omega)}{(\omega_{\mathrm{R}} + \omega + i\Gamma_{\mathrm{R}})(\omega_{\mathrm{R}} - \omega - i\Gamma_{\mathrm{R}})} \tag{3.114}$$

$$\delta\tilde{\phi}(\omega) = \frac{1}{i\omega}\left\{\frac{1}{2}\alpha G_n \delta\tilde{n}(\omega) + \tilde{F}_\phi(\omega)\right\} \tag{3.115}$$

$$\delta\tilde{n}(\omega) = \frac{i\omega\tilde{F}_n(\omega) - \tilde{F}_S(\omega)/\tau_{\mathrm{ph}}}{(\omega_{\mathrm{R}} + \omega + i\Gamma_{\mathrm{R}})(\omega_{\mathrm{R}} - \omega - i\Gamma_{\mathrm{R}})} \tag{3.116}$$

where ω_{R} and Γ_{R} are the angular frequency of the relaxation oscillation and the damping coefficient as discussed before, respectively. From these equations, the noises are much enhanced at the angular frequency equal to the relaxation oscillation, $\omega = \omega_{\mathrm{R}}$. In real lasers, it is sometimes difficult to apply the linear stability analysis for a direct injection current modulation when the modulation is not so small or the effect of spontaneous emissions is not negligible. In those cases, we must numerically solve the rate equations and such an analysis has been reported (Chinone et al. 1978).

3.6.5 *Relative Intensity Noise*

The light output from a semiconductor laser is detected by a high-speed photo receiver. It is converted into an electric signal and analyzed by a spectrum analyzer. For the purpose of these analyses, we need a measure for the relative noise level to the average DC signal power, which is called relative intensity noise (RIN). For a certain angular frequency ω, RIN is defined by (Petermann 1988; Agrawal and Dutta 1993)

$$\mathrm{RIN} = \frac{\Phi_S(\omega)}{\bar{S}^2} \tag{3.117}$$

where $\bar{S}$ is the average power of the laser output. The spectral density Φ_S for the noise component δS is given by Papoulis (1984)

$$\begin{aligned}\Phi_S(\omega) &= \int_{-\infty}^{\infty} \langle \delta S(t)\delta S(t')\rangle \exp\{-i\omega(t-t')\}\mathrm{d}(t-t') \\ &= \lim_{T\to\infty} \frac{1}{T}|\delta\tilde{S}(\omega)|^2\end{aligned} \tag{3.118}$$

From the spectral density calculated from (3.114) to (3.118) together with the relations in (3.117), the RIN is calculated to be

$$\mathrm{RIN} = \frac{2R_{\mathrm{sp}}\{\omega^2 + (1/\tau_s + G_n\bar{S})^2 + G_n^2\bar{S}^2(1 + n/\tau_s R_{\mathrm{sp}}\bar{S}) - 2(1/\tau_s + G_n\bar{S})G_n\bar{S}\}}{\bar{S}\{(\omega_{\mathrm{R}} + \omega)^2 + \Gamma_{\mathrm{R}}^2\}\{(\omega_{\mathrm{R}} - \omega)^2 + \Gamma_{\mathrm{R}}^2\}} \tag{3.119}$$

We have already mentioned that the effects of the noises are much enhanced at the relaxation oscillation frequency. We consider here the noise effects that are less than the relaxation oscillation frequency. As has already been derived, the relaxation oscillation frequency is proportional to the square root of the optical power from a laser and the damping factor is much less than the relaxation oscillation frequency, and then the denominator of (3.119) is proportional to $\bar{S}\omega_{\mathrm{R}}^4 \propto \bar{S}^3$. On the other hand, $\bar{S}$ and $\bar{S}^2$ terms in the numerator may be neglected for low power levels. Therefore, RIN is proportional to $\bar{S}^{-3}$ and the noise level rapidly decreases with the increase of the laser output power (Agrawal and Dutta 1993). Well above the laser threshold, the RIN is usually less than about 10^{-14} (−140 dB) for a 1 Hz bandwidth, which is low enough for the use of lasers as light sources to optical communications and optical data storage systems (Petermann and Arnold 1982; Elsäßer and Göbel 1985).

3.6.6 *Phase Noise and Spectral Linewidth*

Phase noise is calculated from the correlation of the complex field. For example, the power spectrum measured by a Fabry-Perot spectrometer in a real experiment is written by the Fourier transform of the field correlation as

$$\Phi_E(\omega) = \int_{-\infty}^{\infty} \langle E(t)E^*(t+\tau)\rangle \exp(-i\omega\tau)\mathrm{d}\tau \tag{3.120}$$

Here, consider the field having a phase fluctuation of

$$E(t) = \sqrt{S}\exp[-i\{\omega_0 t + \phi + \delta\phi(t)\}] \tag{3.121}$$

where $\delta\phi(t)$ is the time-dependent random fluctuation and S and ϕ are set to be constants. ω_0 is the angular frequency of the laser oscillation. In actual fact, the amplitude (equivalently the photon number) fluctuates, accompanying the phase fluctuation. However, we neglect the effects as a small fluctuation. Substituting (3.121) into (3.120), the power spectrum is given by

$$\Phi_E(\omega) = S\int_{-\infty}^{\infty} \langle \exp(i\phi)\rangle \exp\{-i(\omega-\omega_0)\tau\}\mathrm{d}\tau \tag{3.122}$$

where $\Delta\phi = \delta\phi(t-\tau) - \delta\phi(t)$. Assuming Gaussian statistics for $\delta\phi$, we obtain the following relation (Papoulis 1984):

$$\langle \exp(i\phi)\rangle = \exp\{-\frac{1}{2}\left\langle(\phi)^2\right\rangle\} \tag{3.123}$$

Using (3.115), $\Delta\phi$ is written as

$$\Delta\phi = \frac{1}{2\pi}\int_{-\infty}^{\infty} \Delta\tilde{\phi}(\omega)\{\exp(i\omega\tau) - 1\}\exp(i\omega t)\mathrm{d}\omega \tag{3.124}$$

Then, the ensemble average of the square of $\Delta\phi$ is given by

$$\left\langle(\phi)^2\right\rangle = \frac{1}{\pi}\int_{-\infty}^{\infty} \left\langle|\delta\tilde{\phi}(\omega)|^2\right\rangle(1-\cos\omega\tau)\mathrm{d}\omega \tag{3.125}$$

The spectral power of the field due to the phase fluctuation is calculated by substituting (3.123) into (3.122). The calculation is not straightforward and, instead, it is usually obtained numerically (Henry 1986). Figure 3.4 shows an example of numerical calculations for the power spectrum. With the increase of the output power, the RIN decreases as expected. The higher frequency peaks in the spectra correspond to the relaxation oscillations. Also, the relaxation oscillation frequency increases with the increase of the laser output power. Similar spectral characteristics have also been observed by experiments (Vahala et al. 1983a).

Semiconductor laser materials are usually homogeneous, so that the spectral shape of the laser oscillation is a Lorentzian, which is derived from the fact of an exponential time decay of the coherence of light. We calculate the spectral

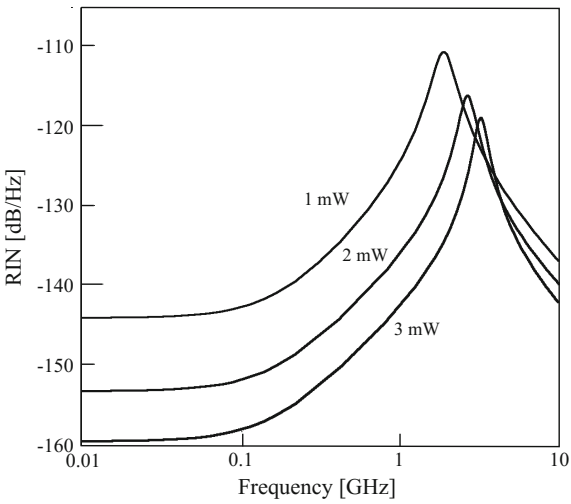

Fig. 3.4 Intensity noise spectrum for several power levels

linewidth of the laser oscillation. Since the fluctuations of the angular frequency $\Delta\omega$ and the phase $\delta\phi$ have the relation $\Delta\omega = \mathrm{d}\delta\phi/\mathrm{d}t$, the power spectrum of the phase noise $\Phi_{\Delta\omega}(\omega)$ is written by

$$\Phi_{\Delta\omega}(\omega) = \omega^2 \langle |\delta\tilde{\phi}(\omega)|^2 \rangle \tag{3.126}$$

Substituting (3.115) into (3.126) and after lengthy calculations, we obtain the approximate form of the spectrum as

$$\Phi_{\Delta\omega}(\omega) = \frac{R_{\mathrm{sp}}}{2S}\left\{1 + \frac{\alpha^2\omega_{\mathrm{R}}^4}{(\omega_{\mathrm{R}}^2 - \omega^2)^2 + (2\omega\Gamma_{\mathrm{R}})^2}\right\} \tag{3.127}$$

There is the following relation between $\Delta\phi$ and the phase noise spectrum

$$\left\langle (\phi)^2 \right\rangle = \frac{1}{\pi}\int_{-\infty}^{\infty} \Phi_{\omega}(\omega)\frac{1-\cos\omega\tau}{\omega^2}\mathrm{d}\omega \tag{3.128}$$

The above integral is not easily calculated in an explicit form, but it is approximated at an angular frequency close to $\omega = 0$ as

$$\left\langle (\phi)^2 \right\rangle = \tau\Phi_{\omega}(0) \tag{3.129}$$

From this result together with (3.122), the correlation function of the field in the presence of phase noise decays exponentially with a time constant of $2/\Phi_{\Delta\omega}(0)$. Also, combining the result with (3.123), it is proved that the power spectral shape has a Lorentzian. The half-width of full maxima (HWFM) is calculated from the relation $\Delta\omega = 2\pi\Delta\nu = \Phi_{\Delta\omega}(0)$ as

$$\Delta\nu = \frac{1}{2\pi}\Phi_{\Delta\omega}(0) = \frac{R_{\mathrm{sp}}}{4\pi S}(1+\alpha^2) \tag{3.130}$$

The spectral linewidth of laser oscillations is calculated from the well-known Schawlow-Townes equation. The linewidth of gas lasers with an almost negligible value of the α parameter is given by $\Delta\nu_0 = R_{\mathrm{sp}}/4\pi\ S$. On the other hand, semiconductor lasers have a non-negligible value of the α parameter and the linewidth of semiconductor lasers is $(1 + \alpha^2)$ times larger than that of ordinary lasers (Henry 1982, 1983, 1986; Petermann 1988; Agrawal and Dutta 1993). The spectral linewidth of semiconductor lasers is usually 10–100 times larger than that of gas lasers and it ranges from several MHz to a hundred MHz without the control for stabilization (Fleming and Mooradian 1981a, b; Elsäßer and Göbel 1984). The spectral linewidth of laser oscillations decreases with an increase in the photon rate, so that the linewidth becomes narrow with an increase of the laser output power. Semiconductor lasers tend to become stable operations for higher output power. Therefore, they frequently show unstable oscillations at lower output power, although unstable behaviors are observed not only at low output power but also at high output power by the introduction of external perturbations.

3.7 Modulation Characteristics

3.7.1 Injection Current Modulation

The unique differentiating feature of semiconductor lasers is the direct modulation for the pump, namely the carrier that is the pump in semiconductor lasers is directly modulated through the injection current. Besides small and compact light sources, semiconductor lasers are suitable light sources of optical communications and information devices because of their direct modulation property. As will be discussed later, a modulation for the injection current itself is the introduction of an extra degree of freedom to semiconductor laser and it induces instability and chaos in the output. On the one hand, chaotic behaviors in semiconductor lasers can also be controlled to stable oscillations by direct injection current modulation. The relaxation oscillation plays a crucial role for the modulation properties in semiconductor lasers.

The efficiency of laser output by the injection current modulation is constant for a small to moderate modulation index when the modulation frequency is less than the relaxation oscillation frequency. On the other hand, the modulation efficiency is greatly degraded over the frequency of the relaxation oscillation and the modulation for the light output over that frequency is not possible (Boers and Vlaardinerbrek 1975; Furuya et al. 1979). The effort to enhance relaxation oscillation frequency of semiconductor lasers has been made to device high efficiency lasers in practical use (Lau and Yariv 1985; Uomi et al. 1985). The injection current modulation

(amplitude modulation) results in the phase modulation (frequency modulation), since the laser oscillation frequency is a function of the injection current. The linear relation is established for the injection current modulation and the increment of the frequency is linearly proportional to the injection current without mode hop. The effect of coupling between the amplitude and the phase comes from the fact that the real and imaginary parts of the refractive index are not independent and they couple with each other. This unique characteristic originated from the nonzero value of the α parameter.

In the following, we discuss the modulation properties when a small signal is applied directly to the injection current. We again employ the method of a small signal modulation used in linear stability analysis. Since we are concerned with the modulation properties, we will not consider noise effects. As an injection current modulation, we assume a time-dependent signal as

$$J(t) = J_{\mathrm{b}} + J_{\mathrm{m}}(t) = J_{\mathrm{b}} + J_{0\mathrm{m}} \sin \omega_{\mathrm{m}} t \tag{3.131}$$

where J_{b} is the bias injection current, J_{m} is the small amplitude of the modulation ($J_{0\mathrm{m}} \ll J_{\mathrm{b}}$), ω_{m} is the modulation angular frequency. The small injection current modulation gives rise to a perturbation to the carrier density δn, and then fluctuations of the photon number δS and the phase $\delta\phi$ are induced through the change of the carrier density. Using the fact that the modulation is very small and from (3.94) to (3.96), the differential equations for the perturbations δS, $\delta\phi$, and δn are given by

$$\frac{\mathrm{d}\delta S(t)}{\mathrm{d}t} = G_n A_s^2 \delta n(t) \tag{3.132}$$

$$\frac{\mathrm{d}\delta\phi(t)}{\mathrm{d}t} = \frac{1}{2}\alpha G_n \delta n(t) \tag{3.133}$$

$$\frac{\mathrm{d}\delta n(t)}{\mathrm{d}t} = -\left(\frac{1}{\tau_s} + G_n A_s^2\right)\delta n(t) - \frac{1}{\tau_{\mathrm{ph}}}\delta S(t) + \frac{J_{\mathrm{m}}(t)}{ed} \tag{3.134}$$

By Fourier transforming these equations, the corresponding components for these perturbations are written by

$$\delta\tilde{S}(\omega) = \frac{G_n A_s^2 \tilde{J}_{\mathrm{m}}(\omega)/ed}{(\omega_{\mathrm{R}} + \omega + i\Gamma_{\mathrm{R}})(\omega_{\mathrm{R}} - \omega - i\Gamma_{\mathrm{R}})} \tag{3.135}$$

$$\delta\tilde{\phi}(\omega) = \frac{1}{2i\omega}\alpha G_n \delta\tilde{n}(\omega) \tag{3.136}$$

$$\delta\tilde{n}(\omega) = \frac{i\omega\tilde{J}_{\mathrm{m}}(\omega)/ed}{(\omega_{\mathrm{R}} + \omega + i\Gamma_{\mathrm{R}})(\omega_{\mathrm{R}} - \omega - i\Gamma_{\mathrm{R}})} \tag{3.137}$$

where $\tilde{J}_{\mathrm{m}}(\omega)$ is the Fourier transform of $J_{\mathrm{m}}(t)$. As is easily understood from the above equations, the modulation for the injection current directly induces fluctuations to the carrier density and, then, it is coupled with the fluctuations of the photon number and the phase through the variation of the carrier density. Thus, instability is intrinsically included in semiconductor lasers as a coupled nonlinear system.

3.7.2 Intensity Modulation Characteristics

From the previous discussion, we calculate the modulation efficiency for the photon number. Using (3.131), the Fourier component of the injection current modulation $\tilde{J}_{\mathrm{m}}(\omega)$ is written by

$$\tilde{J}_{\mathrm{m}}(\omega) = -i\pi J_{0\mathrm{m}}\{\delta(\omega - \omega_{\mathrm{m}}) - \delta(\omega + \omega_{\mathrm{m}})\} \tag{3.138}$$

Substituting the above equation into (3.135), the fluctuation of the photon number is calculated as

$$\delta S(t) = \delta S_0 \sin(\omega_{\mathrm{m}} t + \theta_S) \tag{3.139}$$

where the amplitude δS_0 and the phase θ_S are given by

$$\delta S_0 = \frac{G_n A_s^2 J_{0\mathrm{m}}/ed}{\sqrt{(\omega_{\mathrm{m}}^2 - \omega_{\mathrm{R}}^2 - \Gamma_{\mathrm{R}}^2)^2 + 4\omega_{\mathrm{m}}^2 \Gamma_{\mathrm{R}}^2}} \tag{3.140}$$

$$\theta_S = \tan^{-1}\left(\frac{-2\Gamma_{\mathrm{R}}\omega_{\mathrm{m}}}{\omega_{\mathrm{m}}^2 - \omega_{\mathrm{R}}^2 - \Gamma_{\mathrm{R}}^2}\right) \tag{3.141}$$

The intensity (photon number) of the output from a semiconductor laser is modulated at the same frequency of the injection current modulation and it varies with time proportional to the modulation depth $J_{0\mathrm{m}}$. However, the phase of the modulated intensity is not the same as the injection current modulation and, for example, the signal delay occurs for a modulation below the relaxation oscillation frequency ($\omega_{\mathrm{m}} \ll \omega_{\mathrm{R}}$). The modulation efficiency is greatly enhanced near the relaxation oscillation frequency and takes the maximum at the frequency (Ikegami and Suematsu 1968). Figure 3.5 shows examples of modulation response for different relaxation oscillation frequencies at a damping factor of $\Gamma_{\mathrm{R}} = 3 \times 10^9\ \mathrm{s}^{-1}$. The modulation power is given by $\delta S_0 = \tau_{\mathrm{ph}}\ J_{0\mathrm{m}}/ed$ for $\omega_{\mathrm{m}} \ll \omega_{\mathrm{R}}$. The modulation efficiency at the resonance frequency is about $\omega_{\mathrm{R}}/2\Gamma_{\mathrm{R}}$ times larger than that below the frequency. When the modulation exceeds the relaxation oscillation frequency, the carrier cannot follow the modulation speed of the injection current and the intensity of the modulation rapidly decreases with the increase of the modulation

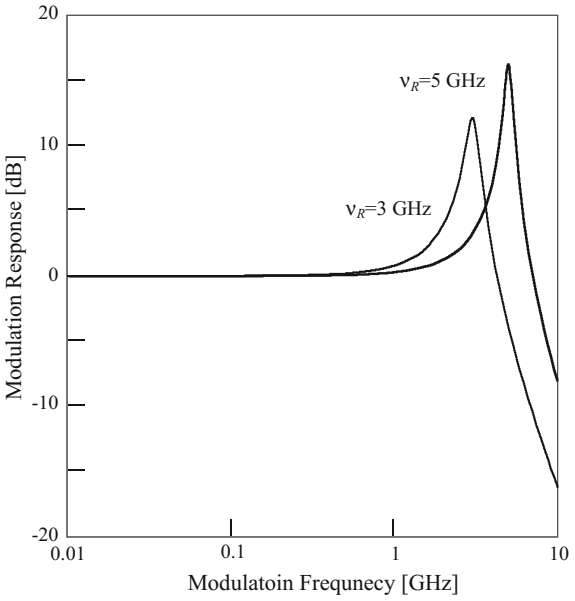

Fig. 3.5 Small signal modulation response at a damping factor Γ_R of 3×10^9 s^{-1}

frequency. Thus, the relaxation oscillation frequency determines the capability of the maximum modulation in semiconductor lasers.

3.7.3 Phase Modulation Characteristics

The injection current modulation induces a change of the phase in laser oscillations known as frequency chirp (Dutta et al. 1984; Linke 1985; Agrawal 1985; Kazarinov and Henry 1987). We write the fluctuation of the frequency as $\delta\nu(t) = \mathrm{d}\delta\phi(t)/\mathrm{d}t/2\pi$. The fluctuation is calculated from the Fourier transform of $\delta\tilde{\phi}(\omega)$ with the relation of (3.136) and is given by

$$\begin{aligned}\delta\nu(t) &= \frac{1}{4\pi^2}\int_{-\infty}^{\infty} i\omega\delta\tilde{\phi}(\omega)\exp(i\omega t)\mathrm{d}\omega \\ &= \frac{\alpha G_n}{8\pi^2 ed}\int_{-\infty}^{\infty}\frac{i\omega\tilde{J}_\mathrm{m}(\omega)}{(\omega_\mathrm{R}+\omega+i\Gamma_\mathrm{R})(\omega_\mathrm{R}-\omega-i\Gamma_\mathrm{R})}\exp(i\omega t)\mathrm{d}\omega\end{aligned} \tag{3.142}$$

From this result, we easily understand that the α parameter, which has a nonzero value in semiconductor lasers, plays an important role for the frequency chirp. For the sinusoidal modulation of the injection current, the frequency of the laser oscillation is modulated by the same frequency as

$$\delta v(t) = \delta v_0 \sin(\omega_m t + \theta_v) \tag{3.143}$$

where the amplitude δv_0 and the phase θ_v are given by

$$\delta v_0 = \frac{\alpha G_n J_{0m}}{4\pi e d} \frac{\omega_m}{\sqrt{(\omega_m^2 - \omega_R^2 - \Gamma_R^2)^2 + (2\omega_m \Gamma_R)^2}} \tag{3.144}$$

$$\theta_v = \frac{\pi}{2} + \tan^{-1}\left(\frac{2\Gamma_R \omega_m}{\omega_m^2 - \omega_R^2 - \Gamma_R^2}\right) \tag{3.145}$$

The modulation efficiency is proportional to the amplitude of the modulation J_{0m} and the amplitude is approximated for the modulation below the relaxation oscillation as

$$\delta v_0 = \frac{\alpha \tau_{ph} \omega_m}{4\pi e d S} J_{0m} \tag{3.146}$$

It is noted that the modulation amplitude is inversely proportional to the photon number and the effect of the modulation on the frequency becomes small for a higher injection current. The conversion efficiency from the injection current to the frequency is about several GHz/mA for ordinary narrow-stripe edge-emitting semiconductor lasers. Figure 3.6 shows the dependence of frequency chirp on the modulation depth of the injection current observed experimentally in various laser structures. For a modulation frequency sufficiently below the relaxation oscillation, the phase has a negligible small value $\theta_v \approx 0$ and the modulated intensity is in-phase with the injection current modulation.

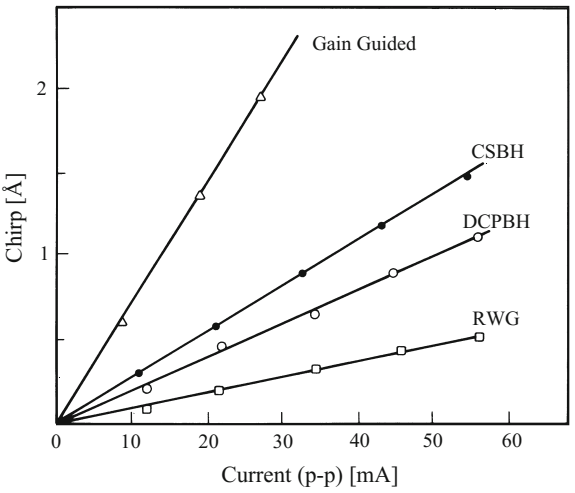

Fig. 3.6 Experimentally measured chirp as a function of the peak-to-peak value of the modulation current for various laser structures at a wavelength of 1.3 μm. *CSBH* channel-substrate buried heterostructure semiconductor laser, *DCPBH* double-channel planar buried heterostructure semiconductor laser, *RWG* ridge waveguide semiconductor laser [after Dutta et al. (1984); © 1984 AIP]

3.8 Waveguide Models of Semiconductor Lasers

3.8.1 Index- and Gain-Guided Structures

Edge-emitting semiconductor lasers with narrow stripe width have common dynamics for external perturbations; however, the parameter range of each stable and unstable characteristic varies from one laser to the other, depending on the laser structures. The dynamics depend on the type of guided structures of light, i.e., gain- or index-guided structure. In addition, they are functions of types of cavity structures such as Fabry-Perot, MQW, or DFB cavity structures. In this subsection, we discuss some wave-guiding models and laser cavity types that affect the laser dynamics in the following chapters. Regarding wave-guiding structures in semiconductor lasers, there are two types of wave-guiding models; one is the index-guided structure, in which we can expect stable laser oscillation with a single longitudinal mode, and the other one is the gain-guided structure, in which the laser behaves rather unstably and it sometimes operates in multi-longitudinal modes (Petermann 1988; Agrawal and Dutta 1993). Each device maker fabricates various types of gain- and index-guided structure lasers for the use of commercial applications.

Figure 3.7 shows typical examples of gain- and index-guided structures. Figure 3.7a is the schematic illustration of the structure of a gain-guide laser at its light exit facet. Due to the presence of insulator regions at p-type electrodes, injected carriers pass through a certain area in the active layer, so that the center of

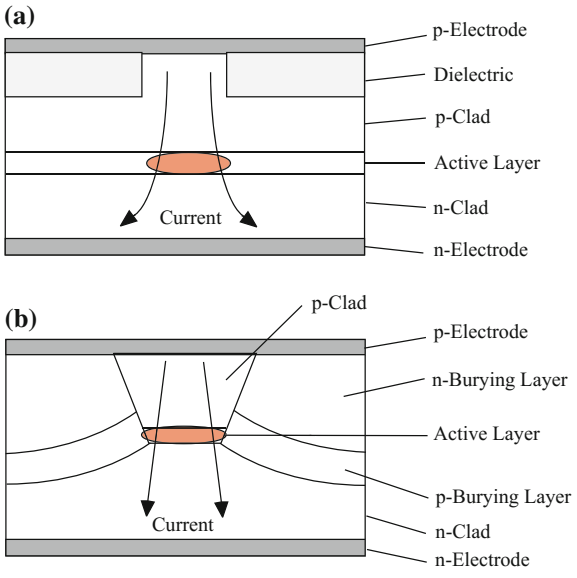

Fig. 3.7 Examples of gain and index-guided laser structures. **a** Gain-guided laser and **b** index-guided laser with buried heterostructure

the active layer only has a high gain. Thus, the laser oscillates around the center of the active region. The laser is easy to fabricate, but it has a low efficiency of light confinement due to the decrease of the refractive index of the active layer by the carrier injection, resulting in leakage of light outside the lasing regions. For the same reason, the emitted light from the laser is usually astigmatic and, in the worst case, the laser has a twin-peaked far-field pattern. The laser easily shares gains for each lasing modes and it sometimes oscillates at multi-longitudinal modes. Another disadvantage of laser oscillations is a low noise performance induced by a high level of spontaneous emission of light. Nevertheless, gain-guided lasers are still used for commercial uses where there is no need to consider high laser performances.

Figure 3.7b is a schematic illustration of the structure of an index-guide laser at its light exit facet. This example is a type of buried hetero-structure, which has a high refractive index and gain waveguide area at the center of the active layer, resulting in high efficiency of confinement of light, similar to an optical fiber structure. Therefore, an index-guided laser has a high quality of emitting beam better than that of a gain-guided laser. The advantages of index-guided lasers are as follows; high efficiency of stimulated emission with a small effect of spontaneous emission, low threshold, oscillation of single longitudinal mode, small astigma, single peak profile of far-filed pattern, and high modulation efficiency. Index-guided semiconductor lasers are widely used as light sources in optical communications and optical data storage systems. The dynamics of semiconductor lasers are strongly affected through the difference in gains in wave-guided structures. Though the universal dynamics and overall chaotic roots for the parameter variations look the same, regardless of the laser structures, each laser with specific structure has characteristic dynamics. The difference between gain- and index-guide structures plays an important role, especially in broad-area semiconductor lasers.

3.8.2 Waveguide Models

In this subsection, we discuss the theoretical treatments of the waveguide models with emphasis on the difference between gain- and index-guided laser structures. In the derivations of the rate equations, we assume that the laser propagates as a harmonic plane wave in the waveguide. A semiconductor laser generally oscillates at a fundamental transverse-electric (TE) mode in the laser cavity, except for the installation of special device structures to force the oscillation to the orthogonal mode, i.e., transverse-magnetic (TM) mode. Therefore, we can approximate plane wave propagation even in the study of laser dynamics. However, we must consider a finite extent of the wave amplitude with elliptic beam profile for propagation of the actual laser. Namely, we must take into account the spatial modes for the lateral and transverse oscillations in a strict sense. The gain for laser oscillation also has a

spatial profile along the active layer and, as a result, the spatial mode profile is affected depending on the waveguide structures. In the following, we briefly develop a theoretical treatment for the lateral spatial modes in narrow-stripe edge-emitting semiconductor lasers by taking into consideration the laser waveguide structures. A narrow-stripe semiconductor laser defined here has a stripe width of 2–3 μm and the theoretical treatment is only valid for lasers with this range. For semiconductor lasers over the stripe width of several micron-meters, we cannot ignore the effects of the higher spatial mode oscillations and their competition in laser dynamics. Waveguide structures play crucial roles for the dynamic properties of vertical-cavity surface-emitting lasers (VCSELs) and broad-area semiconductor lasers, as will be discussed in Chap. 8. In particular, spatio-temporal instability is much enhanced for those lasers with gain-guided structures.

For the mathematical treatment of laser dynamics, we must consider both the temporal and spatial dependences of the Maxwell equation. But we are concerned here with the spatial effects of laser propagation, and the temporal effects may be ignored for a while. We also restrict the discussion of TE-mode propagation. To a good approximation, we can apply the separation of the variables for the electric field using the slab-waveguide model and assume scalar wave propagation (Agrawal and Dutta 1993). Then, the solution of the electric field is approximated by

$$E(x, y, z) = E_0 \psi_y(y) \psi_x(x) \exp(i\beta_z z) \tag{3.147}$$

where x is the lateral coordinate in the active layer, y is the orthogonal coordinate to x, β_z is the propagation constant along the laser cavity, and E_0 is the average amplitude. Substituting (3.147) into the Helmholtz equation, one obtains

$$\frac{1}{\psi_x(x)} \frac{\partial^2 \psi_x(x)}{\partial x^2} + \frac{1}{\psi_y(y)} \frac{\partial^2 \psi_y(y)}{\partial y^2} + \{\varepsilon(x, y) k_0^2 - \beta_z^2\} = 0 \tag{3.148}$$

where $\varepsilon(x, y)$ is the complex dielectric constant generally having the form $\varepsilon(x, y) \approx \varepsilon(x)$ for a slab-waveguide. In the effective index approximation, the transverse field distribution $\psi_y(y)$ is obtained first by solving

$$\frac{\partial^2 \psi_y(y)}{\partial y^2} + \{\varepsilon(x, y) k_0^2 - \beta_{\text{eff}}^2(y)\} \psi_y(y) = 0 \tag{3.149}$$

where $\beta_{\text{eff}}(x)$ is the effective propagation constant at the coordinate x. Substituting (3.149) into (3.148), the lateral field distribution is then obtained by solving

$$\frac{\partial^2 \psi_x(x)}{\partial x^2} + \{\beta_{\text{eff}}^2(x) - \beta_z^2\} \psi_x(x) = 0 \tag{3.150}$$

From the assumption of a thin active layer, i.e., the constant carrier density for the y direction at a fixed x coordinate, the non-time-dependent carrier density equation along the lateral coordinate x is given by the following equation:

$$D_n \frac{\partial^2 n(x)}{\partial x^2} + \frac{J(x)}{ed} - \frac{n(x)}{\tau_s} - G_n\{n(x) - n_0\}E_0^2|\psi_x(x)|^2 = 0 \tag{3.151}$$

where the first term of the equation is the carrier diffusion along the active layer and D_n is the diffusion constant of the carrier density. Usually, the diffusion constant D_n and the gain G_n are also functions of the lateral coordinate x. Non-time-dependent spatial mode analyses can be conducted using (3.149)–(3.151).

3.8.3 *Spatial Modes of Gain- and Index-Guided Lasers*

The mode analysis is simplified for the assumption of the separation of the variables. For the fundamental TE mode, the solution for (3.150) is given by

$$\begin{aligned} \psi_x(x) &= \psi_0 \cos(\kappa_x x) && (|x| \le w/2) \\ &= \psi_0 \cos\left(\frac{\kappa_x w}{2}\right) \exp\left\{-\gamma_x\left(|x| - \frac{w}{2}\right)\right\} && (|x| > w/2) \end{aligned} \tag{3.152}$$

where ψ_0 is the normalization constant, w is the width of the active layer, and κ_x and γ_x are defined by

$$\kappa_x = \sqrt{\beta_{\text{core}}^2 - \beta_{\text{eff}}^2} \tag{3.153a}$$

$$\gamma_x = \sqrt{\beta_{\text{eff}}^2 - \beta_{\text{clad}}^2} \tag{3.153b}$$

In the above equations, β_{core} and β_{clad} are the propagation constants both in the active layer and outside the active layer. The solution can be considered as a Gaussian beam profile with a good approximation. The beam profile for the transverse direction can also be considered as a fundamental Gaussian mode. However, assumption of the fundamental TE mode is only valid for a narrow-stripe edge-emitting semiconductor laser. For broad stripe width or even for a gain-guided laser with narrow-stripe width, we must consider higher spatial modes derived forms (3.150) due to effects such as hole-burning of the carrier. The excitations of higher spatial modes significantly affect laser instabilities.

For an index-guided laser, the wave fronts for the lateral and transverse directions at the exit face are approximated as plane waves. On the other hand, the approximation of plane wave is only valid for the transverse direction in a gain-guided laser. The wave front for the lateral direction must be treated as a divergent spherical wave (Agrawal and Dutta 1993). In a gain-guided laser, the

effective propagation constant becomes a function of the lateral coordinate. We assume the parabolic profile for the propagation constant written by

$$\beta_{\text{eff}} = \beta_{0\text{eff}} - k_0^2 a_c^2 x^2 \tag{3.154}$$

where $\beta_{0\text{eff}}$ is the propagation constant at $x = 0$. The complex parameter a_c is defined by $a_c = a_r - ia_i$ and has a relation with the complex refractive index in (3.39) as follows (Cook and Nash 1975):

$$\text{Re}[\eta_c] = \eta - \frac{a_r^2 - a_i^2}{2\eta} x^2 \tag{3.155a}$$

$$\text{Im}[\eta_c] = -\frac{\eta' + 2a_r a_i x^2}{2\eta} \tag{3.155b}$$

Solving the differential equation for the fundamental spatial mode, one obtains

$$\psi_{x0}(x) = B_0 \exp\left(\frac{1}{2} i k_0 a_i x^2\right) \exp\left(-\frac{1}{2} k_0 a_r x^2\right) \tag{3.156}$$

where B_0 is the normalization constant. The solutions for the higher spatial modes are given by the following Gauss-Hermite function:

$$\psi_m(x) = \text{H}_m\left(\sqrt{k_0 a_c} x\right) \psi_0(x) \tag{3.157}$$

Here, H_m is the Hermite polynomial of order m. As already discussed, the wave front of the transverse direction in a gain-guided laser is assumed to be plane wave, therefore we can only consider the spatial dependence for the lateral direction. From (3.147), the surfaces of constant phase of the complex field in gain-guided lasers are written as

$$\beta_z z + \frac{1}{2} k_0 a_i x^2 = \text{const.} \tag{3.158}$$

The surfaces are cylindrical with a radius of a certain curvature near the coordinate at $x = 0$. Therefore, the phase front of the gain-guided laser at the exit face must be approximately treated as a spherical wave along the lateral direction. Assuming that the difference of the refractive indices between the center and edge of the active layer is small, the curvature is approximated as

$$R_m = \frac{\beta_z}{k_0 a_i} \approx \frac{\eta}{a_i} \tag{3.159}$$

For an index-guided laser, $a_i = 0$ resulting in a plane wave front for the lateral direction. A gain-guided laser has a divergent wave front and it is unstable laser

compared with an index-guided laser. The difference of the instabilities can be implemented by the variations of the gains between the two laser models in the rate equations.

3.8.4 *Effects of Spontaneous Emission in Gain- and Index-Guided Lasers*

The effects of spontaneous emission play crucial roles for laser oscillations. The increase in spontaneous emission in the cavity is counted as a loss of the laser, and results in the increase of the laser threshold. The effects of spontaneous emission are quite different depending on whether the laser structure is a gain-guided type or an index-guided one. The stationary solution for the photon number S_s is related to the spontaneous emission, and is easily derived from (3.94) as

$$S_s = \frac{1}{G_n(n_s - n_{\text{th}})} R_{\text{sp}} \tag{3.160}$$

In actual lasers, the effect of spontaneous emission on the lasing oscillation (photon number) is enhanced due to non-negligible losses from the laser cavity. The enhancement factor K_c is calculated from the traveling wave amplifier model and the corrected stationary solution for the photon number is given by Petermann (1988)

$$S = \frac{1}{G_n(n_s - n_{\text{th}})} K_c R_{\text{sp}} \tag{3.161}$$

with

$$K_c = \left\{ \frac{(r_1 + r_2)(1 - r_1 r_2)}{2 r_1 r_2 \ln(1/r_1 r_2)} \right\}^2 \tag{3.162}$$

where r_1 and r_2 are the facet amplitude reflectivities of the laser cavity. For the reflectivities $r_1 = r_2 \approx 1$, the correction factor is $K_c = 1$ and no correction for spontaneous emission is required. However, in the case of semiconductor lasers, K_c is usually larger than unity. For example, for the cleaved facets of AlGaAs lasers of $r_1^2 = r_2^2 = 0.32$, one obtains $K_c = 1.11$, which is still not significant. On the other hand, large enhancement factors are obtained when one of the laser mirrors is coated for antireflection, as is often the case.

For gain-guided semiconductor lasers, we must consider an additional enhancement of spontaneous emission. The phase fronts in gain-guided lasers are curved, so that energy is carried not only in the axial direction but also in the lateral direction. As a result, the lasing mode in the gain-guided laser captures a larger fraction of spontaneous emission than the lasing mode in the index-guided laser.

This is somewhat similar to the effect of aberrations in lenses. The additional enhancement factor K_{gain} for the spontaneous emission noise of a gain-guided laser is given by Petermann (1979)

$$K_{\text{gain}} = \left\{ \frac{\int |\psi_x(x)|^2 \mathrm{d}x}{\int \psi_x^2(x) \mathrm{d}x} \right\}^2 \tag{3.163}$$

For index-guided lasers, one has the plane phase fronts and $\psi_x^2 = |\psi_x|^2$ yielding $K_{\text{gain}} = 1$. On the other hand, ψ_x is a complex for gain-guided lasers and the value of K_{gain} is always larger than unity. For the fundamental spatial mode oscillation, the factor K_{gain} is calculated as Petermann (1979)

$$K_{\text{gain}} = \sqrt{1 + \left(\frac{a_i}{a_r} \right)^2} \tag{3.164}$$

Here, a_i/a_r is defined as the strength of astigmatism. The strength of astigmatism has the relation with the linewidth enhancement factor (Kirkby et al. 1977)

$$\frac{a_i}{a_r} = \sqrt{1 + \alpha^2} + \alpha \tag{3.165}$$

Using this relation, the additional enhancement factor for spontaneous emission is written as

$$K_{\text{gain}} = \sqrt{2(1 + \alpha^2) + 2\alpha\sqrt{1 + \alpha^2}} \tag{3.166}$$

For a typical value of the linewidth enhancement factor of $\alpha = 4$, the additional enhancement factor is calculated to be $K_{\text{gain}} = 8.2$. Normally, the typical value of the additional enhancement factor for spontaneous emission has a value of the order of 10. On the whole, gain-guided lasers have a strong dependence on spontaneous emission and have higher threshold for laser oscillations as shown in Fig. 3.8 (Petermann and Arnold 1982). The gain-guided lasers are unstable lasers having unclear laser threshold and even larger radiation less than the threshold. These characteristics strongly affect the laser dynamics for time development through the gain factor.

3.8.5 *Laser Types*

Fabry-Perot lasers, MQW lasers, and DFB lasers are typical models of edge-emitting lasers currently commercially available. These lasers are widely used for light sources of optical communications, optical data storage systems, and

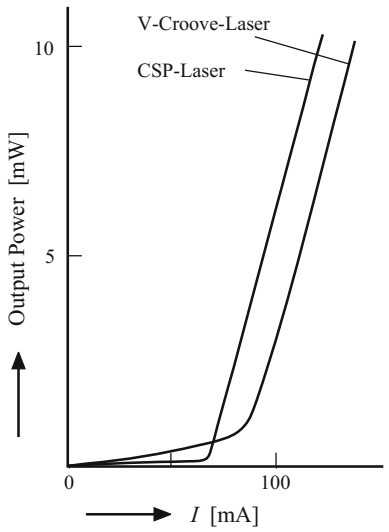

Fig. 3.8 Experimental L-I characteristics of gain- and index-guided semiconductor lasers. *CSP laser* channeled substrate planar laser [after Petermann and Arnold (1982); © 1982 IEEE]

optical information systems. Although the theoretical treatments discussed here have been developed for a type of Fabry-Perot semiconductor lasers, the laser rate equations are commonly applicable to other types of narrow-stripe edge-emitting semiconductor lasers including MQW and DFB lasers. However, each type of laser has different device characteristics and the stable and unstable features of laser oscillations for external perturbations are strongly dependent on each device parameter. For example, a semiconductor laser is easily destabilized by self-optical feedback as will be discussed in Chap. 4, but the external feedback level for unstable chaotic oscillations is different for each laser depending on the values of the device parameters.

Fabry-Perot lasers are easily fabricated and were used in the early days. The theory for the dynamics discussed in the preceding subsections is based on Fabry-Perot structures. The gain for semiconductor laser materials is broad, up to several tens of nanometers and the gain difference for the laser modes in Fabry-Perot lasers is small, so that they tend to oscillate at multi-longitudinal modes. In particular, gain-guided lasers with Fabry-Perot cavity structure show multimode oscillation without exception. Even a single mode Fabry-Perot laser exhibits multimode oscillations at a fast modulation for the bias injection current. From the viewpoint of chaotic dynamics, the Fabry-Perot laser is an unstable laser from external perturbations, showing a wide range of unstable oscillations for the parameter variations.

MQW lasers have many thin quantum-well layers parallel to the active layer. Each quantum-well layer has a thickness ranging from ten to several tens of nanometers, where the confined electrons play like waves within the quantum potentials. Figure 3.9 shows a schematic diagram of AlGaAs multi quantum-well lasers. Figure 3.9a shows the band model for multi quantum-well structure and

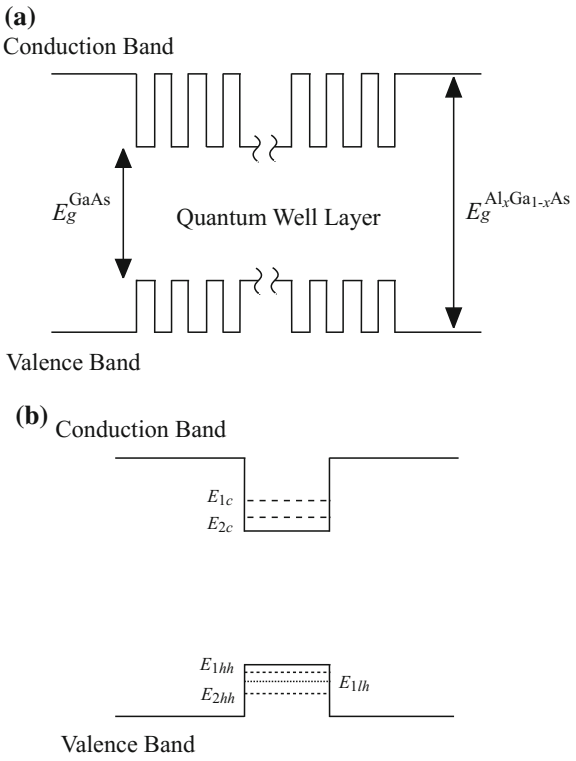

Fig. 3.9 Schematic diagram of AlGaAs multi-quantum well lasers. **a** Band model for the multi-quantum well structure and **b** energy band of a single quantum well with confined particle energy levels of electrons (*c*), heavy holes (*hh*) and light holes (*lh*)

Fig. 3.9b is the schematic representation of the confined particle energy levels of electrons (*c*), heavy holes (*hh*) and light holes (*lh*) in a single quantum-well. Due to the narrow potential well of a GaAs layer sandwiched by AlGaAs layers, the energy levels are quantized and have discrete distributions. The use of multi quantum wells has several advantages over Fabry-Perot lasers with a single thick (~ 10 nm) active layer. The gain for a particular oscillation wavelength can be much enhanced due to the quantum-well structure, and the gain coefficient is usually greater than three times or more compared with a single layer Fabry-Perot laser. The shorter oscillation wavelength is attained compared with a bulk semiconductor laser by the quantization of the energy levels. Figure 3.10 shows modal gain as a function of the injection current with the number of quantum wells in the active layer. As is easily recognized, the differential gain $\partial g/\partial n$ increases with the increase in the number of quantum wells. From (3.89), the relaxation oscillation frequency, which limits the modulation performance, is proportional to the square root of the differential gain, so that we can expect enhancement of the modulation property for multi quantum-well lasers. A multi quantum-well laser has a small linewidth enhancement factor, and unstable parameter regions are much reduced compared with bulk semiconductor lasers. As a result of efficient optical confinement, we can achieve lower threshold lasers with small optical losses. With such excellent performances

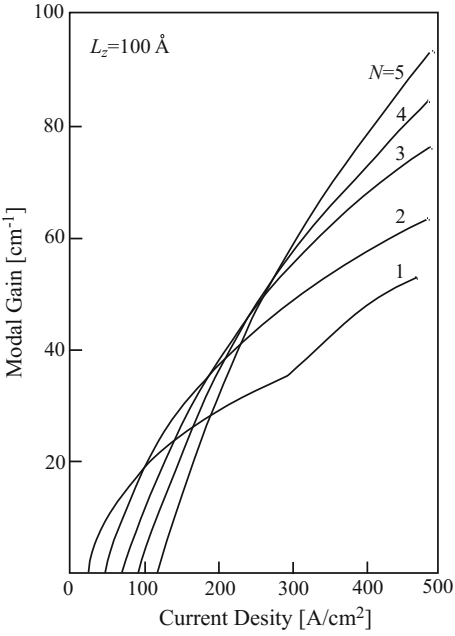

Fig. 3.10 Modal gain as a function of the injection current with the number of quantum wells N. The quantum well thickness is assumed to be 10 nm [after Arakawa and Yariv (1985); © 1985 IEEE]

and reasonable prices for fabrication cost, multi quantum-well lasers are widely used in optical data storage systems and optical information processing systems.

In optical communication systems, a semiconductor laser with single mode and narrow linewidth is desired for good quality of data transmissions. For such purpose, DFB lasers have been developed. Figure 3.11 shows a schematic diagram of the typical $\pi/2$ shifted DFB laser structure along the laser cavity. A DFB laser has a grating structure close to the active layer in the axial direction. Therefore, a preference is obtained for an oscillation wavelength, which fits the grating's period. If the grating has a continuous periodic structure without non-phase shift, the light corresponding to the Bragg wavelength λ_B is not an oscillation mode due to the stop-band. However, light with wavelength λ_B becomes the transmission mode due to the opening of the transmission window in the presence of $\pi/2$ phase shift at the center of the grating structure. This results in stable laser oscillations at the Bragg wavelength. As a disadvantage of the DFB structure, the amplitude of the standing wave is fixed by the grating, so that the effect of carrier hole-burning is much enhanced at the regions of large field amplitudes. Then, the gain at those points decreases and the effect is to lower the laser threshold. This is not too serious, as will be discussed in the following. As a whole, DFB semiconductor lasers are excellent light sources as a dynamic single-mode laser with low chirp suitable for optical communications.

The oscillation frequency reflects the phase condition for the modes of a DFB structure. The required threshold gain g_{th} for the DFB laser modes strongly depends on the respective modes, yielding oscillation angular frequency ω_0. This behavior

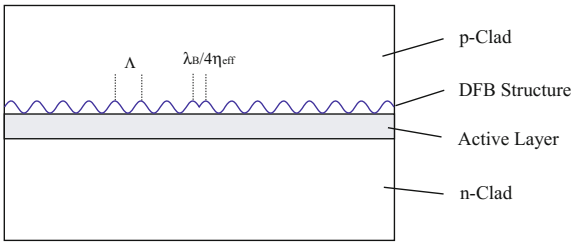

Fig. 3.11 Schematic diagram of the typical $\pi/2$ shifted DFB laser structure. $\Lambda = m\lambda_B/2\eta_{eff}$ (m is the integer number)

differs from a Fabry-Perot type laser, in which equal threshold gain is required for all the resonant modes. The threshold gain for a DFB laser is written by

$$g_{th} = a + a_m \tag{3.167}$$

where a is the loss in the cavity due to optical scattering and is already defined in (3.4). a_m is the loss due to the reflection in the DFB structure. In the case of a Fabry-Perot laser, the reflection loss is explicitly given as $a_m = \ln(1/r_1 r_2)/l$. The detailed analysis for a DFB laser oscillation can be treated by using coupled-wave equations. However, the reflection loss in the DFB laser is not given by an analytical form, and is calculated numerically (McCall and Platzman 1985).

The threshold gain of a DFB laser depends on the coupling strength of the grating structure, namely $\kappa_{DFB}l$ (κ_{DFB} and l being the coupling coefficient and the cavity length). The factor $\kappa_{DFB}l$ is a function of the cavity loss $a_m l$. For a typical coupling strength around $\kappa_{DFB}l = 2$, one obtains the value of the cavity loss $a_m l = 1.4$ for a $\pi/2$ phase shifted DFB laser, which corresponds to the case of the equal facet reflectivity of $R = r^2 = 0.25$ in a Fabry-Perot laser. Therefore, the threshold gain of DFB is higher than that of a Fabry-Perot laser, but is very close to the threshold of Fabry-Perot laser (Petermann 1988). Due to strong non-uniformity of the optical intensity for DFB lasers along the laser length, the spontaneous emission enhancement factor equivalent to the coefficient K_c defined in (3.147) is usually larger than that for Fabry-Perot type lasers with equal cavity loss $a_m l$. If the coupling strength is taken as $\kappa_{DFB}l = 2$ for a non-phase shifted DFB laser, the spontaneous emission factor $K_c = 1.94$ is obtained (Petermann 1988). It is noted that the internal reflectivities at the laser facets have complex values in a strict sense, so that the reflectivity from the external mirror must also be treated as a complex value.

References

G.P. Agrawal, Chirp minimization and optimum biasing for current-modulated coupled-cavity semiconductor lasers. Opt. Lett. **1**, 10–12 (1985)

G.P. Agrawal, N.K. Dutta, *Semiconductor Lasers* (Van Nostrand Reinhold, New York, 1993)

Y. Arakawa, A. Yariv, Theory of gain, modulation response, and spectral linewidth in AlGaAs quantum well lasers. IEEE J. Quantum Electron. **21**, 1666–1674 (1985)

G. Arnold, P. Russer, K. Petermann, Modulation of laser diodes (Chap. 7), in *Semiconductor Devices for Optical Communication*, ed. by H. Kressel. (Springer, Berlin, 1982)
P.M. Boers, M.T. Vlaardinerbrek, Dynamic behavior of semiconductor lasers. Electron. Lett. **11**, 206–208 (1975)
D. Botez, InGaAsP/InP double-heterosturcture lasers: simple expressions for wave confinement, beam width, and threshold current over wide range in wavelength (1.1–1.65 μm). IEEE J. Quantum Electron. **17**, 178–186 (1981)
J. Buss, M.J. Adams, Phase and group indices for double heterostructure lasers. Solid-State Electron. Dev. **3**, 189–195 (1979)
N. Chinone, K. Aiki, M. Nakamura, R. Ito, Effects of lateral mode and carrier density profile on dynamic behaviors of semiconductor lasers. IEEE J. Quantum Electron. **14**, 625–631 (1978)
W.W. Chow, S.W. Koch, M. Sargent III, *Semiconductor Laser Physics* (Springer, New York, 1993)
D.D. Cook, F.R. Nash, Gain-induced guiding and astigmatic output beam of GaAs lasers. J. Appl. Phys. **46**, 1660–1672 (1975)
N.K. Dutta, N.A. Olsson, L.A. Koszi, P. Besomi, R.B. Wilson, Frequency chirp under current modulation in InGaAsP injection lasers. J. Appl. Phys. **56**, 2167–2169 (1984)
W. Elsäßer, E.O. Göbel, Spectral linewidth of gain- and index-guided InGaAs semiconductor lasers. Appl. Phys. Lett. **45**, 353–355 (1984)
W. Elsäßer, E.O. Göbel, Multimode effects in the spectral linewidth of semiconductor lasers. IEEE J. Quantum Electron. **21**, 687–692 (1985)
M.W. Fleming, A. Mooradian, Fundamental line broadening of single-mode (AaAl)As diode lasers. Appl. Phys. Lett. **38**, 511–513 (1981a)
M.W. Fleming, A. Mooradian, Spectral characteristics of external-cavity controlled semiconductor lasers. IEEE J. Quantum Electron. **17**, 44–59 (1981b)
K. Furuya, Y. Suematsu, Y. Sakakibara, M. Yamada, Influence of intraband electronic relaxation on relaxation oscillation of injection lasers. Trans. IECE Jpn. E **62**, 241–245 (1979)
H. Haug, Quantum-mechanical rate equations for semiconductor lasers. Phys. Rev. **184**, 338–348 (1969)
C.H. Henry, Theory of the linewidth of semiconductor lasers. IEEE J. Quantum Electron. **18**, 259–264 (1982)
C.H. Henry, Theory of phase noise and power spectrum of a single mode injection laser. IEEE J. Quantum Electron. **19**, 1391–1397 (1983)
C.H. Henry, Theory of spontaneous emission noise in open resonators and its applications to lasers and optical amplifiers. J. Lightwave Technol. **4**, 288–297 (1986)
T. Ikegami, Y. Suematsu, Resonance-like characteristics of the direct modulation of a junction laser. Proc. IEEE **55**, 122–133 (1967)
T. Ikegami, Y. Suematsu, Carrier lifetime measurement of a junction laser using direct modulation. IEEE J. Quantum Electron. **4**, 148–151 (1968)
K.I. Kallimani, M.J. O'Mahony, Relative intensity noise for laser diodes with arbitrary amounts of optical feedback. IEEE J. Quantum Electron. **34**, 1438–1446 (1998)
R.F. Kazarinov, C.H. Henry, The relation of line narrowing and chirp reduction resulting from coupling of a semiconductor laser to a passive resonator. IEEE J. Quantum Electron. **23**, 1401–1409 (1987)
P.A. Kirkby, A.R. Goodwin, G.H.B. Thompson, P.R. Selway, Observations of self-focusing in stripe geometry semiconductor lasers and the development of a comprehensive model of their operation. IEEE J. Quantum Electron. **13**, 705–719 (1977)
R. Lang, Lateral transverse mode instability and its stabilization in stripe geometry injection laser. IEEE J. Quantum Electron. **15**, 718–726 (1979)
K.Y. Lau, A. Yariv, Ultra-high speed semiconductor lasers. IEEE J. Quantum Electron. **21**, 121–138 (1985)
M. Lax, Fluctuations from the non-equilibrium steady state. Rev. Mod. Phys. **32**, 25–64 (1960)
M. Lax, W.H. Louisell, Quantum noise, XII. density-operator treatment of field and population fluctuations. Phys. Rev. **185**, 568–591 (1969)

A.R. Linke, Modulation induced transient chirping in single frequency lasers. IEEE J. Quantum Electron. **21**, 593–597 (1985)
D. Marcuse, T.P. Lee, On approximate analytical solutions of rate equations for studying transient spectra of injection lasers. IEEE J. Quantum Electron. **19**, 1397–1406 (1983)
S.L. McCall, P.M. Platzman, An optimized $\pi/2$ distributed feedback laser. IEEE J. Quantum Electron. **21**, 1899–1894 (1985)
D.E. McCmber, Intensity fluctuations in the output of cw laser oscillators I. Phys. Rev. **141**, 306–322 (1966)
M. Nakamura, K. Aiki, N. Chinone, R. Ito, U. Umeda, Longitudinal-mode behaviors of mode stabilized $Al_xGa_{1-x}As$ injection lasers. J. Appl. Phys. **49**, 4644–4548 (1978)
M. Osinski, J. Buss, Linewidth broadening factor in semiconductor lasers—an overview. IEEE J. Quantum Electron. **23**, 9–29 (1987)
T.L. Paoli, J.E. Ripper, Direct modulation of semiconductor lasers. Proc. IEEE **58**, 1457–1465 (1970)
A. Papoulis, *Probability, Random Variables, and Stochastic Processes* (McGraw-Hill, New York, 1984)
K. Petermann, Calculated spontaneous emission factor for double-heterostructure injection lasers with gain-induced wave-guiding. IEEE J. Quantum Electron. **15**, 566–570 (1979)
K. Petermann, *Laser Diode Modulation and Noise* (Kluwer Academic, Dordrecht, 1988)
K. Petermann, G. Arnold, Noise and distortion characteristics of semiconductor lasers in optical fiber communication systems. IEEE J. Quantum Electron. **18**, 543–555 (1982)
H. Risken, *The Fokker-Planck Equation: Methods of Solution and Applications* (Springer, Berlin, 1996)
B. Saleh, *Photoelectron Statistics* (Springer, Berlin, 1978)
N. Schunk, K. Petermann, Noise analysis of injection-locked semiconductor injection lasers. IEEE J. Quantum Electron. **22**, 642–650 (1986)
G.H.B. Thompson, *Physics of Semiconductor Laser Devices* (Wiley, Chichester, 1980)
R.S. Tucker, High-speed modulation of semiconductor lasers. J. Lightwave Technol. **3**, 1180–1192 (1985)
K. Uomi, N. Chinone, T. Ohtoshi, T. Kajimura, High relaxation oscillation frequency (beyond 10 GHz) of GaAlAs multi-quantum well lasers. Jpn. J. Appl. Phys. **24**, L539–L541 (1985)
K. Vahala, A. Yariv, Semiclassical theory of noise in semiconductor lasers—part I. IEEE J. Quantum Electron. **19**, 1096–1101 (1983a)
K. Vahala, A. Yariv, Semiclassical theory of noise in semiconductor lasers—part II. IEEE J. Quantum Electron. **19**, 1102–1109 (1983b)
K. Vahala, C. Harder, A. Yariv, Observation of relaxation resonance effects in the field spectrum of semiconductor lasers. Appl. Phys. Lett. **42**, 211–213 (1983a)
K. Vahala, L.C. Chiu, S. Margalit, A. Yariv, On the linewidth enhancement factor α in semiconductor injection lasers. App. Phys. Lett. **42**, 631–633 (1983b)
Y. Yamamoto, AM and FM quantum noise in semiconductor lasers—part I: theoretical analysis. IEEE J. Quantum Electron. **19**, 34–46 (1983)
A. Yariv, P. Yeh, *Photonics: Optical Electronics in Modern Communications*, 6th edn. (Oxford University Press, Oxford, 2007)
T.H. Yoon, C.H. Lee, S.Y. Shin, Perturbation analysis of bistable and period doubling bifurcation in directly-modulated laser diodes. IEEE J. Quantum Electron. **25**, 1993–2000 (1989)

Chapter 4
Theory of Optical Feedback in Semiconductor Lasers

Abstract A semiconductor laser with optical feedback is an excellent model for generating chaos in its output power and the system has proven to be very useful in practical applications. This chapter concerns the theoretical background for instability and chaos induced by optical feedback in narrow-stripe edge-emitting semiconductor lasers, such as Fabry-Perot lasers, multi-quantum well (MQW) lasers, and distributed feedback (DFB) lasers. Particular dynamics of feedback-induced instability and chaos in semiconductor lasers are separately discussed in the following chapter. In this chapter, we focus on the theoretical treatment of optical feedback effects in semiconductor lasers. Lasers show the same or similar dynamics as far as rate equations are described by the same forms. We here assume single mode operations for semiconductor lasers. The dynamics for multimode cases will be discussed in Chap. 8.

4.1 Theory of Optical Feedback

4.1.1 Optical Feedback Effects and Classifications of Optical Feedback Phenomena

The effects of optical feedback in semiconductor lasers have been studied from the beginning of their development (Risch and Voumard 1977; Voumard 1977; Gavrielides et al. 1997). In early 1980, Lang and Kobayashi published a milestone paper on the effects of optical feedback in semiconductor lasers, which initiated an enormous research effort devoted to the study of the dynamics induced by optical feedback. Since then, bistability, instability, self-pulsations, and coherence collapse states have been observed in feedback-induced irregular oscillations in semiconductor lasers (Mils et al. 1980; Glas et al. 1983; Lenstra et al. 1985; Cho and Umeda 1986). In semiconductor lasers, self-optical-feedback effects are frequently used for the control of oscillation frequency, selection of mode, and suppression of side modes. Indeed, the linewidth of laser oscillations can be stabilized by a strong optical feedback and chirping of oscillation frequency can be compensated by

© Springer International Publishing AG 2017

J. Ohtsubo, *Semiconductor Lasers*, Springer Series in Optical Sciences 111,
DOI 10.1007/978-3-319-56138-7_4

optical feedback (Goldberg et al. 1982; Tamburrini et al. 1983; Agrawal 1984; Lin et al. 1984). On the other hand, the semiconductor laser shows unstable oscillations for a certain range of optical feedback levels. The dynamics of semiconductor lasers induced by optical feedback in this range are very interesting not only from the viewpoint of fundamental physics but also for practical applications, since optical feedback effects appear everywhere in optical systems including optical communication systems, optical data storages, and optical measurements. These irregular oscillations are induced by the dynamics involved in laser systems known as chaos described by nonlinear delay differential equations.

Cleaved facets were frequently used as a laser resonator in semiconductor lasers in the early days. Therefore, the reflectivity of laser facets of semiconductor lasers is much lower than that of other lasers such as gas lasers. Since light in a cavity of a semiconductor laser is reflected perpendicularly to the laser facet, the internal amplitude reflectivity r_0 is given by

$$r_0 = \frac{\eta - 1}{\eta + 1} \tag{4.1}$$

where η is the refractive index of the laser material. For example, the refractive index η of the AlGaAs semiconductor laser without any optical coating is about 3.6 and the amplitude reflectivity of the facet is calculated to be $r_0 = 0.565$. The corresponding intensity reflectivity is $R_0 = r_0^2 = 0.32$. Only 32% of the light generated by the stimulated emission is fed back into the laser cavity and the other photons dissipate from the laser cavity (Zah et al. 1987). To make a high power laser, the laser facets are coated appropriately by dielectric films. Then, the rear facet of the cavity usually has a high reflectivity of more than 90% and the front fact has a low reflectivity of less than 10%. This is quite different from other lasers where both facets have high reflectivities close to 100%.

In spite of such a dissipative laser structure, laser oscillations are still possible in semiconductor lasers due to the high efficiency of the conversion from pump to light. For example, the conversion efficiency of electricity to light in semiconductor lasers is usually up to fifty percent. This makes semiconductor lasers different from other lasers. Thus, light goes away from the cavity after a few reflections within the resonator. In other words, semiconductor lasers are easily affected by external light due to optical feedback or optical injection from a different laser. Indeed, the use of optical isolators is essential in optical communication systems to prevent unstable laser operations generated by feedback light from optical components and optical fiber facets. Optical feedback induces various instabilities in semiconductor lasers, for example, noises (actually they are chaotic fluctuations as discussed later) are much enhanced by optical feedback. In optical communications, the quality of signal transmissions has priority, so that optical isolators are used at the expensive of system sizes and costs to reduce feedback noises. On the other hand, optical information equipment, for example, optical data storages, in which serious problems by optical feedback are encountered for the performance of operations, the cost of the system is most important. In those systems, the reduction and control of

noises (actually chaotic oscillations) are essential issues for good systems. For such purpose, the idea of chaos control, which is discussed in Chap. 9, can be applied.

There are many parameters to characterize instabilities and chaos in semiconductor lasers. Every parameter is important for describing the characteristics, however, one important and most useful parameter to figure out the characteristics is the reflectivity of the external mirror. Tkach and Chraplyvy (1986) investigated the instabilities of semiconductor lasers with optical feedback and categorized them into the following five regimes, depending on the feedback fraction.

Regime I Very small feedback (the feedback fraction of the amplitude is less than 0.01%) and small effects. The linewidth of the laser oscillation becomes broad or narrow, depending on the feedback fraction (Kikuchi and Okoshi 1982)

Regime II Small, but not negligible effects (less than $\sim$0.1% and the case for $C > 1$, where the C parameter is a measure of instability, discussed in Sect. 4.2). Generation of the external modes gives rise to mode hopping among internal and external modes (Tkach and Chraplyvy 1985)

Regime III This is a narrow region around $\sim$0.1% feedback. The mode hopping noise is suppressed and the laser may oscillate with a narrow linewidth (Tkach and Chraplyvy 1986)

Regime IV Moderate feedback (around 1%). The relaxation oscillation becomes undamped and the laser linewidth is broadened greatly. The laser shows chaotic behavior and sometimes evolves into unstable oscillations in a coherence collapse state. The noise level is enhanced greatly under this condition (Lenstra et al. 1985)

Regime V Strong feedback regime (higher than 10% feedback). The internal and external cavities behave like a single cavity and the laser oscillates in a single mode. The linewidth of the laser is narrowed greatly (Fleming and Mooradian 1981a, b)

In the above regimes, the quoted fraction is that of the actual optical feedback level into the active layer and it does not mean the reflectivity of the external mirror, since there are scattering and absorption losses of light through optical components. Furthermore, a diffraction loss of light due to a collimator lens usually put in front of the laser facet is not negligible, because the thickness of the active layer is as small as 0.1 μm in ordinary edge-emitting lasers. Therefore, the fraction of optical feedback actually fed back into the active layer becomes one-tenth or less than the intensity reflectivity of the external mirror. However, semiconductor lasers are sensitive enough to destabilize their output power by a small amount of optical feedback of less than 1% of the amplitude. Therefore, an isolation of 40 dB is usually required in optical communication systems to avoid optical feedback effects.

The investigated dynamics of the above regimes were for a DFB laser with a wavelength of 1.55 μm, so that the feedback fraction corresponding to each dynamics scenario described above is not always true for other lasers. However, the

dynamics for other lasers show similar trends for the variations of feedback fraction. The lasers show the same or similar dynamics as far as the rate equations are written in the same forms. As has already been discussed, the rate equations for narrow-stripe edge-emitting semiconductor lasers, such as Fabry-Perot, MQW, and DFB lasers, are described by the same forms. Therefore, these lasers exhibit similar chaotic dynamics, though the parameters may have different values. We are very interested in regime IV that shows chaotic dynamics (Sacher et al. 1989; Mørk et al. 1990a, b, 1992), though it is a small level of optical feedback (the intensity fraction of the feedback is only 0.01%). In actual applications of semiconductor lasers, this regime is important because, for example, the feedback fraction of laser amplitude in Compact Disk systems corresponds to regime IV (Gray et al. 1994). Thus, regime IV is important for the studies of both nonlinear dynamics and applications.

4.1.2 Theoretical Model

The static characteristics of semiconductor lasers with optical feedback can be theoretically investigated with the relations among the reflectivities of internal cavity and external reflector, the gain in a medium, and other static laser parameters. However, the dynamic characteristics must be described by time-dependent equations of the systems. The equations for semiconductor lasers in the presence of optical feedback are easily obtained by modifying the rate equations for the solitary laser discussed in Chap. 3. The schematic model of a semiconductor laser with optical feedback is shown in Fig. 4.1. For a while, we consider that the external reflector is a conventional plain reflection mirror. The effects of other reflectors such as grating and phase conjugate mirrors will be discussed later. Light from a laser is reflected from an external mirror and fed back into the laser cavity with time delay. We assume that the mirror is positioned within the coherence length of the laser. Also, the laser is assumed to be operated at a single mode, although this is not always true in actual situations. The laser sometimes oscillates at multimode under certain parameter conditions of optical feedback even when the laser oscillates at a single mode in the solitary condition. The external feedback effect is added to the equation for the complex field of (3.47) and the field equation is written in the following form (Lang and Kobayashi 1980):

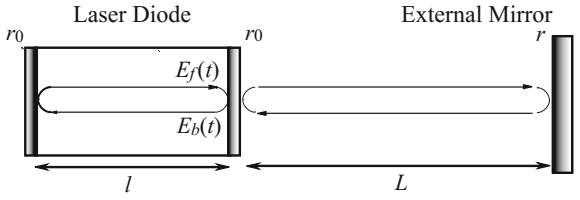

Fig. 4.1 Model of a semiconductor laser with optical feedback

$$\frac{dE(t)}{dt} = \frac{1}{2}(1 - i\alpha)G_n\{n(t) - n_{th}\}E(t) + \frac{\kappa}{\tau_{in}}E(t - \tau)\exp(i\omega_0\tau) \tag{4.2}$$

where κ is the feedback coefficient due to the external optical feedback, $\tau = 2L/c$ (L being the length of the external cavity) is the round trip time of light within the external cavity, ω_0 is the angular oscillation frequency of the laser. The extra term has a delay time τ and the complex field is described by a delay differential equation and this is the origin of instability and chaotic dynamics in semiconductor lasers. The equation is known as the Lang-Kobayashi equation after their derivation.

The feedback coefficient κ can be calculated from considering the multiple reflection effects of light in the external cavity. In Fig. 4.1, we consider the fields propagating forward and backward within the cavity and the extra term added to the laser field from the optical feedback in front of the facet of the resonator. For the steady-state oscillation in the presence of external feedback, the relation between the forward and backward traveling fields at the laser facet, $E_f(t)\exp(-i\omega_0 t)$ and $E_b(t)\exp(-i\omega_0 t)$, is given by (Lang and Kobayashi 1980)

$$E_b(t) = r_0\left\{E_f(t) + \frac{1 - r_0^2}{r_0}r\sum_{m=1}^{\infty}(-r_0 r)^{m-1}E_f(t - m\tau)\exp(im\omega_0\tau)\right\} \tag{4.3}$$

where r is the amplitude reflectivity of the external mirror. In the parenthesis of the above equation, the first term is the ordinary field of reflection in the internal cavity and the second is the effect of the external optical feedback. The semiconductor laser is easily destabilized and shows chaotic dynamics even for a small level of feedback less than a few percent of the amplitude reflectivity. We here consider a steady-state solution as $E_f(t - m\tau) \approx E_f(t)$ and only assume a single reflection for a small external reflection r. Then, the feedback coefficient κ is written by (van Tartwijk and Lenstra 1995)

$$\kappa = \left(1 - r_0^2\right)\frac{r}{r_0} \tag{4.4}$$

We assume that the reflectivities for the front and back facets of the laser cavity are the same at r_0. It is not always true for actual lasers, but the feedback rate for different reflectivities can be calculated straightforwardly. Recent semiconductor lasers have a low intensity reflectivity of the front facet as small as 10% or less by optical coating and, therefore, the lasers are much affected by optical feedback.

The time-dependent phase in the presence of optical feedback plays an important role, since the phase couples with the other variables. For the carrier density, we need not consider the modification of the equation. Similar to the derivations for the rate equations in (3.75)–(3.77), we obtain the rate equations in the presence of optical feedback as follows (Ohtsubo 2002):

$$\frac{dA(t)}{dt} = \frac{1}{2}G_n\{n(t) - n_{th}\}A(t) + \frac{\kappa}{\tau_{in}}A(t-\tau)\cos\theta(t) \tag{4.5}$$

$$\frac{d\phi(t)}{dt} = \frac{1}{2}\alpha G_n\{n(t) - n_{th}\} - \frac{\kappa}{\tau_{in}}\frac{A(t-\tau)}{A(t)}\sin\theta(t) \tag{4.6}$$

$$\frac{dn(t)}{dt} = \frac{J}{ed} - \frac{n(t)}{\tau_s} - G_n\{n(t) - n_0\}A^2(t) \tag{4.7}$$

$$\theta(t) = \omega_0\tau + \phi(t) - \phi(t-\tau) \tag{4.8}$$

We can investigate the dynamics of semiconductor lasers with optical feedback by numerically solving the above equations. In the rate equations for a solitary laser derived from (3.75) to (3.77), the phase does not affect the other variables and, therefore, a semiconductor laser is only described by the field amplitude and carrier density equations. However, we must consider the phase for a time development in the presence of optical feedback, since the phase is related to the other variables through the optical feedback term as shown in the above equations. Then, three coupled equations are essential for semiconductor lasers with optical feedback and they show unstable oscillations and chaotic dynamics in their output powers like three coupled equations in Lorenz systems. In the numerical simulations, the fourth-order Runge-Kutta algorithm is frequently used for the sake of the accuracy of the calculations (Press et al. 1986).

4.2 Linear Stability Analysis for Optical Feedback Systems

4.2.1 Steady-State Solutions

When the fluctuation of the output power is small even in the presence of optical feedback in a semiconductor laser, we assume a steady-state solution for the average field. In this case, we obtain the steady-state solutions for $A(t) = A_s$, $\phi(t) = (\omega_s - \omega_{th})t$, and $n(t) = n_s$ from (4.5) to (4.7) as follows (Tromborg et al. 1984, 1987; Agrawal and Dutta 1993):

$$A_s^2 = \frac{J/ed - n_s/\tau_s}{G_n(n_s - n_0)} \tag{4.9}$$

$$\omega_s - \omega_{th} = -\frac{\kappa}{\tau_{in}}\{\alpha\cos(\omega_s\tau) + \sin(\omega_s\tau)\} \tag{4.10}$$

$$n_s = n_{\text{th}} - \frac{2\kappa}{\tau_{\text{in}} G_n} \cos(\omega_s \tau) \tag{4.11}$$

For zero feedback coefficient $\kappa = 0$, the above equations reduce to the solutions for the solitary laser already given by (3.78)–(3.80). We rewrite (4.10) as

$$\omega_{\text{th}} \tau = \omega_s \tau + C \ \sin(\omega_s \tau + \tan^{-1}\alpha) \tag{4.12}$$

where the C parameter already introduced in the regimes of the dynamics for the optical feedback level in Sect. 4.1.1 is defined by (van Tartwijk and Lenstra 1995)

$$C = \frac{\kappa \tau}{\tau_{\text{in}}} \sqrt{1 + \alpha^2} \tag{4.13}$$

From (4.12), we can calculate modes for laser oscillations in the presence of optical feedback. The relation in (4.12) can be written by

$$\Delta\omega_s \tau = -C \sin(\varphi_0 + \Delta\omega_s \tau) \tag{4.14}$$

where $\Delta\omega_s = \omega_s - \omega_{\text{th}}$ corresponds to the steady-state value of the phase difference $\phi(t) - \phi(t - \tau)$ and $\varphi_0 = \omega_{\text{th}}\tau + \tan^{-1}\alpha$. When $C < 1$, there is only one solution for (4.12), as already discussed, which is dynamically stable and can be identified as a slightly changed solitary laser state. By increasing the C parameter value, the number of the mode solutions increases but is always an odd number. The curves in (C, φ_0) space in Fig. 4.2 that separate the regions of equal number of solutions are given by

$$\varphi_0 = (2m+1)\pi \pm \cos^{-1}\left(\frac{1}{C}\right) \mp C \sin\left\{\cos^{-1}\left(\frac{1}{C}\right)\right\} \tag{4.15}$$

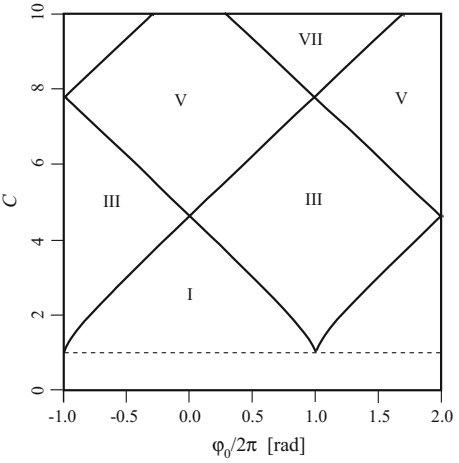

Fig. 4.2 Number of solutions for (4.14) in (C, φ_0) space. The *roman numbers* represent the number of solutions

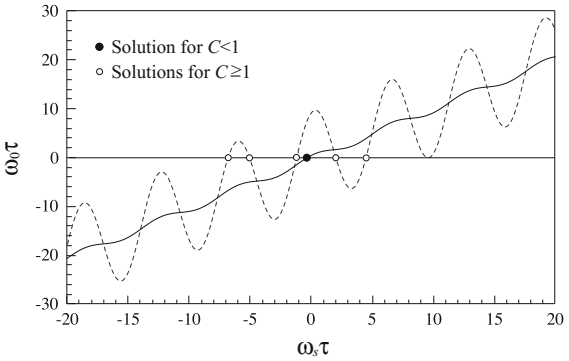

Fig. 4.3 Dependence of steady-state solutions for the phase on the parameter value C. *Solid* and *dashed lines* correspond to $C = 0.76$ and $C = 9.50$, respectively. The *black circle* denotes only one solution for $C < 1$ and *white circles* represent multiple solutions for $C > 1$

where $C \geq 1$ and m is an integer number. This causes a pattern to arise in (C, φ_0) space, as shown in Fig. 4.2 where the roman numbers represent the number of solutions. For $C > 1$, multiple steady-state solutions appear.

The solutions in (4.12) are also graphically calculated as intersections of the curves $y = \omega_{\text{th}}\tau$ and $y = \omega_s\tau + C\sin(\omega_s\tau + \tan^{-1}\alpha)$ as shown in Fig. 4.3 (Fravre 1987; Murakami et al. 1997). When $C < 1$ (for a small optical feedback and a short external cavity), (4.12) has only a single solution and the laser exhibits stable oscillation. If $C > 1$, many possible modes for the laser oscillations (external modes and anti-modes) are generated with the relation among the internal laser modes and the excited external modes, and, then, the laser shows unstable operations. By adjusting the position of the external mirror (which is equivalent to appropriate selection of the round-trip time τ) and setting $\varphi_0 = \omega_{\text{th}}\tau + \tan^{-1}\alpha = 0$ (where $\omega_{\text{th}}\tau = -\tan^{-1}\alpha$ and, thus, the condition $\Delta\omega_s\tau = -C\sin(\Delta\omega_s\tau)$ is satisfied), the higher bound of the coefficient C for a single-mode oscillation of the laser is easily obtained from Fig. 4.3 as $C \approx 3\pi/2$ (Petermann 1988). Above this value $C > 3\pi/2$, many modes are excited and the laser becomes unstable. Complicated dynamics are observable in the output power, however, the laser does not always exhibit unstable oscillations. Even for such unstable regimes, the laser may show stable oscillations. The details of the dynamics will be discussed in Sect. 5.2.

When the C parameter well exceeds the value of unity, many modes are excited in the laser output and the laser becomes truly unstable. Another representation for possible oscillation modes is frequently used in the phase space of the oscillation frequency and the carrier density. Figure 4.4 is such a representation for the parameter space in the $\Delta\omega_s\tau$ versus Δn_s plane. The relation is calculated from (4.10) and (4.11) by eliminating the sine and cosine functions and is given by (Henry 1986)

$$\left(\Delta\omega_s\tau - \frac{\alpha\tau}{2}G_n\Delta n\right)^2 + \left(\frac{\tau}{2}G_n\Delta n\right)^2 = \left(\frac{\kappa\tau}{\tau_{\text{in}}}\right)^2 \tag{4.16}$$

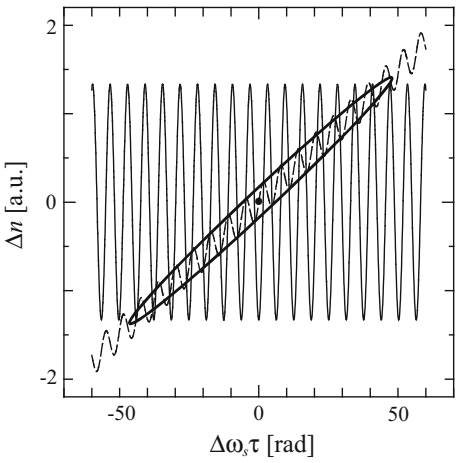

Fig. 4.4 Carrier density change n versus frequency change ω for the possible steady states under external feedback. The crossing points of the solid and broken sinusoidal waves are the locations of the modes. Modes are on an ellipsoid. The *solid dot* at center (0, 0) is the solitary oscillation mode

where $\Delta\omega_s = \omega_s - \omega_{\text{th}}$ and $\Delta n_s = n_s - n_{\text{th}}$. The broken sinusoidal curve in the figure denotes the deviation from the steady state of the oscillation angular frequency $\Delta\omega_s$ and the other sinusoidal curve represents that of the carrier density Δn_s. The crossing points of these two curves are the locations of possible oscillations and they are on the ellipsoid given by (4.16) (thick solid curve in the figure). Those in the lower half are the solutions for stable oscillations (external modes) and those in the upper half are unstable oscillations. Solutions for unstable oscillations are sometimes called anti-mode. The laser oscillates at one of the external modes and the maximum gain mode is the most probable mode for laser oscillation. However, when the laser oscillation is unstable due to external feedback, the mode hops around among the external modes and the anti-modes, thus the laser exhibits chaotic oscillations. One typical instability is the phenomenon known as low-frequency fluctuations (LFFs), in which the laser output power shows frequent irregular dropouts having frequency from MHz to hundred MHz (Mørk et al. 1988; Fischer et al. 1996). The details for the origin of LFFs and their dynamics are again discussed in Sect. 5.3. The solid dot at the center of the ellipsoid in the figure is the solution for the laser oscillation in the solitary laser (solitary mode). The laser without optical feedback, of course, has no fluctuation in the sense of chaotic dynamics and oscillates only at this mode.

4.2.2 Linear Stability Analysis

The stability and instability of laser oscillations in the presence of optical feedback are theoretically studied by the linear stability analysis for the steady-state solutions of the laser variables. In the same manner as a solitary laser, using the rate equations and taking the first order small infinities for the perturbations, the equations for the

field δE, the phase $\delta\phi$, and the carrier density δn are calculated as (Tromborg et al. 1984)

$$\begin{aligned}\frac{\mathrm{d}\delta A(t)}{\mathrm{d}t} &= \frac{1}{2}G_n A_s \delta n(t) - \frac{\kappa}{\tau_{\mathrm{in}}}\cos(\omega_s\tau)\{\delta A(t) - \delta A(t-\tau)\} \\ &\quad - \frac{\kappa}{\tau_{\mathrm{in}}}A_s\sin(\omega_s\tau)\{\delta\phi(t) - \delta\phi(t-\tau)\}\end{aligned} \tag{4.17}$$

$$\begin{aligned}\frac{\mathrm{d}\delta\phi(t)}{\mathrm{d}t} &= \frac{\alpha}{2}G_n A_s \delta n(t) + \frac{\kappa}{\tau_{\mathrm{in}}}\frac{\sin(\omega_s\tau)}{A_s}\{\delta A(t) - \delta A(t-\tau)\} \\ &\quad - \frac{\kappa}{\tau_{\mathrm{in}}}\cos(\omega_s\tau)\{\delta\phi(t) - \delta\phi(t-\tau)\}\end{aligned} \tag{4.18}$$

$$\frac{\mathrm{d}\delta n(t)}{\mathrm{d}t} = -2G_n A_s(n_s - n_0)\delta A(t) - \left(G_n A_s^2 + \frac{1}{\tau_s}\right)\delta n(t) \tag{4.19}$$

Assuming that the perturbations take the forms of $\delta x(t) = \delta x \exp(\gamma\, t)$ ($x = A$, ϕ, and n), the characteristic equations for the condition having non-trivial solutions for the variables δA, $\delta\phi$, and δn are calculated from the following:

$$\begin{vmatrix} \gamma + \frac{\kappa}{\tau_{\mathrm{in}}}K\cos(\omega_s\tau) & \frac{\kappa}{\tau_{\mathrm{in}}}KA_s\sin(\omega_s\tau) & -\frac{1}{2}G_nA_s \\ -\frac{\kappa}{\tau_{\mathrm{in}}}\frac{K}{A_s}\sin(\omega_s\tau) & \gamma + \frac{\kappa}{\tau_{\mathrm{in}}}K\cos(\omega_s\tau) & -\frac{1}{2}\alpha G_n \\ 2A_sG_n(n_s - n_0) & 0 & \gamma + G_nA_s^2 + \frac{1}{\tau_s} \end{vmatrix} = 0 \tag{4.20}$$

where $K = 1 - \exp(-\gamma\tau)$. The oscillation modes for the perturbations are calculated by solving the characteristic equation

$$\begin{aligned}D(\gamma) &= \gamma^3 + 2\left\{-\Gamma_{\mathrm{R}} + \frac{\kappa}{\tau_{\mathrm{in}}}K\cos(\omega_s\tau)\right\}\gamma^2 \\ &\quad + \left\{\omega_{\mathrm{R}}^2 - \frac{4\kappa K\Gamma_{\mathrm{R}}}{\tau_{\mathrm{in}}}\cos(\omega_s\tau) + \left(\frac{\kappa}{\tau_{\mathrm{in}}}K\right)^2\right\}\gamma \\ &\quad - \frac{2\kappa K^2\Gamma_{\mathrm{R}}}{\tau_{\mathrm{in}}} + \frac{\kappa K\omega_{\mathrm{R}}^2}{\tau_{\mathrm{in}}}\{\cos(\omega_s\tau) - \alpha\sin(\omega_s\tau)\} = 0\end{aligned} \tag{4.21}$$

In the above equation, Γ_{R} and ω_{R} are the previously defined parameters of the damping factor and angular frequency of the relaxation oscillation at the solitary mode.

We cannot calculate explicit forms of the solutions for (4.21), since the equation includes the exponential form for the variable γ and, then, the solutions are numerically calculated. The real part of the solution is related to the stability of the mode and the imaginary part of it represents the oscillation frequency of the mode as has already been discussed. When the real part (damping factor) takes a negative value, the mode is stable and the excited oscillation damps out for the time

development with a frequency calculated from the imaginary part. On the other hand, the mode is unstable for a positive value of the real part and the laser shows either regular or irregular oscillations with a typical frequency corresponding to the imaginary part. If the level of optical feedback is low or the condition $\kappa\tau/\tau_{in} \ll 1$ is satisfied, we can assume $|\gamma\tau| \ll 1$ and obtain the analytical form of the solution for γ. Then, the real and imaginary parts, Γ'_R and ω'_R, of the solution are given by (Agrawal and Dutta 1993)

$$\Gamma'_R = \Gamma_R \tag{4.22}$$

$$\omega'_R = \omega_R \sqrt{\frac{1 + (\kappa_c - \alpha\kappa_s)\tau/\tau_{in}}{(1 + \kappa_c\tau/\tau_{in})^2 + (\kappa_s\tau/\tau_{in})^2}} \tag{4.23}$$

where $\kappa_c = \kappa \cos(\omega_s\tau)$ and $\kappa_s = \kappa \sin(\omega_s\tau)$. Of course, (4.22) and (4.23) are equal to (3.86) and (3.87) at no optical feedback, respectively.

The relaxation frequency in the presence of optical feedback shifts from that of the solitary oscillation. Increase or decrease of the frequency shift depends on the signs of κ_c and κ_s, however, it is usually enhanced at moderate optical feedback and takes a larger value than that of the solitary oscillation. For a laser oscillation, the sign of the expression inside the square root in (4.23) must be positive and we obtain the stability condition (Acket et al. 1984; Lenstra et al. 1984)

$$1 + C\cos(\omega_s\tau + \tan^{-1}\alpha) > 0 \tag{4.24}$$

Equation (4.24) denotes that the laser becomes unstable for $C > 1$ as expected, while it is stable for $C < 1$ even if optical feedback is present in semiconductor lasers. We calculated oscillation modes for perturbations of the steady-state values for the variables. The solutions obtained from such characteristic equations are called linear modes, the name comes from the linear stability analysis.

4.2.3 *Linear Mode, and Stability and Instability in Semiconductor Lasers*

For certain ranges of optical feedback level, the output of a semiconductor laser evolves from stable states to chaotic states via unstable periodic oscillations. One or a few frequencies for the solutions derived from the characteristic equation in (4.21) are equal to or close to the typical frequency corresponding to the response of the system. Periodic oscillations in chaotic states are generally not harmonic oscillations, but they include an obscure fundamental frequency and its higher harmonics. In quasi-periodic oscillations, frequency peaks become obscured due to irregular oscillations and no clear spectral peak is observable in complete chaotic states, like white noises. In semiconductor lasers with optical feedback, modes generated by

the internal and external cavities are mixed and the laser oscillates at one or several modes. The other important frequency of laser oscillations besides these modes is the frequency of the relaxation oscillation. Since chaos is a nonlinear phenomenon, many modes are not only related to the internal and external modes and the relaxation oscillation modes but also their sums and differences, and higher harmonics are excited (Cohen et al. 1988; Helms and Petermann 1990; Levine et al. 1995). For a chaotic bifurcation, the laser first becomes unstable with a frequency close to the relaxation oscillation, which is called period-1 oscillation. Next, the external mode is also excited. After that, many modes are excited and the laser oscillates at quasi-periodic oscillation. Then, the laser evolves into chaotic oscillations with complicated and broadened frequency components.

Figure 4.5 is an example of numerically calculated linear modes from (4.21) (Murakami and Ohtsubo 1998). In the figure, the change of modes is shown for the increase of the amplitude reflectivity from the external mirror. The vertical axis is the damping factor (the real part of the solution of the characteristic equation) and the horizontal axis is the frequency of the oscillation (the imaginary part of the solution). For a negative value of the damping factor, the mode damps out for a time evolution even if it is once excited. The value of the real part is negative for the highest mode in the absence of optical feedback (around the frequency of 2.5 GHz in this case) and the laser never gets into unstable oscillations. The frequency corresponds to the relaxation oscillation at the solitary mode. With the increase of the external feedback, the real part of the highest mode at first exceeds zero and the laser becomes unstable with a frequency of the relaxation oscillation (period-1 oscillation). Under the condition in this figure, the C parameter at which the laser at first exhibits unstable oscillation has a value of $C = 2.8$ (calculated from the external reflection of 0.4%). The value is slightly less than $C = 3\pi/2$, which was estimated in the previous section, but the assumption in the previous section is proved to be reasonable. With further increase of the external reflectivity, the damping rates for all the modes increase and the laser becomes less stable. The second highest mode in the presence of optical feedback corresponds to the external cavity mode and the frequency is about 1.5 GHz (approximately equal to the

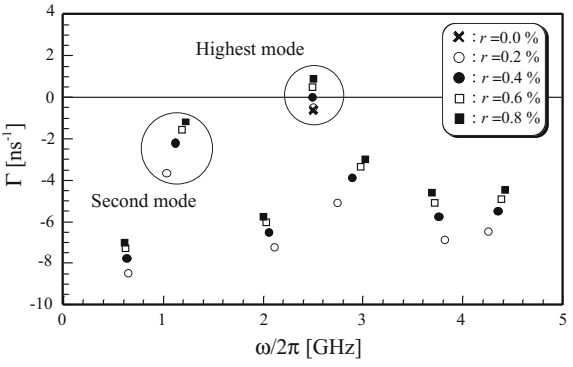

Fig. 4.5 Linear mode distributions at an external cavity length of $L = 10$ cm and a bias injection current of $J = 1.3J_{th}$. The highest mode corresponds to the relaxation oscillation and the second mode to the external cavity mode. With increasing external feedback, the real part of each mode increases and the laser becomes less stable

frequency calculated from the external cavity length of 10 cm). With this mode, the laser shows higher periodic oscillations and it evolves into chaotic oscillations through a bifurcation for the increase of optical feedback (Ye and Ohtsubo 1998). As we recognize from the figure, the external frequency does not have a fixed value, but shifts with the increase of the reflectivity, except for the relaxation oscillation mode, which always almost has a fixed value.

4.2.4 Gain Reduction Due to Optical Feedback

Though direct analyses for the rate equations are essential for investigating the dynamics of semiconductor lasers with optical feedback, the steady-state analysis is still useful and important to obtain parameter conditions for stable and unstable laser operations. Here, we calculate the gain in the presence of optical feedback under a steady-state condition. We assume the same reflectivities calculated in (4.4) (the internal reflectivity r_0 and the external reflectivity r), the effective reflectivity at the front facet taking into account the external mirror at steady state is given by (Koelink et al. 1992; Osmundsen and Gade 1983; Kakiuchida and Ohtsubo 1994; Katagiri and Hara 1994)

$$r_{\mathrm{eff}} = \frac{r_0 + r\exp(i\omega_0\tau)}{1 + r_0 r\exp(i\omega_0\tau)} \tag{4.25}$$

We investigate the gain of laser oscillation in the presence of optical feedback under the condition of a small external reflectivity $r \ll 1$. From the above equation, the effective reflectivity is written by

$$r_{\mathrm{eff}} = |r_{\mathrm{eff}}|\exp(i\phi_r) \approx r_0 + (1 - r_0^2)r\exp(i\omega_0\tau) \tag{4.26}$$

where ϕ_r is the phase of the effective reflectivity. Also, the effective reflectivity $\kappa = (1 - r_0^2)r/r_0$ defined in (4.4) is small enough. Then, the absolute value and phase of the effective reflectivity are approximated as

$$|r_{\mathrm{eff}}| = r_0\{1 + \kappa\cos(\omega_0\tau)\} \tag{4.27}$$

$$\phi_r = \kappa\sin(\omega_0\tau) \tag{4.28}$$

The condition of laser oscillation under optical feedback is also given by the same equation as (3.3) and reads as

$$r_0 r_{\mathrm{eff}}\exp\{2ikl + (g - a)l\} = 1 \tag{4.29}$$

Therefore, the condition of the gain is

$$g_c = a + \frac{1}{l}\ln\left(\frac{1}{r_0|r_{\text{eff}}|}\right) \tag{4.30}$$

The difference between the gains with and without optical feedback for a small value of κ is given by

$$g_c - g_{\text{th}} = -\frac{\kappa}{l}\cos(\omega_0\tau) \tag{4.31}$$

The gain in the presence of optical feedback depends on the round-trip time τ and it changes periodically for the variation of the external cavity length. The mode for the maximum gain is attained at $\omega_0\tau = 2\,m\pi$ (m being an integer). As the gain varies depending on the optical feedback level, we can control or suppress the adjacent modes from the main oscillation mode by using the gain difference in accordance with (4.31) when the external mirror is positioned close to the laser facet. The difference of gains between successive modes in edge-emitting semiconductor lasers is as small as 0.1 cm^{-1} and the condition $\kappa/l < 0.1$ is required for stable laser oscillations (Petermann 1988). For example, with an internal reflectivity of the laser facet of $r_0 = 0.56$ and the internal cavity length of $l = 300$ μm, we obtain the condition of the stable laser oscillation for the external amplitude reflectivity as about $r < 2 \times 10^{-3}$. This value corresponds to that in regimes III to IV already discussed in Sect. 4.1.1 and is equal to the boundary of the regimes between the stable and unstable oscillations.

4.2.5 *Linewidth in the Presence of Optical Feedback*

The linewidth of laser oscillations in the presence of optical feedback is also calculated in the same manner as in Sect. 3.6.6. We consider small perturbations for the steady-state values of the variables in the presence of optical feedback and derive the linewidth from the power spectrum for the time derivative equations for the perturbations. The calculation is rather lengthy but straightforward, so that only the result is given here (Tromborg et al. 1984). Using the linewidth $\Delta\nu$ without optical feedback, the linewidth $\Delta\nu_{\text{ex}}$ in the presence of optical feedback is calculated as

$$\Delta\nu_{\text{ex}} = \frac{\Delta\nu}{F^2} \tag{4.32}$$

The coefficient $F = \text{d}\omega_{\text{th}}/\text{d}\omega_s$ for the reduction (or the broadening) of the spectral line width is calculated from (4.12) and given by

$$F = \frac{d\omega_{th}}{d\omega_s} = 1 + C\cos\left(\omega_s\tau + \tan^{-1}\alpha\right) \tag{4.33}$$

The minimum spectral linewidth is attained when the phase adjustment condition $\omega_s\tau = -\tan^{-1}\alpha$ is satisfied. Then, the spectral linewidth at the minimum condition is given by

$$\Delta v_{ex} = \frac{\Delta v}{(1+C)^2} \tag{4.34}$$

On the other hand, the linewidth for the maximum gain condition at $\omega_s\tau = 2\ m\pi$ is calculated to be

$$\Delta v_{ex} = \frac{\Delta v}{\left(1+\kappa\frac{\tau}{\tau_{in}}\right)^2} \tag{4.35}$$

The linewidth with optical feedback at the maximum gain condition is always less than the value of the solitary oscillation. These results hold for stable laser operations even when the laser is subjected to optical feedback. However, for optical feedback above a certain level, the laser does not oscillate at one of the modes but many modes are simultaneously excited or even drifting or wandering among the modes (external modes and anti-modes) occur. Such oscillations give rise to much noise (actually chaotic fluctuations) and even result in the collapse of coherence. These are the typical features in regimes III and IV in the preceding discussion. At this state, the linewidth of the laser is much broadened to as large as over GHz or more. However, the coherence of the laser recovers and the linewidth becomes narrow for a sufficiently strong optical feedback at regime V.

4.3 Feedback from a Grating Mirror

4.3.1 Plane Grating Optical Feedback

Other than conventional optical feedback reflectors, a grating mirror is frequently used to select the oscillation line in a semiconductor laser or stabilize the oscillation frequency. Grating optical feedback is categorized as one of filtered optical feedback systems and is originally applied for the stabilization of laser oscillations, however, it sometimes induces instabilities in lasers. Before discussing instabilities, we present the theoretical background of grating feedback and stabilization of optical frequency. For a small feedback coefficient and also small detuning between the laser and grating frequencies, the complex field equation can be approximately written by a similar equation of conventional optical feedback as

$$\frac{dE(t)}{dt} = \frac{1}{2}(1 - i\alpha)G_n\{n(t) - n_{th}\}E(t) + \frac{\kappa_g}{\tau_{in}}E(t - \tau)\exp(-i\Delta\omega t + i\omega_g\tau) \quad (4.36)$$

where κ_g is the feedback coefficient from the grating mirror and $\Delta\omega$ is the angular frequency detuning given by $\Delta\omega = \omega_g - \omega_0$ (ω_g being the angular frequency of the grating feedback). However, in general, the optical feedback from the grating mirror is strong and the frequency detuning between the laser oscillation and the grating is as large as up to several nanometers in wavelength. Therefore, the approximation in (4.36) is only valid within a small range of grating feedback. To treat the dynamics of grating feedback in a strict sense, the relation of the phase between the complex fields for the forward and backward propagations as a multiple-reflection model must be taken into account (Pittoni et al. 2001). Instead, we here consider the static model of the grating feedback and some stable and unstable features of the dynamics are presented.

The effective reflectivity of the static model in grating feedback including the laser facet and the grating mirror with multiple reflections is calculated in the same manner as the conventional mirror in (4.25) and is given by (Binder et al. 1990; Genty et al. 2000)

$$r_{eff} = |r_{eff}|\exp(i\phi_r) = \frac{r_0 + r(\omega)\exp(i\omega\tau)}{1 + r_0 r(\omega)\exp(i\omega\tau)} \quad (4.37)$$

The above equation has the same form as (4.25), but the external reflectivity by the grating mirror is a function of the optical frequency $\nu = \omega/2\pi$. The condition of the laser oscillation can be written in the same form as (4.29) and the gain is also given by (4.30). We here apply the steady-state analysis and calculate the conditions for the phase and the gain. Putting the angular frequency of the laser oscillation as $\omega = \omega_g$, the phase condition in the presence of grating optical feedback reads as

$$2\eta\omega_g l/c + \phi_r = 2m\pi \quad (4.38)$$

where m is an integer and $2\eta\omega_g l/c = 2m'\pi$ is the oscillation condition for a solitary laser. From the relation $\Delta(\eta\omega_g) = \omega_{th}\ \Delta\eta + (\omega_g - \omega_{th})\eta$, the change in the round-trip phase $\Delta\phi_d$ compared to $2m\pi$ due to grating tuning is written by

$$\Delta\phi_d = \frac{2l}{c}\{\omega_{th}\Delta\eta + (\omega_g - \omega_{th})\eta\} + \phi_r \quad (4.39)$$

where $\Delta\eta$ is expanded by the carrier density and the angular frequency as

$$\Delta\eta = \frac{\partial\eta}{\partial n}(n - n_{th}) + \frac{\partial\eta}{\partial\omega}(\omega_g - \omega_{th}) \quad (4.40)$$

Using the definition of the refractive index in (3.40), i.e., $\eta_c = \eta - i\eta'$, together with the equalities

$$\frac{\partial \eta}{\partial n} = \alpha \frac{\partial \eta'}{\partial n} = -\frac{\alpha c}{2\omega_{\text{th}}} \frac{\partial g}{\partial n} \tag{4.41}$$

the relation between the carrier density and the gain is written as

$$\frac{\partial \eta}{\partial n}(n - n_{\text{th}}) = -\frac{\alpha c}{2\omega_{\text{th}}}(g_{\text{g}} - g_{\text{th}}) \tag{4.42}$$

where g_{g} is the gain in the presence of grating feedback. Substituting (4.40)–(4.42) into (4.39) together with the relation in (3.8), the phase change reads as

$$\Delta\phi_d = -\alpha(g_{\text{g}} - g_{\text{th}})l + \frac{2\eta_e l}{c}(\omega_{\text{g}} - \omega_{\text{th}}) + \phi_r \tag{4.43}$$

Putting $\Delta\phi_d = 0$ for a possible solution for the laser oscillation and using the internal trip time of light $\tau_{\text{in}} = 2\eta_e l/c$, we obtain

$$\omega_{\text{g}} - \omega_{\text{th}} = \frac{1}{\tau_{\text{in}}}\{\alpha(g_{\text{g}} - g_{\text{th}})l - \phi_r\} \tag{4.44}$$

Then, the reduction of gain in the presence of grating feedback is given by

$$g_{\text{g}} - g_{\text{th}} = \frac{1}{l}\ln\frac{1}{r_0|r_{\text{eff}}(\omega_g)|} \tag{4.45}$$

and the linewidth reduction factor is calculated as

$$F_{\text{g}} = \frac{\mathrm{d}\omega_{\text{th}}}{\mathrm{d}\omega_{\text{g}}} = 1 + \frac{1}{\tau_{\text{in}}}\frac{\mathrm{d}\phi_r}{\mathrm{d}\omega_{\text{g}}} - \frac{\alpha}{\tau_{\text{in}}}\frac{\mathrm{d}}{\mathrm{d}\omega_{\text{g}}}\left\{\ln\frac{1}{|r_{\text{eff}}(\omega_{\text{g}})|}\right\} \tag{4.46}$$

The linewidth of a semiconductor laser with grating optical feedback is finally written as

$$\Delta\nu_{\text{g}} = \frac{\Delta\nu}{F_{\text{g}}^2} \tag{4.47}$$

where $\Delta\nu$ is again the linewidth of the solitary laser defined by (3.130). When the laser beam has a Gaussian profile and a certain diffraction order is selected by the grating as a feedback light, the reflectivity is explicitly given by

$$r(\omega_{\text{g}}) = r_{\text{g}} \exp\left\{-\frac{(\omega_{\text{g}} - \omega_{\text{G}})^2}{\Delta\omega_{\text{G}}^2}\right\} \tag{4.48}$$

where ω_{G} is the selected angular frequency of the grating, r_{g} is its reflectivity, and $\Delta\omega_{\text{G}}$ is the width of the grating resolution at that angular frequency defined by

$\Delta\omega_G = c \tan\theta/w_0$ (θ is the incidence angle of light onto the grating and $2w_0$ is the diameter of the Gaussian beam). The linewidth of a semiconductor laser is narrowed by a grating feedback under stable oscillation. However, it is again noted that the laser becomes unstable even by a grating feedback for a certain range of the feedback strength, either for small or strong grating feedback.

4.3.2 Fiber Bragg Grating Optical Feedback

Fiber Bragg grating is frequently used as compact and frequency selective optical feedback systems. It is easy to study the static effects in semiconductor lasers subjected to optical feedback from fiber Bragg grating based on the theoretical analysis. However, it is not easy to find rigorous theory for the dynamic properties of optical feedback from fiber Bragg grating (time dependent characteristics), since the optical feedback arises from a continuous distributed optical reflection within a finite length L_{FBG} of the fiber Bragg grating and, also, the reflected optical phase coupled to the laser cavity continuously changes. Several theories are proposed for the treatment of the dynamics in semiconductor lasers with optical feedback from fiber Bragg grating (Erdogan 1997; Abdulrhmann et al. 2003; Naumenko et al. 2003). Here, we derive the field equation, which expresses the rough effects of the dynamic properties in semiconductor lasers with fiber Bragg grating optical feedback.

In a system of fiber Bragg grating optical feedback in semiconductor lasers, the feedback field can be similarly given by the field (4.3) as the relation between the forward and backward traveling fields, E_f and E_b, at the laser facet, and is given by

$$E_b(t) = r_0\left[E_f(t) + \frac{1}{2\pi}\frac{1-r_0^2}{r_0^2}\sum_{m=1}^{\infty}\exp(i\omega_0 m\tau)\int_{-\infty}^{\infty}\{-r_0\tilde{r}(\omega)\}^m\tilde{E}_f(\omega)\exp\{i\omega(t-m\tau)\}\mathrm{d}\omega\right] \tag{4.49}$$

where $\tilde{r}(\omega)$ is the frequency response of the reflectivity form the fiber Bragg grating, and $\tilde{E}_f(\omega)$ is the Fourier transform of the time dependent field $E_f(t)$. In above equation, we consider multiple reflection of optical field. The response function $\tilde{r}(\omega)$ is calculated from the coupled-mode theory for the mutually coupled field due to distributed fringes within a finite coupling length of fiber Bragg grating, L_{FBG}, and is given by (Erdogan 1997; Naumenko et al. 2003; Yariv and Yeh 2006)

$$\tilde{r}(\omega) = \frac{-\kappa_{FBG}\sinh\left\{\sqrt{\kappa_{FBG}^2-\delta^2}L_{FBG}\right\}}{\delta\sinh\left\{\sqrt{\kappa_{FBG}^2-\delta^2}L_{FBG}\right\} + i\sqrt{\kappa_{FBG}^2-\delta^2}\cosh\left\{\sqrt{\kappa_{FBG}^2-\delta^2}L_{FBG}\right\}} \tag{4.50}$$

where κ_{FBG} is the magnitude of the coupling coefficient of the fiber Bragg grating, and δ is the phase mismatch between the counter propagating modes that equals $\delta = \eta_{\mathrm{FBG}}(\omega - \omega_{\mathrm{FBG}})/c$ (η_{FBG} and ω_{FBG} being the refractive index of the fiber Brag grating and the Bragg angular frequency, respectively).

Using the above relations, for fiber Bragg grating optical feedback, the second term of the right hand side equation in (4.2) is replaced by the following feedback term:

$$E_{\mathrm{FBG\ feedback}}(t) = \frac{1}{2\pi\tau_{\mathrm{in}}}\frac{r_0^2-1}{r_0^2}\sum_{m=1}^{\infty}\exp(i\omega_0 m\tau + i\theta_0) \int_{-\infty}^{\infty}\{-r_0\tilde{r}(\omega)\}^m\tilde{E}(\omega)\exp\{i\omega(t-m\tau)\}\mathrm{d}\omega \tag{4.51}$$

where θ_0 is a constant phase associated with the grating optical feedback. In (4.51), for $m = 1$ and $\tilde{r}(\omega) = \mathrm{const}$, the equation reduces to additional term of the right-hand side of equation in (4.2), namely, corresponding to conventional optical feedback with a small reflection. For a weak optical feedback from fiber Bragg grating, we consider only a single optical feedback as $m = 1$, and the feedback term becomes

$$E_{\mathrm{FBG\ feedback}}(t) = \frac{1}{\tau_{\mathrm{in}}}\frac{1-r_0^2}{r_0} r\exp(i\omega_0\tau + \theta_0)\cdot r(t)\otimes E(t-\tau) \tag{4.52}$$

where $r(t)$ is the inverse Fourier transform of $\tilde{r}(\omega)$ and $\otimes$ represents convolution operator. Indeed, from theoretical and experimental studies, chaos and low-frequency fluctuations (LFFs) are demonstrated in semiconductor lasers with optical feedback from fiber Bragg grating (Abdulrhmann et al. 2003; Baladi et al. 2016).

4.4 Phase-Conjugate Feedback

A semiconductor laser is frequently used as a light source of phase-conjugate optics (Pochi 1993). Or a phase-conjugate mirror is positively used to return light exactly into the active region in a semiconductor laser, since the light reflected from the phase-conjugate mirror is automatically fed back into the laser cavity due to the generation of the conjugate wave without any additional optical components in the external optical path. The phase-conjugate feedback induces instabilities in the laser oscillation and the dynamics of the laser are not always the same as those from the ordinary feedback reflector. The typical timescale in semiconductor lasers with optical feedback is of the order of a nanosecond, defined by the laser relaxation oscillation frequency. Therefore, typical effects of phase-conjugate feedback occur

when the phase-conjugate mirrors respond as fast as this timescale. Such phase-conjugate mirrors are realized in quick-response Kerr media with large third-order susceptibility and also quick-response photorefractive mirrors of semiconductor materials (Agrawal and Klaus 1991; Agrawal and Gray 1992; van Tartwijk et al. 1992; Langley and Shore 1994; Gray et al. 1993, 1994; Bochove et al. 1997). On the other hand, the dynamics for slow-response photorefractive mirrors, where the response is much slower than the time variations of the laser dynamics, are the same as those for ordinary plain reflection mirrors. For a slow-response photorefractive crystal, for example a $TiBaO_3$ crystal, the laser light automatically returns into the laser cavity, however, the mirror produces the same dynamics of optical feedback as an ordinary reflection mirror (Miltyeni et al. 1995; Liby and Statman 1996; Murakami and Ohtsubo 1999). Only the spatial phase-conjugate characteristic is effective in such optical feedback. In either case of fast or slow response phase-conjugate mirrors, phase-conjugate feedback can be also applied to control the quality of oscillations for semiconductor lasers (Gray et al. 1995; Kurz and Mukai 1996; Anderson 1999).

Figure 4.6 shows an optical setup for generating a phase-conjugate wave by four-wave mixing from a phase-conjugate mirror. We here assume that the phase-conjugate mirror responds much faster than the typical chaotic fluctuations of semiconductor lasers. The angular frequencies of the signal and pump beams at the phase-conjugate mirror are set to be ω_0 and ω_p, respectively, and the generated phase-conjugate wave has a frequency $\omega_c = 2\omega_p - \omega_0$. Therefore, we consider the angular frequency detuning $2\delta = 2(\omega_p - \omega_0)$ between the laser angular frequency and that of the feedback light. Thus, the equation of the complex field E for the semiconductor laser with phase-conjugate feedback is given by

$$\frac{dE(t)}{dt} = \frac{1}{2}(1 - i\alpha)G_n\{n(t) - n_{th}\}E(t) + \frac{\kappa}{\tau_{in}}E^*(t - \tau)\exp\left\{-i2\delta\left(t - \frac{\tau}{2}\right) + i\phi_{PCM}\right\} \tag{4.53}$$

where E^* represents the conjugate field and ϕ_{PCM} is the phase shift induced by the reflection at the phase-conjugate mirror. The final term in the above equation is the effect of phase-conjugate feedback. The rate equations for the field amplitude, the phase, and the carrier density are written as

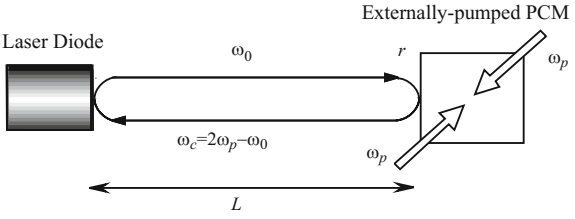

Fig. 4.6 Optical setup in a semiconductor laser with phase-conjugate optical feedback

$$\frac{dA(t)}{dt} = \frac{1}{2}G_n\{n(t) - n_{th}\}A(t) + \frac{\kappa}{\tau_{in}}A(t-\tau)\cos\theta(t) \tag{4.54}$$

$$\frac{d\phi(t)}{dt} = \frac{1}{2}\alpha G_n\{n(t) - n_{th}\} - \frac{\kappa}{\tau_{in}}\frac{A(t-\tau)}{A(t)}\sin\theta(t) \tag{4.55}$$

$$\frac{dn(t)}{dt} = \frac{J}{ed} - \frac{n(t)}{\tau_s} - G_n\{n(t) - n_0\}A^2(t) \tag{4.56}$$

$$\theta(t) = 2\delta\left(t - \frac{\tau}{2}\right) + \phi(t) + \phi(t-\tau) + \phi_{PCM} \tag{4.57}$$

Equations (4.54)–(4.56) are in the same form as (4.5)–(4.7), however, (4.57) is different from (4.8) even for zero detuning ($\delta = 0$). This makes the laser dynamics of phase-conjugate feedback different from those of an ordinary optical feedback reflector.

A typical feature of the dynamics in phase-conjugate feedback is the phase locking phenomenon. The steady-state solutions for the field, the phase, and the carrier density at zero detuning $\delta = 0$ are given by

$$A_s^2 = \frac{J/ed - n_s/\tau_s}{G_n(n_s - n_0)} \tag{4.58}$$

$$\phi_s = \frac{1}{2}\tan^{-1}(-\alpha) \tag{4.59}$$

$$n_s = n_{th} - \frac{2\kappa}{\tau_{in}G_n}\cos(2\varphi_s) \tag{4.60}$$

Namely, the phase is locked to a certain value given by (4.59) in phase-conjugate feedback, while it changes depending on the time in the case of conventional external feedback and the steady-state frequency has multiple solutions (see 4.10). Indeed, the phase-locking phenomenon in phase-conjugate optical feedback is obtained by the numerical simulation as shown in Fig. 4.7a. In this figure, a step current is applied to a semiconductor laser subjected to phase-conjugate optical feedback at time $t = 0$. From the figure, the optical phase is locked to a certain value after transient of the relaxation oscillation. It is noted that the feedback level is so weak that chaotic fluctuation is not visible in the time series. On the other hand, the phase in a case of conventional optical feedback linearly increases for the time lapse as shown in Fig. 4.7b. The result is consistent with the assumption of the steady-state solution for the linear phase change with time introduced in Sect. 4.2.1. It is noted that the optical phase in conventional optical feedback may linearly increase or decrease for the time development. Namely, the sign of $\omega_s - \omega_{th}$ in (4.10) is either positive or negative.

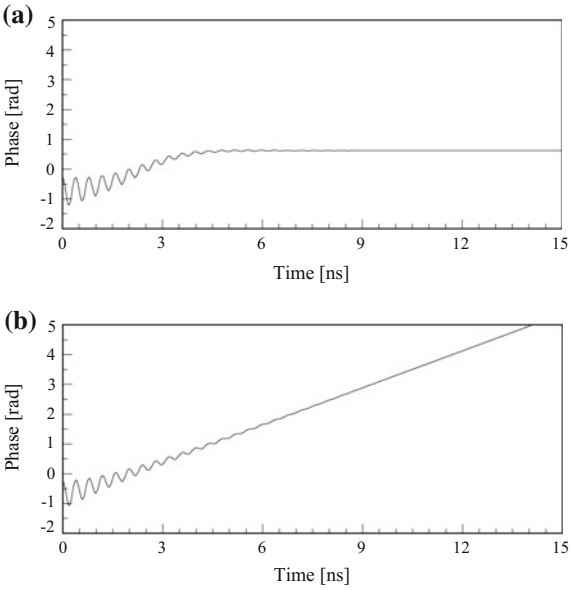

Fig. 4.7 **a** Step response of the bias injection current in phase conjugate optical feedback in a semiconductor laser. After the transient of relaxation oscillation, the phase is locked to a certain level. **b** Step response in conventional optical feedback. The phase is linearly changed for time development

The laser for ordinary optical feedback is very sensitive to short variations of the external mirror compatible with optical wavelength. However, the phase of the laser with phase-conjugate feedback does not show any change for such a small variation of the external mirror. Here, we discussed the case when the phase-conjugate mirror responds immediately after the arrival of the signal beam. The laser dynamics of semiconductor lasers with a finite response time in a phase-conjugate mirror have also been discussed (DeTienne et al. 1997; van der Graaf et al. 1998). For a finite response of a phase-conjugate mirror, the equation for the complex field is given by

$$\frac{\mathrm{d}E(t)}{\mathrm{d}t} = \frac{1}{2}(1 - i\alpha)G_n\{n(t) - n_{\mathrm{th}}\}E(t) + \frac{\kappa}{\tau_{\mathrm{in}}}\exp\left\{-i2\delta\left(t - \frac{\tau}{2}\right)\right\}\int_{-\infty}^{t} E^*(t' - \tau)\exp\left\{-(1 - i\delta t_m)\frac{(t - t')}{t_m}\right\}\mathrm{d}t' \tag{4.61}$$

where t_m is the time that it takes the light to penetrate the phase-conjugate mirror. Above, we assumed a fast-response phase-conjugate mirror, but similar dynamics are obtained for a finite-response phase-conjugate mirror.

4.5 Incoherent Feedback

Coherent optical feedback effects are important in applications of semiconductor lasers. For a long external cavity when the feedback light has an incoherent coupling with the original light in the laser cavity, the rate equations in (4.5)–(4.7) are still applicable for investigating the laser dynamics. Even in incoherent optical feedback, a laser becomes unstable and shows instability and chaos in its output. For example, the dynamics of long external optical feedback from a reflector over the coherence length of a semiconductor laser is treated as those for incoherent schemes. Indeed, the coherence length of a semiconductor laser is usually several tens to a hundred meters, since the linewidth of the laser oscillations is around several mega hertz without any frequency stabilization. Also, polarization-rotated optical feedback under certain conditions is sometimes treated as a system of incoherent optical feedback. In these cases, the returned laser field does not interfere with the inner oscillation field, but acts as the perturbation for carriers and has the coupling with them. Namely, the feedback term is introduced to the carrier density in the rate equations. Through this interaction, the laser shows instabilities.

The model is described by the following rate equations (Otsuka and Chern 1991):

$$\frac{\mathrm{d}S(t)}{\mathrm{d}t} = G_n\{n(t) - n_{\mathrm{th}}\}S(t) \tag{4.62}$$

$$\frac{\mathrm{d}n(t)}{\mathrm{d}t} = \frac{J}{ed} - \frac{n(t)}{\tau_s} - G_n\{n(t) - n_0\}\{S(t) + \kappa' S(t-\tau)\} \tag{4.63}$$

where κ' is the feedback coefficient coupled with the carrier density and τ has the same definition as before (the round-trip time of light in the external cavity). We do not have to consider the phase, since the phenomena come from the incoherent origin. The rate equations are only written by two differential equations, however, they are coupled with each other by the delay differential term. Thus, we can expect instabilities and chaos in semiconductor lasers. One of the typical features in incoherent optical feedback is sustained pulsations in the laser output. The gain saturation term discussed in Sect. 3.3.4 must be taken into account for such pulsations. In incoherent optical feedback in semiconductor lasers, we obtain not only irregular or chaotic pulsations in the laser output but also regular pulsings (such as period-1 oscillations) with high-speed oscillations as fast as picoseconds (Otsuka and Chern 1991). Those regular fast pulsing oscillations are important for the application of light sources in high-speed optical communications.

4.6 Polarization-Rotated Optical Feedback

Generally, narrow-stripe edge-emitting semiconductor laser oscillates at a transverse electric mode (TE mode). On the other hand, the counter polarization mode, i.e., transverse magnetic mode (TM mode), is not a lasing mode and is scarcely excited. The optical gain of a TM mode is slightly less than that of a TE mode and the laser preferredly oscillates at the TE mode due to the nonlinear effect of lasing. However, the TM mode starts to oscillate when the TE mode is coherently coupled to the TM mode through the polarization-rotated optical feedback. We consider here the case of strong optical feedback from a crossed-polarization component, where the orthogonal-polarization component becomes the lasing mode. Figure 4.8 shows two examples of single path systems with orthogonal-polarization optical feedback. Figure 4.8a is a ring-loop model for orthogonal-polarization optical feedback, by which we can avoid multiple-reflection scheme within optical feedback loop. The main oscillated TE mode from a narrow-stripe edge-emitting laser goes through a polarization beam splitter and is converted into a TM mode by $\lambda/4$ and $\lambda/2$ wave-plates. Figure 4.8b is another example of orthogonal-polarization feedback systems. The TE polarized beam enters a Faraday rotator (RT), whose input polarizer is removed, and the beam's polarization rotates 45°. The beam reflected by the feedback mirror is reinjected to the rotator, and this creates an orthogonal polarized beam to the laser oscillation mode (i.e., TM mode). In this configuration, the reflected vertical beam from the laser facet is once passed through the rotator, but it is blocked by the polarizer (PL). Thus, a single feedback loop is guaranteed in this setup. For both systems, the effect of orthogonal-polarization feedback can be described by the same rate equations. For a strong crossed-polarizing optical feedback (say, for example, 10 times larger than ordinary

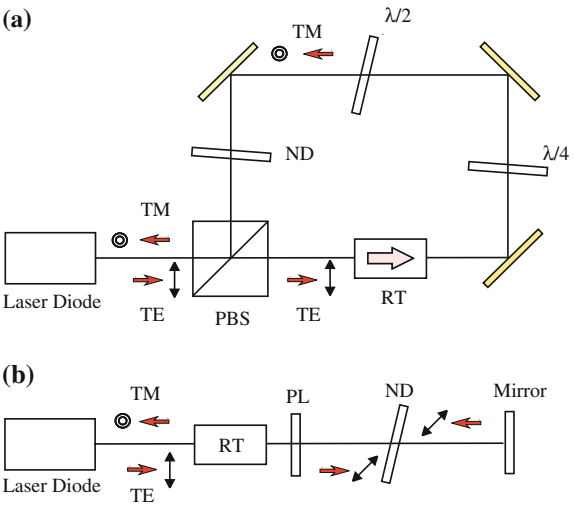

Fig. 4.8 Optical setups of orthogonal polarization feedback in a semiconductor laser. **a** Ring-loop feedback system. *PBS* polarization beam splitter, *RT* Faraday rotator, $\lambda/4$: $\lambda/4$ waveplate, $\lambda/2$: $\lambda/2$ waveplate, *ND* neutral density filter. **b** Single-pass feedback system. *PL* polarizer

parallel-polarization optical feedback to induce chaotic oscillations), the TM oscillation merges in the laser output power besides the TE oscillation mode. In this situation, we can observe quite different dynamics compared with ordinary parallel-polarizing optical feedback and the detail of the dynamics will be discussed in Chap. 5 (Heil et al. 2003).

For the crossed-polarization scheme with strong optical feedback, we must use a coherent model for the laser oscillations, since both the amplitudes of TE and TM modes are time-dependent functions and coherently couple with each other. Then, the rate equations of crossed-polarization feedback system are written as

$$\frac{\mathrm{d}A_{\mathrm{TE}}(t)}{\mathrm{d}t} = \frac{1}{2} G_{n,\mathrm{TE}} \{n(t) - n_{\mathrm{th,TE}}\} A_{\mathrm{TE}}(t) \tag{4.64}$$

$$\frac{\mathrm{d}\phi_{\mathrm{TE}}(t)}{\mathrm{d}t} = \frac{1}{2} \alpha G_{n,\mathrm{TE}} \{n(t) - n_{\mathrm{th,TE}}\} \tag{4.65}$$

$$\frac{\mathrm{d}A_{\mathrm{TM}}(t)}{\mathrm{d}t} = \frac{1}{2} G_{n,\mathrm{TM}} \{n(t) - n_{\mathrm{th,TM}}\} A_{\mathrm{TM}}(t) + \frac{\kappa}{\tau_{\mathrm{in}}} A_{\mathrm{TE}}(t-\tau) \cos\theta(t) \tag{4.66}$$

$$\frac{\mathrm{d}\phi_{\mathrm{TM}}(t)}{dt} = \frac{1}{2} \alpha G_{n,\mathrm{TM}} \{n(t) - n_{\mathrm{th,TM}}\} - \frac{\kappa}{\tau_{\mathrm{in}}} \frac{A_{\mathrm{TE}}(t-\tau)}{A_{\mathrm{TM}}(t)} \sin\theta(t) \tag{4.67}$$

$$\frac{\mathrm{d}n(t)}{\mathrm{d}t} = \frac{J}{ed} - \frac{n(t)}{\tau_s} - \{n(t) - n_0\} \{G_{n,\mathrm{TE}} A_{\mathrm{TE}}^2(t) + G_{n,\mathrm{TM}} A_{\mathrm{TM}}^2(t)\} \tag{4.68}$$

$$\theta(t) = \omega_0 \tau + \phi_{\mathrm{TM}}(t) - \phi_{\mathrm{TE}}(t-\tau) \tag{4.69}$$

where the subscripts TE and TM represent the variables and parameters for TE and TM modes. The gain G_n and the carrier density at threshold n_{th} have different values for the TE and TM modes in a strict sense. When optical feedback is small, the equations for the TM mode (4.66) and (4.67) are eliminated and we can put $A_{\mathrm{TM}}^2(t) \propto A_{\mathrm{TE}}^2(t-\tau)$. Then, replacing (4.64) for the photon number, the relations of (4.62) and (4.63) hold. Crossed-polarization optical feedback plays an important role in VCSELs as will be discussed in Chap. 8. In VCSELs, typical polarization dynamics are observable even for a small amount of optical feedback with crossed-polarization due to the small difference of the gains between the two polarization modes.

4.7 Filtered Feedback

We have discussed several optical feedback schemes and formulated the equations for the models. We can consider systematic treatments for these models (Yousefi and Lenstra 1999; Lenstra et al. 2005; Green and Krauskopf 2006). We here

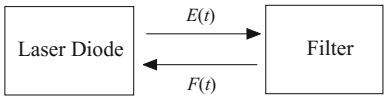

Fig. 4.9 Notation of filtered feedback

formulate the preceding optical feedback models. Also, the formulation can be extended to other feedback models such as optoelectronic feedback models, which will be discussed in Chap. 7. Through the introduction of systematic descriptions, we can give rise to a good perspective for universal understanding of the dynamics in feedback phenomena in semiconductor lasers, i.e., coherent and incoherent optical feedback, phase-conjugate feedback, grating feedback, etc. Figure 4.9 shows the notation of the system for filtered feedback. Assuming that the laser field E and the feedback function given by an external device F are slowly time-dependent amplitudes, the filtered feedback system is written as

$$\frac{\mathrm{d}E(t)}{\mathrm{d}t} = \frac{1}{2}(1 - i\alpha)G_n\{n(t) - n_{\mathrm{th}}\}E(t) + \frac{\kappa_{\mathrm{feedback}}}{\tau_{\mathrm{in}}}F(t) \tag{4.70}$$

We assume that the emitted laser field is $E(t)\mathrm{e}^{-i\omega_0 t} + c.c.$ and the feedback field $F(t)\mathrm{e}^{-i\omega_0 t} + c.c.$. For a linearly responding device, the function is given by

$$F(t) = \int_{-\infty}^{t} r(t' - t)E(t')\mathrm{d}t \tag{4.71}$$

where r (t) represents the response function of the external devices. It is noted that, in a case of phase-conjugate optical feedback, E in (4.71) must be replaced by E^*. The carrier density equation remains the same and is given as

$$\frac{\mathrm{d}n(t)}{\mathrm{d}t} = \frac{J}{ed} - \frac{n(t)}{\tau_s} - G_n\{n(t) - n_0\}|E(t)|^2 \tag{4.72}$$

For simplicity, the response function is assumed to be given by a simple Lorentzian frequency filter. Indeed, the spectral form of the transfer function induced by optical feedback from a grating or Fabry-Perot filter can be given by a Lorentzian shape as will be discussed in Chap. 5. From the Fourier transform relation, the time-dependent response function is given as

$$r(t) = \Lambda \exp\{-\Lambda|t| - i(\omega_c - \omega_0)t\} \tag{4.73}$$

where ω_c is the central frequency of the Lorentz spectrum and Λ is the half-width at half-maximum (HWHM) of the spectrum. Under this assumption, one obtains the differential equation for the feedback as

$$\frac{\mathrm{d}F(t)}{\mathrm{d}t} = \Lambda E(t-\tau)\exp(i\omega_0\tau) - \{\Lambda + i(\omega_c - \omega_0)\}F(t) \tag{4.74}$$

In general, the response does not always have a Lorentzian spectral function in coherent optical feedback. However, a general response function can be expanded by a linear superposition of Lorentz functions and one can generally decompose the response function as a sum of exponential functions of the same type of the equation $r(t) = \Lambda \exp\{-\Lambda|t| - i(\omega_c - \omega_0)t\}$.

From the above discussions, we can figure out general descriptions for the systems with filtered optical feedback. In the following, we will study the explicit forms of the feedback function for some limiting cases. In a conventional optical feedback without frequency filter (usual plane mirror feedback), Λ is assumed to be infinity. In this limit, the differential equation is simply reduced as

$$F(t) = E(t-\tau)\exp(i\omega_0\tau) \tag{4.75}$$

The expression, of course, is the same as the extra term added to the field equation of a semiconductor laser with optical feedback in (4.2). For a very narrow filter case, i.e., $\Lambda \to 0$, (one of such examples is optical injection from a different laser), the feedback function is easily calculated as

$$F(t) = E_{\mathrm{inj}}(t)\exp\{-i(\omega_m - \omega_0)t\} \tag{4.76}$$

Injection-locking instability will be discussed in Chap. 6. The third example is optical feedback from a four-wave mixing phase-conjugate mirror with finite time response and where the feedback field is detuned from the solitary laser, which was discussed in Sect. 4.4. In a four-wave mixing phase-conjugate optical feedback, the differential equation of the response function is modified

$$\frac{\mathrm{d}F(t)}{\mathrm{d}t} = \Lambda E^*(t-\tau)\exp\left\{-2i\delta\left(t-\frac{\tau}{2}\right)\right\} - (\Lambda + i\delta)F(t) \tag{4.77}$$

where δ is the detuning of the angular frequency between the four-wave mixing pump beam ω_p and the reference frequency ω_0, i.e., $\delta = \omega_p - \omega_0$. A system with optoelectronic feedback is also written by the same feedback function as discussed here, and the dynamics of such systems will be treated in Chap. 7.

References

S.G. Abdulrhmann, M. Ahmed, T. Okamoto, W. Ishimori, M. Yamada, An improved analysis of semiconductor laser dynamics under strong optical feedback. IEEE J. Sel. Top. Quantum Electron. **9**, 1265–1274 (2003)

G.P. Agrawal, Line narrowing in a single mode injection laser due to external optical feedback. IEEE J. Quantum Electron. **20**, 468–471 (1984)

G.P. Agrawal, N.K. Dutta, *Semiconductor Lasers*, 2nd edn. (Van Nostrand Reinhold, New York, 1993)
G.P. Agrawal, G.R. Gray, Effect of phase-conjugate feedback on the noise characteristics of semiconductor lasers. Phys. Rev. A **46**, 5890–5898 (1992)
G.P. Agrawal, J.T. Klaus, Effect of phase-conjugate feedback on semiconductor laser dynamics. Opt. Lett. **16**, 1325–1327 (1991)
G.A. Acket, D. Lenstra, J. den Boef, B.H. Verbeek, The influence of feedback intensity on longitudinal mode properties and optical noise in index-guided semiconductor lasers. IEEE J. Quantum Electron. **20**, 1163–1169 (1984)
O.K. Anderson, A.P.A. Fischer, L.C. Lane, E. Louvergneaux, S. Stolte, D. Lenstra, Experimental stability diagram of a diode laser subject to weak phase-conjugate feedback from a Rubidium vapor cell. IEEE J. Quantum Electron. **35**, 577–582 (1999)
F. Baladi, M.W. Lee, J.R. Burie, M.A. Bettiati, A. Boudrioua, A.A. Fischer, High-resolution low-frequency fluctuation map of a multimode laser diode subject to filtered optical feedback via a fiber Bragg grating. Opt. Lett. **41**, 2950–2953 (2016)
J.O. Binder, D. Cormack, A. Somani, Intermodal tuning characteristics of an INGaAsP laser with optical feedback from an external grating reflector. IEEE J. Quantum Electron. **26**, 1191–1199 (1990)
E. Bochove, Theory of a semiconductor laser with phase-conjugate optical feedback. Phys. Rev. A **55**, 3891–3899 (1997)
Y. Cho, M. Umeda, Observation of chaos in a semiconductor laser with delayed feedback. Opt. Commun. **59**, 131–136 (1986)
J.S. Cohen, R.R. Dentine, B.H. Verbeek, The effect of optical feedback on the relaxation oscillation in semiconductor lasers. IEEE J. Quantum Electron. **24**, 1989–1995 (1988)
D.H. DeTienne, G.R. Gray, G.P. Agrawal, D. Lenstra, Semiconductor laser dynamics for feedback from a finite-penetration-depth phase-conjugate mirror. IEEE J. Quantum Electron. **33**, 838–844 (1997)
T. Erdogan, Fiber grating spectra. J. Lightwave Technol. **15**, 1277–1294 (1997)
M.W. Fleming, A. Mooradian, Fundamental line broadening of single-mode (AaAl)As diode lasers. Appl. Phys. Lett. **38**, 511–513 (1981a)
M.W. Fleming, A. Mooradian, Spectral characteristics of external-cavity controlled semiconductor lasers. IEEE J. Quantum Electron. **17**, 44–59 (1981b)
I. Fischer, G.H.M. van Tartwijk, A.M. Levine, W. Elsäßer, E.O. Göbel, D. Lenstra, Fast pulsing and chaotic itinerancy with a drift in the coherence collapse of semiconductor lasers. Phys. Rev. Lett. **76**, 220–223 (1996)
F. Fravre, Theoretical analysis of external optical feedback on DFB semiconductor lasers. IEEE J. Quantum Electron. **23**, 81–88 (1987)
A. Gavrielides, V. Kovanis, T. Erneux, Analytical stability boundaries for a semiconductor laser subject to optical injection. Opt. Commun. **136**, 253–256 (1997)
G. Genty, A. Gröhn, H. Talvitie, M. Kaivola, H. Ludvigsen, Analysis of the linewidth of a grating-feedback GaAlAs laser. IEEE J. Quantum Electron. **36**, 1193–1198 (2000)
P. Glas, R. Müller, A. Klehr, Bistability, self-sustained oscillations, and irregular operation of a GaAs laser coupled to an external resonator. Opt. Commun. **47**, 297–301 (1983)
L. Goldberg, H.F. Taylor, A. Dandrige, J.F. Weller, R.O. Miles, Coherence collapse in single mode semiconductor lasers due to optical feedback. IEEE J. Quantum Electron. **18**, 555–679 (1982)
G.R. Gray, A.T. Ryan, G.P. Agrawal, E.C. Gage, Control of optical-feedback-induced laser intensity noise in optical data recording. Opt. Eng. **32**, 739–745 (1993)
G.R. Gray, D. Huang, G.P. Agrawal, Chaotic dynamics of semiconductor lasers with phase-conjugate feedback. Phys. Rev. A **49**, 2096–2105 (1994)
G.R. Gray, D.H. DeTienne, G.P. Agrawal, Mode locking in semiconductor lasers by phase-conjugate optical feedback. Opt. Lett. **20**, 1295–1297 (1995)
K. Green, B. Krauskopf, Mode structure of a semiconductor laser subject to filtered optical feedback. Opt. Commun. **258**, 243–255 (2006)

C.H. Henry, Theory of spontaneous emission noise in open resonators and its applications to lasers and optical amplifiers. J. Lightwave Technol. **4**, 288–297 (1986)
J. Helms, K. Petermann, A simple analytic expression for the stable operation range of laser diode with optical feedback. IEEE J. Quantum Electron. **26**, 833–836 (1990)
T. Heil, A. Uchida, P. Davis, T. Aida, TE-TM dynamics in a semiconductor laser subject to polarization-rotated optical feedback. Phys. Rev. A **68**, 033811-1–033811-8 (2003)
Y. Katagiri, S. Hara, Increased spatial frequency in interferential undulations of coupled cavity lasers. Appl. Opt. **33**, 5564–5570 (1994)
H. Kakiuchida, J. Ohtsubo, Characteristics of a semiconductor laser with external feedback. IEEE J. Quantum Electron. **30**, 2087–2097 (1994)
K. Kikuchi, T. Okoshi, Simple formula giving spectrum-narrowing ratio of semiconductor laser output obtained by optical feedback. Electron. Lett. **18**, 10–12 (1982)
M.H. Koelink, M. Slot, F.F.M. de Mul, R. Grever, A.C. Graaff, M. Dasse, J.G. Aaroudse, Laser Doppler velocimeter based on the self-mixing effect in a fiber-coupled semiconductor laser: theory. Appl. Opt. **31**, 3401–3408 (1992)
P. Kürz, T. Mukai, Frequency stabilization of semiconductor laser by external phase-conjugate feedback. Opt. Lett. **21**, 1369–1371 (1996)
R. Lang, K. Kobayashi, External optical feedback effects on semiconductor injection properties. IEEE J. Quantum Electron. **16**, 347–355 (1980)
L.N. Langley, K.A. Shore, Intensity noise and linewidth characteristics of laser diodes with phase conjugate optical feedback. IEE Proc.: Optoelectron. **141**, 103–108 (1994)
D. Lenstra, M. van Vaalen, B. Jaskorzynska, On the theory of a single-mode laser with weak optical feedback. Physica **125C**, 255–264 (1984)
L. Lenstra, B.H. Verbeek, A.J. den Boef, Coherence collapse in single-mode semiconductor lasers due to optical feedback. IEEE J. Quantum Electron. **21**, 674–679 (1985)
D. Lenstra, G. Vemuri, M. Yousefi, Generalized optical feedback (Chap. 3), in *Unlocking Dynamical Diversity—Optical Feedback Effects on Semiconductor Lasers*, ed. by D.M. Kane, K.A. Shore (Wiley, Chichester, 2005)
A.M. Levine, G.H.M. van Tartwijk, D. Lenstra, T. Erneux, Diode lasers with optical feedback: stability of the maximum gain mode. Phys. Rev. A **52**, R3436–R3439 (1995)
B.W. Liby, D. Statman, Controlling the linewidth of a semiconductor laser with photorefractive phase conjugate feedback. IEEE J. Quantum Electron. **32**, 835–838 (1996)
C. Lin, C. Burrus, L. Coldren, Characteristics of single-longitudinal mode selection in short-coupled-cavity (SCC) injection lasers. J. Lightwave Technol. **2**, 544–549 (1984)
R.O. Mils, A. Dandrigdge, B. Tveten, H.F. Taylor, T.G. Tgiallorenzi, Feedback induced line broadening in cw channel-substrate planar laser diodes. Appl. Phys. Lett. **37**, 990–992 (1980)
J. Mørk, B. Tromborg, P.L. Christiansen, Bistability and low-frequency fluctuations in semiconductor lasers with optical feedback: a theoretical analysis. IEEE J. Quantum Electron. **24**, 123–133 (1988)
J. Mørk, J. Mark, B. Tromborg, Route to chaos and competition between relaxation oscillations for a semiconductor laser with optical feedback. Phys. Rev. Lett. **65**, 1999–2002 (1990a)
J. Mørk, M. Semkow, B. Tromborg, Measurement and theory of mode hopping in external cavity laser. Electron. Lett. **26**, 284–285 (1990b)
J. Mørk, B. Tromborg, J. Mark, Chaos in semiconductor lasers with optical feedback: theory and experiment. IEEE J. Quantum Electron. **28**, 93–108 (1992)
E. Miltyeni, M.O. Ziegler, M. Hofmann, J. Sacher, W. Elsäßer, E.O. Göbel, D.L. MacFarlane, Long-term stable mode locking of a visible diode laser with phase-conjugate feedback. Opt. Lett. **20**, 734–736 (1995)
A. Murakami, J. Ohtsubo, Dynamics and linear stability analysis in semiconductor lasers with phase-conjugate feedback. IEEE J. Quantum Electron. **34**, 1979–1986 (1998)
A. Murakami, J. Ohtsubo, Dynamics of semiconductor lasers with optical feedback from photorefractive phase conjugate mirror. Opt. Rev. **6**, 350–364 (1999)
A. Murakami, J. Ohtsubo, Y. Liu, Stability analysis of semiconductor laser with phase-conjugate feedback. IEEE J. Quantum Electron. **33**, 1825–1831 (1997)

A. Naumenko, P. Besnard, N. Loiko, G. Ughetto, J.C. Bertreux, Characteristics of a semiconductor laser coupled with a fiber Bragg grating with arbitrary amount of feedback. IEEE J. Quantum Electron. **39**, 1216–1228 (2003)
J. Ohtsubo, Chaotic dynamics in semiconductor lasers with optical feedback (Chap. 1), in *Progress in Optics*, vol. 44, ed. by E. Wolf (North-Holland, Amsterdam, 2002)
J.H. Osmundsen, N. Gade, Influence of optical feedback on laser frequency spectrum and threshold conditions. IEEE J. Quantum Electron. **19**, 465–469 (1983)
K. Otsuka, J.L. Chern, High-speed picosecond pulse generation in semiconductor lasers with incoherent optical feedback. Opt. Lett. **16**, 1759–1761 (1991)
K. Petermann, *Laser Diode Modulation and Noise* (Kluwer Academic, Dordrecht, 1988)
F. Pittoni, M. Gioannini, I. Montrosset, Time-domain analysis of fiber grating semiconductor laser operation in active mode-locking regime. IEEE J. Sel. Top. Quantum Electron. **7**, 280–286 (2001)
Y. Pochi, *Introduction to Photorefractive Nonlinear Optics* (Wiley, New York, 1993)
W.H. Press, B.P. Flannery, S.A. Teukolsky, W.T. Vetterling, *Numerical Recipes: The Art of Scientific Computing* (Cambridge University Press, Cambridge, 1986)
C. Risch, C. Voumard, Self-pulsation in the output intensity and spectrum of GaAs-AlGaAs cw diode lasers coupled to a frequency-selective external optical cavity. J. Appl. Phys. **48**, 2083–2085 (1977)
J. Sacher, W. Elsäßer, E.O. Göbel, Intermittency in the coherence collapse of a semiconductor laser with external feedback. Phys. Rev. Lett. **63**, 2224–2227 (1989)
M. Tamburrini, P. Spano, S. Piazolla, Influence of an external cavity on semiconductor laser phase noise. Appl. Phys. Lett. **43**, 410–412 (1983)
R.W. Tkach, A.R. Chraplyvy, Line broadening and mode splitting due to weak feedback in single frequency 1.5 μm lasers. Electron. Lett. **21**, 1081–1083 (1985)
R.W. Tkach, A.R. Chraplyvy, Regimes of feedback effects in 1.5 μm distributed feedback lasers. J. Lightwave Technol. **4**, 1655–1661 (1986)
B. Tromborg, J.H. Osmundsen, H. Olesen, Stability analysis for a semiconductor laser in an external cavity. IEEE J. Quantum Electron. **20**, 1023–1032 (1984)
B. Tromborg, H. Olssen, X. Pan, S. Saito, Transmission line description of optical feedback and injection locking for Fabry-Perot and DFB lasers. IEEE J. Quantum Electron. **23**, 1875–1889 (1987)
G.H.M. van Tartwijk, D. Lenstra, Semiconductor lasers with optical injection and feedback. Quantum Semiclass. Opt. **7**, 87–148 (1995)
G.H.M. van Tartwijk, H.J.C. van der Linden, D. Lenstra, Theory of a diode laser with phase-conjugate feedback. Opt. Lett. **17**, 1590–1592 (1992)
W.A. van der Graaf, L. Pesquera, D. Lenstra, Stability of a diode laser with phase-conjugate feedback. Opt. Lett. **23**, 256–258 (1998)
C. Voumard, External-cavity-controlled 32 MHz narrow-band cw GaAlAs-diode lasers. Opt. Lett. **1**, 61–63 (1977)
A. Yariv, P. Yeh, *Photonics: Optical Electronics in Modern Communications* (Oxford University Press, Oxford, 2006)
S.Y. Ye, J. Ohtsubo, Experimental investigation of stability enhancement in semiconductor lasers with optical feedback. Opt. Rev. **5**, 280–284 (1998)
M. Yousefi, D. Lenstra, Dynamical behavior of semiconductor laser with filtered external optical feedback. IEEE J. Quantum Electron. **35**, 970–976 (1999)
C.E. Zah, J.S. Osinski, S.G. Menocal, N. Tabatabaie, T.P. Lee, A.G. Dentai, C.A. Burrus, Wide bandwidth and high-power 1.3 μm InGaAsP buried crescent lasers with semi-insulating Fe-doped InP current blocking layers. Electron. Lett. **23**, 52–53 (1987)

Chapter 5
Dynamics of Semiconductor Lasers with Optical Feedback

Abstract Optical feedback in semiconductor lasers gives rise to rich varieties of dynamics and the effects have been extensively studied for the past three decades. Also semiconductor lasers with optical feedback are used as chaotic light sources in many applications discussed in the following chapters. The theoretical background was discussed in the preceding chapter. In this chapter, substantial feedback effects and chaotic dynamics in semiconductor lasers are presented and theoretical and experimental results are given. As fundamental characteristics, feedback induced chaos is investigated for variations of feedback strength and position of the external cavity. Coherent and incoherent feedback effects are also taken into account in the dynamics. The external feedback mirror to a semiconductor laser may not be always a simple reflector (conventional plain mirror) but may be a grating or phase-conjugate mirror. Instabilities are also induced by such reflectors and the dynamics induced by grating and phase-conjugate mirrors are presented.

5.1 Optical Feedback from a Conventional Reflector

5.1.1 Optical Feedback Effects

In this section, we discuss the dynamics of chaos in semiconductor lasers with optical feedback and show various routes to chaos for parameter variations. Figure 5.1 shows experimental examples of chaotic oscillations in a MQW laser with optical feedback. Figure 5.1a shows the laser output for a negligible small optical feedback. The excited relaxation oscillation smoothly decays out after the laser is switched on and we can see only statistical noise induced by spontaneous emissions (in actual fact, the detector noise is included in the waveform). With the increase of optical feedback, the laser shows periodic oscillation in Fig. 5.1b.

© Springer International Publishing AG 2017

J. Ohtsubo, *Semiconductor Lasers*, Springer Series in Optical Sciences 111,
DOI 10.1007/978-3-319-56138-7_5

The scheme corresponds to regimes III–IV discussed in Sect. 4.1.1. The relaxation oscillation frequency of the laser is about 3 GHz, but higher oscillations above GHz are not observable due to the slow response of the oscilloscope in this experiment. Therefore, the observed periodic oscillation of the peak frequency of 451 MHz corresponds to the excited external mode. The reflectivity of the external mirror is 1% in this case. With a further increase of optical feedback, an irregular oscillation of the laser output power is shown in Fig. 5.1c. The oscillation corresponds to regime IV and the coherence of the laser is almost destroyed. Though the fundamental spectral peak of 480 MHz is still visible, the spectrum spreads out, which is a typical feature of quasi-chaotic or weak chaotic oscillations. For optical feedback above this level, we could see no clear peaks in the spectrum and the laser exhibits fully chaotic oscillations.

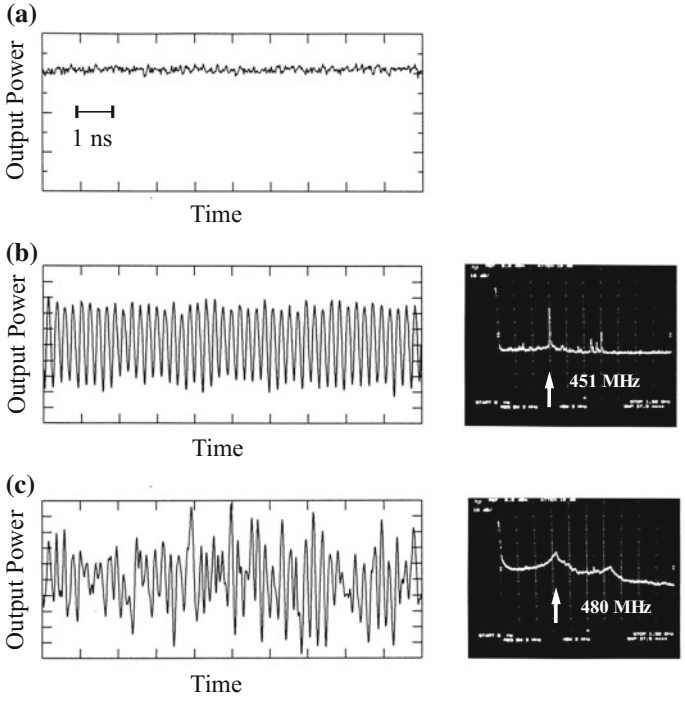

Fig. 5.1 Experimental time series and rf spectra at an injection current of $J = 1.5J_{th}$ and an external cavity length of $L = 30$ cm. **a** Negligible small feedback, **b** period-1 oscillation with small feedback, and **c** chaotic oscillations with strong feedback

5.1.2 Potential Model in Feedback-Induced Instability

In Sect. 4.2.5, we derived the linewidth of a semiconductor laser with weak optical feedback (regimes I–II). The linewidth is reduced according to (4.32) as far as the optical feedback is small enough. When the feedback is in-phase in regime II, the laser is well stabilized and the linewidth is much reduced. But, for an out-of-phase feedback, the linewidth is not reduced any more and the laser shows hopping between the two oscillation modes arising from the external feedback, according to the relation $\omega_s - \omega_{\text{th}} = -\kappa/\tau_{\text{in}}\{\alpha\cos(\omega_s\tau) + \sin(\omega_s\tau)\}$. Figure 5.2 shows an example of optical spectra in regime II (Tkach and Chraplyvy 1986). By a small in-phase optical feedback, the linewidth of the laser is greatly reduced as seen from Figs. 5.2a, b. On the other hand, the laser shows two oscillation modes for a small out-of-phase optical feedback in Fig. 5.2c. The separation of the two peaks corresponds to the external cavity frequency.

Mode hopping between two external modes can be explained by a potential model for the optical feedback system (Lenstra 1991; van Tartwijk and Lenstra 1994). In their model, the hopping is induced by noises and the oscillation is kicked out from one of the potential wells among the possible external modes and falls in another state. To derive the potential model to explain the mode hopping, let us consider the difference between the present and the delayed phases $\Delta\phi(t) = \phi(t) - \phi(t-\tau)$. Assuming that the delay is very small and expanding the delayed phase by the delay time τ, the difference can be expressed as

$$\begin{aligned} \Delta\phi(t) &= \phi(t) - \phi(t-\tau) \\ &\approx \phi(t) - \left\{\phi(t) - \tau\frac{\mathrm{d}\phi(t)}{\mathrm{d}t} + \frac{1}{2}\tau^2\frac{\mathrm{d}^2\phi(t)}{\mathrm{d}t^2}\right\} \\ &\approx \tau\frac{\mathrm{d}\phi(t)}{\mathrm{d}t} - \frac{1}{2}\tau\frac{\mathrm{d}\Delta\phi(t)}{\mathrm{d}t} \end{aligned} \tag{5.1}$$

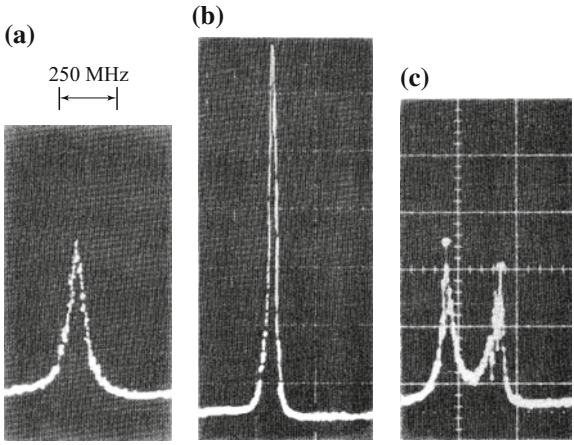

Fig. 5.2 Optical spectra of a semiconductor laser with weak external feedback in regime II. **a** No feedback, **b** −62 dB inphase feedback, and **c** −62 dB out-of-phase feedback [after Tkach and Chraplyvy (1986); © 1986 IEEE]

Here, we used the relation $d^2\phi(t)/dt^2 \approx \{d\phi(t)/dt - d\phi(t-\tau)/dt\}/\tau = d\Delta\phi(t)/dt/\tau$. Assuming the steady-state solutions except for the phase and taking into consideration (4.6) and (5.1), one obtains the relation

$$\frac{d\phi(t)}{dt} = \frac{1}{\tau}\Delta\phi(t) + \frac{1}{2}\frac{d\Delta\phi(t)}{dt} = -\frac{\kappa}{\tau_{in}}\sqrt{1+\alpha^2}\sin\{\theta_0 + \Delta\phi(t)\} + F_\phi(t) \tag{5.2}$$

where F_ϕ is the Langevin noise function for the phase and $\theta_0 = \omega_s\tau + \tan^{-1}\alpha$. Then, the equation of the potential function of the phase difference can be written as

$$\begin{aligned}\frac{d\Delta\phi(t)}{dt} &= -\frac{2}{\tau}\Delta\phi(t) - 2\frac{\kappa}{\tau_{in}}\sqrt{1+\alpha^2}\sin\{\theta_0 + \Delta\phi(t)\} + 2F_\phi(t) \\ &= -\frac{1}{\tau}\frac{d}{d\Delta\phi}[\Delta\phi^2(t) - 2C\cos\{\theta_0 + \Delta\phi(t)\}] + 2F_\phi(t)\end{aligned} \tag{5.3}$$

Considering the term $U(\Delta\phi(t)) = \Delta\phi^2(t) - 2C\cos\{\theta_0 + \Delta\phi(t)\}$ as a potential function and interpreting that a particle moves with the coordinate $\Delta\phi$ in the potential, one obtains the equation for the time development of the phase difference in the potential

$$\frac{d\Delta\phi(t)}{dt} = -\frac{1}{\tau}\frac{d}{d\Delta\phi}U(\Delta\phi(t)) + 2F_\phi(t) \tag{5.4}$$

From this equation, the statistical behaviors of mode hopping can be simulated. Figure 5.3 is an example of numerical simulations based on the potential model for a small optical feedback of −45.7 dB (Mørk et al. 1990a, b). The right figure shows the plots of the potential for different phase values of θ_0. For the in-phase case, the state is trapped to a deep potential well, so that the laser stays stable and oscillates almost at a single frequency. Thus, the laser has a narrow oscillation linewidth. On the other hand, two states compete with each other for the out-of-phase case and the probability for the dwelling time in each state becomes the same. Thus, the laser frequency frequently switches between the two states due to noise. A mode hop to a

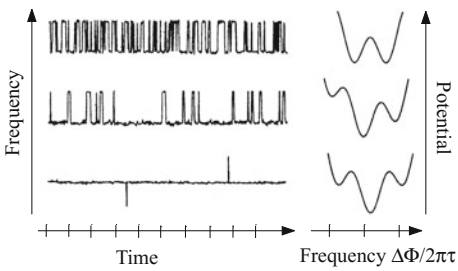

Fig. 5.3 Variations of frequency calculated from the potential model under the condition of $J = 1.84J_{th}$ and $L = 60$ cm. *Left* Time series of frequency, *right* potential. The optical feedback is −45.7 dB. *Lower trace* is for a relative phase of $\theta_0 = 0$ (in-phase), *middle trace* $\theta_0 = 1.4$, and *upper trace* $\theta_0 = \pi$ (out-of-phase) [after Mørk and Tromborg (1990); © 1990 IEEE]

neighboring mode occurs when the noise takes the phase delay beyond one of the potential barriers confining the mode. The barriers for the central mode in the lower potential are higher than the barrier separating the two modes in the upper potential. Since higher barriers are harder to pass, this explains the large difference in mode hopping rates.

5.1.3 *Optical Spectrum in Stable and Unstable Feedback Regimes*

For a feedback parameter C less than unity at regime I, only one solution $\omega\tau$ exists for the phase condition, yielding a linewidth narrowing or broadening depending on the phase $\omega_s\tau$. For the condition $C > 1$ at regime II, multiple solutions exist for the phase condition and it turns out that the emission frequency locks to the solution with the lowest phase noise. At this feedback, mode hopping may occur between modes with a similar amount of phase noise. Especially, for a phase change $\theta_0 = \pi$, two solutions exist with just the same linewidth, yielding strong mode hopping between these two modes as already discussed in the previous subsection. With increasing feedback level at regime III, the frequency splitting of the hopping modes converges to the frequency separation between the external cavity modes and the feedback phase $\omega_s\tau$ for these modes converges the phase $\theta_0 = 2\,m\pi$. Therefore, at this range of feedback, the laser will lock more and more to the feedback phase adjusted for minimum linewidth and mode hopping disappears. Certain saturation in linewidth reduction is obtained for a larger feedback level above −50 dB.

With further increase of the feedback in regime IV, the frequency fluctuations dramatically increase, yielding a tremendous linewidth broadening, which is characteristic for the coherence collapse regime. Figure 5.4 shows experimentally obtained optical spectra at feedback regimes III–IV (Tkach and Chraplyvy 1986). The laser first destabilized with the relaxation oscillation for the increase in the feedback fraction, as shown in Fig. 5.4a. Then, the laser evolves into quasi-periodic oscillations with several spectral peaks in Fig. 5.4b. Finally, the laser shows chaotic oscillation and the linewidth of the spectrum is greatly broadened by the optical feedback. In a sense of laser oscillation, the laser is coherence collapsed and the linewidth is as much as 100 GHz in Fig. 5.4c. However, the laser may be still a single mode in a sense of longitudinal laser oscillation observed such as an optical spectrum analyzer with a resolution of nanometers. The range of each regime strongly depends on the condition of the laser operations, such as laser device structure, bias injection current, and feedback length. However, each regime is clearly identified under the different conditions of the laser operations.

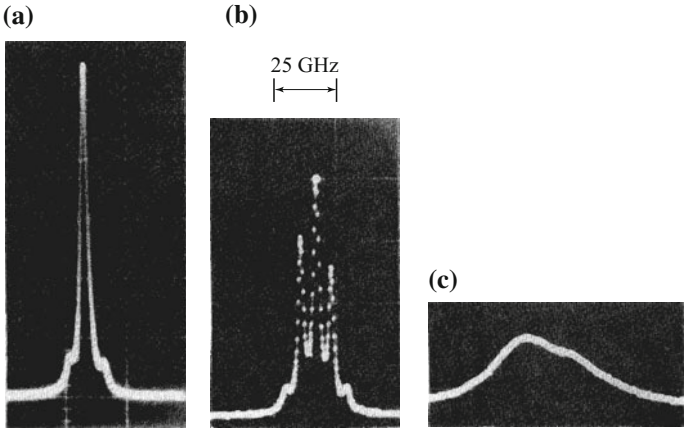

Fig. 5.4 Unstable optical spectra in regimes III–IV. **a** Periodic state with relaxation oscillation at optical feedback of approximately −40 dB, **b** quasi-periodic oscillations at approximately −30 dB, and **c** chaotic state at −20 dB [after Tkach and Chraplyvy (1986); © 1986 IEEE]

In a summary, Fig. 5.5 shows the experimental and theoretical results for spectral narrowing and broadening in the presence of optical feedback in semiconductor lasers (Schunk and Petermann 1988). Spectral linewidth is plotted as a function of feedback fraction. The experiments were conducted for various phase values of $\omega_0\tau$ (where ω_0 is the oscillation frequency of the laser and it is very close to ω_{th}). The roman numbers denote the feedback regimes discussed in Sect. 4.1. The dashed line is the linewidth of the solitary laser. The solid curve is the expected minimum linewidth calculated from the theoretical equation in (4.32) under the assumption of an in-phase condition. The theory well agrees with the experiments at regimes I and II. However, it deviates from the experiments in regime III and complete spectral broadening is observed in regime IV, where the theoretical equation (4.32) cannot be applied. For moderate optical feedback in regimes III and IV, it is difficult to obtain analytical forms to describe the dynamics of semiconductor lasers with optical feedback. In usual, the laser has a rather broad spectral linewidth of several tens of MHz at solitary oscillation. By optical feedback, the linewidth is greatly reduced to 100 kHz at regime III (narrowing of 1/1000 of the original spectral linewidth). This situation is easily understood from analysis for the relative intensity noise (RIN) of the laser output. The RIN abruptly increases at the external feedback level of 10^{-4}. The RIN here is obtained as an average over the frequency range of 5–500 MHz (Schunk and Petermann 1988). In a strong optical feedback regime V, the linewidth is again strongly narrowed and the spectral narrowing by strong optical feedback will be discussed in relation to stabilization of semiconductor lasers in Chap. 10.

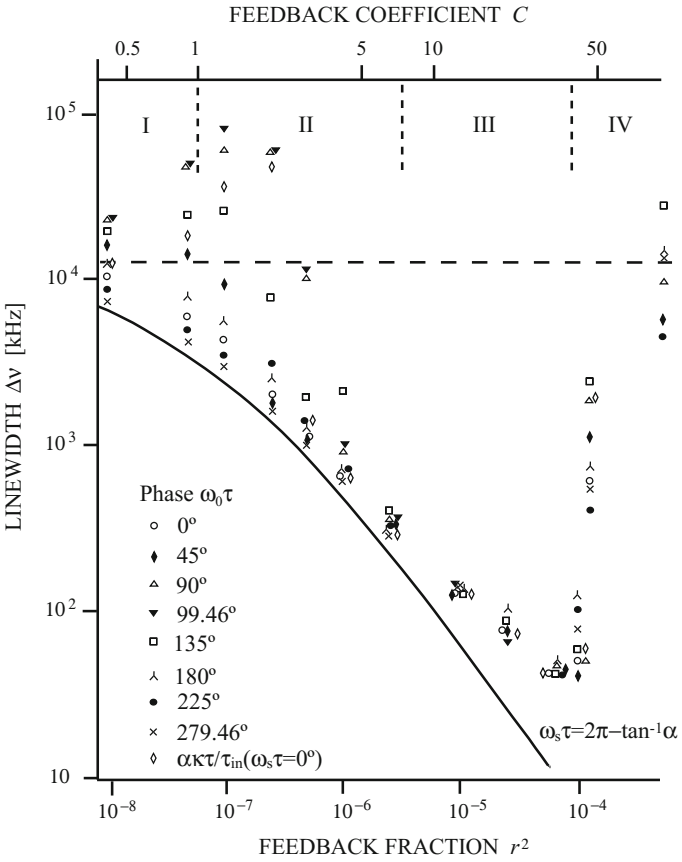

Fig. 5.5 Spectral linewidth versus feedback fraction at an output power of 5 mW and an external cavity length of $L = 50$ cm for various $\omega_0\tau$. The *roman numbers* denote the feedback regimes. *Dashed line* Linewidth of the solitary laser, *solid curve* linewidth of the external cavity laser according to (4.32) at in-phase optical feedback [after Schunk and Petermann (1988); © 1988 IEEE]

5.1.4 *Chaos in Semiconductor Lasers with Optical Feedback*

Next, we numerically investigate routes to chaos for the optical feedback level. Here, we used parameter values of AlGaAs MQW semiconductor lasers of a Channeled Substrate Planer (CSP) type as shown in Table 5.1 (Liu et al. 1995). The values listed in Table 5.1 are typical for semiconductor lasers with visible line; however, other MQW semiconductor lasers of different oscillation lines, such as near-infrared semiconductor lasers used for optical communications, have similar parameter values as those in Table 5.1 (Shibasaki et al. 2006). Figure 5.6 shows the

Table 5.1 Some parameter values for a narrow-stripe edge-emitting semiconductor laser (GaAs-GaAlAs780 nm wavelength)

Symbol	Parameter	Value
G_n	Gain coefficient	7.00×10^{-13} m^3 s^{-1}
α	Linewidth enhancement factor	3.00
r_0	Facet reflectivity	0.565
n_{th}	Carrier density at threshold	2.02×10^{24} m^{-3}
n_0	Carrier density at transparency	1.40×10^{24} m^{-3}
τ_s	Lifetime of carrier	2.04 ns
τ_{ph}	Lifetime of photon	1.93 ps
τ_{in}	Round trip time in laser cavity	8.00 ps
V	Volume of active region	1.2×10^{-16} m^3
ε	Gain saturation coefficient	8.4×10^3 s^{-1}

result of dynamic behaviors of the laser output power at a fixed bias injection current and an external mirror position for the variations of the feedback level. The Langevin noises are excluded in the calculations in order to see the pure dynamics produced by the nonlinear equations. The left row in the figure is time series, the middle row is its attractor, and the right row is the power spectrum. For a small optical feedback, the laser output power is constant. For the external feedback level of 0.5% (2.5×10^{-5} in intensity) shown in Fig. 5.6a, the laser becomes unstable and exhibits a period-1 oscillation. The main frequency of the oscillation is 2.53 GHz and it is very close to the relaxation oscillation frequency of 2.50 GHz at the solitary mode. When the feedback level is raised at 1.0%, a period-2 oscillation appears as shown in Fig. 5.6b. Figure 5.6c shows a chaotic oscillation at the feedback level of 2.0%. When the laser output power shows periodic oscillations, we can see clear spectral peaks, however, at the chaotic state, clear spectral peaks are not observable but the optical spectrum is broadened around the relaxation oscillation frequency.

A chaotic attractor is a trajectory in the phase space of chaotic variables and is frequently used for the analysis of chaotic oscillations (see Appendix A.2). Since the laser output power at a stable oscillation is constant, the attractor (not shown here) is a fixed point in the phase space of the output power and the carrier density. A period-1 signal, as is the case in Fig. 5.6a, is a closed loop. The attractor of a period-2 oscillation is a double-loop as shown in Fig. 5.6b. However, the chaotic attractor behaves in a rather different way from fixed state or periodic oscillations. At chaotic oscillations, the state goes around points within the closed compact space in the attractor; however, it never visits the same point in the space. The trajectory crosses in the attractor in Fig. 5.6c, since it is a projection onto only two-dimensional space. In actual fact, the chaotic trajectory goes around in a multi-dimensional phase space and never crosses in such a space (Mørk and

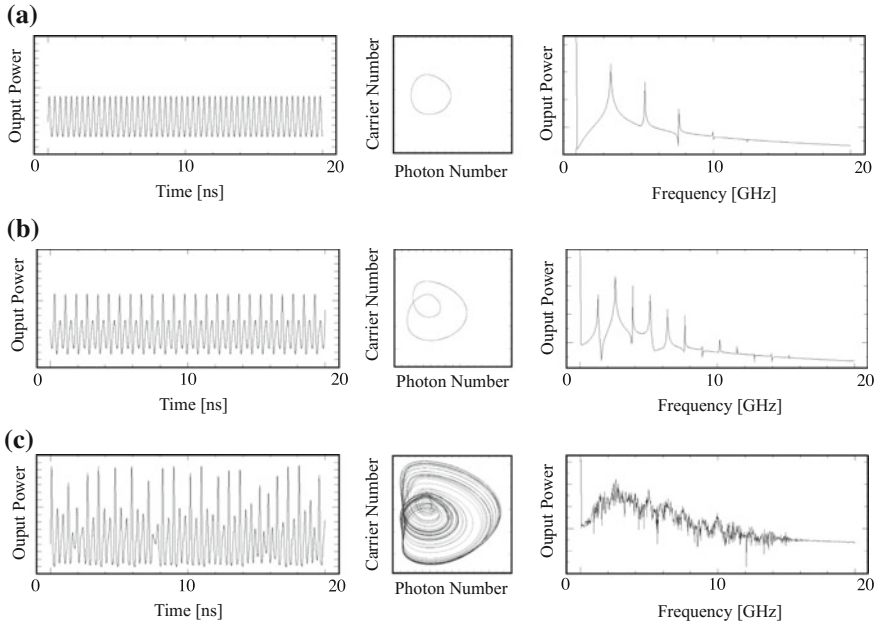

Fig. 5.6 Numerically calculated time series (*left row*), attractors (*middle row*), and power spectra (*right row*) for different feedback ratios at a bias injection current of $J = 1.3J_{th}$ and an external cavity length of $L = 3$ cm. Feedback fractions of the amplitude are **a** $r = 0.005$, **b** $r = 0.01$, and **c** $r = 0.02$

Tromborg 1990; Ye et al. 1993; Li et al. 1993). A chaotic attractor is quite different from other periodic oscillations and looks very strange. Therefore, it is sometimes called a strange attractor (Appendix A.2).

5.1.5 Chaotic Bifurcations

The plot of a bifurcation diagram is used to investigate chaotic evolutions for the change of a certain parameter (see Appendix A.1). A bifurcation diagram is obtained from a time series by sampling and plotting local peaks and valleys of the waveform for a parameter change. Figure 5.7 shows a numerical example of chaotic bifurcation induced by optical feedback in semiconductor lasers. The vertical axis is the local peaks and valleys of the waveform. The horizontal axis is the parameter of the optical feedback level. In Fig. 5.7a the laser is stable for an external feedback of less than 0.35%. The state is called a fixed point. Above this value, a relaxation oscillation appears in the laser output and the diagram has two points corresponding to the peaks and valleys of the period-1 oscillation. When the feedback level exceeds the value of 0.94%, a period-2 oscillation starts and the

output has four states of peaks and valleys. For a further increase of the feedback, the laser evolves into quasi-periodic states and finally chaotic oscillations over the feedback level of 1.36%. The chaotic laser oscillates at the mixed frequencies of the internal and external modes and the relaxation oscillation mode. The evolution such as shown in Fig. 5.7a is called a period-doubling bifurcation or a Hopf bifurcation (the Hopf bifurcation actually has a rigid definition for chaotic evolutions and the example shown here may not be an exact Hopf bifurcation). A test for Hopf bifurcation is frequently used to check chaotic routes and evolutions of the output in nonlinear systems for variations of chaotic parameters (Appendix A.1).

Hopf bifurcation is not the only chaotic evolution but various routes to chaos exist in nonlinear systems. Figure 5.7b is another example. The external cavity length is different from that in Fig. 5.7a, but the other parameters are the same. In this figure, the fixed point evolves into period-1 oscillations; however, the laser becomes quasi-periodic and chaotic states occur immediately after period-1 oscillations for the increase of the feedback parameter. The oscillation is called a quasi-periodic bifurcation to distinguish it from a Hopf bifurcation. Another route is an intermittent route to chaos, which is known as low-frequency fluctuations (LFFs) in semiconductor lasers (Mørk et al. 1988; Fischer et al. 1996). The occurrence and

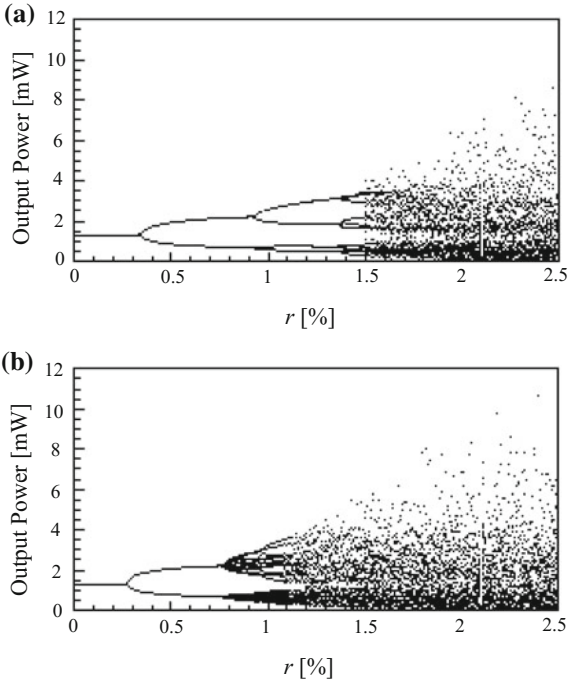

Fig. 5.7 Calculated chaotic bifurcation diagrams at a bias injection current of $J = 1.3J_{th}$. External cavity length of **a** $L = 9$ cm (period-doubling bifurcation) and **b** $L = 15$ cm (quasi-periodic bifurcation)

dynamics of LFFs will be treated in Sect. 5.3. Chaotic bifurcations highly depend on chaos parameters in nonlinear systems (Helms and Petermann 1990; Ritter and Haug 1993a, b; Levine et al. 1995).

We ignored Langevin noises in the numerical calculations to investigate the pure dynamics involved in the nonlinear system. In the presence of noises, chaotic dynamics are barely affected as long as the effect of spontaneous emission is small. In such a case, the maxima and minima of the output in the fixed and periodic states in the bifurcation have finite widths. Thus, the overall features of chaotic dynamics are unchanged by noises. However, spontaneous emission of light plays a crucial role for the dynamics when the photon number in the cavity is small (Yu 1999). In actual experimental situations, it is not easy to obtain a bifurcation diagram for a waveform with high frequency fluctuations such as in a semiconductor laser, since we require a very high-speed digitizing oscilloscope to fully reconstruct the diagram from the time series. One of the characteristic frequencies of chaotic oscillations in semiconductor lasers with optical feedback is the relaxation oscillation frequency. It usually ranges form several GHz to 10 GHz depending on the device parameters and the driving condition. Instead, to analyze chaotic oscillations (oscillations for the relaxation and external-cavity modes) in semiconductor lasers with optical feedback, a rf spectrum analyzer or a Faby-Perot spectrum analyzer is frequently used in experiments.

Chaotic bifurcation diagram for optical feedback is experimentally obtained (Kim et al. 2014, 2015). Figure 5.8a shows an experimental chaotic bifurcation diagram for optical feedback coefficient κ. The laser is a single mode InGaAsP DFB laser that oscillates at wavelength 1550 nm and is biased at $J = 2.38J_{\text{th}}$ (corresponding relaxation oscillation frequency is 7.4 GHz). The external mirror is positioned at $L = 30$ cm from the laser facet and the reflectivity from the external mirror is carefully changed by a combination of a linear polarizer and a quarter-wave plate. Time series from the laser output are obtain by a digital oscilloscope with a bandwidth of 12 GHz, therefore, the main chaotic oscillations are well captured by the experimental setup, since the relaxation oscillation frequency at solitary oscillation, which is a measure of typical frequency of chaotic oscillations, is within an observable frequency range. Figure 5.8b shows the variation of the voltage across the laser diode. As will be discussed in Sect. 11.3.1, the voltage tracks the changes in the carrier density. A decrease (increase) in the carrier density by the optical feedback decreases (increases) the difference between quasi-Fermi levels in the p- and n-type quasi-neutral regions of the laser diode. Then, the voltage provides information on the dynamical variable of the carrier density. Since we could not directly measure the change of carrier density, the voltage variation across the laser diode can be used as a probe for the carrier density in these experiments. We will return the relation between the carrier density and the voltage in Sect. 11.3.1.

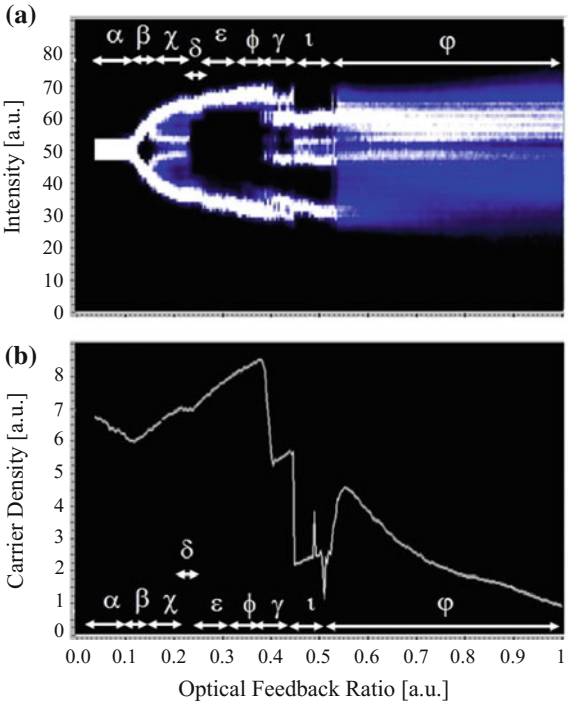

Fig. 5.8 **a** Experimental bifurcation diagram of the laser output power for variations of external feedback at $J = 2.38J_{th}$ and $L = 30$ cm. **b** Voltage variation across the laser diode. Note that the voltage variation is proportional to the carrier density [after Kim et al. (2015); © 2015 APS]

5.1.6 *Dynamics for Injection Current Variations*

The laser output power of semiconductor lasers at solitary oscillations is linearly proportional to the bias injection current. A typical feature of optical feedback in semiconductor lasers is the threshold reduction, which is related to the gain reduction as discussed in Sect. 4.2.4 (Hegarty et al. 1998). Figure 5.9 shows an example of light-injection current (L–I) characteristics experimentally obtained in a semiconductor laser with and without optical feedback. The solid curve is the L–I characteristics for the solitary oscillation and the other curves are with optical feedback. The reductions of the threshold current are about 30% in this case. The angular frequency of the laser at solitary oscillation is a function of the bias injection current and is written as (Petermann 1988)

$$\omega_0 = \omega_c - \frac{\partial \omega_0}{\partial J} J \tag{5.5}$$

where ω_c is the offset angular frequency and $\partial x_0/\partial J$ is the conversion coefficient of the injection current to the angular frequency. Due to the change of the frequency for the increase or decrease of the injection current, the successive external modes

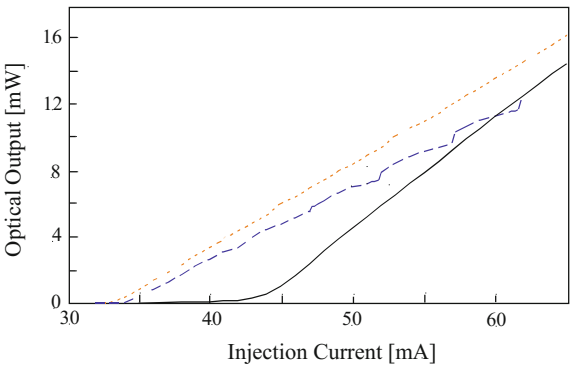

Fig. 5.9 Experimentally obtained light-injection current (L–I) characteristics of semiconductor lasers with optical feedback. *Solid line* Solitary oscillation, *dotted line* external cavity length of L = 15 cm, *broken line* external cavity length of L = 150 cm

are sequentially selected. Then, mode hops occur at certain bias injection currents. This induces instabilities in semiconductor lasers and chaotic oscillations in the laser output power are observed in between the mode jumps.

Figure 5.10a shows an example of output power jumps numerically calculated from the rate equations for the increase of the injection current. The conditions of the calculations correspond to regime III discussed in Sect. 4.1.1. Figure 5.10b is the bifurcation diagram for Fig. 5.10a. A chaotic scenario between successive jumps is observed. At the position after a mode jump, the laser oscillates with period-1, the laser becomes unstable with the increase of the injection current, and, finally, it evolves into chaotic states. The frequency of the period-1 oscillation is almost equal to the relaxation oscillation frequency. The averaged output power is proportional to the injection current, however, periodic power jumps are observed in the output power with a period equal to the increment of the injection current corresponding to the frequency of the external mode (Fukuchi et al. 1999). The conversion coefficient $\partial v_0/\partial J$ is of the order of GHz/mA in ordinary narrow-stripe edge-emitting semiconductor lasers (Petermann 1988). The jump of the output power originates from the external mode alternation, namely, one external mode switches to the next at the jump position. Therefore, for example, a mode hop occurs about every 1 mA for the increment of the bias injection current at an external cavity length of 15 cm. With a further increase of the external optical feedback in regime IV, the laser output power becomes completely unstable and no jump is observable in the L–I characteristic as shown in Fig. 5.10c. In the corresponding bifurcation diagram in Fig. 5.10d, the laser output shows only chaotic oscillations throughout the range in the bias injection current. In an actual situation, the laser output power has a hysteresis with increase or decrease of the injection current. In this numerical simulation, the output power is essentially calculated as a step response, so that the result of the laser output power in Fig. 5.10a corresponds to that for the upward change of the injection current.

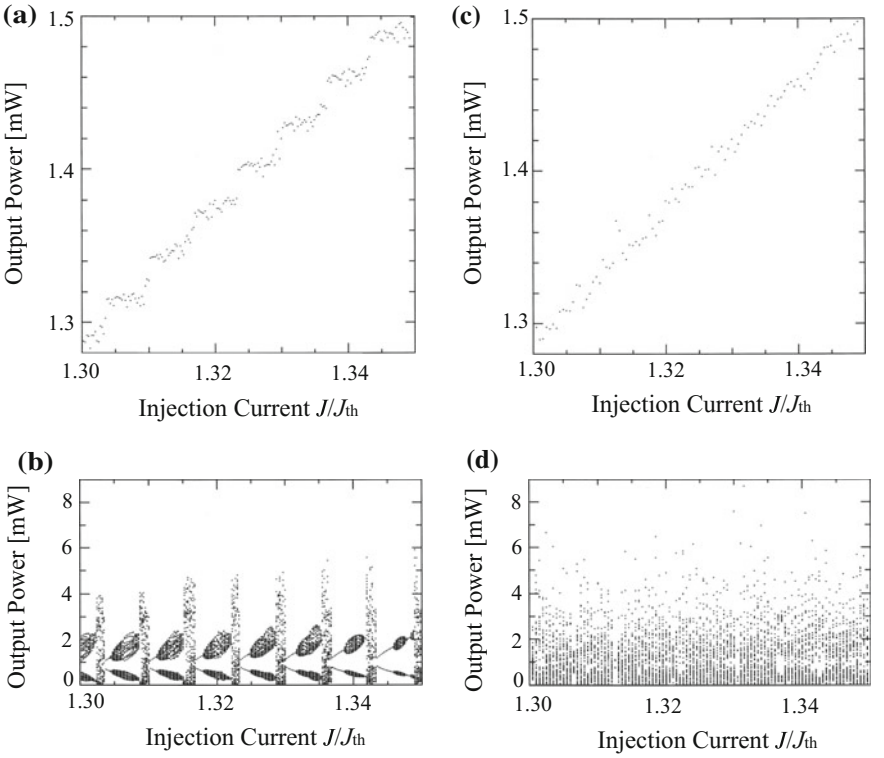

Fig. 5.10 Numerically calculated laser output powers and chaotic bifurcations for the injection current at an external cavity length of L = 15 cm. **a** L–I characteristic at an external reflectivity of r = 0.01. **b** Chaotic bifurcation diagram corresponding to **a**. **c** L–I characteristic at an external reflectivity of r = 0.02. **d** Chaotic bifurcation diagram corresponding to **c**. **c**, **d** are coherence collapse states

Figure 5.11 shows the example of mode jumps obtained from experiments (Fukuchi et al. 1999). In Fig. 5.11a, clear mode jumps occur in the L–I characteristic. Figure 5.11b shows optical spectra observed by a Fabry-Perot spectrometer at the injection currents marked in Fig. 5.11a. At point 'a' followed by a mode jump, the laser oscillation stays stable. With an increase of the injection current at 'd', the relaxation oscillation increases. After that, the laser shows quasi-periodic oscillations with mixed frequencies of the relaxation and external modes, and, then, unstable oscillations before returning to a stable oscillation at 'h.' A similar process is repeated as the injection current increases. The measured relaxation oscillation frequency (for example in spectrum 'd') is 4.5 GHz. Since the external mode frequency (5.0 GHz) is close to the relaxation oscillation frequency in this case, it is not easy to distinguish the external modes with the relaxation oscillation in the spectra. However, the difference between periodic and quasi-periodic oscillations is clear in the figure. The result well coincides with the numerical simulations in

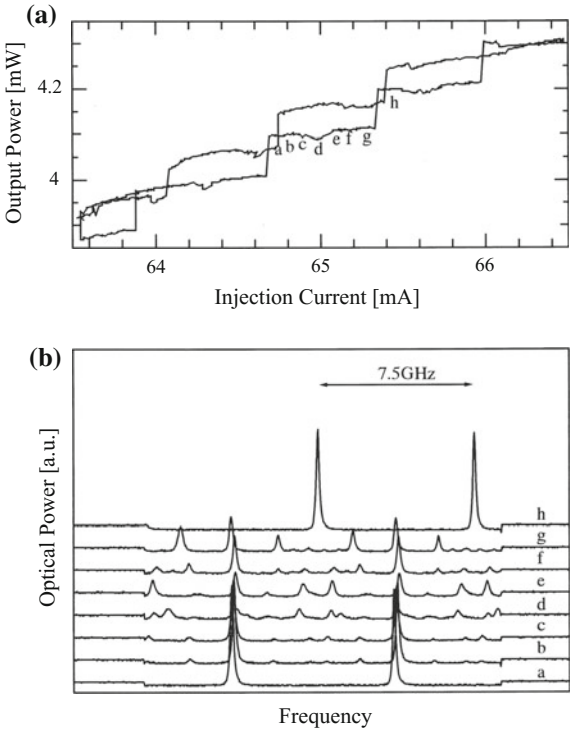

Fig. 5.11 Experimentally obtained L–I characteristic and optical spectra at an external cavity length of $L = 3$ cm and an external reflectivity of $r^2 = 0.03$. **a** Output power versus injection current. **b** Optical spectra corresponding to the marked position in **a**

Fig. 5.10. For a further increase of the optical feedback, no jump is observed in the L–I characteristic. No distinct peak is observable by a Fabry-Perot spectrometer and the coherence of the laser is completely destroyed. As shown in Fig. 5.11a, the laser output power has a hysteresis for increase or decrease of the injection current.

Finally, we briefly refer to the effect of coherence induced by optical feedback in semiconductor lasers. Normally, the spectral linewidth of a semiconductor laser without any stabilization is much broadened due to a finite value of the α parameter compared to other lasers, such as gas lasers. The linewidth of a semiconductor laser with solitary oscillation ranges from several MHz to several tens of MHz. In this case, the averaged coherence length of the laser is over several meters. On the other hand, the linewidth of a semiconductor laser in the presence optical feedback is further broadened over several to several tens of GHz, even if the laser is assumed to be oscillated at single longitudinal mode. When a laser is oscillated at quasi-periodic or weak chaotic states by optical feedback, the time-averaged coherence is maintained around several tens of centimeters. However, the time-averaged coherence is much reduced to less than several centimeters for strong chaotic oscillations or low-frequency fluctuation (LFF) states. The degree of the time-averaged coherence is easily obtained from observation of the visibility for the

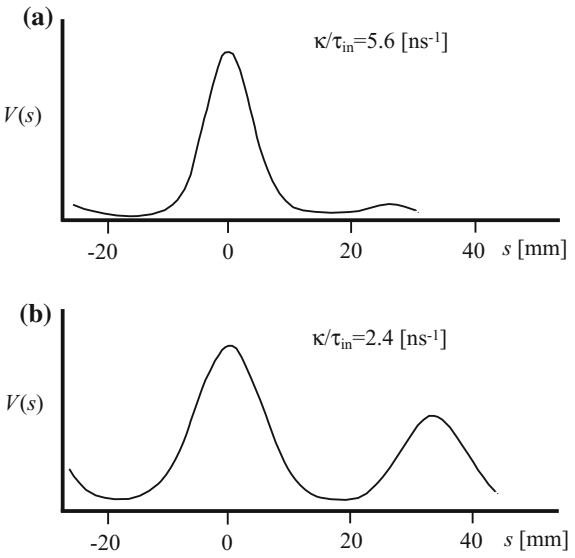

Fig. 5.12 Experimentally observed visibility curve for the arm length difference of a Michelson interferometer. Feedback strengths are **a** $\kappa/\tau_{in} = 5.6\ ns^{-1}$ and **b** $\kappa/\tau_{in} = 2.4\ ns^{-1}$. The external cavity length is $L = 80$ cm and the injection current is $J = 1.51J_{th}$ [after Lenstra et al. (1985); © 1985 IEEE]

laser output by employing a Michelson interferometer. Figure 5.12 is an example of experimental observations of visibility curves in Michelson interferometer (Lenstra et al. 1985). For the increase of optical feedback, the coherence length becomes small. The spectral linewidths calculated from the observation are 11 GHz (corresponding coherence length of 2.0 cm) and 15 GHz (coherence length of 2.7 cm) for Fig. 5.12a and b, respectively. In Fig. 5.12b, the second spectral peak (4.4 GHz) corresponds to the laser relaxation oscillation of the laser. Thus, the large degradation of the averaged coherence due to chaotic oscillations induced by optical feedback must be taken into account.

5.2 Dependence of Chaotic Dynamics on the External Mirror Position

5.2.1 Periodic Stability Enhancement for Variations of the External Cavity Length

We discuss here the dependence of chaotic dynamics on the external cavity length in semiconductor lasers. We consider the case where the change of the external cavity length is much larger than the internal laser cavity length ($\sim$cm) and investigate the stability and instability for the change. Assuming a small external feedback and satisfying the conditions $\omega_R^2 \gg (\kappa/\tau_{in})^2$, $-\kappa\Gamma_R/\tau_{in}$, the characteristic equation (4.21) is approximated by

$$D(\gamma) = \gamma^3 + 2\left\{-\Gamma_R + \frac{\kappa K}{\tau_{in}}\cos(\omega_s\tau)\right\}\gamma^2 + \omega_R^2\gamma + \frac{\kappa K\omega_R^2}{\tau_{in}}\{\cos(\omega_s\tau) - \alpha\sin(\omega_s\tau)\} \tag{5.6}$$

Assuming $\gamma = i\omega$ and substituting it into (5.6), the boundary condition for stable and unstable oscillations is calculated. From the real part of the equation, we obtain

$$-\alpha\sin(\omega_s\tau) + \left\{1 - 2\left(\frac{\omega}{\omega_R}\right)^2\right\}\cos(\omega_s\tau) = -\frac{\left(\frac{\omega}{\omega_R}\right)^2}{\Gamma_R\frac{\kappa}{\tau_{in}}\sin^2\left(\frac{\omega\tau}{2}\right)} \tag{5.7}$$

From the condition for the imaginary part together with the above equation, the boundary condition is given by (Tromborg et al. 1984)

$$\omega^2 - \omega_R^2 = -2\Gamma_R\omega\cot\left(\frac{\omega\tau}{2}\right) \tag{5.8}$$

To investigate the stability and instability dependence, we must numerically solve the condition for τ from (5.8), but we can conjecture from the above equation that the critical point changes periodically for the external cavity length. The round trip time τ corresponding to this period is written by

$$\tau = \frac{2}{\omega}\left[\cot^{-1}\left\{-\frac{1}{2\Gamma_R\omega}(\omega^2 - \omega_R^2)\right\} + m\pi\right] \tag{5.9}$$

From (5.8), $\omega = \omega_R$ is the solution for the periodic boundary and the condition is also given by $\omega_R\tau = 2\ m\pi$ (m is an integer). Namely, the boundary changes periodically for the external cavity length satisfied as $L = mc/2\nu_R$ (ν_R is the relaxation oscillation frequency). Again, the relaxation oscillation frequency plays an important role for the stability and instability of the laser systems.

From the graphical relation between ω and τ in (5.9), we can numerically obtain the solution for the resonance of the laser oscillations (Tromborg et al. 1984; Mørk et al. 1992; Murakami et al. 1997). The intersections of the graph $\omega = \omega_R$ along the round trip time τ are the points where constructive interference is achieved and the stability of the laser for the external reflectivity is much enhanced at these points. In the graph, the intersections crossing at $\omega/\omega_R = 1$ are the values of τ where the boundary of the stability enhancement occurs. We obtain periodic solutions for the intersections and the separation between the successive solutions is exactly equal to the time corresponding to the frequency of the relaxation oscillation. This periodicity is also calculated from the direct numerical simulation for the rate equations. A periodic enhancement of stability for the laser oscillation can be observed for the

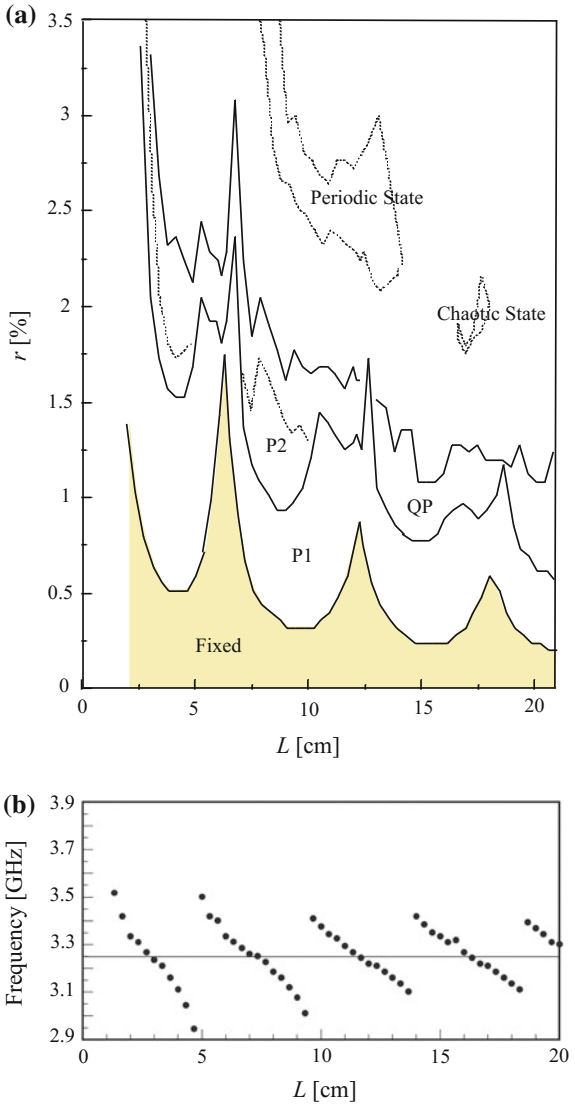

Fig. 5.13 **a** Phase diagram of chaotic oscillations for the external mirror position and the optical feedback level at a bias injection current of $J = 1.3J_{th}$. *Fixed* Fixed state, *P1* period-1 oscillation, *P2* period-2 oscillation, *QP* quasi-periodic oscillation. **b** Excited relaxation oscillation at boundary between fixed and period-1 states. The relaxation oscillation frequency at free running state, which is shown as a *straight line* is 3.25 GHz

change of the external mirror position of the order of centimeters. Figure 5.13a shows the numerical result of the phase diagram of stable and unstable oscillations for the external mirror position and the optical feedback level (Murakami et al. 1997; Murakami 1999). The diagram is numerically obtained for $\omega_0\tau = 0$ in the rate equations in (4.8) and it does not include the effects of a small mirror variation compatible with the optical wavelength. In the figure, "periodic state" within chaotic oscillations denotes the periodic windows frequently observed in chaotic bifurcations.

With the increase of optical feedback at a fixed external cavity length, the laser also becomes unstable at a rather larger external feedback level and fixed point of the laser oscillation evolves into the period-1 state after crossing the boundary. At the external cavity lengths satisfying the condition $L = mc/2v_R$, the laser constructively couples with the external cavity and a larger fraction of feedback light is required to destabilize it. The stable area greatly expands at this location, but the laser rapidly turns out to be unstable after the feedback exceeds the critical point. This corresponds to the quasi-periodic bifurcations of chaos that are shown in Fig. 5.7b. At other mirror locations, the laser easily becomes unstable and rapidly evolves into chaotic states with a small amount of external feedback. The laser evolves rather slowly into unstable and chaotic states for the increase of the external reflectivity at these locations. We can see clear period-doubling bifurcations of the laser oscillations in the mirror position at the bottom of the periodic enhancement. This corresponds to the Hopf bifurcations shown in Fig. 5.7a. The excited relaxation oscillation at the critical point also changes periodically for the external cavity length as shown in Fig. 5.13b. The relaxation oscillation decreases with the increase of the external cavity length. Then, it jumps up at the stability peak and repeats the same process for the increase of the external cavity length.

Also, periodic stability enhancement can be observable for the change of the bias injection current, which is dependent on the optical feedback level. From the stability-enhancement condition of $\omega_R\tau = 2m\pi$ derived from (5.9) together with equation of (3.89), we obtain the condition of periodic stability enhancement for the bias injection current as

$$\frac{\tau}{2\pi}\sqrt{\frac{G_n}{ed}(J - J_{th})} = m \tag{5.10}$$

Then, the periodicity can be found for the square root of the bias injection current ($\sqrt{J/J_{th} - 1} \propto m$) at a fixed round trip time of τ. Figure 5.14 is the result of numerical simulations for chaotic bifurcation boundaries in the phase space of the bias injection current and the optical feedback level at a fixed external mirror position of $L = 15$ cm. Each curve denotes the boundary of the oscillation states. In the figure, the first, second, and third peaks of the stabilities can be read as $\sqrt{J/J_{th} - 1} = 0.48$, $\sqrt{J/J_{th} - 1} = 0.95$, and $\sqrt{J/J_{th} - 1} = 1.40$, respectively, and, thus, the relation in (5.10) approximately holds. As discussed in this subsection, stability and instability of chaotic oscillations in optical feedback systems in semiconductor lasers are strongly dependent on external cavity length, optical feedback level, and bias injection current. Therefore, we must carefully choose these parameter sets from a viewpoint of chaos generations in semiconductor lasers with optical feedback. The periodic feature of the stability enhancement was also confirmed by experiments (Ye and Ohtsubo 1998). The origin of the phenomena is also presented in the next subsection.

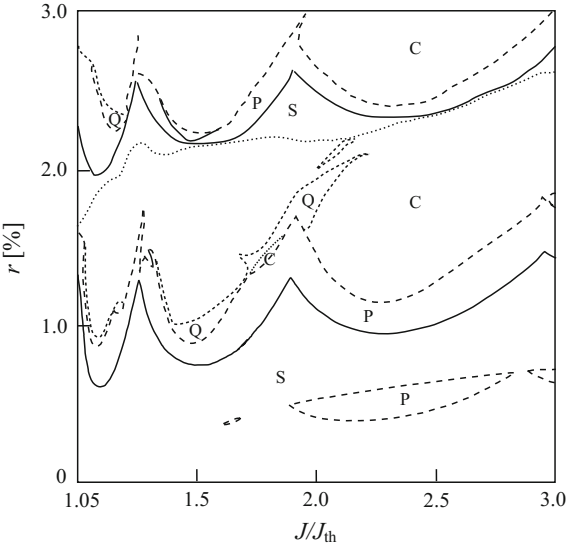

Fig. 5.14 Phase diagram of chaotic oscillations for the bias injection current and the optical feedback level at an external cavity length of L = 15 cm. *S* Stable state, *P* periodic oscillation, *Q* quasi-periodic oscillation, *C* chaotic oscillation. Each *curve* represents the boundary of oscillation

5.2.2 *Origin of Periodic Stability Enhancement*

The periodic stability enhancement for the change of the external cavity length observed in the previous subsection is explained by competitions of linear modes derived from the linear stability analysis for the rate equations (Murakami and Ohtsubo 1998). Figure 5.15 shows mode transition around the third stability peak at the external cavity length of L = 14.0 cm with the external reflectivity of 0.7% corresponding to Fig. 5.13a. In Fig. 5.15a at L = 13.75 cm, mode A is the highest mode and the real part of the mode has a positive value. Then, the oscillation becomes unstable at mode A and this mode plays role in the relaxation oscillation mode. Figure 5.15b is the mode distribution at L = 14.0 cm where the stability of the laser oscillation is locally much enhanced. The reflectivity of 0.7% is selected as slightly less than the feedback level for unstable oscillations. Two modes A and B are competing and the real part of mode A becomes negative. Then, the laser output stays at a stable fixed state and the relaxation oscillation mode is not excited. Figure 5.15c is the mode distribution at the position of the external mirror of L = 14.25 cm. The highest mode switched from A to B and the laser again shows unstable oscillations at mode B. From these results, the stability enhancement along the external cavity length is explained by the mode competition between linear modes near the relaxation oscillation frequency. Once two modes have positive values of their real parts for a larger external optical feedback, the two modes become unstable simultaneously. Thus, the laser is rapidly destabilized and shows

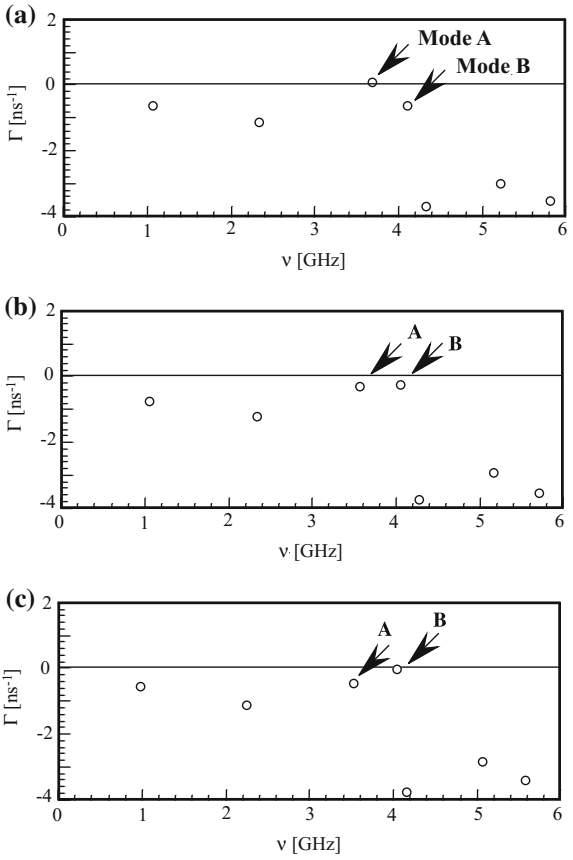

Fig. 5.15 Competition of two modes related to a resonance frequency at $r = 0.05$ and $J = 1.5J_{th}$ for variations of the external cavity length. **a** $L = 13.75$ cm, **b** $L = 14.0$ cm at the stability peak, and **c** $L = 14.25$ cm

chaotic oscillations above the fraction of external feedback. On the other hand, at and around the stability bottoms in Fig. 5.13a, there is only one mode near the relaxation oscillation frequency and the laser shows typical period-doubling bifurcation to chaos.

For a longer external cavity length, the laser is less stabilized with a small fraction of optical feedback as seen from Fig. 5.13a. Usually, a semiconductor laser without any special control for stabilization has a spectral bandwidth of several to several tens of MHz and the coherence is in the order of meters. The optical feedback phenomena from a distant reflector longer than the laser coherence are attributed to the incoherent effect. The rate equations for the two variables of the photon number and the carrier density are enough to describe such phenomena. However, the effects of coherence both for coherent and incoherent feedback are included in the rate equations in (4.5)–(4.7), and we can still use them for numerical calculation of the dynamics in incoherent feedback.

5.2.3 Effects of Linewidth Enhancement Factor

The linewidth enhancement factor α of semiconductor lasers plays an important role in the laser dynamics and the laser instability is greatly enhanced for larger value of the linewidth enhancement factor. In this section, we investigate the dependence of onset of chaos on the linewidth enhancement factor in the presence of optical feedback to semiconductor lasers. For that purpose, we first consider a transfer function from the modulation current to the modulated optical power in a semiconductor laser. Assuming a long external cavity limit (the length of the external mirror is much larger than $c/2\nu_R$), the small-signal transfer function like general control systems can be defined by

$$H_K(i\omega) = \{1 - K(i\omega)\}\frac{H(i\omega)}{1 - K(i\omega)H(i\omega)} \tag{5.11}$$

where $H(i\omega)$ corresponds to the normalized transfer function of the semiconductor laser without optical feedback ($K(i\omega) = 0$) and is given by (Helms and Petermann 1990)

$$H(i\omega) = \frac{1}{\left(i\frac{\omega}{\omega_R}\right)^2 + i\frac{\omega}{\omega_d} + 1} \tag{5.12}$$

Here, $\omega_R = 2\pi\nu_R$ is the resonance angular frequency and $\omega_d = -\omega_R^2/\Gamma_R$ [Γ_R being the damping coefficient defined in (3.86)]. The relation $\omega_d > \omega_R$ ($\omega_R > -\Gamma_R$) holds and $H(i\omega)$ takes its maximum at $\omega \approx \omega_R$. As a result, a resonance peak at $\omega = \omega_R$ appears for $\omega_R/\omega_d \ll 1$. The function $H_K(i\omega)$ is derived for the minimum linewidth mode, since this is the most stable external cavity mode. Also weak feedback and a linewidth enhancement factor $\alpha > 1$ are assumed to derive this equation. Then, the feedback term $K(i\omega)$ is given by

$$K(i\omega) = i\frac{k_c\sqrt{1+\alpha^2}}{\omega}\{1 - \exp(-i\omega\tau)\} \tag{5.13}$$

with the round trip delay τ of the external cavity and the feedback rate $k_c = \kappa/\tau_{in}$.

At a certain feedback level, the transfer function (5.12) exhibits an unstable pole. The existence of such a pole does not necessarily mean that a coherence collapse occurs, since the coherence collapse is described by a very complicated dynamic process. However, the minimum feedback level at which an unstable pole occurs, actually corresponds to the onset of the coherence collapse. A pole in $H_K(i\omega)$ occurs for

$$K(i\omega)H(i\omega) = 1 \tag{5.14}$$

A long external cavity is assumed here, so that $K(i\omega)$ gets maximum for $\exp(i\omega\tau) = 1$ in (5.13), where $\omega\tau$ is an odd multiple of π. Using $\omega \approx \omega_R$ and the condition in (5.14), the critical feedback coefficient $k_{c,\text{critical}}$ reads

$$k_{c,\text{critical}} = \frac{\omega_R^2}{2\omega_d}\frac{1}{\sqrt{1+\alpha^2}} = \frac{1}{2}\frac{\Gamma_R}{\sqrt{1+\alpha^2}} \tag{5.15}$$

Noted that the $k_{c,\text{critical}}$ is derived from the assumption for a large value of the linewidth enhancement factor. Therefore, (5.15) is only valid for $\alpha > 1$. To deduce the expression still applicable to a small value of the linewidth enhancement factor, we employ a following empirical approximation for a large value of the linewidth enhancement factor ($\alpha^2 \gg 1$) (Helms and Petermann 1990):

$$\frac{1}{\sqrt{1+\alpha^2}} \approx \frac{\sqrt{1+\alpha^2}}{\alpha^2} \tag{5.16}$$

Using this relation with (5.15), the critical feedback coefficient is expressed as

$$k_{c,\text{critical}} = \frac{\Gamma_R}{2}\frac{\sqrt{1+\alpha^2}}{\alpha^2} \tag{5.17}$$

For the feedback parameter of a Fabry-Perot laser in (4.4), the critical feedback level where the semiconductor laser starts to show unstable oscillations is given by

$$r_{\text{critcal}} = \frac{\Gamma_R^2\tau_{in}^2\sqrt{1+\alpha^2}}{4\alpha^2\frac{1-r_0^2}{r_0}} \tag{5.18}$$

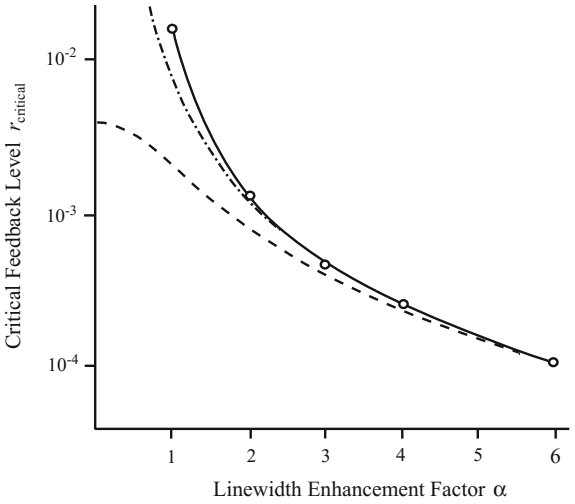

Fig. 5.16 Critical feedback strength for linewidth enhancement factor. *Solid line* Numerically determined critical feedback strength, *dashed line* theoretical prediction from (5.15), *dash-dotted line* theoretical prediction from (5.17) [after Helms and Petermann (1990); © 1990 IEEE]

Figure 5.16 is the plot of the critical feedback strength for the linewidth enhancement factor. The solid line shows the numerically calculated critical feedback strength. While the dashed line is the theoretical prediction obtained from (5.15) and the dash-dotted line is the one from (5.17). Equation (5.17) well represents the critical feedback strength for the linewidth enhancement factor, where the unstable laser oscillation starts. This tolerable feedback level increases with the increasing damping of the relaxation oscillations.

5.2.4 Sensitivity of the Optical Phase

We showed the dependence of the dynamics in semiconductor lasers with optical feedback on the external mirror position in the previous section. The dynamics is strongly dependent on the position of the external mirror not only for the long range of the mirror displacement in the order of centimeter to meter, but also for short variation of the external mirror comparable with optical wavelength. When the length of the external mirror L is short enough and it is less than the internal cavity length ηl (effective cavity length), the mode separation of the internal cavity becomes shorter than that of the external cavity. Then, one of the successive internal modes is sequentially selected by the continuous small change of the external mirror position. When the mode hops, a noise known as mode-hop noise is induced and the laser performance is much deteriorated. In this regime, the coupling between the internal and external cavity is strong, though the laser output power shows a periodic variation with a period of the half wavelength of $\lambda/2$. The laser under this condition is usually stable and rarely shows chaotic oscillations. When the external mirror is located at a length longer than the internal cavity length but it is within the length corresponding to the frequency of the relaxation oscillation, i.e., $\eta l < L < c/2\nu_R$, the laser is still stable as far as the external feedback stays small. However, for a larger feedback level, the laser shows instabilities and it evolves into chaotic oscillations for a further increase of optical feedback. For $L > c/2\nu_R$ but within the coherence length of the laser oscillation, the laser becomes less stable at a smaller feedback level and it is easily destabilized by optical feedback. As will be discussed in the following, the laser output shows chaotic dynamics for a small variation of the external mirror position compatible with optical wavelength λ. Namely, the laser has a phase sensitivity to the change of the external cavity length (Lang and Kobayashi 1980; Osmundsen and Gade 1983; Arimoto and Ojima 1984; Kakiuchida and Ohtsubo 1994).

Figure 5.17 schematically shows the dependence of the optical output for the increase of external optical feedback when the external mirror is positioned at several centimeters to meters in ordinary semiconductor lasers. As far as the optical feedback is very small, very smoothly varying undulation is observed as shown in Fig. 5.17a. With the increase of optical feedback, the amplitude of the modulation grows but shows asymmetric features in the waveform (see Fig. 5.17b). Then, a further increase of optical feedback but still at a modest feedback level, sudden

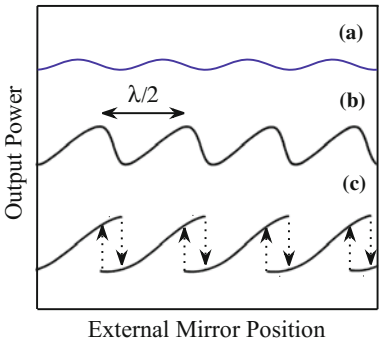

Fig. 5.17 Schematic plot of the dependence of the output power for the change of external mirror position compatible with the optical wavelength. **a** Small feedback with sinusoidal oscillation, **b** moderate feedback with asymmetric oscillation, and **c** strong feedback with hysteresis

jumps of the optical output appear for the variation of the external mirror position. Also, the waveform shows hysteresis depending on the upward or downward variation of the mirror position as shown in Fig. 5.17c (Lang and Kobayashi 1980). The duration of the periodic cycle of the output power is not always equal to $\lambda/2$ but also $\lambda/4$, $\lambda/6$, and so on (Kakiuchida and Ohtsubo 1994). When the optical feedback fraction becomes very large, we can observe such higher order periodic undulations in the optical output. For further increase of optical feedback, the laser oscillations of bistability and multistabilities evolve into irregular chaotic oscillations. Periodic oscillations, which is an interference effect between the internal- and external-cavity fields before the onset of chaos in semiconductor lasers with optical feedback can be applied for interferometric measurements. We will return to the subject and demonstrate some applications based on the phenomena in Chap. 11.

5.2.5 *Chaotic Dynamics for a Small Change of the External Cavity Length*

In Sect. 5.2.1, we assumed a fixed phase of $\omega_0\tau = 0$ and obtained the dependence of the dynamics on the external mirror length for a range of the order of centimeters to meters. We here consider the effects for a small change of the external mirror position, i.e., $\omega_0\tau$ is not zero and the change of the external mirror position is compatible with the optical wavelength. The semiconductor laser is very sensitive to a small change of the external mirror position and the output power varies periodically with length corresponding to half of the optical wavelength. In actual fact, not only periodic oscillations of the laser output power but also chaotic instabilities are observed within such a short variation. When the fraction of optical feedback is small enough, the laser output shows smooth periodic undulations for a change of the external mirror position as discussed in the previous subsection. Various methods for metrological applications (for example, micro-vibration measurement of surfaces compatible with optical wavelength) have been proposed based on the periodic change of the laser output power (Donati et al. 1995). These

techniques are only applicable for the external feedback fraction in the regimes from II to III discussed in Sect. 4.1.1. On the other hand, smooth undulations are no longer observed in regimes III and IV and, instead, chaotic oscillation appears for the change of the external mirror length (Ikuma and Ohtsubo 1998). We show various routes to chaos for such small changes of the external mirror position in the following and also compare the theory with experiments.

Figure 5.18 shows the dynamics of the laser output power numerically calculated for the small change of the external mirror position (Ikuma and Ohtsubo 1998). The wavelength of the laser used is λ = 780 nm, so that the period of undulations is half of the wavelength, $\lambda/2$ = 390 nm. The left column is the variation of the averaged laser output power. The right column is the bifurcation diagram corresponding to the left. When the external feedback is small (Fig. 5.18a), the laser output power smoothly changes for the increase of the external mirror length with a period of $\lambda/2$. The laser stably oscillates at a fixed point even though it shows small periodic undulation for the change of the external mirror position (Fig. 5.18a right). For larger optical feedback, the laser output power periodically changes with a period of $\lambda/2$, however it shows sudden drops and irregular fluctuations (Fig. 5.18b–d). Chaotic bifurcations are clearly visible at larger optical feedback. For example, at the external mirror length around 4.2000 cm in Fig. 5.18d, the laser output power is stable and it oscillates at a single mode. As the external cavity length increases, it suddenly becomes unstable and shows chaotic oscillations. With further increase of the external cavity length, it reduces from the quasi-periodic state to periodic oscillation and finally reaches the stable state. This process repeats with the period equal to $\lambda/2$. In actual fact, there exists a hysteresis of the laser output power for upward and downward changes of the external mirror position. The power drops observed in Fig. 5.18d, e originate from this instability. The waveforms are the time-averaged signals. Hence, the time-resolved signals at a certain external mirror position show fast irregular oscillations with a typical frequency of the relaxation oscillation as is the case for chaos in semiconductor lasers with optical feedback, as has already been discussed. The maximum Lyapunov exponent is frequently used to help the understanding of the dynamic behaviors of nonlinear systems (Appendix A.2). The maximum Lyapunov exponent has a positive value in chaotic regions, while it has zero or negative value in periodic and stable oscillations. At the point where the Lyapunov exponent has a value of less than zero, the laser output power becomes fixed states (single straight line) in the bifurcation diagram. Indeed, the maximum Lyapunov exponent is positive for the chaotic region in Fig. 5.18, while it is negative for stable states (Ikuma and Ohtsubo 1998).

The optical spectrum at stable oscillation in Fig. 5.18a is completely a single mode, though the optical frequency changes with the variation of the optical output power. On the other hand, the coherence of the laser is destroyed due to chaotic oscillations and the laser has several broadened spectral peaks mixed with the relaxation oscillation and external cavity modes (coherence collapse state). We can experimentally observe the evidence of chaotic bifurcations from the laser output power by using a Fabry-Perot spectrometer. Figure 5.19 shows an example of optical spectra obtained by a Fabry-Perot spectrometer for the small change of the

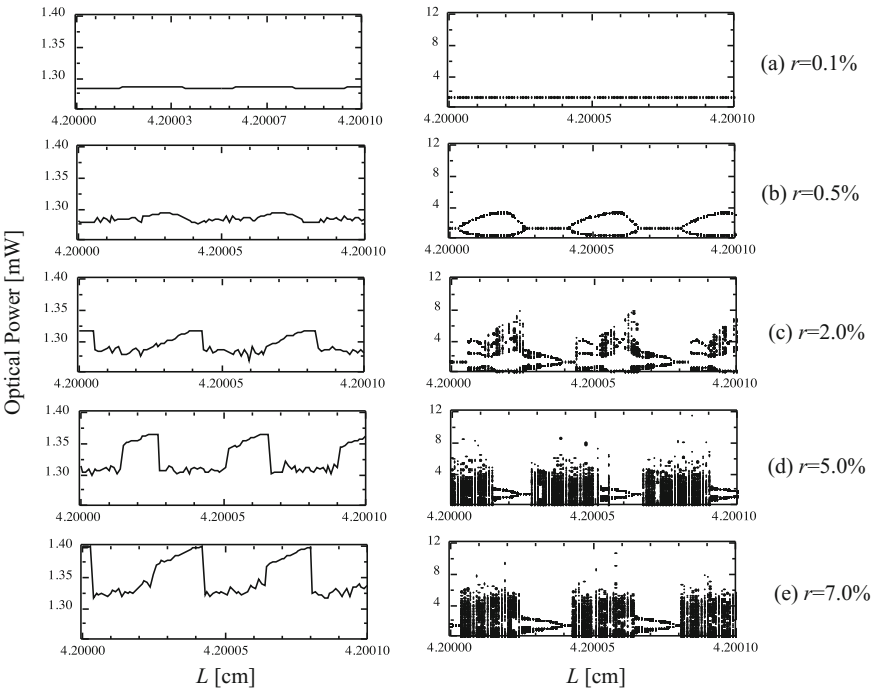

Fig. 5.18 Numerical results of the averaged laser output power (*left*) and the bifurcation diagram (*right*) for a small change of external mirror position at $L = 4.2000$ cm and a bias injection current at $J = 1.3J_{\text{th}}$

mirror position. The external cavity length is increased from bottom to top in this figure. The unstable state (weak chaotic or quasi-periodic oscillation) reduces to periodic oscillation and once stable state, then, it again becomes unstable oscillations with a period equal to half of the wavelength.

We assume a single internal mode oscillation for a semiconductor laser in the above discussion. However, for large external feedback reflectivity, a semiconductor laser sometimes oscillates with multimode. In such a case, we observe periodic undulations with periods not only of $\lambda/2$ but also $\lambda/4$, $\lambda/6$, and so on, for a small change of the external cavity length. Which period emerges in the laser output power variations depends on the absolute external mirror position from the laser facet. For a long-range variation of the external cavity length equal to the order of $\sim$mm or more, there also exists a periodic change of the laser output power with a period equal to the effective internal cavity length when the laser oscillates with multimode (Murakami 1999). At moderate optical feedback, when only a single external mode contributes to the laser oscillation (which occurs at integer multiples of the internal cavity length $m\eta l$ with integer number m), an undulation with period $\lambda/2$ is observed. When two external modes play an important role for the laser oscillation at the external mirror position of $(m + 1/2)\eta l$, an undulation with a

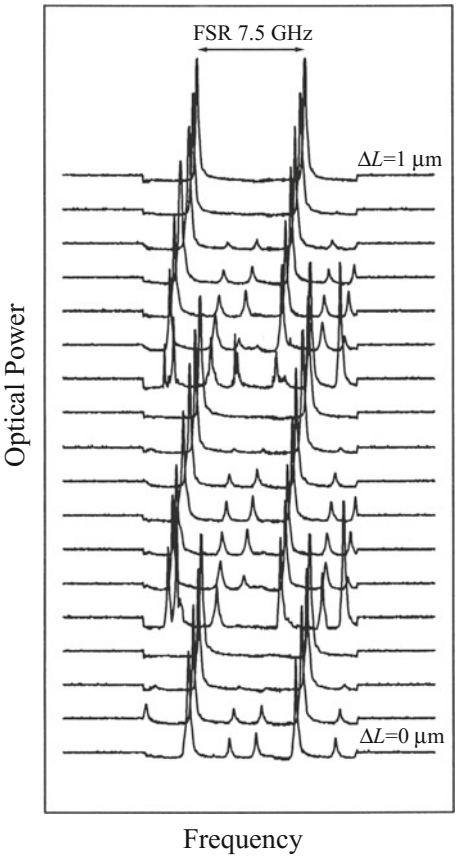

Fig. 5.19 Experimentally observed optical spectra obtained by a Fabry-Perot spectrometer for small change of the external mirror position

period of $\lambda/4$ is observed. Further, at the external mirror position of $(m + 1/3)\eta l$ and $(m + 2/3)\eta l$, an undulation with a period of $\lambda/6$ appears. Similarly, higher order periodic undulations are observed depending on the external mirror position and the excited internal modes. Even in a higher order periodic undulation, there exist chaotic bifurcations within that period. Those effects are well demonstrated by the numerical simulation of the multimode laser rate equations and can be compared with experimental results (Kakiuchida and Ohtsubo 1994).

5.3 Low-Frequency Fluctuations

5.3.1 Low-Frequency Fluctuation Phenomena

Periodic and quasi-periodic bifurcations are typical routes to chaos in nonlinear systems. However, these are not only the chaotic routes. Folding and stretching

variables in the projection process in nonlinear systems, and various possibilities for chaotic routes are generated. Other than periodic and quasi-periodic bifurcations, one of the well-known routes is the intermittent route to chaos (Risch and Voumard 1977; Fujiwara et al. 1981; Temkin et al. 1986; Sano 1994). Low-frequency fluctuation (LFF) is one of chaotic oscillation known as the intermittent chaos of saddle node instability also observed in semiconductor lasers with optical feedback. To study LFFs is very important from the viewpoint of practical applications, since LFFs induce much noise in the laser output power. A typical feature of LFFs is a sudden power dropout with a following gradual power recovery. LFFs occur irregularly in time depending on the system parameters and the frequency of LFFs is usually of the order of MHz to a hundred MHz. Since the frequency of LFFs is much lower than ordinary chaotic fluctuations related to the relaxation oscillations, the phenomena are called low-frequency fluctuations. When waveforms of LFFs are observed by a fast digital oscilloscope, they seem to be continuous signals. However, it is proved that LFF has very fast time structures within the waveform and it consists of a series of fast pulses on the order of picosecond. Indeed, this fast pulsation has been experimentally observed by using a streak camera (Fischer et al. 1996). Though LFFs were first recognized as sudden power dropouts with low frequency in the early days and this was the origin of the name of the phenomena, LFFs have quite different features from the ordinary chaotic behaviors and show a rich variety of dynamics. In the following, we show various dynamics of the phenomena and discuss the origin of LFFs.

LFFs were first observed in the output power above but close to the laser threshold. However, LFFs are phenomena induced by saddle node instability in nonlinear systems, therefore they are also observable in laser oscillations well above the threshold under appropriate conditions of the parameters when the system has saddle node unstable periodic orbits (Pan et al. 1997). LFFs are also observed by injection current modulation and optical injection from a different laser when the laser is subjected to optical feedback (Takiguchi et al. 1998). Various models for the origin of LFFs have been proposed. One of them is the model that LFF is the instability driven by noise in the nonlinear laser system (Tromborg et al. 1997; Eguia et al. 1998; Mørk et al. 1999). Other ones are explained by competitions between modes in a multimode model of the laser (Hegarty et al. 1998), and the crisis between two attractors (van Tartwijk et al. 1995). However, LFFs have been experimentally observed in a single mode laser with optical feedback and they have also been proved to appear in a single mode model by numerical simulations without noise effects. Therefore, LFFs are the deterministic chaos induced by saddle node instability with time-inverted type-II intermittency in semiconductor lasers with optical feedback (Sacher et al. 1989, 1992).

Figure 5.20a is an example of typical LFF waveforms obtained by experiment (Fischer et al. 1996). This is a low-pass filtered waveform and a higher component over nanosecond oscillations is not observable. The typical features of LFFs are frequent power dropouts after stationary output and subsequent gradual power recovery processes as shown in the figure. When the laser is operated close to the threshold, the output power breaks down even below the threshold at the solitary

operation. The frequency strongly depends on the conditions of the laser parameters and the external mirror. The power dropouts occur irregularly and their average frequency is about 5 MHz in this case, hence low-frequency fluctuations. Figure 5.20b shows a time-resolved waveform of LFFs observed by a high-speed streak camera. The waveform consists of a pulse train with an average period of 300 ps. Figure 5.21a is a one-shot of LFFs. To show the power recovery process clearly, one-shot of LFFs is averaged and plotted in Fig. 5.21b. Stepwise power recovery is clearly visible in the figure. In actual fact, relaxation oscillations are included at the onset of each jump in the power recovery, although it is averaged out in this figure. The time duration of each step in the power recovery is equal to the round trip time of light in the external loop. LFFs tend to appear in the laser output when the external cavity length is sufficiently long and the external feedback is large enough (Takiguchi et al. 1999). Under such conditions, saddle node instabilities are easily induced in the system and many external- and anti-modes are generated. As will be discussed later, LFFs are explained as chaotic itinerary among these modes. On the other hand, LFFs are rarely observed for short external cavity length with small optical feedback, since the oscillation modes are sparsely distributed in the phase space. From these results, LFF, which is first recognized as fluctuations of the laser output with a low frequency, is composed of three components of time scales. One is a component of a low-frequency fluctuation with a period around MHz; the second is a component related to the external cavity length; the third is a high frequency component with a period of picoseconds. In the following, several characteristics of LFFs and their origin are described.

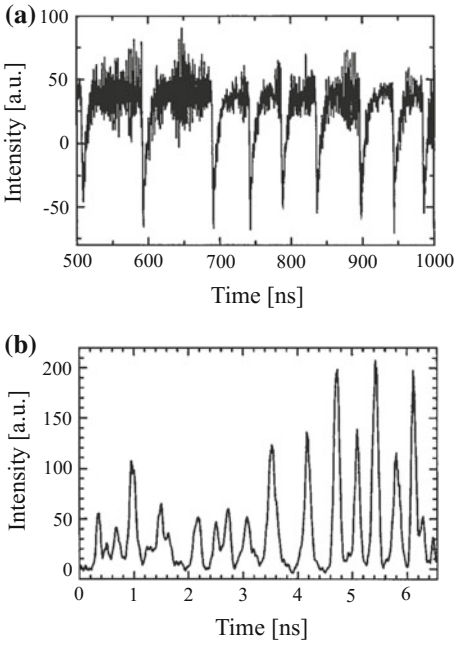

Fig. 5.20 Low-frequency fluctuations in semiconductor lasers with optical feedback at $J = 1.03J_{th}$. **a** Detected by a slow response detector. **b** Observed by a fast streak camera. Delay time is $\tau = 3.6$ ns [after Fischer et al. (1996); © 1996 APS]

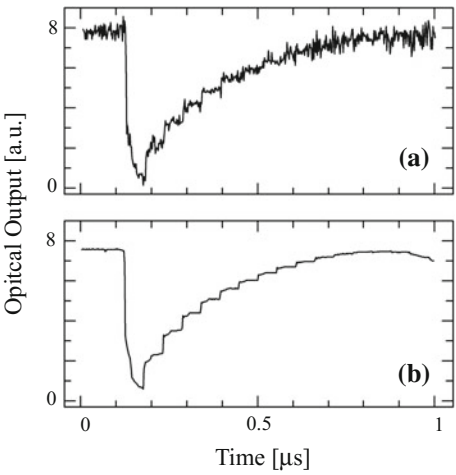

Fig. 5.21 **a** Single shot of LFFs and **b** one-shot of LFFs averaged over 3000 events. The external cavity length and the bias injection current are $L = 8.10$ m and $J = 1.07J_{th}$. The external reflectivity is $r^2 = 0.12$

5.3.2 *Low-Frequency Fluctuation Characteristics*

One typical chaotic evolution is an intermittent route to chaos and low-frequency fluctuations (LFFs) are frequently observed as such chaotic oscillations in semiconductor lasers. Feedback-induced LFFs in semiconductor lasers depend on the bias injection current, the external cavity length, and the feedback level. As a general trend, the frequency of LFFs linearly increases with the increase of the bias injection current. The frequency of LFFs is about several to several tens of MHz when the external mirror is positioned around 10–100 cm. On the other hand, the frequency is less than MHz for a longer external cavity length over 1 m (but the mirror is still positioned within coherence length of the laser). The linear relation between the frequency and the bias injection current is also held in this case. The frequency of LFFs linearly decreases for the increase of the external reflectivity at the bias injection current well above the threshold, however it stays almost constant for the bias injection current close to the threshold (Takiguchi 2002).

LFFs were initially observed near the solitary laser threshold. However, it was later proved that LFFs occur everywhere along the boundary between the optical feedback regimes of IV and V discussed in Sect. 4.1.1. Figure 5.22a shows the diagram of the possible area for the occurrence of LFFs obtained by experiment (Pan et al. 1997). Due to the low internal reflectivity of the front facet of semiconductor lasers, LFFs are observed not only for low injection current close to the laser threshold, but also for a higher injection current. The laser threshold is reduced by the external feedback as discussed, but, under certain conditions of the laser parameters, the slope efficiency decreases and the laser power becomes lower than that of the solitary laser at a higher injection current (see Fig. 5.9). In such cases, LFFs occur at a high injection current and the laser power shows not dropouts but jumpups in LFFs as shown in Fig. 5.22b. Thus, LFFs are universal phenomena observed in semiconductor lasers with optical feedback and they are a typical

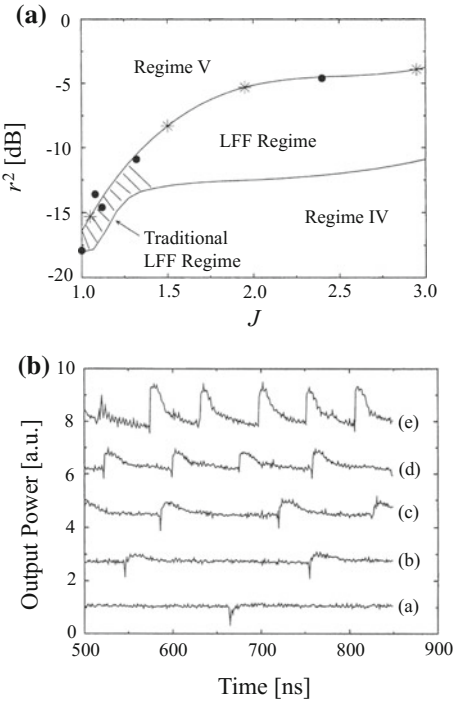

Fig. 5.22 **a** LFF regions between regimes IV and V at $L = 60$ cm. The *horizontal axis* is the injection current and the *vertical axis* is the ratio of the feedback light. *Symbols* denote experimental results and *solid lines* theoretical results. **b** Time series of LFFs for bias injection currents of $J = 1.20J_{th}$, $1.34J_{th}$, $1.48J_{th}$, $1.66J_{th}$, and $2.08J_{th}$ from *bottom* to *top* at $\kappa\tau/\tau_{in} = 240$ [after Pan et al. (1997); © 1997 OSA]

feature of saddle node instabilities involved in nonlinear systems. When LFFs occur, the laser usually oscillates at multimode and a single mode operation of the laser is not always an appropriate model to describe it. However, we can observe LFFs at a single mode operation of the laser as mentioned before (Heil et al. 1998). For example, when a semiconductor laser with optical feedback is operated by selecting a single mode from a grating mirror feedback, we can still observe LFFs under this condition. Furthermore, LFFs are reproduced by the numerical simulation in the laser output power with a single mode model for the rate equations (Sano 1994). LFFs are also simulated at a multimode operation of the laser. In the multimode case, switching of the output power among the modes occurs and the total power shows LFF waveforms, which is the same as those of ordinary chaotic oscillations.

5.3.3 *Origin of Low-Frequency Fluctuations*

LFFs are explained by saddle node and intermittent instability involved in the nonlinear system of semiconductor lasers with optical feedback. LFFs occur not only by self-optical feedback but also by optical injection from a different laser. Another example of the occurrence of LFFs is an injection current modulation in

the presence of optical feedback and, indeed, the laser also shows LFFs by the injection current modulation. However, we focus on the discussion for the origin of LFFs induced by optical feedback. The same or a similar explanation is also applicable for other cases. Phenomena of LFFs are generally explained by employing the model that the laser output power hops around external- and anti-modes of the laser oscillations due to unstable saddle node instability generated by the optical feedback (Sano 1994).

We start the discussion for the external- and anti-modes in the phase space of the oscillation frequency and the carrier density. In semiconductor lasers with optical feedback, we obtain the steady-state solutions from (4.10) and (4.11) as

$$\Delta\omega\tau = -\frac{\kappa\tau}{\tau_{\text{in}}}\sqrt{1+\alpha^2}\sin(\omega_s\tau + \tan^{-1}\alpha) \tag{5.19}$$

$$\Delta n = -\frac{2\kappa}{\tau_{\text{in}}G_n}\cos(\omega_s\tau) \tag{5.20}$$

where $\Delta\omega = \omega_s - \omega_{\text{th}}$ and $\Delta n = n_s - n_{\text{th}}$. Figure 5.23a shows about lower half the distribution of the modes in the phase space of $\Delta\omega - \Delta n$ calculated from (5.19) and (5.20). This corresponds to the case for a long external cavity length with a high level of external feedback. Therefore, the modes are densely distributed. For the case of short external cavity length with a low external feedback, the mode distribution will be sparse. The laser oscillates at one of the stable modes (lower half modes on the ellipsoid). The modes of the upper half on the ellipsoid are unstable and they are not generally stable lasing modes. The black square at the center of the ellipsoid is the mode of the solitary oscillation. The laser without optical feedback oscillates at this single mode. Among the modes in Fig. 5.23a, the most possible mode of the laser oscillation in the presence of optical feedback is the maximum gain mode. However, the laser does not always oscillate at this mode. Folding and stretching the variables induced by nonlinear characteristics in the system due to small fluctuations, the laser may be suddenly trapped to a spiky orbit with a large amplitude oscillation.

At first, we think that the laser initially oscillates around the maximum gain mode and the state of the laser oscillation fluctuates near this mode with small amplitude. In actual fact, this is not the fixed stable mode. Once, the state reaches a point very close to the counterpart anti-mode and, then, the laser may be trapped in the anti-mode. The phase remains unchanged, but the carrier density abruptly jumps up to the value of the solitary oscillation. The sudden jump of the carrier density induces the increase of the phase and the laser shows a sudden power dropout. At this state, the laser output power is almost equal to the free running oscillation. This corresponds to a sudden power dropout of LFF. After that, the laser is trapped by one of the external modes close to the solitary oscillation mode. Then, the state goes around the successive external modes toward the maximum gain mode. This corresponds to the power recovery process of LFF. When the laser reaches the maximum gain mode, the above process is repeated. The occurrence of LFFs is not

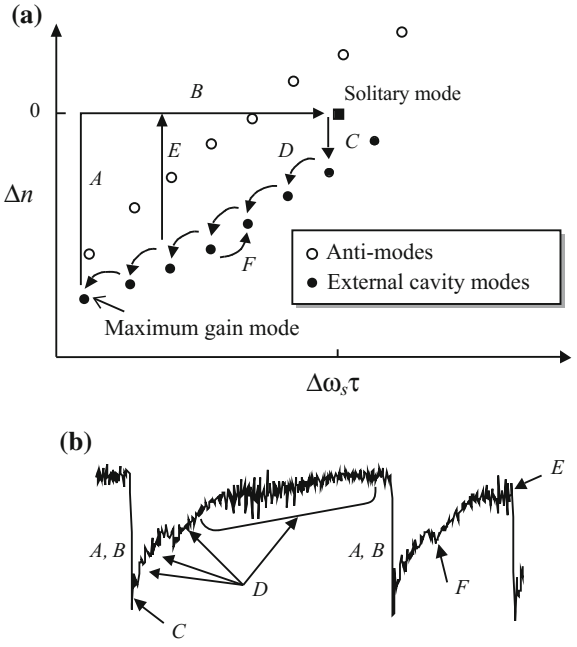

Fig. 5.23 **a** External- and anti-modes in the phase space of the frequency and the carrier density. Only lower half of the ellipsoid of the mode distribution is shown in the graph. **b** Corresponding LFF waveform to **a**

periodic but irregular, since the fluctuations exist in the chaotic itinerary due to the nonlinear effects. For example, when the chaotic oscillation has large amplitude in the power recovery process, the laser may be trapped in the associate anti-mode and a power dropout may occur even before reaching the maximum gain mode. Another case is a reversion of the power recovery and the state goes up against the direction for the maximum gain mode. The corresponding LFF waveform to Fig. 5.23a is also shown in Fig. 5.23b.

Figure 5.24 shows a numerically calculated chaotic itinerary of the laser output power in the phase space of $\Delta\omega - \Delta n$ under a LFF regime. The figure corresponds to almost two cycles of LFFs. Indeed, chaotic itinerary at LFF oscillations was experimentally demonstrated in the phase space between the optical output power and the carrier density (Ray et al. 2006). Also, chaotic LFF itinerary in a phase-space tomography is obtained by simultaneous experimental determination of optical intensity, frequency, and population inversion with high temporal resolution (Brunner et al. 2015). Figure 5.25 shows a phase-space tomography experimentally obtained for intensity dropouts for optical-feedback induced LFFs. The figure represents all three physical dimensions of intensity variations, phase (frequency), and carrier variations after applying 250 MHz low-pass filter for the original time series captured by digital real-time oscilloscope with 16 GHz analog bandwidth. The wavelength of the semiconductor laser is 1543 nm. The laser is biased at $J = 1.04J_{\text{th}}$ and the optical feedback attenuation is about 9 dB with a feedback delay of $\tau = 77.6$ ns. As a matter of fact, the population inversion (carrier density) cannot be directly measured in semiconductor lasers. Instead of measuring the

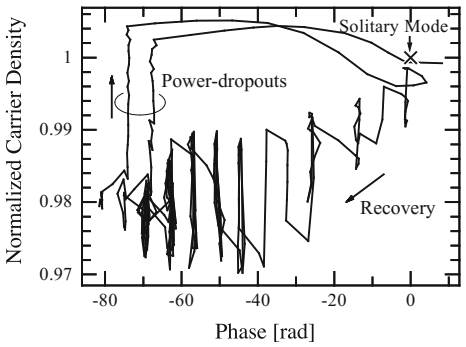

Fig. 5.24 Calculated chaotic itinerary in the phase space of the phase and the carrier density at $J = 1.01J_{th}$, $L = 30$ cm, and $r = 0.1$. Symbol $\times$ is the solitary mode

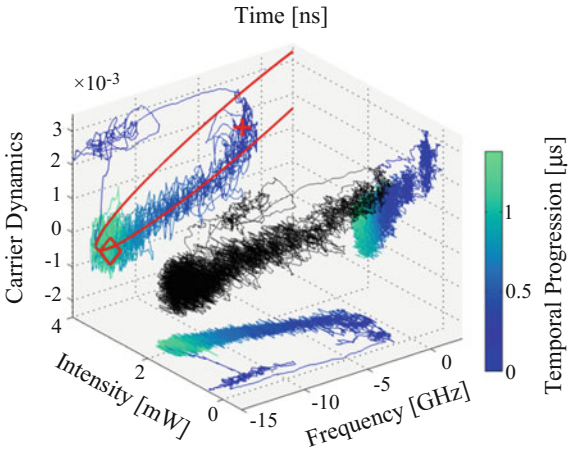

Fig. 5.25 Experimental phase-space tomography of intensity dropouts in LFF regime. *Black line* Three-dimensional trajectory of LFF. *Red line* fitted mode ellipse, *red cross* solitary laser mode, *red diamond* maximum gain mode. The two-dimensional projections include color-coded temporal information [after Brunner et al. (2015); © 2015 APS]

change of the carrier density, the voltage variation across the laser diode is obtained as mentioned in Sect. 5.1.5.

In the meantime, for the wandering from the solitary laser mode to the higher gain mode, chaotic itinerary of LFFs was directly visualized by experiment. Brunner et al. (2012) used a heterodyne technique to extract frequency information from time series of low-frequency fluctuations. In their scheme, a heterodyne signal, created by optical interference of a chaotic laser and a frequency stabilized reference laser with sufficiently narrow linewidth on a photodetector, is recorded with a sufficient analogue bandwidth. Expressing the field amplitudes of the lasers as $E(t) = A(t)\cos(2\pi\nu t)$, the interference signal is given by

$$I(t) = \frac{1}{2}\{A_0^2(t) + A_r^2(t)\} + A_0(t)A_r(t)\cos\{2\pi\Delta\nu_b(t)t\} \tag{5.21}$$

where A_0 and A_{in} are the amplitudes of the chaotic laser and the reference laser, and $\Delta\nu_b$ is the beat induced by the heterodyning. The phase dynamics $2\pi\tau\Delta\nu = \phi(t) - \phi(t-\tau)$ of the chaotic laser is well represented by the beat frequency $\Delta\nu_b$.

The amplitude of the chaotic laser is a function of time, while we can assume that the reference laser has constant amplitude for time. Then, the frequency dynamics can be given by a deconvolution between the cosine term signal in (5.21) and the time dependent amplitude A_0 as

$$S(\nu) = \left[\tilde{I}(\nu) - \frac{1}{2}\{\tilde{A}_0^2(\nu) + \tilde{A}_{\text{in}}^2(\nu)\}\right] \hat{\otimes} \tilde{A}_0(\nu) \tag{5.22}$$

where the symbol $\sim$ over the variable denotes a Fourier transform corresponding to the time function and $\hat{\otimes}$ stands for a deconvolution operator. Finding $S(\nu)$ by experiment, the phase dynamics of LFFs can be obtained.

Figure 5.26a shows an example of LFF oscillations. The laser is biased at $1.03J_{\text{th}}$ and the optical feedback time is $\tau \sim 100$ ns. For the time series, the dynamics of the laser frequency from (5.22) are analyzed by employing a sliding fast Fourier transform (sFFT) with each sliding-time window of 4 ns. Figure 5.26b shows the result of the reconstructed frequency. The frequency detuning between the chaotic laser (at solitary laser mode: SLM) and the reference laser is −3.4 GHz and the higher gain mode region (higher gain region: HGR) exists at around −13 GHz.

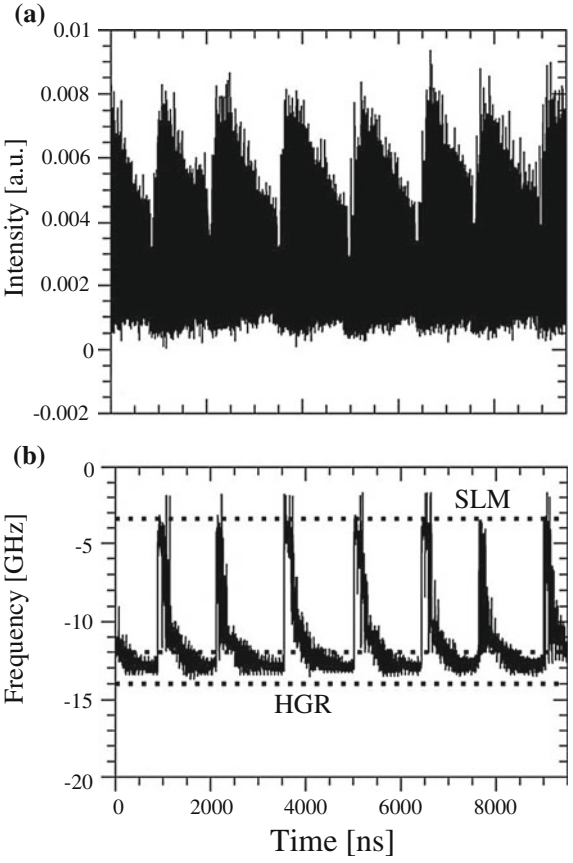

Fig. 5.26 Dynamics of a delayed feedback laser. **a** Time series of the LFF intensity induced by optical feedback and **b** dynamics of the peak spectral component reconstructed from (5.22). The laser is biased at $1.03J_{\text{th}}$ and the optical feedback time is $\tau \sim 100$ ns [after Brunner et al. (2012); © 2012 Nature Pub.]

After dropout in LFFs, the laser is trapped to the solitary mode frequency and gradually recovers toward the high gain mode frequency, which is quite consistent with the theory discussed in this section. The linewidth of the external mode is also calculated from the beating spectrum. The linewidth is around 1 MHz in this laser and the linewidth in the high gain region is slightly less than other frequency region including the solitary laser mode. On the other hand, the relaxation rate at the high gain region is much less than other region. The relaxation rate takes the maximum at the solitary laser mode.

As has already been discussed, LFFs have three time scales of fluctuations. The first one is a fast pulse-like oscillation of the order of several tens of picoseconds. When the laser is oscillated close to one of the external modes, the carrier density changes with large amplitude and it reaches the associated anti-mode, while the phase stays almost constant. This corresponds to a series of fast pulsations. The time scale depends on the fluctuations of the carrier number in the active layer. The second is the transition time between the successive external modes in the stepwise time recovery process. The time is related to the external cavity length and, for example, it is of the order of nanoseconds for the external cavity length of several tens of centimeters. The third time scale is the duration time of power dropout events. This time scale is usually of the order of microseconds, but the period is not fixed, as has already been discussed. We have assumed the steady-state condition to calculate the external- and anti-modes in Fig. 5.23. However, the occurrence of LFFs is of dynamic nature, so that the discussion developed here may not be applicable for such dynamic states in the strict sense. Nonetheless, the approach can explain the overall feature of the LFF dynamics, because chaos itself is generated from small perturbations to the initial state of the laser oscillations.

Finally, we will show a return map of the LFF characteristics to demonstrate typical folding and stretching process in the nonlinear system (Mørk et al. 1999). The relation between the present field and the previous field before time τ can be calculated from (4.2). Reducing the delay differential equations into difference equations, we obtain the relation by Fourier transforming the difference equation. The relation between the Fourier components $\tilde{E}_n(\omega)$ and $\tilde{E}_{n-1}(\omega)$ is given by

$$\tilde{E}_n(\omega) = \frac{\frac{\kappa}{\tau_{\text{in}}}\exp(-i\omega\tau)\tilde{E}_{n-1}(\omega) + \tilde{F}_E(\omega)}{i\omega - \frac{1}{2}(1 - i\alpha)G_n(n - n_{\text{th}})} \tag{5.23}$$

The equation includes the Langevin noise component $\tilde{F}_E(\omega)$, although it is not essential. Calculating the square modulus of (5.23) and converting to the form for the intensity, we obtain a return map for delay time τ. The result is shown in Fig. 5.27. Dots in the figure are the modes of laser oscillations. The modes along the line are stable external modes and the modes below the line are anti-modes. The state of the laser oscillations goes up from small to large intensity and the intensity breaks down to a level close to the threshold. The chain of dots shows the nonlinear nature of the system. The qualitative explanation can be given by this model. To reproduce the irregular occurrence of LFFs, the Langevin term is introduced in the model. When the noise term is not included, LFFs occur periodically with an exact

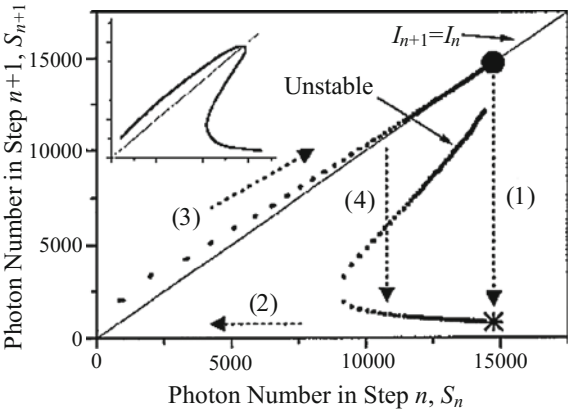

Fig. 5.27 Calculated return-map for LFFs at a feedback level of $\kappa = 0.15$ and an injection current of $J = 1.0J_{th}$. The *arrows* with numbering illustrate how the map is traversed starting from the steady-state point. Notice that the switching at 4 can take place for any value of the photon number in the range where three solutions exist. The *inset* shows a schematic of the full map, which is not accessible in the calculations or in experiments [after Mørk et al. (1999); © 1999 Elsevier]

period. Therefore, it may not reflect real oscillations of LFFs, since the equation is derived from the simplification of the discrete sampling for the rate equations. On the other hand, periodic LFFs are experimentally observed for a strong coupling of light with a short external cavity length (Heil et al. 2001).

5.4 Chaotic Dynamics in Short External Cavity Limit

5.4.1 Stable and Unstable Conditions in Short External Cavity

Most investigations of the dynamics of semiconductor lasers subject to delayed optical feedback have been focused on the so-called long external cavity regime, in which the external cavity length is larger than the corresponding frequency of the relaxation oscillation frequency ν_R. However, in many practical applications in engineering, for example, optical fiber communications or optical storage systems, the typical external cavity is only a few centimeters long. In Sect. 5.2.1, we observed the periodicity of the stability enhancement for the variations of external cavity length. The first period of the stability is almost equal to the length calculated from the relaxation oscillation frequency. Namely, within this optical feedback length, the semiconductor laser becomes stable and shows robustness for the feedback. In the following section, we discuss the dynamics and stability of semiconductor lasers from short external cavity. As a measure of stability and instability in semiconductor lasers, we have already introduced the C parameter. The C parameter includes the round trip time τ and the time is proportional to the external cavity length as

$\tau = 2L/c$. The laser is stable for external optical feedback as far as $C < 1$, namely the short cavity limit. The C parameter is also proportional to the feedback strength κ as (4.13), so that even for a feedback from a short cavity, the laser is not always stable and the stability strongly depends on the external feedback strength. To begin the discussion of the short cavity limit, we first consider the boundary for the stability and instability in the phase space of the feedback time τ and the feedback fraction r.

Here, the condition for the short external cavity in a semiconductor laser is $\nu_R\tau < 1$. Even under a small cavity condition, the laser shows unstable oscillations when the external optical feedback is strong enough. In other word, the laser always has unstable solutions of the oscillation for $\nu_R\tau > 1$. Schunk and Petermann (1989) theoretically predicted that there is an external cavity length below which coherence collapse should not be observed. Figure 5.28 shows the boundary condition below which coherence collapse should not be observed. The boundary is obtained from numerically solving the rate equations in the presence of optical feedback in a semiconductor laser. The relaxation oscillation and α parameter of the laser are assumed to be $\nu_R = 4.4$ GHz and $\alpha = 6$, respectively. The shaded part is the area where unstable laser oscillations are observable. The laser does not always show unstable oscillations in all of this area, but mixed states with stable and unstable oscillations are observable depending on the parameter conditions. For comparison, the boundary of the stable condition for the C parameter ($C \propto r\tau$) is shown as a broken line. A semiconductor laser should be always stable for $C < 1$. As is seen from the figure, the line $C = 1$ is not at all suitable for the criterion of the boundary between the stable and unstable regimes in the strict sense.

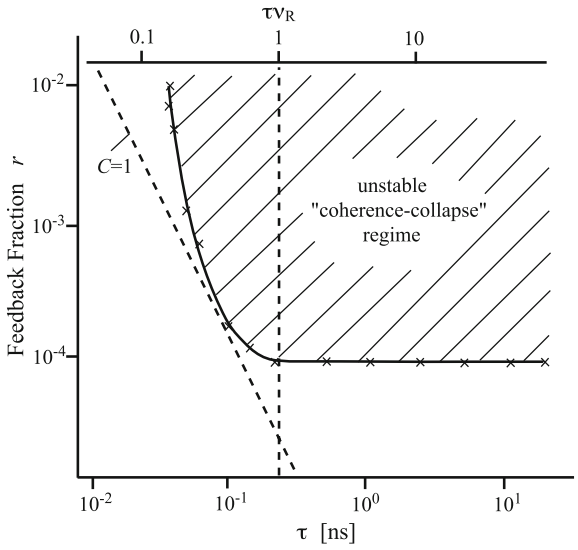

Fig. 5.28 Boundary for stable and unstable states for the feedback time τ and the external reflectivity r. *Solid line* Unstable boundary calculated from the rate equations, *dashed line* line for the feedback coefficient of $C = 1$ [after Schunk and Petermann (1989); © 1989 IEEE]

5.4.2 Regular Pulse Package Oscillations in Short External Cavity

The stability of a semiconductor laser is greatly enhanced for a short external cavity limit, as has been already pointed out. In this limit, the laser tends to oscillate at a LFF regime rather than irregular fast chaotic oscillations. Furthermore, the laser becomes very sensitive to the optical phase due to the strong coupling between the internal and external cavities. Heil et al. (2001) experimentally and theoretically investigated the dynamics of a semiconductor laser with short external cavity. As a typical feature of the dynamics, the laser showed a regular pulse package with a frequency of several hundreds of MHz like a LFF oscillation and each package contained about 10 pulses with a period corresponding to the external cavity length. The frequency of regular pulse package is considerably higher than a frequency with long external cavity ($\sim$10 MHz or less). Pulse-package oscillations are not only unique phenomena observed in narrow-stripe edge-emitting semiconductor lasers but also observed other types of semiconductor lasers. For example, Takeda et al. (2012) demonstrated similar pulse package oscillations in broad-area semiconductor lasers with short optical feedback.

Figure 5.29 shows the results of the dynamic characteristics in a semiconductor laser with optical feedback from a short external cavity. Figures 5.29a and b are the experimental results of observed spectra. In Fig. 5.29a, the laser shows a regular pulse package of an LFF frequency of 390 MHz. The pulse package is very regular and each pulse package consists of a train of regularly spaced light pulses occurring at the round trip frequency. Also, the spectral peak for the external cavity of 4.5 GHz, which corresponds to the short external cavity length of 3.3 cm, is seen. The inset is the direct waveform observed by a digital oscilloscope, but the waveform is smeared out due to the resolution of a digitizer (the bandwidth of 4.5 GHz). The regular pulsating oscillations with fully modulated waveform were confirmed by the observation from a streak camera and each pulse width was observed to be around 10 ps. In Fig. 5.29b, the LFF frequency is 1.195 GHz, which is quite fast, compared to the case of a long external cavity feedback. Only the LFF frequency is shown in the figure, since the external cavity frequency is 14 GHz (corresponding to the external cavity length of 1.1 cm) and the spectral peak is outside the scope of this plot. Under regular pulse package emission, the lasers operate on several longitudinal oscillation modes, which is similar to ordinary LFFs with long external cavity. In all cases of external cavity length in semiconductor lasers, the dynamics is sensitive to optical phase compatible to the optical wavelength. However, strong phase sensitivity is observed in the case of short external cavity optical feedback. In this experiment, the regular pulse package occurs only over a certain phase interval for the ranges of $1.3J_{\mathrm{th}} < J < 1.5J_{\mathrm{th}}$. For $J > 1.5J_{\mathrm{th}}$, the regular pulse package is present for all feedback phase.

Figure 5.29c is the simulation results for regular pulse package oscillations based on the laser rate equations. The threshold reduction due to the optical feedback is 11%. It is noted that the laser intensity is plotted against time

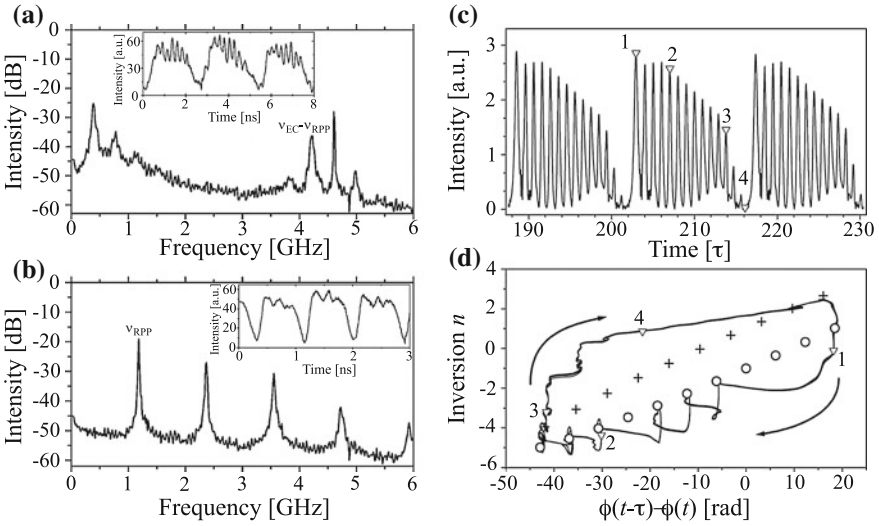

Fig. 5.29 Experimentally observed rf spectra and intensity time series for **a** $L = 3.3$ cm and $J = 1.08J_{th}$ corresponding to $\nu_R = 1.1$ GHz, and **b** $L = 1.1$ cm and $J = 1.80J_{th}$ corresponding to $\nu_R = 3.8$ GHz. **c** Numerical calculation of regular pulse package state and **d** trajectory plotted on the normalized inversion n and phase difference $\phi(t - \tau) - \phi(t)$ plane. The parameters used in the simulations are $J = 1.15J_{th}$ (corresponding relaxation oscillation frequency of $\nu_R = 3.42$ GHz), $L = 1.79$ cm, $1/\tau_{ph} = 5.86 \times 10^{11}$ s^{-1}, $\kappa/\tau_{in} = 7.91 \times 10^{10}$ s^{-1}, $\tau/\tau_{ph} = 70$, and $\tau_s/\tau_{ph} \approx 1710$ [after Heil et al. (2001); © 2001 APS]

normalized to the photon lifetime τ_{ph}. Figure 5.29d shows the trajectory of chaotic oscillations. In the phase space, the location of external modes is indicated by circles and the anti-modes by crosses. The temporal evolution occurs clockwise and the numbers in the figure provide a one-to-one correspondence of time series and phase space portrait. The LFF itinerary for one cycle is similar to that of a long external cavity. One of the remarkable characteristics is that the trajectory always visits the same external cavity modes and the laser shows regular pulses.

Increasing the length of the external cavity, the transition from regular pulse package dynamics to LFF dynamics occurs roughly at $\nu_R \geq \nu_{ex}$ (ν_{ex} being external cavity frequency); the short time scale dynamics become irregular and are dominated by relaxation oscillations. We find remarkable common features in the dynamics of regular pulse package and LFF. In both cases, low-frequency phenomena are present, which correspond to a directed global trajectory along several attractor ruins, resulting in fast intensity pulsations underlying the low-frequency envelope. In the LFF, the trajectory usually backtracks irregularly, and visits different attractor ruins, whereas the trajectory in regular pulse package evolves in a regular way within a well-defined looped channel always along the same series of attractor ruins. Considering the complicated phase space structure of a delay system, this is remarkable and indicates a global orbit underlying to the regular pulse package dynamics. For certain parameter sets, regular states have also been

Table 5.2 Classification of semiconductor laser with moderate optical feedback: short cavity regime versus long cavity regime

	Short cavity	Long cavity
Waveform	Regular pulse package	Low-frequency fluctuation
Frequency relation	$\nu_{ex} > \nu_R$	$\nu_{ex} < \nu_R$
Number of modes in phase space	Small (~ 10)	Large (~ 100)
Phase sensitivity	Qualitative changes	Little qualitative changes
Dynamics on short time scales	Regular fast pulses ($\nu = \nu_{ex}$)	Irregular fast pulses ($\nu_{ave} \approx \nu_R$)

observed in the long cavity regime. However, in the long cavity regime, the fast time scales are dominated by relaxation oscillations, whereas the fast time scales in the short cavity regime are dominated by the external cavity roundtrip frequency. The merging of attractor ruins to a global orbit appears to be a basic phenomenon series expansion of the delay terms in the optical feedback model.

The LFF envelope frequency in the short cavity limit has the dependence of the bias injection current (Heil et al. 2003a). The LFF frequency has a linear relation to the bias injection current and the frequency increases with the increase of the bias injection current. In addition, the linear dependence is independent of the cavity length. The trends are similar to the case of LFFs in long external cavity regimes. The linear relation is remarkable, in spite of the fact that the solitary relaxation oscillation frequency shows a square root scaling with $\nu_R \propto \sqrt{J - J_{th}}$. The relation is also well reproduced by numerical simulations using the rate equations with short cavity external optical feedback. Thus, the regular pulse package envelope frequency cannot be simply associated with the relaxation oscillation frequency. In addition, the frequency is significantly smaller than the relaxation oscillation frequency. The linear scaling and the slow time scales of the regular pulse package envelope frequency already indicate that not the solitary laser characteristics, but rather the structure of the phase space and the corresponding unstable manifolds govern the dynamics of the pulse package. The main differences between long and short cavity limits are summarized in Table 5.2.

5.4.3 Bifurcations of Regular Pulse Package

Regular pulse package in a short cavity is induced by the wandering among the external modes and anti-modes, which is quite similar to the occurrence of LFFs in a long external cavity. In both cases, low frequency phenomena are present connected with a global trajectory along several attractor ruins, and producing pulses when visiting each of them. The transition from regular pulse package to LFF occurs when the delay becomes larger than the relaxation oscillation period. What makes regular

pulse package distinct from LFF is the sensitivity to phase of the back-reflected light. Tabaka et al. (2004) investigated the dynamics and bifurcation scenarios of regular pulse packages in the short external regimes. With increased feedback strength in the short optical feedback regime, regular pulse package may undergo a period-doubling bifurcation cascade. On the bifurcation cascade, they found chaotic coexistent states with a time-periodic solution that originates from a newly born external cavity mode. The external cavity modes exhibit supercritical Hopf bifurcations. From these supercritical Hopf bifurcations emerge branches of time-periodic solutions. They found that the largest region of regular pulse package occurs for delays around half of the relaxation oscillation period of the solitary laser.

Figure 5.30 shows the plot of the point representing the detected regular pulse package dynamics, including regular pulse package of higher order periods (up to period of 10), to obtain representative picture of the regions of the regular pulse package dynamics (Tabaka et al. 2004). The map reveals that regular pulse package dynamics appears for intermediate levels of feedback strength and at delays smaller than the relaxation oscillation period $\tau_R/\tau_{ph} = 170$ (where τ_R is the laser relaxation-oscillation time). This is in agreement with previous observations by Heil et al. (2001), in which they suggest that regular pulse package disappears when the delay approaches the relaxation oscillation period and, then, the transition to LFF takes place. Moreover, in Fig. 5.30, one finds that the largest region of regular pulse package is for delays around half of the relaxation oscillation period. For smaller delays, small windows of regular pulse package are very well identified in Fig. 5.30. For changing phase of the back-reflected light, the structure of this part of the map may be significantly altered. When the phase changes by $\pm\pi$ the windows of regular pulse package shift in such a way that they fit the space in the map, where regular pulse package was not previously present. This phase sensitivity is illustrated in the inset of Fig. 5.30, where the regions of regular pulse package are plotted for two different phase conditions that differ by π. We observe that changing the phase shifts the regions of regular pulse package up and down such that regular

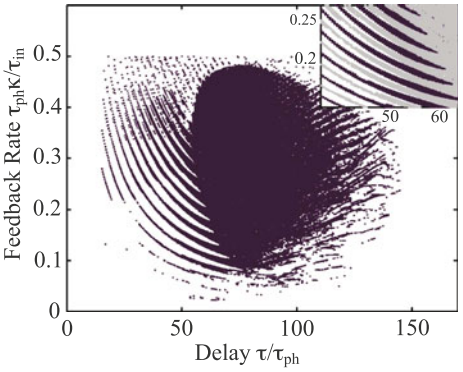

Fig. 5.30 Map of the regular pulse package dynamics in the space of the feedback rate and the delay. The parameters are $J = 1.155J_{th}$, $\alpha = 5$, and $\omega_0\tau = \tan^{-1}\alpha + \pi$. The inset illustrates the phase dependency of regular pulse package: in *black* the map is plotted for $\omega_0\tau = \tan^{-1}\alpha$ and in *gray* $\omega_0\tau = \tan^{-1}\alpha + \pi$ [after Tabaka et al. (2004); © 2004 APS]

pulse package may be found in that interval in the space of the feedback rate and the delay, only if the proper phase condition is chosen. However, from the map we see that it is only true for small delays. For delay times larger than half the relaxation oscillation period the occurrence of regular pulse package dynamics becomes phase insensitive.

5.5 Dynamics in Semiconductor Lasers with Grating Mirror Feedback

The theoretical background of grating feedback in semiconductor lasers has already been discussed in Sect. 4.3. Grating feedback is frequently used to select a certain mode among the possible oscillation lines and to stabilize the oscillation of a semiconductor laser. However, even in a semiconductor laser with grating feedback, instabilities are also observed for a certain range of the feedback level and experimental configurations, since the feedback is the introduction of an additional degree of freedom. The general purpose of grating mirror feedback is the stabilization of semiconductor lasers and a few studies have reported on instability and chaos in semiconductor lasers with grating feedback (Zorabedian et al. 1987; Binder et al. 1990; Detoma et al. 2005). These are the results for conventional feedback from plain grating mirrors. While the effects of grating optical feedback from fiber Bragg grating and volume holographic grating were reported (Naumenko et al. 2003; Ewald et al. 2005), in which similar dynamic behaviors as those of plain grating mirror were observed. Here, we focus only on the origin of instability in semiconductor lasers induced by grating optical feedback. In ordinary grating feedback to stabilize laser oscillation, the feedback fraction is not so small and (4.36) may not be appropriate to describe such a system, since we must take into account multiple reflections between the external grating mirror and the front laser facet. For such a model, the complex fields for the forward and backward propagations as a multiple reflection must be used and the matrix transformation technique taking into account the grating mirror reflection is applied (Pittoni et al. 2001). The method is also effective for the treatment of optical feedback from distributed fiber grating into a semiconductor laser. However, we currently have few tools for analyzing exactly the dynamic properties of grating feedback and we require further formulation for grating feedback in semiconductor lasers. Here, we discuss instabilities in semiconductor lasers with grating feedback by introducing a steady-state analysis.

The relation of the output power versus the detuning between laser and grating mirror frequencies is numerically calculated from (4.36) together with (4.37). Figure 5.31 shows the results (Binder et al. 1990). When the reflectivity of a grating mirror is small, the laser output power shows a continuous variation with small amplitude, since the gain for the laser oscillation smoothly changes. In the figure of the curve P_L, ω_G is the angular frequency of the maximum reflection of the grating mirror given by (4.48). The period of oscillatory power change along the detuning

is related to the wavelength of the laser, the maximum grating frequency, and the external cavity length. In the calculation, the feedback to the active layer is very small, since the internal reflectivity of the laser facet is set to be 2% and the fraction of grating feedback is as small as 3%. However, the laser output power shows hysteresis, as shown in the curve PH when the grating feedback increases (the internal reflectivity of the laser facet and the reflectivity of the grating mirror are assumed to be 0.05 and 13%, respectively, in this calculation). The bistability of the laser output power may predict instability of the laser oscillations in grating optical feedback for the change of the parameters.

The lasing condition for the compound cavity of a semiconductor laser with a grating mirror is also obtained from (4.37). From the phase condition in (4.43) and the amplitude condition in (4.45), the gain and the phase of the laser oscillations in the presence of grating optical feedback are plotted as a function of the frequency detuning. The results are shown in Fig. 5.32 (Genty et al. 2000). The detuning of the grating center frequency is $\nu_G = \omega_G/2\pi$ and the solitary laser frequency $\nu_0 = \omega_0/2\pi$ is set to be $\nu_G - \nu_0 = 20$ GHz. Due to the presence of grating optical feedback, the gain (solid line) and the phase (dotted line) show undulations and the cross points between them are the conditions for possible laser oscillations. The oscillation modes are discretely distributed and each mode has a different gain. The symbol of an open triangle shows the grating mode, but the maximum gain mode, which is denoted by an open rectangle, is different from this mode. Such periodic and skewed gain modes will become the origin of instability in semiconductor lasers with grating optical feedback.

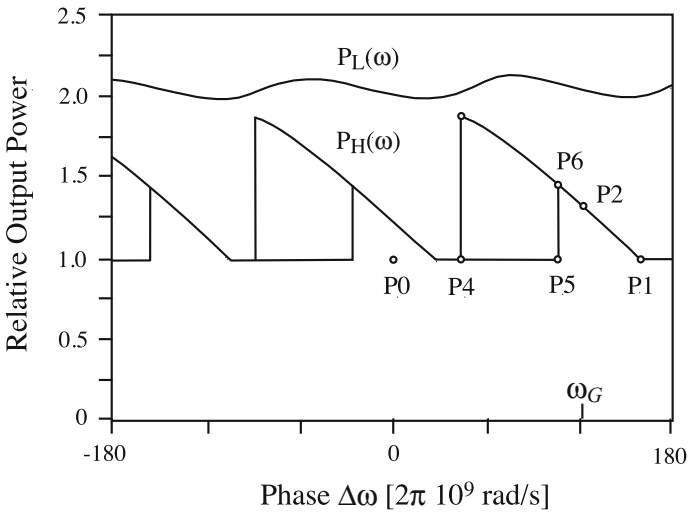

Fig. 5.31 Calculated output power versus tuning characteristics showing continuous tunability for low reflectivity laser (P_L) and hysteresis for high reflectivity laser (P_H) at an external cavity length of $L = 19$ cm and an optical wavelength of $\lambda = 1.3$ μm [after Binder et al. (1990); © 1990 IEEE]

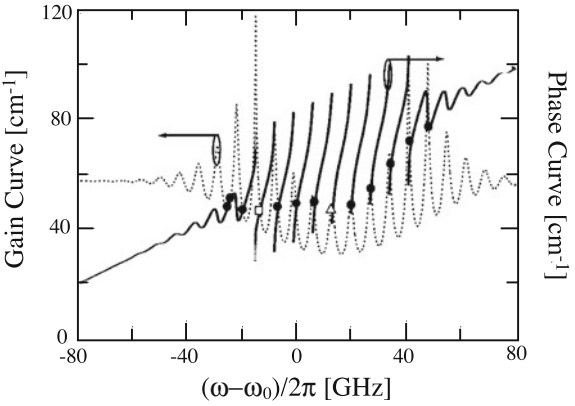

Fig. 5.32 Gain and phase curves as a function of the frequency detuning for $\nu_G - \nu_0 = 20$ GHz. The external cavity length is $L = 12$ cm. The reflectivities of the grating mirror and the internal cavity are $r = 0.25$ and $r_0 = 0.05$, respectively. *Solid line* gain, *dotted line* phase. The *symbols* are the possible oscillation modes [after Genty et al. (2000); © 2000 IEEE]

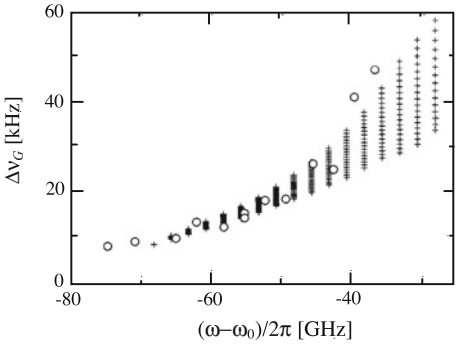

Fig. 5.33 Calculated linewidth (*crossed marks*) as a function of the frequency detuning for variations of the grating orientation. *Open circles* are the measured data. The condition is the same as in Fig. 5.32 [after Genty et al. (2000); © 2000 IEEE]

The linewidth of the laser oscillation in the presence of grating feedback is also calculated from (4.46). Figure 5.33 shows the linewidth for the frequency detuning at a steady-state oscillation under the same condition as in Fig. 5.32 (Genty et al. 2000). The original linewidth of the laser oscillation at the solitary mode is 20 MHz. Therefore, the linewidth of the laser oscillation is much narrowed and the laser is stabilized for negative detuning with a larger absolute value. Possible stable oscillation modes are discretely distributed along the detuning. Also, oscillation modes denoted by the vertical lines (crossed marks) are not continuous lines but discretely distributed. Further, the crossed marks are not on the vertical lines, but have even a negative slope. The theoretical calculation is well coincident with the measured data (open circles). The continuous tuning range for each group is about 20 MHz for the external cavity length of $L = 12$ cm. If the external cavity length is reduced to 1 cm, we can expand the fine tuning range and it becomes 2.5 GHz. When the feedback fraction increases, the effective detuning increases so as to compensate the increase of the photon number due to the optical feedback. As a result, the linewidth of the laser oscillation becomes narrow. For a wide tuning range of the spectral response, we were able to attain a wide tuning range by the

feedback for the wide spectral response of the grating, although the laser hops around among these oscillation modes and instability is enhanced by such hoppings. As a result, chaotic oscillation may be encountered in the dynamics.

5.6 Dynamics in Semiconductor Lasers with Phase-Conjugate Mirror Feedback

5.6.1 Linear Stability Analysis

A linear stability analysis is applied for semiconductor lasers with optical feedback from a phase-conjugate mirror. The procedure is the same as that in Sect. 4.2.1. For simplicity, we first assume a case of zero detuning $\delta = 0$. For small perturbations of δA, $\delta\phi$, and δn in (4.54)–(4.56), we obtain differential equations for the perturbations. Assuming the form of the solutions as $\delta x(t) = \delta x_0 \exp(\gamma t)$ ($x = A$, ϕ, n), the condition for non-trivial solutions of the equations is given by (Murakami et al. 1997)

$$D(\gamma) = \gamma^3 + \gamma^2\left(\frac{1}{\tau_R} + \frac{2\kappa}{\tau_{in}}\cos 2\phi_s\right) + \gamma\left\{\omega_R^2 + \frac{2\kappa}{\tau_R\tau_{in}} + K_1K_2\left(\frac{\kappa}{\tau_{in}}\right)^2\right\} + \left\{\frac{K_1K_2}{\tau_R}\left(\frac{\kappa}{\tau_{in}}\right)^2 + \omega_R^2\frac{K_2\kappa}{\tau_{in}}(\cos 2\phi_s - \alpha\sin 2\phi_s)\right\} = 0 \tag{5.24}$$

where $K_1 = 1 - \exp(-\gamma\tau)$, $K_2 = 1 + \exp(-\gamma\tau)$, $1/\tau_R = -2\Gamma_R$, and ϕ_s is the phase defined by (4.59). The other parameters are the same as those in (4.21). Setting $\gamma = i\omega$ the stability condition for phase-conjugate feedback is calculated from the above equation and given by

$$\omega^2 - \omega_R^2 = -\left(\frac{\omega}{\tau_R} + 2\omega\frac{\kappa}{\tau_{in}}\cos 2\phi_s\right)\tan\left(\frac{\omega\tau}{2}\right) \tag{5.25}$$

Here, we assume that the feedback is small and the relations of $\omega_R^2 \gg (\kappa/\tau_{in})^2$, $\kappa/\tau_{in}\tau_R$ hold.

For conventional optical feedback, $\omega^2 - \omega_R^2$ is proportional to $\cot(\omega\tau/2)$ (see (5.8)), while it is proportional to $\tan(\omega\tau/2)$ in phase-conjugate feedback. Periodic stability conditions with period $\tau = 2\pi/\omega_R$ are obtained both for conventional and phase-conjugate feedback. However, the positions of the external mirror at which the stability condition is satisfied are located alternately along the time axis of τ. Figure 5.34a is the calculated result from the rate equations for the boundary between stable fixed state and period-1 oscillation. The solid line shows the result for the phase-conjugate feedback, while the broken line is for the conventional feedback as already shown in Fig. 5.13a. Periodic stability enhancement is

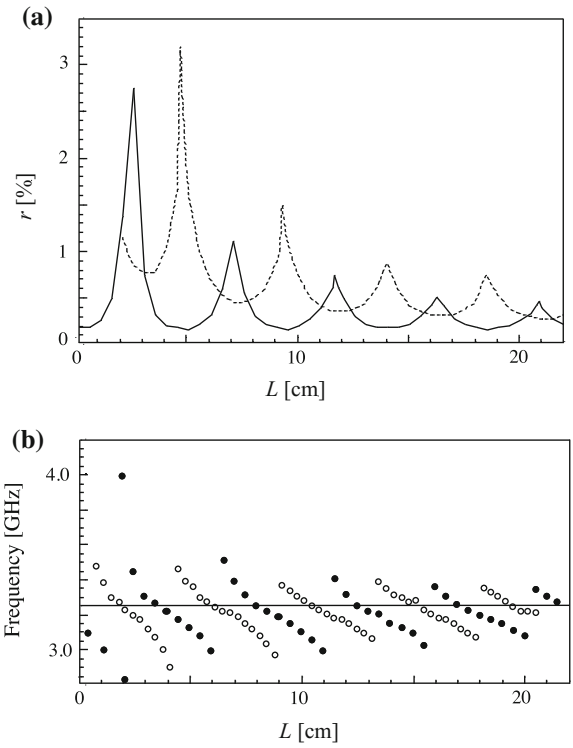

Fig. 5.34 **a** Boundary of fixed stable state at a bias injection current of $J = 1.3J_{th}$. The *solid line* corresponds to the case of phase-conjugate feedback, while the *dotted line* to optical feedback with a conventional plain mirror (corresponding to the stable fixed boundary in Fig. 5.13a). **b** Variations of excited resonance mode frequency. *Black circles* are for phase-conjugate feedback and *white ones* for conventional mirror feedback

observed with a period equal to the length corresponding to the relaxation oscillation frequency of the solitary laser, but stability peaks between the cases for phase-conjugate and conventional mirrors are located alternately with each other. Figure 5.34b shows the accompanying frequency at which the laser is destabilized, i.e., the frequency excited at the stability boundary. Closed circles are for phase-conjugate feedback and the open circles are for conventional optical feedback. The positions of jumps are periodic and the frequency jumps at the stability peaks. Also, the jump positions between the cases for phase-conjugate and conventional mirrors are located alternately with each other.

5.6.2 *Dynamics Induced by Phase-Conjugate Feedback*

In this section, we briefly remark on the dynamics induced by phase-conjugate feedback in the special case of zero detuning $\delta = 0$. Bifurcation diagrams were obtained for optical feedback from a phase-conjugate mirror (Murakami et al. 1997). When the reflectivity is small, the laser stays stable and it evolves into periodic oscillations for the increase of the reflectivity. However, clear period-doubling bifurcation is not visible and the laser soon evolves into

quasi-periodic and chaotic oscillations after stable fixed state. Furthermore, the laser shows less stable oscillations in the phase-conjugate feedback compared with conventional optical feedback. Namely, the laser is easily destabilized by phase-conjugate feedback.

The phase diagram of the chaotic evolutions was calculated and a similar diagram to Fig. 5.13a was obtained, though the positions of periodic stability peaks were different from those of conventional optical feedback. The differences of dynamics between the systems of conventional and phase-conjugate feedback are recognized from their mode distributions. As discussed in Fig. 4.5, the laser was first destabilized by the excitation of the relaxation oscillation modes for the increase of the external reflectivity. The remarkable difference is the distribution of the second modes, which are excited after the relaxation oscillation mode. For conventional optical feedback, the laser evolves into unstable oscillations by the excitation of this mode after period-1 oscillation. The mode corresponds to the fundamental oscillation of the external cavity mode and the frequency is approximately calculated as $\nu = c/2L$ (L being the external cavity length). The frequency of the second mode in the case of phase-conjugate feedback clearly differs from that of conventional optical feedback and the value of the real part of the solution is much higher than that of conventional optical feedback. Therefore, the laser is quickly destabilized by the increase of the phase-conjugate reflectivity (Murakami and Ohtsubo 1998).

The excited second mode frequency in conventional optical feedback is linearly proportional to the external mode frequency with a slope of unity. However, in the phase-conjugate case, the excited mode frequency is less than that for the conventional feedback and it shows a periodic undulation for the change of the external cavity length. The period is also equal to the relaxation oscillation frequency of the solitary laser (Murakami et al. 1997). Chaotic bifurcations also existed for the change of the bias injection current in the presence of phase-conjugate feedback (like in Figs. 5.10 and 5.11). The laser frequency is a function of the bias injection current and modes generated by phase-conjugate feedback are successively selected for the increase of the bias injection current. Then, the output power jumps at the positions of the mode jumps. Also, the positions of jumps in the L–I characteristic in phase-conjugate feedback occur alternately to those of conventional mirror feedback.

5.6.3 *Dynamics in the Presence of Frequency Detuning*

In the preceding section, we ignored the frequency detuning between the pump frequency of the four-wave mixing and the laser oscillation to calculate the dynamics of phase-conjugate feedback. For four-wave mixing phase-conjugate feedback having frequency detuning, different dynamics from a phase-conjugate mirror with degenerate four-wave mixing are observed. In the case of phase-conjugate optical feedback with zero detuning, the laser evolves from stable

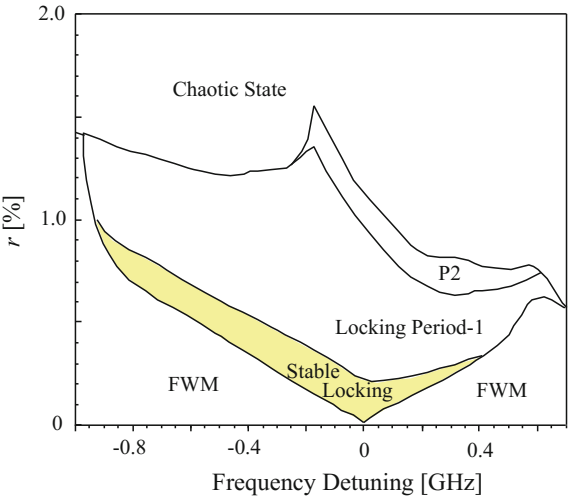

Fig. 5.35 Phase diagram for frequency locking with variation of the detuning in a phase-conjugate mirror. The injection current and the external cavity length are $J = 1.4J_{th}$ and $L = 5$ cm. *P2* Period-2 oscillation, *FWM* four wave mixing

state to chaotic oscillations through a period-doubling like bifurcation. However, different behaviors are observed for the dynamics of non-degenerate four-wave mixing (Murakami et al. 1997). Though it is not clear, we can observe period-1 oscillations with very small amplitude in a region of small phase-conjugate reflectivity. The frequency of the oscillations depends on the external reflectivity, but it is close to the frequency detuning of 2δ. In the presence of feedback from a non-degenerate four-wave mixing mirror, the laser first oscillates at the frequency of the four-wave mixing of $\omega_0 + 2\delta$. For the increase of the feedback reflectivity, the laser oscillation is locked to the pump frequency of $\omega_0 + \delta$ and, then, the laser evolves into chaotic oscillations with the same frequency as the pump. Figure 5.35 shows the phase diagram of the oscillation states in the phase space of the frequency detuning and the phase-conjugate reflectivity. The shaded area in the figure corresponds to stable oscillations with locking state to the laser frequency. Above the area, the region of chaotic bifurcations locked to the pump frequency exists. We did not consider the gain saturation effects in the calculations. When we take into consideration the gain saturation in the rate equations, the detailed dynamics are slightly different from those without the effects, but the fundamental dynamics are almost the same.

5.6.4 *Finite and Slow Response Phase-Conjugate Feedback*

Here, we consider a finite or slow response phase-conjugate feedback in semiconductor lasers. For a finite response of a phase-conjugate mirror, the equation for the complex field has already been given by (4.61). The important parameter of finite response phase-conjugate feedback is the penetration time t_m of light into the

phase-conjugate medium. Depending on this parameter, we observe remarkable shifts of peaks in the stability enhancement curve such as shown in Fig. 5.34. Figure 5.36 shows the stability diagram for the feedback rate $\gamma = \kappa/\tau_{in}$ and the delay time τ (unit of $2\pi/\omega_R$) at three different penetration times (van der Graaf et al. 2001). The parameter Λ in the figure is the same definition as the spectral linewidth defined in the filtered optical feedback in (4.74). For the instantaneous response ($t_m = 0$), the stability peak enhancements are compatible with those of Fig. 5.34, while the peaks shift for the increase of the penetration time. Comparing PCF from an instantaneous response mirror with that from a slow-response mirror, we see that the stability enhances slightly with increasing t_m. This is caused by the mirror induced spectral filtering of the reflected field, suppressing frequencies larger than $1/t_m$. Similar behavior was found in the case of conventional optical feedback (Yousefi and Lenstra 1999). More striking is the shifted location of the stability peaks, which, in view of the time delay in the mirror, resembles a situation of an external round-trip length larger than in an instantaneous-response mirror. The effective round-trip length enhancement is not sharply defined, which reduces the quality of the resonance for large t_m. Since the relative importance of this increases when τ gets smaller, this may explain why the peak at $\omega_R\tau/2\pi = 1/2$ is lower for 400 ps than for shorter response times.

When the response time of a phase-conjugate mirror is very large compared with chaotic variations of semiconductor lasers, the laser behaves completely different from a laser with fast-response phase-conjugate optical feedback. For slower time response of phase-conjugate mirrors, the time dependent features in the dynamics like phase locking phenomenon are lost. For example, the time response of a photorefractive phase conjugate medium, such as a photorefractive crystal of $BaTiO_3$ and $LiNbO_3$, and other photorefractive polymer materials, is very slow compared with time fluctuations of chaotic semiconductor lasers. Therefore, the grating formed in a photorefractive crystal can be considered as a static grating.

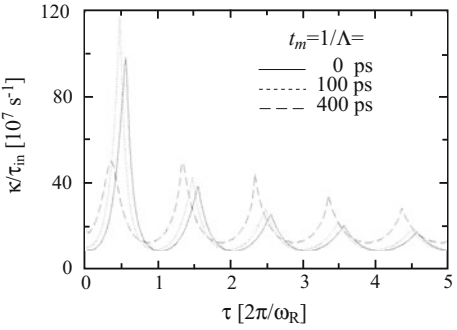

Fig. 5.36 Feedback rate at which the laser changes stability as a function of the cavity roundtrip time τ, normalized to the relaxation oscillation period. The laser is stable for low feedback and becomes unstable upon increasing κ/τ_{in}. In the simulations, the parameters are $\delta = 0$ and $J = 1.05J_{th}$ [after van der Graaf et al. (2001); © 2001 IEEE]

Once the grating is formed in a photorefractive mirror, the dynamics are only governed by the total feedback loop of the pump beam. This loop plays the role of an external cavity length. As a result, the dynamics are completely the same as those for a conventional mirror feedback except for the generation of a spatial phase-conjugate wave. The dynamics in such photorefractive phase-conjugate feedback are quite different from those for a fast-response phase-conjugate mirror. Indeed, the same results as those for conventional optical feedback have been experimentally obtained for a slow-response phase-conjugate mirror using a $BaTiO_3$ crystal (Murakami and Ohtsubo 1999). However, a photorefractive mirror with slow time response may be a good medium as a feedback reflector for positive use of optical feedback effects, since it functions as an automatical feedback reflector without any adjustment for optical components in the systems. The reflection fraction of the feedback beam can be easily controlled by changing the pump ratio for phase-conjugation.

5.7 Dynamics of Incoherent Optical Feedback

For incoherent optical feedback in semiconductor lasers, the dynamics can be described by only two rate equations for the photon number and the carrier density. The feedback effect is included in the field equation for coherent feedback, while it appears as a modulation to carrier density for the case of incoherent optical feedback. The nonlinearity of the system is much enhanced by the delay differential term in the carrier density equation induced by incoherent optical feedback. Thus, instability and chaos can be observed in such a system. The dynamics of semiconductor lasers with incoherent optical feedback is investigated by using the rate equations in (4.62) and (4.63). Instabilities of semiconductor lasers with incoherent feedback have been studied by Otsuka and Chern (1991) and Ishiyama (1999). They carried out numerical simulations for incoherent optical feedback in semiconductor lasers and found sustained pulsations in the laser output. Even without optical feedback in a semiconductor laser, damping oscillation due to relaxation oscillation arises in the laser output. When there is incoherent feedback in a semiconductor laser, the damping oscillation is memorized and then fed back to the laser. The carrier density is intensely modulated by the feedback light, since the feedback is to the carrier density and the laser produces modulated output. The returned light further modulates the carrier density. When the growth rate of pulsations by the positive feedback balances with the damping forces induced by the relaxation oscillation, the laser shows sustained pulsating oscillations.

Figure 5.37 is a numerical example of pulsating oscillations of the output power in a semiconductor laser with incoherent optical feedback (Otsuka and Chern 1991). Changing the bias injection current, the relaxation oscillation frequency increases and, as a result, both the pulsating frequency and the amplitude of pulses increase. In this simulation, the feedback strength and the feedback time are assumed to be $\kappa' = 0.4$ and $\tau = 0.1\tau_s$, respectively. Regular pulsing is not always

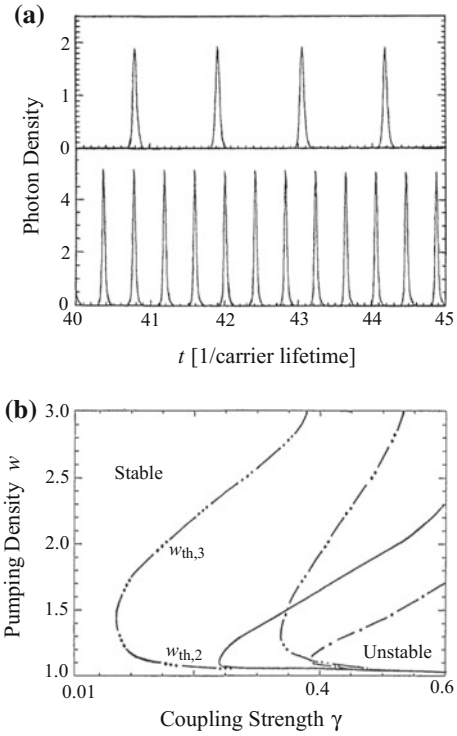

Fig. 5.37 Numerical example for sustained pulsating oscillations in a semiconductor laser with incoherent optical feedback. **a** $J = 1.1J_{th}$ and **b** $J = 1.5J_{th}$. The time axis is normalized by the carrier lifetime τ_s. **c** Stability boundaries for various conditions. *Solid curve* $g = \varepsilon_s \Gamma_T V = 10$ (ε_s, Γ_T, and V are the gain saturation coefficient, the confinement factor, and the volume of the active layer, respectively), $T = \tau/\tau_s = 0.1$, and $\beta = n_0/n_{th} = 0.375$. *Dashed-dotted curve* $g = 20$, $T = 0.1$, and $\beta = 0.375$. *Dashed-double-dotted curve* $g = 10$, $T = 0.05$, and $\beta = 0.375$. *Dashed-triple-dotted curve* $g = 0$, $T = 0.1$, and $\beta = 0$. The normalized pump is defined by $w = J/J_{th}$ and the feedback parameter is $\gamma = \kappa' V$ [after Otsuka and Chern (1991); © 1991 OSA]

observed for all the parameter ranges of the bias injection current and the coupling strength. The region of unstable and pulsating oscillations is calculated in the phase space of the bias injection current and the feedback strength. The phase diagram in Fig. 5.37b is obtained from the linear stability analysis for the rate equations. At a certain feedback strength, the laser shows stable oscillation close to the laser threshold. It evolves into period-1 oscillation (regular pulsing) at the threshold $w_{th,2}$. With the increase of the bias injection current, the pulsing frequency increases and the pulse amplitude grows. However, with further increase of the bias injection current, the damping rate of the relaxation oscillation decreases and the decay rate of the carrier density also decreases. This suppresses the sustained pulsation in the laser output. Above a certain bias injection current ($w_{th,3}$), the feedback-induced modulation is damped out within the delay time and finally the instability vanishes.

Since the occurrence of sustained pulsating oscillations is related to the relaxation oscillation, the bias injection current for the threshold $w_{th,3}$ at which the regular pulsing diminishes decreases with the increase of the delay time and the nonlinear gain.

Sustained pulsating oscillations in semiconductor lasers induced by incoherent optical feedback are used to generate a series of fast pulsing in optical communications. We can easily generate fast pulses shorter than nanosecond (as fast as picosecond) under the conditions for small nonlinear gain and also small confinement factor. In incoherent optical feedback, we have an advantage of designing the pulse sequence with an arbitrary pulsing frequency. Also, the pulse width can be designed by appropriately setting the parameter values. Chern et al. (1993) investigated the dynamics of class B lasers with incoherent optical feedback including semiconductor lasers. They showed the coexistence of two attractors under the same parameter conditions for pulsating oscillations induced by the Q switching effect and sustained relaxation oscillations. They demonstrated that either oscillation occurs depending on the initial condition of the laser oscillation.

Several researches have been conducted into the experimental studies of incoherent optical feedback in semiconductor lasers (Cohen et al. 1990; Yen et al. 1998; Cheng et al. 2003). Figure 5.38a shows examples of experimentally obtained

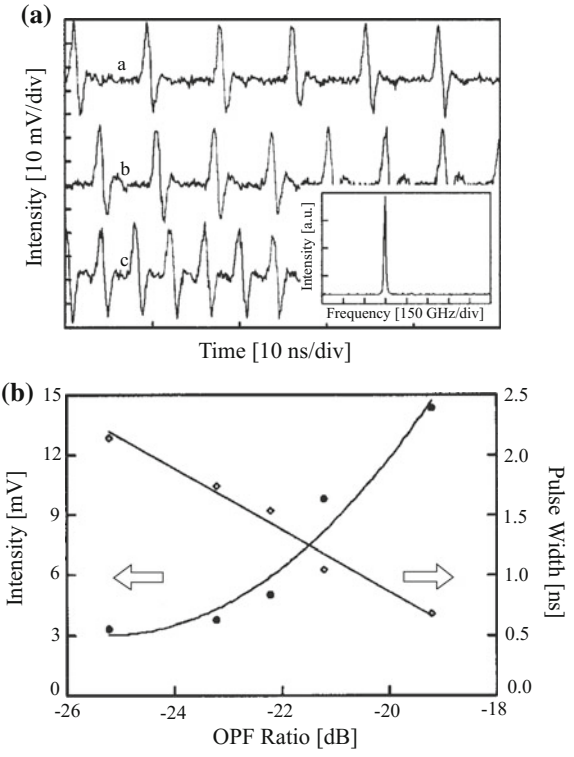

Fig. 5.38 **a** Experimentally obtained sustained pulsating oscillations in semiconductor lasers with incoherent feedback for different external cavity lengths. The external cavity lengths are L = 133.3, 100 and 60 cm from *top* to *bottom*. The optical feedback ratio is −19.2 dB. *Inset* is the optical spectrum obtained by a Fabry-Perot spectrometer. **b** Dependence of pulse width and pulse intensity on the optical feedback ratio at a bias injection current of $J = 1.25J_{th}$ and an external cavity length of L = 75 cm [after Cheng et al. (2003); © 2003 Elsevier]

pulsating oscillations at the bias injection current of $J = 1.3J_{th}$ (Cheng et al. 2003). With the increase of the external cavity length, the frequency of pulses decreases. However, the feedback strength is weak and the pulsing frequency is only about 250 MHz. To obtain pulses with a much higher repetition rate as fast as nanosecond, a stronger feedback ratio is required. The laser used is the single mode near-infrared semiconductor laser of the Fabry-Perot type. The laser oscillates at a single mode as shown in the inset of the figure even when it shows pulsing oscillations. Figure 5.38b also presents experimentally obtained relations between the pulse width and the pulse intensity for the optical feedback ratio. As a general trend, for the increase of the feedback level, the pulse width decreases and the pulse height increases.

5.8 Dynamics of Polarization-Rotated Optical Feedback

5.8.1 TE–TM Mode Dynamics in Polarization-Rotated Optical Feedback

In Sect. 4.6, we formulated the scheme for polarization-rotated optical feedback. Here, we discuss some dynamic properties of polarization-rotated optical feedback in semiconductor lasers. The dynamics of polarization-rotated optical feedback are quite different from those of ordinary optical feedback discussed in the previous sections. Figure 5.39 shows an example of L–I characteristics calculated from the rate equations of polarization-rotated feedback in (4.64)–(4.68) (Heil et al. 2003b). The intensities with optical feedback contain instabilities for the time development, but the plotted L–I characteristics are averaged intensities. As was already discussed, one of the typical features of parallel-polarization optical feedback is the threshold reduction of the injection current for the laser oscillation. However, there is no threshold reduction in the case of polarization-rotated feedback, and the laser oscillation starts at the same bias injection current as the solitary laser. Furthermore, the slope efficiency remains the same as that of the solitary laser. The level of polarization-rotated feedback required to induce instability in the laser output is much higher than that for the case of ordinary optical feedback, as shown in the following discussion, and the level is usually 10 times higher than that in ordinary optical feedback (in amplitude). Another typical feature in ordinary optical feedback is the increase of the laser output power due to the coherent optical injection. On the other hand, the laser output power of polarization-rotated feedback shows little change compared with the solitary case in spite of such large optical feedback. Namely, the laser oscillation is divided into the TE and TM modes, while the total power remains unchanged. It is noted that the temporal waveform of the TM mode is delayed with respect to that of the TE mode by the propagation time τ of the external feedback loop, showing that the TM mode is following the delayed feedback signal. Namely, the TM mode is just a copy of the TE mode with the delay time τ. These results mean that the interaction between the TE- and TM-mode intensities through the carrier density generates chaotic intensities and the dynamics of both the amplitude and phase are governed by the dynamics of the carrier density.

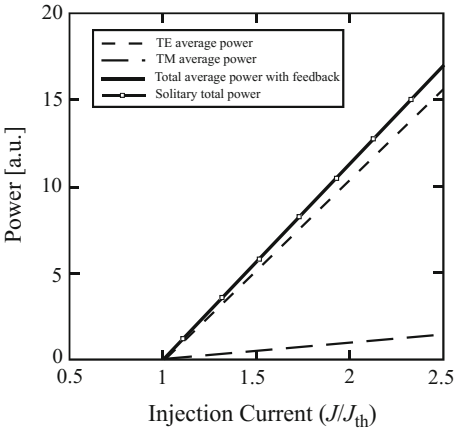

Fig. 5.39 Numerical result of L–I characteristics. *Black thick line* Total output of a laser with TM-mode feedback, *solid line with squares* solitary laser output, *dotted line* TE-component output of the laser with polarization-rotated feedback, *dashed line* TM-component output of the laser with polarization-rotated feedback. The optical feedback ratio is $\kappa/\tau_{in} = 7 \times 10^{10}$ s^{-1} [after Heil et al. (2003b); © 2003 APS]

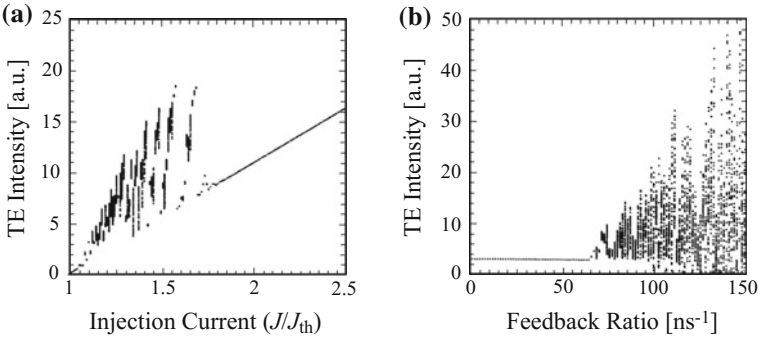

Fig. 5.40 **a** Bifurcation diagram of the intensity dynamics as a function of the injection current. The optical feedback ratio is $\kappa/\tau_{in} = 7 \times 10^{10}$ s^{-1}. **b** Bifurcation diagram of the intensity dynamics as a function of feedback power ratio. The bias injection current is $J = 1.4J_{th}$ [after Heil et al. (2003b); © 2003 APS]

To induce instability in polarization-rotated optical feedback, one requires a strong optical feedback; however, the fully developed chaotic state, as is observed in ordinary optical feedback, is scarcely seen. In most cases, the instability observed in polarization-rotated feedback is quasi-periodic oscillation or week chaotic state. Figure 5.40 shows bifurcation diagrams of chaotic evolutions for the parameters (Heil et al. 2003b). Figure 5.40a is the bifurcation diagram of the TE laser output for the bias injection current at a fixed feedback ratio of $\kappa/\tau_{in} = 7 \times 10^{10}$ s^{-1}. From the figure, when the injection current is increased, one recognizes that the value of the steady-state solution of the carrier density is increased and the laser tends to be

less sensitive to the feedback light. Finally, the laser reached stable oscillation state even in the presence of orthogonal-polarization feedback. In ordinary optical feedback, the laser tends to less unstable for the increase of the bias injection current, but instabilities of the laser persist and never disappear. This is the big difference between polarization-parallel and polarization-rotated optical feedback. Another difference of polarization-rotated feedback is that the positions of the spectral peaks associated the round-trip frequency do not shift with the increase of the bias injection current. This is in contrast to the dynamics of coherent parallel-polarization feedback, where a significant shift and broadening of these peaks occurs for increasing bias injection current. Figure 5.40b shows the bifurcation diagram of TE laser output for the feedback ratio (κ/τ_{in}) at a fixed bias injection current of $J = 1.4J_{th}$. The feedback ratio at which onset of chaos starts is much higher than one order or more for the case of parallel-polarization feedback. The theoretical results discussed here are supported by the experimental results (Heil et al. 2003b).

Above discussions are limiting cases for strong polarization-rotated optical feedback and also with negligible frequency detuning between the two polarization modes. In these cases, the TM mode shows in-phase synchronous oscillations with TE mode having a propagation delay in the optical feedback loop. Therefore, the synchronization in this scheme is originated from optical injection form TE mode to TM mode. However, in general, there exists a frequency difference between TE and TM modes, although it is not large. The existence of the frequency detuning plays an important role in the dynamics of TE–TM mode coupled semiconductor lasers. Indeed, Takeuchi et al. (2008, 2010) experimentally studied TE–TM dynamics for semiconductor lasers with polarization-rotated optical feedback, in which there was a non-zero frequency detuning between the two polarization modes of −870 MHz. They used a moderate optical feedback coefficient of 1.6×10^{10} s^{-1} and observed different dynamics from those in strong polarization-rotated optical feedback. In their results, anti-phase synchronous oscillations between the TE and TM modes were observed and the time delay of the synchronization between the two modes was always zero for the lower rf frequency component than the relaxation oscillation, which corresponds to the central chaotic oscillation frequency. For the moderate polarization-rotated optical feedback, the phenomenon may be considered not as the injection-locking effect from the TE to TM mode, but as the effect of competition between the oscillations of the TE and TM modes, which differs from previous results for in-phase oscillations. This anti-phase dynamics is a typical feature for non-zero frequency detuning. On the other hand, the in-phase dynamics with a loop delay in the polarization-rotated optical feedback system have been explained by optical injection locking.

By the numerical simulations based on the rate equations, it is shown that anti-phase oscillations with zero time lag switch to in-phase oscillations with time lag of the optical feedback loop for the increase of the feedback strength even in the existence of the frequency detuning. The dynamics of TE–TM coupling in polarization-rotated optical feedback strongly depend on the gain difference between the TE and TM modes. The optical gain is determined by the laser

materials, structures, and operating conditions. The gain of the TM mode is usually less than that of TE mode and the dynamics discussed here can be observed for lasers within the gain difference of 10–30%. In actual, a gain of TM mode of about 20% less than that of TE mode was used in the numerical simulations for the dynamics of semiconductor lasers with polarization-rotated optical feedback (Shibasaki et al. 2006; Takeuchi et al. 2010). Smaller the gain difference, stronger the coupling between two polarization mode, and we observe rich TE–TM dynamics. On the other hand, the excitation of TM mode by TE-mode optical injection becomes small and the effects look like as those for incoherent optical feedback. TE–TM mode dynamics are also applied to chaos synchronization and chaotic communications. We again return to this subject in Chaps. 12 and 13.

5.8.2 *Square-Wave Generation in Polarization-Rotated Optical Feedback*

Periodic pulsating oscillations are observed in semiconductor lasers with incoherent optical feedback as discussed in Sect. 5.7. Also, periodic square-wave oscillations are observable in semiconductor lasers with polarization-rotated coherent optical feedback (Gavrielides et al. 2006, 2010). In this subsection, we treat a case of narrow-stripe edge-emitting semiconductor lasers; however, similar square-wave oscillations are also generated in vertical-cavity surface-emitting semiconductor lasers (VCSELs) with polarization-rotated optical feedback as discussed in Sect. 8.3.7. In VCSELs, the gain difference between the two orthogonal polarization modes is very small, while the gain difference of orthogonal modes in edge-emitting semiconductor lasers is fairly larger than that of VCSELs. In addition to the gain difference, the active region of edge-emitting semiconductor laser has a thin guided structure, so that TE mode is a common lasing mode and the orthogonal TM mode is not usually an oscillation mode. However, TM mode is excited and it shows periodic or chaotic oscillations when a strong optical injection induced by polarization-rotated optical feedback exists in edge-emitting semiconductor laser. At the same time, the TE mode also shows periodic or chaotic oscillations in accordance with the TM mode. In usual, the two orthogonal modes synchronously oscillate with each other and they show anti-phase oscillations.

Figure 5.41 is an experimental example of square waves in narrow-stripe edge-emitting semiconductor lasers with polarization-rotated optical feedback at a strong feedback ratio of 37.6% in intensity. It is noted that we can ignore multiple reflection from an external mirror due to an optical configuration employed in Sect. 4.6, although the feedback is strong. Among narrow-stripe edge-emitting semiconductor lasers, square-wave oscillations induced by polarization-rotated optical feedback are typically generated when the gain difference between TE and TM modes is small and the loss difference between the two polarization modes is small enough. In this figure, the frequency of square waves is 5.85 ns, which is

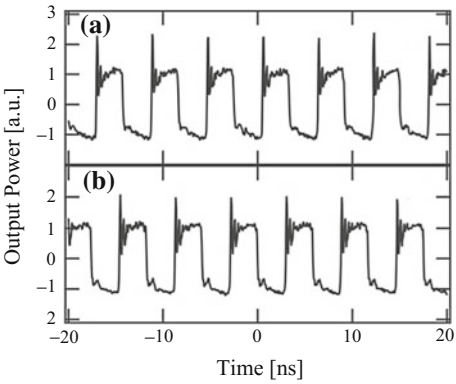

Fig. 5.41 Experimentally observed square-wave modulated oscillations induced by polarization rotated optical feedback. **a** TE-mode oscillation and **b** TM-mode oscillation. The external round-trip time of light is 2.60 ns and the optical feedback ratio is 37.6% in intensity [after Gavrielides et al. (2006); © 2006 OSA]

slightly larger than twice of the round-trip time of light of $\tau = 2.60$ ns in the external loop. It is also noted that the two waveforms show anti-phase oscillations. Similar results of 2τ periodic and anti-phase square-wave oscillations are found for the case of polarization-rotated optical feedback in VCSELs.

In VCSELs, square-wave oscillations due to orthogonal polarization optical feedback are easily observed since the gain difference between the two modes is small as is already discussed. On the other hand, ordinary narrow-stripe edge-emitting semiconductor laser has a larger gain difference and the orthogonal polarization mode only becomes a lasing mode for fairly strong polarization-rotated optical feedback. Gavrielides et al. (2006, 2010) theoretically and experimentally studied chaotic routes and examined the condition for square-wave oscillations. According to their analysis, TM mode is chaotically excited at a feedback level about ten times larger than that for the case of parallel optical feedback. After the excitation of ordinary fast chaotic irregular oscillations, square-wave oscillations are generated for a fairly strong optical feedback. They examined the condition of square-wave generation for a steady-state analysis for the plateaus of periodic square pulses. The condition of the loss difference a_d between the TE and TM modes for square-wave generation is given by

$$a_d \leq \frac{2\kappa}{\tau_{\text{in}}\sqrt{1+\alpha^2}} \tag{5.26}$$

Namely, square-wave oscillations tend to occur at large enough optical feedback coefficient κ and small loss difference a_d. Indeed, the observed square-wave in Fig. 5.41 satisfied this condition. In their numerical simulations of square-wave generations, the conditions of the gain ratio of $G_{n,\text{TM}}/G_{n,\text{TE}} \approx 0.3$, the external optical feedback of $r = 0.2 \sim 0.3$, and the gain loss of $a_d \approx 1/(20\tau_{\text{ph}})$ are used and square-wave oscillations are successfully reproduced. The chaotic routes to square-wave oscillations are not unique and show complex routes. Multiple coexistent states exist even under the same operation condition in the laser oscillations, including complex waveforms with 2τ periodicity.

Coupling of two crossed polarization modes and the following instabilities are typical features in VSCELs, which are discussed in Chap. 8. As mentioned before, the gain difference between two crossed polarization modes in VCSELs is very small compared to common narrow-stripe edge-emitting semiconductor lasers. Therefore, the laser is easily destabilized by parallel- or crossed-polarization optical feedback even when the laser is oscillated at a single polarization mode without external optical feedback. Due to this fact, square-wave oscillations in VCSELs are frequently and easily observed by crossed-polarization optical feedback. The quality of square-wave is strongly related to the dichroism, which is one of the important device parameter of VCSELs, and good square-waves are obtained at rather small bias injection current (Torre et al. 2011; Sukow et al. 2012; Marconi et al. 2013). However, the interaction between the two crossed polarization modes are too strong and the quality of square-wave is not so good compared to that in narrow-stripe edge-emitting semiconductor lasers.

5.9 Dynamics of Filtered Optical Feedback

5.9.1 Filtered Optical Feedback

In this section, as an example of filtered optical feedback, we describe the dynamics of coherent optical feedback from a Fabry-Perot resonator. Filtered optical feedback has become a topic of interest, since it offers the potential to control the laser dynamics through the spectral width of the filter and the detuning from the original laser oscillation frequency. The dynamics of filtered optical feedback from a Fabry-Perot resonator have been extensively investigated in relation to the filter width compared with the relaxation oscillation frequency and external cavity frequency (Fischer et al. 2000, 2004a, b; Yousefi and Lenstra 2003; Erzgräber et al. 2006). The treatments of the filtered feedback from a Fabry-Perot resonator can be applied to other case of coherent optical feedback filter, such as grating optical feedback (Yousefi and Lenstra 1999). For example, using feedback from a diffraction grating is a common method for obtaining single-mode operation of a semiconductor laser. In such cases, a specific spectral component of the diffracted light is fed back to the laser, and this forms a good example of filtered optical feedback. The use of a Michelson interferometer is another example of a filtered optical feedback to control the behaviors of low-frequency fluctuations (LFFs) in a semiconductor laser subject to optical feedback (Rogister et al. 1999). In other applications, an alkali vapor or a filter is placed within the external cavity laser system to frequency stabilize the laser. In such configurations, the laser frequency is locked to one of the transition lines of for example, rubidium or barium, or to a resonance of a Fabry-Perot interferometer (Anderson et al. 1999). All of these systems are equivalent to a semiconductor laser with an external cavity containing a frequency-selective filter.

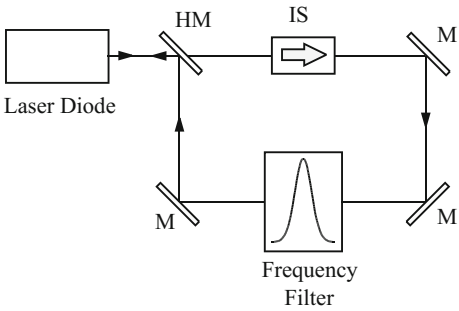

Fig. 5.42 Schematic diagram of unidirectional ring configuration for a filtered optical feedback setup. *HM* Half mirror, *IS* isolator, *M* mirror

The typical feature of filtered coherent optical feedback is frequency oscillations in which the laser intensity is almost constant in spite of the periodic laser frequency oscillations. The complex dynamics behavior in the lasers is rooted in the undamping of the intrinsic relaxations, the relatively large self-phase modulation property of semiconductor lasers, and the feedback delay. The self-modulation property manifests itself as a coupling between amplitude and phase of the laser field and originates from the existence of the non-zero α parameter. The filter can be viewed as a mechanism for restricting the phase space. By the introduction of the filter, the number of external cavity modes decreases and also the modes are also moved around in the phase space. Here, we focus on the effects of coherent optical feedback from frequency filter, and those for filtered optoelectronic feedback will be presented in Chap. 7. Figure 5.42 shows a schematic setup of filtered optical feedback in semiconductor lasers. In wide variety of applications for laser control, an optical feedback from a Fabry-Perot resonator to a semiconductor laser is used instead of a conventional reflector. Usually, we must consider multiple reflections from the filter and (4.73) is replaced by the reflectance for multiple loops for the filter feedback (Yousefi and Lenstra 1999). In the figure, we consider only a system of a single unidirectional ring loop for simplicity and the optical feedback through a single-path Fabry-Perot resonator. With a good approximation, the optical feedback from the Fabry-Perot filter is given by the following Lorentzian shape:

$$R(\omega) = \frac{\Lambda}{\Lambda + i(\omega - \omega_c)} \tag{5.27}$$

where Λ is the full-width at half-maximum (FWHM) of the spectral transmission through the Pabry-Perot filter and ω_c is its center frequency relative to the solitary laser frequency. Consequently, we can assume the relation of (4.73) as the time response function. In the following, we present several dynamics for filtered optical feedback from Fabry-Perot resonator in semiconductor lasers.

5.9.2 External Cavity Modes

In this section, we find the relation of the actual laser oscillations with the solitary oscillation frequency. The first step is to investigate the steady-state regime of the filter external optical feedback system by means of the fixed point analysis for the rate equations including the filtered optical feedback effect described by (4.70), (4.72), and (4.74), i.e., the linear stability analysis, which is the same procedure in Sect. 4.2. We assume the following forms for the steady-state solutions for the optical field, the filter, and the carrier density:

$$E(t) = \sqrt{P_s}\exp(-i\Delta\omega_s t) \tag{5.28}$$

$$F(t) = \sqrt{P_{Fs}}\exp\{-i(\Delta\omega_s t + \theta_s)\} \tag{5.29}$$

$$n(t) = n_s \tag{5.30}$$

where $\Delta\omega_s = \omega_s - \omega_0$ (ω_s and ω_0 being the steady-state and solitary laser oscillation frequency, respectively) and P_s, P_{Fs}, and n_s are the steady-state values for the optical power, the filter transmission optical power, and the carrier density, respectively. Substituting (5.28)–(5.30) into the rate equations, the transcendental equation in $\Delta\omega_s$ can be derived as

$$\Delta\omega_s\tau = -h(\Delta\omega_s)C\sin\left(\Delta\omega_s\tau + \omega_0\tau + \tan^{-1}\alpha - \tan^{-1}\frac{\Delta\omega_s - \omega_c}{\Lambda}\right) \tag{5.31}$$

with

$$h(\Delta\omega_s) = \frac{\Lambda}{\sqrt{\Lambda^2 + (\Delta\omega_s - \omega_c)^2}} \tag{5.32}$$

where ω_c is the relative detuning between the center frequency of the filter and the solitary laser frequency. The C parameter in (5.31) is the measure of the fraction of feedback and has already been defined by (4.13). The constant phase θ_s is also obtained from the linear stability analysis and given by

$$\theta_s = -\omega_0\tau - \tan^{-1}\frac{\Delta\omega_s - \omega_c}{\Lambda} \tag{5.33}$$

For the infinite filter bandwith ($\Lambda \to \infty$), (5.31) reduces to (4.14) of the case of conventional optical feedback. Since $h(\Delta\omega_s)$ in (5.31) is smaller than unity, the relation $h(\Delta\omega_s)C < C = \kappa\tau/\tau_{\text{in}}\sqrt{1+\alpha^2}$ always holds. Therefore, a comparison with conventional optical feedback shows that the number of fixed points for filtered optical feedback is always smaller than for conventional optical feedback.

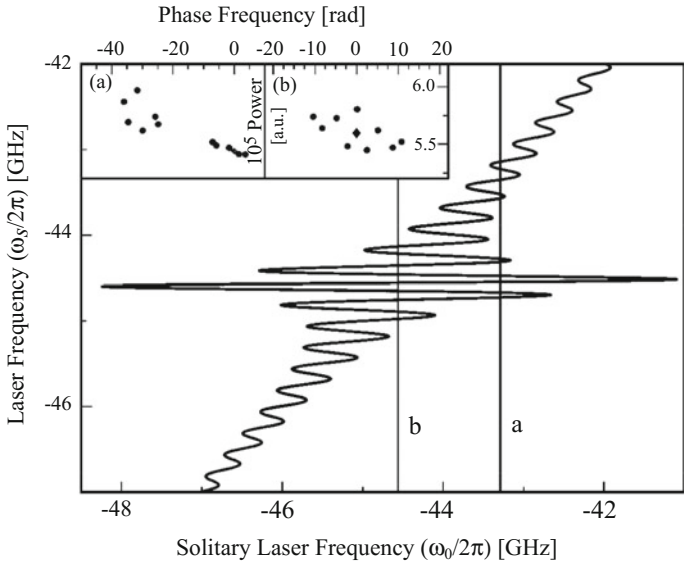

Fig. 5.43 Fixed-point solutions to the phase relation (5.31) in (ω_s, ω_0) plane at $C = 51$ and $\Lambda = 2$ GHz. The *insets* show the fixed points in the ($\phi(t) - \phi(t - \tau)$, P) plane for the two cases **a** and **b** as indicated in the main frame. In **a**, the detuning is large enough to split the fixed-point body into two separate islands, creating a potentially globally bistable situation. In **b**, the filter profile is seen to be superimposed on the standard fixed-point ellipse of conventional optical feedback. The *diamond* in **b** is the solitary mode [after Yousefi and Lenstra (2003); © 2003 AIP]

Figure 5.43 is an example of the fixed point frequencies calculated from (5.31) (Yousefi and Lenstra 1999). In the case of frequency optical feedback, the snake-like contour in Fig. 5.43 is modulated by the filter profile. This is due to the envelope $h(\Delta\omega_s)$ in (5.31) modulating the sine function. This means that, for a given ω_0, the number of external cavity modes is strongly dependent on the detuning of ω_0 with respect to ω_c. For the frequency ω_0 far away from the central frequency ω_c of the filter, $h(\Delta\omega_s)$ will be almost zero, and there will only be a few solutions, while several modes are available for $\omega_0 \approx \omega_c$. Another difference from conventional optical feedback is the phase shift introduced by $C = \kappa\tau/\tau_{\text{in}}\sqrt{1+\alpha^2}$. This term does not exist in the case of conventional optical feedback and it is a consequence of the causality principle (Kramers–Kronig relations) applied to the Lorentzian filter. Figure 5.43 is the case of moderate feedback of intermediate filter where the relation $\nu_{\text{ex}} < \Delta\nu_f < \nu_{\text{R}}$ holds (ν_{ex}, $\Delta\nu_f$, and ν_{R} being the frequencies of the external cavity, the filter bandwidth, and the relaxation oscillation).

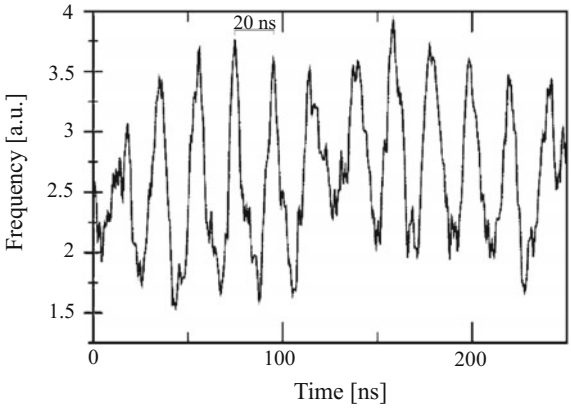

Fig. 5.44 Experimentally observed time series showing oscillations in the frequency of a laser when subject to filtered optical feedback. The period of the oscillations corresponds to an external delay of 6 m (∼20 ns). The HWHM bandwidth of the filter is 700 MHz [after Fischer et al. (2004a); © 2004 AIP]

5.9.3 *Frequency Oscillations and Chaotic Dynamics*

A typical feature of optical feedback from a Fabry-Perot filter is frequency oscillations for which the laser intensity is almost constant, and only the laser frequency oscillates. The origin of this phenomenon has been unclear at present and the further study for understanding the mechanism is still on going. Figure 5.44 shows an experimental example of frequency oscillations in filtered optical feedback in semiconductor lasers (Fischer et al. 2004a). The example corresponds to an intermediate filter case of the frequencies of $\nu_{ex} = 50$ MHz, $\Delta\nu_f = 700$ MHz, and $\nu_R = 4 \sim 5$ GHz. The solitary laser frequency is chosen to be about 200 MHz higher than the center frequency of the Fabry-Perot filter. The observed periodic frequency oscillation is 19.6 ns, which quite agrees with the round trip time of the external delay. From the detailed analysis, the frequency is not simply equal to the round trip time but the round trip time plus the time corresponding to the frequency shift of the filter, $\sim 1/\Lambda$. Even in the frequency oscillation state, the measured laser power shows no evidence of oscillatory behaviors, thus the phenomenon is called "frequency oscillation".

The dynamics of filtered optical feedback in semiconductor lasers are strongly affected both by the frequency relations among the bandwidth of the filter, the external cavity, and the relaxation oscillation of the laser, and the feedback strength from the filter. Erzgräber et al. (2006) investigated the dynamics of filtered optical feedback in semiconductor lasers based on the numerical simulations from the rate equations of (4.70), (4.72), and (4.74). Figure 5.45 shows their results for an intermediate filter case of the frequencies of $\nu_{ex} = 200$ MHz, $\Delta\nu_f = 700$ MHz, and $\nu_R = 4.2$ GHz. For a weak but not such small optical feedback case in Fig. 5.45a, the laser shows relaxation oscillations at a frequency of 4.2 GHz. Since the HWHM of the filter is narrow enough compared to the relaxation oscillation frequency, the intensity I_F transmitted through the filter (and also fed back in the laser cavity) is almost constant. Figure 5.45b is an example of frequency oscillations for the

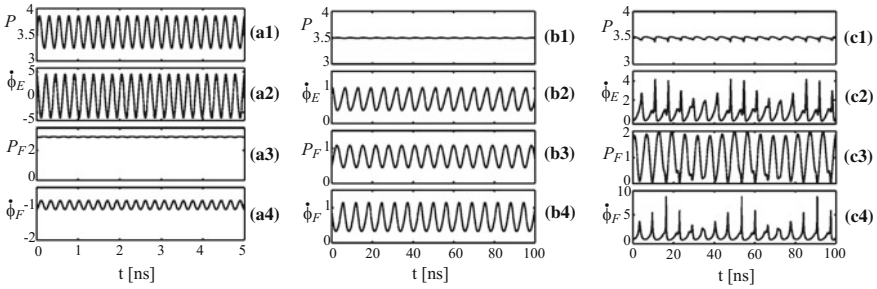

Fig. 5.45 Time series of P (optical power), P_F (feedback power), $\dot{\phi}_E$ (optical frequency), and $\dot{\phi}_F$ (feedback frequency) of **a** relaxation oscillations, **b** frequency oscillations, and **c** quasi-periodic frequency oscillations. From **a**–**c**, $(\tau_{ph}\kappa/\tau_{in}, \omega_0\tau)$ takes the values $(0.02, 4\pi/3)$, $(0.007, -2\pi)$, and $(0.014, -2\pi)$, respectively [after Erzgräber et al. (2006); © 2006 AIP]

dynamics of filtered optical feedback. In contrast to the relaxation oscillations in Fig. 5.45a, the laser intensity is almost constant, while its frequency $\dot{\phi}_E$ oscillated at the typical time period of the addition of the round trip time and the time shift in the frequency filter. Note that the laser frequency $\dot{\phi}_E$ and the feedback intensity I_F are approximately in anti-phase for this frequency oscillation. Fischer et al. (2004a) postulated that the frequency oscillations are interpreted as an interplay between the filter and the laser that compensates for the effects of the amplitude-phase coupling, leading to an effectively zero α parameter. Also, Rogister et al. (1999) argued that filtered optical feedback, in this case from a double mirror, effectively reduces the value of α. Finally, Fig. 5.45c shows that frequency oscillations can undergo further bifurcations, i.e., a torus bifurcation. This dynamical regime differs from the quasi-periodic dynamics associated with relaxation oscillations, in that there is again only very small intensity dynamics. Notice that the frequency oscillations exhibit a slow modulation with a period about 6 times larger than the basic oscillation. This ratio may crucially depend on other parameters.

In the following, we summarize the dynamics of filtered optical feedback in semiconductor lasers. Fischer et al. (2000) systematically investigated the dynamics for the strength of filtered optical feedback. Similar trends to conventional optical feedback have been observed for the increase in feedback strength, although the dynamics are more or less affected by the filter profile and several frequencies related to the filter, the laser device, and the feedback length. Namely, for the increase of the feedback strength (the increase of the C parameter), we can observe discrete external mode selections and hopping, hysteresis for increase or decrease of the bias injection current versus the laser power, and coherence collapse states. Also, following Fischer et al. (2004a), the dynamics of filtered optical feedback in semiconductor lasers are summarized for the frequency relations among the bandwidth of the filter, the external cavity, and the relaxation oscillation of the laser, and the feedback strength from the filter.

1. Wide filter case: $\Delta v_f > v_R$
   Since the filter bandwidth is larger than the relaxation oscillation frequency, the relaxation-oscillation-side-peak falls within the filter profile when the filter is centered at the solitary laser frequency. This case is very close to conventional optical feedback, wherein, one can have several hundred external cavity modes under the filter profile, and so the dynamics can be quite complicated.
2. Intermediate filter case: $v_{ex} < \Delta v_f < v_R$
   One can have a few tens of external cavity modes under the filter profile, such that the dynamics are more complicated than the narrow filter case, but in this regime one has the possibility to control dynamics.
3. Narrow filter case: $\Delta v_f \ll v_R$ and $\Delta v_f < v_{ex}$
   In this case, the filter is so narrow that at most one external cavity mode lies under the filter profile and so the laser prefers to operate on that single external cavity mode. Yet even in this case, dynamics are still possible. One mechanism for dynamics is the destabilization of the external cavity mode through a Hopf bifurcation, leading to undamped relaxation oscillations. Another mechanism is to detune the solitary laser by one relaxation oscillation frequency with respect to the filter center. The feedback channel via the relaxation oscillation side peak will likely give rise to undamped relaxation oscillations. In fact, these two mechanisms are also active in the intermediate case.

References

O.K. Anderson, A.P.A. Fischer, L.C. Lane, E. Louvergneaux, S. Stolte, D. Lenstra, Experimental stability diagram of a diode laser subject to weak phase-conjugate feedback from a Rubidium vapor cell. IEEE J. Quantum Electron. **35**, 577–582 (1999)

A. Arimoto, M. Ojima, Diode laser noise at control frequency in optical videodisc players. Appl. Opt. **23**, 2913–2920 (1984)

J.O. Binder, D. Cormack, A. Somani, Intermodal tuning characteristics of an INGaAsP laser with optical feedback from an external grating reflector. IEEE J. Quantum Electron. **26**, 1191–1199 (1990)

D. Brunner, X. Porte, M.C. Soriano, I. Fischer, Real-time frequency dynamics and high-resolution spectra of a semiconductor laser with delayed feedback. Sci. Rep. **2**, 732-1–732-5 (2012)

D. Brunner, M.C. Soriano, X. Porte, I. Fischer, Experimental phase-space tomography of semiconductor laser dynamics. Phys. Rev. Lett. **115**, 053901-1–053901-5 (2015)

D.L. Cheng, T.C. Yen, J.W. Chang, J.K. Tsai, Generation of high-speed single-wavelength optical pulses in semiconductor lasers with orthogonal-polarization optical feedback. Opt. Commun. **222**, 363–369 (2003)

J.L. Chern, K. Otsuka, F. Ishiyama, Coexistence of two attractors in lasers with delayed incoherent optical feedback. Opt. Commun. **96**, 259–266 (1993)

J. Cohen, F. Wittgrefe, M.D. Hoogerland, J.P. Woerdman, Optical spectra of a semiconductor laser with incoherent optical feedback. IEEE J. Quantum Electron. **26**, 982–990 (1990)

E. Detoma, B. Tromborg, I. Montrosset, The complex way to laser diode spectra: example of an external cavity laser strong optical feedback. IEEE J. Quantum Electron. **41**, 171–182 (2005)

S. Donati, G. Giuliani, S. Merlo, Laser diode feedback interferometer for measurement of displacements without ambiguity. IEEE J. Quantum Electron. **31**, 113–119 (1995)
M.C. Eguia, G.B. Mindlin, M. Giudici, Low-frequency fluctuations in semiconductor lasers with optical feedback are induced with noise. Phys. Rev. E **58**, 2636–2639 (1998)
H. Erzgräber, B. Krauskoph, D. Lenstra, A.P.A. Fischer, G. Vemuri, Frequency versus relaxation oscillations in a semiconductor laser with coherent filtered optical feedback. Phys. Rev. E **73**, 055201-1–055201-4 (2006)
G. Ewald, K.M. Knaak, S.G. Otte, K.D.A. Wendt, H.J. Kluge, Development of narrow-linewidth diode lasers by use of volume holographic transmission gratings. Appl. Phys. B **80**, 483–487 (2005)
I. Fischer, G.H.M. van Tartwijk, A.M. Levine, W. Elsäßer, E.O. Göbel, D. Lenstra, Fast pulsing and chaotic itinerancy with a drift in the coherence collapse of semiconductor lasers. Phys. Rev. Lett. **76**, 220–223 (1996)
A.P.A. Fischer, O.K. Andersen, M. Yousefi, S. Stolte, D. Lenstra, Experimental and theoretical study of filtered optical feedback in a semiconductor laser. IEEE J. Quantum Electron. **36**, 375–384 (2000)
A.P.A. Fischer, M. Yousefi, D. Lenstra, M.W. Carter, G. Vemuri, Filtered optical feedback induced frequency dynamics in semiconductor lasers. Phys. Rev. Lett. **92**, 023901-1–023901-4 (2004a)
A.P.A. Fischer, M. Yousefi, D. Lenstra, M.W. Carter, G. Vemuri, Experimental and theoretical study of semiconductor laser dynamics due to filtered optical feedback. IEEE J. Sel. Top. Quantum Electron. **10**, 944–954 (2004b)
M. Fujiwara, K. Kubota, R. Lang, Low-frequency intensity fluctuation in laser diode with external optical feedback. Appl. Phys. Lett. **38**, 217–220 (1981)
S. Fukuchi, S.Y. Ye, J. Ohtsubo, Relaxation oscillation enhancement and coherence collapse in semiconductor lasers with optical feedback. Opt. Rev. **6**, 365–371 (1999)
A. Gavrielides, T. Erneux, D.W. Sukow, G. Burner, T. McLachlan, J. Miller, J. Amonette, Square-wave self-modulation in diode lasers with polarization-rotated optical feedback. Opt. Lett. **21**, 2006–2008 (2006)
A. Gavrielides, D.W. Sukow, G. Burner, T. McLachlan, J. Miller, J. Amonette, Simple and complex square waves in an edge-emitting diode laser with polarization-rotated optical feedback. Phys. Rev. E **81**, 056209-1–056209-7 (2010)
G. Genty, A. Gröhn, H. Talvitie, M. Kaivola, H. Ludvigsen, Analysis of the linewidth of a grating-feedback GaAlAs laser. IEEE J. Quantum Electron. **36**, 1193–1198 (2000)
S.P. Hegarty, G. Huyet, P. Porta, J.G. McInerney, Analysis of the fast recovery dynamics of a semiconductor laser with feedback in the low-frequency fluctuation regime. Opt. Lett. **23**, 1206–1208 (1998)
T. Heil, I. Fischer, W. Elsäßer, Coexistence of low-frequency fluctuations and stable emission on a single high-gain mode in semiconductor lasers with external optical feedback. Phys. Rev. A **58**, R2672–R2675 (1998)
T. Heil, I. Fischer, W. Elsäßer, A. Gavrielides, Dynamics of semiconductor lasers subject to delayed optical feedback: the short cavity regime. Phys. Rev. Lett. **87**, 243901-1–243901-4 (2001)
T. Heil, I. Fischer, W. Elsäßer, B. Krauskopf, K. Green, A. Gavrielides, Delay dynamics of semiconductor lasers with short external cavities: bifurcation scenarios and mechanisms. Phys. Rev. E **67**, 066214-1–066214-11 (2003a)
T. Heil, A. Uchida, P. Davis, T. Aida, TE-TM dynamics in a semiconductor laser subject to polarization-rotated optical feedback. Phys. Rev. A **68**, 033811-1–033811-8 (2003b)
J. Helms, K. Petermann, A simple analytic expression for the stable operation range of laser diode with optical feedback. IEEE J. Quantum Electron. **26**, 833–836 (1990)
Y. Ikuma, J. Ohtsubo, Dynamics in a compound cavity semiconductor laser induced by small external-cavity-length change. IEEE J. Quantum Electron. **34**, 1240–1246 (1998)
F. Ishiyama, Bistability of quasi periodicity and period doubling in a delay-induced system. J. Opt. Soc. Am. B **16**, 2202–2206 (1999)

H. Kakiuchida, J. Ohtsubo, Characteristics of a semiconductor laser with external feedback. IEEE J. Quantum Electron. **30**, 2087–2097 (1994)
B. Kim, A. Locquet, N. Li, D. Choi, D.S. Citrin, Bifurcation-cascade diagrams of an external-cavity semiconductor laser: experiment and theory. IEEE J. Quantum Electron. **50**, 965–973 (2014)
B. Kim, A. Locquet, D. Choi, D.S. Citrin, Experimental route to chaos of an external-cavity semiconductor laser. Phys. Rev. A **91**, 061802(R)-1–061802(R)-4 (2015)
R. Lang, K. Kobayashi, External optical feedback effects on semiconductor injection properties. IEEE J. Quantum Electron. **16**, 347–355 (1980)
D. Lenstra, Statistical theory of the multistable external-feedback laser. Opt. Commun. **81**, 209–214 (1991)
L. Lenstra, B.H. Verbeek, A.J. den Boef, Coherence collapse in single-mode semiconductor lasers due to optical feedback. IEEE J. Quantum Electron. **21**, 674–679 (1985)
A.M. Levine, G.H.M. van Tartwijk, D. Lenstra, T. Erneux, Diode lasers with optical feedback: stability of the maximum gain mode. Phys. Rev. A **52**, R3436–R3439 (1995)
H. Li, J. Ye, J.G. McInerney, Detailed analysis of coherence collapse in semiconductor lasers. IEEE J. Quantum Electron. **29**, 2421–2432 (1993)
Y. Liu, N. Kikuchi, J. Ohtsubo, Controlling of dynamical behavior of semiconductor lasers with external optical feedback. Phys. Rev. E **51**, R2697–R2700 (1995)
M. Marconi, J. Javaloyes, S. Barland, M. Giudici, S. Balle, Robust square-wave polarization switching in vertical-cavity surface-emitting lasers. Phys. Rev. A **87**, 013827-1–013827-9 (2013)
J. Mørk, B. Tromborg, The mechanism of mode selection for an external cavity laser. IEEE Photonics Technol. Lett. **2**, 21–23 (1990)
J. Mørk, B. Tromborg, P.L. Christiansen, Bistability and low-frequency fluctuations in semiconductor lasers with optical feedback: a theoretical analysis. IEEE J. Quantum Electron. **24**, 123–133 (1988)
J. Mørk, J. Mark, B. Tromborg, Route to chaos and competition between relaxation oscillations for a semiconductor laser with optical feedback. Phys. Rev. Lett. **65**, 1999–2002 (1990a)
J. Mørk, M. Semkow, B. Tromborg, Measurement and theory of mode hopping in external cavity laser. Electron. Lett. **26**, 284–285 (1990b)
J. Mørk, B. Tromborg, J. Mark, Chaos in semiconductor lasers with optical feedback: theory and experiment. IEEE J. Quantum Electron. **28**, 93–108 (1992)
J. Mørk, H. Sabbatier, M.P. Sørensen, B. Tromborg, Return-map for low-frequency fluctuations in semiconductor lasers with optical feedback. Opt. Commun. **171**, 93–97 (1999)
A. Murakami, J. Ohtsubo, Dynamics and linear stability analysis in semiconductor lasers with phase-conjugate feedback. IEEE J. Quantum Electron. **34**, 1979–1986 (1998)
A. Murakami, J. Ohtsubo, Dynamics of semiconductor lasers with optical feedback from photorefractive phase conjugate mirror. Opt. Rev. **6**, 350–364 (1999)
A. Murakami, Dynamics of semiconductor lasers with phase-conjugate optical feedback. Ph.D. Thesis, Shizuoka University (1999)
A. Murakami, J. Ohtsubo, Y. Liu, Stability analysis of semiconductor laser with phase-conjugate feedback. IEEE J. Quantum Electron. **33**, 1825–1831 (1997)
A. Naumenko, P. Besnard, N. Loiko, G. Ughetto, J.C. Bertreux, Characteristics of a semiconductor laser coupled with a fiber Bragg grating with arbitrary amount of feedback. IEEE J. Quantum Electron. **39**, 1216–1228 (2003)
J.H. Osmundsen, N. Gade, Influence of optical feedback on laser frequency spectrum and threshold conditions. IEEE J. Quantum Electron. **19**, 465–469 (1983)
K. Otsuka, J.L. Chern, High-speed picosecond pulse generation in semiconductor lasers with incoherent optical feedback. Opt. Lett. **16**, 1759–1761 (1991)
M.W. Pan, B.P. Shi, G.R. Gray, Semiconductor laser dynamics subject to strong optical feedback. Opt. Lett. **22**, 166–168 (1997)
K. Petermann, *Laser Diode Modulation and Noise* (Kluwer Academic, Dordrecht, 1988)

F. Pittoni, M. Gioannini, I. Montrosset, Time-domain analysis of fiber grating semiconductor laser operation in active mode-locking regime. IEEE J. Sel. Top. Quantum Electron. **7**, 280–286 (2001)
W. Ray, W.S. Lam, P.N. Guzdar, R. Roy, Observation of chaotic itinerancy in the light and carrier dynamics of a semiconductor laser with optical feedback. Phys. Rev. E **73**, 026219-1–026219-5 (2006)
C. Risch, C. Voumard, Self-pulsation in the output intensity and spectrum of GaAs-AlGaAs cw diode lasers coupled to a frequency-selective external optical cavity. J. Appl. Phys. **48**, 2083–2085 (1977)
A. Ritter, H. Haug, Theory of laser diodes with weak optical feedback: 1. Small-signal analysis and side-mode spectra. J. Opt. Soc. Am. B **10**, 130–114 (1993a)
A. Ritter, H. Haug, Theory of laser diodes with weak optical feedback: 2. limit-cycle behavior, quasi-periodicity, frequency locking, and route to chaos. J. Opt. Soc. Am. B **10**, 145–154 (1993b)
F. Rogister, P. Mégret, O. Deparis, M. Blondel, T. Erneux, Suppression of low-frequency fluctuations and stabilization of a semiconductor laser subjected to optical feedback from a double cavity: theoretical results. Opt. Lett. **24**, 1218–1220 (1999)
J. Sacher, W. Elsäßer, E.O. Göbel, Intermittency in the coherence collapse of a semiconductor laser with external feedback. Phys. Rev. Lett. **63**, 2224–2227 (1989)
J. Sacher, D. Baums, P. Panknin, W. Elsäßer, E.O. Göbel, Intensity instabilities of semiconductor lasers under current modulation, external light injection, and delayed feedback. Phys. Rev. A **45**, 1893–1905 (1992)
T. Sano, Antimode dynamics and chaotic itinerancy in the coherence collapse of semiconductor lasers with optical feedback. Phys. Rev. A **50**, 2719–2726 (1994)
N. Schunk, K. Petermann, Numerical analysis of the feedback regimes for a single-mode semiconductor laser with external feedback. IEEE J. Quantum Electron. **24**, 1242–1247 (1988)
N. Schunk, K. Petermann, Stability analysis for laser diodes with short external cavities. IEEE Photonics Technol. Lett. **1**, 49–51 (1989)
N. Shibasaki, A. Uchida, Y. Yoshimori, P. Davis, Characteristics of chaos synchronization in semiconductor lasers subject to polarization-rotated optical feedback. IEEE J. Quantum Electron. **42**, 342–350 (2006)
D.W. Sukow, T. Gilfillan, B. Pope, M.S. Torren, A. Gavrielides, C. Masoller, Square-wave switching in vertical-cavity surface-emitting lasers with polarization-rotated optical feedback: experiments and simulations. Phys. Rev. A **86**, 033818-1–033818-8 (2012)
A. Tabaka, K. Panajotov, I. Veretennicoff, M. Sciamanna, Bifurcation study of regular pulse packages in laser diodes subject to optical feedback. Phys. Rev. E **70**, 036211-1–036211-9 (2004)
A. Takeda, S. Shogenji, J. Ohtsubo, Dynamics and pulse-package oscillations in broad-area semiconductor lasers with short optical feedback. Appl. Phys. Lett. **101**, 231105-1–231105-3 (2012)
Y. Takeuchi, R. Shogenji, J. Ohtsubo, Chaotic dynamics in semiconductor lasers subjected to polarization-rotated optical feedback. Appl. Phys. Lett. **93**, 181105-1–181105-3 (2008)
Y. Takeuchi, R. Shogenji, J. Ohtsubo, Chaos dynamics in semiconductor lasers with polarization-rotated optical feedback. Opt. Rev. **17**, 144–151 (2010)
Y. Takiguchi, Y. Liu, J. Ohtsubo, Low-frequency fluctuation induced by injection-current modulation in semiconductor lasers with optical feedback. Opt. Lett. **23**, 1369–1371 (1998)
Y. Takiguchi, Y. Liu, J. Ohtsubo, Low-frequency fluctuations and frequency-locking in semiconductor lasers with optical feedback. Opt. Rev. **6**, 339–401 (1999)
H. Temkin, N.A. Olsson, T.H. Abeles, R.A. Logan, M.B. Panish, Reflection noise in index-guided InGaAsP lasers. IEEE J. Quantum Electron. **22**, 286–293 (1986)
R.W. Tkach, A.R. Chraplyvy, Regimes of feedback effects in 1.5-m distributed feedback lasers. J. Lightwave Technol. **4**, 1655–1661 (1986)

M.S. Torre, A. Gavrielides, C. Masoller, Numerical characterization of transient polarization square-wave switching in two orthogonally coupled VCSELs. Opt. Express **19**, 20269–20278 (2011)
B. Tromborg, J.H. Osmundsen, H. Olesen, Stability analysis for a semiconductor laser in an external cavity. IEEE J. Quantum Electron. **20**, 1023–1032 (1984)
B. Tromborg, J. Mørk, V. Valichansky, On mode coupling and low-frequency fluctuations in external-cavity laser diodes. J. Opt. B **9**, 831–851 (1997)
W.A. van der Graaf, L. Pesquera, D. Lenstra, Stability and noise properties of diode lasers with phase-conjugate feedback. IEEE J. Quantum Electron. **37**, 562–573 (2001)
G.H.M. van Tartwijk, D. Lenstra, Nonlocal potential for class-B lasers with external optical feedback. Phys. Rev. A **50**, R2837–R2840 (1994)
G.H.M. van Tartwijk, A.M. Levine, D. Lenstra, Sisyphus effect in semiconductor lasers with optical feedback. IEEE J. Sel. Top. Quantum Electron. **1**, 466–472 (1995)
Y. Takiguchi, Chaotic oscillations in semiconductor lasers with optical feedback: control and applications. Ph.D. Thesis, Shizuoka University (2002)
S.Y. Ye, J. Ohtsubo, Experimental investigation of stability enhancement in semiconductor lasers with optical feedback. Opt. Rev. **5**, 280–284 (1998)
J. Ye, H. Li, J.G. McInerney, Period-doubling route to chaos in a semiconductor laser with weak optical feedback. Phys. Rev. A **47**, 2249–2252 (1993)
T.C. Yen, J.W. Chang, J.M. Lin, R.J. Chen, High-frequency optical generation in a semiconductor laser by incoherent optical feedback. Opt. Commun. **150**, 158–162 (1998)
M. Yousefi, D. Lenstra, Dynamical behavior of semiconductor laser with filtered external optical feedback. IEEE J. Quantum Electron. **35**, 970–976 (1999)
M. Yousefi, D. Lenstra, Nonlinear dynamics of a semiconductor laser with filtered optical feedback and the influence of noise. Phys. Rev. E **67**, 046213-1–046213-11 (2003)
S.F. Yu, Nonlinear dynamics of vertical-cavity surface-emitting lasers. IEEE J Quantum Electron. **35**, 331–332 (1999)
P. Zorabedian, W.R. Trutna, L.S. Cutler, Bistability in grating tuned external-cavity semiconductor laser. IEEE J. Quantum Electron. **23**, 1855–1860 (1987)

Chapter 6
Dynamics in Semiconductor Lasers with Optical Injection

Abstract Since the semiconductor laser has unique features of high gain, low facet reflectivity, and amplitude-phase coupling through the α parameter, it is also sensitive to optical injection from a different laser. Locking and unlocking phenomena in optically injected semiconductor lasers have been extensively studied. Especially optical injection locking has been appreciated as a useful tool for controlling and stabilizing laser oscillations. The general application of optical injection is to control the laser and the locking condition is extensively investigated to distinguish the unlocking phenomena. However, little attention has been paid to the unlocking dynamics. Recent studies proved that rich varieties of dynamics, such as the four-wave mixing, period-doubling route to chaos, and non-locking beating, are involved in the unlocking region. In this chapter, we focus on the dynamic characteristics of locking and unlocking regimes in optically injected semiconductor lasers.

6.1 Optical Injection

6.1.1 Optical Injection Locking

Optical injection technique can be used in various applications, for example it is used to reduce intensity, frequency, and partition noises in semiconductor lasers (Furusawa 1996; Schunk and Petermann 1986; Genest et al. 1997), generating microwave signals (Chan and Liu 2004), or producing chaotic signals for secure communications (Liu et al. 2001). The technique is originally developed to lock the frequency and stabilize the oscillation of an optically injected laser. The injection locking system is very simple, as shown in Fig. 6.1. Injection locking is useful for stabilizing the injected laser; however, the lasers sometimes show instability and exhibit a rich variety of dynamics. For optical injection locking, we prepare two

© Springer International Publishing AG 2017

J. Ohtsubo, *Semiconductor Lasers*, Springer Series in Optical Sciences 111,
DOI 10.1007/978-3-319-56138-7_6

lasers with almost the same oscillation frequencies and the frequency detuning between them must usually be within several GHz. A light from a laser under a single-mode oscillation (master laser) is fed into the active layer of the other laser (slave laser). Then, the two lasers synchronize with each other in the same optical frequency under the appropriate conditions of the frequency detuning and the injection strength. The remarkable characteristics of optical injection locking in semiconductor lasers originated from the fact that the α parameter (linewidth enhancement factor) has a nonzero definite value, which makes semiconductor lasers very different from other lasers. As a viewpoint of laser dynamics, an optical injection from a different laser means the introduction of an extra degree of freedom to the semiconductor laser. Therefore, various dynamics are observed by optical injection, including stable and unstable injection locking, instabilities and chaos, and four-wave mixing depending on the locking conditions (Mogensen et al. 1985; Sacher et al. 1992; Lee et al. 1993; Annovazzi-Lodi et al. 1994; Liu and Simpson 1994; Simpson et al. 1995, 1997; Kovanis et al. 1995; Erneux et al. 1996; De Jagher et al. 1996; Gavrielides et al. 1997; Eriksson and Lindberg 2001).

Optical injection technique is originally developed for the stabilization of the injected slave laser, so that, at first glance, it may be surprising that the laser is destabilized by the optical injection. However, as already mentioned, the perturbed laser is a candidate of a chaotic system. Figure 6.2a shows an example of bifurcation diagram of the slave laser for the change of the frequency detuning between the master and slave lasers at a fixed optical injection rate. We can see stable and unlocking oscillations, and various unstable oscillation states for the change of the frequency detuning. Figure 6.2b, c show the time series and rf spectrum at the frequency detuning of $\Delta\nu = 1.0$ GHz. Similarly to chaotic oscillations for the case of optical feedback in the previous chapter, we can observe chaotic oscillations in optical injection systems. As we will see in the following, periodic and unstable oscillations are observed in adjacent to the stable injection locking state. Also, unlocking oscillations are distributed for large values of the frequency detuning. We will later present the instabilities and chaotic dynamics by optical injection and, here, we investigate the principle of optical injection locking in semiconductor lasers.

Again the tool for investigating the characteristics of optical injection locking is the linear stability analysis. We assume that the frequency detuning $\Delta\nu = \Delta\omega/2\pi$

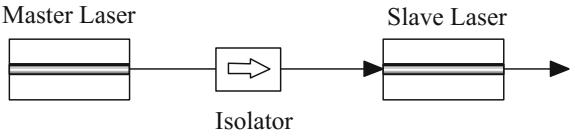

Fig. 6.1 Optical injection system in semiconductor lasers

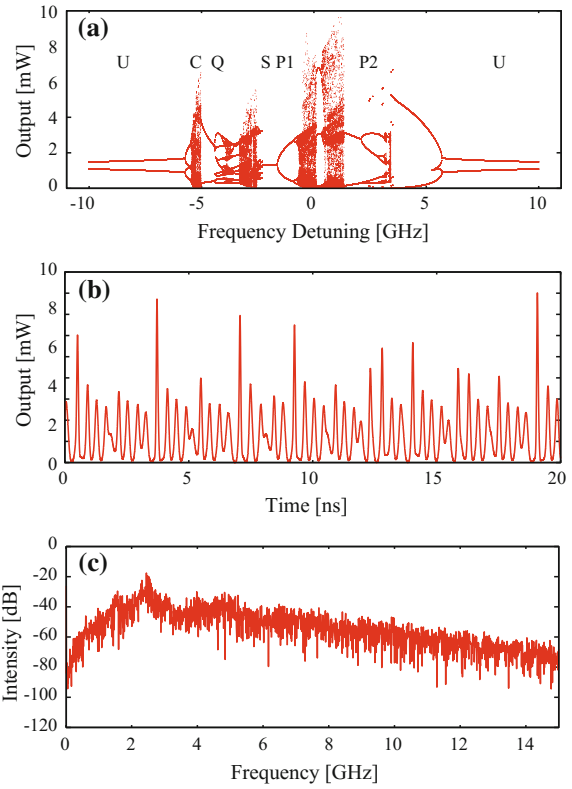

Fig. 6.2 **a** Bifurcation diagram for the frequency detuning at a fixed optical injection ratio of $r_{inj} = 0.03$ (amplitude) and a bias injection current of $J = 1.3J_{th}$. **b** Example of time series of chaotic states at a frequency detuning of $\Delta\nu = +1.0$ GHz. **c** Rf spectrum corresponding to **b**. Some examples of oscillation states in **a** are *S* stable injection locking state, *U* unlocking state, *P1* period-1 oscillation, *P2* period-2 oscillation, *Q* quasi-periodic oscillation, and *C* chaotic oscillation

between the master and slave lasers is small and the fraction of the photon number S_m (optical injection power $S_m = |E_m|^2 = A_m^2$) from a master laser is also small compared with the photon number S_s of a slave laser. As usual, the injection strength to the slave laser may or may not be small, but for the moment, we consider the case of a rather small optical injection. Here, we discuss the effects to understand the principle of optical injection locking. It is also noted that a laser may show instability and chaotic oscillations for a small injection fraction under certain injection conditions, as we will see in the following sections. We use a steady-state complex field $E_m(t) = \sqrt{S_m}\exp\{-i\phi_m(t)\}$ for a master laser and assume the complex field $E_s(t) = \sqrt{S_s}\exp\{-i\phi_s(t)\}$ for a slave laser. The phases ϕ_m and ϕ_s are generally time-dependent functions, but the master laser is under steady-state operation and its phase is assumed to be constant as $\phi_m = 0$. Though the phase of the slave laser generally fluctuates with time, it is approximated as a small fluctuation and assumed to be a constant value when the slave laser is injection locked. Taking these assumptions into consideration, the rate equation for the slave field is written by

$$\frac{dE_s(t)}{dt} = \frac{1}{2}(1 - i\alpha)G_n\{n(t) - n_{th}\}E_s(t) + \frac{\kappa_{inj}}{\tau_{in}}E_m(t)\exp(-i\Delta\omega t) \tag{6.1}$$

where $\Delta\omega = 2\pi\Delta\nu = \omega_m - \omega_s$ is the detuning between the angular frequencies, ω_m and ω_s, for the master and slave lasers, respectively, κ_{inj} is the injection coefficient, and τ_{in} is the round trip time of light in the laser cavity as introduced before. κ_{inj} is related to the actual fraction of the external injection ratio r_{inj} (which is normalized to the average of the absolute value of the field $|E_s|$) as

$$\kappa_{inj} = \frac{r_{inj}}{r_0}\sqrt{\frac{1 - r_0^2}{\eta}} \tag{6.2}$$

where r_0 is the front facet reflectivity of the laser cavity and η is the refractive index of the laser medium, which are the same definitions as before. Even in the presence of optical injection, the carrier density equation accompanying to the field equation remains the same as (3.51).

Sometimes a different equation from (6.1) is used for investigating theoretically the dynamics of injection locking. In spite of the different expression, the same results as those derived from the rate equation in (6.1) are of course obtained. In this expression, using the angular frequency detuning parameter $\Delta\omega$, a new optical field $\hat{E}_s(t)$ is defined as $E_s(t) = \hat{E}_s(t)\exp(-i\Delta\omega t)$. Substituting the variable into (6.1) and eliminating the term $\exp(-i\Delta\omega t)$, we obtain the following new expression for the optical field:

$$\frac{d\hat{E}_s(t)}{dt} = \frac{1}{2}(1 - i\alpha)G_n\{n(t) - n_{th}\}\hat{E}_s(t) + \frac{\kappa_{inj}}{\tau_{in}}E_m(t) + i\Delta\omega\hat{E}_s(t) \tag{6.3}$$

In the meanwhile, the carrier equation only includes the term for the absolute value of the field and has no modification. The new field equation has an extra term of phase so that the dynamics are different from those of the original field itself. However, the resulting dynamics of the laser power and the carrier density remain the same as those derived from (6.1) and can be compared with experiments.

6.1.2 Injection Locking Condition

Optical injection locking is a coherent optical phenomenon, so that the discussion must be based on the complex field instead of the photon number. As the carrier density of the slave laser is affected by optical injection, we put the deviation of it as $\Delta n = n - n_{th}$. We introduce a phase $\psi(t) = \Delta\omega t + \phi_m(t) - \phi_s(t)$ and a small deviation between the photon numbers with and without the optical injection as $S_s - S_{0s}$ (S_{0s} is the photon number of the slave laser in the absence of the optical injection). In a locking state, the phase of the injected laser is locked to a certain value as

$\phi_s(t) - \phi_m(t) = \Delta\omega t + \phi_L$. (Note that the phase of the injection laser, $\phi_m(t)$, can be set to be constant.) Then, we write the locked phase ϕ_L as $\phi_L = -\psi(t) = -\psi_s$. By the use of the representation of $\psi(t)$ instead of $\phi_s(t) - \phi_m(t)$, we can define the rate equations as autonomous equations. Then, we obtain the solutions $S_s - S_{0s}$, ψ_s, and Δn for the steady-state values (Mogensen et al. 1985; van Tartwijk and Agrawal 1998)

$$\frac{1}{2}G_n\Delta n + \frac{1}{\tau_{\text{in}}}\sqrt{\frac{S_{\text{inj}}}{S_s}}\cos\psi_s = 0 \tag{6.4}$$

$$\Delta\omega = \frac{1}{2}\alpha G_n\Delta n - \frac{1}{\tau_{\text{in}}}\sqrt{\frac{S_{\text{inj}}}{S_s}}\sin\psi_s \tag{6.5}$$

$$-\left(\frac{1}{\tau_s} + G_n S_{0s}\right)\Delta n - \left(\frac{1}{\tau_{\text{ph}}} + G_n\Delta n\right)(S_s - S_{0s}) = 0 \tag{6.6}$$

where $S_{\text{inj}} = \kappa_{\text{inj}}^2 S_m$. In the above equation, replacing the fluctuation of the carrier density with $x = G_n\Delta n$ and eliminating the variables ϕ_s and S_s, we obtain the characteristic equation as follows:

$$\begin{aligned} &-\frac{1}{4\tau_s}(1+\alpha^2)x^3 + \left\{\frac{1}{4}(1+\alpha^2)\omega_{\text{R}}^2 + \frac{\alpha\Delta\omega}{\tau_s}\right\}x^2 \\ &-\left(\alpha\Delta\omega\omega_{\text{R}}^2 + \frac{\Delta\omega^2}{\tau_s} + \frac{1}{\tau_{\text{in}}^2}G_n S_{\text{inj}}\right)x + \omega_{\text{R}}^2\left(\Delta\omega^2 - \frac{1}{\tau_{\text{in}}^2}\frac{S_{\text{inj}}}{S_{0s}}\right) = 0 \end{aligned} \tag{6.7}$$

From the above equation, we obtain the solutions for the fluctuation of the carrier density. Eliminating Δn in (6.4) and (6.5), we also hold the relation between the phase ψ_s and the laser powers as

$$\psi_s = \sin^{-1}\left(-\frac{\tau_{\text{in}}\Delta\omega}{\sqrt{1+\alpha^2}}\sqrt{\frac{S_s}{S_{\text{inj}}}}\right) - \tan^{-1}\alpha \tag{6.8}$$

From this relation, we obtain the condition for the phase ψ_s as

$$-\frac{\pi}{2} - \tan^{-1}\alpha \le \psi_s \le \frac{\pi}{2} - \tan^{-1}\alpha \tag{6.9}$$

On the other hand, from the steady-state condition for the carrier density n_s under the existence of optical injection, one reads

$$\Delta n_s = n_s - n_{\text{th}} = -\frac{2}{\tau_{in}G_n}\sqrt{\frac{S_{\text{inj}}}{S_s}}\cos\psi_s \tag{6.10}$$

Δn_s should be negative, so that the phase has the condition as $\psi_s \geq -\pi/2$. Therefore, the range of the phase for stable locking is totally given by (Mogensen et al. 1985)

$$-\frac{\pi}{2} \leq \psi_s \leq \cot^{-1}\alpha \tag{6.11}$$

Finally, the range of the angular frequency for the stable injection locking condition is obtained as

$$-\frac{\sqrt{1+\alpha^2}}{\tau_{\text{in}}}\sqrt{\frac{S_{\text{inj}}}{S_s}} = \Delta\omega_L \leq \Delta\omega \leq \frac{1}{\tau_{\text{in}}}\sqrt{\frac{S_{\text{inj}}}{S_s}} \tag{6.12}$$

Successful optical injection locking occurs at a frequency satisfying the above equation for the injection fraction S_{inj}/S_s. The α parameter encountered in the above equation plays an important role in optical injection locking.

Using the relation of (6.12), the deviation of the carrier density Δn is given by

$$\Delta n = \frac{2\alpha\Delta\omega \pm 2\sqrt{\Delta\omega_L^2 - \Delta\omega^2}}{G_n(1+\alpha^2)} \tag{6.13}$$

In the above equation, the plus and minus signs denote that the corresponding solution for (6.8) has a phase value of zero or π radian. There exist two solutions for the same photon number S_s. One is a stable solution and the other is unstable. In general, optical injection locking occurs at or close to the stable solution. Figure 6.3 shows the areas of optical injection locking in the phase space for the frequency

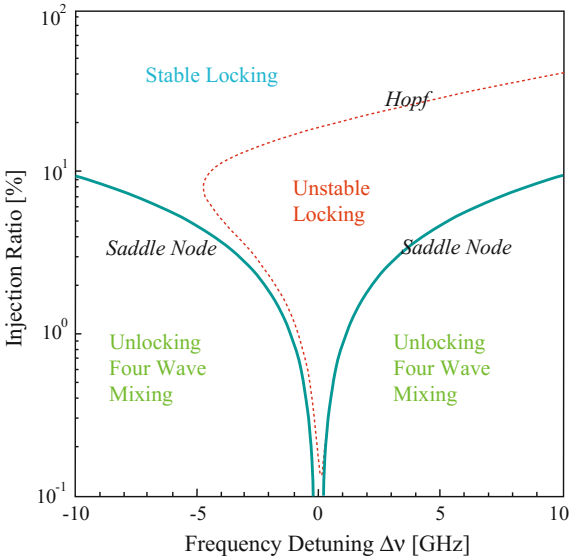

Fig. 6.3 Locking and unlocking regions in the phase space of the frequency detuning and the injection field

detuning between the master and slave lasers and the injection ratio. The solid curves show the boundaries between optical injection locking and non-locking regions. The boundaries are fundamentally saddle node (SN) points from stable to unstable bifurcations. In the non-locking region, we can expect various dynamics such as chaotic oscillations and four-wave mixing when the detuning is not so far from zero. Indeed, we can observe various dynamics when the frequency detuning and the injection ratio are small in these regions. Within the region of the optical injection locking, there are stable and unstable locking areas. The boundary of the unstable and stable injection locking areas is denoted by a dotted curve. The boundary is the Hopf bifurcation point. In the unstable injection locking area, we can also observe chaotic bifurcations for certain parameter ranges. The asymmetric feature of stable injection locking again originated from the fact that the α parameter has a nonzero value in semiconductor lasers.

Figure 6.4 is the detail of the injection map corresponding to Fig. 6.3. Along the boundary of the Hopf bifurcation in the unstable injection locking region, period-1 oscillations emerges and, then, the laser power bifurcates periodic to chaotic oscillations via period-doubling bifurcations for rather weak optical injection strength. On the other hand, along the stable boundary in the negative detuning region, the stable output power evolves into quasi-periodic to chaotic oscillations. In the unstable injection-locking region, the phase of the laser also exhibits periodic oscillation as shown in Fig. 6.5a. As a result, the momentary frequency (the time derivative of the phase, $\mathrm{d}\phi_s(t)/\mathrm{d}t$) also shows periodic oscillation. However, the averaged optical frequency ($\langle \mathrm{d}\phi_s(t)/\mathrm{d}t \rangle$) remains the same as that for the stable injection locking state, namely, the averaged phase is still "locked" to the phase of the injection laser (phase locking state) as depicted in Fig. 6.5b.

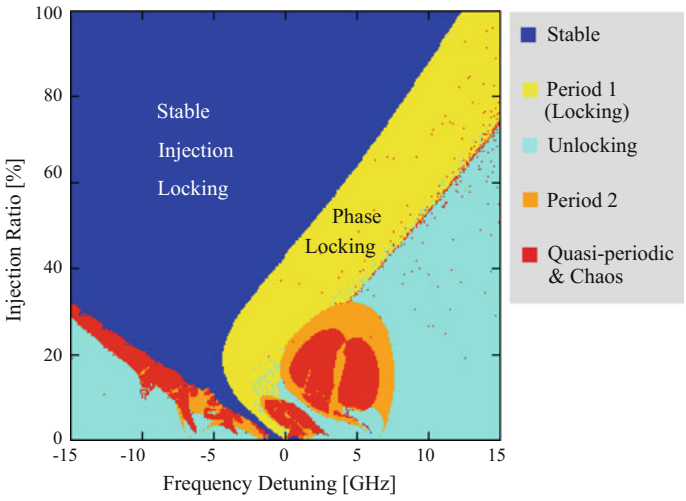

Fig. 6.4 Detailed injection map of the intensity in the phase space of the frequency detuning and the optical injection ratio

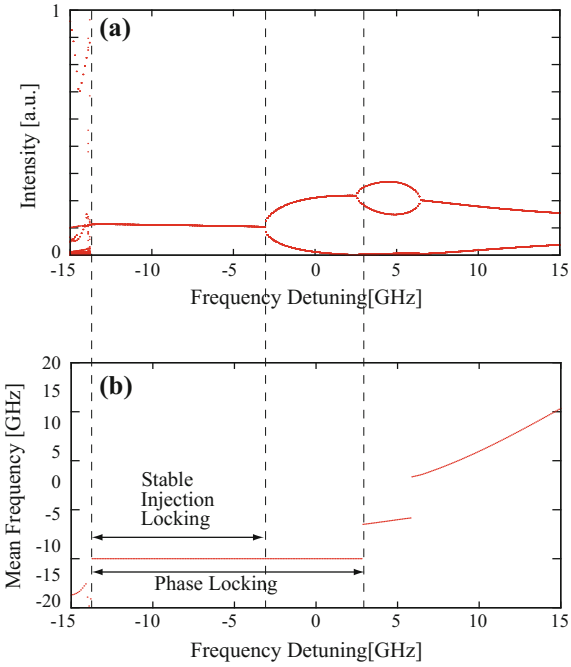

Fig. 6.5 **a** Bifurcation diagram of the intensity at an optical injection ratio of 30%. **b** Bifurcation diagram of the mean phase at an optical injection ratio of 30%

In actual optical injection locking, the hysteresis is observed depending on the continuous increase or decrease of the frequency detuning at a fixed strength of optical injection (Blin et al. 2009; Guo et al. 2013). Figure 6.6 is such a numerical example for an optical injection to a vertical-cavity surface-emitting laser (VCSEL). For the increase of the wavelength detuning (decrease of the frequency detuning from positive to negative), the slave laser is frequency locked to the master laser at around the wavelength detuning of −0.5 nm. Then, the optical power of the slave laser is amplified by optical injection locking for the increase of the detuning. As a result, the locking jumps off to the unlocking state at around the wavelength detuning of 2 nm. However, when the wavelength detuning is decreased from positive to negative, the laser still remains unlocking state even at the jumping point and the optical injection locking starts at smaller wavelength detuning of about 1 nm. Thus, we observe a bistable state of the laser output power for the frequency detuning between 1 and 2 nm. Figure 6.6 is calculated without the effects of optical interference of the laser output powers from the slave laser and the reflection of the master laser in front of the slave laser facet. For example, the front facet reflectivity of VCSELs is very high up to 99.9%, so that we cannot ignore this effect in real situations. Indeed, the output power at the detector plane is considerably changed in a real experiment due to the interference. However, in the numerical simulation in Fig. 6.6, we exclude such effect. Also the hysteresis can be observed for the continuous increase or decrease of the strength of optical injection at a fixed frequency detuning. Note that, from negative to positive frequency detuning in the optical injection map in the phase space of the optical injection strength and the frequency

detuning, the bistable domain is bounded at the left (right in Fig. 6.6 in the case of the wavelength-detuning plot) by the locking boundary of the steady state (saddle-node bifurcation point).

The hyesterses are indeed observed in experiments (Blin et al. 2009; Yang et al. 2010; Guo et al. 2013). Figure 6.7 shows a map of stable and unstable injection locking boundaries with increasing and decreasing frequency detuning. It is noted that the map is plotted for the wavelength detuning. For a fixed injection ratio, the locking range is much wider when the wavelength is increased (decreasing frequency) in Fig. 6.7a. While the stable injection locking range is narrow for the decreasing wavelength (increasing frequency) in Fig. 6.7b. The color indicates the output power of the slave laser induced by the optical injection. The laser used is a

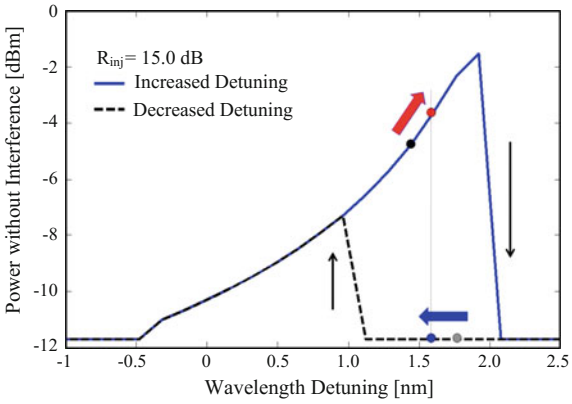

Fig. 6.6 Numerical example of the output power of the slave laser for the wavelength detuning at a fixed optical injection of ratio of 15 dBm. The interference of the output power from the master laser reflection at the slave laser facet is not considered. *Solid line* increase of wavelength, and *dashed line* decrease of wavelength [after Guo et al. (2013); © 2013 OSA]

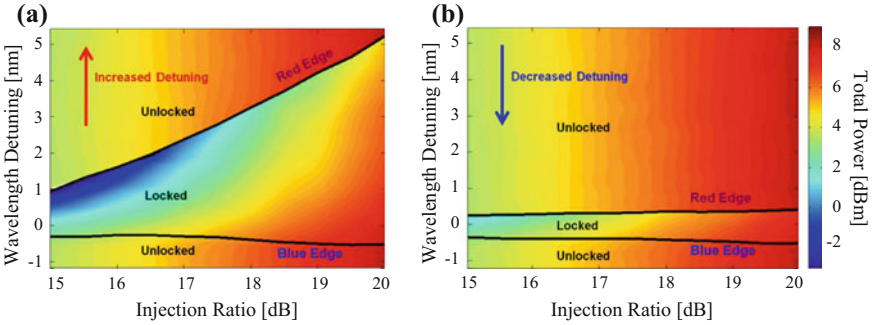

Fig. 6.7 Experimental results of the optical output power on the locking map. **a** With increased wavelength detuning and **b** with decreased wavelength detuning. Note that the interference effects between the reflection of the injected laser at the front facet of VCSEL and the internal laser output due to optical injection are included [after Guo et al. (2013); © 2013 OSA]

VCSEL. In the case of VCSELs, the light from the master laser is strongly reflected at the VCSEL facet and it interferes with the cavity output light. As a result of the strong interference, the total output power of the VCSEL including the interference decreases for optical injection at the stable injection-locking region (see Fig. 6.7). On the other hand, it increases without taking the interference effect into consideration (Yang et al. 2010). Guo et al. (2013) observed an ultra-wide hysteresis cycle of 3.7 nm (473 GHz) for a VCSEL of an operating wavelength at 1531 nm.

6.2 Stability and Instability in Optical Injection Systems

6.2.1 Rate Equations

Side modes are sometimes excited in the oscillation of a semiconductor laser subjected to optical injection even if it operates at a single mode under a solitary condition. Therefore, we must take into account the effect of side modes into the rate equations. The assumption of a single-mode operation can be well applied to a DFB semiconductor laser. However, a single-mode Fabry–Perot semiconductor laser, it is easily destabilized and oscillated at a multimode by the introduction of optical injection. Here, we first rewrite the rate equations of an optically injected semiconductor laser for a single-mode operation and, after that, we introduce the side-mode effect. To investigate the dynamics of optically injected semiconductor lasers, we again introduce the equations of the field amplitudes for the master and slave lasers, $A_m(t)$ and $A_s(t)$, the phase $\psi(t)$, and the carrier density $n(t)$ as

$$\frac{dA_s(t)}{dt} = \frac{1}{2}G_n\{n(t) - n_{\text{th}}\}A_s(t) + \frac{\kappa_{\text{inj}}}{\tau_{\text{in}}}A_m(t)\cos\psi(t) \tag{6.14}$$

$$\frac{d\psi(t)}{dt} = \frac{1}{2}\alpha G_n\{n(t) - n_{\text{th}}\} - \frac{\kappa_{\text{inj}}}{\tau_{\text{in}}}\frac{A_m(t)}{A_s(t)}\sin\psi(t) - \Delta\omega \tag{6.15}$$

$$\frac{dn(t)}{dt} = \frac{J}{ed} - \frac{n(t)}{\tau_s} - G_n\{n(t) - n_0\}A_s^2(t) \tag{6.16}$$

$$\psi(t) = \phi(t) - \Delta\omega t \tag{6.17}$$

In the above equations, we do not consider the gain saturation terms, however, the gain saturation also plays an important role in multimode oscillations in semiconductor lasers with optical injection. For such a case, we can use the relation of (3.45) or (3.46) for the gain saturation effect.

When the side-mode effects are important, the complex field for the main mode is rewritten as (Ryan et al. 1994)

$$\begin{aligned}\frac{dE_s(t)}{dt} &= \frac{1}{2}(1-i\alpha)G_n\{n(t)-n_{th}\}E_s(t) \\ &\quad -\frac{1}{2}\{\varepsilon'|E_s(t)|^2+\theta_c|E_{s'}(t)|^2\}E_s(t)+\frac{\kappa_{inj}}{\tau_{in}}E_m(t)\exp(-i\Delta\omega t)\end{aligned} \tag{6.18}$$

where $E_{s'}$ is the complex field of the side mode and θ_c is the cross-saturation coefficient for the gain. Here, we consider the excitation of one side mode and also take into account the self-saturation effect $\varepsilon' = \varepsilon_s\,(1 - i\alpha)G_n$. The rate equation for the complex field of the side mode is given by

$$\begin{aligned}\frac{dE_{s'}(t)}{dt} &= \frac{1}{2}(1-i\alpha)G_n\{n(t)-n_{th}\}E_{s'}(t) \\ &\quad -\frac{1}{2}\{\varepsilon'|E_{s'}(t)|^2+\theta|E_s(t)|^2\}E_{s'}(t)-\mu_d E_{s'}(t)\end{aligned} \tag{6.19}$$

where the final term is the gain defect of the secondary mode and μ_d is the coupling coefficient called gain defect.

Due to this gain defect, mode switching will be suppressed in this model and the laser is assumed to be always oscillated at the main mode as far as the coefficient has a significant value. Using these two modes, the carrier density equation is written as

$$\frac{dn(t)}{dt} = \frac{J}{ed}-\frac{n(t)}{\tau_s}-G_n\{n(t)-n_0\}\{|E_s(t)|^2+|E_{s'}(t)|^2\} \tag{6.20}$$

In actual fact, many side modes may be excited in the laser oscillations due to optical injection. However, it is proved that the model introduced here well explains mode excitations for real oscillations in a Fabry–Perot semiconductor laser subjected to optical injection.

The laser gain is usually linearized for the carrier density. However, in a strict sense, it is also a function of the photon number and the gain term $g' = (1 - i\alpha)$ $G_n\{n(t) - n_{th}\}$ is replaced by

$$g' = (1-i\alpha)G_n\{n(t)-n_{th}\}+(1-i\alpha')G_P\{|E(t)|^2-|E_0|^2\} \tag{6.21}$$

where G_P is the expansion coefficient for the photon number $S = |E|^2$, α' is the coefficient for the saturation of the output power given by $\alpha' = -(\partial \mathrm{Re}[\chi]/\partial S)/(\partial \mathrm{Im}[\chi]/\partial S)$, and E_0 is the steady-state field amplitude. For the model of a two-level atom in laser oscillations, we can approximate the coefficient α' equal to α, while it reduces to zero under the resonance condition (Simpson et al. 2001). Stability and instability of semiconductor lasers for optical injection are strongly dependent on the linewidth enhancement factor α and also on the coefficient α' of the saturation. It is proved in the following that this nonlinear coefficient α' is related to the suppression of the laser instabilities. Namely, the laser is stabilized for a larger value of this factor, while it shows instabilities for a small

value of it. The damping term μ_d introduced in the side-mode equation in (6.19) also plays an important role in the dynamics as discussed in the following.

In semiconductor laser systems of optical injection, optical feedback, and optoelectronic feedback, we can observe multistability and coexistence states of chaotic oscillations in the dynamics. At coexistence states, the respective chaotic attractor is completely different from others even for a particular set of the parameter values. Which state we can observe is strongly dependent on the initial conditions of the systems. Coexistence states of attractors are not only simulated by numerical calculations, but also experimentally observed. Some such examples in optical injection systems will be discussed in Sect. 6.2.4.

6.2.2 *Chaotic Bifurcations by Optical Injection*

The important parameters in the dynamics of optically injected semiconductor lasers are the frequency detuning between the master and slave lasers and the injection strength from the master to the slave. Figure 6.8 shows the experimental results of the dynamic characteristics in a semiconductor laser subjected to optical injection (Simpson 2003). The figure shows the plots of optical frequencies observed by a Fabry–Perot spectrometer (left column) and rf power spectra obtained by a spectrum analyzer (right column). Chaotic bifurcations are well demonstrated by the plots. We can assume a single-mode operation for the semiconductor laser even in the presence of optical injection, since the laser used is a DFB laser. As is easily recognized from the stability map in Fig. 6.3, the slave laser operates outside of the stable locking region for a small optical injection. When the injection fraction exceeds a certain threshold, the laser is injection-locked by the master laser and operates stably. It is noted that the injection strength defined in the figure is counted outside of the laser and not exactly equal to the intensity injected into the active layer.

In Fig. 6.8a, for a small level of the injection rate of 0.14, the slave laser shows four-wave and multi-wave mixing associated with the unlocked slave laser frequency and has a side peak in the spectrum due to regenerative amplification. The effect of multi-wave mixing becomes distinct in the laser output power at the injection rate of 0.23 in Fig. 6.8b. At the same time, the component corresponding to the relaxation oscillation becomes non-vanishing and the oscillation close to the relaxation oscillation frequency of 4.7 GHz is excited. Also, the spectrum is much broadened. The multi-wave mixing effect is recognized as the phase-modulation like Adler-type frequency pulling toward locking (Simpson 2003). However, the frequency pulling here is somewhat different from the ordinary effect and it is an unstable phenomenon accompanying the relaxation resonance. Frequency-pulled multi-wave mixing components disappear at the injection rate of 0.41 and the multi-wave mixing features are pulled to the injection frequency as shown in Fig. 6.8c. As a result, a sharp and enhanced component of the relaxation oscillation is observed. Therefore, the laser shows a stable oscillation under the condition.

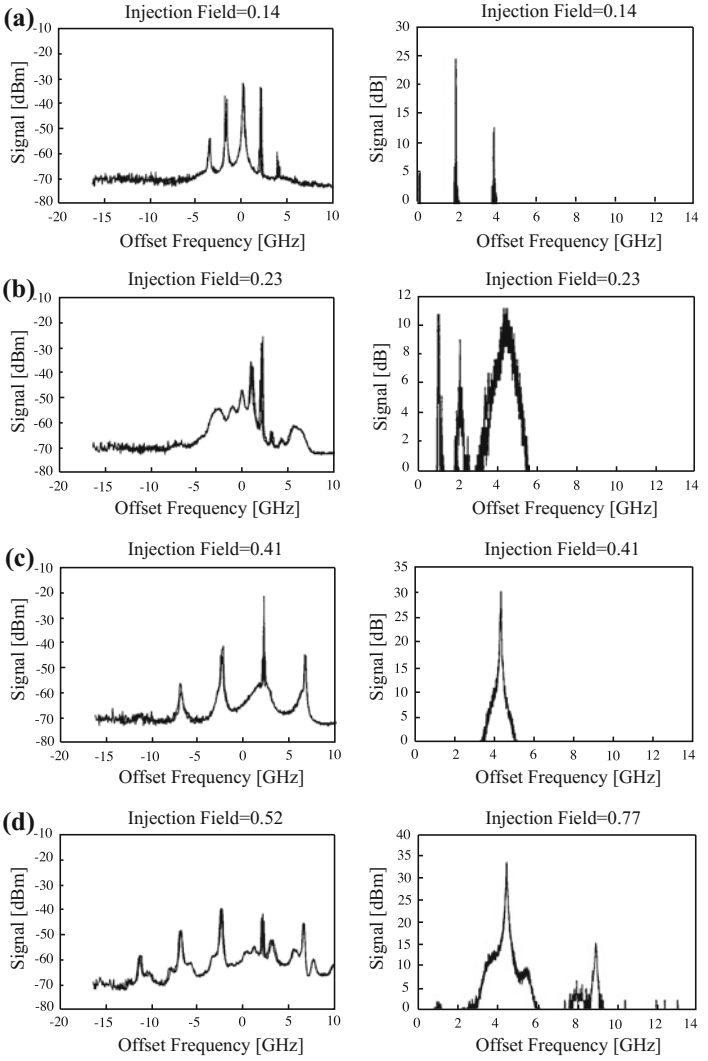

Fig. 6.8 Experimentally observed optical frequencies and rf power spectra corresponding to chaotic bifurcations in semiconductor lasers under optical injection. On the *left* are optical spectra and the *right* are rf spectra. The laser is a single-mode DFB laser at a wavelength of 1557 nm and a bias injection current of $J = 2.0J_{\text{th}}$. The relaxation oscillation frequency at solitary oscillation is 4.7 GHz. The injection rate (intensity) is changed as **a** 0.14, **b** 0.23, **c** 0.41, **d** 0.52, **e** 0.77, **f** 1.02, **g** 1.30, and **h** 3.01, respectively, at a fixed frequency detuning of +2 GHz [after Simpson (2003); © 2003 Elsevier]

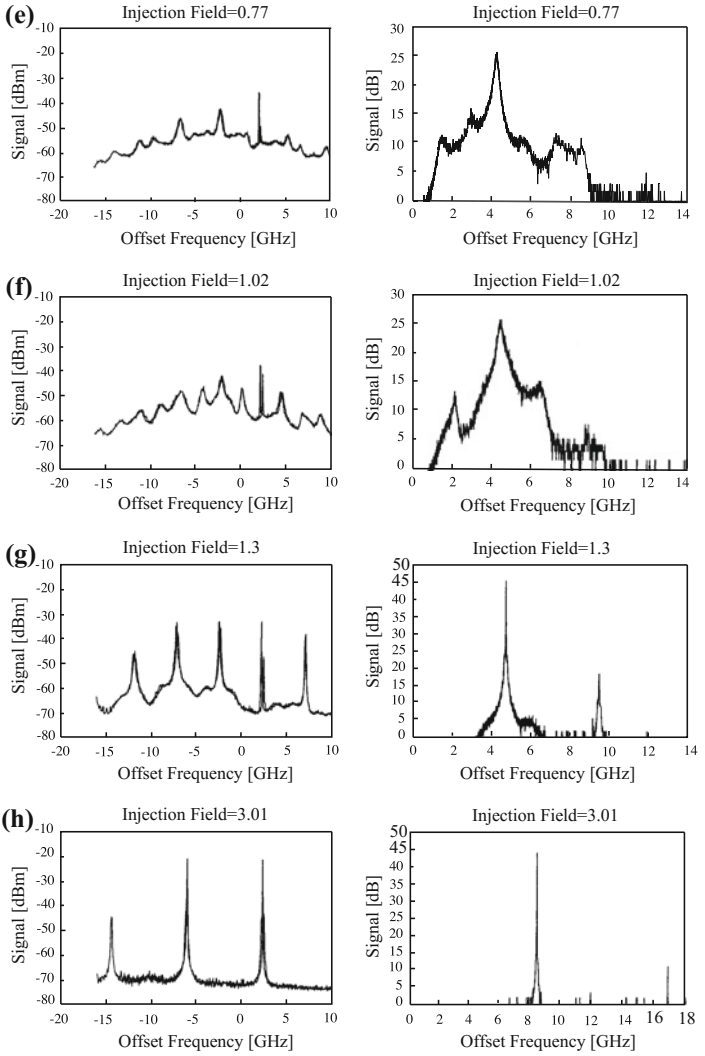

Fig. 6.8 (continued)

Incommensurate frequency is encountered in the dynamics at the injection rate of 0.52 in Fig. 6.8d and the floor of the spectrum becomes broadened. This is a typical feature of the onset of quasi-periodic bifurcation and chaos. The floor of the spectrum further becomes broadened at the injection rate of 0.77 in Fig. 6.8e and

several spectral peaks appear except for the relaxation oscillation component. Within the main peak, we can see two visible peaks. This indicates that the laser corresponds to period-3 oscillation. The oscillation mode within the relaxation oscillation frequency reduces as a single peak at the injection rate of 1.02 and the laser shows period-2 oscillation as shown in Fig. 6.8f. When the injection fraction is large enough at the injection rate of 1.30 in Fig. 6.8g, the laser oscillates at period-1 oscillation with the main frequency corresponding to the relaxation oscillation. The higher harmonics of the period-1 oscillation is also visible. Finally in Fig. 6.8h, at a strong injection rate of 3.01, the laser is completely locked to a certain frequency and shows period-1 oscillation. The locked frequency is different from the relaxation oscillation frequency at the solitary oscillation. This phenomenon is related to the enhancement of the cutoff frequency for the modulation bandwidth of the laser as discussed in the following. In this example, the chaotic evolution is observed for a fixed frequency detuning (+2 GHz). The dynamics are not always the same as those for other conditions of the detuning, but they exhibit typical chaotic routes when the absolute value of the frequency detuning is within several GHz.

In accordance with stable and unstable oscillations in optically injected semiconductor lasers, chaotic bifurcations are numerically calculated taking into consideration the effects of side-mode excitation. Figure 6.9 shows chaotic bifurcations for a change of the injection ratio at a fixed frequency detuning of +2 GHz (Simpson 2003). In Fig. 6.9a, the laser is assumed to be oscillated at a single mode, since it includes the effect of a larger defect with $\mu_d = 0.1$. The laser once evolves from periodic to chaotic oscillations and, then, takes an inverse route of chaotic bifurcations for the increase of the injection ratio. Finally, it reduces to a period-1 state. The behaviors are quite similar to the chaotic route for a single-mode laser discussed in Fig. 6.9. On the other hand, the instability of the laser is suppressed because of the leakage of the power from the main mode to the side mode when the effect of the defect is as small as $\mu_d = 0.001$ in Fig. 6.9b. Under this condition, the laser shows no typical chaotic bifurcations. Figure 6.9c shows the plot of the relative circulating power level in the main mode for single and multimode operations. The power of the main mode is transferred to the side mode and the instability of the laser oscillation is greatly suppressed, when there is a side mode and the injection strength is small. However, the side mode is never excited for a larger value of the defect and the assumption of a single-mode oscillation is well established.

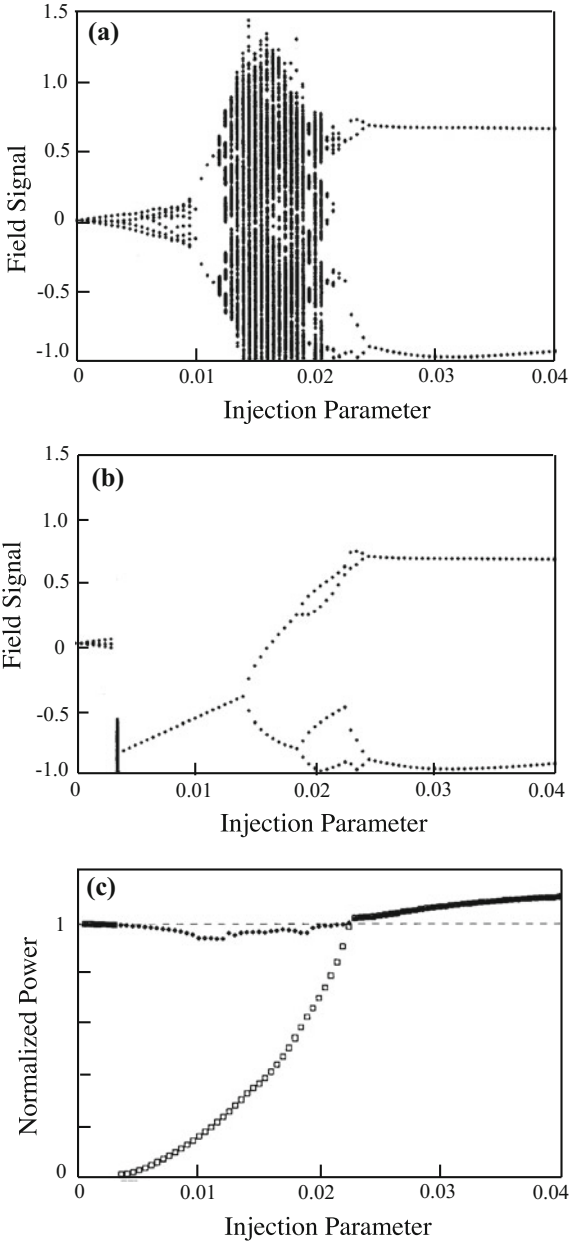

Fig. 6.9 Bifurcation diagram as a function of the injection ratio at a frequency detuning of +2 GHz. **a** Bifurcation diagram for a large gain defect of $\mu_d = 0.1$. The laser oscillates at a single mode. **b** Bifurcation diagram for a small gain defect of $\mu_d = 0.001$. Significant power leaks into the side mode. **c** Relative circulating power. The *symbol of diamonds* is for the single-mode oscillation, while *open squares* denote the case of multimode oscillations [after Simpson (2003); © 2003 Elsevier]

6.2.3 *Chaos Map in the Phase Space of Frequency Detuning and Injection*

We discuss chaos maps in the phase diagram of the frequency detuning and the injection ratio. Stable injection locking is achieved in a region for a certain combination of the frequency detuning and the injection ratio; however, various unstable and chaotic dynamics are observed in unstable locking and unlocking regions. Figure 6.10 shows the chaotic map obtained experimentally from the behaviors of the optical spectra corresponding to Fig. 6.9 (Simpson 2003). The laser is operated at a single mode even in the presence of optical injection and the side mode is suppressed in this laser. It is noted that the vertical axis and the horizontal axis are replaced compared with the plot in Fig. 6.3. The diamond-filled symbol shows in the negative frequency detuning is the boundary between unstable and stable operations. This corresponds to the saddle node boundary between stable locked and unlocked operations. Open diamonds show the unlocking-locking transition in a region of bistability and torus bifurcation. The square mark close to zero detuning is the Hopf bifurcation boundary between stable locked and limit cycle dynamics. The triangle is the boundaries for regions of period-2 dynamics. These period-2 regions include complex dynamics and they are shown by the shaded lines and crosses in the figure. Bounded by the circles is a region of period-4 operation. At injection levels below the saddle node bifurcation line and at low offset frequencies, multi-wave mixing and Adler-type frequency pulling to locking are observed in the lightly shaded regions.

Figure 6.11 shows the experimental result for the map in a semiconductor laser with side-mode excitation by optical injection (Hwang and Liu 2000). The laser used is a conventional Fabry–Perot type edge-emitting laser with a quantum well

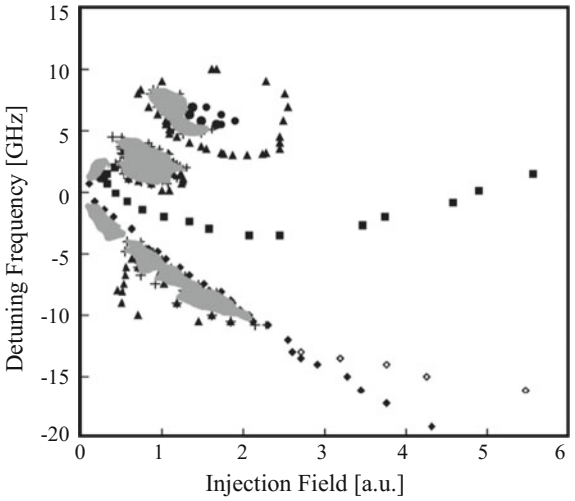

Fig. 6.10 Experimentally obtained chaotic map from the measured optical spectra of a single-mode DFB laser under optical injection. The meaning of each *symbol* is referred to the text [after Simpson (2003); © 2003 Elsevier]

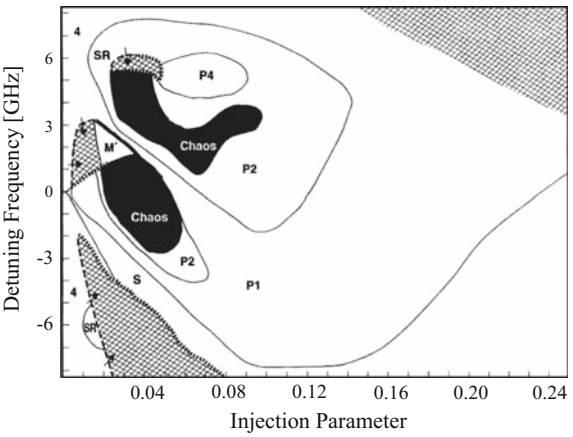

Fig. 6.11 Experimentally obtained chaotic map from the measured optical spectra in a Fabry–Perot laser operating at 827.6 nm. A side mode is excited by optical injection. The bias injection current is $J = 1.67J_{th}$. The detail of the map is discussed in the text [after Hwang and Liu (2000); © 2000 Elsevier]

structure. The back facet of the laser is coated for high reflection and the front output facet is coated for a reflection of a few percent. At the free running state of the laser oscillation, the side mode is suppressed as low as less than 0.5%. The symbols in the figure are 4: a perturbation spectrum with weak regenerative amplification and four-wave mixing sidebands, S: stable injection locking, P1: limit cycle oscillation, P2: period doubling, P4: period quadrupling, chaos: deterministic chaos, M: multi-wave mixing with most output on another longitudinal mode, SR: sub-harmonic resonance, hatched regions: principal output on another longitudinal mode, thin curves: smooth transition between dynamic regions, thick dotted curves: abrupt mode-hop transitions with minor hysteresis, thick broken curves with an arrow: one-way mode hops out of mode, and thick full curves: abrupt transition to/from a region of chaos or multi-wave mixing where there is significant power in another longitudinal mode, from/to a region with power primarily in the principal mode.

For a small injection, the optical injection acts as a perturbation generating weak sidebands at the offset frequency, regenerative amplification, and equally and oppositely shifted four-wave mixing. With increasing both of the frequency detuning and the injection ratio, various instabilities appear in the laser output power. The tendency of periodic bifurcations and chaotic islands in the unstable region is the same as that for a DFB laser. However, distinct chaotic bifurcation is not observable for a Fabry–Perot laser in the region of negative frequency detuning along the stable boundary, while it was observed for a DFB laser (see Fig. 6.10). There is an abrupt mode hop near the locking–unlocking boundary at negative detuning which has a small hysteresis. The analytical studies of the locking–unlocking boundary at negative detuning have shown that there is a region of bistability associated with the locking–unlocking transition (Li 1994a, b). The bistability results from competing attractors representing locked and unlocked solutions for the coupled equations (Lenstra et al. 1993). The carrier density is larger than that for the steady-state n_s under the unlocked solution, while it stays a smaller value for the

locked solution. The gain of the side mode increases with the increase of the carrier density and the refractive index of the active layer accordingly changes. The change induces the transfer of the optical energy from the main mode to side modes. Then, the gain of the main mode is reduced and this sometimes results in frequent mode hop. However, the chaotic dynamics disappears in the output power. On the contrary, instabilities still remain in the dynamics of a single-mode laser without the excitation of the side mode as shown in Fig. 6.10.

Considering the gain defect and using (6.18)–(6.20), stable and unstable maps in the phase space of the frequency detuning and the injection ratio like in Figs. 6.10 and 6.11 can be calculated (Simpson 2003). The results are quite consistent with the experimental results. Namely, the suppression of chaotic dynamics for the excitation of the side mode is well reproduced. Hwang and Liu (2000) numerically calculated maps of stable and unstable regions in the phase space of the frequency detuning and the injection ratio by changing the parameters in the rate equations. They studied the dependence of the parameters for the cavity decay rate $\gamma_c = 1/\tau_{\mathrm{ph}}$, the carrier relaxation rate $\gamma_s = 1/\tau_s$, the differential relaxation rate γ_n, and the nonlinear carrier relaxation rate γ_π. For the change of those parameters, they obtained the following results. (1) The carrier decay rate γ_s affects little change, since the carrier relaxation is usually induced by spontaneous emission of light and it is a small perturbation for the field strength. (2) The laser is stabilized for a small value of the differential relaxation rate γ_n, since the fast carrier diffusion reduces unstable regions. (3) When the nonlinear carrier relaxation rate γ_π increases, the unstable region shrinks and the laser is stabilized. The increase of the nonlinear carrier relaxation rate γ_π results in the change of the carrier density in the active layer and the fluctuation of the optical phase is suppressed. This results in the suppression of frequency fluctuations. Therefore, the laser is stabilized. (4) For a larger value of the α parameter, instability of laser oscillation is enhanced. (5) Stability and instability of semiconductor lasers subjected to optical injection are also dependent on the bias injection current. With increasing the bias injection current, the stable region in the map expands. When a laser is operated at a higher injection current level, the coherent optical power stored in the cavity is higher, thus allowing the laser to be more resistant to the perturbation of the externally injected optical field. This is why stronger externally optical perturbation is required to observe instabilities and chaos in the system at a higher injection current level.

6.2.4 *Coexistence of Chaotic Attractors in Optically Injected Semiconductor Lasers*

A nonlinear system has the nature of multistability under a certain condition of the parameters. Namely, the system may have coexistent states of different chaotic attractors for the same parameter set. Which attractor the system converges to strongly depends on the initial conditions. Indeed, coexistence of chaotic orbits has

been observed in various systems of semiconductor lasers (Masoller and Abraham 1998; Heil et al. 1998, 1999; Sukow et al. 1999; Viktorov and Mandel 2000). In optically injected semiconductor lasers, multistability and coexistence of chaotic attractors have also been studied (Wieczorek et al. 2000, 2001a, b, c, 2002). Here, we present such examples. Under a certain experimental configuration, we always observe a particular chaotic attractor, since the process of obtaining chaotic oscillation is generally the same. Therefore, we usually observe a chaotic oscillation for one of the chaotic attractors in a fixed experimental condition even if multistabilities are involved in the system. However, if the separation between the two coexisting attractors in the high-dimensional phase space is not so far away, switching from one attractor to the other may occur due to, for example, noises involved in the system. Indeed, transition of the state from one chaotic oscillation to another has been experimentally observed (Heil et al. 1998, 1999).

Using the bifurcation theory, it is easy to know whether a nonlinear system has coexisting attractors under the operating condition when the system exhibits bistability or multistability. However, the characteristics of the coexisting attractors cannot be obtained using the bifurcation analysis. With the simulation method, the existence of the bistability or multistability is found by numerically simulating the system with different initial conditions under the same operating parameters. Figure 6.12 shows the numerical result for the map of coexistence states in semiconductor lasers subjected to optical injection (Wieczorek et al. 2000). The plot is a similar one in the phase space as shown in Figs. 6.10 and 6.11, but normalized axes

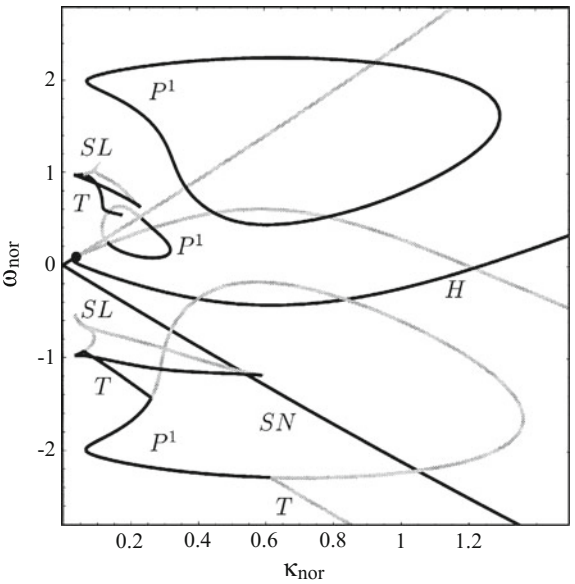

Fig. 6.12 Bifurcation diagram showing coexistence states in the phase space of the normalized frequency detuning and the injection ratio. The *vertical axis* is the normalized frequency of $\omega_{nor} = \Delta\omega/\omega_R$, and the *horizontal axis* of the injection ratio is also normalized as $\kappa_{nor} = \kappa_{inj}A_m/\omega_R\tau_{in}A_{0s}$. P^1 period-doubling bifurcations, *SL* saddle-nodes of limit cycles, *T* torus, *H* Hopf bifurcation, and *SN* saddle-node bifurcation [after Wieczorek et al. (2000); © 2000 Elsevier]

are used. Each point in this plane corresponds to a particular phase portrait, which contains more than one attractor. Black parts of bifurcation curves correspond to supercritical bifurcations in which attractors bifurcate and gray parts correspond to subcritical bifurcations of repelling objects. Subcritical bifurcations are less important from an experimental point of view, but we trace them out as they may produce stable objects for instance in a subcritical torus bifurcation or change to supercritical.

In Fig. 6.12, the region inside the straight line from zero detuning to negative detuning is the stable injection locking area. A detailed explanation of the map is found in the reference (Wieczorek et al. 2000). We here focus on the points that weigh with actual observations. In the stable region, there exist areas for the saddle-node bifurcation (SN) and the Hopf bifurcation (H). When the black part of SN is crossed, one of the bifurcating stationary points is an attractor. It physically corresponds to the laser operating at constant power and at the frequency of the injected light, meaning that the laser locks to the input signal. On the other hand, along the gray part of the curve SN, a repellor and a saddle point bifurcate. Along the black part of H, an attracting periodic orbit is born from the attracting stationary point and this corresponds physically to the undamping of the relaxation oscillation. Physically, the appearance of a new orbit means that some resonance in the laser gets excited, often because the operational parameters $\kappa_{\mathrm{nor}} = \kappa_{\mathrm{inj}} A_m / \omega_{\mathrm{R}} \tau_{\mathrm{in}} A_{0s}$ and $\omega_{\mathrm{nor}} = \Delta\omega/\omega_{\mathrm{R}}$ drive the laser close to the relaxation frequency or its multiples. In Fig. 6.12, the two saddle nodes of the limit cycle bifurcation curves starting with a cusp at $\omega_{\mathrm{nor}} \approx \pm 1$ represent a resonance between the relaxation oscillation frequency of the laser and the detuning of the injected light from the free running laser frequency.

Starting from different initial conditions, the nonlinear system may have different attractors in the phase space, even if the parameters have the same values as shown in the previous figure. Figure 6.13 shows examples of attractors in multistability states in the phase space of the imaginary part of the field, E_y (where the complex field E is given by $E = E_x + i\,E_y$), and the carrier density n (Wieczorek et al. 2000). The plots are the same conditions as those in Fig. 6.12. Figure 6.13a shows the plot of three attractors. Figure 6.13b, c are periodic states of period-1 with small amplitude and large periodic orbit, respectively. Figure 6.13d corresponds to a quasi-periodic oscillation on a torus. As has already been discussed, which of the attractors the system settles down to depends on the initial conditions. Furthermore, when a parameter is swept gradually through a region of multistability, then, one will find hysteresis loops with sudden jumps from one attractor to another at different values of the parameter, depending on the direction of the sweep.

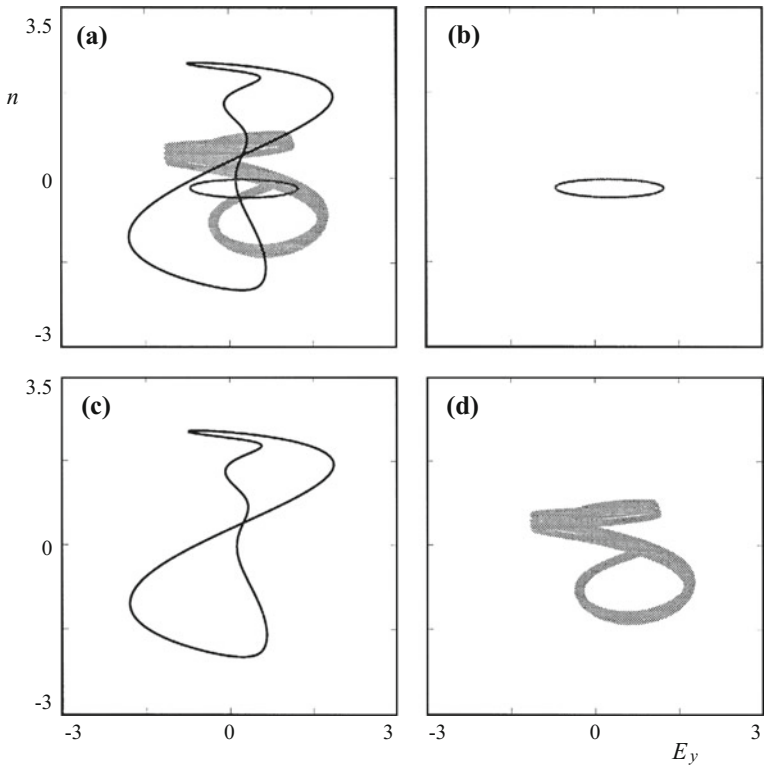

Fig. 6.13 Coexistence state of attractors at $\kappa_{nor} = 0.29$ and $\omega_{nor} = -1.37$. **a** Simultaneous plot of three attractors, **b** running phase solution, **c** large periodic orbit, and **d** quasi-periodic motion on a torus [after Wieczorek et al. (2000); © 2000 Elsevier]

6.3 Enhancement of Modulation Bandwidth and Generation of High Frequency Chaotic Oscillation by Strong Optical Injection

6.3.1 Enhancement of Modulation Bandwidth by Strong Optical Injection

The modulation bandwidth of a semiconductor laser at free running state is limited by the relaxation oscillation frequency. However, when a semiconductor laser is strongly injected under stable conditions, the modulation bandwidth of the slave laser is greatly enhanced. At the same time, the suppression of laser noises is achieved, but the strong modulation gives rise to frequency chirping in the laser oscillation. The effects of noises and frequency chirping under optical injection are critical for the laser operation (Piazzolia et al. 1986; Yabre 1996). In a locking–unlocking bistable state, a large modulation current can unlock the laser. In a state

near or beyond the Hopf bifurcation boundary, the dynamic instability of the laser can lead to high broadband noise and large frequency chirping. Also, the enhancement of the modulation bandwidth of semiconductor lasers subjected to strong injection has been demonstrated (Simpson et al. 1995, 1996; Simpson and Liu 1997; Chen et al. 2000; Wang et al. 1996, 2008). For weak optical injection and optical feedback, the modulation bandwidth is increased due to the increase of the photon number within the internal cavity, since the relaxation oscillation frequency is proportional to the square root of the photon number (see (3.87)). The amount of the shift of the cutoff frequency is up to ten percent at most. However, the cutoff frequency of the laser under strong optical injection is greatly enhanced up to several times the relaxation oscillation frequency of the free running laser. Therefore, a different explanation for the origin of the enhanced modulation bandwidth may be required to understand the phenomenon. The bandwidth-enhanced semiconductor laser is very useful as a broadband light source for optical communications.

Figure 6.14 is an example of experimental results of the enhancement of the modulation bandwidth. For a modulation of a small sinusoidal wave of 12 GHz to the bias injection current, the modulated laser output is attenuated and is only −27.49 dBm without optical injection as shown in Fig. 6.14a, since the modulation is far away from the relaxation oscillation frequency (about 3 GHz). On the other hand, the modulation efficiency is increased up to 10 dBm by a strong optical injection (Fig. 6.14b). As will be discussed in Chap. 13, chaotic carrier frequency is the measure of the maximum data transmission rate in optical secure communications based on chaos synchronization in semiconductor laser systems. The chaotic carrier frequency is also increased by a strong optical injection and a large capacity of the channels for the communication is expected.

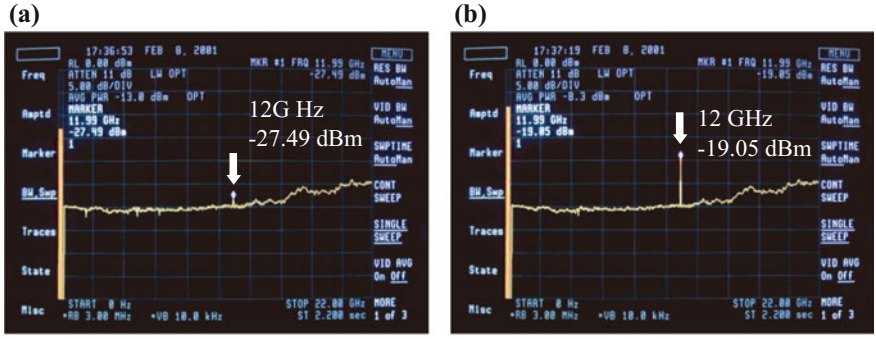

Fig. 6.14 Experimental result of the modulation bandwidth of a strongly optical injection-locked semiconductor laser. The laser is modulated by a small sinusoidal signal at 12 GHz. The modulation efficiency without optical injection is −27.49 dBm. The efficiency with optical injection is −19.05 dBm. The relaxation oscillation frequency of the DFB laser used is 3 GHz at free running state

The enhancement of the modulation bandwidth in a semiconductor laser under strong optical injection is numerically studied based on the rate equations. Wang et al. (1996) investigated the modulation response for a small signal to the bias injection current using a linear stability analysis. Figure 6.15 is the result. The frequency detuning between the master and slave lasers is assumed to be zero in this case. The cutoff frequency read from the resonance frequency is 12.6 GHz for the injection ratio of $S_{inj}/S_s = 0.44$ (curve d), while the relaxation oscillation frequency is 3.4 GHz at the free running state (curve a). In addition, the response is almost flat well below the cutoff frequency and the modulation bandwidth is enhanced up to four times compared with that of the free running state. As has already been discussed, the relaxation oscillation frequency is proportional to the square root of the photon number and the photon number is a function of the bias injection current. To obtain the equivalent modulation bandwidth of 12 GHz for the free running laser, we would require the bias injection current to be seven times larger than that of the free running state, which corresponds to almost 13 times the threshold injection current and might damage the laser. Thus, the method of strong optical injection is effective for greatly enhancing the modulation bandwidth in semiconductor lasers. Wang et al. (1996) conducted a linear stability analysis for the cutoff frequency under strong optical injection and obtained the approximate solution as

$$v_{\text{enhanced}} = \frac{1}{2\sqrt{3}\pi}\left[K_e - \left(\frac{K_a}{S_s}\right)^2 + \left\{\left(\frac{K_a}{S_s}\right)^2 - 4K_e\left(\frac{K_a}{S_s}\right)^2 + K_e^2 - 6K_aK_b\alpha G_n^2(n_s - n_0)\right\}^{1/2}\right]^{1/2} \tag{6.22}$$

where the parameters in the above equation are given by

$$K_e = \frac{1}{\tau_{in}^2}\frac{S_{inj}}{S_s} \tag{6.23}$$

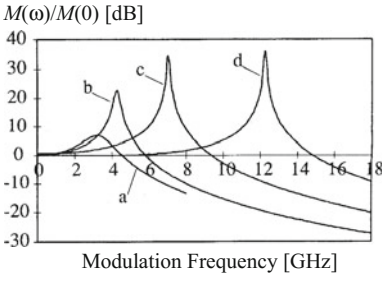

Fig. 6.15 Normalized modulation response of a semiconductor laser at $J = 2.4J_{th}$. *a* Free running laser, *b* $S_{inj}/S_s = 0.011$, *c* $S_{inj}/S_s = 0.092$, *d* $S_{inj}/S_s = 0.44$. S_{inj} and S_s are the photon numbers injected from the master laser and the steady-state value of the free running slave laser [after Wang et al. (1996); © 1996 IEEE]

$$K_a = \frac{2}{\tau_{\text{in}}}\sqrt{S_{\text{inj}}S_s}\cos(\phi_s - \phi_m) = -\left\{G_n(n_s - n_0)(1 - \varepsilon_s S_s) - \frac{1}{\tau_{\text{ph}}}\right\}S_s - R_{\text{sp}} \tag{6.24}$$

$$K_b = \frac{1}{\tau_{\text{in}}}\sqrt{\frac{S_{\text{inj}}}{S_s}}\sin(\phi_s - \phi_m) = \frac{1}{2}\alpha G_n(n_s - n_0) - \Delta\omega \tag{6.25}$$

As will be shown later, the cutoff frequency is linearly proportional to the injection power. Therefore, the origin of the enhancement of the modulation bandwidth does not simply come from the increase of the photon number in the active layer. It is explained by the interference between the optical frequency of the original laser oscillation and the shifted frequency due to the strong optical injection.

The enhancement of the modulation bandwidth is also strongly dependent on frequency detuning between the master and slave lasers. Figure 6.16 shows the dependence of the modulation response in the presence of frequency detuning between the master and slave lasers (Chen et al. 2000). The conditions of the numerical simulations are as follows; the laser is assumed to be an index-guided GaAs/AlGaAs quantum-well laser and is biased at $\hat{J} = 0.67$ (corresponding to $J = 1.67J_{\text{th}}$), where $\hat{J}$ is the scaled injection current defined by $\hat{J} = (J/ed - n_s/\tau_s)/(n_s/\tau_s)$. The injection parameter defined by $\kappa'_{\text{nor}} = (\kappa_{\text{inj}}\tau_{\text{ph}}A_m)/(\tau_{\text{in}}A_s)$ is

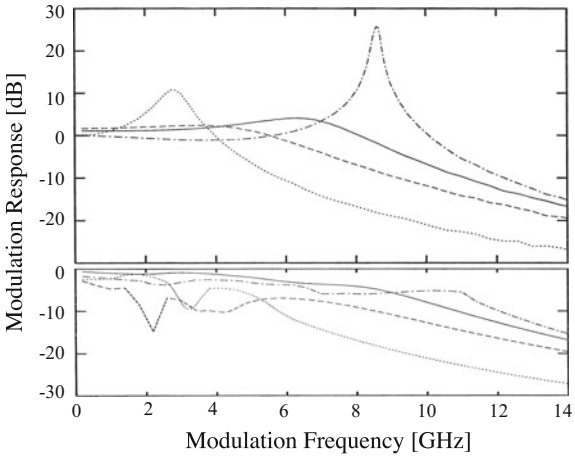

Fig. 6.16 Normalized current modulation response in the presence of the frequency detuning Δv between the master and slave lasers. *Dash–dotted curve* injection locking at Δv = 1 GHz. *Solid curve* injection locking at Δv = −10 GHz. *Dashed curve* injection locking at Δv = −18 GHz. *Dotted curve* free running. The curves in the *upper plot* are the response for m = 1%, and those in the *lower plot* are the responses for m = 100%. The 0 dB in the *lower plot* corresponds to the 0 dB in the *upper plot* in order to make all the response curves comparable [after Chen et al. (2000); © 2000 Elsevier]

fixed at a moderate level $\kappa'_{nor} = 0.2$, while different values of frequency detuning representing different locking conditions are chosen. At $\kappa'_{nor} = 0.2$, the stable locking region is bounded by $\Delta\nu$ = 1 GHz and $\Delta\nu$ = −13 GHz, where $\Delta\nu$ = 1 GHz is the Hopf bifurcation boundary. Between $\Delta\nu$ = −13 GHz and $\Delta\nu$ = −22 GHz is a region of locking–unlocking bistability, where the laser can be either locked or unlocked depending on the initial condition. Under that condition, the laser cannot be locked when the frequency detuning is more negative than −22 GHz. Relative to the free running laser, a broadband noise reduction occurs in the locked region when the injection field is negatively detuned beyond $\Delta\nu$ = −3 GHz. The three representative values of frequency detuning chosen in this case are $\Delta\nu$ = 1 GHz on the Hopf bifurcation boundary (dash-dotted curves in the figures), $\Delta\nu$ = −10 GHz in the stable locking region (solid curves), and $\Delta\nu$ = −18 GHz in the locking-unlocking bistability region (dashed curves).

In the figure, the upper plot shows the response for a small modulation index of m = 1% and the graphs are normalized to the low frequency response of the laser in its free running condition, under the four different operating conditions. The lower plot in Fig. 6.16 shows the distorted current modulation response when the modulation index reaches m = 100%. At a given modulation strength, negatively shifting the frequency detuning of the injected optical field generally reduces the distortion in the current modulation response if the laser remains stably locked. However, when the laser is injection-locked in the bistability region, a high modulation index can cause instability by unlocking the laser. As a result, the modulation response in such an operating condition becomes very irregular, as can be seen from the dashed curve (−18 GHz) in the lower plot of Fig. 6.16. For weak current modulation with small values of the modulation index, the modulation response will be obscured by the intrinsic laser noise. For the change of the modulation index, the laser noise induces insignificant differences between the overall response due to the combined modulation current and intrinsic noise and the modulation response alone when the modulation index m is larger than 1%. Below m = 1%, the relative importance of the laser noise gradually increases and the laser noise induces fluctuations in the response that obscure the modulation response.

Nevertheless optical feedback is strong, the optical injection power in the previous examples is still smaller than the solitary slave laser emission power. For stronger optical injection above the slave optical power, we can expect much broader bandwidth enhancement. Figure 6.17 shows such an example. Lau et al. (2008) experimentally investigated modulation bandwidth for the condition of ultra strong optical injection more than +10 dB and large frequency detuning of about ±100 GHz. The figure shows the boundaries of enhanced resonance frequencies in the phase space of the optical injection ratio and the frequency detuning within the stable region of a used laser. The laser used is an InGaAsP DFB laser of the cavity length of 500 μm operating at a wavelength of 1.55 μm. The bias injection current is $1.3J_{th}$ and the corresponding relaxation oscillation frequency at solitary mode is ν_R = 3 GHz. For an optical injection of 18 dB (the actual optical injection is estimated as about 14 dB due to losses in the optical system) and the

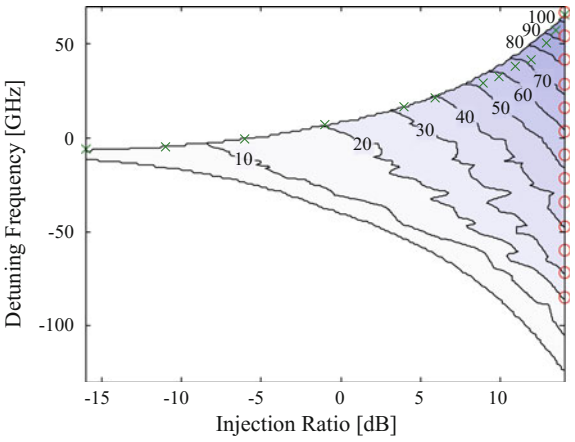

Fig. 6.17 Enhanced resonance frequency as a function of the detuning frequency and the injection ratio. Each value denotes the enhanced boundary resonance frequency [after Lau et al. (2008); © 2008 OSA]

frequency detuning from the solitary laser of +67 GHz, the modulation bandwidth is enhanced up to 107 GHz. By strong optical injection ratio with large frequency detuning, the stable area is largely expanded, especially in the region of strong optical injection. The attained value of the resonance frequency of 107 GHz is not the limitation of the device characteristic itself, but the result is limited only by the response of the equipment. Lau et al. also studied an enhancement of a modulation bandwidth for a VCSEL of a wavelength of 1.55 μm. The laser is biased at $3J_{th}$ with the corresponding relaxation frequency of 5 GHz. The resonance frequency enhancement of 104 GHz is obtained for the optical injection of 13.6 dB and the frequency detuning of +102 GHz.

One of merits of optical injection locking in semiconductor lasers is the increase of rf gain. However, there exists a tradeoff between the enhancement of modulation bandwidth and the increase of rf gain. For a fixed optical injection ratio, the rf gain of a small amplitude modulation for the bias injection current varies with detuning. For a large positive frequency detuning, one can obtain a sharp and high peak of the resonance frequency; however, the gain for the lower frequency component tends to be lower than that for a case of smaller frequency detuning. On the other hand, a high rf gain but a small peak of the resonance frequency is attained for an optical injection with a small frequency detuning. Figure 6.18 shows a summary for such examples obtained by experiments (Chrostowski et al. 2006). Figure 6.18a is a plot for enhanced modulation frequencies for four VCSELs with almost the same optical injection ratios versus wavelength detuning. For the increase of the detuning, the modulation bandwidth is increased (it is noted that the graph is plotted not for the frequency but for the optical wavelength). While, Fig. 6.18b is a plot for enhanced resonance frequency at the injection–current modulation of 1 GHz versus wavelength detuning. With the increase of the frequency detuning, the rf gain decreases. The tradeoff is not only a particular feature for VCSELs but also other types of semiconductor lasers, and the similar trend can be expected for edge-emitting semiconductor lasers.

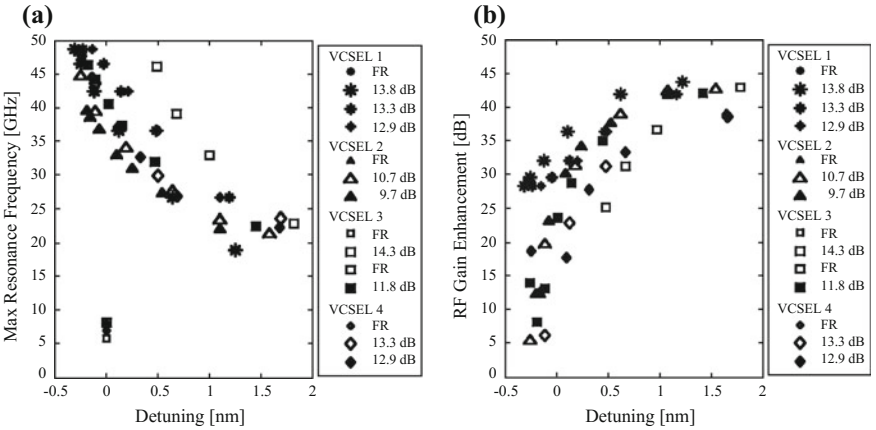

Fig. 6.18 Tradeoff between the resonance frequency and the rf gain. **a** Resonance frequency of four VCSELs versus wavelength detuning. **b** Rf gain measured at 1 GHz for four VCSELs versus wavelength detuning [after Chrostowski et al. (2006); © 2006 IEEE]

6.3.2 *Origin of Modulation Bandwidth Enhancement*

The origin of the enhancement of modulation bandwidth by strong optical injection is explained by Murakami et al. (2003). They consider the frequency shift of the slave laser induced by strong optical injection. The expansion of the modulation bandwidth is realized by the interference between the original optical frequency at the free running state and the shifted frequency after the injection. According to their explanation, the difference between the two frequencies corresponds to the expanded modulation bandwidth. Figure 6.19 schematically shows the model of the frequency shift. Let the angular frequency of the slave laser at the free running state be given by ω_0 and that of the master laser be ω_{inj}. In the figure, the frequency detuning is assumed to be positive, but the other case will be reduced to the same result. By a strong optical injection, the carrier density in the slave laser increases. This induces the change of the optical frequency of the laser oscillation and results in red-shift of the oscillation frequency. Using the change of the carrier density δn, the laser once oscillates at an optical angular frequency ω_{shift} and the shift of the laser angular frequency after the injection is given by

$$\Delta\omega_{\text{shift}} = \frac{1}{2}\alpha G_n \delta n \tag{6.26}$$

The change of the carrier density δn is proportional to the strength of optical injection. The frequency shift given by (6.26) has the same form as the first term in (6.5). In actual fact, the frequency of the slave laser is locked to the frequency of the injection laser (angular frequency of ω_{inj}). Accordingly, the injection-locked laser may operate at a frequency different from its cavity resonance condition, namely

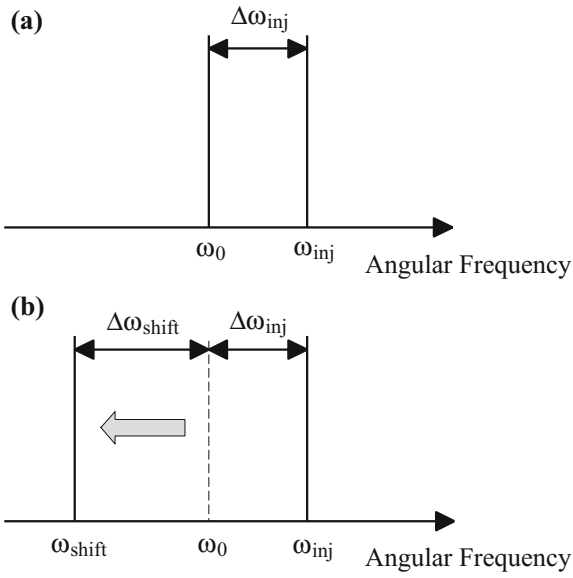

Fig. 6.19 Resonant condition of a semiconductor laser in the presence of optical injection. **a** Spectrum before optical injection. ω_0 is the angular frequency of the solitary laser, ω_{inj} is the frequency of the injected light, and $\Delta\omega_{inj}$ is the frequency detuning between them. **b** Cavity resonant condition under injection locking. ω_{shift} is the cavity resonance frequency shifted from ω_0 by $\Delta\omega_{shift}$ due to optical injection

operating at ω_{inj}, not at ω_{shift}. Such frequency detuning between ω_{inj} and ω_{shift} influences the modulation bandwidth, as predicted by Simpson et al. (1996).

Here, we consider the transient situation. The field corresponding to the shifted cavity resonance ω_{shift} is once excited and interference between the two components of the angular frequencies ω_{shift} and ω_{inj} occurs. Then, the beat between the two frequencies is induced in the output of the slave laser. However, sufficient gain is not allocated to this mode and the oscillation of the mode rapidly decays out, since this is a transient field. The oscillation angular frequency of the slave laser is restored to ω_{inj}. The laser output may exhibit a damping oscillation at the beat frequency due to such transient interference. Note that this damped oscillation differs from the relaxation oscillation in the physical mechanism, because the relaxation oscillation results from an interaction or coupling between photon and carrier through the stimulated emission. Therefore, from (6.5), the resonance angular frequency produced by the interference $\omega_{res} = \Delta\omega_{inj} - \Delta\omega_{shift}$ is given by

$$\omega_{res} = \Delta\omega_{inj} - \Delta\omega_{shift} = -\frac{1}{\tau_{in}}\sqrt{\frac{S_{inj}}{S_s}}\sin\psi_s \tag{6.27}$$

Following the above explanation, the dependence of the resonance frequency in the presence of strong optical injection is calculated (Murakami et al. 2003). Figure 6.20 shows the plots of dependence of the injection ratio (amplitude) and the frequency detuning on the cutoff frequency. Figure 6.20a is the dependence of the cutoff frequency on the injection ratio at the frequency detuning of +0.5 GHz. Under a strong optical injection condition, the cutoff frequency is linearly proportional to the injection ratio in accordance with the prediction in (6.27). In the

figure, three data are plotted; the solid line is the prediction calculated from (6.27), circles are the direct numerical calculation from the rate equations, and triangles are obtained from the linear stability analysis. In strong optical injection of over 30%, the three plots coincide well with each other. Figure 6.20b is the plot of the cutoff frequency for the frequency detuning at a high optical injection ratio of 40%. The cutoff frequency tends to increase with increased detuning from negative to positive values. Thus, the enhancement of the cutoff frequency under strong optical injection is explained by the interference between the injection laser frequency and the implicit frequency shift of the slave laser induced by the strong optical injection.

The definition of the injection and average intensities, S_{inj} and S_s, in (6.27) are the measures in the internal laser cavity. For the external injection intensity $S_{\text{inj,ext}}$, it has the relation with the internal intensity as (Lau et al. 2007)

$$S_{\text{inj}} = \frac{(1 - r_0^2)^2}{r_0^2} \frac{S_s}{S_{s,\text{out}}} S_{\text{inj,ext}} \tag{6.28}$$

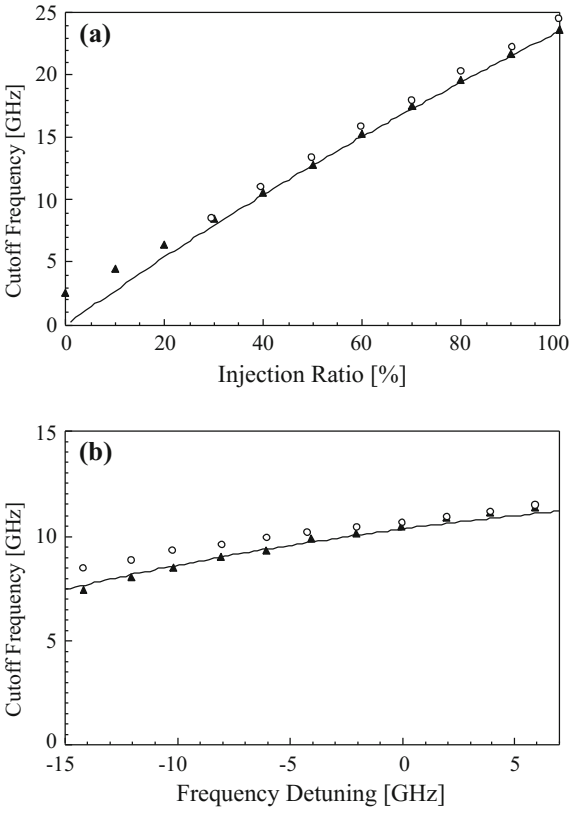

Fig. 6.20 Dependence of the resonance frequency on **a** the injection rate and **b** the frequency detuning. *Circles* represent the numerical results, *triangles* are the results obtained from the stability analysis, and the *solid line* is the theoretical curve of (6.27)

where r_0 is the laser facet reflectivity defined in (4.1) and $S_{s,\text{out}}$ is the average intensity of the slave laser outside of the cavity. For edge-emitting semiconductor lasers, the orders of the magnitudes of internal and external injections are almost the same. In the case of VCSELs, the amount of the internally injected intensity is very small compared with that of the external intensity, since the facet reflectivity of VCSELs is usually higher than 99%. On the other hand, the injection efficiency is proportional to $1/\tau_{\text{in}}$, so that the effect of optical injection to VCSELs is relatively strong due to their short cavity lengths. From (6.27), the attainable maximum enhanced modulation frequency is given by

$$\omega_{\text{res,max}} = \frac{1}{\tau_{\text{in}}}\sqrt{\frac{S_{\text{inj}}}{S_s}} \tag{6.29}$$

As another expression, using the cavity Q factor of lasers, the fraction of the enhanced resonance frequency $\omega_{\text{res,max}}$ can be defined by

$$\omega_{\text{res,max}} = \frac{\omega_0}{2Q}\sqrt{\frac{S_{\text{inj,ext}}}{S_{s,\text{out}}}} \tag{6.30}$$

where ω_0 is the laser frequency and $Q = (\omega_0/v_g)\cdot\{r_0/(1-r_0^2)\}$ (v_g is the group velocity of light in the laser medium). Interestingly, the order of the Q-factor values for common edge-emitting semiconductor lasers and VCSELs are almost the same. For example, a typical edge-emitting semiconductor laser with l = 500 μm and r_0 = 0.3 has the same Q ($Q = 6.7 \times 10^3$) as a typical VCSEL with l = 2 μm and r_0 = 0.995. Therefore, for the same optical injection strength, we can expect almost the similar enhancement of the bandwidth both for them.

The above relation is well coincident with experimental results. From the detailed study, an approximate relation including a small resonance frequency, ω_{res}, due to weak optical injection is obtained as (Lau et al. 2007, 2008, 2009)

$$\omega_{\text{enhanced}}^2 \approx \omega_{\text{R}}^2 + \omega_{\text{res}}^2 \tag{6.31}$$

where ω_{R} is the relaxation oscillation angular frequency of a solitary laser. For a large resonance frequency of $\omega_{\text{res}} \gg \omega_{\text{R}}$ (namely, strong optical injection), the relation $\omega_{\text{enhanced}} = \omega_{\text{res}}$ holds. In accordance with the enhancement of the modulation bandwidth, the damping factor is also enhanced. The damping factor except for near the resonance peak frequency under strong optical injection is approximated as

$$\Gamma_{\text{enhanced}} \approx \Gamma_{\text{R}} - G_n(n_{\text{th}} - n_0) \tag{6.32}$$

where Γ_{R} is the damping factor of the solitary laser defined in (3.86). Note that Γ_{R} is taken as a negative value. Also the damping factor is enhanced by the reduction of gain below threshold. The result is interpreted as follows; the injection-locked

laser resonance is primarily due to energy oscillating between the slave field and phase interfering with the injected light from the master laser. The reduced gain allows a portion of this oscillation energy to be lost to the carrier. We can observe the similarity of the damping enhancement in an RLC oscillator in electric circuits. On the other hand, the damping factor closed to the resonance frequency is given by

$$\Gamma_{\text{enhanced,res}} \approx \frac{\alpha}{\tau_{\text{ph}}\omega_{\text{res}}} G_n S_s - G_n(n_{\text{th}} - n_0) \tag{6.33}$$

Lau et al. (2009) also demonstrated theoretically and experimentally that the modulation bandwidth was further enhanced by amplitude and/or phase modulations of the master laser under strong optical injection.

6.3.3 Visual Solution for Resonance Frequency

The enhancement of the resonance frequency under strong optical injection with relation to the injection ratio and the injection frequency can be easily understood and be visually solved by the trajectory of ellipse for the phase space of $\Delta\omega_{\text{shit}}$ and $\Delta\omega_{\text{inj}}$. Putting $\Delta\omega_{\text{shift}} = x$ and $\Delta\omega_{\text{inj}} = y$ with (6.4), (6.5), and (6.26), the variables x and y are expressed by functions of ψ_{s} as

$$x = -\frac{\alpha}{\tau_{\text{in}}}\sqrt{\frac{S_{\text{inj}}}{S_{\text{s}}}}\cos\psi_{\text{s}} = \alpha A\cos\psi_{\text{s}} \tag{6.34}$$

$$y = -\frac{\sqrt{1+\alpha^2}}{\tau_{\text{in}}}\sqrt{\frac{S_{\text{inj}}}{S_{\text{s}}}}\sin(\psi_{\text{s}} + \tan^{-1}\alpha) = -\sqrt{1+\alpha^2}A\sin(\psi_{\text{s}} + \theta) \tag{6.35}$$

with $A = \frac{1}{\tau_{\text{in}}}\sqrt{\frac{S_{\text{inj}}}{S_{\text{s}}}}$ and $\theta = \tan^{-1}\alpha$. Then, x and y form an ellipse and the implicit equation to describe the relationship can be written by

$$\frac{x^2}{\alpha^2 A^2} + \frac{y^2}{(1+\alpha^2)A^2} - \frac{2\sin\theta}{\alpha\sqrt{1+\alpha^2}A^2}xy = \cos^2\theta \tag{6.36}$$

Using relations with $\sin(\tan^{-1}\alpha) = \alpha/\sqrt{1+\alpha^2}$ and $\cos(\tan^{-1}\alpha) = 1/\sqrt{1+\alpha^2}$, the above equation reads

$$x^2 + \frac{\alpha^2}{1+\alpha^2}y^2 - \frac{2\alpha^2}{1+\alpha^2}xy = \frac{\alpha^2 A^2}{1+\alpha^2} \tag{6.37}$$

Figure 6.21 shows the schematic view of an ellipse of the above equation. Taking into the injection locking condition given by (6.11) as $-\frac{\pi}{2} \le \psi_s \le \cot^{-1}\alpha$ and the definition of (6.1), the value of the solution for x always takes negative. The

possible injection locking solution is displayed as a bold solid line on the ellipse in Fig. 6.21. The upper boundary of the point of positive detuning corresponds to the solution for $-\pi/2$. The value of the angular frequency detuning is $y_+ = A = \sqrt{S_{inj}/S_s}/\tau_{in}$. By lowering the detuning, the solution goes down to the lowest possible injection locking point along the ellipse denoted by y_{min} remaining in the negative x value. The point is the lowest boundary of the solution for the negative detuning (corresponding to the solution for $\cot^{-1}\alpha$). The minimum value of y is $y_{min} = -\sqrt{1+\alpha^2}A$. The x axis denotes the coordinate for the angular frequency shift of $\Delta\omega_{shift}$ and the y axis represents that for the angular frequency of optical injection of $\Delta\omega_{inj}$. Note that the origin of the coordinate denotes the angular frequency of the slave laser. Then, the positive value of y corresponds to positive frequency detuning of optical injection, while the negative value to negative detuning. Consider visual solutions for the resonance frequency from Fig. 6.21. For example, we pay attention to the two points (denoted by blue circles) which intercept the ellipsoid and the line $y = x$ with blue horizontal line with arrows. The right circle denotes the angular frequency detuning and the left circle represents the angular frequency shift. Then, the separation between them is the resonance angular frequency according to (6.27).

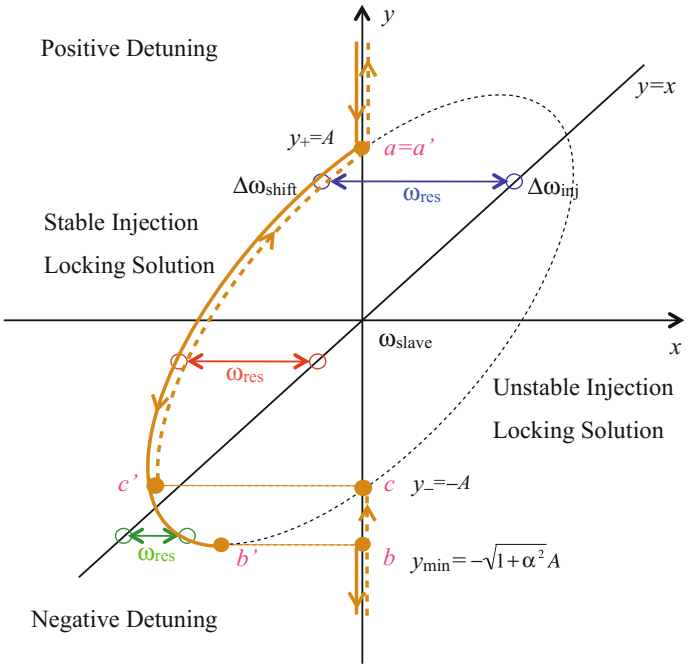

Fig. 6.21 Ellipse model of bandwidth enhancement in the phase space of the frequency detuning, $\Delta\omega_{inj}$, (y axis) and the frequency shift induce by optical injection, $\Delta\omega_{shift}$, (x axis). ω_{res} is the enhanced laser bandwidth. See details in the text

The resonance angular frequency is given by (6.27) and is written by a function of the angular frequency detuning of y as

$$\omega_{\mathrm{res}} = y - x = \frac{1}{1+\alpha^2} y + \frac{\alpha^2}{\sqrt{1+\alpha^2}} \sqrt{A^2 - \frac{y^2}{1+\alpha^2}} \tag{6.38}$$

Then, the possible maximum resonance is attained at $y = y_+ = A$ and the resonance angular frequency takes a value given by (6.29). It is noted that the maximum resonance frequency is inversely proportional to the internal round trip time of light in the laser cavity ($A \propto 1/\tau_{\mathrm{in}}$). The discussion here is for narrow-strip edge-emitting semiconductor lasers, however similar results could be obtained for other semiconductor lasers with different structures. Therefore, we can expect larger resonance frequency for optically injected VCSELs, since the internal round trip time is much smaller than other semiconductor lasers (the round trip time is usually an order of less than two-digit compared to edge-emitting semiconductor lasers). The method of the graphical solution for resonance frequency can also be extended to multimode semiconductor lasers and semiconductor lasers with crossed-polarization oscillations (Guo et al. 2012). The ellipsoid enlarges as the increase of the optical injection ratio under a fixed α parameter value, as remaining the same eccentricity e. While the eccentricity e decreases with the increase of the α parameter under the same optical injection ratio, as remaining the cross points of $\pm y_+$. The α parameter is only a function of the eccentricity as (Guo et al.2012)

$$\alpha = \sqrt{\frac{e^4 + (2-e^2)\sqrt{e^4+4e^2-4}}{8(1-e^2)}} \tag{6.39}$$

Thus, we can calculate the α parameter from the eccentricity of the ellipsoid.

In actual, the resonance has a hysteresis for the continuous increase or decease of the frequency detuning. For example, when the frequency of the master laser is lowered from large positive detuning in Fig. 6.21, the slave laser oscillates at the free-running frequency without locking. At or below point a, the slave laser is locked to the master laser and the laser frequency shifts to $\Delta\omega_{\mathrm{shift}}/2\pi$ along the ellipsoid with stable injection locking condition. For the negative frequency detuning, the slave laser is unlocked at point b' and the frequency of the slave laser shifts to its original frequency (point b). Then, the slave laser again oscillates at the free-running frequency below point b. On the other hand, the slave laser is not locked at point b when the master laser frequency is increased form a large negative detuning frequency, since the black-dot line is the unstable injection locking solution. Then, the slave laser frequency stays the stable free-running oscillation frequency along the brown dotted line. When the master laser frequency reaches at point c, which is a lower cross point of the ellipsoid with y axis, the slave laser frequency jumps to point c' and goes up along the ellipsoid. At point a, the slave laser is again unlocked from the master laser and the laser oscillates at the free-running frequency. To reproduce the hysteresis, a care must be taken in the

numerical calculation for a set of rate equations. At first, either locking or unlocking state is calculated under certain parameter conditions. If the point is a locking stable one, the values of the parameter set for the point must be used for the next simulation. While free running stable values should be used for the unstable unlocking state as is easily understood from Fig. 6.21.

6.3.4 Modulation Response by Strong Optical Injection

The effects of the injection current modulation on the response distortion and the noise compression can be evaluated by eye patterns with digital signals. The capability of data transmission in optical communications is calculated in Fig. 6.22 (Chen et al. 2000). The eye patterns are numerically calculated from the rate equations with strong optical injection. In the numerical simulations, eye patterns

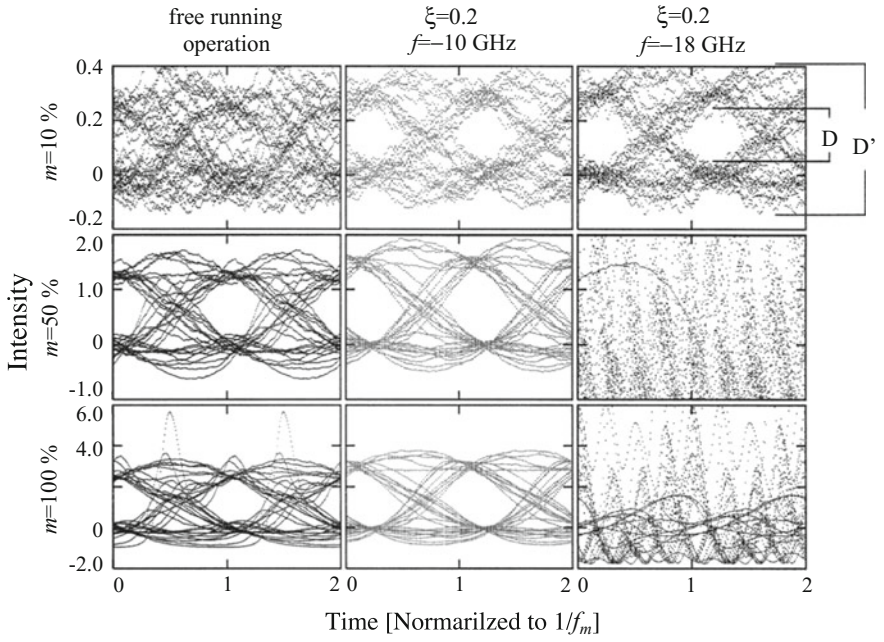

Fig. 6.22 Eye pattern for square wave modulations. The bit rate is chosen as the corresponding resonance frequency for each operating condition: the bit rate f_m = 2.9 GHz is chosen for the free running operation, f_m = 4.7 GHz for $\Delta\nu$ = −18 GHz, and f_m = 6.8 GHz for $\Delta\nu$ = −10 GHz. The optical injection rate ξ is defined as $\xi = \tau_{ph}\kappa_{inj}/\tau_{in}$. The eye opening obtained from the operating condition $\Delta\nu$ = 1 GHz is zero for the range of the bit rate we are concerned with, so the eye patterns are not shown. The intensity of the eye patterns is the differential intensity above or below the corresponding field intensity of the injection-locked laser without current modulation for each operating condition [after Chen et al. (2000); © 2000 Elsevier]

are generated by modulating the injection current of the semiconductor laser under the various operating conditions with a train of random raised-cosine functions:

$$J_m = \sum_{K=0}^{n} C_K h(t - KT) \tag{6.40}$$

$$h(t) = \frac{\sin\left(\frac{\pi t}{T}\right)\cos\left(\frac{\pi\beta_t t}{T}\right)}{\frac{\pi t}{T}\left[1 - \left(\frac{2\pi\beta_t t}{T}\right)^2\right]} \tag{6.41}$$

where C_K is a series of random numbers with the value 0 or 1, which represents digitized information, and $T = 1/f_m$, where the modulation frequency f_m represents the bit rate. The value of the parameter β_t is chosen to be 0.3 in this simulation.

Figure 6.22 shows the eye patterns for different modulation indexes at the modulation frequency of $f_m = 2.9$ GHz. The modulation frequency is equal to the relaxation oscillation frequency of the laser at the free running state. Three different modulation indexes $m = 10$, 50, and 100% are chosen to present the advantages of the injection-locked laser in the stable locking region. The eye patterns obtained in the condition when the laser is injection-locked at $\Delta v = -10$ GHz have clearer eye opening with less distortion or less noise than those obtained in other operating conditions. The relative eye opening shows the same tendency as the noise compression. For a small modulation index of $m = 10\%$, the modulation efficiency is much improved compared with that at the free running state. However, when the modulation index increases, the modulation signal with a modulation index of $m = 50\%$ unlocks the laser for a large negative frequency detuning ($\Delta v = -18$ GHz), resulting in zero eye opening. When the frequency detuning is positively shifted beyond the noise compression region, the eye opening also rapidly decreases to zero. Therefore, the eye opening obtained in the operating condition with $\Delta v = 1$ GHz is zero for a modulation index of any value.

6.3.5 *Suppression of Frequency Chirping by Strong Optical Injection*

It has already been noted that the chirping of frequency due to injection current modulation in a semiconductor laser is much suppressed by a strong optical injection. We here demonstrate an example. Usually, a change in the carrier density causes a change in the refractive index of the laser medium. This change in the index generates frequency chirping, which can place a considerable limitation on the modulation bit rate. The frequency chirping is measured by the normalized chirp to the power ratio CPR, which is defined as follows (Piazzolia et al. 1986):

$$\mathrm{CPR} = \frac{1}{2\pi R_P}\left|\frac{\mathrm{d}\phi}{\mathrm{d}t}\right| \tag{6.42}$$

where R_P is the modulation response. The frequency chirp originates from the linewidth enhancement factor α, which has a nonzero value in a semiconductor laser. Neglecting noise effects in a semiconductor laser and applying a small signal analysis, the relation between the linewidth enhancement factor α and CPR can be obtained by linearizing the rate equations around the locking operating point (Simpson et al. 1996). This relationship between α and the CPR can be expressed as follows:

$$\frac{1}{2\pi R_P}\left|\frac{\mathrm{d}\phi}{\mathrm{d}t}\right| \approx f_m \alpha \sqrt{\frac{f_m^2 + (u - v/\alpha)^2}{f_m^2 + (u + v/\alpha)^2}} \tag{6.43}$$

where u and v are given by

$$u = \frac{\kappa_{\mathrm{inj}}}{2\pi\tau_{\mathrm{in}}}\left|\frac{A_m}{A_s}\right|\cos\phi_L \tag{6.44}$$

$$v = \frac{\kappa_{\mathrm{inj}}}{2\pi\tau_{\mathrm{in}}}\left|\frac{A_m}{A_s}\right|\sin\phi_L \tag{6.45}$$

Here ϕ_L is the phase of the intracavity laser field relative to the injection field. An effective linewidth enhancement factor α_{eff}, which is the modified chirping parameter under injection locking, can be defined as follows:

$$\alpha_{\mathrm{eff}} \approx \alpha \sqrt{\frac{f_m^2 + (u - v/\alpha)^2}{f_m^2 + (u + v/\alpha)^2}} \tag{6.46}$$

Of course, the effective chirping parameter α_{eff} is equal to α when the laser is at the free running state ($u = v = 0$). The dependence of the effective chirping parameter on the modulation frequency f_m is shown in Fig. 6.23 (Chen et al. 2000). The injection locking of the laser at $\Delta\nu = -10$ GHz reduces the effective chirping parameter more than injection locking the laser at $\Delta\nu = -18$ GHz does. Positive shifting of the frequency detuning reduces the effective chirping parameter further until the boundary of the Hopf bifurcation is reached. For a large modulation index, the effective chirping parameter finally reaches that of the free running state. Therefore, the effect of the suppression for the chirping is remarkable for lower modulation frequency. When the effect of the intrinsic noise or that of the nonlinearity of the laser on the frequency chirping are significant, the simple relationship in (6.46) between the CPR and α is no longer valid. In this situation, it is not possible to simply represent the frequency chirping with an effective chirping parameter. Then, the measurement of the frequency chirping including the effects of

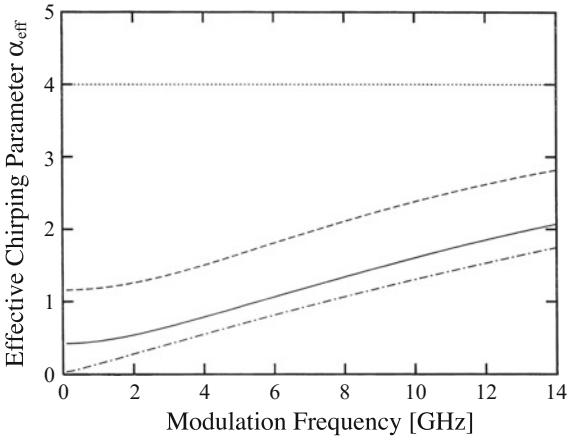

Fig. 6.23 Effective chirping parameter. Each *curve* corresponds directly to the curves in Fig. 6.16 that have the same style [after Chen et al. (2000); © 2000 Elsevier]

the intrinsic noise and the nonlinearity of the laser dynamics under a large modulation current is better quantified directly with the CPR.

From the detailed analysis for CPR, if the laser noise were not present, a significant reduction of the frequency chirping could be achieved by optical injection, and positively shifting the frequency detuning could further reduce the frequency chirping. In reality, however, when the modulation index is small, the chirp is dominated by the laser noise. As a result, the chirp follows the same tendency as the power noise. Therefore, reduction of the frequency chirping in a semiconductor laser is not always guaranteed by injection locking (Chen et al. 2000). A semiconductor laser injection-locked in a locking–unlocking bistable state cannot fully take such benefits because a large modulation current can unlock the laser. Further, one cannot operate in a state near or beyond the Hopf bifurcation boundary because of the high broadband noise and the large frequency chirping associated with the instability of the laser. A semiconductor laser operated in a stable state generally has better current modulation characteristics than in its free running state.

6.3.6 *Generation of High-Frequency Chaotic Oscillation by Strong Optical Injection*

Main chaotic carrier frequency in a semiconductor laser system has almost the same or nearly the relaxation oscillation frequency of the solitary laser. For example, the oscillation very close to the relaxation oscillation frequency is at first excited in a semiconductor laser with optical feedback for the increase of the feedback strength. For a further increase of the feedback, the laser typically shows chaotic oscillations via period-doubling or quasi-period-doubling routes. Therefore, the relaxation oscillation frequency of the laser is the measure of chaotic oscillations and it plays a crucial role in the chaotic dynamics. Especially, the bandwidth of the chaotic signal

is important in the chaotic secure communications discussed in Chap. 13. In such chaotic communications, the generation of a fast chaotic carrier signal is essential for a message transmission with higher bit rate. We here consider the generation of fast chaotic signals in semiconductor lasers both subjected to optical feedback and optical injection. There are two ways for enhancing chaotic carrier frequency by optical injection; one is a simple method in which a chaotic semiconductor laser such as induced by optical feedback is strongly optical-injected by a stable master laser (Wang et al. 2008). The other one is that a chaotic master laser light is strongly injected to a slave laser (Someya et al. 2009). The slave laser may behave stably at solitary mode. For either case, chaotic carrier frequency of an original relaxation oscillation of about 3 GHz is experimentally expanded up to 15–20 GHz under appropriate optical injection conditions. In the preceding sections, we only treated the enhancement of the modulation bandwidth due to optical injection in stable region. However, outside of stable area in the phase space of the frequency detuning and the optical injection ratio, there exist regions of chaotic oscillations as is discussed in Fig. 6.10. Therefore, the discussion for chaotic carrier enhancement under optical injection is not straightforward. In the following, we treat the case of the bandwidth enhancement in chaotic semiconductor laser with optical feedback by strong optical injection from a stable laser. Therefore, we here restrict the discussion of chaotic carrier enhancement for stable region.

Figure 6.24 is a typical power spectrum of chaotic oscillations obtained from a semiconductor laser, which has both external optical feedback and strong optical injection. Without a strong optical injection, the laser shows chaotic oscillation due to the external optical feedback and the spectral peak (though it has a broad peak) is about 3 GHz, which is comparable with the relaxation oscillation of the solitary laser. The original relaxation oscillation frequency is shown by the arrow (left arrow). On the other hand, the frequency of the maximum chaotic oscillation is increased to 14 GHz (right arrow) by a strong optical injection, that is an increase by a factor of 4.6. In this experimental example, the frequency detuning between

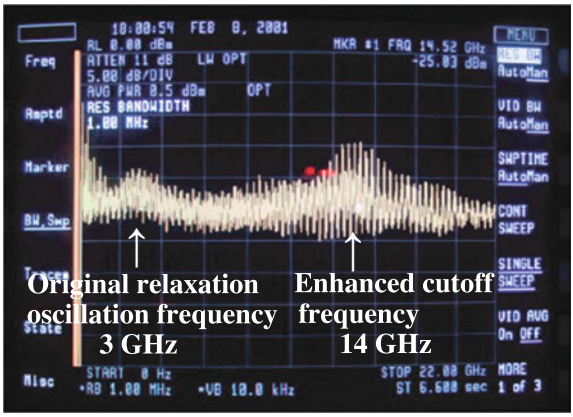

Fig. 6.24 Experimentally obtained chaotic power spectrum with the enhanced cutoff frequency in a DFB semiconductor laser subjected to both optical feedback and strong optical injection. The frequency detuning between the two lasers is −3.44 GHz and the injection ratio is −5.61 dBm. The *left* and *right arrows* indicate the peaks for the chaotic carrier frequencies without and with optical injection, respectively

the master and slave lasers is −3.44 GHz and the optical injection ratio is −5.61 dBm. This condition corresponds to the ordinary stable operation in the absence of external optical feedback.

The enhancement of the chaotic carrier frequency is also numerically calculated based on the rate equations. Figure 6.25 is the result (Takiguchi et al. 2003). Figure 6.25a, b are the time series of chaotic oscillations with and without optical injection, respectively. The relaxation oscillation frequency of the solitary laser is about 2.7 GHz. Figure 6.25c, d are the corresponding rf spectra to Fig. 6.25a, b, respectively. The feedback fraction to the slave laser is taken to be a large value of $\kappa/\tau_{in} = 2.33 \times 10^{10}$ s^{-1} to destabilize the strongly injection-locked laser. In Fig. 6.25d, the chaotic oscillation rapidly decays out over the relaxation oscillation frequency without optical injection. On the other hand, the spectrum in Fig. 6.25c shows a bandwidth-enhanced chaotic oscillation in the presence of a strong optical injection. As can easily be seen both from the time series and the spectrum, the chaotic carrier frequency is greatly expanded up to about 8 GHz by the strong

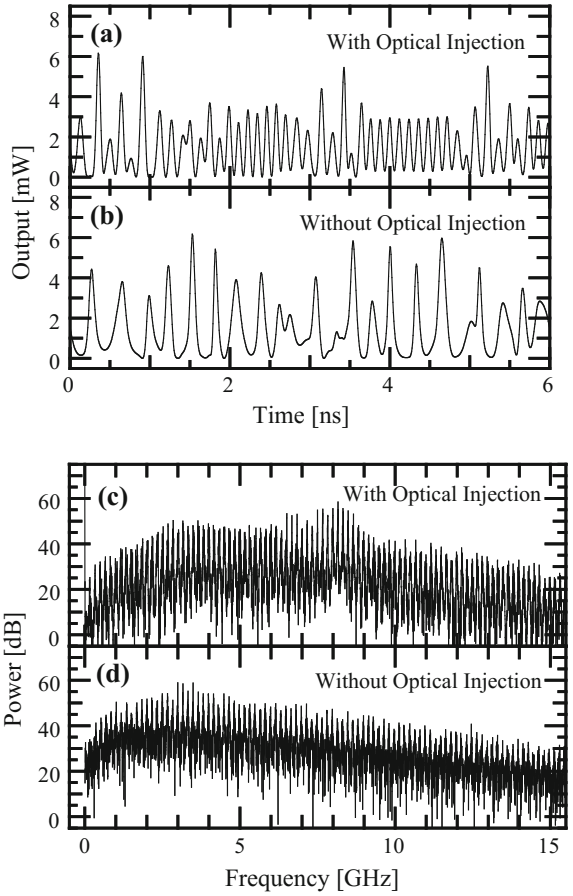

Fig. 6.25 Numerically calculated time series and power spectra of chaotic oscillations in a semiconductor laser with strong optical injection. Time series **a** with and **b** without optical injection. Power spectra **c** with and **d** without optical injection corresponding to **a** and **b**, respectively. The parameter conditions are $J_{s,m} = 1.3J_{th}$, $\tau = 6$ ns, $\kappa/\tau_{in} = 2.33 \times 10^{10}$ s^{-1}, $\kappa_{inj}/\tau_{in} = 1.79 \times 10^{10}$ s^{-1}, and $\Delta\nu = -4$ GHz

optical injection, which is as much as three times that without optical injection in Fig. 6.25d. As shown in the figure, the chaotic carrier frequency is also greatly enhanced by a strong optical injection. However, it is difficult to calculate analytically the exact enhanced bandwidth of the chaotic carrier frequency.

References

V. Annovazzi-Lodi, S. Donati, M. Manna, Chaos and locking in a semiconductor laser due to external injection. IEEE J. Quantum Electron. **30**, 1537–1541 (1994)

S. Blin, O. Vaudel, P. Besnard, R. Gabet, Power- or frequency-driven hysteresis for continuous-wave optically injected distributed-feedback semiconductor lasers. Opt. Express **17**, 9292–9299 (2009)

S.C. Chan, J.M. Liu, Tunable narrow-linewidth photonic microwave generation using semiconductor laser dynamics. IEEE J. Sel. Top. Quantum Electron. **10**, 1025–1032 (2004)

H.F. Chen, J.M. Liu, T.B. Simpson, Response characteristics of direct current modulation on a bandwidth-enhanced semiconductor laser under strong injection locking. Opt. Commun. **173**, 349–355 (2000)

L. Chrostowski, X. Zhao, C.J. Chang-Hasnain, Microwave performance of optically injection locked VCSELs. IEEE Trans. MTT **54**, 788–796 (2006)

P.C. De Jagher, W.A. van der Graaf, D. Lenstra, Relaxation-oscillation phenomena in an injection-locked semiconductor laser. Quantum Semiclass. Opt. **8**, 805–822 (1996)

S. Eriksson, A.M. Lindberg, Periodic oscillation within the chaotic region in a semiconductor laser subjected to external optical injection. Opt. Lett. **26**, 142–144 (2001)

T. Erneux, V. Kovanis, A. Gavrielides, P.M. Alsing, Mechanism for period-doubling bifurcation in a semiconductor laser subject to optical injection. Phys. Rev. A **53**, 4372–4380 (1996)

A. Furusawa, Amplitude squeezing of a semiconductor laser with light injection. Opt. Lett. **21**, 2014–2016 (1996)

A. Gavrielides, V. Kovanis, T. Erneux, Analytical stability boundaries for a semiconductor laser subject to optical injection. Opt. Commun. **136**, 253–256 (1997)

J. Genest, M. Chamberland, P. Tremblay, M. Têtu, Microwave signals generated by optical heterodyne between injection-locked semiconductor lasers. IEEE J. Quantum Electron. **33**, 989–998 (1997)

P. Guo, W. Yang, D. Parekh, A. Xu, Z. Chen, C.J. Chang-Hasnain, An ellipse model for cavity mode behavior of optically injection-locked VCSELs. Opt. Express **20**, 6980–6988 (2012)

P. Guo, W. Yang, D. Parekh, C.J. Chang-Hasnain, A. Xu, Z. Chen, Experimental and theoretical study of wide hysteresis cycles in 1550 nm VCSELs under optical injection. Opt. Express **21**, 3125–3132 (2013)

T. Heil, I. Fischer, W. Elsäßer, Coexistence of low-frequency fluctuations and stable emission on a single high-gain mode in semiconductor lasers with external optical feedback. Phys. Rev. A **58**, R2672–R2675 (1998)

T. Heil, I. Fischer, W. Elsäßer, Influence of amplitude-phase coupling on the dynamics of semiconductor lasers subject to optical feedback. Phys. Rev. A **60**, 634–641 (1999)

S.K. Hwang, J.M. Liu, Dynamical characteristics of an optically injected semiconductor laser. Opt. Commun. **183**, 195–205 (2000)

V. Kovanis, A. Gavrielides, T.B. Simpson, J.M. Liu, Instabilities and chaos in optically injected semiconductor lasers. Appl. Phys. Lett. **67**, 2780–2782 (1995)

E.K. Lau, H.K. Sung, M.C. Wu, Scaling of resonance frequency for strong injection-locked lasers. Opt. Lett. **32**, 3373–3375 (2007)

E.K. Lau, X. Zhao, H.K. Sung, D. Parekh, C.J. Chang-Hasnain, M.C. Wu, Strong optical injection-locked semiconductor lasers demonstrating >100-GHz resonance frequencies and 80-GHz intrinsic bandwidths. Opt. Express **16**, 6609–6618 (2008)

E.K. Lau, L.J. Wong, M.C. Wu, Enhanced modulation characteristics of optical injection-locked lasers: a tutorial. IEEE J. Sel. Top. Quantum Electron. **15**, 618–633 (2009)

E.K. Lee, H.S. Pang, J.D. Park, H. Lee, Bistability and chaos in an injection-locked semiconductor laser. Phys. Rev. A **47**, 736–739 (1993)

D. Lenstra, G.H.M. van Tartwijk, W.A. van der Graaf, P.C. De Jagher, Multiwave-mixing dynamics in a diode laser. SPIE Proc. **2039**, 11–22 (1993)

L. Li, Static and dynamic properties of injection-locked semiconductor lasers. IEEE J. Quantum Electron. **30**, 1701–1708 (1994a)

L. Li, A unified description of semiconductor lasers with external light injection and its application to optical bistability. IEEE J. Quantum Electron. **30**, 1723–1731 (1994b)

J.M. Liu, T.B. Simpson, Four-wave mixing and optical modulation in a semiconductor laser. IEEE J. Quantum Electron. **30**, 957–966 (1994)

J.M. Liu, H.F. Chen, S. Tang, Optical-communication systems based on chaos in semiconductor lasers. IEEE Trans. Circuits Syst. I **48**, 1475–1483 (2001)

C. Masoller, N.B. Abraham, Stability and dynamical properties of the coexisting attractors of an external-cavity semiconductor laser. Phys. Rev. A **57**, 1313–1322 (1998)

F. Mogensen, H. Olesen, G. Jacobsen, Locking conditions and stability properties for a semiconductor laser with external light injection. IEEE J. Quantum Electron. **21**, 784–793 (1985)

A. Murakami, K. Kawashima, K. Atsuki, Cavity resonance shift and bandwidth enhancement in semiconductor lasers with strong light injection. IEEE J. Quantum Electron. **39**, 1196–1204 (2003)

S. Piazzolia, P. Spano, T. Tamburrini, Small signal analysis of frequency chirping in injection locked semiconductor lasers. IEEE J. Quantum Electron. **22**, 2219–2223 (1986)

A. Ryan, G.P. Agrawal, G.R. Gray, E.C. Gage, Optical feedback-induced chaos and its control in multimode semiconductor lasers. IEEE J. Quantum Electron. **30**, 668–679 (1994)

J. Sacher, D. Baums, P. Panknin, W. Elsäßer, E.O. Göbel, Intensity instabilities of semiconductor lasers under current modulation, external light injection, and delayed feedback. Phys. Rev. A **45**, 1893–1905 (1992)

N. Schunk, K. Petermann, Noise analysis of injection-locked semiconductor injection lasers. IEEE J. Quantum Electron. **22**, 642–650 (1986)

T.B. Simpson, Mapping the nonlinear dynamics of a distributed feedback semiconductor laser subjected to external optical injection. Opt. Commun. **215**, 135–151 (2003)

T.B. Simpson, J.M. Liu, Enhanced modulation bandwidth in injection-locked semiconductor lasers. IEEE Photonics Technol. Lett. **9**, 1322–1324 (1997)

T.B. Simpson, J.M. Liu, A. Gavrielides, Bandwidth enhancement and broadband noise reduction in injection-locked semiconductor lasers. IEEE Photonics Technol. Lett. **7**, 709–911 (1995)

T.B. Simpson, J.M. Liu, A. Gaverielides, Small-signal analysis of modulation characteristics in semiconductor laser subject to strong optical injection. IEEE J. Quantum Electron. **32**, 1456–1468 (1996)

T.B. Simpson, J.M. Liu, K.F. Huang, K. Tai, Nonlinear dynamics induced by external optical injection in semiconductor lasers. Quantum Semiclass. Opt. **9**, 765–784 (1997)

T.B. Simpson, F. Doft, E. Strzelecka, J.J. Liu, W. Chang, G.J. Simonis, Gain saturation and the linewidth enhancement factor in semiconductor lasers. IEEE Photonics Technol. Lett. **13**, 776–778 (2001)

H. Someya, I. Oowada, H. Okumura, T. Kida, A. Uchida, Synchronization of bandwidth enhanced chaos in semiconductor lasers with optical feedback and injection. Opt. Express **17**, 19536–19543 (2009)

D.W. Sukow, T. Heil, I. Fischer, A. Gavrielides, A. Hohl-AbiChedid, W. Elsäßer, Picosecond intensity statistics of semiconductor lasers operating in the low-frequency fluctuation regime. Phys. Rev. A **60**, 667–673 (1999)

Y. Takiguchi, K. Ohyagi, J. Ohtsubo, Bandwidth-enhanced chaos synchronization in strongly injection-locked semiconductor lasers with optical feedback. Opt. Lett. **28**, 319–321 (2003)
G.H.M. van Tartwijk, G.P. Agrawal, Laser instabilities: a modern perspective. Prog. Quantum Electron. **22**, 43–122 (1998)
E.A. Viktorov, P. Mandel, Low frequency fluctuations in a multimode semiconductor laser with optical feedback. Phys. Rev. Lett. **85**, 3157–3160 (2000)
J. Wang, M.K. Haldar, L. Li, V.C. Mendis, Enhancement of modulation bandwidth of laser diodes by injection locking. IEEE Photonics Technol. Lett. **8**, 34–36 (1996)
A.B. Wang, Y. Wang, H. He, Enhancing the bandwidth of the optical chaotic signal generated by a semiconductor laser with optical feedback. IEEE Photonics Technol. Lett. **20**, 1633–1635 (2008)
S. Wieczorek, B. Krauskopf, D. Lenstra, Mechanisms for multistability in a semiconductor laser with optical injection. Opt. Commun. **183**, 215–226 (2000)
S. Wieczorek, B. Krauskopf, D. Lenstra, Unnested islands of period doublings in an injected semiconductor laser. Phys. Rev. E **64**, 056204-1–056204-9 (2001a)
S. Wieczorek, B. Krauskopf, D. Lenstra, Sudden chaotic transitions in an optically injected semiconductor laser. Opt. Lett. **11**, 816–818 (2001b)
S. Wieczorek, B. Krauskopf, D. Lenstra, Bifurcation transitions in an optically injected diode laser: theory and experiment. Opt. Commun. **215**, 125–134 (2001c)
S. Wieczorek, T.B. Simpson, B. Krauskopf, D. Lenstra, Global quantitative predictions of complex laser dynamics. Phys. Rev. E **65**, R045207-1–R045207-4 (2002)
G. Yabre, Effect of relatively strong light injection on the chirp-to-power ratio and the 3 dB bandwidth of directly modulated semiconductor lasers. J. Lightwave Technol. **14**, 2367–2373 (1996)
W. Yang, P. Guo, D. Parekh, C.J. Chang-Hasnain, Reflection-mode optical injection locking. Opt. Express **18**, 20887–20893 (2010)

Chapter 7
Dynamics of Semiconductor Lasers with Optoelectronic Feedback and Modulation

Abstract One of the characteristics of semiconductor lasers that is different from other lasers is the direct pump modulation. The disturbance to the injection current is an additional degree of freedom. Therefore, the disturbance to the injection current induces instabilities to semiconductor lasers, and instabilities and chaotic behaviors are indeed observed by the injection current modulation. Another example of disturbances to the injection current is optoelectronic feedback, in which the output from the laser is once detected by a photodetector and, then, the detected photocurrent is fed back into the injection current. A typical feature of instabilities induced by disturbances to the injection current is the regular and irregular pulsations in the laser output. In this chapter, we discuss instabilities and chaotic dynamics of optoelectronic feedback and injection current modulation in semiconductor lasers.

7.1 Theory of Optoelectronic Feedback

7.1.1 Optoelectronic Feedback Systems

Optoelectronic feedback is one of the perturbations to the injection current in semiconductor lasers that induces instabilities. In optical feedback to semiconductor lasers, the phase sensitivity plays a crucial role in the laser dynamics. However, different from optical feedback, we do not need to consider the phase effect in optoelectronic feedback systems, since the phase information is once eliminated by a photodetection in the feedback process. Stable or unstable operations of semiconductor lasers are flexibly and reliably controlled through the injection current (Giacomelli et al. 1989; Loiko and Samson 1992). The dynamics of semiconductor lasers with optoelectronic feedback can be described only by the two equations of

© Springer International Publishing AG 2017

J. Ohtsubo, *Semiconductor Lasers*, Springer Series in Optical Sciences 111,
DOI 10.1007/978-3-319-56138-7_7

the photon number and the carrier density. Therefore, optoelectronic feedback shows different dynamics from those of optical feedback and optical injection in semiconductor lasers.

For optoelectronic feedback through the injection current, there are two categories; one is positive feedback and the other negative feedback. They have different mechanisms for driving the dynamics of the laser. In negative feedback, the feedback current is deducted from the bias injection current and it induces the sharpening of the relaxation oscillation (Lee and Shin 1993). On the other hand, the feedback current is added to the bias injection current in positive feedback and, as a result, the gain switching tends to drive the laser into pulsing states in the output power (Damen and Duguay 1980). Therefore, regular pulsing states induced by positive optoelectronic feedback are used as a light source for periodic pulse trains with short picosecond duration (Paulus et al. 1987). Compared with short-pulse generations by passive mode locking with a saturable absorber (typically 1 ps pulse), Q switching, gain switching (typically 10 ps pulse), or active mode locking with external modulation (typically 10 ps pulse), stable and fast pulses with variable pulse-width can be easily obtained by setting appropriately the external parameters in the optoelectronic feedback system (Inaba 1982; van der Ziel 1985). The repetition rate of the pulses is found to be an integer multiple of the inverse of the feedback-loop delay time that is closest to the relaxation resonance frequency of the laser. Otherwise, when the time for the feedback loop is not coincident with the period of the laser relaxation oscillation or its integer multiples, the competition of the incommensurate periods results in chaotic oscillations in the laser that strongly depend on the feedback time. The chaotic pulses in this system have both chaotic peak intensities and chaotic pulse intervals.

The model of optoelectronic feedback in semiconductor lasers is the same as that treated as the injection current modulation discussed in Sect. 3.7 (Lin and Liu 2003a). Figure 7.1 shows a schematic diagram of optoelectronic feedback in a semiconductor laser. The light emitted from a semiconductor laser is detected by a photodetector and the detected photocurrent is fed back through a bias Tee circuit. The feedback may be positive or negative depending on the polarity of the output of the amplifier in the circuit. In optoelectronic feedback, the modulation is not for the complex field but for the carrier density through the disturbance to the injection current. Therefore, we use the rate equation of the photon number instead of the complex amplitude. Using (3.94) and (3.96), the rate equations for the optoelectronic feedback system are written by

$$\frac{\mathrm{d}S(t)}{\mathrm{d}t} = G_n\{n(t) - n_{\mathrm{th}}\}S(t) \tag{7.1}$$

$$\frac{\mathrm{d}n(t)}{\mathrm{d}t} = \frac{J}{ed}\left\{1 + \xi\frac{S(t-\tau) - S_{\mathrm{offset}}}{S_s}\right\} - \frac{n(t)}{\tau_s} - G_n\{n(t) - n_0\}S(t) \tag{7.2}$$

where ξ is the feedback strength. The system is positive feedback for a positive value of ξ, while it is negative feedback for a negative value. S_s is the steady-state

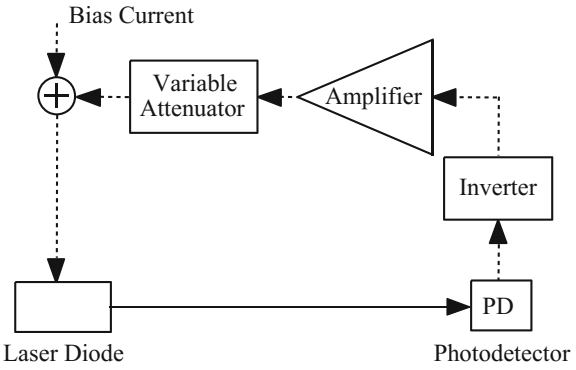

Fig. 7.1 Schematic diagram of an optoelectronic feedback system

value for the photon number and S_{offset} is the constant offset in the feedback loop. The value of the offset may be zero. τ is the feedback time including time responses of the detector and the electronic circuits.

A feedback circuit with time response of 100 ps is easily available at present and the response is sufficient to follow chaotic variations in semiconductor lasers. However, when the time response of the electronic feedback circuit has the same order as the relaxation oscillation of the laser, the effect of the finite response must be taken into account and another differential equation for the feedback current must be introduced besides the photon number and carrier density equations (Lee et al. 1988). We will discuss this point later. Contrary to the case of optical feedback in semiconductor lasers, photon noises induced in the optoelectronic feedback system have less effect, since the feedback is to the carrier density. This is due to the difference of the time scales of the lifetimes of carrier density and photon; the photon lifetime is typically of the order of picoseconds, while the carrier lifetime is much longer than that and it is around nanoseconds. As noted, we do not consider the phase equation and the phase sensitivity are eliminated in the optoelectronic feedback system.

7.1.2 Pulsation Oscillations in Optoelectronic Feedback Systems

The typical feature of optoelectronic feedback in semiconductor lasers is pulsation oscillations. Depending on the feedback conditions, the laser shows various dynamic states of periodic and chaotic oscillations. However, the dynamics strongly depend on whether the system has a positive or negative feedback loop. The details of the dynamics will be given later. Instead, we first present experimental results of pulsation oscillations in optoelectronic feedback systems. Figure 7.2 shows such examples (Tang and Liu 2001b). The laser outputs (left) and its rf spectra (right) are obtained for certain conditions of the feedback delay (the delay time including the

flight of light in the loop of the laser, the detector, and the electric circuit). From Fig. 7.2a–c, the laser evolves a regular pulsing state of constant peak intensity into a quasi-periodic pulsing state. Only one fundamental frequency at 650 MHz is excited in the spectrum in Fig. 7.2a, which has the pulsing frequency of the regular pulses seen in the corresponding time series. However, ripples with small amplitude are included in the spectrum. The laser is not completely stabilized to a periodic state, although the level of the ripples is below 40 dB. The frequency of 140 MHz corresponding to the delay time of the loop is excited as the second oscillation

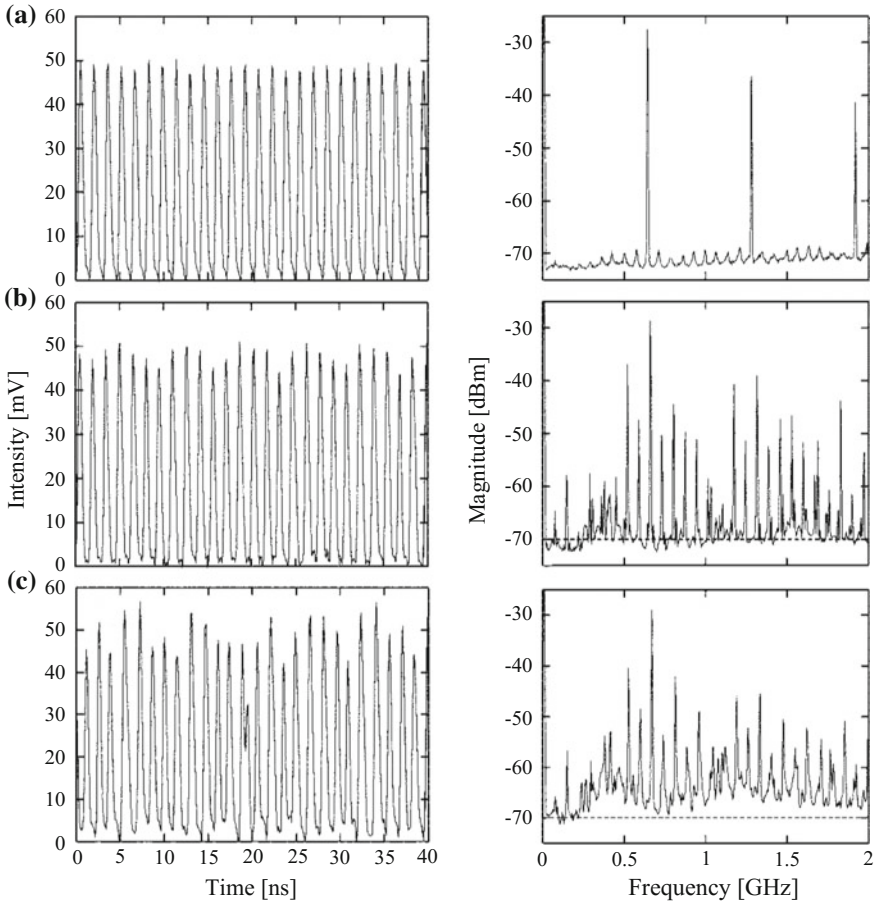

Fig. 7.2 Experimental results of time series and power spectra of various pulsing states for different delay times. **a** Regular pulsing at τ = 7.47 ns. **b** Two-frequency quasi-periodic pulsing at τ = 7.09 ns. **c** Chaotic pulsing at τ = 6.92 ns. The laser used is a single mode DFB laser with a wavelength of 1.33 μm and the bias injection current is $J = 1.34J_{th}$ [after Tang and Liu (2001b); © 2001 IEEE]

frequency in Fig. 7.2b. The two frequencies are incommensurate. Therefore, the laser oscillates at the two fundamental frequencies and the oscillation is in a two-frequency quasi-periodic pulsing state. In Fig. 7.2c, the broadband background is much higher than in Fig. 7.2b, indicated by the dashed reference lines at −70 dBm. All over the spectrum is much broadened and the peak heights of the pulsation oscillation vary irregularly, corresponding to chaotic oscillation. Such chaotic evolution is well reproduced by numerical simulations based on the rate equations.

The feedback delay time and the feedback ratio play crucial roles in the dynamics of optoelectronic feedback systems, as is the case for optical feedback. A map of the dynamics in the phase space of the delay time and the feedback strength is calculated from the numerical simulation for the rate equations. Figure 7.3 shows the map of chaotic routes in the space for the normalized delay of $\hat{\tau} = \tau\nu_R$ (ν_R is the relaxation oscillation frequency) and the feedback strength ξ at a fixed bias injection current (Lin and Liu 2003a). The positive value of ξ is the case for positive feedback and the negative value of ξ for negative feedback as already defined. We find that these systems share the same route to chaos and most of the dynamic states, but the frequency-locked pulsing states are clearly observed only in the negative feedback system. On the other hand, the region of the locking range of the frequency-locked states is too narrow to be observable in the positive feedback. Therefore, small fluctuations in the laser parameters would drive the system into the neighboring quasi-periodic or chaotic states (CO). Although frequency-locked states should generally exist in a two-frequency system, it is very difficult to observe experimentally the locking range of the frequency-locked states in positive optoelectronic feedback systems and they are rarely observable in real experiments.

With the increases of the normalized delay time $\hat{\tau}$ or the feedback strength ξ, the laser output shows very complicated dynamics. The laser evolves into CO through a quasi-periodic route following regular pulsing (RP), two-frequency quasi-periodic pulsing (Q2), three-frequency quasi-periodic pulsing (Q3), and finally chaotic pulsing states (C). Quasi-periodic states are typically observed for strong feedback strength in the positive feedback system. On the other hand, such states are limited within small feedback strength in the negative feedback system. In the mappings, RP, Q2, and Q3 states spread over large areas in the positive feedback system, while CO have large areas in the negative feedback system. Therefore, we could easily obtain CO in the negative feedback system, when we adjust the controllable parameters. Especially, we could observe remarkable chaotic pulsing states at large feedback strengths and long delay times. Another important difference between these two systems is the regions of the frequency-locked (FL) pulsing state. In the positive optoelectronic feedback system, the states that separate the chaos islands are the RP states. However, in the negative optoelectronic feedback system, the

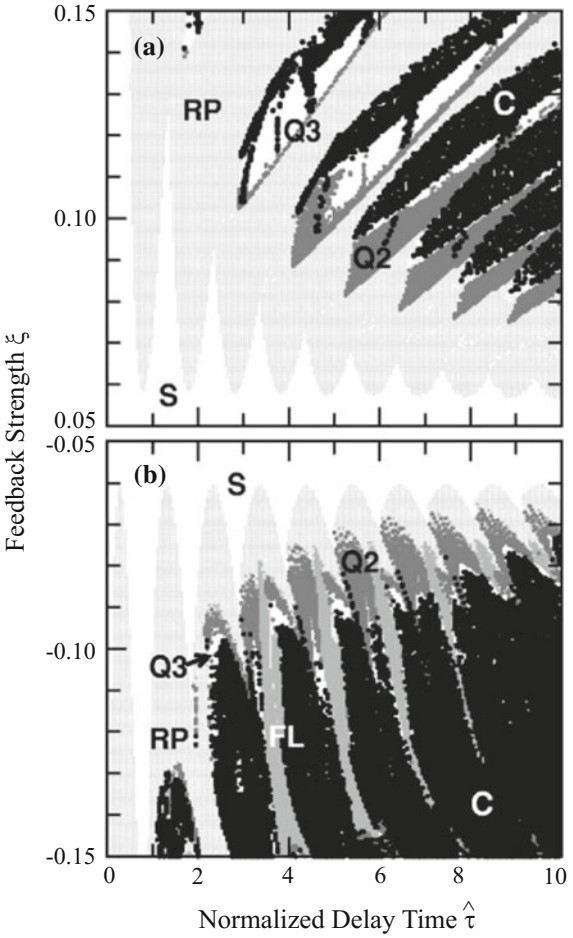

Fig. 7.3 Mappings of dynamic states of **a** positive optoelectronic feedback and **b** negative optoelectronic feedback systems at $J = 1.33J_{th}$. *S* Steady states, *RP* regular pulsing, *Q2* two-frequency quasi-periodic pulsing, *Q3* three-frequency quasi-periodic pulsing, *PL* frequency-locked pulsing, *C* chaotic pulsing [after Lin and Liu (2003a); © 2003 IEEE]

states that separate the chaos islands are the FL pulsing states instead. Thus, the dynamics of optoelectronic feedback systems strongly depends on the positive or negative feedback even for the same delay time and the same strength.

7.2 Linear Stability Analysis for Optoelectronic Feedback Systems

7.2.1 Linear Stability Analysis

The solutions of stability and instability for the parameters in optoelectronic feedback systems are calculated by the linear stability analysis (Pieroux et al. 1994; Grigorieva

et al. 1999). Grigorieva et al. investigated the local dynamics for semiconductor lasers with optoelectronic feedback. Applying the linear stability analysis for (7.1) and (7.2), they obtained the characteristic equation for the system as

$$\gamma^2 + \varepsilon_\tau\left(c_q^2 + 1\right)\gamma + c_q^2\left\{1 + \gamma_0 \exp\left(-\frac{\lambda\tau}{\varepsilon_\tau}\right)\right\} = 0 \tag{7.3}$$

where the normalized parameters are defined by $\varepsilon_\tau = \sqrt{\tau_{\mathrm{ph}}/\tau_s}$, $\gamma_0 = -\tau_{\mathrm{ph}}\xi J/S_s ed$, and $c_q = \sqrt{(q-1)/(1+\gamma_0)}$ ($q = \tau_s\tau_{\mathrm{ph}}G_n(J/ed - n_0/\tau_s)$). From the characteristic equation, we can calculate the boundary for stable and unstable oscillations of the laser. Figure 7.4 is the result. The stable region is located around the zero feedback coefficient ($\gamma_0 = 0$) and the left and right curves are the stability boundaries. The left curve is the stable boundary for the negative feedback, while the right curve is for the positive feedback. These curves correspond to the stable and unstable boundaries in Fig. 7.3, which is obtained from the numerical calculation for the rate equations.

The minimal values of the feedback coefficients for the stable boundaries are the same both for negative and positive feedback and the approximate form is given by

$$\gamma_{0\min} = \varepsilon_\tau \frac{q}{c_{q0}} \tag{7.4}$$

where $c_{q0} = \sqrt{q-1}$ is the value of c_q at $\gamma_0 = 0$. Namely, we require the above minimal value of the injection current to destabilize the laser output in optoelectronic feedback systems, whether it is a positive or negative feedback. The minimal points at $\gamma_{0\min}$ locate periodically for the increase or decrease of the delay time. For a positive feedback, the locations of the minimal points at the delay time are shifted by one-quarter from the multiple period of the relaxation oscillation at a free running laser and the delay is given by

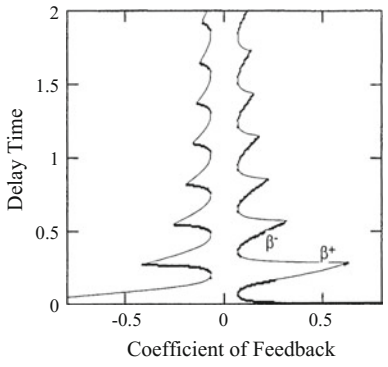

Fig. 7.4 Boundary of stability and instability in the phase space of the feedback coefficient and the delay time at $\varepsilon_\tau^2 = 10^{-3}$ and $q = 1.5$ [after Grigorieva et al. (1999); © 1999 Elsevier]

$$\tau_m = \varepsilon_\tau \frac{2\pi}{c_{q0}}\left(m + \frac{1}{4}\right) \quad m = 1, 2, 3\ldots \tag{7.5}$$

On the other hand, the delay for a negative feedback is given by

$$\tau_m = \varepsilon_\tau \frac{2\pi}{c_{q0}}\left(m + \frac{3}{4}\right) \quad m = 1, 2, 3\ldots \tag{7.6}$$

For a positive feedback, the relaxation oscillation frequency decreases due to the increase of the carrier density and it is calculated as

$$\nu'_{\mathrm{R}} = \frac{c_{q0}}{2\pi\varepsilon_\tau}\left(1 - \frac{\gamma_{0\min}}{2}\right) \tag{7.7}$$

The second term in the parenthesis on the right-hand side of the equation is the effect of the feedback. In the case of a negative feedback, the relaxation oscillation frequency has the same form as (7.7), but the sign of the minimal value is negative and the relaxation oscillation frequency increases due to the reduction of the carrier density.

In the above discussion, we ignore the response time of the electronic circuits in the feedback system. However, we must take the transient effect into consideration, when we cannot neglect the finite response time of the photodetector. Lee et al. (1988) investigated the dynamics of semiconductor lasers with optoelectronic feedback when the photodetector has a finite response and derived the conditions for pulsation oscillations in the laser output power. They introduced the response for the feedback current as a differential equation (Kressel and Butler 1977):

$$\frac{\mathrm{d}i}{\mathrm{d}t} = \frac{1}{\tau_i}(c_1 S_s - i) \tag{7.8}$$

where $i = \tau_s \tau_{\mathrm{ph}} G_n J/ed$ is the normalized feedback current, τ_i is the 3 dB bandwidth of the feedback circuits, c_1 is the conversion efficiency of the photon density to the normalized current through the photodetector including the coupling efficiency. Taking into account the saturation effect of the current, the actual feedback current i_f through an amplifier is modeled by the following equation:

$$i_f = \frac{i_s}{1 + \exp\left\{-\frac{4(i - i_a)G_A}{i_s}\right\}} \tag{7.9}$$

where i_s, i_a, and G_A are the saturation current, the detected photocurrent, and the gain in the circuit, respectively.

Combining (7.1) and (7.2) with (7.8), a linear stability analysis is also applied to a negative optoelectronic feedback system. The loop gain for pulsation oscillations is calculated from the real part of the characteristic equation in the linear stability

analysis. The resonance angular frequency taking into consideration of the finite response of the feedback circuit is given by

$$\omega_{\mathrm{R,feedback}}^2 = \omega_{\mathrm{R}}^2 + \frac{1}{\tau_i}\left\{\frac{1}{\tau_s} + G_n S_s + \frac{1}{\tau_{\mathrm{ph}}}\left(\varepsilon' S_s + \beta_{\mathrm{sp}}\frac{G_n \tau_{\mathrm{ph}} n_0 + 1}{G_n \tau_s S_s}\right)\right\} \tag{7.10}$$

where ω_{R} is the angular frequency of the relaxation oscillation for the infinite time response of the feedback circuit and ε' is the effect of the nonlinear gain $\varepsilon' = \varepsilon_s G_n \tau_s$. The second term on the right-hand side of the equation is the correction of the resonance angular frequency for the finite time response. The equation includes the effects of the nonlinear gain saturation ε_s and the spontaneous emission of light (coefficient β_{sp}). When the value of τ_i is approximated as infinity, namely, the time response is assumed to be instant, the second term in (7.10) is neglected and, then, the resonance frequency becomes exactly equal to the relaxation oscillation frequency at the infinite time response. For a finite time response of the circuit, the resonance frequency increases due to negative optoelectronic feedback. It is noted that the spontaneous emission of light induces the increase of the frequency of the relaxation oscillation as can be easily understood from (7.10). Also, the nonlinear gain shows the same tendency as the effect of spontaneous emission.

7.2.2 *Characteristics of Semiconductor Lasers with Optoelectronic Feedback*

Taking an example for negative optoelectronic feedback, we here present some results of the characteristics in the systems derived from the linear stability analysis. Figure 7.5a shows light-injection-current (L-I) characteristics for a negative optoelectronic feedback (Lee et al. 1988). Since the carrier number in the active layer in negative optoelectronic feedback is reduced from that at the free running state, the laser threshold increases. As a result, we require a larger bias injection current for the same laser output power as that at the solitary oscillation. At the same time, the slope efficiency is reduced. In this model, the saturation effect for the current in the feedback loop is taken into account and, therefore, the slope of the L-I characteristic at a higher injection current is the same as that of the solitary oscillation, although the L-I curve is shifted toward the higher injection current.

Pulsation oscillations in optoelectronic feedback in semiconductor lasers strongly depend on the feedback gain G_A and the response time of the feedback circuit τ_i. The map of pulsing states in the phase space of the feedback gain and the response time is calculated from the linear stability analysis and is plotted in Fig. 7.5b. In Fig. 7.5b, the normalized coordinates of $c_1 G_A$ and τ_s/τ_i are used instead of the feedback gain and the response time. In Fig. 7.5b, the unstable region of pulsations is inside the curves. When the feedback gain is as small as $c_1 G_A \ll 1$, the laser oscillates stably. For larger feedback gain, unstable pulsing starts to

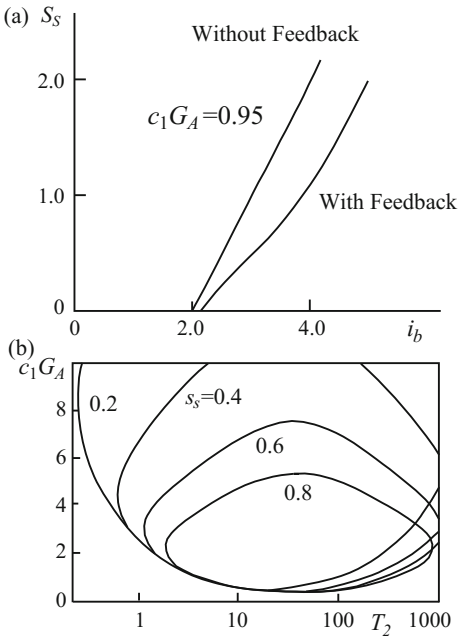

Fig. 7.5 Effects of negative optoelectronic feedback. **a** L-I characteristics. **b** Dependence of pulsing area on photon number or equivalently bias injection current, $T_2 = \tau_s/\tau_i$ and $s_s = G_n\tau_s S_s$. The parameters are $T_1 = \tau_s/\tau_{ph} = 2000$, $i_s = 2.5$, $\beta_{sp} = 10^{-5}$, and $\varepsilon' = 10^{-3}$ [after Lee et al. (1988); © 1988 OSA]

appear. However, the unstable region shrinks and finally disappears at a certain level of the feedback gain. The laser is stabilized for a higher bias injection current and the increase of the photon number (normalized photon number $s_s = G_n\tau_s S_s$) results in the shrinkage of the unstable region. As can be easily understood from the figure, the required closed-loop gain becomes minimum when $1/\tau_i$ is equal to the relaxation oscillation frequency. In this simulation, only the unstable pulsing oscillation boundary is investigated from the linear stability analysis. However, it is noted that various unstable dynamics and routes to chaos, not only the pulsing states but also unstable oscillations and chaotic oscillations, are observable depending on the device and system parameters.

Figure 7.6 shows the waveforms of pulsing states for the feedback current i ($i = G_n\tau_s\tau_{ph}J/ed$), the carrier density n' ($n' = G_n\tau_{ph}n$), and the photon number s ($s = G_n\tau_{ph}S$) at certain parameter conditions (Lee et al. 1988). The excitation of pulsation oscillations in negative optoelectronic feedback is explained as follows; the detected photocurrent from the laser is fed back into the bias injection current with a transient response of the photodetector after the laser oscillation starts at a certain time. The feedback current induces the reduction of the injection current. The injection current may become below the threshold and the laser oscillation stops for a large feedback current. Therefore, the laser oscillates at only the beginning of the rise time of the electronic feedback circuit and emits a very short pulse. When the laser oscillation stops, the feedback current decreases and the injection current to the laser increases. The injection current well exceeds the threshold, and then the next pulse is generated. These processes may be regarded as

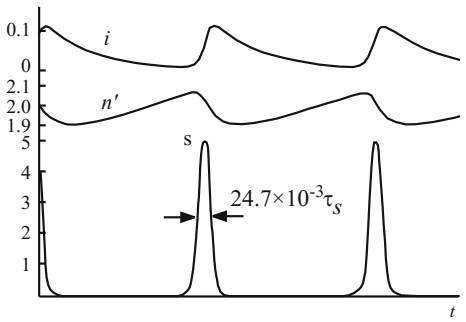

Fig. 7.6 Calculated waveform for current i, carrier density n', and photon number s with $s_s = 0.4$, $i_s = 2.5$, $c_1 G_A = 2.0$, $T_1 = 2000$, $T_2 = 10$, $\beta_{sp} = 10^{-5}$, and $\varepsilon' = 10^{-3}$ [after Lee et al. (1988); © 1988 OSA]

sharpening the extraction of the first spike of the relaxation oscillation. The feedback sharpens the falling edge of the first spike and suppresses the subsequent spikes. Thus, strong pulsation oscillation is generated at a high frequency of the order of the relaxation oscillation frequency (the frequency is shifted to a higher side due to the feedback). The pulse width is easily adjusted by appropriately choosing the feedback gain. Also, the pulse repetition rate can be controlled by the bandwidth $1/\tau_i$ of the amplifier.

7.3 Dynamics and Chaos in Semiconductor Lasers with Optoelectronic Feedback

7.3.1 Chaotic Dynamics in Negative Optoelectronic Feedback

In the previous section, we demonstrated regular pulsing states in semiconductor lasers induced by optoelectronic feedback. In this section, we show in detail unstable and chaotic pulsation oscillations in such systems. As has already been discussed, there are two types of optoelectronic feedback; one is positive and the other is negative. For both cases, we can expect regular pulsing, quasi-periodic pulsing, and chaotic pulsing states in the laser output power. However, the region of the frequency-locked state in the parameter space is very narrow for positive optoelectronic feedback and it is only observable for negative optoelectronic feedback in actual experimental systems (Giacomelli et al. 1989). Similar locking states have been observed in a modulated external cavity injection laser (Lee and Shin 1993) and a modulated self-pulsing semiconductor laser (Lee et al. 1988). These frequency-locked pulsing states are experimentally observed to exhibit a harmonic frequency-locked phenomenon, where the pulsing frequency is locked to a harmonic of the delay loop frequency instead of the delay loop frequency itself.

Numerical simulations for stable and unstable pulsation oscillations for negative optoelectronic feedback were conducted and various pulsing states were observed.

Here, we show the experimental results (Lin and Liu 2003a). In Fig. 7.7, sequential pulsing states including RP, two-frequency quasi-periodic (Q2), quasi-periodic FL (Q-FL), FL, and chaotic (C) states are observed by changing the frequency of the feedback loop from $f_{\text{loop}} = 49$ to 68 MHz. On the way to chaotic evolutions, generations of various frequency components are observed, such as excitations of the relaxation oscillation, the second fundamental frequency (the loop frequency), their harmonics, and their beats. It is also demonstrated that the rotation numbers of these frequency-locked pulsing states show a Devil's staircase structure. Three-frequency quasi-periodic pulsing (Q3) states in which an extra frequency component is added to the two-frequency quasi-periodic state (the relaxation oscillation and the loop frequencies) are observed in the numerical simulations. However, Q3 states are rarely observed in experiments. In this experiment, Q3 states are not observed, since the areas of Q3 states are so small that they are easily shifted to different neighbor states due to disturbances such as noises in the electronic circuit. The other oscillation states were well reproduced in the numerical simulations.

Figure 7.7a is a regular pulsing state for the loop frequency of $f_{\text{loop}} = 68$ MHz. The pulsing frequency is 750 MHz. It is noted that the pulsing frequency of the laser is about one-half of the resonance frequency $f_p \approx \nu_R/2$. Such sub-harmonic oscillation has also been found in a driven van der Pol oscillator (Gilbert and Gammon 2000). When the loop frequency f_{loop} becomes as small as 64 MHz, Q2 states appear. In this state, the pulsation frequency f_p at 760 MHz beats with a frequency at 320 MHz. The latter frequency is about five times that of f_{loop}. The frequency f_p is beating with the fifth harmonic of f_{loop}. Although the noise and the digitization error make the ring expected for a Q2 state diffused in the phase portrait, a ring-like distribution can still be seen (Fig. 7.7b). A Q-FL state between quasi-periodic pulsing and frequency-locked pulsing is observed at the increased loop frequency of 51 MHz as shown in Fig. 7.7c, where three smeared dots can be seen in the phase portrait. We can see the three frequency components of f_p, f_{loop}, and the fifth harmonic of f_{loop}. Figure 7.7d is an example of a frequency locking state. At the lower frequency of f_{loop} equal to 50 MHz, f_{loop} and f_p at 750 MHz become exactly commensurate, and frequency locking occurs. The state is a 5:15 (1:3) frequency locking, where f_{lock} is the fifth harmonic of f_{loop}, $f_{\text{lock}} = 5\, f_{\text{loop}}$, and the pulsing frequency is $f_p = 15\, f_{\text{loop}}$. The laser evolves into a chaotic state for the decrease of f_{loop} to 49 MHz as shown in Fig. 7.7e. The chaotic state (C) is identified by the spread dots in the phase portrait and the random intensity pulses seen in the time series. Hence, the experimental results bear out the simulation study, where the same sequence of states including the RP, Q2, Q-FL, FL, and C states are found and a quasi-periodic route to chaos is verified. Lin and Liu (2003a) further investigated the phenomenon of frequency locking states with various rotation numbers and they obtained a Devil's staircase (which is a typical structure reconstructed from excited frequencies of chaotic oscillation in nonlinear systems) for the relation between the rotation number and the locking frequency.

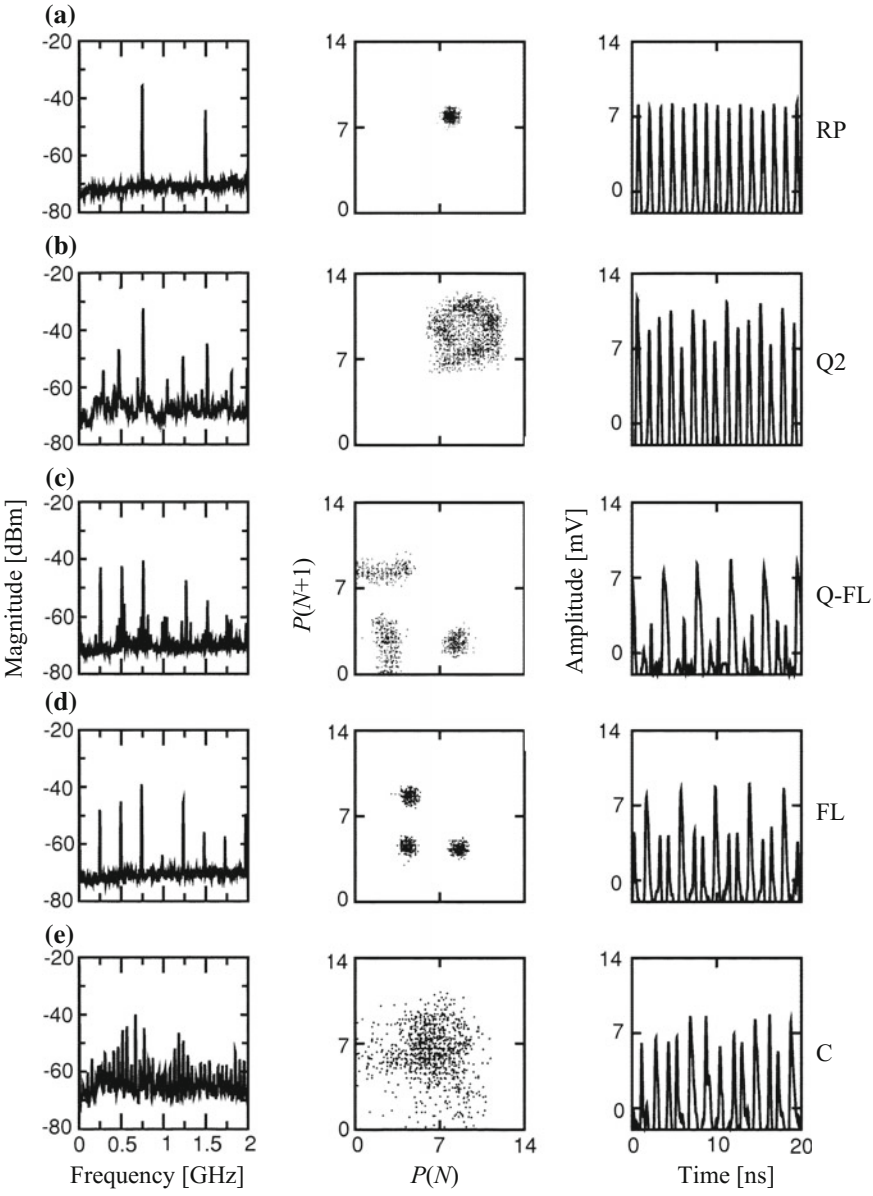

Fig. 7.7 Experimentally measured power spectra, phase portraits, and time series of different pulsing states in negative optoelectronic feedback systems. **a** *RP* Regular pulsing, **b** *Q2* two-frequency quasi-periodic pulsing, **c** *Q-FL* quasi-periodic frequency-locking, **d** *FL* frequency-locking, and **e** *C* chaotic states, where the loop frequencies are 68, 64, 51, 50, and 49 MHz, respectively. The laser used is a DFB laser of the wavelength of 1.299 μm. The bias injection current is $J = 1.17J_{th}$ and the relaxation oscillation frequency at that current is 1.5 GHz [after Lin and Liu (2003a); © 2003 IEEE]

7.3.2 Chaotic Dynamics in Positive Optoelectronic Feedback

Self-sustained pulsations are observed both for negative and positive optoelectronic feedback in semiconductor lasers. However, their dynamics are not always the same. For example, frequency-locked states are the typical feature in negative optoelectronic feedback, while they are rarely observed in positive optoelectronic feedback. The extent of chaotic regions in the parameter space varies. Here, we discuss chaotic evolutions of pulsing states in positive optoelectronic feedback systems and demonstrate that not only the pulse height but also the jitter of pulse sequences shows chaotic behaviors. Figure 7.8 is a numerical result of pulsing states for the variations of the delay time in an optoelectronic feedback system (Tang and Liu 2001b). The normalized delay time is used in the figure and it is defined by $\hat{\tau} = v_R \tau$. With $\hat{\tau} = 7.47$ in A of Fig. 7.8, the time series shows a sequence of regular pulses with a constant pulsing intensity and interval. The corresponding power spectrum has only one fundamental pulsing frequency at $f_1 \approx 2.3$ GHz, which is close to the resonance frequency of the laser. When the delay time is decreased to $\hat{\tau} = 7.25$ in B, the laser enters a two-frequency quasi-periodic pulsing state with the intensity modulated at a certain frequency f_2. The pulses are clearly modulated and the new modulation frequency is read to be $f_2 \approx 320$ MHz. This f_2 is close to, but slightly less than, the inverse of the delay time of the feedback loop. The appearance of two incommensurate frequencies, f_1 and f_2, is the indication of quasi-periodicity. When the delay time is further decreased to $\hat{\tau} = 7.00$ in C, the laser enters a three-frequency quasi-periodic pulsing state as a third frequency at $f_3 \approx 23$ MHz shows up. The component of this frequency f_3 is very small and the frequency is incommensurate with f_1 and f_2. In other delayed feedback systems, such as semiconductor lasers with weak optical feedback (Ritter and Haug 1993a, b) and semiconductor lasers with negative optoelectronic feedback controlling the pump current (Grigorieva et al. 1999), a similar third frequency has also been found. Tang and Liu (2001b) indicated that f_3 is the result of nonlinear interaction between the laser relaxation oscillation and the delayed feedback. Finally, when $\hat{\tau} = 6.48$, the laser enters a chaotic pulsing state, as shown in D. In the CO, not only the pulse height but also the separation becomes chaotic (jitter) and the corresponding spectrum is much broadened.

Phase portraits and spectra of the peak series in the Poincaré sections constructed from the corresponding time series of Fig. 7.8 are calculated and plotted in Fig. 7.9. In the phase portraits, $S(N)$ are the successive peak intensity values of the laser pulses in a given time series, while $T(N)$ are the corresponding time intervals of the pulses. The range of the rf spectra is expanded and the plots show only lower frequency components. In a regular pulsing state in A, the peak series consists of a single constant value, therefore the phase portrait is a single fixed point. In a two-frequency quasi-periodic pulsing state in B, the phase portrait shows a clear circle, since the pulsing frequency f_1 in the power spectrum of the original time series has been eliminated from the data set of the peak series under the Poincaré

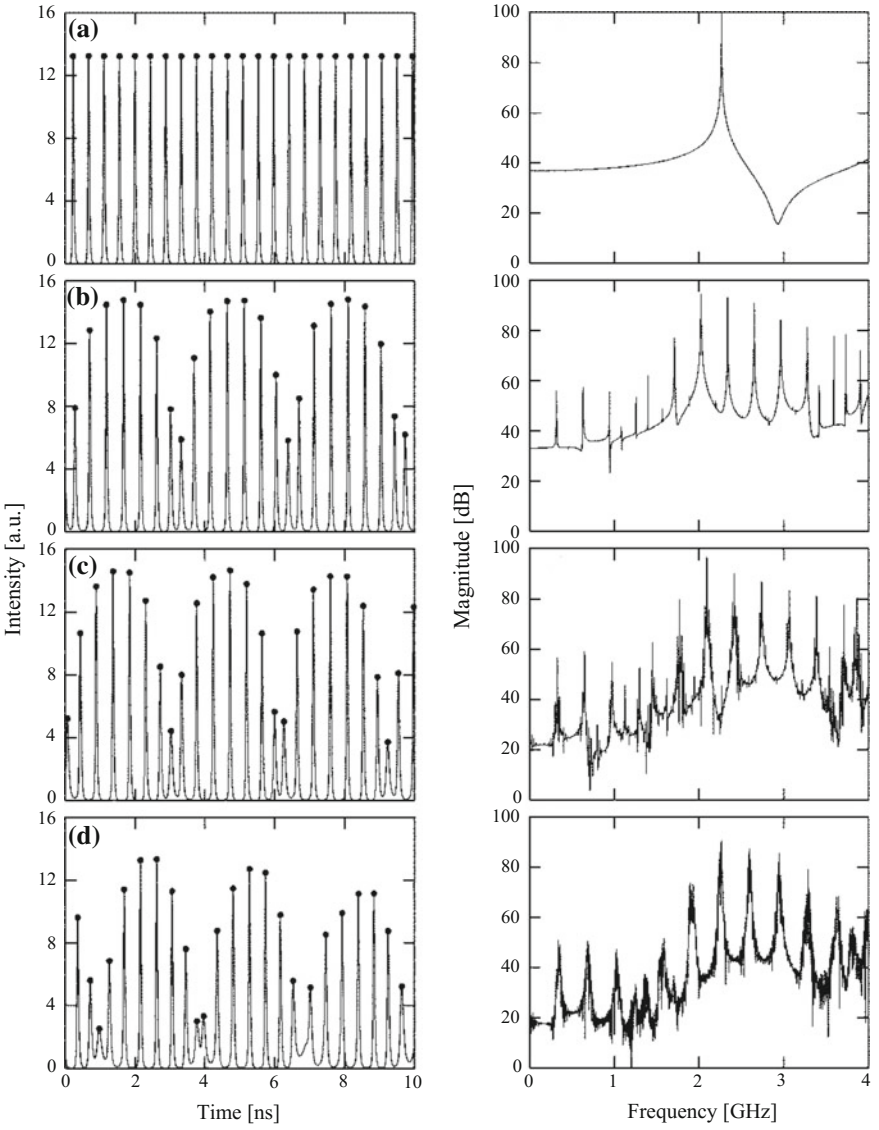

Fig. 7.8 Time series and power spectra of different pulsing states. **a** Regular pulsing at $\hat{\tau} = 7.47$. **b** Two-frequency quasi-periodic pulsing at $\hat{\tau} = 7.25$. **c** Three-frequency quasi-periodic pulsing at $\hat{\tau} = 7.00$. **d** Chaotic pulsing at $\hat{\tau} = 6.48$. The pulse peak intensities are marked by the filled circles in the time series. The calculated spectra have relative magnitudes with decibel increment. In the numerical simulations, the relaxation oscillation frequency is assumed to be $\nu_R = 2.5$ GHz at $J = 1.33J_{th}$ [after Tang and Liu (2001b); © 2001 IEEE]

section and the successive peaks corresponding to f_2 are sampled. In the three-frequency quasi-periodic pulsing state in C, the two incommensurate frequencies f_2 and f_3 are both clearly shown in the spectrum of the peak series and the phase portrait is characterized by a torus. Finally, when the laser enters a chaotic pulsing state as in D, the phase portrait spreads out over a wide range. The phase portraits of $T(N + 1)$ versus $T(N)$ have the same characteristics as those of $S(N + 1)$ versus $S(N)$ at different delay times as shown in a–d of Fig. 7.9. From Figs. 7.8 and 7.9, a positive optoelectronic feedback system fits in a Rulle–Takens–Newhouse three-frequency quasi-periodic scenario to chaos (Tang and Liu 2001b).

To visualize the chaotic route in positive optoelectronic feedback in a semiconductor laser, the bifurcation diagrams are numerically calculated. Bifurcation

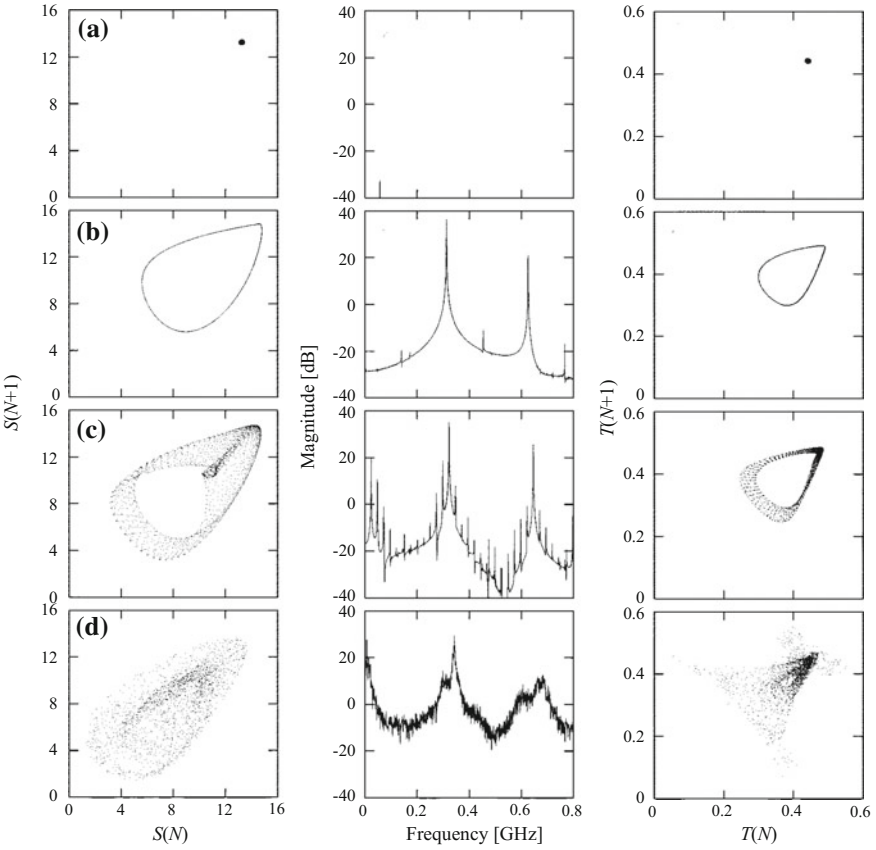

Fig. 7.9 Phase portraits and spectra for peak series extracted from the waveforms in Fig. 7.8. *Left* phase portraits of peak intensities $S(N + 1)$ versus $S(N)$. *Middle* Spectra of peak series. *Right* Phase portraits of the time intervals of pulses $T(N + 1)$ versus $T(N)$. **a–d** Indicate the corresponding pulsing states in Fig. 7.8. In **a**, the *single dot* in the phase portrait is enlarged for visibility [after Tang and Liu (2001b); © 2001 IEEE]

diagrams of the extrema of the peak series versus delay time corresponding to the previous figures (Figs. 7.8 and 7.9) are plotted in Fig. 7.10. Figure 7.10a is the bifurcation diagram with the normalized delay time $\hat{\tau}$ varying from 0 to 10. For a small delay time, the effect of the feedback on the dynamics is not distinct and the feedback increases the laser output slightly over that in the free-running condition. With the increase of the delay time, the laser output shows regular pulsing with constant pulse peak intensity and interval. For a larger delay, the laser follows a quasi-periodic route into chaotic pulsing states. Figure 7.10b is the enlarged bifurcation diagram of a part in Fig. 7.10a denoted by the broken rectangle. A–D in the figure can be compared to the pulsing states in Fig. 7.8. The different pulsing states are indicated by the corresponding arrows, where A is regular pulsing, B is two-frequency quasi-periodic pulsing, C is three-frequency quasi-periodic pulsing, and D is chaotic pulsing.

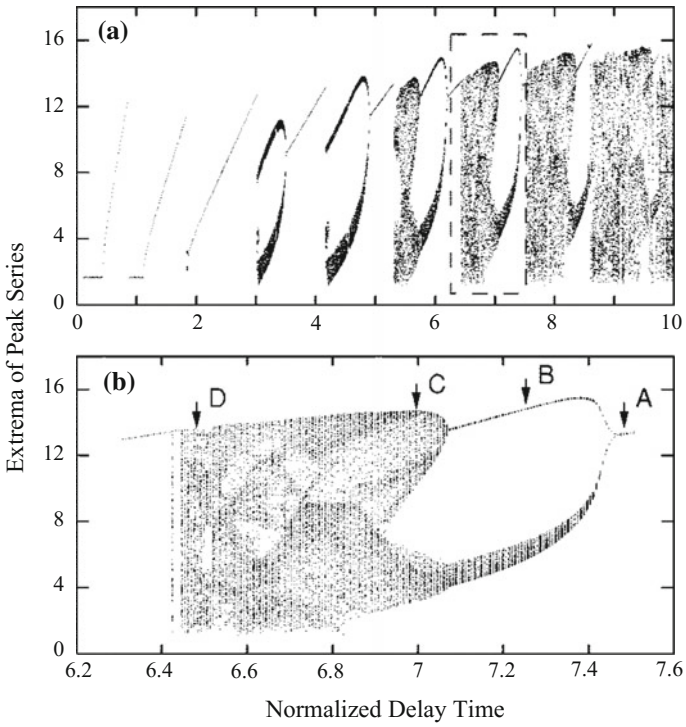

Fig. 7.10 **a** Bifurcation diagram of extrema of peak series with the normalized delay time $\hat{\tau}$ varying from 0 to 10. **b** Enlargement of a small region indicated by dashed rectangle in **a** with identification of various pulsing states. *A–D* Indicate the corresponding pulsing states, as in Fig. 7.8 [after Tang and Liu (2001b); © 2001 IEEE]

7.4 Optoelectronic Feedback with Wavelength Filter

7.4.1 System of Optoelectronic Feedback with Wavelength Filter

The frequency of a semiconductor laser changes as the increase or decrease of the pump for the laser, i.e., the change of the bias injection current in accordance with (5.5). The order of the frequency change is ∼GHz/mA in common narrow-stripe edge-emitting semiconductor lasers. Therefore, we can observe the dynamics induced by the nonlinearity in a semiconductor laser with optoelectronic feedback through a wavelength filter (frequency filter) having a bandwidth of ∼GHz. In such systems, the nonlinearity is greatly enhanced by the introduction of a compulsive time delay longer than the response time of the circuit inserted in the electronic feedback loop. The systems show a rich variety of dynamics, including stable and unstable oscillations and chaos, depending on the delay and other control parameters. Several chaotic systems of optoelectronic feedback with wavelength filter have been proposed in semiconductor lasers. One of them is an optoelectronic system where the emitted light passes through a Fabry–Perot (FP) resonator and the output from the FP is electronically detected and fed back to the laser injection current (Ohtsu 1996). The second example is the use of a birefringent plate in the optical path with the combination of optoelectronic feedback circuits to a semiconductor laser (Goedgebuer et al. 1998a; Larger et al. 1998a). Another system of optoelectronic filtered feedback in a semiconductor laser is an electro-optic (EO) modulation system, in which the emitted light from a semiconductor laser is detected by a photodetector and the signal drives an EO modulator. The light from a different laser goes through the EO module. The light is then detected by a second photodetector and the electric signal with time delay is added to the bias injection current, thus closing the loop (Goedgebuer et al. 2002). This is also an example of filtered optoelectronic systems. These examples are categorized into filtered feedback systems discussed in Sect. 4.7. These systems are used for light sources of chaotic generators in optical secure communications, which will be discussed in Chap. 13. Chaotic communications of encoding and decoding rather lower frequency signals ranging from several kHz to 100 MHz have been demonstrated using chaotic transmitter and receiver systems with optoelectronic filtered feedback (Goedgebuer et al. 1998b, 2002; Larger et al. 1998b). In this section, we describe a system and dynamics of filtered optoelectronic feedback based on a birefringent plate.

Figure 7.11 shows an example of generator of chaos in wavelength using a wavelength tunable semiconductor laser with a nonlinear feedback loop (Larger et al. 1998a). The nonlinearity is induced by the birefringent plate between two crossed polarizers. In a two-electrode semiconductor laser, the wavelength is fixed at a given value λ_0 by adjusting a couple of bias currents (I_0, I_1) on each of the electrodes and can be tuned electronically around λ_0 by varying current I_0 by i, while keeping I_1 constant. The feedback loop consists of a birefringent plate whose fast and slow axes are at 45° to two crossed polarizers PL1 and PL2, a

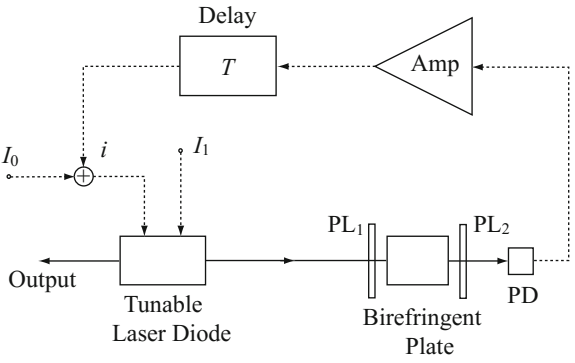

Fig. 7.11 Generator of chaos in wavelength using a wavelength tunable semiconductor laser with a nonlinear feedback loop. *PL* Polarizer, *PD* photo-detector, *Amp* amplifier. *Solid lines* are the optical paths and *dotted lines* are the electronic connections

photodetector (PD) having a time response τ with gain, and a delay line with a retardation time T. The signal is converted to the tuning current i, which is superimposed to the bias current I_0. Hence, the emitted wavelength of the laser is given by $\lambda(t) = \lambda_0 + \Delta\lambda(t)$, where the additional change of the wavelength is proportional to the injection current I and is given by $\Delta\lambda(t) = (\mathrm{d}\lambda/\mathrm{d}i)i(t)$. The power spectrum density of light at the output of PL_2 is a channeled spectrum, which is expressed as

$$NL(\lambda) = \sin^2\left(\frac{\pi D}{\lambda}\right) \approx \sin^2\left(\frac{\pi D}{\lambda_0^2}\lambda - \varphi_0\right) \tag{7.11}$$

where D is the optical-path difference through the birefringent plate and $\phi_0 = \pi D/\lambda_0$. Here, we assume that the additional change of the wavelength $\Delta\lambda$ is much smaller than the wavelength λ_0. Then, the output wavelength of the system is ruled by the following delay differential equation:

$$\lambda(t) + \tau\frac{\mathrm{d}\lambda(t)}{\mathrm{d}t} = \beta_\lambda \sin^2\left\{\frac{\pi D}{\lambda_0^2}\lambda(t-T) - \varphi_0\right\} \tag{7.12}$$

where $\beta_\lambda = PK\mathrm{d}\lambda/\mathrm{d}i$, P and K being the detected optical power by the photodetector and the gain of the amplifier. τ is the time constant of the feedback loop and it is theoretically limited by the wavelength switching time of the semiconductor laser. The time delay T is longer than the response time τ of the loop. Since we consider a long delay compared with the laser response (of the order of nanoseconds) and the delay time T is around milliseconds, we need not take into account the dynamics related to the relaxation oscillation. Therefore, (7.12) is enough to describe the dynamics of wavelength in the tunable semiconductor laser.

7.4.2 Dynamics of Optoelectronic Feedback with Wavelength Filter

In this subsection, we present experimental results of optoelectronic feedback with the wavelength filter that is described in the previous subsection. The laser is a tunable double-electrode distributed Bragg reflector (DBR) semiconductor laser whose wavelength can be tuned continuously without mode hopping. The center wavelength of the laser is $\lambda_0 = 1.550$ μm and the total tuning range is 1.5 nm (corresponding frequency range is 200 GHz). The wavelength is tuned by a DBR-section injection current I_0 and the wavelength tunability is $d\lambda/di = 2$ nm/mA. The birefringent plate was a calcite slab of thickness $d_b = 6$ cm, yielding an optical path difference $D = |n_e - n_o|d_b = 11$ mm between its fast and slow axes, where $n_e = 1.477$ and $n_o = 1.634$ are the extraordinary and ordinary refractive indices, respectively. Then, its spectral transmission curve, which is also the function expressed by (7.11), exhibits seven sinusoidal peaks centered at 1.550 μm inside the 1.5 nm tuning range of the semiconductor laser. The linewidth of the laser is 10 MHz. The response time of the electronic circuit is $\tau = 8.6$ μs, while the delay time is much slower than the response time and is set to be $T = 0.51$ ms.

In the wavelength filtered optical feedback, period-doubling cascade route to chaos is obtained as the increase of the bifurcation parameter β ($\beta = \beta_\lambda \pi D/\lambda_0^2$). Figure 7.12 shows experimental dynamics for different values of the bifurcation parameter β and the corresponding power spectrum. The bifurcation parameter β is tuned by changing electronically the photodetector gain K in the feedback loop. Period-2 in Fig. 7.12a is a typical square waveform. The wavelength emitted by the semiconductor laser oscillates periodically between two states spaced by 41 pm (6.3 GHz). The spectrum in Fig. 7.12b shows odd harmonics whose amplitude decreases with increasing the odd number. The fundamental frequency is $\{2(T + \tau)\}^{-1} = 970$ Hz. Four wavelength states (located at $\lambda_1 = 59$ pm, $\lambda_2 = 66$ pm, $\lambda_3 = 110$ pm, $\lambda_4 = 114$ pm) are obtained in the period-4 regime, as shown in Fig. 7.12c. The spectrum of period-4 in Fig. 7.12d exhibits sub-harmonic peaks at frequencies $\{(2m - 1)/4(T + \tau)\}$ with a positive integer m. The DC background in the spectrum is slightly increased compared with that of the period-2 regime. As β exceeds 2.11 in Fig. 7.12e, f, the peak-to-peak amplitude of these small oscillations increases, yielding a high noise-like level in the spectrum. These oscillations may be regarded as a starting chaotic regime at each of the levels of the period-4 cycle. The time evolution of Fig. 7.12e is termed period-4 chaos. When slightly increasing β from 2.12 to 2.18, the laser enters a period-2 chaos, as shown in Fig. 7.12g, h. The background level in the spectrum is relatively high, but still features harmonic peaks. The two successive regimes period-4 chaos and period-2 chaos illustrate the inverse cascade in the bifurcation diagram. These non-periodic but chaotic regimes with a growing complexity are also in very good agreement with the behaviors observed in earlier experimental investigations (Gibbs 1985). Another example of periodic regime is illustrated in Fig. 7.12i, j, a complicated high-frequency periodic oscillation is observed, which is named as higher harmonic

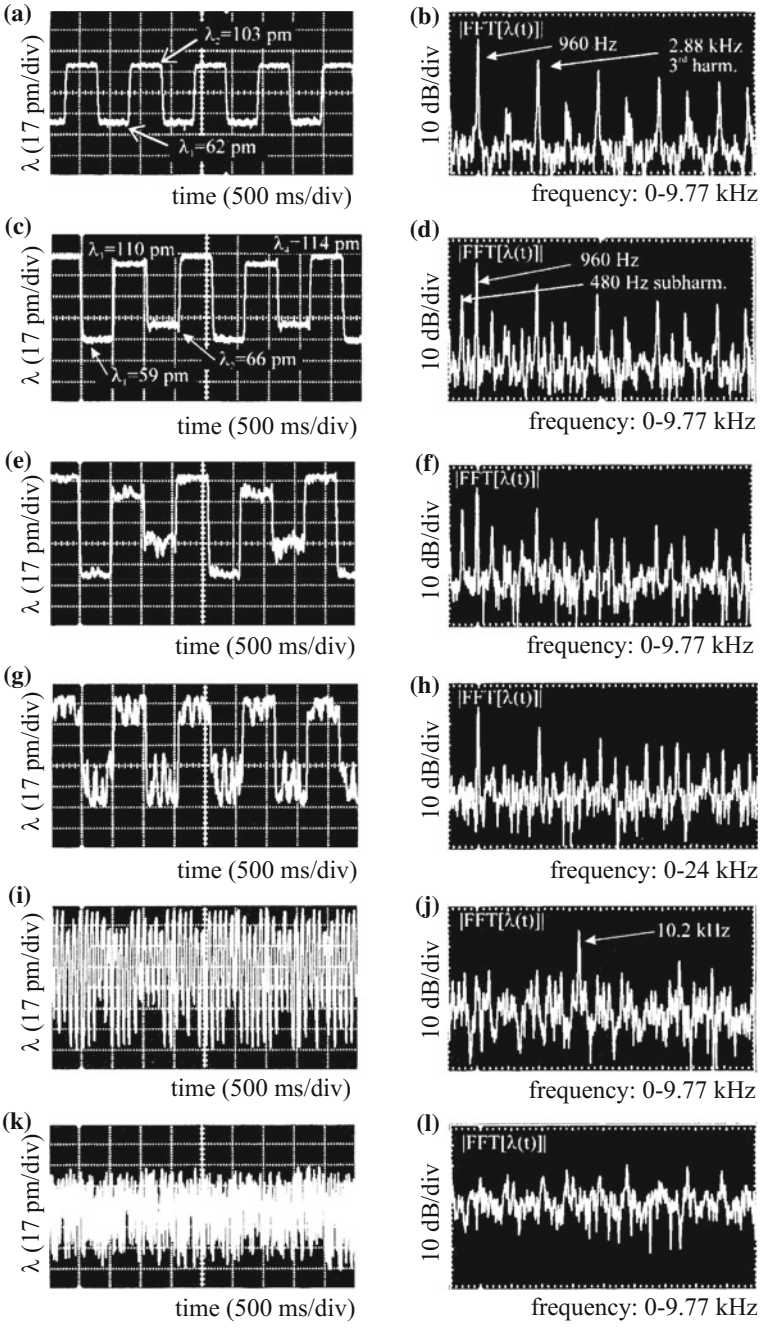

Fig. 7.12 Experimentally obtained time evolution of the wavelength (*left column*) and its FFT spectrum (*right column*) at $\phi_0 = 0.3$ for different values of the bifurcation parameter β. **a**, **b** $\beta = 1.93$, period-2, **c**, **d** $\beta = 2.04$, period-4, **e**, **f** $\beta = 2.12$, period-4 chaos, **g**, **h** $\beta = 2.18$, period-2 chaos, **i**, **j** $\beta = 2.26$, higher harmonic synchronization, and **k**, **l** $\beta = 2.52$, fully developed chaos [after Larger et al. (1998a); © 1998 IEEE]

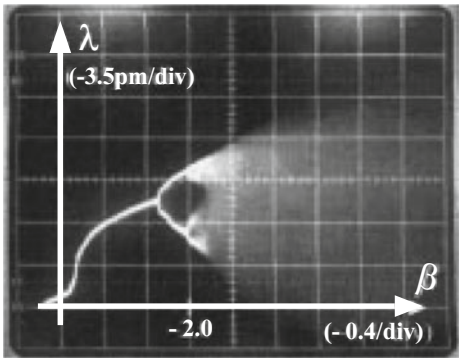

Fig. 7.13 Experimental bifurcation diagram for $\phi_0 = 3$ [after Larger et al. (1998a); © 1998 IEEE]

synchronization. For values of β over 2.5 in Fig. 7.12k, l, fully developed chaos is clearly obtained, without any remaining influence of the higher harmonic synchronization. The spectrum is similar to that of a white noise in the bandwidth of the dynamical system.

Figure 7.13 shows the experimental plot of the bifurcation diagram obtained as $\phi_0 = 0.3$ corresponding to Fig. 7.12. The vertical axis in the figure is the wavelength and the horizontal axis is the bifurcation parameter. The experimental bifurcation diagram quite agrees with the calculated diagram by the delay differential equation in (7.12). The period-doubling cascade (period-2 T_2 and period-4 T_4) route to chaos is obtained as the bifurcation parameter is increased from 0.7 to 2.1. To observe further higher periodic oscillations such as T_8 and T_{16} states, we require a fine tuning of the bifurcation parameter β, but it is very difficult to observe due to existing noises and the limitation for the resolutions of the experimental equipment and also the narrow ranges and the low stabilities of T_8 and higher periods. In usual fact, observations of higher periodic oscillations over period-4 states are rare and difficult in real experiments. When considering the general shape of the doubling cascade, it is also in good agreement with other experimental results (Gibbs 1985).

7.5 Chaotic Dynamics of Semiconductor Lasers Induced by Injection Current Modulation

7.5.1 Instabilities of a Modulated Semiconductor Laser

The output from a semiconductor laser faithfully follows an injection current modulation as far as the modulation is small. On the other hand, for strong injection current modulation, the laser output power clearly exhibits a number of nonlinear characteristics, i.e., harmonic distortion, pulsation different from the modulation frequency, bistability, and period-doubling and quasi-period-doubling routes to

chaos. The routes to chaos in semiconductor lasers have also been intensively studied not only for theoretical interest, but also for practical purposes, especially in the area of analog modulation in optical fiber communications. Chaos in pump-modulated lasers is not the only unique feature in semiconductor lasers. It has also been observed experimentally in solid-state lasers (Klische et al. 1984) and Nd-doped fiber lasers (Phillips et al. 1987). Chaotic phenomena in class B lasers including semiconductor lasers critically depend both on the spontaneous emission (Lee et al. 1985) and the gain saturation (Chen et al. 1985). The spontaneous emission factor and the gain saturation coefficient, which act as damping factors in the small signal analysis, suppress instabilities of semiconductor lasers. Spiky behavior of the photon density by the injection current modulation in semiconductor lasers is used for a light source of picosecond optical pulse generation in various applications (Ito et al. 1981; O'Gorman et al. 1989). When a laser is modulated at a frequency above the intrinsic resonance frequency, the resonance peak shifts towards lower frequency as the modulation current is increased. When the frequency of the noise peak is moved to about a half of the drive frequency, the noise peak begins to be sharpened. That is, the first sub-harmonic is about to be generated. When the modulation current is increased further, the oscillation gradually becomes period-1. Observation of period-4 oscillations in a weakly pulsating laser was reported (Chen et al. 1985), where self-pulsation was induced by optical damage. The observation of a period doubling route to chaos in a Nd-doped fiber laser is also attributed to a very small spontaneous emission factor and gain saturation coefficient (Phillips et al. 1987).

Figure 7.14 is an example of pulsation oscillations by strong modulations for the injection current in a semiconductor laser (Hemery et al. 1990). In the figure, the modulation frequency and index, and the bias injection current are changed. The left plot shows the experimental results and the right shows the theoretical ones. A finite response photodetector is used in the experiment, so that the detector response is also displayed in the middle. In the numerical simulations, the filter effect of the photodetector is taken into account, therefore, the theoretical waveforms are compatible with those of the experiment. The laser is a single-mode Fabry-Perot of an InGaAsP-InP buried heterostructure oscillating at a wavelength of 1.30 μm. The relaxation oscillation frequency depends on the bias injection current and it is less than 3 GHz under the operating conditions. For a high modulation frequency at $f_m = 3.00$ GHz but a moderate modulation index of $m = 0.21$, a waveform similar to the modulation is faithfully reproduced (Fig. 7.14a). For a low modulation frequency and a large modulation index, the laser response still has the same periodicity as the modulation, but several spikes are seen in a single period as shown in Fig. 7.14b. When both the modulation frequency and index are large, period-2 oscillations merge into the laser output power as shown in Fig. 7.14c. However, further large modulation index in Fig. 7.14d, sub-peaks as observed in Fig. 7.14c vanish. Similar results of such period doubling routes have also been reported in semiconductor lasers (Chen et al. 1985; Gallagher et al. 1987; Hori et al. 1988). These behaviors are explained as follows; the laser exhibits intense pulses and the carrier number is abruptly decreased after the

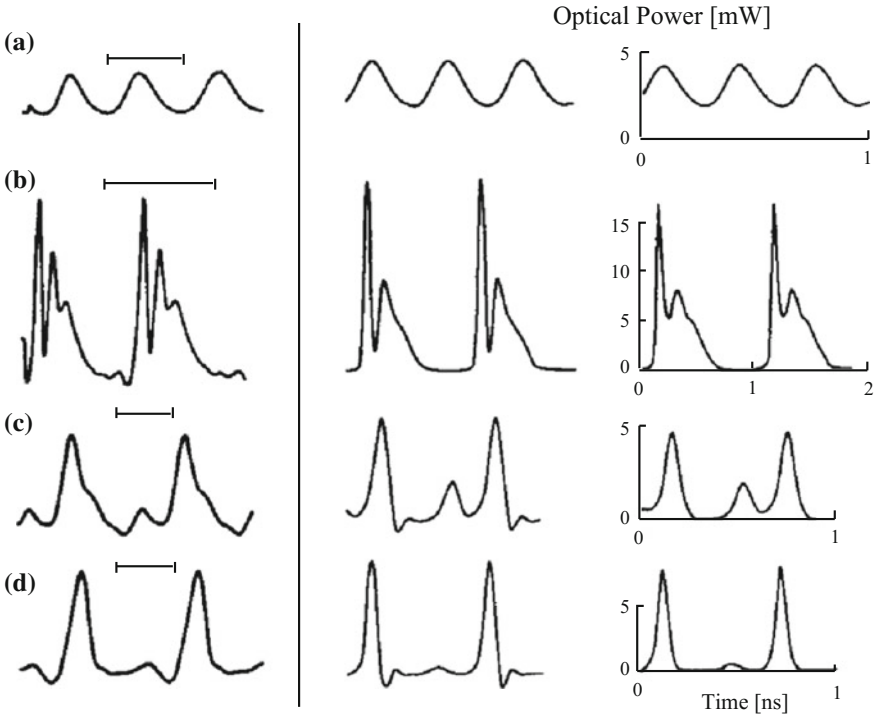

Fig. 7.14 Laser outputs by strong injection current modulation. Experimental (*left*) and theoretical (*right*). *Middle curves* account for the photodetector response in the experiment. The modulation conditions are **a** f_m = 3.00 GHz, m = 0.21, $J = 2.14J_{\text{th}}$, **b** f_m = 1.00 GHz, m = 1.40, $J = 2.14J_{\text{th}}$, **c** f_m = 3.4 GHz, m = 2.30, $J = 1.40J_{\text{th}}$, and **d** f_m = 3.33 GHz, m = 3.60, $J = 1.40J_{\text{th}}$. In each case, the horizontal bar indicates the period of current modulation [after Hemery et al. (1990); © 1990 IEEE]

oscillations of intense pulses when the injection current is strongly modulated. If the modulation frequency exceeds the relaxation oscillation frequency, a longer recovery time than the modulation period is required to restore the carrier number enough for the laser oscillation. Then, the laser may oscillate at a frequency beyond the period of the modulation and result in period-2 oscillations.

7.5.2 Linear Stability Analysis

In optoelectronic feedback systems, the feedback term is applied to the injection current as an additional perturbation as shown in (7.2). In the injection current modulation, the feedback term is replaced by the modulation as discussed in Sect. 3.7. As usual, the modulation may be a sinusoidal one with a modulation

frequency f_m and a modulation index m. Again, the rate equation for the carrier density in the presence of sinusoidal injection current modulation is given by

$$\frac{\mathrm{d}n(t)}{\mathrm{d}t} = \frac{J(t)}{ed}\{1 + m\sin(2\pi f_m t)\} - \frac{n(t)}{\tau_s} - G_n\{n(t) - n_0\}S(t) \tag{7.13}$$

The rate equation for the photon density remains the same as that in (7.1). Several studies have been conducted for the linear stability analysis for the rate equations in the presence of injection current modulation by paying the attention to the nonlinear gain saturation coefficient ε_s and the spontaneous emission factor β_{sp} and discussed stability and instability for the injection current modulation (Yoon et al. 1989; Lee and Shin 1989). They showed resonance frequency shift, bistability, and period-doubling bifurcation in directly modulated semiconductor lasers in the output power. The dynamics is strongly dependent on spontaneous emission and gain saturation. As a result, it is shown that the resonance peak in the frequency response shifts toward lower frequencies as the modulation current is increased, and that it may accompany a hysteresis phenomenon. Similar results have been reported by Harth (1973). His result was obtained by neglecting both the spontaneous emission factor and the gain saturation coefficient. Since the calculation for the steady-state analysis is too complex, we here show only one of the results for the linear stability analyses.

It is known that generation of a period-2 solution or the first period-doubling bifurcation in a directly modulated semiconductor laser is possible by sub-harmonic resonance occurring when the frequency of the driving current is close to twice the small signal resonance frequency (Yoon et al. 1989). Figure 7.15 is an example of domains for the periodic oscillations. At the frequency slightly less than $2\omega_{\mathrm{R}}$, there are hystereses for the increase or decrease of the frequency. It is not explicitly shown in the graph, but coexistence states of two chaotic attractors exist in the region of periodic states (period-1 and period-2) at certain modulation indexes. With an increase of the modulation index from zero, there is no sub-harmonic resonance until $m = m_1$. At that point, the sub-harmonic amplitude suddenly takes a finite value jumping to the upper branch of the amplitude. With decreasing the modulation index on the upper branch, the amplitude of the sub-harmonics decreases and it falls abruptly to zero at $m = m_2$. The existence of a sub-harmonic solution depends on history. Thus, within the region of $m_2 < m < m_1$, two attractors coexist; one is the period-1 and the other is the period-2 (Arecchi et al. 1982). m_1 and m_2 are proportional to the damping constant $\tau_s \Gamma_{\mathrm{R}}$ that increases with the increase of both β_{sp} and ε_s, and is inversely proportional to the normalized carrier decay time $\tau_s/\tau_{\mathrm{ph}}$. Experimental observations of the period-2 solution in pump-modulated lasers have been made (Siemsen 1978; Paoli 1981). In those papers, the authors showed that period-doubling bifurcations via period-4 and period-8 oscillations are excited by the increase of the modulation as parametric resonance in the laser.

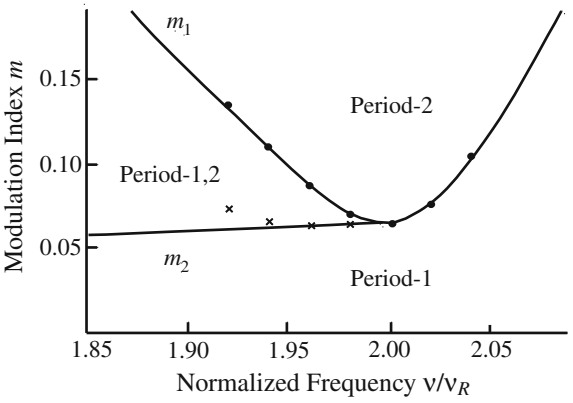

Fig. 7.15 Domain for the first sub-harmonic bifurcation at $\tau_s\Gamma_R = 0.937$. The other used parameters are $G_n\tau_s\tau_{ph}J/ed = G_n\tau_sS_s = 2.8$ and $\tau_s/\tau_{ph} = 3000$ (S_s is the steady-state photon number). *Dots* and *crosses* represent the numerical results and the *solid lines* represent analytical results [after Yoon et al. (1989); © 1989 IEEE]

7.5.3 *Chaotic Dynamics in Modulated Semiconductor Lasers*

Kao et al. (1992), Kao and Lin (1993) investigated the stability and instability for the injection current modulation in the phase space of the modulation frequency and index based on the numerical study for the rate equations. They calculated the maps for the models of Fabry-Perot (FP) laser and the distributed feedback (DFB) lasers. Figure 7.16 is the plot of the map for a small damping factor of $|\Gamma_R/\omega_R| = 0.0469$ with zero nonlinear gain $\varepsilon_s = 0$. Curve HS_m is the boundary of the hysteresis jump of the m-th spiking state; the section with broken line denotes the downward jump. Curves PD_m and PF_m are the boundaries of period-2 and period-4 of the m-th spiking state. The laser oscillation becomes spiky when the modulation current is increased to reach the minimum of the current swing approach to the threshold current level around $m = 0.5$. The laser output shows multiple spikes for $\nu < \nu_R$ and sub-multiple spikes for $\nu > \nu_R$. A minimum modulation current is required for the threshold PD_1 of period-2 state with frequency variation from ν_R to $2\nu_R$. The threshold $HS_{1/2}$ of hysteresis, meanwhile, overlaps with the PD_1 and two types of period-doubling can be observed. Both of them contain half sub-harmonic components in the frequency spectrum and cannot be solely differentiated from the spectra. One is the normal type of period-doubling and is unrelated to the hysteresis. As discussed in Sect. 7.2, the parameters of the nonlinear gain ε_s and the spontaneous emission coefficient β_{sp} play a crucial role for the dynamics.

Not all lasers always show unstable pulsation oscillations for the injection current modulation. In the actual case, some lasers show instabilities for strong injection current modulation, but others not. For example, the dynamics strongly depends on device structures such as FP laser or DFB laser, or the device constants of lasers even for the same laser structures. Bennett et al. (1997) observed period-2 states in a FP laser, while they identified both period-2 and period-3 states in the DFB laser. Figure 7.17 is an example. The FP laser used in the experiments has a wavelength of 1.56 μm biased at $J = 5.88J_{th}$ with a relaxation oscillation frequency

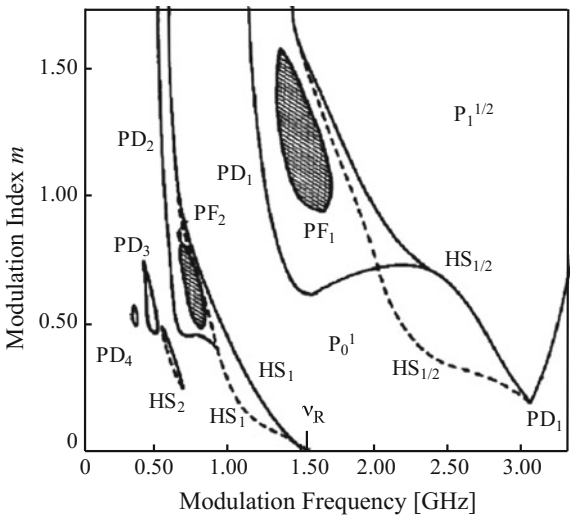

Fig. 7.16 Phase diagram with the modulation frequency and the index at $J = 1.5J_{th}$. The relaxation oscillation frequency of the solitary laser at that frequency is 1.512 GHz. HS_m is the boundary of the hysteresis jump of the m-th spiking state. The section with broken line denotes downward jump. PD_m and PF_m are the boundaries of period-2 and period-4 oscillations of the m-th spiking state [after Kao and Lin (1993); © 1993 IEEE]

of 13.3 GHz. The DFB laser used in the experiments has a wavelength of 1.53 μm biased at $J = 5.26J_{th}$ with the relaxation oscillation frequency of 11.3 GHz. The important parameters for the nonlinear dynamics are the nonlinear gain saturation factor ε_s and the spontaneous emission coefficient β_{sp}. The nonlinear gain saturation factor ε_s is almost the same for those two lasers and the factor of DFB lasers is generally 1.5 times larger than that of FP lasers. On the other hand, the difference of the spontaneous emission coefficient β_{sp} is very large. In general, the coefficient β_{sp} of FP lasers is 50 times larger than that of DFB lasers. Therefore, a FP laser is greatly affected by spontaneous emission of light. This results in less effect for unstable oscillations for the injection current modulation. Figure 7.17a, b are the plots of the map for the regions where unstable behaviors are observed in the experiments. Figure 7.17c, d are the corresponding maps for Fig. 7.17a, b, respectively, obtained by the numerical calculations from the rate equations. PD denotes the regions where period-2 states are recorded and T is the region where a period-3 state is observed. In the FP laser, there is a range of power levels and modulation frequencies over which the period-2 state is observed. In the DFB laser, there are both regions of period-2 and period-3 states. In the region where period-3 oscillation occurs, as the modulation power is increased, the route to period-3 is always via period-doubling. Thus, the dynamics of unstable pulsation oscillations depend on the device parameters, especially on the spontaneous emission coefficient. The theoretical analysis of bifurcation in semiconductor lasers by Yoon et al. (1989) found that lasers with low relaxation damping were more susceptible to bifurcation. This was also observed in the experiments. Liu and Ngai (1993) suggest that the promotion of period-3 in their bulk DFB laser was due to the unusually low value of β_{sp} measured in their laser. The observed period-3 in a DFB laser can be attributed to the low value of β_{sp} measured in that laser.

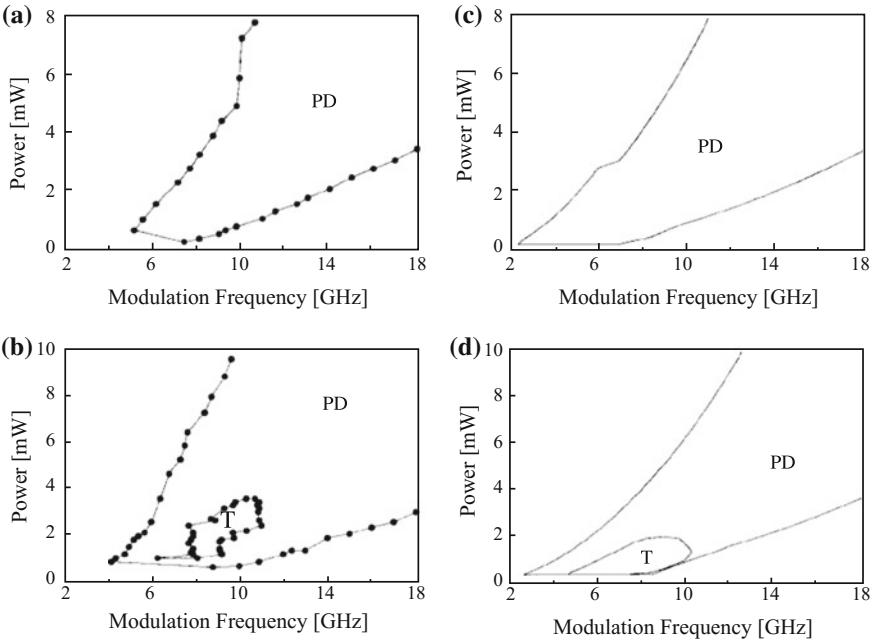

Fig. 7.17 Regions where unstable behaviors are observed. Experimental results for **a** FP laser and **b** DFB laser. **c** and **d** are the corresponding numerical simulations for **a** and **b**, respectively. *PD* Period-2 state, *T* period-3 state [after Bennett et al. (1997); © 1997 IEEE]

7.6 Nonlinear Dynamics of Various Combinations of External Perturbations

7.6.1 Optically Injected Semiconductor Laser Subject to Optoelectronic Feedback

Though a semiconductor laser itself is a stable laser categorized as a class B, the laser is easily destabilized by a single external disturbance, such as optical feedback, optical injection, optoelectronic feedback, or injection current modulation as has already been studied. Other possible perturbations exist. Semiconductor lasers are also destabilized by mixed perturbations with two or more of the above external disturbances and show more complex dynamics. Indeed, such dynamics have been studied because of their importance in practical applications. For laser control to reduce chaotic noises and chaotic communications in semiconductor laser systems, composite external perturbations play essential roles in the systems. In the following, as examples, we discuss the dynamics of semiconductor lasers subjected both to optical injection and optoelectronic feedback, and both to optical feedback and injection current modulation.

At first, we consider the dynamics of semiconductor lasers subjected to optical injection and optoelectronic feedback. In the dynamics in optoelectronic feedback alone, we can observe quasi-periodic routes of chaotic pulsing (Tang and Liu 2001b) and chaotic pulsing states are generated depending on the delay time. On the other hand, a period-doubling route to chaos is identified (Simpson et al. 1994) and the frequency of chaotic oscillations is much enhanced by large optical injection compared with the free running state (Simpson et al. 1995). However, the chaotic oscillations can only be observed for rather small optical injection strength with and without frequency detuning, where careful adjustment of both the injection strength and the frequency detuning is needed to operate the laser in such states (Liu et al. 1997; Simpson et al. 1997).

In the mixed perturbations both of optical injection and optoelectronic feedback, the dynamic states including stable locking, periodic oscillation, chaotic oscillation, regular pulsing, quasi-periodic pulsing, and chaotic pulsing seen in semiconductor lasers subject to either optical injection or delayed optoelectronic feedback alone, can all be found. By controlling the optoelectronic feedback parameters, the bifurcation can be suppressed or inverted in such a manner that high-order periodic or chaotic dynamics are reduced to low-order periodic motions. In a semiconductor laser subject both to optical injection and optoelectronic feedback, coherence collapse is found to be suppressed and the bandwidth broadening effect is observed (Lawrence and Kane 1999). In this system, chaotic evolution can be observed for the change of the optical injection strength. However, there are two ways of chaotic routes, either a period-doubling route to chaotic oscillation states or a quasi-periodic route to chaotic pulsing states, even transient states in-between are identified. A notable expansion and shifting of the chaos region in the parameter space is observed in the system due to a strong optoelectronic feedback effect. The bandwidth of the chaotic state can also be greatly broadened by the introduction of optical injection. This phenomenon of chaos-region broadening and shifting together with the bandwidth enhancement is very important for increasing the bit rate of chaotic communications, which is currently limited by the bandwidth of chaos and the relaxation oscillation frequency of the laser (Tang and Liu 2001a, b; Kusumoto and Ohtsubo 2002).

The mappings of dynamic states of a semiconductor laser subject to optical injection and optoelectronic feedback are numerically calculated and displayed in Fig. 7.18 (Lin and Liu 2003b). The mappings show stable and unstable regions as a function of the normalized optical injection strength of $\kappa'_{\mathrm{nor}} = \kappa_{\mathrm{inj}}(A_m/\tau_{\mathrm{in}})/(A_{0s}/\tau_{\mathrm{ph}})$ and the frequency detuning between the master and slave lasers. The mappings in Fig. 7.18a–d are the plots calculated for different optoelectronic feedback strengths of κ'_{nor}. In the figure, each symbol means S: steady states, P1: period-1, P2: period-2, CO: chaotic oscillation, and P: pulsing states, which include regular pulsing, quasi-periodic pulsing, and chaotic pulsing. With the increase of optoelectronic feedback strength κ'_{nor}, regions of chaotic oscillations greatly expand in the map. When a laser is subjected to optical injection alone, the chaotic region is only restricted for small frequency detuning. On the other hand, when optoelectronic feedback is added to the system, the laser still behaves like a system of

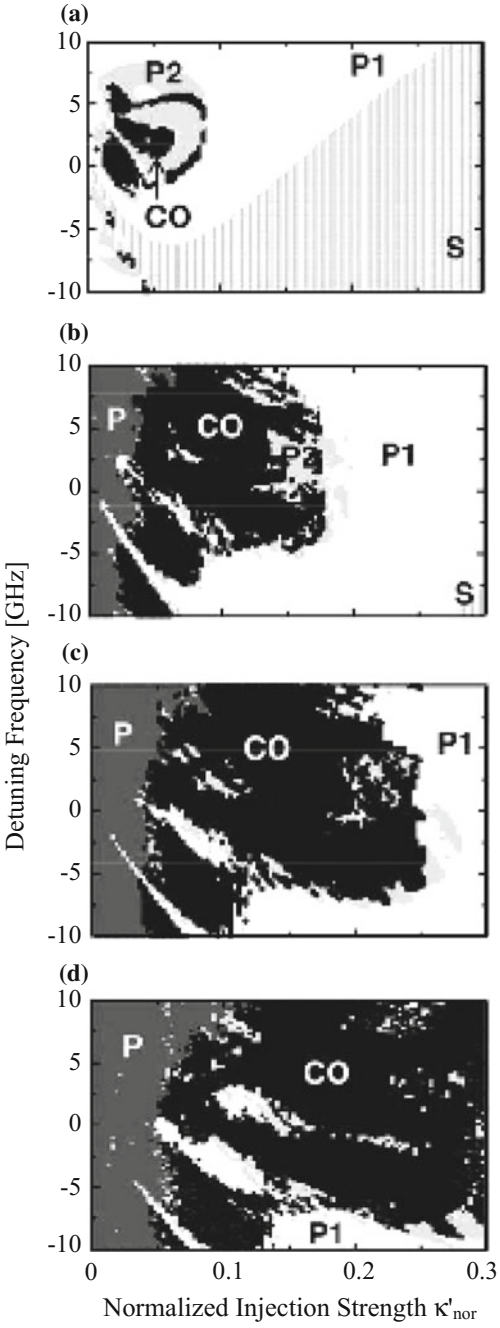

Fig. 7.18 Mappings of dynamic states of the hybrid system where the normalized feedback delay is $\nu_R\tau = 6.8$ and the optoelectronic feedback ratio ξ of **a** 0 (without feedback), **b** 0.16, **c** 0.20, and **d** 0.22, respectively. *S* Steady states, *P1* period-1, *P2* period-2, *CO* chaotic oscillation, *P* pulsing states, which include regular pulsing, quasi-periodic pulsing, and chaotic pulsing. The relaxation oscillation frequency is set to 2.86 GHz [after Lin and Liu (2003b); © 2003 Elsevier]

optical injection alone at a high injection rate, but pulsing states like optoelectronic feedback alone prevail at a lower injection rate as shown in Fig. 7.18b. In between these two states of pulsations and chaotic oscillations, chaotic pulsing states are observed. As the feedback strength is further increased, this expanding and shifting effect is further enhanced as can be seen in Fig. 7.18c, d. Because of the broadening and the shifting caused by the optoelectronic feedback, this hybrid system is able to operate at CO in the strong injection region, where bandwidth enhancement of the CO is expected (Liu et al. 1997). The CO of this system in the strong injection region has bandwidths much broader than the one that can be obtained in a laser subject to optical injection alone. This hybrid system can be used for high-speed chaotic communications, spread-spectrum spectroscopy, or other applications demanding broadband chaos.

7.6.2 *Semiconductor Lasers with Optical Feedback and Modulation*

As shown in the previous section, when one of the mixed perturbations is small, the behavior of the laser is dominated by the other perturbations. As another example, we here discuss the dynamics of semiconductor lasers subjected to optical feedback and modulation. Lawrence and Kane (2002) experimentally examined the chaotic dynamics for such systems, however they considered two modulation methods for the laser power; one is the direct injection current modulation through a bias Tee and the other is the use of an EO modulator put into the path of the optical feedback loop. For the EO modulation, light emitted from the laser is modulated by a lithium niobate EO modulator. Figure 7.19 presents the experimental results for the map of the dynamic states in the phase space of the modulation frequency and index at a fixed external optical feedback. In the experiment, the laser used is a single-mode quantum-well index-guided laser with a wavelength of 850 nm and a maximum emission power of 50 mW. The laser is biased at $J = 1.4J_{\mathrm{th}}$ (the threshold current is 25 mA). Under the operation condition, the relaxation oscillation frequency of the solitary laser is about 2 GHz. The external feedback mirror is positioned at 317 mm (external cavity resonant frequency of 473 MHz) from the front facet of the laser. The external intensity feedback ratio is 0.22, which corresponds to strong optical external feedback. For such strong optical feedback, the laser is generally stabilized and the linewidth of the laser is much narrowed by the feedback. However, the laser is no more stable with the additional strong modulation. Figure 7.19 shows the output states examined for a wide range of modulation frequencies (from 50 MHz to 1 GHz) relative to the external cavity resonant frequency. In the direct injection current modulation in Fig. 7.19a, a rich variety of dynamics can be observed compared with the case for the EO modulation in Fig. 7.19b. When the modulation is small, the laser output powers for both cases show stable oscillations except for regions corresponding to the external cavity frequency and the relaxation oscillation

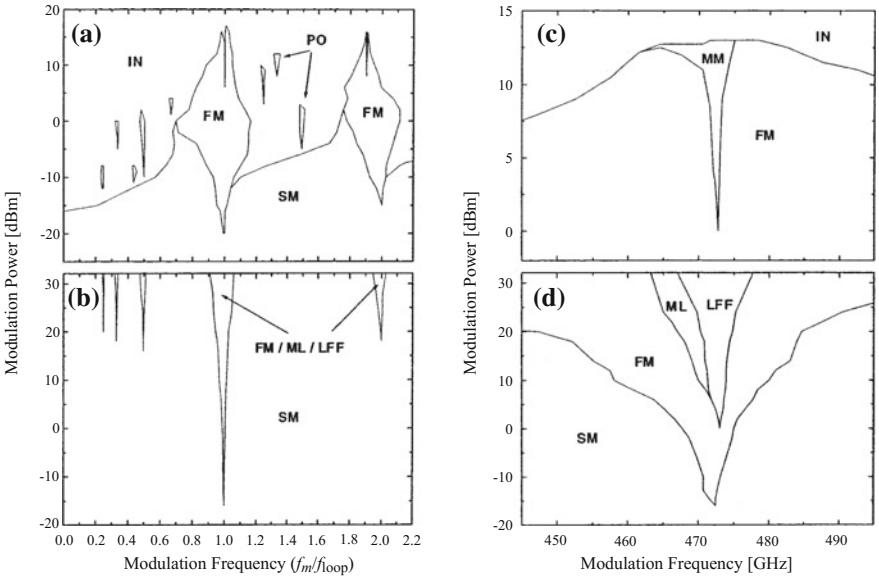

Fig. 7.19 Mappings of dynamic states in the parameter space of the modulation power and the modulation frequency from 50 MHz to 1 GHz ($0.1–2.0 f_{loop}$) for **a** direct injection current modulation and **b** electro-optic modulation. Enlarged mappings for **c** direct injection current modulation and **d** electro-optic modulation corresponding to the dynamic states in **a** and **b** close to the external cavity resonance frequency (473 MHz), respectively. *IN* Temporal instability, *MM* multimode instability, *FM* frequency modulation, *LFF* low-frequency fluctuation, *ML* mode-locking, *SM* single-mode small-signal modulation, *PO* periodic orbit [after Lawrence and Kane (2002); © 2002 IEEE]

frequency. Large regions of FM and multimode output are observed at modulation frequencies close to multiples of the external cavity resonant frequency. The dominant state for the injection current is a temporal instability. At the temporal instability states, we can see distinct regions of periodic oscillation. In the EO modulation in Fig. 7.19b, the laser shows much different features from the case of the direct injection current modulation. FM lasing, mode-locking, and low-frequency fluctuations (LFFs) are observed for small regions centered at sub-harmonics and multiples of the external cavity resonant frequency.

Figure 7.19c, d show the enlarged plots of the dynamics concerning the modulation frequency corresponding to those of Fig. 7.19a, b, respectively. The center frequency of the plots is the external feedback frequency. For the direct modulation with low modulation powers (0 dBm) in Fig. 7.19c, the output is typical of an FM laser. As the modulation frequency is tuned close to the external cavity resonant frequency, the power modulation depth remains constant but the frequency modulation index increases. This enhancement occurs at a resonant frequency near the external cavity resonant frequency, dependent on the feedback level and the external cavity length (Lucero et al. 1988). For increased modulation power, there is

a region of multimode output (labeled MM in the figure) centered at a detuning of 2 MHz from the external cavity resonant frequency. This region is characterized by an oscillation on multiple external cavity modes (Schremer et al. 1988). Such an optical state is similar to the coherence-collapsed state observed in semiconductor lasers operated with optical feedback in regime IV.

When EO modulation is applied, the system behaves somewhat differently as shown in Fig. 7.19d. At modulation frequencies near the external cavity resonance, four distinct states are observed. For low modulation powers, or large detuning, the output is a single frequency. This represents very small signal modulation (labeled SM). As the modulation power is increased or the detuning from the external cavity resonant frequency is decreased, an FM lasing region is observed. This results in lower asymmetry in the FM sideband pairs. A further increase in the modulation power or decrease in the frequency detuning results in a multimode instability. However, this instability is an intermittent state similar to the LFF state observed in semiconductor lasers with optical feedback at low injection currents. For the EO case, the instability close to the external cavity resonant frequency is predicted to occur theoretically using an iterative model based on a perturbation approach. It is attributed to mode competitions between external cavity modes and coupled cavity modes. The theory predicts a dynamic state consisting of large quasi-periodic amplitude modulation with irregular intermittent behavior over longer time scales, similar to the coherence-collapse state in semiconductor lasers with optical feedback but with greater periodic structure than is generally observed for the case of optical feedback alone (Spencer et al. 1999).

References

F.T. Arecchi, R. Meucci, G.P. Puccioni, J.R. Tredicce, Experimental evidence of subharmonic bifurcations, multistability, and turbulence in a Q-switched gas laser. Phys. Rev. Lett. **49**, 1217–1220 (1982)

S. Bennett, C.M. Snowden, S. Iezekiel, Nonlinear dynamics in directly modulated multiple quantum-well laser diodes. IEEE J. Quantum Electron. **33**, 2076–2083 (1997)

Y.C. Chen, H.G. Winful, J.M. Liu, Subharmonic bifurcations and irregular pulsing behavior of modulated semiconductor lasers. Appl. Phys. Lett. **47**, 208–210 (1985)

T.C. Damen, M.A. Duguay, Optoelectronic regenerative pulser. Electron. Lett. **16**, 166–167 (1980)

D.F.G. Gallagher, I.H. White, J.E. Carroll, R.G. Plumb, Gigabit pulse position bistability in semiconductor lasers. J. Lightwave Technol. **5**, 1391–1398 (1987)

G. Giacomelli, M. Calzavara, F.T. Arecchi, Instabilities in a semiconductor laser with delayed optoelectronic feedback. Opt. Commun. **74**, 97–101 (1989)

H.M. Gibbs, *Optical Bistability: Controlling Light with Light* (Academic Press, New York, 1985)

T. Gilbert, R.W. Gammon, Stable oscillations and devil's staircase in the van der Pol oscillator. J. Bifurcation. Chaos **10**, 155–164 (2000)

J.P. Goedgebuer, L. Larger, H. Porte, F. Delorme, Chaos in wavelength with a feedback tunable laser diode. Phys. Rev. E **57**, 2795–2798 (1998a)

J.P. Goedgebuer, L. Larger, H. Porte, Optical cryptosystem based on synchronization of hyperchaos generated by a delayed feedback tunable laser diode. Phys. Rev. Lett. **80**, 2249–2252 (1998b)

J.P. Goedgebuer, P. Levy, L. Larger, C.C. Chen, W.T. Rhodes, Optical communication with synchronized hyperchaos generated electrooptically. IEEE J. Quantum Electron. **38**, 1178–1183 (2002)

E.V. Grigorieva, H. Haken, S.A. Kaschenko, Theory of quasi-periodicity in model of lasers with delayed optoelectronic feedback. Opt. Commun. **165**, 279–292 (1999)

H. Inaba, *Optical Devices and Fibers* (North-Holland, Amsterdam, 1982)

W. Harth, Large signal direct modulation of injection lasers. Electron. Lett. **9**, 532–533 (1973)

H. Hemery, L. Chusseau, J.M. Lourtioz, Dynamic behaviors of semiconductor lasers under strong sinusoidal current modulation: modeling and experiments at 1.3 μm. IEEE J. Quantum Electron. **26**, 633–641 (1990)

Y. Hori, H. Serizawa, H. Sato, Chaos in directly modulated semiconductor lasers. J. Opt. Soc. Am. B **5**, 1128–1133 (1988)

H. Ito, H. Yokoyama, S. Murata, H. Inaba, Generation of picosecond optical pulses with highly RF modulated AlGaAs DH laser. IEEE J. Quantum Electron. **17**, 663–670 (1981)

Y.H. Kao, H.T. Lin, Virtual Hopf precursor of period-doubling route in directly modulated semiconductor lasers. IEEE J. Quantum Electron. **29**, 1617–1623 (1993)

Y.H. Kao, C.H. Tsai, C.S. Wang, Observation of bifurcation structure in a rf driven semiconductor laser using an electronic simulator. Rev. Sci. Instrum. **63**, 75–79 (1992)

W. Klische, H.R. Telle, C.O. Weiss, Chaos in a solid-state laser with a periodically modulated pump. Opt. Lett. **9**, 561–563 (1984)

H. Kressel, J.K. Butler, *Semiconductor Lasers and Hetero-Junction LEDs* (Academic Press, New York, 1977)

K. Kusumoto, J. Ohtsubo, 1.5-GHz message transmission based on synchronization of chaos in semiconductor lasers. Opt. Lett. **27**, 989–991 (2002)

L. Larger, J.P. Goedgebuer, J.M. Merolla, Chaotic oscillator in wavelength: A new setup for investigating differential difference equations describing nonlinear dynamics. IEEE J. Quantum Electron. **34**, 594–601 (1998a)

L. Larger, J.P. Goedgebuer, F. Delorme, Optical encryption system using hyperchaos generated by an optoelectronic wavelength oscillator. Phys. Rev. E **57**, 6618–6624 (1998b)

J.S. Lawrence, D.M. Kane, Injection locking suppression of coherence collapse in a diode laser with optical feedback. Opt. Commun. **167**, 273–282 (1999)

J.S. Lawrence, D.M. Kane, Nonlinear dynamics of a laser diode with optical feedback systems subject to modulation. IEEE J. Quantum Electron. **38**, 185–192 (2002)

C.H. Lee, S.Y. Shin, Transformation of rate equations and approximate transient solutions for semiconductor lasers. IEEE J. Quantum Electron. **25**, 878–884 (1989)

C.H. Lee, S.Y. Shin, Self-pulsing spectral bistability, and chaos in a semiconductor laser diode with optoelectronic feedback. Appl. Phys. Lett. **62**, 922–924 (1993)

C.H. Lee, T.H. Yoon, Y. Shin, Period doubling and chaos in a directly modulated laser diode. Appl. Phys. Lett. **46**, 95–97 (1985)

C.H. Lee, S.Y. Shin, S.Y. Lee, Optical short-pulse generation using diode laser with negative optoelectronic feedback. Opt. Lett. **13**, 464–466 (1988)

F.Y. Lin, J.M. Liu, Nonlinear dynamics of a semiconductor laser with delayed negative optoelectronic feedback. IEEE J. Quantum Electron. **39**, 562–568 (2003a)

F.Y. Lin, J.M. Liu, Nonlinear dynamical characteristics of an optically injected semiconductor laser subject to optoelectronic feedback. Opt. Commun. **221**, 173–180 (2003b)

H.F. Liu, W.F. Ngai, Nonlinear dynamics of a directly modulated 1.55 μm InGaAsP distributed feedback semiconductor laser. IEEE J. Quantum Electron. **29**, 1668–1675 (1993)

J.M. Liu, H.F. Chen, X.J. Meng, T.B. Simpson, Modulation bandwidth noise, and stability of semiconductor laser subjected to strong injection locking. IEEE Photonics Technol. Lett. **9**, 1325–1327 (1997)

N.A. Loiko, A.M. Samson, Possible regimes of generation of a semiconductor laser with a delayed optoelectronic feedback. Opt. Commun. **93**, 66–72 (1992)
A.J. Lucero, R.W. Tkach, R.M. Derosier, Distortion of the frequency modulation spectra of semiconductor lasers by weak optical feedback. Electron. Lett. **24**, 337–339 (1988)
J. O'Gorman, B.J. Hawdon, J. Hegarty, Frequency locking and quasiperiodicity in a modulated external cavity injection lasers. J. Appl. Phys. **66**, 57–60 (1989)
M. Ohtsu, *Frequency Control of Semiconductor Lasers* (Wiley-Interscience, New York, 1996)
T.L. Paoli, Optical response of a stripe-geometry junction laser to sinusoidal current modulation at 1.2 GHz. IEEE J. Quantum Electron. **17**, 675–680 (1981)
P. Paulus, R. Langenhorst, D. Jäger, Stable pulsations of semiconductor lasers by optoelectronic feedback with avalanche photodiodes. Electron. Lett. **23**, 471–472 (1987)
M.W. Phillips, H. Gong, A.I. Ferguson, D.C. Hanna, Optical chaos and hysteresis in a laser-diode pumped Nd-doped fibre laser. Opt. Commun. **61**, 215–218 (1987)
D. Pieroux, T. Erneux, K. Otsuka, Minimal model of class-B laser with delayed feedback: cascading branching of periodic solutions and period-doubling bifurcation. Phys. Rev. A **50**, 1822–1829 (1994)
A. Ritter, H. Haug, Theory of laser diodes with weak optical feedback: 1. small-signal analysis and side-mode spectra. J. Opt. Soc. Am. B **10**, 130–114 (1993a)
A. Ritter, H. Haug, Theory of laser diodes with weak optical feedback: 2. limit-cycle behavior, quasi-periodicity, frequency locking, and route to chaos. J Opt. Soc. Am. B **10**, 145–154 (1993b)
A. Schremer, T. Fujita, C.F. Lin, C.L. Tang, Instability threshold resonances in directly modulated external-cavity semiconductor lasers. Appl. Phys. Lett. **52**, 263–265 (1988)
D. Siemsen, Observation of inherent oscillations and subharmonic resonances in the light output GaAs DH lasers. Int. J. Electron. **45**, 63–67 (1978)
T.B. Simpson, J.M. Liu, A. Gavrielides, V. Kovanis, P.M. Alsing, Period-doubling route to chaos in a semiconductor laser subject to optical injection. Appl. Phys. Lett. **64**, 3539–3541 (1994)
T.B. Simpson, J.M. Liu, A. Gavrielides, Bandwidth enhancement and broadband noise reduction in injection-locked semiconductor lasers. IEEE Photonics Technol. Lett. **7**, 709–911 (1995)
T.B. Simpson, J.M. Liu, K.F. Huang, K. Tai, Nonlinear dynamics induced by external optical injection in semiconductor lasers. Quantum Semiclass. Opt. **9**, 765–784 (1997)
P.S. Spencer, D.M. Kane, K.A. Shore, Coupled-cavity effects in FM semiconductor lasers. J. Lightwave Technol. **17**, 1072–1078 (1999)
S. Tang, J.M. Liu, Synchronization of high-frequency chaotic optical pulses. Opt. Lett. **26**, 596–598 (2001a)
S. Tang, J.M. Liu, Chaotic pulsing and quasi-periodic route to chaos in a semiconductor laser with delayed opto-electronic feedback. IEEE J. Quantum Electron. **37**, 329–336 (2001b)
J.P. van der Ziel, Mode locking of semiconductor lasers, in *Semiconductors and Semimetals,* vol. 22, Part B, ed. by W.T. Tsang (Academic, Orlando, 1985)
T.H. Yoon, C.H. Lee, S.Y. Shin, Perturbation analysis of bistable and period doubling bifurcation in directly-modulated laser diodes. IEEE J. Quantum Electron. **25**, 1993–2000 (1989)

Chapter 8
Instability and Chaos in Various Laser Structures

Abstract Narrow-stripe edge-emitting structure is not the only one for semiconductor lasers. Other than these, various kinds of laser structures of semiconductor lasers have been proposed and some of them are now in practical use. For example, vertical-cavity surface-emitting semiconductor lasers (VCSELs) are expected as the next generation laser light sources for optical communications and optical memory systems, and broad-area semiconductor lasers are promising light sources for high power laser applications. Quantum-dot semiconductor laser is a new laser structure expected as a light source for highly coherent beam emission. The region of light emission from the laser is well confined in a certain spatial point in the active area, namely a quantum dot, and the energy levels related to light emission are perfectly quantized by a quantum-dot structure. Another example of recent semiconductor laser is quantum-cascade laser, which is a THz light source. Though a quantum-cascade laser is one of the semiconductor lasers, the laser structure and light emission process are completely different from other semiconductor lasers based on inter-band optical transitions. Such a laser also shows different dynamics from conventional semiconductor lasers. They have their own unique characteristic properties. Here, we do not discuss the details of each device structure and its characteristics, but we introduce the rate equations for such lasers and present their dynamic properties. These new laser structures have extra degrees of freedom and show instabilities and chaotic dynamics without any introduction of external perturbations. In this chapter, we discuss the dynamics of these new lasers both for solitary oscillations and external perturbations.

8.1 Multimode Lasers

8.1.1 Multimode Operation of Semiconductor Lasers

Before discussing the dynamics of semiconductor lasers with various structures different from narrow-stripe edge-emitting lasers, we show the rate equations for multimode operating narrow-stripe edge-emitting lasers. In the preceding chapters,

© Springer International Publishing AG 2017

J. Ohtsubo, *Semiconductor Lasers*, Springer Series in Optical Sciences 111,
DOI 10.1007/978-3-319-56138-7_8

semiconductor lasers were assumed to be operating at a single longitudinal mode, however, the laser sometimes oscillates at multimode due to noises when it is biased at a low injection current close to the threshold, otherwise it oscillates at multimode originating from their device structures even for a higher bias injection current. It intrinsically oscillates at multimode by the introduction of external perturbations such as optical external feedback. Figure 8.1 shows a multimode spectrum of a Fabry-Perot semiconductor laser operating close to the threshold. Even for a laser operating at a single mode with suppressed side mode, the side mode does not damp out by optical feedback or optical injection, and the laser dynamics are much affected by the mode behaviors as shown in Chap. 6. Semiconductor lasers at solitary condition may be operated with multimode as a nature of the device structure, since the laser has a broad gain bandwidth. The separation of the longitudinal modes of an ordinary semiconductor laser is more than 100 GHz (the corresponding wavelength separation is $\sim$1 nm) due to a short internal cavity length. However, the gain profile is as large as 20 nm or more and it has the possibility of multimodal oscillations with several oscillation lines. In semiconductor lasers of various device structures different from narrow-stripe edge-emitting lasers, they usually operate at multimode without any external perturbations, since they originally include extra variables (extra degrees of freedom) besides those for narrow-stripe edge-emitting lasers. We will discuss these dynamics later. Here, we first discuss the dynamics of narrow-stripe edge-emitting semiconductor lasers operating at multimode.

Semiconductor lasers have broad gain bandwidth, which is a unique feature different from other lasers. Therefore, there exist many possible oscillation lines within the bandwidth. The gain curve is sometimes assumed as a parabolic function, although, in actual fact, the gain profile has asymmetry as discussed in Sect. 3.4. The gain for shorter wavelength (higher energy of carrier or higher frequency oscillation) tends to be large by the band-filling effects under the condition of constant temperature and carrier injection. Also, semiconductor lasers with multimode operation are much affected by this effect (Petermann 1988). The optical powers are equally distributed to respective modes below the laser threshold. However, the transfer of the power to the side modes is much restrained well above the threshold and the power of the main mode increases resulting in a single-mode

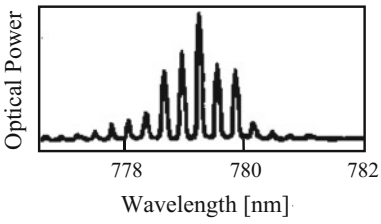

Fig. 8.1 Optical spectrum of a multimode Fabry-Perot semiconductor laser

oscillation. This phenomenon is well reproduced from the calculations of the rate equations for taking into consideration the multimode effects and the theory and experiments show good coincidence. The effect of side mode suppression is strongly dependent on spontaneous emission of light and the large spontaneous emission coefficient β_{sp} forces the excitation of side modes.

8.1.2 Theoretical Model of Multimode Lasers

The rate equations for the photon number and the carrier density for multimode semiconductor lasers are given by the following equations (Petermann 1988):

$$\frac{dS_j(t)}{dt} = \left[G_{n,j}\left\{n(t) - n_{th,j}\right\}\right]S_j(t) + R_{sp}(\omega_j) \tag{8.1}$$

$$\frac{dn(t)}{dt} = \frac{J(t)}{ed} - \frac{n(t)}{\tau_s} - \sum_{j=-M}^{M} G_{n,j}\{n(t) - n_0\}S_j(t) \tag{8.2}$$

where subscript j is for the j-th mode and $2M + 1$ is the total mode number. $j = 0$ is the main mode. The final term in (8.1) is the effect of spontaneous emission of light. It is noted that it is not only a function of time but also a function of optical frequency. For incoherent rate equations, we do not need to consider the phase equation, since it does not couple with the other equations. The above two equations are enough to describe the primary characteristics induced by multimode oscillations in a solitary laser. On the other hand, in an actual situation, we must consider the nonlinear saturation effect for the gain and the cross-saturation effect in the photon number rate equation. Further, we must use the complex field equation instead of the photon number rate equation, when we consider coherent effects such as optical feedback. For coherent phenomena, the phase equation plays a crucial role for the dynamics as has already been discussed. Such an instance will be treated later in this subsection.

At first, we study the side mode suppression ratio (MSR) in a multimode semiconductor laser. Assuming $2M + 1$ oscillation lines within the gain profile and approximating the gain as a parabolic curve, the gain is written as

$$G_{n,j} = G_n\left\{1 - \left(\frac{j}{M}\right)^2\right\} \tag{8.3}$$

where $M = \Delta\nu_g/\Delta\nu_l$, $\Delta\nu_g$ is the frequency width of the gain profile and $\Delta\nu_l$ the frequency of the longitudinal mode spacing. The laser output power of the j-th

mode for the steady-state solution is calculated from the rate (8.1) and (8.2) as (Petermann 1988; Agrawal and Dutta 1993)

$$S_j \approx \frac{R_{\mathrm{sp}}(\omega_j)}{\frac{1}{\tau_{\mathrm{ph}}} - G_{n,j}(n_s - n_0)} \approx \frac{\tau_{\mathrm{ph}} R_{\mathrm{sp}}(\omega_j)}{\delta + \left(\frac{j}{M}\right)^2} \tag{8.4}$$

where n_s and n_0 is the steady-state value of carrier density and carrier number at transparency, and $\delta = 1 - G_n \tau_{\mathrm{ph}}(n_s - n_0) = \tau_{\mathrm{ph}} R_{\mathrm{sp}}/S_0$. Note that the relation $G_n \tau_{\mathrm{ph}}(n_s - n_0) \approx 1$ is used for the final form of (8.4). From this relation, we obtain the side mode suppression ratio as

$$\mathrm{MSR} = \frac{S_0}{S_1} = 1 + \frac{1}{\delta M^2} = 1 + \frac{S_0}{\tau_{\mathrm{ph}} R_{\mathrm{sp}}} \left(\frac{\Delta v_l}{\Delta v_g}\right)^2 \tag{8.5}$$

For a semiconductor laser which is assumed to be a single mode operation, the value of MSR is larger than 20.

A single mode operation at a high bias injection current is expected for index-guided semiconductor lasers, since the spontaneous emission coefficient is as small as less than $\beta_{\mathrm{sp}} \approx 10^{-4}$. However, the side mode suppression is weak for gain-guided semiconductor lasers with a larger spontaneous emission coefficient of $\beta_{\mathrm{sp}} \approx 10^{-3}$ and the laser tends to be oscillated with multimode. As a primary effect, a side mode is suppressed for the increase in the injection current above the threshold and the optical power is concentrated to the main mode. In actual laser oscillation, there are effects of spatial hole-burning due to standing-wave nature along the laser propagation and spectral hole-burning due to the broadening of the gain profile for the increase in the optical power. As results, the side mode is suppressed and the optical power is transferred to the main mode (Agrawal and Dutta 1993). These effects cause instabilities for the main mode and play an important role for chaotic dynamics in semiconductor lasers. Similar effects are observed for optical injection to semiconductor lasers as shown in Fig. 6.9. Other effects to destabilize the main mode and enhance the side modes are the beating between the main and side modes and the four-wave mixing in the oscillation modes. The effects are strongly dependent on laser types, materials, and confinement of light in the active layer.

We have derived the multimode rate equations for semiconductor lasers in the incoherent case. However, we must take into account the effects of the nonlinear gain saturation and cross-gain saturation. Also, we must use the coherent rate equations for a semiconductor laser when the laser is subjected to external optical feedback or optical injection. When a semiconductor laser oscillates at a multimode with $2M + 1$ oscillation lines, the rate equations for the complex field and the carrier density are written as (Ryan et al. 1994)

$$\frac{dE_j(t)}{dt} = \frac{1}{2}(1 - i\alpha)G_{n,j}\{n(t) - n_{th,j}\}E_j(t) - \frac{1}{2}\left\{\varepsilon_{sj}|E_j(t)|^2 + \sum_{m=-M}^{M}\theta_{mj}|E_m(t)|^2\right\}E_j(t) \tag{8.6}$$

$$\frac{dn(t)}{dt} = \frac{J}{ed} - \frac{n(t)}{\tau_s} - \sum_{m=-M}^{M}\left[K_m G_{n,m}\{n(t) - n_0\}\right]|E_m(t)|^2 \tag{8.7}$$

where $E_j(t)$ is the field of the j-th mode, ε_{sj} and θ_{mj} ($m = j$) are the nonlinear self- and cross-saturation coefficients, respectively, and K_m is the mode gain coefficient. We omitted the Langevin noise terms in (8.6), however, it may be added where necessary.

The nonlinear saturation coefficient $\alpha' = -(\partial \mathrm{Re}[\chi]/\partial S)/(\partial \mathrm{Im}[\chi]/\partial S)$ for the photon number discussed in Sect. 6.2 is ignored in the above equation. The saturation coefficients ε_{sj} and θ_{mj} do not have large values and they are in the order of 10^4 s^{-1}. In the carrier density equation, we also ignore the mode interferences for the carrier recombination because it has small effects. A semiconductor laser operating at multimode is an unstable laser and it is easily affected by external perturbations. A multimode semiconductor laser shows mode competitions and mode switching induced by the nonlinear interactions among the modes. Mode partition noise is one of the dominant effects in multimode oscillating lasers and it is a non-negligible effect (Ahamed and Yamada 2002). Each oscillation mode includes a very large relative intensity noise (RIN) and it sometimes causes problems in actual use. However, as a total intensity, a multimode semiconductor laser with partition noise has the same order of RIN as a single mode laser, since the partition noises are averaged out (Petermann 1988). Using (8.6), the rate equation for the complex field in a multimode semiconductor laser with optical feedback is given by

$$\frac{dE_j(t)}{dt} = \frac{1}{2}(1 - i\alpha)G_{n,j}\{n(t) - n_{th,j}\}E_j(t) - \frac{1}{2}\left\{\varepsilon_j|E_j(t)|^2 + \sum_{m=-M}^{M}\theta_{mj}|E_m(t)|^2\right\}E_j(t) + \frac{\kappa_j}{\tau_{in}}E_j(t-\tau)\exp(i\omega_j\tau) \tag{8.8}$$

In the following, the dynamics of multimode semiconductor lasers subjected to external optical feedback are numerically investigated. Table 8.1 shows typical values of device parameters for a multimode semiconductor laser frequently used in numerical simulations (Ryan et al. 1994).

Table 8.1 Characteristic device parameters for a multimode semiconductor laser at an oscillation wavelength of 780 nm (GaAs-GaAlAs laser)

Symbol	Parameter	Value
G_n	Gain coefficient	2.05×10^{-13} m^3 s^{-1}
α	Linewidth enhancement factor	4.00
r_0	Facet reflectivity	0.556
n_{th}	Carrier density at threshold	4.00×10^{24} m^{-3}
n_0	Carrier density at transparency	1.40×10^{24} m^{-3}
τ_s	Lifetime of carrier	2.00 ns
τ_{ph}	Lifetime of photon	1.88 ps
τ_{in}	Round trip time in laser cavity	6.00 ps
V	Volume of active region	1.25×10^{-16} m^3
ε_{sj}	Nonlinear self-saturation coefficient	1.70×10^4 s^{-1}
θ_{mj}	Nonlinear cross-saturation coefficient	1.60×10^3 s^{-1}

8.1.3 *Dynamics of Multimode Semiconductor Lasers with Optical Feedback*

When the frequency corresponding to the round-trip time of light in the external cavity is small enough compared with the relaxation oscillation frequency, the difference in the dynamics between single mode and multimode semiconductor lasers is not distinct. However, if the external cavity length becomes short and the corresponding frequency exceeds the relaxation oscillation frequency, they show different dynamics. Figure 8.2 shows an example of the difference. Bifurcation diagrams in the phase space of the carrier density and the external feedback rate are calculated both for single mode and multimode semiconductor lasers (Ryan et al. 1994). For the multimode laser, five modes are assumed. In Fig. 8.2a, b, the multimode laser is stable compared with the single mode laser and a feedback level of ten times larger than the solitary case is required to destabilize the laser. Namely, the multimode semiconductor laser is less sensitive to optical feedback than the single mode semiconductor laser as far as the conditions of the device parameters are the same. This result can be understood qualitatively by noting that all modes contribute to the damping of relaxation oscillations. Even though an individual mode may be unstable in solitary oscillation, simultaneous lasing of all modes preserves the steady state over a large range of the external feedback. The situation is quite similar to the effect of averaged RIN in multimode semiconductor lasers (Petermann 1988). Also, chaotic regions are much thinner compared to the single mode case.

At chaotic oscillations of a multimode semiconductor laser, the bifurcation diagrams cannot tell us whether all of the modes simultaneously oscillate, or whether one of the modes, or a small number of them are the dominant oscillation modes. Figure 8.3 shows the simulation result for waveforms of each oscillation mode in a multimode semiconductor laser (Ryan et al. 1994). Figure 8.3 is the

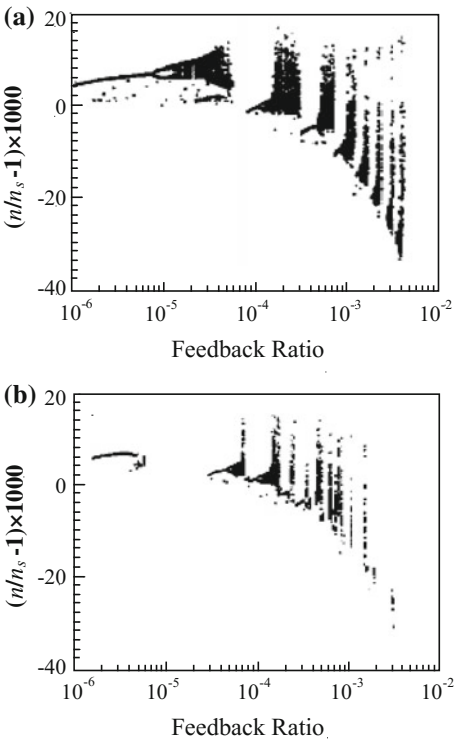

Fig. 8.2 Bifurcation diagrams of the carrier density for optical feedback rate. **a** Single-mode laser. **b** Multimode laser with five oscillation lines. The external cavity length is L = 10 cm, which corresponds to a frequency of 1.5 GHz. The relaxation oscillation frequency of the laser is assumed as 0.7 GHz. The same device parameters are assumed for both cases [after Ryan et al. (1994); © 1994 IEEE]

calculations of waveforms without and with optical feedback. Each waveform is averaged for a 10 ns time window to clearly show the difference. Switching among the modes is not distinct for the solitary oscillation, although the change of the main mode for the time evolution is visible as shown in Fig. 8.3a. The solitary laser exhibits mode partition fluctuations, but it remains multimoded most of the time. The total optical power at the solitary oscillation is almost constant for time. However, in Fig. 8.3b, only one of the modes is dominant for a certain time duration and the other mode is suppressed, when the laser shows chaotic dynamics induced by the optical feedback. The main mode changes to the other mode after a certain time duration in a random manner. At the moment of mode hopping, the total output power sustains irregular spikes. Switching among modes is a typical feature of multimode semiconductor lasers subjected to optical feedback. From the detailed study of the dynamics, it is understood that only one or few of the possible oscillation modes become the dominant mode for a certain time duration and the modes alternately switch in a random manner. When the mode number is small, only one mode tends to oscillate in chaotic manner and oscillations of the other modes are suppressed. Especially, a mode of shorter wavelength tends to show

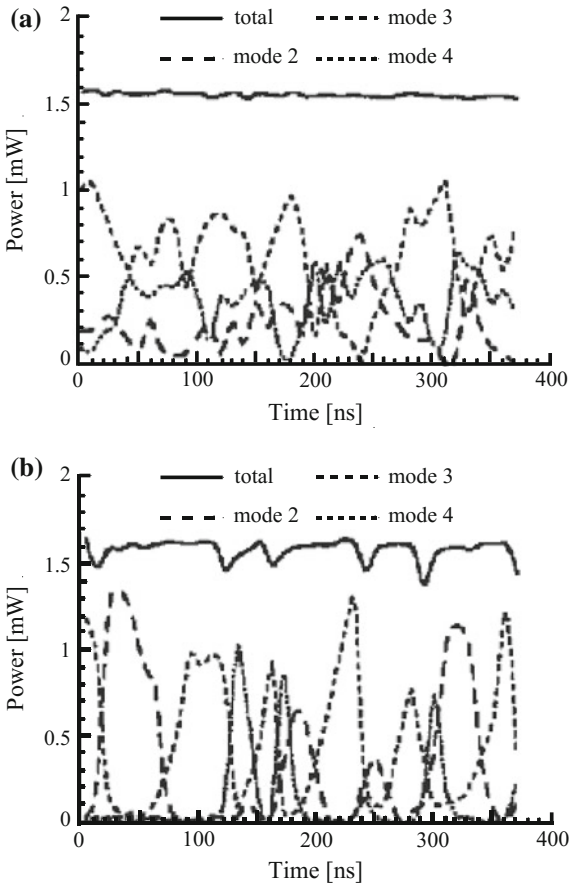

Fig. 8.3 Waveform of each mode in a multimode semiconductor laser corresponding to Fig. 8.2. Three modes are displayed. **a** Almost steady-state oscillation without optical feedback and **b** chaotic oscillation with optical feedback. The intensity feedback ratio is 5×10^{-4} [after Ryan et al. (1994); © 1994 IEEE]

chaotic oscillations for small optical feedback due to the asymmetry of the gain profile. Indeed, this mode switching has been experimentally observed (Ikuma and Ohtsubo 1998).

8.2 Self-Pulsating Lasers

8.2.1 Theory of Self-Pulsating Lasers

Self-pulsating semiconductor lasers are used as light sources for digital versatile disks (DVD) in optical data storage systems, since noises (actually chaotic irregular oscillations) induced by optical feedback from a disk surface are greatly suppressed by self-pulsations. Also, a technique of high frequency injection current modulation in CW operating semiconductor lasers is used to reduce optical feedback noises in

optical disk systems. Self-pulsating semiconductor lasers are fabricated to reduce feedback noises using pulsation oscillations originating from their device structures without external control circuits. The pulsation frequency depends on each device and the bias injection current, and ranges typically from several hundreds of MHz to the order of GHz. The self-pulsation semiconductor laser itself is unstable and sometimes shows instability for a certain region of the bias injection current even without external perturbations. The structure of self-pulsation lasers is almost the same as edge-emitting lasers except for saturable absorbing regions adjacent to the active layer as shown in Fig. 8.4. The width of the active region is usually the same size as that of edge-emitting semiconductor lasers. However, this is not the only structure of self-pulsating semiconductor lasers. The other example is a type of weak index guide (WIG) and the saturable absorbing layer is installed above the active region. The type of adjacent saturable absorbing layers (SALs) shown in Fig. 8.4 is assumed in the following discussion. However, the results are straightforwardly applicable to the WIG model.

In Fig. 8.4a the cross-section of the front facet of a self-pulsating semiconductor lasers is represented. The saturable absorbing regions are installed at both sides of the active layer. Figure 8.4b is the carrier distribution along the active layer. The size of the active region has almost the same dimension as that of common narrow-stripe edge-emitting semiconductor lasers. Carriers injected into the active region rapidly decay out to the regions of the saturable absorbers. Figure 8.4c is the profile of the output power at lasing oscillation. The whole distributions of the carriers and the optical power from the active layer to the saturable absorbing regions are determined by the boundary conditions in the same manner as the treatment of the light transmission in an optical wave guide (Yamada 1993). The time constant τ_{12} of the carrier diffusion from the active layer to the absorbers is given as

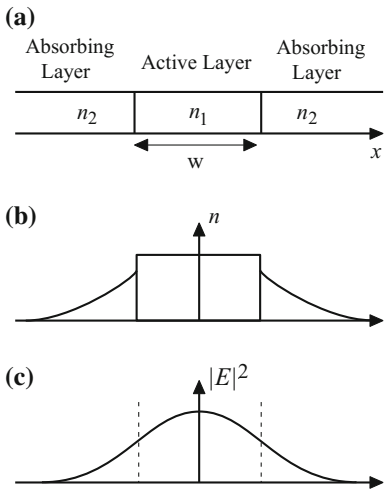

Fig. 8.4 Model of self-pulsating semiconductor lasers. **a** Cross-section of the front facet of the laser, **b** carrier distribution, and **c** optical profile. The center is the active region and both sides of the active layer are the carrier absorbing regions

$$\tau_{12} = \frac{w^2}{2D} \tag{8.9}$$

where w is the width of the active layer and D is the diffusion constant. At the same time, the carrier diffusion also occurs from the saturable absorbing regions to the active layer. Since the total number of the electrons $V_1 n_1 + V_2 n_2$ should be unchanged, the time constant τ_{21} of the carrier diffusion from the absorbers to the active layer is given as

$$\tau_{21} = \frac{V_2}{V_1}\tau_{12} \tag{8.10}$$

where V_1 and V_2 are the volumes of the active and absorbing regions, and n_1 and n_2 are the carrier densities at the active and absorbing regions, respectively. The linearized gains for the active and absorbing regions have different values, therefore we must use appropriate gains for them in the numerical simulations. Also, the carrier densities above which the lasing gain becomes positive, i.e., transparent, differ from each other.

Before introducing the rate equations for self-pulsating semiconductor lasers, the mechanism of self-sustained pulsating oscillations in a SAL type laser is briefly explained. At the carrier number less than the laser threshold, carriers are accumulated in the active region by the carrier injection. When the carrier number exceeds the laser threshold, the laser oscillation starts. The carriers are rapidly absorbed by the diffusion to the saturable absorbing regions. The carrier diffusion is reduced due to the increase of the carrier number in the saturable absorbing regions, and this results in the increase of the photon number. However, the increase of the photon number causes the depletion of carriers in the active region and the decrease of the carrier number is accelerated by the diffusion of the carriers to the saturable absorbing regions. Then, the carrier number falls below the laser threshold and, finally, the laser oscillation stops. After the halt of the laser oscillation, the carrier number again increases and the next pulsating oscillation starts. This process repeats again and again and the laser shows self-sustained pulsation oscillations. The accumulation time of carriers to show lasing oscillation is typically about 1 ns (corresponding to a pulsating oscillation frequency of 1 GHz) and the width of the pulses is $\sim$100 ps.

In the following, we assume a single mode oscillation for a self-pulsating semiconductor laser, however, actual lasers are more or less multimode oscillations. Therefore, the dynamics derived from the theory do not always coincide well with the experimental results unlike in the cases of narrow-stripe edge-emitting lasers. However, we can discuss approximate characteristics of self-pulsating semiconductor lasers, such as pulsating oscillations, pulsing frequency, and L-I characteristics. Several theoretical models have been proposed and some of them are listed in the reference (Carr and Erneux 2001), although the fundamental idea of the models is the same. Here, we assume a single mode model for a self-pulsating semiconductor laser and we introduce an additional carrier density equation for the saturable

absorbing regions of the rate equations in a narrow-stripe edge-emitting semiconductor laser (Yamada 1993, 1996). Due to the presence of the saturable absorbing regions, carriers in the active region rapidly decay toward the absorbing regions and pulsations occur in the laser output. In such a structure, we must take into account the carrier density equations in the absorbing regions.

The rate equations for the complex amplitude E and the carrier densities n_1 and n_2 for the active and absorbing regions describing self-pulsation semiconductor lasers are written as

$$\frac{dE(t)}{dt} = \frac{1}{2}(1 - i\alpha)[G_{n1}\{n_1(t) - n_{th1}\} + G_{n2}\{n_2(t) - n_{th2}\}]E(t) \tag{8.11}$$

$$\frac{dn_1(t)}{dt} = \frac{J}{ed} - \frac{n_1(t)}{\tau_{s1}} - \frac{n_1(t) - n_2(t)}{\tau_{12}} - G_{n1}\{n_1(t) - n_{01}\}|E(t)|^2 \tag{8.12}$$

$$\frac{dn_2(t)}{dt} = -\frac{n_2(t)}{\tau_{s2}} - \frac{n_2(t) - n_1(t)}{\tau_{21}} - G_{n2}\{n_2(t) - n_{02}\}|E(t)|^2 \tag{8.13}$$

Here, subscripts 1 and 2 denote the quantities for the active and absorbing regions, respectively, and τ_{12} and τ_{21} are the carrier diffusions from regions 1–2 and vice versa, respectively, as has already been defined. In the field equation, we ignored the nonlinear gain saturation effect. However, it may play an important role in self-pulsating semiconductor lasers, since the photon density becomes large due to pulsating oscillations even for a short time duration. We take into account the nonlinear gain in such a case as discussed in Sect. 3.3.4. However, we can simulate approximate characteristics of self-pulsating semiconductor lasers without considering the gain saturation effect and the term is sometimes omitted. Self-pulsation semiconductor lasers were originally aimed to reduce the effect of optical feedback noises, however, the RIN is sometimes enhanced under certain conditions of the feedback. Furthermore, they are essentially unstable lasers and they sometimes show unstable or chaotic oscillations under certain ranges of the bias injection current even at solitary oscillations.

8.2.2 *Instabilities at Solitary Oscillations*

The self-pulsating semiconductor laser itself is an unstable laser and regular pulsating oscillation is considered as a kind of period-1 state on the way to chaotic evolution. Typical features of chaotic states in a self-pulsating semiconductor laser are pulsing oscillations with irregular pulse amplitude and jitters. The characteristics of self-pulsating semiconductor lasers are strongly dependent on the device structure and parameters. Figure 8.5 shows an example of an experimental L-I characteristic of a self-pulsating semiconductor laser at solitary oscillation. The laser is a SAL type and has a maximum output power of 5 mW with an oscillation

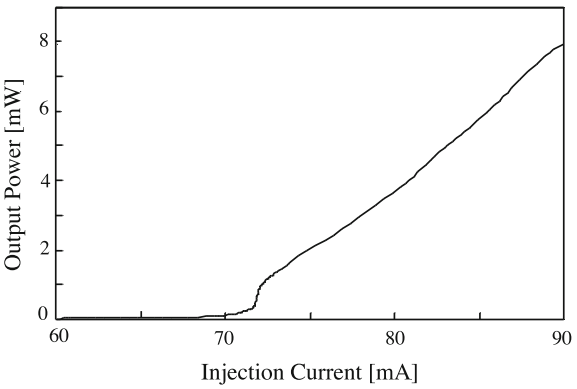

Fig. 8.5 L-I characteristic of a self-pulsating semiconductor laser. The laser is an AlGaInP multi-quantum well laser operating at a wavelength of 650 nm and a maximum output power of 5 mW

wavelength of 650 nm. The oscillation above the threshold is divided into unstable and stable regions for the bias injection current. The threshold current is about 70 mA, which is much higher than that of ordinary narrow-stripe edge-emitting semiconductor lasers, because the strong carrier dissipation exists due to the presence of the saturable absorbing regions. Another difference is the vague threshold. The laser power does not linearly increase for the bias injection current close to the threshold, but it has a hysteresis. As demonstrated later, bistability is reproduced by the numerical simulations from the rate equations.

In the L-I characteristic, the laser output shows the bistable state above the threshold. In this region, the laser exhibits pulsating oscillation, but it is unstable. A waveform and its rf spectrum in this region are plotted in Fig. 8.6a. The pulse peak changes irregularly and the waveform shows a broad chaotic spectrum. Well above the laser threshold, the laser shows regular pulsing states with constant peak and separation as shown in Fig. 8.6b. However, even for such stabilized operations at solitary mode, the laser may be destabilized by optical feedback. Stability or instability of the laser operations for optical feedback is discussed in the next subsection. It is noted that every self-pulsating semiconductor laser does not always show the same L-I characteristics as in Fig. 8.5. A laser with regular pulsing states is suitable for a read-light source in DVD systems to avoid optical feedback from a disk surface.

The L-I characteristic is numerically calculated from the rate equations (8.11)–(8.13). Typical parameter values of red light self-pulsating semiconductor lasers are listed in Table 8.2. Because of the pulsation characteristics of laser oscillations, the values of the gain coefficients are larger than those of narrow-stripe edge-emitting semiconductor lasers. Figure 8.7 is an example of the calculated L-I characteristic (van Tartwijk and San Miguel 1996). After the lasing oscillations, the laser shows bistability for the bias injection current between 48 and 58 mA and chaotic pulsating oscillations are observable in this region. For the bias injection current from 58 to 125 mA, the laser oscillates at stable regular pulsing states. Over the bias injection current of 125 mA, the laser shows stable CW oscillations. In the

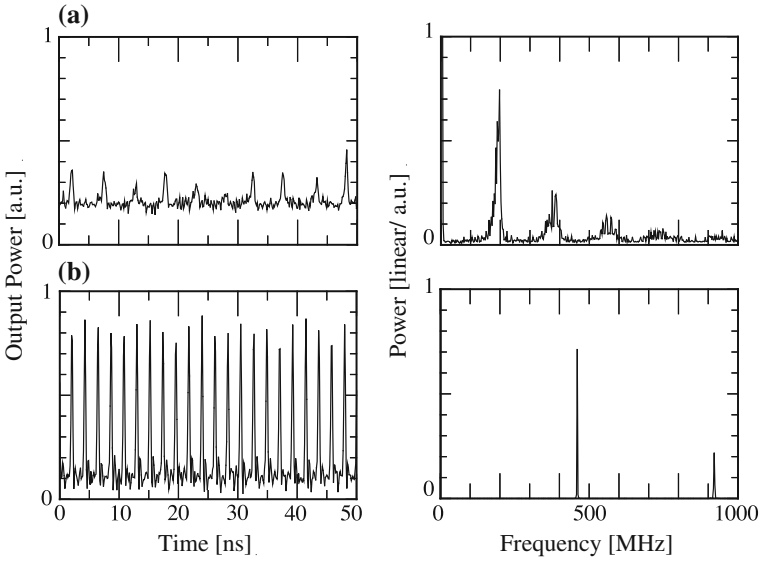

Fig. 8.6 Waveforms (*left*) and rf spectra (*right*) in Fig. 8.5. **a** Unstable region at a bias injection current of 74 mA and **b** stable regular pulsating oscillation at 80 mA

Table 8.2 Characteristic device parameters for a self-pulsating semiconductor laser at an oscillation wavelength of 650 nm (AlGaInP laser)

Symbol	Parameter	Value
G_{n1}	Gain coefficient in active region	3.08×10^{-12} m^3 s^{-1}
G_{n2}	Gain coefficient in saturable absorbing region	1.24×10^{-13} m^3 s^{-1}
α	Linewidth enhancement factor	4.00
n_{01}	Carrier density at transparency in active region	1.40×10^{24} m^{-3}
n_{02}	Carrier density at transparency in saturable absorbing region	1.60×10^{24} m^{-3}
τ_{s1}	Lifetime of carrier in active region	2.49 ns
τ_{s2}	Lifetime of carrier in saturable absorbing region	1.25 ns
τ_{12}	Diffusion time	2.65 ns
τ_{ph}	Lifetime of photon	2.72 ps
V_1	Volume of active region	0.72×10^{-16} m^3
V_2	Volume of saturable absorbing region	0.46×10^{-16} m^3

numerical simulations, noises induced by spontaneous emission strongly affect the pulsing frequency. At regular pulsing states without considering noises, the pulsing frequency smoothly increases with the increase of the bias injection current. In the presence of noises, a kink is observed in the characteristic curve of the pulsing frequency and the bias injection current (van Tartwijk and San Miguel 1996; Mirasso et al. 1999).

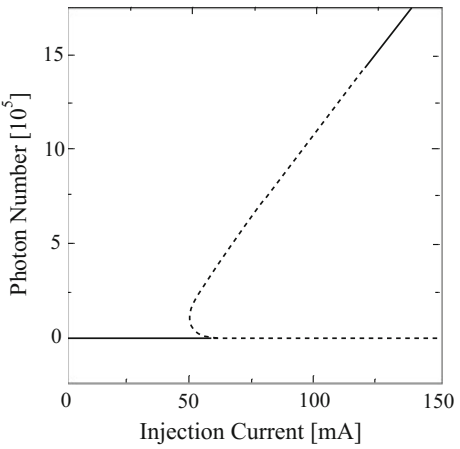

Fig. 8.7 Theoretically calculated L-I characteristic of a self-pulsating semiconductor laser [after van Tartwijk and San Miguel (1996); © 1996 IEEE]

The theoretical calculation in Fig. 8.7 well reproduces the behaviors of unstable and stable pulsating oscillations. However, the CW operation of self-pulsating lasers is not observable in experiments. The CW operation in Fig. 8.7 is achieved at a high bias injection current and such a high bias injection current may damage the laser. Another example of discrepancy between the theory and the experiment is the pulse width of the waveform. The theoretically calculated pulse width is much smaller than the actual width. For example, the calculated pulse width is typically 10 ps, but the observed pulse usually has a width of around 100 ps. As has already been mentioned, the improvement of the theoretical model of the rate equations is still required to explain well the experimental data (Yamada 1998b). The other reason for the discrepancy is the assumption of a single-mode operation for self-pulsating lasers. It is well known that self-pulsating semiconductor lasers oscillate at multimode with many oscillation lines.

Characteristics of InGaN self-pulsating semiconductor lasers with an operating wavelength of 395 nm have been investigated (Tronciu et al. 2003). Since the difference between the carrier lifetimes of the active and saturable absorbing layers is much greater than that of red light self-pulsating semiconductor lasers, the lasers show quite different dynamics from red self-pulsating lasers. For example, the carrier lifetime of the active layer is 2.0 ns, while that of the saturable absorbing layer is only 0.1 ns. The rate equations are fundamentally the same as those in (8.11)–(8.13), but Tronciu et al. took into account the effects of the outer regions besides the active and absorbing layers in the numerical simulations. Figure 8.8 shows some numerical and experimental results. They used the model of a WIG-type laser. Close to the threshold, the laser oscillates at the CW operation without hysteresis like in Fig. 8.8a, which is quite different from the operation of red self-pulsating lasers. At a certain bias injection current, the laser at first shows self-pulsating oscillation. However, the laser recovers stable states for a bias injection current above 200 mA. The dynamics is strongly dependent on the laser

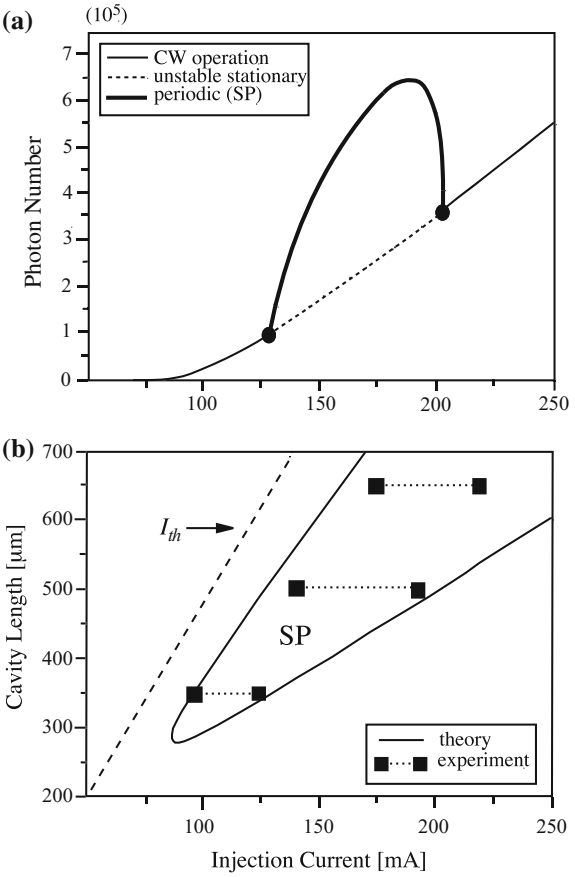

Fig. 8.8 Characteristics of an InGaN self-pulsating semiconductor laser with an oscillation wavelength of 395 nm. **a** Calculated bifurcation diagram for a laser cavity length of 500 μm. The self-pulsation region is observable from 125 to 200 mA. The other range of the injection current is a stable CW operation. **b** Self-pulsation range in the plane of laser cavity length versus injection current. Experimentally obtained ranges of the self-pulsation are indicated with *dotted lines* [after Tronciu et al. (2003); © 2003 IEEE]

cavity length. The self-pulsation range (SP) for the laser cavity length is investigated in Fig. 8.8b. We can see the agreement between the theoretical and experimental results.

8.2.3 *Instability and Chaos by Optical Feedback*

The self-pulsating semiconductor laser is fabricated as a low noise light source in optical data storage systems. However, the reduction of feedback noise is not always achieved for every feedback condition. The self-pulsating semiconductor laser has a periodic pulsation with a frequency ranging from several hundreds MHz to GHz depending on the bias injection current. There is a congenial range of optical feedback lengths to suppress feedback noise. The self-pulsating semiconductor laser sustains a forced oscillation due to the device structure and the

feedback noise is reduced for a wide range of the feedback conditions. On the other hand, outside this region, the laser undergoes more noises than that of edge-emitting semiconductor lasers. Also, the laser shows chaotic behaviors for the modulation under certain bias injection current ranges. At first, we consider feedback-induced noises in a self-pulsating semiconductor laser. There are two schemes of optical feedback in self-pulsating semiconductor lasers; coherent and incoherent feedback depending on the relation between the pulse separation and the feedback length. When the feedback length is small enough compared with the pulsing separation and close or less than the pulse width, the effect is coherent. For the condition $T_p > \tau$ (T_p being the pulse separation), the rate equation for the complex field is given by

$$\begin{aligned}\frac{\mathrm{d}E(t)}{\mathrm{d}t} = &\frac{1}{2}(1-i\alpha)[G_{n1}\{n_1(t)-n_{\mathrm{th1}}\}+G_{n2}\{n_2(t)-n_{\mathrm{th2}}\}]E(t)\\ &+\frac{\kappa}{\tau_{\mathrm{in}}}E(t-\tau)\exp(i\omega_0\tau)\end{aligned} \tag{8.14}$$

The equation is the same as that for the coherent case of narrow-stripe edge-emitting semiconductor lasers except for the effects of the gain term in the saturable absorbing regions. The rate equations for the carrier densities under coherent feedback remain unchanged as in (8.12) and (8.13).

On the other hand, the rate equation of the complex field is written the same as (8.11) for incoherent optical feedback, however, the carrier density equation for the active layer in (8.12) must be changed and the incoherent feedback term is added to this equation, when $T_p < \tau$. The rate equation for the carrier density is given as

$$\begin{aligned}\frac{\mathrm{d}n_1(t)}{\mathrm{d}t} = &\frac{J}{ed}-\frac{n_1(t)}{\tau_{s1}}-\frac{n_1(t)-n_2(t)}{\tau_{12}}-G_{n1}\{n_1(t)-n_{01}\}\\ &\times\left\{|E(t)|^2+\kappa_i\left(1-R_0^2\right)R|E(t-\tau)|^2\right\}\end{aligned} \tag{8.15}$$

where R_0 and R are the intensity reflectivities of the front facet of the laser and the external reflector, respectively, and κ_i is the intensity coupling coefficient to the active layer.

We show some numerical results for the dynamics of self-pulsating semiconductor lasers subjected to coherent optical feedback. Figure 8.9 is an example (Yamada 1998a, b). Figure 8.9a shows the time series of the laser oscillation without optical feedback. In the figure, n_1 and n_2 are the carrier densities of the active and saturable absorbing regions, respectively, and S is the photon number. n_4 is the carrier density at the current blocking region installed above the saturable absorbing layer. The laser oscillates at the regular pulsing state and the pulsing frequency is 1.29 GHz. The calculated RIN at the solitary oscillation is less than −130 dB/Hz for the lower frequency component. Figure 8.9b shows the waveforms for the same variables under optical feedback. The feedback ratio is set to be 3.3% in the average field amplitude. In the presence of optical feedback, the laser still

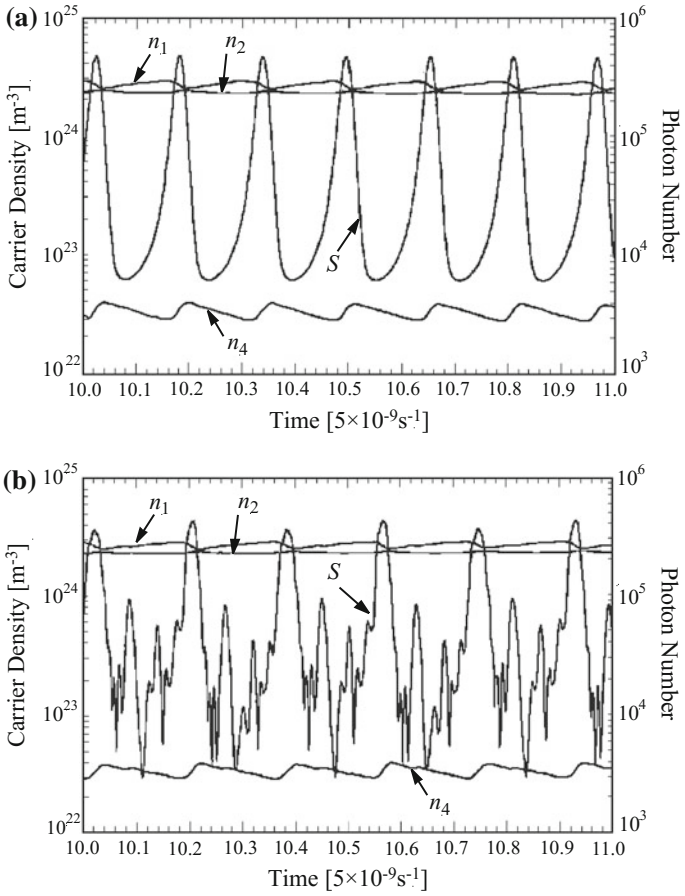

Fig. 8.9 Times series of the variables in a self-pulsating semiconductor laser at $J = 1.69J_{th}$. **a** Without optical feedback and **b** with optical feedback of 3.3% of the average field amplitude. The external cavity length is $L = 4$ cm. n_1: carrier density in the active region, n_2: carrier density in the saturable absorbing region, n_4: carrier density in the current blocking region, and S photon number [after Yamada (1998a); © 1998 IEICE]

shows a pulsating oscillation. However, the laser output power is disturbed by the feedback and the laser shows a chaotic oscillation. The pulse period is larger than that of the solitary oscillation and its average frequency is 1.07 GHz. It is noted that the pulse height also fluctuates and the RIN is greatly enhanced up to −90 dB/Hz for the lower frequency component.

van Tartwijk and San Miguel (1996) numerically studied the effects of optical feedback in self-pulsating semiconductor lasers and calculated pulse periods and jitters (the standard deviation from the average period) without and with optical feedback. As results, the pulse period decreases with the increase of the bias injection current and, at the same time, the jitter becomes small. Increasing the

feedback time, the pulse period increases and, then, a sudden jump-down is observed at a certain feedback distance. The jump in the pulse period must be attributed to a switch of the locked-pulse frequency to a neighboring compound cavity mode, i.e., the resulting resonance frequency of the laser mode with relaxation oscillations and one of the external cavity resonance frequencies. A similar trend can be observed for the pulse jitter. There is also phase sensitivity of coherent optical feedback in a self-pulsating semiconductor laser as expected from (8.14). When the feedback is small, the pulse period keeps almost the same value as that of the solitary oscillation. However, the jitter has the minimum value at a certain small feedback ratio. The increase in jitter after the optimum value manifests itself by a multi-peaked, very broad pulse period distribution. The effects agree well with the period-doubling route to chaos (Kuznetsov et al. 1986). The dynamics of coherent optical feedback is extensively studied in self-pulsating semiconductor lasers, because the lasers are used as light sources for DVD systems in which the optical feedback length is typically within several centimeters. On the other hand, the typical feedback length is several tens of centimeters to meters when the lasers are used as light sources for optical measurements. The effects for this range are incoherent.

8.2.4 *Instability and Chaos by Injection Current Modulation*

A few studies have been reported for the modulation properties of self-pulsating semiconductor lasers. The lasers show unstable oscillations by the modulation to the bias injection current, and also exhibit chaotic behaviors at large modulation index. For the variations of irregular pulse peaks, we can see similar chaotic bifurcations to those in ordinary narrow-stripe edge-emitting semiconductor lasers such as discussed in Chap. 7 (Winful et al. 1986; Juang et al. 1999, 2000; Jones et al. 2001). It is shown that the occurrence of chaotic oscillations is critically dependent on the modulation frequency. Periodic bands of chaotic dynamics are found to exist at multiples of the relaxation oscillation frequency. Not only stable pulsations resonance to the modulation frequency (locking oscillation), but also unstable pulsations and unique frequency-locked pulsations in which multiple spikes appear within some modulation period are found.

Fukushima et al. (2002) investigated experimentally and theoretically the dynamics of self-pulsating semiconductor lasers with injection current modulated and observed chaotic bifurcations for the pulsation frequency and the pulse height. Figure 8.10 shows some typical output waveforms observed by the experiments. The scales in the figure denote the period of modulation. The modulation index for the bias injection current is set to be $m = 1.06$. Each periodic state is defined as P_k^l, where k stands for the ratio of the fundamental period of the pulse train to the modulation period and l stands for the number of spikes in the fundamental period of the pulse train. Without rf modulation, the laser shows stable pulsation at a

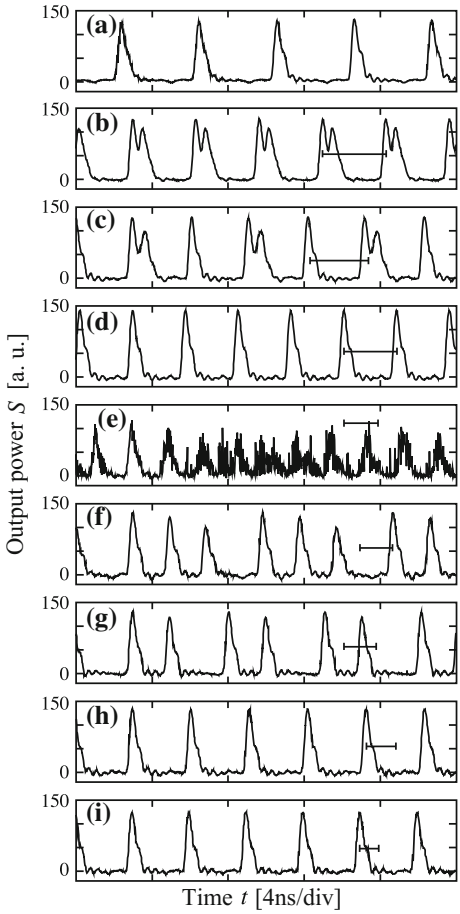

Fig. 8.10 Experimentally observed temporal waveforms of output optical pulses at a bias injection current of 59.5 mA and a modulation index of $m = 1.06$. **a** Without rf modulation, **b** P_1^2: pulsation at $f_m = 300.0$ MHz, **c** P_2^3: pulsation at $f_m = 327.0$ MHz, **d** P_1^1: pulsation at $f_m = 360.0$ MHz, **e** unstable pulsation at $f_m = 562.0$ MHz, **f** P_4^3: pulsation at $f_m = 584.0$ MHz, **g** P_3^2: pulsation at $f_m = 592.0$ MHz, **h** P_2^1: pulsation at $f_m = 650.0$ MHz, and **i** P_3^1: pulsation at $f_m = 1000.0$ MHz. The bar in each plot is the fundamental period of the modulation [after Fukushima et al. (2002); © 2002 JSAP]

self-pulsation frequency of 245.7 MHz, as shown in Fig. 8.10a. Under rf modulation, as the modulation frequency f_m increases, the output optical pulse train is locked to the modulation frequency (P_1^1 pulsation) or its sub-harmonics (P_2^1 and P_3^1 pulsations) as shown in Fig. 8.10d, h, and i. In the boundary regions of these frequency-locked pulsations, unstable pulsation occurs as shown in Fig. 8.10e. It is speculated that the unstable region contains both quasi-periodic pulsation and chaotic pulsation. In the boundary regions, unique frequency-locked pulsations are also observed. One is P_1^2 pulsation in which two spikes appear within one modulation period, as shown in Fig. 8.10b. Another is P_2^3 pulsation in which two spikes and a single spike appear alternately. The others are P_4^3 and P_3^2 pulsations in which three or two spikes appear within four or three modulation periods as shown in Fig. 8.10f, g, respectively.

The experimental results are summarized in Fig. 8.11. Figure 8.11a shows the characteristics of pulsation frequency versus modulation frequency. The figure

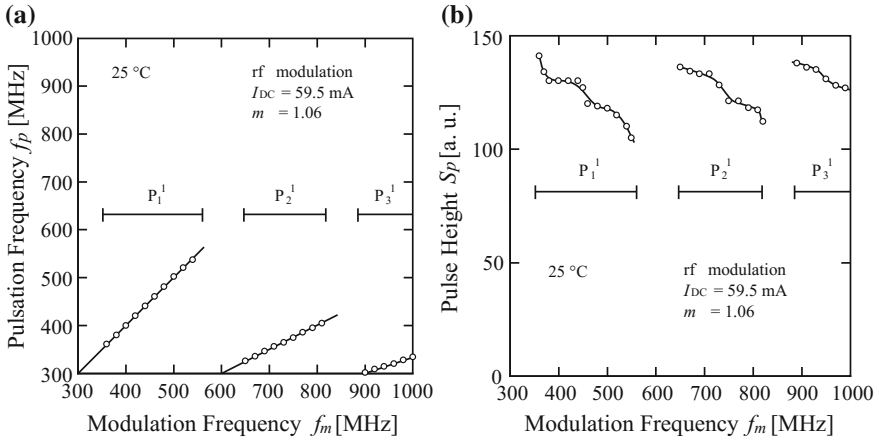

Fig. 8.11 **a** Characteristics of pulsation frequency versus modulation frequency under rf modulation. **b** Dependence of the pulse height on the modulation frequency under the frequency-locked pulsations of P_1^1, P_2^1, and P_3^1 [after Fukushima et al. (2002); © 2002 JSAP]

shows the regions of frequency-locked states for the modulation frequency. In between the frequency-locked states for the modulation frequency, we can observe unstable and chaotic oscillations as shown in Fig. 8.10e. Figure 8.11b shows the dependence of the pulse height on the modulation frequency under P_1^1, P_2^1, and P_3^1 pulsations. Under P_1^1 pulsation, the pulse height decreases gradually as the modulation frequency increases and eventually the pulsation becomes unstable at the modulation frequency of 560 MHz. Then P_2^1 pulsation occurs at 647 MHz. Here, the pulse height again returns to a high level. The same phenomenon is observed under P_2^1 and P_3^1 pulsations. The modulation index used in this experiment is rather high. However, similar trends in those results were obtained for lower modulation index, although each region of frequency-locked state shifts for lower modulation frequency. Fukushima et al. (2002) also compared the theoretical results with those experiments and demonstrated that the theory based on the rate equations of (8.11)–(8.13) with injection current modulation well explains their experiments.

8.3 Vertical-Cavity Surface-Emitting Lasers

8.3.1 Structure of Vertical-Cavity Surface-Emitting Lasers

Vertical-cavity surface-emitting lasers (VCSELs) are promising devices of light sources for optical information processing and communications. Currently, VCSELs from visible wavelengths to near infrared (1.5 μm) are fabricated and their output powers reach as high as several tens of milliwatts. Also, a device that has a

high modulation bandwidth of over 10 GHz with a low RIN of less than −140 dB is fabricated. A VCSEL has a disk structure with light coming out from the top or bottom of the substrate surface. Various types of device structures have been proposed. Index- and gain-guiding structures are used for the confinements of carrier and light in VCSELs such as those for edge-emitting semiconductor lasers. Each guiding structure has merits and demerits in the laser oscillations, but the differences of the stable and unstable effects between those device structures are usually small compared with those in edge-emitting semiconductor lasers, since the length of the laser cavity is much smaller than that of edge-emitting semiconductor lasers. The details of VCSEL structures can be found in the book by Li and Iga (2002). Here, we do not discuss the details of device structures and device characteristics, but discuss the dynamics. As an example, the distributed Bragg reflector (DBR) VCSEL is shown in Fig. 8.12. The thickness of the active layer is approximately equal to the wavelength of light λ. The top view of the laser looks like a disk and its diameter is several to tens of μm. For special use, a disk diameter over 100 μm has been fabricated. In these devices, the reflectivity of the bottom surface is almost 100% and the top reflectivity of the DBR structure is more than 99%. The laser light comes out from the top. Though the internal reflectivity is very high compared with edge-emitting semiconductor lasers, VCSELs are also sensitive to optical feedback and optical injection. The photon number in the active volume is much less than that of edge-emitting lasers, and a few external photons would cause instabilities in the laser oscillations. VCSELs even for different device structures are described by the same or similar rate equations for the field and the carrier density.

There are many advantages of VCSELs for practical purposes. Since the VCSEL has a symmetric space structure, we can expect a circular beam as its output, while the beam profile of the edge-emitting laser has astigmatism. Due to a short cavity length compatible with the wavelength of light and very high reflectivity of light in the internal cavity, the laser is a very low threshold device, as low as ∼μA. From this same reason, we can produce a stabilized oscillation with a single mode that has a large mode separation (∼40 THz). Another merit of VCSELs is the easiness of devising laser arrays because of the surface-emitting structure. However, VCSELs

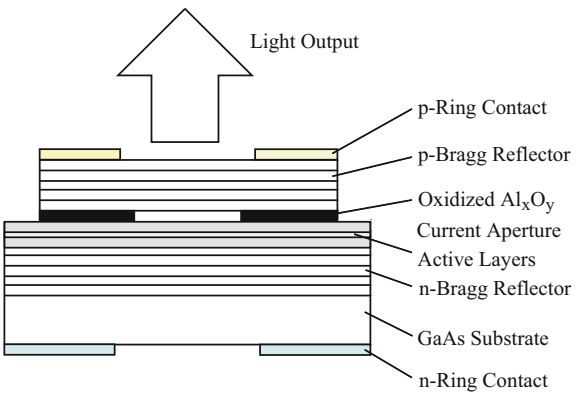

Fig. 8.12 Distributed Bragg reflector VCSEL structure

have unstable features for their operations even without any external perturbations. In addition to the time-dependent phenomena, the space structures and the polarization modes give rise to instability and chaotic dynamics in VCSELs. Spatial hole-burning and multi-transverse mode oscillations are often observed in the laser output to cause instabilities such as spatial-mode and polarization switching. Therefore, the VCSEL itself is an unstable laser. To describe the dynamics of VCSELs, several models have been proposed. Each model has the advantages for explaining respective particular dynamics of real VCSELs. In the following, some of them are introduced.

8.3.2 Spatial-Mode Expansion Model

The rate equations of VCSELs are similar to those for the narrow-stripe edge-emitting laser except for the spatial terms. For a certain polarization mode, the field equation is given as (Valle et al. 1995a, b; Law and Agrawal 1997a, b; Law 1997)

$$\frac{\mathrm{d}E_j(t)}{\mathrm{d}t} = \frac{1}{2}(1 - i\alpha)\left\{G_j(t) - \frac{1}{\tau_{\mathrm{ph},j}}\right\}E_j(t) \tag{8.16}$$

where $G_i(t)$ is the modal gain for the j-th mode, defined as

$$G_j(t) = \frac{\int_0^d \int_0^{2\pi} \int_0^{R_a} G(r,\phi,t)|\psi_j(r,\phi)|^2 |A_j \sin(\beta_j z)|^2 r\mathrm{d}r\mathrm{d}\phi\mathrm{d}z}{\int_0^L \int_0^{2\pi} \int_0^{R} |\psi_j(r,\phi)|^2 |A_j \sin(\beta_j z)|^2 r\mathrm{d}r\mathrm{d}\phi\mathrm{d}z} \tag{8.17}$$

where $G(r, \phi, t)$ is the local gain and is written by $G(r,\phi,t) = G_n\{n(r,\phi,t) - n_0\}$. The upper limits in the integration, d is the thickness of the active region, L is the length of the laser cavity, and R and R_a are the radius of index-guided area and the active area. ψ_j is the eigen-function for the j-th spatial mode, A_i is a normalization constant for the propagation mode, and β_j is the propagation constant of light for the j-th mode. E_j is the field amplitude for the laser oscillation of the j-th spatial component, and the total complex amplitude from a VCSEL is written as

$$\mathbf{E}_{\mathrm{total}}(r,\phi,z,t) = \frac{1}{2}\sum_{j=1}^{M} \hat{\mathbf{e}}_j E_j(t)\psi_j(r,\phi)A_0 \sin(\beta_z z)\exp(-i\omega_{\mathrm{th},j}t) + c.c. \tag{8.18}$$

where M is the total number of the spatial modes, $\hat{\mathbf{e}}_j$ is the polarization vector for the j-th mode, β_z is the propagation constant for the z direction, and A_0 is the normalization coefficient. Since the carrier diffusion in the radial direction must be taken into account for the VCSEL oscillation due to a large aperture size, the rate equation for the carrier density is written as

$$\frac{\mathrm{d}}{\mathrm{d}t}n(r,\phi,t) = D\nabla_T^2 n(r,\phi,t) + \frac{J(r,\phi)}{ed} - \frac{n(r,\phi,t)}{\tau_s} - \frac{\Gamma_d}{d}\sum_{j=1}^{M} G_{nj}\{n(r,\phi,t) - n_0\}\left|E_j(t)\psi_j(r,\phi)\right|^2 \tag{8.19}$$

where D is the coefficient for the carrier diffusion, the subscript T denotes the operation for the transverse coordinates, and Γ_d is the confinement factor for the longitudinal direction in the active layer given as

$$\Gamma_d = \int_0^d |A_0 \sin(\beta z)|^2 \mathrm{d}z \tag{8.20}$$

Here, the thickness of the active layer d is smaller than the total length of the laser cavity l, thus $\Gamma_d < 1$. In the derivation of the carrier density equation (8.19), we must consider the depletion of carriers for laser emission and take into account the interference terms for the external product of the vector polarizations. However, the frequency difference of the modes is usually of the order of several tens of GHz to one hundred GHz. As a result, the beating of these i and j terms, $\exp\{-i(\omega_i - \omega_j)t\}$, has a high frequency and the carrier cannot follow the oscillation. Therefore, we can neglect this effect and (8.19) becomes a good approximation for the dynamics of the carrier density.

The eigen-function for the j-th mode ψ_j is a function of the polar coordinate calculated for a particular structure of the VCSEL. For example, for a weak index-guide cylindrical structure with two polarization states corresponding to the spatial LP_{01} mode, it is written by the Bessel function of the first kind $\mathrm{J}_0(z)$ and the modified Bessel function of the second kind $\mathrm{K}_0(z)$ and has the following form:

$$\psi_j(r,\varphi) = \begin{cases} \dfrac{\mathrm{J}_0\left(u_{1j}r/R_a\right)}{\mathrm{J}_0\left(u_{1j}\right)} & \text{for } r \le R_a \\ \dfrac{\mathrm{K}_0\left(w_{1j}r/R_a\right)}{\mathrm{K}_0\left(w_{1j}\right)} & \text{for } r > R_a \end{cases} \tag{8.21}$$

where R_a is the radius of the active area and u_{1j} and w_{1j} are the first roots of the eigen-value equation for the j-th polarization mode

$$\frac{u_j \mathrm{J}_1\left(u_j\right)}{\mathrm{J}_0\left(u_j\right)} = \frac{w_j \mathrm{K}_1\left(w_j\right)}{\mathrm{K}_0\left(w_j\right)} \tag{8.22}$$

They have a relation of $u_{1j}^2 + w_{1j}^2 = V_j^2$. V_j is the normalized frequency defined as

$$V_j = \frac{2\pi R_a \sqrt{\eta_{1j}^2 - \eta_j^2}}{\lambda} \tag{8.23}$$

where λ is the wavelength of light in vacuum and η_{1j} and η_j are the refractive indices for the j-th mode in the active area and the clad region.

8.3.3 Spin-Flip Model

The spatial mode model well represents the spatial behaviors of VCSELs, however, it takes a long time to perform numerical calculations. Alternative models to show the dynamics of VCSELs have been proposed. The spin-flip model is an excellent one for analyzing the behaviors of polarization switching and polarization-mode oscillation in the lowest spatial mode. In the derivation of the rate equations in the previous subsection, we consider the polarization effects in VCSELs in (8.18). However, in the physical terms, we must take into account the effects of electron spin states associated with light emission in the polarization dynamics of VCSELs. Specifically, left and right circularly polarizations of laser light emission are related to spin states of electrons in the conduction and valence bands. This is the origin of the polarization oscillations in VCSELs, and results in a rich variety of polarization dynamics including polarization switching frequently observed in VCSELs. San Miguel et al. proposed a spin-flip model for the rate equations of VCSELs by taking into account spin dynamics (San Miguel et al. 1995; Martín-Regalado et al. 1997; Sciamanna et al. 2002a, b). The model couples the polarization state of the electric field to the semiconductor medium by including the magnetic sublevels of the conduction and valence bands (the angular momentum numbers of electron) in quantum well devices. It is shown that laser dynamics depend significantly on the value of the relaxation rate. The polarization switching is included by the assumption of the population difference between the carrier densities with positive- and negative-spin values. From these equations, the dynamics of the laser oscillations for the lower order spatial mode can be easily explained, and the results are entirely coincident with the model discussed in the previous subsection. Although the dynamics of polarization dynamics in VCSELs can be well defined by the model, these rate equations are usually applicable to the lowest spatial-mode oscillation. In the following, we derive the expressions for the rate equations based on the spin dynamics.

In VCSELs, the thickness of the laser cavity is thin and less than the optical wavelength and light comes out vertically from the substrate surface (along the z-direction), so that the degeneration of spin states of electrons in heavy-hole and light-hole bands is resolved along the z-direction and we must take into account the difference between down- and up-spin states. In the case of edge-emitting semiconductor laser, the thickness of the active layer is also very thin, however, light comes out perpendicular to the z-direction and we need not consider the spin states.

Only the total carrier number is important for the dynamics in edge-emitting semiconductor laser, while the sum and difference of carrier number play the important role in the VCSEL dynamics. Figure 8.13 shows the four-level model for polarization dynamics in quantum-well VCSELs (San Miguel et al. 1995; Martín-Regalado et al. 1997; Martín-Regalado 1997). In Fig. 8.13, γ_J^{-1} is the spin relaxation time. In the spin dynamics model of laser transitions, the magnetic quantum numbers in the lower edge of the conduction band have $J_z = \pm 1/2$ in accordance with down- and up-spin states. On the other hand, the magnetic quantum numbers for heavy holes in the upper valence band have values of $J_z = \pm 3/2$, since we can neglect the effect of light holes in quantum-well VCSELs. In the quantum state numbers, the same sign corresponds to the same spin state. Photon emitted from + spin state corresponds to left circular polarization, while photon from − spin state to right circular polarization. In the model, the decay rate γ_J accounts for the mixing of the populations with opposite value of J_z. This parameter is introduced to model spin-flip relaxation processes.

We next consider the effects of cavity anisotropies, which can be modeled in the two equations for the time evolution of the field amplitudes with two circular polarizations by replacing the linear loss rate with a matrix whose Hermitian part is associated with amplitude losses and whose anti-Hermitian part gives linear and circular phase anisotropies (also known as birefringence and circular dichroism, respectively). For VCSELs, it is known that there are two preferred modes of linear polarization that coincide with the crystal axes. These two modes have a frequency splitting associated with the birefringence of the medium. This can be modeled by a linear phase anisotropy given by a parameter γ_p, which represents the effect of different indexes of refraction for the orthogonal linearly polarized modes. In addition, the two modes may have a slightly different gain-to-loss ratio that can be related to the anisotropic gain properties of the crystal; the slightly different position of the frequencies of the modes with respect to the gain versus frequency curve, and different cavity geometries for the differently polarized modes. These effects can be

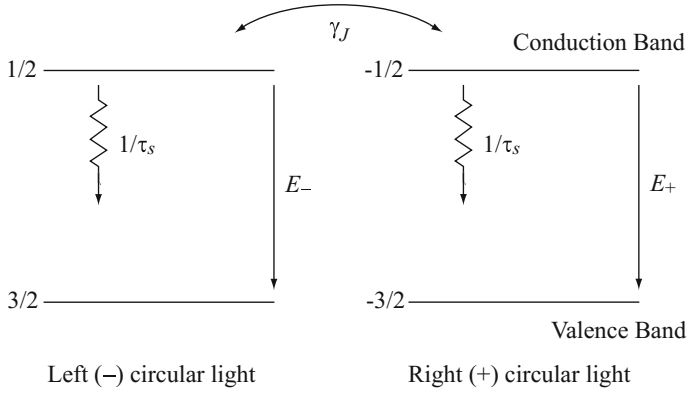

Fig. 8.13 Four-level spin-flip model for polarization dynamics in quantum-well VCSELs

modeled by an amplitude anisotropy with parameter γ_a. We assume here for simplicity that the directions of linear phase and amplitude anisotropy coincide, so that both are diagonalized by the same basis states.

We now derive the rate equations for double-crossed linearly polarized light. Electron spin is associated with photon spin. We start the description of circularly polarized light for the fields of photons in such a case. The laser light field is coupled to two population inversion variables; n is the sum of the upper state and lower state populations and n_J is the number of the difference between the population inversions (upper and lower state population difference) on the two distinct channels with positive or negative value of J_z (quantum spin number). Namely, in semiconductor lasers, n represents the total carrier number in excess of its value at transparency. Then, the rate equations for the fields with right (+) and left (−) circularly polarized states are given as (San Miguel et al. 1995)

$$\frac{\mathrm{d}E_{\pm}(t)}{\mathrm{d}t} = \frac{1}{2}(1 - i\alpha)G_n\left\{n_{\pm}(t) - \frac{1}{G_n\tau_{\mathrm{ph}}}\right\}E_{\pm}(t) - \left(\gamma_a - i\gamma_p\right)E_{\mp}(t) \tag{8.24}$$

where $n_{\pm}(t) = n(t) \pm n_J(t) - n_0$ (n_0 is the total carrier density at transparency), and γ_a and γ_p are the linear anisotropies representing dichroism and birefringence discussed above. Note that signs between the spin states and the subscripts of the fields are opposite. The rate equations for the carrier density with spin-down and spin-up, $n_{\pm}$, are written

$$\begin{aligned}\frac{\mathrm{d}n_{\pm}(t)}{\mathrm{d}t} = {} & \frac{J}{ed} - \frac{1}{2\tau_s}\{n_+(t) + n_-(t)\} \\ & \mp \frac{1}{2\tau_J}\{n_+(t) - n_-(t)\} - 2G_n n_{\pm}(t)|E_{\pm}(t)|^2\end{aligned} \tag{8.25}$$

where $1/\tau_J$ is the spin-flip rate.

Using the conversion relations between linearly polarized lights and circularly polarized lights, $E_x = (E_+ + E_-)/\sqrt{2}$ and $E_y = i(E_+ - E_-)/\sqrt{2}$, and also the relations of the sum of the carrier number of down- and up-spin states n and the spin-state difference n_J, $n_+ = n + n_J - n_0$ and $n_- = n - n_J - n_0$, the equations for the linearly polarized fields are given as

$$\frac{\mathrm{d}E_x(t)}{\mathrm{d}t} = \frac{1}{2}(1 - i\alpha)G_n\left[\{n(t) - n_{\mathrm{th}}\}E_x(t) - in_J(t)E_y(t)\right] - \left(\gamma_a - i\gamma_p\right)E_x(t) \tag{8.26}$$

$$\frac{\mathrm{d}E_y(t)}{\mathrm{d}t} = \frac{1}{2}(1 - i\alpha)G_n\left[\{n(t) - n_{\mathrm{th}}\}E_y(t) + in_J(t)E_x(t)\right] + \left(\gamma_a - i\gamma_p\right)E_y(t) \tag{8.27}$$

The rate γ_p reads to a frequency difference of $2\gamma_p$ between the x- and y-polarized solutions (the x-polarized solution having the lower frequency when γ_p is positive). The decay rate γ_a reads to threshold difference for these two linearly polarized solutions, with the y-polarized solution having the lower threshold when γ_a is

positive. In actual fact, the frequency difference between the two linear modes depends on both the parameters γ_p and γ_a. Similarly, the equations for the total carrier density and the difference of the spin states are calculated as

$$\begin{aligned}\frac{dn(t)}{dt} = \frac{J}{ed} - \frac{n(t)-n_0}{\tau_s} - G_n\{n(t)-n_0\}\left\{|E_x(t)|^2 + |E_y(t)|^2\right\} \\ + iG_n n_J(t)\left\{(E_y(t)E_x^*(t) - E_x(t)E_y^*(t)\right\}\end{aligned} \tag{8.28}$$

$$\begin{aligned}\frac{dn_J(t)}{dt} = -\frac{n_J(t)}{\tau_J} - G_n n_J(t)\left\{|E_x(t)|^2 + |E_y(t)|^2\right\} \\ + iG_n\{n(t)-n_0\}\left\{(E_y(t)E_x^*(t) - E_x(t)E_y^*(t)\right\}\end{aligned} \tag{8.29}$$

The total carrier number n has a decay rate $1/\tau_s$ associated with spontaneous decay, while the carrier difference n_J has a decay rate $1/\tau_J = 1/\tau_s + 2\gamma_J$. The rate γ_J accounts for the mixing of the populations with opposite value of J_z, which was introduced to model spin-flip relaxation process and assumed to have the same value for the conduction and valence bands.

One of the typical features of VCSELs is a sharp polarization switching for the increase or decrease of the bias injection current. Figure 8.14 shows an example of polarization switching in VCSELs. Figures 8.14a and b are an experimentally observed L-I characteristic and a simulation result calculated from (8.26)–(8.29) using the parameter values of $\gamma_p = 1.0\ \text{ns}^{-1}$ and $\gamma_a = 45\ \text{ns}^{-1}$. In this case, the y-polarization mode is the starting main mode above the threshold and it switches to the x-polarization mode for the increase of the bias injection current. Though the switching point does not correspond with each other, a sharp polarization switching is well reproduced by the numerical simulation. It is noted that the frequency difference of the laser oscillations between y- and x-polarization modes is about +6 GHz at a bias injection current of 4 mA, although the lasing power of the x-polarization mode is very small at this bias injection current.

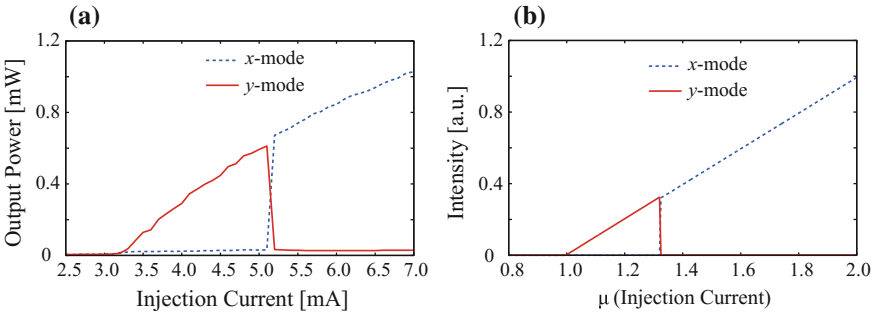

Fig. 8.14 L-I characteristics of VCSELs. **a** Experimental L-I characteristic and **b** L-I characteristic calculated by the spin-flip model

Normalized versions of the above rate equations are widely used for numerical investigations of VCSEL dynamics (Martín-Regalado et al. 1997). Using the normalizations of the variables as $E'_{\pm} = \sqrt{\tau_s G_n} E_{\pm}$ and $n'_{\pm} = n' \pm n'_J = G_n \tau_{ph} n_{\pm}$ ($n' = G_n \tau_{ph}(n - n_0)$ and $n'_J = G_n \tau_{ph} n_J$), the field and carrier density equations for circularly polarized states read as

$$\frac{dE'_{\pm}(t)}{dt} = \frac{1}{2\tau_{ph}}(1 - i\alpha)\{n_{\pm}(t) - 1\}E'_{\pm}(t) - (\gamma_a - i\gamma_p)E'_{\mp}(t) \tag{8.30}$$

$$\frac{dn'_{\pm}(t)}{dt} = \frac{1}{\tau_s}\mu - \frac{1}{2\tau_s}\{n'_{+}(t) + n'_{-}(t)\} \mp \frac{1}{2\tau_J}\{n'_{+}(t) - n'_{-}(t)\} - \frac{2}{\tau_s} n'_{\pm}(t)\left|E'_{\pm}(t)\right|^2 \tag{8.31}$$

where μ is the current density normalized to the threshold, $\mu = J/J_{th}$. On the other hand, for linearly polarized case, the field equations of the two components are written as

$$\frac{dE'_x(t)}{dt} = \frac{1}{2\tau_{ph}}(1 - i\alpha)\left[\{n'(t) - 1\}E'_x(t) - in'_J(t)E'_y(t)\right] - (\gamma_a - i\gamma_p)E'_x(t) \tag{8.32}$$

$$\frac{dE'_y(t)}{dt} = \frac{1}{2\tau_{ph}}(1 - i\alpha)\left[\{n'(t) - 1\}E'_y(t) + in'_J(t)E'_x(t)\right] + (\gamma_a - i\gamma_p)E'_y(t) \tag{8.33}$$

The equations for the total carrier density and the carrier difference are given as

$$\begin{aligned}\frac{dn'(t)}{dt} = -\frac{1}{\tau_s}\Bigg[n'(t)\left\{1 + \left(\left|E'_x(t)\right|^2 + \left|E'_y(t)\right|^2\right)\right\} - \mu \\ -in'_J(t)\left\{E'_y(t)E'^{*}_x(t) - E'_x(t)E'^{*}_y(t)\right\}\Bigg]\end{aligned} \tag{8.34}$$

$$\begin{aligned}\frac{dn'_J(t)}{dt} = -\frac{1}{\tau_J}n'_J(t) - \frac{1}{\tau_s}\Bigg[n'_J(t)\left\{\left|E'_x(t)\right|^2 + \left|E'_y(t)\right|^2\right\} \\ -in'(t)\left\{E'_y(t)E'^{*}_x(t) - E'_x(t)E'^{*}_y(t)\right\}\Bigg]\end{aligned} \tag{8.35}$$

Several spin relaxation processes for electrons and holes have been identified in semiconductors, such as scattering by defects, exchange interactions between electrons and holes, and exciton–exciton exchange interactions (Martín-Regalado et al. 1997). From experimental measurements of spin relaxation times in quantum wells, the relaxation time is of the order of tens of picoseconds. Since typically $\tau_s \approx 1$ ns, and $\tau_{ph} \approx 1$ ps, the spin mixing τ_J occurs on an intermediate timescale between that of the field decay and that of the total carrier population difference decay. Hence, the dynamics of the difference in spin states n_J cannot be adiabatically eliminated for the time scales of interest. The rate equations including the magnetic sublevels of the conduction and valence bands are applied to analyses for

the dynamics of VCSEL polarizations such as polarization switching and polarization instabilities (Sciamanna et al. 2003b, c; Sciamanna and Panajotov 2005, 2006; Masoller et al. 2006). In particular, fruitful results are obtained for explanations of the dynamics for orthogonal optical injection and stabilization in VCSELs. For the treatments of dynamics related to higher spatial modes, we need the rate equations discussed in the previous subsection. The spin-flip model is essentially developed for explaining the polarization dynamics in VCSELs in the fundamental spatial mode. However, it can be extended to the model including higher spatial modes (Valle et al. 2007). In this book, we use mainly the theoretical treatments in the previous subsection, which includes the spatial effects. However, the model of the magnetic sublevels is also used for VCSEL dynamics when necessary.

8.3.4 Two-Gain Model

The rate equations for narrow-stripe edge-emitting semiconductor lasers have been modified and used to study the dynamics of VCSELs, since they are very simple and easier to perform steady-state analyses and numerical simulations (Danckaerta et al. 2002; Hong et al. 2005). In the rate equations, the complex fields E_x and E_y for the two polarization directions in the orthogonal x and y coordinates at a single spatial mode oscillation are given as

$$\frac{\mathrm{d}E_x(t)}{\mathrm{d}t} = \frac{1}{2}(1 - i\alpha)G_{n,x}\{n(t) - n_{\mathrm{th},x}\}E_x(t) \tag{8.36}$$

$$\frac{\mathrm{d}E_y(t)}{\mathrm{d}t} = \frac{1}{2}(1 - i\alpha)G_{n,y}\{n(t) - n_{\mathrm{th},y}\}E_y(t) \tag{8.37}$$

where $G_{n,x}$ and $G_{n,y}$ are the gain coefficients for the polarization modes, and $n_{\mathrm{th},x}$ and $n_{\mathrm{th},y}$ are the carrier densities at threshold. We here introduced the different gain coefficients for the orthogonal polarization modes. The carrier density equation is given as

$$\frac{\mathrm{d}n(t)}{\mathrm{d}t} = \frac{J}{ed} - \frac{n(t)}{\tau_s} - G_{n,x}\{n(t) - n_{0,x}\}|E_x(t)|^2 - G_{n,y}\{n(t) - n_{0,y}\}|E_y(t)|^2 \tag{8.38}$$

where $n_{0,x}$ and $n_{0,y}$ are the carrier densities at transparency for the respective modes.

For the main lasing mode above the threshold, the gain is saturated, however, the gain of the counterpart polarization mode is a function of the bias injection current. At a certain bias injection current, the oscillation mode is switched from the main polarization mode to the sub-polarization mode. Then, the gain of the sub-mode saturates and the gain of the original main mode decreases for the further increase of the bias injection current. Figure 8.15 is an example of two orthogonal gain

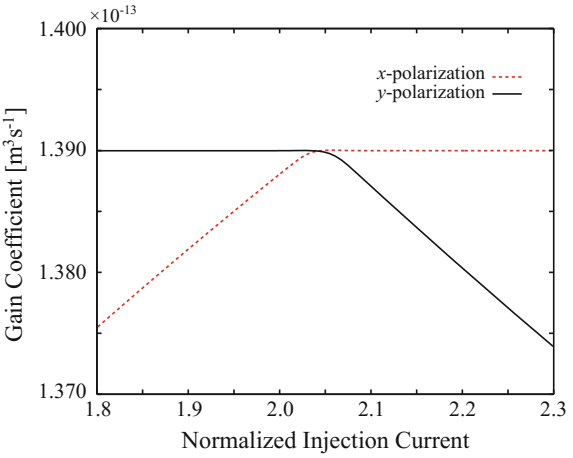

Fig. 8.15 Example of gain coefficients for two orthogonal polarization modes for increase of the bias injection current calculated from the spatial-mode model discussed in Sect. 8.3.2. μ is the normalized bias injection current to the threshold as $\mu = J/J_{\text{th}}$. The polarization switching point is set to $\mu = 2.04$

coefficients calculated from the spatial model, which is discussed in Sect. 8.3.2. In this case, the y-polarization mode is the main oscillation mode above the threshold. At a bias injection current $\mu = 2.04$, the laser oscillation is switched to the x-polarization mode. During the oscillation mode, the corresponding gain is clamped to a constant value, while the counterpart mode linearly increases or decreases for the change of the bias injection current. Therefore, from the gain coefficients in Fig. 8.15, we introduce the difference of the gain coefficients $G_{n,x}$ and $G_{n,y}$ as

$$G_{n,y} - G_{n,x} = G_0\left(1 - \frac{J}{J_{sw}}\right) \tag{8.39}$$

where G_0 is a certain constant and J_{sw} is the switching current at which the polarization alteration occurs. We here assume that the y-polarization mode is the original laser oscillation mode above the threshold and x-polarization mode is the sub-mode. Also, the gains below or above the polarization switching current are defined as

$$G_{n,y} = G_{0y} = \text{constant} \quad \text{for } J \leq J_{sw} \tag{8.40a}$$

$$G_{n,x} = G_{0x} = \text{constant} \quad \text{for } J > J_{sw} \tag{8.40b}$$

For the example of the spatial-mode model in Fig. 8.15, we obtain the gain constants as $G_0 = 2.00 \times 10^{-15}$ m^3 s^{-1} and $G_{0y} = G_{0x} = 1.39 \times 10^{-13}$ m^3 s^{-1}. Using the two-gain model, we can describe a sharp polarization switching such as observed in Fig. 8.14. In the spatial-mode model in Sect. 8.3.2, the difference between the gain coefficients of the two polarization modes is implicitly included through the refractive indices in the orthogonal gains defined in (8.19), so that we do not explicitly introduce the terms for the gain difference in the rate equations. While the difference is explicitly included as the parameters of birefringence and dichroism, γ_p and γ_a, in the spin-flip model in Sect. 8.3.3.

8.3.5 *Characteristics of VCSELs in Solitary Oscillations*

Even in the absence of external perturbations, VCSELs sometimes show unstable behaviors depending on the bias injection current. Spatial and polarization modes play important roles in the dynamic behavior of VCSELs. Higher spatial modes are easily excited for a higher bias injection current. Figure 8.16 shows the beam profiles for the lowest three spatial modes along the radial direction of a VCSEL (Linearly Polarized modes; LP_{01}, LP_{11}, and LP_{21} modes). These modes are calculated from (8.21)–(8.23). Due to the spatial hole-burning effects, the carrier distribution has a dip at the center of the disk in a VCSEL and the higher spatial modes tend to oscillate for a large bias injection current (Law and Agrawal 1997b). Figure 8.17 shows the experimentally obtained near-field images of the oscillation modes (Degen et al. 1999). The disk diameter of the VCSEL is 6 μm. The patterns are obtained by changing the bias injection current. Higher spatial modes are excited for the increase of the bias injection current. The excitation of higher modes strongly depends on the disk diameter. For ordinary applications of VCSELs, a circular Gaussian beam of the lowest mode is desirable. To obtain such a clean beam, the diameter of a VCSEL must be small, but it is difficult to attain a high power operation at the same time.

In semiconductor materials, there exists the difference of the refractive indices between the components for the principal axis and the orthogonal axis to it because of the distortion and birefringence of the materials. The difference between the indices is very small and it is 10^{-3}–10^{-4}. For ordinary edge-emitting semiconductor lasers, the difference can be ignored due to a large asymmetric configuration for the TE and TM modes in the active layer and the laser usually operates at only TE mode. However, the difference plays a crucial role for the operations of VCSEL,

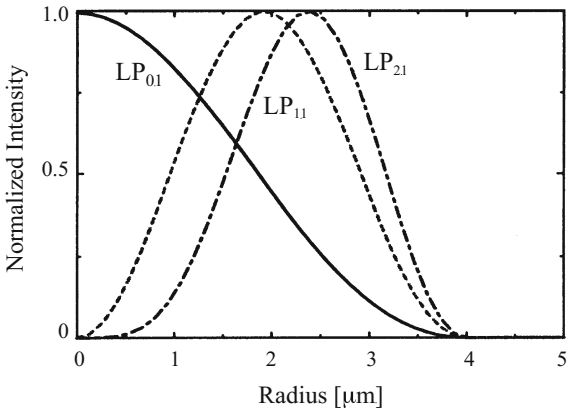

Fig. 8.16 Spatial mode distributions for LP_{01}, LP_{11}, and LP_{21} modes in VCSELs. The radius of the disk is assumed as 4 μm

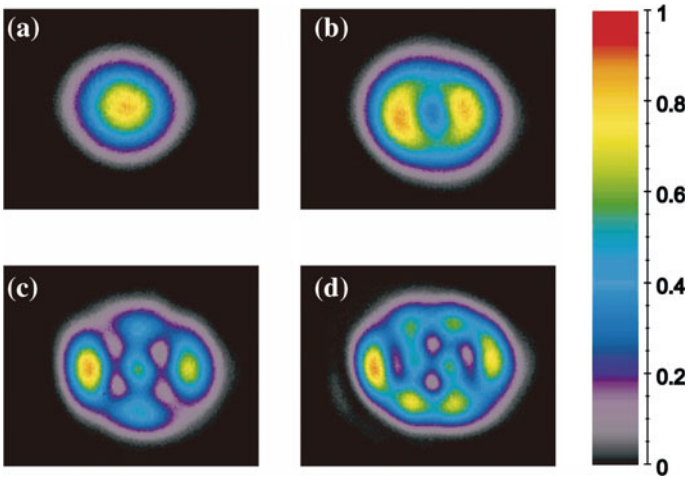

Fig. 8.17 Experimentally obtained near-field images of VCSEL with 6 μm diameter at an injection current of **a** 3.0, **b** 6.2, **c** 14.7, and **d** 18 mA [after Degen et al. (1999); © 1999 OSA]

since it has a circular disk structure of the light-emitting facet. Then, there is an ambiguity for the polarization direction of the laser oscillation. A VCSEL usually oscillates at a polarization mode along the optic axis of the material (*y*-polarization mode) when the laser is biased at a low injection current. However, the polarization mode may switch from this mode to the orthogonal one (*x*-polarization mode) for the increase of the bias injection current. This switching is mainly induced by the distortion or the birefringence of the laser material as discussed above. Taking into consideration the birefringence of laser materials, the polarization switching is well reproduced by the numerical simulations from (8.16)–(8.19) (Giudici et al. 1999; Danckaerta et al. 2002).

At a low bias injection current, the carrier density has a maximum value at the center of the disk in the active area and the carrier density smoothly decreases toward the edge of the disk. However, for a large bias injection current, hole-burning of carriers occurs at the center of the disk. Then, the carrier density takes the maximum value a little away from the center of the disk. This induces the excitation of the orthogonal mode and the suppression of the original mode, since, for example, the hole-burning due to the birefringence causes the transfer of the optical energy from the *y*-mode to the *x*-mode. Then, the laser oscillation is switched from the *y*-mode to the *x*-mode. The effects are distinct for VCSELs with large birefringence and small disk size. Which polarization mode is the main lasing oscillation strongly depends the device parameters and the bias injection current. Under certain conditions, only one of the polarization modes oscillates, while both polarization modes simultaneously oscillate with a stable manner for another case. Even, both polarizations would become unstable oscillation modes. Figure 8.18

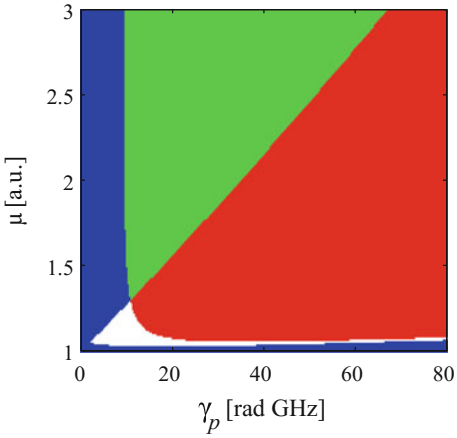

Fig. 8.18 Stability and instability of x and y polarized states of a solitary VSCEL. μ is the normalized injection current and γ_p is the birefringence. *Red region* stable x-polarization state, *blue region* y-polarization state, *white region* both stable polarization state, and *green region* neither stable polarization state. The parameters are $1/\tau_{ph} = 300\ ns^{-1}$, $1/\tau_s = 2\ ns^{-1}$, $1/\tau_J = 50\ ns^{-1}$, $\gamma_a = 0.4\ ns^{-1}$ and $\alpha = 3$ [after Torre et al. 2011; © 2011 OSA]

shows a map of oscillation modes in a space of bias injection current and the birefringence parameter in a free-running VCSEL (Torre et al. 2011).

The L-I characteristic of a VCSEL experimentally obtained for a disk diameter of 3 μm is already shown in Fig. 8.14a. The laser is a typical single spatial mode VCSEL of a wavelength of 780 nm and a maximum power of 2.0 mW, since the diameter is rather small compared with spatially multimode VCSELs such as shown in Fig. 8.17. In Fig. 8.14a, the laser at first oscillates at the main polarization mode (y-polarization mode) above the threshold current of 3.1 mA, but it switches to the orthogonal polarization mode (x-polarization mode) at the bias injection current of 5.2 mA. After the switching, the laser stably oscillates at the orthogonal polarization mode. Usually, the polarization switching has a hysteresis for the increase or the decrease in the bias injection current. Whether we can observe clear switching of the polarization modes or not, strongly depends on the characteristics of the laser materials and the device structures. Some VSCELs do not show clear polarization switching for the change of the bias injection current. Different from edge-emitting semiconductor lasers, two orthogonal polarization modes are easily excited simultaneously owing to a small gain difference between the two modes. The laser is longitudinally a single mode, since the total cavity length in VCSELs is as small as around 1 μm and the free spectral range of the cavity is very large. For the same reason, the conversion efficiency from the current to the frequency is very large compared with that of edge-emitting semiconductor lasers (see Sect. 5.1.6). Indeed, the laser in Fig. 8.14a has a conversion efficiency of 128 GHz/mA. Due to a short cavity length compared with edge-emitting semiconductor lasers (usually, the cavity length is several hundred times less than that of an edge-emitting

semiconductor laser), the change of the refractive index for the increase or decrease of the bias injection current causes a very large frequency change in the laser oscillation through the relation of $\Delta\nu \approx c(1 - \Delta\eta/\eta)/2\eta l$, where $\Delta\nu$ and $\Delta\eta$ are the frequency change and the change of the refractive index, respectively.

Even in solitary oscillations, VCSELs show dynamic characteristics. One such type of dynamics is the anti-phase irregular oscillation of the optical power between the two polarization modes (Fujiwara and Ohtsubo 2004). Figure 8.19 shows an experimental example of anti-phase oscillations of the y- and x-polarization modes in a VCSEL. Unstable pulsations and bistability are sometimes observed at the switching point of the two polarization modes (Tang et al. 1997). However, not only at the switching point of the two polarization modes but also at certain bias injection currents different from the switching point, does the laser show fast unstable oscillations and the two polarization modes oscillate at anti-phase manner in time. When the output power of the y-polarization mode goes down, the output power of the x-polarization mode grows up, and vice versa. This anti-phase oscillation is frequently observed in chaotic VCSELs subjected to optical feedback and injection current modulation (Besnard et al. 1997, 1999).

In a common narrow stripe semiconductor laser, the optical phase is assumed to be zero for the time development at its steady state as shown in (3.79). On the other hand, when an optical feedback is applied to such a laser, the phase linearly changes (either increase or decrease of the phase depending on external parameters) for time as discussed in Sect. 4.2.1. Linear change of optical phase is a common feature of the instability in semiconductor lasers. Since VCSELs are essentially unstable lasers, for example, they include polarization instability even when the laser is operating at a main single polarization mode. We here discuss only the instability of polarization modes and we do not consider the spatial-mode instability (namely, VCSELs are operating at the fundamental spatial-mode.) In a spin-flip model, the optical phase of a VCSEL operating at a solitary mode is easily calculated from the steady-state analysis for (8.32)–(8.35). Assuming that a VCSEL is operating at a y-polarization mode and the steady-state solution of the phase is given as $d\phi_y/dt = C_p$ (where ϕ_y

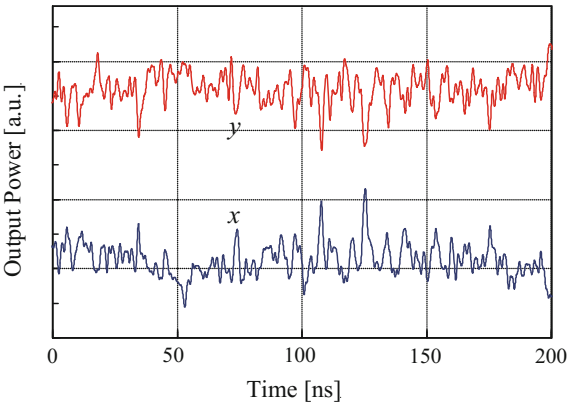

Fig. 8.19 Example of antiphase oscillations of y- and x-polarization modes in a VCSEL at solitary oscillation

is the phase component of the y mode and C_p is a constant), we obtain the relation as $C_p = \gamma_p - \gamma_a\alpha$. Namely, the phase linearly increases or decreases at a slope C_p for time. If a VCSEL is operating at a single x-polarization mode, the constant phase slope can be calculated as $C_p = \alpha\gamma_a - \gamma_p$. Also, the optical phase variation for time can be numerically calculated from the rate equations (8.32)–(8.35) in a solitary VCSEL. The result of the slope for a polarization mode is well coincident with the theoretically expected value of C_p under the corresponding device parameters. Even VCSEL operates at a single polarization mode, the two orthogonal modes actually pull against each other and this predation effect causes the linear change of the optical phase as similar to unstable optical feedback effects in common narrow-stripe semiconductor lasers. Linear optical phase change for time is also observed in solitary BALs (see for example, time varying optical phase variations in Fig. 12.5).

8.3.6 Spatio-Temporal Dynamics in VCSELs

Lasers with spatial structures such as VCSELs and broad-area lasers have spatiotemporal dynamics induced by diffraction of light and hole-burning of carriers in the laser cavity. In the case of VCSELs, the cavity length is short, so that the effect of the diffraction of light inside the cavity can be neglected. However, the effect of carrier hole-burning plays a crucial role for transverse-mode oscillations. The polarization dynamics of VCSEL are strongly related to carrier hole-burning, and the laser shows picosecond instabilities even at solitary oscillations. Time averaged polarization dynamics in VCSELs, such as dynamics of near-field patterns for the bias injection current, were extensively studied, while a few studies of spatiotemporal dynamics were reported (Mulet and Balle 2002; Barchanski et al. 2003; Valle et al. 2007). In this subsection, we present some experimental results for the spatio-temporally resolved polarization dynamics and discuss the underlining mechanism. Figure 8.20 shows the experimental results of spatiotemporal dynamics of a VCSEL obtained by a temporally resolved imaging by differential analysis, which allows us to extract the full two-dimensional evolution of the near-field intensity on time scales of 10 ps (Barchanski et al. 2003). The laser used is an oxidized VCSEL with an oscillation wavelength of 852 nm and a maximum output power of 3.8 mW. The VCSEL has a disc diameter of 14 μm.

Figure 8.20a shows the laser outputs of the two polarization modes for the time evolution after a step impulse, in which each polarization mode shows relaxation oscillation after the switch-on. A period of 10 μs of the pulse prevents the occurrence of thermal effects in the experiments. The laser is biased at $2.3J_{\text{th}}$. At this bias injection current, the frequency of the relaxation oscillation is about 3 GHz. In this figure, the 90° polarization mode is the main oscillation mode. After about 3 ns from switch-on, the laser settles down to steady-state oscillation. Figure 8.20b shows snapshots for the evolution of the near-field intensity in the VCSEL after the

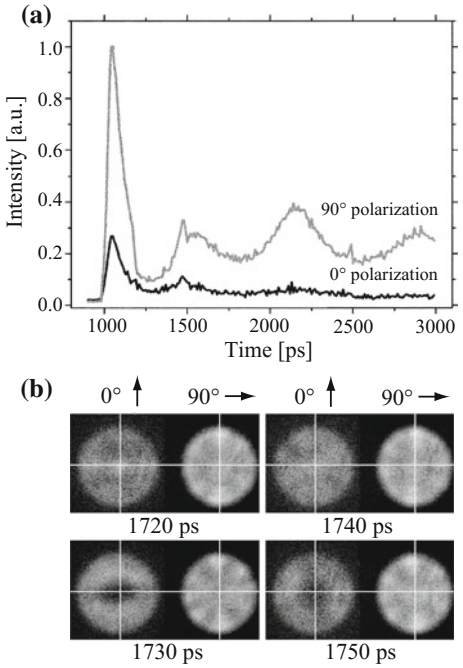

Fig. 8.20 **a** Evolution of relaxation oscillations extracted from the differential images of the near-field polarization-resolved patterns. *Gray curve* 90° polarization mode (dominant oscillation mode), *black curve* 0° polarization mode. **b** Snapshots for the evolution of near-field intensity of the VCSEL after the second relaxation oscillation peak. In each snapshot, the *left* shows the 0° polarization mode and the *right* 90° polarization mode. The crossing point of the overlaid crosshair is the center of the laser [after Barchanski et al. (2003); © 2003 IEEE]

second relaxation oscillation peak. In order to allow measurements, a displacement prism was used in the detection path to separate the laser beam into two orthogonal polarization patterns. The near-field polarized patterns of the laser was detected as an integrated image of 36,000 events by a CCD camera with a fast shutter time $\sim$200 ps using gating triggers synchronized with the driving pulses for the bias injection current. The images in Fig. 8.20b give evidence for a rich dynamical behavior in the emission profile in both polarization directions. In the 0° polarization mode, the intensity change of the center of the disc aperture is clearly seen, namely, the center is filled with a bright spot at 1720 ps, however, the center of the aperture remains mostly dark at 10 ps later. The intensity at 1740 ps is nearly uniform over the whole aperture, and then the center is again dark at 1750 ps. In the near-field patterns of the 90° polarization mode, we can see clear rotational flicker of the bright spots of the laser oscillations. For example, bright spots of the intensity rotate by 5° counterclockwise from 1720 to 1730 ps, while they rotate by 5° clockwise from 1740 to 1750 ps. This kind of rotational flicker is attributed to the spatial hole-burning of the carrier density in the laser cavity. Spatial hole-burning has been identified as a very important effect contributing to the observed dynamics on the examined timescales, especially for lasers having a spatial structure. Similar nonlinear dynamical behaviors have already been found and well investigated in the field of broad-area semiconductor lasers as known filamentation effects, which will be discussed in the following section.

Every transverse mode in a VCSEL corresponds to a different wavelength. Therefore, by spectrally resolving the near-field emission intensity, it is possible to investigate the dynamics of each mode separately. Figure 8.21 shows spectrally resolved near-field patterns of the VCSELs. In the observations, a spectrometer was used in the detection path to obtain spectrally resolved near-field patterns of the laser oscillations. The horizontal axis represents the spatial coordinate, and the vertical axis is a combination of both spatial and spectral coordinates, with the wavelength increasing from the bottom to top of each snapshot. The large birefringence splitting, which is the spectral spacing among the fundamental Gaussian modes in orthogonal polarization directions, is quite noticeable. The estimation of the birefringence splitting, performed with an optical spectrum analyzer having a maximal resolution of 0.05 nm, provides a value of approximately 0.11 nm, or 50 GHz, respectively. The first image at 1430 ps, within the second relaxation oscillation peak, shows two more mode orders than during the first relaxation oscillation peak, though the near-field pattern at the first relaxation oscillation peak is not shown here. At 1930 ps, about ten modes occur in the near-field intensity within the observed area. While the relative intensity among the 90° polarization modes mostly remains uniform, there is a drastic change in the modal behavior in the 0° polarization mode. Throughout the evolution, the four-lobed mode, which is the second oscillation mode, remains as an oscillation mode and all other modes of the 0° polarization direction show a relative smaller intensity. The fundamental Gaussian mode in the 90° polarization mode is spectrally aligned at the same position as the bright four-lobed mode in the 0° polarization mode. This spectral alignment implies the importance of spectral interactions related to the spatial carrier hole-burning effects. Namely, the fundamental mode, observed in the 90° polarization direction, has its intensity concentrated in the center of the aperture. In contrast, the intensity of the four-lobed mode is concentrated in the periphery of the

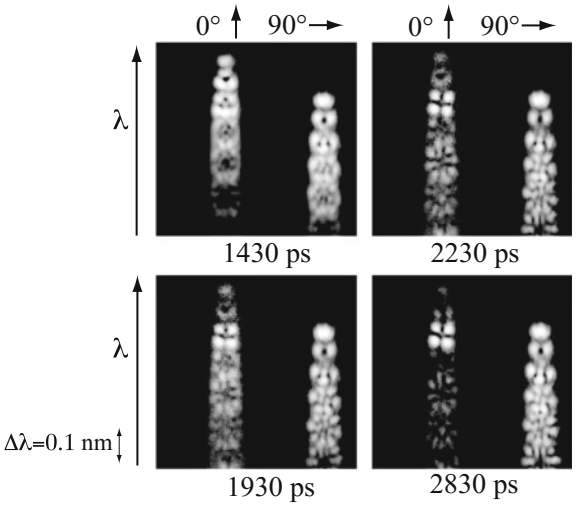

Fig. 8.21 Spectrally resolved near-field patterns for time evolution. In each snapshot, the *left* shows the 0° polarization mode and the *right* 90° polarization mode. The wavelength increases from *bottom* to *top* of each snapshot. The snapshots show the intensity change during 100 ps [after Barchanski et al. (2003); © 2003 IEEE]

aperture, resulting in a minimal spatial overlap of both modes. The complementary oscillation between the two polarization modes originates from a competition of both polarization directions for the available gain in the active medium. The dynamics of VCSELs even at solitary oscillation still remains an interesting research field, providing further insight into the fundamental physics of semiconductor lasers and promising device optimization.

8.3.7 Optical Feedback Effects in VCSELs

VCSELs have a high reflective mirror of the Bragg reflector within the cavity as much as the internal reflectivity of higher than 99% to realize a low laser threshold. However, the total photon number within the cavity is much smaller than that of an edge-emitting semiconductor laser and the laser is also affected by a small number of photons from an external reflector. For a small optical feedback, (8.16) is modified and the rate equations for the complex field are written as

$$\frac{\mathrm{d}E_j(t)}{\mathrm{d}t} = \frac{1}{2}(1 - i\alpha)G_{nj}\{n(r,\phi,t) - n_{\mathrm{th},j}\}E_j(t) + \frac{\kappa}{\tau_{\mathrm{in}}}E_j(t-\tau)\exp(i\omega_0\tau) \quad (8.41)$$

The other equations for the total complex field amplitude and the carrier density remain unchanged. Equation (8.41) looks like the same form as that for narrow-stripe edge-emitting semiconductor lasers. However, the rate equations of the total field and the carrier density are the functions not only of time but also space and, as a result, the laser shows complicated behaviors compared with narrow-stripe edge-emitting semiconductor lasers. Mutual interactions between the two polarization modes also affect the dynamics. Spatial mode competitions may also play an important role for the dynamics under a large bias injection current. Therefore, we must take into account the essential terms of the spatial polarization modes for numerical calculations of the dynamics.

Since the laser cavity length of a VCSEL is less than the optical wavelength and much smaller than those of other semiconductor lasers, the separations both for the longitudinal and transverse modes are much larger than for other lasers. Therefore, we can well apply the approximation for a single longitudinal mode operation as far as the laser has a small disk size or is biased at a modest injection current. However, the competition among spatial and polarization modes arises at a higher bias injection current. In the following, we show some characteristics of optical feedback effects in VCSELs. Unstable oscillations of VCSELs induced by optical feedback have been numerically calculated (Law and Agrawal 1998). Table 8.3 is a typical set of parameters used in the numerical simulations. Figure 8.22 shows a numerically calculated time series of the laser output for the change of the external feedback ratio. The diameter of the laser disk is 4 μm and the laser is oscillated with the lowest single mode or the lowest two spatial modes (LP_{01} and LP_{11} modes). However, a single polarization mode is assumed at solitary oscillation. From

Table 8.3 Characteristic device parameters for a VCSEL at an oscillation wavelength of 850 nm

Symbol	Parameter	Value
G_n	Gain coefficient	2.90×10^{-12} m^3 s^{-1}
Γ_d	Confinement factor	0.1
α	Linewidth enhancement factor	3.80
r_1	Output facet reflectivity	0.9975
r_2	Bottom reflectivity	0.9995
n_{th}	Carrier density at threshold	3.80×10^{24} m^{-3}
n_0	Carrier density at transparency	1.75×10^{24} m^{-3}
τ_s	Lifetime of carrier	1.00 ns
τ_{ph}	Lifetime of photon	3.30 ps
γ_J^{-1}	Lifetime of spin	30 ps
τ_{in}	Round trip time in laser cavity	22.6 fs
D	Diffusion constant	30 cm^{2}s^{-1}
l	Cavity length	1.00 μm
d	Active layer thickness	0.20 μm
R_a	Radius of active layer	4.00 μm

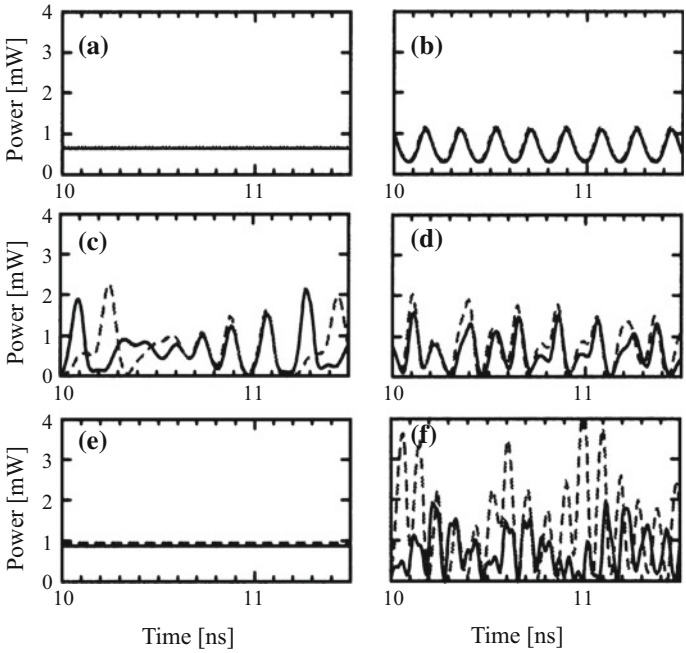

Fig. 8.22 Temporal evolutions of the output power under two-mode operation with a 4 μm disc contact (weak coupling) VCSEL for several feedback levels. *Solid* and *dashed curves* represent the LP_{01} and LP_{11} modes, respectively. External feedback rate κ of **a** 0, **b** 1.6×10^{-4}, **c** 5×10^{-4}, **d** 8.9×10^{-4}, **e** 1.6×10^{-3}, and **f** 2.8×10^{-3} [after Law and Agrawal (1998); © 1998 OSA]

Fig. 8.22a–d, the two modes show period-doubling like evolutions to chaotic states. However, once they become a fixed oscillation in Fig. 8.22e and again evolve into fully chaotic oscillations in Fig. 8.22f. Spontaneous emission of light is ignored in these calculations, however, it strongly affects the dynamics when the laser oscillates at chaotic states. Some such effects are the increase of noise floor and the broadening of the chaotic carrier frequency.

As dynamics of narrow-stripe edge-emitting semiconductor lasers, low-frequency fluctuations (LFFs) have been observed. LFFs are not only the typical features of narrow-stripe edge-emitting semiconductor lasers, but also they are observed in various types of semiconductor lasers. Fujiwara et al. (2003) have experimentally observed LFFs in VCSELs with optical feedback from a distant reflector. Similar LFF characteristics to those of narrow-stripe edge-emitting semiconductor lasers, sudden power dropout and gradual power recovery, are observed for the *y*-polarization mode with the lowest spatial mode of LP_{01} at a low bias injection current. Under an LFF oscillation for the *y*-polarization mode, the output power of the orthogonal *x*-polarization mode also shows synchronous waveforms of LFFs with the *y*-polarization mode, but it is an anti-phase oscillation. Similar to the dynamics of narrow-stripe edge-emitting semiconductor lasers, coexistent states of LFFs and stable oscillations are sometimes observed close to the threshold current. The polarization switching is suppressed or even eliminated by parallel optical injection at higher optical feedback ratio, while the laser shows chaotic oscillations at a single polarization mode when the feedback is not so strong (Hong et al. 2004; Aoyama et al. 2011). Also, the coherence of the laser is fairly collapsed at LFF states. However, the laser still holds a single longitudinal-mode operation, because of the large separation of the cavity modes (Chang-Hasnain et al. 1991). The dynamic properties of LFFs in VCSELs have been demonstrated by numerical simulations using the model of the population difference between the carrier densities with positive and negative spin values, i.e., spin-flip model (Masoller and Abraham 1999a; Sciamanna et al. 2003a, b, c).

Figure 8.23 shows time-averaged effects of polarization-selected optical feedback in a VCSEL. A VCSEL used in the experiments has the disc diameter of 16 μm and the oscillation wavelength of 780 nm with a maximum optical power of 10 mW. The external mirror is located at 90 cm away from the front facet of the laser. For a reference, the L-I characteristics of solitary mode together with near-field oscillation patterns at 7.0, 12.0, 18.0, and 24.0 mA are displayed in Fig. 8.23a. For steady-state oscillations, the complementary features of the oscillation patterns between the two polarization modes are clear, especially at higher bias injection current, which is the typical nature of VCSELs either for fast or slow dynamics. This laser has no clear polarization switching between the crossed polarization modes. As noted, L-I characteristics of VCSELs strongly depend on device structures and used materials. Though the total L-I characteristic shows an almost linear relation for the increase of the bias injection current, each polarization

component has quite different features depending on the respective VCSEL structures. For example, the L-I characteristics of *y*- and *x*-polarization modes are quite different from those for one in Fig. 8.14 that shows a clear polarization switching. As a result, the near-field pattern for each VCSEL is also dependent on the device structures. For the case of total optical feedback in Fig. 8.23b, the threshold of the *y*-polarization mode slightly reduces from 6.4 to 6.2 mA, while the threshold of the *x*-polarization mode increases from 6.4 to 6.8 mA. The slope efficiency increases due to the optical feedback, but only slight changes of the L-I curves are visible. However, the spatial modes are affected by the optical feedback, especially in higher bias injection current. In the case of *y*-polarization optical feedback, the trends of the threshold reduction are almost the same as for the case of the total optical feedback. However, the crossed polarization component (*x*-polarization mode) is greatly suppressed. On the other hand, two modes compete with each other in the case of *y*-polarization feedback. As a result, the laser becomes less stable at this amount of the optical feedback and it is oscillated with lower spatial orders. Polarization selective optical feedback provides quite interesting dynamics of VCSELs, and it is very important from the viewpoint of laser control.

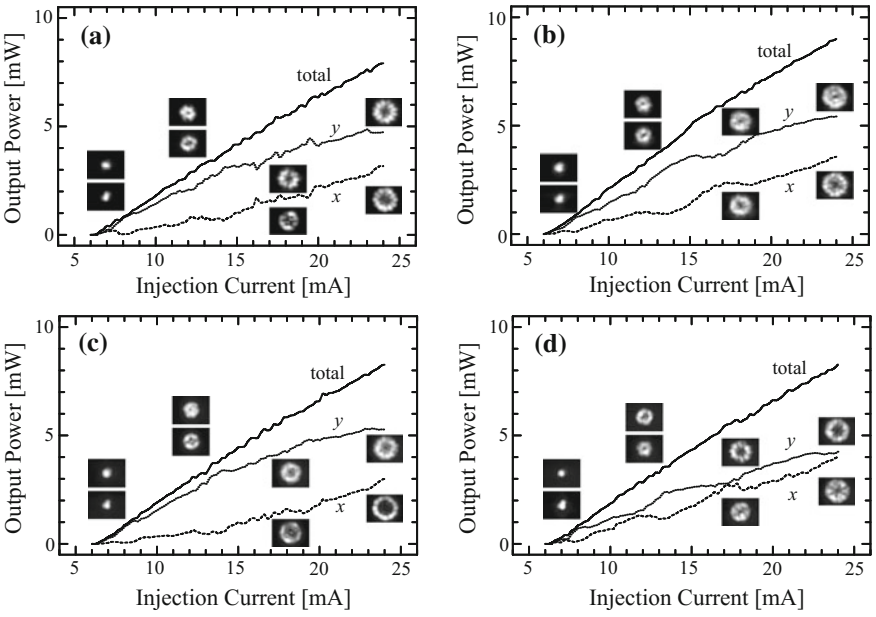

Fig. 8.23 Effects of optical feedback in VCSELs. Experimentally obtained L-I characteristics and near-field patterns for **a** solitary oscillations, **b** total optical feedback (intensity feedback of 9.8%), **c** *y*-polarization feedback (feedback of 6.1%), and **d** *x*-polarization feedback (feedback of 6.0%). The *upper* mode patterns in the *insets* are for the *y*-polarization mode, while the *lower* ones for the *x*-polarization mode

8.3.8 Square-Wave Generation in VCSELs

VCSELs have been newly developed and they themselves show various dynamics under solitary oscillations and external perturbations. Therefore, the dynamics have not been well understood yet and studies are still undergoing. As another example of dynamics in VCSELs, we here show self-oscillation properties when a portion of the laser output power is injected back into the laser after having rotated its polarization by 90° with respect to the initial laser polarization state (Jiang et al. 1993). When the two polarization components of the lights are orthogonally returned to the laser from a reflector with short distance, the *y*-polarization component coherently couples with the *x*-polarization component and the *x*-polarization component also coherently couples with the *y*-polarization component in as far as the corresponding oscillation wavelengths are assumed to be almost the same. Figure 8.24 shows the experimental waveforms of self-modulations in VCSELs. In this experiment, a laser that shows a clear polarization switching is used.

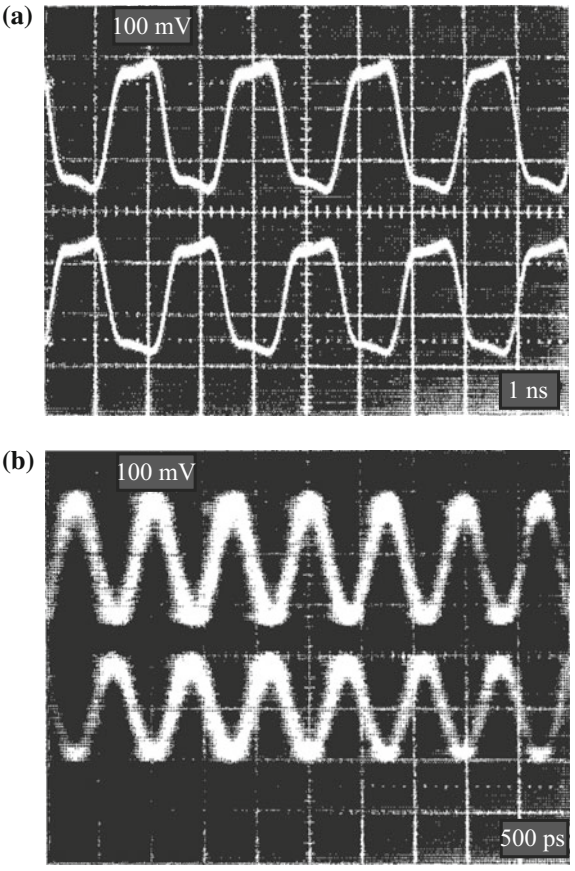

Fig. 8.24 Waveforms of polarization self-modulation signals corresponding to extended cavity lengths of **a** 16.5 cm and **b** 5.3 cm at a bias injection current of $J = 1.51J_{th}$. The bias injection current is above the point of the polarization switching. *Upper trace* *y*-polarization, *lower trace* *x*-polarization [after Jiang et al. (1993); © 1993 AIP]

Self-modulations are observed both for the bias injection currents above and below the polarization switching point. As square wave is observed for a long external feedback, while sinusoidal waveforms are observed for a short external feedback. As can easily be recognized, the waveforms of the *y*- and *x*-polarization components show anti-phase oscillations. The frequency of the oscillation is half of the frequency for the external cavity length. The polarization rotation feedback induces polarization injection locking in the VCSEL and leads to a switching of the polarization state, then, self-modulation occurs in its output. The phenomenon is quite similar to injection locking in a regenerative amplifier, where very weakly injected light is sufficient to lock the laser to the incident frequency. Under the same configuration, a self-modulation with a frequency of 6 GHz is obtained for a short cavity length of 1 cm. These self-modulation oscillations can be used as light sources for high-speed pulse sequences. Masoller and Abraham (1999a, b) presented the numerical simulations for the model considering the population difference between the carrier densities with positive- and negative-spin values in VCSELs and obtained the generations of self-modulation square waves. It is noted that similar square-wave generation is also observed in narrow-stripe edge-emitting semiconductor lasers with polarization-rotated optical feedback as discussed in Sect. 5.8.2. In that case, the frequency of pulses is also twice of the round-trip time of light in the external feedback loop. Therefore, square-wave generation is a universal feature in any semiconductor lasers with polarization-rotated optical feedback. However, it is again noted that the quality of square-wave generated by polarization-rotated optical feedback in VCSELs is not so good compared to that in narrow-stripe edge-emitting semiconductor lasers, since the interaction between the two crossed-polarization modes are too strong.

8.3.9 Short Optical Feedback in VCSELs

In Sect. 5.4.2, we discussed typical regular pulse package dynamics with LFFs induced in short cavity optical feedback in narrow-stripe edge-emitting semiconductor lasers. Regular pulse package dynamics are also observed in VCSELs with short cavity optical feedback. However, VCSEL has complex dynamics of orthogonal polarization modes and the characteristics of the pulse package are substantially affected by the polarization dynamics. Thus, we cannot observe exact regular pulse oscillations as in the case of narrow-stripe edge-emitting semiconductor lasers, due to the competitions of the crossed-polarization modes. Though the device structure of VCSELs is fairly different from that of common semiconductor lasers, the relaxation oscillation frequency is mainly determined by the gain coefficient and the photon lifetime (see 3.87). Thus, the relaxation oscillation frequency is almost the same order as that of narrow-stripe edge-emitting semiconductor lasers as far as the emitting light powers are the same. The definition of short cavity is that the cavity length is within the length corresponding to the relaxation oscillation frequency, which is usually less than centimeters. For example, in a

VCSEL with a very short external cavity condition ($\sim$10 μm), the laser and the external cavity conform a composite cavity and one polarization mode shows a periodic undulation of the output power for a period of $\lambda/2$ with the change of the external cavity length. In this state, the other mode is also excited alternately to the orthogonal mode, thus showing anti-phase oscillation for the external cavity length (Arteaga et al. 2006).

Tabaka et al. (2006) investigated the pulse package dynamics with LFFs including polarization modes in a short external cavity VCSEL. As a result, for the increase of the injection current, switching from one polarization mode to the other with orthogonal polarization direction is observed. The existence of the two polarization modes in VCSELs can give rise to an additional polarization mode competition dynamics in the presence of feedback. Figure 8.25 shows the experimental results of the polarization resolved dynamics. The VCSEL with an oscillation wavelength of 986 nm has the solitary threshold of I_{th} = 3.7 mA and shows polarization switching at the bias injection current of I = 4.2 mA. The external cavity length is 6.5 cm and the mirror reflectivity is 0.3, which results in a threshold reduction of 22% from the solitary laser oscillation. The relaxation oscillation

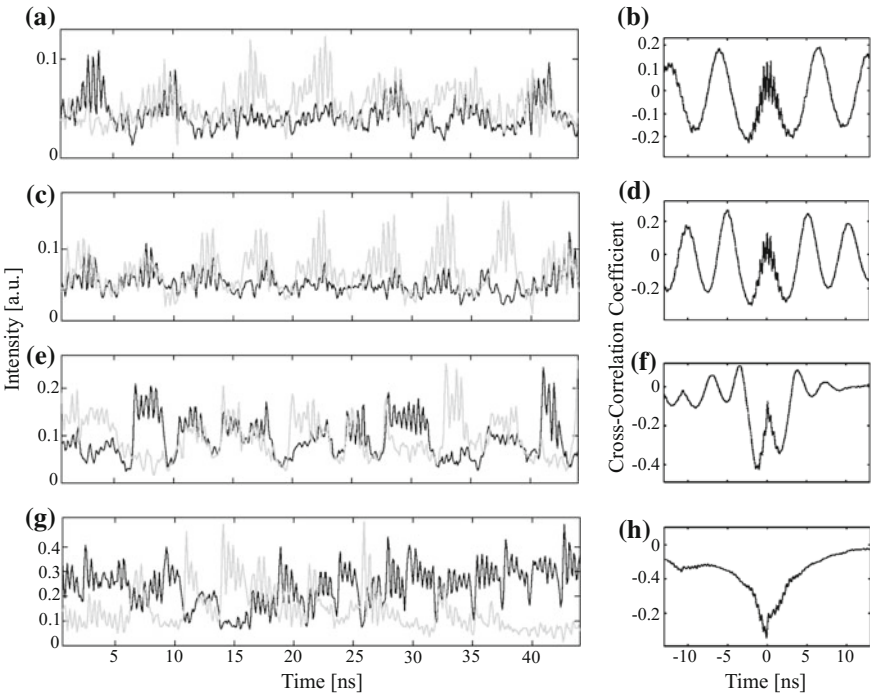

Fig. 8.25 Polarization resolved dynamics of a VCSEL in the pulse package regime for the injection current. *Left column* is time series and *right column* the corresponding cross-collation function. **a**, **b** I = 3.2 mA, **c**, **d** I = 3.4 mA, **e**, **f** I = 3.8 mA, and **g**, **h** I = 5.0 mA. *Gray plot* corresponds *y*-polarization and *black plot* *x*-polarization [after Tabaka et al. (2006); © 2006 AIP]

frequency at $I = 5.2$ mA corresponds to the external cavity length of 6.5 cm. Therefore, the observed dynamics in Fig. 8.25 satisfy the short cavity condition. In Fig. 8.25a the amplitude of the peaks is still small and the shape of the single pulse package envelope is not very regular. However, the envelope of the packages can be clearly identified, which indicates that the pulse packages in the two polarization modes are almost periodic with a characteristic frequency. The pulse package dynamics in the two polarization modes can be much better recognized at $I = 3.4$ mA, in Fig. 8.25c. In actual fact, the total intensity shows a quite regular pulse package oscillation, but the polarization resolved pulse package dynamics is not as regular as for the total intensity. The reason for this is that we observe polarization-mode competition, underlying the pulse package dynamics, reducing the regularity of the pulse package dynamics in each polarization mode. This mechanism becomes more relevant at a higher injection current, approaching the polarization switching point. A gradual loss of the regularity in the pulse package dynamics as the bias injection current is increased from 3.2 to 3.8 mA. In the time series in Fig. 8.25, the pulse package dynamics temporarily take place in one of the polarization modes only in some cases and the second mode is almost turned off. In other cases the pulse package dynamics take place in the two polarization modes simultaneously. The first case of dynamics, in which the pulses are emitted in one polarization mode only, is referred to as type I pulse packages. The second case of dynamics, in which the pulse package dynamics take place in the two polarization modes simultaneously, is called type II pulse packages. Similar interplay of the feedback induced complex dynamics and polarization-mode competition has been found numerically in the long external cavity regime (Sciamanna et al. 2003a) and experimentally confirmed (Naumenko et al. 2003; Sondermann et al. 2003).

The cross-correlation functions corresponding to the left column are shown in the right column of the figure. By increasing the injection current, we observe a continuous decrease of the modulation amplitude at the timescale of the multiples of the pulse package envelope until the peaks completely vanish, which we demonstrate in Fig. 8.25h. At higher levels of the bias injection current, the laser first emits pulses with high amplitudes while the amplitude of the following pulses progressively decreases. Moreover, in the regime of high injection currents, well above the polarization switching point, the cross-correlation function becomes negative for all time lags. This substantial change in the shape of the cross-correlation function can be associated with a remarkable change of the pulse package dynamics, reflecting a gradual transition from type II pulse package to type I one.

8.3.10 Optical Injection Dynamics in VCSEL

We have discussed optical injection phenomena in narrow-stripe edge-emitting semiconductor lasers in Chap. 6. The technique is developed for frequency-locking and stabilizing injected lasers, but the lasers are sometimes destabilized by optical

injection and show a rich variety of chaotic dynamics for certain ranges of the injection parameters as has already been discussed. In the case of narrow-stripe edge-emitting semiconductor laser, the laser usually emits a light with a linear polarization (TE mode) and the same polarization is used as an injection light. Once in a while, polarization-rotated optical injection (TM mode injection) is applied to obtain a chaotic light source in narrow-stripe edge-emitting semiconductor lasers. Normally, the excitation of the orthogonal mode is very small in ordinary edge-emitting semiconductor lasers. However, the situation completely changes in VCSELs, since the lasers have the ambiguity of oscillations for polarization directions. In VCSELs, optical injection including the polarization direction plays a crucial role in the dynamics of the laser oscillations even if the laser is oscillated at a certain fixed polarization with a solitary mode. Depending on the injection conditions, the laser shows a rich variety of dynamics; stable and unstable injection locking, and even chaotic oscillations by the optical injection. The typical feature of the dynamics is the polarization switching between the two orthogonal polarization modes. Further, the polarization is greatly affected by small changes of the bias injection current or the device temperature may result in a polarization switching between the two linearly polarized modes. Control of the VCSEL polarization is a major issue in telecommunication applications. For well polarization controlled VCSELs, polarization switching may be interesting for the development of all optical switches.

The typical feature of VCSEL oscillations is the polarization switching for the increase or decrease of the bias injection current. By optical injection, the laser shows different dynamics depending on the injection direction for the polarization mode and also the frequency detuning. As a general trend, the polarization switching current is almost fixed to that of the solitary oscillation for a small optical injection. For the increase of optical injection level, the switching current increases. Finally, the polarization switching is eliminated for a strong optical injection like the effect of optical feedback and the laser oscillates at only a single polarization mode (injected polarization direction), although the particular mode may show chaotic oscillations. In optical injection to a VCSEL, we can obtain a similar injection map of Fig. 6.4 in Sect. 6.1.2 as far as the injection polarization direction is the same as the oscillation mode of the VCSEL (Li et al. 1996; Ryvkinn et al. 2004; Hurtado et al. 2010). However, polarization switching dynamics encounter for an orthogonal polarization injection and the laser shows a rich variety of dynamics in its output power and polarizations. Figure 8.26 shows examples of dynamic-state maps in the phase space of the optical injection and the frequency detuning calculated from the spin-flip model discussed in Sect. 8.3.3. Here, we show different conditions of the polarization directions of optical injection and the bias injection points. The important parameters related to the polarization switching current and the laser oscillation frequency are set to $\gamma_p = 30\ \mathrm{ns}^{-1}$ and $\gamma_a = 1\ \mathrm{ns}^{-1}$. Under this condition, the normalized polarization switching current is $\mu_{\mathrm{sw}} = 1.3$ and the frequency difference between the y- and x-polarization oscillations is about 9 GHz. Figure 8.26a, b are the results for parallel optical injections, while Fig. 8.26c, d are those for orthogonal optical injection. Figure 8.26a is the map for the optical injection to the y-polarization when the laser oscillates at the y-

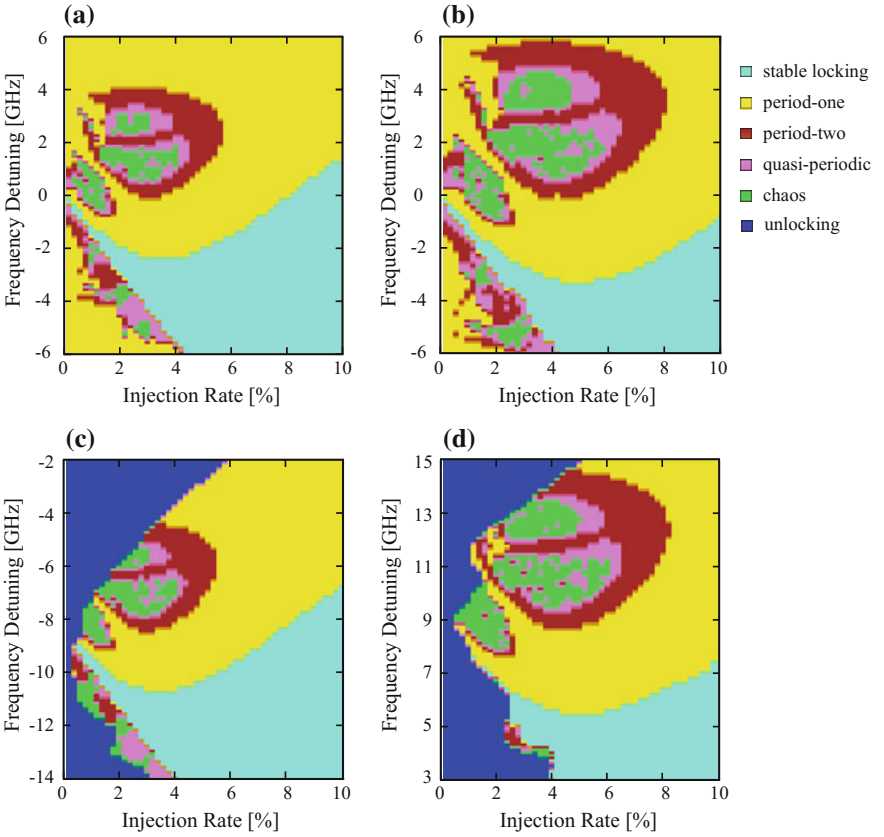

Fig. 8.26 Maps of dynamic states of an optically injected VCSEL in the phase space of the optical injection rate and the frequency detuning between the injection laser and the VCSEL. The maps are calculated from the spin-flip model. The polarization switching current is $\mu = 1.3$. Parallel optical injection maps for the oscillation modes at **a** $\mu = 1.2$ (y-polarization mode is injected) and **b** $\mu = 1.4$ (x-polarization mode is injected). Orthogonal optical injection maps for the non-oscillation modes at **c** $\mu = 1.2$ (x-polarization mode is injected) and **d** $\mu = 1.4$ (y-polarization mode is injected)

polarization mode ($\mu = 1.2$). On the other hand, Fig. 8.26b is that for the optical injection to the x-polarization under the laser oscillation at the x-polarization mode ($\mu = 1.4$). The general trends of the dynamics are quite similar to the case of narrow-stripe edge-emitting semiconductor lasers. As is expected, for higher bias injection, the stable oscillation region shrinks and chaotic oscillation areas are expanded. Figure 8.26c is the map for the optical injection to the x-polarization when the laser oscillates at the y-polarization mode ($\mu = 1.2$). While, Fig. 8.26d is that for the optical injection to the y-polarization under the laser oscillation at the x-polarization mode ($\mu = 1.4$). In the maps of the orthogonal optical injections, the offset frequency detunings of ± 9 GHz correspond to the frequency differences

between the two polarization components of the laser oscillations. Except for the offset of the frequency detuning, one obtains similar dynamics for parallel optical injection to VCSELs. However, it is noted that unlocking regions are widely observed at lower injection ratio in these cases.

In order to represent the richness of the polarization dynamics in VCSELs with orthogonal optical injection including wide range of frequency detuning and also large dynamic range of optical injection power, the map of the boundaries of different dynamics is experimentally drawn as usual in the phase space of the frequency detuning and the injection power in Fig. 8.27 (Altés et al. 2006; Gatare et al. 2006). The laser is under the *x*-polarization oscillation with a single spatial mode (the fundamental transverse mode) above the polarization switching point, hence the main *y*-polarization mode is suppressed. The injection power in the horizontal axis in Fig. 8.27 is normalized to the solitary oscillation power at this bias point. The VCSEL is externally injected by the linear polarization light with *y*-polarization mode and the *x*-polarization mode dynamics of the laser is investigated. The thin solid and gray lines are the polarization switching boundaries (switch-on points) for the increase of the bias injection current. While the dashed and the thick solid lines are polarization switching boundaries (switch-off points) for the decrease of the bias injection current. In the regions S1 and S2, the frequency of VCSEL emission is locked to the master laser. However, in the case of S2, it is the first order transverse mode and not the fundamental transverse mode that locks to the master laser, the fundamental transverse mode then being suppressed. The unlocking of the first order transverse mode happens at smaller values of the injection power,

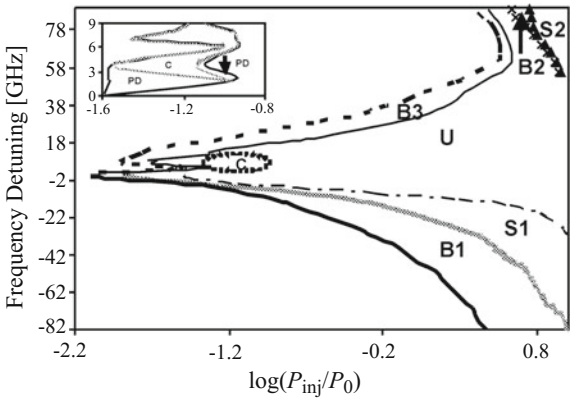

Fig. 8.27 Mapping of the dynamics of a VCSEL subject to optical injection in the phase space of the frequency detuning and the optical injection power. The laser is oscillated at the *y*-polarization mode above the polarization switching point. The injected linear polarization light is set to be the *x* mode. *Thin solid line* and *gray line* are polarization-switching boundaries for the increase of the bias injection current. *Dashed line* and *thick solid line* are polarization-switching boundaries for the decrease of the bias injection current. *B1*, *B2*, *B3* bistable regions, *S1*, *S2* stable injection-locking regions, *U* unlocking region, *C* chaotic region. The *inset* shows period-doubling (*PD*) dynamics around the region of instabilities C [after Altés et al. (2006); © 2006 IEEE]

describing bistable region B2 between the fundamental and the first order transverse mode both with the same polarization.

In Fig. 8.27, two polarization bistable regions are observed in a regime of fundamental mode emission, which correspond to two different ways of polarization switching. The first one is with frequency locking in region B1 and is confined between the gray and the thick solid lines. The second polarization bistable region of B3 is confined between the dash and the thin solid lines where the polarization switching happens without frequency locking. The two bistable regions are connected at a detuning of 2 GHz, which coincides with the birefringence frequency splitting between the two linear polarization modes. This means that when the master laser is biased at the frequency of the *y* mode (the suppressed mode under the bias injection current) a dramatic change of dynamics occurs from polarization switching with injection locking to polarization switching without locking. For larger positive or negative detunings, the switching power is larger, and moreover the switching power is larger for a negative than for a positive detuning value. This experimental feature agrees with theoretical results on a VCSEL rate equation model (Sciamanna and Panajotov 2005). It is noted that the widths of the injection-locking regions S1 and S2 and of the bistability region B1 increase with the detuning. On the other hand, the width of the bistability region B3 remains approximately constant when changing the frequency detuning. This bistable region B3 is also strongly influenced by the locking of the first order linear polarization mode (S2). For small positive detunings ranging from about 0–10 GHz, complicated dynamics like wave mixing, sub-harmonic resonance, sustained limit cycle oscillation, period doubling, and chaotic regimes (C) are observed as shown in the inset in Fig. 8.27. The example shown here is the polarization dynamics of orthogonally injected VCSELs at the bias injection current above the polarization switching point. Similar but somewhat different dynamics can be found for the bias injection current below the polarization switching point (*y*-polarization mode oscillations) and *x*-polarized optical injection (Sciamanna and Panajotov 2005, 2006).

8.4 Broad-Area Semiconductor Lasers

8.4.1 Theoretical Model of Broad-Area Semiconductor Lasers

The high power semiconductor laser is a promising laser device for various industrial applications of high-energy optical sources, since the power conversion efficiency from electricity to light in those semiconductor lasers is much higher than in other lasers (the efficiency is more than 50%). Such high power and high efficiency lasers can be used for light sources of laser welding, pumps for solid-state lasers, and laser fusion. Also high power semiconductor lasers are used as light

sources for laser printing and laser display. Currently, a high power semiconductor laser over 1 kW of output is devised by stacking lasers as arrays. One of the technologies for high power semiconductor lasers is a broad-area laser that has a broad stripe width ($\sim$100 μm which is about twenty times or more larger than that for ordinary narrow-stripe edge-emitting semiconductor lasers). The broad-area semiconductor laser has a broad stripe width of the active region as its name suggests. Therefore, the effects of the carrier diffusion and the diffraction of light in the active region are essential for such a structure (Diehl 2000; Gehrig and Hess 2003). As discussed in the following, spatial filament oscillation is one of the typical dynamics observed in broad-area semiconductor lasers. However, filamentation effects are generally stronger in a nitride quantum-well gain medium than in that of a conventional near-infrared semiconductor lasers, because of heavier electron and hole effective masses. In addition, there is strong quantum-well width dependence because of the quantum-confined Stark effect (Chow and Amano 2001). Therefore, InGaN semiconductor laser behaves like a broad-area semiconductor laser even when the stripe width of the laser is only a few microns. Other than that, the broad-area semiconductor laser has the same structure as ordinary narrow-stripe edge-emitting semiconductor lasers. Figure 8.28 is an example of the device structures. The thickness of the active layer is larger than that of ordinary narrow-stripe edge-emitting semiconductor lasers, but the oscillation of the TE mode is usually expected. However, under special installation of the device structures such as stress-induced anisotropy for the device, a broad-area semiconductor laser may oscillate at the TM mode. The internal cavity length is of the same order as for narrow-stripe edge-emitting semiconductor laser or several times larger than that. The longitudinal dimension is typically 1 mm. Except for wide stripe, the laser usually has a high reflectivity of light at the back facet and a low reflectivity at the front facet to avoid catastrophic optical damage (COD), which is discussed in Sect. 8.4.3. The output power of a broad-area laser is more than 100 mW and even 10 W oscillation is realized as a single emission light source.

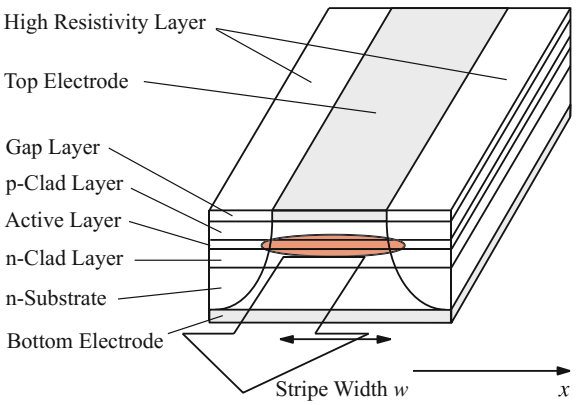

Fig. 8.28 Device structure of a broad-area semiconductor laser. The stripe width w of the active layer is as broad as $\sim$100 μm

Except for the advantage of high power operation, the qualities of the laser beam show rather poor performances. For example, broad-area semiconductor lasers usually operate at multimode both for the longitudinal and transverse modes. Depending on the bias injection current, spatial mode excitation or suppression occurs in the laser beam. As an ordinary tendency, the laser transversely oscillates with a few lower spatial modes at low bias injection current, while higher spatial modes are further excited with the increase of the bias injection current. This effect originates from the increased importance of carrier dynamics; with increasing current the nonlinear spatial and spectral dynamics lead to an increased rise in the gain for the higher spatial modes. Moreover, the carrier-induced refractive index induces dynamic filamentations in the gain medium, which is a principal cause of multimode dynamics. The far-field pattern of a broad-area laser typically has a twin-peak at low bias injection current. There exists a carrier hole-burning effect in the active region along the stripe width at high bias injection current. The positions of the hole-burning change and fluctuate with time and this gives rise to pulsating oscillations with picosecond and fast spatio-temporal filamentations (Hess et al. 1995; Marciante and Agrawal 1998; Scholz et al. 2008). Filamentation of broad-area semiconductor lasers, which shows zigzag motions of high intensity peaks along the internal cavity (typically the time size is several tens of picoseconds and the spatial size of several micron-meters), is one of the typical features of broad-area semiconductor lasers and it much deteriorates the laser performance. The broad-area semiconductor laser is also sensitive to external perturbations. In the following, we discuss the dynamics both without and with external perturbations.

The broad-area semiconductor laser itself is also an unstable device due to the spatial dependence in the laser oscillations (i.e., the spatial variation is an additional degree of freedom). Broad-area semiconductor lasers usually oscillate with multimode, however, we assume a single longitudinal mode operation for simplicity. Even for the assumption, it is proved that we can well reproduce fundamental dynamics of broad-area semiconductor lasers. Starting from the Helmholtz equation for the complex laser field $E(x, t)$ (x is the coordinate perpendicular to the laser thickness in the active layer, i.e., the direction along the laser stripe width), the rate equation is given as (Rahman and Winful 1994; Merbach et al. 1995; Levy and Hardy 1997; Marciante and Agrawal 1997):

$$\begin{aligned}\frac{\partial E(x,t)}{\partial t} &= iD_e \frac{\partial^2 E(x,t)}{\partial x^2} + \frac{1}{2}(1 - i\alpha)G_n\{n(x,t) - n_{\text{th}}\}E(x,t) \\ &\quad + in_2 k_0 |E(x,t)|^2 E(x,t)\end{aligned} \tag{8.42}$$

where $D_e = c/2k_0\eta^2$ is the diffraction coefficient of light (k_0 being the wavenumber in vacuum). The first term on the right-hand side of the equation is the diffraction effect due to the broad active area. The last term in the right-hand side of equation is the Kerr effect induced by the nonlinear property of the semiconductor laser materials and it is added as a phenomenological effect. The Kerr coefficient is very small and it may be neglected for a lower bias injection current, while it plays an

important role for the increase of the pump. Typically, the Kerr coefficient of a GaAs semiconductor material is $n_2 \sim 1 \times 10^{-17}$ m^2/W, although it depends on the optical wavelength. Also, we must take into account the nonlinear gain saturation at higher bias injection current [see (3.45) and (3.46)]. The diffusion effect must also be included in the rate equation for the carrier density $n(x, t)$ and it is written as

$$\frac{\partial n(x,t)}{\partial t} = D_n \frac{\partial^2 n(x,t)}{\partial x^2} + \frac{J}{ed} - \frac{n(x,t)}{\tau_s} - G_n\{n(x,t) - n_0\}|E(x,t)|^2 \qquad (8.43)$$

where D_n is the diffusion coefficient of the carrier and it is defined as $D_n = l_d^2/\tau_s$ (l_d is the diffusion length). In reality, the injection current is a function not only of time but also of the x coordinate. The dynamics of broad-area semiconductor lasers at solitary oscillations are numerically simulated from (8.42) and (8.43). Table 8.4 is an example of characteristic parameters of broad-area semiconductor lasers.

To explain the dynamics not only for the externally emitting light field but also within the laser cavity, a different model for broad-area semiconductor lasers is sometimes employed. In this model, the field amplitude and carrier density in the active region of a broad-area semiconductor laser fluctuate in time and space both for the transverse and longitudinal directions, i.e., x and z directions (z is the direction of light propagation). To analyze the internal local field and carrier density, we must take into account the internal field for the propagating and counter propagating waves and the polarization of the matter. Then, the electromagnetic field equation is numerically solved by using a finite difference time domain

Table 8.4 Characteristic device parameters for a broad-area semiconductor laser at an oscillation wavelength of 780 nm

Symbol	Parameter	Value
G_n	Gain coefficient	2.00×10^{-13} m^3 s^{-1}
α	Linewidth enhancement factor	3.00
r_1	Front facet reflectivity	0.05
r_2	Back facet reflectivity	0.95
n_{th}	Carrier density at threshold	5.11×10^{24} m^{-3}
n_0	Carrier density at transparency	1.30×10^{24} m^{-3}
τ_s	Lifetime of carrier	3.00 ns
τ_{ph}	Lifetime of photon	1.88 ps
τ_{in}	Round trip time in laser cavity	6.00 ps
D_e	Diffraction coefficient	1.44 m^2 s^{-1}
D_n	Carrier diffusion coefficient	30 cm^2 s^{-1}
l	Cavity length	500 μm
w	Stripe width	50 μm
d	Thickness of active layer	0.05 μm

(FDTD) method (Acachihara et al. 1993; Hess and Kuhn 1996a, b; Simmendinger et al. 1999). Therefore, such a model is sometimes used to investigate the internal distributions of carrier density and optical field. In the model, the field equation for the forward and backward propagations $E^{+}(x, z, t)$ and $E^{-}(x, z, t)$ along the z direction in the internal active region is given as

$$\begin{aligned} &\pm\frac{\partial E^{\pm}(x,z,t)}{\partial z}+\frac{\eta}{c}\frac{\partial E^{\pm}(x,z,t)}{\partial t} \\ &\quad=\frac{i}{2k}\frac{\partial^2 E^{\pm}(x,z,t)}{\partial x^2}-\left(\frac{\alpha_s}{2}+i\gamma_w\right)E^{\pm}(x,z,t)+\frac{i}{2}\frac{\Gamma(x)}{\eta^2\varepsilon_0 l}P_N^{\pm}(x,z,t) \end{aligned} \tag{8.44}$$

and the carrier density $n(x, z, t)$ reads as

$$\frac{\partial n(x,z,t)}{\partial t}=D_n\left\{\frac{\partial^2 n(x,z,t)}{\partial x^2}+\frac{\partial^2 n(x,z,t)}{\partial z^2}\right\}+\frac{J(x,z)}{ed}-\frac{n(x,z,t)}{\tau_s}-G_{E,P}(x,z,t) \tag{8.45}$$

where l is the internal cavity length of the laser, α_s is the linear absorption term, γ_w is the parameter related to transverse and vertical variations of the refractive index due to the waveguide structure, and $\Gamma(x)$ is the confinement factor. $P_N^{\pm}(x, z, t)$ is the nonlinear polarization of the matter accompanying the laser oscillation and is written as

$$P_N^{\pm}=\frac{2}{V}\sum_k d_{cv}(k)p_r^{\pm}(k) \tag{8.46}$$

where $d_{cv}(k)$ is the optical dipole matrix element and $p_r^{\pm}(k)$ is the microscopic polarization function. The macroscopic generation rate $G_{E,P}$ in (8.45) is given as

$$\begin{aligned} G_{E,P}(x,z,t)=&-\chi''\frac{\varepsilon_0}{2\hbar}\left\{|E^{+}(x,z,t)|^2+|E^{-}(x,z,t)|^2\right\} \\ &+\left[\frac{-i}{2\hbar}\{E^{+}(x,z,t)P^{+*}(x,z,t)-E^{-}(x,z,t)P^{-*}(x,z,t)\}+c.c.\right] \end{aligned} \tag{8.47}$$

where χ'' is the imaginary part of the susceptibility. When the variables for the z direction in (8.44) and (8.45) change slowly in time, the equations reduce to the rate equations at the exit face of the laser given by (8.42) and (8.43).

8.4.2 Dynamics of Broad-Area Semiconductor Lasers at Solitary Oscillations

In this subsection, the dynamics of broad-area semiconductor lasers at solitary oscillations are described. The L-I characteristic is the same as that for narrow-stripe edge-emitting semiconductor lasers, but the threshold current is much higher because of the broad stripe width and the need of the high carrier injection rate. The laser threshold current is usually larger than 100 mA. In the previous theoretical model, we assume a single mode oscillation for a broad-area semiconductor laser, however, most of the actual broad-area semiconductor laser oscillates with multi-modes. Figure 8.29 shows an example of spectrally resolved near-field pattern taken by a double-pass grating spectrometer (Stelmakh and Flowers 2006). The InGaAs-InGaP broad-area semiconductor laser has about ten oscillation lines (longitudinal modes) operating at a bias injection current of 600 mA ($J = 2.3J_{th}$). The main oscillation wavelength is $\lambda \approx 980$ nm, the stripe width is $w = 100$ μm, and the cavity length of $l = 1008$ μm. Among the longitudinal modes, two lines are shown in the photograph. In the figure, m denotes the number of the longitudinal modes, while p represents the number of the lateral modes. For example, $p = 0$ corresponds to the fundamental transverse mode (TEM_{00} mode) in the m-th longitudinal mode. In this laser, the separation of the longitudinal modes is about 60 GHz ($\sim$1.25 Å) and the successive lateral modes have a separation of 2–3 GHz. Therefore, in a strict sense, we must use multimode equations for the real laser model to compare with experiments. However, the single mode model can reproduce well the fundamental characteristics of broad-area semiconductor lasers as will be discussed in the last of this section. In usual, it takes a long time to calculate numerically the rate equations for broad-area semiconductor lasers, since the time step for the numerical calculations is as small as femtosecond due to the existence of a diffraction coefficient D_e, which contains a parameter of the laser wavelength. Therefore, the following examples of the numerical simulations are the results for a single longitudinal mode assumption.

As discussed, the rate equations depend on the x coordinate and the spatial modes play a crucial role for the dynamics. Then, we cannot ignore the spatial dependence and must take into account the higher transverse modes. Further, the laser undergoes spatial and temporal complex dynamics due to the self-focusing effects induced by the hole-burning of carriers and the diffraction of light. We will describe the fast dynamics later and, instead, we here discuss the time-averaged far-field profile of a laser oscillation. The output profile of broad-area semiconductor lasers has a significant wavefront distortion and the effect is remarkable for the laser of the gain-guided structure that is easy to fabricate. The far-field pattern of a broad-area semiconductor laser typically has a twin-peak profile. For multi-transverse mode lasers, the beam quality factor is introduced to evaluate the beam quality. The beam quality factor M^2 of a far-field pattern for a laser is defined as (Hodgson and Weber 1997)

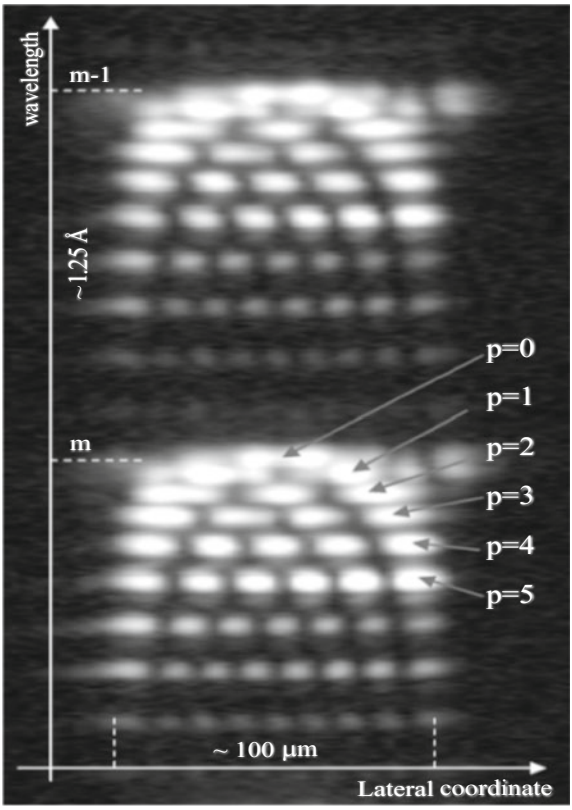

Fig. 8.29 Spectrally resolved near-field pattern of an InGaAs-InGaP broad-area semiconductor laser with a stripe width of 100 μm. Two of about ten longitudinal modes are shown in the photograph. m is the number of longitudinal modes and p corresponds to lateral modes [after Stelmakh and Flowers (2006); © 2006 IEEE]

$$M^2 = \frac{D_m \theta_m}{d_0 \theta_0} \approx \left(\frac{D_m}{d_0}\right)^2 \tag{8.48}$$

where d_0 and D_m are the diameters of the ideal Gaussian beam and the observed beam, and θ_0 and θ_m are the divergence angles for the ideal and observed beams, respectively. The value of the beam quality factor M^2 is unity for the ideal beam, but the value for broad-area semiconductor lasers usually ranges from 10 to 50 depending on the bias injection current and the stripe width.

Figure 8.30 shows a plot of experimental far-field patterns of a broad-area semiconductor laser for a change of the bias injection current. The profile is spatially averaged. At a lower bias injection current, the laser profile has a single lobe, while the laser shows a typical twin-peak pattern for a higher injection current. The extent of the divergence of the beam in the far field is roughly determined by the average particle size of the filamentation. From this relation, the spatial size of the filamentation at the exit facet of the laser is given as (Hülsewede et al. 2001)

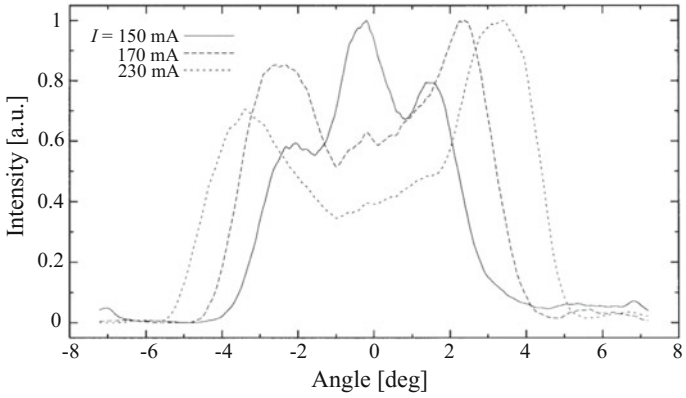

Fig. 8.30 Experimental far-field beam profile of a broad-area semiconductor laser. The laser oscillates at 780 nm and has a stripe width of 50 μm. The threshold current is 140 mA

$$\sigma = \frac{4\lambda}{\pi\theta} \tag{8.49}$$

where θ is the diffraction angle at the far-field plane. In Fig. 8.30, the divergence angle is $\theta = 0.17$ radians and the corresponding spatial size of the filamentation at $I = 230$ mA is estimated as 6 μm.

A laser with a non-negligible spatial structure shows instabilities without any external perturbations. Another example is VCSELs, as we have already discussed. Next, we show a typical example of spatio-temporal dynamics in broad-area semiconductor lasers. Figure 8.31 is numerically calculated near-field and far-field patterns of a broad-area semiconductor laser for a stripe width of 50 μm at a bias injection current of $J = 1.5J_{\text{th}}$. Figure 8.31a, b are the time-resolved near-field and far-field patterns with a time window of 1 ns. The horizontal axis is the position of the exit face of the broad-area semiconductor laser and the vertical axis is the time development of the output power. In the near-field pattern (NFP), we can see that bright spot particles move back and forth in a zigzag manner along the stripe width. This coil-like pattern is called a filament and it is a typical structure of the light output in broad-area semiconductor lasers. Figure 8.31b shows the corresponding time-resolved far-field pattern (FFP). Figure 8.31c, d are the time-averaged NFP and FFP. In the time-averaged NFP, the light outputs of the both edges in the active region are enhanced. The corresponding time-averaged FFP shows a twin-peaked pattern, which is typically observed in experiments. The calculated M^2 factor in the FFP is about $M^2 = 10$. The filament structures are indeed observed in experiments. Figure 8.32 is a filamentation oscillation experimentally observed by a streak camera in a near-field output of a broad-area semiconductor laser (Fischer et al. 1996; Burkhard et al. 1999). The width of migrating filaments is typically around 10 μm and it takes them about several picoseconds to migrate from one edge of the active region to the other. Figure 8.32a is the numerical simulation for the

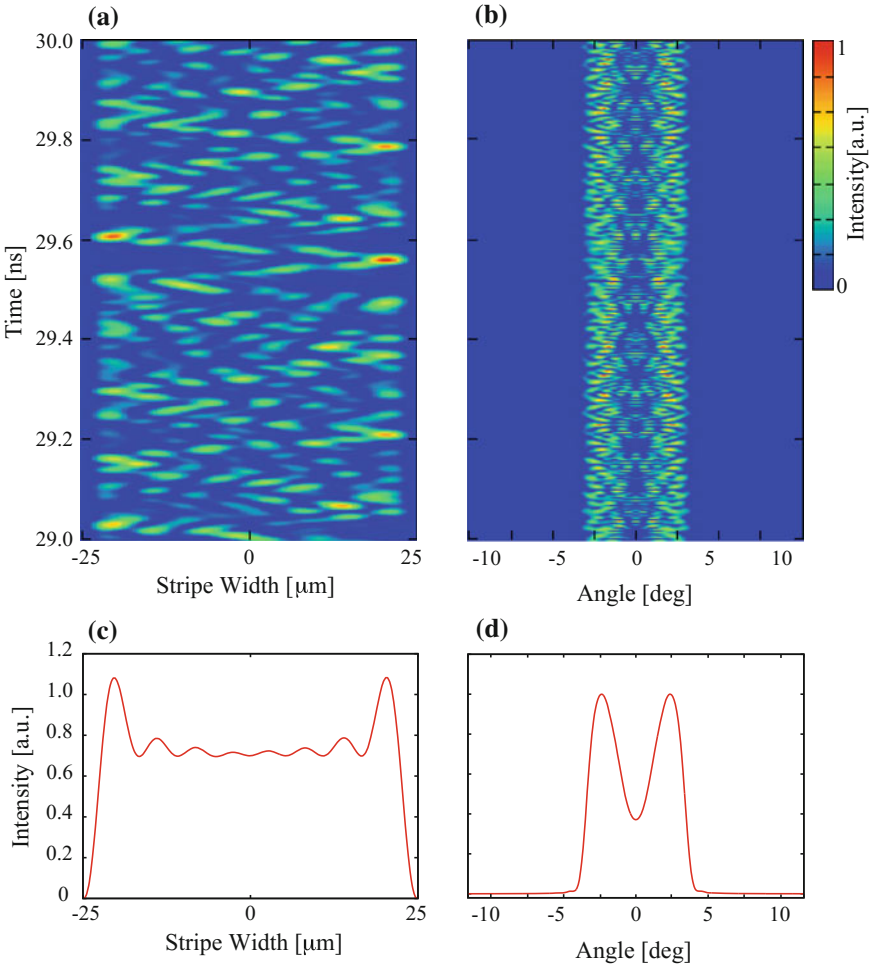

Fig. 8.31 Time-resolved **a** near-field pattern (NFP) and **b** far-field pattern (FFP) of an index-guided structure broad-area semiconductor laser at a bias injection current of $J = 1.5J_{th}$. The stripe width is 50 μm. Time-averaged **c** NFP and **d** FFP

experiment for Fig. 8.32b. Though the model is a single mode, the calculated filamentation is quite similar to the experimental one. Since filamentation is one of chaotic oscillations, the steady-state solution of the optical phase of a solitary broad-area semiconductor laser is not a fixed value for the time development. It is noted that the steady-state solution of the phase of narrow-stripe edge-emitting semiconductor lasers can be set to zero as described in (3.79), while the optical phase linearly changes in the presence of optical feedback as shown in Sect. 4.2.1. Similarly, the optical phase of a solitary broad-area semiconductor laser shows linear change for the time, since it is still an unstable laser. We will again discuss

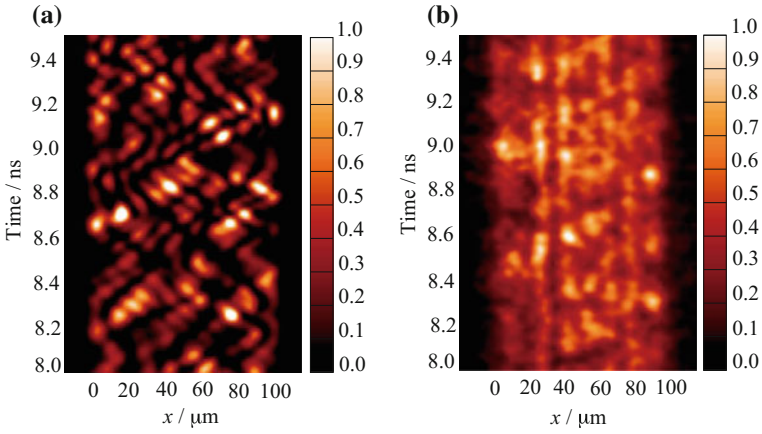

Fig. 8.32 Near-field pattern of filamentation in a broad-area semiconductor laser. **a** Numerical simulation of filamentation. **b** Experimentally observed filamentation by a streak camera. The bias injection current is $J = 2.0J_{\text{th}}$. The laser has a stripe width of 100 μm and the oscillation wavelength is 814 nm. The parameters of the theoretical result are compatible with those of the experiment. The horizontal axis corresponds to the exit face of the active region and the vertical axis is the time evolution [after Fischer et al. (1996); © 1996 EDP Sciences]

the steady-state solution of the optical phase in Sect. 12.3.7. Filamentation is universally observed not only for wide stripe lasers but also for semiconductor laser arrays.

The origin of dynamic filamentation in broad-area semiconductor lasers is not fully understood yet. However, the phenomena can be related to the effects of self-focusing, diffraction, and spatial hole-burning, which depends on spatial carrier diffusion as the relevant physical mechanisms (Hess et al. 1995; Hess and Kuhn 1996b). The self-focusing tends to guide high intensity regions resulting in a decrease of the optical gain. Thus, in the neighboring regions, the gain is higher. In addition, diffraction couples light into this neighboring region so that the spot of high intensity starts to migrate. At the edges of the active area, coupling via diffraction occurs only to one side, leading to a change of direction of migration. Figure 8.33 shows the intensity distribution of the internal cavity calculated from Maxwell-Bloch equations discussed in the previous subsection that include both the space dependence and the momentum dependence of the charge carriers and the polarization of matter (Hess and Kuhn 1996b). The bottom of each plot is the front facet with a lower internal intensity reflectivity of 0.33 and the top is the back facet with a higher reflectivity of 0.99. Bright spots of filamentation move with the time evolutions. Other than broad-area semiconductor lasers with constant stripe width, various types of broad-area lasers have been proposed (Levy and Hardy 1997; Fukushima 2000). To control and reduce the effect of filamentation, a flared laser having a tapered cavity has been used. In such lasers, the filamentation has been reduced but different complex spatio-temporal dynamics have been encountered.

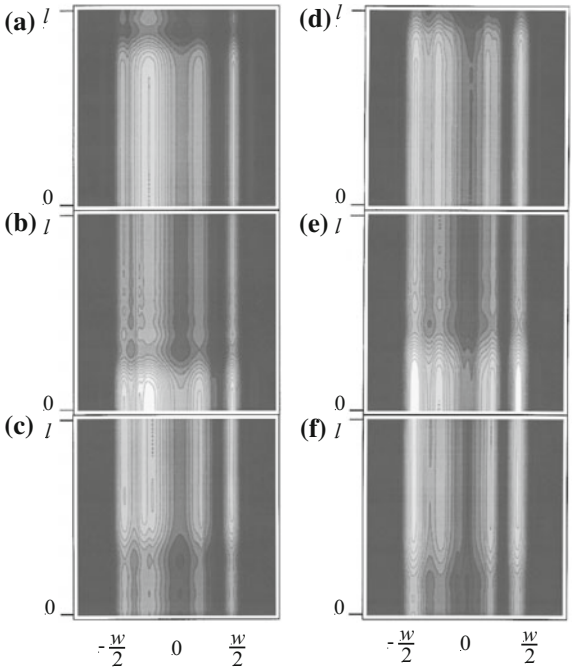

Fig. 8.33 Propagation of filamentary structures in a broad-area semiconductor laser. The individual plots display snapshots showing the equi-intensity regions of the intracavity intensity. At time **a** $t = t_0$, **b** $t_0 + 1$, **c** $t_0 + 2$, **d** $t_0 + 2.8$, **e** $t_0 + 3.5$, and **f** $t_0 + 4.5$ ps. *Dark shading* corresponds to low intensity and *bright colors* to areas of high intensity. The out-coupling facet (mirror reflectivity of 0.33) is located at the lower edge of each square. The highly reflecting back-coupling mirror (mirror reflectivity of 0.99) is at the upper edge. The longitudinal extension corresponds to 250 μm; the total transverse width ($w = 50$ μm) is 70 μm [after Hess and Kuhn (1996b); © 1996 APS]

We discussed the dependences of the laser dynamics on index- and gain-guide structures in ordinary narrow-stripe edge-emitting semiconductor lasers and the differences between them in Sect. 3.8.1. In the case of narrow-stripe edge-emitting semiconductor lasers, the dynamics strongly depend on the structures not only for solitary oscillations but also for oscillations under external perturbations. However, the differences are reflected only to the parameter values in the rate equations and particular time-dependent dynamics only change for the ranges of the parameter values, whether the laser is an index- or gain-guide structure. Nevertheless, lasers with gain-guide structure show unstable oscillations from the dynamics point of view. On the other hand, a broad-area semiconductor laser has a spatial structure along the stripe width (index- and gain-guided structures) and the differences between the structures give rise to large differences to the spatio-temporal dynamics. The dynamics of filamentations, which are the typical fast dynamics in

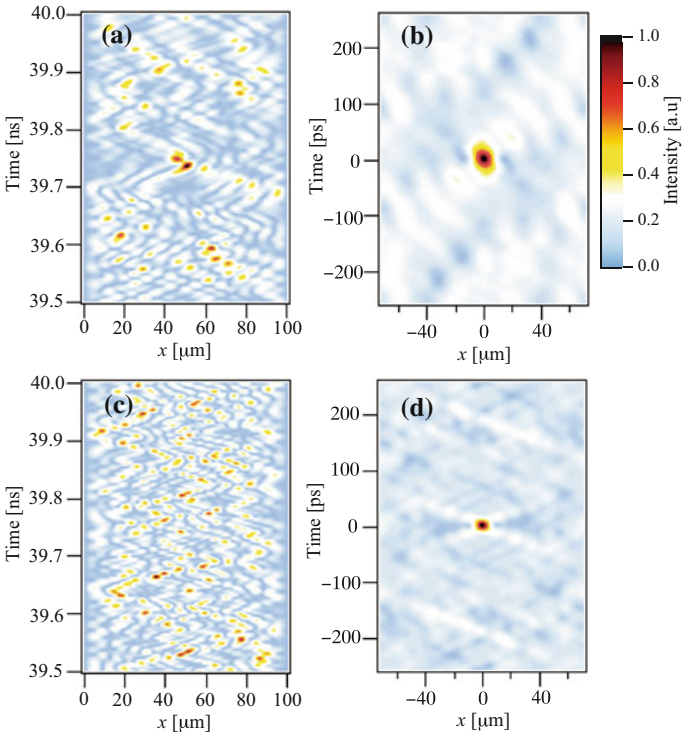

Fig. 8.34 Numerical simulations for near-field patterns in broad-area semiconductor lasers (*left column*) and their spatio-temporal correlations (*right column*) at $J = 1.5J_{th}$. **a** and **b** Index-guide semiconductor laser, and **c** and **d** gain-guide semiconductor laser. Both lasers have the same stripe widths of 100 μm. Parabolic profiles for the gain, the refractive index, the injection current distribution along the stripe width are assumed in the gain-guide semiconductor laser

broad-area semiconductor lasers, are strongly affected by the waveguiding structures.

Figure 8.34 shows the results of numerical simulations for filamentations in index- and gain-guide structures in broad-area semiconductor lasers, which have the same stripe width of 100 μm and the same bias injection current of $1.5J_{th}$. In the numerical simulations, the same form of the rate equations (8.42) and (8.43) is assumed, but, in the gain-guide laser, it is assumed that the gain, the refractive index, and the injection current distribution have appropriate parabolic spatial distributions along the stripe width. Figure 8.34a, b show the near-field patterns at the exit faces of the lasers and their space–time correlation functions. The time and spatial sizes of the filaments in the index-guide laser calculated from the correlation function are 4.1 μm and 27 ps, respectively, while those for the gain-guide laser are 2.9 μm and 12 ps, respectively. Namely, the gain-guide laser is less stable laser than the index-guide laser and the filaments strongly migrate back and forth along the active layer in the gain-guide laser as far as the values of the device parameters

for both the structures are the same. For the increase in the bias injection current, the spatio-temporal size of filaments shrinks and filaments shows strong zig-zag motions along the active layer, as a result, both the lasers similarly become less stable.

This fluctuation of microscopic filaments reflects the performances of macroscopic laser oscillations. Figure 8.35 shows experimental results of the time-averaged intensity distributions at the exit faces of index- and gain-guide broad-area semiconductor lasers for the bias injection current. The horizontal axis points to the exit face of the laser and the intensity distribution at each bias injection current is normalized. Each streak along the bias injection current corresponds to averaged filamentations. We can see different dynamics for several levels of the bias injection current. As already seen in Fig. 8.31, the enhancement of the powers at both edges of the active layer is observable irrespective of the guided structures. Although the two lasers have different stripe widths, values of device parameters, and oscillation frequencies, we can recognize that the gain-guide laser is less stable laser (Asatuma et al. 2006). In actual, broad-area semiconductor lasers oscillate at multimode both for longitudinal and lateral components as discussed above. In spite of the fact, a single-mode model both for longitudinal and lateral modes is frequently employed for studying the dynamics of broad-area semiconductor lasers. Figure 8.35c shows an example of calculated averaged near-field patterns for

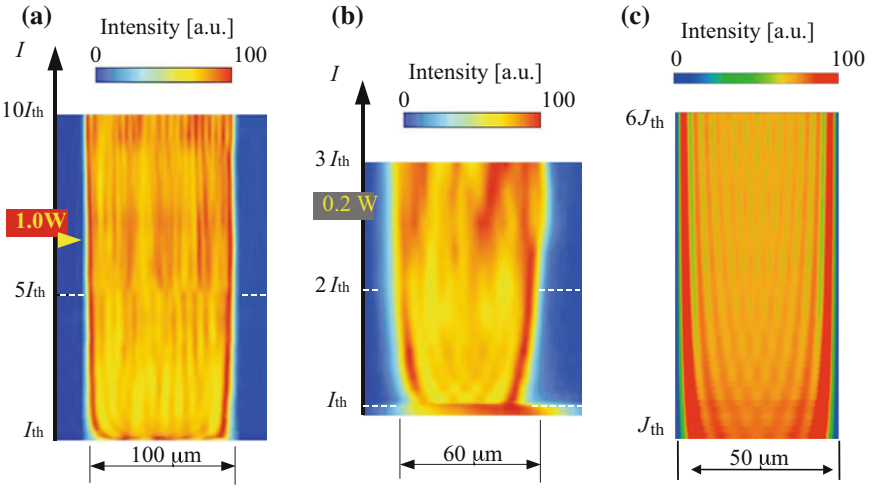

Fig. 8.35 Averaged near-field patterns for index- and gain-guide semiconductor lasers for the increase of the bias injection current. **a** Near-field pattern for an AlGaAs index-guide laser having a stripe width of 100 μm and oscillating at a wavelength of 808 nm. The threshold current is I_{th} = 160 mA. **b** Near-field pattern for an AlGaInP gain-guide laser having a stripe width of 60 μm and oscillating at a wavelength of 642 nm. The threshold current is I_{th} = 191 mA. **c** Numerically calculated averaged near-field pattern for an index-guide semiconductor laser with a stripe width of 50 μm. A single mode both for longitudinal and lateral modes is assumed for the calculation. Courtesy of SONY Cooperation

index-guided broad-area semiconductor lasers, where a single mode model for the rate equations in (8.42) and (8.43) is used. The figure can be compatible with the experimental result in Fig. 8.35a. Thus, the primary properties of broad-area semiconductor lasers can be approximately characterized even by using a single mode model in the numerical simulations.

8.4.3 *Optical Feedback Effects in Broad-Area Semiconductor Lasers*

Instabilities in broad-area semiconductor lasers are enhanced by external perturbations. In this subsection, we present some instabilities and chaotic dynamics in broad-area semiconductor lasers subjected to optical feedback. The field equation in the presence of optical feedback is given as

$$\begin{aligned}\frac{\partial E(x,t)}{\partial t} &= iD_e\frac{\partial^2 E(x,t)}{\partial x^2} + \frac{1}{2}(1-i\alpha)G_n\{n(x,t)-n_{\text{th}}\}E(x,t) \\ &\quad + \frac{\kappa}{\tau_{\text{in}}}E(x,t-\tau)\exp(i\omega_0\tau)\end{aligned} \tag{8.50}$$

In the above equation, the feedback light is always returned to the original position in the active area, however, the assumption may not always be true in experimental situations. The light is intentionally fed back to a different position to control the oscillation and beam profile. In that case, we must introduce the term for the space-dependent optical feedback. The spatial coupling plays an important role in the laser dynamics and a locking of the laser oscillations can be expected. The beam quality inevitably deteriorates due to the broad stripe width, however, fabrication of high power laser is at present the primary interest for the development for broad-area lasers and few studies have been reported for the enhancement of beam qualities. However, now the beam quality becomes the important issue for the applications of broad-area semiconductor lasers, for example, a light source for the second harmonic generation of solid-state lasers, laser welding and cutting, optical data storage, and display. Thus, a beam with good quality is expected. One of the beam controls is optical feedback. Figure 8.36 shows a numerical example of the effects of short optical feedback in a broad-area semiconductor laser at the bias injection current of $J = 1.5J_{\text{th}}$, the external amplitude reflectivity of $r = 0.06$, and the external mirror length of $L = 0.75$ cm. In the optical feedback, a partial reflection mirror of the width of 15 μm corresponding to the near field is used, so that the lower spatial modes are enhanced in the resulting oscillation. Figure 8.36a is the time-resolved NFP. Except for optical feedback, the condition is the same as that in Fig. 8.31. The filaments shows a rather regular pattern compared with the irregular oscillation of spatio-temporal pattern in Fig. 8.31a. At the same time, the side-peak intensities in Fig. 8.31c in the time-averaged NFP are suppressed and the twin-peak pattern of FFP in Fig. 8.31d becomes a single lobe pattern.

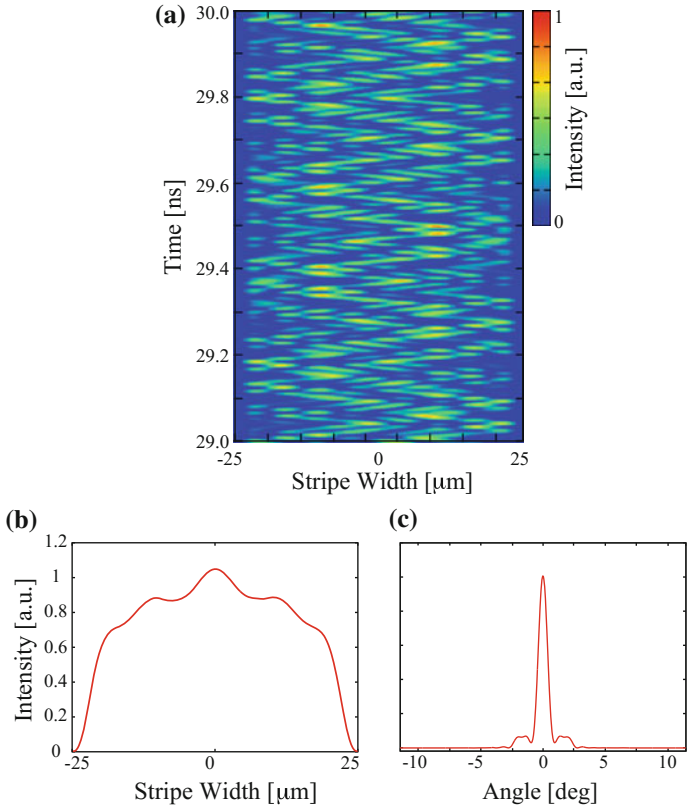

Fig. 8.36 Effect of short optical feedback with a partial reflection mirror of the width of 15 μm corresponding to the near field. **a** Time-resolved NFP at a bias injection current of $J = 1.5J_{th}$, an external amplitude reflectivity of $r = 0.06$, and an external mirror length of $L = 0.75$ cm. Time-averaged **b** NFP and **c** FFP

Dynamics similar to those of narrow-stripe edge-emitting semiconductor laser have been experimentally observed by optical feedback to broad-area semiconductor lasers. We show here one of the chaotic evolutions; the evolution of intermittent oscillations to regular chaotic states for the increase of the injection current. Figure 8.37 is an example of chaotic evolutions for the bias injection current at the external cavity length of $L = 30$ cm. The threshold of the used laser is about 140 mA. Figure 8.37a is the laser output power at the free running state just above the threshold. With the optical feedback, the reduction of the threshold is also observed in the broad-area semiconductor laser and the reduction rate is 13.9% for the external feedback rate of 6% (in intensity). When the laser is biased at a low injection current, LFFs are observed. In the power recovery process after the power dropout, the time scale of each step is also the same as the time calculated from the external cavity length. With the increase of the bias injection current, the frequency

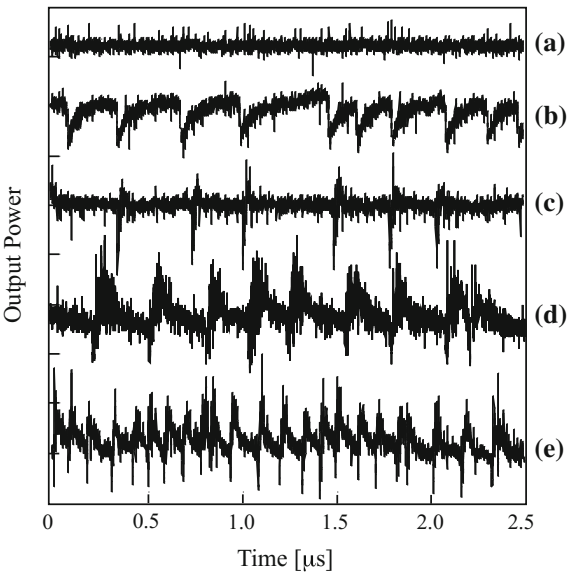

Fig. 8.37 Experimentally observed chaotic evolution for the bias injection current in a broad-area semiconductor laser. **a** Solitary oscillation at 140 mA. Optical feedback at bias injection currents **b** 150, **c** 162, **d** 170, and **e** 190 mA. The external cavity length is L = 30 cm and the external feedback strength is 6% in intensity. The laser used is the same as in Fig. 8.30

of LFFs changes and the inverse LFFs in which power jump-ups instead of power dropouts appear are observed at the bias injection current of 170 mA. Around this bias injection current, there is a kink of the L-I characteristic and the phase of the laser oscillation changes to a different state. At a further increase of the bias injection current, the laser behaves with normal chaotic oscillations, although the waveform still shows LFF-like oscillation (not fully chaotic oscillation in ordinary sense).

In a short optical feedback regime, one can observe similar dynamics of pulse packages as those in narrow-stripe semiconductor lasers. However, there are two schemes of pulse packages; one is a periodic envelope of an LFF frequency with a modulation of the fast oscillation corresponding to the external optical feedback loop, which is a familiar pulse package observed in a narrow-stripe edge-emitting semiconductor laser, which is discussed in 5.4.2. The other one is a pulse package of an envelope of the external optical feedback loop with the fast regular oscillation of filament pulses, which is a unique feature in broad-area semiconductor lasers (Tachikawa et al. 2010). Edge-emitting semiconductor lasers are also very sensitive to the phase. Phase sensitivity also exists in broad-area semiconductor lasers subjected to optical feedback and the dynamics are much affected by the absolute phase of the external cavity (Martín-Regalado et al. 1996a, b). The other effects of frequency-filtered optical feedback, spatial-filtered optical feedback, and grating feedback have been studied (Gaciu et al. 2007). We return the subject of optical feedback in broad-area semiconductor lasers from the viewpoint of laser control in Chap. 10.

One of the important issues for the practical applications of broad-area semiconductor lasers, such as laser cutting, is catastrophic optical damage (COD)

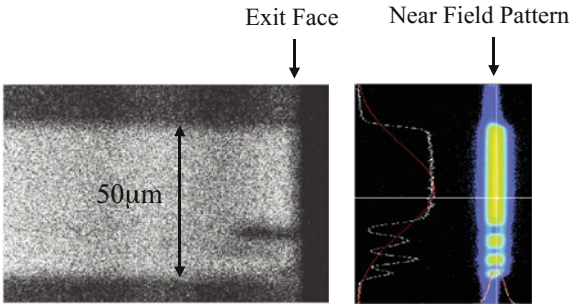

Fig. 8.38 Catastrophic optical damage (COD) induced by optical feedback in an index-guided broad-area semiconductor laser with a 50 μm stripe width and an oscillation wavelength of 808 nm. *Left* top view of the front facet. COD can be seen in the lower part of the laser. *Right* intensity profile of the cathode luminescence image at the front facet. Dips of light emissions corresponding to the front facet can be seen. Courtesy of SONY Cooperation

induced by optical feedback from a target. In ordinary narrow-stripe edge-emitting semiconductor lasers, catastrophic optical damage is also a serious problem when the laser is biased at a high injection current. The performance of the laser oscillations is significantly degraded by catastrophic optical damage and, worst case, the laser oscillation stops by the damage. The catastrophic optical damage is a critical problem in laser cutting using high power broad-area semiconductor lasers. Takiguchi et al. (2006) investigated the conditions for the occurrence of catastrophic optical damage in broad-area semiconductor lasers from the viewpoint of laser dynamics. Figure 8.38 shows an example of catastrophic optical damage observed in an AlGaAs index-guide broad-area semiconductor laser having a stripe width of 50 μm. Under filamentation oscillations in broad-area semiconductor laser, a large power is concentrated to a filament within a short time, and this effect together with large optical feedback intensity may damage the laser. Thus, microscopic filamentations greatly affect the catastrophic optical damage, but the detailed study for catastrophic optical damage with the relation of laser dynamics has not been fully understood yet. The study is very important to prevent fatal catastrophic optical damage in broad-area semiconductor lasers as a practical issue.

8.4.4 Effects of Optical Injection in Broad-Area Semiconductor Lasers

Similar to the optical feedback effects in broad-area semiconductor lasers, the injection of an external coherent resonant light can lead to the excitation and selection of specific transverse modes depending on the power and spatial profile of the injected light field (Gaciu et al. 2007; Takimoto et al. 2009). Except for the

spatial dependence of the injected field, the field in the presence of optical injection can be described by the same equation as (6.1) and is given as

$$\frac{\partial E(x,t)}{\partial t} = iD_e \frac{\partial^2 E(x,t)}{\partial x^2} + \frac{1}{2}(1 - i\alpha)G_n\{n(x,t) - n_{\text{th}}\}E(x,t) + \frac{\kappa_{\text{inj}}}{\tau_{\text{in}}} E_m(x,t)\exp(-i\Delta\omega t) \tag{8.51}$$

Again, E_m is the field of the injection laser, κ_{inj} is the injection fraction, and $\Delta\omega$ is the frequency detuning between the injection laser and the broad-area laser.

Figure 8.39 shows numerical results of optical injection to a broad-area semiconductor laser (Takimoto et al. 2009). The stripe width of the active layer is 50 μm and the continuous-wave injection beam has a rectangular shape with a width of 40 μm. The beam is symmetrically injected related to the center of the active layer. The frequency detuning is assumed to be $\Delta\omega = 0$ GHz at the bias injection current of $1.5J_{\text{th}}$. The upper plots are the time-resolved filament patterns and the lower traces are the time-averaged intensity profiles of the near-field patterns. The external

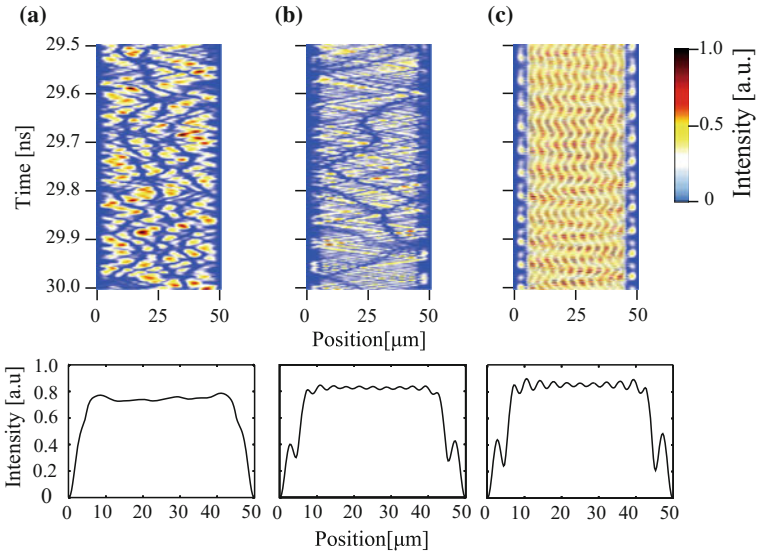

Fig. 8.39 Numerical results of optical injection at external injection ratios of **a** $r_{\text{inj}} = 0.4$, **b** 1.2, and **c** 1.6 at a frequency detuning of $\Delta\omega = 0$ GHz and a bias injection current of $1.5J_{\text{th}}$. The internal reflectivity of the active layer and the refractive index of the laser medium are assumed as $r_0 = 0.1$, and $\eta = 3.59$, respectively. *Upper plots* time-resolved filament patterns and *lower graphs* time-averaged near-field patterns

injection ratio r_{inj} defined by (6.2) is used as a measure of optical injection. At $r_{\mathrm{inj}} = 0.4$ in Fig. 8.39a, the laser still exhibits irregular oscillations, but the filament behavior differs from that of a solitary oscillation (compare with the solitary oscillation in Fig. 8.31) and the temporal duration of the filament is reduced. In the presence of optical injection, the side peak intensities, which exist at solitary oscillation, are suppressed and the laser beam has a flat top-hat profile, as shown in the time-averaged profile. Such a flat top-hat beam shape is very important for practical applications. At $r_{\mathrm{inj}} = 1.2$ in Fig. 8.39b, the laser still undergoes irregular oscillations, but some regular structure can be seen in the pattern and the filament durations are shorter. However, the flat-topped beam profile collapses and spatial periodicity is enhanced with a further increase in the optical injection, thus resulting in the excitation of higher spatial modes as shown in the time-averaged near-field pattern. At $r_{\mathrm{inj}} = 1.6$ in Fig. 8.39c, the near-field pattern shows a remarkable periodic structure and higher spatial modes are strongly excited. Spatio-temporal and spatio-spectral dynamics induced by optical injection are also studied by Gaciu et al. (2007).

8.5 Laser Arrays

Semiconductor laser arrays are also important devices for light sources with high power radiation. The laser may be composed of arrays of broad-area lasers to make an extremely high power laser device. However, here we assume that the arrays consist of ordinary narrow-stripe edge-emitting lasers and consider the interaction among the laser elements. When the separation between the laser arrays is very small, each laser interferes and instability sometimes occurs in the total laser output. In a strict sense, we must consider all the effects of the diffraction and the carrier diffusion as already discussed in Sect. 8.4 (Münkel et al. 1996). However, we consider the situation that the coupling of lights among arrays is a dominant effect and that it is more important than those of the diffraction and the carrier diffusion. We also assume that the coupling only between the neighborhood lasers is strong, as is often the case. Thus, the rate equations for the field amplitude and the carrier density of the j-th element are given as (Winful and Rahman 1990; Winful 1992)

$$\frac{\mathrm{d}E_j(t)}{\mathrm{d}t} = \frac{1}{2}(1 - i\alpha)G_n\{n_j(t) - n_{\mathrm{th}}\}E_j(t) - i\frac{\kappa_a}{\tau_{\mathrm{in}}}\{E_{j+1}(t) + E_{j-1}(t)\} \tag{8.52}$$

$$\frac{\mathrm{d}n_j(t)}{\mathrm{d}t} = \frac{J}{ed} - \frac{n_j(t)}{\tau_s} - G_n\{n_j(t) - n_0\}|E_j(t)|^2 \tag{8.53}$$

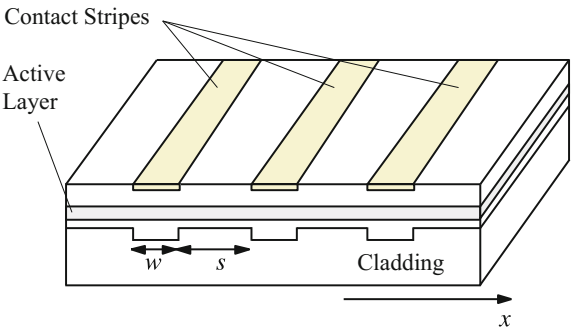

Fig. 8.40 Model of a multi-stripe semiconductor laser array. Only three stripes are displayed

where κ_a is the coupling ratio between the neighborhood laser elements. The spontaneous emission term is neglected in the above equations. For the numerical calculation of the rate equations, the number of laser arrays is $N + 1$ and the boundary condition is $E_0 = E_N = 0$. The rate equation for the field amplitude has the same form as the well-known equation of the coupled map lattice (CML). The CML shows typical spatio-temporal instabilities and chaos. Therefore, semiconductor laser arrays are essentially chaotic systems. Winful (1992) investigated chaotic dynamics and synchronization of laser arrays based on this model.

As a different approach for the analysis of semiconductor laser arrays, the model of periodic carrier confinement and injection is proposed by extending the theory of broad-area semiconductor lasers (Merbach et al. 1995; Martín-Regalado et al. 1996a, b). In multi-stripe laser arrays, the rate equations remain the same as (8.42) and (8.43). However, the laser is assumed to have a discrete multi-stripe structure along the x-direction as shown in Fig. 8.40. The confinement of the gain arises periodically in the active region. Then, we introduce a periodic confinement factor $\Gamma(x)$ in the wave-guide. Also, the bias injection current $J(x)$ is assumed as a periodic function with the same period. Using these assumptions, the dynamics of the multi-stripe laser are numerically investigated. For the laser arrays, filamentations are also observed. Figure 8.41 shows an example of numerically calculated filamentations (Merbach et al. 1995). The laser has a ten-stripe. We can see filamentations among laser arrays and the dynamics strongly depends on the bias injection current. In Chap. 10, we also return to the control of unstable operation of laser arrays subjected to optical feedback from the viewpoint of laser control.

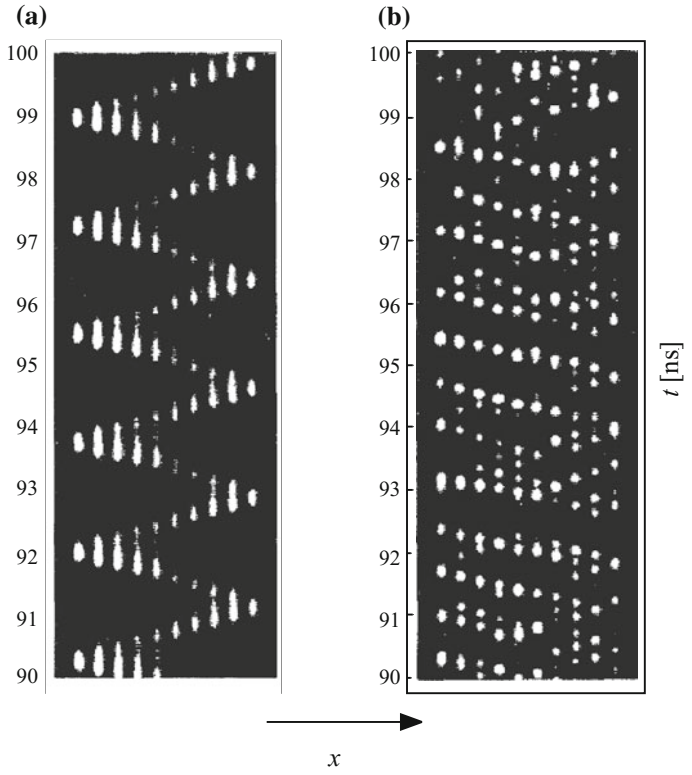

Fig. 8.41 Numerical plots of the spatio-temporal output power of a ten-stripe laser array for two different injection currents. **a** $I = 34$ mA: periodic state and **b** $I = 44$ mA: chaotic state. The threshold current for each stripe is $I_{th} = 36$ mA. The stripe width is $w = 5.0$ μm and the stripe separation is $s = 5.8$ μm [after Merbach et al. (1995); © 1995 APS]

8.6 Quantum-Dot Semiconductor Lasers

8.6.1 Theory of Quantum-Dot Semiconductor Lasers

Quantum-dot semiconductor laser is an important light source for high-speed data communication applications, since it is insensitive to temperature variations and optical feedback, and provides features of high modulation bandwidth and low chirp. The device structure of a quantum-dot laser is almost the same as common narrow-stripe edge-emitting semiconductor lasers. However, in the active layer, small quantum dots as small as nano-meter size are fabricated, usually by a self-assembled method of the crystal. A common quantum-dot semiconductor laser is not a single layer device, but several thin quantum-well layers with quantum dots are piled up in the active region. An electron and a hole are captured in a single dot and behave like zero-dimensionally confined particles with a fixed energy state.

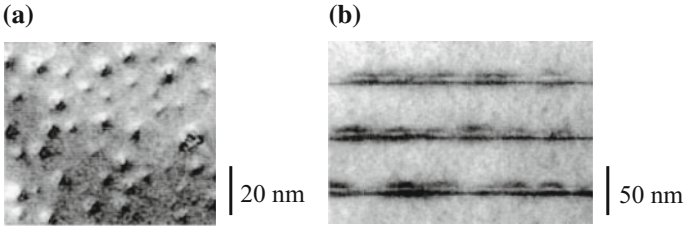

Fig. 8.42 Example of a self-assembled quantum-dot structure. **a** Plane view and **b** cross-section view [after Shoji et al. (1997); © 1997 IEEE]

Thus, the light emitted from a quantum-dot semiconductor laser shows a high coherence state. The crystal growth, the device characteristics, and their theoretical treatments have been given in a book of Sugawara (1999). Figure 8.42 is an example of a self-formed quantum-dot structure of InAs in an active region of GaAs (Shoji et al. 1997). Figure 8.42a show a plane view of quantum dots. It is desirable that quantum dots stand in a line on the wetting quantum-well layer and the size of each quantum dot should be the same. However, the control of the crystal growth is very difficult. In spite of irregularities of the size and the position, the laser can emit a high quality beam. The grown quantum dots in Fig. 8.42b are 20 nm in diameter and 5 nm in height. The areal coverage is about 10%.

The behaviors of quantum-dot semiconductor lasers are interesting from the viewpoint of nonlinear dynamics. We must consider electron and hole scattering rates to and from dots in the active layer. Therefore, we must introduce the extra differential equations to describe the dynamics. In usual, an addition of extra degree of freedom induces less stable operations for the system. Nevertheless, quantum-dot

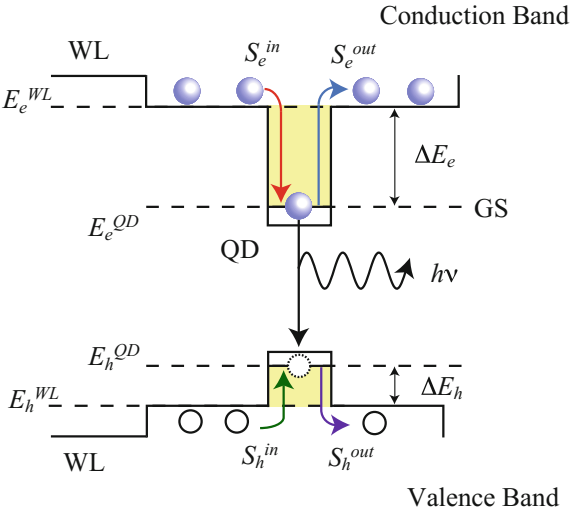

Fig. 8.43 Energy band structure of quantum-dot semiconductor lasers. *WL* quantum-well wetting layer, *QD* quantum dot, *GS* ground state level of a quantum dot, *E* energy level for corresponding state, *ΔE* energy difference, S^{in} capture rate, S^{out} escape rate

semiconductor laser is a stable light source even compared with common narrow-stripe edge-emitting semiconductor lasers. Physically, this stability is explained by the limitation of the light-emitting region to a confined dot structure. To describe the dynamics, we need to introduce a microscopic model of the quantum-dot structure (Erneux et al. 2007; Lüdge et al. 2008, 2010; Lüdge and Schöll 2009; Grillot et al. 2009; Lüdge 2011; Otto 2014). Figure 8.43 is the model of the energy band-structure of a quantum-dot semiconductor laser. Beside the two-level energy states (conduction and valence bands) in common semiconductor lasers, the energy band for a quantum dot is introduced. In this model, we here only consider the ground state (GS) of the energy level for a quantum dot. As far as the bias injection current is not large, the model can well describe the dynamics. For higher bias injection current, the exited states of the energy level should be taken into account (Grillot et al. 2009). In the microscopic model, the dynamics of electron and hole should be treated separately, since the effective masses for electron and hole are different and the carrier scattering rates from the wetting layer to a dot S^{in} and from a dot to the wetting layer S^{out} are also different. In the figure, the subscripts of e and h stand for electron and hole. In the microscopic model, the carrier scatterings into and from quantum dots (Auger process and carrier-phonon interaction) play important roles in the dynamics.

Using the band model in Fig. 8.43, the rate equation for the optical field is given by (Lüdge and Schöll 2009)

$$\frac{\mathrm{d}E(t)}{\mathrm{d}t} = \frac{1}{2}(1 - i\alpha)\left[\Gamma WA\left\{n_e(t) + n_h(t) - N^{\text{QD}}\right\} - \frac{1}{\tau_{\text{ph}}}\right]E(t) \tag{8.54}$$

where Γ is the optical confinement factor, W is the Einstein coefficient, and A is the area of the active region. N^{QD} denotes twice the density of the active quantum dots, taking into account spin degeneracy. n_e and n_h are the two-dimensional electron and hole densities in the dots, i.e., the densities are defined as a unit of a single layer. The rate equations for the densities of electrons w_e and holes w_h in the quantum-well wetting layer (WL) is given as

$$\frac{\mathrm{d}w_e(t)}{\mathrm{d}t} = \frac{J}{e} - S_e^{\text{in}}\frac{N^{\text{sum}}}{N^{\text{QD}}}\left\{N^{\text{QD}} - n_e(t)\right\} + S_e^{\text{out}}\frac{N^{\text{sum}}}{N^{\text{QD}}}n_e(t) \tag{8.55}$$

$$\frac{\mathrm{d}w_h(t)}{\mathrm{d}t} = \frac{J}{e} - S_h^{\text{in}}\frac{N^{\text{sum}}}{N^{\text{QD}}}\left\{N^{\text{QD}} - n_h(t)\right\} + S_h^{\text{out}}\frac{N^{\text{sum}}}{N^{\text{QD}}}n_h(t) \tag{8.56}$$

where J is the injection current density. N^{sum} is twice the total quantum-dot density as given by experimental surface imaging, which accounts for reduced gain because due to the size distribution of the quantum dots, namely the active quantum dots N^{QD}, match the mode energy for lasing. A crucial contribution to the dynamics of quantum-dot semiconductor lasers is given by non-radiative carrier–carrier scattering rates. S_e^{in} and S_h^{in} are the electron and hole capture rates into the quantum-dot levels in this process, while S_e^{out} and S_h^{out} are the electron and hole escape rates from

the quantum-dot levels. The scattering times for electrons and holes are given by $\tau_e = 1/\left(S_e^{\text{in}} + S_e^{\text{out}}\right)$ and $\tau_h = 1/\left(S_h^{\text{out}} + S_h^{\text{out}}\right)$, respectively. As specific equations for quantum-dot semiconductor lasers, we need the following carrier density equations of quantum dots:

$$\frac{\mathrm{d}n_e(t)}{\mathrm{d}t} = S_e^{\text{in}}\left\{N^{\text{QD}} - n_e(t)\right\} - S_e^{\text{out}} n_e(t) - WA\left\{n_e(t) + n_h(t) - N^{\text{QD}}\right\}|E(t)|^2 \tag{8.57}$$

$$\frac{\mathrm{d}n_h(t)}{\mathrm{d}t} = S_h^{\text{in}}\left\{N^{\text{QD}} - n_h(t)\right\} - S_h^{\text{out}} n_h(t) - WA\left\{n_e(t) + n_h(t) - N^{\text{QD}}\right\}|E(t)|^2 \tag{8.58}$$

As an example, the values of device parameters for quantum-dot semiconductor lasers are listed in Table 8.5.

Strictly speaking, we must use the above five-variable model to explain the dynamics of quantum-dot semiconductor lasers, however, for the easiness of analytical calculations, such as an analysis for steady-state characteristics, a reduced model is sometimes used (O'Brien et al. 2004; Erneux et al. 2007). In this model, the carrier densities of electrons and holes in the wetting layer are assumed to be the same and the carrier densities in quantum dots also obey the same dynamics. Therefore, the carrier density equations in the wetting layer reduce to a single carrier density equation. Also the carrier density equations in a quantum dot are replaced as a probability density equation of a single carrier occupation. Then, this model contains three variables of the field E, the occupation probability density ρ of

Table 8.5 Characteristic device parameters for a quantum-dot semiconductor laser with five-variable model at an oscillation wavelength of 1.30 μm

Symbol	Parameter	Value
W	Einstein coefficient	0.7 ns^{-1}
Γ	Confinement factor	2.25×10^{-3}
A	WL normalization area	4×10^{-9} m^2
N^{QD}	Twice total QD density of lasing group	0.6×10^{14} m^{-2}
N^{sum}	Twice total QD density	20×10^{14} m^{-2}
α	Linewidth enhancement factor	0.9
τ_{ph}	Lifetime of photon	10 ps
τ_{in}	Round trip time in laser cavity	24 ps
ΔE_e	Ground state energy difference for electron	190 meV
ΔE_h	Ground state energy difference for hole	69 meV
m_e	Effective mass of electron	$0.043m_0$
m_h	Effective mass of hole	$0.45m_0$
m_0	Mass of electron	9.11×10^{-31} kg
r_0	Facet reflectivity	0.565

electron and hole pair in a quantum dot, and the carrier density n in the wetting layer as follows:

$$\frac{dE(t)}{dt} = \frac{1}{2}(1 - i\alpha)\left[g_0\vartheta\{2\rho(t) - 1\} - \frac{1}{\tau_{ph}}\right]E(t) \tag{8.59}$$

$$\frac{d\rho(t)}{dt} = -\frac{\rho(t)}{\tau_d} - g_0\{2\rho(t) - 1\}|E(t)|^2 + \left[\{1 - \rho(t)\}R_{cap} - \rho(t)R_{esc}\right] \tag{8.60}$$

$$\frac{dn(t)}{dt} = \frac{J}{e} - \frac{n(t)}{\tau_s} - 2N_d\left[\{1 - \rho(t)\}R_{cap} - \rho(t)R_{esc}\right] \tag{8.61}$$

where g_0 is the gain coefficient, ϑ is the conversion coefficient from the total gain to the two-dimensional surface given by $\vartheta = 2N_d\Gamma/d_d$, N_d is the total carrier density, and d_d is the thickness of quantum dots. R_{cap} and R_{esc} are the carrier capture and escape rates in and from a dot, respectively. The carrier capture rate is given by $R_{cap} = Cn^2 + Bn$, where C is the carrier–carrier scattering coefficient (Auger capture coefficient) and B is the carrier–phonon scattering coefficient. These rates correspond to the carrier–carrier scattering rates defined in (8.54)–(8.58), however the rates for electrons and holes are assumed to be the same in (8.60). In the five-variable model, these parameters are the functions of the carrier densities in the wetting layer. In spite of a rough picture of the model, the fundamental dynamics and the trends of the laser oscillations can be explained to some extent. The model is particularly useful for the primary study of the steady-state behaviors in quantum-dot semiconductor lasers. The values of the parameters used in this model are listed in Table 8.6.

Table 8.6 Characteristic device parameters for a quantum-dot semiconductor laser with three-variable model at an oscillation wavelength of 1.30 μm

Symbol	Parameter	Value
g_0	Gain coefficient	1.8×10^{-11} m^3 s^{-1}
ϑ	Conversion coefficient	2.4×10^{22} m^{-3}
N_d	Total carrier density	2×10^{15} m^{-2}
d_d	Thickness of dot	10 nm
α	Linewidth enhancement factor	1.2
r_0	Facet reflectivity	0.565
τ_{ph}	Photon lifetime	3 ps
τ_d	Carrier lifetime in dot	1 ns
τ_s	Carrier lifetime in well	1 ns
τ_{in}	Round trip time in laser cavity	8 ps
Γ	Confinement factor	0.06
R_{cap}	Carrier capture rate	10^{11} s^{-1}
R_{esc}	Carrier escape rate	1.25×10^{10} s^{-1}

8.6.2 *Quantum-Dot Semiconductor Lasers in Solitary Oscillations*

We here discuss some characteristics of quantum-dot semiconductor lasers at solitary oscillation based on the five-variable model. The scattering rates are not constant but they depend on the carrier densities in the quantum-well wetting layer. They are calculated from microscopic Auger in- and out-scatterings. The calculation is not straightforward and they are not given by analytical forms. Therefore, we here only show examples of numerical results for the scattering rates. Figure 8.44 shows the scattering rates of electrons and holes for the carrier densities in the wetting layer at the ground state energy difference for electron of ΔE_e = 190 meV and the ground state energy difference for hole ΔE_h = 69 meV. We can see the strong dependence of the scattering rates on the carrier densities in the wetting layer. Figure 8.45a shows the steady-state occupation probabilities of carriers in a dot as a function of the bias injection current under the same condition of Fig. 8.44. For a low bias injection current in Fig. 8.45a, the difference of occupations of electron and hole is large, but it becomes small for the increase of the bias injection current and stays constant values. On the other hand, the difference of the carrier densities in the wetting layer is rather small for the all range of the bias injection current as shown in Fig. 8.45b. Thus, the difference of the occupation probabilities between electrons and holes in quantum dots plays a crucial role in the dynamics of quantum-dot semiconductor lasers.

The damping rate for a step response of the laser output for the bias injection current in quantum-dot semiconductor lasers is very high compared with that of quantum-well lasers. The fact is confirmed experimentally and theoretically. Figure 8.46 shows a comparison of experimental and simulation results for some fundamental characteristics in a quantum-dot semiconductor laser (Lüdge and

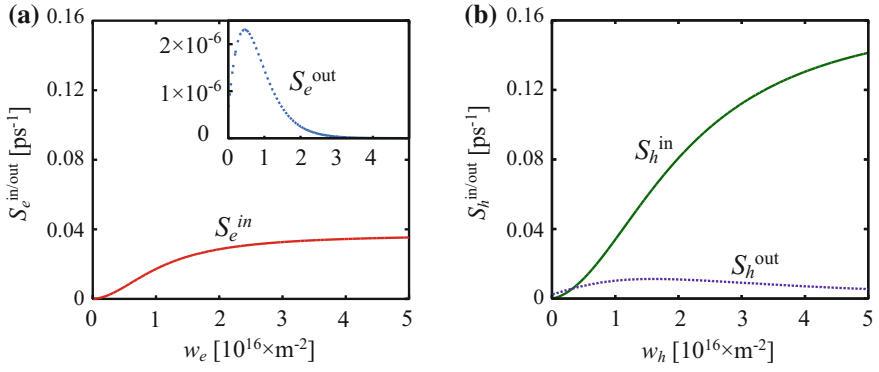

Fig. 8.44 Carrier–carrier scattering rates of **a** electrons (S_e^{in} and S_e^{out}) and **b** holes (S_h^{in} and S_h^{out}) for the carrier densities in the wetting layer at ΔE_e = 190 meV and ΔE_h = 69 meV. *Solid lines* capture rates. *Dotted lines* escape rates

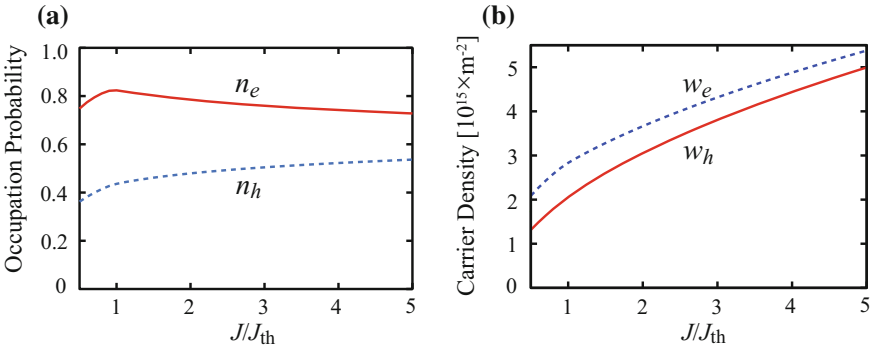

Fig. 8.45 **a** Steady-state occupation probabilities of carriers in a dot for the bias injection current. **b** Steady-state carrier densities in the quantum-well wetting layer for the bias injection current. *Solid lines* electrons. *Dotted lines* holes

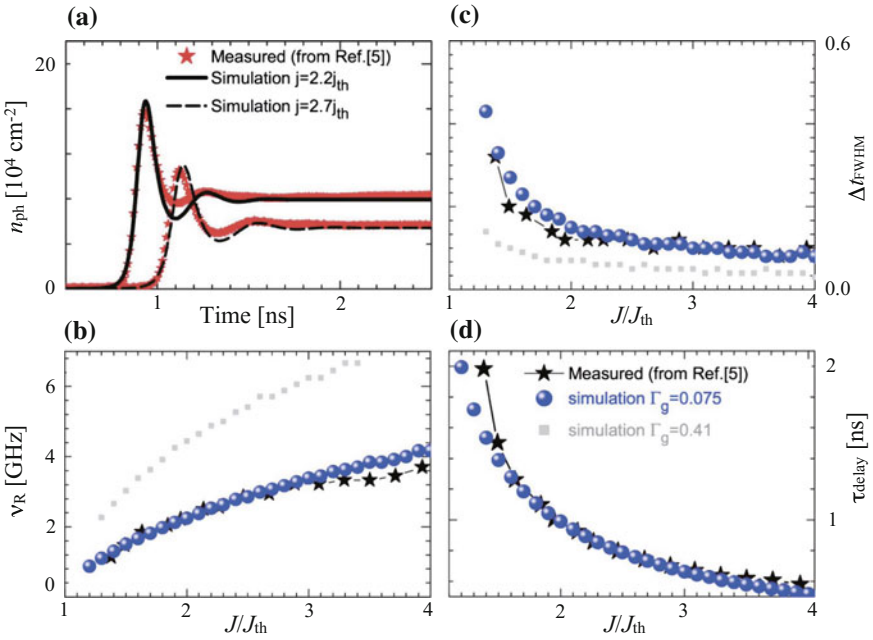

Fig. 8.46 Characteristics of a quantum-dot semiconductor laser. **a** Step response of bias injection currents at $2.2J_{th}$ and $2.7J_{th}$. *Stars* are the experimental results. **b** Frequency of the relaxation oscillation for the bias injection current. *Stars* are the experimental results and *dots* are the simulated results. **c** Width of the first relaxation oscillation peak. **d** Turn-on delay time. Γ_g is the geometric confinement factor, which is related to the confinement factor as $\Gamma = \Gamma_g N^{QD}/N^{sum}$ [after Lüdge and Schöll (2009); © 2009 IEEE]

Schöll 2009). Figure 8.46a is a turn-on transient at the bias injection currents of $2.2J_{th}$ and $2.7J_{th}$. The symbol of stars corresponds to the experimental and the simulation results are obtained from the five-variable model in (8.54)–(8.58). We can see fast decays of the relaxation oscillations. Figure 8.46b–d are the frequency of the relaxation oscillation ν_R, the width of the first relaxation oscillation peak Δt_{FWHM}, and the turn-on delay τ_{delay} for the variation of the bias injection current. The microscopic five-variable model well reproduces the experimental results. Except for the fast damping rate in Fig. 8.46a, the other characteristics are compatible with those for quantum-well semiconductor lasers.

8.6.3 *Optical Feedback Effects in Quantum-Dot Semiconductor Lasers*

Since quantum-dot semiconductor laser has a fast damping rate as discussed in the previous subsection, it is robust for external perturbations such as optical feedback and optical injection. The optical feedback effects in quantum-dot semiconductor lasers have been studied theoretically and experimentally (O'Brien et al. 2004; Huyet et al. 2004; Viktorov et al. 2006; Otto et al. 2010). For example, the field equation with optical feedback in the microscopic model is written as

$$\begin{aligned}\frac{dE(t)}{dt} &= \frac{1}{2}(1-i\alpha)\left[\Gamma WA\left\{n_e(t)+n_h(t)-N^{QD}\right\}-\frac{1}{\tau_{ph}}\right]E(t) \\ &\quad+\frac{\kappa}{\tau_{in}}E(t-\tau)\exp(i\omega_0\tau)\end{aligned} \tag{8.62}$$

and the other four equations of the carrier densities in quantum-well and quantum-dot layers remain the same as (8.54)–(8.58). Similar to the dynamics of quantum-well semiconductor lasers, LFFs and fast chaotic oscillations are observed depending on the length of an external reflector, the external reflectivity, and the bias injection current. However, we need a larger external feedback power to destabilize the laser compared with quantum-well semiconductor lasers.

Figure 8.47 shows examples of chaotic bifurcation diagrams induced by optical feedback for quantum-well and quantum-dot semiconductor lasers. Since the device structure and the parameters are different for the two lasers, it is difficult to perform completely direct comparisons of the dynamics. However, the device parameters are carefully chosen to compare the characteristics. The bifurcation diagram for the quantum-dot semiconductor laser is calculated from the microscopic five-variable model. As similar to optical feedback effects in quantum-well semiconductor lasers as those observed in Figs. 5.7 and 5.13, the output power from a quantum-dot semiconductor laser with optical feedback shows chaotic evolutions for the variations of chaotic parameters (optical feedback strength, optical feedback time, injection current, and so on). Although quantum-dot semiconductor lasers, for

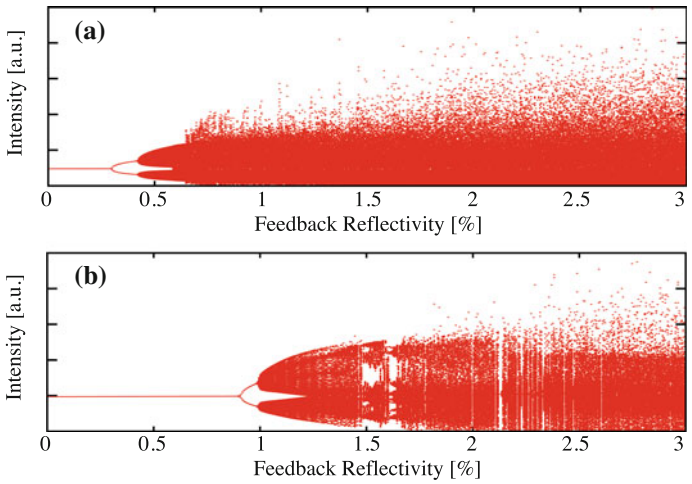

Fig. 8.47 Chaotic bifurcation diagrams induced by optical feedback. Bifurcation diagrams for **a** quantum-well and **b** quantum-dot semiconductor lasers. The length of the external reflector is $L = 45$ cm and the bias injection current is set to $J = 1.5J_{\text{th}}$

example, show stable oscillations for the increase of the optical feedback strength, the outline of route to chaos in both cases is almost the same. The robustness for optical feedback in quantum-dot semiconductor lasers is related to the structure of the optical cavity and a small value of the α parameter. Also, the stability and instability of quantum-dot semiconductor lasers with optical feedback are strongly dependent on the dot density. The fabrication of high-density GaAs quantum dots up to 7.3×10^{15} m^{-2} is proposed by droplet epitaxy (Jo et al. 2012). Within the range of quantum-dot density from 1×10^{15} m^{-2} to 10×10^{15} m^{-2}, which is currently available dot density, it is demonstrated by numerical simulations that the stability against optical feedback and other perturbations is greatly enhanced for the increase of the dot density. From the figures, we can also conclude that the quantum-dot semiconductor laser is less sensitive to optical feedback and we need much higher feedback power to destabilize the laser.

8.6.4 Optical Injection Effects in Quantum-Dot Semiconductor Lasers

Quantum-dot semiconductor laser has a high damping rate and a small α parameter. This high damping and small α parameter have been cited as the principal reason for the increased stability of such devices when subject to optical feedback, optical injection, and mutual coupling configurations. Therefore, it behaves like a class A laser rather than a class B laser for an optical injection (Goulding et al. 2007;

Erneux et al. 2010). A typical feature of optical injection to a class B laser with nonzero α parameter is an asymmetric shape of the stable injection-locking region in the phase-space map of the optical injection and the frequency detuning as shown in Fig. 6.4. While, a class A laser such as He–Ne laser with visible oscillation shows a symmetric shape of the stable injection-locking region. Quantum-dot semiconductor laser with optical injection shows similar dynamics to a class A laser as for optical injection, however, various dynamics can be found at the boundaries of the stable optical injection-locking region. One of typical characteristics of quantum-dot semiconductor lasers is a pulsation oscillation like the axon of the giant Atlantic squid when perturbed above certain threshold level. The pulses are evidence of a large excursion in the phase space of the system. Indeed, for optical injection, quantum-dot semiconductor laser shows single pulses and double excitable pulses at one boundary of the stable injection-locking region at high injection strength with finite frequency detuning. Theoretical considerations show that these pulses are related to a saddle-node bifurcation on a limit cycle as in the Adler equation.

Figure 8.48 shows the boundaries of the stable optical injection-locking region in quantum-dot semiconductor laser (Erneux et al. 2010). Figure 8.48a is an experimental result of the phase diagram for a DFB quantum dot semiconductor laser of an oscillation wavelength of 1.30 μm. The bias injection current is set to $1.5J_{th}$. The solid lines in Fig. 8.48 are the boundary of saddle-node (SN) bifurcations, and the dashed lines are that of Hopf (H) bifurcations. The

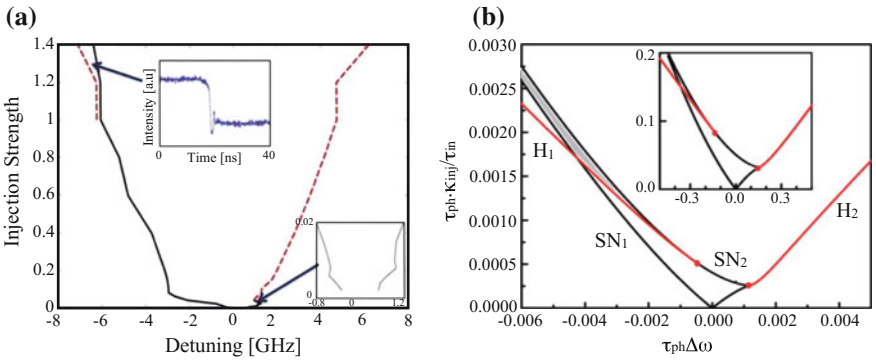

Fig. 8.48 **a** Experimental stability diagram in the phase space of the frequency detuning and the injection strength (intensity). The *lines* are the stability boundary for optical injection. *Solid line* saddle-node bifurcation boundary, and *dashed line* Hopf bifurcation boundary. *Upper inset* switching between two locked states with different intensities, and *lower inset* zoom of the region of low injection strength where the locking is via a saddle-node bifurcation for both signs of the detuning. **b** Analytic stability diagram calculated from three-variable model at $J = 1.2J_{th}$, $\alpha = 1.2$, and $\tau_{ph} = 2$ ps. *SN* saddle-node bifurcation point, *H* Hopf bifurcation point. The *shaded region* denotes the domain of steady-state bistability. The *dots* are fold-Hopf points where Hopf and SN bifurcation lines merge. The *inset* shows the stability diagram for an injected class A laser [after Erneux et al. (2010); © 2010 OSA]

inside of the lines are the stable injection-locking region. Various dynamics are observed, but the one of different features of injection locking from those of conventional quantum-well semiconductor lasers is rather a symmetrical shape of the injection-locking region and the domain of bistable operation, in which coexistence of two stable locking states exists. The Hopf bifurcation line differs from that which occurs for an injected quantum-well semiconductor lasers and, in particular, it does not cross the zero detuning line as shown in the inset in Fig. 8.48a. The phase diagram is not similar to that of ordinary class B laser, but similar to that of class A laser. More precisely, quantum-dot semiconductor lasers exhibit both Class A and Class B dynamics, depending on the carrier capture parameters by analyzing a following three-variable rate-equation model.

To investigate optical-injection dynamics, the following field equation of the three-variable model is employed:

$$\frac{\mathrm{d}E(t)}{\mathrm{d}t} = \frac{1}{2}(1 - i\alpha)\left[g_0\vartheta\{2\rho(t) - 1\} - \frac{1}{\tau_{\mathrm{ph}}}\right]E(t) + \frac{\kappa_{\mathrm{inj}}}{\tau_{\mathrm{in}}}E_m(t)\exp(-i\Delta\omega t) \quad (8.63)$$

The other two equations are the same as (8.60) and (8.61). Figure 8.48b shows the phase diagram theoretically calculated from the three-variable model. The dots are fold-Hopf points where Hopf and SN bifurcation lines merge. The shaded region denotes the domain of steady-state bistability, which is compatible with the experiment. At higher injection levels and for positive detuning, the locking is via a Hopf bifurcation (H2), and there is no SN bifurcation. For negative detunings, there is a domain of bistability between two locked states, because of a Hopf bifurcation that stabilizes the lower intensity branch (H1). The dynamics is fairly similar to those of an injected class A laser, which is shown in the inset in Fig. 8.48b. The general trends of optical-injection dynamics in Fig. 8.48b are well coincident with those of the experiment in Fig. 8.48a. Figure 8.49 shows an example of bifurcation diagrams for the variations of frequency detuning in optically injected quantum-dot semiconductor lasers, in which the three-variable model (8.58)–(8.60) is used. Figure 8.49a, b show bifurcation diagrams for intensity and mean frequency, respectively. The mean frequency is the same definition as that in Sect. 6.1.2, namely, it is defined by the time average of the momentary frequency, $\langle d\phi(t)/dt\rangle$. Different from the case of quantum-well semiconductor lasers in Fig. 6.5, period-1 oscillations are clearly observed not only in the positive frequency detuning region but also in negative one. Except for period-1 oscillations in the region of negative frequency detuning, overall trends for bifurcations in quantum-dot semiconductor lasers resemble with those in quantum-well semiconductor lasers.

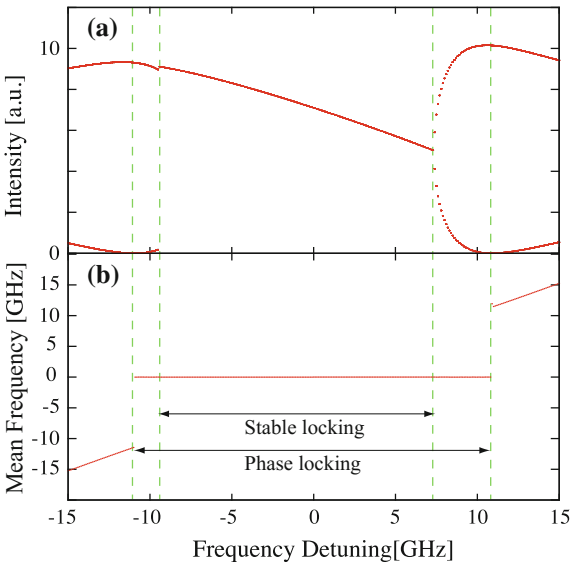

Fig. 8.49 Bifurcation diagram of optically injected quantum-dot semiconductor lasers. **a** Bifurcation diagram of the intensity. **b** Bifurcation diagram of the mean phase. The optical injection ratio is 50% (r_{inj} = 0.5)

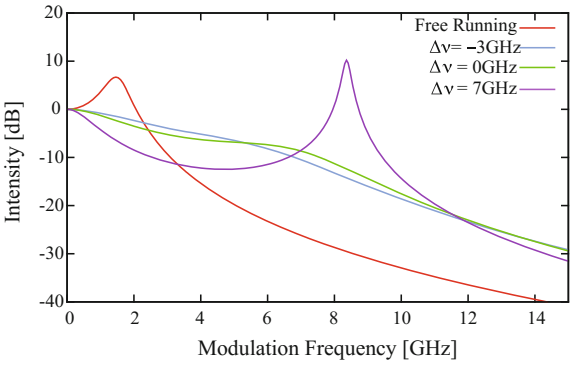

Fig. 8.50 Numerical calculation of modulation responses in the presence of optical injection in a quantum-dot semiconductor laser at $J = 1.5J_{th}$. The optical injection ratio is 50%. $\Delta\nu$ denotes frequency detuning

8.6.5 *Bandwidth Enhancement in Optically Injected Quantum-Dot Semiconductor Lasers*

The modulation bandwidth of semiconductor lasers is greatly enhanced by optical injection as discussed in Sect. 6.3. Similar to other types of semiconductor lasers, the modulation bandwidth of quantum-dot semiconductor lasers can be enhanced by optical injection. Figure 8.50 shows an example of modulation responses for various frequency detunings between the injection laser and the slave quantum-dot semiconductor laser. The three-variable model is used for the numerical

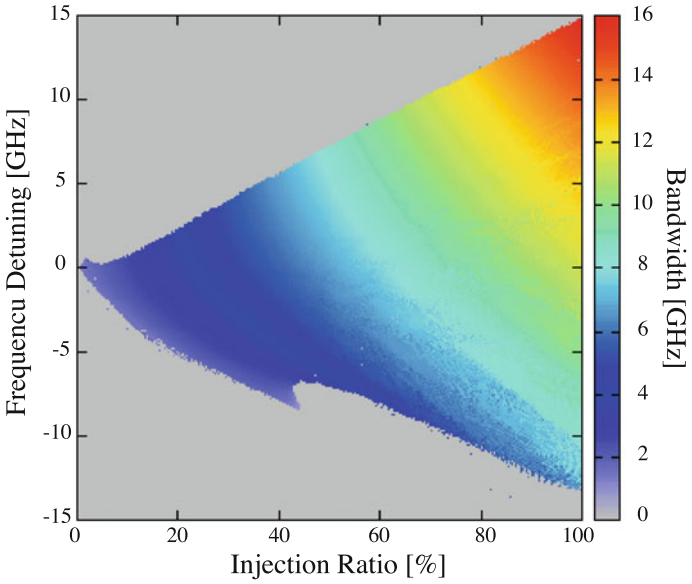

Fig. 8.51 Numerical calculation of bandwidth enhancement induced by optical injection in a quantum-dot semiconductor laser at $J = 1.5J_{th}$

calculations. The trends of the modulation response are quite similar to those in Figs. 6.16 and 6.17, and the resonance peak is greatly shifted toward higher frequency at positive frequency detuning compared with the modulation response of no optical injection. On the other hand, resonance peak is not distinct for negative detuning, however, the modulation efficiency is greatly enhanced to higher frequency. Figure 8.51 shows the summary of bandwidth enhancement within the stable locking region in a quantum-dot semiconductor laser. Similar trends of the enhancement of modulation bandwidth as that of a DFB laser in Fig. 6.17 are obtained. The original bandwidth is 1.46 GHz without optical injection, while the bandwidth is enhanced up to 15.9 GHz in this modulation map. The magnification of the modulation bandwidth (the ratio of the bandwidth with and without optical injection) in quantum-dot semiconductor lasers is generally greater than those in quantum-well semiconductor lasers and VCSELs. As discussed in this section, quantum-dot semiconductor lasers behave like somewhat those of stable class A lasers from a viewpoint of dynamics. However, overall dynamics are almost similar to those of common quantum-well semiconductor lasers.

8.7 Quantum-Cascade Semiconductor Lasers

8.7.1 Principle of Quantum-Cascade Semiconductor Lasers

Different from conventional quantum-well semiconductor laser, which uses optical transitions between conduction and valence bands (inter-band), semiconductor laser that is based on inter-subband optical transitions within conduction band has been developed (Faist et al. 1994; Gmachl et al. 2001; Wójcik et al. 2011a, b; Scalari et al. 2009; Jirauschek and Kubis 2014; Razeghi et al. 2015; Vitiello et al. 2015). The laser has several stages of cascades consisting of super-lattice structures and is called quantum-cascade semiconductor laser (QCL). The light emission of this laser is based on inter-subband optical transitions, therefore the carrier related to laser radiation is only electron. Quantum-cascade lasers emit THz light from mid-infrared (wavelength of several μm) to far-infrared (several hundreds μm) oscillations either at pulse or CW operations. However, it is difficult to obtain a laser from an oscillation wavelength between 30 and 60 μm, since the energy in this region corresponds to that of longitudinal optical phonon (LO phonon). In a long optical wavelength, cooling for the device is essential, however, a laser (GaInAs/AlInAs/InP quantum-cascade laser) operating at room temperature is reported. Quantum-cascade semiconductor laser can emit high power as much as 1 W and has a narrow oscillation linewidth as small as 150 kHz, while conventional quantum-well semiconductor laser has a linewidth around 10 MHz. Quantum-cascade lasers are of great interest, since they can be used for detection of toxic chemicals and gases by mid-infrared spectroscopy. Also self-mixing interferometry in quantum-cascade lasers provides useful and indispensable tool for mechanical measurements in THz regions, since fast and efficient photodetectors are not available in this wavelength. Their narrow linewidths make them attractive in coherent applications, such as free-space short-range communications due to the Wi-Fi capabilities of terahertz waves and large supposed bandwidth modulation. Also their large direct intensity modulation bandwidth is attractive for optical communication systems. Some of different characteristics of quantum-cascade semiconductor lasers from conventional quantum-well semiconductor lasers are listed in Table 8.7. The main difference concerning the laser dynamics is a short relaxation time of carriers due to the use of inter-subband optical transitions. Another difference is the polarization mode of the laser oscillations. Due to the selection rules for inter-subband optical transitions, only transverse-magnetic (TM) mode oscillations is allowed, since electrons are interact with polarized light perpendicular to the plane of the quantum wells (Dhirhe et al. 2012; Janassek et al. 2016).

Figure 8.52 shows a schematic model of the band structure in a quantum-cascade semiconductor laser. The laser consists of a multi-stage quantum cascade. In the figure, a single period is drawn. A single photon is emitted by the transition in the subbands when an electron passes through each quantum cascade. Each stage consists of the active region and the injection region. The electron that is

Table 8.7 Difference of the characteristics between conventional quantum-well semiconductor lasers (QWLs) and quantum-cascade semiconductor lasers (QCLs)

	QWLs	QCLs
Optical transitions	Inter-band	Inter-subband
Carriers	Electrons and holes	Electrons
α Parameter	Large	Small
Oscillation linewidth	Broad ($\sim$10 MHz)	Narrow ($\sim$100 kHz)
Polarization mode	TE	TM
Output power	Proportional to injection current	Proportional to injection current and number of cascades
Stripe width[a]	Few μm	Larger than 10 μm
Thickness of active region[a]	Less than 1 μm	Larger than 10 μm
Relaxation time of carrier	$\sim$1 ns	$\sim$1 ps

[a]Note that the size of QCL is strongly dependent on the emission wavelength

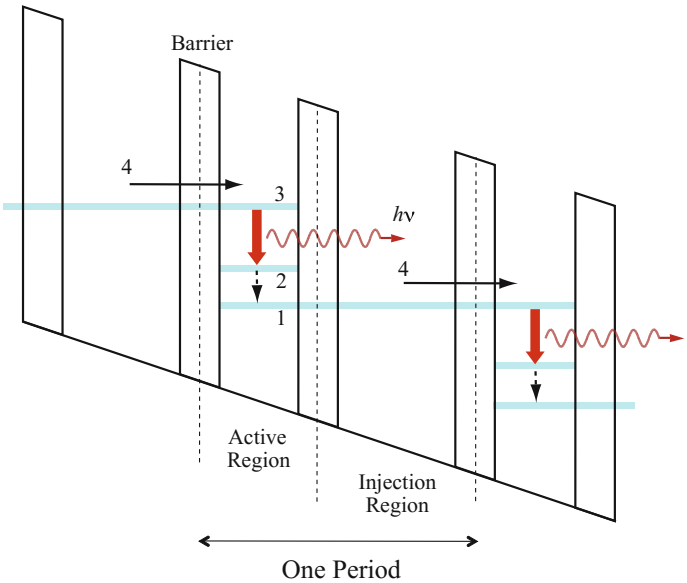

Fig. 8.52 Schematic model of quantum-cascade lasers using inter-subband four-level active medium. Each stage consists of active and injection regions. *4* Injector, *3* upper level of laser emission, *2* lower level of laser emission, and *1* ground state

once emitted photon is reused in the next stage, therefore, the external quantum efficiency is very high and the laser power is proportional to the number of the stages. In actual, each region consists of several layers of quantum-well structures.

For optical transitions, the laser is described by a two-level model, however four energy levels are related to the light emission as shown in the figure. A carrier is injected from the injection region and goes through a tunnel barrier 4. The injected carrier at the level 3 emits a photon and transitions to the level 2. The carrier is pulled out form the level 2 to the ground state 1 by the fast sub-picosecond time relaxation process. This carrier is again injected to the next stage. Several stages, usually several to more that ten stages, are piled up along the direction perpendicular to the substrate and, thus, forming quantum cascades. The emission wavelength is easily controlled by designing the thicknesses of the active and injection regions and also the inside quantum-well layers, even for the same material, which is quite different from conventional quantum-well semiconductor lasers. Indeed, the design of the subband ranging from several tens to 100 meV is possible for the same materials and we can obtain a quantum-cascade semiconductor laser with a desired optical wavelength.

8.7.2 *Linewidth Enhancement Factor of Quantum-Cascade Semiconductor Lasers*

In conventional diode lasers, the linewidth enhancement factor (α factor) is typically 3–7, and arises because the conduction and valence bands involved in the laser transition have opposite curvature in *k*-space, resulting in a spectrally asymmetric differential gain. In contrast, both laser subbands of a quantum-cascade semiconductor laser are within the conduction band, and exhibit the same reciprocal space curvature. It has thus been predicted that the lasers should display a symmetric differential gain and a zero α factor. However, it is not true for real quantum-cascade semiconductor lasers for several reasons and the lasers usually have small but nonzero value of the linewidth enhancement factor. Therefore, the lasers behave like not class B lasers as dynamic characteristics but rather class A lasers. There are several methods to measure a linewidth enhancement factor in a semiconductor laser and the same techniques can be also applied to measure the parameter in a quantum-cascade semiconductor laser. Among them, the measurement using self-mixing effect in semiconductor laser is a promising one due to the lack of compact and sensitive detectors in the THz band (Staden et al. 2006; Green et al. 2008; Lim et al. 2011). The method of self-mixing in semiconductor lasers is well studied in quantum-well semiconductor lasers and applications of self-mixing interferometry including the measurement of linewidth enhancement factor are discussed in Chap. 11.

Figure 8.53 shows an example of the measurements of linewidth enhancement factor using self-mixing effects in quantum-cascade semiconductor lasers (Staden et al. 2006). The laser is a DFB quantum-cascade laser of an internal cavity length

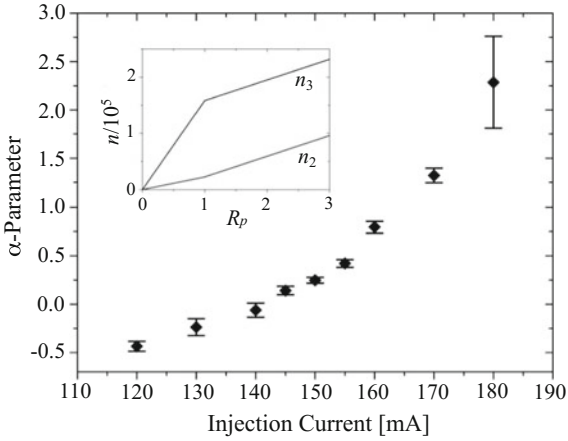

Fig. 8.53 α parameter as a function of the injection current. The *inset* shows the dependence of the carrier population of the upper and lower levels on the pump parameter $R_p = J/J_{th}$ [after Staden et al. (2006); © 2006 OSA]

of $L = 1$ mm, a width of the active region of $w = 10$ μm, and an oscillation wavelength of $\lambda = 5.45$ μm. The laser is cooled and its threshold current is 115 mA at 82 K. The linewidth enhancement factor has a value close to zero near the threshold, however, it varies largely depending on the bias injection current and has a large value at higher injection current. This is a remarkable difference with respect to near-infrared interband semiconductor lasers, for which α is expected to be approximately constant. One of possible reasons for this increase could be the detuning effect of the resonator mode with respect to the gain curve. It is known that for inter-band semiconductor lasers a relative red-shift of the resonator mode with respect to the gain peak results in an increase of the linewidth enhancement factor (α factor). For quantum-cascade semiconductor lasers, an increase of temperature as well as an increase of injection current results in a red-shift of the gain spectrum. Further, a steady-state analysis based on the rate equations discussed in the next subsection, the carrier densities of the upper and lower laser levels both increase above threshold with increasing injection current, even though the difference of both densities above threshold remains constant, accounting for gain clamping. This behavior follows from the rate equations for quantum-cascade semiconductor lasers and is depicted in the inset of the figure. It is in contrast to inter-band semiconductor lasers, where the carrier density is pinned above threshold. The monotonic increase of the carrier density certainly influences the material susceptibility, and thus it alters the linewidth enhancement factor. As another example, Green et al. (2008) measured the linewidth enhancement factor for a quantum-cascade semiconductor laser of an optical wavelength of $\lambda = 116$ μm. They obtained the linewidth enhancement factor from 0.2 to 0.5 depending on the bias current ranging form J to $2J_{th}$. The variation is small but it still depends on the bias injection current.

8.7.3 Rate Equations of Quantum Cascade Semiconductor Lasers

A quantum-cascade laser consists of a large number of layers constituting active and injector regions. An accurate design requires a large number of rate equations (Donovan et al. 2001). However, it is not convenient to treat them for the visualization of interplay between various parameters. Therefore, to obtain a reduced set of equations, we here consider a two-level lasing quantum well together with a lifetime describing carrier removal. As a result, the model of a quantum-cascade laser of N_p periods, are written by the following simple rate equations (Haldar 2005; Petitjean et al. 2011; Meng and Wang 2012):

$$\frac{\mathrm{d}S(t)}{\mathrm{d}t} = N_p G\{n_3(t) - n_2(t)\}S(t) - \frac{S(t)}{\tau_{\mathrm{ph}}} + \beta\frac{n_3(t)}{\tau_{\mathrm{sp}}} \tag{8.64}$$

$$\frac{\mathrm{d}n_3(t)}{\mathrm{d}t} = \frac{J}{ed} - \frac{n_3(t)}{\tau_3} - G\{n_3(t) - n_2(t)\}S(t) \tag{8.65}$$

$$\frac{\mathrm{d}n_2(t)}{\mathrm{d}t} = \frac{n_3(t)}{\tau_{32}} - \frac{n_2(t)}{\tau_2} + G\{n_3(t) - n_2(t)\}S(t) \tag{8.66}$$

S is the photon number, n_3 is the carrier density at energy level 3, and n_2 is the carrier density at energy level 2 in Fig. 8.52. Here, G is the gain coefficient, τ_{ph} is the photon lifetime, τ_{sp} is the spontaneous relaxation time, τ_3 is the electron lifetime at level 3, τ_{32} the phonon scattering time from level 3 to 2, τ_2 is the electron lifetime at level 2, β is the spontaneous emission factor. From the steady-state analysis for the rate equations, the threshold current for laser oscillations is given by

$$J_{\mathrm{th}} = \frac{ed}{N_p G\tau_{\mathrm{ph}}\tau_3(1 - \tau_2/\tau_{32})} \tag{8.67}$$

Thus, we require the condition of $\tau_{32} > \tau_2$ for laser oscillations. In a steady state, the carrier density of common semiconductor lasers is clamped to that of the threshold, n_{th}, after the lasing starts. However, different from common semiconductor lasers, above but close to the threshold, the carrier densities n_3 and n_2 increase for the increase of the bias injection current as $n_3 \approx (\tau_3/ed)J$ and $n_2 \approx (\tau_3\tau_2/\tau_{32}ed)J$. Namely, the carrier densities have linear relations to the bias injection current as depicted in the inset in Fig. 8.53. Table 8.8 lists some parameter values used for numerical calculations in the above equations (Petitjean et al. 2011).

One of the characteristics related to the dynamics in quantum-cascade semiconductor laser is a very short carrier lifetime, by which the laser shows significant differences in comparison with conventional semiconductor lasers based on

Table 8.8 Characteristic device parameters for a quantum-cascade semiconductor laser at an oscillation wavelength of 103 μm

Symbol	Parameter	Value
v	Frequency	2.9 THz
N_p	Number of period	30
Γ	Confinement factor	0.27
w	Cavity width	80 μm
L	Cavity length	3.0 mm
r^2	Facet reflectivity	0.29
η_g	Mode-group index	3.3
α_i	Cavity loss	2.4×10^{-3} m^{-1}
G	Gain coefficient	6.75×10^{-9} m^3 s^{-1}
I_{th}	Threshold current	200 mA
β	Spontaneous emission factor	1×10^{-5}
τ_2	Electron lifetime at level 2	0.3 ps
τ_3	Electron lifetime at level 3	1.1 ps
τ_{31}	Phonon scattering time $3 \rightarrow 1$	2.4 ps
τ_{32}	Phonon scattering time $3 \rightarrow 2$	2.0 ps
τ_{ph}	Photon lifetime	3.7 ps
τ_{sp}	Spontaneous relaxation time	7.0 ns

inter-band optical transitions. Due to fast carrier decay rate, the laser has a small damping characteristic for a step response and behaves like class A lasers. Figure 8.54 shows a small signal response of a quantum-cascade laser calculated

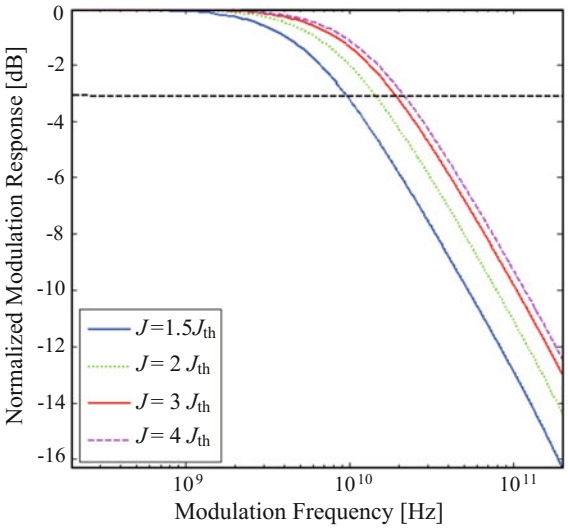

Fig. 8.54 Numerical example of small signal response in a quantum-cascade laser at λ = 9 μm, N_p = 40, τ_{ph} = 9.91 ps and τ_3 = 0.66 ps [after Meng and Wang (2012); © 2012 OSA]

from the above three equations (Meng and Wang 2012). In an inter-band semiconductor laser, the modulation bandwidth is simply determined by the relaxation oscillation time and the oscillation frequency is increased as the square root of the optical power. Thus, in common semiconductor lasers, the relaxation oscillation frequency is usually several to ten GHz within the operation injection current range. However, a high modulation characteristic is obtained in a quantum-cascade semiconductor laser as shown in Fig. 8.54. For the bias injection current of $J = 4J_{th}$, the 3-dB cutoff frequency of 21 GHz is obtained. Further, resonance peak, which is usually observed close to the cutoff frequency in conventional semiconductor lasers, is not visible in the responses. The 3-dB optical bandwidth increases with optical power, but unlike that for inter-band lasers, it initially increases approximately linearly with optical power, not as the square root of the optical power. To explain the detailed dynamics of quantum-cascade semiconductor lasers, the extraction time of the electrons to pass through the different periods should be taken into account (Rana and Ram 2002; Gensty and Elsäßer 2005; Petitjean et al. 2011). To account the extraction time of the electrons to pass from the fundamental level of a certain period to the excited one of the next period, one more equation has to be reintegrated. The rate equations are consequently based on a three-level scheme with four equations (one for each of the three levels of the electrons and one for the photons).

8.7.4 *Nonlinear Interactions in Quantum-Cascade Semiconductor Lasers*

Nonlinear phase coupling of laser modes in quantum-cascade semiconductor lasers leads to a variety of ultrafast and coherent phenomena; synchronization of transverse modes, beam steering, multimode instability, and generation of mode-locked ultra-short pulses. The inhomogeneous saturation leads to spectral and spatial hole-burning, which, in turn, gives rise to multimode operation and nonlinear coupling between laser modes. This nonlinear coupling is phase sensitive and under certain conditions may lead to frequency and phase locking of laser modes. To discuss coherent interplays in quantum-cascade semiconductor lasers, the equation for the field is necessary instead of the photon number equation in the preceding subsection. For the purpose of explaining nonlinear phase coupling in multimode quantum-cascade semiconductor lasers, the coherent rate-equation model based on the two-level Maxwell-Bloch equations are derived (Wójcika et al. 2010, 2011a, b). The derivation is almost equal to that derived in Chap. 2.

The electron flow through the typical active region of a quantum-cascade semiconductor laser can be roughly approximated by a four-level laser scheme. The four-level scheme can be further reduced to the effective two-level scheme if we take into account that the scattering time from lower laser level 3 to level 2 in Fig. 8.52 is very short ($\sim$0.2 ps) due to resonant LO-phonon emission. Therefore,

level 3 stays almost empty and we can neglect its population. Then, one can write the equation for the population inversion $W = n_3 - n_2$ between laser levels 3 and 2. The total field is expanded by the eigen-function of the x and y coordinates $\psi(\mathbf{r}_\perp)$ ($\mathbf{r}_\perp = (x, y)$) as

$$E_{\text{total}}(\mathbf{r}, t) = \sum_i E_i(z, t)\psi_i(\mathbf{r}_\perp) \tag{8.68}$$

where ψ_i is the eigen-function for the i-th mode. Then, the rate equations for the field component E_i, the polarization P and the population inversion W are given by

$$\frac{\partial E_i(z,t)}{\partial t} + \frac{c}{\eta_i}\frac{\partial E_i(z,t)}{\partial z} + (\alpha_i + i\delta_i)E_i(z,t) = i\frac{4\pi\omega_0}{\eta_i\sigma}\int_{ar} P(z,t)\psi_i(\mathbf{r}_\perp)\mathrm{d}V \tag{8.69}$$

$$\frac{\partial P(z,t)}{\partial t} + \gamma_\perp P(z,t) = \frac{iN_A\mu^2}{2\hbar}W(z,t)\sum_i E_i(z,t)\psi_i(\mathbf{r}_\perp) \tag{8.70}$$

$$\frac{\partial W(z,t)}{\partial t} + \gamma_{||}\{W(z,t) - W_p\} = \frac{i}{\hbar N_A}\sum_i \{E_i^*(z,t)P(z,t) - E_i(z,t)P^*(z,t)\} \tag{8.71}$$

where $\gamma_\perp$ is the longitudinal relaxation coefficient, $\gamma_\parallel$ is the transverse relaxation coefficient, N_A is the density of atoms in the unit volume, μ is the dipole moment of the laser transition, W_p is the pump, η_i is the modal refractive index, α_i is the modal loss, $\delta_i = \omega_i - \omega_0$ is the detuning of the i-th mode (ω_i) from the central frequency (ω_0), and σ is the cross section of the waveguide. The integration in (8.69) is taken over the active region.

The fast relaxation times for population inversion, $\gamma_\parallel^{-1} \approx 1$ ps, and polarization, $\gamma_\perp^{-1} \approx 0.1$ ps, characteristic of quantum-cascade semiconductor lasers allow us to adiabatically eliminate both variables. This remarkable stability of the transverse mode locking is the consequence of another peculiar feature of the lasers; ultrafast gain recovery time of the order of 1 ps. This timescale is much shorter than the cavity round-trip time and the photon lifetime, which makes the laser a class A laser. Ultrafast gain recovery time leads to over-damped relaxation oscillations as discussed in the previous subsection, which stabilizes phase locking, as compared to class B lasers where phase locking of transverse modes is more difficult to achieve because of prominent relaxation oscillation resonance. In common semiconductor lasers, phase locking is primarily due to density modulation of free carriers, which is proportional to the linewidth enhancement factor α. In quantum-cascade lasers, the total electron density is not affected by the laser field and the linweidth enhancement factor is much smaller. In this case, the mode coupling is due to gain saturation across an inter-subband atomic-like laser transition and the concomitant strong spatial hole-burning, which favors multimode operation. Figure 8.55 shows an example of nonlinear phase couplings in

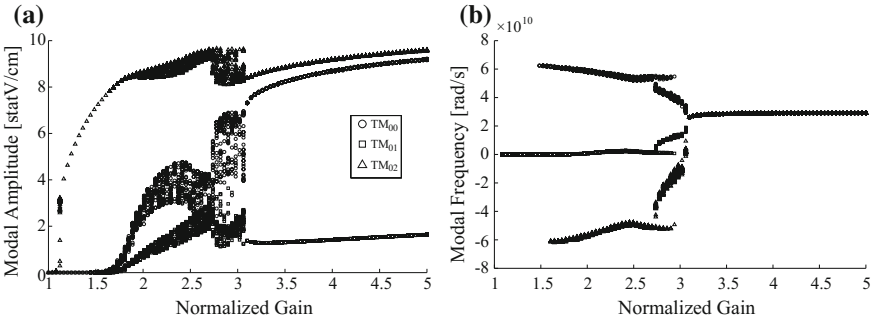

Fig. 8.55 Stable steady-state solutions for three TM modes (TM_{00}, TM_{01}, and TM_{02}) as a function of the linear gain normalized to the threshold gain for the TM_{02} mode. **a** Modal amplitudes and **b** modal frequencies [after Wójcik et al. (2010); © 2010 SPIE]

quantum-cascade semiconductor lasers. The laser is operated with three TM modes (TM_{00}, TM_{01}, and TM_{02}), which are assumed in coincident with a real experiment. Figure 8.55a, b are the amplitude and frequencies of all stable steady-state solutions, respectively (only the field equation is taken into account). The frequency of each mode in Fig. 8.55 is defined as a derivative of the total phase; it is constant when the steady state is reached. The simulations reveal the existence of a certain critical current above which there is only one stable steady-state solution. A remarkable feature of this solution is that frequencies of all modes are locked to the same frequency. Below this critical current, there are multiple steady-state solutions with different uncorrelated frequencies and phases. The model can well explain coherent interplays in real quantum-cascade semiconductor lasers with multimode oscillations.

8.7.5 *Effects of Optical Feedback in Quantum-Cascade Semiconductor Lasers*

For coherent effects of optical feedback and optical injection in quantum-cascade semiconductor lasers, a similar equation for the complex field E as those discussed in the pervious sections can be employed instead of the photon number equation in (8.64).

$$\frac{\mathrm{d}E(t)}{\mathrm{d}t} = \frac{1}{2}(1 - i\alpha)\left[N_p G\{n_3(t) - n_2(t)\} - \frac{1}{\tau_{\mathrm{ph}}}\right]E(t) \tag{8.72}$$

Quantum-cascade semiconductor lasers still have non-zero value of the α parameter and, as a result, the lasers are more or less sensitive to optical feedback and optical injection. Optical feedback or optical injection term is added to the right-hind side

of the equation in (8.72) when necessary. The carrier density equations remain the same as (8.65) and (8.66). Room temperature quantum-cascade semiconductor lasers are an attractive solution for trace gas sensing applications that require fast, portable, high sensitivity measurements such as environmental monitoring and medical diagnostics. Therefore, the study of optical feedback effects in quantum-cascade semiconductor lasers is important, since the coherence of the lasers is high (the oscillation linewidth is as small as $\sim$100 kHz) and an isolator in this wavelength region is not available. Nevertheless, a little study for the dynamics of quantum-cascade semiconductor lasers with optical feedback has been conducted (Hugi et al. 2010). One of the reasons for lacking the study is that the lasers behave like class A lasers and we need much larger optical feedback to induce instabilities such as periodic oscillations and chaos in comparison with conventional semiconductor lasers. We here only remark some aspects of the current study of the optical feedback effects.

As the study for the optical feedback from plain mirror and grating mirror, the effects for the linewidth narrowing, spectroscopic characteristics of laser oscillations, and RIN enhancement and reduction have been reported (Luo et al. 2001; Totschnig et al. 2002; Petitjean et al. 2011). The dynamic phenomena correspond to those of small optical feedback effects in inter-band quantum-well semiconductor lasers. Since currently available quantum-cascade semiconductor lasers have small value of α parameter, they are robust for optical feedback and exhibit little chaotic instability. Also, they show no relaxation oscillation for a step response at solitary oscillations, and this results in the insensitivity for optical feedback. On the other hand, we can reproduce instabilities even in quantum-cascade semiconductor lasers in numerical simulations when we change the relaxation constants for the carrier decays as close to those of quantum-well semiconductor lasers. However, such values of the carrier decays are not realistic in actual devices. Therefore, we cannot find remarkable chaotic routes for optical feedback in quantum-cascade semiconductor lasers. While, we can still observe self-mixing effects (period-one oscillations) in quantum-cascade semiconductor lasers subjected to optical feedback, which is an indication of onset of chaos and one of the routes to chaos. Indeed, various measurements using self-mixing interferometer have been proposed in quantum-cascade semiconductor lasers with optical feedback. The subjects will be treated in Chap. 11.

8.7.6 Enhancement of Modulation Bandwidth in Quantum-Cascade Semiconductor Lasers

Similar to optical-injection phenomena in quantum-well semiconductor lasers, the effect of optical injection in quantum-cascade semiconductor lasers is an interesting issue left for the future study. We here numerically demonstrate some of the dynamic properties of optical injection in quantum-cascade semiconductor lasers.

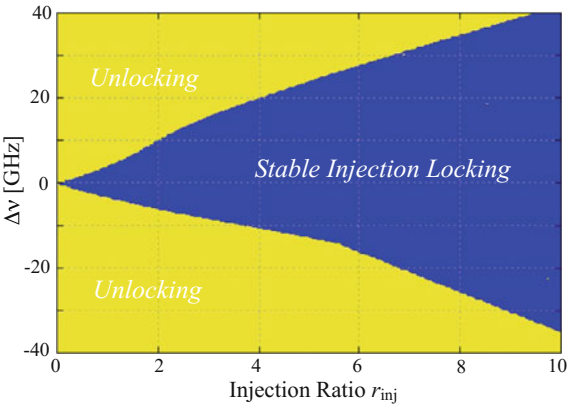

Fig. 8.56 Locking and unlocking optical injection map of a quantum-cascade semiconductor laser in the phase space of the optical injection ratio and the frequency detuning at $\alpha = 1$, $\lambda = 5$ μm, and $J = 3J_{th}$

Figure 8.56 shows an example of optical injection map of quantum-cascade semiconductor lasers in the phase space of the optical injection strength and the frequency detuning. Compared with that in common quantum-well semiconductor lasers, only two classes of locking states (stable injection locking region and unlocking region) are visible, and periodic bifurcations and chaotic oscillations are scarcely observed. Another difference is the almost symmetric shape of the stable injection-locking region for the positive and negative frequency detuning $\Delta\nu$, which is the typical feature of the optical injection characteristics in class A lasers. By changing the values of the relaxation times for carriers in the numerical simulations, chaotic oscillations are even reproduced in quantum-cascade semiconductor lasers induced by optical injection. However, the values of the time constants would be far from those of real devices.

As similar to those of common semiconductor lasers, the modulation bandwidth of quantum-cascade semiconductor lasers is greatly enhanced by strong optical injection. Figure 8.57 shows some examples of modulation characteristics in the presence of optical injection at rather strong optical injection of $r_{inj} = 10$. The definition of r_{inj} is the same one as used in (6.2). In a solitary mode, quantum-cascade semiconductor lasers exhibit no relaxation oscillation. Little enhancement of the modulation bandwidth is observed even for a strong optical injection at zero frequency detuning. The modulation efficiency is deteriorated for a negative frequency detuning. On the other hand, for a positive frequency detuning, the laser shows a relaxation oscillation and the modulation bandwidth is greatly enhanced compared with that of the solitary oscillation, though the peak power of the relaxation oscillation is still lower than those observed in common semiconductor lasers induced by optical injection with positive frequency detuning. Not shown in this figure, the laser even exhibits relaxation oscillation at a larger negative frequency detuning under stronger optical injection. The overall behaviors for the effects of optical injection in quantum-cascade semiconductor lasers are similar

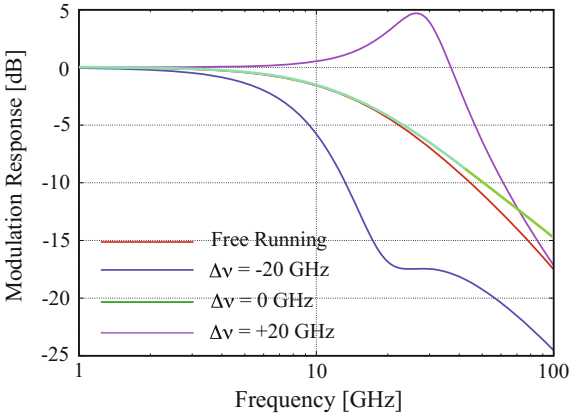

Fig. 8.57 Modulation response in the presence of optical injection at $\alpha = 1$, $\lambda = 5$ μm, and $J = 3J_{th}$. The optical injection ratio is $r_{inj} = 10$

to those of common semiconductor lasers as shown in Fig. 6.17. By appropriately selecting the conditions of optical injection, the modulation bandwidth is enhanced up to 100 GHz. Figure 8.58 shows the result of the modulation bandwidth (3 dB cutoff bandwidth) within the stable injection locking region. The original bandwidth (without optical injection) is 14 GHz. As discussed in Fig. 8.57, the enhancement of the bandwidth is distinct for large positive frequency detuning and strong optical injection. However, higher enhancement of modulation bandwidth is observed at the edge of the negative frequency detuning with larger optical injection. In this region, a large relaxation oscillation peak appears in the modulation response. The maximum modulation bandwidth of about 90 GHz is obtained in the case.

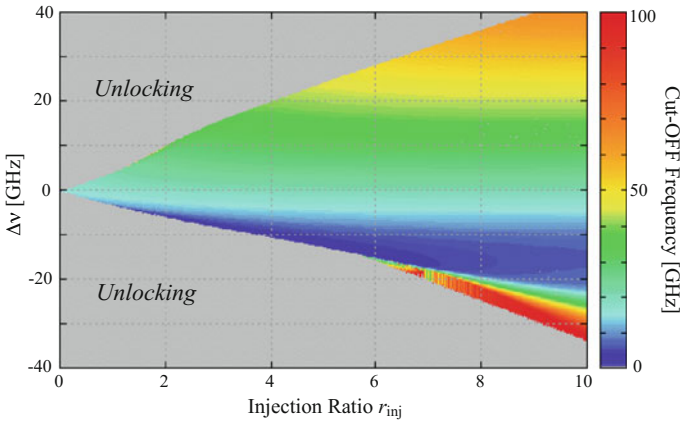

Fig. 8.58 Enhancement of cutoff modulation frequency by optical injection at $\alpha = 1$, $\lambda = 5$ μm, and $J = 3J_{th}$

References

H. Acachihara, O. Hess, E. Abraham, Spatiotemporal chaos in broad-area semiconductor lasers. J. Opt. Soc. Am. B **10**, 658–665 (1993)

G.P. Agrawal, N.K. Dutta, *Semiconductor Lasers* (Van Nostrand Reinhold, New York, 1993)

M. Ahamed, M. Yamada, Influence of instantaneous mode competition on the dynamics of semiconductor lasers. IEEE J. Quantum Electron. **38**, 682–693 (2002)

J.B. Altés, I. Gatare, K. Panajotov, H. Thienpont, M. Sciamanna, Mapping of the dynamics induced by orthogonal optical injection in vertical-cavity surface-emitting lasers. IEEE J. Quantum Electron. **42**, 198–207 (2006)

H. Aoyama, S. Tomida, R. Shogenji, J. Ohtsubo, Chaos dynamics in vertical-cavity surface-emitting semiconductor lasers with polarization-selected optical feedback. Opt. Commun. **284**, 1405–1411 (2011)

M.A. Arteaga, H.J. Unold, J.M. Ostermann, R. Michalzik, H. Thienpont, K. Panajotov, Investigation of polarization properties of VCSELs subject to optical feedback from an extremely short external cavity—part II: experiments. IEEE J. Quantum Electron. **42**, 102–107 (2006)

T. Asatuma, Y. Takiguchi, S. Frederico, A. Furukawa, S. Hirata, Successive phase change and stability of near-field patterns for broad-area laser diodes. SPIE Proc. **6104**, 105–111 (2006)

A. Barchanski, T. Gensty, C. Degen, I. Fischer, W. Elsäßer, Picosecond emission dynamics of vertical-cavity surface-emitting lasers: spatial, spectral, and polarization-resolved characterization. IEEE J. Quantum Electron. **39**, 850–858 (2003)

P. Besnard, F. Robert, M.L. Charès, G.M. Stéphan, Theoretical modeling of vertical-cavity surface-emitting lasers with polarized optical feedback. Phys. Rev. A **56**, 3191–3205 (1997)

P. Besnard, M.L. Charès, G. Stéphan, F. Robert, Switching between polarized modes of a vertical-cavity surface-emitting laser by isotropic optical feedback. J. Opt. Soc. Am. B **16**, 1059–1064 (1999)

T. Burkhard, M.O. Ziegler, I. Fischer, W. Elsäßer, Spatio-temporal dynamics of broad area semiconductor lasers and its characterization. Chaos, Solitons Fractals **10**, 845–850 (1999)

T.W. Carr, T. Erneux, Dimensionless rate equations and simple conditions for self-pulsing in laser diodes. IEEE J. Quantum Electron. **37**, 1171–1177 (2001)

C.J. Chang-Hasnain, J.P. Harbison, G. Hasnain, A.C. Von Lehmen, L.T. Florez, N.G. Stoffel, Dynamics, polarization, and transverse mode characteristics of vertical cavity surface emitting lasers. IEEE J. Quantum Electron. **27**, 1402–1409 (1991)

W.W. Chow, H. Amano, Analysis of lateral-mode behavior in broad-area InGaN quantum-well lasers. IEEE J. Quantum Electron. **37**, 265–273 (2001)

J. Danckaerta, B. Naglera, J. Alberta, K. Panajotova, I. Veretennicoff, T. Erneux, Minimal rate equations describing polarization switching in vertical-cavity surface-emitting lasers. Opt. Commun. **201**, 129–137 (2002)

C. Degen, I. Fischer, W. Elsäßer, Transverse modes in oxide confined VCSELs: influence of pump profile, spatial hole burning, and thermal effects. Opt. Express **5**, 38–47 (1999)

D. Dhirhe, T.J. Slight, B.M. Holmes, D.C. Hutchings, C.N. Ironside, Quantum cascade lasers with an integrated polarization mode converter. Opt. Express **23**, 25711–25717 (2012)

R. Diehl, *High-power Diode Laser, Fundamentals, Technology, Applications* (Springer, Berlin, 2000)

K. Donovan, P. Harrison, R.W. Kelsall, Self-consistent solutions to the intersubband rate equations in quantum cascade lasers: analysis of a GaAs/$Al_xGa_{1-x}As$ device. J. Appl. Phys. **89**, 3084–3090 (2001)

T. Erneux, E.A. Viktorov, P. Mandel, Time scales and relaxation dynamics in quantum-dot lasers. Phys. Rev. A **76**, 023819-1–023819-7 (2007)

T. Erneux, E.A. Viktorov, B. Kelleher, D. Goulding, S.P. Hegarty, G. Huyet, Optically injected quantum-dot lasers. Opt. Lett. **35**, 937–939 (2010)

J. Faist, F. Capasso, D.L. Sivco, C. Sirtori, A.L. Hutchinson, A.Y. Cho, Quantum cascade laser. Science **264**, 553–556 (1994)
I. Fischer, O. Hess, W. Elsäßer, E. Göbel, Complex spatio-temporal dynamics in the near-field of broad-area semiconductor laser. Europhys. Lett. **35**, 579–584 (1996)
N. Fujiwara, J. Ohtsubo, Synchronization in chaotic vertical-cavity surface-emitting semiconductor lasers. SPIE Proc. **5349**, 282–289 (2004)
N. Fujiwara, Y. Takiguchi, J. Ohtsubo, Observation of low-frequency fluctuations in vertical-cavity surface-emitting lasers. Opt. Lett. **28**, 896–898 (2003)
T. Fukushima, Analysis of resonator eigenmodes in symmetric quasi-stadium laser diodes. J. Lightwave Technol. **18**, 2208–2216 (2000)
T. Fukushima, H. Miyazaki, T. Ando, T. Tanaka, T. Sakamoto, Nonlinear dynamics in directly modulated self-pulsating laser diodes with a highly doped saturable absorption layer. Jpn. J. Appl. Phys. **41 Part 1**, 117–124 (2002)
N. Gaciu, E. Gehrig, O. Hess, Control of broad-area laser dynamics with delayed optical feedback (Chap. 22), in *Handbook of Chaos Control*, ed. by E. Schöll, G. Schuster (Wiley-VCH, Weinheim, 2007)
I. Gatare, M. Sciamanna, J. Buesa, H. Thienpont, K. Panajotov, Nonlinear dynamics accompanying polarization switching in vertical-cavity surface-emitting lasers with orthogonal optical injection. Appl. Phys. Lett. **88**, 101106-1–101106-3 (2006)
E. Gehrig, O. Hess, *Spatio-temporal Dynamics and Quantum Fluctuations in Semiconductor Lasers* (Springer, Heidelberg, 2003)
T. Gensty, W. Elsäßer, Semiclassical model for the relative intensity noise of intersubband quantum cascade lasers. Opt. Commun. **256**, 171–183 (2005)
M. Giudici, S. Balle, T. Ackemann, S. Barland, J.R. Tredicce, Polarization dynamics in vertical cavity surface-emitting lasers with optical feedback: experiment and model. J. Opt. Soc. Am. B **16**, 2114–2123 (1999)
C. Gmachl, F. Capasso, D.L. Sivco, A.Y. Cho, Recent progress in quantum cascade lasers and applications. Rep. Prog. Phys. **64**, 1533–1601 (2001)
D. Goulding, S.P. Hegarty, O. Rasskazov, S. Melnik, M. Hartnett, G. Greene, J.G. McInerney, D. Rachinskii, G. Huyet, Excitability in a quantum dot semiconductor laser with optical injection. Phys. Rev. Lett. **98**, 153903-1–153903-4 (2007)
R.P. Green, J.H. Xu, L. Mahler, A. Tredicucci, F. Beltram, G. Giuliani, H.E. Beere, D.A. Ritchie, Linewidth enhancement factor of terahertz quantum cascade lasers. Appl. Phys. Lett. **92**, 071106-1–071106-3 (2008)
F. Grillot, K. Veselinov, M. Gioannini, I. Montrosset, J. Even, R. Piron, E. Homeyer, S. Loualiche, Spectral analysis of 1.55-μm InAs-InP(113)B quantum-dot lasers based on a multipopulation rate equations model. IEEE J. Quantum Electron. **45**, 872–878 (2009)
M.K. Haldar, A simplified analysis of direct intensity modulation of quantum cascade lasers. IEEE J. Quantum Electron. **41**, 1349–1355 (2005)
O. Hess, T. Kuhn, Maxwell-Bloch equations for spatially inhomogeneous semiconductor lasers. I theoretical formulation. Phys. Rev. A **54**, 3347–3359 (1996a)
O. Hess, T. Kuhn, Maxwell-Bloch equations for spatially inhomogeneous semiconductor lasers. II spatiotemporal dynamics. Phys. Rev. A **54**, 3360–3368 (1996b)
O. Hess, S.W. Koch, J.V. Moloney, Filamentation and beam propagation in broad-area semiconductor lasers. IEEE J. Quantum Electron. **31**, 35–43 (1995)
N. Hodgson, H. Weber, *Optical Resonators* (Springer, London, 1997)
Y. Hong, P.S. Spencer, K.A. Shore, Suppression of polarization switching in vertical-cavity surface-emitting lasers by use of optical feedback. Opt. Lett. **29**, 2151–2153 (2004)
Y. Hong, R. Ju, P.S. Spencer, K.A. Shore, Investigation of polarization bistability in vertical-cavity surface-emitting laser subjected to optical feedback. IEEE J. Quantum Electron. **41**, 619–624 (2005)
A. Hugi, R. Maulini, J. Faist, External cavity quantum cascade laser. Semicond. Sci. Technol. **25**, 083001-1–083001-14 (2010)

R. Hülsewede, J. Sebastian, H. Wenzel, G. Beister, A. Kanauer, G. Erbert, Beam quality of high power 800 nm broad-area laser diodes with 1 and 2 mm large optical cavity structure. Opt. Commun. **192**, 69–75 (2001)

A. Hurtado, A. Quirce, A. Valle, L. Pesquera, M.J. Adams, Nonlinear dynamics induced by parallel and orthogonal optical injection in 1550 nm vertical-cavity surface-emitting lasers (VCSELs). Opt. Express **18**, 9423–9428 (2010)

G. Huyet, D. O'Brien, S.P. Hegarty, J.G. McInerney, A.V. Uskov, D. Bimberg, C. Ribbat, V.M. Ustinov, A.E. Zhukov, S.S. Mikhrin, A.R. Kovsh, J.K. White, K. Hinzer, A.J. SpringThorpe, Quantum dot semiconductor lasers with optical feedback. Phys. Stat. Sol. (a) **201**, 345–352 (2004)

Y. Ikuma, J. Ohtsubo, Dynamics in a compound cavity semiconductor laser induced by small external-cavity-length change. IEEE J. Quantum Electron. **34**, 1240–1246 (1998)

S. Jiang, Z. Pan, M. Dagenais, R.A. Morgan, K. Kojima, High-frequency polarization self-modulation in vertical-cavity surface-emitting lasers. Appl. Phys. Lett. **63**, 3545–3547 (1993)

P. Janassek, S. Hartmann, A. Molitor, F. Michel, W. Elsäßer, Investigations of the polarization behavior of quantum cascade lasers by Stokes parameters. Opt. Lett. **41**, 305–308 (2016)

C. Jirauschek, T. Kubis, Modeling techniques for quantum cascade lasers. Appl. Phys. Rev. **1**, 011307-1–011307-51 (2014)

M. Jo, T. Mano, Y. Sakuma, K. Sakoda, Extremely high-density GaAs quantum dots grown by droplet epitaxy. Appl. Phys. Lett. **100**, 212113-1–212113-3 (2012)

R.J. Jones, P. Rees, P.S. Spencer, K.A. Shore, Chaos and synchronization of self-pulsating laser diodes. J. Opt. Soc. Am. B **18**, 166–172 (2001)

C. Juang, M.R. Chen, J. Juang, Nonlinear dynamics of self-pulsating laser diodes under external drive. Opt. Lett. **24**, 1346–1348 (1999)

C. Juang, T.M. Hwang, J. Juang, W. Lin, A synchronization scheme using self-pulsating laser diodes in optical chaotic communication. IEEE J. Quantum Electron. **36**, 300–304 (2000)

M. Kuznetsov, D.Z. Tsang, J.N. Walpole, Z.L. Liau, E.P. Ippen, Chaotic pulsation of semiconductor lasers with proton-bombarded segment, in *Optical Instabilities*, vol. 4, ed. by R.W. Boyd, M.G. Raymer, L.M. Narducci (Cambridge University Press, Cambridge, 1986)

J.Y. Law, Static, dynamic, and noise characteristics of vertical-cavity surface-emitting lasers. Ph. D. Thesis, University of Rochester, (1997)

J.Y. Law, G.P. Agrawal, Effects of spatial hole burning on gain switching in vertical-cavity surface-emitting lasers. IEEE J. Quantum Electron. **33**, 462–468 (1997a)

J.Y. Law, G.P. Agrawal, Mode-partition noise in vertical-cavity surface-emitting lasers. IEEE Photonics Technol. Lett. **9**, 437–439 (1997b)

J.Y. Law, G.P. Agrawal, Feedback-induced chaos and intensity-noise enhancement in vertical-cavity surface-emitting lasers. J. Opt. Soc. Am. B **15**, 562–569 (1998)

G. Levy, A.A. Hardy, Chaotic effects in flared lasers: a numerical analysis. IEEE J. Quantum Electron. **33**, 26–32 (1997)

H. Li, K. Iga, *Vertical-Cavity Surface-Emitting Laser Devices* (Springer, Berlin, 2002)

H. Li, T.L. Lucas, J.G. McInerney, M.W. Wright, R.A. Morgan, Injection locking dynamics of vertical cavity semiconductor lasers using conventional and phase conjugate injection. IEEE J. Quantum Electron. **32**, 22–235 (1996)

Y.L. Lim, P. Dean, M. Nikolić, R. Kliese, S.P. Khanna, M. Lachab, A. Valavanis, D. Indjin, Z. Ikonić, P. Harrison, E.H. Linfield, A.G. Davies, S.J. Wilson, A.D. Rakić, Demonstration of a self-mixing displacement sensor based on terahertz quantum cascade lasers. Appl. Phys. Lett. **99**, 081108-1–081108-3 (2011)

K. Lüdge, Modeling quantum dot based Laser devices (Chap 1), in *Nonlinear Laser Dynamics,* ed. by K. Lüdge. (Wiley-VCH, Weinheim, 2011)

K. Lüdge, E. Schöll, Quantum-dot lasers-desynchronized nonlinear dynamics of electrons and holes. IEEE J. Quantum Electron. **45**, 1396–1401 (2009)

K. Lüdge, M.J.P. Bormann, E. Malić, P. Hövel, M. Kuntz, D. Bimberg, A. Knorr, E. Schöll, Turn-on dynamics and modulation response in semiconductor quantum dot lasers. Phys. Rev. B **78**, 035316-1–035316-11 (2008)

K. Lüdge, R. Aust, G. Fiol, M. Stubenrauch, D. Arsenijević, D. Bimberg, E. Schöll, Large-signal response of semiconductor quantum-dot lasers. IEEE J. Quantum Electron. **46**, 1755–1762 (2010)

G.P. Luo, C. Peng, H.Q. Le, S.S. Pei, W.Y. Hwang, B. Ishaug, J. Um, J.N. Baillargeon, C.H. Lin, Grating-tuned external-cavity quantum-cascade semiconductor lasers. Appl. Phys. Lett. **78**, 2834–2836 (2001)

J.R. Marciante, G.P. Agrawal, Spatio-temporal characteristics of filamentation in broad-area semiconductor lasers. IEEE J. Quantum Electron. **33**, 1174–1179 (1997)

J.R. Marciante, G.P. Agrawal, Spatio-temporal characteristics of filamentation in broad-area semiconductor lasers: experimental results. IEEE Photonics Technol. Lett. **10**, 54–56 (1998)

J. Martin-Regalado, Polarization properties of vertical-cavity surface-emitting lasers. Ph.D. Thesis, Universitat de les Illes Balears, (1997)

J. Martín-Regalado, G.H.M. van Tartwijk, S. Balle, Mode control and pattern stabilization in broad-area lasers by optical feedback. Phys. Rev. A **54**, 5386–5393 (1996a)

J. Martín-Regalado, S. Balle, N.B. Abraham, Modeling spatio-temporal dynamics of gain-guided multistripe and broad-area lasers. IEE Proc.: Optoelectron. **143**, 17–23 (1996b)

J. Martín-Regalado, J.F. Prati, N.B. Abraham, Polarization properties of vertical-cavity surface-emitting lasers. IEEE J. Quantum Electron. **33**, 765–783 (1997)

C. Masoller, N.B. Abraham, Low-frequency fluctuations in vertical-cavity surface-emitting semiconductor lasers with optical feedback. Phys. Rev. A **59**, 3021–3031 (1999a)

C. Masoller, N.B. Abraham, Polarization dynamics in vertical-cavity surface-emitting lasers with optical feedback through a quarter-wave plate. Appl. Phys. Lett. **74**, 1078–1080 (1999b)

C. Masoller, M.S. Torre, P. Mandel, Influence of the injection current sweep rate on the polarization switching of vertical-cavity surface-emitting lasers. J. Appl. Phys. **99**, 026108-1–026108-3 (2006)

B. Meng, Q.J. Wang, Theoretical investigation of injection-locked high modulation bandwidth quantum cascade lasers. Opt. Express **20**, 1450–1464 (2012)

D. Merbach, O. Hess, H. Herzel, E. Schöll, Injection induced bifurcations of transverse spatiotemporal patterns in semiconductor arrays. Phys. Rev. E **52**, 1571–1578 (1995)

C.R. Mirasso, G.H.M. van Tartwijk, E. Hernández-García, D. Lenstra, S. Lynch, P. Landais, P. Phelan, J. O'Gorman, W. Elsäßer, Self-pulsating semiconductor lasers: theory and experiment. IEEE J. Quantum Electron. **35**, 764–770 (1999)

J. Mulet, S. Balle, Spatio-temporal modeling of the optical properties of VCSELs in the presence of polarization effects. IEEE J. Quantum Electron. **38**, 291–305 (2002)

M. Münkel, F. Kaiser, O. Hess, Spatio-temporal dynamics of multi-stripe semiconductor lasers with delayed optical feedback. Phys. Lett. A **222**, 67–75 (1996)

A.V. Naumenko, N.A. Loiko, M. Sondermann, T. Ackemann, Description and analysis of low-frequency fluctuations in vertical-cavity surface-emitting lasers with isotropic optical feedback by a distant reflector. Phys. Rev. A **68**, 033805-1–033805-16 (2003)

D. O'Brien, S.P. Hegarty, G. Huyet, Sensitivity of quantum-dot semiconductor lasers to optical feedback. Opt. Lett. **29**, 1072–1074 (2004)

C. Otto, *Dynamics of Quantum Dot Lasers: Effects of Optical Feedback and External Optical Injection* (Springer Science & Business Media, 2014)

C. Otto, K. Lüdge, E. Schöll, Modeling quantum dot lasers with optical feedback: sensitivity of bifurcation scenarios. Phys. Stat. Sol. (b) **247**, 829–845 (2010)

K. Petermann, *Laser Diode Modulation and Noise* (Kluwer Academic, Dordrecht, 1988)

Y. Petitjean, F. Destic, J.C. Mollier, C. Sirtori, Dynamic modeling of terahertz quantum cascade lasers. IEEE J. Sel. Top. Quantum Electron. **17**, 22–29 (2011)

L. Rahman, H. Winful, Nonlinear dynamics of semiconductor arrays: a mean field model. IEEE J. Quantum Electron. **30**, 1405–1406 (1994)

F. Rana, R.J. Ram, Current noise and photon noise in quantum cascade lasers. Phys. Rev. B **65**, 125313-1–125313-29 (2002)
M. Razeghi, Q.Y. Lu, N. Bandyopadhyay, W. Zhou, D. Heydari, Y. Bai, S. Slivken, Quantum cascade lasers: from tool to product. Opt. Express **23**, 8462–8475 (2015)
A. Ryan, G.P. Agrawal, G.R. Gray, E.C. Gage, Optical feedback-induced chaos and its control in multimode semiconductor lasers. IEEE J. Quantum Electron. **30**, 668–679 (1994)
B.S. Ryvkinn, K. Panajotov, E.A. Avrutin, I. Veretennicoff, H. Thienpont, Optical-injection-induced polarization switching in polarization-bistable vertical-cavity surface-emitting lasers. J. Appl. Phys. **96**, 6002–6007 (2004)
M. San Miguel, Q. Feng, J.V. Moloney, Light polarization dynamics in surface-emitting semiconductor lasers. Phys. Rev. A **52**, 1729–1740 (1995)
G. Scalari, C. Walther, M. Fischer, R. Terazzi, H. Beere, D. Ritchie, J. Faist, THz and sub-THz quantum cascade lasers. Laser Photon Rev. **3**, 45–66 (2009)
D. Scholz, H. Braun, U.T. Schwarz, S. Brüninghoff, D. Queren, A. Lell, U. Strauss, Measurement and simulation of filamentation in (Al,In)GaN laser diodes. Opt. Express **16**, 6846–6859 (2008)
M. Sciamanna, K. Panajotov, Two-mode injection locking in vertical-cavity surface-emitting lasers. Opt. Lett. **30**, 2903–2905 (2005)
M. Sciamanna, K. Panajotov, Route to polarization switching induced by optical injection in vertical-cavity surface-emitting lasers. Phys. Rev. A **73**, 023811-1–023811-17 (2006)
M. Sciamanna, T. Erneux, F. Rogister, O. Deparis, P. Mégret, M. Blondel, Bifurcation bridges between external-cavity modes lead to polarization self-modulation in vertical-cavity surface-emitting lasers. Phys. Rev. A **65**, 041801-1–041801-4 (2002a)
M. Sciamanna, F. Rogister, O. Deparis, P. Mégret, M. Blondel, T. Erneux, Bifurcation to polarization self-modulation in vertical-cavity surface-emitting lasers. Opt. Lett. **27**, 261–263 (2002b)
M. Sciamanna, C. Masoller, N.B. Abraham, F. Rogister, P. Mégret, M. Blondel, Different regimes of low-frequency fluctuations in vertical-cavity surface-emitting lasers. J. Opt. Soc. Am. B **20**, 37–39 (2003a)
M. Sciamanna, C. Masoller, F. Rogister, P. Mégret, N.B. Abraham, M. Blondel, Fast pulsing dynamics of a vertical-cavity surface-emitting laser operating in the low-frequency fluctuation regime. Phys. Rev. A **68**, 015805-1–015805-4 (2003b)
M. Sciamanna, A. Valle, P. Mégret, M. Blondel, K. Panajotov, Nonlinear polarization dynamics in directly modulated vertical-cavity surface-emitting lasers. Phys. Rev. E **68**, 016207-1–016207-4 (2003c)
H. Shoji, Y. Nakata, K. Mukai, Y. Sugiyama, M. Sugawara, N. Yokoyama, H. Ishikawa, Lasing characteristics of self-formed quantum-dot lasers with multistacked dot layer. IEEE J. Sel. Top. Quantum Electron. **3**, 188–195 (1997)
C. Simmendinger, D. Preißer, O. Hess, Stabilization of chaotic spatiotemporal filamentation in large broad area lasers by spatially structured optical feedback. Opt. Express **5**, 48–54 (1999)
M. Sondermann, H. Bohnet, T. Ackemann, Low-frequency fluctuations and polarization dynamics in vertical-cavity surface-emitting lasers with isotropic feedback. Phys. Rev. A **67**, 021802-1–021802-4 (2003)
N. Stelmakh, M. Flowers, Measurement of spatial modes of broad-area diode lasers with 1-GHz resolution grating spectrometer. IEEE Photonics Technol. Lett. **18**, 1618–1620 (2006)
M. Sugawara, *Self-assembled InGaAs/GaAs Quantum Dots* (Academic Press, San Diego, 1999)
A. Tabaka, M. Peil, M. Sciamanna, I. Fischer, W. Elsäßer, H. Thienpont, I. Veretennicoff, K. Panajotov, Dynamics of vertical-cavity surface-emitting lasers in the short external cavity regime: pulse packages and polarization mode competition. Phys. Rev. A **73**, 013810-1–013810-14 (2006)
T. Tachikawa, S. Takimoto, R. Shogenji, J. Ohtsubo, Dynamics of broad-area semiconductor lasers with short optical feedback. IEEE J. Quantum Electron. **46**, 140–149 (2010)
Y. Takiguchi, T. Asatsuma, S. Hirata, Effect of the threshold reduction on a catastrophic optical mirror damage in broad-area semiconductor lasers with optical feedback. SPIE Proc. **6104**, 61040X (2006)

S. Takimoto, T. Tachikawa, R. Shogenji, J. Ohtsubo, Control of spatio-temporal dynamics of broad-area semiconductor lasers by strong optical injection. IEEE Photonics Technol. Lett. **21**, 1051–1053 (2009)
X. Tang, J.P. van der Ziel, B. Chang, R. Johnson, J.A. Tatum, Observation of bistability in GaAs quantum-well vertical-cavity surface-emitting lasers. IEEE J. Quantum Electron. **33**, 927–932 (1997)
M.S. Torre, A. Gavrielides, C. Masoller, Numerical characterization of transient polarization square-wave switching in two orthogonally coupled VCSELs. Opt. Express **19**, 20269–20278 (2011)
G. Totschnig, F. Winter, V. Pustogov, J. Faist, A. Müller, Mid-infrared external-cavity quantum-cascade laser. Opt. Lett. **27**, 1788–1800 (2002)
V.Z. Tronciu, M. Yamada, T. Ohno, S. Ito, T. Kawakami, M. Taneya, Self-pulsation in an InGaN laser—theory and experiment. IEEE J. Quantum Electron. **39**, 1509–1514 (2003)
A. Valle, J. Sarma, K.A. Shore, Spatial hole-burning effects on the dynamics of vertical-cavity surface-emitting laser diodes. IEEE J. Quantum Electron. **31**, 1423–1431 (1995a)
A. Valle, J. Sarma, K.A. Shore, Dynamics of transverse competition in vertical cavity surface-emitting laser diodes. Opt. Commun. **115**, 297–302 (1995b)
A. Valle, I. Gatare, K. Panajotov, M. Sciamanna, Transverse mode switching and locking in vertical-cavity surface-emitting lasers subject to orthogonal optical injection. IEEE J. Quantum Electron. **43**, 322–333 (2007)
G.H.M. van Tartwijk, M. San Miguel, Optical feedback on self-pulsating semiconductor lasers. IEEE J. Quantum Electron. **32**, 1191–1202 (1996)
E.A. Viktorov, P. Mandel, I. O'Driscoll, O. Carroll, G. Huyet, J. Houlihan, Y. Tanguy, Low-frequency fluctuations in two-state quantum dot lasers. Opt. Lett. **31**, 2302–2304 (2006)
M.S. Vitiello, S. Scalari, B. Williams, P. De Natale, Quantum cascade lasers: 20 years of challenges. Opt. Express **23**, 5167–5182 (2015)
J. von Staden, T. Gensty, W. Elsäßer, G. Giuliani, C. Mann, Measurements of the α factor of a distributed-feedback quantum cascade laser by an optical feedback self-mixing technique. Opt. Lett. **31**, 2574–2576 (2006)
A.K. Wójcik, A. Belyanin, N. Yu, L. Diehl, F. Capasso, Nonlinear coupling of transverse modes in quantum cascade lasers. Opt. Eng. **49**, 111114-1–111114-10 (2010)
A.K. Wójcik, N. Yu, F. Capasso, A. Belyanin, Nonlinear optical interactions of laser modes in quantum cascade lasers. J. Mod. Opt. **58**, 727–742 (2011a)
A.K. Wójcik, N. Yu, L. Diehl, F. Capasso, A. Belyanin, Self-synchronization of laser modes and multistability in quantum cascade lasers. Phys. Rev. Lett. **106**, 133902-1–133902-4 (2011b)
H.G. Winful, Instability threshold for an array of coupled semiconductor lasers. Phys. Rev. A **46**, 6093–6094 (1992)
H.G. Winful, L. Rahman, Synchronized chaos and spatiotemporal chaos in arrays of coupled lasers. Phys. Rev. Lett. **65**, 1575–1578 (1990)
H.G. Winful, Y.C. Chen, J.M. Liu, Frequency locking, quasi-periodicity, and chaos in modulated self-pulsating semiconductor lasers. Appl. Phys. Lett. **48**, 616–618 (1986)
M. Yamada, A theoretical analysis of self-sustained pulsation phenomena in narrow-stripe semiconductor lasers. IEEE J. Quantum Electron. **29**, 1330–1336 (1993)
M. Yamada, Theoretical analysis of noise-reduction effects in semiconductor lasers with help of self-sustained pulsation phenomena. J. Appl. Phys. **79**, 61–71 (1996)
M. Yamada, Computer simulation of feedback induced noise in semiconductor lasers operating with self-sustained pulsation. IEICE Trans. Electron. **E81-C**, 768–780 (1998a)
M. Yamada, A theoretical analysis of quantum noise in semiconductor leasers operating with self-sustained pulsation. IEICE Trans. Electron. **E81-C**, 290–298 (1998b)

Chapter 9
Chaos Control and Applications

Abstract We cannot foresee the future of chaotic evolutions, since a small deviation of the initial condition in a nonlinear system results in a completely different solution of the system output. However, chaos can be controllable. Of course, a nonlinear system does not always show unstable oscillations. Or the system can be controlled and stabilized to a steady state by appropriately shifting the parameters even when the system originally outputs irregular chaotic oscillations. In such control, the perturbations for the system may be large and the system is switched to another state from the original oscillation by the parameter shifts. However, the idea of chaos control is completely different from ordinary control methods. The perturbation for a nonlinear system is very small and affects the state of the system very less. In chaos control, the system is controlled to a nearby unstable periodic or fixed orbit (saddle node point of the system). In this chapter, we discuss the method of chaos control and give some applications in semiconductor laser systems. We also demonstrate suppression of unstable oscillations in semiconductor lasers.

9.1 General Methods of Chaos Control

9.1.1 OGY Method

The physical models we encounter in real situations have more or less nonlinear characteristics, nevertheless the techniques of linearization for the systems are frequently applied and only their linear parts are used for convenience, especially in engineering. Therefore, chaos induced by nonlinear effects is usually an unfavorable phenomenon and we keep away from such irregular oscillations in practical applications (Schöll and Schuster 2008; Ohtsubo 2008). However, chaos is controllable and the first paper on chaos control was published by Ott et al. (1990). A nonlinear system includes various parameters and irregular oscillations of the output are generated under certain conditions in multidimensional parameter space.

© Springer International Publishing AG 2017

J. Ohtsubo, *Semiconductor Lasers*, Springer Series in Optical Sciences 111,
DOI 10.1007/978-3-319-56138-7_9

However, the operating point is not always embedded into the chaotic sea on every side. As usual, under a parameter condition, there is a possibility of the existence of unstable periodic orbits (UPO) close to the operating point of the system. Or luckily enough, a fixed point may exist near the point. Ott, Grebogi, and Yorke proposed an algorithm (OGY method) that applies appropriately estimated minute perturbations to an accessible system parameter to select and stabilize certain nearby periodic orbit (unstable periodic orbit). Whether the method works well or fails depends on the availability of the possible nearby unstable saddle node points and the extent of the basin of unstable orbits. This idea indicates that a chaotic system can be turned into a system with multipurpose flexibility, meaning that one can obtain various desired orbits in a simple system without dramatically modifying the configuration of the system. This method is called chaos control. The details of chaos control proposed by Ott, Grebagi, and Yorke can be found in Appendix A.3. Here, we briefly describe the idea of chaos control based on their proposal.

The application of the OGY method requires the full mathematical description of a nonlinear model. We need the attractors or the Poincaré map in advance to analyze and control the system. Based on this information, the parameter is perturbed by the mathematical method and the system is forced to fall down onto an unstable periodic orbit. Therefore, the OGY algorithm is difficult to apply to real experimental systems. The method comes from a rather mathematical basis and can only be applicable for experimental situations where one knows explicitly the exact parameter values in the dynamical system, since the parameter values are important for the calculations of unstable periodic orbits. Although the method is difficult to apply in actual situations of chaos control, it is modified and new techniques applicable to actual experimental systems are proposed by taking over the essence of the OGY method. It is noted that the idea of chaos control is a small perturbation to a nonlinear system and the original chaotic attractor is affected little by the perturbation. If the chaotic attractor is disturbed by the perturbation and the state is switched to another one, the method is not called chaos control in a strict sense. It may be a control of chaos, but not ‘chaos control’.

9.1.2 Continuous Control Method

A fundamental problem existing in the OGY algorithm is the applicability for the control of high-dimensional chaotic systems. Although some attempts were made to adapt this technique to the experimental control of high-dimensional dynamics, the requirements for the knowledge about the attractors and their calculations obstruct the application of the algorithm to the real time control of high-dimensional chaos. As alternative methods of chaos control for the applications to real systems, several chaos control techniques have been proposed. One of them is a continuous control proposed by Pyragas (1992). Figure 9.1 shows the schematic diagram for the

control method. In the Pyragas method, which is called the continuous control method, a part of the output in a nonlinear system is detected with a delay τ_e that has an intrinsic time of the period of the chaotic attractor. The difference between the present $y(t)$ and delayed outputs $y(t - \tau_e)$ is fed back into the original system. This characteristic time τ_e can be calculated either from the theoretical model or from the experimental estimation. The feedback signal is given by (Pyragas 1992, 1993, 2001; Kittel et al. 1994; Naumenko et al. 1998)

$$u(t) = \xi_K\{y(t - \tau_e) - y(t)\} \tag{9.1}$$

where ξ_K is an appropriate feedback gain. An example of the continuous control is given in Appendix A.3. As mentioned above, τ_e is the delay time and is chosen to be near or equal to the response time of the system. When the system is controlled, the amount of the feedback reduces to zero and the output is stabilized to a periodic or fixed state that corresponds to one of the unstable periodic orbits involved in the nonlinear system. The necessary condition in the continuous control method is only the delay time τ_e and the appropriate set of the feedback parameter enables the system to fall down to a periodic or a fixed state even when it originally outputs chaotic oscillations. It is easy to implement the method by using electronic circuits when the system response is not so fast. The method is also applicable to chaotic semiconductor laser systems.

9.1.3 *Occasional Proportional Method*

The other powerful method for the application in experimental systems is the occasional proportional feedback (OPF) method (Hunt 1991; Roy et al. 1992; Liu and Ohtsubo 1994). The OPF method modifies the OGY algorithm. The OPF method also perturbs one of the system control parameters by carefully feeding back a part of the output signal. It creates only small alterations of the attractor and pushes the system so as to stabilize it to the periodic orbit. Digital and analog electronic circuits, such as comparator and sample/hold circuits, are required for the

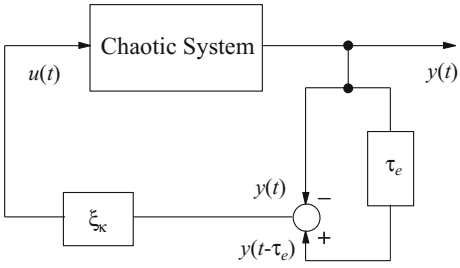

Fig. 9.1 Model of the continuous chaos control method. $y(t)$: output, τ_e: feedback delay, ξ_K: feedback gain, $u(t)$: feedback signal

implementation of the method and periodic components of the attractor are extracted from the chaotic output of the system. Then, the system is stabilized to a periodic orbit by appropriately setting a synchronous signal. The seeding synchronous signal is estimated from the system parameters. Therefore, we require the information only for the characteristic time of the system, such as the delay time, in advance. However, we do not need the exact characteristic time but only a rough estimate of it. When the parameters are set within certain ranges of the appropriate values, a signal for the chaos control is autonomous output. The control signal is a pulse-like one much smaller than the chaotic oscillations and the level is also small enough for the assumption of minute perturbation for the system in chaos control. It is noted that the control signal is continuously generated in the OPF method even after the control has succeeded. This is different from the continuous control in which the control signal is eliminated after the success of the control.

Since the OPF technique is implemented using analog and digital electronic circuits, the control can be performed very fast and is applicable to a variety of nonlinear systems. However, different from the continuous control method, the electronic circuits used in the OPF method are not simple and the implementation may not be easy for a nonlinear system with fast response over nanosecond oscillations. It is also pointed out that the OPF method is essentially a limited case of the OGY algorithm, when the contracting direction of the chaos attractor is infinite in strength. In laser systems, the controls of chaotic oscillations have been successfully performed based on the OPF method. The OPF method has been applied for stabilization and control for class B lasers with slow relaxation oscillations, such as solid-state lasers, fiber lasers, and CO_2 lasers (Roy et al. 1992; Ciofini et al. 1999). In semiconductor lasers, the method is also applied to the control in optoelectronic hybrid systems. Such an example is demonstrated in Chap. 11.

9.1.4 Sinusoidal Modulation Method

Chaotic oscillations in semiconductor lasers related to the relaxation oscillations are usually on the order of nanosecond and close attention must be paid to making the control circuits even when the control is possible. Here, we discuss a different method of chaos control that is very simple and suitable for practical use in systems with fast chaotic oscillations. As discussed in Chap. 4, there exist unstable periodic orbits (modes), for example, in a semiconductor laser with optical feedback. The accompanying frequencies for the modes are numerically calculated from the linear stability analysis for the system. Some of them have periodic solutions with a negative damping coefficient and they are the candidates for unstable periodic orbits (periodic solutions) close to the operating point of the system. Therefore, we think of the control of the system applying a sinusoidal modulation to one of the

accessible parameters. Thus, one may expect to stabilize a chaotic oscillation to a periodic state by applying a small perturbation for a chaos parameter and a new category of chaos control is established as far as the perturbation is small enough and the original state is not so far from the periodic state (Liu et al. 1995; Kikuchi et al. 1997).

In the nonlinear system to be controlled, we apply this method of sinusoidal modulation to one of the accessible chaos parameters. Choosing an appropriate frequency f_0 from the mode analysis, the modulation with a small modulation index m for the parameter is given by

$$u(t) = u_o\{1 + m\sin(2\pi f_0 t)\} \tag{9.2}$$

However, modulation frequencies derived from the linear stability analysis do not always work for the stabilization. Whether or not the control goes well depends on the extent of the basin of the attractor for the control frequency and the modulation depth. The method is an alternative one for the OPF control, since the periodic synchronous perturbation generated from the control circuits of the OPF method is replaced by a simple sinusoidal periodic signal. The sinusoidal modulation control is very easy to apply and the fast modulation is easily attained through the injection current modulation. Therefore, the method is frequently used in semiconductor laser systems.

9.2 Chaos Control in Semiconductor Lasers

9.2.1 Continuous Control

The continuous control method is suited for a system with fast chaotic oscillations in semiconductor lasers. In this section, we show an example of stabilization for chaotic oscillations induced by optical feedback in semiconductor lasers based on the continuous control method. The chaotic output from a semiconductor laser is once detected by a photodetector and electronically fed back into the bias injection current of the laser. The control signal is the difference between the detected intensities from the laser at present and before the time τ_e. Using the feedback gain ξ_K, the term for the injection current in the carrier density equation in (4.7) is replaced by

$$J = J_b[1 + \xi_K\{S(t - \tau_e) - S(t)\}] \tag{9.3}$$

where J_b is the bias injection current without control. The second term in the parenthesis in the right-hand side equation is the control signal corresponding to $u(t)$ in (9.1). The delay time τ_e for the control is usually chosen to be the same as the optical feedback time. However, there is an optimum time delay for the control

depending on the parameter conditions and it is not always the same value as the optical feedback time τ, but it is usually very close to it. The feedback in (9.3) looks like similar to the optoelectronic feedback discussed in Chap. 7, however, it is not the same. After the continuous control has succeeded and the output of the laser is forced to a periodic or fixed oscillation, the control signal is eliminated ($S(t - \tau_e) = S(t)$) and the original state is little affected by the control.

Little work has been reported on the implementation of continuous chaos control in semiconductor laser systems. Instead of showing continuous chaos control, we here show a numerical example of dynamics states in chaotic semiconductor lasers subjected to optical feedback based on (9.3). Figure 9.2 shows the numerical example of bifurcation diagrams for a change of the control parameters (Turovets et al. 1997). Chaotic oscillations under this condition are not LFFs but irregular fast oscillations. Figure 9.2a shows the bifurcation diagram without feedback signal. We can see period-doubling chaotic bifurcation for the increase of the external

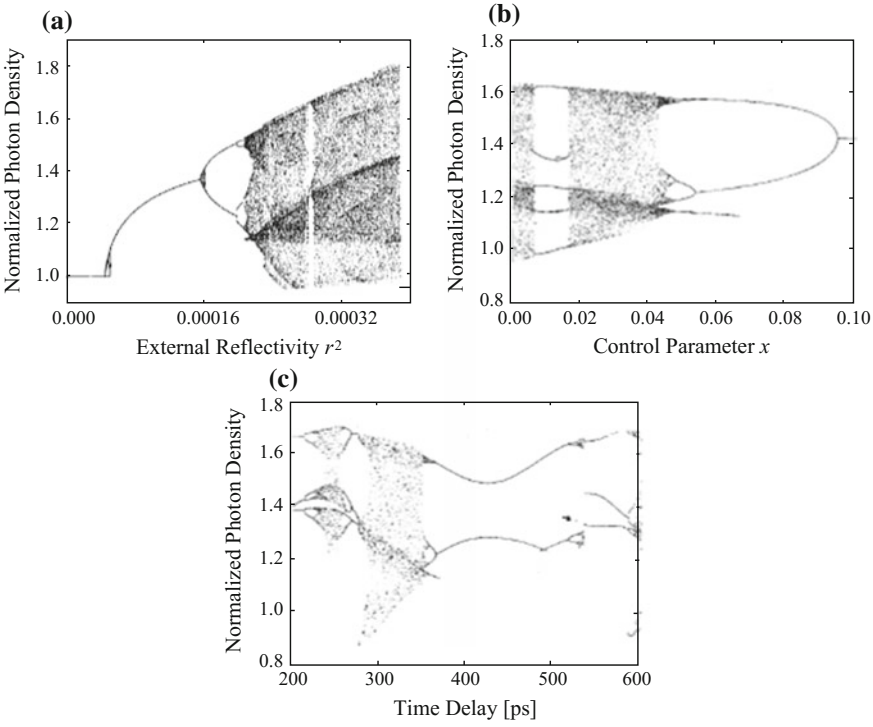

Fig. 9.2 Numerical continuous chaos control at $\xi_K = 0.05/S_0$ (S_0 is the average photon number) and $J_b = 2.0J_{\text{th}}$. The relaxation oscillation frequency at the bias injection current is about 3 GHz. **a** Bifurcation diagram for a change of the external reflectivity r^2 without control at $\tau = 0.23$ ns. **b** Bifurcation diagram with chaos control for a change of feedback coefficient $x = \xi_K S_0$ at $r^2 = 0.000256$ and $\tau_e = 0.36$ ns. **c** Bifurcation diagram with control for a change of delay time τ_e at $x = \xi_K S_0 = 0.05$ and $r^2 = 0.000256$ [after Turovets et al. (1997); © 1997 OSA]

reflectivity r^2. Figure 9.2b shows a bifurcation diagram for the change of the feedback coefficient $x = \xi_K S_0$ at $r^2 = 0.000256$. For the increase of the feedback coefficient, we can see an inverse period-doubling bifurcation. The chaotic states are stabilized at periodic states or even at fixed states for the increase of the control parameter. The delay time of the optoelectronic feedback circuit is set to $\tau_e =$ 0.36 ns and the delay is almost equal to the delay time in the optical feedback loop. The bifurcations are much dependent on the delay time τ_e. For the original chaotic state with $x = 0$, the laser output is stabilized to, for example, a periodic state by the change of the control parameter. However, the change may not be small and there exists a residual of the control signal in this case after the state is shifted to a stable oscillation. Figure 9.2c shows the bifurcation diagram for the change of the delay time τ_e at a fixed control parameter where the original state of the laser output is a period-2 oscillation.

In actual fact, the delay τ_e is electronically generated by an analog circuit and the control signal is fed back into the bias injection current of the laser. Therefore, we must design a fast response circuit for fast chaotic oscillations. As discussed in Chap. 7, the finite response of the electronic circuits, including photodetector and amplifier, is always encountered besides of the setting of the delay τ_e. For real systems, we must take into account these effects. It is again noted that a perturbation for the chaos control must be very small and the system is scarcely affected by the control (Naumenko et al. 1998). Therefore, it is not easy to realize laser stabilization in the strict sense of chaos control. Nevertheless, the analysis of finding stable points in the bifurcation diagram gives rise to a good indication for the control of irregular oscillations of the system even if the control signal does not have small value and the residual of the control is not small.

9.2.2 *Occasional Proportional Feedback Control*

The OPF technique is effective for the control of rather slow response laser systems such as solid-state lasers, but it is not easy to apply the method for fast oscillating lasers. Therefore, the OPF control in chaotic semiconductor lasers has not been reported to date. Here, we show an example of the system construction of OPF control in a chaotic semiconductor laser subjected to optical feedback. Figure 9.3 shows a schematic diagram of the control. A chaotic output from the laser is detected by a photodetector (PD) and is converted into a time dependent electric signal $x(t)$. A variable offset is added to $x(t)$ to bring it within a window of adjustable width. When the waveform transits within the window, the window comparator outputs a pulse, with the pulse width coincident with the length of transition. Meanwhile, a synchronous signal is generated by a pulse generating circuit. The frequency of the synchronous signal is related to the delay and relaxation times of the system. When the synchronous signal is coincident with the pulse from the window comparator, the sample/hold circuit is activated and acquires the waveform voltage. A gate with adjustable time width is employed to select only a

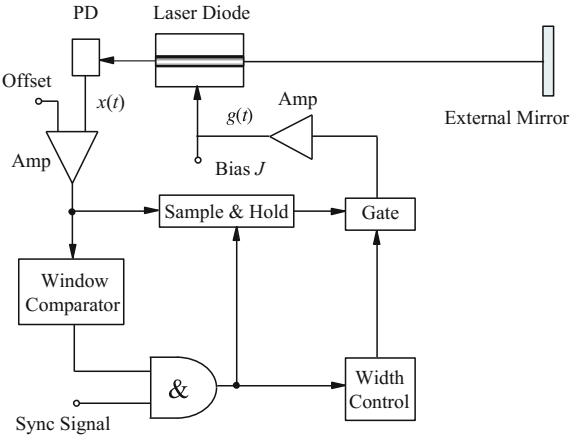

Fig. 9.3 Schematic diagram of the occasional proportional feedback (OPF) control in a semiconductor laser with optical feedback

part of the sampled signal. An amplifier with variable gain, offset, and polarity delivers the control signal $g(t)$ to the drive current of the semiconductor laser diode and perturbs the injection current.

The control signal $g(t)$ must be less than several percent of the bias injection current and it is a pulse like signal with a pulse width that is much shorter than the delay time of the optical feedback. By the control, the chaotic state is always pushed to a periodic or fixed orbit close to the initial point, but the control signal is continuously generated and never dies out. This is different from the result of the continuous control method. Various periodic states can be designed not only for chaotic oscillations but also for stable oscillation states by a small control signal generated by the OPF system adjusting the offset for the amplifier and the window comparator, or appropriately setting the synchronous signal of the AND gate. For design of the OPF control, we require the information about the delay in the nonlinear system in advance. Then, the synchronous signal is appropriately set in the control circuit.

9.2.3 Sinusoidal Modulation Control

The chaos control methods discussed above more or less require the detection of the chaotic signal, the processing of the post-detection signal, and feedback of it to the laser. Therefore, it is sometimes difficult to implement the methods for fast response nonlinear laser systems in practical applications. There is a simple way to realize chaos control suitable for systems with fast chaotic oscillations. We performed the linear stability analysis for the steady states in chaotic semiconductor laser systems in Sect. 4.2.3. The real parts of the solutions for the characteristic equation derived from the linear stability analysis represent the damping rate of the oscillations and the imaginary parts denote the accompanying frequencies. The frequencies obtained

are the candidates for periodic oscillations of unstable saddle node points which are embedded into the system close to the initial operating point. In accordance with this fact, the chaotic system can be controlled to a periodic or fixed state by modulating the accessible parameter with one of the frequencies obtained by the linear stability analysis. The control method works indeed as long as unstable periodic orbits are not far away from the operating point. In a semiconductor laser with optical feedback, a sinusoidal injection current modulation is the easiest way to perform the control. The modulation is applied to the bias injection current in (4.7) as

$$J = J_b\{1 + m\ \sin(2\pi f_0 t)\} \tag{9.4}$$

where f_0 is the modulation frequency calculated from the linear stability analysis and m is the modulation index with a small amplitude. There is an allowable range for the parameter values of f_0 and m for successful control. The robustness for the control depends on the extent of the attractor and the basin of each possible linear mode.

In the following, the sinusoidal modulation control to the injection current in semiconductor lasers with optical feedback is described. Figure 9.4 shows the plot of the mode distribution calculated from the linear stability analysis for the system (Liu et al. 1995; Kikuchi et al. 1997). Under the operating condition, the laser shows chaotic oscillations. All the calculated modes within this region have negative real values, therefore, the calculated modes are candidates for unstable periodic solutions. However, the stability of the modes and the robustness for the control are different from one mode to another and must be investigated by using bifurcation diagrams for the control parameters. We focus on the mode indicated by the arrow in the figure and use this mode as the sinusoidal modulation control.

Figure 9.5 shows an example of chaos control using a sinusoidal modulation to the injection current in a semiconductor laser with optical feedback. The sinusoidal

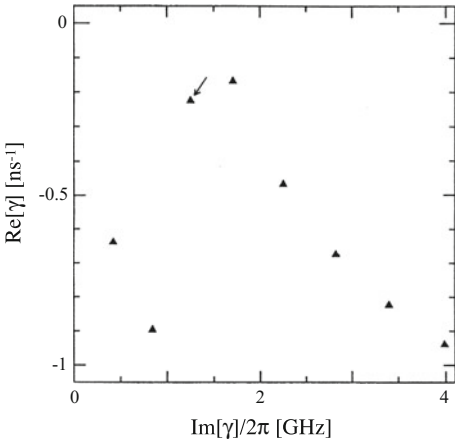

Fig. 9.4 Linear mode distribution for the chaotic output in a semiconductor laser with optical feedback at $J = 1.1J_{th}$, $r = 0.015$, and $L = 25.5$ cm. Under the operation condition, the laser originally shows chaotic oscillation

modulation control is performed by modulating the injection current with the modulation frequency of f_0 = 1.251 GHz and the modulation index of m = 2.1% of the bias injection current. The modulation index is sufficiently small for satisfying the assumption of little effect for the original chaotic state to the system. The chaotic waveform in Fig. 9.5a is controlled to a period-1 oscillation by the modulation of one of the mode frequencies as shown in Fig. 9.5b. Figure 9.5c, d are the attractors for Fig. 9.5a, b, respectively, in the phase space of the laser output power and the carrier density. The chaotic attractor in Fig. 9.5c is controlled to the periodic state in Fig. 9.5d. The robustness of the method for parameter variations is an important issue. In this method, there is a finite modulation range of the parameters for effective control, for example, successful control is achieved within the range of several tens to a hundred MHz centered at the exact mode frequency. However, the extent of the attractor after the control is slightly deformed by the modulation. One of the important issues of chaos control is the response time after the control signal is switched on. The time required for successful control using sinusoidal modulation has been studied by Uchida et al. (1999). According to their results, the time required for reaching the stabilization has statistical distributions for each trial, but the characteristic time is roughly ten times the laser relaxation oscillation (equivalently ten times the typical time scale of chaotic oscillations).

9.2.4 *Optical Control*

Injection current modulation is not the only technique to modulate accessible parameters for the implementation of chaos control in semiconductor lasers. As an alternative modulation method for chaos control, we here show an example of the introduction of an extra mirror in the feedback loop to control chaotic oscillations in a semiconductor laser (Liu et al. 1996; Liu and Ohtsubo 1997; Ruiz-Oliveras and Pisarchik 2006). Figure 9.6 shows the optical chaos control system using double external mirrors. One of the mirrors is the external mirror that gives rise to chaotic oscillations in the semiconductor laser and the second mirror is used for the control. In this system, a beat signal induced by the mixing of lights from the two mirrors plays the same role for a sinusoidal modulation as the bias injection current modulation in the previous section. We have already performed the linear stability analysis for a single external mirror in Sect. 4.2. In the same manner as in the single mirror case, the linear stability analysis is applied to the rate equations with double external mirrors. Depending on the feedback times from the two mirrors, the solutions for the optical oscillation frequency are determined from the following equation:

$$\omega_s - \omega_{\mathrm{th}} = -\frac{\kappa_1}{\tau_{\mathrm{in}}}\{\alpha\cos(\omega_s\tau_1) + \sin(\omega_s\tau_1)\} - \frac{\kappa_2}{\tau_{\mathrm{in}}}\{\alpha\cos(\omega_s\tau_2) + \sin(\omega_s\tau_2)\} \tag{9.5}$$

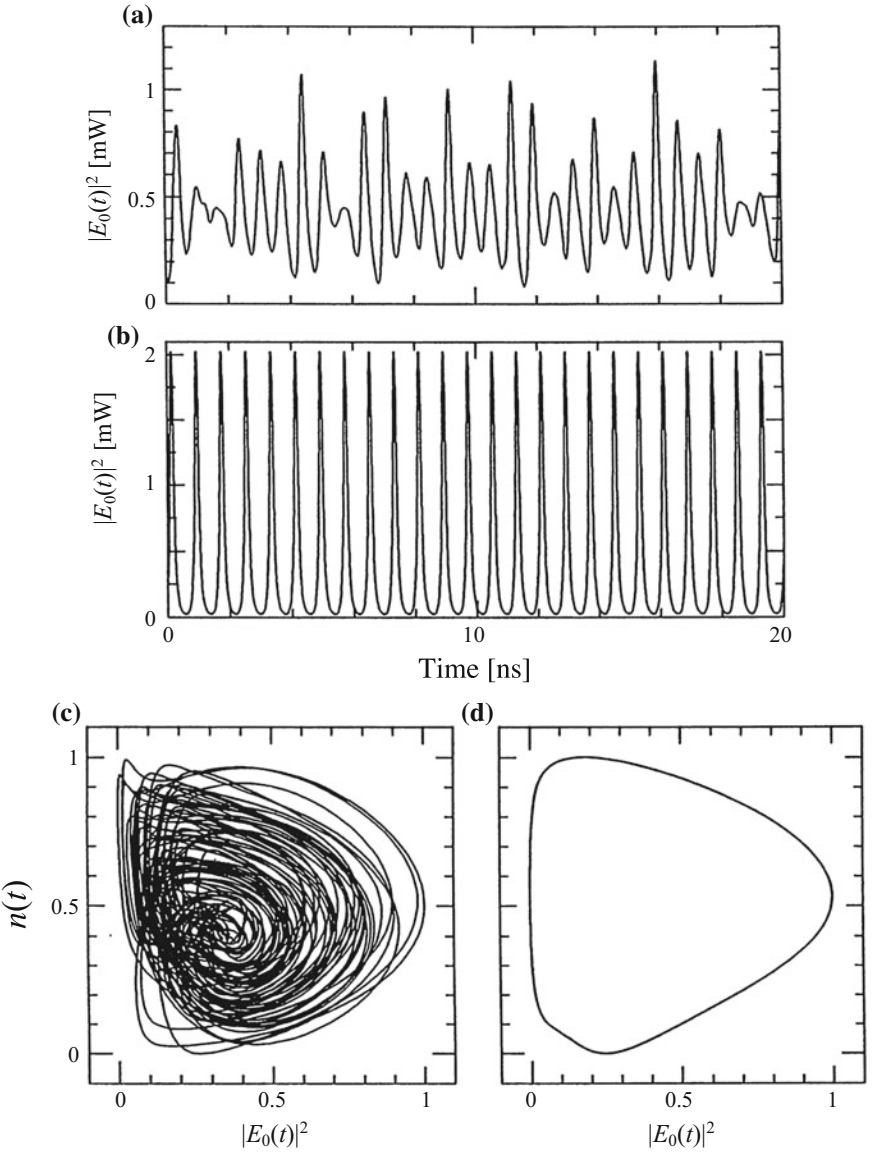

Fig. 9.5 Sinusoidal modulation control using the parameters in Fig. 9.4. **a** Original chaotic oscillation of the laser output without control. **b** Controlled period-1 oscillation using the mode frequency indicated by the *arrow* in Fig. 9.4. The modulation depth is 2.1% of the bias injection current. **c**, **d** are attractors corresponding to **a**, **b**, respectively

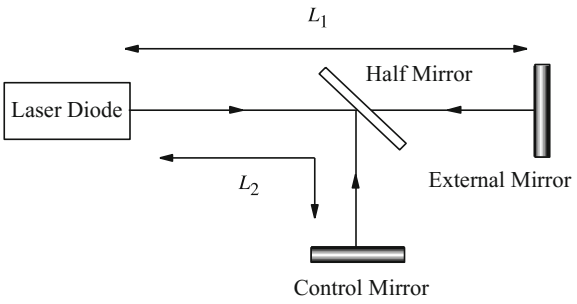

Fig. 9.6 Schematic diagram of the optical sinusoidal modulation control

where ω_s is the angular frequency for the steady-state oscillation, and subscripts 1 and 2 are for the first (external) and second (control) mirrors, respectively. The solution of the above equation is added to the steady-state phase and this additional term has the effect of a sinusoidal modulation for the control of the system.

In the strict sense of chaos control, the additional optical feedback term in (9.5) must be small not to disturb the original feedback system. However, the system is usually affected strongly by the second feedback mirror and the system might not fall into a nearby unstable periodic orbit by the control, but it is pulled apart from an accompanying anti-mode by the interference and is forced to another periodic or fixed state far from the original state. The system after the control may have a different attractor from the original one and, therefore, such a control is not categorized into chaos control with small perturbation in the sense of OGY control. However, the technique is sometimes effective for stabilizing chaotic irregular oscillations. In the following, we demonstrate the control method for stabilizing LFF oscillations in semiconductor lasers with optical feedback as an example of optical control. When LFFs occur, the oscillation mode always accompanies an unstable anti-mode as explained in Sect. 5.3. The oscillation mode is a stable mode close to or at the maximum gain mode of the laser oscillation. During chaotic itinerary due to the perturbation, the state is once trapped into the anti-mode and this induces low-frequency fluctuations. If the system is separated apart from the anti-mode by the control, the laser is forced to a stable oscillation. The steady-state solutions for the photon number and the carrier density in the double-cavity system are written by

$$A_s^2 = \frac{J/ed - n_s/\tau_s}{G_n(n_s - n_0)} \tag{9.6}$$

$$n_s = n_{\text{th}} - \frac{2\kappa_1}{\tau_{\text{in}} G_n}\cos(\omega_s \tau_1) - \frac{2\kappa_2}{\tau_{\text{in}} G_n}\cos(\omega_s \tau_2) \tag{9.7}$$

To realize the control, we make the condition where the accompanying anti-mode of only the first mirror is separated from the maximum gain mode by the introduction of the second mirror according to the steady-state solutions in between (9.6) and (9.7).

Figure 9.7 shows the phase diagram for the carrier density $n(t)$ and the phase $\psi(t) = \phi(t) - \phi(t - \tau) + \omega_0\tau$ ($\omega_0 = \omega_{th}$) in the presence of the control (Rogister et al. 1999). Without the second mirror in Fig. 9.7a, the laser is trapped in one of the anti-modes (denoted by asterisks) close to the maximum gain mode (black dot) and shows chaotic oscillation (chaotic trajectory of LFFs in the figure). By the introduction of the second mirror in Fig. 9.7b, anti-modes are separated far away from the oscillation modes (open circles) and the laser does not show catastrophic oscillations like LFFs. In Fig. 9.7b, the attractor still looks chaotic but with a compact attractor and the laser oscillates at a quasi-periodic state near one of the external modes. With the increase of the feedback level from the second mirror, the laser is stabilized at a periodic state with an attractor of a close loop in Fig. 9.7c and finally forced to a fixed state at the maximum gain mode (black dot) in Fig. 9.7d. Figure 9.8 is an experimental result for the control of LFFs (Rogister et al. 2000). The figure shows optical spectra observed by a Fabry–Perot spectrometer for the change of the external feedback level. The feedback strength of the second mirror is estimated from the threshold reduction rate by the feedback and it is written on the

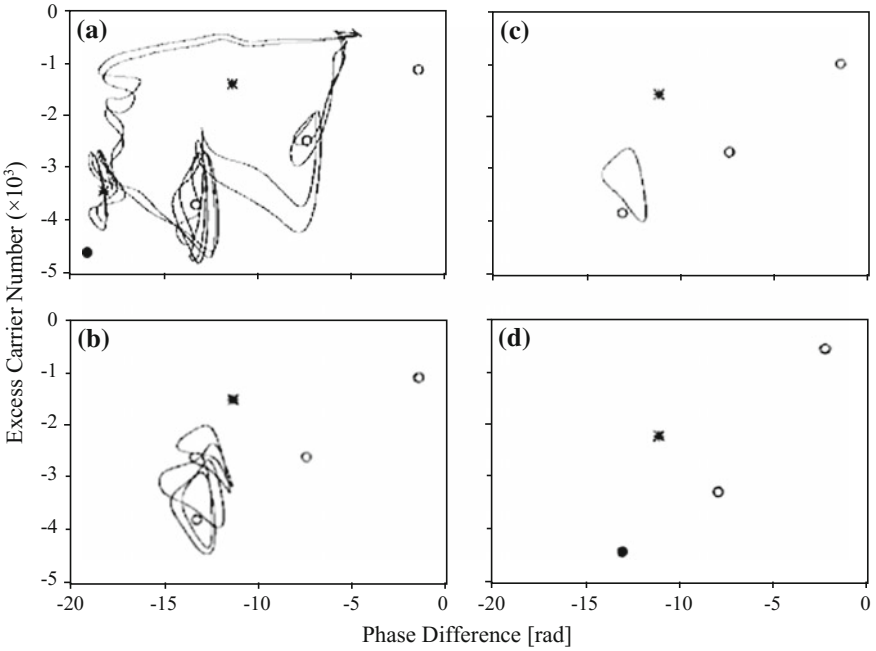

Fig. 9.7 Phase trajectories observed in the phase space ($\phi(t) - \phi(t - \tau_1) + \omega_0\tau$, $n(t)$). *Asterisks* Anti-modes, *open circles* unstable external cavity modes, *filled circles* stable external cavity modes. **a** LFF for $\kappa_1\tau_{ph}/\tau_{in} = 0$. **b** Quasi-periodic behavior with frequency locking for $\kappa_1\tau_{ph}/\tau_{in} = 0.5 \times 10^{-3}$. **c** Limit cycle corresponding to periodic behavior for $\kappa_1\tau_{ph}/\tau_{in} = 1.0 \times 10^{-3}$. **d** Stationary behavior for $\kappa_1\tau_{ph}/\tau_{in} = 4.0 \times 10^{-3}$. The laser locks into a stable external cavity mode. The feedback ratio of the first mirror is $\kappa_1\tau_{ph}/\tau_{in} = 4.6 \times 10^{-3}$ in all cases. The delay times are $\tau_1 = 1$ ns and $\tau_2 = 0.2$ ns [after Rogister et al. (1999); © 1999 OSA]

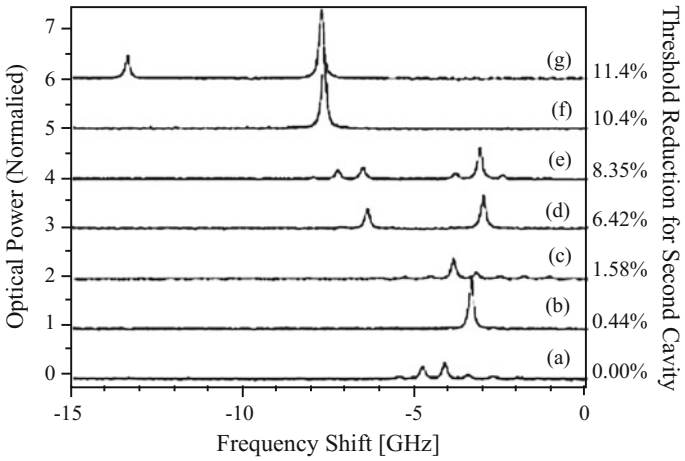

Fig. 9.8 Experimental optical spectra measured in the double cavity configuration as a function of threshold reduction owing to the feedback strength of the second mirror. *a* LFFs in the absence of second feedback. The increase of the feedback strength of the second mirror leads to stabilization (*b* and *f*) interspersed with unstable regions (*c*–*e* and *g*). The optical spectra have been normalized with respect to the maximum of trace *b*. Single-mode oscillation of the laser is guaranteed by a grating mirror put into the path of the optical feedback loop for the second mirror. The feedback fraction is estimated by the reduction rate of the threshold current due to the feedback. The feedback strength of the first mirror is fixed at 7.1% counted by the threshold reduction in all cases. The bias injection current is just above the threshold and the lengths of the external mirrors are L_1 = 21 cm and L_2 = 19 cm [after Rogister et al. (2000); © 2000 OSA]

right-hand side of the figure. Without the control by the second mirror, the coherence of the laser oscillation collapses due to LFF oscillations as shown in Fig. 9.8a. In Fig. 9.8b, f, the laser output power shows fixed constant states and the laser oscillates at single mode. The laser shows a period-1 state with the frequency of the relaxation oscillation in Fig. 9.8d. Thus, the laser is controlled to a periodic or fixed state by appropriately choosing the feedback strength of the second mirror. The noise for the lower frequency component is also much suppressed by the control (Rogister et al. 1999).

9.3 Controlling Chaos and Noise Suppression

9.3.1 Noise Suppression by Sinusoidal Modulation

The main noise source in free running semiconductor lasers is the spontaneous emission of photons in laser media. Noises in semiconductor lasers are greatly enhanced by optical feedback. The detailed definition and descriptions for the noise characteristics in semiconductor lasers can be found in the book by Petermann

(1988). The general description of noise effects and relative intensity noise (RIN) in semiconductor lasers are also given in Sect. 3.6 in this book. We again define the RIN in relation to the noise of the optical power δS to the mean power $\langle S \rangle$ according to [see (3.117)]

$$\mathrm{RIN} = \frac{\langle \delta S^2 \rangle}{\langle S \rangle^2} \tag{9.8}$$

where the optical output power from the laser is defined by $S(t) = \langle S \rangle + \delta S(t)$. In actuality, the feedback induced irregular intensity fluctuation is not a noise but a chaotic fluctuation. However, the effects of the phenomena are similar to noises in free running semiconductor lasers. Therefore, we use the same notation for the feedback induced irregular fluctuations.

Figure 9.9 shows an experimentally obtained RIN in the presence of optical feedback in a Fabry-Perot semiconductor laser. The RIN is plotted for the external feedback strength (intensity), however the actual feedback to the active layer is much less than the externally calculated reflectivity due to the losses and absorption of light through the optical components and the diffraction loss of the focusing lens. At an external reflectivity around 0.1% (compatible with around 0.001% in theoretical calculation), the RIN has almost the same level as the solitary oscillation. Above this level, the RIN abruptly increases and reaches the maximum value at the external reflectivity of 1% (the corresponding theoretical feedback strength is about 0.1–0.01%). Without optical feedback, RIN for ordinary narrow-stripe edge-emitting semiconductor lasers under solitary oscillations is less than −140 dB/Hz. However, in the presence of optical feedback, the RIN increases to much higher than −125 dB/Hz in the feedback regions of III–V (chaotic and coherence collapse regimes) as discussed in Sect. 4.1. In these regions, we can observe the broadening of the oscillation linewidth, chaotic behaviors of the laser output, and the coherence collapse state of the laser. A laser with a RIN above −125 dB/Hz cannot be used as a light source for optical data storage systems

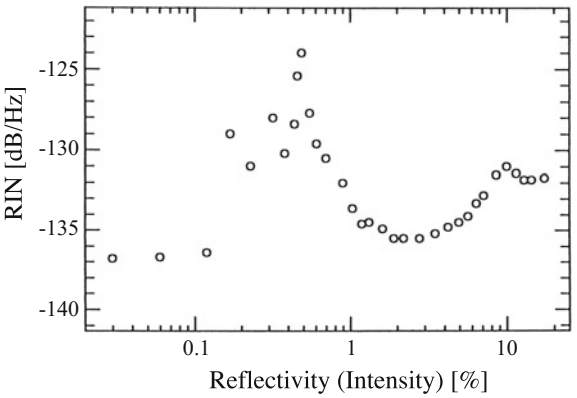

Fig. 9.9 Experimentally obtained RIN in a semiconductor laser with optical feedback. The laser is a Fabry–Perot type with an oscillation wavelength of 780 nm at the maximum power of 5 mW. The bias injection current is $J = 1.5J_{\mathrm{th}}$ and the external cavity length is $L = 20$ cm

because of the increase of bit-rate errors. Although the feedback level in this regime is very small, it affects the performance of the laser operation. To know the dynamics in this feedback regions are also very important from the viewpoint of practical applications, such as the use for optical data storage systems, since the returned light from the disk surface in those systems is almost of the same order. On the other hand, the RIN decreases with further increase of the feedback level. The noise characteristics are dependent not only on the reflectivity of the external mirror, but also on other system parameters such as the bias injection current and the external mirror position.

Unstable oscillation of semiconductor lasers subjected to optical feedback was stabilized by the introduction of a sinusoidal modulation to the injection current as shown in the previous section. Figure 9.10 shows the numerical result of the noise suppression by the sinusoidal modulation method (Kikuchi et al. 1997). The RIN of the solitary laser is about −140 dB/Hz in the lower frequency region (solid line). A frequency peak at about 3 GHz is the relaxation oscillation component. In the presence of optical feedback, the noise is extremely enhanced and it is about −120 dB/Hz in the lower frequency region as is shown as the broken line in the figure. The noise level exceeds the allowed criterion for a light source of the optical data storage system. The dotted line shows the result of the control. One of the mode frequencies (in this case, it is 2.38 GHz) is chosen as a control frequency and the laser is modulated by this frequency through the injection current modulation. By the modulation, the laser shows synchronous oscillation (period-1) and the RIN in the lower frequency region is reduced to −130 dB/Hz. The modulation amplitude is small and $m = 0.15$. The noise level attained by the control is enough for the requirement of a light source for the optical data storage system.

The modulation index of $m = 0.15$ used in Fig. 9.10 may be still larger from the viewpoint of chaos control. The modulation more or less affects the laser oscillation and a closer investigation shows deviations of the chaos attractor from the original one. The modulation index must be less than about 0.01 for the ideal chaos control.

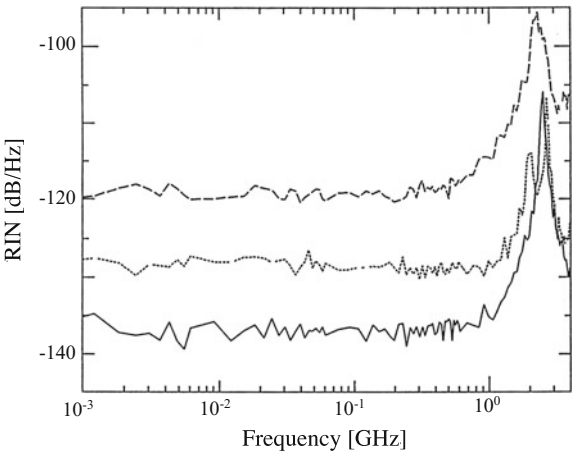

Fig. 9.10 RIN for the sinusoidal modulation control based on the numerical simulation. *Solid line* RIN of solitary oscillation, *broken line* RIN for optical feedback without control, *dotted line* RIN for sinusoidal control. The modulation frequency is 2.38 GHz and the modulation index is 0.15

Nevertheless, the laser is stabilized by a rather small signal compared with ordinary forced sinusoidal control without optimized frequency. In optical data storage systems, the suppression of optical feedback noise is an important issue. The light is reflected from a disk surface and is returned into the laser active layer. The feedback light induces much noise in the laser and causes serious problems for the performance of the data read-out. In actual optical data storage systems, a high frequency injection current modulation on the order of several hundreds MHz to one GHz has been employed to suppress feedback-induced noises (Arimoto et al. 1986; Gray et al. 1993). In such optical data storage systems, the modulation index over $m = 1.0$ was frequently used. The modulation depth is much larger than that of the chaos control and a laser is sometimes brought below the threshold by the modulation.

It is known from the empirical basis that there is a best modulation frequency for each optical data storage system. From the viewpoint of chaos control in semiconductor laser systems, the high frequency modulation technique is closely related to the sinusoidal modulation control in chaos control, in which the chaotic orbit is stabilized to a periodic oscillation, though the modulation depth is much larger than the expected chaos control. The strong modulation technique used for optical compact disk and DVD systems is considered as a forced oscillation to the light source. However, the method does not always work for every selected modulation frequency. As we have discussed in Chap. 7, strong modulation to a semiconductor laser sometimes gives rise to unstable chaotic oscillations. Therefore, the optimized modulation frequency has some relation to the sinusoidal modulation control of chaos, even though the modulation frequency is selected on the empirical basis. A self-pulsation laser is also used for light sources of DVD in optical data storage systems. The chaos control algorithm introduced here may give us important information for the design of such devices and systems. The essence of chaos control is that the control does not change the original dynamics of the nonlinear system. However, the original dynamics may be changed due to very small but non-negligible modulation amplitude. In that case, the idea of chaos control is still effective for the control of an existing unstable periodic orbit as far as the modulation is small.

To decide the optimum frequency in the sinusoidal modulation control, we must establish the model for a real system and estimate the frequency. However, it is not easy to obtain all the parameter values of the system in advance. Nevertheless, we can guess the frequencies. The relaxation oscillation frequency of the laser is one of the candidates for the optimum frequency. Another one is the external cavity frequency and its higher harmonics. From the linear stability analysis, the mode frequencies of the optical feedback system are not always equal to the exact external cavity frequencies, but there exist mode frequencies close to the external cavity frequency. As has already been discussed, there is a certain extent for the tolerance of the modulation frequency for a successful chaos control. In reality, which frequency is the best for the control and suppression of noises must be examined

and tested by using each possible frequency. Noise induced by optical feedback is much suppressed by the best selection of the modulation frequency and, thus, the laser is stabilized with a smaller modulation power.

9.3.2 *Stability and Instability of LFFs by Injection Current Modulation*

Low-frequency fluctuation (LFF) is one of the typical instabilities of semiconductor lasers with optical feedback. Even when the laser seems to be oscillated at a stable state under optical feedback, the laser becomes unstable by the injection current modulation and shows LFF oscillations for certain ranges of the modulation frequency. However, the laser shows stable oscillations for other frequency ranges. On the contrary, the laser oscillating at the LFF state due to optical feedback can be stabilized by the injection current modulation with appropriate frequencies. There exist typical time scales of the laser oscillation in optical feedback systems and the external mode is usually very close to one of the linear modes derived from the linear stability analysis. Here, we show the control of LFFs by the injection current modulation with a frequency close to the external cavity mode. For a detuned modulation from the external-mode frequency, the laser shows LFFs under certain parameter conditions. However, the laser output with LFFs is experimentally stabilized to a synchronous oscillation by a modulation frequency close to the external mode (Takiguchi et al. 1998; 1999b). The modulation frequencies are not exactly equal to the external-mode frequency calculated from the external cavity length. In the experimental study by Takiguchi et al. (1998, 1999a, b, c), LFF oscillations from a semiconductor laser subjected to optical feedback were suppressed by the injection current modulation with the resonance frequency with small modulation index (about −10 dB). By the modulation, the laser oscillation is locked to the control frequency, but the locking range is very narrow. For example, the modulation frequency for the stable oscillation is several hundreds of MHz at the external cavity length of the order of 10 cm, but the range of the modulation frequency for stable oscillations is at most several MHz. Stabilization of LFFs has also been reproduced by numerical simulations. The stabilization of LFFs by the injection current modulation is considered to be the same technique as the sinusoidal modulation control discussed above.

Figure 9.11 shows the stabilization of LFFs by the injection current modulation (Takiguchi et al. 2002). Figure 9.11a is an example of LFFs by the injection current modulation with the frequency far away from the external cavity frequency. The laser is originally a single-mode laser, but it oscillates at multimode and the coherence of the laser is completely destroyed, as is observed from the spectrum in a Fabry–Perot spectrometer. On the other hand, the laser is stabilized and oscillates at a single mode for the frequency close to the external cavity mode (note that it is not exactly equal to the external cavity frequency). The laser oscillates at single mode and also recovers its coherence as can be seen from the optical spectra both of

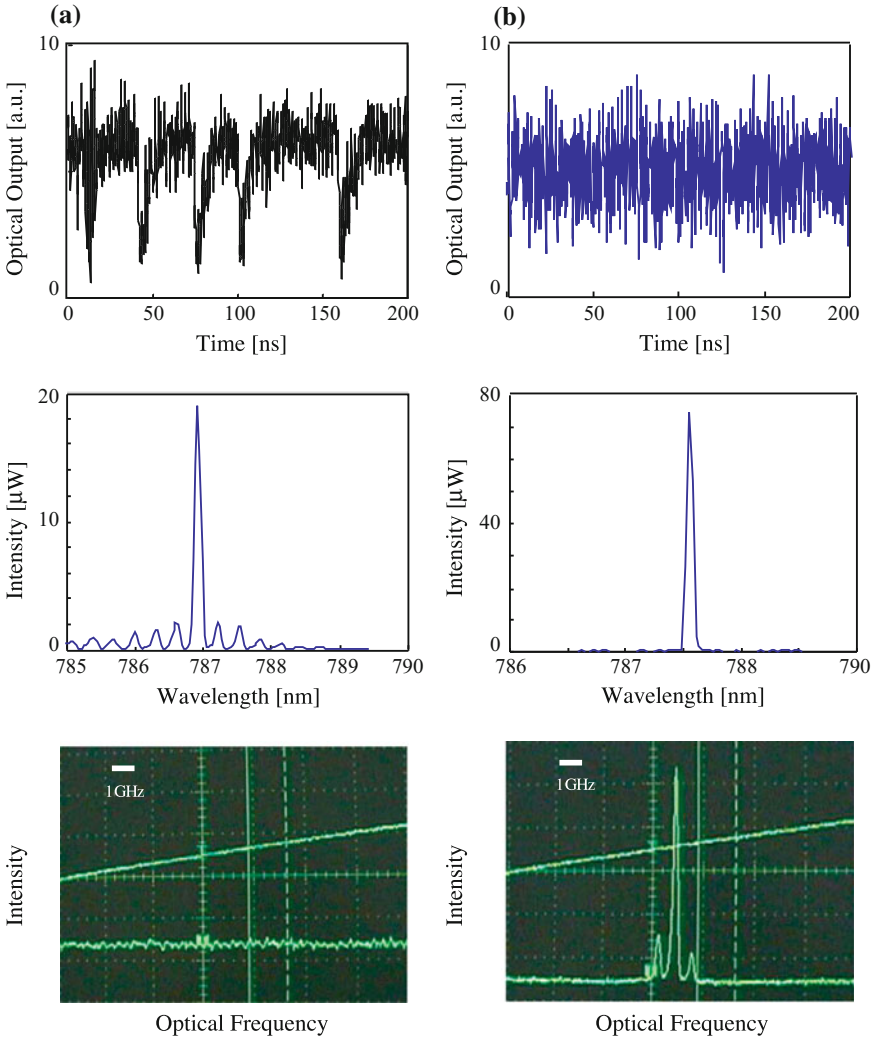

Fig. 9.11 Experimental results of modulation induced LFFs and stabilization in the semiconductor laser with optical feedback. The external cavity length is $L = 27$ cm. *Top* to *bottom* Waveform of LFFs, optical spectrum observed by a spectrum analyzer, and optical spectrum observed by a Fabry–Perot spectrometer. **a** LFFs for a modulation frequency of 390 MHz and a modulation depth of −4 dBm. **b** Stabilized oscillation for a modulation frequency of 548 MHz and a modulation depth of −4 dBm. The external cavity frequency is 556 MHz

the spectrum analyzer and the Fabry–Perot spectrometer. The small spectral sub-peaks appeared at the main mode in the Fabry–Perot spectrometer correspond to the components of the modulation. The laser is also stabilized by the injection current modulation with frequencies of the higher harmonics of the fundamental frequency of the external cavity mode.

9.3.3 Chaos Targeting

We have discussed the optical control method in Sect. 9.2.4 in which the laser oscillation was fixed to the maximum gain mode by the introduction of the second mirror. A similar technique can be applied to stabilize feedback induced chaotic oscillations so as to lower the state onto the maximum gain mode by adjusting the optical phase. The control method is called dynamic targeting (Wieland et al. 1997; Hohl and Gavrielides 1998). The dynamic targeting is generally realized by compensating the parameter values to shift and stabilize the laser oscillation when the system becomes an unstable state. From (4.10), the condition of the stability, i.e., the maximum gain mode condition is given by

$$\omega_{\mathrm{th}}\tau = \frac{\kappa_1}{\tau_{\mathrm{in}}}\tau\alpha \mod 2\pi \tag{9.9}$$

When the system does not satisfy this condition, the laser becomes unstable and shows LFFs and chaotic oscillations. Therefore, we could adjust the parameters to stabilize the laser when the system deviates from this condition. The laser is forced to a fixed state by controlling the bias injection current to satisfy the condition of (9.9), since the optical frequency ν_0 can be changed by the bias injection current according to the relation of (5.5).

Figure 9.12 is an example of the results for dynamic targeting control (Hohl and Gavrielides 1998). The bifurcation diagram in Fig. 9.12a is a calculated bifurcation cascade of a semiconductor laser subjected to optical feedback at the pump of $S = \frac{2\tau_{\mathrm{ph}}}{G_n\tau_s}\left(\frac{J}{ed} - \frac{n_{\mathrm{th}}}{\tau_s}\right) = 0.001$ for the change of the feedback fraction $\kappa\tau_{\mathrm{ph}}/\tau_{\mathrm{in}}$, where κ is the feedback parameter defined previously. For the change of the optical feedback level, the laser shows a bifurcation cascade from stable state, period-doubling, to chaotic oscillations. The dashed curve denotes the stabilized laser intensity when the feedback phase is adjusted by means of the optical frequency ν_0 as the feedback strength is increased. For the adjustment of the phase x, the rate equation of the field is written by

$$\frac{\mathrm{d}E(t)}{\mathrm{d}t} = \frac{1}{2}(1 - i\alpha)G_n\{n(t) - n_{\mathrm{th}}\}E(t) + \frac{\kappa}{\tau_{\mathrm{in}}}E(t-\tau)\,\exp\{i(\omega_0 - x)\tau\} \tag{9.10}$$

By the extra phase $x\tau$ in (9.10), the laser oscillation is fixed to the maximum gain mode. In actuality, the laser output decreases due to the decrease of the bias injection current by the adjustment. The laser output decreases for the increase of the feedback strength but stabilizes to a fixed state as shown in Fig. 9.12b. Thus, the system under irregular oscillations can always be pulled back by dynamic targeting control. It is again noted that the dynamic targeting is not categorized as chaos control in the sense of the OGY method, since the system is always changed to a different chaotic state by dynamic targeting.

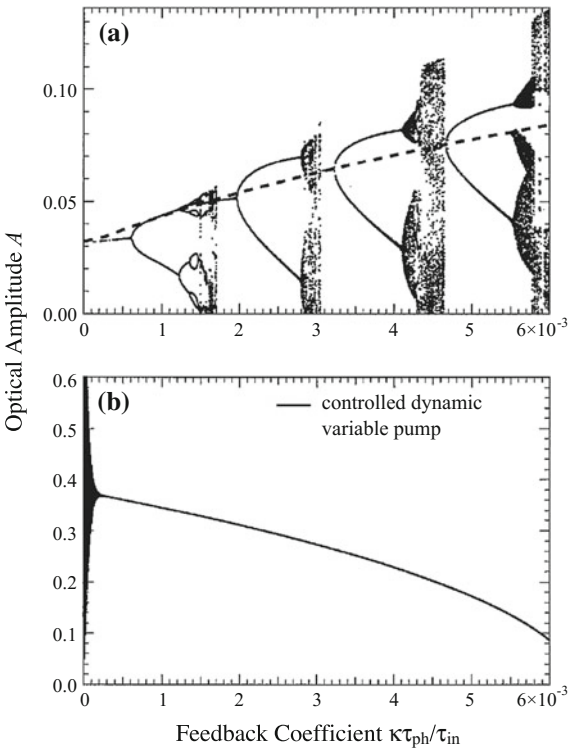

Fig. 9.12 **a** Computed bifurcation cascade for a semiconductor laser with optical feedback. The *dashed curve* shows the stabilized laser intensity as the feedback phase is adjusted by means of ω_0 as the feedback strength is increased. **b** Stabilization of laser intensity by varying the injection current by $\Delta S = 0.17\Delta\omega_0$ (corresponding to 1.1 GHz/mA). The intensity is stabilized and falls off as the injection current is decreased. The parameter conditions are $L = 15$ cm, $\omega_0\tau = -1.45$ rad, and $\alpha = 4$. The feedback ratio here is defined by $\kappa\tau_{ph}/\tau_{in}$. The conversion relation from the injection current to the optical frequency $\delta J = 0.085(\tau_s/\tau_{ph})G_n ed\Delta\omega_0$ is used [after Hohl and Gavrielides (1998); © 1998 OSA]

References

A. Arimoto, M. Ojima, N. Chinone, A. Oishi, T. Gotoh, N. Ohnuki, Optimum conditions for the high frequency noise reduction method in optical videodisk system. Appl. Opt. **25**, 1398–1403 (1986)

M. Ciofini, A. Labate, R. Meucci, M. Galanti, Stabilization of unstable fixed points in the dynamics of a laser with feedback. Phys. Rev. E **60**, 398–402 (1999)

G.R. Gray, A.T. Ryan, G.P. Agrawal, E.C. Gage, Control of optical-feedback-induced laser intensity noise in optical data recording. Opt. Eng. **32**, 739–745 (1993)

A. Hohl, A. Gavrielides, Experimental control of a chaotic semiconductor laser. Opt. Lett. **23**, 1606–1608 (1998)

E.R. Hunt, Stabilizing high-period orbits in a chaotic system: the diode resonator. Phys. Rev. Lett. **67**, 1953–1955 (1991)

N. Kikuchi, Y. Liu, J. Ohtsubo, Chaos control and noise suppression in external-cavity semiconductor lasers. IEEE J. Quantum Electron. **33**, 56–65 (1997)
A. Kittel, K. Pyragas, R. Richter, Prerecorded history of a system as an experimental tool to control chaos. Phys. Rev. E **50**, 262–268 (1994)
Y. Liu, J. Ohtsubo, Experimental control of chaos in a laser-diode interferometer with delayed feedback. Opt. Lett. **19**, 448–450 (1994)
Y. Liu, J. Ohtsubo, Dynamics and chaos stabilization of semiconductor lasers with optical feedback from an interferometer. IEEE J. Quantum Electron. **33**, 1163–1169 (1997)
Y. Liu, N. Kikuchi, J. Ohtsubo, Controlling of dynamical behavior of semiconductor lasers with external optical feedback. Phys. Rev. E **51**, R2697–R2700 (1995)
Y. Liu, J. Ohtusbo, S.Y. Ye, Dynamical and coherent characteristics of semiconductor lasers with external optical feedback. SPIE Proc. **2886**, 120–127 (1996)
A.V. Naumenko, N.A. Loiko, S.I. Turovets, P.S. Spencer, K.A. Shore, Controlling dynamics in external-cavity laser diodes with electronic impulsive delayed feedback. J. Opt. Soc. Am. B **15**, 551–561 (1998)
J. Ohtsubo, Chaos and control in semiconductor lasers (Chap. 22), in *Handbook of Chaos Control*, ed. by E. Schöll, G. Schuster (Wiley, Weinheim, 2008)
E. Ott, C. Grebogi, J.A. Yorke, Controlling chaos. Phys. Rev. Lett. **64**, 1196–1199 (1990)
K. Petermann, *Laser Diode Modulation and Noise* (Kluwer Academic, Dordrecht, 1988)
K. Pyragas, Continuous control of chaos by self-controlling feedback. Phys. Lett. A **170**, 421–428 (1992)
K. Pyragas, Predictable chaos in slightly perturbed unpredictable chaotic systems. Phys. Lett. A **181**, 203–210 (1993)
K. Pyragas, Control of chaos via an unstable delayed feedback controller. Phys. Rev. Lett. **86**, 2265–2268 (2001)
F. Rogister, P. Mégret, O. Deparis, M. Blondel, T. Erneux, Suppression of low-frequency fluctuations and stabilization of a semiconductor laser subjected to optical feedback from a double cavity: theoretical results. Opt. Lett. **24**, 1218–1220 (1999)
F. Rogister, D.W. Sukow, A. Gavrielides, P. Mégret, O. Deparis, M. Blondel, Experimental demonstration of suppression of low-frequency fluctuations and stabilization of an external-cavity laser diode. Opt. Lett. **25**, 808–810 (2000)
R. Roy, T.W. Murphy, T.D. Maier, Z. Gills, E.R. Hunt, Dynamical control of a chaotic laser: experimental stabilization of a globally coupled system. Phys. Rev. Lett. **68**, 1259–1262 (1992)
F.R. Ruiz-Oliveras, A.N. Pisarchik, Phase-locking phenomenon in a semiconductor laser with external cavities. Opt. Express **14**, 12859–12866 (2006)
E. Schöll, H.G. Schuster, *Handbook of Chaos Control* (Wiley, Weinheim, 2008)
Y. Takiguchi, Y. Liu, J. Ohtsubo, Low-frequency fluctuation induced by injection-current modulation in semiconductor lasers with optical feedback. Opt. Lett. **23**, 1369–1371 (1998)
Y. Takiguchi, Y. Liu, J. Ohtsubo, Low-frequency fluctuations and frequency-locking in semiconductor lasers with optical feedback. Opt. Rev. **6**, 339–401 (1999a)
Y. Takiguchi, Y. Liu, J. Ohtsubo, Low frequency fluctuation in semiconductor lasers with long external cavity feedback and its control. Opt. Rev. **6**, 424–432 (1999b)
Y. Takiguchi, H. Fujino, J. Ohtsubo, Experimental synchronization of chaotic oscillations in external cavity semiconductor lasers in low-frequency fluctuation regime. Opt. Lett. **24**, 1570–1572 (1999c)
Y. Takiguchi, H. Kan, J. Ohtsubo, Modulation induced low-frequency fluctuations in semiconductor lasers with optical feedback and their suppression by synchronous modulation. Opt. Rev. **9**, 234–237 (2002)
S.I. Turovets, J. Dellunde, K.A. Shore, Nonlinear dynamics of a laser diode subjected to both optical and electronic feedback. J. Opt. Soc. Am. B **14**, 200–208 (1997)
A. Uchida, T. Sato, T. Ogawa, F. Kannari, Characteristics of transients among periodic attractors controlled by high-frequency injection in a chaotic laser diode. IEEE J. Quantum Electron. **35**, 1374–1381 (1999)
J. Wieland, C.R. Mirasso, D. Lenstra, Prevention of coherence collapse in diode lasers by dynamic targeting. Opt. Lett. **22**, 469–471 (1997)

Chapter 10
Stabilization of Semiconductor Lasers

Abstract Chaos and instabilities are not only the effects in semiconductor lasers with external perturbations. Semiconductor lasers are also strongly stabilized by external perturbations under appropriate parameter conditions. Optical injection from a different laser is a typical example of laser stabilizations. Other examples are weak or strong optical feedback, phase-conjugate optical feedback, grating optical feedback, and optoelectronic feedback. The longitudinal and transverse modes, frequency, power, and polarizations of semiconductor lasers are stabilized by external perturbations. Stabilizations are especially important in newly developed semiconductor lasers (VCSELs, broad-area semiconductor lasers, laser arrays, and so on), since these lasers involve instabilities even in their solitary oscillations. In this chapter, stabilization and control of semiconductor lasers are discussed based on rather simple configurations of external perturbations. Other than these examples, we present laser stabilizations using photonic structures and quantum-dot structures for newly developed lasers. The control methods introduced here may not be chaos control discussed in the previous chapter, but they are closely related to the ideas of dynamic and chaos controls in semiconductor lasers.

10.1 Linewidth Narrowing by Optical Feedback

10.1.1 Linewidth Narrowing by Strong Optical Feedback

The spectral line of edge-emitting semiconductor laser usually has a width of several to several tens of MHz even its solitary oscillation, which is 100 times larger than ordinary lasers. Such broad spectral linewidth mainly originates from the existence of a non-zero linewidth enhancement factor known as the α parameter, which is discussed in Sect. 3.6.6. For applications for coherent optical communications and coherent optical measurements, it is essential to use frequency-stabilized and narrow-linewidth light sources. The linewidth of a solitary narrow-stripe edge-emitting semiconductor laser is determined by the device parameters and given by (3.130) as $\Delta\nu = R_{sp}(1 + \alpha^2)/(4\pi S)$. Therefore, we can

© Springer International Publishing AG 2017

J. Ohtsubo, *Semiconductor Lasers*, Springer Series in Optical Sciences 111,
DOI 10.1007/978-3-319-56138-7_10

reduce the linewidth by appropriate designs for a semiconductor laser; the use of semiconductor materials with small α parameter, lower spontaneous emission rate R_{sp}, and higher bias injection current (higher photon rate). As a different technique, the linewidth of semiconductor lasers can be reduced by weak optical feedback as discussed in Sect. 5.1.3. The linewidth narrowing induced by optical feedback is realized within the ranges of feedback regimes II–III and the linewidth is reduced by a factor of two or three from that of the solitary laser. However, with the increase of optical feedback level, the semiconductor laser is destabilized by the feedback and shows instabilities in feedback regime IV. As a result, the linewidth is much broadened of the order of GHz and the laser finally reaches coherence collapse state. On the contrary, further increase of the optical feedback level over several percents in amplitude, the laser is again stabilized by strong optical feedback and the linewidth is greatly reduced compared with the solitary oscillation linewidth. This effect can be used for laser stabilization. Many studies for linewidth narrowing induced by strong optical feedback in semiconductor lasers have been reported previously (Fleming and Mooradian 1981; Patzak et al. 1983; Wyatt and Devlin 1983; Chraplyvy et al. 1986; Kazarinov and Henry 1987; Tromborg et al. 1987). By using a complex feedback system and careful tuning of the system, Stoehr et al. (2006) achieved ultra-narrow linewidth control as small as 1 Hz. They used a complex system consisting of a semiconductor laser locked in a single stage to a stable high-finesse reference cavity. The phase locking technique with the combination of optical feedback and injection were frequently used for realizing ultra-narrow linewidth and the method is promising for applications in optical communications. However, we discuss here rather simple optical feedback systems for linewidth narrowing in semiconductor lasers.

First, we discuss the linewidth in semiconductor lasers with strong optical feedback (regime V) from a plain reflector. For narrowing the linewidth of a semiconductor laser, the combination of a low front facet reflectivity and a high back facet reflectivity, which are achieved by antireflection (AR) coating techniques, is frequently used to perform the effective reduction of the linewidth. Strong optical feedback is applied to such an AR-coated semiconductor laser. Therefore, we assume different internal reflectivities for the front and back facets as r_1 and r_2, respectively. Then, the composite reflectivity at the front facet together with the external reflector, which was already discussed in (4.25), can be written by

$$r_{\mathrm{eff}} = \frac{r_1 + r\exp(i\omega_0\tau)}{1 + r_1 r\exp(i\omega_0\tau)} \tag{10.1}$$

For a small external reflectivity r, (10.1) reduces to (4.26) corresponding to a weak optical feedback case. According to (4.32), the linewidth in the presence of optical feedback is given by

$$\Delta\nu_{ex} = \frac{\Delta\nu}{F^2} = \frac{R_{sp}(1+\alpha^2)}{4\pi S_s F^2} \tag{10.2}$$

where S_s represents the steady-state solution for the laser intensity in the presence of optical feedback. The linewidth narrowing factor F is calculated from (Tromborg et al. 1987)

$$F = 1 + \frac{\alpha}{\tau_{in}}\mathrm{Re}\left[\frac{d\ln r_{eff}}{d\omega_0}\right] - \frac{1}{\tau_{in}}\mathrm{Im}\left[\frac{d\ln r_{eff}}{d\omega_0}\right] \tag{10.3}$$

The above equations can be applied to general cases of optical feedback level and the factor F reduces (4.33) for a weak optical feedback in regimes II and III. However, for strong optical feedback, we must use the reflectivity r_{eff} in (10.1). It is noted that the above relations are only valid for stable oscillations of semiconductor lasers and they are not applicable to chaotic oscillations in feedback regimes III–IV. As discussed above, a low front facet reflectivity is sometimes used for the linewidth reduction. In the limit of $r_1 = 0$, the composite reflectivity reads $r_{eff} = r\exp(i\omega_0\tau)$ and the resulting linewidth is given by

$$\Delta\nu_{ex,min} = \frac{\Delta\nu}{\left(1+\frac{\tau}{\tau_{in}}\right)^2} \tag{10.4}$$

For $\tau/\tau_{in} \gg 1$, the above equation is approximated as

$$\Delta\nu_{ex,min} = \frac{\Delta\nu}{\left(\frac{\tau}{\tau_{in}}\right)^2} \tag{10.5}$$

For example, the linewidth of a solitary semiconductor laser can be reduced to 1/1000 by appropriately choosing the optical feedback level, the external cavity length, and the front facet reflectivity.

Figure 10.1 shows the instance of linewidth narrowing by strong external optical feedback (Patzak et al. 1983). The solid lines represent the numerical results for the linewidth as a function of R_1 for different external reflectivities of $R = r^2$ normalized at that for $R_1 = r_1^2 = 0$. The laser assumed is an InGaAsP laser with an oscillation wavelength of 1.5 μm and the internal cavity length of 190 μm. The external cavity length is set to be 20 cm. The minimum linewidth of $\Delta\nu_{ex,min}$ is 2 kHz. The solid circle in the figure is the experimental result for a strong optical feedback in the reference (Wyatt and Devlin 1983). The experimental conditions of the used laser system are $R_1 = 0.04$ and $R = 0.04$. The reduced linewidth of 10 kHz in the experiment is well coincident with the theoretical expectation. The linewidth of the solitary laser is ~10 MHz and the linewidth is reduced at a factor of three by the strong optical feedback. As another example, Chraplyvy et al. (1986) also conducted an experiment for linewidth reduction by strong optical feedback for an

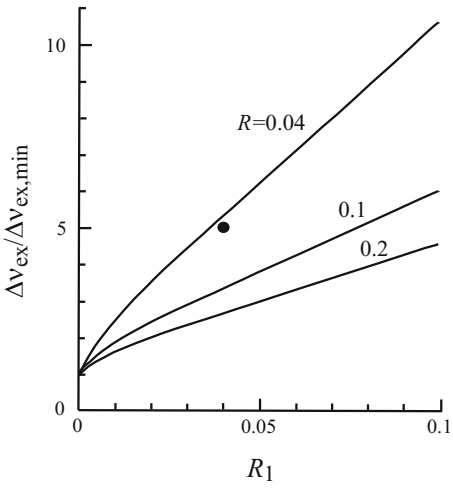

Fig. 10.1 Numerical simulations for the normalized linewidth of a semiconductor laser as a function of the facet reflectivity $R_1 = r_1^2$. $\Delta\nu_{ex,min}$ = 2 kHz is the minimum linewidth for $R_1 = r_1^2 = 0.04$, $R_2 = r_2^2 = 0.31$, and $R_2 = r_2^2 = 0.04$. *Solid circle* is the experimental result [after Patzak et al. (1983); © 1983 IEE]

InGaAsP DFB laser with an oscillation wavelength of 1.5 μm and internal cavity length of 250 μm. Under the conditions of the internal reflectivity of 0.04, the external cavity length of 18 cm, and the external reflectivity of 0.16, they obtained a linewidth of 40 kHz for the original oscillation linewidth of ∼10 MHz. The reduction of the linewidth by a factor of three is typical in this method.

10.1.2 Linewidth Narrowing by Grating Feedback

Grating optical feedback is used for the purpose of the selection of longitudinal modes and the stabilization for the selected mode in semiconductor lasers. We have already introduced the dynamic properties induced by grating optical feedback in semiconductor lasers in Sect. 5.5. In the previous discussion, we presented the theoretical background of the dynamics of grating feedback and showed some numerical results. Here, we show some experimental results for grating feedback in semiconductor lasers from a viewpoint of linewidth narrowing. The essential effects in grating feedback are the same as those of optical feedback from a plain mirror. However, grating feedback enables desirable frequency selection for the laser oscillations, side-mode suppressions, and lowering the frequency jitter. Figure 10.2 shows the example of linewidth narrowing by grating feedback in a semiconductor laser for different three external cavity lengths of L = 25, 50, and 100 cm (Olesen et al. 1983). The used laser is a single-mode InGaAsP semiconductor laser of cleaved facets with the oscillation wavelength of 1.55 μm and the internal cavity length of 310 μm. The laser stably oscillates in a single mode less than the bias injection current of $1.8J_{th}$, but it oscillates at a multimode over that injection current. The linewidth of the free-running laser is rather large and it is 45 MHz. The grating mirror is a diffraction grating of 600 grooves/mm and the blaze wavelength of

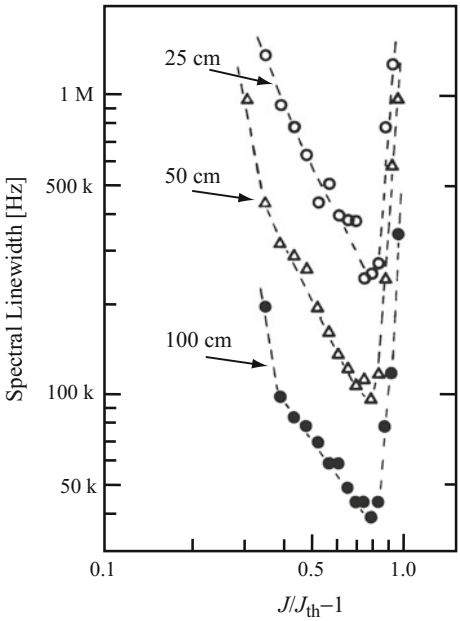

Fig. 10.2 Linewidth reduction for the bias injection current in a semiconductor laser with grating optical feedback for the external cavity lengths of 25, 50, and 100 cm [after Olesen et al. (1983); © 1983 JSAP]

1.25 μm, arranged in a Littrow configuration. The external cavity length (external phase) is finely tuned over a few micron-meter using a piezo-electric element in the optical feedback loop. The estimated optical feedback fraction is around 10^{-4} in intensity, so that the feedback corresponds to weak to moderate optical feedback. In Fig. 10.2, the linewidth inversely proportional to the bias injection current, which is consistent with the relation in (10.2). The linewidth is also reduced by the increase in the external cavity length in accordance with the increase of the C parameter. Over the bias injection current of $1.8J_{th}$, the linewidth of the laser rapidly increases due to multimode oscillations. In this example, the minimum linewidth of 40 kHz is achieved by the grating optical feedback under the conditions of the external cavity length of L = 100 cm and the bias injection current at $1.79J_{th}$. Except for the conventional plain grating mirror, fiber Bragg grating, and volume holographic grating are used as alternative feedback mirrors (Naumenko et al. 2003; Ewald et al. 2005). Ewald et al. (2005) demonstrated linewidth reduction up to 7 kHz using optical feedback from a volume holographic grating for a no special AR-coated semiconductor laser operating at the oscillation wavelength of 852 nm.

10.1.3 Linewidth Narrowing by Phase-Conjugate Optical Feedback

Phase-conjugate optical feedback discussed in Chaps. 4 and 5 can also be used as the linewidth control of semiconductor lasers. For phase-conjugate mirrors, they are

categorized into fast or slow response natures with respect to the response time of semiconductor lasers (mainly carrier response time of semiconductor lasers). The dynamics of respective phase-conjugate effects are different with each other. However, in either case, a spatial phase-conjugate wave is generated from a phase-conjugate mirror, so that the method has the advantages of self-alignment and aberration correction through the optical components. It is expected that these properties will result in good coupling back into the laser and give rise to the active use for the laser stabilization. In the strict sense, instantaneous phase-conjugate mirror is not available and we must more or less consider the effects of finite response of phase-conjugate mirror. Therefore, slow response phase-conjugate mirror, such as $BaTiO_3$ photorefractive crystal, is used for the purpose of alignment free optical feedback due to the generation of only a spatial phase-conjugate wave. Many studies for the stabilization of semiconductor lasers with phase-conjugate optical feedback were reported (Vahala et al. 1986; Kürz and Mukai 1996; Kürz et al. 1996; Liby and Statman 1996; Vainio 2006).

First, we discuss the linewidth narrowing induced by fast response phase-conjugate mirror in semiconductor lasers. Kürz and Mukai (1996) and Kürz et al. (1996) employed a broad-area semiconductor laser as a fast phase-conjugate device. Figure 10.3 shows the experimental setup of the system. An AlGaAs broad-area semiconductor laser, which is biased at less than but very close to the threshold, is pumped by a frequency-stabilized tunable semiconductor laser and a probe beam from a semiconductor laser to be stabilized is injected to the broad-area laser. The phase-conjugated wave is generated from the broad-area laser and it is fed back into the probe laser. The frequency from the pump laser is appropriately chosen and it is stabilized less than the oscillation linewidth of 20 kHz. The front and back facet reflectivities of the broad-area laser are 0.05 and 0.95, respectively, to generate easily a phase-conjugate wave. Since the stripe width of the broad-area laser is wide and is 50 μm, the probe beam can be injected at a non-zero angle with respect to the pump beam, which causes the emission of amplified pump, probe, and phase-conjugate signals in distinct spatial direction. The pump beam, back

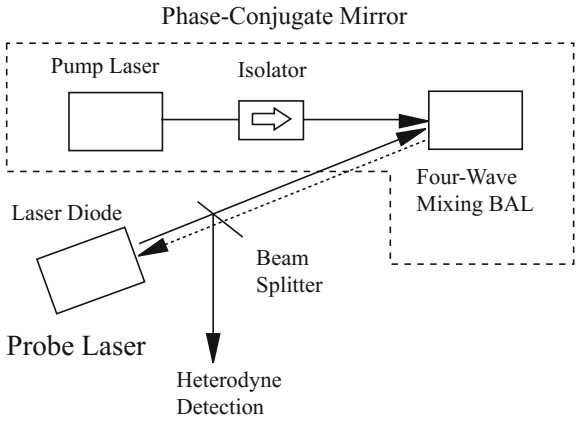

Fig. 10.3 Experimental setup for stabilizing a semiconductor laser with phase-conjugate optical feedback from a four-wave mixing broad-area semiconductor laser (BAL)

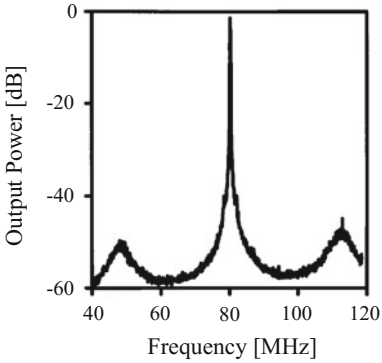

Fig. 10.4 Power spectrum of a stabilized semiconductor laser measured with a delayed self-heterodyne technique [after Kürz and Mukai (1996); © 1996 OSA]

reflected beam from the back facet, and probe beam conform to a four-wave mixing configuration and the phase-conjugate wave is generated back to the laser to be controlled. Using the broad-area semiconductor laser as a phase-conjugate material, the external incidence angle of 5.2° is possible in this configuration, which corresponds to the internal angle of 1.4° between the pump and probe beams. The response time is dependent on the carrier lifetime and the diffusion constant of the carrier density grating inside the broad-area laser. The response time of the phase-conjugate mirror is estimated around 1 ns. The probe laser, which is the stabilized laser, is an uncoated single-stripe semiconductor laser with the oscillation wavelength of 830.6 nm. The free-running laser has a linewidth of 5 MHz at the bias injection current with the mode suppression ratio of 30 dB.

Figure 10.4 shows the experimental result of the linewidth narrowing (Kürz and Mukai 1996). The broad-area semiconductor laser is biased at 98% of the threshold and as small as less than 1% of the probe laser power is injected to the broad-area laser, giving a phase-conjugate reflectivity of 6%. The observed phase-conjugate feedback to the probe laser is about 1 μW (6×10^{-5} of its output power). Figure 10.4 is the power spectrum measured by a delayed self-heterodyne technique. The observed spectral linewidth is 25 kHz, which is close to the instrument resolution of 14 kHz in this measurement. The strong side-mode suppression of 50 dB is also visible in the figure, thus not only the linewidth narrowing but also the reduction of the side-mode suppression ratio is attained by the phase-conjugate optical feedback. The dependence of the side-mode frequency separation $c/4L$ ($L = 2.29$ m corresponding to the side-mode frequency separation of 32.7 MHz) confirmed that the origin of the spectral narrowing comes not from conventional optical feedback effect (for the conventional case, this would be $c/2L$) but phase-conjugate optical feedback effect. In spite of such long external cavity length, the laser is stabilized more than for hours due to the phase-conjugate optical feedback.

Contrary to the case of fast phase-conjugate optical feedback, the effects of spatial phase-conjugation are only dominant for the dynamics of semiconductor lasers with a slow-response phase-conjugate reflector. Therefore, the linewidth of

semiconductor laser with slow response phase-conjugate optical feedback is written by the similar form as the case of conventional optical feedback as

$$\Delta\nu_{\mathrm{pc}} = \frac{\Delta\nu}{\left\{1 + C\cos\left(\phi_{\mathrm{pc}} + \tan^{-1}\alpha\right)\right\}^2} \tag{10.6}$$

where $\Delta\nu$ is again the oscillation linewidth for a solitary semiconductor laser. We assume a weak phase-conjugate optical feedback in the above equation. In conventional optical feedback from a plain reflector, the constant phase ϕ_{pc} in (10.6) is replaced by $\omega_s\tau$, where ω_s is the steady-state value of the oscillation frequency and τ is the round-trip time of light in the feedback loop. Therefore, the linewidth from a conventional optical feedback shows a periodic change for the increase or decrease of the external mirror position. However, the phase-conjugate feedback is phase insensitive as has already been discussed in Chaps. 4 and 5, even for a slow response phase-conjugate mirror. The phase is determined by the boundary conditions of the laser and the device characteristics of the phase-conjugate mirror. We can assume the constant phase as integer multiple of 2π, i.e., $\phi_{\mathrm{pc}} = 2\,m\pi$. Then, the linewidth monotonically decreases for the increase of the length of the phase-conjugate mirror, since the C parameter is simply proportional to the delay time τ. For $\phi_{\mathrm{pc}} = 2\,m\pi$, the reduced linewidth is given by

$$\Delta\nu_{\mathrm{pc}} = \frac{\Delta\nu}{\left(1 + \kappa\frac{\tau}{\tau_{\mathrm{in}}}\right)^2} \tag{10.7}$$

In actual fact, the reflected light at the phase-conjugate mirror has a constant phase shift, so that we must take into account this effect. When the phase shift satisfies the condition as $\phi_{\mathrm{pc}} + \tan^{-1}\alpha = 2\,m\pi$, one obtains the minimum spectral linewidth given by

$$\Delta\nu_{\mathrm{pc}} = \frac{\Delta\nu}{(1 + C)^2} \tag{10.8}$$

Several experimental studies for linewidth narrowing in semiconductor lasers with slow response phase-conjugate optical feedback have been reported (Vahala et al. 1986; Liby and Statman 1996; Vainio 2006). For example, using an uncoated single-mode semiconductor laser with optical feedback from a photorefractive $BaTiO_3$ mirror, the linewidth is reduced one-tenth of that of the free-running laser (Liby and Statman 1996). In this example, the system has a four-wave mixing configuration and the power reflectivity of 0.2% is used. The linewidth reduction is not only the effect of phase-conjugate optical feedback. Another important aspect is the elimination of frequency jitter of the laser oscillations. The fact comes from the slow-response of the photorefractive mirror. Any jitter from the central lasing frequency does not have enough time to write a new holographic grating. Only that central frequency is coupled back into the laser. Due to static gratings compared to

the dynamics of the laser fluctuation, long-term frequency stability is achieved. Vainio (2006) attained the linewidth reduction as small as 25 kHz in an anti-reflection-coated semiconductor laser with strong phase-conjugate optical feedback from a Ce-doped $BaTiO_3$ photorefractive mirror. Since the front facet of the internal reflectivity is as very small as 10^{-4} in this case, strong feedback is realized with relatively small phase-conjugate signal from a self-pumped phase-conjugate configuration. In this experiment, a long life frequency stability of 1.5×10^{-8} during 100 s is observed. Thus, not only the linewidth reduction, but also stable center oscillation frequency, is attained even by slow response phase-conjugate optical feedback.

10.1.4 Linewidth Narrowing by Resonant Optical Feedback

Resonant optical feedback is one of the methods for stabilization and linewidth narrowing in semiconductor lasers (Laurent et al. 1989; Li and Abraham 1989; Iannelli et al. 1993). For example, the linewidth of an AlGaAs semiconductor laser oscillating at 780 nm is stabilized to 20 Hz by a resonant optical feedback using a spectral line from a rubidium atomic vapor (Hashimoto and Ohtsu 1987). Another example, which is frequently used, is optical feedback from a Fabry–Perot resonator. Here, we introduce the stabilization of the spectral line in semiconductor lasers with resonant optical feedback from a Fabry–Perot interferometer. Figure 10.5 shows the geometry of the optical feedback locking system from a Fabry–Perot resonator. The beam from a semiconductor laser is sent through a tilted confocal Fabry–Perot interferometer to avoid the optical feedback effect of the direct reflected beam. Only the transmission-like beam (type II beam shown in the figure) is coupled with the light of the internal laser cavity. For a single-mode semiconductor laser under weak optical feedback from a Fabry–Perot resonator, the rate equations for the complex field is written by (Laurent et al. 1989)

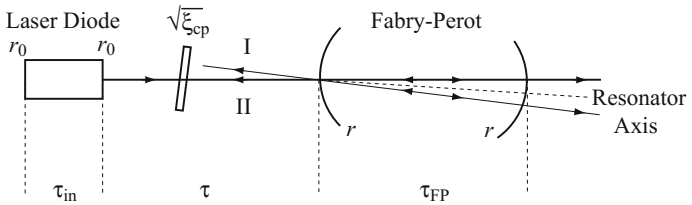

Fig. 10.5 Schematic of optical feedback locking system from a Fabry-Perot resonator. To obtain a transmission type (II) beam for the optical feedback, the resonator axis is slightly tilted, thus avoiding a reflection type (I) beam into the laser cavity

$$\frac{dE(t)}{dt} = \frac{1}{2}(1 - i\alpha)G_n\{n(t) - n_{th}\}E(t) + \sum_{m=0}^{\infty} \frac{\kappa_m}{\tau_{in}} E(t - \tau_m)\exp\{i\omega_0\tau_m - i\phi(t - \tau_m)\} \tag{10.9}$$

where the extra feedback term is the effect of multiple interferences of the beam in the Fabry–Perot resonator. Here, the m-th feedback coefficient is given by

$$\kappa_m = \sqrt{\xi_{cp}}\frac{1 - r_0^2}{r_0} r\left(1 - r^2\right)r^{4m} \tag{10.10}$$

where ξ_{cp} denotes the power mode coupling factor, $\tau_m = \tau + (2m + 1)\tau_{FP}$ is the round-trip delay time between the laser and the Fabry–Perot resonator for each reflection from the cavity (τ_{FP} being the round-trip time in the Fabry–Perot cavity), r_0 is the facet reflectivity of the semiconductor laser, and r is the mirror reflectivity of the Fabry–Perot resonator.

From a steady-state analysis similar to that in Sect. 4.2, we obtain the solution for the laser oscillation frequency as

$$\omega_{th}\tau = \omega_s\tau + C_{FP}\frac{\sin\left\{\omega_s(\tau + \tau_{FP}) + \tan^{-1}\alpha\right\} - r^4\sin\left\{\omega_s(\tau - \tau_{FP}) + \tan^{-1}\alpha\right\}}{1 + K^2\sin^2(\omega\tau_{FP})} \tag{10.11}$$

where the modified C parameter for resonant optical feedback from a Fabry–Perot resonator is given by

$$C_{FP} = \frac{\sqrt{1 + \alpha^2}}{\tau_{in}}\tau\sqrt{\xi_{FP}}\frac{1 - r_0^2}{r_0}\frac{r(1 - r^2)}{(1 - r^4)^2} \tag{10.12}$$

and the factor K is defined by

$$K = \frac{2r^2}{1 - r^4} \tag{10.13}$$

For a high-finesse Fabry–Perot $r \approx 1$, the modified C_{FP} parameter is given by

$$C_{FP} \approx \frac{\sqrt{1 + \alpha^2}}{\tau_{in}}\tau\sqrt{\xi_{FP}}\frac{1}{2}\frac{F_{FP}}{F_0} \tag{10.14}$$

where $F_{FP} \approx \pi r^2(1 - r^4)^{-1}$ and $F_0 = \pi r_0\left(1 - r_0^2\right)^{-1}$ are the finesses of the Fabry–Perot and laser cavities, respectively. Employing a similar derivation of the linewidth for a solitary laser discussed in Sect. 3.6.6, the linewidth of the laser oscillation under optical feedback from a Fabry–Perot resonator is calculated as

$$\Delta\nu_{\mathrm{FP}} = \frac{\Delta\nu}{\left(1 + 2C_{\mathrm{FP}}\frac{\tau_{\mathrm{FP}}}{\tau}\right)^2} \tag{10.15}$$

where $\Delta\nu$ is the linewidth of the free-running laser given by (3.130). For a large optical feedback $C_{\mathrm{FP}}\tau_{\mathrm{FP}}/\tau \gg 1$, the linewidth can be simply written by

$$\Delta\nu_{\mathrm{FP}} = \frac{\Delta\nu_0}{\xi_{\mathrm{FP}}\left(\frac{\tau_{\mathrm{FP}}}{\tau}\frac{F_{\mathrm{FP}}}{F_0}\right)^2} \tag{10.16}$$

where $\Delta\nu_0 = R_{\mathrm{sp}}/(4\pi S)$ is the Schawlow-Townes linewidth. The form of the linewidth is quite similar to (10.5), but it is important to note that this expression no longer contains the linewidth enhancement factor α. This means that the confocal Fabry–Perot cavity imposes the laser frequency and thereby can be interpreted as a decoupling of the phase noise to the amplitude noise.

Employing a resonant optical feedback from a Fabry–Perot interferometer, Laurent et al. (1989) demonstrated the reduction of the linewidth from 20 MHz of a free-running semiconductor laser to 4 kHz in a single-mode GaAlAs semiconductor laser. They used a GaAlAs Fabry–Perot semiconductor laser with the oscillation wavelength of 850 nm. The conditions for the linewidth narrowing are as follows: the free-spectral-range (FSR) of 375 MHz, the finesse of the Fabry–Perot of ~ 100, the cavity length of the Fabry–Perot resonator of 200 mm, and $\tau \approx 2\tau_{\mathrm{FP}}$. Several studies for linewidth narrowing of the order of kHz have been reported in semiconductor lasers with Fabry–Perot optical feedback (Dahmani et al. 1987). Zhao et al. (2012) experimentally demonstrated linewidth narrowing of 125 kHz in a grating feedback semiconductor laser at a wavelength of 689 nm. Further, applying resonant optical feedback from a high-finesse Fabry–Perot cavity to the grating feedback semiconductor laser, they realized the linewidth narrowing of 100 Hz and its instantaneous linewidth to 30 Hz. The laser phase noise is significantly reduced by more than 50 dB in the frequency range from 10 Hz to 10 kHz. While, Liang et al. (2015) used a miniature self-injection locked distributed-feedback laser at a wavelength of 1.55 μm by resonant optical feedback from a MgF_2 high-quality-factor (Q factor) crystalline whispering-gallery-mode resonator. The Q factor is as large as 6×10^9. The free running laser has 2 MHz linewidth. The resonator itself is all integrated in a single package and occupies less than 1 cm^3 volume. The system is highly stabilized for thermal drift. They realized linewidth narrowing of 30 Hz integral linewidth as well as sub-Hz instantaneous linewidth by the heterogeneously integrated, chip-scale semiconductor laser. Also, the laser phase noise is significantly reduced by more than 50 dB in the frequency range from 10 Hz to 10 kHz. The method of the resonant Fabry–Perot optical feedback provides not only narrowing the laser's linewidth but also the stabilization of the center-oscillation-frequency of the laser.

10.2 Linewidth Narrowing by Optoelectronic Feedback

In the applications of linewidth in semiconductor lasers, the method of optoelectronic feedback has the advantages of high stability, reproducibility, flexibility, and controllability over the optical feedback methods, since the feedback is negative and the noise and fluctuation induced by photons from the laser are averaged out due to the slower response of carriers than the photon lifetime. Also, the feedback loop can be designed accurately through a computer simulation, as is the case when designing conventional analog feedback electronic circuits. Here, we discuss linewidth narrowing in semiconductor lasers with negative optoelectronic feedback. Figure 10.6 shows the schematic diagram of the feedback system. The light from the laser passes through a frequency-selected Fabry–Perot resonator and detected by a photodetector. The current signal is amplified and is negatively fed back into the bias injection current of the laser. The stability of this feedback system strongly depends on the noise performance of the detector. Further, the detected signal by the photodetector fluctuates due to the fluctuation of the laser frequency, $\delta\nu(t)$, induced by the spontaneous emission in the laser cavity. The fluctuation is proportional to the laser output power P and the fluctuation of the transmittance of the Fabry–Perot interferometer $\delta T_{\mathrm{FP}}(\nu)$, namely, $\delta P = P\delta T_{\mathrm{FP}}(\nu)$. The stability of feedback is also affected by the noise performance of the photodetector and the linewidth is determined by taking into account these factors.

The variation of the minimum detectable power $\delta P_{\min}$ of the photodetector is defined from the noise theory for optical detectors (Ohtsu and Kotajima 1985). The detectors concerned here are solid-state detectors. From the theory, we can derive the relation of the signal-to-noise ratio (SNR) for a FM noise detection, $\mathrm{S/N} = \delta P/\delta P_{\min}$. For the SNR of S/N = 1, we define the minimum detectable frequency fluctuation for $\delta\nu(t)$ as $\delta\nu_{\min}$, and consider that the square of $\delta\nu_{\min}$ corresponds to the magnitude of the Allan variance for the minimum detectable FM noise. Then, we obtain the following relation between the Allan variance R_E and the minimum fluctuation $\delta\nu_{\min}$:

$$R_E(\tau) = \left\langle \frac{E(t)E^*(t+\tau)}{|E(t)|^2} \right\rangle = \exp\left\{ i2\pi\nu_0\tau - 2(\pi\tau)^2 \cdot \sigma_F^2(\tau) \right\} \tag{10.17}$$

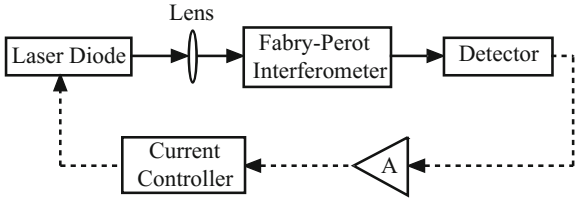

Fig. 10.6 Schematic diagram of an optoelectronic feedback system for the stabilization of a semiconductor laser. The *solid line* corresponds to optical path and the *broken line* to electronic connection

where $\sigma_F^2 = \delta v_{\min}^2$ is the variance of the power spectrum of the FM feedback noise and it is usually assumed to have a Gaussian variation. The Fourier transformed spectrum has a Lorentzian shape. Using these relations, the half-width of half-maximum (HWHM) of the spectral line can be calculated and finally given by (Ohtsu and Kotajima 1985)

$$\Delta v_{\mathrm{FBm}} = \frac{8}{9\pi}\left(\frac{c}{\eta_{\mathrm{FP}} L_{\mathrm{FP}}}\right)^2 \frac{(1-R_{\mathrm{FP}})^2}{R_{\mathrm{FP}}} \frac{Fk_{\mathrm{B}}T + \frac{h\nu_0}{\xi}M}{P} \tag{10.18}$$

where the subscript FP denotes for Fabry–Perot resonator, η_{FP} is the refractive index of the resonator, L_{FP} is the internal cavity length, R_{FP} is the internal reflectivity of resonator mirrors, F is the noise figure of the detector, k_{B} is the Boltzmann constant, T is the temperature, M is the excess noise factor, ξ is the quantum efficiency of the laser, and P is the incident light power into the Fabry–Perot resonator.

Figure 10.7 shows the numerical result of the attainable minimum linewidth Δv_{FBm} of the feedback system for the reflectance of the Fabry–Perot resonator calculated from (10.18) (Ohtsu and Kotajima 1985). Typical values of the excess noise factors for an avalanche photodiode (APD) $M = 9$ and a PIN photodiode $M = 1$ are used in the numerical calculations. The minimum linewidth is reduced by the increase of the reflectance and strongly depends on the excess noise factor. From Fig. 10.7, the linewidth can be ultimately reduced to a value less than 1 kHz when $L_{\mathrm{FP}} = 10$ mm and $R_{\mathrm{FP}} > 0.9$. This makes the electrical feedback a quite promising technique to realize an ultra-narrow linewidth. Figure 10.8 shows the experimental results of oscillation linewidths for the variation of the normalized injection current for different reflectances of the Fabry–Perot interferometer (Ohtsu and Kotajima 1985). The laser used is a single-mode DFB semiconductor laser with the oscillation wavelength of 1.50 μm. Two types of Fabry–Perot filters consisted of rod of fuzed silica with the cavity lengths of 10 mm are used and the reflectance of the interferometers are $R_{\mathrm{FP}} = 0.90$ and 0.95. The gain and bandwidth of the

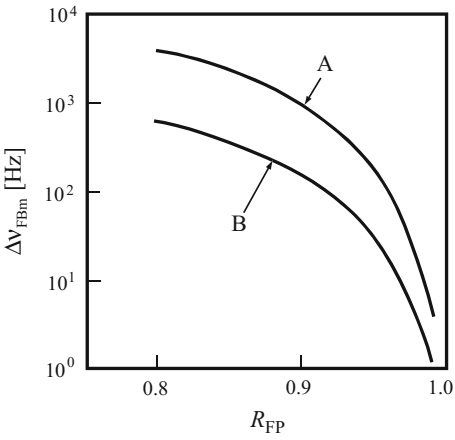

Fig. 10.7 Attainable linewidth reduction for the reflectance of the Fabry–Perot interferometer. **a** Ge-APD detector, and **b** Ge-PIN detector. The parameters are $T = 293$ K, $\nu_0 = 2 \times 10^{14}$ Hz, $P = 3$ mW, $n_{\mathrm{FP}} = 1.4$, $L_{\mathrm{FP}} = 10$ mm, $F = 25$, $\eta = 0.73$ [after Ohtsu and Kotajima (1985); © 1985 IEEE]

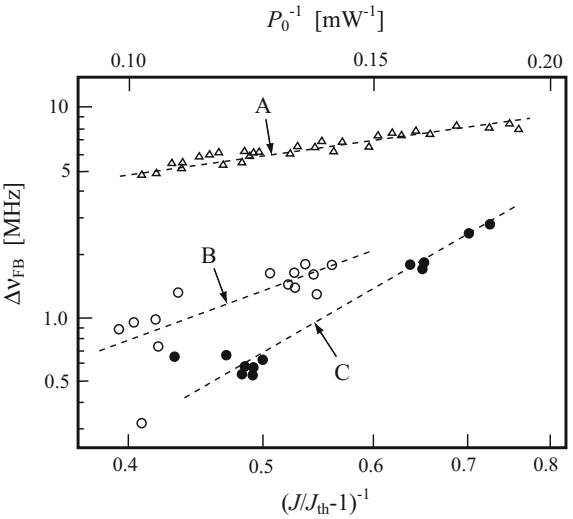

Fig. 10.8 Linewidth for the inverse of the normalized injection current for different reflectances of the Fabry–Perot interferometer. *A* Solitary sate, *B* $R_{FP} = 0.9$, and *C* $R_{FP} = 0.95$ [after Ohtsu and Kotajima (1985); © 1985 IEEE]

amplifier in the electronic feedback circuit are 30 dB and 100 MHz, respectively, and the feedback delay of the circuit is 13 ns. Depending on the reflectivity of the Pabry-Perot mirrors, a power law is established for the normalized injection current (namely the laser output power). A linewidth narrower than 1 MHz is obtained by feedback and the minimum linewidth in this graph is 330 kHz. Modifying the experimental system, Ohtsu et al. (1990) demonstrated a linewidth reduction of 560 Hz for an AlGaAs laser of 830 nm wavelength by optoelectronic feedback and for the cavity length of the Fabry–Perot resonator of 30 mm. The original linewidth of the free-running laser is 3.45 MHz, so that the reduction of factor of four is achieved in this experiment.

10.3 Stabilization in Lasers with Various Structures

10.3.1 Noise Suppression in Self-pulsation Semiconductor Laser

Noise suppression in semiconductor lasers caused by external perturbations is an important issue not only for narrow-stripe edge-emitting lasers but also for other newly developed semiconductor lasers. We showed some numerical results for the dynamics of self-pulsating semiconductor laser subjected to coherent optical feedback in Sect. 8.2. The noise performance of self-pulsating semiconductor lasers with optical feedback is strongly dependent on the external cavity conditions. Figure 10.9 shows the calculated relative intensity noises (RINs) under different feedback condition (Yamada 1998). The RIN at solitary oscillation is well below the required

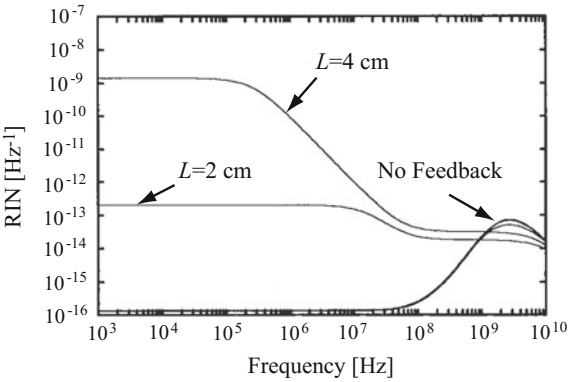

Fig. 10.9 RIN of a self-pulsating semiconductor laser in the presence of optical feedback at $J = 1.69J_{th}$. The feedback ratio is 3.33% [after Yamada (1998); ©1998 IEICE]

noise level for the use of optical data storage systems and the noise is only enhanced close to the relaxation oscillation frequency. However, for the optical feedback at 3.3% in amplitude and the external reflector length of $L = 4$ cm ($\tau = 0.27$ ns), the noise level of the lower frequency component increases up to −90 dB/Hz. The laser at this noise level cannot be used for a light source in optical data storage systems (the tolerance for external feedback noise is less than −125 dB/Hz). On the contrary, the feedback noise is greatly suppressed by as much as less than −130 dB/Hz at the external cavity length of $L = 2$ cm ($v = 0.13$ ns), which is below the noise level required in optical data storage systems. The essence of chaos control is that a chaotic state is shifted to a periodic or a fixed state (saddle node points) embedded in the chaotic sea in the parameter space by a small perturbation to the parameters. The operation point may not be always situated close to such unstable saddle node points. When the state is close enough to the unstable saddle node points, the control is successful. However, it would fail when the state is far from such points. The origin of instability induced by optical feedback in self-pulsating semiconductor laser is explained by the inappropriate combination of the operating condition of the system including the laser device parameters. Therefore, it is not easy to suppress optical feedback noise only from the design of the parameters and structure of semiconductor devices. We must consider the whole system for the optimizing operation condition for the use of self-pulsating semiconductor lasers in optical data storage systems.

10.3.2 Stabilization of VCSELs

Semiconductor laser is essentially a stable class B laser; however, it is only true for narrow-stripe edge-emitting lasers in the absence of external perturbations, which are described by simple rate equations with time development. Newly developed semiconductor lasers have additional degrees of freedom compared with ordinary narrow-stripe edge-emitting semiconductor lasers and they are not stable lasers any

more. They show unstable chaotic oscillations without any external perturbations as discussed in Chap. 8. Therefore, the stabilization in those lasers even in their solitary oscillations is an important issue in practical applications. Those lasers are either stabilized by external control or by installation of some control structures inside the device. To reduce unstable oscillations, the idea of chaos control is still effective for stabilizing those lasers. In VCSELs, the linewidth narrowing and the stabilization of the spatial modes are important and the lasers are controlled by optical feedback and optical injection in the same manner as those for narrow-stripe edge-emitting semiconductor lasers. A VCSEL usually oscillates at the lowest fundamental spatial mode, when it is biased close to the threshold. However, depending on the device parameters, the laser may show a polarization switching between two polarization modes even for a single spatial mode oscillation. With the increase of the bias injection current, higher spatial modes are ready to oscillate and the instability of the laser increases. Therefore, the control and stabilization to the fundamental Gaussian mode with fixed polarization are essential in the applications of VCSELs at any bias injection current.

Optical feedback and optical injection are effective for the control and the stabilization of the polarization mode (Marino et al. 2003; Romanelli et al. 2005). In a short cavity optical feedback regime, the laser is periodically stabilized with synchronizing periodic stability enhancement for the change of the external cavity length as described in Sects. 5.4 and 8.3 (Arteaga et al. 2007). Another important issue is the stabilization of VCSELs for the injection current modulation in the presence of optical feedback, which is a possible situation for optical data storage systems. The VCSEL sometimes shows unstable oscillations due to the existence of the two perturbations. Yu (1999) conducted numerical simulations for such a model in VCSELs and discussed the stability and instability of the laser oscillations from a viewpoint of the device designs. To obtain high single-mode output power (of the order of a few milliwatts and over) within a large range of injection currents could be interesting for communication systems and optical data storage systems. For these applications, it is important to avoid multimode oscillation in large aperture devices and to control the polarization of the emitted light. This requires us to develop methods for achieving the control of the transverse and polarization modes emitted by VCSELs. Several approaches have been undertaken to increase the single-mode output power of VCSELs; increasing the cavity length, hybrid implant oxide VCSELs, surface etching, or implementing a passive anti-guide region (Marino et al. 2003). In this subsection, we present the control and stabilization both of the spatial and polarization modes to a single mode in a VCSEL using a frequency selective optical feedback from a grating mirror, even when the laser is biased at a higher injection current.

Figure 10.10 shows an experimental example of the controls by frequency selective optical feedback in a VCSEL (Marino et al. 2003). The VCSEL used has a disc diameter of 16 μm and oscillates at the wavelength of 840 nm. The laser has the threshold current of 1.6 mA. At the threshold, the VCSEL emits only in its fundamental transverse mode, but the two orthogonal polarizations are active. Figure 10.10a shows the free-running polarization-resolved optical spectra at the

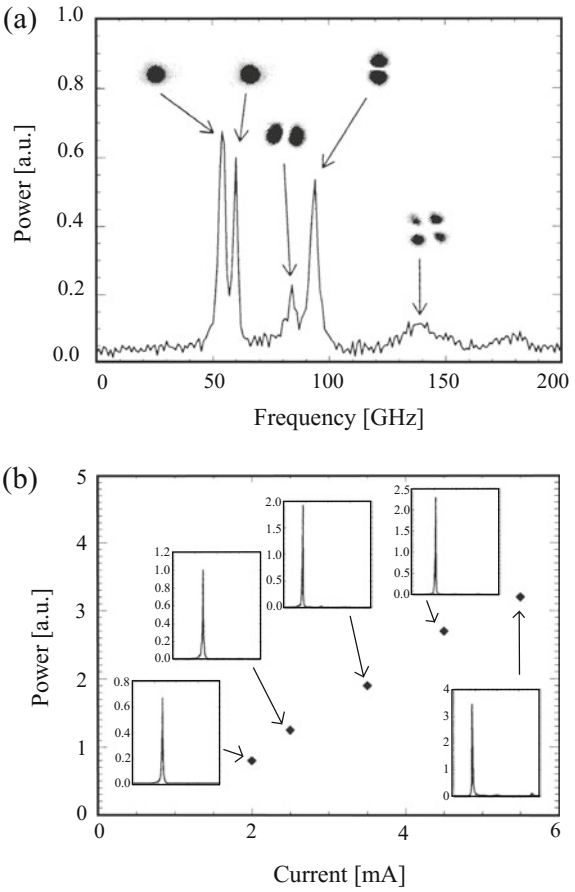

Fig. 10.10 Single-mode operation of a VCSEL induced by frequency selective optical feedback. **a** Optical spectra and frequency-resolved transverse profiles of multi-spatial-mode and polarization oscillations at free-running state. **b** Result of the control [after Marino et al. (2003); © 2003 IEEE]

bias injection current of 1.7 mA. In Fig. 10.10a, the third-order transverse mode is close to the threshold and only one of the polarization modes is visible. The separation between the two polarization modes within the same spatial component is about 10 GHz, while the successive spatial-mode separation is about 40 GHz. For the control, the emitted light from the VCSEL is optically fed back into the laser cavity using the first-order reflection of a diffraction grating in the grazing incidence configuration (Littman external cavity), thus frequency selective optical feedback is achieved. The external cavity length is 15 cm, corresponding to a free spectral range of 1 GHz. Using the frequency selective control, Marino et al. (2003) selected any of the two polarization components of a particular spatial mode among the spatial modes. For this purpose, the grating lines rotated at 45° with respect to the orthogonal polarization modes to obtain the grating efficiency for the both polarization components be the same.

From the point of view of the applications, it could be very important to optimize the single fundamental mode output power and the pump current range of stable

single-mode operation. Figure 10.10b shows the result of control of one of the polarization modes (main mode) with the fundamental transverse component. In this occasion, the polarization direction is taken to be perpendicular to the grating lines in order to have the strongest feedback as possible. The threshold reduction induced by the optical feedback is $\sim 10\%$. During the measure, the tuning mirror angle is readjusted because of the modal frequency shift due to the current change. In Fig. 10.10b, we observe the fundamental single-mode emission until $I \approx 4$ mA ($2.5I_{\mathrm{th}}$) the corresponding output power is 2.7 mW. At this current, the output power of the solitary laser is 1.9 mW and four transverse modes are emitting. Within this range of currents, the emission is stable and the polarization is perpendicular to the grating rulings. For higher injection currents, the output starts to loose stability and higher order transverse modes appear.

Other than the control of VCSELs by external optical feedback, optically pumped vertical-external-cavity surface-emitting lasers known as VECSELs are emerging as an important category of semiconductor lasers (Holm et al. 1999; Fan et al. 2006). Optical pumping of these devices allows high power (0.1–1.0 W), circularly symmetric TEM_{00} mode laser operation to be achieved without the need for post-growth processing and at modest cost. Another example is the use of the effect of external optical feedback on the transient response of anti-resonant reflecting optical waveguide (ARROW) VCSELs (Chen and Yu 2004). The proper design of ARROW can suppress the excitation of high-order transverse leaky modes, as well as increase the critical feedback strength so that stable high power single-mode operation of VCSELs can be obtained even under the influence of strong external optical feedback. The control of spatial modes using the installation of photonic structures in VCSELs, which is discussed in the following section, is categorized into this technique. The control and stabilization of spatial and polarization modes are still important issues for the applications of VCSELs.

10.3.3 Stabilization of Broad-Area Semiconductor Lasers

Control of the emission properties of broad-area semiconductor lasers is also an important issue, such as for pump source for solid-state lasers, spectroscopy, and material processing. Shaping beam profile and recovering laser coherence in broad-area semiconductor lasers are expected for the practical applications (Champagne et al. 1995; Simmendinger et al. 1999a, b; Wolff and Fouckhardt 2000; Raab and Menzel 2002; Lawrence and Kane 2002; van Voorst et al. 2006). Several schemes to control and stabilize for the emission properties of broad-area semiconductor lasers have been proposed. Some of them are based on the improvements of device structures and the others are based on external control. Examples of the latter case include injection locking in a master-slave configuration, frequency selective optical feedback, and spatial filtering optical feedback. In broad-area semiconductor lasers, we can expect the similar techniques of laser control and stabilization as those for narrow-stripe edge-emitting semiconductor

lasers. However, we must take into account unique characteristics of the dynamic properties of broad-area semiconductor lasers originated from the large stripe width. One of the instabilities that strongly affect the oscillation properties and the beam qualities is the filamentation effect discussed in Sect. 8.4. Though the filamentation is an irregular and fast phenomenon in time, it is controllable by ordinary external perturbations to broad-area semiconductor lasers. Indeed, several studies were reported for the selection and control of spatial oscillation modes using the method of optical feedback (Martín-Regalado et al. 1996; Mandre et al. 2003, 2005; Wolff et al. 2003; Chi et al. 2005). Even by such simple control, the filamentation of a broad-area semiconductor laser is greatly suppressed and the time-averaged beam profile, the oscillation linewidth, the beam profile, and the power stability, are much improved.

First, we discuss the stabilizations of unstable oscillations induced by filamentation in broad-area semiconductor lasers based on spatially filtered optical feedback. Figure 10.11 is an experimental example of chaos control of a broad-area semiconductor laser by optical feedback (Mandre et al. 2003, 2005). The laser is a broad-area semiconductor laser with the stripe width of 100 μm and the output power of 1 W operating in pulse mode to minimize thermal effects. The output power is fed back into the active region by an external mirror with a spatial filter. The spatial filtering is very simple, and is accomplished by the intrinsic beam divergence. Depending on the shape of the spatial filter (the shape of the reflecting mirror curvature), the filamentation can be controlled and even completely eliminated for a certain condition of the filter configuration. The external mirror is positioned at 10 mm from the laser facet and the reflectivity of the mirror is about 50% in intensity. The free-running laser shows unstable oscillations with filamentations like that shown in Fig. 8.32. Figure 10.11 shows a plot of near-field patterns at the laser exit face observed by a streak camera (Mandre et al. 2003). The horizontal axis is the position of the laser exit face and the vertical axis is the time development for the laser oscillation. The optical feedback is switched on at time $t = 0$ ns. Figure 10.11a shows a plot of filamentation for a lower bias injection current at $J = 1.75J_{\mathrm{th}}$, while Fig. 10.11b is for a higher injection at $J = 3.0J_{\mathrm{th}}$. For the lower bias injection current, filamentation is greatly suppressed by the feedback after a certain time lapse from the switch-on (around 8 ns) and the averaged spatial beam profile becomes almost single. For the higher bias injection current, the filamentation is not completely eliminated, however it is enough suppressed compared with filamentations under no control compared with Fig. 8.32. In usual fact, thermal lensing due to the high carrier density concentration in the active layer may increasingly affect the beam characteristics at high pump current, thus leading the degradation of the beam quality. Nevertheless, stabilization of the emission dynamics is still achieved by the scheme even at high operation currents.

Next, we show coexistence states of chaotic attractors in broad-area semiconductor lasers subjected to optical feedback. This indicates the possibility of the control for broad-area semiconductor lasers by the method of optical feedback (Fujita and Ohtsubo 2005). The coexistence states of chaotic attractors were already described in Sect. 6.2.4. Similar effects are also observed in broad-area

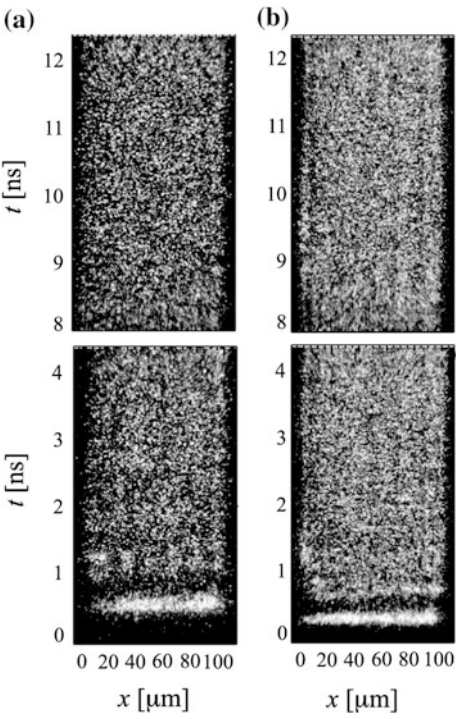

Fig. 10.11 Experimentally controlled filamentations in a broad-area semiconductor laser by spatially filtered optical feedback. Near-field patterns observed by a streak camera at the bias injection currents of **a** $J = 1.75J_{th}$ and **b** $J = 3.0J_{th}$ [after Mandre et al. (2003); © 2003 OSA]

semiconductor lasers. Figure 10.12 shows an experimental example of coexistence states of chaotic oscillations in a broad-area semiconductor lasers. The initial condition determined the convergence to one of the coexistent chaotic attractors. Once the system falls on a certain chaotic orbit, the system always goes around the same chaotic attractor. However, if the perturbation to the system is strong enough, there is a possibility of the system to switch from one chaotic orbit to another. Figure 10.12a shows a time trace in such a case. The laser is suddenly trapped to a steady-state oscillation with constant output from LFF oscillation. In this experiment, the laser alternately switches from stable to unstable oscillations for the period of several to several tens of milliseconds. When the laser shows a LFF oscillation, it oscillates at multimode as easily understood from the optical spectrum in Fig. 10.12b (upper plot). However, the optical spectrum in Fig. 10.12b (lower plot) is almost single for the constant part of the output power in Fig. 10.12a. One of typical features of broad-area semiconductor lasers is a twin-peak intensity profile of the far-field pattern as observed in Fig. 8.31. Figure 10.12c shows the twin-peak far-field pattern at the LFF oscillation in Fig. 10.12a. On the other hand, the pattern is a single lobe when the stable oscillation is achieved (Fig. 10.12d). The spatial mode of the laser oscillation is also stabilized to the lowest spatial mode. The beam profile and the coherence are easily controlled and stabilized not only by grating mirror feedback but also by conventional optical feedback and

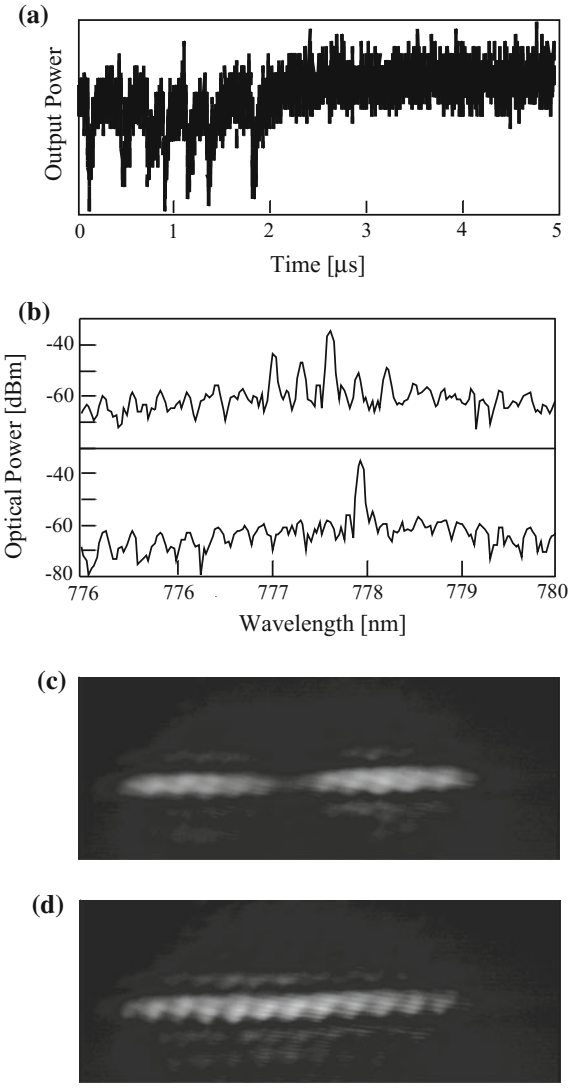

Fig. 10.12 Experimental example of coexistence states of chaotic attractors in a broad-area semiconductor laser at $J = 1.0J_{th}$. **a** Coexistence state of LFFs and stable oscillation. **b** Optical spectra at LFF state (*upper plot*) and stable oscillation (*lower plot*). Near-field spatial patterns at **c** LFF state and **d** stable oscillation. The stripe width of the laser is 50 μm. The external cavity length is $L = 30$ cm and the feedback strength is 5% of the average intensity

phase-conjugate feedback (Lawrence and Kane 2002; van Voorst et al. 2006; Gaciu et al. 2007). As already discussed in Sect. 8.4.3, the control of delayed optical feedback by spatial-mode selection and mode reduction is also effective for shaping the beam profile of broad-area semiconductor lasers (see Fig. 8.36). The control of the beam qualities of broad-area semiconductor lasers is important for practical applications and is still an ongoing issue.

The method of optical injection is also effective for suppression of filamentations and shaping of the beam profile in broad-area semiconductor lasers (Kaiser et al. 2004; Takimoto et al. 2009). As discussed in Sect. 8.4.4, the higher spatial modes

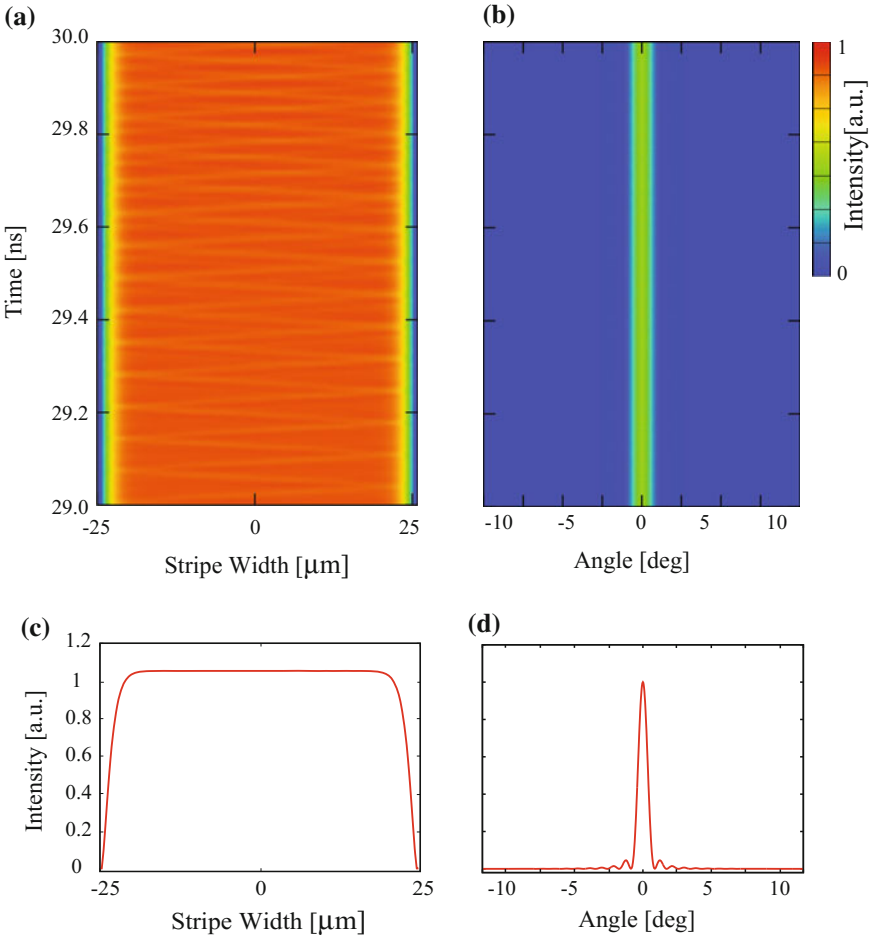

Fig. 10.13 Numerical beam shaping by optical injection. **a** Time-resolved near-field pattern and **b** time-resolved far-field pattern. **c** Time-averaged beam profile at near-field and **d** time-averaged beam profile at far-field. The injection amplitude ratio is 1.2 (intensity ratio of 1.44) and the frequency detuning of 0 GHz. The bias injection current is set to $1.5J_{\text{th}}$

are much suppressed by optical injection and the typical side-peak enhanced near-field pattern in Fig. 8.31 can be reduced to a flat top-hat pattern in Fig. 8.39. Thus, we can expect a narrow beam at the far field, which is convenient for applications. The important parameters for these purposes are again the injection ratio and the frequency detuning between the slave broad-area semiconductor laser and the injection laser. The resulting beam pattern also depends on the injection width at the front face of the active region. Figure 10.13 shows a numerical example of beam shaping in optically injected broad-area semiconductor lasers. For a strong optical injection ratio of 1.2 (amplitude) and a zero frequency detuning,

filamentations are forced to a plain pattern as shown in Fig. 10.13a, although a periodic structure with a small undulation can be seen. The corresponding time-averaged near-field pattern in Fig. 10.13c shows almost the diffraction-limited profile coincident with the aperture width. The time-resolved far-field pattern in Fig. 10.13b also shows little fluctuation for the time development. The time-averaged far-field pattern in Fig. 10.13d almost looks like a diffraction pattern from the rectangular aperture, which is the same as the stripe width, hence the beam quality factor of $M^2 \approx 1$ is obtained. Here, we showed a numerical case of a clean beam profile for rather strong optical injection; however, it is desirable from an application viewpoint that the power from the injection laser is less than the injected broad-area semiconductor laser. In the numerical examples, periodic filamentations appear above the injection ratio of 0.3 and the regularity increases for the increase of the injection ratio. However, the quality of beam profile deteriorates for a higher injection ratio above 1.2. Thus, the optimum optical injection ratio exists to obtain a good beam quality. In the current example, a strong optical injection is employed at the bias injection current of $1.5J_{\mathrm{th}}$. So that the strong injection fraction in this case does not destroy the laser as is easily recognized from the actual laser operations as shown in Fig. 8.35.

10.3.4 Stabilization of Laser Arrays

The control of laser arrays is important for the implementation of high power semiconductor lasers. The technique of optical feedback is also used for the control of laser arrays (Münkel et al. 1996, 1997; Martín-Regalado et al. 1996; Chi et al. 2003). Narrowing the spectral linewidth of a multi-array stack of semiconductor lasers is very important, especially for high power applications of semiconductor lasers, such as in material processing and laser welding. Stacked arrays of semiconductor lasers are also controlled by external optical feedback. Zhu et al. (2005) conducted the linewidth narrowing of stacked semiconductor laser arrays by grating optical feedback. In their experiment, the spectral power of the narrowed laser is increased up to approximately 3.5 times that of the free-running case. The method of optical feedback is also effective for the control and stabilization of the oscillation line, beam profile, and power stability in laser arrays. As discussed in Sect. 8.5, the same technique for calculating rate equations in broad-area semiconductor laser is used for the numerical simulations for laser arrays. Figure 10.14 shows a numerical example of the control of a semiconductor laser array with five elements (Münkel et al. 1997). The laser shows unstable chaotic oscillations at the free running state. When the optical feedback is applied to the array at a time of $t = 30$ ns, each laser oscillation is stabilized within 1–2 ns after the switching. The lasers at the free running state behave like pulsation oscillations, but each laser oscillates at almost spatially single mode after the control. The phase sensitivity also plays an important role for laser oscillations and the effects must be taken into account for the control. As another example of stabilization of laser arrays,

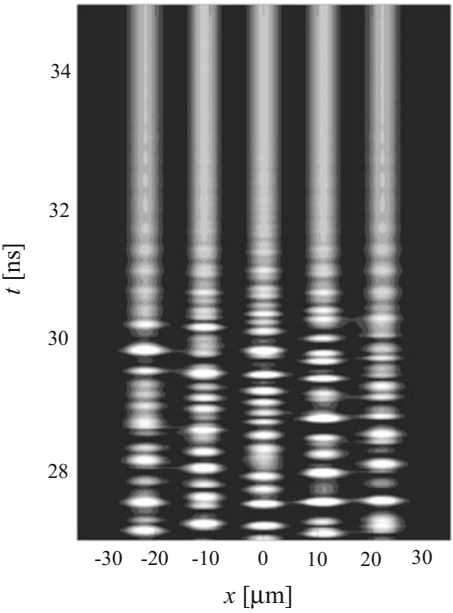

Fig. 10.14 Numerical result of the spatio-temporal dynamics of a five-stripe laser at $J = 4.0J_{th}$, $\kappa = 3 \times 10^{-2}$, and $\tau = 0.0877$ ns, where the feedback is switched on at $t = 30$ ns. The stripe width of each array is 5 μm and the separation of the lasers is 6 μm [after Münkel et al. (1997); © 1997 APS]

coherently coupled VCSEL arrays are important for their potential to create a high brightness low-diffraction beam. For the aim of coherently coupled VCSEL arrays, Gao et al. (2016) employed bottom-emitting photonic crystal ion-implanted arrays, where the coherent in-phase arrays emit from the substrate side. To improve current spreading and trying to avoid optical loss for enhancing the coherence property of VCSEL laser arrays, bottom emitting photonic crystal ion-implanted VCSEL arrays, where the coherent arrays emit from the substrate side, is fabricated. They successfully demonstrated 3 × 3 coherent VCSEL arrays in experiment. A few theoretical and experimental studies on the control of laser arrays have been reported, but little has been investigated on the control of actual laser arrays. The model described here is considered as rather strong coupling between the adjacent laser elements. The control of laser arrays with loose coupling is also an important issue as a real model, but the study is left for the future.

10.4 Controls in Nobel Structure Lasers

10.4.1 Photonic VCSELs

To control and stabilize newly developed semiconductor lasers, external control techniques have been developed. We discussed some instances in the previous section. In this section, we present topics of controls of newly developed semiconductor lasers based on installations of device structures. The first example is a

photonic structure installed in adjacent to a laser exit face in VCSELs. Single-mode operation of lasers is important for the diffraction limit of the output beam in various applications. VCSEL is expected to operate by stable oscillations at the fundamental single spatial mode with a fixed polarization direction. The stable single mode laser with small beam divergence angle is advantageous for reliable high-speed data transmission. Even for short-distance links, multimode VCSELs undergo various problems at high modulation frequencies. In addition to the single-mode operation, the control and stabilization of the output polarization are essential for most applications. In spite of strong demand for single-mode operations, stable single spatial mode of VCSEL is difficult to obtain with a high output power, as discussed in the preceding sections. In general, a large device size enhances the maximum output power while degrading the single-mode stability due to the thermal lens effect and carrier non-uniformity. To attain single-mode VCSELs with high output power, the improvement of device structures such as anti-guide optical confinement was proposed. However, we here discuss a different method by installing a photonic structure on the top of the device as a post-processed technique, although it has some tradeoffs, for example for the cavity loss or current confinement. Periodic structure with some small defects or holey structure is a common technique for photonic VCSELs (Furukawa et al. 2004; Lee et al. 2004; Liu et al. 2004; Terhalle et al. 2008). The excitation of higher spatial modes is suppressed and the laser is forced to stay to a single mode by a photonic structure installed on the top of the exit surface of the laser cavity.

Furukawa et al. (2004) employed triangular-shaped holes as a photonic structure for the purpose of increasing the field penetration of higher order spatial modes to the hole side. Figure 10.15 shows an example of the holey structures, which has 12 triangular holes. The holey structure is installed on the top of the DBR reflector of an oxide-confined VCSEL. The holes are aligned so that they surrounded the center

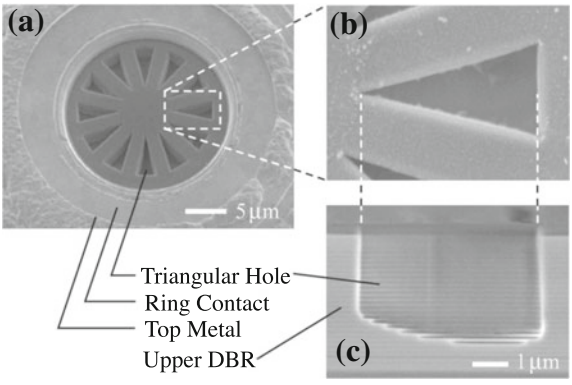

Fig. 10.15 Example of scanning electron microscope images of a triangular holey structure with twelve holes. **a** Full top view. **b** Magnified top view of triangular hole. **c** Cross-sectional side view of the hole formed on upper multilayer DBR [after Furukawa et al. (2004); © 2004 AIP]

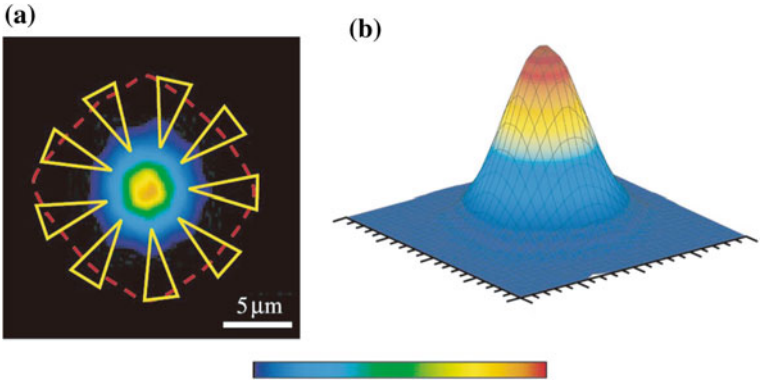

Fig. 10.16 Emission pattern from a photonic VCSEL with nine triangular holes. **a** Near-field pattern at the maximum laser output power of 2 mW. The solid line shows positions of triangular holes and the dashed line represents the oxide aperture. **b** Far-field pattern of the VCSEL [after Furukawa et al. (2004); © 2004 AIP]

modal area and the tip penetrates the oxide aperture. Figure 10.16 shows the result of the stabilizations for another holey structure with nine triangular holes. The figure shows the near- and far-field patterns at the maximum output power. The dashed line in Fig. 10.16a denotes the boundary of the oxide aperture of a diameter of 15 μm. The holes are aligned sufficiently close together with a relatively large penetration of 4 μm to the oxide aperture. The half-maximum diameter of the near-field pattern is 3.1 μm and the half-maximum divergence angle is 6.4°, which agrees closely with the diffraction limit of the near-field pattern. The side-mode suppression ratio is greatly enhanced and the ratio of 45–50 dB is attained. There are several variations for photonic structures to control emissions in semiconductor lasers. A monolithically integrated surface grating on top of VCSELs is another example of the structures (Debernardi et al. 2005), by which the oscillation wavelength is selected to coincide with the grating frequency and the polarization of the laser oscillations is controlled to the direction perpendicular to the grating lines.

10.4.2 Control of Mode Distribution Through Etched Microstructure in Broad-Area Semiconductor Lasers

In the previous subsection, a photonic structure is installed onto the exit face of a VCSEL to control spatial modes. The control and selection of spatial modes are also an important issue to obtain a good quality beam in broad-area semiconductor lasers. In broad-area semiconductor lasers, an etched microstructure is fabricated along a p-contact layer of the laser waveguide as a one of methods to control spatial modes (Crump et al. 2008; Chen et al. 2009). Figure 10.17 shows such an example for an etched microstructure broad-area semiconductor laser with operating at a

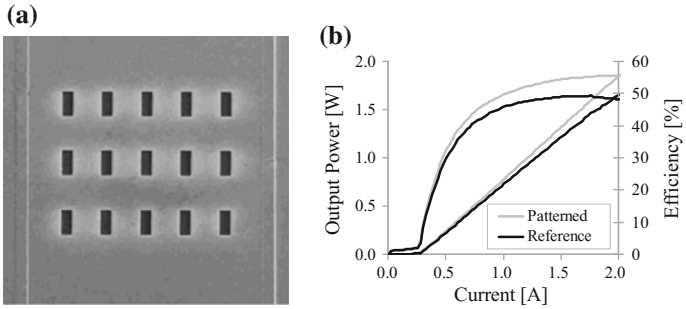

Fig. 10.17 **a** SEM image of the focused ion beam etched hole pattern in the laser stripe. **b** L-I characteristics and conversion efficiencies from current to light of the etched and unetched broad-area semiconductor lasers [after Chen et al. (2009); © 2009 AIP]

wavelength of 808 nm. Figure 10.17a is the top view of a scanning electron microscope (SEM) image along the laser stripe with the etched mode-stabilizing holes. Three aligned rows of holes are employed along the cavity length of 1 mm, but the induced index perturbation is located within the laser cavity, away from either laser facet, to avoid possible mirror damage. The size of the holes is 5 μm wide and the separation between the rectangular holes is 20 μm, thus, the holes are uniformly distributed across the 100 μm wide laser stripe. These holes are milled to a sufficient depth to allow some interaction with the optical mode, but not so deep as to introduce significant losses or penetrate the active region. These air holes overlap weakly with the optical field in the device, just touching the waveguide region. The air holes act as scattering centers, adjusting optical intensity from low spatial order to high order lateral modes or vice versa. Figure 10.17b shows L-I characteristics (straight lines above the threshold) for the patterned and unpatterned lasers. The laser with etched holes shows improvement in slope efficiency due to the increased overlap of the optical mode with the lateral gain profile. The curves in the figure are the conversion efficiencies from current to light. The efficiency is also much improved by the etched microstructure on the laser stripe. The method is proved to be effective for beam shaping in broad-area semiconductor lasers.

10.4.3 Quantum-Dot Broad-Area Semiconductor Lasers

The importance of beam shaping for broad-area semiconductor lasers was discussed in Sect. 10.3.3. The beam quality of broad-area semiconductor lasers is strongly affected by filamentations, so that the suppression of the effects is essential in applications. It is well known that beam filamentation in semiconductor laser strongly depends on the linewidth enhancement factor a (Marciante and Agrawal 1998). Quantum-dot devices exhibit less filamentation than quantum-well devices,

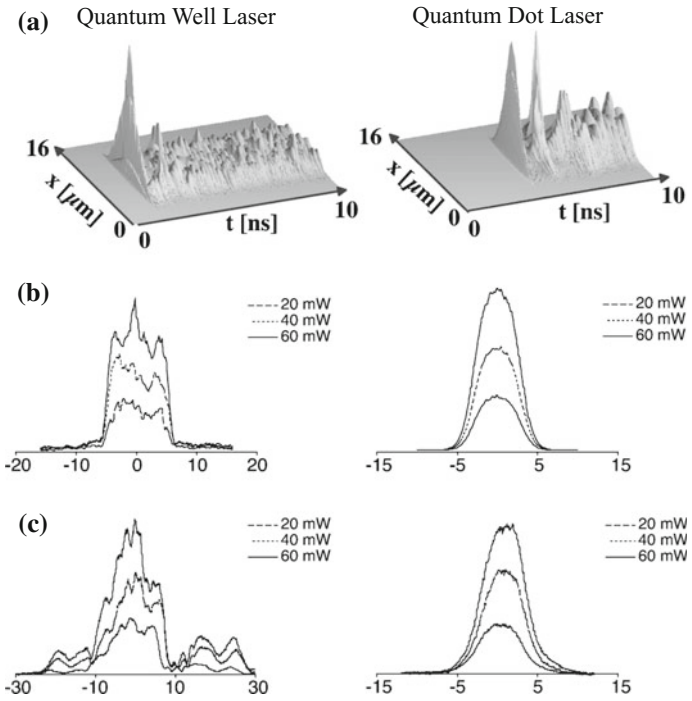

Fig. 10.18 Filamentation control by quantum-dot structure in a broad-area semiconductor laser. *Left* quantum-well laser, and *right* quantum-dot laser. **a** Time resolved dynamic behaviors after laser switch-on (numerical simulation). Averaged near-field patterns for **b** theory and **c** experiments [after Gehrig et al. (2004); © 2004 AIP]

since the quantum-dot structure can reduce the linewidth enhancement factor, resulting in suppression of filamentations compared to quantum-well lasers. In the quantum-dot laser, the strong localization of carrier inversion and the small amplitude-phase coupling enable a significant improvement of beam quality compared to quantum-well lasers of identical geometry and material parameters (Gehrig and Hess 2002; Smowton et al. 2002; Ribbat et al. 2003; Gehrig et al. 2004). For the description of a quantum-dot structure, some modifications for the rate equations of ordinary broad-area semiconductor lasers are necessary to account for the characteristics of a quantum-dot laser ensemble as discussed in Sect. 8.6.

Figure 10.18 shows the comparisons of the beam qualities between quantum-dot and quantum-well lasers obtained by numerical simulations and experiments. For the numerical simulations, we here employ the microscopic model of the carrier dynamics (Gehrig and Hess 2002; Gehrig et al. 2004), which is quite similar to that discussed in Sect. 8.6.1. Quantum dots at an appropriate density are embedded into the active region of the laser cavity. In the presence of quantum dots, the dynamic motions of filaments are greatly suppressed and the laser can emit fairly stable beam compared with quantum-well semiconductor lasers. The laser is an InGaAs

quantum-dot laser (dot density 10^{15} m^{-2}) of the strip-width of 6 μm at the wavelength of 1.1 μm. The laser has a rather small stripe width, but it is enough to show the dynamic properties of filamentations typically observed in broad-area semiconductor lasers. Depending on the dot density and each size of quantum dot, the laser shows inhomogeneous broadening, which results in the change of the linewidth enhancement factor. The α parameter can be even negative under a certain operating condition of the laser and the filamentation behavior of a quantum-dot laser should be drastically different from a quantum-well laser. As easily seen from Fig. 10.18a, the quantum-well laser has strong filamentations, while the quantum-dot laser is well stabilized enough after the switch-on relaxation oscillation. The averaged beam profiles both for the simulations and the experiments are shown in Fig. 10.18b, c. The averaged beam profiles for quantum-well laser contain irregular peaks in their envelopes, which is the effect of filamentations of the order of picosecond. On the other hand, the good quality beam profiles are obtained for the quantum-dot laser. The beam quality factor M^2 ($M^2 = (D_m/d_0)^2$: D_m and d_0 being the diameters for the observed and ideal Gaussian beams defined in (8.48)) is much reduced in comparison with that of quantum-well lasers. For fiber coupling purposes, the beam quality of $M^2 < 2$ is desirable. The obtained beam quality of the quantum-dot laser well satisfies the demand for such application. Quantum-dot lasers have a much better beam quality compared to quantum-well lasers of the same geometry and the same material parameters. The strong localization of the carriers in the dots in combination with the reduced amplitude phase coupling thus guarantees a good spatial quality. In VCSELs, quantum-dot structure is sometimes used to control unstable oscillations such as polarization-mode switching, higher spatial-mode excitations, and mode competitions. The instabilities have been reduced by introducing physical distortions to the laser materials. The polarization mode of VCSEL is also stabilized to a single mode by embedding quantum dots into the active layer (Huffaker et al. 1998; Yu et al. 2006). Quantum-dot structures are promising to stabilize laser oscillations not only in ordinary narrow-stripe edge-emitting semiconductor lasers but also in newly developed semiconductor lasers.

References

M.A. Arteaga, M. López-Amo, H. Thienpont, K. Panajotov, Role of external cavity reflectivity for achieving polarization control and stabilization of vertical cavity surface emitting laser. Appl. Phys. Lett. **90**, 031117-1–031117-3 (2007)

Y. Champagne, S. Mailhot, N. McCarthy, Numerical procedure for the lateral-mode analysis of broad-area semiconductor lasers with an external cavity. IEEE J. Quantum Electron. **31**, 795–810 (1995)

N.S. Chen, S.F. Yu, Transient response of ARROW VCSELs under external optical feedback. IEEE Photonics Technol. Lett. **16**, 1610–1612 (2004)

C. Chen, P. Leisher, S. Patterson, P. Crump, Y.K. Kim, K. Choquette, Stabilization of lateral mode transients in high-power broad area semiconductor lasers. Appl. Phys. Lett. **94**, 011107-1–011107-3 (2009)

M.J. Chi, B. Thestrup, J.L. Mortensen, M.E. Nielsen, P.M. Petersen, Improvement of the beam quality of a diode laser with two active broad-area segments. J. Opt. A **5**, S338–S341 (2003)

M. Chi, B. Thestrup, P.M. Petersen, Self-injection locking of an extraordinarily wide broad-area diode laser with a 1000-μm-wide emitter. Opt. Lett. **30**, 1147–1149 (2005)

A.R. Chraplyvy, K.Y. Liou, R.W. Tkach, G. Eisenstein, Y.K. Jhee, T.L. Koch, P.J. Anthony, U.K. Chakrabarti, Simple narrow-linewidth 1.5 μm InGaAsP DFB external-cavity laser. Electron. Lett. **22**, 88–90 (1986)

P. Crump, P. Leisher, T. Matson, V. Anderson, D. Schulte, J. Bell, J. Farmer, M. DeVito, R. Martinsen, Y.K. Kim, K.D. Choquette, G. Erbert, G. Tränkle, Control of optical mode distribution through etched microstructures for improved broad area laser performance. Appl. Phys. Lett. **92**, 131113-1–131113-3 (2008)

B. Dahmani, L. Hollberg, R. Drullinger, Frequency stabilization of semiconductor lasers by resonant optical feedback. Opt. Lett. **12**, 876–878 (1987)

P. Debernardi, J.M. Ostermann, M. Feneberg, C. Jalics, R. Michalzik, Reliable polarization control of VCSELs through monolithically integrated surface gratings: a comparative theoretical and experimental study. IEEE J. Sel. Top. Quantum Electron. **11**, 107–116 (2005)

G. Ewald, K.M. Knaak, S.G. Otte, K.D.A. Wendt, H.J. Kluge, Development of narrow-linewidth diode lasers by use of volume holographic transmission gratings. Appl. Phys. B **80**, 483–487 (2005)

L. Fan, M. Fallahi, J.T. Murray, R. Bedford, Y. Kaneda, A.R. Zakharian, J. Hader, J.V. Moloney, W. Stolz, S.W. Koch, Tunable high-power high-brightness linearly polarized vertical-external-cavity surface-emitting lasers. Appl. Phys. Lett. **88**, 021105-1–021105-3 (2006)

M.W. Fleming, A. Mooradian, Spectral characteristics of external-cavity controlled semiconductor lasers. IEEE J. Quantum Electron. **17**, 44–59 (1981)

Y. Fujita, J. Ohtsubo, Optical-feedback-induced stability and instability in broad-area semiconductor lasers. Appl. Phys. Lett. **87**, 031112-1–031112-3 (2005)

A. Furukawa, S. Sasaki, M. Hoshi, A. Matsuzono, K. Moritoh, T. Baba, High-power single-mode vertical-cavity surface-emitting lasers with triangular holey structure. Appl. Phys. Lett. **85**, 5161–5163 (2004)

N. Gaciu, E. Gehrig, O. Hess, Control of broad-area laser dynamics with delayed optical feedback (Chap. 22), in *Handbook of Chaos Control,* ed. by E. Schöll, G. Schuster (Wiley-VCH, Weinheim, 2007)

Z. Gao, B.J. Thompson, G. Ragunathan, M.T. Johnson, B. Rout, K.D. Choquette, Bottom-emitting coherently coupled vertical cavity laser arrays. IEEE Photonics Techonol. Lett. **28**, 513–515 (2016)

E. Gehrig, O. Hess, Mesoscopic spatiotemporal theory for quantum-dot lasers. Phys. Rev. A **65**, 033804-1–033804-16 (2002)

E. Gehrig, O. Hess, C. Ribbat, R.L. Sellin, D. Bimberg, Dynamic filamentation and beam quality of quantum-dot lasers. Appl. Phys. Lett. **84**, 1650–1652 (2004)

M. Hashimoto, M. Ohtsu, Experiments on a semiconductor laser pumped rubidium atomic clock. IEEE J. Quantum Electron. **23**, 446–451 (1987)

M.A. Holm, D. Burns, A.I. Ferguson, M.D. Dawson, Actively stabilized single-frequency vertical-external-cavity AlGaAs laser. IEEE Photonics Technol. Lett. **11**, 1551–1553 (1999)

D.L. Huffaker, H. Deng, D.G. Deppe, 1.15-μmwavelength oxide-confined quantum-dot vertical-cavity surface-emitting laser. IEEE Photonics Technol. Lett. **10**, 185–187 (1998)

J.M. Iannelli, Y. Shevy, S.J. Kitching, A. Yariv, Linewidith reduction and frequency stabilization of semiconductor lasers using dispersive losses in an atomic vapor. IEEE J. Quantum Electron. **29**, 1253–1261 (1993)

J. Kaiser, I. Fischer, W. Elsäßer, E. Gehrig, O. Hess, Mode-locking in broad-area semiconductor lasers enhanced by picosecond-pulse injection. IEEE J. Sel. Top. Quantum Electron. **10**, 968–973 (2004)

R.F. Kazarinov, C.H. Henry, The relation of line narrowing and chirp reduction resulting from coupling of a semiconductor laser to a passive resonator. IEEE J. Quantum Electron. **23**, 1401–1409 (1987)

P. Kürz, T. Mukai, Frequency stabilization of semiconductor laser by external phase-conjugate feedback. Opt. Lett. **21**, 1369–1371 (1996)

P. Kürz, R. Nagar, T. Mukai, Highly efficient phase conjugation using spatially non-degenerate four-wave mixing in a broad-area laser diode. Appl. Phys. Lett. **68**, 1180–1182 (1996)

P.H. Laurent, A. Clairon, C.H. Bréant, Frequency noise analysis of optically self-locked diode lasers. IEEE J. Quantum Electron. **25**, 1131–1142 (1989)

J.S. Lawrence, D.M. Kane, Broad-area diode lasers with plane-mirror and phase-conjugate feedback. J. Lightwave Technol. **20**, 100–104 (2002)

K.H. Lee, J.H. Baek, I.K. Hwang, Y.H. Lee, G.H. Lee, J.H. Ser, H.D. Kim, H.E. Shin, Square-lattice photonic-crystal vertical-cavity surface-emitting lasers. Opt. Express **17**, 4136–4143 (2004)

H. Li, N.B. Abraham, Analysis of the noise spectra of a laser diode with optical feedback from a high-finesse resonator. IEEE J. Quantum Electron. **25**, 1782–1793 (1989)

W. Liang, V.S. Ilchenko, D. Eliyahu, A.A. Savchenkov, A.B. Matsko, D. Seidel, L. Maleki, Ultralow noise miniature external cavity semiconductor laser. Nat. Comm. **6**, 7371–7376 (2015)

B.W. Liby, D. Statman, Controlling the linewidth of a semiconductor laser with photorefractive phase conjugate feedback. IEEE J. Quantum Electron. **32**, 835–838 (1996)

H. Liu, M. Yan, P. Shum, H. Ghafouri-Shiraz, D. Liu, Design and analysis of anti-resonant reflecting photonic crystal VCSEL lasers. Opt. Express **18**, 4269–4274 (2004)

S.K. Mandre, I. Fischer, W. Elsäßer, Control of the spatiotemporal emission of a broad-area semiconductor laser by spatially filtered feedback. Opt. Lett. **28**, 1135–1137 (2003)

S.K. Mandre, I. Fischer, W. Elsäßer, Spatiotemporal emission dynamics of a broad-area semiconductor laser in an external cavity: stabilization and feedback-induced instabilities. Opt. Commun. **244**, 355–365 (2005)

J.R. Marciante, G.P. Agrawal, Spatio-temporal characteristics of filamentation in broad-area semiconductor lasers: experimental results. IEEE Photonics Technol. Lett. **10**, 54–56 (1998)

F. Marino, S. Barland, S. Balle, Single-mode operation and transverse-mode control in VCSELs induced by frequency-selective feedback. IEEE Photonics Technol. Lett. **15**, 789–791 (2003)

J. Martín-Regalado, G.H.M. van Tartwijk, S. Balle, M. San Miguel, Mode control and pattern stabilization in broad-area lasers by optical feedback. Phys. Rev. A **54**, 5386–5393 (1996)

M. Münkel, F. Kaiser, O. Hess, Spatio-temporal dynamics of multistripe semiconductor lasers with delayed optical feedback. Phys. Lett. A **222**, 67–75 (1996)

M. Münkel, F. Kaiser, O. Hess, Stabilization of spatiotemporally chaotic semiconductor laser arrays by means of delayed optical feedback. Phys. Rev. E **56**, 3868–3875 (1997)

A. Naumenko, P. Besnard, N. Loiko, G. Ughetto, J.C. Bertreux, Characteristics of a semiconductor laser coupled with a fiber Bragg grating with arbitrary amount of feedback. IEEE J. Quantum Electron. **39**, 1216–1228 (2003)

M. Ohtsu, S. Kotajima, Linewidth reduction of a semiconductor laser by electrical feedback. IEEE J. Quantum Electron. **21**, 1905–1912 (1985)

M. Ohtsu, M. Murata, M. Kourogi, FM noise reduction and subkilohertz linewidth of an AlGaAs laser by negative electronic feedback. IEEE J. Quantum Electron. **26**, 231–241 (1990)

H. Olesen, S. Saito, T. Mukai, T. Saitoh, O. Mikami, Solitary spectral linewidth and its reduction with external grating feedback for a 1.55 μm InGaAsP BH laser. Jpn. J. Appl. Phys. **22**, L664–L666 (1983)

E. Patzak, A. Sugimura, S. Satio, T. Mukai, H. Olesen, Semiconductor laser linewidth in optical feedback configurations. Electron. Lett. **19**, 1026–1027 (1983)

V. Raab, R. Menzel, External resonator design for high-power laser diodes that yields 400 mW of TEM_{00} power. Opt. Lett. **27**, 167–169 (2002)

Ch. Ribbat, R.L. Sellin, I. Kaiander, F. Hopfer, N.N. Ledentsov, D. Bimberg, A.R. Kovsh, V.M. Ustinov, A.E. Zhukov, M.V. Maximov, Complete suppression of filamentation and superior beam quality in quantum-dot lasers. Appl. Phys. Lett. **82**, 952–954 (2003)

M. Romanelli, J.P. Hermier, E. Giacobino, A. Bramati, Demonstration of single-mode operation of a vertical-cavity surface-emitting laser with optical feedback: the intensity-noise-measurement approach. J. Opt. Soc. Am. B **22**, 2596–2600 (2005)

C. Simmendinger, D. Preißer, O. Hess, Stabilization of chaotic spatiotemporal filamentation in large broad area lasers by spatially structured optical feedback. Opt. Express **5**, 48–54 (1999a)

C. Simmendinger, M.M. Münkel, O. Hess, Controlling complex temporal and spatio-temporal dynamics in semiconductor lasers. Chaos, Solitons Fractals **10**, 851–864 (1999b)

P.M. Smowton, E.J. Pearce, H.C. Schneider, W.W. Chow, M. Hopkinson, Filamentation and linewidth enhancement factor in InGaAs quantum dot lasers. Appl. Phys. Lett. **81**, 3251–3253 (2002)

H. Stoehr, F. Mensing, J. Helmcke, U. Sterr, Diode laser with 1 Hz linewidth. Opt. Lett. **31**, 736–738 (2006)

S. Takimoto, T. Tachikawa, R. Shogenji, J. Ohtsubo, Control of spatio-temporal dynamics of broad-area semiconductor lasers by strong optical injection. IEEE Photonics Technol. Lett. **21**, 1051–1053 (2009)

B. Terhalle, N. Radwell, P. Rose, C. Denz, T. Ackemann, Control of broad-area vertical-cavity surface emitting laser emission by optically induced photonic crystals. Appl. Phys. Lett. **93**, 151114-1–151114-3 (2008)

B. Tromborg, H. Olssen, X. Pan, S. Saito, Transmission line description of optical feedback and injection locking for Fabry-Perot and DFB lasers. IEEE J. Quantum Electron. **23**, 1875–1889 (1987)

K. Vahala, K. Kyuma, A. Yariv, S.K. Kwong, M. Cronin-Golomb, K.Y. Lau, Narrow linewidth, single frequency semiconductor laser with a phase conjugate external cavity mirror. Appl. Phys. Lett. **49**, 1563–1565 (1986)

M. Vainio, Phase-conjugate external cavity diode laser. IEEE Photonics Technol. Lett. **18**, 2047–2049 (2006)

P.D. van Voorst, H.L. Offerhaus, K.J. Boller, Single-frequency operation of a broad-area laser diode by injection locking of a complex spatial mode via a double phase conjugate mirror. Opt. Lett. **31**, 1061–1063 (2006)

S. Wolff, H. Fouckhardt, Intra-cavity stabilization of broad area lasers by structured delayed optical feedback. Opt. Express **7**, 222–227 (2000)

S. Wolff, A. Rodionov, V.E. Sherstobitov, H. Fouckhardt, Fourier-optical transverse mode selection in external-cavity broad-area lasers: experimental and numerical results. IEEE J. Quantum Electron. **39**, 448–458 (2003)

R. Wyatt, W.J. Devlin, 10 kHz linewidth 1.5 μm InGaAsP external cavity laser with 55 nm tuning range. Electron. Lett. **19**, 110–112 (1983)

M. Yamada, Computer simulation of feedback induced noise in semiconductor lasers operating with self-sustained pulsation. IEICE Trans. Electron. **E81-C**, 768–780 (1998)

S.F. Yu, Nonlinear dynamics of vertical-cavity surface-emitting lasers. IEEE J. Quantum Electron. **35**, 332–331 (1999)

H.C. Yu, J.S. Wang, Y.K. Su, S.J. Chang, F.I. Lai, Y.H. Chang, H.C. Kuo, C.P. Sung, H.P.D. Yang, K.F. Lin, J.M. Wang, J.Y. Chi, R.S. Hsiao, S. Mikhrin, 1.3-μm InAs-InGaAs quantum-dot vertical-cavity surface-emitting laser with fully doped DBRs grown by MBE. IEEE Photonics Technol. Lett. **18**, 418–420 (2006)

Y. Zhao, Y. Li, Q. Wang, F. Meng, Y. Lin, S. Wang, B. Lin, S. Cao, J. Cao, Z. Fang, T. Tianchu Li, E. Zang, 100-Hz linewidth diode laser with external optical feedback. IEEE Photonics Technol. Lett. **24**, 1795–1798 (2012)

H. Zhu, I.C. Ruset, F.W. Hersman, Spectrally narrowed external-cavity high-power stack of laser diode arrays. Opt. Lett. **30**, 1342–1344 (2005)

Chapter 11
Metrology Based on Chaotic Semiconductor Lasers

Abstract On the way to chaotic evolution, periodicity, bistability, and multistability are observed, such as in the outputs of semiconductor lasers with optical feedback. The system of optical feedback in a semiconductor laser, whose output shows periodic oscillations, is sometimes called self-mixing semiconductor laser. In a periodic state, the laser output shows not simply periodic oscillation but also hysteresis. Novel applications have been proposed based on these phenomena, for example, a displacement measurement is performed by counting the fringes obtained from bistable self-mixing interference between the internal field and the optical feedback light in the laser cavity. The direction of the displacement is simultaneously determined from asymmetric waveforms showing hysteresis. Also correlation of signals between scattering and reference chaotic lights can be applied for remote sensing from distant reflecting targets. We discuss various methods for optical metrology based on self-mixing interference effects and correlation techniques in semiconductor lasers. This chapter does not deal with the detailed descriptions of the methods and their accuracies but with the introduction of the principles of the methods.

11.1 Optical Feedback Interferometers

11.1.1 Bistability and Multistability in Feedback Interferometers

Laser interferometry is a well-established technique for the measurement of vibrations and displacement of objects. In the interferometry, for example, the displacement of the order of optical wavelength is measured from the fringe analysis of sinusoidal variations of signals from the interferometer output. We have investigated the self-mixing effects in semiconductor lasers with optical feedback in Chap. 4. We have also shown that the laser output exhibited periodic undulations with half of the optical wavelength for the change of the external cavity length

© Springer International Publishing AG 2017

J. Ohtsubo, *Semiconductor Lasers*, Springer Series in Optical Sciences 111,
DOI 10.1007/978-3-319-56138-7_11

under an appropriate condition of the external reflectivity. In self-mixing semiconductor lasers, the returned light from an external reflector interferes with the internal laser oscillation and the original field in the laser cavity plays a role for the reference wave. Therefore, we can conduct interferometric measurements using semiconductor lasers with optical feedback based on the same principle as the ordinary laser interferometers and we can obtain the absolute position, displacement, and vibration of the external reflector.

In this interferometric measurement, we use periodic oscillations, especially period-1 states, prior to chaotic oscillations on the way to period doubling bifurcations. Since self-mixing in semiconductor lasers is a nonlinear effect, not only the absolute value of the displacement but also the additional information of the direction of motion (whether the object is approaching or is going away from the laser) can be easily determined from the analysis for the fringe pattern. A semiconductor laser itself plays a role not only as a light source but also as a self-mixing detector in the measurement. In commercially available semiconductor lasers, a photodiode is usually installed within the laser package as a monitor of the laser output power and we can use it as a detector for the fringe analysis. Therefore, we can construct a very compact sensor for the interferometric measurements. Also, we do not require complex processing for the post-detection signal. However, it is noted that the technique is limited to a certain range of the reflectivity of the external reflector. For large reflectivity of the external reflector, the detected signal may not be a periodic oscillation but a chaotic irregular oscillation. We cannot apply the method for such a case of a large reflectivity of the external reflector.

In the following, we investigate the interferometric measurements using bistable states (period-1 states) of light outputs in self-mixing semiconductor lasers discussed in Chap. 4. The optical configuration is the same as that in Fig. 4.1 and the rate equations of the model are given by (4.5)–(4.7). In the presence of optical feedback in a semiconductor laser, the oscillation angular frequency changes from ω_0 (the solitary oscillation) to ω_s. The relation between the two angular frequencies is given by

$$\omega_0 \tau = \omega_s \tau + C \sin(\omega_s \tau + \tan^{-1} \alpha) \tag{11.1}$$

where $C = \kappa\tau\sqrt{1+\alpha^2}/\tau_{\text{in}}$. The dynamics in semiconductor lasers subjected to optical feedback strongly depend on the C parameter. We are interested in the parameter region of $C \approx 1$ in this section, where the laser shows periodic states prior to the onset of chaotic oscillations. Using (4.9)–(4.11), the steady-state value of the laser output is given by

$$S_s = A_s^2 = \frac{\frac{\tau_s J}{ed} - n_s + \frac{2\kappa}{G_n \tau_{\text{in}}} \cos \omega_s \tau}{1 - \frac{2\kappa\tau_{\text{ph}}}{\tau_{\text{in}}} \cos \omega_s \tau} \frac{\tau_{\text{ph}}}{\tau_s} \tag{11.2}$$

Since we are considering a rather small coefficient κ of optical feedback, the difference between the laser output powers with and without optical feedback is small. Then, the difference can be approximated as follows:

$$\Delta S = S_s - S_s|_{\kappa=0} \approx \Delta S_0 \cos \omega_s \tau \tag{11.3}$$

where $\Delta S_0 = 2\kappa\tau_{ph}^2(J/ed - n_s/\tau_s)/\tau_{in}$. In actual fact, ΔS is a time dependent function because the carrier density also varies with time by the optical feedback. We introduce a normalized function $F(t)$ as $F(t) = \Delta S(t)/\Delta S_0$. Substituting (11.3) into (11.1) and using the relation $\omega_0\tau = 2kL$, the external cavity length as a function of time t is given by

$$L(t) = \frac{1}{2k}\left[\cos^{-1} F(t) + \frac{C}{\sqrt{1+\alpha^2}}\left\{\alpha F(t) + \sqrt{1-F^2(t)}\right\} + 2m\pi\right] \quad \frac{dF}{dt}\cdot\frac{dL}{dt} < 0 \tag{11.4a}$$

$$L(t) = \frac{1}{2k}\left[-\cos^{-1} F(t) + \frac{C}{\sqrt{1+\alpha^2}}\left\{\alpha F(t) - \sqrt{1-F^2(t)}\right\} + 2(m+1)\pi\right] \quad \frac{dF}{dt}\cdot\frac{dL}{dt} > 0 \tag{11.4b}$$

where m is a non-negative integer number (m = 0, 1, 2, …). The laser output varies for the change of the external cavity length, but the waveform has asymmetric features depending whether the external reflector moves toward or away from the laser. Then, we can determine the displacement of the external reflector and also the direction of movement in accordance with the relation in (11.4)

Next, we investigate the effect of optical feedback at bistable states of the laser output power. For a small optical feedback of C = 0.6, for example, the laser output power is a periodic oscillation as shown in Fig. 11.1a and the period is just half of the optical wavelength (Donati et al. 1995). The variation of the waveform is smooth, but it is not a symmetrical shape as expected from the above discussion. In this numerical simulation, it is assumed that the external mirror is moving away from the laser, i.e., the phase $\omega_0\tau$ is increasing. If the phase $\omega_0\tau$ is decreasing, the laser output shows the reversed waveform to Fig. 11.1a. Therefore, we can determine the direction of the movement from the shape of the waveform. For a large value of a C parameter of C = 3, the laser output power still varies with the period of $\lambda/2$, but shows hysteresis as shown in Fig. 11.1b. At this parameter value, the laser output power takes bistable states for a certain range of the phase. Therefore, we can expect a significant difference between the shapes of the waveforms for the increase or decrease of the external mirror position. With further increase of the C parameter value, skew of the waveform is enhanced and the laser output takes multistable states. These multistable states are rarely observed in actual situations and the laser behaves as the chaotic oscillations under these conditions, since multistable states are usually “unstable” in real systems.

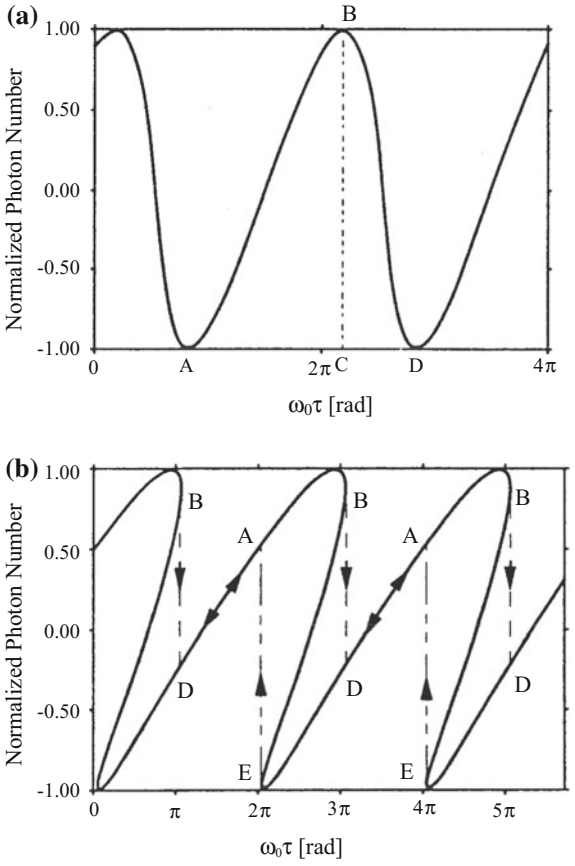

Fig. 11.1 Numerical calculation of the laser output power ΔS for the phase $\omega_0\tau$. **a** $C = 0.6$ and **b** $C = 3$ with hysteresis. The linewidth enhancement factor is chosen as $\alpha = 6$ [after Donati et al. (1995); © 1995 IEEE]

Figure 11.2 presents the experimental results of self-mixing signals for different optical feedback strengths (Giuliani et al. 2001). The external reflector is put on a loudspeaker and the loudspeaker is driven by a sinusoidal signal in Fig. 11.2a. When the feedback is small in Fig. 11.2b (the feedback strength in intensity is roughly estimated as 10^{-7}), the laser output power shows a periodic undulation whose period is equal to half of the optical wavelength. In Fig. 11.2c (the feedback strength of 10^{-5}), the laser output power is quite different from the periodic state in Fig. 11.2b. The waveform is still periodic, but the waveform for the increase of the phase is completely different from that for the decrease. Then, the absolute value of the displacement of the external reflector is obtained by counting the peaks of the undulations in the waveform and the direction of the movement is clearly discriminated by examining the waveform. The feedback intensity of 10^{-5} corresponds to the periodic state just before the onset of chaotic evolution in a semiconductor laser with optical feedback. For the large feedback strength of 10^{-4} in Fig. 11.2d (corresponding to a moderate to strong feedback in regime IV), the coherence of the laser is completely destroyed and periodicity is not visible in the waveform. As a

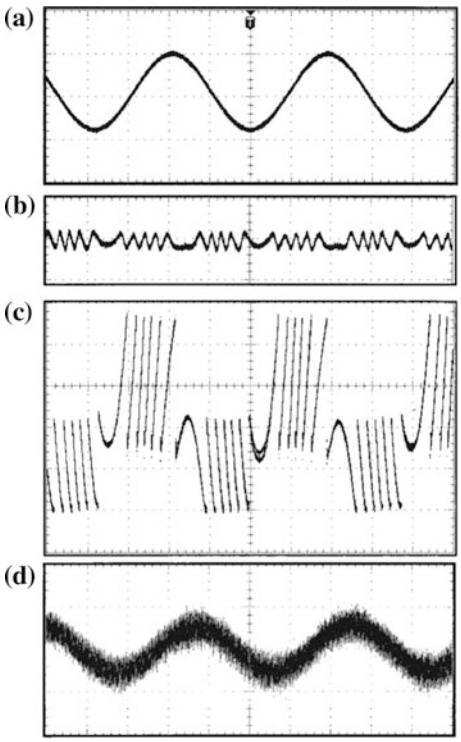

Fig. 11.2 Experimentally observed self-mixing signals for the change of an external reflector. **a** Driving sinusoidal signal of the external reflector. Laser output signals for external reflectivities of **b** 10^{-7} with periodic state, **c** 10^{-5} with hysteresis, **d** 10^{-4} with coherence collapse state. The driving signal corresponds to the change of the external reflector for 1.3 μm/div. The oscillation wavelength of the laser used is 800 nm. The time scale is 1 ms/div [after Giuliani et al. (2001); © 2001 SPIE]

result, the laser output power exhibits a similar waveform to the driving signal. However, the signal is broadened due to the modulation of fast chaotic oscillations. It is also noted that the offset phase of the signal is generally not always equal to that of the driving signal.

11.1.2 Interferometric Measurement in Self-mixing Semiconductor Lasers

We can measure the change of the external cavity length on the order of half of the optical wavelength by using self-mixing effect in semiconductor lasers and also determine the direction of the change. Based on these principles, we here discuss the concrete methods for the measurement of displacement, vibration, and absolute position of the external reflector. Each measurement includes a particular processing algorithm for the detected signals, however, the fundamental methods of signal processing for those measurements still contain the common technique (Donati et al.

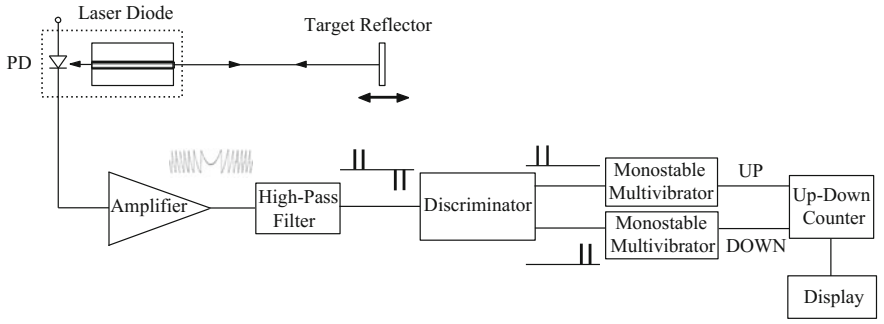

Fig. 11.3 Basic circuits of the signal processing for interferometric measurements in self-mixing semiconductor lasers

1995; Donati 2012; Taimre et al. 2015). Before discussing each technique, we take the measurement for the displacement of an external reflector as an example and show the detection and analysis for periodic signals in the self-mixing laser output. Figure 11.3 is an example of the signal processing systems. The light reflected from a target mirror is mixed with the original laser field in the laser cavity and the mixed signal is detected by a photodiode installed in the laser package. The detected signal passes through an amplifier and a high-pass filter. Then, the up- and down-edges of the periodic signal for every $\lambda/2$ period are counted by a counter. As a result, the displacement of the target reflector including the direction of the movement during the counting is calculated. The basic resolution of the measurement is $\lambda/2$ in this technique. It is noted that the SNR of the self-mixing interferometer using semiconductor lasers is limited by the efficiency of the coupling photodiode, and it is about 20 dB poorer than of conventional interferometry with the 50/50 half mirror (Giuliani et al. 2002). However, we can construct a very simple measurement system with high flexibility by the self-mixing interferometer using semiconductor lasers. In the following discussions, we assume that the laser output due to the mixing is a periodic signal with period $\lambda/2$ without notice.

In the following, we show typical signals observed in the self-mixing semiconductor lasers. We take an example of the displacement measurement of an external target under an appropriate condition of the external optical feedback for bistability operation of $C > 1$. Figure 11.4 is an experimental self-mixing signal for a sinusoidal displacement of the object. In the figure, the upper trace is the experimental self-mixing signal for a sinusoidal target displacement of 3.3 μm peak-to-peak amplitude and 1 kHz frequency. The lower trace is an analogue derivative of a self-mixing signal, showing up- and down-pulses, where the states of up- and down-pulses correspond whether the target is coming toward or going away from the laser. By this approach, displacement of retro-reflective target has been successfully measured over 1 m distance with an allowed maximum speed of 0.4 m/s, solely limited by electronic bandwidth. The maximum target distance is limited by the coherence length of semiconductor lasers, being usually several

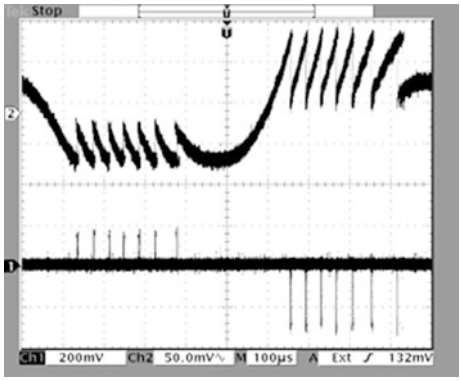

Fig. 11.4 *Upper trace* experimental self-mixing signal obtained for a sinusoidal target displacement of 3.3 µm peak-to-peak amplitude and 1 kHz frequency, *lower trace* analogue derivative of the self-mixing signal, showing up/down-pulses. The timescale is 100 µs per division [after Giuliani et al. (2002); © 2002 IOP]

meters to 10 m. For an appropriate target reflectivity satisfying the condition $C > 1$, the self-mixing signal becomes a sawtooth-like waveform and, then, an accuracy better than $\lambda/2$ can be achieved by linearization of the interferometric fringe, i.e., the function defined in (11.4) is approximated by ideal sawtooth. A resolution of 65 nm has been achieved using a semiconductor laser with a wavelength of 780 nm, in which the resolution is improved by a factor of 6 with respect to conventional fringe counting technique (Servagent et al. 1998). Residual inaccuracy is caused by the nonlinearity of the actual self-mixing waveform. In the following section, we discuss several particular examples of the self-mixing measurements in semiconductor lasers.

11.2 Applications in Feedback Interferometer

11.2.1 Displacement and Vibration Measurement

In the signal processing system in Fig. 11.3, we obtain the number N of counted pulses as the output and the number is assumed to be large enough. Then, the displacement ΔL ($L = L_0 + \Delta L$, L_0 being the offset length) of the external reflector is given by the following relation (Donati et al. 1996; Merlo and Donati 1997):

$$\Delta L = N\frac{\lambda}{2} + O(\lambda) \approx N\frac{\lambda}{2} \tag{11.5}$$

where $O(\lambda)$ is the residual of the counts. The direction of the displacement is determined from the total counted number of the up- and down-edges. Therefore, N has a plus or minus sign. Vibration measurement of an external reflector is also conducted by the same principle. For vibration measurement, the follow-up for time varying signals is important. The measurement is intrinsically limited by the response of the laser, i.e., the relaxation oscillation. Although the time response of

the laser is over nanosecond, the total response of the measurement system with fast electronic circuits is generally up to nanosecond. Still, the electronic response is much faster than time variations of the ordinary mechanical vibrations we are considering.

The detection of a target displacement is the basic for interferometric measurement. We have shown an example of displacement measurement using self-mixing semiconductor lasers in the previous section. Here, we discuss vibration measurement in a self-mixing interferometer, which is the same principle as displacement measurement. When the amplitude of a target reflector under vibration is large enough (larger than the optical wavelength), we can obtain the frequency of the vibration from a Fourier transform analysis for the detected signal in the interferometer. Regardless of the optical feedback strength, the maximum frequency contained in the self-mixing signal for the case of a target vibrating at a frequency f_0 with amplitude ΔL is proportional to the product $f_0 \Delta L$. Indeed, a sinusoidal object vibration of 140 Hz frequency and 7.86 μm peak-to-peak amplitude is successfully measured by the method (Scalise 2002). However, only the product can be measured by the method, and we cannot obtain details of the vibration, such as the profile of the vibration amplitude.

To reconstruct a waveform of an object vibration, a closed loop technique is proposed. The principle of the measurement and the processing electronic circuits after the detection of a self-mixing signal are shown in Fig. 11.5 (Giuliani et al. 2003). At a moderate optical feedback of $C > 1$, we obtain a sawtooth-like interferometric signal as an output form the self-mixing in a semiconductor laser has already been discussed. Figure 11.5a shows the principle of linear measurement of small target vibrations by locking the interferometer phase to half a fringe in the

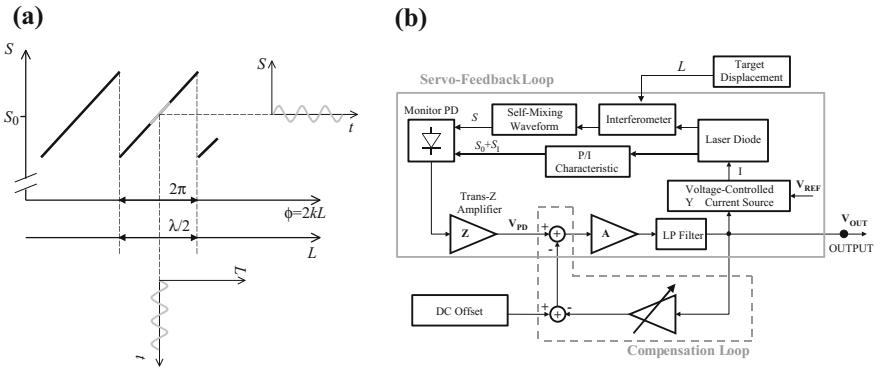

Fig. 11.5 **a** Principle of linear measurement of small target vibrations by locking the interferometer phase to half a fringe in the moderate feedback regime. The vertical axis represents the power emitted by the semiconductor laser, where S_0 is the power emitted by the unperturbed semiconductor laser. The horizontal axes represent interferometric phase and target displacement, respectively. **b** Block diagram for the self-mixing vibrometer accomplishing the phase-locking and phase-nulling techniques. The details of input and output variables and each block are explained in the text [after Giuliani et al. (2003); © 2003 IOP]

moderate feedback regime, where the interferometric signal can be approximated as having a triangular shape. For a moment, we consider a small amplitude object vibration. At an operating offset intensity at S_0, the self-mixing output S is linearly proportional to the vibration amplitude and the waveform of the vibration is directly observed by an oscilloscope as far as the peak-to-peak amplitude of the object vibration is within $\lambda/2$.

By employing an additive active phase-tracking method, the maximum measurable vibration amplitude can be extended up to several hundred-micron meters. The active phase-tracking system is designed so that a constant number of wavelengths are contained in the path from the semiconductor laser to the target. Figure 11.5b shows the block diagrams of the signal processing system. The blocks contained in the solid box constitute the servo-feedback loop and the blocks contained in the dashed box make up the compensation path. The main block is the self-mixing interferometer operating in the moderate feedback regime, whose phase must be kept at a constant value, corresponding to half an interferometric fringe. The target displacement ΔL acts as a perturbation to the system, and it generates a variation $\Delta\phi$ of the interferometric phase. The phase variation $\Delta\phi$ causes a proportional variation ΔS in the power emitted by the laser through the self-mixing effect given by $\Delta S = \beta_{\mathrm{tr}}\Delta\phi$ (β_{tr} being the slope coefficient of the triangular transfer characteristics of the interferometer). The power variation is detected by the monitor photodiode and converted into the voltage signal ΔV_{PD} by the trans-impedance amplifier, which is given by the relation as $\Delta V_{\mathrm{PD}} = \sigma Z \Delta S$ (σ is the net efficiency of the photodiode and Z is the trans-resistance). This signal is then amplified by a factor A, low-pass filtered, and fed to the input of the voltage-controlled laser current source with admittance Y, thus generating a variation I of the injection current as $\Delta I = AY\Delta V_{\mathrm{PD}}$. This, in turn, gives rise to a variation $\Delta\lambda$ of the laser wavelength such that $\Delta\lambda = \Delta I \cdot \mathrm{d}\lambda/\mathrm{d}I$. The feedback loop ensures that the phase variation generated by the laser wavelength variation is exactly opposite (at least at first order) to that caused by target displacement. The amplified error signal V_{OUT} fed to the current source is a perfect replica of the target displacement, and it constitutes the instrument output.

Figure 11.6 is an example of vibration measurements using the self-mixing vibrometer (Giuliani et al. 2003). The object is a loudspeaker driven by a square wave of 10 Hz. The semiconductor laser used is a commercial single-mode Fabry–Perot type with maximum power of 40 mW at the oscillation wavelength of 800 nm. The distance from the laser to the target is 80 cm. The amplitude of the vibration is much lager than $\lambda/2$, but we can obtain the full waveform of the oscillations as shown in the figure. As we can see, the damped resonance oscillations of the loudspeaker are clearly visible. In usual, the resolution of self-mixing interferometry is $\lambda/2$. A method for vibration measurement below $\lambda/2$ is proposed by combining optical feedback effect and frequency modulation to the laser bias injection current (Jha et al. 2016), in which they demonstrate vibration amplitude below $\lambda/2$ with a resolution of a few nanometers.

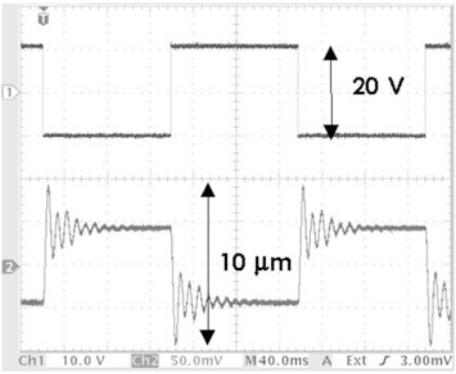

Fig. 11.6 Examples of vibration measurement. The target is a loudspeaker with a black paper surface driven by a 10 Hz square wave. *Upper traces* loudspeaker drive signal, *lower traces* vibrometer output signal [after Giuliani et al. (2003); © 2003 IOP]

11.2.2 Absolute Position Measurement

When the injection current of a semiconductor laser is modulated, not only the laser output power, but also the oscillation frequency of the laser, change in accordance with the relation in (5.5). The same periodic undulation signal like in Fig. 11.2b or c is observed for the laser output under the condition of the C parameter of $C \approx 1$ when a ramp signal is applied to the bias injection current of a semiconductor laser at a fixed external mirror position. The period of the undulations is equal to $c/2L$. For the measurement of the absolute position of a target (distance), a ramp signal, which has a linear increase or decrease for the time development, is usually used. By the ramp modulation, the oscillation frequency is also linearly changed. For a change of the injection current, the wavelength of the laser oscillation varies as $\Delta\lambda$, then the change of the wavenumber Δk is written by

$$\Delta k = -2\pi \frac{\Delta\lambda}{\lambda^2} = 2\pi \frac{\Delta v}{c} \tag{11.6}$$

where Δv is the frequency change due to the injection current variation. For the reflecting mirror positioned at L from the laser facet, the change of the optical phase in the self-mixing interferometer due to the modulation is $\Delta\phi = \Delta k \cdot 2L$. The quantity of $\Delta\phi/2\pi$ is the number of interferometric fringes occurring from the wavelength variation $\Delta\lambda$ observed in the self-mixing interferometer, which is given by the following relation:

$$\frac{\Delta k \cdot 2L}{2\pi} = N + O(N) \tag{11.7}$$

Here, $O(N)$ again represents the residual of fringe number, which corresponds to the maximum error in the distance measurement. By counting the number of fringes, one obtains the distance of the reflector from the laser facet, and the distance L is given by

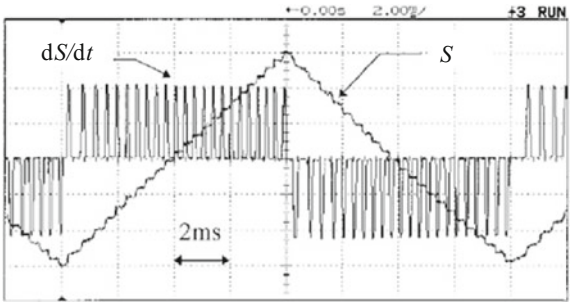

Fig. 11.7 Self-mixing signal for absolute distance measurement, obtained for a 0.8 mA current modulation in a Fabry–Perot semiconductor laser. The pulses are the analogue derivative of the laser output power, which corresponds the fringes to be counted for the distance measurement [after Giuliani et al. (2002); © 2002 IOP]

$$L = \frac{\lambda^2}{2\Delta\lambda}N = \frac{c}{2\Delta v}N \tag{11.8}$$

Figure 11.7 shows the detected output power S of the laser swept by a ramp signal (Giuliani et al. 2002). Looking more closely, the signal resembles stepwise variations of the output power, although the macroscopic change of the detected signal shows a linear increase or decrease for the time development. This step-wise change is induced by the selections of successive resonance external modes by the variation of the bias injection current for the laser; thus the output power shows not a smooth change but a step-wise change. The analogue derivative of the laser output power $\mathrm{d}S/\mathrm{d}t$ becomes a train of pulse-like signals, and this corresponds to the fringe signals discussed before. Counting the number of fringes for the duration of the ramp signal, we obtain the absolute distance with the relation in (11.8). The error in this measurement is the quantization error of fringes and the error corresponds to the maximum residual of the fringe counting in (11.7). Thus, the maximum error is given by $c/2\Delta v$. Mourat et al. (2000) conducted the distance measurement using the self-mixing interferometer of a tunable multi-electrode DBR semiconductor laser having continuous tunable range up to 375 GHz and attained the accuracy of the measurement less than 0.5 mm for the distance of the order of meters. The accuracy is quite coincident with the theoretical resolution of $c/2\Delta v$ = 0.4 mm.

11.2.3 Angle Measurement

Self-mixing interferometry is also applied for small angle measurement. In the angle measurement, coherence collapse states like in Fig. 11.2d is used (Giuliani et al. 2001). Figure 11.8 shows the experimental setup for small angle measurement

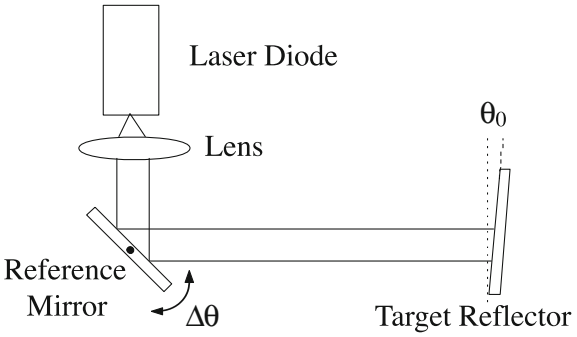

Fig. 11.8 Experimental setup for angle measurement in a self-mixing semiconductor laser. The external mirror under test is tilted with a small angle θ_0. The reference mirror is dithered with small amplitude

in a self-mixing semiconductor laser. An external mirror under to test is tilted with a small angle θ_0 for the optical axis. In the optical setup, the direction of the illuminating light beam is changed by a reference mirror and the beam is directed to the reflector under the test. The feedback level is in regime IV and the laser output power shows coherence collapse states as shown in Fig. 11.2d when $\theta_0 = 0$. For a nonzero tilt angle, the feedback strength from the reflected light decreases with the increase of the tilt angle, but the reflected light is still fed back into the laser cavity and the tilt is such a small angle. In the measurement, the reference mirror put into the optical path is dithered with small amplitude of the tilt angle $\Delta\theta$. At the reference mirror angle for compensating the reflector tilt θ_0, the amount of the feedback light takes the maximum value. When the tilt of the reference mirror is a periodic function with time, the laser shows synchronous output with the modulation. However, the phase of the detected periodic function differs from that of the modulation due to the initial offset angle θ_0. Figure 11.9 shows the experimental results of the laser outputs in the angle measurement. In this figure, signal B corresponds to zero tilt of the external mirror and the output power includes the second harmonic component due to rather strong optical feedback. However, the

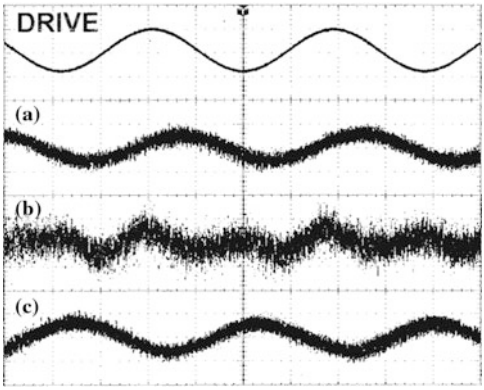

Fig. 11.9 Waveforms of self-mixing laser outputs. *Upper trace* drive signal of the reference mirror. Laser output powers *A* with negative tilt, *B* zero tilt, and *C* positive tilt. The frequency of the driving signal is 180 Hz [after Giuliani et al. (2001); © 2001 SPIE]

initial phases of signals A and C are shifted from that of the driving signal and the small angles are calculated from the phase shifts. The tilt angle of the external mirror has a linear relation with the detected phase shifts for a certain range of the tilt. In this technique, we need some calibration for a particular setup of the experiment. We can perform a small tilt angle detection on the order of 10^{-6}–10^{-4} rad based on this technique.

11.2.4 Measurement of the Linewidth Enhancement Factor

The linewidth enhancement factor α of a semiconductor laser is an important parameter for deciding its dynamical characteristics. As discussed in Chap. 3, the real and imaginary parts of the complex susceptibility in semiconductor lasers are not determined independently, but they have a certain relation. This fact gives rise to the nonzero finite value of the linewidth enhancement factor. For most lasers such as gas lasers, the value of the linewidth enhancement factor α is zero, while it has a value around $\alpha = 3 \sim 7$ in semiconductor lasers (see Sect. 3.3.3). As a result, the linewidth of the laser oscillation is broadened by as much as several tens of MHz up to 100 MHz. On the other hand, for lasers with a linewidth enhancement factor of $\alpha = 0$, the linewidth is usually less than MHz as discussed in Chap. 3. There are several methods to measure the factor (Okoshi et al. 1980). It is also measured by analyzing the laser output power for a sinusoidal modulation of the external mirror position in a self-mixing interferometer. For a certain range of the optical feedback strength of an external reflector, a periodic sawtooth-like wave is observed for the change of the external cavity length in the laser output power. Several methods of the measurement of the linewidth enhancement factor α have been proposed based on self-mixing interferometry. In the following, we show an example of a direct calculation of the linewidth enhancement factor.

The linewidth enhancement factor can be easily calculated form a periodic sawtooth-like signal from the output in self-mixing interferometry (Yu et al. 2004, 2005). The relation between the intensity variations ΔS and the feedback phase $\phi_0 = \omega_0 \tau$ in a small optical feedback system is given by (11.3) with (11.1). Such a variation is schematically shown in Fig. 11.10. From typical phase values in the intensity variation under appropriate feedback conditions, we can directly calculate the α parameter of a semiconductor laser. We define following four phases $\phi_1 \sim \phi_4$ to calculate the parameter as shown in Fig. 11.10. The maximum intensity of a phase ϕ_1 corresponding to $\omega_s \tau = 0$ is obtained as

$$\phi_1 = C \sin(\tan^{-1} \alpha) \tag{11.9}$$

The phase ϕ_2 crossing at zero from plus to minus sign is given by

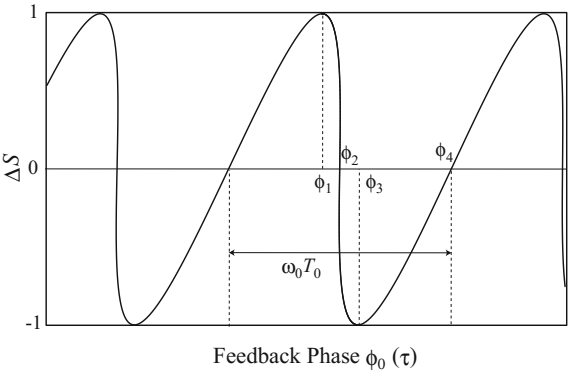

Fig. 11.10 Configuration of a sawtooth-like signal and definitions of the phases to calculate the linewidth enhancement factor

$$\phi_2 = \frac{\pi}{2} + C\,\cos(\tan^{-1}\alpha) \tag{11.10}$$

The minimum intensity of a phase ϕ_3 at $\omega_s\tau = \pi$ reads

$$\phi_3 = \pi - C\,\sin(\tan^{-1}\alpha) \tag{11.11}$$

Finally, the phase ϕ_4 crossing at zero from minus to plus is given by

$$\phi_4 = \frac{3\pi}{2} - C\,\cos(\tan^{-1}\alpha) \tag{11.12}$$

In real observations, the intensity ΔS is a time-varying signal, in which the phases $\phi_1 \sim \phi_4$ correspond to times $T_1 \sim T_4$, respectively. Then, the α parameter is calculated to be

$$\alpha = \frac{\phi_3 - \phi_1 - \pi}{\phi_4 - \phi_2 - \pi} = \frac{T_3 - T_1 - T_0/2}{T_4 - T_2 - T_0/2} \tag{11.13}$$

where T_0 is the period of the fringe in the time domain. Based on this procedure, Yu et al. (2005) obtained the values of the α parameter from 2.2 to 3.3 for commercially available common DFB and MQW semiconductor lasers.

When an optical feedback intensity behaves like a sawtooth wave, the linewidth enhancement factor can also be obtained by the above same optical system from the calculation of the two-phase separations; one is the separation between a zero-crossing phase of the approaching signal and the phase at the adjacent down-edge, and the other is the separation between a zero-crossing phase of the leaving signal and the phase at the adjacent up-edge. Form the comparison between the two-phase values, the linewidth enhancement factor can be calculated either graphically or numerically (Yu et al. 2004). The values of the linewidth enhancement factor from 2.2 to 4.9 are experimentally obtained for various different lasers with different oscillation wavelength. The other example of the measurement for

linewidth enhancement factor is a statistical method (Giuliani and Norgia 2000). A semiconductor laser intrinsically contains statistical noises and the laser has frequency fluctuations. It is proved that the average of the jitter observed in the sawtooth-like waves of the interference fringes in optical feedback is linearly proportional to the linewidth of the laser oscillation. Then, we can calculate the linewidth enhancement factor from the relation (3.130). The values of the linewidth enhancement factor measured using the proposed technique are in good agreement with those obtained by using the self-heterodyne method (Okoshi et al. 1980). It is finally noted that, as pointed out in Sect. 8.7.2, self-mixing effects are very suited for the measurement of the linewidth enhancement factor in quantum-cascade semiconductor lasers. It is difficult to fabricate a photodetector within a quantum-cascade semiconductor laser and, furthermore, a fast response photodetector is not available in THz wavelength. Instead of using a photodetector in self-mixing interferometry, the voltage variations across the laser diode induced by self-mixing effects can be employed for the detection of mixing signals. We will treat the subject in the next section.

11.3 Sensing of Self-mixing Signal Across Laser Diode Voltage

11.3.1 Detection Principles

A photodiode is usually installed into commercialized semiconductor lasers with common package. The photodiode is set close the back facet of the active layer and the light output power from the laser can be monitored. In self-mixing interferometry, which has been discussed in the previous sections, a photodiode installed into a semiconductor laser is used to realize a compact sensor. However, in some types of semiconductor lasers, it is not easy to install a photodetector within a laser package. For example, in vertical-cavity surface-emitting lasers (VCSELs), the back facet reflectivity of light is very high close to 100% and the laser power is rather weak less than a few mW compared to other semiconductor lasers, so that a packaged photodiode is not usually available in VCSELs. In the meantime, we have no compact THz photodetector for the detection of optical power in quantum-cascade semiconductor lasers (QCLs). External photodetectors are used for QCLs. They are usually large-scale devices with slow time response and need cooling to attain efficient light detections. Even using external photodetector in those semiconductor lasers, self-mixing interferometry is still a useful tool for various measurements as discussed in the preceding sections. Instead of using an external photodetector, the voltage variations across the laser diode induced by self-mixing effects can be employed for the detection of mixing signals. In especial, it has a great advantage to use the voltage as the detection of mixing signals in QCLs without using a large-scale external photodetector. Also, the time response of

the voltage is as fast as the laser bandwidth. This compares favorably with the bandwidth of the integrated photodetector that is typically in the range form tens of kHz up to MHz as it original intention is only to monitor the DC power level in the laser. The change of the voltage across a laser diode and the reduction of the threshold have been reported from early time in common semiconductor lasers (Mitsuhashi et al. 1981). The change of the voltage can be explained by the photoconduction effect and a reduction of the quasi-Fermi level related to the enhanced stimulated emission induced by optical feedback.

Since semiconductor lasers are diodes as electronic devices, the current-voltage (I-V) characteristic is given by Agrawal and Dutta (1993)

$$I = I_s\{\exp(\beta V) - 1\} \approx I_s \exp(\beta V) \tag{11.14}$$

where I_s is the saturation parameter, $\beta = e/\eta_i k_B T$ (e being the electron charge, η_i the ideality factor, k_B the Boltzmann constant, and T the temperature), and V is the voltage across the semiconductor laser. For GaAs devices, the ideality factor in the parameter β is around $\eta_i \approx 2$ with a good approximation. Above the laser threshold in free running laser, the voltage across the laser saturates because the carrier density saturates. Then, the voltage is proportional to the bias injection current ($V = RI$: R is the series resistance of the diode). Figure 11.11 shows an example of an I-V characteristic together with a light-current (L-I) characteristic of a QCL of 10 μm wide ridge structure emitting at $\lambda = 8$ μm under the temperature of 200 K (Gordon et al. 2008). Above the threshold, the voltage is linearly proportional to the current until the saturation of current. This feature is not only special for QCLs but also commonly observed in other semiconductor lasers. In the presence of optical feedback to a semiconductor laser above threshold, the threshold carrier density (n_{th}) is reduced and, at the same time, the threshold current (current density J_{th}) decreases. Then, the voltage V across the diode decreases, e.g. $V \propto n$ (Ray et al. 2006).

For narrow-stripe edge-emitting semiconductor laser, the relation between the voltage across the laser and the carrier density can be easily derived from the I-V

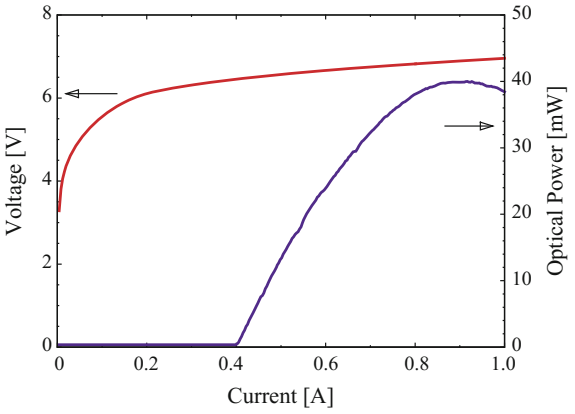

Fig. 11.11 Current-voltage (I-V) and light-current (L-I) characteristics above threshold obtained in a 10 μm wide ridge CW quantum-cascade semiconductor laser emitting at 8 μm under 200 K [after Gordon et al. (2008); © 2008 APS]

characteristics. The carrier density n can be similarly written by the following equation as (11.14) for the change of the voltage ΔV due to optical feedback:

$$n = n_s + \Delta n = n_{0s} \exp\{\beta(V_s + \Delta V)\} \tag{11.15}$$

where n_{0s} is the constant saturation carrier density and V_s is the voltage without optical feedback. Since Δn is very small and $\Delta n / n_s \ll 1$, we have an approximate form as

$$\frac{\Delta n}{n_s} = \exp(\beta \Delta V) - 1 \approx \beta \Delta V \tag{11.16}$$

Then, taking (4.11) into consideration, the change of the voltage reads

$$\Delta V = -\frac{2\kappa}{\beta n_s \tau_{in} G_n} \Delta n \cos \omega_s \tau \tag{11.17}$$

This means that an increase in laser power coincides with a decrease in laser junction voltage, while the two quantities are out of phase. Thus, the voltage across the diode can be used as a detector for a signal from self-mixing interferometry. However, the amount of the voltage change in common semiconductor lasers with optical feedback is very small as from a few mV to 10 mV.

11.3.2 Self-mixing Interferometry in VCSELs

Since the internal back reflectivity in a VCSEL cavity is almost 100% due to high reflectivity DBR mirror, it is not easy to obtain light intensity with a good sensitivity from a photodiode installed within the laser device. One can employ an external photodiode in self-mixing interferometry in VCSELs at the expense of the sensor size. However, an advantage of the compact sensor is impaired. In the meantime, there are a few examples to make a detector integrated into the back of VCSEL structure (Gorecki et al. 2001). Using such devices, a self-mixing interferometric sensor for optical storage memory and near-field scanning optical microscopes (SNOMs) is developed based on the same principles as those in the previous sections. However, it is still difficult to fabricate such devices for practical applications. Instead of an internal photodiode, the voltage across the laser diode can be used to detect the change of feedback light from an external reflector (Hashizume et al. 2002). Figure 11.12 shows an example of voltage detection across a VCSEL when an external diffuse reflector is driven by a small sinusoidal signal (piezo-electric (PZT) drive) and the reflected light is fed back into the laser cavity (Lim et al. 2006). Figure 11.12a is a small sinusoidal drive signal applied to the reflector. Figure 11.12b is the variations of the laser output detected by an external photodiode, which is a similar one detected by an internal photodiode

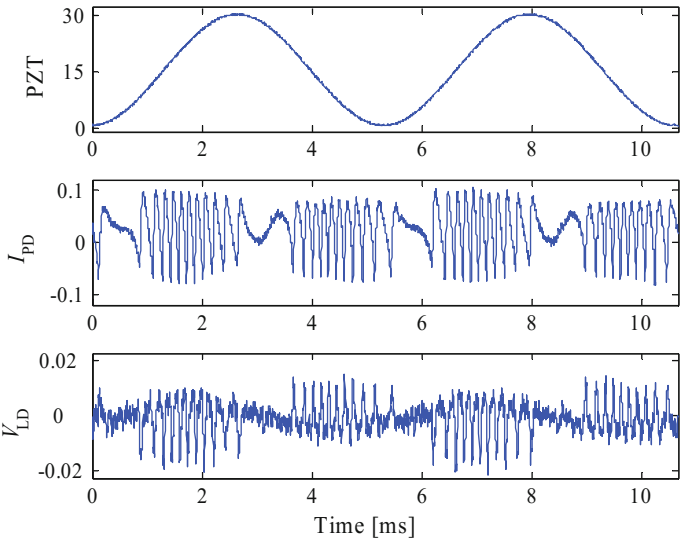

Fig. 11.12 Self-mixing in a VCSEL for target displacement. **a** Drive signal for the reflector, **b** light variations detected by an external photodetector, and **c** voltage across the laser [after Lim et al. (2006); © 2008 SPIE]

installed within the package in a common edge-emitting semiconductor laser. Figure 11.12c is the variations of the voltage across the VCSEL. Although the sensitivity of the detection for the voltage is lower than that for internal photodiodes, the method is still effective for the detection of self-mixing signals in VCSELs. Also the voltage signal has an advantage over photocurrent detection as the direction discrimination of the motion of the external reflector.

Figure 11.13 shows an example of two-dimensional distance measurement using voltage detection in a self-mixing VCSEL (Heinis et al. 2006). The sample is a plain glass plate containing a thin layer of gold (Au) deposited on it. The emitted light from the VCSEL is coupled into a single-mode optical fiber. The fiber end is located a few microns above the sample. From the relation in (11.3), we have $\Delta S = \Delta S_0 \cos(\pi z/\lambda)$ for the change of optical output in the self-mixing interferometry, where z is the distance between the laser and the sample. For the change of the voltage across the laser, we obtain the similar relation as $\Delta V \propto \cos(\pi z/\lambda)$. Figure 11.13a is a two-dimensional optical output detected by an external photodiode. The two-dimensional scanning area for the sample is $60 \times 60\ \mu m^2$. The sample is tilted against the laser facet, so that a similar pattern to an interferometric fringe is observed. Also an increase of fringe contrast can be visible when passing from the glass to Au layer, due to the reflectivity jump between both layers. To enhance the resolution of the measurement, the optical fiber is carried by a piezoelectric (PZT) actuator and the distance between the laser and the sample is changed by modulating the applied voltage to the PZT. For a small change of the PZT, δ ($\delta \ll \lambda$), and the modulation frequency f_0, namely, the change of the

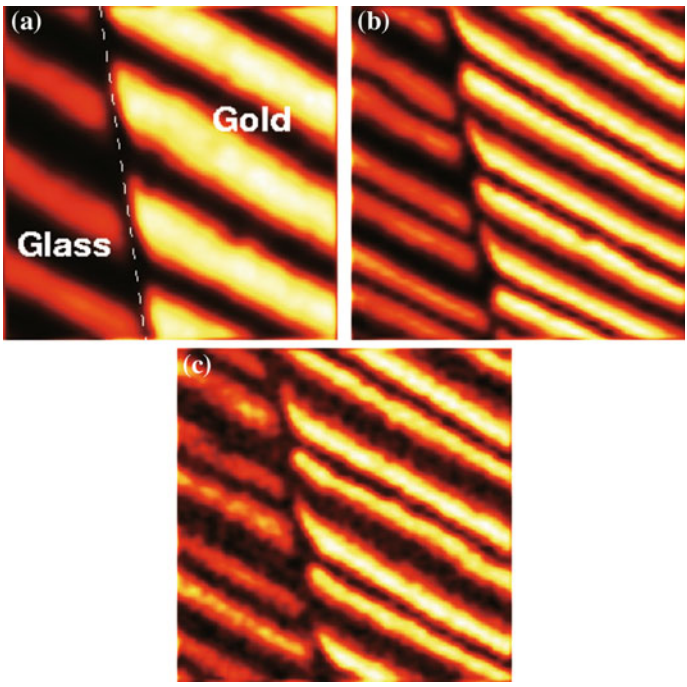

Fig. 11.13 Two-dimensional imaging using self-mixing interferometry in a VCSEL. **a** Optical interference image, **b** optical image obtained by an external photodetector with z-scan, and **c** voltage image with z-scan [Heinis et al. (2006); © 2006 OSA]

distance $z + \delta \cos(2\pi f_0 t)$, the modulated voltage after extracted by a lock-in amplifier is given by

$$\Delta V \propto \left| \sin\left(\frac{\pi}{\lambda} z\right) \right| \tag{11.18}$$

Figure 11.13b, c are the two-dimensional patterns by an external photodiode and the voltage across the laser, respectively. One can obtain almost the same SNR for the detections of the external photodetector and the internal voltage. The principle can be applied to miniature parallel scanning probe optical microscopes, such as confocal microscope, where the use of an external photodetector is avoided. Self-mixing interferometry using VCSELs has an advantage for intrinsic two-dimensional sensor. Namely, two-dimensional information for various mechanical measurements such as position, displacement, and vibration can be simultaneously obtained as a map by using VCSEL arrays. Indeed, distribution on the surface of a rotating disc is obtained as a two-dimensional image from self-mixing interferometry in VCSEL arrays (Lim et al. 2009).

11.3.3 Self-mixing Interferometry in QCLs

Since quantum-cascade laser (QCL) is a semiconductor laser device and the facet reflectivity of the cavity is lower less than several tens of percents like those in other edge-emitting semiconductor lasers (see, for example, Table 8.8), the laser is sensitive to optical feedback. Therefore, self-mixing interferometry is a useful tool to investigate mechanical measurements and other physical parameters based on optical feedback in THz regions and we can use the same principle as discussed in the previous sections. However, it is difficult to fabricate photodetector inside the package of a QCL for the detection of the change of the laser intensity induced by optical feedback. Instead of the use of internal photodetector, the voltage across the laser diode can be used as detection for self-mixing signals, as has already been discussed. Figure 11.14 shows an example of self-mixing interferometric measurement in QCLs (Lim et al. 2011). The sample to be measured is a vibrating aluminum plated attached to a speaker cone and the laser is a quantum-cascade laser with an emission wavelength of $\lambda = 115$ μm (corresponding optical frequency of 2.6 THz). The target is located 47 cm away from the laser facet and the amplitude of vibration is about 100 μm driven by a sinusoidal waveform. The displacement of the motion is detected either with or without obstruction by opaque materials (in visible optical wavelength). Figure 11.14a is a sinusoidal driving signal to the speaker and Fig. 11.14b is the expected self-mixing signal numerically calculated from (11.1) and (11.3) for a small C parameter. Figure 11.14c is an experimentally measured voltage across the laser diode without obstruction. The measured interferogram contains a phase lag due to the inertia of the electromechanical system. Figure 11.14c, e are the results for the change of the voltage with different obstructions between the laser and the target. Since the effective distance between the laser and the target changes depending on the obstruction, the phase shift occurs for each interferogram in Fig. 11.14c–e. In Fig. 11.14c–e, red points correspond to experiments and the black lines are estimated interferograms for $C = -0.74$ and $\alpha = -0.09$. Figure 11.14f is the recovered target displacement calculated from the result in Fig. 11.14c.

Two- and three-dimensional measurements of object profiles can be obtained from the same technique as above. Figure 11.15 shows examples for two- and three-dimensional profile measurements. The samples are mounted on a moving x-y stage and the distance from the laser to the targets is measured at each driving step (250 μm step) by the self-mixing technique (Dean et al. 2011). The QCL is the same as used in the previous one ($\lambda = 115$ μm). Figure 11.15a is the result of a three-dimensional measurement for a scalpel blade. The fringes observed in the image represent the surface morphology of the object with adjacent fringes corresponding to a longitudinal displacement of half a wavelength. In this measurement, the target is obstructed behind a polyethylene FedEx envelope. Figure 11.15b is the calculated modulation transfer function (MTF) of the system. Figure 11.15c is the result of a high-resolution image of a British two-pence coin (259 × 259 pixels). Thus, not only point detection but also two- and three-dimensional measurements,

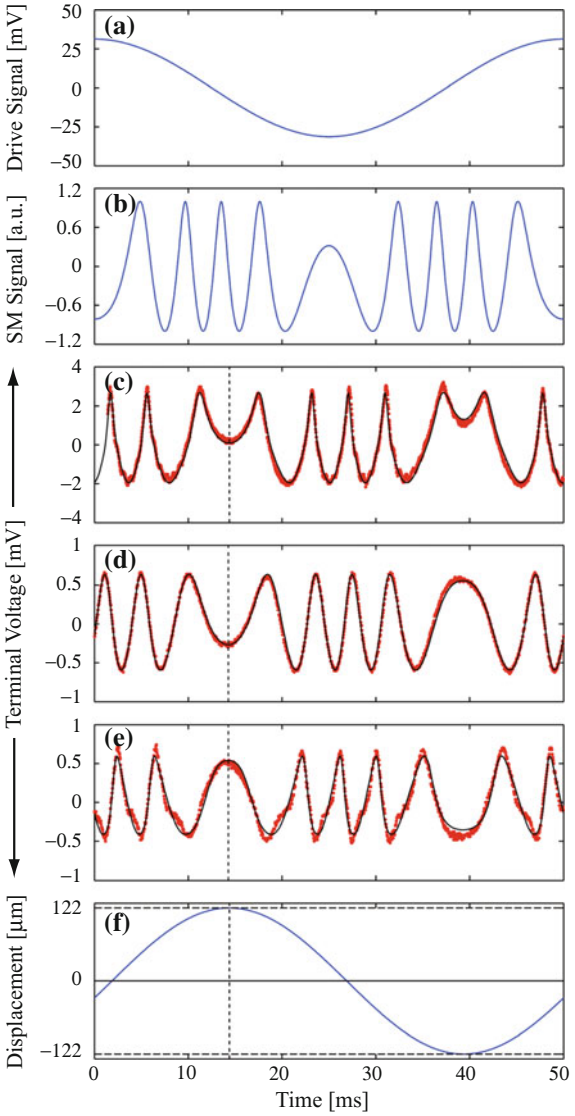

Fig. 11.14 Self-mixing interferometric measurement in a QCL. **a** Driving signal to the target, **b** expected self-mixing signal by the simulation, and **c** self-mixing voltage signal without obstruction. Self-mixing voltage signal obstructed by **d** a black cloth and **e** an HDPE FedEx® envelope. **f** Recovered target displacement from the result in (**c**). In **c**–**e**, the acquired signals are shown as *red dots* and the fits are plotted with *black solid lines* [after Lim et al. (2011); © 2011 AIP]

such as for displacement, vibration, and surface profile, even though clothing or fabrics can be performed based on the voltage detection in self-mixing QCLs. The method offers high sensitivity imaging at THz frequencies without the need for an external THz detector.

As discussed in Sect. 8.7.2, one of the important parameters in QCLs is the linewidth enhancement factor (α parameter), since it greatly varies depending on the bias injection current. Therefore, the measurement of α parameter is very important in QCLs. As already discuss in Sect. 11.2.4, the similar technique as ordinary

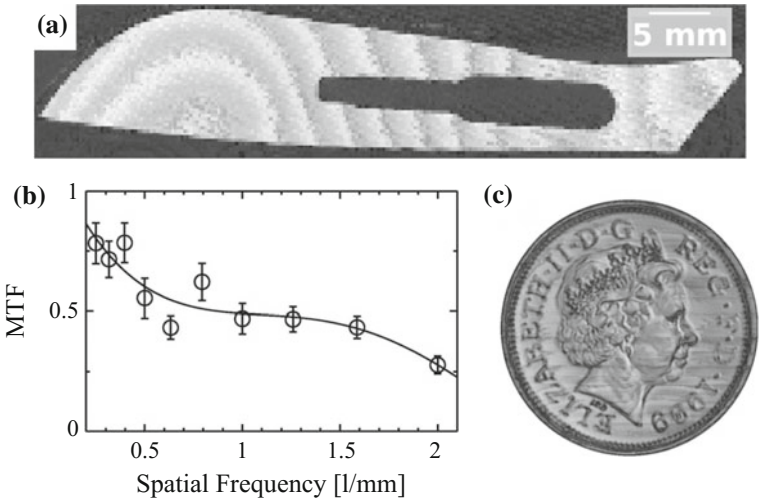

Fig. 11.15 Self-mixing interferometric measurements in a QCL obtained by the voltage change across the laser diode. **a** Three-dimensional image of a scalpel blade obscured behind a polyethylene FedEx® envelope. **b** Modulation transfer function (MTF) of the system. **c** A high-resolution image of a British two-pence coin (diameter = 25.9 mm) [after Dean et al. (2011); © 2011 OSA]

semiconductor lasers can be applied to the measurement of α parameter of QCLs. Indeed, the first application of self-mixing effects in QCLs is the measurement of α parameter (von Staden et al. 2006). Based on the method developed by Yu et al. (2004) for common semiconductor lasers, they obtained the results shown in Fig. 8.53 for a quantum-cascade laser of a wave length of $\lambda = 5.45$ μm. Green et al. (2008) applied the same technique to a quantum-cascade laser oscillating at $\lambda = 116$ μm (2.55 THz) and obtained the value of $\alpha = 0 \sim 0.5$ within the range of the bias injection current of $1.4J_{th} \sim 2.0J_{th}$. The measurement of α parameter in QLDs is very important and the self-mixing technique to measure α parameter in QCLs has great advantage as a simple, compact, and easy method. As another example, the interferometric method induced by optical feedback in QCLs can be also applied to biological imaging. Lim et al. (2014) demonstrated the feasibility of a biological technique using a QCL operating at 2.59 THz to perform coherent imaging of porcine tissue samples and showed the potential of this new THz biomedical imaging technique for in vivo studies, by virtue of a reflection geometry and useful tissue penetration depth enabled by the large THz powers emitted by a QCL. The technique opens a pathway towards automatic measurement for the discrimination of healthy tissue types for the study of normal physiology and possible therapeutic approaches.

11.4 Self-mixing Doppler Velocimetry

11.4.1 Velocity Measurement

For a continuous movement of an external reflector, the output power from the laser by self-mixing exhibits a Doppler beat signal. The field rate equation for such a continuous movement as a function of time t needs to be modified for practical numerical simulations. Velocity measurement is considered as a continuous change of the external mirror position, however, as discussed in the previous section, it can be easily analyzed by the extension of the displacement measurement as the first approximation. When the external mirror moves, the detected signal changes as $\Delta S = \Delta S_0 \cos\omega_s \tau$ in accordance with (11.3). The external cavity round-trip time τ is a time dependent function and is proportional to the external cavity length L. Considering the angle θ of the motion for the optical axis, the round-trip time τ is written by (Bosch et al. 2001)

$$\tau(t) = \frac{2}{c}(L_0 \pm vt \cos\theta) \tag{11.19}$$

where v is the speed of the external mirror and L_0 is the offset distance of the reflector from the laser facet at $t = 0$. The signs of the velocity term account for the direction of the motion; the plus sign is for the object moving away from the laser and the minus sign is for moving toward the laser. The self-mixing in semiconductor lasers is of the heterodyne detection and the term related to the velocity in (11.19) corresponds to a Doppler shift component in the self-mixing (Groot and Gaillatin 1989; Shinohara et al. 1989; Aoshima and Ohtsubo 1992). As has already been discussed in the displacement measurement, we can discriminate the direction of the movement from the shape of waveforms of the self-mixing signal. Two-dimensional velocity measurement is easily implemented by extending the one-dimensional measurement.

Figure 11.16 shows an experimental self-mixing signal in time-domain from a rough rotating disc with a small feedback fraction $C < 1$ (Giuliani et al. 2002). In Fig. 11.16a, the self-mixing amplitude is strongly deformed by speckle modulation compared with a flat reflecting surface. Therefore, it may be difficult to extract the velocity information from the time signal by the fringe counting technique, as done in the displacement measurement. However, the harmonic component corresponding to the disc velocity is easily obtained from the Fourier spectrum as shown in Fig. 11.16b, although the spectrum has a broadened peak due to the speckle effect. Using the technique of the self-mixing in semiconductor lasers, velocity measurements ranging from a rigid surface of $\sim$100 m/s to a slow blood flow of $\sim$mm/s have been performed (Özdemir et al. 2000; Giuliani et al. 2002).

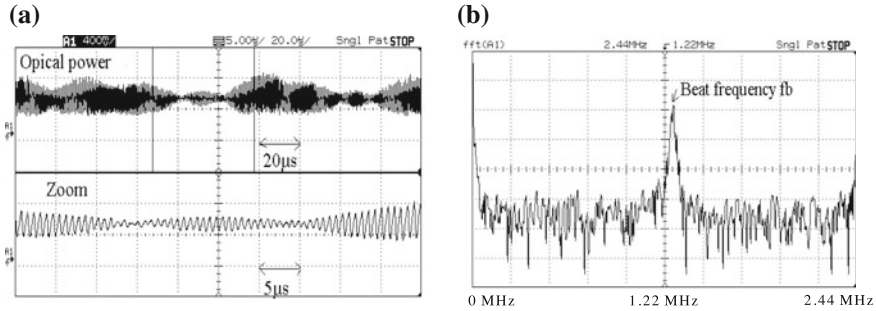

Fig. 11.16 Example of velocity measurements using a self-mixing semiconductor laser. **a** Time-domain self-mixing signal for velocity measurement on a rotating diffusing target. **b** FFT spectrum of the signal. The Doppler beat frequency 1.46 MHz corresponds to a speed of 0.56 m/s [after Giuliani et al. (2002); © 2002 IOP]

11.4.2 Rigorous Rate Equations of Self-mixing Doppler Effects

As mentioned in the previous subsection, the field equation in the presence of time-dependent continuous change of the external mirror must be modified from (4.2) in a static optical feedback case. As a first step to derive the rigorous equation of optical feedback for a continuously moving reflector, we derive the form of the feedback field in the presence of the Doppler effect. At the exit facet of the laser, the complex field of the feedback light including optical frequency oscillations, $\hat{E}_{\text{feedback}}(t)$, from a moving reflector with a constant vector velocity v is given by the following equation (Durst et al. 1976):

$$\hat{E}_{\text{feedback}}(t) = E(t-\tau)\exp\{i(\mathbf{k}_i \cdot \mathbf{r}_i + \mathbf{k}_s \cdot \mathbf{r}_s) - i\omega_0 t\} \tag{11.20}$$

where $\mathbf{k}_i$ and $\mathbf{k}_s$ are the vector wavenumbers to and from the reflector at time t, $\mathbf{r}_i$, and $\mathbf{r}_s$ are the accompanying position vector coordinates, and ω_0 is the angular frequency of the internal laser oscillation. The equation is for a single optical feedback and is valid for a weak optical reflection. We apply the relations $\mathbf{r}_i = \mathbf{r}_i' + \mathbf{v}t$, $\mathbf{r}_s = \mathbf{r}_s' - \mathbf{v}t$, $\mathbf{k}_i \approx \mathbf{k}_i'$, $\mathbf{k}_s \approx \mathbf{k}_s'$, $\mathbf{k}_s = -\mathbf{k}_i$, $\mathbf{r}_s = -\mathbf{r}_i$, $\mathbf{r}_s' = -\mathbf{r}_i'$, and $|\mathbf{k}_i| = |\mathbf{k}_s| = k = \omega_0/c$, where $\mathbf{r}'$ and $\mathbf{k}'$ correspond to respective variables at time $t = 0$. Then, the complex field is written as

$$\hat{E}_{\text{feedback}}(t) = E(t-\tau)\exp\{i\omega_0\tau_0 - i(\omega_0 - \omega_d)t\} \tag{11.21}$$

where τ_0 is the offset round-trip time of light $\tau_0 = 2L_0/c$ and ω_d is the Doppler shifted angular frequency $\omega_d = 2\pi v_d = 2\omega_0 v/c$. τ is the round-trip time of light scattered from the moving object and is written as

$$\tau = \frac{\mathbf{r}_i - \mathbf{r}_s}{c} = \frac{2}{c}(L_0 + vt) \tag{11.22}$$

Here, the expression is the same as (11.19), however, we assume that $\theta = 0$ and the plus or minus sign is included in the parameter v depending on whether the reflector is approaching to or leaving from the front facet of the laser. Since the round-trip time τ is a function of time t, it is difficult to directly perform numerical calculations simply applying the feedback field of (11.21) into (4.2).

Substituting (11.22) into (11.21), the delay field is explicitly written by

$$E(t-\tau) = E(t - \tau_0 - \frac{2v}{c}t) = E\{a(t - \tau_0')\} \tag{11.23}$$

where $a = 1 - 2v/c$ and $\tau_0' = \tau_0/a$. Since the velocity of interest is much smaller than the speed of light $v \gg c$ and, thus, a is very close to unity, τ_0' is approximated as

$$\tau_0' \approx \tau_0(1 + \frac{2v}{c}) \tag{11.24}$$

Therefore, the feedback field has a time scale, at, different from the original field $E(t)$. To adjust different time scales within the same differential equation, the method of Mellin transform is effective. A function of t, $E\{(1-\varepsilon)t\}$ with a small value of ε can be expanded as a non-scaled function $E(t)$ by virtue of the Mellin transform (Gradshteyn and Ryzhik 1980). Then, the function $E\{(1-\varepsilon)t\}$ is approximated as

$$E\{(1-\varepsilon)t\} \approx E(x) - \varepsilon t \frac{\mathrm{d}E(t)}{\mathrm{d}t} \tag{11.25}$$

Note that the above equation looks like a simple approximation as a Taylor series expansion. However, the result is not self-evident, since $E\{(1-\varepsilon)t\}$ is a function of a scaled variable. Putting $a = 1 - \varepsilon$ and replacing t as $t - \tau_0'$, the delay differential field equation for Doppler self-mixing is finally given by Ohtsubo et al. (2009):

$$\begin{aligned}\frac{\mathrm{d}E(t)}{\mathrm{d}t} = &\frac{1}{2}[(1-i\alpha)G_n\{n(t) - n_{\mathrm{th}}\}]E(t) \\ &+ \frac{\kappa}{\tau_{\mathrm{in}}}\left\{E(t-\tau_0') - \frac{2v}{c}(t-\tau_0')\frac{\mathrm{d}E(t-\tau_0')}{\mathrm{d}t}\right\}\exp\{i(\omega_0\tau_0 + \omega_d t)\}\end{aligned} \tag{11.26}$$

Using (11.24), we can perform numerical calculations not only for periodic beating signal but also for chaotic oscillations in the presence of continuous time-dependent external mirror movement. For the carrier density n, which is the counterpart variable for calculating the dynamics in self-mixing semiconductor lasers, the same equation as that for optical feedback from a fixed reflector can be used.

Figure 11.17 shows numerical examples of time series of Doppler shifted waveform. The offset position of the external reflector is $L_0 = 9$ cm and the laser is

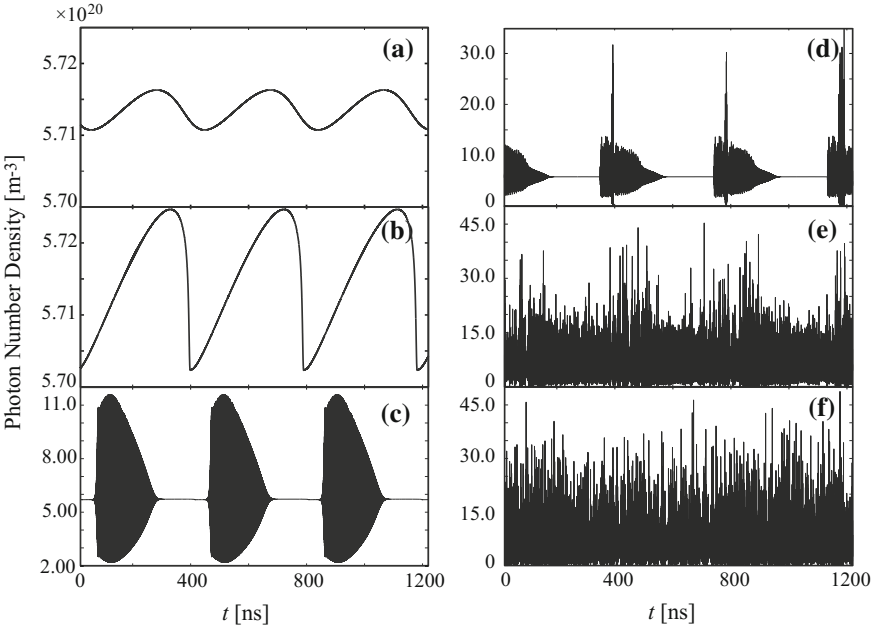

Fig. 11.17 Time series of the Doppler-shifted waveform (photon number density) for variations of external mirror reflectivities. **a** $r = 0.000402$, **b** $r = 0.00161$, **c** $r = 0.00241$, **d** $r = 0.0109$, **e** $r = 0.0153$, **f** $r = 0.0233$. The offset position of the external reflector is $L_0 = 9$ cm and the laser is biased at $J = 1.3J_{th}$. The parameter values almost similar to those listed in Table 5.1 are used for the numerical simulations

biased at $J = 1.3J_{th}$. The other parameter values used are almost the same as those in Table 5.1. Therefore, the chaotic bifurcation diagram is the same as that in Fig. 5.7a and the laser evolves into chaotic oscillations through like a Hopf bifurcation. As the external reflectivity increases, the output power of the self-mixing semiconductor laser shows sinusoidal oscillations in Fig. 11.17a and sawtooth-like periodic oscillations in Fig. 11.17b. The Doppler frequency is $\nu_d = 2.55$ MHz (equivalent to a time period of 391.5 ns). Over a certain breaking point, the laser becomes unstable and oscillates with a burst-like waveform as shown in Fig. 11.17c. While Fig. 11.17c does not show it clearly, the frequency of the periodic burst corresponds to the relaxation oscillation. Even for such unstable oscillations, the Doppler frequency is still visible in the waveform. In Fig. 11.17d, the main Doppler frequency is still preserved, but the laser becomes less stable. If we replace the time scale with an external cavity length, very similar waveforms as those shown in Fig. 11.17a, b are observed for static optical feedback for a discrete change in the mirror position. However, different dynamics are observed for a range of intermediate optical feedback ratios, which are not observed for a static displacement. For moderate optical feedback, the periodicity of the Doppler effect is barely detectable, as shown in Fig. 11.17e. However, with a further increase in the

external reflectivity in Fig. 11.17f, the laser output shows completely chaotic oscillation and no Doppler frequency component is observed in the waveform.

11.5 Chaotic Lidar

For an optical remote sensing technology, LIDAR (Light Detection And Ranging, or it is sometimes called Laser Rader), that can measure the distance or the properties of a target, has been developed since 1970s. In this technique, either short-pulses or random pulse sequences modulated by microwave range is used as a source for illuminating a target. In the common short-pulse technique, the time of flight is measured directly and the range resolution, which is determined by the pulse width, is typically in the range of meters. As an alternative technique, pseudorandom code-modulated CW lidar has been developed. In this technique, target detection and localization are accomplished either by correlating the signal waveform reflected or backscattered from the target with the time-delayed reference waveform or by interfering them optically with a Michelson interferometer, where the range resolution is determined by the bandwidth of the modulated waveform. Based on this technique, higher resolution that measured by short-pulse light sources is attained up to 5 cm. Instead of random modulation, chaotic lidar has been proposed (Lin and Liu 2004a, b). As discussed in this book, chaos in semiconductor lasers exhibits very high-speed oscillations and has very broad bandwidth with flat spectral profile in microwave region. Therefore, it is very suited for a light source of lidar. Further, compared with conventional radars, chaotic lidar has the advantages of very high-range resolution, unambiguous correlation profile, possibility of secure detection, low probability of intercept, and high electromagnetic compatibility. The needs of high-speed random-code generation and modulation electronics no longer exist and the ambiguity caused by the limited length of pseudorandom codes or a repeated waveform is also eliminated because a chaotic waveform never repeats itself. One of promising applications similar to chaotic lidar is a chaotic correlation optical time-domain reflectometer (CC-OTDR). Wang et al. (2008) successfully demonstrated an OTDR for measuring the distribution of the reflectivity along an optical fiber transmission line based on the chaotic correlation technique by experiment. In the following, we will discuss the principle of chaotic lidar and its performance.

Figure 11.18 shows a schematic setup of a chaotic lidar. The light source is a high-speed chaotic semiconductor laser. Chaotic oscillations in semiconductor lasers are generated by for examples, optical injection, optical feedback, or opto-electronic feedback. An optical isolator is placed right after the chaotic laser to prevent unwanted optical feedback. The chaotic output is split by a polarizing beam splitter into two beams, one serving as the probe beam and the other as the reference. By rotating the angle of the half-wave plate relative to the polarizing beam splitter, the power ratio between these two beams can be adjusted. The probe beam is directed to the target, and the signal light that is backscattered or reflected from

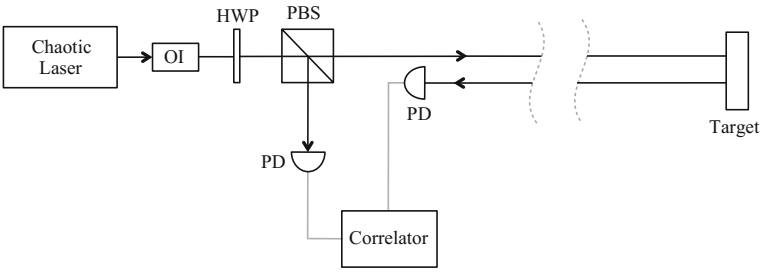

Fig. 11.18 Schematic setup of a chaotic lider. *OI* optical isolator, *HWP* half-wave plate, *PBS* polarization beam splitter, *PD* photodetector

the target. In a practical field application, high power semiconductor laser is used as a light source, and telescope transmitter and receiver are used to transmit and detect chaotic signals. The signal is collected and detected by a combination of lens and detector. The detection and ranging are realized by correlating the signal waveform reflected back from the target with a delayed reference waveform. The performance of the lidar is mainly determined by the generated chaotic state. To have a δ-function-like correlation trace that has a highest possible resolution and lowest possible detection ambiguity, chaotic lidar should be operated in a state that its chaotic waveform has similar properties to those of white noise, such as a flat, smooth, and broad spectrum more than 10 GHz, and a noise-like time series. Chaotic lidar has a much higher range resolution benefiting from the broad bandwidth of the optical chaos. Indeed, due to the very broad bandwidth of the chaotic waveform that can be easily generated by a semiconductor laser, a centimeter-range resolution is readily achieved.

Figure 11.19a shows a numerical example of autocorrelation traces of the time series of generated chaotic light with a correlation length of 200 ns (Lin and Liu 2004a). The chaotic oscillations generated by optical injection to a semiconductor laser with the injection strength of 0.046 in amplitude and the frequency detuning of 0 GHz between the master and slave lasers at the bias injection current of $2J_{\text{th}}$. The laser has a free-running relaxation frequency of 12 GHz at this bias injection current. A narrow correlation spike without any apparent side-lobe is visible and its full-width at half-maximum (FWHM) of the spike, namely, the range resolution, is 0.9 cm, which is much higher than the resolution of a conventional radar. To quantify the performance in a radar system, the peak side-lobe level (PSL) is frequently used. Peak side-lobe level is defined as the ratio of the maximum side-lobe to the peak; it is associated with the probability of a false signal in a particular range bin due to the presence of a target in a neighboring range bin. The peak side-lobe level for the chaotic signal is shown for the correlation length in Fig. 11.19b. The peak side-lobe level for the chaotic signal shows a better correlation performance than those of any other lidar systems. Thus, the chaotic waveform generated by an optically injected semiconductor has superior characteristics for radar applications without the need of any sophisticated microwave circuit.

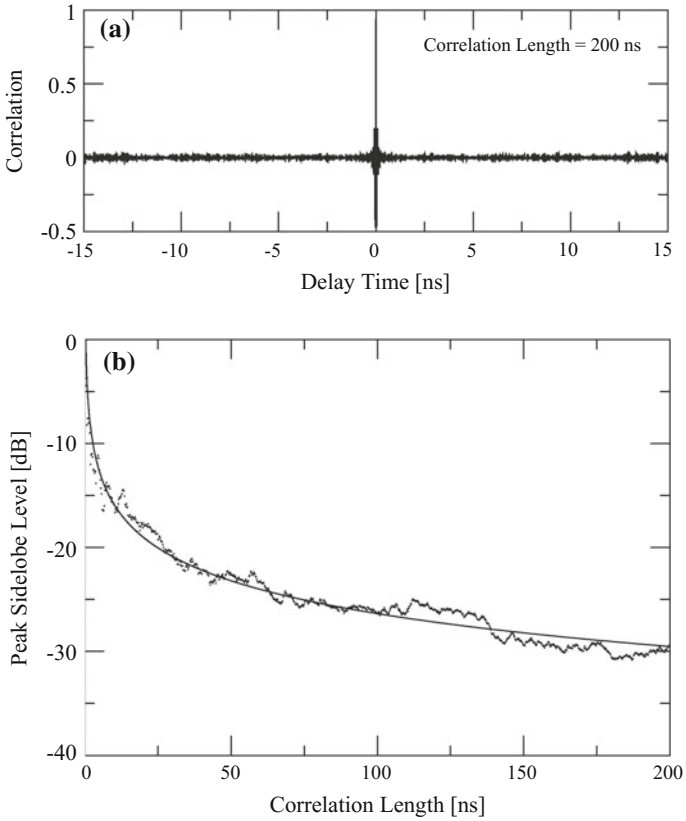

Fig. 11.19 **a** Numerical example of autocorrelation for a chaotic oscillation generated by optical injection. **b** Peak side-lobe level versus correlation length. The *solid line* is the regression. To generate chaos in the semiconductor laser, optical injection is used. The injection strength is 0.046 (amplitude) and the frequency detuning between the injected and slave lasers is 0 GHz [after Lin and Liu (2004a); © 2004 IEEE]

To demonstrate the feasibility of chaotic lidar, a laboratory experiments were carried out (Lin and Liu 2004b). Figure 11.20 shows the result of cross-correlation obtained by a target moving about 50 cm in the line of sight. The laser used is a single-mode distributed feedback InGaAsP/InP semiconductor laser with a wavelength of 1.3 μm. Chaotic oscillations are generated by optical injection under appropriate conditions of the optical injection and the frequency detuning, and the bandwidth of the chaotic signal is measured to be more than 15 GHz. The target mirror is arranged at about 2 m away from the chaotic lidar system on a translation stage. Set of signal and reference waveforms are first obtained and the cross-correlation trace of them is plotted in Fig. 11.20 (the curve corresponds to a correlation peak at 2.1 ns). By translating the mirror about 50 cm away in the line of sight, a second set of signal and reference waveforms are obtained, and their cross-correlation trace is plotted (the curve corresponds to a correlation peak at

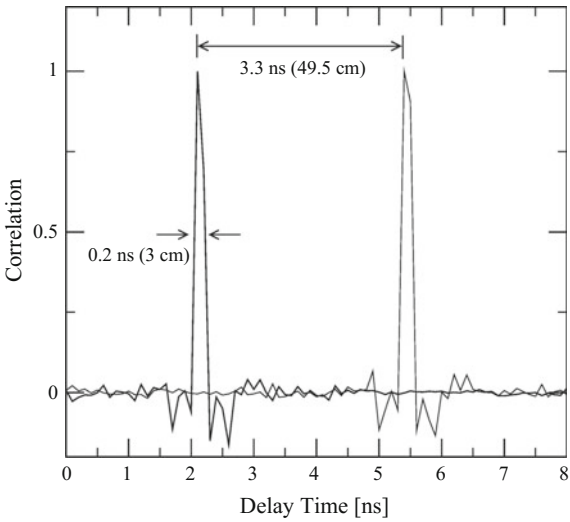

Fig. 11.20 Cross-correlation traces of a target moving about 50 cm in the line of sight [after Lin and Liu (2004b); © 2004 IEEE]

5.4 ns). In both cases, the correlation lengths to acquire chaotic data are 2 μs. From the separation between the correlation peaks, the relative range difference is measured to be 49.5 cm showing a sub-centimeter accuracy in ranging. A 3-cm range resolution is achieved with a 0.2-ns FWHM of the cross-correlation peak. However, the resolution is not the limitation for the essential system but the limitation for the equipment used in the experiment. The peak side-lobe level is calculated to be 27 dB and the signal-to-noise ratio of 27.5 dB is obtained in this experiment. The chaotic lidar system has an excellent performance in correlation such that target detection can be done unambiguously with a very high resolution.

11.6 Active Feedback Interferometer and Applications

11.6.1 Stability and Bistability in Active Feedback Interferometer

Another type of feedback interferometer is a system of a two-arm interferometer with optoelectronic feedback. Here, we discuss the feedback of the interference light to the bias injection current of a semiconductor laser. Such a system is considered as a kind of filtered feedback systems discussed in Sect. 4.7. For example, in a Twyman-Green interferometer, the optoelectronic feedback technique is applied to stabilize the fringe of the interferometer output from disturbances such as mechanical vibrations. Such a system opens wide applications for the fringe analysis and measurements of laser interferometer under various circumstances of the atmosphere (Yoshino et al. 1987). Figure 11.21 is an example of laser interferometers with optoelectronic feedback. The interferometer output is detected by a photodetector through a small pinhole. The

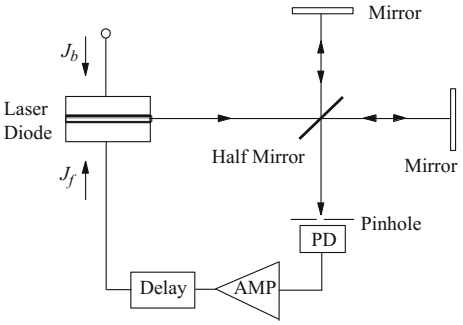

Fig. 11.21 Model of a Twyman-Green active feedback interferometer. The fringe of the interferometer output is detected by a photodetector (PD) through a pinhole smaller than the fringe spacing

diameter of the pinhole is assumed to be much smaller than the fringe spacing. The detected photocurrent is fed back to the bias injection current of the light source of the semiconductor laser. The principle of the stabilization of the interferometer is as follows; the detected optical power deviates when the fringe is disturbed by the external perturbation. Then, the detected photocurrent changes and the injection current to the laser is modulated. The change of the laser output power induces the optical frequency change so as to compensate and cancel the fluctuations of the fringe intensity at the detection point. The variation of the optical frequency is at most several GHz in ordinary feedback interferometers. We can ignore the effect of disturbance by the optical frequency change on the accuracy of the interferometric measurement, since the ratio of the change to the center optical frequency is only less than 10^{-5}. However, care must be taken with respect to the feedback strength. In this active interferometer, stability, multistability, and chaos appear in the laser output depending on the feedback strength and the response time of the feedback loop. In the following, we discuss the principle and behaviors of the active feedback interferometer, and applications for chaos control and signal generations.

We have investigated the effects of optoelectronic feedback in semiconductor lasers in Chap. 7. A similar treatment can be applied to the active interferometer, but the feedback signal is an interference fringe. The rate equations we use are

$$\frac{\mathrm{d}S(t)}{\mathrm{d}t} = G_n\{n(t) - n_{\mathrm{th}}\}S(t) + R_{\mathrm{sp}} \tag{11.27}$$

$$\frac{\mathrm{d}n(t)}{\mathrm{d}t} = \frac{1}{ed}\{J - \xi x(t)\} - \frac{n(t)}{\tau_s} - G_n\{n(t) - n_0\}S(t) \tag{11.28}$$

where $x(t)$ is the term of optoelectronic feedback. As discussed in Chap. 7, the electronic feedback circuit usually has a finite time response and the variable $x(t)$ follows a differential equation similar to (7.8). Here, we write the response of the feedback term as follows:

$$\tau_i \frac{dx(t)}{dt} = -x(t) + \frac{J_f(t)}{\xi} \tag{11.29}$$

where τ_i is again the response time of the electric circuit and J_f is the feedback current to the bias injection current. $x(t)$ is the variable of the feedback and it corresponds to the photon number as a physical quantity. Therefore, ξ is the conversion efficiency from the current density to the photon number. The feedback current of the active interferometer is easily calculated as (Ohtsubo and Liu 1990; Liu and Ohtsubo 1992a, b)

$$J_f(t) = \xi x_b - G_A \xi x(t)[1 + b\cos\{\kappa_i x(t) - \phi_0\}] \tag{11.30}$$

where x_b is the reference signal in the feedback circuit and G_A is the gain of the circuit. The cosine term on the right-hand side of (11.30) denotes the fringe in the interferometer output and b is the visibility of the fringe. ϕ_0 is an offset phase in the interferometer. The laser frequency is changed by the feedback current. The cosine term in (11.30) is the effect of the frequency change. Using the optical frequency v_0 without feedback, the frequency $v(t)$ in the presence of feedback is written by $v(t) = v_0 - \beta_f x(t)$. Then, the argument of the cosine function reads

$$-\kappa_i x(t) + \phi_0 = -\frac{4\pi D_i v(t)}{c} = -\frac{4\pi D_i \beta_f}{c} x(t) + \frac{4\pi D_i v_0}{c} \tag{11.31}$$

where D_i is the difference of the interferometer arms and β_f is the conversion efficiency from the photon number to the oscillation frequency in the semiconductor laser.

If the responses of the electronic circuits and the laser are much faster than the time-varying external disturbances for the interferometer, only (11.30) is sufficient to describe the system characteristics of the active interferometer. We here discuss the stability and instability of the system when the response time of the feedback circuit is fast enough, $\tau_i \sim 0$. Indeed, possible mechanical vibrations for the interferometer are less than 1 kHz. Therefore, solutions of stability, bistability, and multistability of the laser output are investigated from the crossing points for the graph of $y = x(t)$ and $y = J_f(t)$ in (11.30). When the disturbance for the interferometer is small enough, we can obtain a stable solution of the interferometer. In this active interferometer, the configuration of the imbalance interferometer is essential, since the feedback signal depends on the difference according to (11.31). The interferometer is always stabilized at a certain fringe pattern as far as the deviation or distortion of the fringe pattern by the disturbance is smaller than the fringe separation. Thus, we can attain robust interferometric measurement under unfavorable conditions of disturbances and the fringe analysis is performed under such severe conditions. When the disturbance is large enough with exceeding the fringe spacing, multistable states appear in the laser output and hops of the optical frequency through the feedback are induced. This gives rise to chaotic behaviors in the

laser output (Ohtsubo and Liu 1990; Liu 1994). It is noted that the technique of the active interferometer cannot be applied for the phase scanning interferometer, since the phase shift of the fringe is an essential technique in the phase scanning interferometry.

The active interferometer shows rich varieties of dynamics when the feedback circuit has a time delay. By the introduction of the delay, the system exhibits stability, instability, and chaotic states depending on the feedback delay and ratio. We here consider the following modified equation for (11.31) for the delayed system (Liu and Ohtsubo 1992a, b):

$$J_f(t) = \xi x_b - G_A \xi x(t - \tau_e)[1 + b\cos\{\kappa_i x(t - \tau_e) - \phi_0\}] \tag{11.32}$$

where τ_e is the delay time in the feedback circuit. Figure 11.22 shows the calculated bifurcation diagram of the laser output for the change of the reference signal (the bias injection current). The bifurcation diagram is obtained by assuming the difference equation described by (11.32) instead of solving the continuous rate equations. The laser output clearly shows typical chaotic evolution via period doubling bifurcation. Figure 11.23 shows experimentally obtained waveforms in the active interferometer for the change of reference signal level. With increasing the reference signal level, the laser output evolves from a periodic oscillation into chaotic states. The period $2T$ of the period-1 oscillation in Fig. 11.23a is about $2T = 0.22$ ms and it is almost equal twice the delay time of the circuit of $\tau_e = 0.10$ ms. The difference of time $T - \tau_e = 0.01$ ms is equal to the intrinsic delay τ_i of the whole circuit except for the extra delay circuit. In this chaotic system, we can easily design periodic orbits by appropriately choosing the system parameters and generate arbitrary waveform sequences in the laser output prior to chaotic states. These higher harmonic oscillations are used for the applications of chaotic associative memory (Liu and Ohtsubo 1992b, 1993, 1994b).

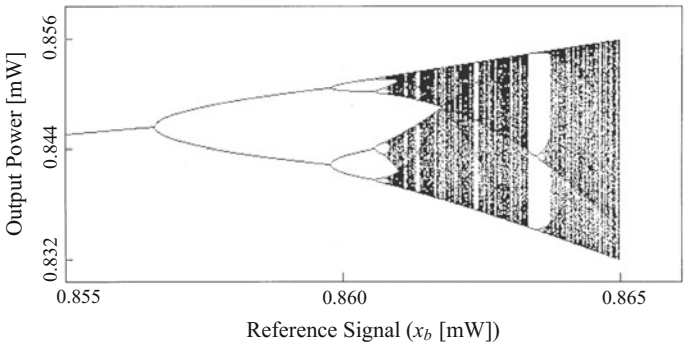

Fig. 11.22 Bifurcation diagram of the laser output in an active delay feedback interferometer for change of the bias injection current. The parameters are $G_A = 0.05$, $\kappa_i = 32\pi$, and $\phi_0 = 0$

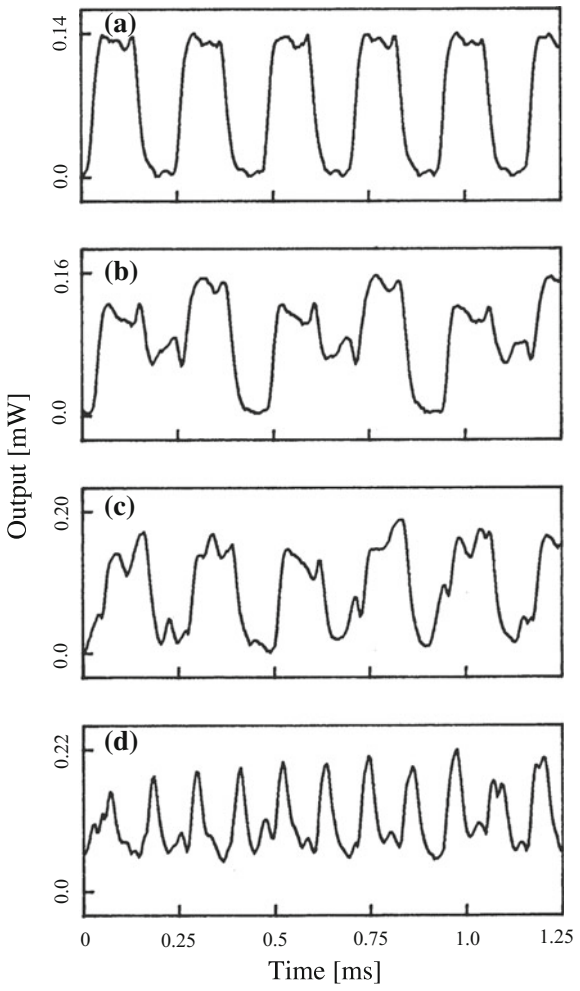

Fig. 11.23 Chaotic oscillations in an active delayed feedback interferometer at $G_A = 0.05$, $\kappa_i = 32\pi$, and $\phi_0 = 0$, and $\tau = 0.1$ ms. **a** $x_b = 0.423$ mW with period-1 state, **b** $x_b = 0.30$ mW with period-4 state, **c** $x_b = 0.473$ mW with period-1 chaos, and **d** $x_b = 0.573$ mW with fully developed chaos

11.6.2 Chaos Control in Active Feedback Interferometers

Chaotic oscillations in active delayed feedback interferometers can be also controlled to periodic or fixed states based on the chaos control method. In this subsection, we describe chaos control in the active interferometer by the occasional proportional feedback (OPF) method. The active feedback interferometer was originally designed for the isolation of rather slow response mechanical vibrations. Therefore, the system is very suited of the OPF technique (Liu and Ohtsubo 1994a, b). We employ the OPF control system discussed in Fig. 9.3. Figure 11.24 shows the schematic diagram for the OPF control in the active interferometer. From the detected output power from PD1, an appropriate sampling control signal is

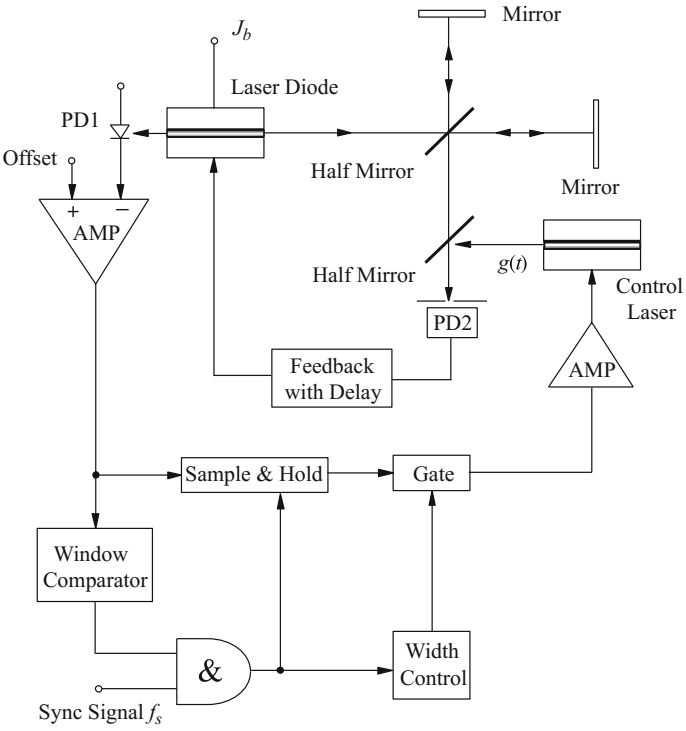

Fig. 11.24 OPF control for chaotic oscillations in an active delay feedback interferometer

generated in the OPF control circuit with a synchronous signal (Sync Signal) and the control signal with small amplitude is overlapped into photodetector PD2 for the fringe detection as a small perturbation. After successful control, the chaotic output of a laser oscillation is fixed to a periodic state.

Figure 11.25 is the experimental result of the OPF control. The delay time of the circuit is $\tau_e = 2.0$ ms. Under the experimental condition, the laser exhibits chaotic oscillation as shown in Fig. 11.25a. The typical frequency of the chaotic signal is 0.24 kHz and it is almost equal to the sum of the times τ_i and τ_e. For the frequency of the synchronous signal in the control circuit of 2.64 kHz, the system is controlled to a periodic state. In Fig. 11.25b, the controlled waveform is the 11th harmonics of the fundamental period-1 orbit. On the other hand, the laser is controlled to the 7th harmonics of the fundamental period-1 orbit for the synchronous frequency of 5.04 kHz in Fig. 11.25c. The corresponding sampling frequency used as a control signal $g(t)$ is 21 multiples of the fundamental frequency. In delay differential systems, we can design and generate arbitrary multi-valued waveforms (isomer signals) of higher periodic orders for the fundamental periodic oscillation by adding extra control circuits to the systems (Liu and Ohtsubo 1991; Liu et al. 1994). In this

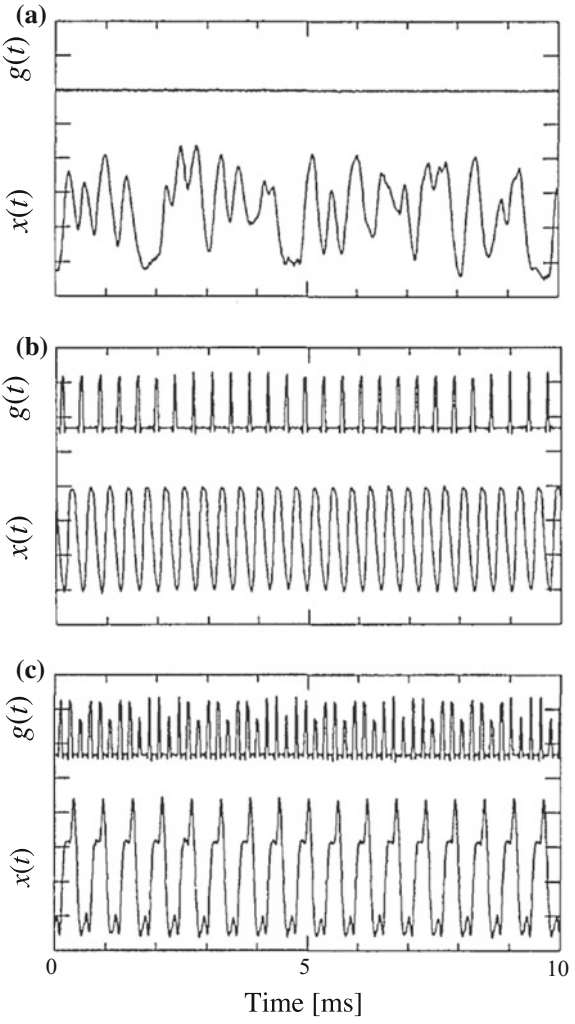

Fig. 11.25 Experimental results of the chaos control in an active delay feedback interferometer. **a** Chaotic oscillation without control. **b** 11th harmonics of fundamental period-1 orbit with control (synchronous frequency is 2.64 kHz). **c** 7th harmonic oscillation of fundamental period-1 orbit with control (synchronous frequency is 5.04 kHz). The delay time of the circuit is τ_e = 2.0 ms. *Upper trace* of each figure is the control signal $g(t)$ (arbitrary amplitude) and *lower trace* is the controlled waveform $x(t)$

example, the control signal is a very small perturbation to the chaotic oscillation and its amplitude is less than 3% of the bias injection current. Therefore, the OPF control applied here is approximately considered as a category of chaos control in the meaning of the OGY algorithm. In the OGY method, the control signal is eliminated after the success of the control, but the control signal is continuously lasting with the same level. In the OPF method, the system must be always pushed by the control signal to fix a certain attractor of unstable periodic orbit.

References

G.P. Agrawal, N.K. Dutta, *Semiconductor Lasers* (Van Nostrand Reinhold, New York, 1993)
T. Aoshima, J. Ohtsubo, Two-dimensional vector LDV using laser diode frequency change and self-mixing effect. Opt. Commun. **92**, 219–224 (1992)
T. Bosch, N. Servagent, S. Donati, Optical feedback interferometry for sensing application. Opt. Eng. **40**, 20–27 (2001)
P. Dean, Y.L. Lim, A. Valavanis, R. Kliese, M. Nikolić, S.P. Khanna, M. Lachab, D. Indjin, Z. Ikonić, P. Harrison, A.D. Rakić, E.H. Linfield, A.G. Davies, Terahertz imaging through self-mixing in a quantum cascade laser. Opt. Lett. **36**, 2587–2589 (2011)
S. Donati, Developing self-mixing interferometry for instrumentation and measurements. Laser Photon. Rev. **6**, 1–25 (2012)
S. Donati, G. Giuliani, S. Merlo, Laser diode feedback interferometer for measurement of displacements without ambiguity. IEEE J. Quantum Electron. **31**, 113–119 (1995)
S. Donati, L. Falzoni, S. Merlo, A PC-interfaced, compact laser-diode feedback interferometer for displacement measurements. IEEE Trans. Instrum. Meas. **45**, 942–947 (1996)
F. Durst, A. Melling, J.H. Whitelaw, *Principles and Practice of Laser Doppler Anemometry* (Academic Press, New York, 1976)
G. Giuliani, M. Norgia, Laser diode linewidth measurement by means of self-mixing interferometry. IEEE Photonics Technol. Lett. **12**, 1028–1030 (2000)
G. Giuliani, S. Donati, M. Passerini, T. Bosch, Angle measurement by injection detection in a laser diode. Opt. Eng. **40**, 95–99 (2001)
G. Giuliani, M. Norgia, S. Donati, T. Bosch, Laser diode self-mixing technique for sensing applications. J. Opt. A: Pure Appl. Opt. **4**, S283–S294 (2002)
G. Giuliani, S. Bozzi-Pietra, S. Donati, Self-mixing laser diode vibrometer. Meas. Sci. Technol. **14**, 24–32 (2003)
A. Gordon, C.Y. Wang, L. Diehl, F.X. Kärtner, A. Belyanin, D. Bour, S. Corzine, G. Höfler, H.C. Liu, H. Schneider, T. Maier, M. Troccoli, J. Faist, F. Capasso, Multimode regimes in quantum cascade lasers: from coherent instabilities to spatial hole burning. Phys. Rev. A **77**, 053804-1–053804-18 (2008)
C. Gorecki, S. Khalfallah, H. Kawakatsu, Y. Arakawa, New SNOM sensor using optical feedback in a VCSEL-based compound-cavity. Sens. Actuators A **87**, 113–123 (2001)
I.S. Gradshteyn, I.M. Ryzhik, *Table of Integral, Series, and Products* (Academic Press, New York, 1980)
R.P. Green, J.-H. Xu, L. Mahler, A. Tredicucci, F. Beltram, G. Giuliani, H.E. Beere, D.A. Ritchie, Linewidth enhancement factor of terahertz quantum cascade lasers. Appl. Phys. Letts. **92**, 071106-1–071106-3 (2008)
P.J. Groot, G.M. Gaillatin, Backscatter-modulation velocimetry with an external-cavity laser diode. Opt. Lett. **14**, 165–167 (1989)
J. Hashizume, S. Shinada, F. Koyama, K. Iga, Reflection induced voltage change of surface emitting laser for optical probing. Opt. Rev. **9**, 186–188 (2002)
D. Heinis, C. Gorecki, S. Bargiel, B. Cretin, Feedback-induced voltage change of a vertical-cavity surface-emitting laser as an active detection system for miniature optical scanning probe microscopes. Opt. Express **14**, 3396–3405 (2006)
A. Jha, F.J. Azcona, S. Royo, Frequency-modulated optical feedback interferometry for nanometric scale vibrometry. IEEE Photonics Technol. Lett. **28**, 1217–1220 (2016)
Y.L. Lim, K. Bertling, P. Rio, J.R. Tucker, A.D. Rakić, Displacement and distance measurement using the change in junction voltage across a laser diode due to the self-mixing effect. Proc. SPIE **6038**, 378–387 (2006)
Y.L. Lim, N. Nikolic, K. Bertling, R. Kliese, A.D. Rakić, Self-mixing imaging sensor using a monolithic VCSEL array with parallel readout. Opt. Express **17**, 5517–5525 (2009)

Y.L. Lim, P. Dean, M. Nikolić, R. Kliese, S.P. Khanna, M. Lachab, A. Valavanis, D. Indjin, Z. Ikonić, P. Harrison, E.H. Linfield, A.G. Davies, S.J. Wilson, A.D. Rakić, Demonstration of a self-mixing displacement sensor based on terahertz quantum cascade lasers. Appl. Phys. Lett. **99**, 081108-1–081108-3 (2011)

Y.L. Lim, T. Taimre, K. Bertling, P. Dean, D. Indjin, A. Valavanis, S.P. Khanna, M. Lachab, H. Schaider, T.W. Prow, H.P. Soyer, S.J. Wilson, E.H. Linfield, A.G. Davies, A.D. Rakić, High-contrast coherent terahertz imaging of porcine tissue via swept-frequency feedback interferometry. Biomedical Opt. Express **5**, 3981–3989 (2014)

F.Y. Lin, J.M. Liu, Chaotic radar using nonlinear laser dynamics. IEEE J. Quantum Electron. **40**, 815–820 (2004a)

F.Y. Lin, J.M. Liu, Chaotic lidar. IEEE J. Sel. Top. Quantum Electron. **10**, 991–997 (2004b)

Y. Liu, J. Ohtsubo, Observation of higher-harmonic bifurcations in a chaotic system using a laser diode active interferometer. Opt. Commun. **85**, 457–461 (1991)

Y. Liu, J. Ohtsubo, Chaos in an active interferometer. J. Opt. Soc. Am. B **9**, 261–265 (1992a)

Y. Liu, J. Ohtsubo, Period three-cycle in a chaotic system using a laser diode active interferometer. Opt. Commun. **93**, 311–317 (1992b)

Y. Liu, J. Ohtsubo, Regeneration spiking oscillation in semiconductor laser with a nonlinear delayed feedback. Phys. Rev. A **47**, 4392–4399 (1993)

Y. Liu, J. Ohtsubo, Experimental control of chaos in a laser-diode interferometer with delayed feedback. Opt. Lett. **19**, 448–450 (1994a)

Y. Liu, J. Ohtsubo, Controlling chaos of a delayed optical bistable system. Opt. Rev. **1**, 91–93 (1994b)

Y. Liu, J. Ohtsubo, Y. Shoji, Accessing of high mode oscillations in a delayed optical bistable system. Opt. Commun. **105**, 193–198 (1994)

Y. Liu, Study of chaos in a delay-differential system with a laser diode active interferometer. Ph.D. Thesis. Shizuoka University, (1994)

S. Merlo, S. Donati, Reconstruction of displacement waveforms with a single-channel laser diode feedback interferometer. IEEE J. Quantum Electron. **33**, 527–531 (1997)

Y. Mitsuhashi, J. Shimada, S. Mitsutsuka, Voltage change across the self-coupled semiconductor laser. IEEE J. Quantum Electron. **17**, 1216–1225 (1981)

G. Mourat, N. Servagent, T. Bosch, Distance measurements using the self-mixing effect in a 3-electrode DBR laser diode. Opt. Eng. **39**, 738–743 (2000)

J. Ohtsubo, Y. Liu, Optical bistability and multistability in active interferometer. Opt. Lett. **15**, 731–733 (1990)

J. Ohtsubo, H. Kumagai, R. Shogenji, Numerical study of Doppler dynamics in self-mixing semiconductor lasers. IEEE Photonics Technol. Lett. **21**, 742–744 (2009)

T. Okoshi, K. Kikuchi, A. Nakayama, Novel method for high resolution measurement of laser output spectrum. Electron. Lett. **16**, 630–631 (1980)

S.K. Özdemir, S. Shinohara, S. Takamiya, H. Yoshida, Noninvasive blood flow measurement using speckle signals from a self-mixing laser diode: in vitro and in vivo experiments. Opt. Eng. **39**, 2574–2580 (2000)

W. Ray, W.S. Lam, P.N. Guzdar, R. Roy, Observation of chaotic itinerancy in the light and carrier dynamics of a semiconductor laser with optical feedback. Phys. Rev. E **73**, 026219-1–026219-5 (2006)

L. Scalise, Self-mixing feedback laser doppler vibrometry. SPIE Proc. **4827**, 374–384 (2002)

N. Servagent, F. Gouaux, T. Bosch, Measurements of displacement using the self-mixing interference in a laser diode. J. Opt. **29**, 168–173 (1998)

S. Shinohara, H. Naito, H. Yoshida, H. Ikeda, M. Sumi, Compact and versatile self-mixing type semiconductor laser doppler velocimeters with direction discrimination circuit. IEEE Trans. Instrum. Meas. **38**, 574–577 (1989)

J. von Staden, T. Gensty, W. Elsäßer, G. Giuliani, C. Mann, Measurements of the a factor of α distributed-feedback quantum cascade laser by an optical feedback self-mixing technique. Opt. Lett. **31**, 2574–2576 (2006)

T. Taimre, M. Nikolié, K. Bertling, Y.L. Lim, T. Bosch, A.D. Rakí, Laser feedback interferometry: a tutorial on the self-mixing effect for coherent sensing. Adv. Optics Photonics **7**, 570–631 (2015)

A.B. Wang, Y. Wang, H. He, Enhancing the bandwidth of the optical chaotic signal generated by a semiconductor laser with optical feedback. IEEE Photonics Technol. Lett. **20**, 1633–1635 (2008)

T. Yoshino, M. Nara, S. Mnatzakanian, B.S. Lee, T.C. Strand, Laser diode feedback interferometer for stabilization and displacement measurements. Appl. Opt. **26**, 892–897 (1987)

Y. Yu, G. Giuliani, S. Donati, Measurement of the linewidth enhancement factor of semiconductor lasers based on the optical feedback self-mixing effect. IEEE Photonics Technol. Lett. **16**, 990–992 (2004)

Y. Yu, J. Xi, E. Lia, J.F. Chicharo, Measuring the linewidth enhancement factor of semiconductor lasers based on weak optical feedback effect. SPIE Proc. **5628**, 34–39 (2005)

Chapter 12
Chaos Synchronization in Semiconductor Lasers

Abstract Another important application of chaotic semiconductor lasers is chaotic secure communications. The key to chaotic communications is chaos synchronization between two nonlinear systems. If two nonlinear chaotic systems operate independently, the two systems never show the same output because of the sensitivity of chaos for the initial conditions. However, when a small portion of a chaotic output from one nonlinear system is sent to the other, the two systems synchronize with each other and show the same output under certain conditions of the system parameters. This scheme is called chaos synchronization. It is very surprising that two chaotic systems share the same waveform, since chaos is sensitive to the initial conditions and its future is unpredictable. In this chapter, we overview chaos synchronization in chaotic semiconductor laser systems for the introduction of the secure chaos communications discussed in Chap. 13.

12.1 Concept of Chaos Synchronization

12.1.1 Chaos Synchronization

We cannot expect the same chaotic oscillation for two nonlinear systems even when they are the same configuration having the same parameter values, because chaos has strict sensitivity to the initial conditions of the parameters. For example, two chaotic systems with the same parameters may at first output similar signals when the difference between the initial conditions is small enough in the ordinary sense. Then, the two signals show a small difference with lapse of time and, then, the difference rapidly increases for further time development. Finally, the two systems behave in a completely different manner as far as the difference between the initial conditions is not zero. However, there is a possibility of showing the same output in two nonlinear systems if the two systems possess a common subsystem with the same parameter values, otherwise if a small amount of the signal from one of the two systems is transmitted to the other. Under this condition, the systems output completely the same chaotic signal. The scheme is called "chaos synchronization."

© Springer International Publishing AG 2017

J. Ohtsubo, *Semiconductor Lasers*, Springer Series in Optical Sciences 111,
DOI 10.1007/978-3-319-56138-7_12

It is noted that chaos synchronization is not only a unique phenomenon limited to two chaotic systems, but is universally observed many coupled nonlinear elements. For example, many fireflies in a forest wink their light coherently after initial random chaotic twinkling of respective fireflies (Renato and Strogatz 1990; Strogatz et al. 1993). Crowd synchrony on the Millennium Bridge is another example of chaos synchronization for many coupled nonlinear elements, which was caused by synchronous lateral excitation by many random steps of the pedestrian walks (Strogatz et al. 2005; Eckhardt et al. 2007). One of the well-known systems of chaos synchronization is the Huygens' pendulum clocks mounted on the same wooden beam (Huygens 1986). We will return to the subject of chaos synchronization in many coupled nonlinear elements in Chap. 14. Here, we focus on chaos synchronization between two semiconductor laser systems and study the synchronization properties between them.

The idea of chaos synchronization between two nonlinear systems was proposed by Pecora and Carroll (1990, 1991). They used a Lorenz system with three variables for the demonstration. In their system, an output from one of the variables as a subsystem in a transmitter was sent to a receiver. Then, they showed chaotic synchronization between the transmitter and receiver systems. In actual, earlier study of the mathematical aspects of chaos synchronization had been studied by Fujisaka and Yamada in 1983. After their proposal, synchronization phenomena in various chaotic systems including lasers have been reported. The idea and principle of chaos synchronization are described in Appendix A.4. Chaos synchronization between two nonlinear systems is not self-evident and this is a real surprise, since we cannot expect the same output even for the same two chaotic systems as far as the two systems are isolated from each other. The origin of chaos synchronization has not been fully understood yet and the theoretical background has not been established. However, chaos synchronization has been observed by numerical simulations and experiments in various nonlinear systems. In laser systems, synchronization of chaos was experimentally demonstrated in CO_2 lasers (Sugawara et al. 1994) and solid-state lasers (Roy and Thornburg 1994). After that, many theoretical and experimental researches for chaos synchronization in various laser systems including semiconductor lasers were published.

Here, we show the general idea of chaos synchronization. Figure 12.1 is a one-to-one system of chaos synchronization. The receiver of chaotic system 2 consists of the same configuration as chaotic transmitter system 1 and also has the same device characteristics as those of system 1. A small portion of the transmitter output is sent to the receiver. In Fig. 12.1a, the transmitter signal is unidirectionally coupled to the receiver and the chaotic output from the receiver synchronizes with the transmitter under an appropriate condition. In laser systems, an optical isolator is usually used to realize unidirectional coupling and the laser output from the transmitter is optically injected to the receiver laser. As a matter of fact, transmitter and receiver lasers may not be the same types as chaotic light sources, or even the transmitter may not be the same kind of laser as the receiver laser. As far as the transmitter can simulate and transmit a possible chaotic waveform of the receiver laser with the same optical frequency, successful chaos synchronization can be

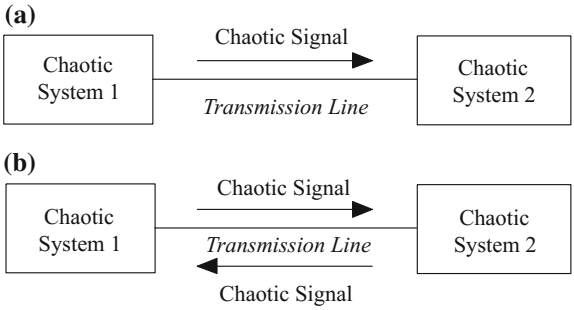

Fig. 12.1 General idea of chaos synchronization of a one-to-one transmitter–receiver system

achieved. Indeed, a virtual chaotic waveform numerically simulated by a computer is also used as a transmitter signal to a real receiver laser for chaos synchronization. Chaos synchronization is realized for a negative value of the maximum conditional Lyapunov exponent for the difference between the transmitter and receiver signals. Figure 12.1b is a chaos synchronization system of the mutual coupling of signals. Unidirectional systems are mainly used for secure chaotic data communications, however, we can perform simultaneous data transmissions using mutual coupling systems and the properties of those systems have been studied as a chaos synchronization scheme.

Chaos synchronization is attained not only in one-to-one transmitter–receiver systems but also in the multiple transmitter–receiver systems shown in Fig. 12.2. In this system, all the transmitters and receivers may be the same system, but each transmitter laser exhibits different chaotic output from the others. In this case, the parameter values for each pair of the transmitter and receiver systems must be the same and they become the key for chaos synchronization. Otherwise, a transmitter is a different system from each other and one of the receivers may play a

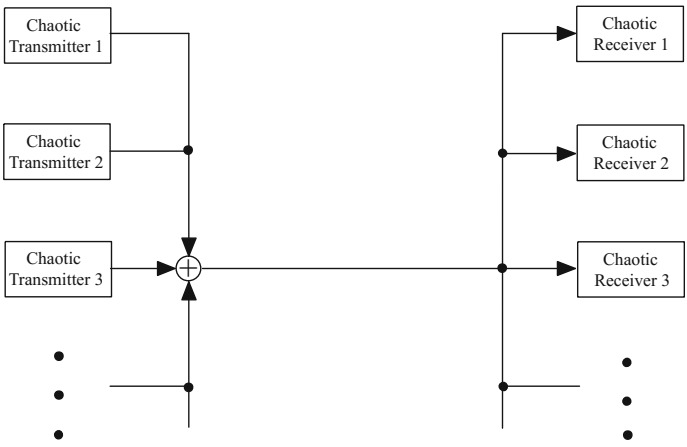

Fig. 12.2 Multiple transmitter–receiver systems of chaos synchronization

counterpart to the transmitter. Chaotic signals from the transmitters are sent through a single transmission line and broadcasted to each receiver. In the receiver systems, each chaotic signal from the transmitters only synchronizes with the corresponding receiver having the same system and device characteristics. Indeed, chaos synchronization has been demonstrated in a few of multiple transmitter–receiver systems (Liu and Davis 2000). Other examples are one-to-many and many-to-one optical chaos synchronization and communication systems (Zhang et al. 2008). They numerically demonstrated chaos synchronization in such systems and successfully recovered original messages both for one-to-many and many-to-one systems.

In the proposal of chaos synchronization by Pecora and Carroll, the system is divided into two subsystems. In their model, the transmitter has two subsystems, while the receiver has only one of the two subsystems (for details, the reader is referred to Appendix A.4). The chaotic signal from one of the subsystems is transmitted to the receiver. Then, the receiver conforms the complete chaotic system by the signal transmission and the receiver synchronizes with the transmitter under an appropriate condition of the parameters. The idea of chaos synchronization was immediately applied in real electronic circuit systems after the proposal by Pecora and Carroll (Cuomo et al. 1993). However, the method is not straightforwardly applicable to laser systems, since we cannot divide the dynamics of laser variables into subsystems.

Chaos synchronization strategies developed for most nonlinear systems, such as nonlinear electronic circuits, cannot be directly implemented on semiconductor lasers because of a number of significant differences between semiconductor lasers and other nonlinear dynamical systems. The differences are as follows:

1. A semiconductor laser is an integrated entity that cannot be easily decomposed into subsystems.
2. For a given laser, it is not possible to arbitrarily adjust its intrinsic dynamical parameters and they can be only varied through their linear dependence on the laser power by varying the bias point of the laser.
3. One of its dynamical variables, the carrier density, is not directly accessible externally and, therefore, cannot be used to couple the transmitter and receiver lasers for synchronization.
4. When the output field of the transmitter laser is transmitted and coupled to the receiver laser, both its magnitude and phase are transmitted and coupled. It is not possible to only transmit and couple the magnitude but not the phase, or only the phase but not the magnitude.

By using a driving signal to link two chaotic systems, synchronization can be achieved if the difference between the outputs of the two systems possesses a stable fixed point with zero value. As an alternative technique in laser systems, the difference between certain variables in transmitter and receiver lasers can be used as control parameters for synchronization (Annovazzi-Lodi et al. 1996). In semiconductor lasers, master–slave configurations are frequently used as chaos

synchronization systems suitable for chaotic secure communications. The schemes of optical feedback, optical injection, and optoelectronic feedback are used as typical chaotic generators in semiconductor lasers. Chaos synchronization in particular systems is discussed in the subsequent sections in this chapter. They are mostly numerical demonstrations of chaos synchronization, however, several experimental results have been reported.

12.1.2 Generalized and Complete Chaos Synchronization

There are two different origins of chaos synchronization in nonlinear delay differential systems, such as in semiconductor laser systems of optical feedback and optoelectronic feedback. One is synchronization of chaotic signals based on optical injection phenomena. The other is complete chaos synchronization in which the two systems can be written by a set of the identical rate equations in a mathematical sense. We will discuss the two synchronization schemes in this section. In the ordinary sense, chaos synchronization occurs immediately after a receiver receives a chaotic signal from a transmitter when the transmitter and the receiver are divided into several subsystems (see Appendix A.4). In this case, the time lag of the signal in the receiver system is defined by time τ_c, which is the transmission time of signal from the transmitter to the receiver. Namely, using the chaotic signals $\mathbf{y}(t)$ and $\mathbf{y}'(t)$ from the transmitter and receiver systems, respectively, the relation

$$\mathbf{y}'(t) = K_p \mathbf{y}(t - \tau_c) \tag{12.1}$$

is obtained (Ohtsubo 2002a). In (12.1), K_p is the proportional coefficient, and $\mathbf{y}$ and $\mathbf{y}'$ are essentially vector variables. In laser systems, this type of chaos synchronization is achieved by optical injection locking and amplification of signals from the transmitter to the receiver. This is the well-known phenomenon of injection locking in laser systems. The receiver output is usually an amplified signal of the transmitted field (the gain is not necessary larger than unity). Therefore, an excellent synchronized waveform is obtained in the receiver system when the amplification is faithfully achieved. However, distortions are usually introduced to the injection-locked waveforms and the correlation between the transmitter and receiver outputs is less than unity. This scheme is called generalized synchronization.

On the other hand, there exists a different scheme of chaos synchronization from the generalized one in delay differential systems. We assume a system like a delay differential system such as optical feedback or optoelectronic feedback in a semiconductor laser. The differential equation in the transmitter output $\mathbf{y}(\mathbf{t})$ is described by

$$\frac{\mathrm{d}\mathbf{y}(t)}{\mathrm{d}t} = f\{\mathbf{y}(t), \boldsymbol{\mu}_p\} + \kappa_{p0}\mathbf{y}(t-\tau) \tag{12.2}$$

where $\boldsymbol{\mu}_p$ is the vector of chaos parameters, κ_{p0} is the feedback coefficient in the system, τ is the delay time, and f is the nonlinear function describing the delay differential system. Assuming that a small portion of the transmitter signal is sent to the receiver, the receiver equation is written by

$$\frac{\mathrm{d}\mathbf{y}'(t)}{\mathrm{d}t} = f\{\mathbf{y}'(t), \boldsymbol{\mu}_p\} + \kappa_{p1}\mathbf{y}'(t-\tau) + \kappa_{p2}\mathbf{y}(t-\tau_c) \tag{12.3}$$

where κ_{p1} is the feedback coefficient in the receiver system, κ_{p2} is the coupling coefficient between the transmitter and the receiver, τ_c is again the transmission time of the signal from the transmitter to the receiver. From a comparison between (12.2) and (12.3), we obtain the condition for the equivalent forms of the two differential equations as

$$\mathbf{y}'(t) = \mathbf{y}(t - \Delta t) \tag{12.4}$$

$$\Delta t = \tau_c - \tau \tag{12.5}$$

$$\kappa_{p0} = \kappa_{p1} + \kappa_{p2} \tag{12.6}$$

Under the above conditions, the receiver system is mathematically described by the equivalent equation such as that of the transmitter system and the receiver generates completely the same output as the transmitter (not an amplified signal but a complete copy of the transmitter signal), since the two systems posses the same seeding signal through the coupling. Therefore, the synchronization scheme is called complete chaos synchronization and it is distinguished from generalized synchronization of chaotic oscillations. The above examples are of chaos synchronization for unidirectionally coupled nonlinear systems. However, we can consider mutually coupled systems for chaos synchronization. In that case, there are also two types of chaos synchronization, i.e., generalized and complete schemes. We will discuss chaos synchronization in mutually coupled laser systems later in this chapter.

The difference between the complete and generalized synchronization is clear from (12.1) and (12.4) and the scheme of chaos synchronization in a particular system is easily distinguished by investigating the time lag between the transmitter and receiver outputs. Figure 12.3 shows the relations of time lags in the two schemes. The receiver outputs a synchronized waveform immediately after it receives the transmitter signal in generalized chaos synchronization in Fig. 12.3a. Therefore, the time lag between the two outputs is always τ_c. On the other hand, a synchronous chaotic signal in the receiver is generated in advance to receiving the transmitter signal for complete chaos synchronization as shown in Fig. 12.3b. The

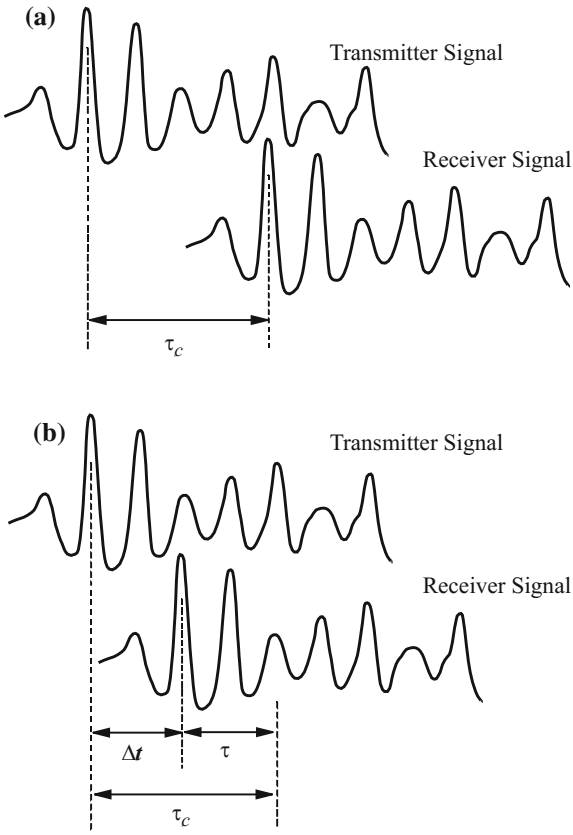

Fig. 12.3 Time lag between transmitter and receiver waveforms in chaos synchronization. Time lags **a** in generalized chaos synchronization and **b** in complete chaos synchronization. τ_c is the transmission time of the signal from the transmitter to the receiver and τ is the optical feedback time in the transmitter and receiver systems

time lag $\Delta\tau$ in the complete chaos synchronization is less than the signal transmission time between the transmitter and receiver systems. Complete chaos synchronization is sometimes called anticipating chaos synchronization due to its origin (Masoller 2001). However, it has been proved that anticipating chaos synchronization is not a unique phenomenon in delay differential systems, but also it is universally observed in differential systems. Indeed, Voss (2000) demonstrated anticipating chaos synchronization in a Rössler system that is described by a set of simple differential equations. Further, it is proved that anticipating chaos synchronization is not equivalent to complete chaos synchronization. Kusumoto and Ohtsubo (2003) observed anticipating chaos synchronization based on the injection-locking phenomenon in semiconductor lasers with optical feedback. The investigation of chaos synchronization for the mathematical and physical backgrounds is still undergoing and many subjects are left for future study.

12.2 Theory of Chaos Synchronization in Semiconductor Lasers with Optical Feedback

12.2.1 Model of Synchronization Systems

There are two schemes of chaos synchronization in delay differential systems. A semiconductor laser subjected to optical feedback is a delay differential system and different dynamics like the Lorenz system are observed (see Appendix A.4). The systems of semiconductor lasers with optical feedback have been frequently used for chaotic generators in chaos synchronization and numerous reports have been published (Ohtsubo 2002b; Uchida et al. 2005; Uchida 2012 and the references therein). In the following, detailed explanations of synchronization in chaotic semiconductor lasers subjected to optical feedback are given. Examples for some other systems will be presented later.

In laser systems, a small portion of the output from one of variables (usually the laser output power or the complex field) is sent to the receiver laser instead of sharing common variables. Chaos synchronization is very sensitive to parameter mismatches between the transmitter and receiver systems. For example, even for semiconductor lasers coming from the same wafer, we cannot expect exactly the same oscillation frequencies for the transmitter and receiver lasers under the same bias injection current. That is in itself a reason why chaos synchronization is difficult to achieve in laser systems. However, laser frequency is easily tuned by changing the bias injection current and a slave laser frequency can be locked to a master laser by optical injection within a certain range of the frequency detuning. Therefore, we can achieve robust chaos synchronization using the frequency-pulling effect by carefully choosing the parameter conditions.

Chaos synchronization is achieved not only in a master–slave configuration of transmitter and receiver systems but also in a mutual coupling system (Fujino and Ohtsubo 2001; Heil et al. 2001). We can see complicated dynamics in mutual coupling systems compared with those in unidirectionally coupled systems. A few studies have been reported for chaos synchronization in mutual coupling systems and the study is still undergoing. We can still apply mutual coupling systems to chaotic secure communications, but some modifications of data transfers between transmitter and receiver lasers from that of unidirectional systems are necessary. The topic is treated in Chap. 13. As other applications of mutually coupled systems, they are used for phase locking and control of laser arrays (Winful and Rahman 1990; Sauer and Kaiser 1998; Garcia-Ojalvo et al. 1999). Chaos synchronization has been extensively studied in class B lasers and many experimental results have been reported. The semiconductor laser with optical feedback is the excellent model of chaos synchronization both for the theoretical and experimental studies.

We here discuss systems for chaos synchronization in semiconductor lasers with optical feedback (Ohtsubo 2002a). Figure 12.4 schematically shows the chaos synchronization systems. Figure 12.4a shows a unidirectional coupling system in which the receiver laser is isolated from the transmitter laser by an optical isolator.

Both the transmitter and receiver systems have optical feedback loops and this configuration is called a closed-loop system. In Fig. 12.4b, the system is also a unidirectional coupling, but the receiver system does not have a feedback loop. This asymmetric system is called an open-loop system. The robustness and accuracy of chaos synchronization in the open-loop system are quite different from those in the closed-loop system. In chaos synchronization, the transmitter must output a chaotic signal. However, the output from the receiver systems may or may not be chaotic without receiving the transmitter signal. Chaos synchronization is achieved by an injection of a chaotic signal. As a matter of fact, Fig. 12.4b shows a special case of Fig. 12.4a. Indeed, the system in Fig. 12.4a reduces to the system in Fig. 12.4b, when we put the reflectivity of the external reflector equal to zero. We mostly discuss chaos synchronization for the closed-loop configuration of Fig. 12.4a, but the open-loop system is implicitly included in the discussion. Figure 12.4c is a mutual coupling system. Here, the isolator in Fig. 12.4a is removed. Then, each laser behaves as a transmitter and a receiver. In this system, each laser outputs different chaotic signals or steady-state signals before coupling. After the coupling, the two lasers output the same chaotic signal. In mutual coupling systems, chaotic oscillations, and chaos synchronization are also possible without the use of external mirrors. Namely, chaotic oscillations both for transmitter and receiver lasers can be attained when the two lasers directly couple with each other and one of the lasers plays a kind of a role for external mirror to the counterpart laser. Also an open-loop system is another option for mutual coupling configuration. There are also two synchronization schemes (complete and generalized schemes) in the mutual coupling case.

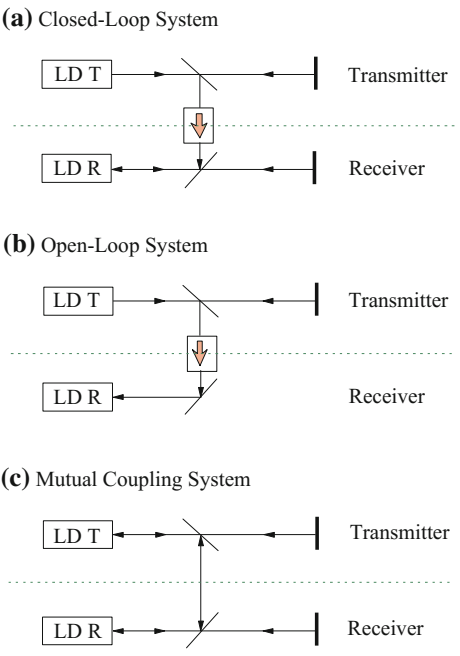

Fig. 12.4 Schematic diagram of chaos synchronization systems in semiconductor lasers with optical feedback. **a** Symmetric unidirectional coupling system, **b** asymmetric unidirectional coupling system, and **c** mutual coupling system. *LD T* transmitter laser, *LD R* receiver laser

12.2.2 Rate Equations in Unidirectional Coupling Systems

In this section, we investigate the theoretical treatment for chaos synchronization in the unidirectional coupling closed-loop system shown in Fig. 12.4a. The rate equations for the transmitter and receiver lasers are written by the same equations as those for the model discussed in Chap. 4 except for the light transmission term in the receiver rate equations (Ahlers et al. 1998). The rate equations for the transmitter laser are written by

$$\frac{dA_T(t)}{dt} = \frac{1}{2} G_{n,T}\{n_T(t) - n_{th,T}\}A_T(t) + \frac{\kappa_T}{\tau_{in,T}} A_T(t - \tau_T)\cos\theta_T(t) \tag{12.7}$$

$$\frac{d\phi_T(t)}{dt} = \frac{1}{2}\alpha_T G_{n,T}\{n_T(t) - n_{th,T}\} - \frac{\kappa_T}{\tau_{in,T}}\frac{A_T(t-\tau_T)}{A_T(t)}\sin\theta_T(t) \tag{12.8}$$

$$\frac{dn_T(t)}{dt} = \frac{J_T}{ed} - \frac{n_T(t)}{\tau_{s,T}} - G_{n,T}\{n_T(t) - n_{0,T}\}A_T^2(t) \tag{12.9}$$

$$\theta_T(t) = \omega_{0,T}\tau + \phi_T(t) - \phi_T(t - \tau_T) \tag{12.10}$$

where subscript T represents the transmitter laser. The rate equations for the receiver laser read

$$\begin{aligned}\frac{dA_R(t)}{dt} = {} & \frac{1}{2} G_{n,R}\{n_R(t) - n_{th,R}\}A_R(t) \\ & + \frac{\kappa_R}{\tau_{in,R}} A_R(t - \tau_R)\cos\,\theta_R(t) + \frac{\kappa_{cp}}{\tau_{in,R}} A_T(t - \tau_c)\cos\,\xi_c(t)\end{aligned} \tag{12.11}$$

$$\begin{aligned}\frac{d\phi_R(t)}{dt} = {} & \frac{1}{2}\alpha_R G_{n,R}\{n_R(t) - n_{th,R}\} - \frac{\kappa_R}{\tau_{in,R}}\frac{A_R(t-\tau_R)}{A_R(t)}\sin\theta_R(t) \\ & - \frac{\kappa_{cp}}{\tau_{in,R}}\frac{A_T(t-\tau_c)}{A_R(t)}\sin\xi_c(t)\end{aligned} \tag{12.12}$$

$$\frac{dn_R(t)}{dt} = \frac{J_R}{ed} - \frac{n_R(t)}{\tau_{s,R}} - G_{n,R}\{n_R(t) - n_{0,R}\}A_R^2(t) \tag{12.13}$$

$$\theta_R(t) = \omega_{0,R}\tau + \phi_R(t) - \phi_R(t - \tau_R) \tag{12.14}$$

$$\xi_c(t) = \omega_{0,T}\tau_c + \phi_R(t) - \phi_T(t - \tau_c) - \Delta\omega t \tag{12.15}$$

where subscript R denotes the receiver lasers, κ_{cp} is the injection rate from the transmitter to the receiver laser, and $\Delta\omega$ is the angular frequency detuning. The last terms in (12.11) and (12.12) are the effect of the chaotic signal from the transmitter. When the external feedback is zero in the receiver system, i.e., $\kappa_R = 0$, the model reduces to the open-loop system in Fig. 12.4b.

12.2.3 Generalized Chaos Synchronization

One of the origins of chaos synchronization in a semiconductor laser with optical feedback is the injection-locking and amplification phenomenon in a system modeled by delay differential equations. The condition for complete chaos synchronization, which is discussed in the next subsection, is very strict and most cases of chaos synchronization observed in lasers are based on the injection-locking and amplification phenomenon. Therefore, experimental results of chaos synchronization in laser systems were mostly for generalized chaos synchronization. We here consider the condition for the generalized chaos synchronization in a system of a semiconductor laser with optical feedback. For generalized chaos synchronization, the average optical power injected to the receiver laser is large, as much as several tens of percent in amplitude (several percent in intensity), while it is much less than several percents for the case of complete chaos synchronization. In generalized chaos synchronization, the relation between the field amplitudes for the transmitter and receiver lasers is given by

$$A_{\mathrm{R}}(t) \propto A_{\mathrm{T}}(t - \tau_c) \tag{12.16}$$

Namely, the synchronized chaotic output in the receiver is generated upon receiving the transmitter signal. Therefore, the time lag between the outputs of the transmitter and receiver lasers is equal to the transmission time τ_c.

12.2.4 Complete Chaos Synchronization

Next, we consider the conditions where the two systems of the transmitter and receiver lasers are written by the identical set of equations, namely, the conditions for complete chaos synchronization. The model of chaotic generators for the transmitter and the receiver is also a semiconductor laser with optical feedback. We assume that the device parameters in the two lasers are the same and the two lasers oscillate at the same frequency, i.e., zero frequency detuning $\Delta\omega = \omega_{0,m} - \omega_{0,s} = 0$. Further, the lasers are biased at the same injection current and the external feedback conditions are also the same for the transmitter and receiver lasers, except for different values of the feedback coefficients, κ_{T} and κ_{R}. Under these assumptions, the conditions for complete chaos synchronization read (Ohtsubo 2002b)

$$A_{\mathrm{R}}(t) = A_{\mathrm{T}}(t - \Delta t) \tag{12.17}$$

$$\phi_{\mathrm{R}}(t) = \phi_T(t - \Delta t) - \omega_0 \Delta t (\mathrm{mod}\, 2\pi) \tag{12.18}$$

$$n_{\mathrm{R}}(t) = n_{\mathrm{T}}(t - \Delta t) \tag{12.19}$$

$$\kappa_{\mathrm{T}} = \kappa_{\mathrm{R}} + \kappa_{cp} \tag{12.20}$$

$$\Delta t = \tau_c - \tau \tag{12.21}$$

The delay differential equations (12.11)–(12.13) in the receiver laser have completely identical forms to those in (12.7)–(12.9) of the transmitter laser. The scheme is called compete chaos synchronization. The receiver laser outputs the synchronous chaotic signal before receiving the transmitted signal by anticipating it in advance to the time $\tau = \tau_{\mathrm{T}} = \tau_{\mathrm{R}}$. The parameters in the two laser systems must be identical to satisfy the conditions for complete chaos synchronization, however, there are certain ranges of tolerances for the parameter mismatches when we allow a little deterioration of the correlation between the transmitter and receiver outputs. Usually, it is not easy to achieve complete chaos synchronization in real laser systems, especially in delay optical feedback systems, and a few experimental studies for complete chaos synchronization have been reported (Liu et al. 2002).

12.2.5 Mutual Coupling Systems

We discuss chaos synchronization in mutually coupled semiconductor lasers modeled in Fig. 12.4c. For simplicity, we put the reflectivities of external mirrors in the transmitter and receiver systems equal to zero without loss of generality, i.e., we remove the external mirrors. In the mutual coupling system, each laser plays a role for the virtual external mirror to the counterpart laser. Therefore, even without the optical feedback loop, the lasers can show chaotic oscillations due to mutual optical injections, as discussed in Chap. 6. Mutual coupling lasers with optical feedback is a straightforward extension of the discussion here. We can also observe both complete and generalized chaos synchronization in mutually coupled semiconductor lasers (Hohl et al. 1997, 1999). The rate equations for one of the lasers are written by

$$\frac{\mathrm{d}A_1(t)}{\mathrm{d}t} = \frac{1}{2}G_{n,1}\{n_1(t) - n_{\mathrm{th},1}\}A_1(t) + \frac{\kappa_{\mathrm{inj},2}}{\tau_{\mathrm{in},1}}A_2(t - \tau_c)\cos\theta_1(t) \tag{12.22}$$

$$\frac{\mathrm{d}\phi_1(t)}{\mathrm{d}t} = \frac{1}{2}\alpha_1 G_{n,1}\{n_1(t) - n_{\mathrm{th},1}\} - \frac{\kappa_{\mathrm{inj},2}}{\tau_{\mathrm{in},1}}\frac{A_2(t - \tau_c)}{A_1(t)}\sin\theta_1(t) \tag{12.23}$$

$$\frac{\mathrm{d}n_1(t)}{\mathrm{d}t} = \frac{J_1}{ed} - \frac{n_1(t)}{\tau_{s,1}} - G_{n,1}\{n_1(t) - n_{0,1}\}A_1^2(t) \tag{12.24}$$

$$\theta_1(t) = \omega_{0,1}\tau + \phi_1(t) - \phi_2(t - \tau_c) + \Delta\omega t \tag{12.25}$$

The rate equations for the other laser are also given by symmetrical forms as

$$\frac{dA_2(t)}{dt} = \frac{1}{2} G_{n,2}\{n_2(t) - n_{th,2}\}A_2(t) + \frac{\kappa_{inj,1}}{\tau_{in,2}} A_1(t - \tau_c)\cos\theta_2(t) \tag{12.26}$$

$$\frac{d\phi_2(t)}{dt} = \frac{1}{2}\alpha_2 G_{n,2}\{n_2(t) - n_{th,2}\} - \frac{\kappa_{inj,1}}{\tau_{in,2}}\frac{A_1(t - \tau_c)}{A_2(t)}\sin\theta_2(t) \tag{12.27}$$

$$\frac{dn_2(t)}{dt} = \frac{J_2}{ed} - \frac{n_2(t)}{\tau_{s,2}} - G_{n,2}\{n_2(t) - n_{0,2}\}A_2^2(t) \tag{12.28}$$

$$\theta_2(t) = \omega_{0,2}\tau + \phi_2(t) - \phi_1(t - \tau_c) - \Delta\omega t \tag{12.29}$$

where subscripts 1 and 2 are for the respective lasers and $\Delta\omega = \omega_1 - \omega_2$ is the angular frequency detuning between the two lasers.

In the mutual coupling systems, there are also two solutions of chaos synchronization; one is based on injection-locking and amplification phenomena and the other is complete chaos synchronization. For the case of synchronization due to injection-locking, one of the two lasers plays the role of a master laser and the other is a slave. Then, the relation between the two amplitudes is written by

$$A_2(t) \propto A_1(t - \tau_c) \tag{12.30}$$

or

$$A_2(t - \tau_c) \propto A_1(t) \tag{12.31}$$

These are no exact solutions for (12.22)–(12.29) in a mathematical sense. However, these relations are confirmed by numerical simulations and experiments. Most cases of chaos synchronization observed in real experiments in mutually coupled semiconductor lasers are based on generalized chaos synchronization. In these cases, the optical transmission power is as large as several tens of percent of the average amplitude of the chaotic variation. The percentage is almost the same as that in a unidirectional coupling system of a generalized chaos synchronization scheme. Which laser becomes master or slave (leader or lagger laser) is determined by the differences of the operating conditions of the lasers and the parameter mismatches.

On the other hand, there is an identical solution for complete chaos synchronization in mutually coupled semiconductor lasers, since the transmitter and receiver systems have mathematically symmetrical forms as far as the device parameters and driving conditions are identical. The conditions follow

$$\Delta\omega = 0 \tag{12.32}$$

$$A_2(t) = A_1(t) \tag{12.33}$$

$$\phi_2(t) = \phi_1(t) \tag{12.34}$$

$$n_2(t) = n_1(t) \tag{12.35}$$

Namely, the two lasers simultaneously output the same chaotic signals even for a finite transmission time τ_c of light. The scheme is also considered as anticipating chaos synchronization. However, the complete chaos synchronization under the current configuration is only limited to the case without Langevin noises. In actual systems, there exist Langevin noises and the synchronization is fairly affected by the laser noises. An isochronal solution of complete chaos synchronization is easily reduced to an achronal state due to the presence of the noises in spite of highly symmetrical conditions of two mutually coupling lasers. The detail is again discussed in Sect. 12.7.1.

12.3 Chaos Synchronization in Semiconductor Lasers with an Optical Feedback System

12.3.1 Chaos Synchronization—Numerical Examples

We here show some numerical simulations of chaos synchronization in the open-loop systems shown in Fig. 12.4b. Figure 12.5 shows examples of generalized and complete chaos synchronization (Murakami and Ohtsubo 2002). Figure 12.5a shows a chaotic signal to be transmitted. Figure 12.5b shows the receiver output under the condition of generalized chaos synchronization and Fig. 12.5c shows the correlation plot between the waveforms of Fig. 12.5a, b. Figure 12.5d shows the receiver output under the condition of complete chaos synchronization and Fig. 12.5e is the correlation plot between the waveforms of Fig. 12.5a, d. The optical transmission power is 22% ($\kappa_{cp}/\tau_{in,R} = 74.9\ ns^{-1}$) in the generalized chaos synchronization. On the other hand, it is as small as 1.5×10^{-4} % ($\kappa_{cp}/\tau_{in,R} = 1.96\ ns^{-1}$) in the complete case. The time for the light transmission between the transmitter and receiver lasers is set to zero for simplicity in this figure. Therefore, the time lag between the two lasers is zero for generalized synchronization, while it is -1 ns for complete chaos synchronization. An excellent correlation between the transmitter and receiver outputs is obtained for the complete chaos synchronization. The difference of the time is exactly equal to the theoretically expected time lag $\Delta\tau$. Thus, we can distinguish the type of chaos synchronization by investigating the time lag between the transmission signal and the receiver output.

The attractors in the transmitter and receiver lasers show the same orbit under complete chaos synchronization, since the two systems follow completely the identical equations. Then, the receiver output traces the same orbit as that of the transmitter due to injection of a small seed from the transmitter. On the other hand,

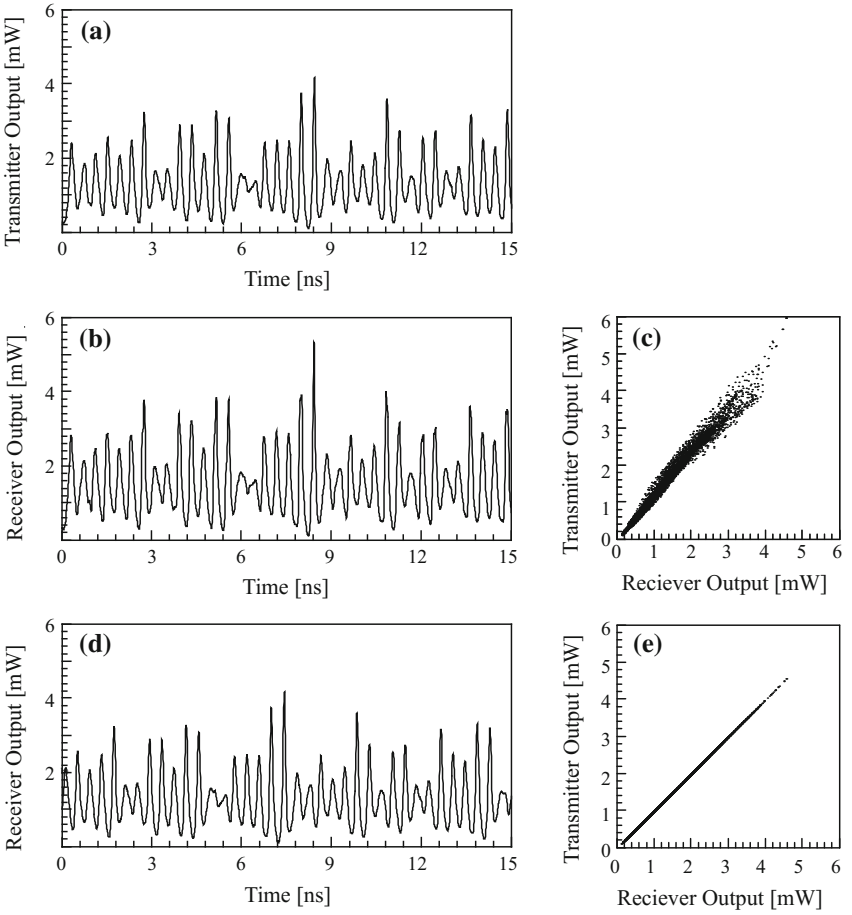

Fig. 12.5 Chaos synchronization in a closed-loop system. **a** Chaotic transmission signal, **b** receiver output of generalized chaos synchronization at $\kappa_{cp}/\tau_{in,R} = 74.9\ ns^{-1}$, **c** correlation plot between **a** and **b**, **d** receiver output of complete chaos synchronization at $\kappa_{cp}/\tau_{in,R} = 1.96\ ns^{-1}$, and **e** correlation plot between **a** and **d**. The conditions are $J = 1.3J_{th}$, $\tau = 1$ ns, $\kappa_T/\tau_{in,T} = 1.96\ ns^{-1}$, and $\Delta\omega = 0$

the receiver output is an amplified copy of the transmitter signal in generalized chaos synchronization. Therefore, the synchronized signal almost looks the same as the waveform of the transmitter, however, the chaotic attractor in the receiver laser has some deviations from that of the transmitter. Figure 12.6 shows chaotic attractors of the receiver laser in the phase space of the laser output power and the carrier density. Figure 12.6a is the chaotic attractor of the transmitter signal in Fig. 12.5a. Figure 12.6b is the chaotic attractor of the receiver output corresponding to Fig. 12.5b. The general view of the orbit is quite similar to Fig. 12.6a, but they are different. The extent of the orbit in Fig. 12.6b is slightly larger than that

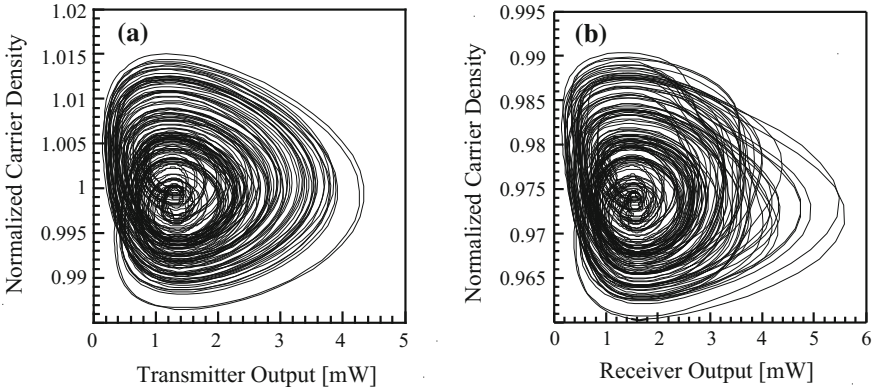

Fig. 12.6 Chaotic attractors in the phase space of the laser output power and the carrier density. **a**, **b** Chaotic attractors corresponding to Fig. 12.5b, d respectively

of Fig. 12.6a and the receiver signal is amplified. Also, the carrier density in Fig. 12.6b is lowered to less than the threshold by the strong optical injection from the transmitter laser and this results in the reduction of the gain. For the case of complete chaos synchronization in Fig. 12.5d, the chaotic orbit of the receiver laser is the same as in Fig. 12.6a. From these facts, generalized chaos synchronization is clearly a different phenomenon from complete chaos synchronization.

Optical injection is widely used for signal transmission from transmitter to receiver lasers in chaotic communications. When we consider optical injection, the stable and unstable map, which is discussed in Chap. 6, is very useful to know the injection properties. Here, we show the conditions and distributions of successful chaos synchronization using the map. Figure 12.7 presents the map of stable and unstable injection-locking areas. The boundaries of stable and unstable injection-locking, and unlocking for the solitary laser are shown as solid curves in the figure. The vertical axis is the optical injection (in intensity) from the transmitter to the receiver laser and the horizontal axis is the frequency detuning between the transmitter and receiver lasers. Excellent chaos synchronization is attained at the dark areas in the map. The error of chaos synchronization in the figure is defined by the following equation:

$$\sigma_{\text{error}} = \frac{\langle |S_{\text{T}} - S_{\text{R}}| \rangle}{\langle S_{\text{R}} \rangle} \tag{12.36}$$

where S_{T} and S_{R} are the intensities of the transmitter and receiver lasers, and $< >$ denotes the ensemble average. Generalized chaos synchronization occurs in a wide range of the frequency detuning and the optical injection in the stable injection-locking area, while complete chaos synchronization takes place at the unstable injection-locking area. From the comparison of this map with Fig. 6.4,

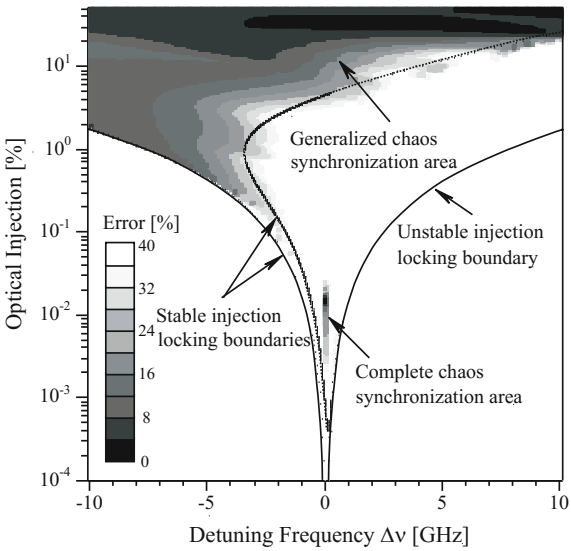

Fig. 12.7 Map of stable and unstable injection locking in the receiver laser and areas of generalized and complete chaos synchronization. An open-loop optical feedback system is assumed. The reflectivity of the external optical feedback mirror in the transmitter system is 10^{-2}% in intensity

complete chaos synchronization is attained at chaotic states within the unstable injection-locking area in a simple optical injection-locked laser. The area of complete chaos synchronization is very narrow with zero detuning and small optical injection due to the requirement of strict parameter coincidence.

The effects of parameter mismatches between the transmitter and receiver systems are very important for applications of chaos synchronization to secure optical communications. Figure 12.8 shows the plots of synchronization errors for the mismatches of various laser device parameters. Figure 12.8a shows the errors of generalized chaos synchronization. The permissible errors for the parameter mismatches are large in generalized chaos synchronization and we can expect robust chaos synchronization. However, the synchronization errors are always larger than 1% of the average laser intensity variations, since the origin of the synchronization comes from optical injection-locking and amplification phenomena, and distortions of the synchronous waveform from the transmitter signal are always presented. From the investigation of the transmitter and receiver waveforms, they are still quite similar with each other when the errors for the parameter mismatches are less than a few percent. It is noted that the best synchronization is not always attained at zero parameter mismatches. Figure 12.8b is the effects of parameter mismatches in complete chaos synchronization. As expected, chaos synchronization is achieved with high accuracy at almost zero parameter mismatches and the synchronization errors rapidly increase with the increase of the parameter mismatches. Thus, strict conditions are required for successful chaos synchronization in the complete case.

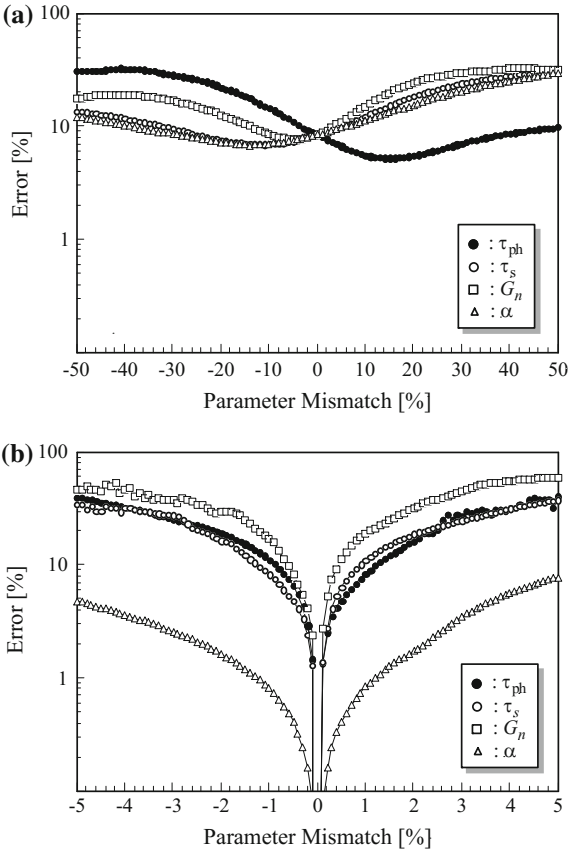

Fig. 12.8 Calculated synchronization error as a function of parameter mismatch. τ_{ph} photon lifetime, τ_s carrier lifetime, G_n gain, and α linewidth enhancement factor. **a** Generalized and **b** complete chaos synchronization. The parameter values are the same as those in Fig. 12.5

12.3.2 Chaos Synchronization—Experimental Examples

Chaos synchronization in semiconductor lasers with optical feedback has been reported in real experimental systems (Takiguchi et al. 1999a, b, c; Fujino and Ohtsubo 2000; Fischer et al. 2000a, b; Sivaprakasam et al. 2000). In this section, we show some examples of experimental results for chaos synchronization. Figure 12.9 shows the experimental results of chaos synchronization in a closed-loop system discussed in Fig. 12.4a. Figure 12.9a is the output waveforms of the transmitter and receiver lasers without signal transmission. As far as the two lasers are isolated, the output powers have no correlation as shown in Fig. 12.9b. When a fraction of the transmitter output is sent to the receiver, the synchronous waveform in Fig. 12.9c is obtained. The transmitted optical power from the transmitter to the receiver is rather strong, as much as 4.6% of the average power of the receiver laser. Therefore, the synchronization is a generalized case. In Fig. 12.9a, the two lasers show chaotic outputs. However, it is not always necessary for the receiver laser to be oscillated at a chaotic state and the receiver laser may be

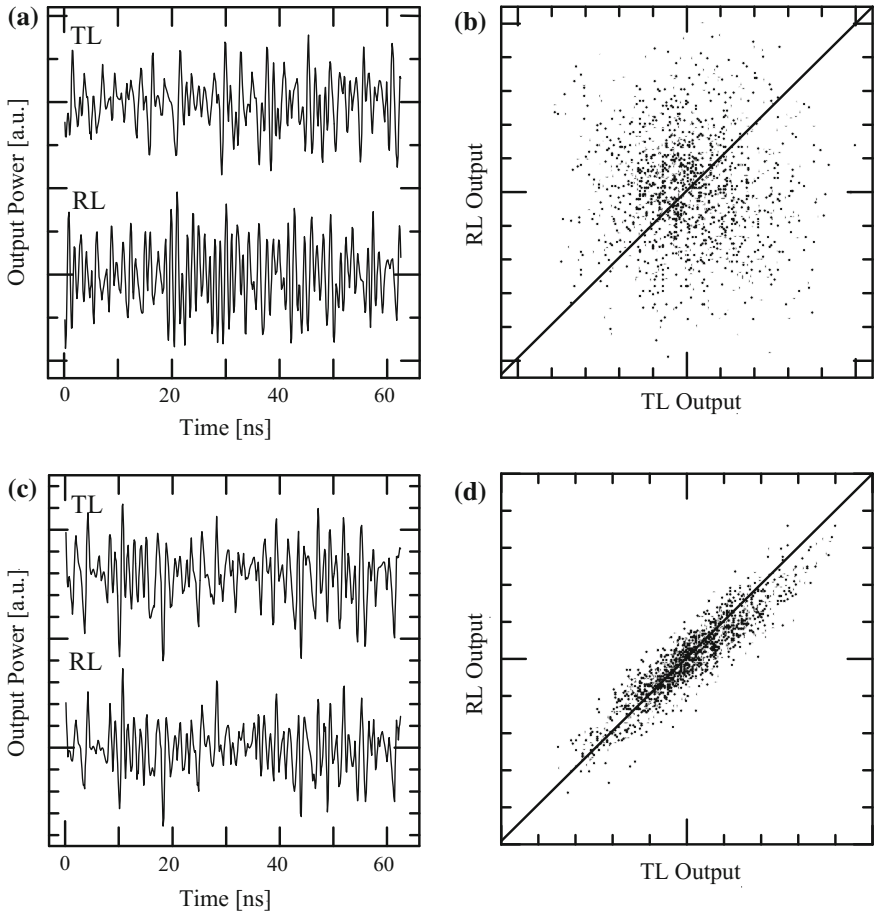

Fig. 12.9 Experimental chaos synchronization in a closed-loop system. **a** Waveforms of transmitter and receiver lasers without coupling. **b** Correlation plot for (**a**). **c** Waveforms of the transmitter and receiver lasers with coupling. The transmitted optical power is 4.6% of the average optical power of the receiver laser. **d** Correlation plot for (**c**)

a steady-state oscillation even in the presence of optical feedback. The feedback level in the receiver laser is usually less than that in the transmitter laser and the receiver laser may show a synchronous chaotic oscillation after the optical injection from the transmitter. Chaos synchronization has been also demonstrated in an open-loop system. Of course, the receiver laser oscillates at a steady state without coupling of the transmitter signal in that case. The robustness of chaos synchronization is much dependent on whether the system is an open- or closed-system. We will again discuss the differences in Chap. 13.

Only a few experimental studies have been reported for complete chaos synchronization, since the conditions of complete chaos synchronization are too severe

to be achieved in real experiments (Sivaprakasam et al. 2001; Liu et al. 2002a). At complete chaos synchronization, the time lag of the waveforms between the transmitter and receiver lasers is given by $\Delta\tau = \tau_c - \tau$. Liu et al. (2002a) conducted complete chaos synchronization in an open-loop system of semiconductor lasers with optical feedback. They changed the external cavity length and examined the time lag between the transmitter and receiver signals. They observed the change of the time lag proportional to the external cavity length (the proportional coefficient is negative) and showed that their schemes were for complete chaos synchronization. In their experiment, the parameters of the transmitter and receiver lasers were carefully chosen to have almost the same characteristics and the initial frequency detuning between the transmitter and receiver lasers was set to be less than several tens of MHz.

12.3.3 Anticipating Chaos Synchronization

Anticipating chaos synchronization was at first introduced as a synchronization phenomenon peculiar to nonlinear delay differential systems. Later, it was proved that anticipating chaos synchronization is also observed in low dimensional dissipative systems described by simple differential equations (Ahlers et al. 1998; Voss 2000; Ohtsubo 2002b). Voss demonstrated that anticipating chaos synchronization is realized in a Rössler system (continuous system) that is described by three differential equations. Therefore, anticipating chaos synchronization is not only a unique feature in delay differential systems, but also it is a universal phenomenon in chaotic nonlinear systems. In chaos synchronization systems of semiconductor lasers with optical feedback, anticipating chaos synchronization is also observed outside of the parameter regions for ordinary complete chaos synchronization in the stable and unstable injection-locking map. In that case, the chaos synchronization originates from optical injection-locking and amplification effects, but the time lag of the waveforms between the transmitter and receiver lasers is equal to that of anticipating synchronization.

Kusumoto and Ohtsubo (2003) conducted a detailed study of chaos synchronization in the stable injection-locking area in Fig. 12.7. Figure 12.10 shows their results. Figure 12.10a plots the anticipating chaos synchronization in the stable injection-locking area. The time lag corresponds to that of anticipating synchronization, but the synchronization originates from the ordinary injection-locking effect. Within the white ellipsoid in the figure, the value of the correlation coefficient between waveforms of the transmitter and receiver lasers exceeds 0.94. In this open-loop system, the optical feedback ratio in the transmitter system is as high as 0.3. Complete chaos synchronization is achieved around the optical injection rate of 0.3 at zero frequency detuning (marked A). Of course, the synchronization is an anticipating one under this condition. However, the area of anticipating chaos synchronization expands over a wide region in the stable injection-locking map. For example, the synchronization at point B is still an anticipating one as a time lag of

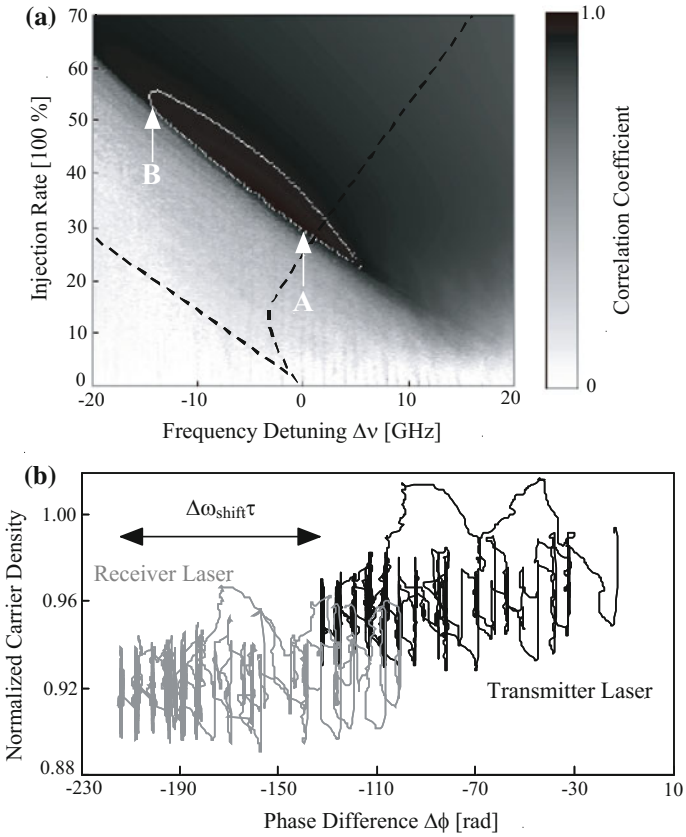

Fig. 12.10 **a** Anticipating chaos synchronization region in the phase space of the frequency detuning $\Delta\nu$ and the optical injection rate in an open-loop system. The feedback rate in the transmitter system is 0.3. **b** Chaotic trajectories for the transmitter and receiver lasers at point B in (a). The trajectories are plotted in the phase space of the phase difference $\Delta\phi = \phi_j(t) - \phi_j(t - \tau)$ and the normalized carrier density $n_j/n_{\mathrm{th},j}$ (j = T or R). *Black trace* is for the transmitter laser and *gray trace* for the receiver laser

the waveforms, but the synchronization originates from the injection-locking effect. Figure 12.10b plots the trajectories of the transmitter and receiver outputs corresponding to point B in Fig. 12.10a. The plot is in the phase space of the phase difference and the normalized carrier density. Black trace denotes the trajectory for the transmitter laser and gray trace is for the receiver laser. If the chaos synchronization is complete, the trajectory of the transmitter laser perfectly overlaps with that of the receiver in the map. However, the two trajectories are separated from each other in the phase space. This phase shift between the two trajectories is equal to the frequency detuning between the two lasers. Also the carrier density of the receiver laser is lowered by the optical injection. This fact proves that the

phenomenon originates from optical injection-locking and amplification. According to the detailed study by Peters-Flynn et al. (2006), the laser output that is categorized as anticipating chaos synchronization in the stable injection-locking area in Fig. 12.10 sometimes shows a mixed state of waveforms corresponding to anticipating and injection amplification signals. The two states irregularly switch in time in their numerical simulations. The details of the phenomena and the origin of the switching are not fully understood yet. Anticipating chaos synchronization is not a unique phenomenon accompanying complete chaos synchronization, but it is a universal nature in nonlinear chaotic systems.

12.3.4 Bandwidth Enhanced Chaos Synchronization

We discussed the enhancement of the cutoff frequency in a chaotic semiconductor laser by a strong optical injection in Sect. 6.3. Such semiconductor lasers are used as light sources of chaotic generators for chaos synchronization and communications (Takiguchi et al. 2003; Someya et al. 2009). The cutoff frequency can be varied by adjusting the fraction of the optical injection. For example, a modulation bandwidth of $\sim$20 GHz for the original relaxation oscillation frequency of 3–4 GHz was attained by strong optical injection. In chaotic communications, the maximum data transmission rate is determined by the cutoff frequency of chaotic carrier signals and the cutoff frequency is roughly equal to the maximum modulation bandwidth of the laser. Higher modulation bandwidth is also demanded in various applications such as direct modulations in semiconductor lasers. Figure 12.11 shows the schematic diagram of open-loop chaos synchronization systems with enhanced chaotic frequency (Takiguchi et al. 2003). Both the transmitter and receiver semiconductor lasers, LD T and LD R, are strongly injected from external semiconductor lasers, LD1 and LD2, with the same characteristics of the device parameters. Both the transmitter and receiver lasers oscillate at the stable injection-locked state in the absence of optical feedback. Figure 12.12 demonstrates a numerical example of bandwidth-enhanced chaos synchronization. The conditions are the same as those in Fig. 6.25. Therefore, the main chaotic frequencies of the two lasers at solitary oscillations are 2.7 GHz and the main chaotic frequency is expanded to 8 GHz. The upper trace in Fig. 12.12a is a time series of the transmitter output and the lower one is that of the receiver. The frequency detuning between the transmitter and receiver lasers is set to be zero and the observed time lag is equal to $\Delta t = \tau_c - \tau = -6$ ns ($\tau_c = 0$ and $\tau = 6$ ns). Therefore, the synchronization scheme is for the complete case or so-called anticipating chaos synchronization. Figure 12.12b is the correlation plot. The correlation coefficient is calculated to be 0.954 and the two lasers show good synchronization. However, we obtain a better figure of the correlation coefficient for complete chaos synchronization in the absence of strong optical injection. The range for small

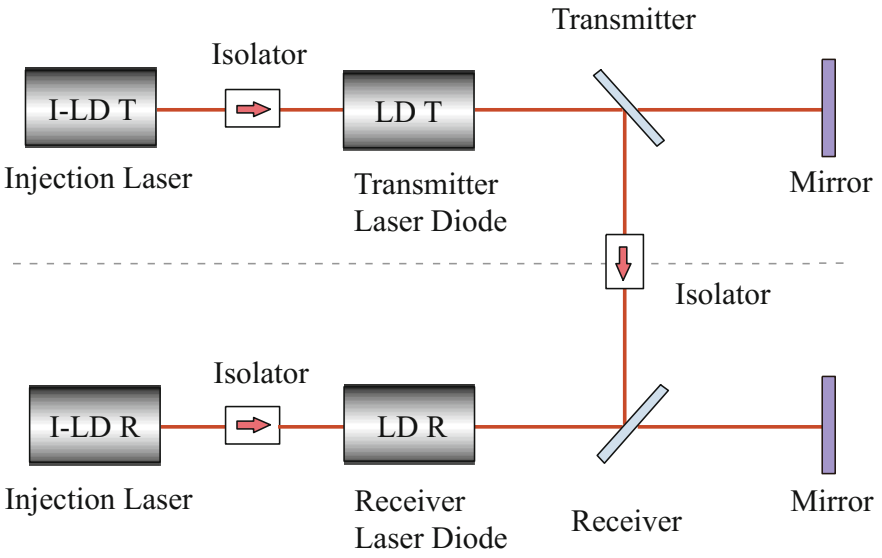

Fig. 12.11 Schematic diagram of a bandwidth-enhanced chaos synchronization system. *I-LD T* and *I-LD R* are the injection lasers to the transmitter and receiver lasers. *LD T* and *LD R* are the transmitter and receiver lasers

synchronization error is very narrow for the parameter mismatches in the complete case. Even if the two lasers have the same device parameters and operate under the same conditions, chaos synchronization is realized under the limited parameter values and their ranges are usually very narrow.

12.3.5 Incoherent Synchronization Systems

The frequency detuning of the transmitter and receiver lasers plays a crucial role for the performance of chaos synchronization when the two lasers coherently couple. The difference of the frequencies must be at least within a few GHz. As discussed in Sect. 5.7, we can observe chaotic oscillations in systems of semiconductor lasers with incoherent optical feedback. Chaos synchronization is also realized in incoherent systems. We do not pay particular attention to the frequency detuning in this system. In an incoherent optical setup, the feedback light in the transmitter system is incoherently coupled with the internal laser field. We assume that the transmission light is also incoherently coupled to the receiver laser. In incoherent chaos synchronization, we do not need to consider the rate equation for the optical phase. Therefore, the model is described by the equations for the photon number and the carrier density. For the transmitter laser, we obtain (Rogister et al. 2001).

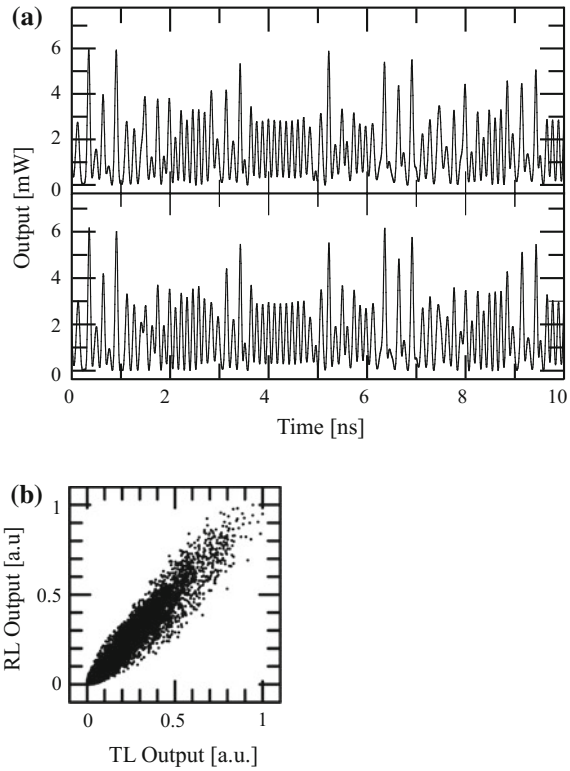

Fig. 12.12 Bandwidth-enhanced chaos synchronization in semiconductor lasers with optical feedback. **a** Chaotic time series (*upper trace* transmitter output and *lower trace* receiver output) and **b** their correlation plot. The time lag of $\Delta t = -6$ ns between the two waveforms is compensated. The conditions for the lasers are the same as those in Fig. 6.25. The synchronization scheme is complete

$$\frac{\mathrm{d}S_{\mathrm{T}}(t)}{\mathrm{d}t} = G_{n,\mathrm{T}}\{n_{\mathrm{T}}(t) - n_{\mathrm{th,T}}\}S_{\mathrm{T}}(t) + R_{\mathrm{sp,T}} \tag{12.37}$$

$$\frac{\mathrm{d}n_{\mathrm{T}}(t)}{\mathrm{d}t} = \frac{J_{\mathrm{T}}}{ed} - \frac{n_{\mathrm{T}}(t)}{\tau_{s,\mathrm{T}}} - G_{n,\mathrm{T}}\{n_{\mathrm{T}}(t) - n_{0,\mathrm{T}}\} \times \{S_{\mathrm{T}}(t) + \kappa_{\mathrm{T}}' S_{\mathrm{T}}(t - \tau_{\mathrm{T}})\} \tag{12.38}$$

For the receiver

$$\frac{\mathrm{d}S_{\mathrm{R}}(t)}{\mathrm{d}t} = G_{n,\mathrm{R}}\{n_{\mathrm{R}}(t) - n_{\mathrm{th,R}}\}S_{\mathrm{R}}(t) + R_{\mathrm{sp,R}} \tag{12.39}$$

$$\frac{\mathrm{d}n_{\mathrm{R}}(t)}{\mathrm{d}t} = \frac{J_{\mathrm{R}}}{ed} - \frac{n_{\mathrm{R}}(t)}{\tau_{s,\mathrm{R}}} - G_{n,\mathrm{R}}\{n_{\mathrm{R}}(t) - n_{0,\mathrm{R}}\} \times \{S_{\mathrm{R}}(t) + \kappa'_{\mathrm{R}} S_{\mathrm{R}}(t - \tau_{\mathrm{R}}) + \kappa_{\mathrm{cp}} S_{\mathrm{T}}(t - \tau_c)\} \tag{12.40}$$

Also, the subscripts T and R are for the transmitter and receiver lasers. The feedback light is coupled to the carrier density as a delayed signal. The final term in (12.40) is the coupling of incoherent light from the transmitter. Since the coupling between the transmitter and receiver lasers is incoherent, the receiver laser is not injection-locked. However, complete chaos synchronization is also achieved under the appropriate conditions. Assuming all the device parameters of the two lasers to be the same, the conditions read

$$S_{\mathrm{R}}(t) = S_{\mathrm{T}}(t - \Delta t) \tag{12.41}$$

$$n_{\mathrm{R}}(t) = n_{\mathrm{T}}(t - \Delta t) \tag{12.42}$$

where $\Delta t = \tau_c - \tau$. Under these conditions, complete anticipating chaos synchronization is realized. Indeed, the condition for the frequencies of the lasers is not included in the coupling equations.

12.3.6 Polarization Rotated Chaos Synchronization

Chaotic oscillations of semiconductor lasers are observed not only by parallel-polarization optical feedback, but also by polarization-rotated optical feedback. The system of polarization-rotated optical was described in Sects. 4.6 and 5.8.1. The dynamics of polarization-rotated chaos synchronization were studied theoretically and experimentally (Sukow et al. 2004, 2005, 2006; Shibasaki et al. 2006; Takeuchi et al. 2010). A semiconductor laser with polarization-rotated optical feedback can be used as a light source for a system of chaotic synchronization and communications. Here, we discuss chaos synchronization in a system of semiconductor lasers with polarization-rotated optical feedback. As an example, take a chaotic generator shown in Fig. 4.7b. The system we consider is shown in Fig. 12.13, in which the laser light with TE mode emitted from a transmitter laser (LD T) passes through a Faraday rotator and is reflected by a mirror. The feedback light again passes through the Faraday rotator and fed back into the laser cavity as a TM mode light (cross-polarized component to the TE mode). A part of the TE mode light is divided by a beam splitter and is fed to the receiver laser through a set of an isolator and a Faraday rotator as the TM mode light. Then, the crossed-polarization light is injected to the receiver laser. Thus, the polarization-rotated chaos synchronization is realized under appropriate conditions for the transmitter and receiver lasers.

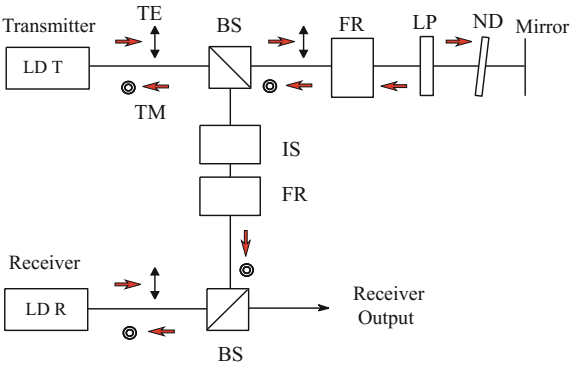

Fig. 12.13 System of a polarization-rotated open-loop chaos synchronization system. *LD T* transmitter laser, *LD R* receiver laser, *TE* TE polarization mode, *TM* TM polarization mode, *FR* Faraday rotator (45° rotation), *IS* isolator, *PL* polarizer, *ND* neutral density filter

In the open-loop chaos synchronization system in Fig. 12.13, the rate equations for the transmitter read (Shibasaki et al. 2006)

$$\frac{\mathrm{d}E_{\mathrm{T,TE}}(t)}{\mathrm{d}t} = \frac{1}{2}(1 - i\alpha_{\mathrm{T}})G_{n,\mathrm{T,TE}}\{n(t) - n_{\mathrm{th,T,TE}}\}E_{\mathrm{T,TE}}(t) \tag{12.43}$$

$$\begin{aligned}\frac{\mathrm{d}E_{\mathrm{T,TM}}(t)}{\mathrm{d}t} &= \frac{1}{2}(1 - i\alpha_{\mathrm{T}})G_{n,\mathrm{T,TM}}\{n(t) - n_{\mathrm{th,T,TM}}\}E_{\mathrm{T,TM}}(t) \\ &+ \frac{\kappa}{\tau_{\mathrm{in}}}E_{\mathrm{T,TE}}(t-\tau)\exp[i\{-\Delta\omega_{\mathrm{TE,TM}}t + \omega_{0,\mathrm{T}}\tau + \phi_{\mathrm{T,TM}}(t) - \phi_{\mathrm{T,TE}}(t-\tau)\}]\end{aligned} \tag{12.44}$$

$$\begin{aligned}\frac{\mathrm{d}n(t)}{\mathrm{d}t} &= \frac{J_{\mathrm{T}}}{ed} - \frac{n(t)}{\tau_{s,\mathrm{T}}} - \{n(t) - n_{0,\mathrm{T}}\} \\ &\times \{G_{n,\mathrm{T,TE}}|E_{\mathrm{T,TE}}(t)|^2 + G_{n,\mathrm{T,TM}}|E_{\mathrm{T,TM}}(t)|^2\}\end{aligned} \tag{12.45}$$

For the receiver systems, the rate equations are written by

$$\frac{\mathrm{d}E_{\mathrm{R,TE}}(t)}{\mathrm{d}t} = \frac{1}{2}(1 - i\alpha_{\mathrm{R}})G_{n,\mathrm{R,TE}}\{n(t) - n_{\mathrm{th,R,TE}}\}E_{\mathrm{R,TE}}(t) \tag{12.46}$$

$$\begin{aligned}\frac{\mathrm{d}E_{R,TM}(t)}{\mathrm{d}t} &= \frac{1}{2}(1 - i\alpha_{\mathrm{R}})G_{n,\mathrm{R,TM}}\{n(t) - n_{\mathrm{th,R,TM}}\}E_{\mathrm{R,TM}}(t) \\ &+ \frac{\kappa_{\mathrm{cp}}}{\tau_{\mathrm{in,R}}}E_{\mathrm{T,TE}}(t-\tau_c) \\ &\exp\{-i\Delta\omega t + i\omega_{0,\mathrm{T}}\tau + i\phi_{\mathrm{R,TM}}(t) - i\phi_{\mathrm{T,TE}}(t-\tau_c)\}\end{aligned} \tag{12.47}$$

$$\begin{aligned}\frac{\mathrm{d}n(t)}{\mathrm{d}t} &= \frac{J_{\mathrm{R}}}{ed} - \frac{n(t)}{\tau_{s,\mathrm{R}}} - \{n(t) - n_{0,\mathrm{R}}\} \\ &\times \{G_{n,\mathrm{R,TE}}|E_{\mathrm{R,TE}}(t)|^2 + G_{n,\mathrm{R,TM}}|E_{\mathrm{R,TM}}(t)|^2\}\end{aligned} \tag{12.48}$$

where subscripts TE and TM stand for two crossed polarization modes, subscript T and R correspond to for the transmitter and receiver lasers, $\Delta\omega_{TE,TM}$ represents the frequency detuning between TE and TM modes in the transmitter laser, $\Delta\omega$ is the frequency detuning between the transmitted light and the TM light in the receiver laser. The other parameters are the same meaning defined in Sect. 12.2.2. The dynamic properties of the transmitter and receiver lasers in polarization-rotated chaos synchronization are numerically studied by using these coupling equations. The frequency detuning between the TE and TM modes sometimes plays an important role, although it is usually small. Indeed, a frequency detuning of −870 MHz is experimentally observed and the dynamics and synchronization properties are fairly affected by the detuning (Takeuchi et al. 2010).

In transmitter and receiver systems in semiconductor lasers with polarization-rotated optical feedback, one can attain both regimes of chaos synchronization, i.e., complete and generalized cases. Figure 12.14 shows numerical examples of polarization-resolved waveforms both for complete and generalized chaos synchronization in polarization-rotated optical feedback regimes. It is noted that these are examples for zero frequency detuning between the TE and TM modes with fairly strong optical injection from TE to TM modes. When the injection ratio from the transmitter to the receiver lasers is equal to the optical feedback ratio in the transmitter laser, namely, $\kappa = \kappa_{cp}$, complete chaos synchronization can be achieved under appropriate parameter conditions, which is the same case for non-rotated optical feedback. For complete synchronization, the TE mode waveform of the transmitter laser completely synchronizes with the TE mode waveform of the receiver laser, and the TM mode of the response laser also synchronizes with the TM mode of the drive laser, as shown in Fig. 12.14a, c. Without loss of generality, the transmission time from the transmitter to the receiver lasers is equal to the delay time in the feedback loop in the transmitter, i.e., $\tau = \tau_c$. Therefore, the time lag between the synchronized signals is zero in complete chaos synchronization. In this configuration, the receiver output is a complete copy of the transmitter signal. On the other hand, for a strong optical injection $\kappa = 3\kappa_{cp}$, the receiver laser is injection-locked to the transmitter laser. Then, the receiver output of TM mode is an amplified version of the transmitted chaotic signal of the TE mode oscillation from the transmitter laser as shown in Fig. 12.14b, d. The time lag between the waveforms of the TE mode in the transmitter laser and the TM mode in the receiver laser is τ_c, which is the evidence of generalized chaos synchronization. In this example, the TE mode in the receiver laser is completely suppressed and only the TM polarization component is the oscillation mode.

As in the case for synchronization in semiconductor lasers with normal (non-polarization-rotated) optical feedback, the chaos in the two regimes (complete and generalized synchronization) are distinguishable by the delay of the chaotic waveform with respect to that of the injected signal. From the detailed study for polarization-rotated chaos synchronization, it is proved that chaos synchronization can be performed even if there is a large mismatch in the optical frequencies of the

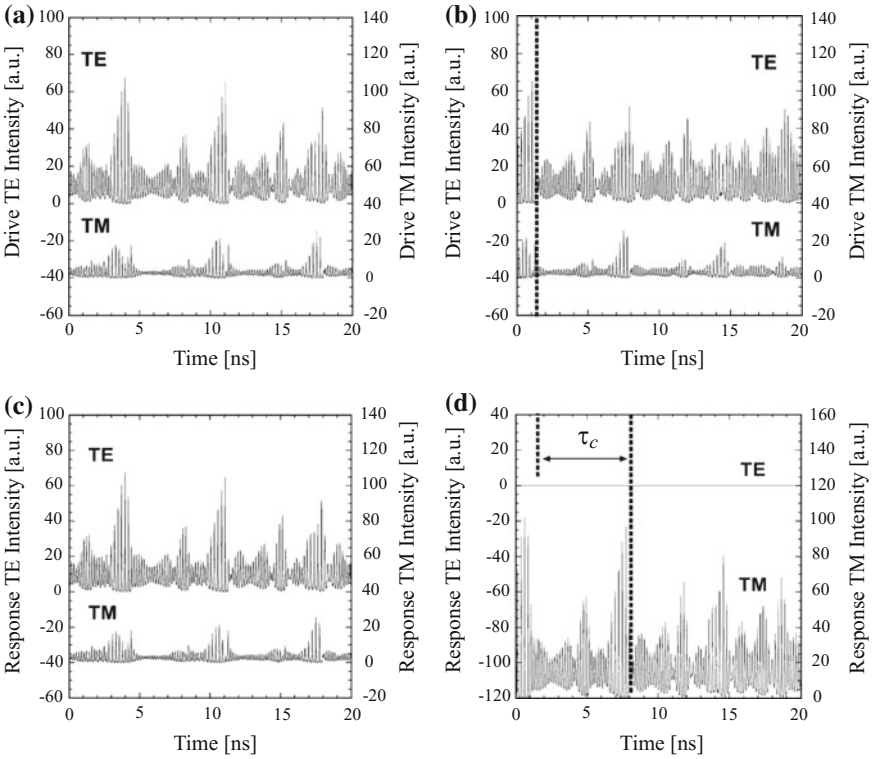

Fig. 12.14 Numerically calculated temporal waveforms of TE and TM mode intensities at synchronization. **a**, **c** Complete chaos synchronization for the transmitter and the receiver lasers, respectively, at $\kappa = \kappa_{cp}$. **b**, **d** Generalized chaos synchronization for the transmitter (drive) and receiver (response) lasers, respectively, at $\kappa = 3\kappa_{cp}$ [after Shibasaki et al. (2006); © 2006 IEEE]

lasers (Shibasaki et al. 2006). It is worth noting that synchronization can be maintained in the presence of the detuning by adjusting appropriately the injection strength between the transmitter and receiver lasers. This feature is very different from the case of semiconductor lasers with non-polarization-rotated optical feedback, where complete synchronization is only very weakly robust against detuning. Good synchronization can be maintained at the condition of positive detuning and small injection strength and at the condition of negative detuning and large injection strength. This asymmetric feature may result from the α parameter (linewidth enhancement factor) of semiconductor lasers, in the sense that chaos synchronization in semiconductor lasers with polarization-rotated optical feedback does not require strict matching of optical frequency. This feature of robustness with respect to optical frequency is particularly important for practical implementations of secure communication systems using chaos synchronization.

12.3.7 Synchronization in Broad-Area Semiconductor Lasers

There are a large number of studies for the fundamental characteristic of chaos synchronization in common narrow-stripe semiconductor lasers. Other than the study in narrow-stripe semiconductor lasers, chaos synchronization has been demonstrated in various types of semiconductor lasers, for example, in vertical-cavity surface-emitting semiconductor lasers (Fujiwara et al. 2003; Hong et al. 2004). However, there is little study for chaos synchronization in broad-area semiconductor lasers (BALs). Even in solitary oscillations, broad-area semiconductor lasers show very fast chaotic oscillation that is called filamentation as fast as picosecond in time. Further, they exhibit various different dynamics induced by external perturbations, such as optical feedback and optical injection as discussed in Sects. 8.4 and 10.3.3. Due to their high power oscillations, broad-area semiconductor laser is expected to use as a source of optical communications in space. Here, we demonstrate chaotic filament synchronization between two broad-area semiconductor lasers. We assume that a transmitter laser is a broad-area semiconductor laser subjected to optical feedback and the laser output with filament oscillations is sent to a receiver laser with similar device characteristics (an open loop system). The rate equations of the optical field for the transmitter and receiver lasers are the same as discussed in (8.42) except for optical feedback and injection terms, and they are written in the following forms:

$$\begin{aligned}\frac{\partial E_{\mathrm{T,R}}(x,t)}{\partial t} &= iD_e\frac{\partial^2 E_{\mathrm{T,R}}(x,t)}{\partial x^2} + \frac{1}{2}(1-i\alpha)G_n\{n(x,t)-n_{\mathrm{th}}\}E_{\mathrm{T,R}}(x,t)\\ &+ \frac{\kappa}{\tau_{\mathrm{in,T}}}E_{\mathrm{T}}(x,t-\tau_{\mathrm{T}})\exp(i\omega_0\tau)\\ &+ \frac{\kappa_{\mathrm{cp}}}{\tau_{\mathrm{in,R}}}E_{\mathrm{R}}(x,t-\tau_c)\exp(-i\Delta\omega t)\end{aligned} \tag{12.49}$$

where the subscripts T and R stand for the transmitter and receiver lasers, respectively. The carrier number equations remain the same forms as (8.43). In this occasion, we assume that the transmitter output is precisely fed into the position of the active layer in the receiver laser with one-to-one correspondence in space. In the followings, we show some numerical examples for chaos synchronization in broad-area semiconductor lasers in the level of filament fluctuations.

Before showing the results of synchronization, we briefly discuss the phase in solitary broad-area semiconductor lasers. For a common solitary semiconductor laser with narrow strip structure, the steady-state solution of the phase associated with the complex field is zero for the time development. On the other hand, in the presence of optical feedback in a narrow-stripe semiconductor laser as discussed in Sect. 4.2.1, the steady-state solution of the phase ϕ is not zero, but its time derivative is constant as $\mathrm{d}\phi/\mathrm{d}t = \omega_s - \omega_{\mathrm{th}}$, where ω_s is the oscillation angular frequency of the laser and ω_{th} is the threshold angular frequency. Similar to optical

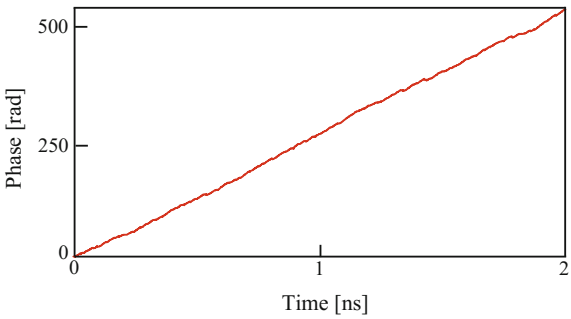

Fig. 12.15 Optical phase of a broad-area semiconductor laser at solitary oscillation for time variations

feedback effects in narrow-stripe semiconductor lasers, the optical phase of a solitary BAL linearly changes with time as shown in Fig. 12.15, although it contains small fluctuations. Namely, the optical phase in filament oscillations of a solitary BAL is similar to a steady-state phase in the presence of optical feedback in common narrow-stripe semiconductor lasers. However, the phase change for time is much faster than that in common narrow-stripe semiconductor lasers with optical feedback.

Since a solitary broad-area semiconductor laser shows irregular filament oscillations even without optical feedback, one can still use it as a chaotic source. Then, we can expect chaos synchronization when an output from a transmitter of a broad-area semiconductor laser at solitary oscillation is fed into a receiver of a solitary broad-area semiconductor laser. However, we here consider a transmitter system of a broad-area semiconductor laser subjected to optical feedback. By applying optical feedback to a transmitter laser, various different filament oscillations can be generated. Then, the chaotic oscillation is transmitted to a receiver broad-area semiconductor laser. The receiver laser is assumed to be oscillated at solitary mode. When the optical injection from the transmitter laser to the receiver laser is rather strong, one obtain generalized chaos synchronization and the delay of the synchronization is always τ_c, which is the transmission time of light. Figure 12.16a shows the intensity correlation function between the two lasers. Each output is integrated along the stripe width at a time instance (namely, time resolved total intensity). Since the maximum correlation is achieved at delay time equal to zero (note that the transmission time of light τ_c is set to be zero in the numerical simulation), this corresponds to generalized chaos synchronization. In this case, the optical injection coefficient to the receiver broad-area semiconductor laser is larger than the optical feedback coefficient in the transmitter, i.e., $\kappa_{ex} < \kappa_{inj}$. On the other hand, complete synchronization is observed at $r_{ex} = 0.06$ and $r_{inj} = 0.10$ as shown in Fig. 12.16b. In this case, the optical injection coefficient in the receiver laser is nearly equal to that of the optical feedback in the transmitter laser, namely, $\kappa_{ex} \approx \kappa_{inj}$, and the time delay of the correlation peak is equal to $\Delta t = \tau_c - \tau_{ex} = -1$ ns. The time delay of the correlation denotes that the synchronization is perfect (complete synchronization).

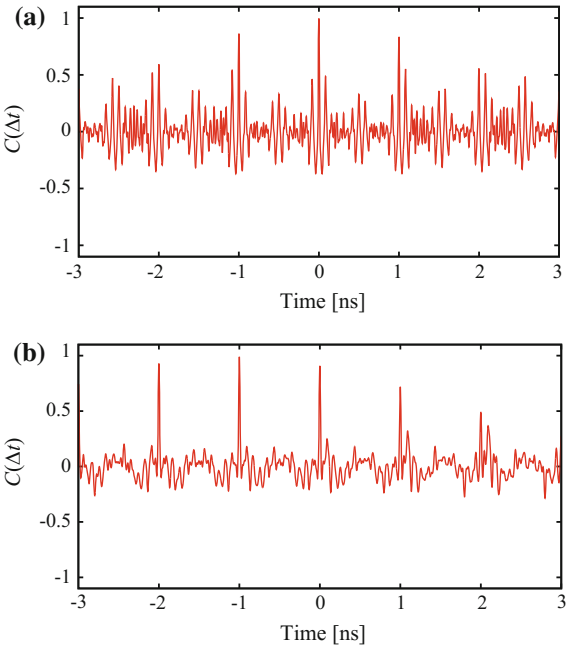

Fig. 12.16 **a** Time correlation of the total intensities between two broad-area semiconductor lasers at $r_{ex} = 0.01$, $r_{inj} = 0.20$ ($\kappa_{ex} < \kappa_{inj}$), and $\tau_{ex} = 1$ ns. **b** Time correlation at $r_{ex} = 0.06$, $r_{inj} = 0.10$ ($\kappa_{ex} \approx \kappa_{inj}$), and $\tau_{ex} = 1$ ns. τ is set to be zero in this case

In the meantime, to confirm the completeness of synchronization, the relations for the optical phase and the carrier density must be studied, since anticipating chaos synchronization does not always mean complete synchronization as discussed in Sect. 12.3.3 (Alers et al. 1998; Kusuomoto and Ohtsubo 2003). Namely, in addition to the anticipated intensity synchronization between the two intensity waveforms, the conditions of (12.18) and (12.19) for the optical phase ϕ and the carrier density n must be satisfied. Then, we construct phase maps for the time variations of the optical phase and the carrier density at the center of the coordinate in the active region, $x = 0$. Figure 12.17 shows the chaotic trajectories for the transmitter and receiver lasers in the phase space of the normalized carrier density $n_{T,R}(t)/n_{th}$ and the phase difference $\Delta\phi_{T,R} = \phi_{T,R}(t) - \phi_{T,R}(t - \tau_{ex})$. Figure 12.17a corresponds to the phase map for the generalized chaos synchronization in Fig. 12.16a. The red curve represents the trajectory for the receiver laser, while the green one denotes that for the transmitter laser. Due to the carriers diffusion to the direction to the edges of the active layer and the effects of carrier hole-burning, the carrier density at the center of the active layer greatly decreases in comparison with the threshold carrier density, n_{th}, when the lasers are biased well above the threshold. Therefore, the normalized carrier densities are much smaller than unity. The situation is quite different from the case of the trajectories obtained in common narrow-stripe semiconductor lasers in Fig. 12.10b. In Fig. 12.17a, the two trajectories do not coincide with each other and the averaged carrier density of the transmitter laser is larger than that of the receiver, so that the scheme is generalized

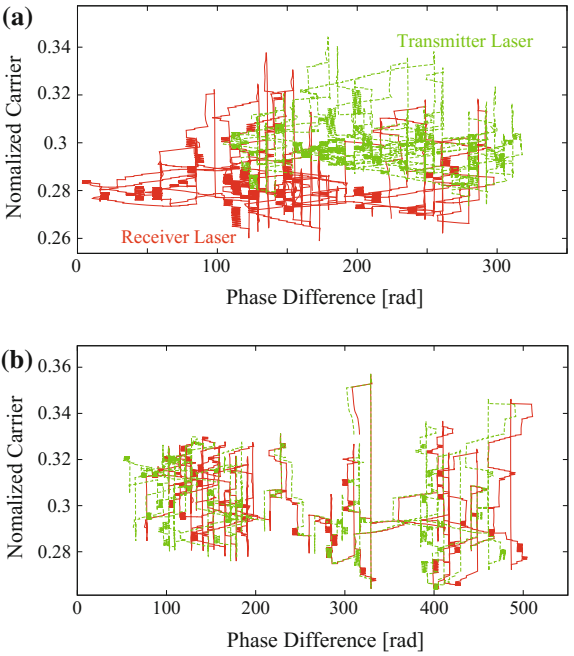

Fig. 12.17 Chaotic trajectories in the phase space of the normalized carrier density $n_{T,R}(t)/n_{th}$ and the optical phase difference $\Delta\phi_{T,R} = \phi_{T,R}(t) - \phi_{T,R}(t - \tau_{ex})$ at $x = 0$. **a** Generalized synchronization corresponding to Fig. 12.16a, b complete synchronization corresponding to Fig. 12.16b. *Green trajectory* Transmitter laser. *Red trajectory* Receiver laser

synchronization. Figure 12.17b corresponds to the phase map for the complete chaos synchronization in Fig. 12.16b. Although there exist small deviations between the two trajectories, they are almost coincident with each other. Then, it is concluded that the scheme is complete chaos synchronization.

12.4 Chaos Synchronization in Optically Injected Lasers

12.4.1 Theory of Chaos Synchronization in Optically Injected Lasers

Semiconductor lasers exhibit chaotic oscillations by optical injection from a different laser as discussed in Chap. 6. We can use an optically injected laser as a light source for chaos synchronization as depicted in Fig. 6.1. However, an optical injection system is not a delay differential system, so that complete chaos synchronization is not generally realized in this system. We can also consider two types of synchronization systems; closed- and open-loop systems (Chen and Liu 2000). Both the transmitter and receiver lasers are optically injection-locked from external lasers in the closed-loop system, while only the transmitter laser is injection-locked in the case of the open-loop system. The open-loop system is also a special case of

the closed-loop system. In the following, we formulate chaos synchronization in closed-loop systems of optically injected semiconductor lasers.

The optical injection-locking semiconductor laser is a coherent system. Therefore, the model must be described by the rate equations of the field, the phase, and the carrier density

$$\frac{\mathrm{d}A_{\mathrm{T}}(t)}{\mathrm{d}t} = \frac{1}{2}G_{n,\mathrm{T}}\{n_{\mathrm{T}}(t) - n_{\mathrm{th,T}}\}A_{\mathrm{T}}(t) + \frac{\kappa_{\mathrm{inj,T}}}{\tau_{\mathrm{in,T}}}A_{\mathrm{inj,T}}(t)\cos\,\theta_{\mathrm{T}}(t) \tag{12.50}$$

$$\frac{\mathrm{d}\phi_{\mathrm{T}}(t)}{\mathrm{d}t} = \frac{1}{2}\alpha_{\mathrm{T}}G_{n,\mathrm{T}}\{n_{\mathrm{T}}(t) - n_{\mathrm{th,T}}\} - \frac{\kappa_{\mathrm{inj,T}}}{\tau_{\mathrm{in,T}}}\frac{A_{\mathrm{inj,T}}(t)}{A_{\mathrm{T}}(t)}\sin\theta_{\mathrm{T}}(t) \tag{12.51}$$

$$\frac{\mathrm{d}n_{\mathrm{T}}(t)}{\mathrm{d}t} = \frac{J_{\mathrm{T}}}{ed} - \frac{n_{\mathrm{T}}(t)}{\tau_{s,\mathrm{T}}} - G_{n,\mathrm{T}}\{n_{\mathrm{T}}(t) - n_{0,\mathrm{T}}\}A_{\mathrm{T}}^2(t) \tag{12.52}$$

$$\theta_{\mathrm{T}}(t) = -\Delta\omega_{\mathrm{T}}t + \phi_{\mathrm{T}}(t) - \phi_{\mathrm{inj,T}}(t) \tag{12.53}$$

The parameters in the above equations are essentially the same as those of previous equations. $\Delta\omega_{\mathrm{T}}$ is the frequency detuning between the transmitter laser and the injection laser. The receiver laser driven by the transmitted signal can be described by

$$\begin{aligned}\frac{\mathrm{d}A_{\mathrm{R}}(t)}{\mathrm{d}t} = &\frac{1}{2}G_{n,\mathrm{R}}\{n_{\mathrm{R}}(t) - n_{\mathrm{th,R}}\}A_{\mathrm{R}}(t) + \frac{\kappa_{\mathrm{inj,R}}}{\tau_{\mathrm{in,R}}}A_{\mathrm{inj,R}}(t)\cos\,\theta_{\mathrm{R}}(t)\\ &+ \frac{\kappa_{\mathrm{cp}}}{\tau_{\mathrm{in,R}}}A_{\mathrm{T}}(t-\tau_c)\cos\,\xi_c(t)\end{aligned} \tag{12.54}$$

$$\begin{aligned}\frac{\mathrm{d}\phi_{\mathrm{R}}(t)}{\mathrm{d}t} = &\frac{1}{2}\alpha_{\mathrm{R}}G_{n,\mathrm{R}}\{n_{\mathrm{R}}(t) - n_{\mathrm{th,R}}\} - \frac{\kappa_{\mathrm{inj,R}}}{\tau_{\mathrm{in,R}}}\frac{A_{\mathrm{inj,R}}(t)}{A_{\mathrm{R}}(t)}\sin\theta_{\mathrm{R}}(t)\\ &- \frac{\kappa_{\mathrm{cp}}}{\tau_{\mathrm{in,R}}}\frac{A_{\mathrm{T}}(t-\tau_c)}{A_{\mathrm{R}}(t)}\sin\xi_c(t)\end{aligned} \tag{12.55}$$

$$\frac{\mathrm{d}n_{\mathrm{R}}(t)}{\mathrm{d}t} = \frac{J_{\mathrm{R}}}{ed} - \frac{n_{\mathrm{R}}(t)}{\tau_{s,\mathrm{R}}} - G_{n,\mathrm{R}}\{n_{\mathrm{R}}(t) - n_{0,\mathrm{R}}\}A_{\mathrm{R}}^2(t) \tag{12.56}$$

$$\theta_{\mathrm{R}}(t) = -\Delta\omega_{\mathrm{R}}t + \phi_{\mathrm{R}}(t) - \phi_{\mathrm{inj,R}}(t) \tag{12.57}$$

$$\xi_c(t) = \omega_{0,\mathrm{T}}\tau_c + \phi_{\mathrm{R}}(t) - \phi_{\mathrm{T}}(t-\tau_c) + \Delta\omega t \tag{12.58}$$

where $\Delta\omega_{\mathrm{R}}$ is the detuning between the receiver and injection lasers, and $\Delta\omega$ is also the detuning between the transmitter and receiver lasers. As can be understood from these equations, chaos synchronization in the systems originates from injection-locking and amplification. Under the special conditions of

$$\frac{1}{\tau_{\mathrm{ph,R}}} = \frac{1}{\tau_{\mathrm{ph,T}}} \mp \frac{2\alpha\kappa_{\mathrm{cp}}}{\tau_{\mathrm{in,R}}\sqrt{1+\alpha^2}} \tag{12.59}$$

$$\omega_{0,\mathrm{T}}\tau_c = -\cot^{-1}\alpha \tag{12.60}$$

$$\Delta\omega = 0 \tag{12.61}$$

$$\Delta\omega_{\mathrm{R}} = \Delta\omega_{\mathrm{T}} \tag{12.62}$$

we obtain complete chaos synchronizations (Liu et al. 2001a, b, c)

$$A_{\mathrm{R}}(t) = A_{\mathrm{T}}(t-\tau_c) \tag{12.63}$$

$$\phi_{\mathrm{R}}(t) = \phi_{\mathrm{T}}(t-\tau_c) \tag{12.64}$$

In (12.59), minus sign is for $\sin(\omega_{0,\mathrm{T}}\tau_c) > 0$, while plus sign is for $\sin(\omega_{0,\mathrm{T}}\tau_c) < 0$. We assume without loss of generality that the other parameter values of the two lasers are the same and the phases of the injection lasers, $\phi_{\mathrm{inj,R}}(t) = \phi_{\mathrm{inj,T}}(t)$, are constant. The condition in (12.59) contains the internal device parameters (τ_{ph} and α) and the external coupling constant. Therefore, it is usually difficult to realize complete chaos synchronization in this system, since the adjustment of the parameters is extremely difficult in real devices and experiments.

12.4.2 *Examples of Chaos Synchronization in Optically Injected Lasers*

Figure 12.18 shows the experimental results of chaos synchronization using chaotic semiconductor lasers by optical injection (Liu et al. 2001a). The system used is an open-loop system and, therefore, optical injection is only presented in the transmitter system. The frequency detuning between the transmitter and injection lasers is changed to generate various chaotic states. Chaos synchronization is realized at period-1, period-2, and chaotic oscillations. Figure 12.19 plots the numerical results of synchronization errors for the parameter mismatches in the system (Chen and Liu 2000). The figure corresponds to the synchronization errors in complete chaos synchronization. The errors of synchronization are asymmetry for the parameter mismatches, which is similar to the trend for the case of the optical feedback system in Fig. 12.8b. The tolerances for the differential carrier relaxation rate, the nonlinear carrier relaxation rate, and the linewidth enhancement factor are much less effective, but the mismatch of the cavity decay rate $1/\tau_{\mathrm{ph}}$ greatly affects the performance of chaos synchronization. In real devices, we could not easily access and vary the device parameters, therefore we must carefully select lasers with similar characteristics even if the lasers come from the same wafer. It is said that semiconductor laser devices have parameter mismatches within 5–20% in industrial standards. In

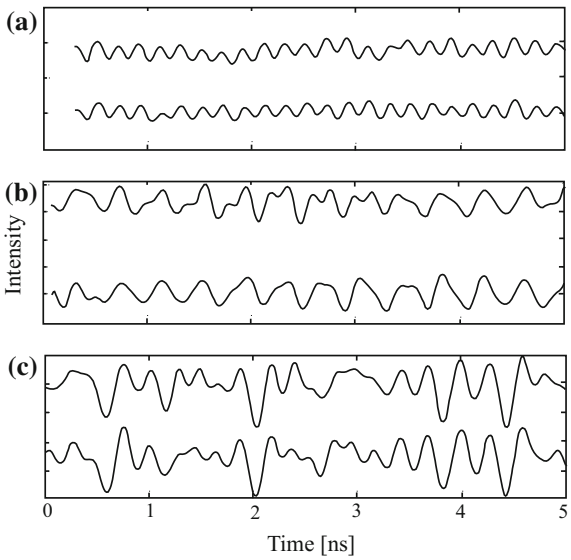

Fig. 12.18 Experimental chaos synchronization using chaotic semiconductor lasers by optical injection. The system is an open-loop. The frequency detuning between the transmitter and injection lasers is changed to generate various chaotic states at a fixed injection rate. Synchronized waveforms at **a** period-1, **b** period-2, and **c** chaotic oscillations. In each figure, the *upper trace* is the transmitter output and the *lower trace* is the receiver output. The lasers used are DFB lasers with an oscillation wavelength of 1.3 μm. The chaos synchronization is achieved under the complete condition [after Liu et al. (2001a); © 2001 IEEE]

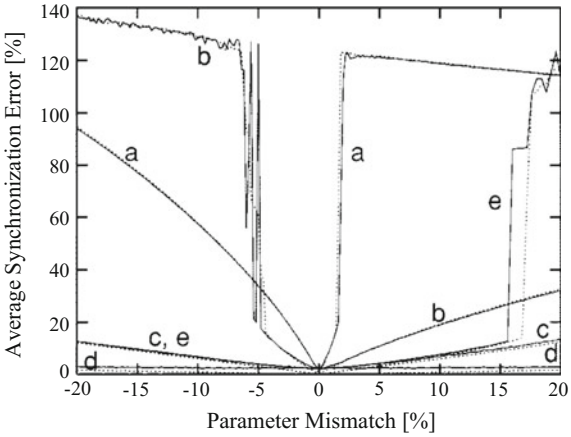

Fig. 12.19 Synchronization error (%) versus parameter mismatch (%). Solid curves *a*, *b*, *c*, *d*, and *e* correspond to parameters of cavity decay rate, spontaneous carrier decay rate, differential carrier relaxation rate, nonlinear carrier relaxation rate, and linewidth enhancement factor, respectively. The intrinsic Langevin noise is considered in the simulation. Each corresponding *dotted curve* is obtained without including the intrinsic noise [after Chen and Liu (2000); © 2000 IEEE]

real lasers, we must also take noise effects into account. Therefore, the coupling coefficient κ_{cp} from the transmitter to the receiver lasers must be larger than a certain value to take on a negative value for the conditional Lyapunov exponent.

12.5 Chaos Synchronization in Optoelectronic Feedback Systems

12.5.1 Theory of Chaos Synchronization in Optoelectronic Feedback Systems

We discussed chaotic oscillations in optoelectronic feedback in semiconductor lasers in Chap. 7. We here assume the chaotic generators of optoelectronic feedback lasers depicted in Fig. 7.1. In optoelectronic feedback systems, the rate equations for the photon number and the carrier density are enough for describing the systems. Optoelectronic feedback systems in semiconductor lasers have an advantage of excellent synchronization performance over optical feedback and optical injection systems. Since the time scale of the relaxation for the carrier density is three figures larger than that of the photon lifetime, the performance, and the accuracy of chaos synchronization in optoelectronic feedback systems are different from those of optical feedback and optical injection systems. The points will be again discussed in the next chapter from the viewpoint of data transmission capability in chaotic communications. The rate equations for the photon number and the carrier density in a transmitter of optoelectronic feedback are written by

$$\frac{\mathrm{d}S_{\mathrm{T}}(t)}{\mathrm{d}t} = G_{n,\mathrm{T}}\{n_{\mathrm{T}}(t) - n_{\mathrm{th,T}}\}S_{\mathrm{T}}(t) + R_{\mathrm{sp,T}} \tag{12.65}$$

$$\begin{aligned}\frac{\mathrm{d}n_{\mathrm{T}}(t)}{\mathrm{d}t} = {} & \frac{J_{\mathrm{T}}}{ed}\{1 + \xi_{\mathrm{T}}S_{\mathrm{T}}(t-\tau_{\mathrm{T}})\} \\ & - \frac{n_{\mathrm{T}}(t)}{\tau_{s,\mathrm{T}}} - G_{n,\mathrm{T}}\{n_{\mathrm{T}}(t) - n_{0,\mathrm{T}}\}S_{\mathrm{T}}(t)\end{aligned} \tag{12.66}$$

where ξ_{T} is the coefficient of the optoelectronic feedback circuit in the transmitter. The rate equations for the receiver laser are given by

$$\frac{\mathrm{d}S_{\mathrm{R}}(t)}{\mathrm{d}t} = G_{n,\mathrm{R}}\{n_{\mathrm{R}}(t) - n_{\mathrm{th,R}}\}S_{\mathrm{R}}(t) + R_{\mathrm{sp,R}} \tag{12.67}$$

$$\begin{aligned}\frac{\mathrm{d}n_{\mathrm{R}}(t)}{\mathrm{d}t} = {} & \frac{J_{\mathrm{R}}}{ed}\{1 + \xi_{\mathrm{R}}S_{\mathrm{R}}(t-\tau_{\mathrm{R}}) + \xi_{\mathrm{cp}}S_{\mathrm{T}}(t-\tau_c)\} \\ & - \frac{n_{\mathrm{R}}(t)}{\tau_{s,\mathrm{R}}} - G_{n,\mathrm{R}}\{n_{\mathrm{R}}(t) - n_{0,\mathrm{R}}\}S_{\mathrm{R}}(t)\end{aligned} \tag{12.68}$$

where ξ_R is the coefficient of the optoelectronic feedback circuit in the receiver and ξ_{cp} is the coupling coefficient from the transmitter to the receiver lasers. As discussed in Chap. 7, when the electronic feedback circuit has a finite time response, the feedback terms $s(t) = \xi_T S_T(t - \tau_T)$ and $s(t) = \xi_R s_R(t - \tau_R) + \xi_{cp} S_T(t - \tau_c)$ are replaced by the following integral equation:

$$y(t) = \int_{-\infty}^{t} f(t' - t)s(t')\mathrm{d}t' \tag{12.69}$$

where $f(t)$ is the response function of the electronic circuit. The optoelectronic feedback system is also a delay differential system like the optical feedback system. However, the optoelectronic feedback system is quite different from optical feedback and optical injection systems. For example, the chaotic output from optoelectronic feedback is generally irregular pulsing states. The driving signal to the laser in the optoelectronic feedback system is also a chaotic signal, but the signal is not linearly proportional to the optical output power (Liu et al. 2001b). Chaos synchronization in optoelectronic feedback is generally a complete type (Tang et al. 2001).

12.5.2 Examples of Chaos Synchronization in Optoelectronic Feedback Systems

Figure 12.20 shows the results of experimental chaos synchronization in an open-loop optoelectronic feedback system (Tang et al. 2001). As discussed in Chap. 7, the typical feature of chaotic oscillations in optoelectronic feedback systems is periodic or irregular pulsations of the laser output power. In the figure, chaos synchronization is achieved for various states of chaotic oscillations by changing the feedback time τ_T in the electronic feedback circuit. The synchronization scheme is complete chaos synchronization. Figure 12.21 shows the numerical simulation for the model. Figure 12.21a is the bifurcation diagram for the normalized delay time $\hat{\tau} = \tau v_R$ in the transmitter laser. Figure 12.21b is the maximum conditional Lyapunov exponent. Here, the parameter c_p is defined by

$$c_p = 1 - \frac{\xi_R}{\xi_T + \xi_{cp}} \tag{12.70}$$

When the system is a closed-loop, $c_p = 0$, while $c_p = 1$ for an open-loop. From this figure, the maximum conditional Lyapunov exponent in the open-loop system is smaller than that of the closed-loop system. Therefore, the open-loop system can achieve stable chaos synchronization compared with the closed-loop system. The effects of parameter mismatches for chaos synchronization have also been studied in optoelectronic feedback systems and similar results as for optical feedback systems are obtained (Abarbanel et al. 2001).

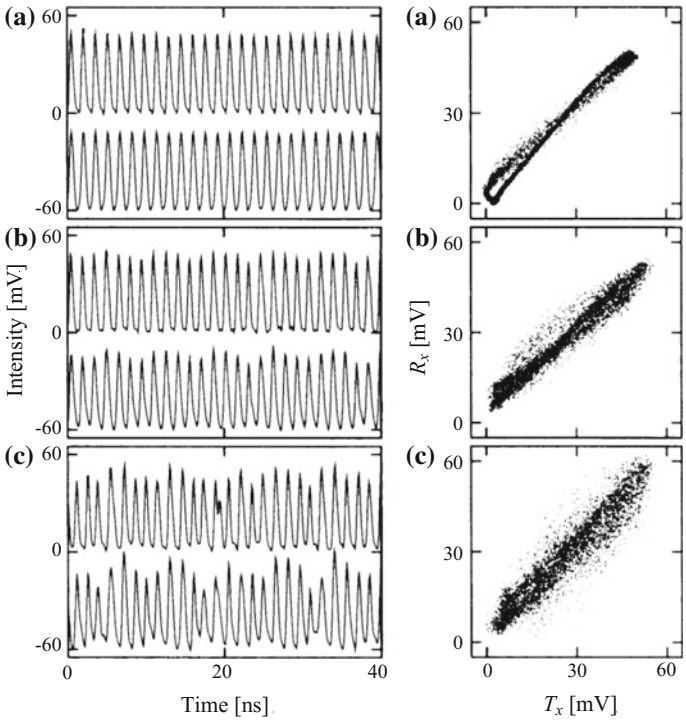

Fig. 12.20 Time series and correlation plots of synchronization at three different pulsing states under $c_p = 1$. **a** Regular pulsing at $\tau = 7.47$ ns, **b** two-frequency quasi-periodic pulsing at $\tau = 7.09$ ns, **c** chaotic pulsing at $\tau = 6.92$ ns. In **a**–**c**, the *upper trace* is for the transmitter and the *lower trace* is for the receiver. The *left row* is the time series and the *right row* is the correlation plots. The laser is a DFB laser with an oscillation wavelength at 1.30 μm. The relaxation oscillation frequency of the laser is 2.5 GHz at the operating condition [after Tang et al. (2001); © 2001 OSA]

12.6 Chaos Synchronization in Injection Current Modulated Systems

Semiconductor lasers are sensitive to injection current modulation and sometimes show chaotic oscillations for certain conditions both of the device parameters and the modulation frequency and index as discussed in Chaps. 6 and 7. However, chaotic oscillations by the frequency modulation occur only under limited conditions in ordinary narrow-stripe edge-emitting semiconductor lasers. Therefore, we briefly introduce a chaos synchronization system using a frequency modulated self-pulsating semiconductor laser as a chaotic light source. The output from a self-pulsating semiconductor laser shows regular pulsating oscillations for the ideal case. The laser is used as a light source of a digital versatile disk system. However, the laser easily exhibits chaotic oscillations (irregular pulsing states) under an

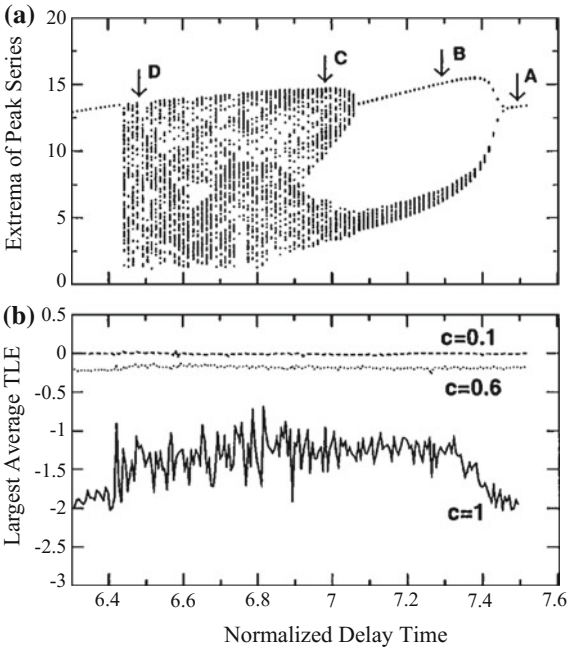

Fig. 12.21 Conditions for stable route-tracking synchronization. **a** Bifurcation diagram. *A* regular pulsing, *B* two-frequency quasi-periodic pulsing, *C* three-frequency quasi-periodic pulsing, *D* chaotic pulsing. **b** Largest average conditional Lyapunov exponent (transverse Lyapunov exponent, TLE) of the coupled system for the same dynamic states as in (**a**) under different coupling strengths, c_p = 0.1, 0.6, and 1 [after Tang et al. (2001); © 2001 OSA]

appropriate combination of the modulation frequency and index for the bias injection current as discussed in Sect. 8.2. In the chaotic oscillations, pulse heights of the pulsating output irregularly fluctuate and this fluctuation is proved to be chaotic. Jones et al. (2001) numerically demonstrated chaos synchronization in symmetrical modulation systems. They used a very high frequency modulation of 3.4 GHz with a large modulation index of 0.3. Their model was a coherent coupling between the transmitter and receiver lasers. However, incoherent coupling must be taken into account through a long transmission line between the transmitter and receiver systems, since a self-pulsating semiconductor laser has once brought almost below the laser threshold after a pulsation. Only a few studies have been published on chaos synchronization in modulated semiconductor lasers to date.

12.7 Chaos Synchronization in Mutually Coupled Lasers

12.7.1 Mutually Coupled Edge-Emitting Semiconductor Lasers

Mutually coupled oscillators are of great interest because of the important insight they provide into coupled physical, chemical, and biological systems. Mutually coupled semiconductor lasers can be used for a system of chaos synchronization.

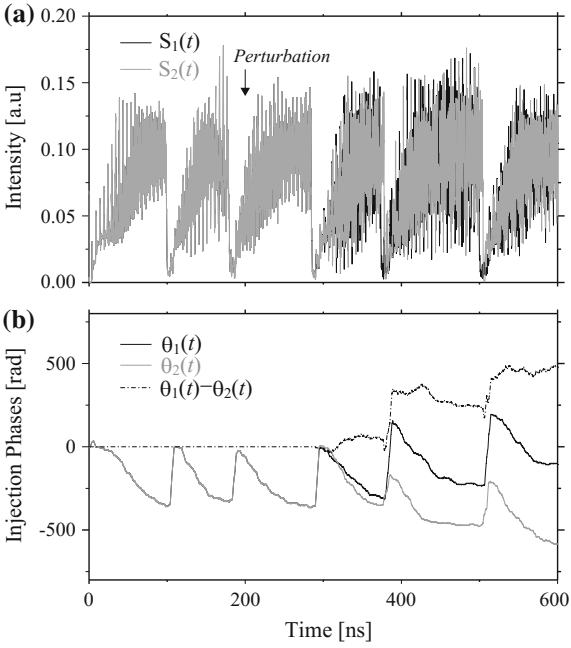

Fig. 12.22 Numerical simulation describing the transition phenomenon from the isochronal to achronal solution due to perturbations of Langevin noises applied at t = 200 ns. **a** Intensity time traces and **b** dynamics of the injection phases. The parameters are τ_c = 5 ns, κ_{cp}/τ_{in} = 20 ns^{-1}, and J/J_{th} = 1 [after Mulet et al. (2004); © 2004 IOP]

However, the dynamics have not been fully studied in semiconductor lasers, since the straightforward applications of the systems such as for secure communications are not easy. Example of chaotic secure communications based on mutual coupling systems is discussed in Chap. 13. Further, many mutual-coupling semiconductor lasers and their synchronization exhibit similar properties as those of nonlinear networks in synaptic neurons. The topics are treated in Chap. 14. In this subsection, we concern chaos synchronization in mutually coupled two narrow-stripe edge-emitting semiconductor lasers (Hohl et al. 1997, 1999; Heil et al. 2001; Mirasso et al. 2002; Mulet et al. 2002, 2004; Klein et al. 2006). In an unbalanced mutual coupling system, (for example, frequency detuned system or parameter mismatched system), one of the lasers become the leader of chaos synchronization and the other is the lagger as concerning to their time series as discussed in Sect. 12.2.5. In accordance with the discussion in Sect. 12.2.5, chaos synchronization originated by injection-locking phenomena can be studied and the detail of the conditions for chaos synchronization in leader-lagger configurations of chaotic waveforms is found in literature (Heil et al. 2001). Here, we focus on the transition phenomenon of chaos synchronization in an intrinsically complete configuration. As mentioned in Sect. 12.2.5, an isochronal solution in the mutual coupling semiconductor lasers is easily transitioned to an achronal state due to the presence of noises in spite of highly symmetrical conditions.

Figure 12.22 shows a numerical example of transitions from complete to generalized chaos synchronization in a symmetrical system of mutual coupling

semiconductor lasers (Mulet et al. 2004). In the numerical simulation, the coupled two lasers without optical feedback have the same device parameters and driving conditions. In Fig. 12.22a, the time traces of the two lasers at first output completely the same waveforms, since the rate equations do not include the noise terms. However, the output powers deviate with each other and the synchronization is transitioned to achronal state from complete isochronal one after the noises are switched on at $t = 200$ ns. Since the lasers are biased at low current $J/J_{\mathrm{th}} = 1$, the output powers show LFFs. Figure 12.22b shows the dynamics of the phases [θ_1 and θ_2 in (12.25) and (12.29)] and their difference. Before the perturbation is applied, the two phases completely show identical traces. However, after one transient LFF following the perturbation, the two phase traces deviate with each other. In the situation of a highly symmetrical mutual coupling system, which laser becomes the leader or lagger is determined by statistically. Further, the leader is once switched to the lagger and at the other occasion it returns to the leader.

The process is described by the statistical potential model, which has already discussed in Sect. 5.1.2, and the transition is kicked by the Langevin noises. To show the physical effects clearly, the case for a low bias injection current is shown in Fig. 12.22. However, similar phenomena are also observed at higher bias injection current with fast chaotic oscillations whose main frequency component corresponds to the laser relaxation oscillation. We cannot avoid statistical noises in real semiconductor lasers, so that we only observe leader and lagger chaotic signals in experimental mutual coupling systems with symmetrical configuration, even if the two coupling lasers are carefully prepared to take the same characteristics. It is noted that such instability of the switching between leader and lagger configurations occurs only for symmetrical systems. When an asymmetry is introduced for a synchronization system of mutual coupling semiconductor lasers with optical feedback, we obtain a fixed relation of the time lag between the laser outputs even for complete chaos synchronization scheme as will be discussed in Sect. 13.5. Synchronization is also attained in polarization-rotated mutual coupling systems and synchronous oscillations of square-wave forms between two lasers have been demonstrated (Sukow et al. 2010). Oscillations of square-wave forms and anti-phase synchronization are typical features in semiconductor lasers with polarization-rotated optical feedback as discussed in Sect. 5.8.2. The tolerances for the parameter mismatches in mutually coupled narrow-stripe edge-emitting semiconductor lasers have also been discussed (Avila and Leite 2009; Hicke et al. 2011).

In the following, we will discuss the effects of frequency detuning on the synchronization and introduce the basic mechanism to the instabilities induced by the laser coupling and the associated symmetry breaking in mutually coupled semiconductor lasers. The coupling time between the two semiconductor lasers is τ_{c}, however the primary frequency component of chaotic oscillations involved in two mutually coupled semiconductor lasers is equal to $\nu_c = 1/2\tau_c$. As discussed above, the two mutually coupled lasers without considering frequency detuning show achronal synchronization when we take into account intrinsic laser noises. By randomly driven by noises, a leader to synchronization frequently switches from

one laser to the other in time. On the other hand, when we take into account frequency detuning between two lasers, the system reduces to one of delay synchronization. In this case, the leader laser has a higher oscillation frequency than that of the lagger laser. About 1 GHz of detuning is enough to switch from achronal to delay synchronization in the mutually coupled system. It is noted that, even without considering laser noises, the two mutually coupled semiconductor lasers show delay synchronization in numerical simulations. The symmetry is also broken by the frequency detuning even without considering laser noises in numerical simulations. As already noted, the primary frequency component is $\nu_c = 1/2\tau_c$. In the case of the existence of frequency detuning, this means that the lagger laser plays a role for a feedback mirror to the leader laser and the leader laser receives an equivalent optical feedback from it after a round trip of light. Thus, in the mutually coupled two-laser system with a frequency detuning, the laggard laser acts as a driving force of the chaotic dynamics (Heil et al. 2001). The situation will be cleared in the next chapter (Sect. 13.5.2), where we will discuss chaos-pass filtering effect in signal transmission in a system in mutually coupled semiconductor laser systems.

12.7.2 Mutually Coupled VCSELs

Several reports have also been published for chaos synchronization with mutually coupled VCSELs (Spencer et al. 1998; Spencer and Mirassso 1999; Fujino and Ohtsubo 2001). In mutually coupled VCSELs, two orthogonal polarization modes are simultaneously excited and the polarization dynamics must be taken into account. We here show chaos synchronization in mutually coupled VCSELs in LFF regimes (Fujiwara et al. 2003). In the experiments, mutually coupled VCSELs without external mirrors are used. Even when the lasers are stable at the free running state, they exhibit chaotic oscillations under mutual coupling. Figure 12.23 shows the results of chaos synchronization. Figure 12.23a plots time series and their optical spectra of the *x*-polarization components of the two lasers at LFF oscillations. Figure 12.23b shows the results for the *y*-polarization components. The lasers are biased at low injection currents and their spatial modes are the lowest ones, i.e., LP_{01} mode. In the experiment, the two polarization modes are mutually coupled with each other. In this example, chaos synchronization occurs by the coupling with the *x*-polarization components and one of the outputs of the orthogonal *y*-polarization components synchronizes to the other under the anti-correlation effect. This fact is easily understood from the observation of optical spectra in the figure. Anti-phase correlation of the two orthogonal polarization components is a typical feature in VCSELs. At the solitary oscillations, the *y*-polarization modes are dominant lasing modes and the laser powers are almost concentrated to the *y*-polarization modes. On the other hand, the *x*-polarization modes increase and become the dominant modes after the mutual coupling. The laser oscillation of VCSEL2 lags with respect to VCSEL1 with 4 ns (the

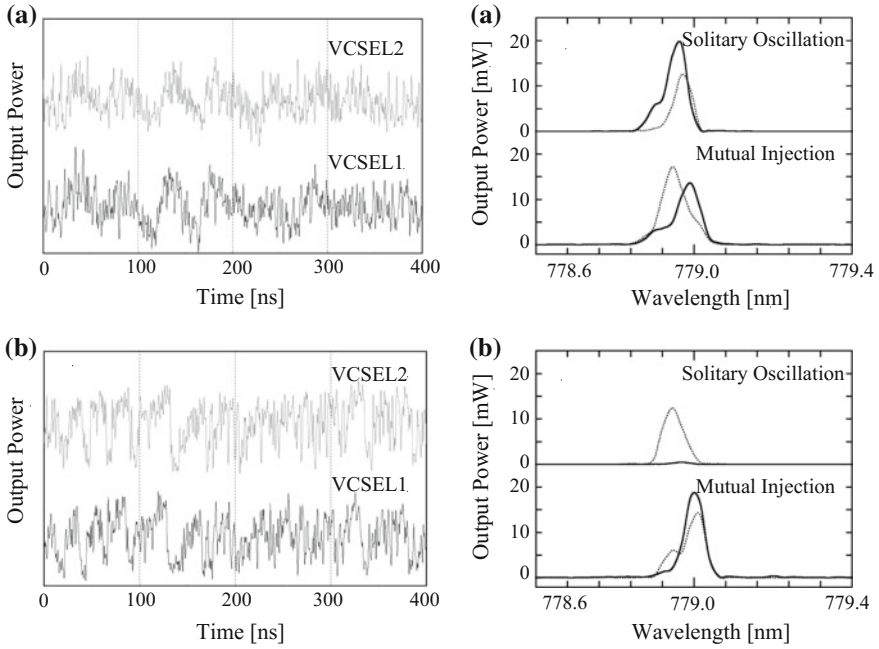

Fig. 12.23 Chaos synchronization in mutually coupled VCSELs in LFF regime. **a** *x*-polarization mode and **b** *y*-polarization mode. *Left* is the time series and *right* is the corresponding optical spectra. *Solid curves* VCSEL 1, *dotted curves* VCSEL2. The coupling time of light between the two lasers is 4 ns

transmission time of light from one laser to the other), therefore the synchronization is a generalized case. Fujiwara and Ohtsubo (2004) also showed chaos synchronization for a selective polarization mode in mutually coupled VCSELs. Though the other mode is not coupled, the remaining modes synchronize with the anti-phase correlation effect. Chaos synchronization in VCSELs occurs even for the two different spatial modes as far as detuning of the oscillation frequencies is negligibly small.

12.7.3 Optoelectronic Mutually Coupled Semiconductor Lasers

The dynamics and chaos synchronization for mutually coupled systems in semiconductor lasers with optoelectronic feedback was studied by Tang et al. (2004). In the system, mutual coupling can act as a negative feedback to stabilize the coupled oscillators or it can increase the complexity of the system inducing a highly complex chaos depending on the operating conditions. A quasi-periodicity and

period-doubling bifurcation, or a mixture of the two, is found in such a system. Also, the system exhibits a unique state of stabilizing and quenching the oscillation amplitude of two pulsating oscillators, a phenomenon known as "death by delay". Although the chaotic waveforms are very complex with broad spectra, a high quality of synchronization between the chaotic waveforms is observed. Such synchronization is achieved because of the effect of mutual coupling and the symmetric design between the two lasers. Figure 12.24 shows a schematic diagram for semiconductor lasers with mutual optoelectronic coupling. The fundamental chaotic oscillator is the same as the system of optoelectronic feedback as discussed in Sect. 12.5.1. A part of an emitted light from semiconductor laser LD 1 is once detected by photodetector PD 1 and electronically fed back into the bias injection current of the laser with delay τ_1. On the other hand, the other light is detected by photodetector PD 2 and fed into the bias injection current of semiconductor laser LD 2 with transmission time T_1. Similarly, semiconductor laser LD 2 also has an optoelectronic feedback loop with time delay τ_2. A part of an emitted light from the laser LD 2 is also fed into the first laser with transmission time T_2, thus, mutual coupling of the system is attained.

The system of the mutual coupling lasers can be easily described by extending the discussion in Sect. 12.5. For semiconductor laser LD 1, one reads

$$\frac{\mathrm{d}S_1(t)}{\mathrm{d}t} = [G_{n1}\{n_1(t) - n_{\mathrm{th1}}\}]S_1(t) \tag{12.71}$$

$$\begin{aligned}\frac{\mathrm{d}n_1(t)}{\mathrm{d}t} = &\frac{J_1(t)}{ed}\{1 + \xi_{f1}S_1(t-\tau_1) + \xi_{\mathrm{cp1}}S_2(t-T_2)\} \\ &- \frac{n_1(t)}{\tau_{s1}} - G_{n1}\{n_1(t) - n_{01}\}S_1(t)\end{aligned} \tag{12.72}$$

Here, we assume an instantaneous response of the electronic feedback circuit, however, we can apply (12.69) for a finite response of the circuit. For the second laser, the coupling equations can be written as symmetric forms as above equations by

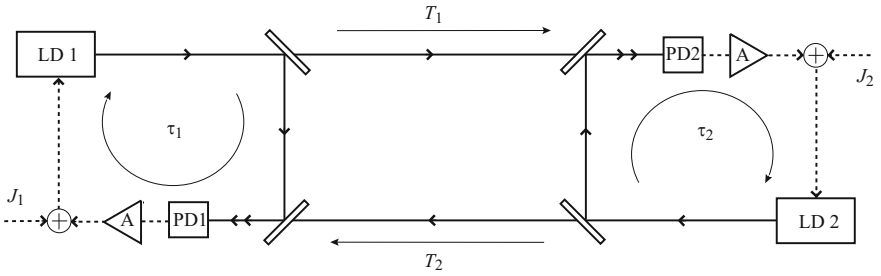

Fig. 12.24 Schematic diagram of mutually coupled semiconductor lasers with optoelectronic feedback. *LD* laser diode, *PD* photodiode, *A* amplifier, *I* bias injection current

$$\frac{\mathrm{d}S_2(t)}{\mathrm{d}t} = [G_{n2}\{n_2(t) - n_{\mathrm{th}2}\}]S_2(t) \tag{12.73}$$

$$\begin{aligned}\frac{\mathrm{d}n_2(t)}{\mathrm{d}t} = &\frac{J_2(t)}{ed}\{1 + \xi_{f2}S_2(t-\tau_2) + \xi_{\mathrm{cp}2}S_1(t-T_1)\} \\ &- \frac{n_2(t)}{\tau_{s2}} - G_{n2}\{n_2(t) - n_{02}\}S_2(t)\end{aligned} \tag{12.74}$$

In mutually coupled semiconductor lasers, not only that the output of one laser is coupled into the dynamics of the other laser, but also that the time delay introduced by the mutual coupling further increases the dimension of the degree of freedom in the coupled lasers. Consequently, a lot of interesting dynamics have been observed in such mutually coupled semiconductor lasers. For example, optoelectronic feedback can drive the semiconductor lasers into nonlinear oscillations, such as regular pulsing, quasi-periodic pulsing, or chaotic pulsing under certain conditions of the device and feedback parameters. One of typical features in this system is a death by delay, in which two limit-cycle oscillators suddenly stop oscillating due to a time-delayed coupling between these oscillators by tuning the feedback parameters (Tang et al. 2004). The phenomenon of death by delay has been observed in many other mutually coupled limit-cycle oscillators, which do not necessarily have a delayed feedback. In the mutually coupled optoelectronic feedback systems described by (12.71)–(12.74), we can observe periodic death islands of the laser oscillations at a certain coupling strength for the increase of the coupling delay time $T_1 + T_2$. In reality, there is always a bandwidth limitation from the components such as the amplifiers, the photodetectors, and even the lasers. Consequently, the mutually coupled semiconductor laser system is not only highly nonlinear but also highly dispersive. The system can have a quasi-periodic pulsing route, a period-doubling pulsing route, or a mixture of these two bifurcations to chaos. The system has very interesting properties as a viewpoint of nonlinear dynamics. However, we here focus on the synchronization properties of the system.

Experimental and theoretical studies for synchronization of mutually coupled semiconductor lasers with optoelectronic feedback were reported by Tang et al. (2004) and Chiang et al. (2005). The two semiconductor lasers are operated in states of regular oscillations or quasi-periodic oscillations under the effect of optoelectronic feedback before the mutual coupling is applied. Once the mutual coupling is applied, dramatic effects can be observed on the original nonlinear oscillations. Figure 12.25 shows an experimental example of chaos synchronization in this system. Without mutual coupling, the waveforms from the two lasers may exhibit either typical pulsing states or chaotic pulsing states at certain oscillation conditions. In this case, the waveform from PD 1 is a regular pulsing state with one fundamental frequency, while that from PD 2 is a quasi-periodic pulsing state as shown in Fig. 12.25a. With mutual coupling, highly complex chaotic outputs form the two lasers are observed under the conditions of $T_1 = T_2 = \tau_1 = \tau_2 = 15.4$ ns as shown in Fig. 12.25b. It is noted that the two waveforms have a zero time lag and

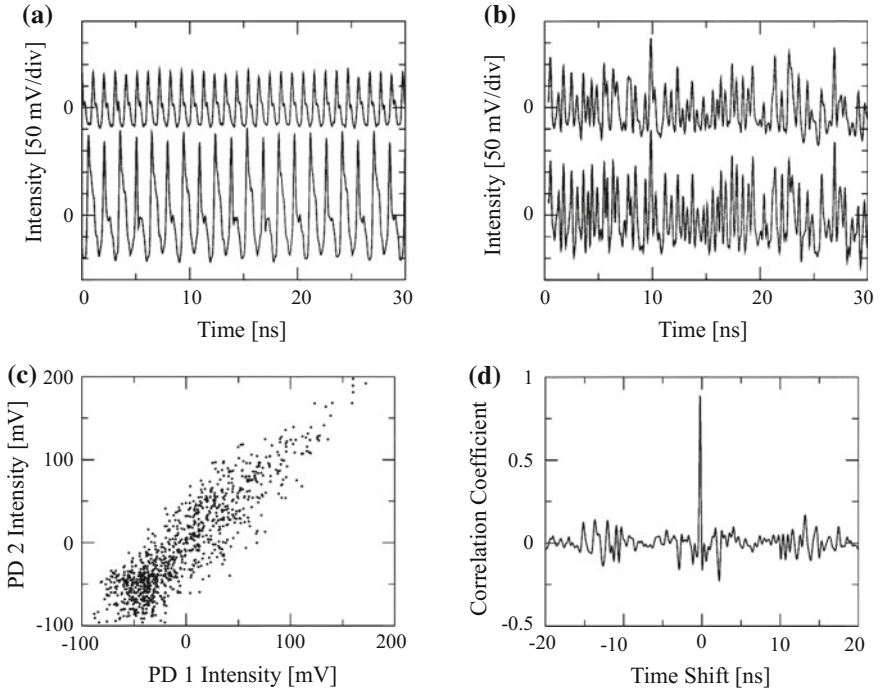

Fig. 12.25 Experimental chaos synchronization in semiconductor lasers with mutual optoelectronic coupling. $T_1 = T_2 = 15.4$ ns and $\tau_1 = \tau_2 = 5.4$ ns. **a** Time series of regular pulsing states in the two lasers before mutual coupling. **b** Chaotic time series after mutual coupling. **c**, **d** Correlation plot of the photodiode outputs after mutual coupling [after Tang et al. (2004); © 2004 IEEE]

the type of synchronization is complete. Figure 12.25c, d show the correlation plot between the outputs form PD 1 and PD 2, and the time shifted correlation, respectively. The detailed properties of chaos synchronization in mutually coupled semiconductor lasers with optoelectronic feedback were reported in the references (Chiang et al. 2005, 2006).

12.8 Common-Chaotic-Signal Induced Synchronization in Semiconductor Lasers

In the preceding sections, we discussed chaos synchronization with two coupled lasers, either in unidirectionally or mutually coupled configuration. However, we can introduce a third chaotic laser in the systems of chaos synchronization. In this configuration, transmitter and receiver lasers are simultaneously injected by the same chaotic signal from the third drive laser and, thus, the accuracy of chaos

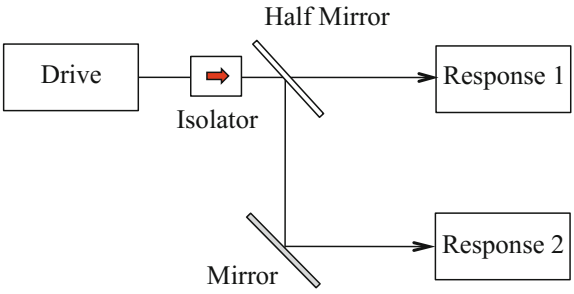

Fig. 12.26 Drive and response configuration in a chaos synchronization system. Two response laser are injected by chaotic light from the drive laser

synchronization between the transmitter and receiver lasers is greatly enhanced. For example, we prepare three chaotic systems consisting of semiconductor lasers with optical feedback; one is assigned to the driving system and the others are used for the response systems. Then, the output from the drive unidirectionally injects the response lasers (Yamamoto et al. 2007; Oowada et al. 2009). The other instance is a mutual coupling system with a third driving laser. In this system, in-between transmitter and receiver lasers, the third laser is introduced as a buffer of the chaotic signal transmissions (Fischer et al. 2006; Vicente et al. 2008). In both cases, we can obtain higher correlations between the transmitter and receiver chaotic signals compared with common two-laser synchronization systems. Figure 12.26 shows a system for the first case. Any chaotic systems may be used as a drive and responses, however, we here assume optical feedback systems of semiconductor lasers for all three systems. The response systems may not be the same characteristics to the drive system. On the other hand, the two response systems are required to have closely similar characteristics with each other not only for the device characteristics but also for the operation conditions. The output powers from response 1 and response 2 show similar chaotic oscillations by the injection of a chaotic signal from the drive system. The driving chaotic signal and the synchronous response signals may not have good correlations, since the adjustment of the parameters between the drive and the responses are rather loose. However, we can obtain a good correlation between the two response systems. The phenomena are confirmed not only by numerical simulations but also by experiments.

Figure 12.27 shows an experimental example of chaos synchronization in drive-response systems. In this case, the driving system is a semiconductor laser with optical feedback (feedback delay time of 4 ns), however, the response systems are solitary semiconductor lasers without optical feedback. The three lasers are all the same DFB lasers with oscillation wavelength of 1.55 μm, which come from the same wafer. At the operation conditions, the response lasers have the same optical wavelength of 1547.356 nm, while the drive laser is biased at lower current and its oscillation wavelength is 1547.376 nm (the corresponding frequency detuning between the drive and response lasers is −2.5 GHz). Since the frequency detuning is not large, the response lasers are injection-locked to the drive laser and they oscillate similar chaotic signal to the drive laser. Figure 12.27a–d are the results of

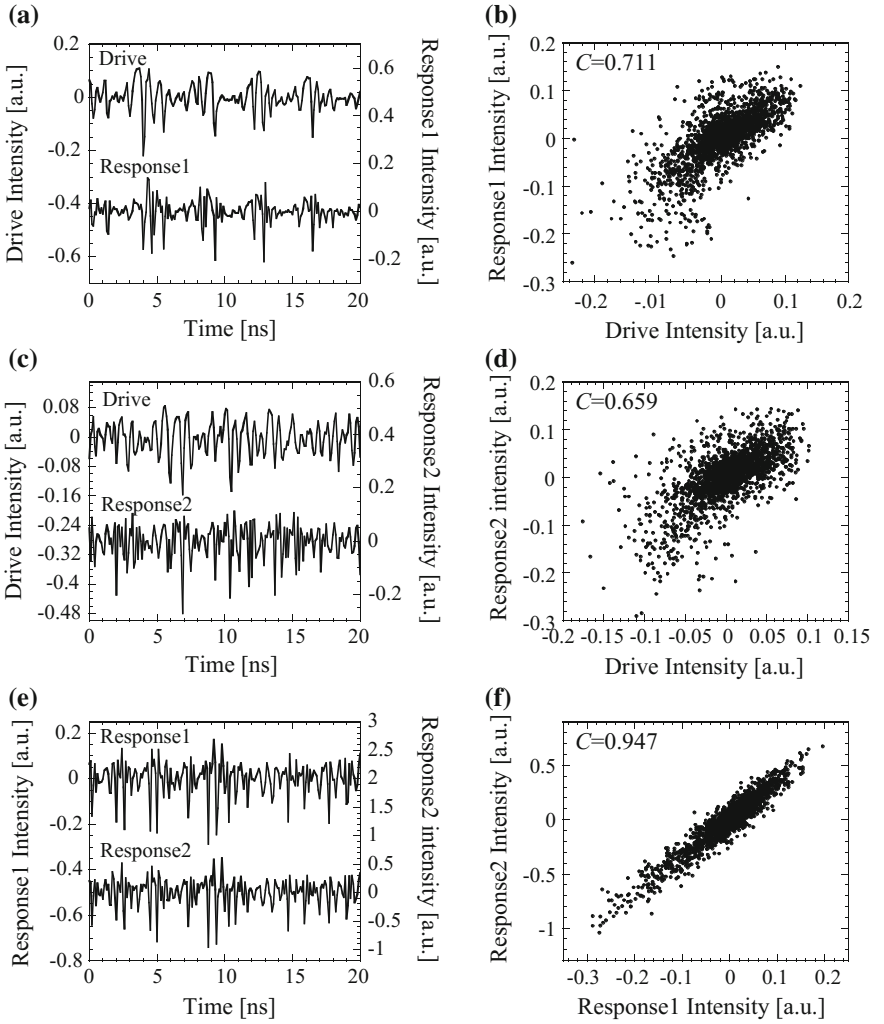

Fig. 12.27 Experimental result of temporal waveforms and corresponding correlation plots for **a**, **b** Drive and Response 1, **c**, **d** Drive and Response 2, and **e**, **f** Response 1 and Response 2. The coupling delay time (4.0 ns) between the two temporal waveforms is compensated in (**a**–**d**). The cross correlation values are **b** 0.711, **d** 0.659, and **f** 0.947 [after Yamamoto et al. (2007); © 2007 OSA]

chaos synchronization. The coupling delay time between the two temporal waveforms is compensated in the time traces in Fig. 12.27a, c. As is seen from these figures, the response lasers shows similar chaotic waveforms to the response laser, however, the correlation is not so high as around 0.7. On the other hand, the correlation between the response lasers has a high correlation as much as 0.947. In ordinary chaos synchronization systems with two unidirectionally coupled

semiconductor lasers, the good correlation values from 0.8 to 0.9 are usually obtained by experiments as far as the synchronization is originated from the effects of optical injection-locking and amplification. Taking the facts into consideration, we can much enhance the correlation of chaos synchronization by the introduction of the third chaotic laser. Although the effects are demonstrated by experiments and corresponding numerical simulations, the mechanism of the enhancement is not fully understood yet. We will return to the subject of synchronization and consistency in coupled semiconductor lasers, and the importance of common driving nonlinear elements for synchronization in Chap. 14.

References

H.D.I. Abarbanel, M.B. Kennel, L. Illing, S. Tang, H.F. Chen, J.M. Liu, Synchronization and communication using semiconductor lasers with optoelectronic feedback. IEEE J. Quantum Electron. **37**, 1301–1311 (2001)

V. Ahlers, U. Parlitz, W. Lauterborn, Hyperchaotic dynamics and synchronization of external-cavity semiconductor lasers. Phys. Rev. E **58**, 7208–7213 (1998)

V. Annovazzi-Lodi, S. Donati, A. Scirè, Synchronization of chaotic injected-laser systems and its application to optical cryptography. IEEE J. Quantum Electron. **32**, 953–959 (1996)

J.F.M. Avila, J.R.R. Leite, Time delays in the synchronization of chaotic coupled lasers with feedback. Opt. Express **24**, 21442–214451 (2009)

H.F. Chen, J.M. Liu, Open-loop chaotic synchronization of injection-locked semiconductor lasers with gigahertz range modulation. IEEE J. Quantum Electron. **36**, 27–34 (2000)

M.C. Chiang, H.F. Chen, J.M. Liu, Experimental synchronization of mutually coupled semiconductor lasers with optoelectronic feedback. IEEE J. Quantum Electron. **41**, 1333–1340 (2005)

M. Chiang, H.F. Chen, J.M. Liu, Synchronization of mutually coupled systems. Opt. Commun. **261**, 86–90 (2006)

K.M. Cuomo, A.V. Oppenheim, S.H. Stogatz, Synchronization of Lorenz-based chaotic circuits with applications to communications. IEEE Trans. Circuits Syst. II **40**, 626–633 (1993)

B. Eckhardt, E. Ott, S.H. Strogatz, D.M. Abrams, A. McRobie, Modeling walker synchronization on the Millennium Bridge. Phys. Rev. E **75**, 021110-1–021110-10 (2007)

I. Fischer, Y. Liu, P. Davis, Synchronization of chaotic semiconductor laser dynamics on sub-nanosecond time scales and its potential for chaos communication. Phys. Rev. A **62**, 011801-1–011801-4 (2000a)

A.P.A. Fischer, O.K. Andersen, M. Yousefi, S. Stolte, D. Lenstra, Experimental and theoretical study of filtered optical feedback in a semiconductor laser. IEEE J. Quantum Electron. **36**, 375–384 (2000b)

I. Fischer, R. Vicente, J.M. Buldú, M. Peil, C.R. Mirasso, M.C. Torrent, J. Garciá-Ojalvo, Zero-lag long-range synchronization via dynamical relaying. Phys. Rev. Lett. **97**, 123902-1–123902-4 (2006)

H. Fujino, J. Ohtsubo, Experimental synchronization of chaotic oscillations in external cavity semiconductor lasers. Opt. Lett. **25**, 625–627 (2000)

H. Fujino, J. Ohtsubo, Synchronization of chaotic oscillations in mutually coupled semiconductor lasers. Opt. Rev. **8**, 351–357 (2001)

H. Fujisaka, T. Yamada, Stability theory of synchronized motion in coupled-oscillator systems. Prog. Theor. Phys. **69**, 1240–1248 (1983)

N. Fujiwara, J. Ohtsubo, Synchronization in chaotic vertical-cavity surface-emitting semiconductor lasers. SPIE. Proc. **5349**, 282–289 (2004)

N. Fujiwara, Y. Takiguchi, J. Ohtsubo, Observation of the synchronization of chaos in mutually injected vertical-cavity surface-emitting semiconductor lasers. Opt. Lett. **28**, 1677–1679 (2003)
J. Garcia-Ojalvo, J. Casademont, C.R. Mirasso, M.C. Torrent, J.M. Sancho, Coherence and synchronization in diode-laser arrays with delayed global coupling. Int. J. Bifurcat. Chaos **9**, 2225–2229 (1999)
T. Heil, I. Fischer, W. Elsäßer, J. Mulet, C.R. Mirasso, Chaos synchronization and spontaneous symmetry breaking in symmetrical delay-coupled semiconductor lasers. Phys. Rev. Lett. **86**, 795–798 (2001)
K. Hicke, O. D'Huys, V. Flunkert, E. Schöll, J. Danckaert, I. Fischer (2011) Mismatch and synchronization: influence of asymmetries in systems of two delay-coupled lasers. Phys. Rev. E. **83**, 056211-1–056211-11
A. Hohl, A. Gavrielides, T. Erneux, V. Kovanis, Localized synchronization in two coupled non-identical semiconductor lasers. Phys. Rev. Lett. **78**, 4745–4748 (1997)
A. Hohl, A. Gavrielides, T. Erneux, V. Kovanis, Quasi-periodic synchronization for two delay-coupled semiconductor lasers. Phys. Rev. A **59**, 3941–3949 (1999)
Y. Hong, M.W. Lee, P.S. Spencer, K.A. Shore, Synchronization of chaos in unidirectionally coupled vertical-cavity surface-emitting semiconductor lasers. Opt. Lett. **29**, 1215–1217 (2004)
C. Huygens, *Christiaan Huygens' the Pendulum Clock, or, Geometrical Demonstrations Concerning the Motion of Pendula as Applied to Clocks* (Iowa State Press, USA 1986)
J. Ohtsubo, Chaotic dynamics in semiconductor lasers with optical feedback (Chap.1), in *Progress in Optics*, vol. 44, ed. by E. Wolf (North-Holland, Amsterdam, 2002a)
R.J. Jones, P. Rees, P.S. Spencer, K.A. Shore, Chaos and synchronization of self-pulsating laser diodes. J. Opt. Soc. Am. B **18**, 166–172 (2001)
E. Klein, N. Gross, M. Rosenbluh, W. Kinze, L. Khaykovich, I. Kanter, Stable isochronal synchronization of mutually coupled chaotic lasers. Phys. Rev. E **73**, 066214-1–066214-4 (2006)
K. Kusumoto, J. Ohtsubo, Anticipating chaos synchronization at high optical feedback rate in compound cavity semiconductor lasers. IEEE J. Quantum Electron. **39**, 1531–1536 (2003)
Y. Liu, P. Davis, Dual synchronization of chaos. Phys. Rev. E **61**, R2176–R2179 (2000)
J.M. Liu, H.F. Chen, S. Tang, Optical-communication systems based on chaos in semiconductor lasers. IEEE Trans. Circuits Syst. I **48**, 1475–1483 (2001a)
J.M. Liu, H.F. Chen, S. Tang, Synchronization of chaos in semiconductor lasers. Nonlinear Anal. **47**, 5741–5751 (2001b)
Y. Liu, H.F. Chen, J.M. Liu, P. Davis, T. Aida, Communication using synchronization of optical-feedback-induced chaos in semiconductor lasers. IEEE Trans. Circuits Syst. I **48**, 1484–1490 (2001c)
Y. Liu, Y. Takiguchi, P. Davis, T. Aida, S. Saito, J.M. Liu, Experimental observation of complete chaos synchronization in semiconductor lasers. Appl. Phys. Lett. **80**, 4306–4308 (2002)
C. Masoller, Anticipation in the synchronization of chaotic semiconductor lasers with optical feedback. Phys. Rev. Lett. **86**, 2782–2785 (2001)
C.R. Mirasso, M. Kolesik, M. Matus, J.K. White, J.V. Moloney, Synchronization and multimode dynamics of mutually coupled semiconductor lasers. Phys. Rev. A **65**, 013805-1–013805-4 (2002)
J. Mulet, C. Masoller, C.R. Mirasso, Modeling bidirectionally coupled single-mode semiconductor lasers. Phys. Rev. A **65**, 063815-1–063815-12 (2002)
J. Mulet, C.R. Mirasso, T. Heil, I. Fischer, Synchronization scenario of two distant mutually coupled semiconductor lasers. J. Opt. B: Quantum Semiclass. Opt. **6**, 97–105 (2004)
A. Murakami, J. Ohtsubo, Synchronization of feedback-induced chaos in semiconductor lasers by optical injection. Phys. Rev. A **65**, 033826-1–033826-7 (2002)
J. Ohtsubo, Chaos synchronization and chaotic signal masking in semiconductor lasers with optical feedback. IEEE J. Quantum Electron. **38**, 1141–1154 (2002)
I. Oowada, H. Ariizumi, M. Li, S. Yoshimori, A. Uchida, K. Yoshimura, P. Davis, Synchronization by injection of common chaotic signal in semiconductor lasers with optical feedback. Opt. Express **17**, 10025–10034 (2009)

L.M. Pecora, T.L. Carroll, Synchronization in chaotic systems. Phys. Rev. Lett. **64**, 821–824 (1990)
L.M. Pecora, T.L. Carroll, Driving systems with chaotic signals. Phys. Rev. A **44**, 2374–2384 (1991)
S. Peters-Flynn, P.S. Spencer, S. Sivaprakasam, I. Pierce, K.A. Shore, Identification of the optimum time-delay for chaos synchronization regimes of semiconductor lasers. IEEE J. Quantum Electron. **42**, 427–434 (2006)
E.M. Renato, S.H. Strogatz, Synchronization of pulse-coupled biological oscillators. SIAM J. Appl. Math. **50**, 1645–1662 (1990)
F. Rogister, A. Locquet, D. Pieroux, M. Sciamanna, O. Deparis, P. Megret, M. Blondel, Secure communication scheme using chaotic laser diodes subject to incoherent optical feedback and incoherent optical injection. Opt. Lett. **26**, 1466–1469 (2001)
R. Roy, K.S. Thornburg Jr., Experimental synchronization of chaotic lasers. Phys. Rev. Lett. **72**, 2009–2015 (1994)
M. Sauer, F. Kaiser, On-off intermittency and bubbling in the synchronization break-down of coupled lasers. Phys. Lett. A **243**, 38–46 (1998)
N. Shibasaki, A. Uchida, Y. Yoshimori, P. Davis, Characteristics of chaos synchronization in semiconductor lasers subject to polarization-rotated optical feedback. IEEE J. Quantum Electron. **42**, 342–350 (2006)
S. Sivaprakasam, E.M. Shahverdiev, K.A. Shore, Experimental verification of the synchronization condition for chaotic external cavity diode lasers. Phys. Rev. E **62**, 7505–7507 (2000)
S. Sivaprakasam, E.M. Shahverdiev, P.S. Spencer, K.A. Shore, Experimental demonstration of anticipating synchronization in chaotic semiconductor lasers with optical feedback. Phys. Rev. Lett. **87**, 154101-1–154101-3 (2001)
H. Someya, I. Oowada, H. Okumura, T. Kida, A. Uchida, Synchronization of bandwidth-enhanced chaos in semiconductor lasers with optical feedback and injection. Opt. Express **17**, 19536–19543 (2009)
P.S. Spencer, C.R. Mirassso, Analysis of optical chaos synchronization in frequency-detuned external-cavity VCSEL's. IEEE J. Quantum Electron. **35**, 803–809 (1999)
P.S. Spencer, C.R. Mirasso, P. Colet, K.A. Shore, Modeling of optical synchronization of chaotic external-cavity VCSEL's. IEEE J. Quantum Electron. **34**, 1673–1679 (1998)
S.H. Strogatz, I. Stewart, Coupled oscillators and biological synchronization. Sci. Am. **269**, 68–68 (1993)
S.H. Strogatz, D.M. Abrams, A. McRobie, B. Eckhardt, E. Ott, Crowd synchrony on the Millennium Bridge. Nature **438**, 43–44 (2005)
T. Sugawara, M. Tachikawa, T. Tsukamoto, T. Shimizu, Observation of synchronization in laser chaos. Phys. Rev. Lett. **72**, 3502–3506 (1994)
D.W. Sukow, K.L. Blackburn, A.R. Spain, K.J. Babcock, J.V. Bennett, A. Gavrielides, Experimental synchronization of chaos in diode lasers with polarization-rotated feedback and injection. Opt. Lett. **29**, 2393–2395 (2004)
D.W. Sukow, A. Gavrielides, T. Erneux, M.J. Baracco, Z.A. Parmenter, K.L. Blackburn, Two-field description of chaos synchronization in diode lasers with incoherent optical feedback and injection. Phys. Rev. A **72**, 043818-1–043818-6 (2005)
D.W. Sukow, A. Gavrielides, T. McLachlan, G. Burner, J. Amonette, J. Miller, Identity synchronization in diode lasers with unidirectional feedback and injection of rotated optical fields. Phys. Rev. **74**, 023812-1–023812-8 (2006)
D.W. Sukow, A. Gavrielides, T. Erneux, B. Mooneyham, K. Lee, J. McKay, J. Davis, Asymmetric square waves in mutually coupled semiconductor lasers with orthogonal optical injection. Phys. Rev. E **81**, 025206-1–025206-4 (2010)
Y. Takeuchi, R. Shogenji, J. Ohtsubo, Chaos synchronization of semiconductor lasers with polarization-rotated optical feedback and polarization-rotated optical injection. Opt. Rev. **17**, 467–475 (2010)
Y. Takiguchi, Y. Liu, J. Ohtsubo, Low-frequency fluctuations and frequency-locking in semiconductor lasers with optical feedback. Opt. Rev. **6**, 339–401 (1999a)

Y. Takiguchi, Y. Liu, J. Ohtsubo, Low frequency fluctuation in semiconductor lasers with long external cavity feedback and its control. Opt. Rev. **6**, 424–432 (1999b)
Y. Takiguchi, H. Fujino, J Ohtsubo, Experimental synchronization of chaotic oscillations in external cavity semiconductor lasers in low-frequency fluctuation regime. Opt. Lett. **24**, 1570–1572 (1999c)
Y. Takiguchi, K. Ohyagi, J. Ohtsubo, Bandwidth-enhanced chaos synchronization in strongly injection-locked semiconductor lasers with optical feedback. Opt. Lett. **28**, 319–321 (2003)
S. Tang, H.F. Chen, J.M. Liu, Stable route-tracking synchronization between two chaotically pulsing semiconductor lasers. Opt. Lett. **26**, 1489–1491 (2001)
S. Tang, R. Vicente, M.C. Chiang, C.R. Mirasso, J.M. Liu, Nonlinear dynamics of semiconductor lasers with mutual optoelectronic coupling. IEEE J. Sel. Top. Quantum Electron. **10**, 936–943 (2004)
A. Uchida, F. Rogister, J. García-Ojalvo, R. Roy, Synchronization and communication with chaotic laser systems (Chap.5), in *Progress in Optics,* vol. 48, ed. by E. Wolf (North-Holland, Amsterdam, 2005)
A. Uchida, *Optical Communication with Chaotic Lasers* (Wiley-VCH, Weinheim, 2012)
R. Vicente, I. Fischer, C.R. Mirasso, Synchronization properties of three delay-coupled semiconductor lasers. Phys. Rev. E **78**, 066202-1–066202-11 (2008)
H.U. Voss, Anticipating chaotic synchronization. Phys. Rev. E **61**, 5115–5119 (2000)
H.G. Winful, L. Rahman, Synchronized chaos and spatiotemporal chaos in arrays of coupled lasers. Phys. Rev. Lett. **65**, 1575–1578 (1990)
T. Yamamoto, I. Oowada, H. Yip, A. Uchida, S. Yoshimori, K. Yoshimura, J. Muramatsu, S. Goto, P. Davis, Common-chaotic-signal induced synchronization in semiconductor lasers. Opt. Express **15**, 3974–3980 (2007)
W.L. Zhang, W. Pan, B. Luo, X.H. Zou, M.Y. Wang, One-to-many and many-to-one optical chaos communications using semiconductor lasers. IEEE Photonics Technol. Lett. **20**, 712–714 (2008)

Chapter 13
Chaotic Communications in Semiconductor Lasers

Abstract Chaotic data encoding or scrambling is a technology for overcoming the difficulties of the digital methods in secure communications. Using chaotic lasers as light sources, high-speed and broadband secure communications can be established. In this chapter, we discuss cryptographic applications of chaos in semiconductor lasers. The technique we treat in this chapter is an analog chaotic encryption and decryption. Messages to be sent are encoded into chaotic time series generated from a chaotic semiconductor laser and decoded by a chaotic laser with the same characteristics. The key for chaotic communications is chaos synchronization, which we discussed in the previous chapter. In chaotic communications, a small message is embedded into a chaotic laser carrier and the total signal is sent to the receiver. Only the chaotic oscillation is reproduced based on chaos synchronization and a chaos-pass filtering effect in the receiver laser. By subtracting the receiver output from the transmission signal, the message is successfully decoded.

13.1 Message Encryption in a Chaotic Carrier and Its Decryption

13.1.1 Chaotic Communications

The development of efficient technologies for high-speed and massive data transmissions is an urgent subject in the rapidly growing information-oriented society. One of the important issues of information and communication networks is the security problem. In secure data transmissions, a message to be sent is usually encoded by computer software and the security of encoding is guaranteed by the complexity of the calculations necessary to decode the original message. However, the development of digital computer technology is so fast that the standard code for scrambling data in secure communication systems can be soon decoded by a fast computer. On the other hand, the enhancement of the complexity of calculations for encoding and decoding messages may lose real-time processing of data transmissions. In the meantime, the method of quantum computing has been developed as

© Springer International Publishing AG 2017

J. Ohtsubo, *Semiconductor Lasers*, Springer Series in Optical Sciences 111,
DOI 10.1007/978-3-319-56138-7_13

one of the candidates to decipher quickly encoded data in standard secure communication systems. As an alternative method, chaotic communications have been proposed for high-speed and broadband capabilities with hardware based secure communications (Kennedy et al. 2000; Dachselt and Schwarz 2001).

There are two techniques for chaos-based secure communications; one is digital encoding and the other is analog encryption. As examples of digital techniques, the method of code scrambling based on chaotic signal generations such as discrete-sequence (DS) optical code division multiple access (CDMA) is used for chaos communications. The method of chaos CDMA uses long life chaotic non-correlated data sequences embedded into the chaotic orbits as CDMA codes. It is verified that the generated codes have an advantage over the existing Gold series for the irregularity and non-correlation properties (Chen et al. 2001). Chaos induced by semiconductor lasers is also effective to generate a series of ultrafast physical random numbers suitable for broadband optical communications (Uchida et al. 2008). The related topic will be treated in Chap. 15. Another example is the technique of secure chaos key generation instead of random numbers in ordinary secure communication systems (Uchida et al. 2003a). In this chapter, we are concerned with the analog method, since chaos in laser systems is best suited for analog data encryption and decryption by nature. In the analog technique, when a fraction of a chaotic signal from a transmitter is sent to a receiver, the two systems synchronize with each other under certain conditions, as discussed in the previous chapter. Not only the two system configurations but also the chaos parameters of the two systems must be the same for perfect chaos synchronization. The merits of the use of semiconductor lasers in chaotic communications are clear, since light is the carrier of modern basic communication channels and the generation of high-speed and broadband signals is easily attained compared with, e.g., nonlinear electronic circuits. Chaotic communications require special hardware to generate a chaotic signal and to realize synchronization. Even if one tries to decode messages by computing or guessing chaotic states from the signals obtained, it is very difficult to decode messages by available techniques without knowledge of the chaos keys because they are embedded into high-dimensional chaotic spaces (Ohtsubo 2002b).

First, we show the basic idea of analog chaos communications. Figure 13.1 shows the model for analog chaos communication systems. The basic of the technique is chaos synchronization between two nonlinear systems, transmitter and receiver, as already noted. A message with small amplitude (compared with the chaotic variations of the transmitter output) is embedded into a chaotic carrier in the transmitter. The chaotic carrier with the message is sent to the receiver through the communication channel. In the receiver, the system only synchronizes to the chaotic signal from the transmitter. Then, the message is decoded by subtracting the receiver output from the transmitted signal. If the amplitude of the message is small enough, we can achieve successful chaos synchronization even if the transmission signal includes the perturbation (message) to the chaotic signal. However, small signal approximation is not always necessary. For example, a message may be comparable with chaotic variations in the chaos modulation (CMO) technique as discussed later.

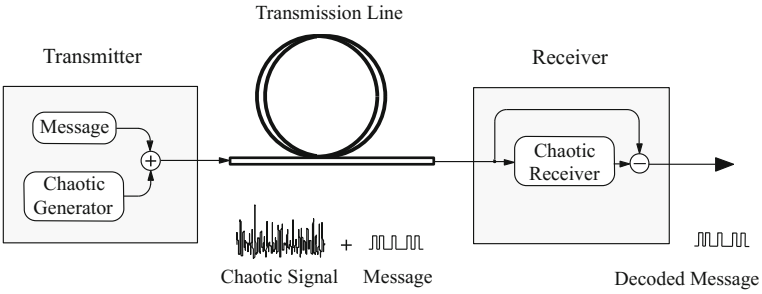

Fig. 13.1 General concept of chaos synchronization with analog data encryption

Chaotic data communications using laser systems are categorized into three classes depending on the techniques of message encoding and decoding (Ohtsubo 2002a, b; Liu et al. 2002b; Ohtsubo and Davis 2005; Uchida 2012). They are chaos masking (CMA), CMO, and chaos shift keying (CSK). Each method can be mathematically formulated by laser rate equations in transmitter and receiver lasers and the dynamic behaviors of the systems can be described by these rate equations. Even for optical communications, we can also generate chaotic oscillations from nonlinear electronic circuits and transmit a chaotic signal converted by optoelectronic devices through optical channels. However, the carrier of communications is light and laser chaos is best suited for such purposes. Therefore, many systems using chaos of various laser systems have been proposed for chaos synchronization and communications. In spite of existing work, we still need extensive studies about many subjects to put the systems into practical use, for example, the degree of security, the accuracy of synchronization for parameter mismatches between transmitter and receiver systems, robustness of communications, and other things.

13.1.2 Chaos Masking

Following the proposal of chaos synchronization in nonlinear systems (Pecora and Carroll 1991; Carroll and Pecora 1991), the possibility of secure communications was pointed out based on chaos synchronization. They used electronic circuits to realize Lorenz chaos (see Appendix A.4). In their method, a chaotic signal (one of three variables, x) in a transmitter system is sent to a receiver system as a synchronous signal. At the same time, a chaotic variable z in the transmitter with a small message m is sent to the receiver and chaos synchronization between the transmitter and receiver systems could be achieved. The receiver system consists of a subsystem of the variables y and z. After subtracting the synchronized signal z' in the receiver from the transmitted signal $z + m$, the message is successfully decoded. The technique is essentially categorized into the method of CMA. However, two different channels were required for the data transmission in their method. Cuomo

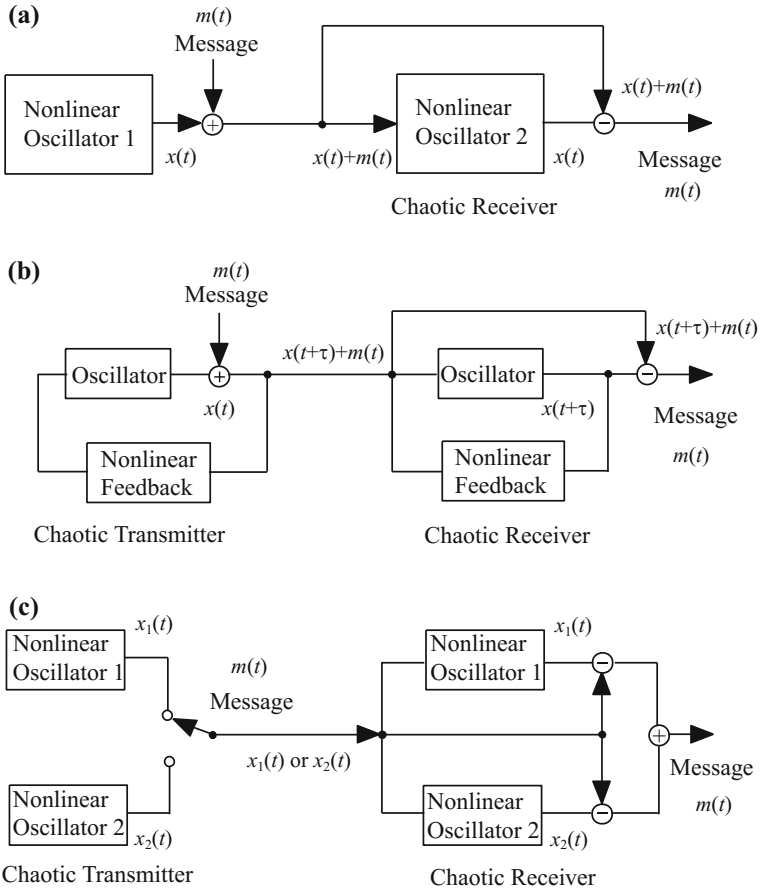

Fig. 13.2 General schemes of optical communications in analog chaotic systems. Models of **a** chaos masking (CMA), **b** chaos modulation (CMO), and **c** chaos shift keying (CSK)

et al. (1993) proposed a method of chaotic communication using a single transmission channel for the same Lorenz system as that of Pecora and Carroll.

In a laser system, we cannot divide the system into subsystems as shown in Appendix A.4. Therefore, a fraction of a chaotic laser output power from a transmitter is sent to a receiver laser through a single communication channel. Figure 13.2 shows the general three schemes of optical communications in analog chaotic systems. Figure 13.2a shows the system of CMA, where a small message $m(t)$ is embedded into a chaotic carrier $x(t)$ in a transmitter and, then, the signal of $x(t) + m(t)$ is sent to a receiver. The receiver system is the same as that of the transmitter and the two systems are operating at the same parameter values. Only the chaotic signal of $x(t)$ is reproduced in the receiver system if the amplitude of the message is small enough. Then, the message $m(t)$ is decoded by subtracting the

receiver output $x(t)$ from the transmission signal $x(t) + m(t)$. To hide a message into chaotic carriers securely (namely, mask the message) and to reproduce good quality of a decoded message, the amplitude of the message must be sufficiently small compared with the averaged chaotic carrier signal. Usually, the fraction is less than 1% of the average chaotic power.

13.1.3 Chaos Modulation

In the method of CMO shown in Fig. 13.2b, both a chaotic carrier and a message conform a new chaotic oscillation in the nonlinear system (Liu et al. 2001a, 2002b; Ohtsubo and Davis 2005). Therefore, a message embedded into the chaotic carrier may not be small. The transmitter and receiver systems can be described by the equivalent mathematical differential equations. Therefore, complete chaos synchronization is achieved in the system and an excellent synchronous signal can be obtained in the receiver output. The method resembles CMA, however, CMO is essentially a different technique from CMA. As shown in Fig. 13.2b, a message is mixed with a chaotic carrier in the nonlinear oscillator and the two signals conform a new chaotic state different from the original one. In CMO, a delayed feedback system is usually used as a chaotic generator. The new chaotic signal is given by $x(t + \tau) = f\{x(t) + m(t)\}$ after the delay time τ, where f is the nonlinear function of the system. This new signal together with the message $x(t + \tau) + m(t + \tau)$ is sent to the receiver. Since the transmitter and the receiver are the same nonlinear systems, the chaotic oscillation $x(t + \tau) = f\{x(t) + m(t)\}$ is exactly reproduced in the receiver system as chaos synchronization. By subtracting the synchronized chaotic signal $x(t + \tau)$ from the transmitted signal $x(t + \tau) + m(t + \tau)$, we can decode the message. Sometimes, the message is decoded by dividing the transmitted signal by the synchronized chaotic signal in the receiver. From the point-of-view of encoding and decoding message, the method of CMO has no restriction on the magnitude of the message as a secure communication, since both the chaotic carrier and the message conform new chaotic states in the nonlinear systems. However, in the optics case, the message is usually decoded as an intensity $S(t) = |E(t)|^2$. Therefore, the amplitude of the message must be small enough when we use the ordinary message decoding technique. Furthermore, the degree of security for data transmissions becomes worse when the signal level of a message is large. Therefore, the amplitude of a message in CMO should also be small.

13.1.4 Chaos Shift Keying

The signal shift keying technique, which is frequently used in ordinary communication systems, is also applicable to chaotic data transmissions. Figure 13.2c is an example of such system diagrams. In CSK, two chaotic states $x_1(t)$ and $x_2(t)$ are

generated in a transmitter system. The switching itself to send either chaotic state is a message $m(t)$. In the receiver system, each state $x_1(t)$ or $x_2(t)$ is detected by the technique of chaos synchronization. Therefore, two sets of chaotic generators are usually prepared both for the transmitter and the receiver. However, the difference between two chaotic states in the CSK system must be very small, since the message can be easily estimated from the attractors when the difference of chaotic oscillations between the two states is too large. In chaos synchronization in nonlinear systems, the time required for the synchronization between receiver and transmitter is finite for the switching of chaotic states. Therefore, we must take into account the transient and finite response of signals for practical use of the systems.

13.1.5 Chaotic Data Communications in Laser Systems

Shortly after the proposal of chaos synchronization by Pecora and Carroll, Colet and Roy (1994) demonstrated chaos synchronization in laser systems using loss modulated solid-state lasers by numerical simulations and predicted the possibility of chaotic communications based on such nonlinear systems. They experimentally showed chaotic data transmission of a binary bit-sequence with a rate of 100 kbps in the system. VanWiggeren and Roy (1998a, b) demonstrated data transmission for secure communications based on CMO using laser systems. They proposed a ring fiber laser system with an optical feedback loop (delay loop) as a chaotic generator. A message to be transmitted was put into the feedback loop as a modulation, then, a new chaotic oscillation was produced in the feedback system. They successfully demonstrated data transmission higher than a bit rate of 100 Mbps. Goedgebuer et al. (1998) and Larger et al. (1998) also reported chaotic data transmission based on optoelectronic feedback using wavelength-to-current conversion systems in semiconductor lasers. Their method was also categorized into CMO. Other CMO systems were also proposed by using laser systems (Luo et al. 2000; Abarbanel et al. 2001; Liu et al. 2001c; Tang et al. 2001). Tang and Liu (2001) experimentally demonstrated data transmission of a pseudo-random binary bit-sequence with a 2.5 Gbps non-return-to-zero (NRZ) signal corresponding to the OC-48 standard bit rate in optoelectronic feedback semiconductor laser systems.

After the demonstration of chaotic communications based on CMO, the method of CMA was widely studied theoretically and experimentally because of the ease of implementation in semiconductor laser systems (Mirasso et al. 1996; Sánchez-Díaz et al. 1999; Sivaprakasam and Shore 1999, 2000a, b; White and Moloney 1999; Jones et al. 2000; Rogister et al. 2001). Annovazzi-Lodi et al. (1996, 1997) proposed a method of CSK using semiconductor lasers with optical feedback. Also studies on chaotic communications based on CSK in various laser systems have been reported (Liu and Davis 2001; Davis et al. 2001; Mirasso et al. 2002). Almost all these systems used chaotic oscillations in class B lasers, such as solid-state lasers, fiber lasers, and semiconductor lasers. In chaotic laser communications, the

effects of optical feedback, optical injection from a different laser, and optoelectronic feedback have been frequently used to generate chaotic signals.

Liu et al. (2002b) investigated three configurations of systems using semiconductor lasers (optical injection-locking, optical feedback, and optoelectronic feedback systems) and compared the performances of data transmissions for three different techniques (CMA, CMO, and CSK). As a result, the optoelectronic feedback system with CMO showed excellent performance for data transmissions. As discussed later, chaotic carrier frequency, which is closely related to the relaxation oscillation of the solitary laser, is an important measure of the capability of data transmissions and semiconductor lasers with high frequency response are indispensable as high-speed chaotic generators for that purpose. Distributed feedback (DFB) lasers of near infrared wavelength oscillations are frequently used for chaotic laser communications, since they are suitable for chaotic light sources of ordinary optical communication systems with high frequency response. Vertical-cavity surface-emitting lasers (VCSELs) are also promising devices for future semiconductor lasers and also chaotic lasers. Other lasers such as MQW lasers with visible oscillations may be used for chaotic light sources for short-range communications. However, we assume edge-emitting lasers as chaotic generators in the following. Even if device structures are different from each other, the system that is described by the same laser rate equations shows the same dynamics of chaotic oscillations as discussed earlier.

As stated in Chap. 12, there are two types of mechanisms of chaos synchronization; one is complete chaos synchronization and the other is synchronization of chaotic oscillation by optical injection locking and amplification. In a delay differential system, there is a solution for complete chaos synchronization where transmitter and receiver lasers can be described by mathematically identical forms of the equations. On the other hand, we can expect synchronization of chaotic oscillations based on the injection-locking phenomenon in nonlinear amplifying systems in the chaotic transmitter and receiver lasers. We can use both systems for secure communications based on chaos synchronization, although the degree of security is different in the two schemes.

13.2 Cryptographic Applications in Optical Feedback Systems

13.2.1 Chaotic Communications in Optical Feedback Systems

In this section, we focus on chaotic secure communications using systems of semiconductor lasers with optical feedback. Sánchez-Díaz et al. (1999) numerically studied chaotic communications based on CMA in the systems and demonstrated data transmissions of a bit rate of 4 Gbps. In their method, a direct modulation to

the injection current in a transmitter semiconductor laser was used as the message encoding, therefore the technique was in principle CMO rather than CMA. However, it is assumed to be CMA as long as the modulation amplitude of a message is very small. Annovazzi-Lodi et al. (1996) proposed a CSK system in semiconductor lasers with optical feedback using systems consisting of a single chaotic transmitter and two chaotic receivers. Mirasso et al. (2002) also proposed a CSK system using a single chaotic generator of a semiconductor laser with optical feedback both for a transmitter and a receiver. They numerically demonstrated data transmissions of a bit rate of 2 Gbps. The technique is called ON/OFF CSK. A lot of theoretical and numerical studies on chaotic data transmissions and communications have been reported in semiconductor lasers with optical feedback. However, only a few studies have been published for experimental data transmission of binary messages in optical feedback systems with bit rate over gigabit-per-second (Argyris et al. 2005). Also few theoretical and experimental studies have been reported for CMO in systems of semiconductor lasers with optical feedback (Liu et al. 2001c). A system of a semiconductor laser with optical feedback has a merit for its simplicity, especially in CMA and CSK. However, we need extra devices for the message modulation in CMO, such as electro-optic (EO) modulators.

Using a chaotic generator of a semiconductor laser with optical feedback, we formulate the rate equations for transmitter and receiver lasers. Figure 13.3 shows the schematic diagram of chaotic communications in semiconductor lasers with optical feedback. Embedding a message into the transmitter system, the transmitter can be modeled by the following coupled equations for the complex field E and the carrier density n, according to the configurations of unidirectionally coupled semiconductor lasers with optical feedback (Ohtsubo 2002a; Liu et al. 2002b):

$$\begin{aligned}\frac{\mathrm{d}E_{\mathrm{T}}(t)}{\mathrm{d}t} &= \frac{1}{2}(1-i\alpha_{\mathrm{T}})G_{n,\mathrm{T}}\{n_{\mathrm{T}}(t)-n_{\mathrm{th,T}}\}E_{\mathrm{T}}(t) \\ &\quad + \frac{\kappa_{\mathrm{T}}}{\tau_{\mathrm{in,T}}}E_{\mathrm{T}}(t-\tau_{\mathrm{T}})\exp(i\omega_{0,\mathrm{T}}\tau_{\mathrm{T}}) + \eta_{\mathrm{CMO}}m_{\mathrm{CMO}}(t)\end{aligned} \tag{13.1}$$

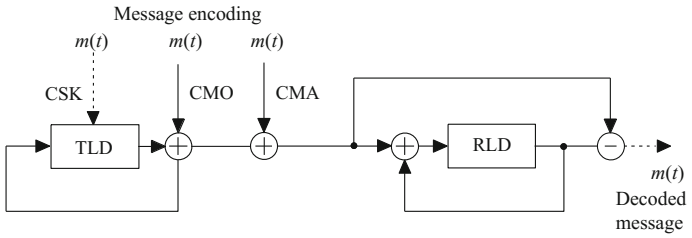

Fig. 13.3 Schematic diagram of chaotic communications in semiconductor lasers with optical feedback. $m(t)$ is a message signal to be embedded. The position for each message encoding scheme is shown in the figure. *Solid lines* are optical connections and *broken lines* are electronic connections

$$\begin{aligned}\frac{\mathrm{d}n_{\mathrm{T}}(t)}{\mathrm{d}t} &= \frac{J_{\mathrm{T}}}{ed}\{1+\eta_{\mathrm{CSK}}m_{\mathrm{CSK}}(t)\} \\ &\quad -\frac{n_{\mathrm{T}}(t)}{\tau_{s,\mathrm{T}}} - G_{n,\mathrm{T}}\{n_{\mathrm{T}}(t)-n_{0,\mathrm{T}}\}|E_{\mathrm{T}}(t)|^2\end{aligned} \tag{13.2}$$

whereas the receiver driven by the transmitted signal can be described by

$$\begin{aligned}\frac{\mathrm{d}E_{\mathrm{R}}(t)}{\mathrm{d}t} &= \frac{1}{2}G_{n,\mathrm{R}}(1-i\alpha_{\mathrm{R}})\{n_{\mathrm{R}}(t)-n_{\mathrm{th,R}}\}E_{\mathrm{R}}(t) \\ &\quad + \frac{\kappa_{\mathrm{R}}}{\tau_{\mathrm{in,R}}}E_{\mathrm{R}}(t-\tau_{\mathrm{R}})\exp(i\omega_{0,\mathrm{R}}\tau_{\mathrm{R}}) \\ &\quad + \frac{\kappa_{\mathrm{cp}}}{\tau_{\mathrm{in,R}}}E_{\mathrm{T}}(t-\tau_c)\exp(i\omega_{0,\mathrm{T}}\tau_c - i\Delta\omega t) \\ &\quad + \eta_{\mathrm{CMA}}m_{\mathrm{CMA}}(t-\tau_c)+\eta_{\mathrm{CMO}}m_{\mathrm{CMO}}(t-\tau_c)\end{aligned} \tag{13.3}$$

$$\frac{\mathrm{d}n_{\mathrm{R}}(t)}{\mathrm{d}t} = \frac{J_{\mathrm{R}}}{ed} - \frac{n_{\mathrm{R}}(t)}{\tau_{s,\mathrm{R}}} - G_{n,\mathrm{R}}\{n_{\mathrm{R}}(t)-n_{0,\mathrm{R}}\}|E_{\mathrm{R}}(t)|^2 \tag{13.4}$$

where $\Delta\omega = \omega_{0,\mathrm{T}} - \omega_{0,\mathrm{R}}$, κ_{cp} is the coupling coefficient of light from the transmitter to the receiver, $m_{\mathrm{CMA}}(t)$, $m_{\mathrm{CMO}}(t)$, and $m_{\mathrm{CSK}}(t)$ are the message sequences corresponding to CMA, CMO, and CSK systems, respectively, and η_{CMA}, η_{CMO}, and η_{CSK} are the actual modulation coefficients for each system. For example, when we consider a chaotic communication system with CMA, we put $\eta_{\mathrm{CMA}} \neq 0$, and $\eta_{\mathrm{CMO}} = \eta_{\mathrm{CSK}} = 0$. The modulation depth of the message in chaotic secure communications is generally very small so as not to disturb the chaotic attractors. In actual systems, the perturbation due to the message encoding is not for amplitude but for optical intensity, except for the case of injection current modulation. However, we can approximately assume amplitude perturbation as far as it is very small compared with the average chaotic amplitudes. Otherwise, we could formulate rate equations for intensity perturbations for the numerical simulations.

As can be easily recognized from (13.1)–(13.4), there is a condition where the rate equations in the transmitter are mathematically identical to those in the receiver in a CMO system. Thus, complete chaos synchronization is performed in this system. On the other hand, for the other cases (CMA and CSK systems), a message always behaves as a small perturbation to each chaotic system. Therefore, the modulation coefficients η_{CMA} and η_{CSK} must be small enough to achieve good chaos synchronization. They should be usually less than 1% of the average of the chaotic fluctuations.

13.2.2 Chaos Masking in Optical Feedback Systems

In the following, we describe the particular technique for each modulation scheme in optical feedback systems. In CMA, a small message to be sent is added to a chaotic carrier from the transmitter laser. The system under consideration is the same as in Fig. 13.2a. In CMA, we set $\eta_{\mathrm{CMA}} \neq 0$ and $\eta_{\mathrm{CMO}} = \eta_{\mathrm{CSK}} = 0$ in (13.1)–(13.4). Since there is a message term on the right hand side of the receiver (13.3), complete chaos synchronization is not realized in this system in a strict sense. However, we can approximately observe complete chaos synchronization as long as the modulation depth of the message is small enough. The accuracy of chaos synchronization depends on the parameter mismatches for the chaos keys. For example, chaos synchronization with high accuracy is achieved when the total light input to the receiver laser both from the external reflector and the transmitter laser is almost equal to the amount of external feedback in the transmitter.

In spite of the presence of the perturbation for a message in a transmitted signal, only the chaotic carrier is reproduced in the receiver output in CMA. This phenomenon is known as chaos-pass-filtering. This fact is verified by numerical and experimental studies (Ohtsubo 2002b). The phenomenon of chaos-pass-filtering in nonlinear systems is not obvious and needs some explanation. The origin of chaos-pass-filtering will be discussed in the following subsection. A small message is also considered as a perturbation for a chaotic system like noises in the system. It seems that noises are discriminated from intrinsic chaotic dynamics induced in the nonlinear system. As far as perturbation in a system is small, original chaotic dynamics is preserved in the transmitted signal. As is easily understood, the message in CMA is decoded by subtracting the receiver output from the transmitted signal of the chaotic carrier together with the message. The accuracy of the decoding becomes worse when the modulation depth of the message increases, though it depends on the synchronization schemes (complete or optical injection-locking regime). Further, the security of data transmissions is degraded with the increase of the modulation depth, since the message may be directly visible in the transmitted signal.

In CMA, a message is added to a chaotic carrier generated from a transmitter. For example, a chaotic carrier is modulated through an EO modulator, which is an intensity modulation to the chaotic carrier. However, an alternative method is frequently used for encoding a message. A message is simply added to the bias injection current and it is an easier way to modulate intensities in semiconductor lasers. Strictly speaking, it is a technique of CMO rather than CMA. However, it reduces to the method of CMA when the level of a message is small enough. Indeed, a lot of theoretical and experimental work has been published based on the same techniques of injection current modulation as message encoding in the system.

Before showing the results for data transmissions and decoding of messages in CMA, the unique phenomenon of chaos-pass-filtering is discussed. Figure 13.4 shows an experimental example for chaos synchronization when a message is

embedded into the transmitter signal (Kusumoto and Ohtsubo 2002). The message is added to a chaotic carrier as an injection current modulation in the transmitter laser and it is a sinusoidal wave with a frequency of 1.5 GHz. The relaxation oscillation frequency of the solitary laser is about 4 GHz. The two chaotic waveforms look the same as shown in Fig. 13.4a and they are synchronized with each other in spite of the presence of the message. The synchronization is also confirmed by the correlation plot. Even in the presence of the message in the transmitter laser, the correlation coefficient between the two laser outputs is 0.86, which is high enough for message decoding in chaotic communications based on chaos synchronization. Figure 13.4b shows the rf spectra corresponding to the waveforms in Fig. 13.4a. Besides the broad spectral peaks of the external cavity mode and its higher harmonics, a sharp spectral peak for the message of 1.5 GHz is clearly visible in the transmitter spectrum. On the other hand, the spectrum bears resemblance to that of the transmitter but no distinct spectral component for the message is present in the receiver spectrum due to a chaos-pass-filtering effect. As a result, we can extract the message simply by subtracting the reproduced chaotic signal in the receiver laser from the transmitted signal, thus, chaotic communication is realized. The receiver laser generates only the intrinsic chaotic oscillations the same as that from the transmitter if the message embedded into the chaotic carrier is small enough. The effect of the insensitivity for small external perturbations to chaos can be considered as a different phenomenon such as the sensitivity of chaos for initial conditions. Chaos seems to distinguish external perturbations and the system nonlinearity.

Looking at the spectrum of the transmitted signal in Fig. 13.4, the question may arise that the message may be extracted by filtering the waveform with a narrow band-pass filter at the message frequency. Figure 13.5 shows the filtered waveforms for the decoded message as well as the transmitted signal and the receiver output. The waveforms are the results for a narrow band-pass filter of ± 100 MHz centered at the message frequency of 1.5 GHz. The decoded message is a simple subtraction of the receiver output from that to the transmitter. The decoded message is reproduced as a good sinusoidal oscillation, which is almost the same signal as the original message. However, the filtered waveforms for the transmitted signal and the receiver output are not good harmonic signals and they are even not in-phase with the message signal. The degree of the security of communications must be evaluated for actual data of binary bit-sequences. However, the results obtained in Fig. 13.5 show some of evidence for the security in the present systems.

As an example of a signal transmission of binary data in CMA, numerical results by Sánchez-Díaz et al. (1999) are shown. They conducted data transmissions of pseudo-random bit-sequences of a 4 Gbps NRZ signal in a closed-loop system. The message is a small perturbation of 0.5% of an averaged chaotic oscillation in the transmitter and it is fed to the injection current to the laser as a direct modulation. Since the perturbation is sufficiently small, the method is considered as CMA. They also assumed the nonlinear effect of signal transmissions through optical fibers between the transmitter and receiver systems. Figure 13.6 shows their results. In

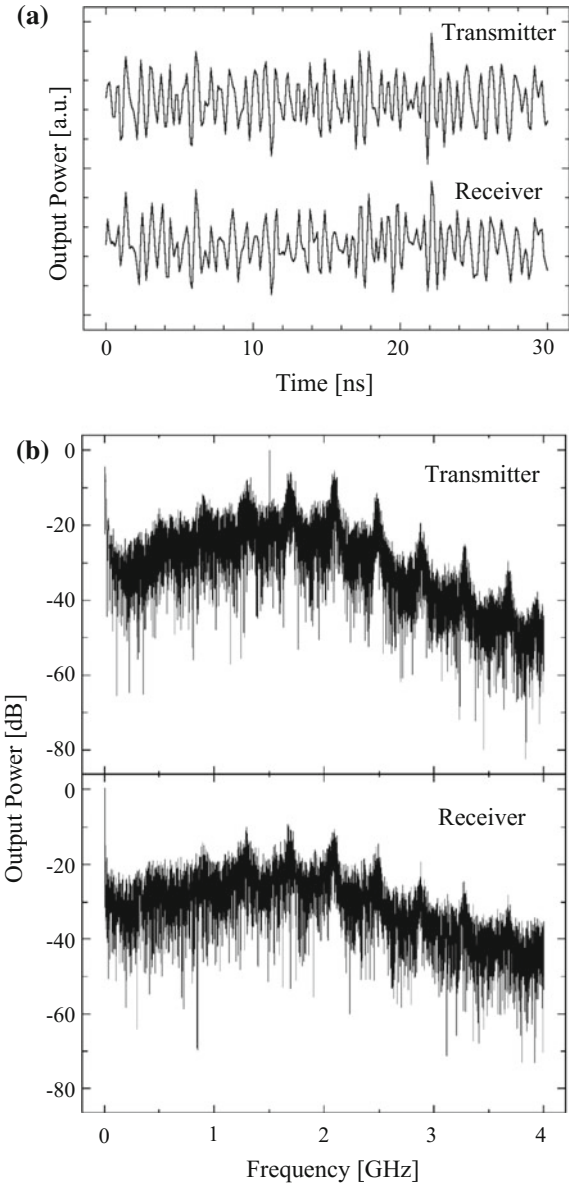

Fig. 13.4 Chaos-pass-filtering effect. **a** Waveforms of the transmitted signal and the receiver output in a closed-loop system of semiconductor lasers with optical feedback. A message of a sinusoidal wave of a frequency of 1.5 GHz with a modulation depth of −14 dB is included in the transmitter signal. **b** Corresponding rf spectra to (**a**). The synchronization is based on an optical injection-locking scheme

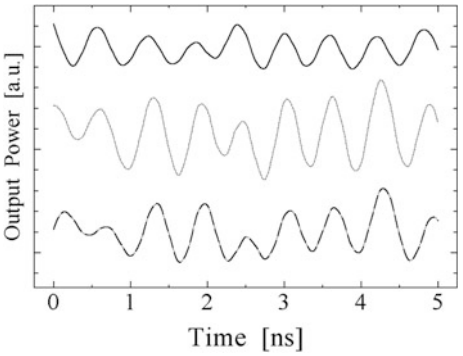

Fig. 13.5 Message decoding for signals in Fig. 13.4a with a narrow band-pass filter of ±100 MHz centered at a message frequency of 1.5 GHz. Decoded message (*upper trace*) and transmitter (*middle trace*) and receiver (*bottom trace*) outputs

their method, the decoded signal is obtained by the comparison of the transmitted signal $E_{\text{trans}}(t)$ ($\propto E_{\text{T}}(t)$) with the decoded one $E_{\text{R}}(t)$ as

$$m'(t) = \sqrt{\frac{|E_{\text{trans}}(t)|^2}{|E_{\text{R}}|^2}} - 1 \tag{13.5}$$

The fidelity of the chaotic signal after the transmission through the optical fiber may be degraded due to a nonlinear dispersion effect in the fiber. The data transmission in optical fiber is described by the following nonlinear Schrödinger equation (Sánchez-Díaz et al. 1999):

$$\begin{aligned} i\frac{\partial E(z,T)}{\partial z} = &-\frac{i}{2}\alpha_f E(z,T) + \frac{1}{2}\beta_2 \frac{\partial^2 E(z,T)}{\partial T^2} \\ &- \gamma_{\text{non}}|E(z,T)|^2 E(z,T) \end{aligned} \tag{13.6}$$

where $E(z, T)$ is the slowly varying complex field, z is the propagation distance, and T is the time measured in the reference frame moving at the group velocity. γ_{non} is the nonlinear parameter that takes into account the optical Kerr effect, α_f is the fiber loss, and β_2 is the second-order dispersion parameter of optical fiber. They also used a low-pass Fabry–Perot filter with a bandwidth of 5 GHz to obtain the final decoded message of Fig. 13.6f, though a higher order Butterworth electronic filter is usually used. Excellent chaos synchronization was attained in spite of the effect of nonlinear optical fiber transmission through 50 km and the message was successfully reconstructed.

The quality of the reproduced chaotic signal and, accordingly, the decoded message in the receiver are degraded by the transmission through the nonlinear optical fiber. The system performance at the modulation of 2 Gbps is displayed in Fig. 13.7 for different propagation length in optical fiber (Sánchez-Díaz et al. 1999). Whether the message is included in the chaotic carrier or not, the synchronization becomes worse for a long fiber transmission and the quality of the decoding becomes worse accordingly. The degradation comes from both the

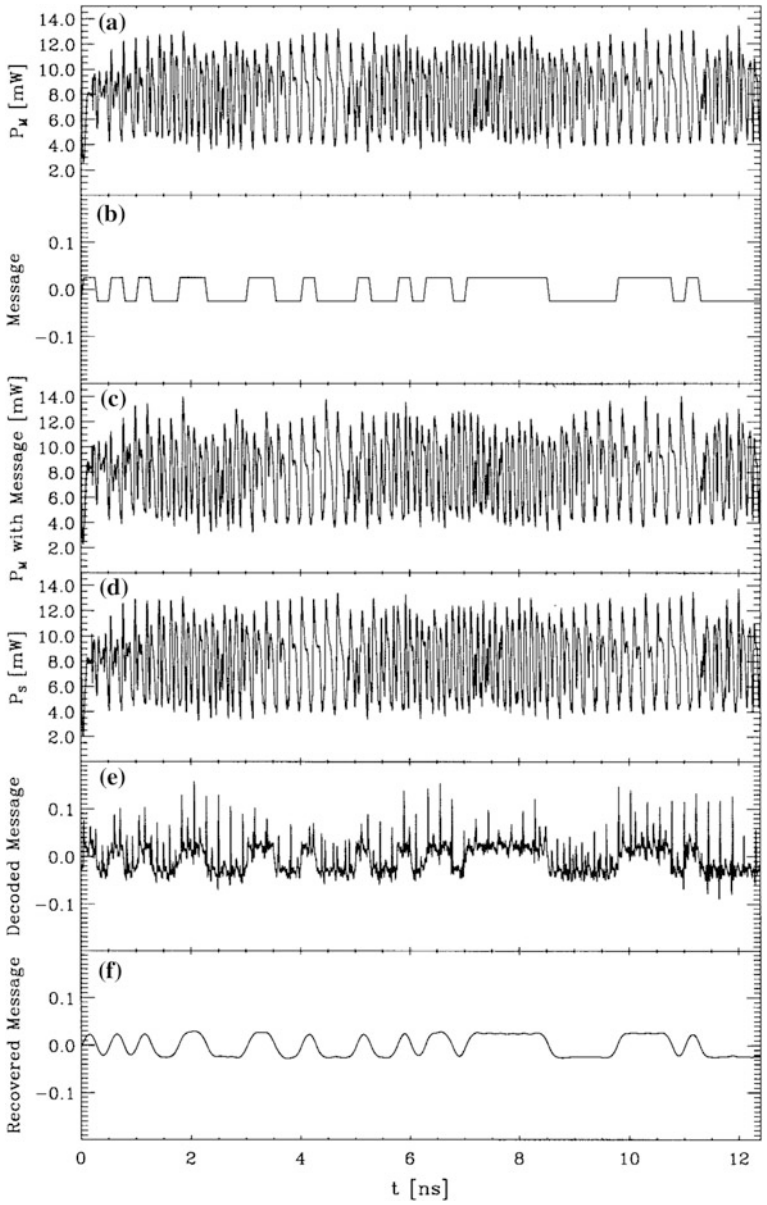

Fig. 13.6 Chaotic communications based on CMA in semiconductor lasers with optical feedback. **a** Chaotic oscillation from the transmitter, **b** binary bit-sequence for data transmission, **c** chaotic waveform together with a message, **d** synchronized chaotic oscillation in the receiver after data transmission through a nonlinear optical fiber of 50 km, **e** decoded signal, and **f** low-pass filtered waveform for the decoded signal [after Sánchez-Díaz et al. (1999); © 1999 IEEE]

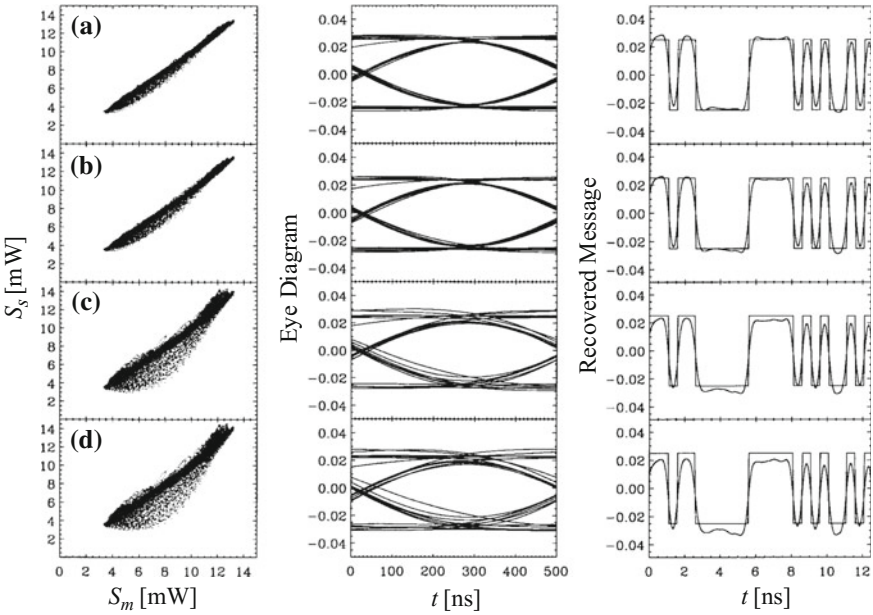

Fig. 13.7 Signal recovery for fiber transmissions of 50, 100, 150, and 200 km from **a** to **d**, respectively. The *left* column shows the correlation plots between the chaotic carrier in the transmitter without a message and the receiver output at synchronization. The *middle* shows the corresponding eye patterns. The *right* shows the decoded messages after filtering [after Sánchez-Díaz et al. (1999); © 1999 IEEE]

dispersion and nonlinearities of optical fiber. In actual optical fiber transmission, there is a loss of light through the optical fiber. Therefore, an in-line amplifier is placed at a certain distance in practical optical fiber communications. This may cause further degradation of chaotic signals due to the enhancement of the nonlinear effects after the amplification. In-line amplifiers would aggravate the negative effect of the fiber nonlinearities on the synchronization.

13.2.3 Chaos Modulation in Optical Feedback Systems

In CMO, we put $\eta_{\mathrm{CMO}} \neq 0$ and $\eta_{\mathrm{CMA}} = \eta_{\mathrm{CSK}} = 0$ in (13.1)–(13.4). A message is added within the transmitter, for example in the feedback loop in Fig. 12.4a, and the transmission signal of $E(t + \tau) = f\{E(t) + m_{\mathrm{CMO}}(t)\}$ is generated and transmitted to the receiver. The original chaotic signal together with the message conforms a new chaotic signal and, therefore, the message may essentially have large amplitude. However, care must be taken when embedding a large message signal into chaotic oscillations, since the message itself may explicitly appear in the transmission signal for the worst case. For this reason, a message with small

amplitude is usually used in CMO. The method of CMO is approximately equal to CMA when an encoding message is small enough.

We present a numerical example of the CMO method. This scheme requires the achievement of complete chaos synchronization and hence is usually difficult to realize by experiment (Liu et al. 2002a). The possibility of transmission of a NRZ pseudo-random binary sequence at 2.5 Gbps using CMO was demonstrated by numerical simulation. Figure 13.8 shows the results (Liu et al. 2001c). In this example, it is assumed that an EO modulator is inserted into the optical feedback loop, and is used to modulate the feedback signal as $m_{\mathrm{CMO}}(t) = 1 + b_m$ for "1" and $m_{\mathrm{CMO}}(t) = 1 - b_m$ or "0", where $b_m (b_m < 1)$ is the modulation depth. Figure 13.8a shows the dependence of the synchronization error on the amplitude of the embedded signal b_m, and Fig. 13.8b is the dependence of the bit error rate on the frequency of the detuning between the transmitter and receiver lasers, both with noise added (triangles) and without noise (circles). The results show good

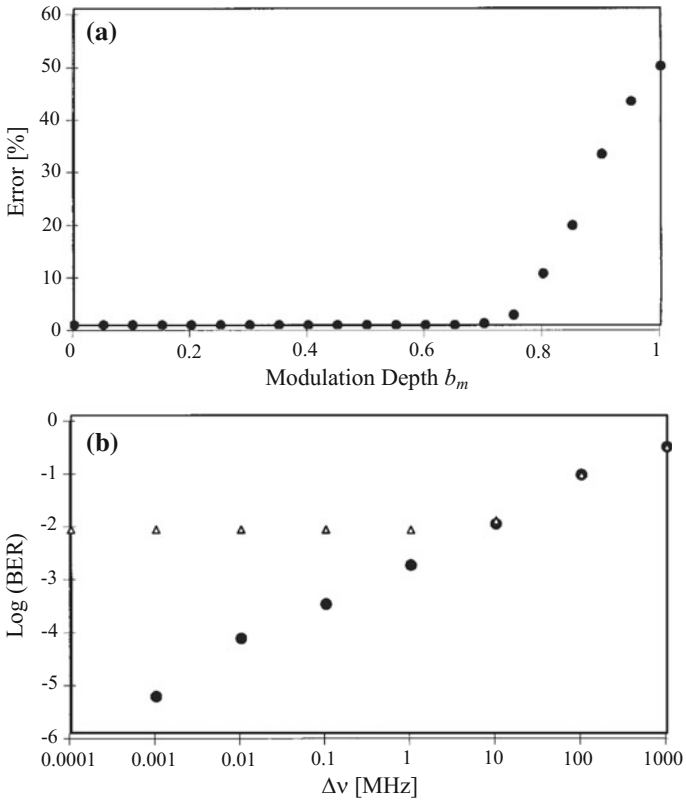

Fig. 13.8 Calculated synchronization error and bit error rate (BER) for normalized dimensionless bias injection currents of 0.67, normalized feedback and injection ratios of 0.01. **a** Synchronization error versus modulation amplitude b_m. **b** BER versus frequency detuning at a modulation factor of $b_m = 0.15$. *Black dots* no noise, *triangles* noise at SNR = 40 dB

synchronization for a wide range of relative modulation amplitudes and sensitive dependence of the bit error rate (BER) on the detuning, which are strong features of the CMO method using complete synchronization.

13.2.4 Chaos Shift Keying in Optical Feedback Systems

A set of chaotic generators is usually required both for transmitter and receiver systems in CSK. Indeed, chaotic signals from two transmitters are switched according to the binary value of 0 or 1 of a message sequence and they are sent to the two receivers. The receivers synchronize to the corresponding transmitters and the decoding is done by the synchronization. Annovazzi-Lodi et al. (1997) used a single transmitter consisting of a semiconductor laser with optical feedback in CSK instead of two transmitters. A NRZ binary message is put into the injection current of the laser at a certain bias point. According to the message, two chaotic states are generated and they are sent to the receiver. The difference between the two chaotic attractors must be sufficiently small not to be distinguished easily for secure communications. The receiver is a set of chaotic generators and they have the same characteristics except for the injection currents. The injection currents are set at either the high or low value of the binary message. Then, each receiver synchronizes with the corresponding chaotic state and synchronous and asynchronous (chaotic bursts) signals are obtained for the time sequence from comparison between the transmitted signal and the receiver output. Figure 13.9 shows one of the receiver outputs in the CSK system. The square waveform is a message to be transmitted and the error signal is the receiver output. The other receiver laser outputs the compensating signal to the waveform in Fig. 13.9. Then, the message is decoded from these two signals.

When two nonlinear chaotic systems synchronize with each other, the receiver does not respond immediately after it receives a chaotic signal from the transmitter. Usually, the receiver outputs the synchronous signal after a certain transient time. In a CSK system, the chaotic oscillation switches from one state to the other according to the ON/OFF signals. Therefore, we must consider the synchronization recovery time after the switching of signals. This limits the efficiency of the possible bit rate of the data transmission. This synchronization recovery time depends on each system configuration (open- or close-loop system) and the device and system parameters. The typical frequency of a chaotic carrier in semiconductor lasers with optical feedback is of the order of the relaxation oscillation frequency at the solitary oscillation and a message frequency must be less than this. The time required for the synchronization in CSK is from nanosecond to several nanoseconds depending on the system parameters (Vicente et al. 2002). On the other hand, it is possible for CMA and CMO methods to achieve higher data transmissions than the relaxation oscillation frequency, since chaotic oscillations in the systems have broadband characteristics over the relaxation oscillations. In the CSK discussed here, the transmitter laser is directly modulated by a message through the injection current,

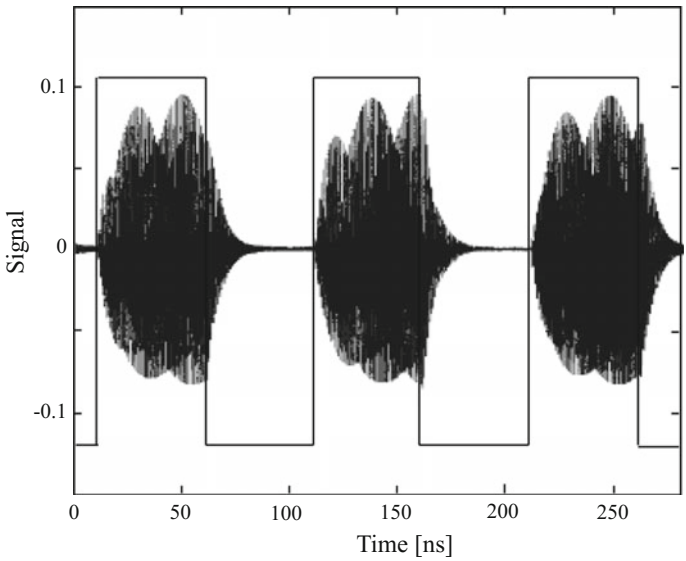

Fig. 13.9 Square message to be transmitted in a CSK system and error signal from one of the receiver outputs. The system has a single transmitter of a semiconductor laser with optical feedback and the receiver consists of two optical feedback systems [after Annovazzi-Lodi et al. (1997); © 1997 IEEE]

so that it looks like a method of CMO. However, the original chaotic attractor is not affected by the modulation. It is distinguished from CMO as long as the amplitude of the message is small (less than 1% of the averaged chaotic oscillation). The synchronization recovery time will be discussed in Sect. 13.9.

13.2.5 Chaotic Communications in Incoherent Optical Feedback Systems

Incoherent optical feedback systems are also used for chaotic communications based on chaos synchronization as discussed in the previous chapter. In the systems, the laser output power from the transmitter is coupled with the carrier density of the receiver laser. Therefore, we do not need to consider the optical phase and tune the optical frequencies between the transmitter and receiver lasers. As a result, we can easily achieve chaos synchronization. However, the grade of the security in the communications is deteriorated, since one of the keys for secure chaotic communications is eliminated. Nevertheless, the output generated by a semiconductor laser with incoherent optical feedback is a higher dimensional chaos and the system has enough complexity for secure communications. It is still not easy to reproduce the transmitter chaos in the receiver without knowing the chaos

parameters in the system. Rogister et al. (2001) conducted chaotic data transmission based on CSK using incoherent optical feedback systems by numerical simulations. The synchronization system is the same as in Sect. 12.3.5. They succeeded in the data transmission of 250 Mbps pseudo-random-bit sequences with excellent quality using ON/OFF CSK. The level of the message was only 0.3% of the bias injection level and the secure communication was achieved by hiding the data behind the chaotic signal.

13.2.6 Chaos Pass Filtering Effects

The effect of chaos-pass filtering is essential to attain successful secure communications by hiding messages behind chaotic signals in chaos synchronization systems. In accordance with the effect, the chaotic signal, which is transmitted from the transmitter laser, is only reproduced by the receiver laser even if the transmitted signal includes a message. Thus, the message is correctly decoded by subtracting the chaos signal of the receiver laser from the transmitted signal under appropriate conditions for the synchronization system. However, the above expression of 'chaotic signal is only reproduced' may not be correct. As will be discussed later, the effect of the chaos-pass filtering is that the main component of the chaotic signal from the transmitter laser is closely copied in the receiver laser and the chaos transmittance is usually equal to or larger than unity, while the transmittance of the message, whose frequency component is less than the relaxation oscillation, is much less than unity. Several studies for the effects of chaos-pass filtering have been reported both theoretically and experimentally (Uchida et al. 2003b; Paul et al. 2004; Murakami and Shore 2005, 2006). Especially, chaos-pass filtering plays a crucial role in chaos masking systems. In the following, we discuss the effect of chaos-pass filtering in semiconductor lasers with optical feedback.

Consider a CMA system in semiconductor laser with optical feedback described by (13.1)–(13.4) and assume three different sinusoidal modulations for the injection current J_T in the transmitter laser as messages. Figure 13.10 shows the calculated transfer function between the transmitted signal and the receiver output. The chaos synchronization system assumed here is a type of open-loop and the synchronization is generalized one. To show the effect of chaos-pass filtering explicitly, the ratio of the optical injection from the transmitter to the receiver laser is as large as 50%. A transmission rate of several percents from the transmitter to the receiver is sufficient to attain chaos synchronization in the laser system and, indeed, such a small rate is usually used in a synchronization system using chaotic semiconductor lasers. The parameters of the solitary laser without optical feedback are $J = 1.3J_{th}$ and $\nu_R = 2.43$ GHz. The optical delay in the transmitter laser is set to be $\tau = 1$ ns and the frequency detuning between the transmitter and receiver lasers is assumed to be -0.1 GHz. Figure 13.10a shows the power spectra for the transmitter signal including the messages and the synchronized receiver output. The power spectrum of the receiver laser is vertically shifted by -15 dB to show clearly the difference.

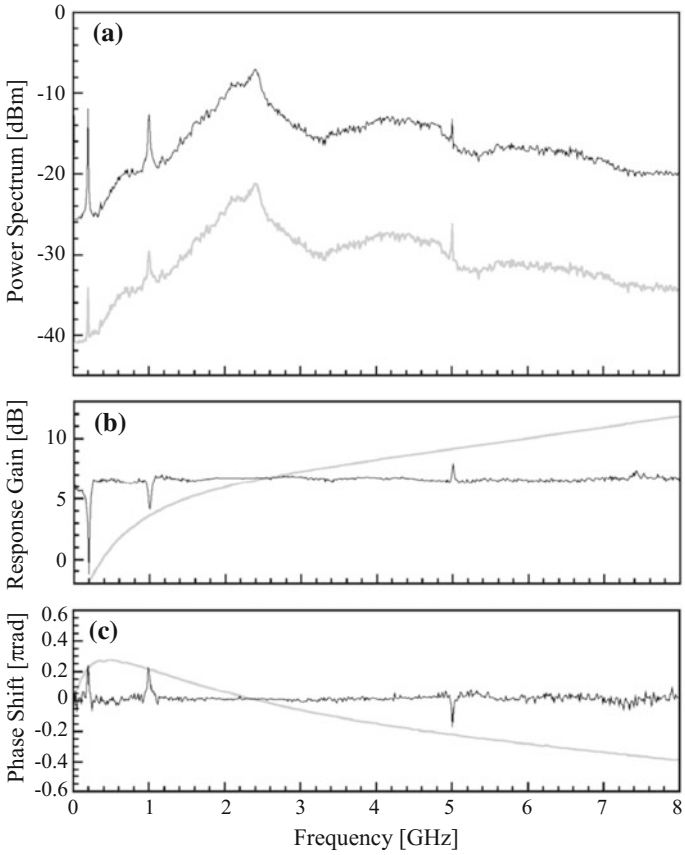

Fig. 13.10 Transfer functions in a chaos synchronization system. The injection ratio from the transmitter to the receiver laser is 50%. The transmitting signal from the transmitter is a chaotic signal together with three sinusoidal messages with modulation frequencies of 0.2, 1.0, and 5.0 GHz. The modulation indices are 0.05, 0.05, and 0.10, respectively. **a** Power spectra for the transmitter signal and the receiver output. *Solid line* transmitter, *gray line* receiver. The receiver spectrum is vertically shifted by −15 dB. **b** Transfer function from the transmitter to the receiver. *Solid line* transfer gain, *gray line* transfer function for a sinusoidal modulation only (modulation index is 0.05). **c** Phase shift between the transmitter signal and the receiver output. *Solid line* phase shift between the transmitter signal and the receiver output, *gray line* phase shift for a sinusoidal modulation only (modulation index is 0.05) [after Murakami and Shore (2005); © 2005 APS]

The frequency component of the chaotic signal is concentrated from 1 to 10 GHz. In the both spectra, embedded spectral peaks of sinusoidal signals are clearly seen. From the closer look at the two spectra, the spectra in the lower frequency components in the receiver are largely suppressed. On the other hand, the signal higher than the relaxation oscillation frequency is much enhanced in the receiver side.

Figure 13.10b shows the response ratio between the transmitter signal and receiver output. Since the injection rate from the transmitter to the receiver is strong

as much as 50% in this case, the gain of the chaotic signal component in the receiver laser is much lager than 0 dB. As for the message components, it is seen from the figure that the transmission rates for the lower frequency components below the solitary relaxation oscillation frequency are greatly decreased compared with the transmission gain of the chaotic signal, while the transmission rate for the higher frequency component is larger than unity. The gray line in the figure shows the transfer function from the transmitter to the receiver laser for only sinusoidal modulation with a modulation index of 5% to the solitary transmitter laser. The crossover point of the chaotic gain and the sinusoidal modulation response is exactly equal to the relaxation oscillation frequency of the semiconductor laser at solitary oscillation. Figure 13.10c shows the phase shift between the transmitter signal and the receiver laser. The solid line represents the phase shift, which is calculated from the Fourier components of the transmitter signal and the receiver output. There is no phase shift for the chaotic transmittance, while the sinusoidal signals with lower frequency components have a positive phase shift and the higher frequency component has a negative shift. The gray line shows the phase shift for only sinusoidal modulation with a modulation index of 5% to the solitary transmitter laser, which corresponds to the gray line in Fig. 13.10b. Again, the crossover point of the chaotic phase shift and the phase shift for the sinusoidal modulation is exactly equal to the relaxation oscillation frequency. It is noted that the phase shift becomes $-\pi$ at the resonant frequency by the strong optical injection from the transmitter to the receiver laser, when only a sinusoidal modulation is transmitted (though the resonant frequency is 12.7 GHz in this case and the frequency is out-of-scope in this graph).

As discussed above, the frequency components of chaotic signals concentrate at and around the relaxation oscillation frequency and they typically range from 1 to 10 GHz in chaotic semiconductor lasers. Another interesting point is that the transfer function of a chaotic signal from the transmitter to the receiver is almost constant for all the frequency range. On the other hand, the transfer function of a sinusoidal signal has frequency dependence. Namely, a sinusoidal signal has a small response gain for lower frequency less than the relaxation oscillation, while a sinusoidal signal with higher frequency has a larger response gain than 0 dB. Thus, the difference for the response gains between chaotic and sinusoidal signals is the origin of the chaos-pass-filtering effects. As another issue, the direct injection current modulation for the transmitter laser as a message encryption deteriorates the performance of chaos synchronization. Therefore, an external modulation for chaotic signals using an EO modulator is frequently used. Uchida et al. (2003b) studied the effects of chaos-pass-filtering in a CMA system using semiconductor lasers with optical feedback, and obtained similar results for the response between the transmitter and the receiver as discussed here. It is derived from the above discussion that chaotic carrier frequency, which is limited by the resonant oscillation frequency of semiconductor laser, must be much greater than a main message frequency to attain higher data-bit transmission in chaotic semiconductor laser systems. Thus, the use of semiconductor lasers, which have high modulation bandwidth, is essential for massive chaotic secure communications.

13.3 Cryptographic Applications in Optical Injection Systems

We can apply the systems of semiconductor lasers subjected to optical injection discussed in Sect. 12.4 to chaotic communications. Figure 13.11 shows the schematic diagram of the chaotic communications. Message encoding and decoding schemes are the same as the systems of optical feedback in Fig. 13.3. For CMA, CMO, and CSK, the equations for the transmitter laser are written by

$$\begin{aligned}\frac{\mathrm{d}E_{\mathrm{T}}(t)}{\mathrm{d}t} &= \frac{1}{2}(1-i\alpha_{\mathrm{T}})G_{n,\mathrm{T}}\{n_{\mathrm{T}}(t)-n_{\mathrm{th,T}}\}E_{\mathrm{T}}(t) \\ &\quad + \frac{\kappa_{\mathrm{inj,T}}}{\tau_{\mathrm{in.T}}}\{1+\eta_{\mathrm{CMO}}m_{\mathrm{CMO}}(t)\}E_{\mathrm{T}}(t)\exp(-i\Delta\omega_{\mathrm{T}}t)\end{aligned} \tag{13.7}$$

$$\begin{aligned}\frac{\mathrm{d}n_{\mathrm{T}}(t)}{\mathrm{d}t} &= \frac{J_{\mathrm{T}}}{ed}\{1+\eta_{\mathrm{CSK}}m_{\mathrm{CSK}}(t)\} - \frac{n_{\mathrm{R}}(t)}{\tau_{s,\mathrm{R}}} \\ &\quad - G_{n,\mathrm{T}}\{n_{\mathrm{T}}(t)-n_{0,\mathrm{T}}\}|E_{\mathrm{T}}(t)|^2\end{aligned} \tag{13.8}$$

where $\Delta\omega = \omega_{\mathrm{inj,T}} - \omega_{0,\mathrm{T}}$ is the frequency detuning between the injection laser and the transmitter laser. Whereas the receiver driven by the transmitted signal can be described by

$$\begin{aligned}\frac{\mathrm{d}E_{\mathrm{R}}(t)}{\mathrm{d}t} &= \frac{1}{2}(1-i\alpha_{\mathrm{R}})G_{n,\mathrm{R}}\{n_{\mathrm{R}}(t)-n_{\mathrm{th,R}}\}E_R(t) \\ &\quad + \frac{\kappa_{\mathrm{inj,R}}}{\tau_{\mathrm{in.R}}}E_{\mathrm{R}}(t)\exp(-i\Delta\omega_{\mathrm{R}}t) \\ &\quad + \frac{\kappa_{\mathrm{cp}}}{\tau_{\mathrm{in.R}}}\{1+\eta_{\mathrm{CMO}}m_{\mathrm{CMO}}(t-\tau_c)\}E_{\mathrm{T}}(t-\tau_c)\exp(-i\Delta\omega_{\mathrm{T,R}}t+i\omega_{0,\mathrm{T}}\tau_c) \\ &\quad + \eta_{\mathrm{CMA}}m_{\mathrm{CMA}}(t-\tau_c)\end{aligned} \tag{13.9}$$

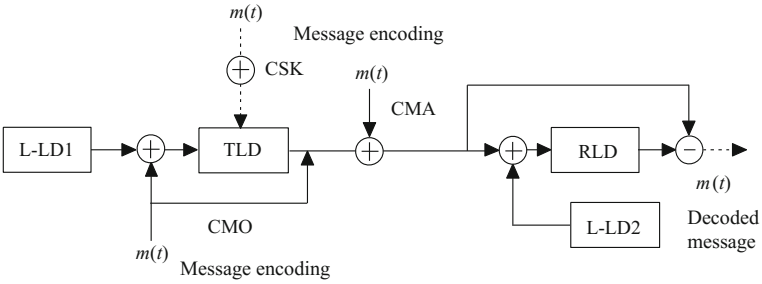

Fig. 13.11 Schematic diagram of chaotic communications in semiconductor lasers with optical injections. $m(t)$ is a message signal to be embedded. The position for each message-encoding scheme is shown in the figure. *Solid lines* are optical connections and *broken lines* are electronic connections

$$\frac{dn_R(t)}{dt} = \frac{J_R}{ed} - \frac{n_R(t)}{\tau_{s,R}} - G_{n,R}\{n_R(t) - n_{0,R}\}|E_R(t)|^2 \tag{13.10}$$

where $\Delta\omega_{T,R} = \omega_{0,T} - \omega_{0,R}$ is the angular frequency detuning between the transmitter and receiver lasers. Optical modulations of messages (CMA and CMO) are assumed to be applied to the complex fields, however EO modulators are usually used as intensity modulations. We need some modifications of the above rate equations for the intensity modulations. Nevertheless, (13.7)–(13.10) are again a good approximation for the optical injection systems as far as the modulation amplitude is small enough.

Figure 13.12 presents a numerical example of chaotic communications in a system of semiconductor lasers subjected to optical injection (Liu et al. 2001a). The figure is a message transmission of a 2.5 Gbps signal based on CMO. In the transmitter laser, a chaotic carrier is generated at the appropriate injection ratio and the frequency detuning in the optical injection configuration. A binary message is encoded into the chaotic carrier. There are two schemes of chaotic modulations to the optical field in CMO; additive modulation and multiplicative modulation. This case is for additive modulation. After subtracting the receiver output from the transmitted signal and low-pass filtering it (bottom of the figure), they obtained a decoded message with good quality. The system of optical injection is also phase sensitive like the system of coherent optical feedback (Heil et al. 2003). We must pay attention to the optical phase to achieve good quality of communications.

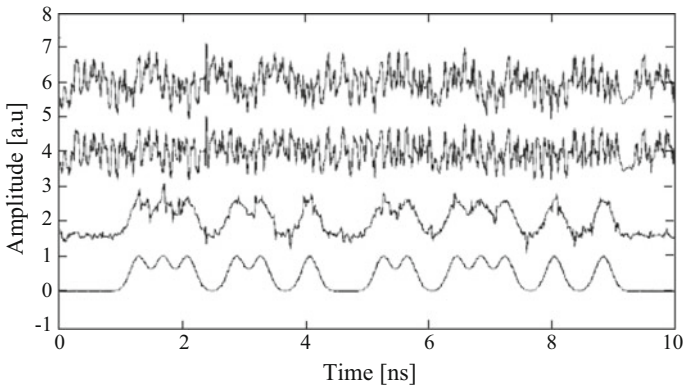

Fig. 13.12 Numerical example of message transmission in semiconductor lasers with optical injection in CMO. The system is an open loop and the message is a 2.5 Gbps signal. From *top* to *bottom* transmitted signal including message, receiver output, decoded signal by subtraction of the receiver output from the transmitted signal, and low-pass filtered signal for the decoded message [after Liu et al. (2001a); © 2001 IEEE]

13.4 Cryptographic Applications in Optoelectronic Systems

We here describe chaotic communications in semiconductor lasers with optoelectronic feedback systems. The system is incoherent coupling and the light from the laser is once detected by a photodetector. Then, the photocurrent is fed back into the bias injection current of the laser. Therefore, noises originating from photons are averaged out due to slow response of the carrier lifetime and high performance for synchronization between the transmitter and receiver lasers can be expected. A message is embedded into fast chaotic pulsation oscillations from sub-nanosecond to picosecond and high-speed chaotic data transmissions are also expected due to the availability of high-speed electronic circuits. Figure 13.13 shows a model of chaotic communication systems in semiconductor lasers with optoelectronic feedback. The system can be described by only the photon number and the carrier density. A message is directly added to the laser intensity or the bias injection current, which is not the case for the systems of optical feedback and optical injection. The following formulation can be widely used in real optoelectronic systems without modification. For the transmitter, the rate equations read

$$\frac{\mathrm{d}S_{\mathrm{T}}(t)}{\mathrm{d}t} = G_{n,\mathrm{T}}\{n_{\mathrm{T}}(t) - n_{\mathrm{th,T}}\}S_{\mathrm{T}}(t) + R_{\mathrm{sp,T}} \tag{13.11}$$

$$\begin{aligned}\frac{\mathrm{d}n_{\mathrm{T}}(t)}{\mathrm{d}t} = &\frac{J_{\mathrm{T}}}{ed}\{1 + \eta_{\mathrm{CSK}}m_{\mathrm{CSK}}(t)\}\{1 + s_{\mathrm{T}}(t)\} \\ &- \frac{n_{\mathrm{T}}(t)}{\tau_{s,\mathrm{T}}} - G_{n,\mathrm{T}}\{n_{\mathrm{T}}(t) - n_{0,\mathrm{T}}\}S_{\mathrm{T}}(t)\end{aligned} \tag{13.12}$$

$$s_{\mathrm{T}}(t) = \xi_{\mathrm{T}}S_{\mathrm{T}}(t - \tau_{\mathrm{T}}) + \eta_{\mathrm{CMO}}m_{\mathrm{CMO}}(t - \tau_{\mathrm{T}}) \tag{13.13}$$

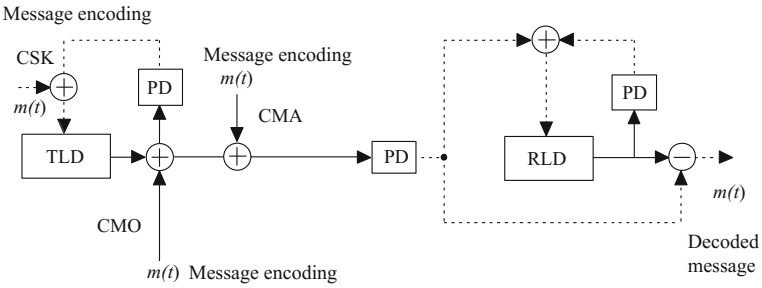

Fig. 13.13 Schematic diagram of chaotic communications in semiconductor lasers with optoelectronic feedback. $m(t)$ is a message signal to be embedded. The position for each message encoding scheme is shown in the figure. *Solid lines* are optical connections and *broken lines* are electronic connections

When the system response is continuous, $s_T(t)$ is replaced by a continuous response function in the same manner as in (12.69) as

$$y_T(t) = \int_{-\infty}^{t} f(t'-t)s_T(t')dt' \tag{13.14}$$

whereas the receiver driven by the transmitted signal can be described by

$$\frac{dS_R(t)}{dt} = G_{n,R}\{n_R(t) - n_{th,R}\}S_R(t) + R_{sp,R} \tag{13.15}$$

$$\frac{dn_R(t)}{dt} = \frac{J_R}{ed}\{1 + s_R(t)\} - \frac{n_R(t)}{\tau_{s,R}} - G_{n,R}\{n_R(t) - n_{0,R}\}S_R(t) \tag{13.16}$$

$$s_R(t) = \xi_R S_R(t - \tau_R) + \xi_{cp} S_T(t - \tau_c) + \eta_{CMO} m_{CMO}(t - \tau_c) \tag{13.17}$$

Similarly, $s_R(t)$ is replaced by a continuous response function for a finite response of the electronic feedback circuits.

Figure 13.14 shows the experimental results of chaotic communications in semiconductor lasers with optoelectronic feedback in CMO. The system is open loop. A message is a pseudo-random signal of an NRZ pulse sequence. The message is embedded into the bias injection current with additive modulation. As discussed in Sect. 12.5, open-loop configuration shows better quality of chaos synchronization and modulation (Tang and Liu 2001; Liu et al. 2002b). Figure 13.14a shows the plot of signals for data transmission and decoding. The decoded signal (the third signal from the top) well reproduces the original message above the threshold level (dotted line). From the time lag, it is recognized that the synchronization is a complete type, although the time lag is compensated to compare the waveforms. Since chaotic signals generated in semiconductor lasers with an optoelectronic feedback system are pulse-like irregular oscillations, additive modulation is suited for CMO rather than multiplicative modulation. Figure 13.14b shows the eye pattern for the decoded message. A good quality of opened eyes is obtained.

13.5 Chaotic Communications in Mutually Coupled Semiconductor Lasers

13.5.1 Communications in Mutually Coupled Semiconductor Lasers

Mutually coupled two chaotic systems can be used for secure communications (Klein et al. 2006; Vicente et al. 2007). Although it is not easy to perform directly

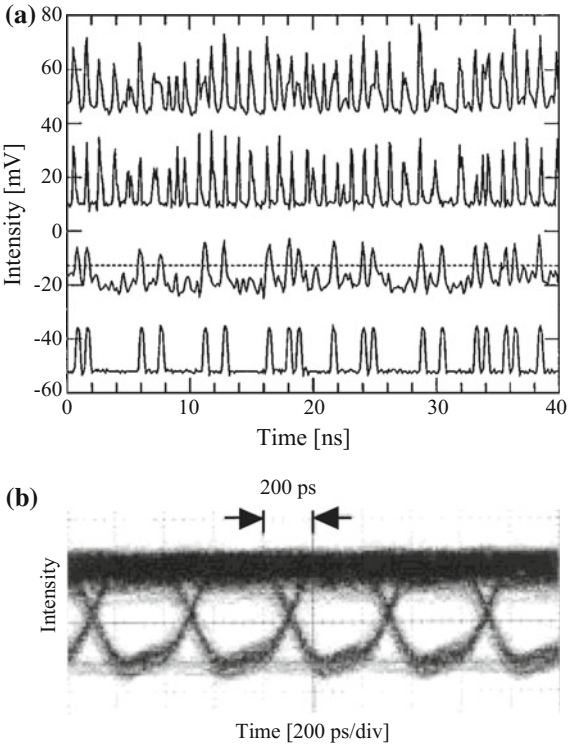

Fig. 13.14 Experimental example of message transmission in semiconductor lasers with optoelectronic feedback in CMO. The system is an open-loop using DFB lasers at a wavelength of 1.30 μm and the message is a 2.5 Gbps signal. **a** From *top* to *bottom* transmitted signal including message, receiver output, decoded filtered signal, and original message [after Tang and Liu (2001); © 2001 OSA]. **b** Eye pattern of the decoded signal [after Liu et al. (2002b); © 2002 IEEE]

secure data transmissions and communications, this scheme, for example, allows one to negotiate a key through a public channel as is discussed in the followings. We here consider a mutual coupling system described in Fig. 12.4c. The two lasers simultaneously transmit respective data through a single transmission channel. Vicente et al. (2007) proposed an asymmetric configuration of the mutual coupling system. In their system, the two lasers have different optical feedback lengths of external reflectors. The two lasers even synchronize developing a leader-laggard-type dynamics with one laser following the other by the coupling delay. This symmetry breaking complicates the simultaneous transmission of information in both directions. The type of chaos synchronization in this system is complete in spite of the asymmetric configuration and, moreover, the two lasers show a leader-laggard dynamics. Messages of "0" and "1" are embedded to the lasers through the injection currents and the messages are simultaneously transmitted to one laser to the other and vice versa. Based on chaos synchronization in the system, they numerically obtained the difference of the two messages. The proposed scheme is the system of simultaneously exchange information between the two lasers by using a single communication channel.

Figure 13.15 shows a result of data transmissions through mutual chaotic communications (Vicente et al. 2007). Figure 13.15a is a pseudo-random digital

message of 1 Gbps embedded into the injection current in one of the lasers, $m_1(t)$. The amplitude of the message is $0.12J_{th}$. Figure 13.15b is the message in the counterpart laser, $m_2(t)$. Figure 13.15c is the expected subtraction of messages $\Delta m(t) = m_1(t) - m_2(t - \Delta\tau)$ with a given time lag ($\Delta\tau = 1$ ns in this case). Figure 13.15d is the calculated intensity difference ΔS after filtering with a fifth-order Butterworth filter with a cutoff frequency of 0.8 GHz. Thus, one can successfully obtained the difference of the embedded messages based on the mutual coupling system under appropriate synchronization conditions. In this system, the maximum encoding rate depends on the inverse of the resynchronization time after a bit arrives at one of the lasers. In the numerical conditions, it is $\sim$0.3 ns. Consequently, a maximum bit rate of about 3 Gbps could be achieved.

Next, we must discuss the security aspects of data transmissions in the mutual coupling system, since both output powers from the two lasers can be accessible from the same communication channel. Therefore, an eavesdropper could easily

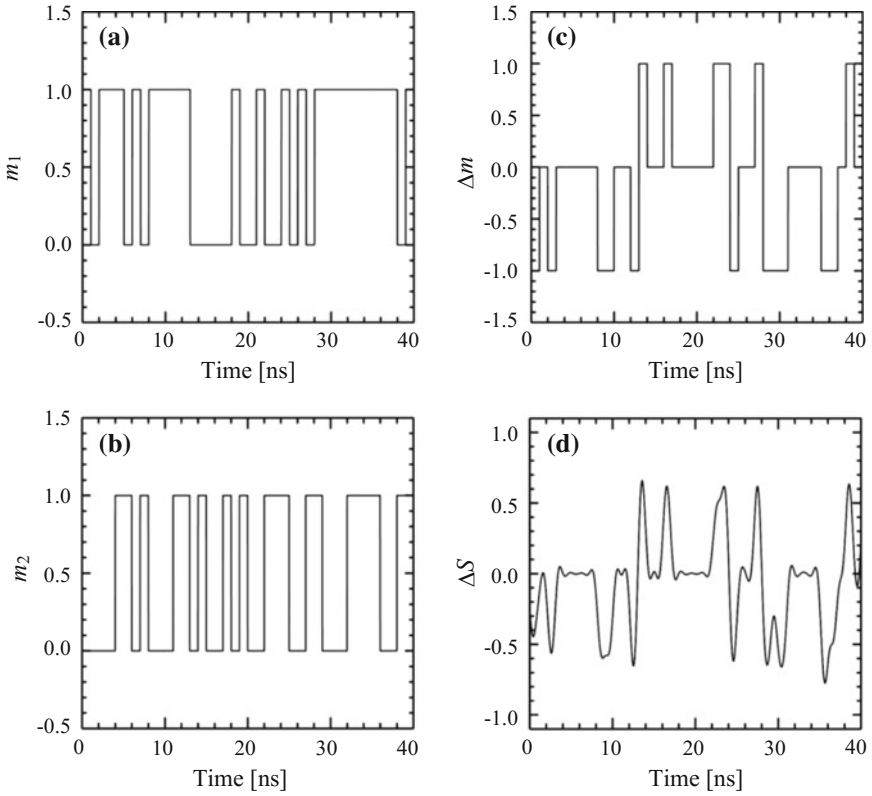

Fig. 13.15 Messages and decryption in mutual coupling semiconductor lasers. Messages from **a** laser 1 (m_1) and **b** laser 2 (m_2). **c** Expected subtraction of messages with time compensation. **d** Decrypted signal (ΔS) through a fifth-order Butterworth filter with a cutoff frequency of 0.8 GHz [after Vicente et al. (2007); © 2007 OSA]

monitor the difference of the messages. For the detected difference, a level of 1 in the message difference would clearly indicate that at the proper time the bit associated with one laser was a "1," while the one sent by the other laser was a "0." A similar argument holds when the message difference is −1. Only when the message difference is zero, which is the case for the coding of the same bit in both lasers, the eavesdropper has no clue as to which are the bits that are being sent. Thus, the mutual coupling configuration could be used to simultaneously negotiate a key for secret data transmissions (Mislovaty et al. 2003). The sender and the receiver can agree to discard those bits that are different from each other while accepting that the key that is formed by the first N bits that coincide with each other. Thus, a key is encrypted with the same level of security as in a unidirectional chaos communication scheme. A secure key exchange cryptosystem based on identical chaos synchronization in mutual coupled semiconductor lasers with additional optical feedback is experimentally demonstrated (Porte et al. 2016). Private key generation rates up to 11 Mbps over a public channel is obtained.

13.5.2 *Chaos-Pass Filtering Effects in Mutually Coupled Systems*

An effect of chaos-pass filtering is not only a unique feature in unidirectionally coupled semiconductor lasers but also it is observed in a mutually coupled system. As discussed in 12.7.1, a system with two mutually coupled semiconductor lasers shows delay synchronization when the two lasers have a frequency detuning. Different from the above section, the configuration under consideration is a simple system of two mutually coupled semiconductor lasers as discussed in 12.7.1. We consider a frequency mismatch (frequency detuning) between the two lasers. This scheme can be also used as communication systems hiding a message into chaotic waveforms, since not zero-lag but delay synchronization is established in this system. We here only discuss a chaos-pass filtering effect. Figure 13.16 shows the experimental results of optical spectra of chaotic signals in the leader and lagger lasers when a small sinusoidal modulation to the bias injection current is applied to one of the two lasers (Heil et al. 2001). The frequency detuning between the leader and lagger lasers is 2.5 GHz and the modulation frequency is 508 MHz. The optical coupling time between the two lasers is $\tau_c = 3.83$ ns and the corresponding frequency for the round trip time of optical feedback to the leader laser from the lagger is $\nu_c = 1/2\tau_c \sim 130$ MHz. Figure 13.16a is a case for the modulation to the lagger laser, while Fig. 13.16b is for the modulation to the leader laser. We can see the primary frequency component of the optical coupling at $\sim$130 MHz. The lower frequency peaks correspond to LFF components. The modulation frequency is very close to one of the higher-order components of the optical coupling time at $\sim 4\nu_c$. When the modulation is applied to the lagger laser (gray spectrum in Fig. 13.16a), the modulation peak is clearly present with comparable intensity in the leader laser

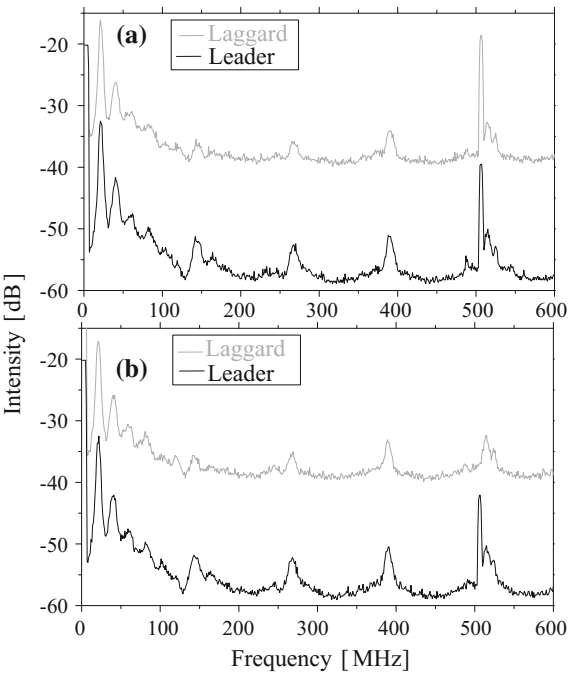

Fig. 13.16 Chaos pass filtering effects. RF spectra of mutual coupling semiconductor lasers under leader-laggard configuration with a small sinusoidal modulation of 508 MHz. **a** Modulation for the laggard. **b** Modulation for the leader. The injection currents are almost close to the laser threshold of solitary oscillations [after Heil et al. (2001); © 2001 APS]

(black spectrum in Fig. 13.16a). On the other hand, in Fig. 13.16b, the dominant modulation peak in the leader spectrum is not present in the laggerd spectrum. The chaos pass filtering effect in the mutual coupling semiconductor lasers can be explained as follows. The chaotic signal of the leader synchronizes the lagger laser, whereas the lagger laser acts as a driving force of the chaotic dynamics. This asymmetric nature of the system manifests itself in these different physical roles of the subsystems. The leader laser synchronizes the lagger laser results in the synchronous dynamical behavior delayed by the coupling time τ_c. Then, the driving role of the lagger laser leads to the observed feedback like dynamical behavior. The signal of the leader laser synchronizes the lagger laser and it is in turn injected into the leader with a delay of $2\tau_c$ after the oscillation of the original leader signal. Consequently, the dynamics of the delay-coupled lasers is comparable to the dynamics of a single laser subject to optical feedback with a delay of $2\tau_{ex}$.

13.6 Chaotic Communications in Drive-Response Systems

In Sect. 12.8, we discussed the enhancement of the correlation in chaos synchronization introducing a third laser as a common drive chaotic system to twin chaotic lasers (transmitter and receiver lasers). We can expect high performance of chaotic communications based on this method. In the following, we present numerical

examples of chaos synchronization in common chaos drive system to transmitter and receiver systems. Annovazzi-Lodi et al. (2008, 2010a, b) proposed systems of optical injection discussed in Sect. 12.8 and optoelectronic driving. Here, we show an example of optoelectronic driving system, in which the drive chaotic signal is once detected by photodetectors and the photocurrents are fed to transmitter and receiver lasers as a common chaotic driving signals (Annovazzi-Lodi et al. 2008). We assume chaotic systems of semiconductor lasers with optical feedback both for the driving chaotic system and the twin response systems. The device parameters and the operating conditions may be different between the driving system and the response systems. On the other hand, in the response systems, the transmitter and the receiver should have almost the same device parameters and operating conditions to obtain good chaos synchronization between them. As a result, the quality of chaos synchronization between the drive and response systems may not be high, while a good correlation between the transmitter and receiver outputs can be attained due to the common chaotic driving. A message embedding into the transmitter chaos is sent to the receiver. Thus, the injection current to the laser is given by $J_T(t) = J_{T0} + J_D(t) + J_M(t)$, where J_{T0} is the constant bias injection current, $J_D(t)$ is the chaotic current from the driver, and $J_M(t)$ is the current corresponding to the message. The transmitted signal is once detected by a photodetector. The injection current to the receiver laser is given by $J_R(t) = J_{R0} + J_D(t)$, where J_{R0} is the constant bias injection current. Then, the output from the receiver laser is subtracted from the transmitted signal and, finally, the decrypted message can be obtained.

Figure 13.17 is a result of numerical simulation (Annovazzi-Lodi et al. 2008). The delay times of optical feedback both in the drive and response systems are set to be the same, however the characteristics of the drive laser are fairly different from those of the response lasers. To represent the actual conditions of experiments, Langevin noises of the lasers, shot noise of the detectors, and Johnson noise of the 50 Ω termination resistance are taken into account in the numerical simulations. Under the conditions, they obtained the correlation coefficient of 0.68 between the drive and response outputs, while it is as high as 0.98 between the transmitter and receiver lasers under the common chaos driving. The message shown in Fig. 13.17a is a pseudo-random NRZ digital signal at 100 Mbps modulated by the carrier in amplitude with 100% modulation depth. The level of the embedded message is 2.86% of the bias injection current of the transmitter laser. Figure 13.17b is the output power from the transmitter laser without optical feedback and in the absence of chaotic driving signal from the third laser. Since various noise sources are taken into account, the observed output power from the laser would not be like the trace in Fig. 13.17a but in b in real experiment. Figure 13.17c shows the transmission signal including the transmitter chaos and the message and Fig. 13.17d is the decrypted message through a band-pass filter with a 400 MHz bandwidth around the carrier frequency. The decrypted message is almost equal to the time trace in Fig. 13.17b, thus, a high quality data reconstruction with secure chaotic encryption is attained by the method of drive and response configurations. The system requires an extra communication channels from the driver to the response systems.

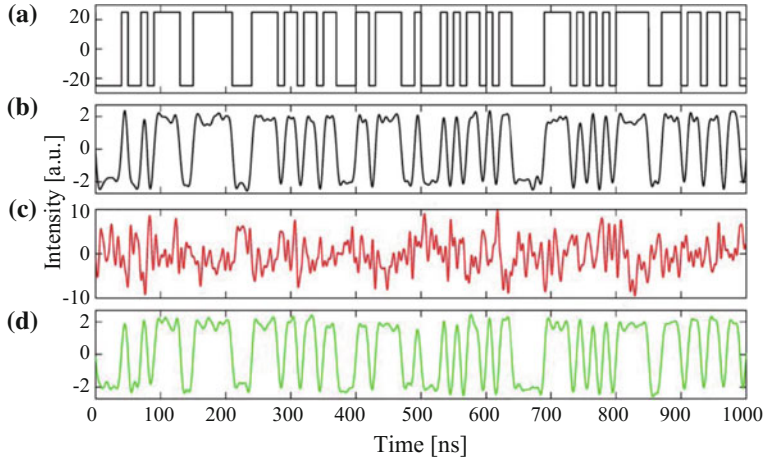

Fig. 13.17 Simulated message transmission in Drive-Response systems. **a** Original message, **b** transmitter light output without chaos and off drive signal, **c** transmission signal of chaotic oscillation plus hidden message, and **d** decrypted message with drive signal. The signal, which is transmitted on a 4.65 GHz carrier, is 100 Mbps. The Langevin noise terms of the lasers and shot noises terms of photodetectors are taken into account [after Annovazzi-Lodi et al. (2008); © 2008 IEEE]

Annovazzi-Lodi et al. proposed an application of the system for free-space broadcasting of the driving chaotic signal and communications using a diffuser. Therefore, the method may be useful as local signal scrambler in a small room communications. They also discussed the effects of parameter mismatches for chaos synchronization and the quality of message reconstructions in the systems.

13.7 Performance of Chaotic Communications

We have discussed chaotic communications for three message encryption schemes (CMA, CMO, and CSK) in three different systems of semiconductor lasers (optical feedback, optical injection, and optoelectronic feedback systems). Each scheme in each system has merit and demerit for chaotic data transmissions. Liu et al. (2002b) numerically compared the performances of chaos communications for these methods. Figure 13.18 shows the results of the comparison of the performance for the three systems of (a) optical feedback, (b) optical injection, and (c) optoelectronic feedback. A message is a 10 Gbps pseudo-random pulse sequence. The relaxation oscillation frequency of the laser assumed is set to be 12 GHz at the operating bias injection current. Open-loop configurations are assumed for all the systems. For CMA and CMO in optical feedback and optical injection systems, the ratio of the amplitude for the encoding message to that of the chaotic amplitude is set at 0.05. For the CSK system, the injection current is modulated as an ON/OFF

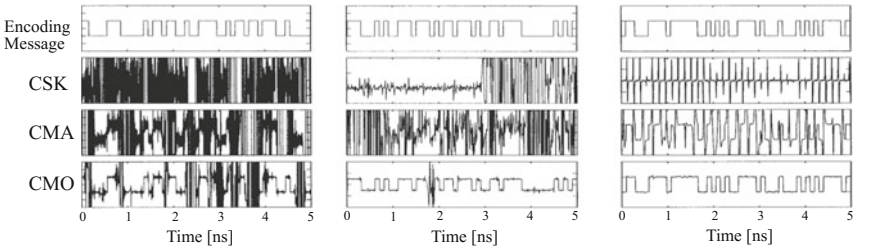

Fig. 13.18 Comparison of the performance for chaotic communications in semiconductor laser systems at data transmission rate of 10 Gbps. **a** Optical feedback system, **b** optical injection system, and **c** optoelectronic feedback system. All the systems are open loop. From *top* to *bottom* in each figure: encrypted message, decoded signal in CSK, decoded signal in CMA, and decoded message in CMO [after Liu et al. (2002b); © 2002 IEEE]

modulation and the corresponding modulation index to the optical field is taken to be the same as those in CMA and CMO. At the modulation index of 0.05, signal-to-noise ratio (SNR) of 30 dB has the channel noise at a level of an equivalent laser linewidth of $\Delta\nu = 0.66$ MHz. On the other hand, the modulation index is assumed to be 0.2 in the optoelectronic feedback system.

A finite response time is required for chaos synchronization in a receiver system when each message is transmitted. In CSK, the chaotic state is always switched in accordance with the binary message and the receiver cannot follow the ON/OFF switching of the chaotic states. Thus, the performance of synchronization becomes worse and one cannot recover the message for the worst case. The basis of chaotic communications is that a message signal attached to the chaotic carrier, which is very small in comparison with the size of the trajectory as a chaotic attractor, will be averaged out and has almost no effect on the duplication of the chaotic trajectory. The whole chaotic carrier waveform can then be reproduced very precisely through all the local predictor functions. However, as already discussed, a message is essentially a perturbation for the chaotic attractor of a transmitter output in CMA and CSK even when it is small, thus the synchronization deviation increases for large message amplitude. On the other hand, for CMO, the symmetry of the transmitter and receiver systems is preserved even if a message is embedded into the transmitter. Therefore, the system of CMO is robust for synchronization deviation compared with CMA and CSK. As a result, we can successfully recover the message with good quality for CMO in the system of optoelectronic feedback as shown in Fig. 13.18c. The synchronization is interrupted by synchronization deviation and bursts at the high data-transmission rate of 10 Gbps even for CMO in the systems of optical feedback and optical injection, and one cannot obtain the original messages. In all systems, the messages are not recovered in the CSK and CMA schemes in Fig. 13.18. For a higher data-transmission rate, a system of optoelectronic feedback with CMO is best suited for chaotic communications.

The reason why the system of optoelectronic feedback is better than those of optical feedback and optical injection for chaos synchronization has been discussed in Sect. 12.5.1. The carrier lifetime plays an important role in the system of optoelectronic feedback, while the photon lifetime is crucial for the other systems. The photon noises are averaged out in the system due to a slow response of the carrier and, as a result, the system is robust for photon noises. As far as the response of the electronic circuits can follow the chaotic signal, we can expect good chaos synchronization and faithful message decoding. The measure of the performance for a communication system is the bit error rate (BER) for the decoded message as a function of the signal-to-noise ratio (SNR) in the transmission channel. The SNR is defined as (Liu et al. 2002b)

$$\mathrm{SNR} = 10 \log \frac{S_m}{\sigma_n^2} \tag{13.18}$$

where S_m is the power of the transmitted message, and $\sigma_n^2 = N_0/2\ T_b$ is the variance of the channel noise with $N_0/2$ being the power spectral density of the channel noise and T_b being the bit duration. The channel SNR is a function of the channel noise, which is taken to additive white Gaussian noise, and the bit energy of the transmitted message, which depends on the modulation index of the message. BER arises from synchronization errors and bursts induced by channel errors and spontaneous emission noises in the lasers. The synchronization error σ_{error} has already been defined in (12.36).

Simply good quality of synchronization does not guarantee good retrieval of a message signal due to the sensitivity of the synchronized trace to any perturbation, including the perturbation caused by the intrinsic noise of the transmitter and that of the receiver. If some perturbation temporarily desynchronizes the synchronized transmitter and receiver for a period-of-time, the message signal within this period cannot be recovered. Therefore, the robustness of synchronization has to be considered in chaotic communications. Desynchronization could happen if the synchronized trace has any positive conditional Lyapunov exponent for a period-of-time while any perturbation is acting on this synchronized trace. It depends on the value of the positive conditional Lyapunov exponent and the strength of the perturbation during that period of time.

The synchronization error is categorized into two origins of synchronization deviation, which is associated with the accuracy of synchronization and desynchronization bursts, which is related to the robustness of synchronization in the system. The correlation coefficient of chaos synchronization between the transmitter and receiver lasers is usually not close to unity, although the two chaotic signals are similar. The deterioration of the correlation coefficient corresponds to the synchronization error. On the other hand, the chaotic output in the receiver completely differs from the transmitter signal at the occurrence of desynchronization bursts and the transmitter and receiver outputs have no correlation. Desynchronization burst is observed at the marginal region of the allowed parameter mismatches for the synchronization. The occurrence of desynchronization burst depends on the

combination of chaotic parameters in the systems. It is an essential phenomenon in chaos synchronization systems with parameter mismatches. Even when the parameters of the transmitter and receiver systems are equal, desynchronization burst may suddenly occur by noises in the electronic circuits. The bits error caused by synchronization deviation is measured by the concept of synchronized bit error rate

$$\text{SBER} = \frac{\text{error bits caused by desynchronization bursts}}{\text{total number of bits tested}} \tag{13.19}$$

The desynchronized bit error rate (DBER) induced by desynchronization bursts is defined by

$$\text{DBER} = \frac{\text{error bits caused by synchronization deviation}}{\text{total number of bits tested}} \tag{13.20}$$

Then, the total BER is simply defined by the sum of the SBER and the DBER as

$$\text{BER} = \text{DBER} + \text{SBER} \tag{13.21}$$

Figure 13.19 is the result of BERs calculated by numerical simulations under the assumption of SNR = 30 dB (Liu et al. 2002b). BER can be improved by applying a filter to the decoded messages. In this example, the testing filter used for examining the characteristics of error reduction is a digital Chbyshev Type I filter with the cutoff frequency equal to the bit rate, the sampling frequency equal to 20 times the cutoff frequency, 0.5 dB ripple on the pass-band and −30 dB attenuation on the stop-band. The best performance of BER is obtained for the optoelectronic feedback system with CMO, which is a good coincidence with the result in Fig. 13.18. Figure 13.19b is the performance of BER obtained by changing the bit rate of the data transmission in CMO schemes. The BERs in optical feedback and optical injection systems stay constant for the change of the bit rate. However, we can expect a great improvement of BER in optoelectronic feedback systems for a lower data-transmission rate.

13.8 Security of Chaotic Communications

The successful demonstrations of chaotic data transmissions in laser systems including semiconductor lasers, and solid-state lasers, and fiber lasers have proved that these schemes are robust to some degree. However, there is still much to be done in terms of evaluating the robustness and practical tradeoffs with the security based on parameter sensitivity. The security in chaotic communications is guaranteed by the coincidence of the system parameters between the transmitter and receiver including the device parameters and the operation conditions of the lasers.

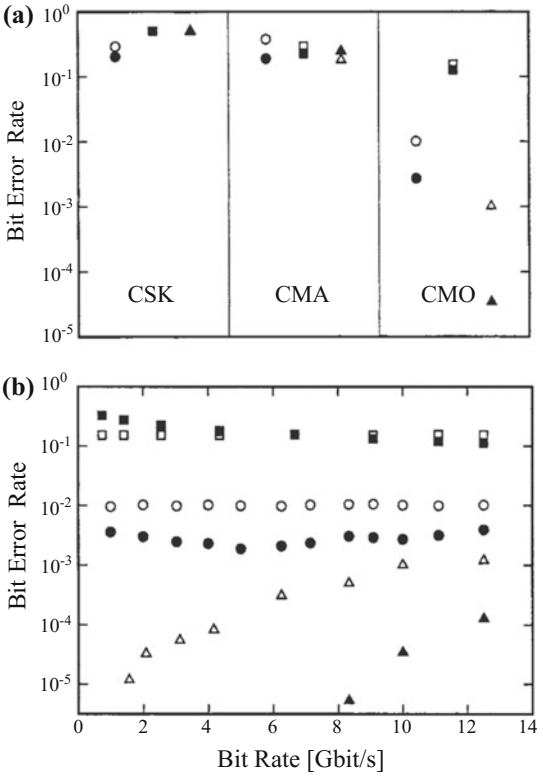

Fig. 13.19 Performance of BER. **a** BERs for optical injection system (marked as *circles*), optical feedback system (marked as *squares*), and optoelectronic feedback system (marked as *triangles*) of three different encryption schemes. The *solid* symbols mark the BER after the filtering, and the *open* symbols mark the BER before the filtering. **b** BER versus bit rate for three systems under CMO. The meanings of the symbols are the same as those in **a**. The relaxation oscillation frequency of the lasers is assumed to be 12 GHz [after Liu et al. (2002b); © 2002 IEEE]

Namely, one cannot achieve chaos synchronization in the system without knowing parameters as a key for communications even if one can know the system configurations. Chaotic communications are essentially hardware-based techniques. However, we can make a virtual system of the chaotic communication on computer software when we know completely the system configurations and their mathematical descriptions. Even for such a case, it is still difficult to imitate the synchronous chaotic signal without knowing each system parameter value. Therefore, the tolerance for the parameter mismatch is quite important for the realization of secure chaotic communications and we require systems that have strict conditions for the parameter mismatches for communications. However, as noted, there is a tradeoff of the difficulty for the range of synchronization in real systems.

One of the aspects of the security of messages hidden in chaotic waveforms is the difficulty of separating the message from the chaotic carrier by analyzing recorded waveforms. It has been demonstrated that systems with low-dimensional chaos are not secure for data transmissions, in the sense that a low-dimensional attractor is easily reconstructed from time series data, and system parameters are easily estimated from this attractor (Short 1994, 1996). Decoding without knowing key parameters becomes more difficult with the increase of the dimension of the

chaotic dynamics (Dachselt and Schwarz 2001). The chaotic signal from a semiconductor laser with optical feedback, as described by the theoretical model, is embedded in an infinite dimensional system due to the delay. However, the actual dimension of the dynamics is typically much lower, being restricted by the intrinsic response times in the laser. Quantitative analysis of the dimension of the synchronized chaos and the degree of security remains an important challenge for future study. Here, we limit our discussion to the issue of the matching of the receiver laser for message recovery by synchronization.

Another important issue is the noise problem. Not only optical and electronic circuits to generate chaotic signals but also optical channels include noises; however, there is little study on the effects of noises on the performance of chaotic communications. The result of Fig. 13.19 is such an instance. It is a well-known result that chaos is sensitive to the initial conditions of the system. When the systems include noises, it may be considered that they disturb the systems and the receiver is not able to output synchronous oscillations even if the two nonlinear systems consist of the same components and have the same parameters. Contrary to the expectations, two nonlinear systems can synchronize with each other even they include noises. This fact is verified by numerical simulations and experiments, although the basis for the phenomenon has not been theoretically proved yet. Chaos induced by the nonlinearity of a system and statistical noises are completely separated and the system seems to discriminate them. Although noises are additive to chaotic signals, a chaotic evolution of a system is essentially determined by the pure initial conditions of the system without noises. For example, a chaotic attractor has slight deviations from the original one in the presence of noises, but the chaotic route and chaotic dynamics do not change, while, for example, the maxima and minima of the output in fixed and periodic states in the bifurcation are not points but have finite widths due to the external noises.

There are two types of chaos synchronization; one is complete chaos synchronization and the other is generalized chaos synchronization. In the following, we discuss the differences of the security in chaotic communications between the two types of synchronization. Take as an example optical feedback systems. As shown in Fig. 12.7, complete chaos synchronization is only realized at zero frequency detuning and a lower optical injection in the map of the unstable injection-locking region. On the other hand, generalized chaos synchronization is attained in a wide range of frequency detuning and optical injection in the stable injection-locking region. From the standpoint of security, the conditions for generalized chaos synchronization are loose compared with those for the complete case. We have investigated the effects of mismatches of the laser device parameters for chaos synchronization in Fig. 12.8. In that case, good synchronization is attained for a very small range of the parameter mismatches in complete chaos synchronization and the accuracy of synchronization rapidly becomes worse for the increase of the parameter mismatches. On the other hand, the tolerance for the parameter mismatches is rather large for the case of the generalized chaos synchronization. Strict conditions are imposed for the case of complete chaos synchronization and, as a result, the security is better than that of generalized chaos synchronization. As a

whole, the scheme of complete chaos synchronization is suited for chaotic communications with respect to a high degree of security.

Another interest concerning the security of chaotic communications is the dependence of the system structures, namely the system is either open loop or closed loop. Each system has advantages and disadvantages as discussed in the preceding sections. Since the receiver is not subject to feedback in the open-loop system, this configuration is mechanically more stable and easier to implement compared with the closed-loop system. The open-loop system is also very robust against frequency detuning and small parameter mismatch, and has a shorter resynchronization time. On the contrary, the closed-loop is less stable in spite of high degree of synchronization. Therefore, not only the device parameters but also the external conditions have to be matched within high precision, otherwise the synchronization quality is greatly deteriorated. In general, the closed-loop system is less robust than the open-loop system and has a longer resynchronization time. However, the degree of synchronization in the open-loop system is worse than that in the closed loop, especially when the open loop is working in the strong injection regime. The use of large amplitude modulations makes the message less encrypted. Soriano et al. (2009) investigated the degree of security in a system of semiconductor lasers with optical feedback. They used the average mutual information as a measure for correlations between two signals and tested for a CMO system both for the open and closed configurations. As results, they numerically found that higher privacy and security could be achieved when the closed-loop scheme is used in the receiver architecture, instead of the open-loop scheme.

The methods of analog chaotic communications are based on the technique of embedding or hiding a message into a chaotic carrier as a secure code. The study of the security issue is still under way. Finally, we here briefly address other alternative techniques proposed at present. Among them, the method of code scrambling based on chaotic signal generations as discrete-sequence optical CDMA is used for chaos communications as digital techniques as discussed before (Kennedy et al. 2000). In the meanwhile, the study has been carried out on developing chaotic algorithms, algorithms using the iteration of nonlinear functions, to efficiently generate random sequences with improved randomness and correlation properties for use in spread-spectrum, code-division multiplexing and error correction (Chen and Wornell 1998; Chen et al. 2001; Uchida et al. 2003a). Since a chaotic time series is truly an irregular oscillation, which is not predictable for the future. Using this property, one can generate fast physical random numbers from such as chaos from semiconductor lasers. Such example is treated in Chap. 15. In any event, it is noted that the methods of analog message encoding and decoding discussed here may not be the best ones for secure optical communications for chaotic data transmissions or for ultimate secure communication systems.

13.9 Chaotic Carrier and Bandwidth of Communications

The relaxation oscillation frequency is an important indicator of the maximum possible rate of data transmissions in chaotic systems of semiconductor lasers. The relaxation oscillation frequency ν_R of the solitary laser is given by $\nu_R = \sqrt{gS/\tau_{ph}}/2\pi$ (see (3.87)). The relaxation oscillation frequency of currently available semiconductor lasers is of the order of several GHz to 10 GHz. Chaotic variations in semiconductor lasers has a broad spectrum and the attainable maximum frequency is usually larger than the relaxation oscillation frequency of the solitary lasers. Therefore, we can transmit a signal, which contains higher frequency components than the relaxation oscillation. For example, a message that contains more than the frequency components over 10 GHz was successfully transmitted in a chaotic communication system (Liu et al. 2001b). Also, over 100 Mbps messages were transmitted through a communication channel composed of systems of solid-state lasers that had a relaxation oscillation frequency of less than several MHz (VanWiggeren and Roy 1998a, b).

The semiconductor laser with a high frequency of chaotic carrier is desirable as a light source of chaotic communications to perform high data-rate transmission. Semiconductor laser with fast response is also essential for other applications such as common optical communications and mass-data storage systems. By carefully choosing parameters of semiconductor materials and device structures, the effort for fabricating faster response semiconductor lasers is still ongoing. However, the attainable frequency for the relaxation oscillation is limited only by improving the materials and the device structures. On the other hand, the relaxation oscillation frequency can be greatly enhanced by strong optical injection from different lasers as discussed in Sect. 6.3.2. Wang et al. (1996) theoretically investigated the enhancement of the relaxation oscillation frequency of a semiconductor laser by using a small signal stability analysis of the laser rate equations at the stable injection-locking steady-state and gave an example where the relaxation oscillation frequency of the injected laser at the solitary oscillation of 3 GHz was increased up to 12 GHz by strong optical injection. Thus, a semiconductor laser with enhanced modulation bandwidth by strong optical injection is effective as a light source for chaotic communications with the capability of faster data transmissions.

The receiver laser does not respond immediately after the transmitter signal is injected to the receiver laser and a finite transition time is required for synchronization. The transition time depends on the device parameters and the system configurations. We again consider a particular example. The model is an optical feedback system and the scheme of CSK. The synchronization recovery time affects the quality of synchronization especially in ON/OFF CSK systems. The transition time is directly governed by the synchronization recovery time. So far, there have been few systematic studies of the recovery time for chaos synchronization. Vicente et al. (2002) investigated the synchronization recovery time for open- and closed-loop systems of semiconductor lasers with optical feedback. Figure 13.20 shows the numerical results of the synchronization time as a function of the external

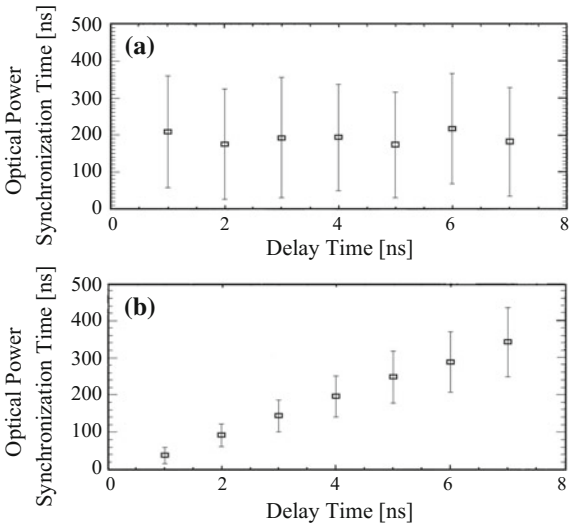

Fig. 13.20 Synchronization recovery time as a function of the external-cavity round-trip time in semiconductor lasers with optical feedback. The message-encoding scheme is CSK. **a** Open-loop and **b** closed-loop systems [after Vicente et al. (2002); © 2002 IEEE]

cavity round trip time τ of the transmitter system. In Fig. 13.20a, the recovery time is independent of the delay time in the open-loop system and the average time required for the synchronization is very small, about 0.2 ns. The reason for the constant delay time for the variation of the external cavity length is that the receiver laser does not need to adjust the time of synchronization for the parameters of the external cavity length, since the external cavity does not exist in the receiver of the open-loop system. On the other hand, the recovery time of the closed-loop system increases for the increase of the external cavity length (delay time). The time required in this case is much longer than that of the open-loop system. It is of the order of several tens of nanoseconds. In actual fact, there exist sudden bursts of synchronization even after chaos synchronization is achieved. This burst behavior also degrades the quality of chaos communications and the property of synchronization bursts remains an important problem.

13.10 Chaos Communications in the Real World

13.10.1 Chaos Masking Video Signal Transmissions

Many theoretical studies have been reported for secure communications using chaotic semiconductor lasers. Also, at the laboratory level, experimental chaotic communications have been demonstrated for data transmissions of sinusoidal signals and pseudorandom bit-sequence signals based on various data encryption

methods. However, only a few studies have been reported on chaotic data transmission for real data. Larger et al. (2001) demonstrated data transmission of voice signals using chaotic semiconductor lasers with EO feedback through wavelength filters, which is the same system as discussed in Sect. 7.4. In that system with a CMO scheme, an AM voice signal encrypted into transmitter chaos is transmitted on a radio frequency and the signal is successfully decrypted in the receiver system. In the following, we show another example of real world data transmissions of video signals at 2.4 GHz sideband frequency embedded into chaotic carrier in semiconductor lasers with optical feedback.

Figure 13.21 shows a CMA system for video data transmission using a chaotic generator of semiconductor laser with optical feedback (Annovazzi-Lodi et al. 2005). The light source is a DFB semiconductor laser of an oscillation wavelength at 1.55 μm. To make the laser chaotic oscillations, the emitted light is fed back from a tip of a transmission fiber, which is located at 3 cm from the laser facet. The DFB lasers used were selected between first neighbors on the same wafer. As a chaos synchronization system, the system is an open-loop configuration and there is no optical feedback in the receiver system. The injection current is biased at $1.5I_{th}$ and the value of each parameter for the transmitter and receiver lasers, such as bias injection currents and temperatures, is finely tuned to coincide with each other. The levels both for the optical feedback in the transmitter and the transmission signal from the transmitter to receiver laser is set to be around 1% in the experiment. A message is obtained as a modulation of another DFB laser and is added to chaotic

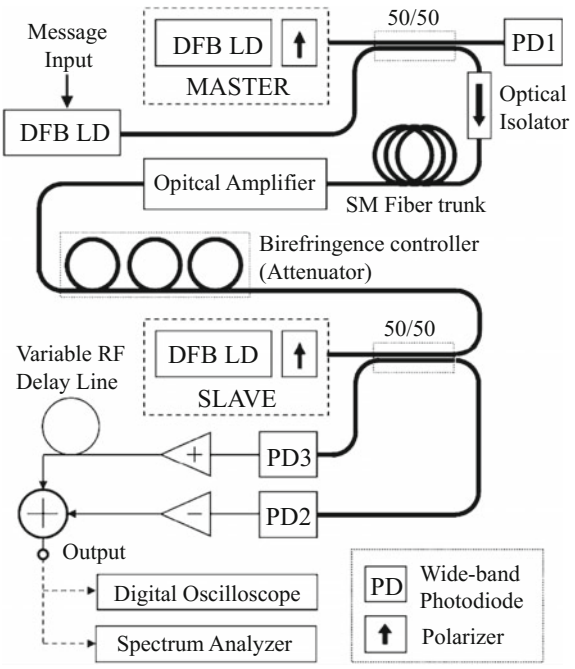

Fig. 13.21 Video signal encoding and decoding system using a chaos masking method with 1.2 km fiber transmission [after Annovazzi-Lodi et al. (2005); © 2005 IEEE]

transmission signal (signal from Master laser) though 50/50 fiber coupler. The fiber length of the data transmission between the transmitter and the receiver is of about 1.2 km. After transmission, the signal is amplified through a semiconductor optical amplifier to increase the maximum injection level from the transmitter into the receiver. Then, the signal passed through a birefringence controller to trim and adjust the injection level to the receiver laser. Subtracting from the reproduced chaotic signal from the transmitted one, the decoded message is recovered. The type of chaos synchronization in this system is one for generalized synchronization (injection and amplification synchronization).

Figure 13.22 shows the results of data transmissions for a still TV pattern. In the system, a composite video signal with amplitude-modulated frequency at 2.4 GHz is used as a message. The quality of the received signal has been evaluated after synchronous detection and baseband filtering at the receiver output node. The signal amplitude has been adjusted as a compromise among efficient masking, low signal distortion, and good quality of the recovered message. In Fig. 13.22, three photographs of the monitor screen are shown. Figure 13.22a is an original pattern to be transmitted without added chaos. Figure 13.22b shows the picture hidden within chaos and represents the message as it would be recovered by an eavesdropper. Figure 13.22c shows the extracted message after synchronization. The signal level has been adjusted as a tradeoff between sufficient image masking by chaos and acceptable image quality after chaos cancelation. Figure 13.22c is obtained by setting the AM sideband level at about 4 dB over chaos. In these conditions, the SNR of S/N = 16–18 dB is obtained for the decoded message.

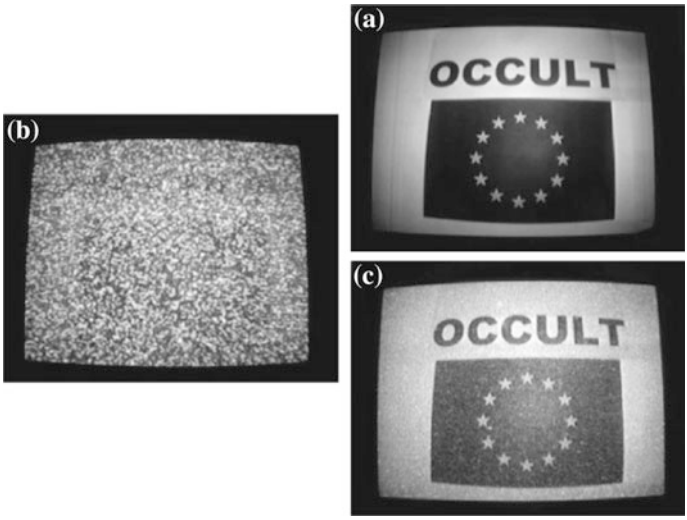

Fig. 13.22 TV frames of a still image transmitted by the setup of Fig. 13.21. **a** Original image to be send, **b** encoded pattern with chaotic signal, and **c** decoded pattern [after Annovazzi-Lodi et al. (2005); © 2005 IEEE]

13.10.2 *Chaotic Signal Transmissions Through Public Data Link*

Argyris et al. (2005) tested the effectiveness of chaotic data transmission in the existing public optical communication links. They employed two chaotic communication systems using semiconductor lasers as light sources; one is an EO open-loop system and the other is all optical open-loop system both based on CMA technique. Figure 13.23 shows the schematics of the systems. Figure 13.23a shows a chaotic EO synchronization system. In this system, chaos is not generated from the nonlinearity of the semiconductor laser itself but from the nonlinear delayed response of light due to delayed optoelectronic hybrid feedback through EO modulator (an integrated EO Mach–Zehnder interferometer: MZ). The system has very high response over 10 GHz and is frequently used as a chaos generator (Gibbs 1985; Davis 1990). The lasers used are DFB semiconductor lasers with an oscillation

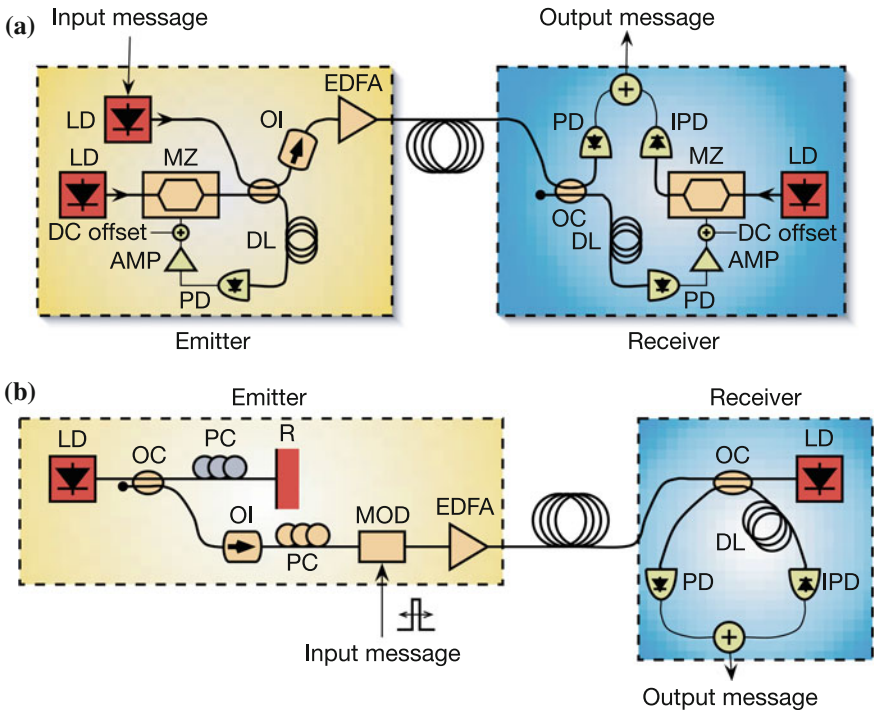

Fig. 13.23 Setups for two optical chaos communication systems. **a** Electro-optic open-loop system. **b** All optical open-loop system. *LD* laser diode, *MZ* electro-optic Mach–Zehnder interferometer, *PD* photodiode, *AMP* electronic amplifier, *OI* optical isolator, *DL* delay line, *EDFA* erbium-doped fiber amplifier, *OC* optical fiber coupler, *IPD* sign-inverting amplified photodiode, *R* digital variable reflector, *PC* polarization controller, *MOD* modulator [after Argyris et al. (2005); © 2005 Nature Pub.]

wavelength of 1.55 μm. A message to be sent, generated from another DFB laser, is simply added to chaotic signals through a 50/50 fiber coupler, which is an additive CMA scheme. The bandwidth of the system estimated is about 7 GHz.

Figure 13.23b shows the second case of all optical system. The transmitter is a DFB semiconductor laser subjected to optical feedback from a digital variable reflector (R) located 6 m from the laser. The system is almost the same as one for the video signal transmission system in the previous subsection. A polarization controller (PC) is used within the cavity to adjust the polarization state of the light reflected back from the variable reflector. The message is added via a $LiNbO_3$ Mach–Zehnder modulator (MOD) at the transmitter's output. The scheme is multiplicative CMA. The bandwidth of the all-optical system is less than that of the EO system and it is about 5 GHz. In both schemes, an erbium-doped fiber amplifier (EDFA) is used to compensate for the power lost upon transmission. Decoding is performed via subtraction of the transmitted signal from the signal filtered by the receiver. Operationally, the subtraction is performed by adding the photocurrents coming from an ordinary and a sign-inverting amplified photodiode (PD and IPD, respectively). Also the type of chaos synchronization in this system is one for generalized synchronization as is usually the case for real chaos communication systems.

Figure 13.24 shows the results for laboratory experiments of eye diagrams in the EO setup after transmission of a binary message through single-mode optical fiber of 50 km and dispersion compensation fiber of 6 km. The message is a pseudo-random bit sequence of $2^7 - 1$ bits and the transmission rate is 3 Gbps. The observed BERs are of the order of 10^{-7}. As already discussed, the performance of data transmission for all optical scheme is usually poor compared with that for the EO system. The transmission rate to attain the similar performance of BER as that in the EO system is about 1 Gbps.

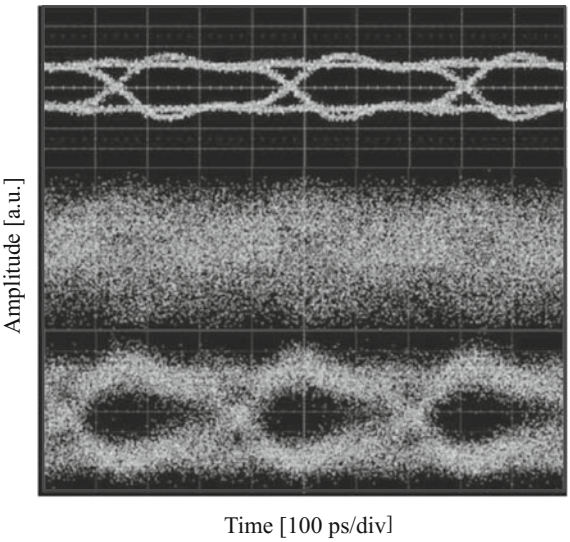

Fig. 13.24 Laboratory test of eye diagrams in the electro-optic system through 50 km fiber transmission. *Top trace* test message, *middle trace* encoded signal, *bottom trace* decoded message [after Argyris et al. (2005); © 2005 Nature Pub.]

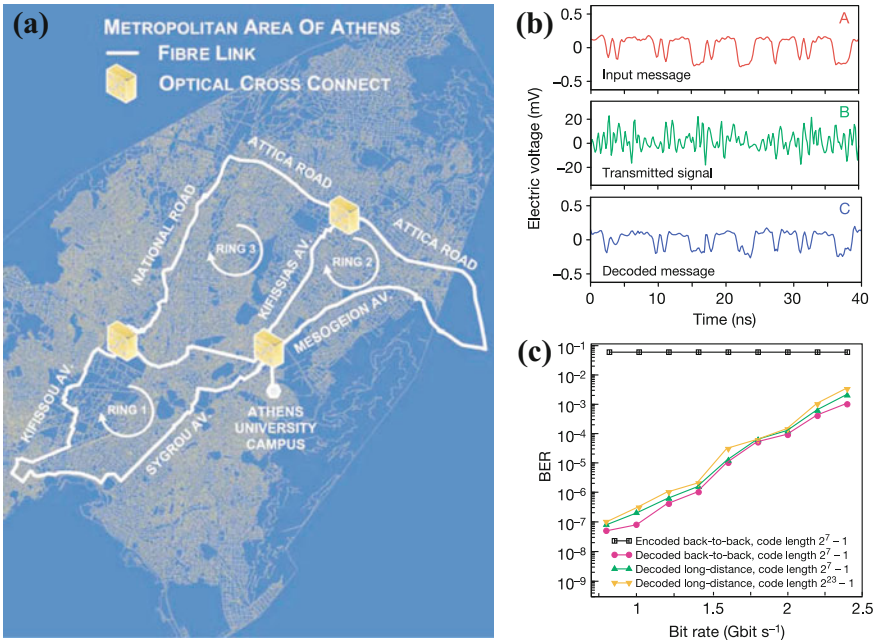

Fig. 13.25 Field experiment of fiber transmission. **a** Chaos-encoded data transmissions in the optical communication network of Athens, Greece. **b** Time trances of 1 Gbps message. *Trace A* applied message of BER $< 10^{-12}$, *trace B* carrier with the encoded message of BER $\approx 6 \times 10^{-2}$, *trace C* recovered message after 120 km transmission of BER $\approx 10^{-7}$. **c** Bit error rate (BER) performance. *Squares* encoded signal, *circles* back-to-back decoded message, *triangles* decoded message after transmission for two different code lengths [after Argyris et al. (2005); © 2005 Nature Pub.]

To test performance under 'real-world' conditions of chaotic communications, the chaos-based all optical transmission system were implemented using an installed optical network infrastructure of single-mode fiber belonging to the metropolitan area network of Athens, Greece. The network has a total length of 120 km. The topology consists of three fiber rings, linked together at specific cross-connect points as shown in Fig. 13.25a. Through three cross-connect points, the transmission path follows the Ring-1 route, then the Ring-2 route, and finally the Ring-3 route. To cancel the chromatic dispersion that would be induced by the single-mode fiber transmission, a dispersion compensation fiber module is used in the link. Also, to compensate the optical losses and filtering of amplified spontaneous emission noise, EDFA and optical filters are used along the optical link. The pair of lasers of the transmitter and the receiver is selected to exhibit parameter mismatches that are constrained below 3%. The mean optical power injected into the receiver has been limited to 0.8 mW, to avoid possible damage of the anti-reflective coating of the slave laser. Test messages are NRZ pseudo-random bit sequences applied by externally modulating the chaotic carrier by means of a modulator. The message

amplitude is attenuated by 14 dB with respect to the carrier to maintain the message security in the communications. As a result, the BER of the transmitted signal after filtering is always larger than 6×10^{-2}, which is the instrumentation limit. A good synchronization performance of the transmitter–receiver setup leads to an efficient cancellation of the chaotic carrier and, thus, satisfactory decoded messages are obtained as shown in Fig. 13.25b. Figure 13.25c shows the performance of the chaotic transmission system for different message bit rates up to 2.4 Gbps for two different code lengths of $2^7 - 1$ and $2^{23} - 1$. All BER values have been measured after filtering the subtracted electric signal, by using low-pass filters with bandwidth adjusted each time to the message bit rate. For transmission rates in the gigabit per second range, the recovered message exhibits BER values lower than 10^{-7}. For higher transmission rates, the corresponding BERs increase due to the fact of imperfect synchronization, as shown in Fig. 13.25c. For the implementation of chaos systems in real optical communication networks, system integrations as compact chips for chaotic light generators are indispensable. We will present the development of photonic integrated circuits for chaotic light generators in Chap. 15.

References

H.D.I. Abarbanel, M.B. Kennel, L. Illing, S. Tang, H.F. Chen, J.M. Liu, Synchronization and communication using semiconductor lasers with optoelectronic feedback. IEEE J. Quantum Electron. **37**, 1301–1311 (2001)

V. Annovazzi-Lodi, S. Donati, A. Sciré, Synchronization of chaotic injected-laser systems and its application to optical cryptography. IEEE J. Quantum Electron. **32**, 953–959 (1996)

V. Annovazzi-Lodi, S. Donati, A. Sciré, Synchronization of chaotic lasers by optical feedback for cryptographic applications. IEEE J. Quantum Electron. **33**, 1449–1454 (1997)

V. Annovazzi-Lodi, M. Benedetti, S. Merlo, M. Norgia, B. Provinzano, Optical chaos masking of video signals. IEEE Photonics Technol. Lett. **17**, 1995–1997 (2005)

V. Annovazzi-Lodi, G. Aromataris, M. Benedetti, S. Merlo, Secure chaotic transmission on a free-space optics data link. IEEE J. Quantum Electron. **44**, 1089–1095 (2008)

V. Annovazzi-Lodi, G. Aromataris, M. Benedetti, M. Hamacher, S. Merlo, V. Vercesi, Close-loop three-laser scheme for chaos-encrypted message transmission. Opt. Quant. Electron. **42**, 143–156 (2010a)

V. Annovazzi-Lodi, G. Aromataris, M. Benedetti, Private message transmission by common driving of two chaotic lasers. IEEE J. Quantum Electron. **46**, 258–264 (2010b)

A. Argyris, D. Syvridis, L. Larger, V. Annovazzi-Lodi, P. Colet, I. Fischer, J. Garcia-Ojalvo, C.R. Mirasso, L. Pesquera, A.K. Shore, Chaos-based communications at high bit rates using commercial fibre-optic links. Nature **438**, 343–346 (2005)

T.L. Carroll, M.L. Pecora, Synchronizing chaotic circuits. IEEE Trans. Circuits Syst. **38**, 453–456 (1991)

B. Chen, G. Wornell, Analog error-correcting codes based on chaotic dynamical systems. IEEE Trans. Commun. **46**, 881–890 (1998)

C.C. Chen, K. Yao, K. Umeno, E. Biglieri, Design of spread-spectrum sequences using chaotic dynamical systems and ergodic theory. IEEE Trans. Circuits Syst. I **48**, 1498–1509 (2001)

P. Colet, R. Roy, Digital communication with synchronized chaotic lasers. Opt. Lett. **19**, 2056–2058 (1994)

K.M. Cuomo, A.V. Oppenheim, S.H. Stogatz, Synchronization of Lorenz-based chaotic circuits with applications to communications. IEEE Trans. Circuits Syst. II **40**, 626–633 (1993)

F. Dachselt, W. Schwarz, Chaos and cryptography. IEEE Trans. Circuits Syst. I **48**, 1498–1500 (2001)
P. Davis, Application of optical chaos to temporal pattern search in a nonlinear optical resonator. Jpn. J. Appl. Phys. **29**, L1238–L1240 (1990)
P. Davis, Y. Liu, T. Aida, Chaotic wavelength hopping device for multi-wavelength optical communications. IEEE Trans. Circuits Syst. I **48**, 1523–1527 (2001)
H.M. Gibbs, *Optical Bistability: Controlling Light with Light* (Academic Press, New York, 1985)
J.P. Goedgebuer, L. Larger, H. Porte, Optical cryptosystem based on synchronization of hyperchaos generated by a delayed feedback tunable laser diode. Phys. Rev. Lett. **80**, 2249–2252 (1998)
T. Heil, I. Fischer, W. Elsäßer, Chaos synchronization and spontaneous symmetry-breaking in symmetrically delay-coupled semiconductor lasers. Phys. Rev. Lett. **89**, 795–798 (2001)
T. Heil, J. Mulet, I. Fischer, C.R. Mirasso, M. Peil, P. Colet, W. Elsäßer, ON/OFF phase shift keying for chaos-encrypted communication using external-cavity semiconductor lasers. IEEE J. Quantum Electron. **38**, 1162–1169 (2003)
R.J. Jones, S. Sivaprakasam, K.A. Shore, Integrity of semiconductor laser chaotic communications to naïve eavesdroppers. Opt. Lett. **22**, 1663–1665 (2000)
M.P. Kennedy, R. Rovatti, G. Setti, *Chaotic Electronics in Telecommunications* (CRC Press, Boca Raton, 2000)
E. Klein, N. Gross, E. Kopelowitz, M. Rosenbluh, L. Khaykovich, W. Kinzel, I. Kanter, Public channel cryptography based on mutual chaos pass filters. Phys. Rev. E **74**, 046201-1–046201-4 (2006)
K. Kusumoto, J. Ohtsubo, 1.5-GHz message transmission based on synchronization of chaos in semiconductor lasers. Opt. Lett. **27**, 989–991 (2002)
L. Larger, J.P. Goedgebuer, F. Delorme, Optical encryption system using hyperchaos generated by an optoelectronic wavelength oscillator. Phys. Rev. E **57**, 6618–6624 (1998)
L. Larger, J.P. Goedgebuer, V.S. Udaltsov, W.T. Rhodes, Radio-transmission system using high dimensional chaotic oscillator. Electron. Lett. **37**, 594–595 (2001)
Y. Liu, P. Davis, Synchronized chaotic mode hopping in DBR lasers with delayed opto-electric feedback. IEEE J. Quantum Electron. **37**, 337–352 (2001)
J.M. Liu, H.F. Chen, S. Tang, Optical-communication systems based on chaos in semiconductor lasers. IEEE Trans. Circuits Syst. I **48**, 1475–1483 (2001a)
J.M. Liu, H.F. Chen, S. Tang, Synchronization of chaos in semiconductor lasers. Nonlinear Anal. **47**, 5741–5751 (2001b)
Y. Liu, H.F. Chen, J.M. Liu, P. Davis, T. Aida, Communication using synchronization of optical-feedback-induced chaos in semiconductor lasers. IEEE Trans. Circuits Syst. I **48**, 1484–1490 (2001c)
Y. Liu, Y. Takiguchi, P. Davis, T. Aida, S. Saito, J.M. Liu, Experimental observation of complete chaos synchronization in semiconductor lasers. Appl. Phys. Lett. **80**, 4306–4308 (2002a)
J.M. Liu, H.F. Chen, S. Tang, Synchronized chaotic optical communications at high bit rates. IEEE J. Quantum Electron. **38**, 1184–1196 (2002b)
L.G. Luo, P.L. Chu, H.F. Liu, 1-GHz Optical communication system using chaos in erbium-doped fiber lasers. IEEE Photonics Technol. Lett. **12**, 269–271 (2000)
C.R. Mirasso, P. Colet, P. Garcia-Fernandez, Synchronization of chaotic semiconductor lasers: application to encoded communications. IEEE Photonics Technol. Lett. **8**, 299–301 (1996)
C.R. Mirasso, J. Mulet, C. Masoller, Chaos shift-keying encryption in chaotic external-cavity semiconductor lasers using a single-receiver scheme. IEEE Photonics Technol. Lett. **14**, 456–458 (2002)
R. Mislovaty, E. Klein, I. Kanter, W. Kinzel, Public channel cryptography by synchronization of neural networks and chaotic maps. Phys. Rev. Lett. **91**, 118701-1–118701-4 (2003)
A. Murakami, K.A. Shore, Chaos-pass filtering in injection-locked semiconductor lasers. Phys. Rev. A **72**, 053810-1–053810-8 (2005)
A. Murakami, K.A. Shore, Analogy between optically driven injection-locked laser diodes and driven damped linear oscillators. Phys. Rev. A **73**, 043804-1–043804-9 (2006)

J. Ohtsubo, Chaotic dynamics in semiconductor lasers with optical feedback (Chap.1), in *Progress in Optics,* vol. 44, ed. by E. Wolf (North-Holland, Amsterdam, 2002a)
J. Ohtsubo, Chaos synchronization and chaotic signal masking in semiconductor lasers with optical feedback. IEEE J. Quantum Electron. **38**, 1141–1154 (2002b)
J. Ohtsubo, P. Davis, Chaotic optical communication (Chap.10), in *Unlocking Dynamical Diversity–Optical Feedback Effects on Semiconductor Lasers,* ed. by D. Kane, K.A. Shore (Wiley, Chichester, 2005)
J. Paul, M.W. Lee, K.A. Shore, Effects of chaos pass filtering on message decoding quality using chaotic external-cavity laser diodes. Opt. Lett. **29**, 2497–2499 (2004)
L.M. Pecora, T.L. Carroll, Driving systems with chaotic signals. Phys. Rev. A **44**, 2374–2384 (1991)
X. Porte, M.C. Soriano, D. Brunner, I. Fischer, Bidirectional private key exchange using delay-coupled semiconductor lasers. Opt. Lett. **41**, 2871–2874 (2016)
F. Rogister, A. Locquet, D. Pieroux, M. Sciamanna, O. Deparis, P. Megret, M. Blondel, Secure communication scheme using chaotic laser diodes subject to incoherent optical feedback and incoherent optical injection. Opt. Lett. **26**, 1466–1469 (2001)
A. Sánchez-Díaz, C.R. Mirasso, P. Colt, P. García-Fernández, Encoded Gbit/s digital communications with synchronized chaotic semiconductor lasers. IEEE J. Quantum Electron. **35**, 292–296 (1999)
K.M. Short, Step toward unmasking secure communications. Int. J. Bifurcat. Chaos **4**, 959–979 (1994)
K.M. Short, Unmasking a modulated chaotic communication scheme. Int. J. Bifurcat. Chaos **6**, 367–375 (1996)
S. Sivaprakasam, K.A. Shore, Signal masking for chaotic optical communication using external-cavity diode lasers. Opt. Lett. **24**, 1200–1202 (1999)
S. Sivaprakasam, K.A. Shore, Critical signal strength for effective decoding in diode laser chaotic optical communications. Phys. Rev. E **61**, 5997–5999 (2000a)
S. Sivaprakasam, K.A. Shore, Message encoding and decoding using chaotic external-cavity diode lasers. IEEE J. Quantum Electron. **36**, 35–39 (2000b)
M.C. Soriano, P. Colet, C.R. Mirasso, Security implications of open- and closed-loop receivers in all-optical chaos-based communications. IEEE Photonics Technol. Lett. **21**, 426–428 (2009)
S. Tang, J.M. Liu, Message encoding/decoding at 2.5 Gbits/s through synchronization of chaotic pulsing semiconductor lasers. Opt. Lett. **26**, 1843–1845 (2001)
S. Tang, H.F. Chen, J.M. Liu, Stable route-tracking synchronization between two chaotically pulsing semiconductor lasers. Opt. Lett. **26**, 1489–1491 (2001)
A. Uchida, *Optical Communication with Chaotic Lasers* (Wiley-VCH, Weinheim, 2012)
A. Uchida, P. Davis, S. Itaya, Generation of information theoretic secure keys using a chaotic semiconductor laser. Appl. Phys. Lett. **83**, 3213–3215 (2003a)
A. Uchida, P. Davis, Y. Liu, Characteristics of chaotic masking in synchronized semiconductor lasers. IEEE J. Quantum Electron. **39**, 963–970 (2003b)
A. Uchida, K. Amano, M. Inoue, K. Hirano, S. Naito, H. Someya, I. Oowada, T. Kurashige, M. Shiki, S. Yoshimori, K. Yoshimura, P. Davis, Fast physical random bit generation with chaotic semiconductor lasers. Nat. Photonics **2**, 728–732 (2008)
G.D. VanWiggeren, R. Roy, Communication with chaotic lasers. Science **279**, 1198–1200 (1998a)
G.D. VanWiggeren, R. Roy, Optical communication with chaotic waveforms. Phys. Rev. Lett. **81**, 3547–3550 (1998b)
R. Vicente, T. Pérez, C.R. Mirasso, Open-versus closed-loop performance of synchronized chaotic external-cavity semiconductor lasers. IEEE J. Quantum Electron. **38**, 1197–1204 (2002)
R. Vicente, C.R. Mirasso, I. Fischer, Simultaneous bidirectional message transmission in a chaos-based communication scheme. Opt. Lett. **32**, 403–405 (2007)
J. Wang, M.K. Haldar, L. Li, V.C. Mendis, Enhancement of modulation bandwidth of laser diodes by injection locking. IEEE Photonics Technol. Lett. **8**, 34–36 (1996)
J.K. White, J.V. Moloney, Multichannel communication using an infinite dimensional spatiotemporal chaotic systems. Phys. Rev. A **59**, 2422–2426 (1999)

Chapter 14
Semiconductor Laser Networks: Synchrony, Consistency, and Analogy of Synaptic Neurons

Abstract Synchronization among coupled elements is universally observed in nonlinear systems, such as in food chain and coupled synaptic neurons as well as coupled semiconductor lasers. Using nonlinear elements showing similar characteristics of synaptic neurons, the behaviors of real neural networks can be effectively investigated and information processing that is similar to the human brain can be performed based on such systems. The typical features of neurons are excitability of the output from external stimuli, inhibition of conflicted inputs, spiking oscillations even including chaos, and synchronization among coupled neurons. As nonlinear dynamics point of view, semiconductor lasers have the similarity with synaptic neurons. Also, neuro-inspired information processing, which mimics the functions of the neuron dynamics, is discussed using nonlinear delay feedback systems such as a semiconductor lasers with optical feedback. The keys for common dynamics of such systems are the consistency of drive-response nonlinear systems and the synchronization properties between distant nonlinear elements. In this chapter, starting from a small number of coupled semiconductor lasers, we investigate the dynamics and synchronization properties of many coupled semiconductor laser networks. We also present a new type of information process and its application based on reservoir computing, in which a single semiconductor laser subjected to optical feedback is used as a reservoir in the neural networks.

14.1 Nonlinear Networks and Coupled Semiconductor Lasers

14.1.1 Coupled Nonlinear Networks

Other than chaotic semiconductor lasers, there are many nonlinear elements that exhibit chaotic dynamics and they have common characteristics. Before discussing the detailed dynamics of coupled nonlinear elements, we at first show an example of phenomena observed in many coupled nonlinear elements. The example is the crowd synchrony of the London Millennium footbridge that crosses the Thames.

© Springer International Publishing AG 2017

J. Ohtsubo, *Semiconductor Lasers*, Springer Series in Optical Sciences 111,
DOI 10.1007/978-3-319-56138-7_14

On its opening day in 2000, the bridge experienced large vibration, which was caused by synchronous lateral excitation by many random steps of the pedestrian walks (Strogatz et al. 2005). The stiffness of the bridge was not strong enough and the motion of the pedestrian forced damped harmonic oscillations of the bridge. Then, they are modeled by a dashpot with soft spring. In this model, many pedestrian crowding finally results in sway of bridge with synchronous way (Eckhardt et al. 2007). Namely, in the crowd synchrony, each pedestrian crossing the bridge is assumed as a nonlinear node and the dynamics induced by the many pedestrian walks on the bridge are modeled as coupled nonlinear networks. The sway of the bridge was finally avoided by improving the stiffness. This is a clear example of phenomena induced by many coupled elements in nonlinear networks. Such synchronization induced by many coupled nonlinear oscillators is sometimes called crowd synchrony. Phenomena of crowd synchrony are widely observed in networks of many coupled nonlinear oscillators and elements, even in biological systems (Strogatz and Stewart 1993). For example, it is well known that thousands of fireflies flash in a synchronous way even when they initially flash in a random manner in time. Each insect plays a role of a nonlinear element and it initially has its own rhythm to flash, but the sight of its neighbors' lights brings that rhythm in harmony with those around it. One of the important properties of these phenomena from a viewpoint of the dynamics is consistency (Uchida et al. 2004; Pérez and Uchida 2011) where the same response output can be observed by using a repeated drive signal.

14.1.2 Chaotic Semiconductor Lasers and Neurons

A system of many coupled synaptic neurons is a typical example of nonlinear networks. As a nonlinear element, neuron has the properties of excitability from external stimuli, inhibition to conflicted signals, oscillatory nature even including chaos, and ability of networking. The dynamics and the synchronization properties in real coupled synaptic neurons have experimentally been investigated and the numerical simulations to explain them have also done on the basis of the Hodgkin-Huxley model for the action potential of synaptic neuron (Hodgkin and Huxley 1952; Hansel et al. 1993; Traub et al. 1996; Beierlein et al. 2000; Guillery 2005). One of the most important features of the synaptic neuron networks is zero-lag synchronization among distant elements. Simultaneous firing between distant neurons induced by zero-lag synchronization is essential for information processing such as in the brain (Fukuda et al. 2006; Vicente et al. 2008; Soriano et al. 2013a). Despite the space separations and the time delay for signal transmissions, not only between a single neuron and another, but also between different groups of neurons indeed show synchronization at zero time delay (Fischer et al. 2006; Vicente et al. 2008). Zero-lag synchronization in nonlinear elements and groups of nonlinear elements plays an important role in information processing for solving complex problems, which are hard to carry out by a traditional digital

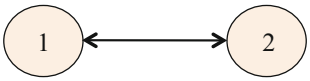

Fig. 14.1 Model of mutually coupled two nonlinear elements. A *circle* denotes a nonlinear element and an *arrow* with *straight line* represents signal transmission

computing, and compatibility among systems spaced in distant places eases the restriction of the use of them in spite of the existence of signal transmission delays. In general, the response time of synaptic neurons is on the order of milliseconds, however the time required signal transmission between neurons is ten times longer than the response time. On the other hand, photonics systems, such as chaotic semiconductor lasers, provide faster response time of nonlinear elements over nanosecond. Then, we can expect very fast signal handling in photonics.

There exist many nonlinear elements, which show similar dynamics to synaptic neurons, although they have not exactly the same characteristics as neurons (Milo et al. 2002). Chaotic semiconductor lasers also show the similar dynamics as those of synaptic neurons and also other nonlinear network elements. As a model of nonlinear network elements, semiconductor laser systems have the advantage of ease of treatments both for theory and experiments. One of the notable features of semiconductor lasers is the fast time response on the order of nanoseconds as discussed above. The appearance of zero-lag synchronization simply depends on the topological configuration of the networks rather than each property of a particular element to consist of nonlinear networks. For example, we consider a system of mutually coupled two nonlinear elements with symmetrical configuration in Fig. 14.1 (two mutually coupled nonlinear elements of any types). From the symmetry, we can expect zero-lag synchronization and, indeed, zero-lag synchronization is mathematically demonstrated on the basis of the numerical model without considering noises involved in the systems. However, real systems contain intrinsic noises in the nonlinear elements. In that case, symmetry breaking of isochronal synchronization occurs and, as a result, the leader element for synchronization alternately switches from one element to the other with time in a random manner. For example, real lasers contain intrinsic spontaneous emission noises and the phenomenon, which is called achronal synchronization, is observed in mutually coupled two semiconductor lasers as already discussed in Sect. 12.7.1 (Mulet et al. 2004). In the following, taking chaotic semiconductor laser as a nonlinear element, we investigate the dynamics and the synchronization properties, especially zero-lag synchronization in rather small number of coupling nodes.

14.1.3 Semiconductor Lasers as Chaotic Elements

We consider chaotic semiconductor lasers as nonlinear network elements and study the properties for zero-lag synchronization in the systems. We here use two

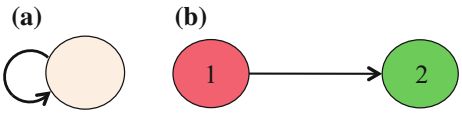

Fig. 14.2 Schematic illustration of fundamental chaotic elements in semiconductor laser systems. **a** Semiconductor laser with optical feedback. A *circle* denotes a semiconductor laser and a *semi-circle* with an *arrow* represents an optical feedback loop. **b** Optical injection in semiconductor lasers. An *arrow* with *straight line* denotes optical injection

fundamental systems in semiconductor lasers to consist of nonlinear chaotic networks. One of the methods to make a chaotic semiconductor laser is self-optical feedback, which is discussed in Chap. 4. The notation used in this chapter is shown in Fig. 14.2a. As already discussed, depending on the appropriate conditions of optical feedback and device parameters, the laser shows chaotic oscillations. The complex field in the presence of optical feedback is well defined in (4.2). Another important method to make chaotic semiconductor lasers is optical injection from an external master laser as shown in Fig. 14.2b. As discussed in Chap. 6, the optical injection technique is usually used to make a stable slave laser for amplitude, frequency, and optical phase depending on the appropriate optical injection strength and the frequency detuning between the master and slave lasers. However, outside of the stable optical injection-locking region in the phase space of the injection parameters, the laser shows periodic and even chaotic oscillations. The complex field for an optically injected semiconductor laser is defined in (6.1). We use these two schemes as fundamental elements (nodes) of nonlinear networks in coupled semiconductor lasers. In coupled semiconductor laser networks, the coupling conditions, namely, the strengths of optical feedback and optical injection, the delay time of optical feedback, and signal transmission delay from one laser to the other, play curial roles for synchronization of the systems.

Finally, let us remind two schemes of chaos synchronization. As discussed in Sect. 12.1.2, there are two types of chaos synchronization. These schemes are not only applied to the dynamics of chaotic semiconductor lasers but also those for other chaotic nonlinear elements. One is complete chaos synchronization, in which the two laser outputs perfectly show the same waveforms. In this case, the two systems are mathematically described by the equivalent differential equations. For example, when a chaotic signal from a semiconductor laser system is transmitted to the other, the receiver laser exactly exhibits synchronous oscillations before receiving chaotic signal from the transmitter. Therefore, the scheme is sometimes called anticipated chaos synchronization (see Sect. 12.1.2). The other scheme is generalized chaos synchronization, in which the receiver laser shows synchronous oscillations immediately after receiving the transmitter signal. Therefore, the time lag between the transmitter and receiver lasers is always equal to the transmission time of the chaotic signal. Generalized chaos synchronization is caused by optical injection and amplification in semiconductor lasers. In networks of many coupled semiconductor lasers, the two types of chaos synchronization are still observed.

14.2 Two Coupled Semiconductor Lasers

14.2.1 Two Unidirectionally Coupled Semiconductor Lasers

The simplest networks are two unidirectionally coupled semiconductor lasers already discussed in Sect. 12.2. They are used for chaotic secure communications. Again, we review and summarize the main points again. In Fig. 14.3a, when the device characteristics of two semiconductor lasers are almost the same and the conditions described in Sect. 12.2.4 are satisfied, complete chaos synchronization is attained. For the optical power balance, zero-lag synchronization in this system is realized when the optical feedback coefficient in laser 1 is equal to the optical injection coefficient from laser 1 to laser 2, i.e. $\kappa_{ex} = \kappa_{inj1,2}$ (κ_{ex} corresponds to κ in (4.2) and $\kappa_{inj1,2}$ corresponds to κ_{cp} in (12.11)). As for the conditions for the optical feedback delay τ_{ex} and the signal transmission time τ_{inj}, zero-lag synchronization is attained at $\tau_{ex} = \tau_{inj}$ [τ_{ex} corresponds to τ in (4.2), and τ_{inj} is equal to τ_c in (12.11)]. Then, the zero-lag synchronization corresponds to complete chaos synchronization and the delay between the two lasers becomes $\Delta t = \tau_{inj} - \tau_{ex} = 0$. Similarly, in the closed-loop systems, zero-lag synchronization is expected when the strengths of the optical feedback and the optical injection in the two lasers balance, $\kappa_{ex1} = \kappa_{inj1,2} + \kappa_{ex2}$, and the times of the optical feedback delay and the optical injection are the same, $\tau_{ex1} = \tau_{inj1,2} = \tau_{ex2}$. If the optical feedback strength and the optical injection power do not balance, the two lasers show generalized synchronization and the time lag between the two lasers becomes τ_{inj}, which is equal to the coupling time between them. Throughout this chapter, it is noted that the same color of lasers represents zero-lag synchronization, while different colors belong to different class of synchronization.

14.2.2 Two Mutually Coupled Semiconductor Lasers

Another example of two coupled semiconductor lasers is the configuration of a mutually coupled system as discussed in Sect. 12.7. Since the system in Fig. 14.4a has a symmetric layout and the two lasers are mathematically described by the same differential equations, we could expect zero-lag synchronization in the laser outputs without considering noises in the systems. However, despite the symmetry, the

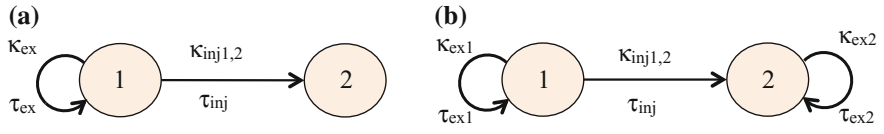

Fig. 14.3 Two unidirectionally coupled semiconductor lasers with optical feedback. **a** Open loop system and **b** closed loop system. κ_{ex} is the optical feedback coefficient and κ_{inj} is the optical coupling coefficient. τ_{ex} is the optical feedback delay and τ_{inj} is the optical injection time

system shows achronal chaos synchronization due to intrinsic spontaneous emission noises of the two lasers. The presence of laser noises induces symmetry breaking of synchronization and the leader laser for synchronization alternately switches from one laser to the other with time in a random manner (Heil et al. 2001). Theoretically, the potential model in the systems explains this symmetry breaking with noises as discussed in Sect. 12.7.1 (Mulet et al. 2004). Indeed, two mutually coupled semiconductor lasers become achronal synchronization as shown in the correlation plot between the two laser intensities in Fig. 14.5a and also the achronal synchronization is verified by the corresponding experiment in Fig. 14.5b. Therefore, we must take intrinsic laser noises into consideration in the following numerical calculations.

How can we realize zero-lag synchronization in a two mutually coupled semiconductor lasers? Remember the configuration in Fig. 14.3a. If the additional element, which enhances the nonlinearity, is attached to the system, the nonlinear elements could show synchronous oscillations between them. An achronal synchronization system in two mutually coupled lasers, such as in Fig. 14.4a, can be changed to a system of zero-lag synchronization when an optical feedback loop is added to one of the lasers. Then, we put an optical feedback loop to one of the lasers as shown in Fig. 14.4b. Laser 1 is driven by itself and also laser 2, while laser 2 is driven only by laser 1. In this case, the self optical-feedback plays a role for a driving force to the entire system and the two lasers show zero-lag synchronization. When the optical feedback time is equal to that of the coupling time between the two lasers, and the total optical power of optical injection and optical feedback in laser 1 is equal to the optical injection power from laser 1 to laser 2, the two lasers synchronize with zero-time delay. The delay and coupling times, τ_{ex} and τ_{inj}, are assumed to be the same here and after, otherwise noted. Also, the frequency detuning among semiconductor lasers is assumed to be zero, although it is an important factor for synchronization in real semiconductor lasers. Zero-lag synchronization in this system is demonstrated in Fig. 14.5c. We here assumed that the delay time τ_{ex} is equal to the signal transmission time τ_{inj} for the zero-lag condition,

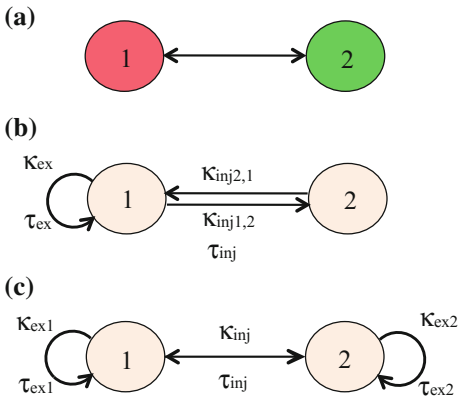

Fig. 14.4 Two mutually coupled semiconductor lasers. **a** Mutual coupling, **b** mutual coupling with a single optical feedback loop, and **c** mutual coupling with double optical feedback loops

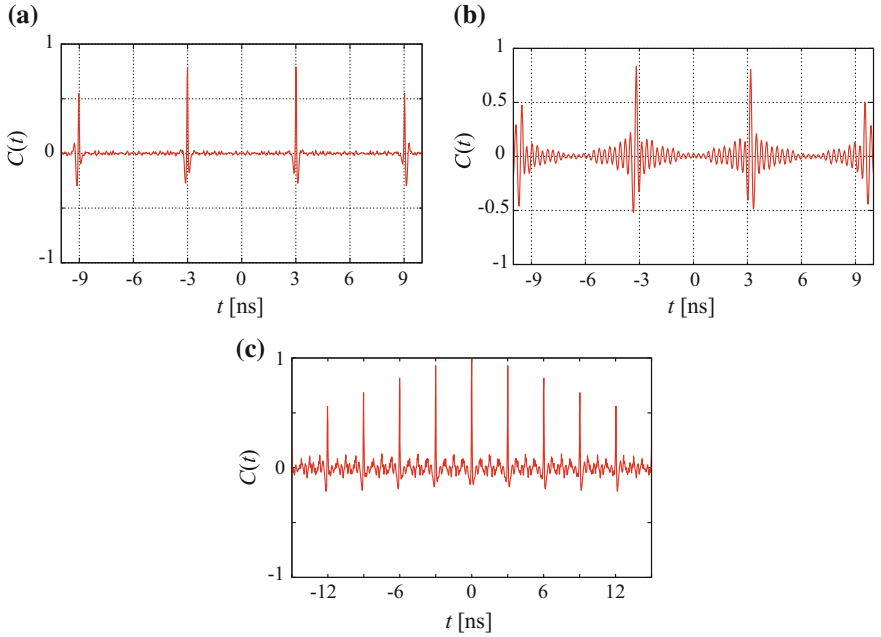

Fig. 14.5 Correlation $C(t)$ of the intensities of two mutually coupled semiconductor lasers. **a** Numerical calculation at $\kappa_{ex} = \kappa_{inj}$ ($r_{inj} = 0.3$) and $\tau_{ex} = \tau_{inj} = 3$ ns corresponding to Fig. 14.4a. r_{inj} is equal to the optical injection ratio defined in (6.2). **b** Experimental result at $\kappa_{ex} = \kappa_{inj}$ ($r_{inj} = 0.7$) and $\tau_{ex} = \tau_{inj} = 3$ ns corresponding to Fig. 14.4a. **c** Numerical calculation at $\kappa_{inj2,1} = \kappa_{ex}$ ($r_{inj2,1} = 0.15$), $\kappa_{inj1,2} = 2\kappa_{inj2,1}$ and $\tau_{ex} = \tau_{inj} = 3$ ns corresponding to Fig. 14.4b

however the relation between the times is rather loose. For example, if the condition $\tau_{ex} = 2\tau_{inj}$ holds, we can also expect zero-lag synchronization in this system. Similarly, zero-lag synchronization is attained when optical feedback loops are added both semiconductor lasers. Form the above discussions, the system symmetry is a condition for the zero-lag synchronization in chaotic semiconductor lasers. But the condition is not enough. The existence of a driving laser is one of the necessary conditions to realize zero-lag synchronization in nonlinear networks. This point will be clearly demonstrated in the following sections. Finally, it is noted that rather strong periodicity of the waveforms can be seen in the correlation function in Fig. 14.5c. The waveforms correspond to dynamic states of weak chaos (Heiligenthal et al. 2011, 2013). When a chaotic state is strong, periodicity in the intensity from a semiconductor laser is fairly suppressed and only small periodic signatures are visible in its autocorrelation function. In networks of coupled semiconductor lasers, the laser output shows either weak or strong chaotic state depending both on the optical coupling strength and the optical coupling time among lasers.

14.3 Three Coupled Semiconductor Lasers

14.3.1 Three Coupled Lasers

Two-node networks are too simple to investigate general nonlinear networks in semiconductor lasers, although some inspirations for the dynamics for lager number of coupled network elements can be recollected. The module for the first step to investigate complex nonlinear elements is a three-node network. Figure 14.6 shows 13 potential modules for coupled three-node networks (Milo et al. 2002). In these cases, each circle is a solitary laser. If we include optical feedback to lasers, the number of connections becomes 69. Thus, even for only coupled three-node nonlinear elements, we can expect a variety of the dynamics. 6 out of 13 are chain connections and the other 7 are ring connections. All of them are not useful for real networks and the useful ones are limited. Asterisks denote useful connections and standard modules are named in the figure. The modules are frequently referred to real networks, namely, module 3 is a network observed in the systems of food chains, modules 7, 12, and 13 are typical connections in the Internets, module 10 usually appears in the networks of electronic circuits, and module 11 is a good example for electronic circuits and connections of synaptic neurons. In the followings, we investigate the detailed dynamics for three mutual-coupled chain (module 4), three unidirectional-coupled ring (ring 10), and three mutual-coupled ring (module 13) as the important laser motifs. Theoretical and experimental studies of the dynamics for three coupled semiconductor lasers have been extensively

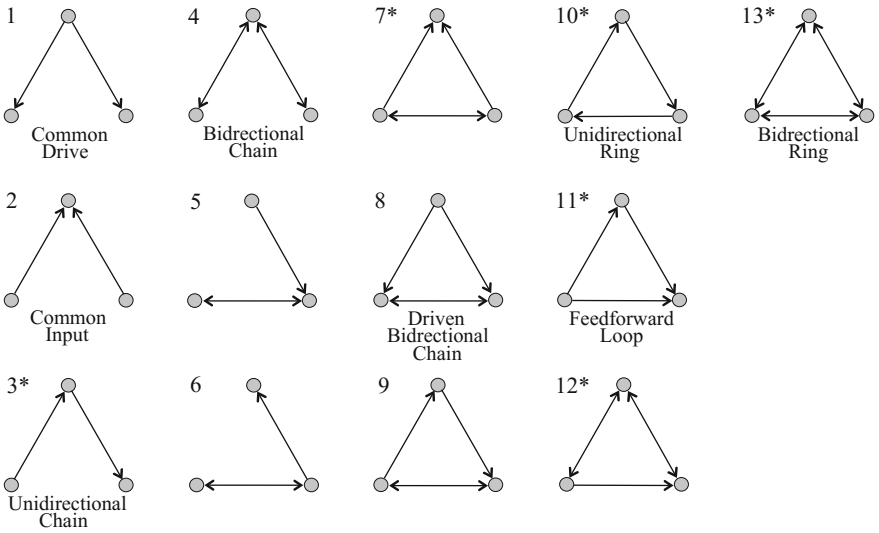

Fig. 14.6 13 potential modules for three-node networks. *Asterisks* denote useful connections for real networks

performed (Fischer et al. 2006; González et al. 2007; Aviad et al. 2012; Soriano et al. 2013a; Ohtsubo et al. 2015).

14.3.2 Three Chain-Coupled Semiconductor Lasers

Figure 14.7 shows some examples of three chain-coupled semiconductor lasers. Figure 14.7a is a system of unidirectionally coupled chain lasers. The field equations for the fundamental chain coupling with N lasers are written by

$$\frac{\mathrm{d}E_j(t)}{\mathrm{d}t} = \frac{1}{2}(1 - i\alpha)G_n\{n_j(t) - n_{\mathrm{th}}\}E_j(t) + \frac{\kappa_{j-1}}{\tau_{\mathrm{in}}}E_{j-1}(t - \tau)\exp(i\omega_0\tau) \tag{14.1}$$

where $E_0\,(t) = 0$ and $j = 1, \ldots, N$. Figure 14.7a corresponds to $N = 3$. In this case, under certain conditions of optical injection, laser 2 shows chaotic oscillations by the optical injection from laser 1. Then, laser 2 behaves like a chaotic laser as a semiconductor laser with optical feedback, which is similar to that of a simple optical injection in Fig. 14.2b, and laser 3 synchronizes with laser 2 under an appropriate condition of the optical injection strength. By installing an optical feedback loop to laser 1 as shown in Fig. 14.7b the network reduces to a system of zero-lag synchronization, which is a direct extension of unidirectionally coupled two semiconductor lasers with optical feedback in Fig. 14.3a.

On the other hand, the field equations in a system of mutually coupled chain lasers are written by the following form:

$$\begin{aligned}\frac{\mathrm{d}E_j(t)}{\mathrm{d}t} = {} & \frac{1}{2}(1 - i\alpha)G_n\{n_j(t) - n_{\mathrm{th}}\}E_j(t) + \frac{\kappa_{j-1}}{\tau_{\mathrm{in}}}E_{j-1}(t - \tau)\exp(i\omega_0\tau) \\ & + \frac{\kappa_{j+1}}{\tau_{\mathrm{in}}}E_{j+1}(t - \tau)\exp(i\omega_0\tau)\end{aligned} \tag{14.2}$$

where $E_0\,(t) = 0$ and $E_{N+1}(t) = 0$. Figure 14.7c is a chain of mutually coupled three lasers for $N = 3$ in above equations. In this system, the outer two lasers have symmetry viewing from the center laser. Then, the outer lasers show zero-lag synchronization; however, the central laser shows delayed synchronization against the outer lasers. Figure 14.8 shows an example of the cross-correlations between two of three lasers in this scheme. $C_{ij}(t)$ is a cross-correlation function for the intensities of the i-th and j-th semiconductor lasers. The two outer lasers show zero-lag synchronization as shown in Fig. 14.8a. However, the center laser is always delayed from the outer lasers as shown in Fig. 14.8b, c. Namely, the outer lasers become leader lasers for synchronization in this configuration. Similar results of zero-lag synchronization have been obtained for mutually coupled chain neurons, in which the Hodgkin-Huxley model is used for the numerical simulations (Mulet et al. 2004). The results of synchronization in synaptic neurons are shown in Fig. 14.9. The outer neurons, N1 and N3, synchronize with each other at zero-time

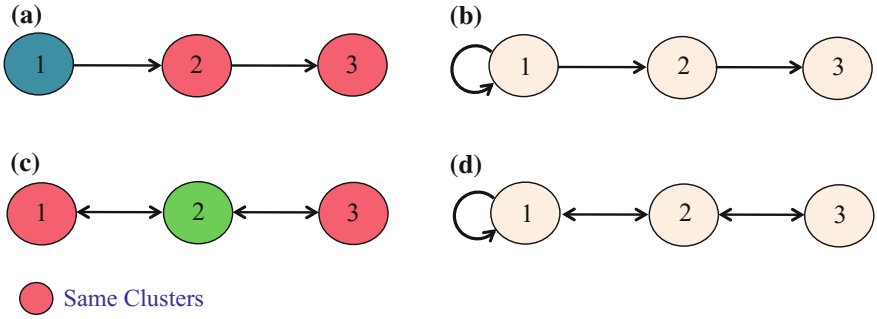

Fig. 14.7 Three-coupled laser chain. **a** Unidirectional optical injection, **b** unidirectional coupling with optical feedback, **c** mutual coupling, and **d** mutual coupling with optical feedback

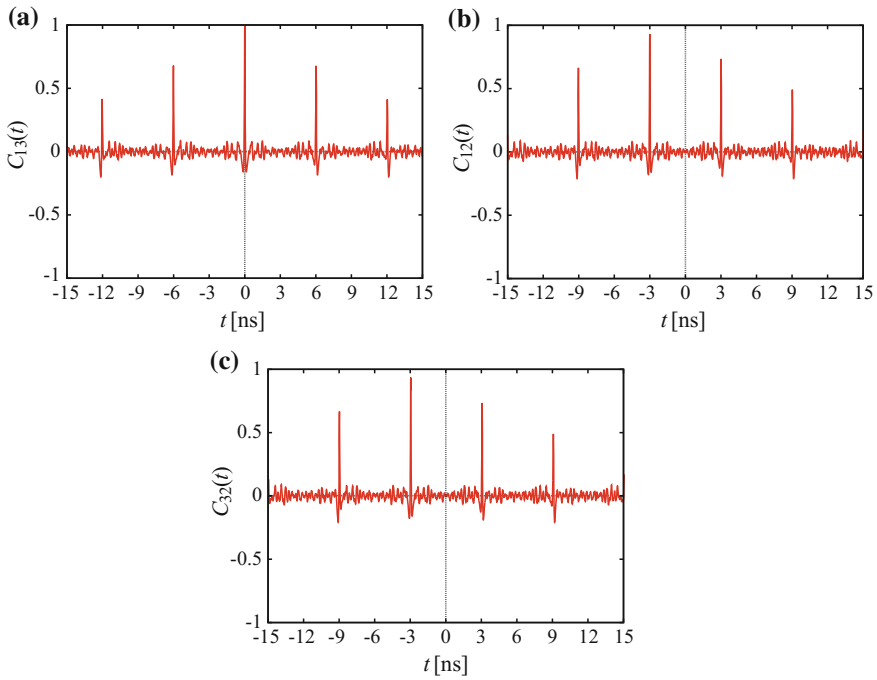

Fig. 14.8 Numerical results of intensity cross-correlations in mutually coupled chain lasers in Fig. 14.7c. **a** $C_{13}(t)$, **b** $C_{12}(t)$, and **c** $C_{32}(t)$ under conditions of $\kappa_{12} = \kappa_{21} = \kappa_{23} = \kappa_{32}$ ($r_{\text{inj}} = 0.4$) and $\tau = 3$ ns

delay, whereas the center neuron delays from the two outer neurons (the delay is about 20 ms). Although the membrane potential from the output of neurons shows chaotic pulsation oscillations, the results of correlations are well coincident with those of intensities from chaotic semiconductor lasers.

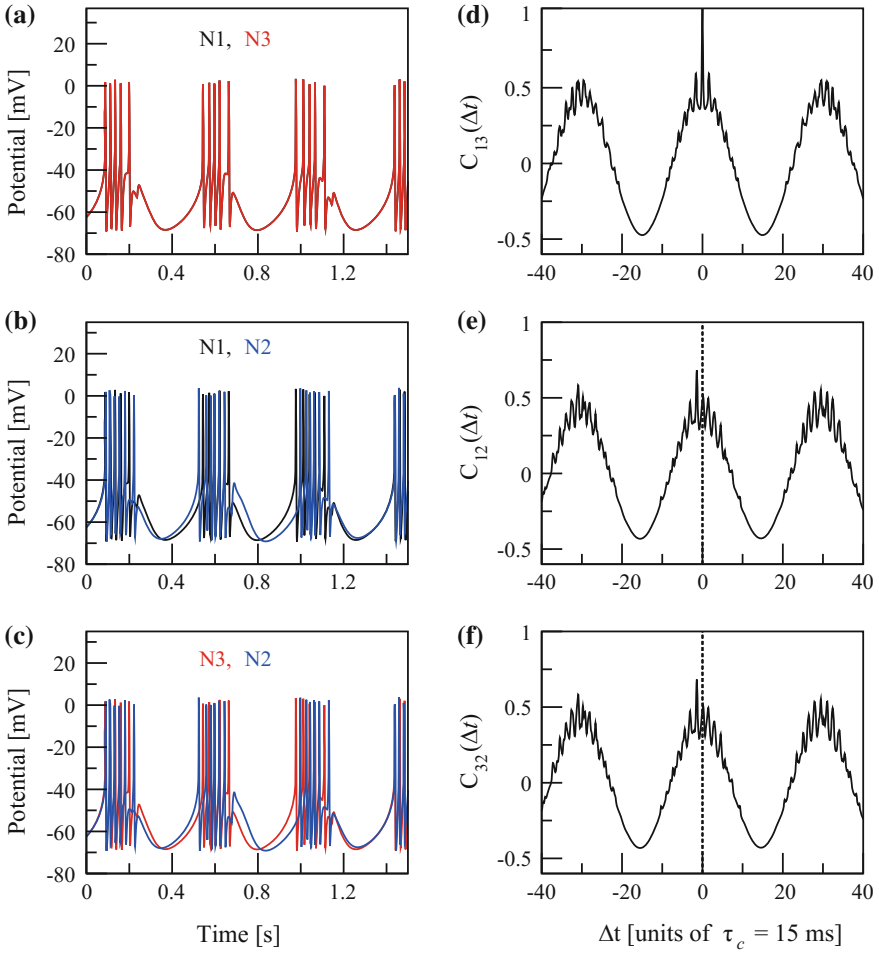

Fig. 14.9 Numerically calculated correlation of three mutually coupled chain neurons in the Hodgkin-Huxley model. *Left column* time series of three neurons, N1, N2, and N3. *Right column* corresponding cross-correlation [after Fischer et al. (2006); © 2006 APS]

As discussed later, the system shown in Fig. 14.7c is the simplest case of sublattice (2 clusters) synchronization. A system of mutually coupled chain lasers can be reduced to zero-lag synchronization by installing an optical feedback loop to the outer lasers. Figure 14.7d is an example of such systems. This is quite consistent with the case in Fig. 14.4b. Zero-lag synchronization is realized when the driving force of the optical feedback is strong enough and the total power of optical feedback and injection in every laser is assumed to be the same. If the two outer lasers have optical feedback loops, the system also becomes zero-lag synchronization.

14.3.3 Three Ring-Coupled Semiconductor Lasers

Next examples are ring laser systems. The field equations for unidirectionally coupled ring lasers are written by the same forms as that in (14.1), but the boundary condition is $E_0(t) = E_N(t)$ ($N = 3$) due to the ring coupling. A ring configuration of three unidirectionally coupled lasers is shown in Fig. 14.10a. We could also expect zero-lag synchronization owing to the symmetry of the system if we ignore intrinsic laser noises. However, as discussed earlier, we must consider laser noises for synchronization and the system is reduced to delay synchronization as shown in Fig. 14.11a. Namely, the delay of the output from each optically injected laser is equal to the coupling time from the injection laser. Once the lasers become chaotic, the correlation peak of delay synchronization increases for the increase of the injection ratio as shown in Fig. 14.11b. By adding an optical feedback loop to one of three unidirectionally coupled ring lasers in Fig. 14.10a, the system of delay synchronization is changed to that of zero-lag synchronization on the time average. Even at this state, the lasers sometimes show instantaneous delay synchronization, however, the delay of the signals does not always occur in order. For example,

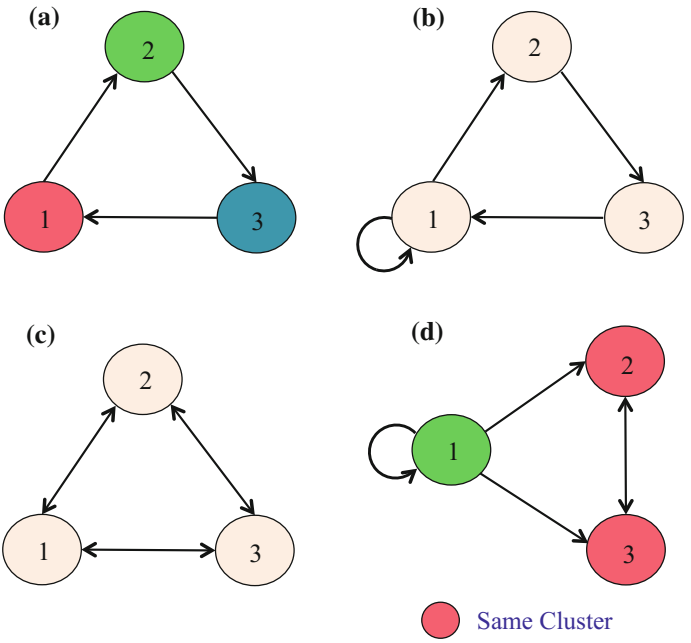

Fig. 14.10 Three coupled ring lasers. **a** Three unidirectionally coupled lasers and **b** addition of an optical feedback loop to one of the lasers in **a**. **c** Three mutually coupled lasers. **d** Importance of a driving laser for synchronization in a three coupled system

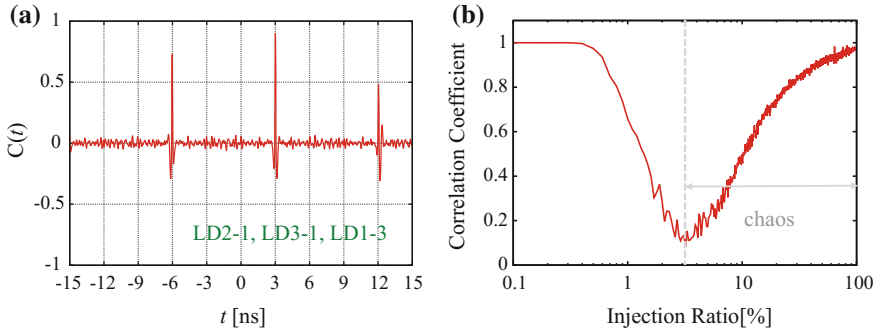

Fig. 14.11 Intensity correlation of unidirectionally coupled ring lasers in Fig. 14.10a. **a** Numerical calculated correlation of adjacent lasers at $r_{inj} = 0.3$. **b** Correlation coefficient of adjacent lasers for the optical injection ratio from one laser to the other

when the lasers show chaotic low-frequency fluctuations, the dropout of the intensities randomly occurs in time among three lasers due to intrinsic laser noises. Namely, local time bursts of the synchronization are observed among the lasers and, as a result, the value of the correlation coefficient is usually less than unity (Buldu et al. 2007). An addition of optical feedback loop to one of lasers in the configuration in Fig. 14.10a is shown in Fig. 14.10b. The optical feedback installed in laser 1 becomes a driving force to the entire laser system and all lasers show zero-lag synchronization under appropriate optical injection conditions in spite of the original ring lasers show delay synchronization even if the lasers contain spontaneous emission noises.

Figure 14.10c shows a system of three mutually coupled ring lasers. The field equations for a mutually coupled ring lasers are also written by the same forms as that in (14.2), but the boundary conditions are $E_0(t) = E_N(t)$ and $E_{N+1}(t) = E_1(t)$ ($N = 3$). In this case, each laser mutually drives the other adjacent lasers and this results in zero-lag synchronization, even if the lasers contain noises. The importance of driving force is clearly demonstrated in Fig. 14.10d. In this system, a chaotic laser with optical feedback (laser 1) commonly drives two lasers (lasers 2 and 3) and, then, the two lasers show zero-lag synchronization even if they are mutually coupled. The system is a good example for the consistency for a model of drive-response systems. In the case of mutual coupling systems, the synchronization is complete and the correlation coefficient becomes unity. Therefore, the system is very suited for mutual optical communications. Indeed, Buldú et al. (2007) proposed a system for chaotic secure communications based on chaos masking method.

14.4 Four Coupled Semiconductor Lasers

14.4.1 Four Chain-Coupled Semiconductor Lasers

The dynamics of four chain-coupled semiconductor lasers can be inferred from those of two- and three-coupled laser chains. Figure 14.12a shows a chain of four mutually coupled lasers. In this configuration, similar results as those for the three chain-coupled lasers in Fig. 14.7c are observed, since a mutually coupled laser of laser 4 is simply added to the outside of the system in Fig. 14.7c. Therefore, laser 1 and laser 3 are driven by laser 2 and, similarly, laser 2 and laser 4 are driven by laser 3. Thus, synchronous oscillations of lasers alternately appear, and two-cluster synchronization is established in the system under appropriate conditions of optical injection. Laser 1 and laser 3 form one cluster of zero-lag synchronization, and laser 2 and laser 4 belong the other cluster of zero-lag synchronization. The scheme is sometimes called sublattice synchronization. The same results are expected for larger number of mutually coupled chain more than four lasers. From this result, we can easily recognize that Fig. 14.7c is the simplest case of sublattice (two clusters) synchronization. When an optical feedback loop is added to one of the outer lasers as shown in Fig. 14.12b, all the lasers are forced to undergo zero-lag synchronization which is similar to the case in Fig. 14.7d. In this system, the lasers show zero-lag synchronization for the conditions where the optical feedback and delay times are equal, namely, $\tau_{ex} = \tau_{inj}$, and the total optical powers in all nodes balance, namely, $\kappa_{ex} + \kappa_{inj2,1} = \kappa_{inj1,2} = \kappa_{inj3,2} = \kappa_{inj2,3} = \kappa_{inj4,3} = \kappa_{inj3,4}$. Thus, zero-lag synchronization in semiconductor laser networks strongly depends on the topology of nonlinear networks.

14.4.2 Four Ring-Coupled Semiconductor Lasers

A ring configuration of four unidirectionally coupled lasers is shown in Fig. 14.13a. Despite the symmetry of the system, we cannot expect zero-lag synchronization owing to the existence of intrinsic laser noises. Instead, the outputs of adjacent lasers show delayed synchronization similar to that in the system in Fig. 14.10a. On

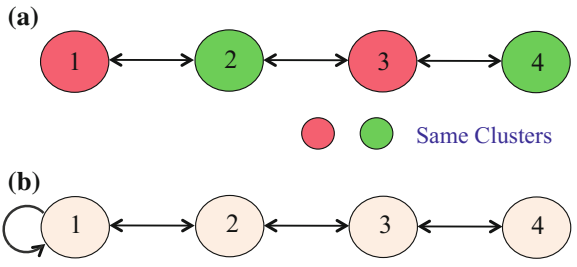

Fig. 14.12 Four chain-coupled semiconductor lasers. **a** Four lasers with mutually coupled chain and **b** addition of an optical feedback loop to one of the outer lasers in (**a**)

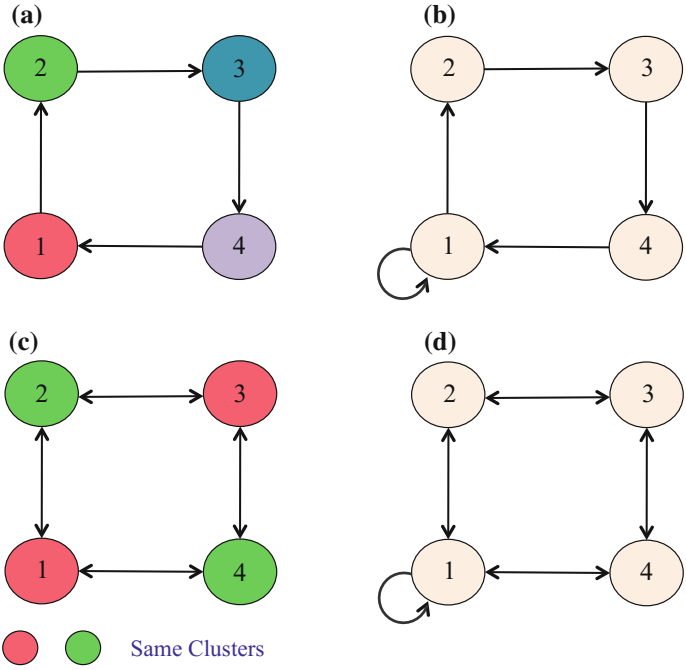

Fig. 14.13 Four ring semiconductor lasers. **a** Four unidirectionally coupled lasers, **b** four unidirectionally coupled lasers with optical feedback, and **c** four mutually coupled lasers. **d** Addition of optical feedback loop to one of the lasers in (**c**)

the other hand, the diagonal pairs show achronal synchronization, since, for example, laser 1 and laser 3 are mutually coupled via buffer lasers. Namely, this case is equal to a two mutually coupled laser system similar to that in Fig. 14.4a via the relay lasers (laser 2 and laser 4). Similar to the case of three unidirectionally coupled lasers, four unidirectionally coupled lasers in Fig. 14.10b forces to a system of zero-lag synchronization by the introduction of an optical feedback loop to one of the lasers as shown in Fig. 14.13b.

Figure 14.13c shows a system of four mutually coupled ring lasers. Similarly to the case of two mutually coupled lasers, the adjacent lasers show achronal synchronization as plotted in Fig. 14.14a, due to the existence of laser noises. The adjacent pairs are the same configuration of two mutually coupled lasers as similar to that in Fig. 14.4a and this results in achronal synchronization between the pair lasers. On the other hand, the diagonal pairs become zero-lag synchronization, as shown in Fig. 14.14b. The zero-lag synchronization is explained as follows. Laser 1 and laser 3, for example, are driven by the same lasers, laser 2 and laser 4, respectively, and, as a result, the diagonal pairs output synchronous oscillations at zero time delay. However, the adjacent pairs, for example, laser 1 and laser 2 have no common driving laser. Then, the network shows sublattice synchronization (two-cluster synchronization). The correlation coefficients are calculated for the

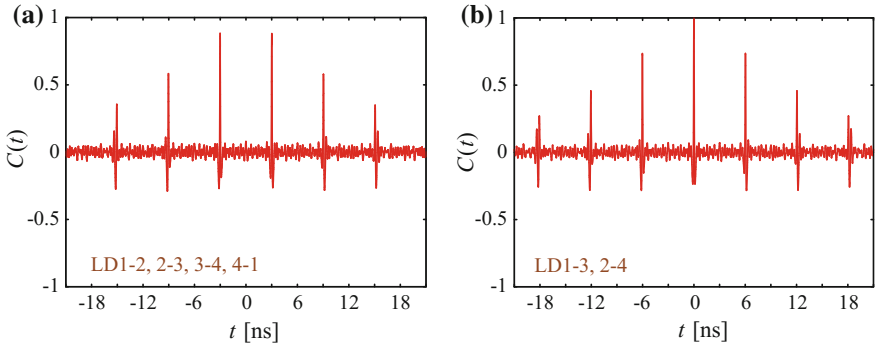

Fig. 14.14 Numerically calculated correlations of **a** adjacent pairs (achronal synchronization), and **b** diagonal pairs (zero-lag synchronization) in Fig. 14.13b under conditions of equal optical injections ($r_{inj} = 0.2$) and $\tau = 3$ ns

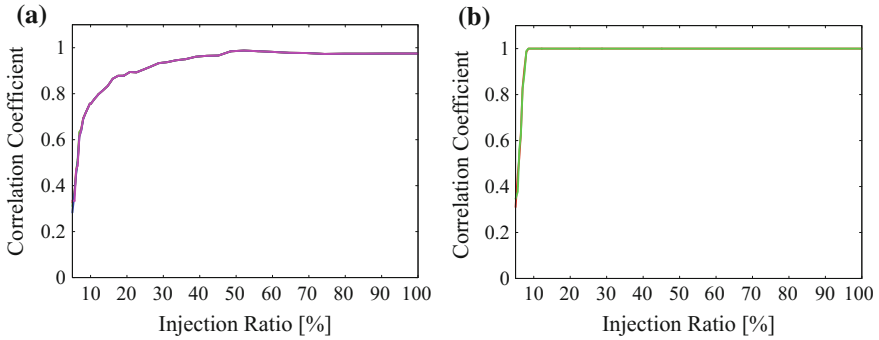

Fig. 14.15 Correlation coefficient for the optical injection strength in four mutually coupled semiconductor lasers. Coefficients of **a** adjacent pairs and **b** diagonal pairs

optical injection strength and are shown in Fig. 14.15. Figure 14.15a shows the correlation coefficient of the adjacent pairs, in which the value of the highest coefficient either $\tau = +3$ or $\tau = -3$ ns is plotted (noted that the correlation peaks have almost the same value). While, Fig. 14.15b corresponds to the correlation coefficient of diagonal pairs at $\tau = 0$ ns. The diagonal pairs show good zero-lag synchronization for the optical injection strength over 10%.

The system of the sublattice synchronization shown in Fig. 14.13c forces to a system of zero-lag synchronization when an optical feedback loop is added to one of the lasers. The configuration is shown in Fig. 14.13d, in which an optical feedback loop is added to laser 1. The part of two mutually coupled lasers, laser 1 with optical feedback and laser 2, is the same system as that in Fig. 14.4b. Then, the adjacent lasers, laser 1 and laser 2, show zero-lag synchronization and the entire system reduces to one of zero-lag synchronization. The conditions for zero-lag synchronization are the same as before, namely, the total power of optical feedback

and optical injection in every laser balances with each other. As discussed above, the extra feedback loop plays a role for the driving force to the whole system.

14.5 Star-Coupled Semiconductor Lasers

14.5.1 Unidirectional Coupled Hub-Star Systems

The issues treated in the dynamic of hub-star coupled systems in semiconductor lasers are closely related to those of the consistency in common drive-response nonlinear systems. For example, in a system of two similar semiconductor lasers, which are unidirectionally driven by a common chaotic semiconductor laser, the synchronization properties between the two lasers are interesting problem from a viewpoint of nonlinear dynamics. We already discussed the properties of chaos synchronization in drive-response systems in Sect. 12.8. Here, we consider a system in which many star lasers are optically injected from a chaotic hub laser in a unidirectional manner as shown in Fig. 14.16. The hub semiconductor laser may show chaotic oscillations induced by a self-optical-feedback loop, while star lasers are stable unless optical injection from the hub-laser. As the mathematical models for the hub (center) laser and the star lasers, the field equations are defined by

$$\frac{\mathrm{d}E_h(t)}{\mathrm{d}t} = \frac{1}{2}(1 - i\alpha)G_n\{n_h(t) - n_{\mathrm{th}}\}E_h(t) + \frac{\kappa_h}{\tau_{\mathrm{in}}}E_h(t - \tau_h)\exp(i\omega_h\tau_h) \tag{14.3}$$

$$\frac{\mathrm{d}E_j(t)}{\mathrm{d}t} = \frac{1}{2}(1 - i\alpha)G_n\{n_j(t) - n_{\mathrm{th}}\}E_j(t) + \frac{\kappa_j}{\tau_{\mathrm{in}}}E_h(t - \tau_j)\exp(-i\Delta\omega_{hj}\tau_j) \tag{14.4}$$

where $E_h(t)$ and $E_j(t)$ ($j = 1, \ldots, N$) are the optical fields for the hub and star lasers, respectively, $\Delta\omega_{hj}$ is the frequency detuning between the hub and star lasers. The

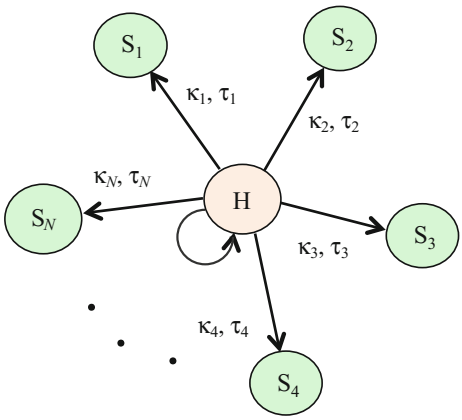

Fig. 14.16 Unidirectionally coupled hub-star laser systems. *H* is a hub laser with optical feedback and S_j represents a star laser

other notations are similar to the systems of optical feedback and optical injection in semiconductor lasers discussed in the previous chapters.

In usual situation, we cannot ignore the frequency detuning among semiconductor lasers, however, we here assume a case of zero frequency detuning for simplicity ($\Delta\omega_{hj} = 0$). When a chaotic signal from the hub laser is broadcasted to the star lasers. Under appropriate operating conditions of the star lasers (such as the bias injection currents and the optical injection strength), the star lasers also show chaotic oscillations. All star lasers may show synchronous chaotic oscillations with zero-time delay when the optical injection strengths κ_j and the optical injection time τ_j are identical. On the other hand, the perfect synchronization between the hub laser and the star lasers is not always satisfied. This means that the model is categorized into that in a drive-response system and the synchronization implies consistency problems in nonlinear networks. When κ_j and τ_j are identical, all star lasers are mathematically described by the equivalent differential equations and the lasers show complete synchronization including optical phase. In the mean time, for different optical injection time τ_j under appropriate conditions of coupling strengths, the output intensities of the pair star lasers, S_j and S_i, still show synchronous oscillations with each other at a time delay, $\Delta t = \tau_j - \tau_l$. However, the phase synchronization is not guaranteed in this case, since the lasers contain intrinsic spontaneous emission noises and the transmitted lights from hub to star lasers include phase difference due to optical propagation. When we ignore spontaneous emission noises in the numerical simulation, the synchronization becomes complete. However real lasers always have spontaneous emission noises.

14.5.2 Mutually Coupled Hub-Star Systems

For example, pendulum clocks mounted on the same wooden beam, all the pendulums swing in the synchronous way without one's noticing it (Huygens 1986). Another example of mutually coupled chaotic systems is the crowd synchrony of the Millennium Bridge in London as discussed in Sect. 14.1.1. When multiple dynamical elements that interact with each other through a common coupling medium (mutually coupled regime), the elements reach synchronization over a critical value of the operating parameters. Next example that we treat is a system of mutually coupled hub-star lasers. A hub-star network consisting of semiconductor lasers is also a good example of crowd synchrony of nonlinear dynamic elements. Also, mutually coupled hub-star laser systems are of importance from the viewpoint of the practical application in real networks, many studies for the models have been reported (Zhang et al. 2008; Zamora-Munt et al. 2010; Aviad et al. 2012; Bourmpos et al. 2012, 2013; Cohen et al. 2012; Xiang et al. 2016). Here, the central laser (hub laser) plays the role of a coupling medium analogous to the bridge structure in pedestrian synchronization and the star lasers interact with each other through the hub laser, which results in synchronous oscillation of the star lasers. The models of

hub-star lasers that are discussed here are closely related to neuron networks and other nonlinear networks that are suitable for investigating the properties of crowd synchrony in many coupled nonlinear elements.

The star-hub semiconductor laser system is one of the models of crowd synchrony in nonlinear networks. Zamora-Munt et al. (2010) discussed the phenomena of crowd synchrony of the optical outputs in star lasers when random detuning among laser oscillation frequencies was introduced. They investigate the dynamics up to the connection of one hundred star lasers and show that the transition to synchronization occurs for a critical number of coupled lasers and strongly depends on the coupling strength via a power law with negative exponent, in agreement with the crowd synchronization transition reported in the Millennium Bridge. Namely, when the number of the nodes (star lasers) increases, the star lasers easily synchronize with each other. Also, an analogy between crowd synchrony and multi-layer neural network architectures is found, in which many non-identical dynamical elements (star semiconductor lasers) communicating indirectly via a few mediators (hub lasers) can synchronize (Cohen et al. 2012). They show that the multi-layer architecture undergoes a sharp transition to crowd synchrony when the number of elements or strength of coupling is large enough. A universal phase transition to crowd synchrony with hysteresis is observed for the change of the coupling strength.

The systems of mutually coupled hub-star lasers are quite similar to that discussed in the previous section, however the hub laser discussed here shows chaotic oscillation without self-optical-feedback. We consider such mutually coupled systems and a particular example of three star lasers is shown in Fig. 14.17. As the mathematical models for the mutually coupled hub (center) and star lasers, the field equations are defined by

$$\frac{\mathrm{d}E_h(t)}{\mathrm{d}t} = \frac{1}{2}(1 - i\alpha)G_n\{n_h(t) - n_{\mathrm{th}}\}E_h(t) + \sum_{j=1}^{N}\frac{\kappa_j}{\tau_{\mathrm{in}}}E_j\big(t - \tau_j\big)\exp\big(-i\Delta\omega_{jh}\tau_j\big) \tag{14.5}$$

$$\frac{\mathrm{d}E_j(t)}{\mathrm{d}t} = \frac{1}{2}(1 - i\alpha)G_n\big\{n_j(t) - n_{\mathrm{th}}\big\}E_j(t) + \frac{\kappa_j}{\tau_{\mathrm{in}}}E_h\big(t - \tau_j\big)\exp\big(-i\Delta\omega_{hj}\tau_j\big) \tag{14.6}$$

where $E_h(t)$ and $E_j(t)$ (j = 1, …, N) are again the optical fields for the hub and star lasers, respectively, $\Delta\omega_{jh}$ and $\Delta\omega_{hj}$ are the frequency detuning between the hub and star lasers. One of the primitive configurations of a system of mutually coupled hub-star lasers is three-chain laser discussed in Sect. 14.3.2. By adding an extra laser to the center laser in Sect. 14.3.2, it reduces to a system of three-star lasers (N = 3) as shown in Fig. 14.17. We first consider an example of synchronization among star lasers under the conditions, in which all of the mutual coupling time τ_j, the optical injection strength r_{inj} ($r_{\mathrm{inj}} = \sqrt{P_h/P_s}$; P_h and P_s being the solitary optical powers of the hub and star lasers), and the bias injection current J_{th}, are equal, τ_j = 3 ns, r_{inj} = 0.4, and $J = 1.3J_{\mathrm{th}}$, respectively. Other device parameters of

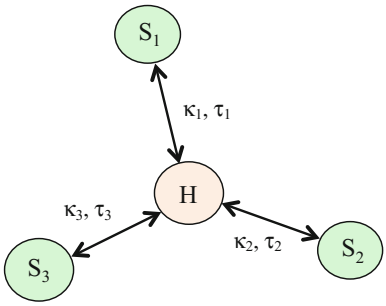

Fig. 14.17 Example of hub and three-star laser system

semiconductor lasers are the same as listed in Table 5.1. Then, we obtain zero-lag synchronization among star lasers with chaotic oscillations. Even when star lasers synchronize with each other, they may or may not synchronize with the hub laser. Namely, the hub laser plays a role for a drive to the star lasers and the star lasers become responses in the drive-response system.

At the same configuration in Fig. 14.17, we change one of the optical coupling strength (for example, the strength of S_3 is changed to 0.6 and the others remain the same as before). Figure 14.18a shows the cross-correlation between S_1 and S_2, while Fig. 14.18b represents the cross-correlation between S_1 (S_2) and S_3. Namely, the correlation between the lasers with different optical coupling strengths decreases, while that with the same group of the coupling strength almost unchanged. Similar results are obtained when a number of star lasers are larger than three and the coupling strength of one of the star lasers is changed. Also the role of the optical strengths for synchronization can be changed by the bias injection current. For example, similar phenomena as Fig. 14.18 are observed when one of the bias injection currents of the star lasers is changed at the fixed optical coupling strength for all hub-star lasers.

Next, we consider the situation where one of the coupling times τ_j among the hub laser and the star lasers is changed at the same configuration shown in

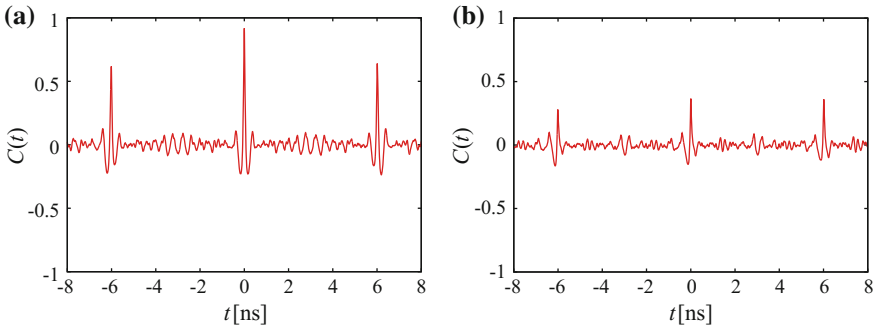

Fig. 14.18 Cross correlations of star lasers when the coupling strengths (r_{inj}) of two lasers are 0.3 and the other is 0.6. **a** Correlation between S_1 and S_2. **b** Correlation between S_1 (S_2) and S_3

Fig. 14.17. For example, we assume that $\tau_1 = \tau_2 \neq \tau_3 = 6$ ns and $\kappa_1 = \kappa_2 = \kappa_3$. Then, all the star lasers synchronize with each other and the star lasers, S_1 and S_2, become zero-lag synchronization. The laser, S_3, still show a synchronized oscillation with the other star lasers, however it is delayed 3 ns ($\Delta t = \tau_3 - \tau_1$) from S_1 and S_2. The result is the same as that of the unidirectional coupling systems as discussed in the previous subsection. At this state, the phase synchronization is also not guaranteed. The same results are observed for a number of star lasers more than three. Even when all the coupling times of the star lasers are different, they show synchronous oscillations, but synchronization delays are determined by the light transmission time from the hub laser to respective star lasers. Indeed, the same results of the delay synchronization in hub-star laser systems with a large number of star nodes were numerically obtained by Xiang et al. (2016) and they also discussed the effects of frequency detuning among star lasers. Thus, the hub laser plays a role for a driving force in the drive-response systems and chaotic oscillations in the hub laser are broadcasted to the star lasers. Then, the star lasers show crowd synchrony.

14.5.3 Group Synchrony in Hub-Star Laser Systems

Finally, we discuss sub-group synchronization in hub-star laser systems. As an example, we assume four star lasers, $S_1 \sim S_4$, mutually coupled with a hub-laser and the coupling delay times are all the same. Among them, two star lasers, S_1 and S_2 (group A), have the same coupling strength, while the other two, S_3 and S_4 (group B), also have the same coupling strength but it is different form the former one. Under appropriate conditions of the other parameters, the same group becomes zero-lag synchronization, but the different group shows unsynchronized oscillations. These group synchronous and asynchronous states are well reproduced by changing the bias injection currents of the star-lasers instead of changing the optical injection strengths. The systems are suitable for secret communications among small group networks. In a system of N star-lasers, the similar results obtained in a four-star-laser system can be observed. When two of the star nodes among N lasers only have a common coupling strength and it is different from those of other star lasers, the two lasers or the other N-2 lasers respectively show zero-lag synchronization under appropriate conditions. But the different groups have no correlation. Even for a system of N star lasers, secret communications are still possible among certain groups of them.

14.6 Many Coupled Semiconductor Lasers

14.6.1 Examples of Many Coupled Semiconductor Lasers

In the preceding sections, we discussed the dynamics and synchronization properties for rather simple networks with a small number of laser nodes. In actual, real neuron networks have a variety of couplings and connections among many neurons. In semiconductor lasers, we can also consider various types of connections of laser elements as network topology. For example, Nixon et al. (2011, 2012) experimentally studied the synchronization properties in large networks of solid-state lasers. In semiconductor lasers, synchronous and asynchronous dynamics were reported in large number of coupled network nodes (Aviad et al. 2012; Argyris et al. 2016). Argyris et al. (2016) experimentally investigated generalized synchrony in a network of 16 mutually coupled semiconductor lasers. They reported the effects of mismatches of the lengths of coupling fibers and the frequency detunings among lasers on the synchronization performance. They also demonstrated that cluster synchronization is possible in this networks by different setting conditions for the operating parameters among lasers. In the followings, we show some typical examples of N-coupled semiconductor laser networks. We assume that network configurations have symmetry and the times for the connections between lasers and the optical feedback loops are the same. Figure 14.19a is a model of N unidirectionally coupled lasers. If laser 2 shows chaotic oscillations by optical injection from laser 1, the following lasers may exhibit zero-lag synchronization under the symmetrical configuration. When we attach an optical feedback loop to laser 1, the system is a straightforward extension of the system discussed in Fig. 14.3a. We can also expect zero-lag synchronization in the system under appropriate condition of optical coupling strength. In the system of mutually coupled chain lasers in Fig. 14.19b, a synchronized pair alternately appears and a sublattice (two cluster) synchronization system is established as the same manner as those in Figs. 14.7c and 14.12a. Figure 14.19c is an example of star coupled systems. As is discussed in the previous section, it is frequently used in computer networks and is one of models of crowd synchrony in semiconductor laser networks.

Figure 14.19d shows N-coupled unidirectional ring semiconductor laser networks. For odd number of coupled lasers, successive lasers are expected to show delay synchronization due to laser noises as discussed in the case of three coupled ring laser networks in Sect. 14.3.3. For even number of coupled lasers, the adjacent lasers also show delay synchronization, however, the every other pairs exhibit achronal synchronization. This is explained as follows: the alternate lasers have the same topology as two mutually coupled lasers through the relay lasers as similar to that discussed in four unidirectionally coupled ring lasers in Sect. 14.4.2. As a secondary effect of unidirectionally coupled semiconductor laser networks, the delay-time signature (such as induced by optical injection and optical feedback), which appears in the output intensities, can be extensively suppressed. In delay

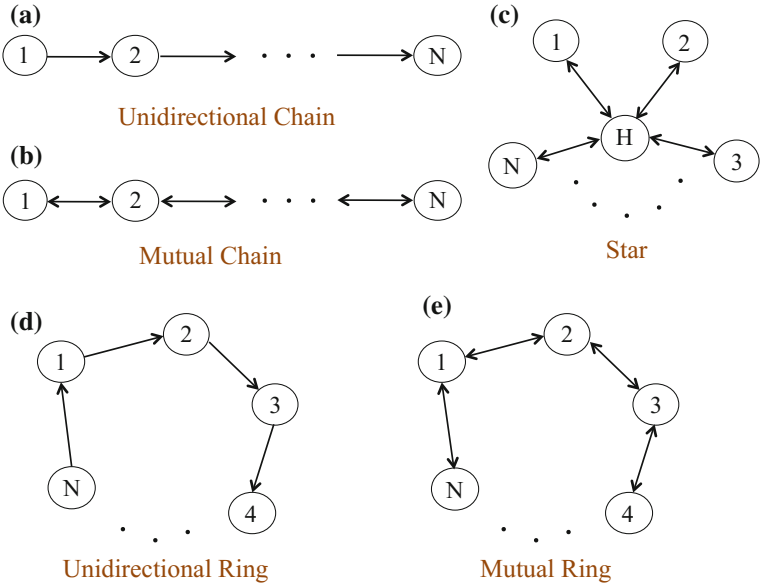

Fig. 14.19 Some examples of *N* coupled semiconductor lasers. **a** Unidirectionally coupled chain, **b** mutually coupled chain, **c** star coupling, **d** unidirectionally coupled ring, and **e** mutually coupled ring

coupled nonlinear systems and also finite time coupling systems, the time signatures inevitably encounter as shown in Fig. 14.8. The time signature is easily obtained from the calculation of correlation functions or/and mutual information from chaotic laser intensities. It is an important secret key for chaotic secure communications and it also greatly deteriorates the performance of the generations of random bits using chaotic semiconductor lasers. So the suppression of time-delay signature in chaotic semiconductor lasers is very important when one uses chaotic signals as carriers in optical security systems. The sub-peaks appeared in the correlation functions of chaotic intensities can be suppressed in proportion to the increase of the coupling number of nodes (Van der Sande et al. 2008). Therefore, the suppression of the time-delay signature using coupled laser networks is greatly appreciated from viewpoint of applications of chaos.

Figure 14.19e is an example of *N*-coupled mutual ring lasers. Different from unidirectionally coupled ring lasers, the number of synchronization clusters depends on the number of coupling elements. When the number of coupling nodes is odd, all lasers synchronize at zero time delay. Namely, the system has only a single cluster in synchronization. On the other hand, for an even number of nodes, a pair of adjacent lasers shows achronal synchronization, while the alternate pairs exhibit zero-lag synchronization. Figure 14.20a, b show examples of five and six mutually coupled ring lasers. In a case of five nodes in Fig. 14.20a, we consider counter-clockwise signal transmission and pay, for example, attention to laser 1.

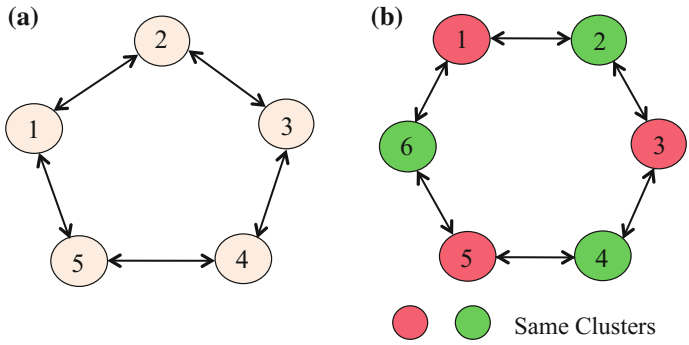

Fig. 14.20 Synchronization clusters in odd and even numbers of mutually coupled ring lasers. **a** Five nodes (*odd number*) and **b** six nodes (*even number*)

Laser 1 and laser 4 are driven by the common laser, laser 5, and they show zero-lag synchronization. Similarly, laser 4 and laser 2 are driven by the common laser, laser 3. Then, laser 1 is driven by the adjacent laser 2 with zero-time delay. Thus, all lasers synchronize with zero-time delay. In a case of six mutually coupled ring lasers, laser 1 and laser 5 show zero-lag synchronization due to the same driving laser, laser 6. Similarly, laser 5 and laser 3 become zero-lag synchronization, and laser 3 and laser 1 also become zero-lag synchronization. Namely, driving lasers alternately appear and two-cluster synchronization (sublattice synchronization) is established in this system. Thus, alternate pairs show zero-lag synchronization and the adjacent pairs exhibit achronal synchronization. From these results, it is concluded that the topology of the networks determines the number of synchronization clusters and the synchronization properties in nonlinear networks despite particular characteristics of nonlinear elements. The properties are common natures for any nonlinear elements similar to synaptic neurons.

14.6.2 Synchronization Properties Depending on Topological Configurations

In this subsection, we demonstrate examples of synchronizations in combined two small semiconductor laser networks, which are stand out in the natures of topological configurations (Nixon et al. 2011, 2012). In Fig. 14.21, a system of zero-lag synchronization is combined with a system of sublattice synchronization. The zero-lag synchronization system consists of three mutually coupled ring lasers and the two-cluster synchronization system is a five mutually coupled laser chain. The outer laser in the latter system, laser 1, is replaced by three mutually coupled ring lasers as shown in Fig. 14.21a. As a result, the entire system shows synchronous oscillations at zero-time delay. Namely, the ring laser system becomes a strong

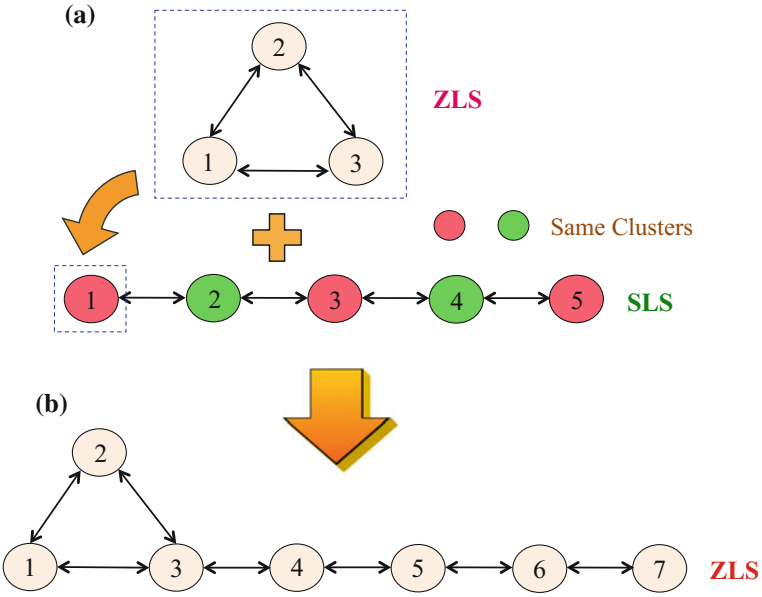

Fig. 14.21 Combination of ring and chain laser networks. **a** Original two networks; three mutually coupled ring lasers and five mutually coupled laser chain. **b** Combined networks

driving force to the whole system and the total system reduces to zero-lag synchronization. Thus, the system of the three mutually coupled laser ring plays a similar role as an optical feedback loop such as in Fig. 14.7b. Figure 14.22 shows another example of synchronization in combined systems. A system of three mutually coupled ring lasers with zero-lag synchronization is combined with that of six mutually coupled ring lasers with sublattice synchronization. Two mutually coupled elements, laser 1 and laser 2 in the six mutually coupled ring lasers are replaced by the three ring lasers. Then, the whole system becomes zero-lag synchronization. Also, the three mutually coupled lasers play a role of a driving force to the entire system and this results in zero-lag synchronization of the combined system as shown in Fig. 14.22b. Again, as a common nature of nonlinear elements, the synchronization properties and the number of synchronization clusters in the networks are essentially determined by their topological configurations. Further, a common driving force plays a crucial role for zero-lag synchronization in nonlinear networks. Finally, it is pointed out that the topology of the systems only tells the potential of zero-lag or cluster synchronization. Whether the system really shows a particular synchronization strongly depends on the operating parameters such as optical injection strength and other laser parameters. Especially, intrinsic noises of nonlinear elements will play a crucial role for synchronization.

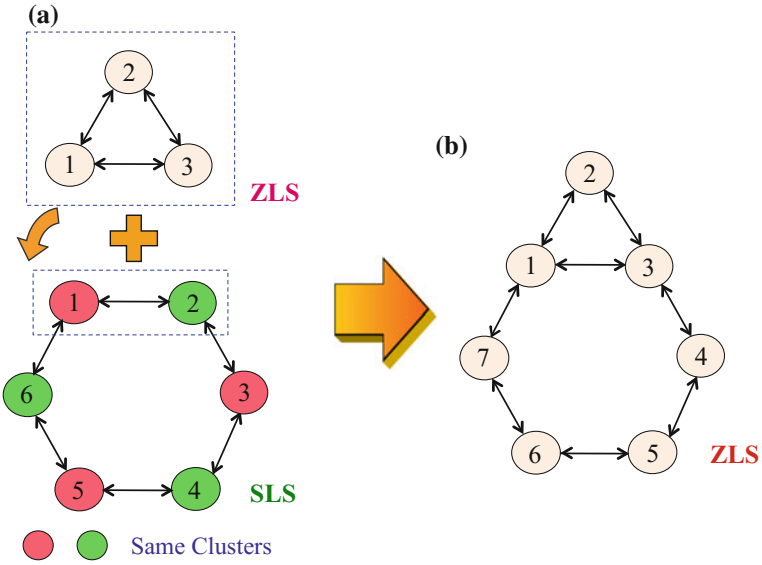

Fig. 14.22 Combined two ring laser networks. **a** Original two networks; three mutually coupled ring lasers and six mutually coupled ring lasers. **b** Combined networks

14.6.3 Greatest Common Divisor Rule in Coupled Semiconductor Laser Networks

We show that the number of synchronization clusters in nonlinear networks is strongly related to their topological configurations in the preceding subsections. Then, what is the rule to determine the number of synchronization clusters for a given network? One of the hints is the greatest common divisor (GCD) rule. Following the GCD rule, the number of synchronization clusters in nonlinear networks is given by the GCD of the number of laser nodes, m, and topology of the network connections, n (Kanter et al. 2011a, b, c; Vardi et al. 2012; Aviad et al. 2012; Rosin et al. 2013; Ohtsubo et al. 2015). We employ a notation of GCD[m, n] = p, where GCD denotes an operator for a greatest common divisor for m and n, and p is the resulting number of synchronization clusters. The same results as those of the preceding sections for the number of synchronization clusters are derived in accordance with the GCD rule. For examples, a system of three mutual coupled ring lasers, as shown in Fig. 14.10c, becomes zero-lag synchronization (a single cluster), since GCD[3,2] = 1. For four ring lasers with a mutually coupled system, as shown in Fig. 14.13c, the system has two synchronization clusters since GCD[4,2] = 2. If an optical feedback loop is added to one of the lasers in Fig. 14.13d, the GCD becomes GCD[4,2,1] = 1 and the system reduces to a single cluster, namely, zero-lag synchronization. In the case of large networks, an odd number of mutually coupled nodes, as shown in Fig. 14.20a, GCD[5,2] = 1 and the network shows

zero-lag synchronization, while in the case of an even number of nodes, as shown in Fig. 14.20b, GCD[6,2] = 2 and the network shows a two-cluster synchronization (sublattice synchronization). It is noted that the rule of GCD only says a possibility of synchronization, cluster-*p* synchronization, in a particular network. Namely, for certain networks, cluster synchronization that is derived from GCD is only realized for limited ranges of system parameters (in the case of semiconductor laser networks, optical feedback and injection strengths of κ_{ex} and κ_{inj} are the important parameters).

14.7 Reservoir Computing and Application

14.7.1 Neuro-Inspired Information Processing

We discussed the analogy between synaptic neurons and coupled semiconductor lasers from viewpoints of the dynamics and synchronization properties. To mimic synaptic neurons, spiking oscillations, which are the specific characteristics of neurons, can be generated from excitable nonlinear devices and the similar dynamics as neurons are reproduced. The information processing using semiconductor lasers that exploit the dynamical analogy of spiking oscillations between semiconductor photo-carriers and neuron biophysics is reviewed by Prucnal et al. (2016). Another approach to mimic synaptic neurons is not to directly generate spiking oscillations but to simulate the equivalent dynamics as a function of synaptic neurons. In both cases, photonics can provide fast information processing similar to synaptic neurons, and photonic neurons and/or laser neurons promise extreme improvements in computational power efficiency.

In the following, we discuss the latter case of mimicking synaptic neurons and treat a new type of information processing based on delay differential systems, which imitate the behaviors in synaptic neurons. Without going into the biological details of a neuron in the brain, the mathematical principle of the computational abilities of the brain can be simulated by digital computers. Further, a hardware implementation of artificial neural networks is possible by using various nonlinear elements instead of a neuron. In those artificial neural networks, it is fundamental to employ many nonlinear elements to constitute the networks, which mimic the dynamic behaviors of neurons. Instead of using many coupled nonlinear network elements, only a single delayed feedback loop can also play a role for artificial neural networks, and the information processing is categorized into reservoir computing. For example, in a semiconductor laser with optical feedback as a reservoir, we assume many imaginary nodes at different positions on the feedback loop, which play a role for neurons, and the optical intensity of each node at a certain time is allocated to the output of a neuron in the reservoir system. Related to the subject in this chapter, the key is the consistency of the response of the output from the system for repeated same or similar inputs to the reservoir. The methods,

implementations, and applications of reservoir computing will be discussed in the following sections. Here, we discuss the difference between traditional artificial neural networks and the networks in reservoir computing.

Based on the behaviors of synaptic neurons, Hopfield (1982, 1984) proposed artificial neural network architecture, which is suitable for solving tasks on digital computers. This enables to effectively perform optimization problems and pattern recognitions for partial images, for one of examples, a traveling salesman problem, which is very difficult to calculate by computers based on a traditional Von Neumann architecture due to exhaustive search for the digital computation. The studies related to the methods of machine learning had been existed before Hopfield, however, the study of mimicking neural networks made rapid progress since then, and various procedures related to the Hopfield model have been reported and have been successfully applied to various complex problems, which were difficult to calculate in ordinary digital computation. These methods are in general recurrent neural networks including self-feedback and connections among nonlinear elements which mimicking neuron behaviors in the human brain. In recurrent neural networks, the performance of information processing is strongly related to the connection weights of nodes (neurons) in input and output interfaces, and network nodes, which are connected to each other through the recurrent networks. In those recurrent neural networks, the optimizations of the weights for all the connections are always required to obtain successful results by the learning processes. The algorithms are complex and the network training usually takes huge amounts of calculations.

In artificial neural networks, the nonlinearity of network elements is essential and a sigmoid function has been frequently used as a nonlinear response function in traditional neural networks. According to the training of the connection weights in the networks, an input signal is transformed into a high dimensional state space in which the signal is represented. Then, it reshapes the signal onto a linear one through nonlinear separation of the input signal and the final result, which is necessary to be separated or classified, is obtained from the output layer. In the real brain, the delay occurs between two distant neurons in cerebral cortex due to the axonal conduction delay. It is important to note that two neurons show zero-lag synchronization in spite of the delay. The delay induces complex dynamics to the network system and the system shows an ambivalent impact on the dynamical behavior, either stabilizing or destabilizing (chaos). These are the same situations for coupled semiconductor lasers as discussed in the preceding sections. The response of semiconductor lasers is very fast over nanosecond, while the connection delay of neurons is tens of milliseconds. Therefore, realizations based on photonics systems are feasible using semiconductor lasers as nonlinear elements in neural networks, including real-time processing capabilities.

14.7.2 Neural Networks and Reservoir Computing

The training procedure of a recurrent neural network is very complex, and the training becomes highly nonlinear and requires a lot of computational power. To reduce the complexity in recurrent neural networks for the calculation of the connection weights in the learning process, the method of reservoir computing has been proposed in the early 2000s (Jaeger 2001; Maass et al. 2002). Contrary to recurrent neural networks, in reservoir computing, the connections between the input layer and the reservoir and, also, the internal connections of nodes in the networks are fixed. Only the training of the output weights is required according to the information to be reconstructed. By using this procedure, the training becomes linear. Therefore, this approach has the great advantage over that of recurrent neural networks and the calculations for the weight connections are much reduced. Figure 14.23a shows the general concept of traditional recurrent neural networks. The feedback signals through the training are always required to the respective

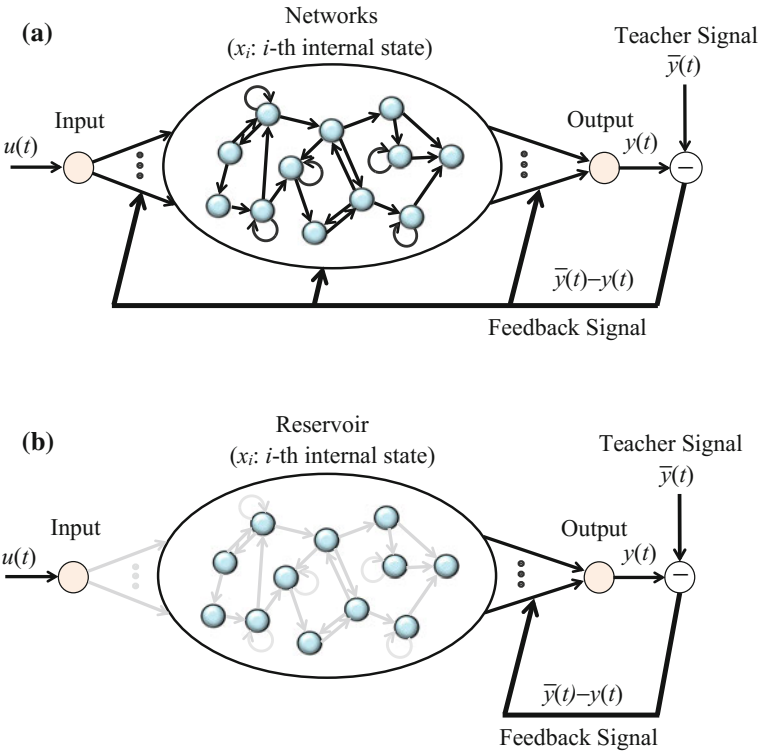

Fig. 14.23 **a** Traditional neural networks. The network is recurrent and the neurons are all connected with certain weights. The weights of the connections are obtained through the learning for the target task. **b** Networks of reservoir computing. The learning is only performed between the reservoir nodes and the output layers, and they are fixed

layers, e.g., input, networks, and output layers. While, in reservoir computing, the feedback signals are only applied to the connections between the network and output layers as mentioned above as shown in Fig. 14.23b. The simplified version of reservoir computing, which is based on the analogy between neuron networks and single-delay nonlinear systems, has been proposed (Appeltant et al. 2011; Appeltant 2012). The aim of this section is an introduction of reservoir computing using a single semiconductor laser subjected to optical feedback. Therefore, we do not discuss the details of the methods and mathematical background of reservoir computing. The general method of reservoir computing and its mathematical procedures can be found in the report (Jaeger 2001).

The general system for reservoir computing consists of three layers, namely, input layer, reservoir, and output layers as depicted in Fig. 14.23b. In the input layer, an input signal multiplied by connection weights (usually random weights) is fed into the networks of the reservoir. The reservoir consists of many nonlinear nodes, which play a role like neurons. It is one of recurrent neural networks with fixed connections. Namely, in the internal network, nodes are mutually connected and, also, they include self-feedback. To achieve the excellent performance of information processing, a large number of reservoir nodes are required and the number of reservoir nodes over several hundreds is used in ordinary networks. The reservoir responds transient states for the input. In the output layer, the output for the input data is calculated as a linear combination of transient values of virtual nodes with the output weights (trained weights). The output weights are optimized by minimizing the mean-square error between the target function and the output from the reservoir through the learning process.

Followings are the key properties of reservoir computing for projecting of input state onto high-dimensional feature space;

1. The response of the reservoir networks must have the properties of consistency and approximation. The responses to same inputs must be consistent and two closed enough inputs yield the same output. At the same time, the reservoir should not be too sensitive and, as a result, similar or alike inputs should not be associated to different classes. On the contrary, the reservoir should exhibit sufficiently different dynamical responses to inputs belonging to different classes. The result of reservoir computing must be reproducible and the system must robust against noises adjacent with inputs or internal noises included in the network elements.
2. As a reservoir performance, the system should have the abilities of separation and classification for different inputs. Namely, different enough inputs must be classified into different outputs. In the reservoir, a low-dimensional input is mapped onto high-dimensional states through the connections of many nonlinear nodes, which constructs a hyper-plane that has a property of separating different classes of data.
3. The dynamics of the reservoir should exhibit a fading memory or a short-term memory. The reservoir state should have some influences of inputs from the recent past, but it should be independent for the inputs from the distant past. The

property is indispensable for the classification and processing of temporal sequences for which the history of the signal is important.

4. As for the connections of reservoir nodes, the connections are randomly chosen and kept fix without trained for possible inputs, which is quite different from the traditional neural networks. According to the learning, the transient states of reservoir nodes are appropriately weighted and the linear summation of the results is read out at the output layer, resulting optimum solution for a certain task. Thus, the training algorithm can be drastically simplified to a linear classifier.

In the following sections, a simplified system for common reservoir computing and its application are introduced. The system uses a semiconductor laser with optical feedback as a reservoir and imaginary nodes are allocated on the optical feedback loop.

14.7.3 Reservoir Computing and Implementation

Appeltant et al. (2011) proposed a simple reservoir computing system that uses a single delay feedback loop instead of using many nodes as reservoir elements. Nonlinear nodes are assumed to be existed on the separated positions in the feedback loop as the imaginary ones, and the transient states from the nodes play a role for the reservoir outputs. The method was tested by opto-electronic delay-feedback circuits, and optical and electronic hybrid delay-feedback systems. To give an indication on the processing power of a reservoir, a wide range of benchmark tasks are successfully demonstrated (Larger et al. 2012; Paquot et al. 2012). Also, all-optical reservoir computing employing the saturation effects of a semiconductor optical amplifier as nonlinearity is reported (Duport et al. 2012). The performance of reservoir computing depends on the characteristics of each nonlinear element, however, over-all system operations do not depend them (Larger et al. 2012). In accordance with this fact, a single semiconductor laser with optical feedback, which is one of the main subjects in this book, can be used as a reservoir. This type of all-optical reservoir computing is also demonstrated (Brunner et al. 2013; Hicke et al. 2013; Nakayama et al. 2016).

According to Fig. 14.23b, we show a brief mathematical representation for general reservoir computing. The reservoir computing implementation we work with is closely related to echo state networks (Jaeger and Haas 2004). For a sampled data, the node states $\mathbf{x}(n)$ at time step n are computed in the following equation:

$$\mathbf{x}(n) = f\left\{\mathbf{W}_{\text{res}}^{\text{res}}\mathbf{x}(n-1) + \mathbf{W}_{\text{in}}^{\text{res}}\mathbf{u}(n-1) + \mathbf{W}_{\text{bias}}^{\text{res}}\right\} \tag{14.7}$$

where $f(\bullet)$ is the nonlinear function that represents the reservoir, and $\mathbf{u}(n-1)$ is the input at time step $n-1$, $\mathbf{W}_{\text{res}}^{\text{res}}$ is reservoir connection weights, $\mathbf{W}_{\text{in}}^{\text{res}}$ is connection weights between the input and reservoir, and $\mathbf{W}_{\text{bias}}^{\text{res}}$ is a random bias matrix. In some

cases, feedback from the output to the reservoir nodes is also included. In a simplified formulation, the output vector $\mathbf{y}(n)$ is a weighted linear combination of the node states, a constant bias value, and the input signals themselves:

$$\mathbf{y}(n) = \mathbf{W}_{\text{res}}^{\text{out}}\mathbf{x}(n) + \mathbf{W}_{\text{in}}^{\text{out}}\mathbf{u}(n-1) + \mathbf{W}_{\text{bias}}^{\text{out}} \tag{14.8}$$

Again, the matrices $\mathbf{W}_{\text{XXX}}^{\text{out}}$ are the connection weights for the output. In reservoir computing, only the matrices in (14.8) are optimized through the training to minimize the error $\langle(\mathbf{y} - \bar{\mathbf{y}})^2\rangle$ between the calculated output values and the required output values $\bar{\mathbf{y}}$.

Using the essence of above calculation, simple dynamical systems with delayed feedback are proposed as reservoir computing (Appeltant et al. 2011). The basic principle is shown in Fig. 14.24, which consists of a single nonlinear delay feedback loop (feedback delay time is τ) as a reservoir. For an original input stream $u(t)$, it is converted to piecewise function $I(t)$ (Fig. 14.24a; $I(t) = u(n)$) by sampling, which is constant during one delay interval τ. Next, a mask function is multiplied to $I(t)$. The mask function is a piecewise constant function during θ with period τ. The values of the mask function during each interval of length θ are chosen independently and it has a random distribution (usually, it has binary values). Within the delay loop in the reservoir, we define N equidistant points separated in time by $\theta = \tau/N$. These N equidistant points represent the virtual nodes. The value of θ should have enough larger than the response time T_0 of the system (in a case of a semiconductor laser with optical feedback, this corresponds to the laser relaxation time τ_{R}). The condition comes from the requirement for the characteristic of fading memory of reservoir nodes. Then, the input function is $J(t) = M(t)I(t)$ as shown in Fig. 14.24b. The reason for the introduction of such mask is that the node states would show transient responses, which satisfy the condition of the consistency for the input and output relation in the reservoir.

In usual, the sum of the weighted input $\gamma J(t)$ (γ is an adjustment parameter) and one delayed signal $x(t - \tau)$ through the loop becomes the input to the reservoir to the next step. With this procedure, we obtain N different, time-multiplexed transient states $x_i(t)$, with integer i. The induced nonlinear transient states should contain a maximum amount of information about the injected input. Therefore, the system must be kept sufficiently far from reaching a steady state during its dynamical response. The output of the nonlinear nodes is depicted in Fig. 14.24c. The final step for the output is the summation of these induced transient states $x_i(t)$ with the multiplexed weights. This is done by calculating a linear combination of the laser output intensities. For the requirement of the approximation and the consistency property in machine learning, the system has to be capable of generating reproducible and consistent transients. Appeltant et al. (2011) used a simple sum of the final output as follows:

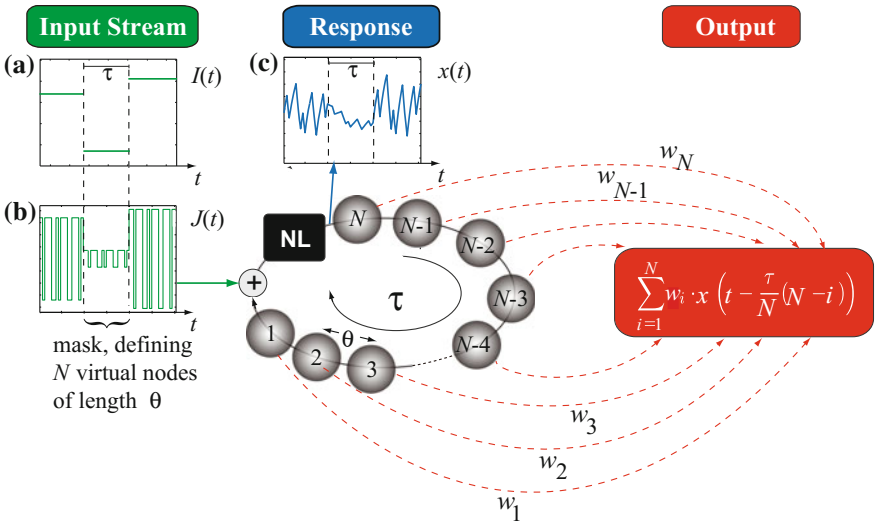

Fig. 14.24 Three layers of a reservoir computing with a delayed feedback system. **a** Three time steps of sampled time series $I(t)$. τ is the loop delay. **b** Input time series $J(t)$ with a random binary mask function $M(t)$ to the nonlinear delay loop. **c** Response function $x(t)$ of the nonlinear node. Final output in the output layer is the linear sum of the state functions of nodes and the learning weights [after Appeltant et al. (2011); © 2011 Nature Pub.]

$$y(n) = \sum_{i=1}^{N} w_i x\{n\tau - \theta(N - i)\} \tag{14.9}$$

Here, w_i is again the weight for the i-th node obtained from the training. As it is noted that a random mask function is applied to the input signal, since the node states should have transient response for satisfying the consistency condition. For most case, a mask function has a binary random function during period θ. On the other hand, other mask functions, such as a multi-valued random function, are sometimes used to reduce the noise effects (Soriano et al. 2013b; Appeltant et al. 2014).

14.7.4 Application of Reservoir Computing to Time Series Perdition

In our brain, thanks to the dynamic activity of neuron networks, we can extract clear and necessary information from insufficient external stimuli such as a blurry photo and a partial image. Inspired by our brain, we can mimic the brain's information processing by the artificial neural networks instead of a traditional Von Neumann

architecture, which executes a set of preprogrammed instructions. Without entering the biological details of a neuron, we can mimic the function of neuron networks by simulating it based on the mathematical principle. The method of reservoir computing is not only effective for solving such complex problems but also provides faster information processing than that of traditional digital computing. Reservoir computing allows for solving tasks such as pattern recognition, classification of signals, time series prediction, and dynamical system modeling. For examples, based on various delay feedback systems as reservoir, spoken digit recognition (Appeltant et al. 2011; Brunner et al. 2013), electrocardiogram (ECG) classification (Escalona-Moran et al. 2015), and chaotic time series prediction (Brunner et al. 2013; Nakayama et al. 2016) have been successfully demonstrated. In the following, we discuss reservoir computing using a single semiconductor laser with optical feedback and present the application of it to the prediction of chaotic time series.

A system of a single semiconductor laser with optical feedback, which is discussed in the previous section, is used as a reservoir (Brunner et al. 2013). The experimental system is a similar one as that in Fig. 14.24. A semiconductor laser operating at the emission line of $\lambda = 1.542$ μm and the relaxation oscillation frequency at free running state varies from 1.4 to 5 GHz depending on the bias injection current. The response time T_0 of the system is approximately equal to the relaxation time. The node separation θ should satisfy the condition of the fading memory and θ should be much less than T_0. In the following example, θ is taken as $\theta / T_0 = 0.2$. For successful information processing, a significant number of different nonlinear transients are required in the feedback loop. The feedback delay is set to be $\tau = 77.6$ ns and the number of nodes is $N = 388$, thus, the node separation is $\theta = 200$ ps. An input to the reservoir, i.e., to a semiconductor laser with optical feedback, is applied through the bias injection current or optical injection from another tunable laser. The optical output from the feedback loop corresponding to each node is detected and the weight calculated from the training is multiplied. Then, the final result is calculated as a linear sum of the results in a digital manner.

Figure 14.25 is an experimental result for a chaotic time-series prediction task of the Santa Fe time-series competition, data set A (Weigend and Gershenfeld 1993). The data set, created by a class C far-infrared NH_3 laser operating in a chaotic state (Huebner et al. 1989), consists of 4000 data points, from which is used 80% for training and 20% for testing and five-fold cross-validation. Figure 14.25a shows the original chaotic time series. The best estimation is obtained at the bias injection current close to the threshold of $I_b = 7.62$ mA and the feedback attenuation 10 dB. Figure 14.25b represents transient states (internal node states) for bias injection currents of $I_b = 7.62$ (green), 9.2 (red) and 10.78 mA (black). Figure 14.25c is the output time series at $I_b = 7.62$ mA (black; target, and red; predicted). The best performance is obtained for I_b close to the laser threshold, with a prediction error of 10.6% at a prediction rate of 1.3×10^7 points per second (corresponding to injecting information at a rate of 1 Byte per clock cycle τ). This type of tasks is

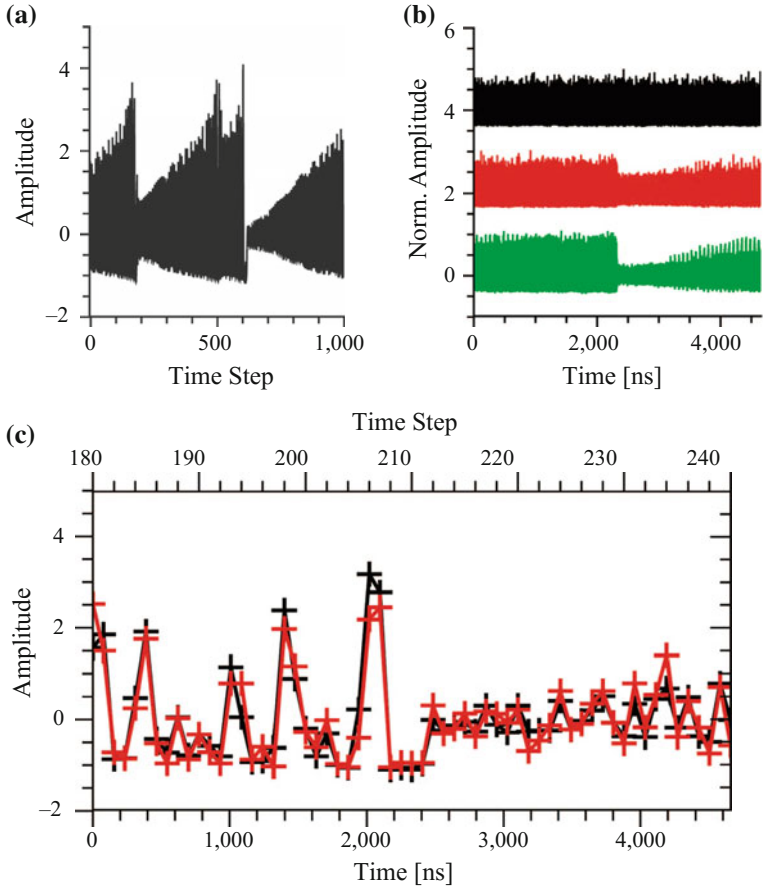

Fig. 14.25 Original and predicted trace, and corresponding transients. **a** Sample of target chaotic time series of Santa Fe data. **b** Experimental transient states (internal reservoir states) for the bias injection current of $I_b = 7.62$ (*green*), 9.2 (*red*) and 10.78 mA (*black*). **c** Target (*black*) and predicted (*red*) time series at $I_b = 7.62$ mA. The upper horizontal axis is the time step corresponding to the original target time step. The lower horizontal axis represents the temporal duration for the prediction in **b** [after Brunner et al. (2013); © 2013 Nature Pub.]

greatly affected by noises compared with other tasks such as pattern recognition for partial images. To reduce the noise effects, they actually employed a six-valued mask, with a random selection from the values. As benchmark tests to evaluate the information processing capability of their scheme, Brunner et al. (2013) also performed parallel spoken digit/speaker recognition and obtained a highest data rate of 1.1 GB/s with low error rate of 0.014%.

References

L. Appeltant, M.C. Soriano, V. Van der Sande, J. Danckaert, S. Massa, J. Dambre, B. Schrauwen, C.R. Mirasso, I. Fischer, Information processing using a single dynamical node as complex system. Nat. Commun. **2**, 468–474 (2011)

L. Appeltant, Reservoir computing based on delay-dynamical systems. Joint Ph.D. Thesis, Vrije Universiteit Brussel and Universitat de les Illes Balears, (2012)

L. Appeltant, G. Van der Sande, J. Danckaert, I. Fischer, Constructing optimized binary masks for reservoir computing with delay systems. Sci. Rep. **4**, 3629–3633 (2014)

A. Argyris, M. Bourmpos, D. Syvridis, Experimental synchrony of semiconductor lasers in coupled networks. Opt. Express **24**, 5600–5615 (2016)

Y. Aviad, I. Reidler, M. Zigzag, M. Rosenbluh, I. Kanter, Synchronization in small networks of time-delay coupled chaotic diode lasers. Opt. Express **20**, 4352–4359 (2012)

M. Beierlein, J.R. Gibson, B.W. Connors, A network of electrically coupled interneurons drives synchronized inhibition in neocortex. Nat. Neurosci. **3**, 904–910 (2000)

M. Bourmpos, A. Argyris, D. Syvridis, Sensitivity analysis of a star optical network based on mutually coupled semiconductor lasers. J. Lightwave Technol. **30**, 2618–2624 (2012)

M. Bourmpos, A. Argyris, D. Syvridis, Analysis of the bubbling effect in synchronized networks with semiconductor lasers. IEEE Photonic Technol. Lett. **25**, 817–820 (2013)

D. Brunner, M.C. Soriano, C.R. Mirasso, I. Fischer, Parallel photonic information processing at gigabyte per second data rates using transient states. Nat. Commun. **4**, 1364–1400 (2013)

J.M. Buldú, M.C. Torrent, J. García-Ojalvo, Synchronization in semiconductor laser rings. J. Lightwave Technol. **25**, 1549–1554 (2007)

E. Cohen, E. Rosenbluh, I. Kanter, Phase transition in crowd synchrony of delay-coupled multilayer laser networks. Opt. Express **18**, 19683–19689 (2012)

F. Duport, B. Schneider, A. Smerieri, M. Haelterman, S. Massar, All-optical reservoir computing. Opt. Express **20**, 22783–22795 (2012)

B. Eckhardt, E. Ott, S.H. Strogatz, D.M. Abrams, A. McRobie, Modeling walker synchronization on the Millennium Bridge. Phys. Rev. E **75**, 021110-1–021110-10 (2007)

M. Escalona-Moran, M.C. Soriano, I. Fischer, C.R. Mirasso, Electrocardiogram classification using reservoir computing with logistic regression. IEEE J. Biomed. Health Inf. **19**, 892–898 (2015)

I. Fischer, R. Vicente, J.M. Buldú, M. Peil, C.R. Mirasso, M.C. Torrent, J. Garciá-Ojalvo, Zero-lag long-range synchronization via dynamical relaying. Phys. Rev. Lett. **97**, 123902-1–123902-4 (2006)

T. Fukuda, T. Kosaka, W. Singer, R.A.W. Galuske, Gap junctions among dendrites of cortical GABAergic neurons establish a dense and widespread intercolumnar network. J. Neurosci. **26**, 3434–3443 (2006)

C.M. González, C. Masoller, M.C. Torrent, J. García-Ojalvo, Synchronization via clustering in a small delay-coupled laser network. Europhys. Lett. **79**, 64003-1–64003-6 (2007)

R.W. Guillery, Review: observations of synaptic structures: origins of the neuron doctrine and its current status. Phil. Trans. Ray. Soc. B **360**, 1281–1307 (2005)

D. Hansel, G. Mato, C. Meunier, Phase dynamics for weakly coupled Hodgkin-Huxley neurons. Europhys. Lett. **23**, 367–372 (1993)

T. Heil, I. Fischer, W. Elsäßer, J. Mulet, C.R. Mirasso, Chaos synchronization and spontaneous symmetry-breaking in symmetrically delay-coupled semiconductor lasers. Phys. Rev. Lett. **86**, 795–798 (2001)

S. Heiligenthal, T. Dahms, S. Yanchuk, T. Jüngling, V. Flunkert, I. Kanter, E. Schöll, W. Kinzel, Strong and weak chaos in nonlinear networks with time-delayed couplings. Phys. Rev. Lett. **107**, 234102-1–234102-5 (2011)

S. Heiligenthal, T. Jüngling, O. D'Huys, D.A. Arroyo-Almanza, M.C. Soriano, I. Fischer, I. Kanter, W. Kinzel, Strong and weak chaos in networks of semiconductor lasers with time-delayed couplings. Phys. Rev. E **88**, 012902-1–012902-13 (2013)

H. Hicke, M.A. Escalona-Morán, D. Brunner, M.C. Soriano, I. Fischer, C.R. Mirasso, Information processing using transient dynamics of semiconductor lasers subject to delayed feedback. IEEE J. Sel. Top. Quantum Electron. **19**, 1501610-1–1501610-10 (2013)

A.L. Hodgkin, A.F. Huxley, A quantitative description of membrane current and its application to conduction and excitation in nerve. J. Physiol. **117**, 500–544 (1952)

J. Hopfield, Neural networks and physical systems with emergent collective computational abilities. Proc. Natl. Acad. Sci. **79**, 2554–2558 (1982)

J. Hopfield, Neurons with graded response have collective computational properties like those of two-state neurons. Proc. Natl. Acad. Sci. **81**, 3088–3092 (1984)

U. Huebner, N.B. Abraham, C.O. Weiss, Dimensions and entropies of chaotic intensity pulsations in a single-mode far-infrared NH_3 laser. Phys. Rev. A **40**, 6354–6365 (1989)

C. Huygens, *Christiaan Huygens' the Pendulum Clock, or, Geometrical Demonstrations Concerning the Motion of Pendula as Applied to Clocks* (Iowa State Press, 1986)

H. Jaeger, The 'echo state' approach to analyzing and training recurrent neural networks. Technical Report GMD Report 148, German National Research Center for Information Technology (2001)

H. Jaeger, H. Haas, Harnessing nonlinearity: predicting chaotic systems and saving energy in wireless communication. Science **304**, 78–80 (2004)

I. Kanter, M. Zigzag, A. Englert, F. Geissler, W. Kinzel, Synchronization of unidirectional time delay chaotic networks and the greatest common divisor. Europhys. Lett. **93**, 60003-1–60003-6 (2011a)

I. Kanter, E. Kopelowitz, R. Vardi, M. Zigzag, W. Kinzel, M. Abeles, D. Cohen, Nonlocal mechanism for cluster synchronization in neural circuits. Europhys. Lett. **93**, 66001-1–66001-6 (2011b)

I. Kanter, E. Kopelowitz, R. Vardi, M. Zigzag, D. Cohen, W. Kinzel, Nonlocal mechanism for synchronization of time delay networks. J. Stat. Phys. **145**, 713–733 (2011c)

L. Larger, M.C. Soriano, D. Brunner, L. Appeltant, J.M. Gutierrez, L. Pesquera, C.R. Mirasso, I. Fischer, Photonic information processing beyond turing: an optoelectronic implementation of reservoir computing. Opt. Express **5**, 188–200 (2012)

W. Maass, T. Natschläger, H. Markram, Real-time computing without stable states: a new framework for neural computation based on perturbations. Neural Comput. **14**, 2531–2560 (2002)

R. Milo, S. Shen-Orr, S. Itzkovitz, N. Kashtan, D. Chklovskii, U. Alon, Network motifs: simple building blocks of complex networks. Science **298**, 824–828 (2002)

J. Mulet, C.R. Mirasso, T. Heil, I. Fischer, Synchronization scenario of two distant mutually coupled semiconductor lasers. J. Opt. B: Quantum Semiclass. Opt. **6**, 97–105 (2004)

J. Nakayama, K. Kanno, A. Uchida, Laser dynamical reservoir computing with consistency: an approach of a chaos mask signal. Opt. Express **24**, 8679–8692 (2016)

M. Nixon, M. Friedman, E. Ronen, A.A. Friesem, N. Davidson, I. Kanter, Synchronized cluster formation in coupled laser networks. Phys. Rev. Lett. **106**, 223901-1–223901-4 (2011)

M. Nixon, M. Friedman, E. Ronen, A.A. Friesem, N. Davidson, I. Kanter, Controlling synchronization in large laser networks. Phys. Rev. Lett. **108**, 214101-1–214101-5 (2012)

J. Ohtsubo, R. Ozawa, M. Nanbu, Synchronization of small nonlinear networks in chaotic semiconductor lasers. Jpn. J. Appl. Phys. **54**, 072702-1–072702-6 (2015)

Y. Paquot, F. Duport, F. Smerieri, J. Dambre, B. Schrauwen, M. Haelterman, S. Massar, Optoelectronic reservoir computing. Sci. Rep. **2**, 287–292 (2012)

T. Pérez, A. Uchida, Reliability and synchronization in a delay-coupled neuronal network with synaptic plasticity. Phys. Rev. E **83**, 061915-1–061915-6 (2011)

P.R. Prucnal, B.J. Shastri, T.F. de Lima, M.A. Nahmias, A.N. Tait, Recent progress in semiconductor excitable lasers for photonic spike processing. Adv. Opt. Photon. **8**, 228–299 (2016)

D.P. Rosin, D. Rontani, D.J. Gauthier, E. Schöll, Control of synchronization patterns in neural-like Boolean networks. Phys. Rev. Lett. **110**, 104102-1–104102-5 (2013)

M.C. Soriano, J. Garcıá-Ojalvo, C.R. Mirasso, I. Fischer, Complex photonics: dynamics and applications of delay-coupled semiconductors lasers. Rev. Mod. Phys. **85**, 421–470 (2013a)

M.C. Soriano, S. Ortín, D. Brunner, L. Larger, C.R. Mirasso, I. Fischer, L. Pesquera, Optoelectronic reservoir computing: tackling noise-induced performance degradation. Opt. Express **21**, 12–20 (2013b)

S.H. Strogatz, I. Stewart, Coupled oscillators and biological synchronization. Sci. Am. **269**, 102–109 (1993)

S.H. Strogatz, D.M. Abrams, A. McRobie, B. Eckhardt, E. Ott, Crowd synchrony on the Millennium Bridge. Nature **438**, 43–44 (2005)

R.D. Traub, M.A. Whittington, I.M. Stanford, J.G. Jefferys, A mechanism for generation of long-range synchronous fast oscillations in the cortex. Nature **383**, 621–624 (1996)

A. Uchida, A. McAllister, R. Roy, Consistency of nonlinear system response to complex drive signals. Phys. Rev. Lett. **93**, 244102-1–244102-4 (2004)

G. Van der Sande, M.C. Soriano, I. Fischer, C.R. Mirasso, Dynamics, correlation scaling, and synchronization behavior in rings of delay-coupled oscillators. Phys. Rev. E **77**, 055202(R)-1–055202(R)-4 (2008)

R. Vardi, A. Wallach, E. Kopelowitz, M. Abeles, S. Marom, I. Kanter, Synthetic reverberating activity patterns embedded in networks of cortical neurons. Europhys. Lett. **97**, 66002-1–66002-6 (2012)

R. Vicente, L.L. Gollo, C.R. Mirasso, I. Fischer, G. Pipa, Dynamical relaying can yield zero time lag neuronal synchrony despite long conduction delays. Proc. Natl. Acad. Sci. **105**, 17157–17162 (2008)

A.S. Weigend, N.A. Gershenfeld, Time series prediction: forecasting the future and understanding the past. http://www-psych.stanford.edu/∼andreas/Time-Series/SantaFe.html, 1993

S.Y. Xiang, A.J. Wen, W. Pan, Synchronization regime of star-type laser network with heterogeneous coupling delays. IEEE Photonic Technol. Lett. **28**, 1988–1991 (2016)

J. Zamora-Munt, C. Masoller, J. García-Ojalvo, R. Roy, Crowd synchrony and quorum sensing in delay-coupled lasers. Phys. Rev. Lett. **105**, 264101-1–264101-4 (2010)

W.L. Zhang, W. Pan, B. Luo, X.H. Zou, M.Y. Wang, One-to-many and many-to-one optical chaos communications using semiconductor lasers. IEEE Photonic Technol. Lett. **20**, 712–714 (2008)

Chapter 15
Physical Random Number Generations and Photonic Integrated Circuits for Chaotic Generators

Abstract The strong demands for increased security in data exchange and communications in optical networks have directed a considerable part of research to physical layer data encryption techniques and, for such purpose, higher bit rates of random number generations have been expected. One of the methods based on the dynamics in semiconductor lasers is the use of chaotic time series to generate ultrafast random bit streams as a physical layer. Optical techniques are not only suitable for high-speed random number generations but also for having the good conformity for data transmission in existing optical channels. In this chapter, the principle and practice of physical random number generations based on chaotic dynamics in semiconductor lasers are discussed. The subjects related to the generations of high quality random bit sequences are also presented. For the implementation of the techniques in real systems, the miniaturization and integration of light sources as chaotic generators are essential to perform stable generations of random number bit sequences. Such systems are also expected as light sources in chaotic secure communications discussed in the preceding chapter. For this aim, deigns, and applications of all optical photonic integrated circuits for chaotic generators are presented. Finally, an application of the systems to random key distributions in quantum cryptographic systems is demonstrated.

15.1 Introduction to Physical Random Number Generations

Random number generations play fundamental role in most algorithms and systems in cryptographic applications (Stinson 1995). Generators of random numbers are divided into two categories; one is pseudo-random number generators and the other is physical random number generators. In modern digital electronic information systems, pseudo-random numbers are widely used for cryptographic data communications (Knuth 1996). Finite sequences of numbers generated by pseudo-random generators are at present considerably random to pass statistical tests of randomness in practical applications. However, sequences of

© Springer International Publishing AG 2017

J. Ohtsubo, *Semiconductor Lasers*, Springer Series in Optical Sciences 111,
DOI 10.1007/978-3-319-56138-7_15

pseudo-random numbers generated deterministically from the same seed will be identical, and this can cause serious problems for applications in security or parallel computation systems. Truly random numbers should be un-reproducible as well as statistically unbiased. For this reason, physically random processes are often used as entropy sources in random number generators. As physical entropy sources for nondeterministic random number generations, random phenomena, for examples, thermal noise in resistors and frequency jitter of electronic oscillators have been used in combination with deterministic pseudo-random number generators. However, rates of nondeterministic random number generators are usually very slow compared to than pseudo-random generators due to limitations of the rate and power of the mechanisms for extracting bits from physical noises. Consequently, it is very difficult to obtain fast random bit streams only from "noises" induced by the electronic circuits and the typical rates are limited to around 10 Mbps (Bucci et al. 2003). Therefore, much faster physical random number generations based on different mechanisms are expected in conjunction with the conformity of communications in optical channels.

To overcome the difficulty of the low speed of random number generators, optical techniques have been introduced. Nondeterministic random number generations rely on stochastic physical processes, the most appealing examples of which are based on fundamental quantum principles such as uncertainty. Spontaneous quantum noises and thermal laser noises have frequently been used as the main techniques for the generations of physical random numbers. These quantum random number generators include two-path splitting of single photons, photon number path entanglement, time of generation or counting of photons, fluctuations of the vacuum state using homodyne detection techniques as well as interferometric schemes. For example, Qi et al. (2010) proposed the method of quantum random number generations by measuring phase noise of a single-mode DFB laser and attained the generation speed at 500 Mbps. Williams et al. (2010) used amplified spontaneous emission generated in an Er/Yb-doped fiber and demonstrated the sampling rate of random bit sequences of 12.5 Gbps. Symul et al. (2011) generated random number bit sequences at 2 Gbps based on fluctuations of the vacuum state using homodyne detection techniques. Li et al. (2011) examined an optoelectronic system for simultaneously generating parallel, independent streams of random bits using spectrally separated noise signals obtained from a single optical source. They used a pair of non-overlapping spectral filters and a fiber-coupled superluminescent LED and produced two independent 10 Gbps random bit streams, for a cumulative generation rate of 20 Gbps. Nie et al. (2015) achieved the highest bit rates of 68 Gbps using phase diffusion quantum random number generation in phase fluctuated lasers. Abellan et al. (2016) made an indium phosphide photonic integrated circuit for random number generation, whose chip

size is only 6×2 mm. Their system is based on two-laser interference and heterodyne detection and it is able to generate random numbers at rates higher than 1 Gbps.

On the other hand, deterministic chaos can be applied for the generations of random number sequences, whose principle is quite different from those of quantum nature of light. Indeed, chaos induced by semiconductor lasers with optical feedback has been used as a noisy light sources to make random number sequences and proved that such systems could be generated random number bits much faster than the existing optical methods (Uchida et al. 2008; Uchida 2012). The advantages of the use of chaos for random number generations are the robustness and stability of the method, and also the easiness for integration of the system as a compact photonic circuit. At present, the speed of random number generations of several giga sampling per second has been demonstrated in real time, while the post-processing techniques enabled the speed over several hundreds of giga sampling per second to tera sampling per second. The technique is very promising for ultrafast random number generators, however, the essential limitation of the speed for chaotic random number generators and the detailed performance of the systems are not clear. The study is still ongoing and these subjects are left for the future issues.

15.2 Signatures in Optical Feedback Induced Chaos

Systems of semiconductor lasers with optical feedback are widely used to generate chaotic time series and they are employed for cryptographic applications as we discussed in the previous chapter. We here present the characteristics of chaotic signals induced by optical feedback systems in semiconductor lasers and their applications to physical random number generations. In delayed hyper-chaotic systems, the security of chaotic communications is guaranteed by the computational complexity to reconstruct a high-dimensional attractor from the time series. For such purpose, a noise-like appearance of a chaotic carrier is expected to conceal messages into chaotic waveforms. A chaotic signal inevitably contains the time signatures of the optical feedback loop and the relaxation oscillation of the semiconductor laser, which can be easily inferred from the analysis of the time correlation for the signal. Otherwise, the knowledge of the time delay allows for the projection of the high-dimensional attractor onto a reduced-dimensional phase space, which makes the system vulnerable to low-computational-complexity identification techniques (Rontani et al. 2007, 2009; Wu et al. 2010). Therefore, it is essential to hide the signatures of these time constants in the waveform of chaotic carrier, since these time constants are important keys in chaos-based secure

communications. In those applications, the existence of some periodicities in the chaotic waveforms might be allowed as far as they are not related to the time constants. On the other hand, periodicities in chaotic waveforms should be eliminated for the applications of physical random number generations. If the periodic structures in the chaotic waveforms were significant, some periodic recurrences might not be avoided in the extracted random number-bit sequences. So periodic components in time series should be as small as possible for the applications of random number generations based on chaotic semiconductor lasers as well as secure communications discussed in Chap. 13. The point for applications will be again discussed in Sect. 15.4.

The system of semiconductor laser subjected to optical feedback considered here is the same as discussed in Chap. 4 and we use the same equations as (4.5)–(4.7) to theoretically describe the system. To investigate time-delay signatures in chaotic waveforms, the autocorrelation function is commonly employed. As another measure to estimate periodicity exiting in a time series, the mutual information is frequently used. For the photon number $S = |A|^2$, the autocorrelation function C for the time delay Δt is written by

$$C(\Delta t) = \frac{\langle \{S(t-\Delta t) - \bar{S}\}\{S(t) - \bar{S}\}\rangle}{\sqrt{\langle S(t-\Delta t) - \bar{S}\rangle^2 \langle S(t) - \bar{S}\rangle^2}} \tag{15.1}$$

where $\bar{S}$ is the mean value of photon number. Meanwhile, the mutual information I is defined by

$$\mathrm{I}(\Delta t) = \sum_{S(t-\Delta t), S(t)} p\{S(t-\Delta t), S(t)\} \log \frac{p\{S(t-\Delta t), S(t)\}}{p\{S(t-\Delta t)\} p\{S(t)\}} \tag{15.2}$$

where $p\{S(t-\Delta t), S(t)\}$ is the joint probability, and $p\{S(t)\}$ and $p\{S(t-\Delta t)\}$ are the marginal probability densities. The mutual information (sometimes known by the archaic term trans-information) of two random variables is a quantity that measures the mutual dependence of the two random variables and the mutual information is especially used for determining the embedding delay parameters. Using these measures, time signatures in chaotic waveforms in semiconductor lasers with optical feedback are examined in the following.

Figure 15.1 shows some experimental results for chaotic time series and their time-delay signatures (the autocorrelation function and the mutual information) for the variations of the optical intensity feedback strength (Wu et al. 2010). The laser used is a single mode DFB laser operating with a wavelength at 1.55 μm. The laser is biased at $1.09I_{\mathrm{th}}$ (I_{th}: threshold current) and the corresponding relaxation oscillation time (the inverse of the relaxation oscillation frequency) is $\tau_{\mathrm{R}} = 0.55$ ns. The optical delay in the external feedback in the semiconductor laser is set to $\tau = 2$ ns.

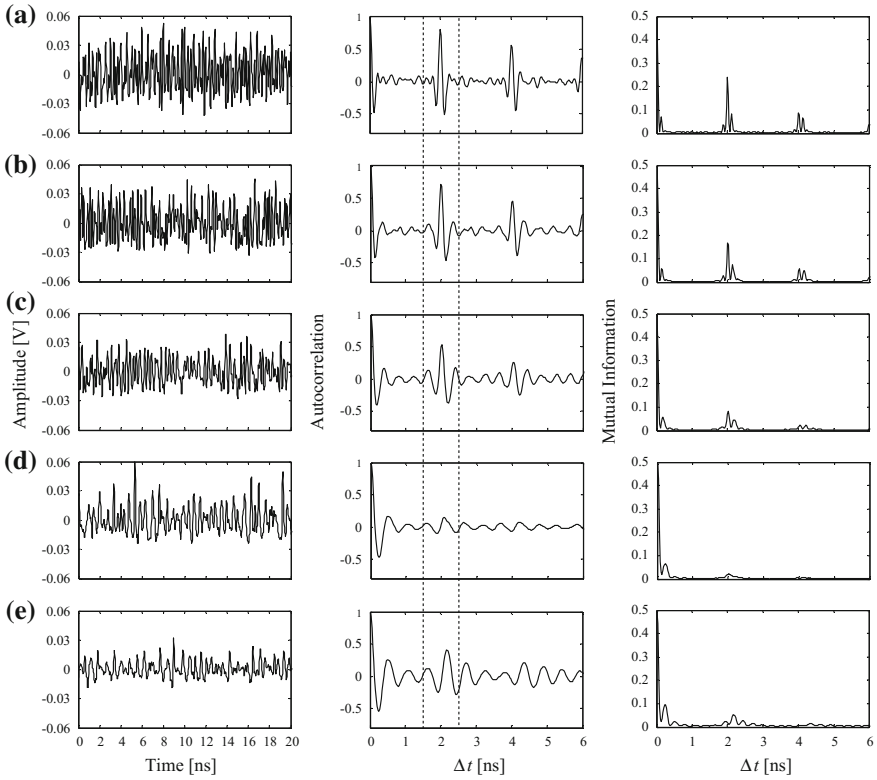

Fig. 15.1 Experimentally obtained chaotic time series for different optical feedback strengths at the optical feedback time of $\tau = 2$ ns, the laser relaxation time of $\tau_R = 0.55$ ns, and the bias injection current of $1.09I_{th}$ (*left column*). Calculated autocorrelation functions (*middle column*) and mutual information (*right column*). Feedback intensity strengths of **a** 0.038, **b** 0.019, **c** 0.0064, **d** 0.0013, and **e** 0.0003 [after Wu et al. (2010); © 2010 OSA]

In Fig. 15.1, the time-delay signature around $\Delta t = \Delta t_p = 2$ ns is significant for higher optical feedback ratio (Fig. 15.1a), while the peak intensity decreases with the decrease of the optical feedback ratio. However, it again increases at the optical feedback ratio at $\gamma = 0.0003$ in Fig. 15.1e (γ is the intensity ratio of optical feedback normalized to the solitary laser power in this case). Thus, there exist an optimum strength of optical feedback to reduce the correlation peak. In this example, the correlation peak is much suppressed at the optical feedback strength of $\gamma = 0.0013$ (Fig. 15.1d) and the time-delay signature is almost shielded into the background fluctuations. For the small feedback strength at Fig. 15.1e, the time-delay signature corresponding to the external feedback time τ is not remarkable, while the time component τ_R for the relaxation oscillation is enhanced and could be estimated as about 0.55 ns from the figure.

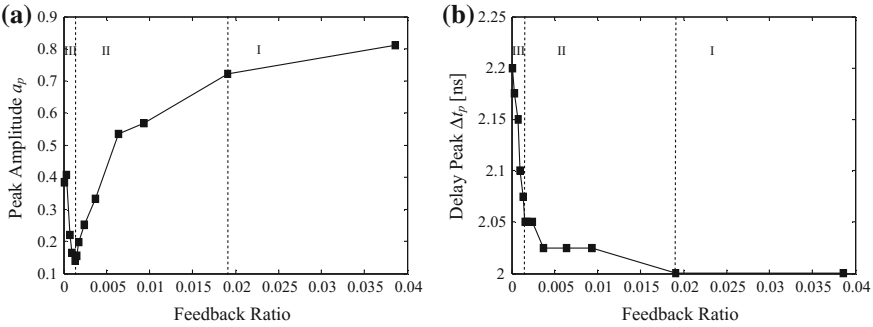

Fig. 15.2 **a** Amplitudes of the maximum correlation peaks and **b** their delay times for the optical injection strength. The experimental conditions are the same as those in Fig. 15.1 [after Wu et al. (2010); © 2010 OSA]

Figure 15.2 shows the evolution of the time-delay signature for the external feedback strength. Figure 15.2a gives the variations of the first maximum amplitude a_p for the external feedback strength, while Fig. 15.2b plots the variations of the peak delay time Δt_p. From these two curves, the evolution of the time-delay signature could be roughly divided into three regions. For $\gamma > 0.019$ (region I), the time-delay signature is obvious and the identified delay well conforms to the expected time of $\Delta t_p \approx 2$ ns. For $0.0013 < \gamma < 0.019$ (region II), the amplitude a_p of time-delay signature attenuates significantly with the decrease of the feedback strength, and the weakest time-delay signature is obtained at $\gamma \approx 0.003$. Meantime, the identified delay begins to deviate from the expected time of $\Delta t_p \approx 2$ ns. For $\gamma < 0.0013$ (region III), the amplitude of time-delay signature again increases. However, the deviation between the identified Δt_p and the exact feedback delay τ is expanded. The experimental results are qualitatively confirmed by the theory (Rontani et al. 2007, 2009). The dip of the amplitude a_p for the increase of the feedback strength is explained by the transition of chaos from weak to strong and, then for further increase, strong to weak chaos (Heilignethal et al. 2011, 2013). When the laser shows strong chaotic oscillations, the amplitude is significantly lowered and shows a small signature of chaos for the feedback parameters. As for hiding the relaxation oscillation time, we can use the relation in Fig. 5.13b. Namely, the relaxation oscillation frequency in the presence of optical feedback varies for the change of the optical delay. Therefore, the exact relaxation oscillation frequency of the solitary laser cannot be obtained when the optical delay is set to slip from the exact time of the relaxation oscillation frequency.

As discussed above, in a system of semiconductor laser with optical feedback, high-dimensional chaos is typically found where the optical feedback strength is large, but the time-delay value is easily retrieved from the analysis of the chaotic output using straightforward techniques. For hiding time-delay signatures in semiconductor lasers with optical feedback, we here summarize some useful results for security application in chaotic communications according to the detailed study

by Rontani et al. (2009). By their analysis, a careful tuning of the external cavity round-trip time with respect to the intrinsic laser relaxation oscillation frequency leads to situations where the time-delay signature is lost in the chaotic laser output. Also the bias injection current plays an important role for the existence of time-delay signatures. When the optical feedback rate is moderate and the injection current is set at rather lower bias (weak chaotic state) such that the relaxation–oscillation period of the laser is close to the optical delay ($\tau \approx \tau_R$), the time-delay identification becomes extremely difficult, thus improving the security of chaos-based communications using external cavity semiconductor lasers. Rontani et al. also proved that a time-delay signature is hardly retrievable from either the autocorrelation function or the mutual information for sufficiently close values of τ and τ_R when an eavesdropper does not know any information about the system and system parameters.

To suppress the signature of the delay time in optical feedback loop, we can use a system of unidirectional ring configuration consisting of a large number of identical semiconductor lasers. Consider a case for N coupled unidirectionally coupled ring semiconductor lasers with coupling delay of τ/N. Then, the model can be described by the following rate equations:

$$\frac{dE_j(t)}{dt} = \frac{1}{2}(1 - i\alpha)G_n\{n_j(t) - n_{th}\}E_j(t) + \frac{\kappa}{\tau_{in}}E_{j-1}\left(t - \frac{\tau}{N}\right)\exp\left(i\omega_0\frac{\tau}{N}\right) \quad (15.3)$$

$$\frac{dn_j(t)}{dt} = \frac{J}{ed} - \frac{n_j(t)}{\tau_s} - G_n\{n_j(t) - n_0\}\left|E_j(t)\right|^2 \quad (15.4)$$

where $j = 0, 1, \ldots, N$, and $E_0(t) = E_N(t)$. It is noted that (15.3) is the similar equation of (14.1). For the case of $N = 1$, the system reduces to a single laser with optical feedback. When $N = 2$, it is a system of two mutually coupled semiconductor lasers. For $N \geq 3$, the system becomes a configuration of unidirectionally coupled ring semiconductor lasers. Figure 15.3 shows numerical calculation of time series and the time correlations of the laser output from N-coupled semiconductor lasers (Van der Sande et al. 2008). As usual, discrete frequency peaks related to the external mode is visible for $N = 1$ (for the case of a semiconductor laser subjected to optical feedback). However, for the increase of the coupling number, the peaks become less defined and, finally, the signature of the delay loop is completely eliminated for a large coupling number of $N = 100$ as easily observed autocorrelation in Fig. 15.3l. It is noted that the amplitude of the first peak of the autocorrelation decreases for the increase of the coupling number N. Namely, the amplitude of the first peak of the autocorrelation in the N coupled ring laser system is equal to that of the N-th peak in the single optical feedback system. For example, the value of the fourth autocorrelation peak in Fig. 15.3c is equal to that of the first peak in Fig. 15.3i. Also, an exponential scaling law is applied for the decrease of the correlation peaks for respective coupled ring system. Thus, the correlation properties of a ring with N elements can be deduced from the autocorrelation of the single delayed feedback system (equivalent single ring element). The reason of the

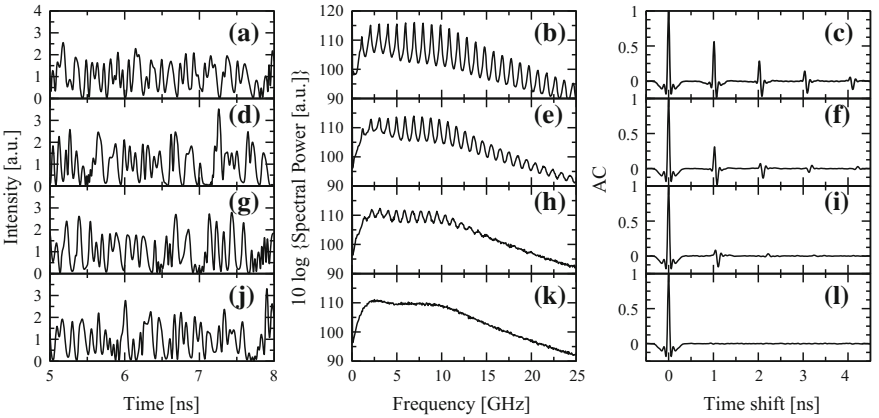

Fig. 15.3 Suppression of signature of the delay time in a ring laser. *Left column* time traces of intensities, *middle column* power spectra, *right column* autocorrelation functions. **a**–**c** Semiconductor laser with delayed optical feedback, **d**–**f** two bidirectionally coupled semiconductor lasers, **g**–**i** 4 semiconductor lasers in a ring configuration, and **j**–**l** 100 semiconductor lasers in a ring configuration [after Van der Sande et al. (2008); © 2008 APS]

suppression of the signature can be interpreted by coherence collapse of semiconductor lasers (Wang and Petermann 1991). Namely, for sufficiently large number of N, the injected field acts as a spontaneous emission noise source yielding the broadband spectrum as the corresponding nonlinear response of semiconductor lasers. This is not only a unique phenomenon that is observed in a system of coupled semiconductor lasers, and suppression of correlation peaks induced by delay can be also observed in any unidirectionally coupled nonlinear chaotic oscillators.

15.3 Probability Distributions of Chaotic Signals

Any chaotic time series exhibits irregular oscillations like noises, however, their spectra are not exactly white and their amplitudes are not Gaussian-like distributions. For example, time series of real experimental data, which are usually low-frequency-cut signals, have skewed waveforms for above or below the zero bias as shown in Fig. 15.1. Furthermore, they even contain periodic structures. For the purpose of physical random number generations, noise-like signals should have symmetrical distributions as thoroughly as possible, otherwise a true random number sequence could not be generated and the generated 0 and 1 distribution may have a bias. To eliminate the bias, the system for random number generators discussed in the next section uses two chaotic systems to equalize the ratio 0 and 1 of random number sequences, and compensates the effect of skewed amplitude distributions of chaotic outputs from optical feedback induced semiconductor

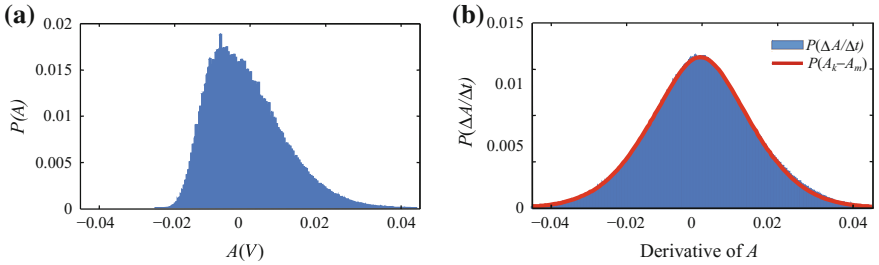

Fig. 15.4 **a** Histogram of the chaotic laser intensity obtained by an 8-bit analogue–digital converter (ADC). **b** Histogram of the derivative of the laser intensity as obtained from the time series of the laser intensities. *Red line* represents a histogram generated directly from the histogram shown in **a** [after Reidler et al. (2009); © 2009 APS]

lasers. Another example to eliminate the skew is the method of differentiation for the skewed time series. Indeed, a symmetrical distribution function close to a Gaussian shape is obtained by time-differentiating a chaotic signal from a semiconductor laser with optical feedback at least for amplitude distributions, which is suitable for the use of physical random number generations.

Figure 15.4 shows an experimental example of amplitude distributions for time-differentiated chaotic signals induced by optical feedback in a semiconductor laser (Reidler et al. 2009). To obtain time-differentiated chaotic signals, a semiconductor laser operating at 656 nm is biased at $1.55J_{\mathrm{th}}$ and the external optical feedback time is set to 12.22 ns. The chaotic time series is detected by a photodetector with a 3-dB low-frequency cutoff of 10 kHz and it is digitized by an 8-bit analogue-to-digital converter (ADC) triggered by a 2.5 GHz clock (the digital oscilloscope used has an analogue bandwidth of 12 GHz). The original sampling rate of the digitizer is 40 GSample/s. A 2.5 GHz digitized data set is used to eliminate the signature of the relaxation oscillation time, which is incommensurate with the sampling rate and the external optical feedback time. Figure 15.4a plots the histogram of the directly sampled chaotic laser intensity. The histogram of the sampled amplitudes is obtained from a 100 μs long data stream. The distribution is asymmetric, therefore an attempt for a random number sequence generated from such time series would result in some bias for a 0 and 1 distribution. Then, the raw data of the 2.5 GHz sampling is converted into a time series consisting of the derivative of the ADC signal amplitudes, A_t, as $\Delta_t = A_t - A_{t-1}$. The result is shown in Fig. 15.4b. The histogram exhibits a very high degree of symmetry and it is suitable for bins of random number generations. Since adjacent Δ_t values may be still temporally correlated even if the original amplitudes are random, one might expect that such a series is not a good candidate for a random sequence. This difficulty is further solved, however, by taking into account only the m least-significant-bits (LSBs) of each Δ_t and relying on the chaotic nature of the time varying laser intensity. We will return the subject in Sect. 15.4.2. It is noted that a care must be taken to use such time-differentiated signals in real systems.

Namely, noises (statistical noises) encountered from a photodetector and/or the laser itself might cause unwanted troubles to generate a random number sequence, since chaos is completely different from statistical noises.

15.4 Chaotic Physical Random Number Generations

15.4.1 Principles of Chaotic Physical Random Number Generations

The first physical random number generators using chaotic semiconductor lasers were proposed by Uchida et al. (2008). They demonstrated a fast physical random number generations as fast as 1.7 Gbps. However, the generation speed was not for the intrinsic limitation of the method but for the limitation of their available devices and electronic instrument. The potential of the proposed method is much faster than the obtained one and, indeed, faster random number generations based on the same principle will be introduced in the following subsections. After the demonstration, a lot of related works and the modification and improvement of the method for faster random number generations have been proposed. We here discuss random number generation based on the proposed method, since the system contained a lot of insights and the essence for physical random number generations using chaotic semiconductor lasers. Figure 15.5 shows the scheme for generation of random bits using two chaotic lasers. In each chaotic laser, a chaotic signal is induced by optical feedback in a semiconductor laser. The outputs from the chaotic lasers are respectively detected by fast photodetectors and converted to binary bit sequences by 1-bit sampling at a fixed sampling rate according to a common clock pulse. The two independent binary digital signals obtained from the two chaotic lasers are then combined by an exclusive-OR (XOR) operation. The output signal from the XOR operation is a stream of random bits with a non-return-to-zero (NRZ) format that is suitable for high-speed data communications. The reason for the use of two chaotic

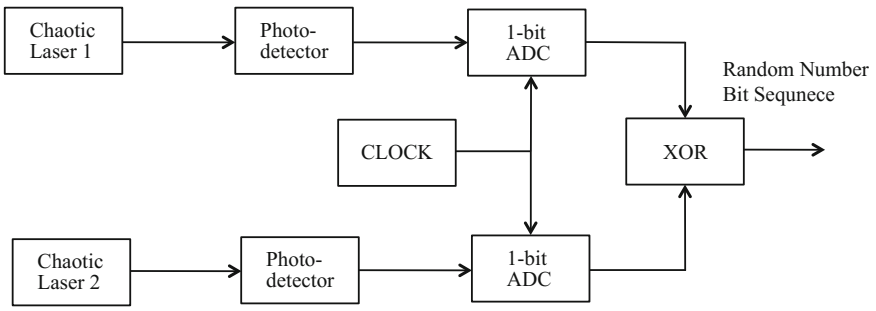

Fig. 15.5 Schematic diagram of random bit generator with two independent chaotic lasers based on 1-bit ADC with Exclusive-OR (XOR) operation

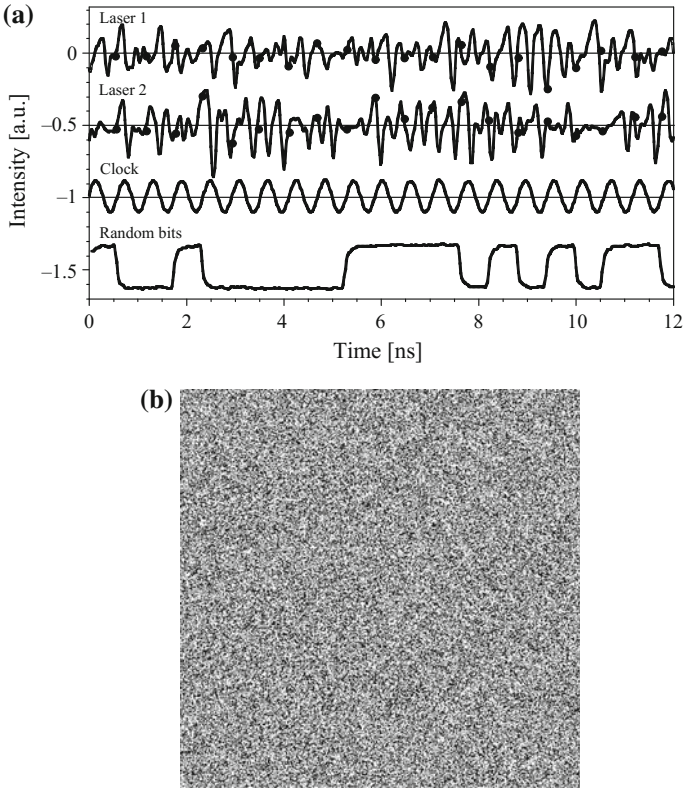

Fig. 15.6 Output signals from an experimental system of the random number generator. **a** Temporal waveforms of the laser output signals, the external clock, and the corresponding random bit sequence. From *top* to *bottom* output from laser 1, output from laser 2, clock, and generated random numbers, respectively. **b** Random bit patterns in a two-dimensional plane. Bits 1 and 0 are converted into *black* and *white dots*, respectively, and placed from left to right (and from *top* to *bottom*); 500 × 500 bits are shown [after Uchida (2011); © 2011 LSJ]

lasers is the elimination of the effect of skewed amplitude distributions of chaotic outputs from optical feedback induced semiconductor lasers as discussed in Sect. 15.3. Also the effects of time-delay signatures on the resulted random number streams discussed in Sect. 15.2 can be greatly reduced by the use of two chaotic lasers. The combination of sequences from two independent sources using XOR operation is a common simple method for improving randomness. It is proved that combining two chaotic lasers is enough to generate good random number sequences in the gigahertz regime. However, certain tuning measures based on characteristics of the chaotic dynamics (for example, such as tuning of the threshold voltages to eliminate the bias at the 1-bit ADCs) are also required to achieve good randomness.

Figure 15.6 shows the results of random number generations using chaotic semiconductor lasers (Uchida 2011). In Fig. 15.6a, the first two time series are the

raw chaotic laser outputs. Each chaotic signal is generated by a single mode DFB semiconductor lasers with optical feedback through an optical fiber. Different optical feedback delays are introduced for the two lasers to avoid similar time signatures of the chaotic waveforms. Then, the delay time of optical feedback for laser 1 is $\tau_1 = 54.26$ ns and that for laser 2 is $\tau_2 = 75.52$ ns. Also the lasers are set to have different characteristic times of the relaxation oscillations at the solitary modes by controlling the bias injection currents. The time for the relaxation oscillation is $\tau_{R1} = 0.326$ ns (relaxation oscillation frequency of $\nu_{R1} = 3.1$ GHz) for laser 1 and $\tau_{R2} = 0.350$ ns ($\nu_{R2} = 2.9$ GHz) for laser 2. The third time series in Fig. 15.6a is a clock with a frequency of 1.7 GHz ($\tau_{sa} = 0.588$ ns) to sample the chaotic amplitudes. Solid dots marks in the chaotic signals in Fig. 15.6a are points sampled at the rising edge of the clock and these values are used for XOR operations to generate a random number sequence. The threshold values for the ADCs are shown as solid lines. The scales for all time constants τ_1, τ_2, τ_{R1}, τ_{R2}, and τ_{sa} are incommensurate and these help to reduce the correlation between the chaotic pulse sequence segments. Thus, better quality of random number sequences is expected under these configurations. The binary signals obtained from each laser are combined by a logical XOR operation to generate a single random bit and the final result of the bit sequence is shown in the bottom in Fig. 15.6a. Figure 15.6b shows an example of maps for a long bit sequence generated by the system. The bit sequence is plotted in a two-dimensional plane. Bits "1" and "0" are converted into white and black dots, respectively, and placed from left to right (and from top to bottom). 500 by 500 bits are shown. It can be seen that there are neither obvious patterns nor structures and that the ratio of 1 and 0 is almost equal, as we expect from a random generation process.

The generated random bit sequences must be tested whether they are truly random sequences. For the test for a random number sequence, several test schemes have been proposed (Marsaglia 1995, 1990; Rukhin et al. 2010). Among them, the most representative statistical tests are the National Institute of Standard Technology (NIST) test suite (NIST Special Publication 800-22 Revision 1a; Rukhin et al. 2010) and they are mostly used as a statistical test suite for random-bit number sequences. The tests for the generated random-bit sequences are performed for $n = 1000$ samples of 1 Mbit sequences for all the NIST tests (the total amount of test data is 1 Gbit data) (Uchida et al. 2008; Uchida 2011). The pass criteria for the tests are chosen based on the length of the sequence and a specified significance level. The significance level of $\alpha = 0.01$ (Note that parameter α here is not the linewidth enhancement factor in the previous notation. The notation is used here, since α is commonly used for such statistical tests) is used for the p-values of each sequence test, and the P-value (uniformity of p-values) obtained for each test should be larger than 0.0001. Here, the p-value is a function of the observed sample results relative to a statistical model, which measures how extreme the observation is. The statistical significance α is defined as a measure whether it is unlikely to have occurred by chance. For "Success" using 1000 samples of sequences and significance level of $\alpha = 0.01$, the proportion of sequences satisfying p-value $> \alpha$ should

Table 15.1 Results of NIST special publication 800-22 statistical tests for randomness

Statistical test	P-value	Proportion	Result
Frequency	0.366918	0.9920	Success
Block-frequency	0.639202	0.9900	Success
Cumulative-sums	0.101311	0.9920	Success
Runs	0.223648	0.9920	Success
Longest-run	0.603841	0.9890	Success
Rank	0.031012	0.9900	Success
FFT	0.274341	0.9910	Success
Nonperiodic-templates	0.013760	0.9810	Success
Overlapping-templates	0.893482	0.9910	Success
Universal	0.903338	0.9920	Success
Approximate-entropy	0.880145	0.9920	Success
Random-excursions	0.142248	0.9836	Success
Random-excursions-variant	0.068964	0.9869	Success
Serial	0.440975	0.9860	Success
Linear-complexity	0.291091	0.9970	Success
Total			15

For "Success" using 1000 samples of 1 Mbit data. For the tests which produce multiple P-values and proportions, the worst case is shown

be in the range of $(1-\alpha) \pm \sqrt{(1-\alpha)\alpha/n} = 0.99 \pm 0.0094392$. For the tests which produce multiple p-values and proportions, the worst case of the calculated results is shown in Table 15.1. Bit sequences obtained from the experiment passed all the NIST test. Another example of statistical test suite is called Diehard test suite and it is also frequently used to check the randomness for random number sequences (Marsaglia 1995). The generated random number sequences also passed the test. The stability of statistics and the success for the statistical tests strongly depend on the effective generations of even probability for 0 and 1 random-bit numbers and these can be performed by adaptive control of the detection threshold for chaotic signals in the proposed method.

In Sect. 15.2, we discussed the existence of chaotic signatures induced by optical feedback in semiconductor lasers. For the purpose of random number generations, the amplitudes of chaotic signatures should be as small as possible to minimize the periodicities appeared in chaotic signals. Furthermore, the locations of characteristic times for chaotic signatures induced by the optical feedback loops and the relaxation oscillations of the solitary lasers should be incommensurate. In the following, we investigate the correlations of the chaotic laser outputs used for random number generations and corresponding random-bit sequences. Figure 15.7 shows experimental examples of the autocorrelation functions of each of the two chaotic laser outputs and the corresponding random-bit sequences as a function of delay time (Hirano et al. 2009). The left column in Fig. 15.7 is the results for a set of different external cavity lengths of L_1 = 2.0 m (the corresponding delay time is

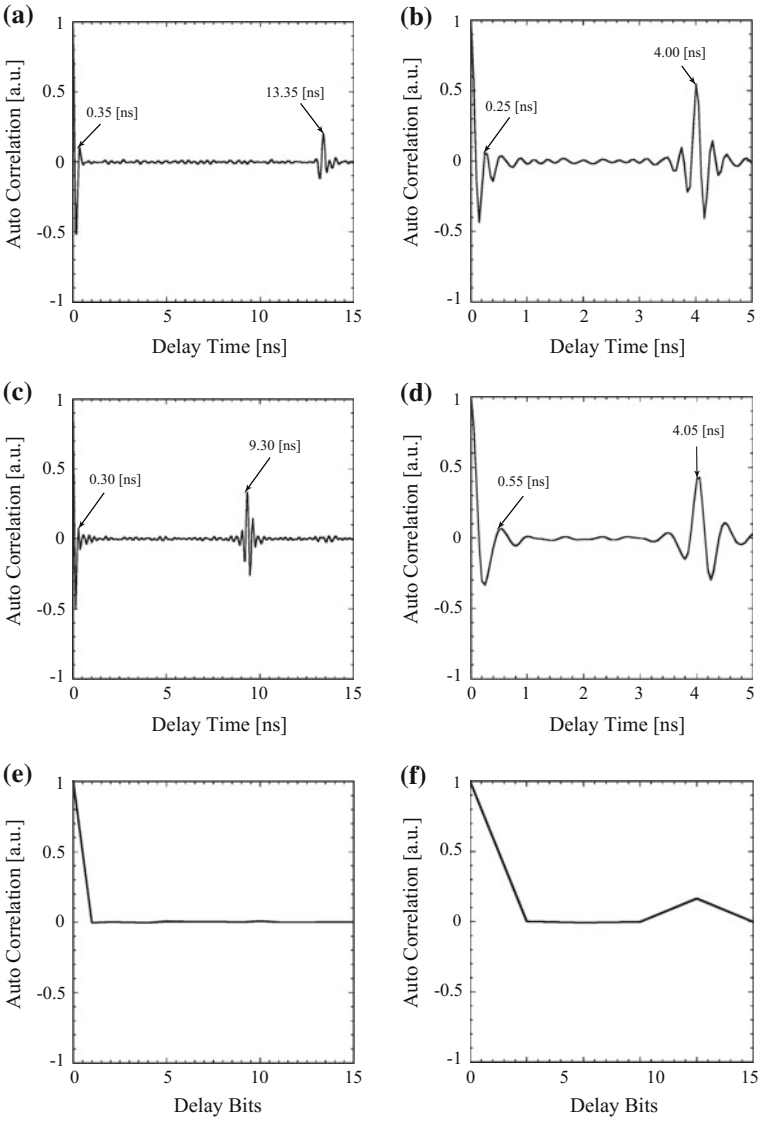

Fig. 15.7 Examples of autocorrelation functions of two chaotic laser outputs and the corresponding random bit sequences as a function of delay time. *Left column* $L_1 = 2.0$ m and $L_2 = 1.4$ m, *right column* $L_1 = 0.6$ m and $L_2 = 0.6$ m. **a** and **b** Outputs from Laser 1, **c** and **d** outputs from Laser 2, and **e** and **f** random bits [after Hirano et al. (2009); © 2009 IEEE]

$\tau_1 = 13.35$ ns for laser 1) and $L_2 = 1.4$ m (the corresponding delay time is $\tau_2 = 9.30$ ns for laser 2), while the right column is those for a set of the identical external cavity lengths of $L_1 = L_2 = 0.6$ m. The times for relaxation oscillation

frequencies of the solitary DFB lasers used in this experiment are $\tau_{R1} = 0.38$ ns ($\nu_{R1} = 2.62$ GHz) and $\tau_{R2} = 0.29$ ns ($\nu_{R2} = 3.42$ GHz), respectively.

The autocorrelation function of each chaotic laser output has chaotic signatures of two dominant peaks that correspond to the inverse of the relaxation oscillation frequency and the external cavity frequency. When the external cavity lengths are different in Fig. 15.7a, c, the time constants τ_1 and τ_2 are incommensurate with each other. Figure 15.7e shows the autocorrelation function of the random-bit sequences obtained from the two chaotic waveforms of Fig. 15.7a, c at the clock frequency of $\tau_{sa} = 1.0$ GHz (the sampling time is 1.0 ns). The autocorrelation function has no significant peak except at zero delay and, then, the bit streams passed all the NIST tests. For the same external cavity length of the two lasers, $L_1 = L_2 = 0.6$ m, the autocorrelation functions are plotted as shown in Fig. 15.7b, d. Both of the autocorrelation functions for the two lasers have the same peak value around 4.0 ns, corresponding to the delay times for the external optical feedback loops. The autocorrelation function of the random-bit sequence is similarly calculated from these two chaotic waveforms at the clock frequency of 1.0 GHz and is plotted in Fig. 15.7f. In Fig. 15.7f, a small peak is observed at 4 bit, corresponding to the external cavity round-trip delay time divided by the sampling time. Since the external cavity lengths of the two lasers are set to the same value and the sampling time is low-order commensurate to the external cavity delay time (1.0 and 4.0 ns, respectively), the peak of autocorrelation remains at 4 bit in the generated random bits. Thus, the bit streams failed the NIST tests. In general, correlation peaks appear when the external cavity lengths of the two lasers are set to a low-order commensurate ratio. This demonstrates that the two external cavity frequencies and the clock frequency need to have an incommensurate ratio (or at least a high-order commensurate ratio) to avoid periodic recurrences in the extracted bit sequences. As discussed here, eliminations of chaotic signatures in delay differential systems are essential for the applications to physical random number generations. For the suppression and elimination of time signatures in chaotic semiconductor lasers, several methods have been proposed. For examples, double optical feedback in semiconductor lasers and the generation of chaos by mutually coupled semiconductor lasers were proposed and chaotic signatures were greatly suppressed or even completely eliminated (Wu et al. 2009, 2011). Also, a system of unidirectional ring configuration consisting of a large number of identical semiconductor lasers is a good candidate for a chaos generator to eliminate chaotic signatures, which is discussed in Sect. 15.2.

15.4.2 Fast Chaotic Random Number Generators

For the expanding demand for higher speed of data transmissions in the traffics in optical communications, faster random number generations are further expected. Several methods to realize high-speed random number generations have been proposed (Reidler et al. 2009; Argyris et al. 2010b; Hirano et al. 2010; Kanter et al.

2010; Sakuraba et al. 2015). Since typical chaotic oscillations in semiconductor lasers are related to the relaxation oscillation frequency, the use of a laser that has a fast relaxation oscillation frequency is essential. However, the typical relaxation oscillation frequency of common semiconductor lasers is limited to about 10 GHz at the solitary oscillation. To enhance the bandwidth of chaotic oscillations in semiconductor lasers, the technique of strong optical injection from a different laser can be used as discussed in Sect. 6.3.6. As another different category of techniques to realize high-speed random number generators, multi-bit samplings (multi-bit ADC) can be used for chaotic time series instead of 1-bit ADC. In this technique, m sampled bits out of n multi-bit data (namely, n-bit ADC sampling with $m < n$) at each sampling point are used to calculate for random bit sequences. By this method, we can attain random number generations m times faster than that for 1-bit ADC at the same sampling frequency. It is noted that the use of the full bits for the random number generations would cause some correlations in the calculated bit sequences, since the probability distribution for the full-bit ADC raw data has a skew as discussed in Sect. 15.3. The use of less bits extracted from the full ADC bits is somewhat equivalent to the differentiation for chaotic time series and, as a result, we obtain even distributions of 0 and 1 bits in the calculated random number sequences.

Figure 15.8 shows an example of a schematic diagram for fast random bit generations. In this configuration, a chaotic output from a semiconductor laser subjected to optical feedback is injected to another semiconductor laser, which has no external feedback in itself. The chaos injected laser is forced to chaotic oscillations by a strong optical injection. By the strong optical injection, the chaotic bandwidth is greatly enhanced under appropriate conditions of optical injection. Indeed, Hirano et al. (2010) obtained a chaotic bandwidth of 16.1 GHz for the original bandwidth of 6.6 GHz in the experiment of fast random number generations. In this system, the bandwidth-enhanced chaotic laser is used as a light source for random number generations. In the previous section, two chaotic lasers are employed for random number generations, however, the single chaotic output from

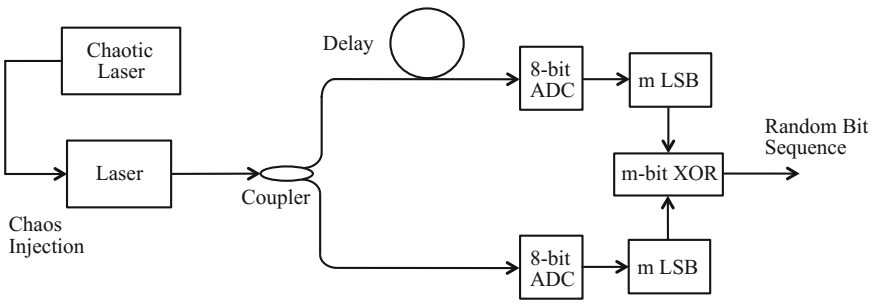

Fig. 15.8 Schematic diagram for a random bit generator with a bandwidth-enhanced chaotic semiconductor laser using multi-bit operation. *Delay* optical delay line, *ADC* analogue-to-digital converter, *LSB* Least Significant Bit, *XOR* exclusive-OR operation

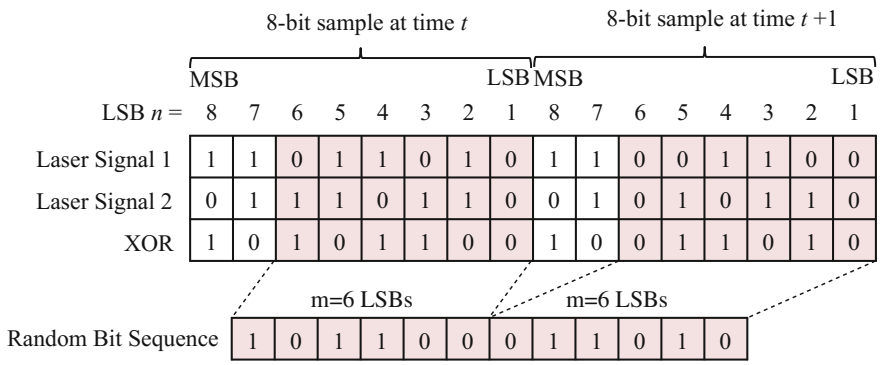
8-bit sample at time t
8-bit sample at time t +1
MSB
LSB
MSB
LSB
LSB n = 8 7 6 5 4 3 2 1 8 7 6 5 4 3 2 1
Laser Signal 1 1 1 0 1 1 0 1 0 1 1 0 0 1 1 0 0
Laser Signal 2 0 1 1 1 0 1 1 0 0 1 0 1 0 1 1 0
XOR 1 0 1 0 1 1 0 0 1 0 0 1 1 0 1 0
m=6 LSBs
m=6 LSBs
Random Bit Sequence 1 0 1 1 0 0 0 1 1 0 1 0

Fig. 15.9 Processing method for generating random bit sequence using multiple significant bits (n = 1, …, 8). Example for m = 6. *MSB* Most Significant Bit

the laser is used here. The chaotic laser output is then divided into two signals. One of the two is guided to an 8-bit ADC through optical fiber, while the other passes through an optical delay line and is fed to another 8-bit ADC. By appropriately choosing the optical delay time, we can set an incommensurate time offset to the time signatures of two chaotic signals at the ADCs, then the two signals equivalently behave like chaotic outputs from two different semiconductor lasers as discussed in the previous subsection.

From each 8-bit digitized output, a subset of lower m ($m < 8$) LSB are extracted and interleaved to generate a random bit sequence by bitwise XOR operation. Note that lower bits less than 8-bit are used to avoid unwanted correlations of the resulted bit streams as mentioned before. The method of multi-bit random number generations is shown in Fig. 15.9. The laser output at a sampling time is digitized as 8-bit data by ADC and the delayed laser output at the same time is also digitized as 8-bit data. Then, each corresponding bit is compared and takes an XOR operation. The lower m bits (in this case, m = 6 bits) are extracted from the resulted XOR data and we finally obtain random bit sequences in the bottom of Fig. 15.9. Hirano et al. (2010) used experimental chaotic data of 8-bit and 12.5 GHz sampling and conducted fast random number generations as a post-detection simulation. As a result, they successfully performed equivalent random number generations at 75 Gbps (12.5 GHz × 6-bit) using 6-bit LSBs for the XOR operation. The generated random number sequences less than 6-bit LSBs all passed the NIST tests, however, the tests almost failed for the sets of data for 7- and 8-bit LSBs. By the detailed study of Hirano et al., they proved that even and uniform distributions of 0 and 1 bits were obtained when the data sets of equal to or less than 6-bit out of 8-bit signals were used for the random number generations in real experimental chaotic waveforms.

Using experimentally obtained chaotic outputs of m LSBs (m is less than the full digitized bits), several studies for fast random number generations have been reported in off-line processing. Reidler et al. (2009) have shown that sequences passing statistical tests of randomness can be achieved at higher bit rates from a

single chaotic semiconductor laser by extracting more than 1-bit per sample in off-line processing of experimental chaotic laser time series. For data produced by differentiation of raw chaotic outputs as discussed in Sect. 15.3, a rate equivalent to 12.5 Gbps was achieved by extracting 5 bits from the difference in 8-bit samples acquired at 2.5 GHz sampling rate. Ordinary digital oscilloscope over the digitizing speed of giga hertz has an 8-bit A/D converter. However, the oscilloscope's 8-bit A/D converter, along with the internal 16-bit ADC and the rest processing units, can provide a "word-type", noise-enhanced, 16-bit output binary sequence for each sample. Using 16-bit ADC for chaotic outputs generated from an integrated photonic circuit of a semiconductor laser with optical feedback (the detail of the device structure as a chaotic generator will be presented in Sect. 15.5), Argyris et al. (2010b) demonstrated generations of random bit sequences as high as 140 Gbps. In their method, 14-bit LSBs are extracted form 16-bit raw data at a rate of 10 GHz sampling to eliminate the skew and ununiformity of signals in post-processing from A/D sampled data by an digital oscilloscope and truly random bit streams with 140 Gbps are generated. Kanter et al. (2010) used higher order derivatives for raw chaotic output signals to calculate random number generations and attained at high bit-rate generation up to 300 Gbps using a single chaotic semiconductor laser by retaining 15-bit LSBs of the value from the 16th derivative of the digitized chaotic laser intensity at 20 GHz sampling per second. Sakuraba et al. (2015) reported fast random number generations of the sampling speed of 1.2 Tbps by experiment. They expanded the chaotic bandwidth of a single semiconductor laser of 12.0–35.2 GHz using three-cascaded chaotic semiconductor lasers. After detecting analogue-to-digital converted chaotic signals of 8-bit with 100 GSample/s, they used 6-bit for the post processing. Applying bit-inversion and XOR-operations for the multi-bit generated signals, the maximum generation rate at 1.2 Tbps (100 GSample/s $\times$ 6-bit $\times$ 2-data) is equivalently achieved.

For the use of differentiated signals in random number generations, the effects of physical noises in semiconductor laser itself, photodetector, and A/D converter, which are potential additional sources of randomness, should be separated from the laser chaos. Also the original bandwidth of chaos from the laser outputs should be taken into account. Namely, in parallel with noise problems, we must consider the true capacity of information when we process a raw chaotic data for the application of it to fast random number generations. The processing might not always mean the enhancement of the capacity of information originally contained in the raw data, even if the method of fast random number generations would pass the statistical tests. Whether each method is truly sound or not for the application must be checked based on the rigid information theory. Such discussion is left for the future study. In these works for ultrahigh bit-rate generations of true random number sequences, advanced electrical post-processing off-line methods have been employed based on either the difference between delayed 8-bit or 16-bit samples or high-order derivatives using off-line memory buffers for intermediate sequences storage. Or they employed optical decorrelation techniques using a relatively complex configuration with coupled lasers for chaotic signal bandwidth enhancement and suppression of time signatures. A strong motivation for using direct sampling of optical chaos for

random number generations is to reduce the dependence on digital electronic operations. The digital electronic techniques only may not be easier to implement at high frequencies and, in principle, it is very difficult to increase the rate for generation of nondeterministic bits. From these points of view, it is very important to increases the bandwidth of the laser chaos used for random number generators.

15.4.3 All Optical Chaotic Random Number Generators

To avoid the limitation by the bottleneck of electronic signal processing and conformity to optical channels in data transmissions, all optical random number generator has been proposed. The proposed system performs all signal processing only in the optical domain, with no digital electronic circuit control. The system consists of a wide bandwidth chaotic laser, an all optical sampler, and an all optical comparator. Figure 15.10 shows an example of all optical systems (Wang et al. 2010).

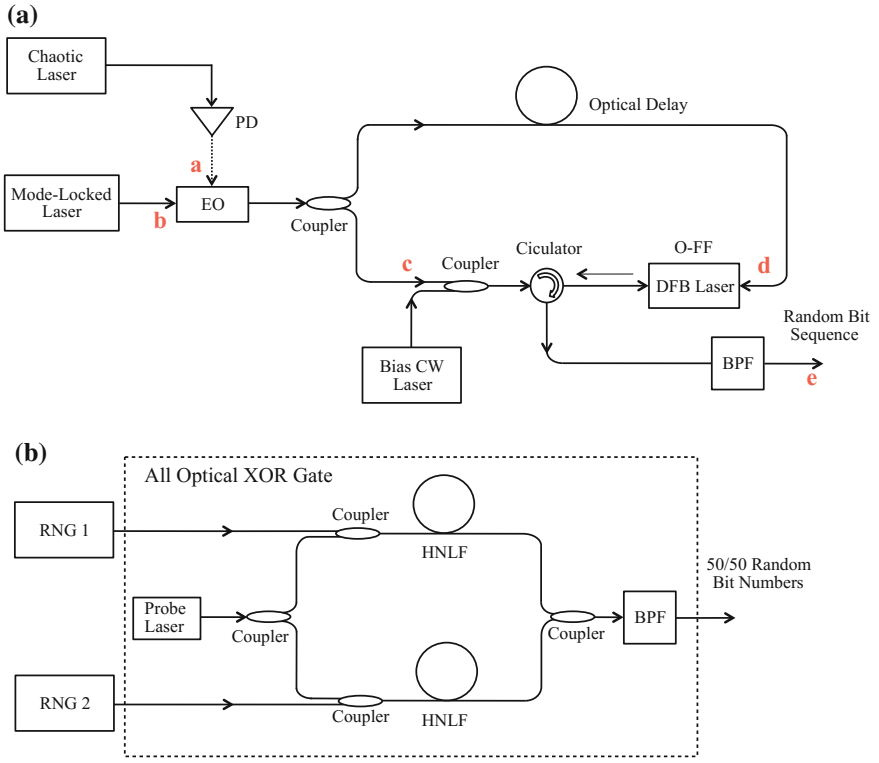

Fig. 15.10 Schematic diagrams for all optical random number generations. **a** Random number generator (RNG). *PD* photo-detector, *EO* Electro-Optical modulator, *O-FF* optical filp-flop, *BPF* optical band-pass filter. For points $a-e$, examples for time signals are plotted in Fig. 15.11. **b** All optical XOR gate to eliminate the bias of "0" and "1" distributions from RNGs. *RNG* random number generator, *HNLF* highly nonlinear fiber

The system consists of two parts. One is for generations of random bit sequences (Fig. 15.10a) and the other is post-processing of all optical XOR gate to eliminate unwanted bias for the first state of the random number bit sequences (Fig. 15.10b). In Fig. 15.10a, the chaotic output induced by such as a semiconductor laser with optical feedback in once detected by a photodetector (PD). The detected signal is fed to the applied voltage to an electro-optic (EO) light modulator. Optical clock pulses generated by a mode-locked laser pass through the EO modulator and the amplitudes of pulses are sampled and modulated by the chaotic signal. Then, the modulated pulse train is split into two identical trains by a coupler. One of the two pulse trains is injected into the right-hand side of a DFB laser through an optical fiber delay line, while the other pulse trains is injected into the left-hand side combined with a continuous wave (CW) of bias laser light, which has a slightly different oscillation wavelength from the DFB laser. The different path lengths for the two pulse trains are used to eliminate correlations of chaotic signals at the DFB laser. Here, the DFB laser acts as an all optical filp-flop (O-FF), which plays the role of quantizing the chaotic signal (Huybrechts et al. 2008). The DFB laser exhibits bistable characteristics due to the dual inputs with the constant light offset. Only when the pulse power injected into the DFB laser from the left or right facet is above the threshold, the DFB laser will be correspondingly switched off or on. Thus, the quantizing to the chaotic laser can be achieved. The output from the O-FF DFB laser passes through a band-pass-filter (BPF) and the resulting random number sequence is obtained.

Figure 15.11 shows numerical examples of the time series marked at a–e in Fig. 15.10a (Wang et al. 2010). The detected signal in Fig. 15.11a by the photodetector (PD) is a chaotic irregular oscillation. Figure 15.11b is the optical clock pulses from the mode-locked laser with Gaussian shape of the pulse width of 7 ps and the repetition frequency of 5 GHz. Figure 15.11c shows the modulated pulse train after the coupler, which is injected into the DFB laser from its left facet. Figure 15.11d is the identical pulse train delayed by 100 ps on the right side of the DFB laser. Figure 15.11e is an output waveform of the O-FF DFB laser through the band-pass-filter transmitting only the light of the DFB laser. As a final result, one can obtain bit sequences of “0” or “1” with an extinction ratio of 30 dB with a duration time of 200 ps (5 Gbps).

The obtained random number sequences from the random number generator (RNG) in Fig. 15.10a may contain an unwanted bias and show a nonuniform ratio of 0 and 1 random bit distribution. To eliminate the effects, the random number sequence need to be exclusive-or processed by an all optical XOR gate as shown in Fig. 15.10b. In this optical circuit, all optical XOR gate is based on a Mach–Zehnder interferometer with an identical highly nonlinear fiber (HNLF) transmission in each arm (Li et al. 2010). A CW beam from a probe laser is split by a coupler into two arms as an interferometer input light, and the output of two independent random number generators (RNGs) are respectively launched into arm 1 and arm 2 as control light through couplers. The control light induces the phase shift of the probe light due to the cross phase modulation in HNLF. After that, the probe light is finally exported through another coupler of the interferometer output. A band-pass-filter (BPF) at the wavelength of the probe beam is utilized to remove

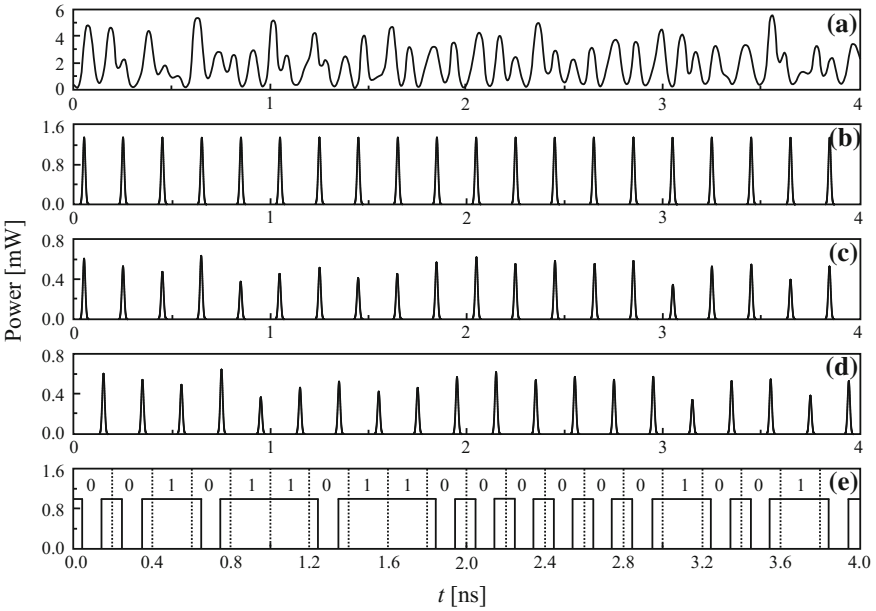

Fig. 15.11 Temporal waveforms of the random number generator. Corresponding sampling points of the random number generator system are shown in Fig. 15.10a. **a** Output from the chaotic laser. **b** Sampling optical clock pulses. **c** Modulated pulse train. **d** Modulated pulse train delayed by 100 ps. **e** Raw random bit sequence [after Wang et al. (2010); © 2010 IEEE]

the control light. The interaction between the random number sequence and the CW light in HNLF is theoretically given by the following nonlinear optical transmission equation:

$$i\frac{\partial E_j(z,T)}{\partial z} = -\frac{i}{2}\alpha_f E_j(z,T) + \frac{1}{2}\beta_2\frac{\partial^2 E_j(z,T)}{\partial T^2} - \gamma_{\text{non}}\left\{\left|E_j(z,T)\right|^2 + 2\sum_{l\neq j}\left|E_l(z,T)\right|^2\right\}E_j(z,T) \tag{15.5}$$

The above equation is almost same as the nonlinear Schrödinger equation in (13.6) except for the cross correlation term (final term). In (15.5), j, l is chosen to be 1 or 2, and E_1 and E_2 represent the complex field amplitudes of the probe laser light and the control light, respectively. The output power of probe light can be expressed by

$$P_{\text{out}} = \frac{1}{2}P_{\text{in}}\{1 - \cos(\phi_{\text{CW}} - \phi_{\text{CCW}})\} \tag{15.6}$$

where P_{in} is the power of the CW probe light. ϕ_{CW} and ϕ_{CCW} are the phase shifts induced by the control lights, respectively, which are proportional to the power of the input random number signals (control lights). When the signal is "1" level, the phase of the probe light has a π radian phase-shift, while the phase of the probe light keeps invariable when the signal is "0" level. Finally, by passing through a band-pass filter with the wavelength of the probe beam, the all optical XOR function can be obtained and accordingly the single random bit sequence with better randomness can be generated. In real experiments of all optical circuit, Erbium doped optical fiber amplifiers (EDFA), optical attenuators, polarization controllers, and optical isolators are inserted in the optical circuits, where and when necessary. By numerical simulations, Li et al. (2010) demonstrated all optical random number generations at a rate of 10 Gbps, which passed all standard statistical tests.

15.5 Photonic Integrated Circuit for Chaotic Generators

For practical applications of chaos to secure optical communications based on chaos synchronization discussed in Chap. 13 and to random number generations in the present chapter, integrated photonic circuits are expected for robust and stable chaotic light sources. For example, configurations of free-space external cavities or fiber-coupled optical feedback loops have been employed to generate chaotic oscillations in semiconductor lasers in those laboratory experiments. However, such external cavities are not sufficiently stable. Therefore, the miniaturization of the configurations through photonic integrations has been proposed. The devices are monolithically installed on a planner integrated circuit. Key elements of such devices are a semiconductor laser, an amplifier, a passive waveguide, and a phase control section. In the early days, similar devices have been developed for light sources of active mode-locking and self pulsating oscillations, which are known as multi-section lasers (Kawaguchi 1994; Bauer et al. 2004; Yousefi et al. 2007). Those integrated photonic circuits usually have short active feedback cavity. Although, they were not suitable for generations of chaotic waveforms appropriate for the use of chaotic communications and chaotic random number generations, they still exhibited bistabilities, multistabilities, and even chaotic dynamics in their outputs. Indeed, a semiconductor laser, followed by a phase section and an active feedback element, forms a very short complex photonic circuit that provides several types of dynamics and bifurcations under optical feedback strength and phase control. After the demonstrations of chaotic secure communications and chaotic random number generations, photonic integrated circuits as chaos generators have been proposed (Argyris et al. 2008; Tronciu et al. 2010; Harayama et al. 2011; Soriano et al. 2013). These integrated circuits usually have a long passive waveguide to generate higher dimensional chaos as their light outputs and come up with various ideas to control chaotic behaviors appropriate for those applications. In the following, we show an example of such devices.

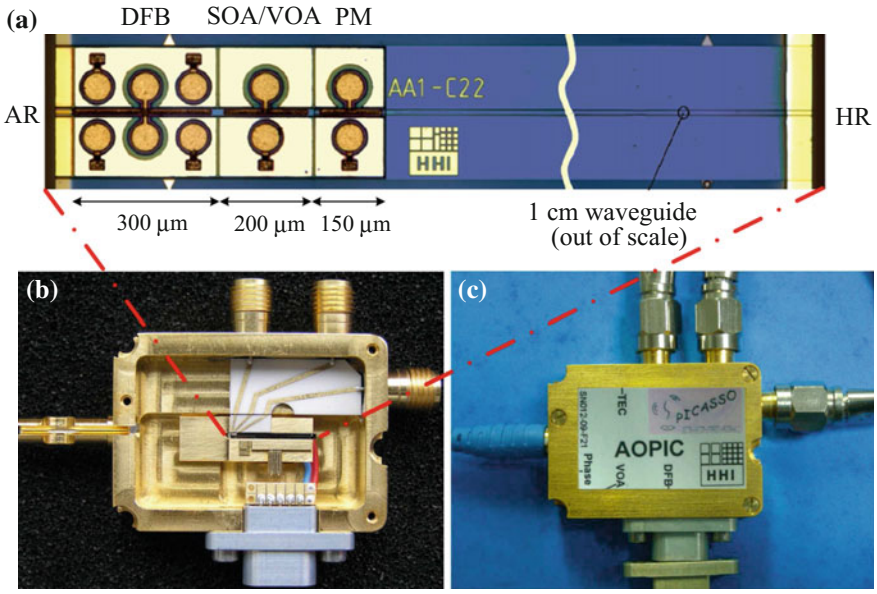

Fig. 15.12 Monolithically integrated photonic circuit for a chaos generator. **a** The device. *DFB* DFB laser, *HR* highly reflective coated mirror, *SOA/VOA* variable gain/absorption section, *PM* phase modulation section. The length of the waveguide is 1 cm-long. The output optical signal is emitted from the front anti-reflective (AR) facet of the DFB laser. **b** Internal structure of the packaging module. **c** Packaged module [after Argyris et al. (2010a); © 2010 OSA]

Figure 15.12 shows photographs of a photonic monolithic integrated chaos generator (Argyris et al. 2008, 2010a). In Fig. 15.12a, the device consist of an InGaAsP distributed feedback (DFB) semiconductor laser with the cavity length of 300 µm at the oscillation wavelength of 1.561 µm (most left of the photograph) and external cavity with the rear facet of the photonic integrated circuit that is highly reflective coated (HR) mirror (most right of the photograph). The chaotic light output is obtained through the anti-reflection (AR) coated interface. The cavity includes various active and passive sections of a variable gain or absorption section (SOA/VOA), a phase section (PM) and a 1-cm long passive waveguide. The passive waveguide is grown by a selective area epitaxial growth. The overall resonator length is defined by the internal laser facet and the chip facet of the waveguide which is highly reflective coated (intensity reflectivity of 95%). Short external cavities (lengths up to a few centimeters in the air) would require a relatively strong optical feedback in order to generate high-dimensional dynamics. The selected length of 1 cm provides an increased effective feedback round-trip time (the total optical feedback time is 280 ps and the corresponding round-trip feedback loop is 8.4 cm in free space connection), therefore enhancing the probability to encounter fully chaotic behavior.

The integration of the gain-absorption section emerges from the requirement to control the optical feedback strength. To produce chaotic attractors highly complex, the short external cavity length is selected. Depending on the biasing current of the DFB laser and the feedback strength, the bandwidth of the chaotic carrier may be increased from several GHz up to 20 GHz. The gain-absorption section offers the control on the optical feedback strength. At no bias, this section leads to a specific optical power feedback ratio equal to 1.6%, which is predetermined by the inherent losses of the external cavity. For positive biasing to this section, it plays as a semiconductor optical amplifier (SOA) and the feedback ratio can be increased up to 5%, while, for negative biasing, it acts as a variable optical attenuator (VOA). In this device, highly chaotic oscillations are generated for SOA operation, while only periodic or stable oscillations are obtained for VOA operation. Consequently, a very wide range of optical feedback values can be set and thus various types of dynamics can be generated. The phase section (PM) accurately tunes the round-trip time of the cavity with sub-wavelength resolution; this operation is extremely crucial for synchronization with other matched devices that might exhibit a small mismatch in the cavity length. The phase section allows for fine-tuning that can almost continuously go over beyond 2π, even several multiples of it. The internal structure of the packaging module is shown in Fig. 15.12b. Micro-strip lines connect the different active sections of the photonic integrated circuit with SMA connectors, while thermo-electric cooling of the device provides extremely stable temperature control. Fiber-chip coupling is performed by a tapered-end fiber with antireflective coating. Figure 15.12c is the packaged module.

Using the developed photonic integrated circuit, the dynamic properties are experimentally and numerically investigated. The bias injection current to the laser is not crucial for achieving enhanced nonlinear dynamics when it is kept well above threshold. For a negative biasing to the gain-absorption section (VOA operation), only limit cycle dynamics or stable solutions are observed excluding any chaos dynamics. On the other hand, various dynamics are obtained at zero biasing to the gain-absorption section depending on the bias current to the phase section. By increasing the bias phase current, the observed dynamics states are periodically repeated over 2π phase change, and limit cycles, quasi-chaotic states, and fully chaotic states can be observed in the laser outputs. For fully coherence-collapsed chaotic states, the radio-frequency (rf) spectrum of the output signal becomes broadband and extends up to the cutoff frequency of 8 GHz. When the gain-absorption section is slightly positively biased, the gain in the cavity compensates the internal losses and results in the increase of the optical power feedback ratio. As a result, broad-spectrum chaotic dynamics appear in the laser outputs and the phase dependence on the dynamics is deteriorated. For moderate bias of the gain-absorption at the bias current of +10 mA, the optical feedback ratio rises to 3.3% and the output shows fully chaotic states independent of any phase condition.

Figure 15.13 corresponds to such case (Argyris et al. 2008). Figure 15.13a shows the phase plot in the space of present and delayed intensities. We can see smoothed broad spectrum in Fig. 15.13b which is suitable for chaotic generators in practical applications. For the experimental data, the chaotic dimension is

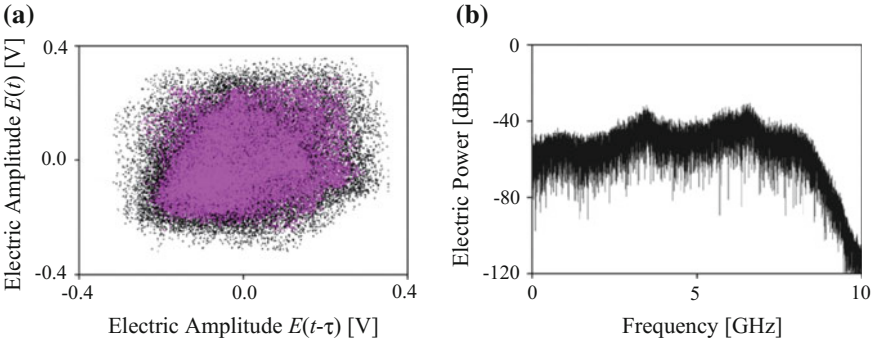

Fig. 15.13 Experimental results of chaos generations from the photonic integrated circuit at a bias injection current of $3I_{th}$ (I_{th} = 10.6 mA), a gain-absorption current of +10 mA (SOA operation), and a phase bias current of 2.9 mA. **a** Phase plot and **b** corresponding rf spectrum [after Argyris et al. (2008); © 2008 APS]

calculated and, as a result, the correlation dimension is 4.8 ± 0.3. It is noted that the bandwidth of the photodetector used in this experiment is 8 GHz, so that the optical power in the rf spectrum is rapidly decreases above the cutoff frequency. Any further increase in the gain-absorption current does not provide any alteration in the characteristics of the chaotic spectrum in this device. As for the long-run stability of the device, the precise thermo-electric cooling of the devices, by using the appropriate packaging for the photonic integrated circuit, provides controllability and operating stability, not only in terms of wavelength and optical power, but also in terms of the spectral distribution of the chaotic carrier and the phase matching conditions. The stability analysis was performed in the developed system and showed that the incorporated chaotic photonic integrated circuits proved to be a reliable solution for applications of chaotic secure communications and chaotic random number generations, after operating continuously for hundreds of hours.

Photonic integrated circuits as chaotic light generators have actually been tested for several systems of chaotic secure communications and random number generations. Argyris et al. (2010a) used two integrated closed-loop systems of semiconductor lasers with optical feedback (which is the same photonic integrated circuit in Fig. 15.12) and performed chaotic secure data communications through 100 km optical fiber transmission based on a chaos masking method as discussed in Chap. 13. The identical chaos generating photonic integrated circuits were able to synchronize and reproduce the same carriers and realized data exchanges up to 2.5 Gbps with bit error rates below 10^{-12} through forward error correction techniques. Tronciu et al. (2010) developed a similar photonic integrated circuit for chaotic secure communications. Their integrated device consisted of a DFB laser, two passive sections, two phase sections, and a narrow air gap. The air gap plays a role for multipath external optical feedback to control chaotic behaviors and eliminate chaotic signatures appropriate for chaos-based communications as discussed in Chap. 13. One of the two phase sections could be used to insert messages

through phase modulation for the purpose of chaotic secure communications. They tested the device to chaos masking data transmission at 1 Gbps and obtained a raw bit error rate of 10^{-4} in the decoded message that yields error-free transmission through suitable forward error correction methods.

On the other hand, integrated chaos generators were applied to random number generations. As already discussed in Sect. 15.4.2, Argyris et al. (2010b) conducted random bit generations using the single photonic integrated circuit. They successfully demonstrated 140 Gbps random number generations by the multi-bit post-processing technique at 10 GHz sampling. Harayama et al. (2011) performed 2.08 Gbps physical random bit generations in real time based on their original photonic integrated circuits with the same configuration of two chaotic generators as that in Sect. 15.4.1. Beside the applications of chaotic secure communications and random number generations, several integrated circuits for chaotic systems have been proposed. For example, Wünsche et al. (2005) reported a photonic integrated circuit for the study of the dynamics of mutual-coupled semiconductor lasers. These systems also provide compact and stable chaotic oscillators and the study would have significances not only for the investigation of detailed fundamental chaotic dynamics but also for future possible applications.

15.6 Application for Random Number Key Distribution with Chaotic Semiconductor Lasers

Quantum key distribution (QKD) has been widely investigated to realize unconditional secure communication (Gisin et al. 2002). In order to properly implement such a high-speed QKD system, a high-speed physical random bit generator is indispensible. However, traditional physical random number generators were too slow to satisfy the requirement of high-speed QKD systems as discussed in Sect. 15.1. Then, the fast random number generators introduced in Sect. 15.4 can be applied to realize high-speed QKD in quantum secure communications. In the following, the system and the performance of differential phase-shift quantum key distribution (DPS-QKD) using chaotic random number generators are described (Honjo et al. 2009). In the DPS-QKD, the key generation rate strongly depends on the modulation speed of the phase of a pulse train. Furthermore, fast random number generations are expected for the longer transmission distance and the higher key generation rate in QKD systems. Figure 15.14 shows a schematic diagram of DSP-QKD systems. In the transmitter (Alice), a laser light (LD) is modulated by an intensity modulator (IM) at a certain clock and a pulse train is generated. The phase of the pulse train is randomly modulated by 0 or π for each pulse through a phase modulator (PM) synchronized to the clock. The chaotic random number generator (C-RNG) discussed in Sect. 15.4 can be used as a random modulator. The obtained optical pulse is attenuated at an attenuator (ATT) and is sent to the receiver (Bob) with an average photon number of less than one per pulse. In the receiver

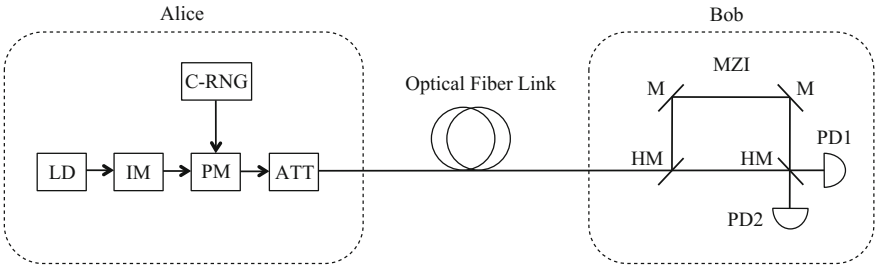

Fig. 15.14 Schematic diagram of differential phase shift quantum key distribution (QKD). *LD* laser diode, *IM* intensity modulator, *PM* 0 and π phase modulator, *ATT* attenuator, *C-RNG* chaotic random number generator, *MZI* Mach–Zehnder interferometer, *HM* half mirror, *M* mirror, *PD* photodetector

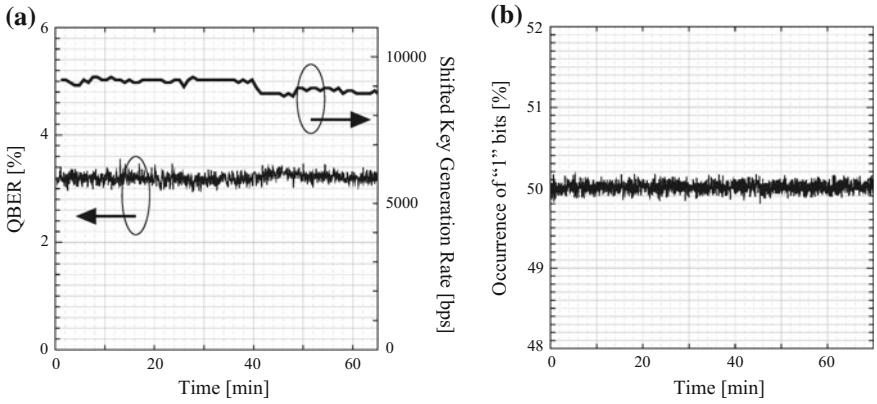

Fig. 15.15 Experimental results of quantum key distribution. **a** Quantum bit error rate (QBER) and shifted key generation rate. **b** Occurrence of "1" bits for the fast physical random bit generator used in the experiment [after Honjo et al. (2009); © 2009 OSA]

side, the phase difference between two sequential pulses is measured by a 1-bit delay Mach–Zehnder interferometer (MZI). Then, the photon arrival time and which detector clicked are examined. Thus, the random bit sequences sent by Alice are reconstructed. Separately, the protocol to retrieve the phase modulation information is prepared between Alice and Bob through an open communication channel.

Figure 15.15 shows the experimental result of DPS-QKD (Honjo et al. 2009). They used a synchronized 1 GHz clock to the intensity modulation of a DFB laser (LD in Fig. 15.14) and also to the phase modulation through a chaotic random number generator. The optical pulse train is randomly phase shifted by 0 or π through the phase modulator driven by random bit sequences from the chaotic random number generator, which consists of almost the same configuration as introduced in Fig. 15.5. Then, the optical pulse is attenuated to 0.2 photons per

pulse and then transmitted to the receiver over 25 km dispersion shifted fiber. In the receiver side, the phase difference between the two sequential pulses is detected through a 1-bit delay Mach–Zehnder interferometer that is stably adjusted by controlling the temperature of the waveguide chip. Figure 15.15a shows the sifted key generation rate and quantum bit error rate as a function of time. The figure indicates the continuous operation over an hour and generated sifted keys at a rate of 9.0 kbps with an average quantum-bit error rate of 3.2%. Figure 15.15b shows the ratio of 1 or 0 bit generated from the used random number generator as a function of time. This confirmed the stability of the operation of the physical random bit generator for the quantum key distribution experiment. The physical random bit generator with chaotic semiconductor lasers provides stable random bit signal continuously throughput a 1-h duration in the experiment. Thus, a physical random bit generator with chaotic semiconductor lasers is a promising candidate for the true random bit generator in a high-speed QKD system. Yoshimura et al. (2012) extended the method by employing a system of one-drive and two-response configuration to generate chaotic signals. The phases of the response lasers are randomly modulated and this generates a pair of secure secret sequences for the random number generations. Then, they obtained the real-time secret key generation rate of 182 kbps for the modulation of 2 MHz.

References

C. Abellan, W. Amaya, D. Domenech, P. Muñoz, J. Capmany, S. Longhi, M.W. Mitchell, V. Pruneri, Quantum entropy source on an InP photonic integrated circuit for random number generation. Optica **3**, 989–994 (2016)

A. Argyris, M. Hamacher, K.E. Chlouverakis, A. Bogris, D. Syvridis, Photonic integrated device for chaos applications in communications. Phys. Rev. Lett. **100**, 14101-1–14101-4 (2008)

A. Argyris, E. Grivas, M. Hamacher, A. Bogris, D. Syvridis, Chaos-on-a-chip secures data transmission in optical fiber links. Opt. Express **18**, 5188–5198 (2010a)

A. Argyris, S. Deligiannidis, E. Pikasis, A. Bogris, D. Syvridis, Implementation of 140 Gb/s true random bit generator based on a chaotic photonic integrated circuit. Opt. Express **18**, 18763–18768 (2010b)

S. Bauer, O. Brox, J. Kreissl, B. Sartorius, M. Radziunas, J. Sieber, H.J. Wünsche, F. Henneberger, Nonlinear dynamics of semiconductor lasers with active optical feedback. Phys. Rev. E **69**, 016206-1–016206-10 (2004)

M. Bucci, L. Germani, R. Luzzi, A. Trifiletti, M. Varanonuovo, A high-speed oscillator-based truly random number source for cryptographic applications on a smart card IC. IEEE Trans. Comput. **52**, 403–409 (2003)

N. Gisin, G. Ribordy, W. Tittel, H. Zbinden, Quantum cryptography. Rev. Mod. Phys. **74**, 145–195 (2002)

T. Harayama, S. Sunada, K. Yoshimura, P. Davis, K. Tsuzuki, A. Uchida, Fast nondeterministic random-bit generation using on-chip chaos lasers. Phys. Rev. A **83**, 031803(R)-1–031803(R)-4 (2011)

S. Heiligenthal, T. Dahms, S. Yanchuk, T. Jüngling, V. Flunkert, I. Kanter, E. Schöll, W. Kinzel, Strong and weak chaos in nonlinear networks with time-delayed couplings. Phys. Rev. Lett. **107**, 234102-1–234102-5 (2011)

S. Heiligenthal, T. Jüngling, O. D'Huys, D.A. Arroyo-Almanza, M.C. Soriano, I. Fischer, I. Kanter, W. Kinzel, Strong and weak chaos in networks of semiconductor lasers with time-delayed couplings. Phys. Rev. E **88**, 012902-1–012902-13 (2013)
K. Hirano, K. Amano, A. Uchida, S. Naito, M. Inoue, S. Yoshimori, K. Yoshimura, P. Davis, Characteristics of fast physical random bit generation using chaotic semiconductor lasers. IEEE J. Quantum Electron. **45**, 1367–1378 (2009)
K. Hirano, T. Yamazaki, S. Morikatsu, H. Okumura, H. Aida, A. Uchida, S. Yoshimori, K. Yoshimura, T. Harayama, P. Davis, Fast random bit generation with bandwidth-enhanced chaos in semiconductor lasers. Opt. Express **18**, 5512–5524 (2010)
T. Honjo, A. Uchida, K. Amano, K. Hirano, H. Someya, H. Okumura, K. Yoshimura, P. Davis, Y. Tokura, Differential-phase-shift quantum key distribution experiment using fast physical random bit generator with chaotic semiconductor lasers. Opt. Express **17**, 9053–9061 (2009)
K. Huybrechts, G. Morthier, R. Baets, Fast all-optical flip-flop based on a single distributed feedback laser diode. Opt. Express **16**, 11405–11410 (2008)
I. Kanter, Y. Aviad, I. Reidler, E. Cohen, M. Rosenbluh, An optical ultrafast random bit generator. Nat. Photon. **4**, 58–61 (2010)
H. Kawaguchi, *Bistabilities and Nonlinearities in Laser Diodes* (Artech House, London, 1994)
D. Knuth, *The Art of Computer Programming, Seminumerical Algorithms*, vol. 2, 3rd edn. (Addison-Wesley, Boston, 1996)
P. Li, Y.C. Wang, J.Z. Zhang, All-optical fast random number generator. Opt. Express **18**, 20360–20369 (2010)
X. Li, A.B. Cohen, T.E. Murphy, R. Roy, Scalable parallel physical random number generator based on a superluminescent LED. Opt. Lett. **36**, 1020–1022 (2011)
G. Marsaglia, Diehard: a battery of tests of randomness. (1995) http://www.stat.fsu.edu/pub/diehard/
G. Marsaglia, A. Zaman, W.W. Tsang, Toward a universal random number generator. Stat. Probab. Lett. **9**, 35–39 (1990)
Y.Q. Nie, L. Huang, Y. Liu, F. Payne, J. Zhang, J.W. Pan, The generation of 68 Gbps quantum random number by measuring laser phase fluctuations. Rev. Sci. Instrum. **86**, 063105-1–063105-6 (2015)
B. Qi, Y.M. Chi, H.K. Lo, L. Qian, High-speed quantum random number generation by measuring phase noise of a single-mode laser. Opt. Lett. **35**, 312–314 (2010)
I. Reidler, Y. Aviad, M. Rosenbluh, I. Kanter, Ultrahigh-speed random number generation based on a chaotic semiconductor laser. Phys. Rev. Lett. **103**, 024102-1–024102-4 (2009)
D. Rontani, A. Locquet, M. Sciamanna, D.S. Citrin, Loss of time-delay signature in the chaotic output of a semiconductor laser with optical feedback. Opt. Lett. **32**, 2960–2962 (2007)
D. Rontani, A. Locquet, M. Sciamanna, D.S. Citrin, S. Ortin, Time-delay identification in a chaotic semiconductor laser with optical feedback: a dynamical point of view. IEEE J. Quantum Electron. **45**, 879–891 (2009)
A. Rukhin, J. Soto, J. Nechvatal, M. Smid , E. Barker, S. Leigh, M. Levenson, M. Vangel, D. Banks, A. Heckert, J. Dray, S. Vo, A statistical test suite for random and pseudorandom number generators for cryptographic applications. Nat. Inst. Stand. Technol. (Special Publication) 800–22 Revision 1a (2010)
R. Sakuraba, K. Iwakawa, K. Kanno, A. Uchida, Tb/s physical random bit generation with bandwidth-enhanced chaos in three-cascaded semiconductor lasers. Opt. Express **23**, 1470–1490 (2015)
M.C. Soriano, J. Garcıá-Ojalvo, C.R. Mirasso, I. Fischer, Complex photonics: dynamics and applications of delay-coupled semiconductors lasers. Rev. Mod. Phys. **85**, 421–470 (2013)
D.R. Stinson, *Cryptography: Theory and Practice* (CRC Press, Boca Raton, 1995)
T. Symul, S.M. Assad, P.K. Lamb, Real time demonstration of high bitrate quantum random number generation with coherent laser light. Appl. Phys. Lett. **98**, 231103-1–231103-3 (2011)
V.Z. Tronciu, C.R. Mirasso, P. Colet, M. Hamacher, M. Benedetti, V. Vercesi, V. Annovazzi-Lodi, Chaos generation and synchronization using an integrated source with an air gap. IEEE J. Quantum Electron. **46**, 1840–1846 (2010)

A. Uchida, K. Amano, M. Inoue, K. Hirano, S. Naito, H. Someya, I. Oowada, T. Kurashige, M. Shiki, S. Yoshimori, K. Yoshimura, P. Davis, Fast physical random bit generation with chaotic semiconductor lasers. Nat. Photon. **2**, 728–732 (2008)

A. Uchida, Review on ultra-fast physical number generators based on optical random phenomena. Rev. Laser Eng. **39**, 508–514 (2011). (in Japanese)

A. Uchida, *Optical Communication with Chaotic Lasers* (Wiley-VCH Weinheim, 2012)

G. Van der Sande, M.C. Soriano, I. Fischer, C.R. Mirasso, Dynamics, correlation scaling, and synchronization behavior in rings of delay-coupled oscillators. Phys. Rev. E **77**, 055202(R)-1–055202(R)-4 (2008)

J. Wang, K. Petermann, Noise analysis of semiconductor lasers within the coherence collapse regime. IEEE J. Quantum Electron. **27**, 3–9 (1991)

Y. Wang, P. Li, J. Zhang, Fast random bit generation in optical domain with ultrawide bandwidth chaotic laser. IEEE Photonics Technol. Lett. **22**, 1680–1682 (2010)

C.R.S. Williams, J.C. Salevan, X. Li, R. Roy, T.E. Murphy, Fast physical random number generator using amplified spontaneous emission. Opt. Express **23**, 23584–23597 (2010)

J.G. Wu, G.Q. Xia, Z.M. Wu, Suppression of time delay signatures of chaotic output in a semiconductor laser with double optical feedback. Opt. Express **17**, 20124–20133 (2009)

J.G. Wu, G.Q. Xia, X. Tang, X.D. Lin, T. Deng, L. Fan, Z.M. Wu, Time delay signature concealment of optical feedback induced chaos in an external cavity semiconductor laser. Opt. Express **18**, 6661–6666 (2010)

J.G. Wu, Z.M. Wu, X. Tang, X.D. Lin, T. Deng, G.Q. Xia, G.Y. Feng, Simultaneous generation of two sets of time delay signature eliminated chaotic signals by using mutually coupled semiconductor lasers. IEEE Photonics Technol. Lett. **23**, 759–781 (2011)

H.J. Wünsche, S. Bauer, K. Kreissl, O. Ushakov, N. Korneyev, F. Henneberger, E. Wille, H. Erzgräber, M. Peil, W. Elsäßer, I. Fischer, Synchronization of delay-coupled oscillators: a study of semiconductor lasers. Phys. Rev. Lett. **94**, 163901-1–163901-4 (2005)

K. Yoshimura, J. Muramatsu, P. Davis, T. Harayama, H. Okumura, S. Morikatsu, H. Aida, A. Uchida, Secure key distribution using correlated randomness in lasers driven by common random light. Phys. Rev. Lett. **108**, 070602-1–070602-5 (2012)

Y. Yousefi, Y. Barbarin, S. Beri, E.A.J.M. Bente, M.K. Smit, R. Nötzel, D. Lenstra, New role for nonlinear dynamics and chaos in integrated semiconductor laser technology. Phys. Rev. Lett. **98**, 044101-1–044101-4 (2007)

Appendix
Chaos

Abstract Chaos is observed in a wide variety of nonlinear systems, not only in physical and engineering systems, but also in biological systems and, even, in sociology and economy. However, the same or similar tools of mathematics can be applied to respective systems. In the Appendix, some common tools for the analyses of chaotic systems are presented.

About Chaos in Nonlinear Systems

Chaos is a phenomenon observed in a nonlinear system described by a certain set of differential equations and shows irregular oscillations for time or spatial evolutions (Lorenz 1963). However, Lorenz was not the first who noticed chaos. Two years earlier than Lorenz chaos, Ueda found chaotic attractor in a mixed van der Pol and Duffing oscillator (Ueda et al. 1992). More than that, Poincaré already reached the idea of chaos in 1800s. He showed the sensitivity to initial condition in dynamical nonlinear systems (Poincaré 1913). Namely, in the nonlinear systems, a small error in the former will produce an enormous error in the latter and prediction becomes impossible. Furthermore, 200 years earlier, Huygens (1986) demonstrated chaos synchronization in pendulum clocks mounted on the same wooden beam. He showed that all the pendulums swing in the synchronous way without one's noticing it. Incidentally, the word “chaos” was not defined by Lorenz. Li and Yorke (1975) first used “chaos” in their paper, ‘Period three implies chaos.’ The discovery of Lorenz chaos and its brief history were compactly introduced by Motter and Campbell (2013).

We must distinguish chaos from the observations of random events, such as flipping of a coin. Namely, chaos is a disorder in a system written by deterministic equations. Chaos is observed in a wide variety of nonlinear systems, not only in physical and engineering systems, but also in biological systems and, even, in sociology and economy. Nonlinearity of a system is one of the important factors to observe chaos. Whether the system is continuous or discrete, it is a good candidate for a chaotic system, but the nonlinearity itself does not always guarantee chaotic oscillations in the system. Chaos occurs in a nonlinear system under appropriate

© Springer International Publishing AG 2017

J. Ohtsubo, *Semiconductor Lasers*, Springer Series in Optical Sciences 111,
DOI 10.1007/978-3-319-56138-7

parameter conditions and also certain parameter ranges. Chaos has a rigid definition for the irregular oscillations of the output from the system. Whether the output from a system is chaos or not is determined by the rigorous procedures using mathematical tools, such as attractors, the Lypunov exponent, and the Poincaré map of the output (Abarbanel 1996). In the following, we discuss what chaos is, what it looks like, and how chaotic data are analyzed. Also, as unique features of chaos, we show some examples of useful techniques for practical applications: control of chaos and chaos synchronization. The Appendix does not aim at the rigid mathematical descriptions of chaos, but it intends to show the general aspects of chaos and gives some useful tools for the analyses of chaos for reading this book.

The following is a list of some additional reading for the general concept and mathematical treatments of chaos. The readers interested in physical and mathematical backgrounds of chaos and also the treatment of chaotic data may consult the following books.

H.D.I. Abarbanel, *Analysis of Observed Chaotic Data* (Springer-Verlag, New York, 1996)

G.L. Barker, J.P. Gollub, *Chaotic Dynamics, An Introduction* (Cambridge University Press, Cambridge, 1990)

R.L. Devaney, *An Introduction to Chaotic Dynamical Systems, Second edn.* (Addison-Wesley, New York, 1989)

K. Kaneko, I. Tsuda, *Complex Systems: Chaos and Beyond: A Constructive Approach with Applications in Life Sciences* (Springer Science & Business Media, 2011)

H. Nagashima, Y. Baba, *Introduction to Chaos: Physics and Mathematics of Chaotic Phenomena* (IOP Pub, Bristol, 1998)

E. Ott, *Chaos in Dynamical Systems, Second edn.* (Cambridge University Press, Cambridge, 2002)

E.A. Jackson, *Perspectives of Nonlinear Dynamics*, vol.1, vol.2 (Cambridge University Press, Cambridge, 1991)

S.H. Strogatz, *Nonlinear Dynamics and Chaos: with Applications to Physics, Biology, Chemistry, and Engineering* (Westview Press, 2014)

J.M.T. Thompson, H.B. Stewart, *Nonlinear Dynamics and Chaos, Geometrical Methods for Engineers and Scientists* (John Wiley & Sons, New York, 1986)

L. Tuckerman, *Order within Chaos* (John Wiley & Sons, New York, 1986)

A.1 Nonlinear Chaotic Systems

A.1.1 Discrete Systems

We consider the occurrence of an event that becomes the new input of the system and causes the next events. Namely, the system is described by discrete difference

equations. We assume a nonlinear response of a discrete system and write its output as $x(n)$

$$x(n+1) = f\{x(n); \mu\} \tag{A.1}$$

where n denotes the step of the occurrence, $f(x)$ is the nonlinear function, and μ is the system parameter. In general, $x(n)$ is a vector and the parameter μ is also a vector. Logistic mapping is the well-known mathematical relation for a discrete chaotic system. We consider the logistic map with a variable x and a parameter μ given by

$$x_{n+1} = \mu x_n (x_n - 1) \tag{A.2}$$

This is a simple mapping using a quadratic function. It is stable and its solution converges to a fixed point for any initial value of $x(n)$ as far as the value of the parameter μ is roughly less than 3. The output x shows an oscillation for the evolution of n when the parameter μ has a value larger than 3. With a further increase in the parameter value, the system shows period-doubling oscillatory solutions and, finally, reaches irregular chaotic oscillations. Figure A.1a shows such an example for the parameter value of μ = 3.8. This irregularity is completely

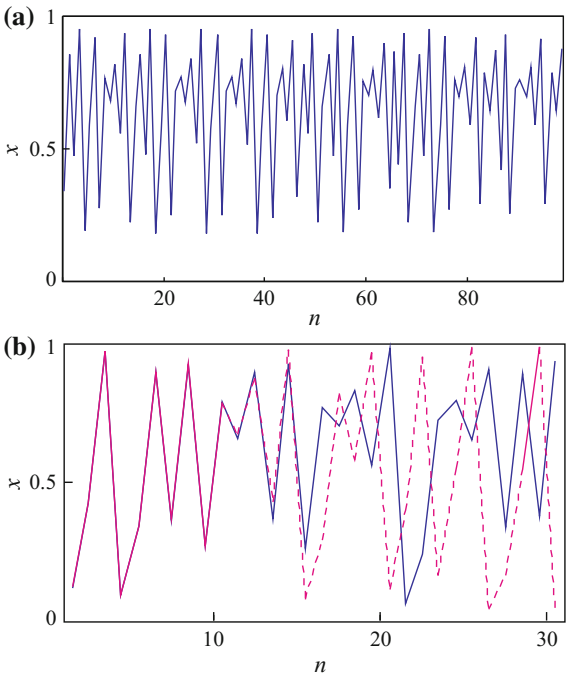

Fig. A.1 Chaotic oscillations in logistic mapping. **a** Chaotic oscillation at μ = 3.8. **b** Sensitivity for initial conditions. *Solid line* x_0 = 0.12000 and *broken line* x_0 = 0.12001

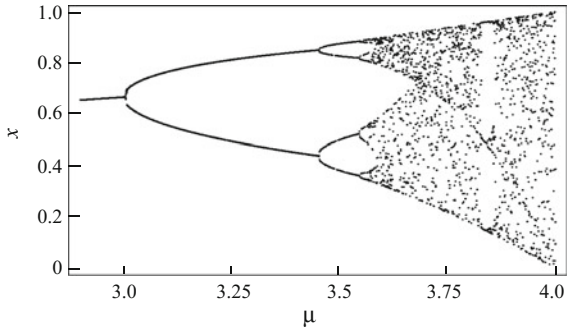

Fig. A.2 Bifurcation diagram for logistic mapping

different from the random fluctuations observed in stochastic processes. The irregularity is simply derived from the deterministic difference equation in (A.2) and the irregularity is called "chaos." One of the unique features of chaos is the sensitivity for the initial condition. In the numerical calculation in (A.2), we can never obtain the same waveform for different initial values even if the difference is extremely small. Figure A.1b is the demonstration of the sensitivity for the initial condition. In the figure, we choose two initial conditions with a slight difference of $x_0 = 0.12000$ and $x_0 = 0.12001$. At first, x shows a quite similar orbit, however the difference between the two orbits deviate from each other and, finally, show completely different oscillations for the evolution of the event. This is a typical nature of the sensitivity for the initial conditions in a chaotic system.

From the plot of the maxima and minima of the variable x for the evolution of step n, we obtain a map for the parameter μ as shown in Fig. A.2. The map is called a bifurcation diagram or a chaotic bifurcation diagram. From this plot, we can see that a fixed point of the output x evolves to periodic oscillations and period-doubling oscillations occur for the increase of the parameter μ. Finally, the output x behaves with completely irregular oscillations at high values of the parameter μ, namely, chaotic oscillations. The type of bifurcation is called a period-doubling bifurcation. Period-doubling bifurcation is not the only chaotic route, but other routes for chaotic evolutions exist depending on the configuration of systems and chaos parameters, for example, quasi-period-doubling bifurcations and intermittent chaotic bifurcations. A bifurcation diagram is important to know how the dynamics of a system change for the parameters. We can make similar plots of bifurcation diagrams for the change in the parameters for any chaotic systems and know the chaotic evolution route of the system output. The fact that such complex dynamics are induced from a simple relation in (A.2) is surprising. Indeed, we can observe complex dynamics in optical systems with discrete nonlinear properties.

A.1.2 Continuous Systems

Continuous systems have more or less nonlinear aspects. For engineering applications, linear response is usually assumed even when a system has nonlinearity, or the linearization is frequently applied for the nonlinear system within suitable ranges of parameters, because nonlinear systems are too complex to be modeled and analyzed. They show unwanted irregular oscillations for a wide range of the change in variables. Therefore, only linear parts of the systems are a good model for engineering applications. Until recently, analysis for nonlinear systems was only of fundamental interest as concerns the dynamic behaviors of the systems. However, many phenomena of nonlinear behaviors have been observed in engineering models. For example, strange relaxation oscillations were observed in a triode used for electric circuits, which is a chaotic oscillation and is now known as a van der Pol oscillator (van der Pol 1926). Chaos, which is irregular oscillations induced in deterministic nonlinear systems, became common understanding after the work done by Lorenz (1963), who investigated the behaviors of convective flow for the atmospheric model. He obtained three differential equations for the model by appropriately scaling the three variables. In spite of the simple forms of the three differential equations, one cannot obtain analytical solutions and needs numerical calculations. Later, it was proved that lasers were described by the same Lorenz equations with three variables (Haken 1975).

Here, we show an example of chaotic oscillations in a continuous nonlinear system. We consider a system of damping oscillation driven by an external force known as the Duffing spring model. The Duffing model is described by

$$\frac{\mathrm{d}^2x}{\mathrm{d}t^2} + k\frac{\mathrm{d}x}{\mathrm{d}t} + x^3 = B\cos\omega t \tag{A.3}$$

where x is the variable for the displacement of the spring, ω is the angular frequency of the external driving force, B is the amplitude of the external force, and k is the coefficient of the friction. Using the notation $y = \mathrm{d}x/\mathrm{d}t$, the Duffing equation is written by the following two differential equations:

$$\frac{\mathrm{d}x}{\mathrm{d}t} = y \tag{A.4}$$

$$\frac{\mathrm{d}y}{\mathrm{d}t} = -ky - x^3 + B\cos\omega t \tag{A.5}$$

Namely, a nonlinear chaotic system is generally described by a vector variable $\mathbf{u}$ and a nonlinear function f as

$$\frac{\mathrm{d}\mathbf{u}}{\mathrm{d}t} = f(\mathbf{u};\boldsymbol{\mu}) \tag{A.6}$$

This equation is quite similar to the discrete nonlinear system described in (A.1). $\boldsymbol{\mu}$ is the vector parameter of the system. The Duffing model is essentially a damping oscillation system, but it shows various stable and unstable oscillations depending on the parameter.

Figure A.3a plots the trajectory of the variables x and y for the parameter values of $k = 0.225$, $B = 0.3$, and $\omega = 1$. The output of the system converges to a periodic

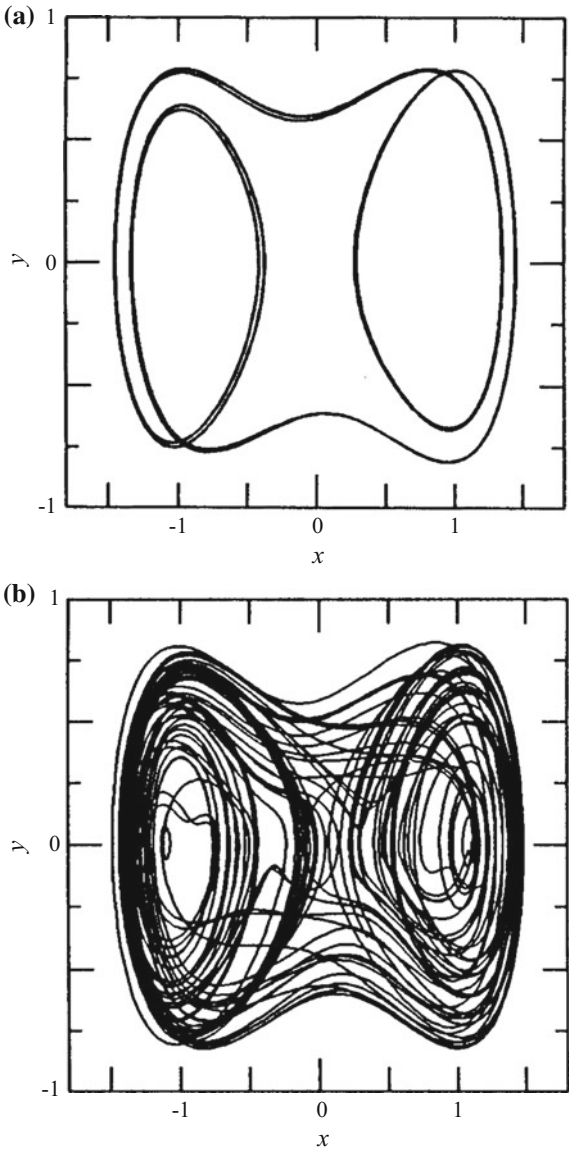

Fig. A.3 Attractors of Duffing system. **a** Periodic attractor for $k = 0.225$, $B = 0.3$, and $\omega = 1$. **b** Chaotic attractor for $k = 0.5$, $B = 0.3$, and $\omega = 1$

orbit (periodic attractor) for the time evolution. The diagram in Fig. A.3a is called a "phase space" and the attraction in the phase space is called "attractor." When $k = 0.5$, $B = 0.3$ $\omega = 1$, the orbit shows a complicated trajectory within a limited compact space as shown in Fig. A.3b. The attractor is so strange that it is called a "strange attractor." A strange attractor is a typical feature of chaotic dynamics. Complex dynamics appear to be such a simple differential equation. Chaos generated from various differential systems for physical and engineering models has been extensively studied after the discovery of chaos by Lorenz. The energy from a physical or engineering system is generally dispersed for the time evolution and such a system is called a dissipative system. In a dissipative system, the volume of the trajectory generally shrinks in the phase space in accordance with the dispersion of energy. However, for dissipative chaotic systems, the trajectory stays within a finite volume in the phase space for the time evolution like in Fig. A.3b due to the presence of an external drive force and it shows a strange attractor. On the other hand, for a system that holds the conservation of energy, the attractor is always fixed within a finite area in the phase space.

A.1.3 Delay Differential Systems

The system described by delay differential equations is a nonlinear system as it is. For the control of a system, a fraction of the output is usually fed back into the system with a finite delay time. When the delay cannot be ignored in order to consider the system response, the system must be described by delay differential equations. In this book, we treat various delayed feedback systems in semiconductor lasers. The general form of a delay differential system is given by the following equation:

$$\frac{\mathrm{d}\mathbf{u}(t)}{\mathrm{d}t} = f\{\mathbf{u}(t-\tau);\boldsymbol{\mu}\} \tag{A.7}$$

where τ is the delay time in the system. As demonstrated in this book, we can observe a rich variety of chaotic dynamics in delay differential systems. The complexity of a system described by delay differential equations is much stronger than that of simple differential systems, since the mapping of a delayed system is of continuous nature. The chaotic dimension (discussed in Sect. A.2.3) of differential systems is low, while it is high for delay differential systems. Therefore, a delay differential system is sometimes referred to as a high-dimensional chaotic system.

A.2 Analysis and Characteristic Descriptions for Chaotic Data

A.2.1 Phase Space, Attractor, and Poincaré Map

We have already shown some tools for the analysis of chaotic oscillations in nonlinear systems. We discussed the phase space for chaotic systems in Sect. A.1.2. We here first go into details of the explanation for the phase space. The phase space of a dynamical system is a mathematical space with orthogonal coordinate directions representing each of the variables needed to specify the instantaneous state of the system. A phase map may be constructed in several ways. For the Lorenz system, for example, the state of the system can be described by three variables x, y, and z and parameters σ, r, and b as

$$\frac{\mathrm{d}x}{\mathrm{d}t} = -\sigma(x - y) \tag{A.8}$$

$$\frac{\mathrm{d}y}{\mathrm{d}t} = -xz + rx - y \tag{A.9}$$

$$\frac{\mathrm{d}z}{\mathrm{d}t} = xy - bz \tag{A.10}$$

Figure A.4 shows the time evolution of Lorenz equations with a diagram in a three-dimensional phase space. The diagram is called the phase portrait and the orbit is called the trajectory in the phase space. The Lorenz system gives an excellent instance of what we called a strange attractor. We see a beautiful butterfly-shaped attractor on which a trajectory starting from any initial point will come back to the near neighborhood of the initial point but never precisely repeat it. An important feature of the phase portrait is that two trajectories will never cross each other. This non-crossing property derives from the fact that both past and future states of a deterministic system are uniquely determined by the system state at a given time. A crossing of trajectories inevitably introduces ambiguity into past and future states and contradicts the assumed uniqueness of the trajectory. However, a projection of a higher dimensional space onto a plane might show apparent crossings which do not represent actual interactions. The phase portraits for the periodic, quasi-periodic, and chaotic time variations in general appear to be a limit cycle, a torus, and a strange attractor, respectively, as shown in Sect. A.2.2.

Poincaré Map

The Poincaré map introduced by H. Poincaré is a classical technique for analyzing a dynamical system. It is obtained by viewing the trajectory stroboscopically. It is

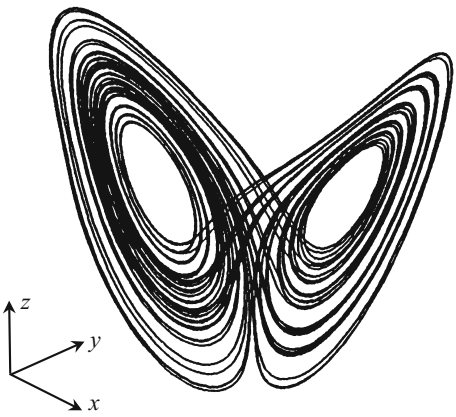

Fig. A.4 Lorenz attractor for parameter values of $\sigma = 10$, $r = 28$; and $b = 8/3$

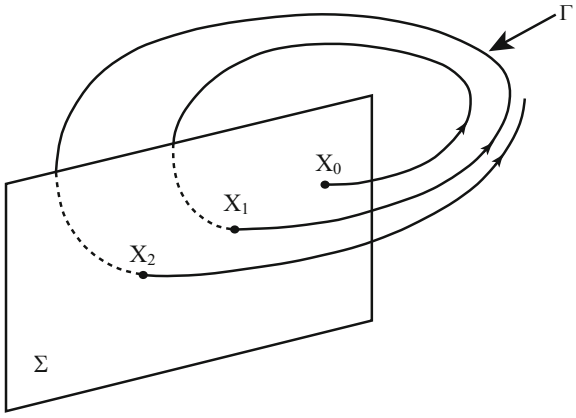

Fig. A.5 Poincaré map of an n-th order autonomous system. Γ: n-dimensional trajectory, Σ: $(n-1)$-dimensional hyper plane

also a useful tool for understanding the characteristics of nonlinear systems. For an n-dimensional trajectory Γ as shown in Fig. A.5, take an $(n-1)$-dimensional hyper plane Σ transverse to the trajectory at X_0. The trajectory emanating from X_0 will hit Σ at X_1, X_2, … at the following transversings. The Poincaré map P is defined as

$$X_{k+1} = \mathrm{P}(X_k) = \mathrm{P}\{\mathrm{P}(X_{k-1})\} = \mathrm{P}^2(X_{k-1}) = \cdots \tag{A.11}$$

where k is an integer. The Poincaré map replaces the continuous dynamical system into a discrete map, which is much easier to deal with mathematically. With the Poincaré map, one can dramatically reduce the data number that is especially necessary in the experiments. As demonstrated in Sect. A.2.2, one can easily distinguish among the periodic, quasi-periodic, and chaotic variations from the

appropriate Poincaré maps. In particular, the Poincaré map for chaotic systems exhibits remarkable features. The map does not result in a simple geometrical structure and, when it is magnified, the fine structure resembles the gross one. Namely, the system trajectory has a fractal structure.

A.2.2 Steady-State Behaviors

We can classify dynamical systems in terms of their steady-state solutions and describe some typical examples for particular cases. The steady state refers to the asymptotic behavior of the system as time t approaches infinity. Typically four different types of steady-state behaviors can be identified to chaotic system. Each steady state will be described from the following different points of view: in the time domain, in the frequency domain, in the phase space, and in the Poincaré map. We here mainly focus on the Poincaré maps for chaotic systems.

Equilibrium Points

An equilibrium point x^0 of an autonomous system is a constant solution in (A.6). In most cases, this means $f(x^0;\ \mu) = 0$ or $x^0 = f(x^0;\ \mu)$. The phase portrait for an equilibrium point is the point itself.

Periodic Solutions

A time-dependent variable $x(t)$ is periodic if $x(t + T) = x(t)$ for all t and some minimal period T. For a model of Duffing's equations in (A.4) and (A.5), a periodic solution was plotted in Fig. A.3a. Such a closed curve is called a limit-cycle as it can be regarded as a diffeomorphic copy of a cycle. The corresponding Poincaré map is displayed in Fig. A.6a by sampling the trajectory with the driving period. The Poincaré map for a periodic solution in general consists of finite points and the number of points depends on the sampling period.

Quasi-Periodic Solutions

A quasi-periodic solution is the sum of periodic solutions each of whose frequency is a linear coupling of a finite set of base frequencies. The simplest case is the one with two frequencies. We here consider the van der Pol equations to demonstrate how quasi-periodic solutions arise in dynamical systems. The van der Pol equations read as

$$\frac{\mathrm{d}x}{\mathrm{d}t} = y \tag{A.12}$$

$$\frac{\mathrm{d}y}{\mathrm{d}t} = \mu\left(1 - x^2\right)y - x + \gamma\cos\omega t \tag{A.13}$$

In the van der Pol equations, there exist two periodic components; one is the driving signal with the period $T_1 = 2\pi/\omega$ and the other is the intrinsic oscillation whose period T_2 depends on the system parameters. When T_2 is synchronized with T_1,

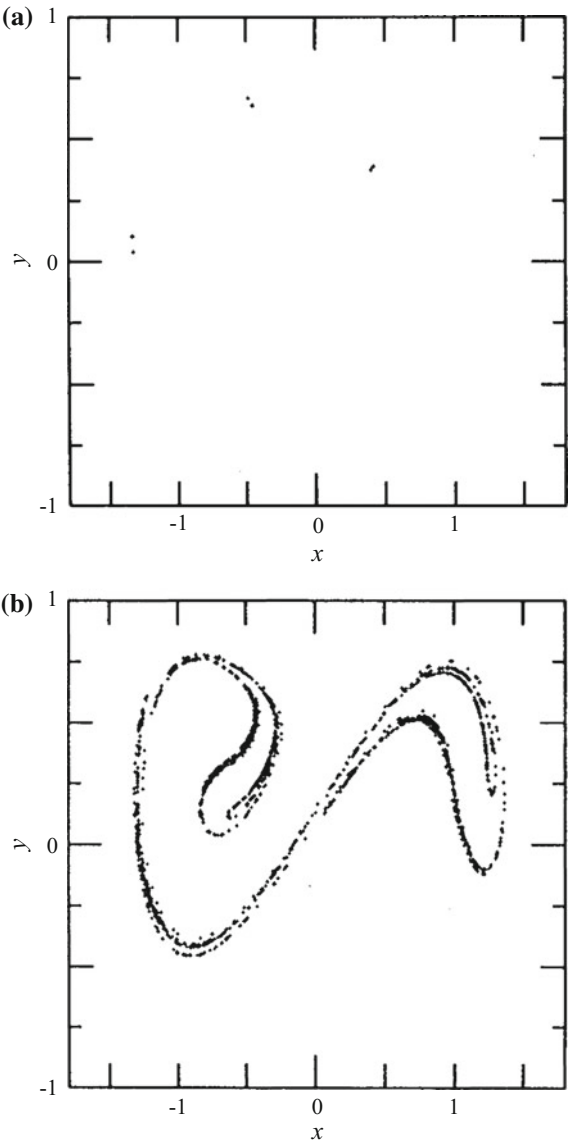

Fig. A.6 Poincaré map for Duffing oscillation. **a** Map for periodic oscillation for Fig. A.3a. **b** Map for chaotic oscillation for Fig. A.3b

there appears a periodic oscillation. However, if T_1 and T_2 are incommensurate and neither of them can dominate the output, the system has a quasi-periodic behavior. An example of the quasi-periodic solutions in the van der Pol model is shown in Fig. A.7. Figure A.7a shows a time series for the quasi-periodic solution. The spectrum (Fig. A.7b) consists of main spectral peaks corresponding to the intrinsic oscillation frequencies of the system and the tightly spaced side bands due to the

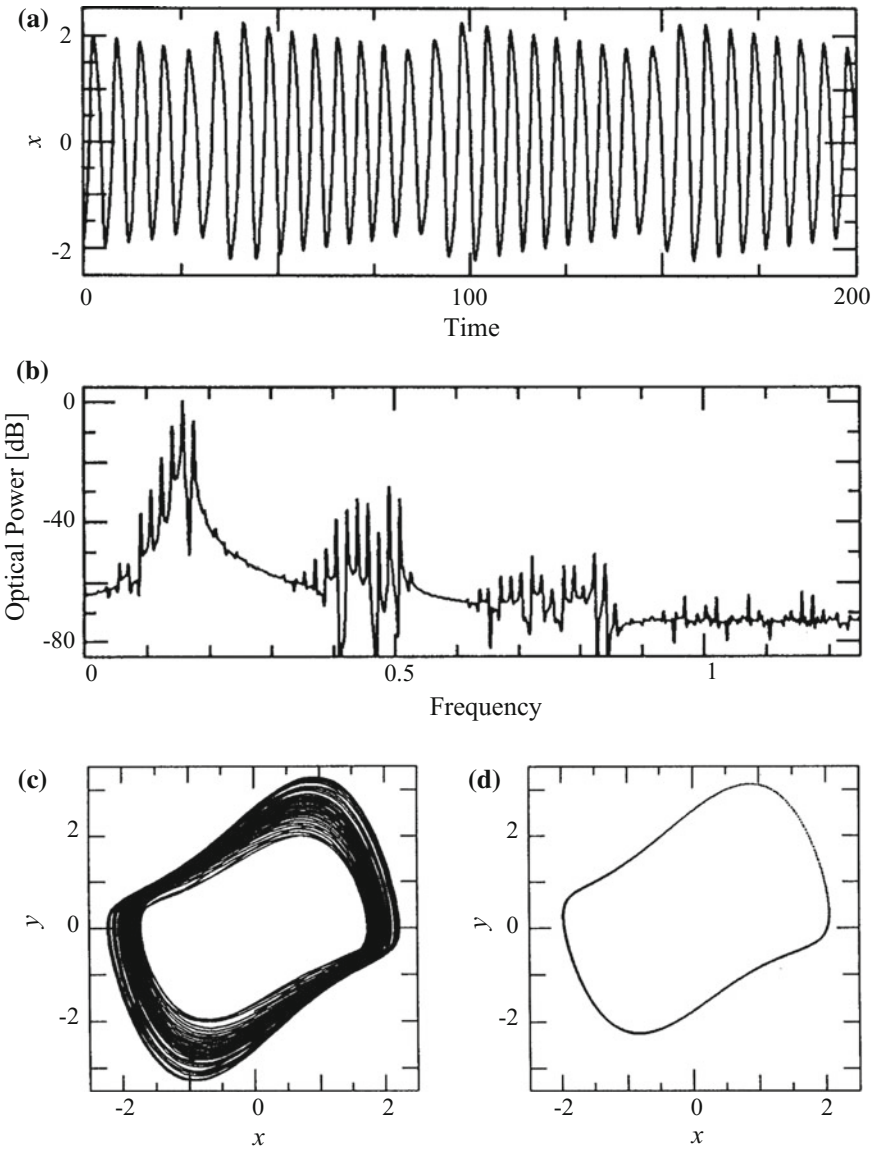

Fig. A.7 Quasi-periodic solution for van der Pol oscillator at $\mu = 1$, $\gamma = 0.5$, and $\omega = 1.1$. **a** Chaotic oscillation, **b** power spectrum, **c** attractor, and **d** Poincaré map

driving signal. The difference between the intrinsic frequency and the driving frequency can be measured from the spacing of the harmonics within the sideband. The corresponding attractor is plotted in Fig. A.7c. In the phase space, the trajectory lies on a diffeomorphic copy of the two-torus as shown in Fig. A.8. Since the

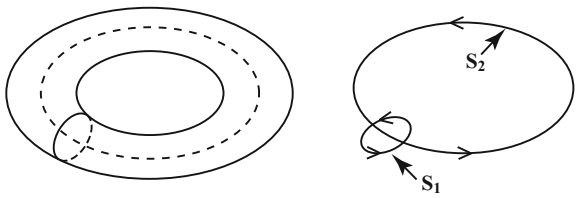

Fig. A.8 Torus with two periodic components denoted as S_1 and S_2

trajectory is a curve and two-torus is a surface, not every point on the torus lies on the trajectory, however, it can be shown that the trajectory repeatedly passes closely every point on the torus in an arbitrary manner. Depending on the sampling period, the Poincaré map for the quasi-periodic solutions appears as various limit cycles. In the van der Pol model, we obtain a Poincaré map by sampling the trajectory with the driving period as in Fig. A.7d.

Chaos

Chaos is different from any one of the above three solutions. Once more we recall Duffing's equations to generate the chaotic attractor in Fig. A.3b. It behaves with more irregular oscillations than those of periodic and quasi-periodic states. In general, the spectrum becomes broadened, and no distinct spectral peak is visible, but has a continuous broadband spectral structure. The Poincaré map corresponding to Fig. A.3b shows a very interesting structure and is displayed in Fig. A.6b.

A.2.3 Fractal Dimension and Correlation Dimension

We here discuss some statistical measures of chaotic attractors by introducing the concept of the fractal dimension. A chaotic trajectory has generally a fractal structure as discussed in Sect. A.2.1. We first start from the capacity dimension. For simplicity, a geometric structure, i.e., a limit cycle, a torus, or a chaotic attractor, is regarded as a set. Consider a set located in an m-dimensional phase space. Imagine we cover the attractor by $N(\varepsilon)m$-dimensional boxes of ε on each side. The capacity dimension d_c is defined as

$$d_c = \lim_{\varepsilon \to 0} \frac{\log N(\varepsilon)}{\log(1/\varepsilon)} \tag{A.14}$$

For a dissipative dynamical system such as a delay differential model, the attractor is located in an m-dimensional phase space (embedding space), but the fractal dimension is in general less than the embedding dimension m. Furthermore, chaotic attractors generally have non-integer dimension.

There are several kinds of definitions about the fractal dimension. For an experimental data or a model of a high-dimensional dynamical system, another type of dimension is more efficient in data calculation than the capacity dimension. The

method is the correlation dimension d_g. Suppose that many points are scattered over a set and consider the correlation between any two points. The typical number of neighbors of a given point will vary more rapidly with the distance from that point if the set has higher dimension than otherwise. The correlation dimension may be computed from the correlation function $C(\rho)$ defined by

$$C(\rho) = \lim_{N\to\infty} \frac{1}{N^2} \sum_{i,j=1}^{N} \theta\left(\rho - \left|x_i - x_j\right|\right) \tag{A.15}$$

where x_i and x_j are the points on the attractor, $\theta(y)$ is the Heaviside function ($\theta(y) = 1$ for $y > 0$ and $\theta(y) = 0$ for $y < 0$) and N is the number of the points randomly chosen from the entire data set. The Heaviside function simply counts the number of the points within a radius ρ of the point x_i, and $C(\rho)$ gives the average function of the points within ρ. The correlation dimension is defined by the variation of $C(\rho)$ with ρ approaching zero as

$$C(\rho) \approx \rho^{d_g} \quad (\rho \to 0) \tag{A.16}$$

Therefore, the correlation dimension is obtained from the slope of the graph of $\log C(\rho)$ versus $\log\rho$.

A.2.4 Lyapunov Exponent

The fractal dimension provides a qualitative measure of the singularity of the chaotic attractor. However, it is a static measure and, from the fractal dimension, we know nothing about how the trajectory varies in the phase space as the time evolution. Moreover, this kind of measure has no explicit relation with the most important characteristics of chaos, i.e., the sensitivity to the initial condition. Therefore, we have to resort to some dynamical measure—the method is known as the Lyapunov exponent.

The basic idea of the Lyapunov exponent is to measure the average rate of the divergence for the neighboring trajectories on the attractor. The direction of the maximum divergence or convergence locally changes on the attractor. The motion must be monitored at each point along the trajectory. Therefore, a small sphere is defined, whose center is a given point on the attractor and whose surface consists of phase points from nearby trajectories. As the center of the sphere and its surface points evolve in time, the sphere becomes an ellipsoid with the principal axes in the directions of the contraction and the expansion. The average rates of the expansion or the contraction along the principal axes are the Lyapunov exponents. For the i-th principal axis, the corresponding exponent is defined by

$$\lambda_i = \lim_{t\to\infty}\left\{\frac{1}{t}\frac{L_i(t)}{L_i(0)}\right\} \tag{A.17}$$

where $L_i(t)$ is the radius of the ellipsoid along the i-th principal axis at time t. In this expression, the growth rate is always measured along the i-th principal axis, but the absolute orientation in the phase space of that axis is not fixed. It is impractical to perform the actual computation in the way suggested in the definition, because the initially close phase points would soon diverge from each other by distances approaching the size of the attractor, and the computation would then fail to capture the local rates of the divergence and the contraction. Therefore, vectors connecting the surface of the ellipsoid to the center must be shrunk periodically or renormalized to ensure that the size of the ellipsoid remains small and that its surface points correspond to trajectories near that of the center point. The calculation algorithm for the Lyapunov exponent from time series can be found in Abarbanel (1996).

There are some important points related to the Lyapunov exponents as discussed in the following:

(1) For a chaotic system, at least one of the Lyapunov exponents must be positive to allow the sensitive dependence on the initial conditions.

(2) According to the definition of the Lyapunov exponents, a small volume V in the phase space will change in time as

$$V(t) = V_0 \exp\left(\sum_{i=1}^{n}\lambda_i t\right) \tag{A.18}$$

and hence the rate of the change of the volume $V(t)$ is simply

$$\frac{\mathrm{d}V(t)}{\mathrm{d}t} = \sum_{i=1}^{n}\lambda_i V(t) \tag{A.19}$$

Therefore, for a dissipative chaotic system, the sum of all the Lyapunov exponents must be negative, i.e., $\sum_i \lambda_i < 0$.

(3) If we order λ_i (i = 1, 2, …, n) as $\lambda_1 > \lambda_2 > \cdots > \lambda_n$, then the Lypapunov dimension, d_l, is defined as

$$d_l = j + \frac{\lambda_1 + \lambda_2 + \cdots + \lambda_j}{\left|\lambda_{j+1}\right|} \tag{A.20}$$

where j is the number of the Lyapunov exponents, which gives a positive sum, but adding λ_{j+1} would make the sum negative, i.e., $\sum_{i=1}^{j}\lambda_i > 0$ but $\sum_{i=1}^{j+1}\lambda_i < 0$. The relationship among the capacity dimension d_c, the correlation dimension d_g,

and the Lyapunov dimension d_l is $d_c \leq d_g \leq d_l$. The equality holds only for the case that the points on the fractal are approximately uniformly distributed (Abarbanel 1996).

A.3 Chaos Control

A.3.1 Controlling Chaos

Real physical and engineering systems are more or less chaotic systems. Stable control for nonlinear systems is essential for practical applications. However, a system sometimes seems to be out of control for any parameters when it operates under chaotic oscillations. The state of the system is surrounded by chaotic sea and the system could not be stabilized by any parameter changes as far as the change is small. However, there always exist stable islands scatteredly located not far from the operating point of the system (they are usually not exact stable points but unstable periodic orbits). By appropriately choosing a perturbation to the system and attracting the state to such a stable orbit, one might successfully stabilize the system even when the original state is a chaotic oscillation. This kind of stabilization is called "chaos control." Chaos control is different from the ordinary technique of forced control in respect to a small perturbation for the system. In ordinary forced control, the power imposed to the system is so large that the original state of the system is completely changed after the control. On the other hand, the applied signal in chaos control is small enough not to change the original state and the system with chaotic oscillation is attracted to a periodic or even a fixed state by the small perturbation. The dynamics of the original state is not changed after the control is achieved. This is the idea of chaos control. Of course, a chaotic state may also be stabilized to a stable oscillation by a large control signal. This is different from chaos control, but it is categorized into ordinary forced control. The principle of chaos control was first proposed by Ott et al. (1990). They gave the mathematical proof of chaos control for chaotic systems and the method is now called OGY method or OGY algorithm after their names. In the following, we present a brief proof of the OGY algorithm. However, the application of the OGY method requires the full mathematical description of a nonlinear model. We need the attractors or the Poincaré map in advance to analyze and control the system. It is sometimes difficult to apply the OGY method for the control of practical systems. As an alternative method (but it still has an essence of the OGY algorithm), we also introduce the continuous chaos control methods, which are applicable to real experimental systems.

A.3.2 Method of Chaos Control

OGY Algorithm

Take as an example a single-input two-dimensional discrete nonlinear system and consider chaos control in the system. The system is written as

$$\mathbf{x}_{n+1} = f(\mathbf{x}_n, \mu) \tag{A.21}$$

where f is again the nonlinear function and μ is the control parameter. We assume that the system has a fixed point at $\mu = \mu_0$, namely

$$\mathbf{x}_f = f(\mathbf{x}_f, \mu_0) \tag{A.22}$$

The operating point for the system parameter μ is assumed to be close to the parameter μ_0 with the accompanying output $\mathbf{x}_f$. We define the difference of the outputs $\mathbf{x}_n$ and $\mathbf{x}_f$ as

$$\xi_n = \mathbf{x}_n - \mathbf{x}_f \tag{A.23}$$

Since the difference ξ is small, we linearize the difference and set the control signal μ_n so as to force the original state $\mathbf{x}_n$ to the stable state $\mathbf{x}_f$. The relation is given as

$$\xi_{n+1} = \mathbf{M}_n + \mathbf{a}\mu_n \tag{A.24}$$

where $\mathbf{M}$ and $\mathbf{a}$ are Jacobian matrices for the variable $\mathbf{x}$ and the parameter μ at the fixed points, respectively. The point we consider is a type of saddle node unstable point. Then, one of the eigenvalues of $\mathbf{M}$ must be $|\lambda_u| > 1$ and the other one is $|\lambda_s| < 1$. We write the eigenvectors for respective eigenstates as $\mathbf{e}_u$ and $\mathbf{e}_s$, and define the accompanying contravariant basis vectors $\mathbf{v}_u$ and $\mathbf{v}_s$. Using the vector relations of $\mathbf{v}_u \cdot \mathbf{e}_u = \mathbf{v}_s \cdot \mathbf{e}_s = 1$ and $\mathbf{v}_s \cdot \mathbf{e}_u = \mathbf{v}_u \cdot \mathbf{e}_s = 0$, the matrix $\mathbf{M}$ is written as

$$\mathbf{M} = [\,\mathbf{e}_u \quad \mathbf{e}_s\,] \begin{bmatrix} \lambda_u & 0 \\ 0 & \lambda_s \end{bmatrix} \begin{bmatrix} \mathbf{v}_u \\ \mathbf{v}_s \end{bmatrix} = \lambda_u \mathbf{e}_u \cdot \mathbf{v}_u + \lambda_s \mathbf{e}_s \cdot \mathbf{v}_s \tag{A.25}$$

When a small control signal is applied to put the difference ξ_{n+1} on the stable orbit in accordance with (A.24), the difference ξ_{n+1} is parallel to the vector $\mathbf{e}_s$. Then, we obtain the condition

$$\mathbf{v}_u \cdot \xi_{n+1} = 0 \tag{A.26}$$

Taking into account the relations in (A.24) and the condition of $\mathbf{v_n} \cdot \mathbf{a} \neq 0$ from (A.24), we obtain the following signal suitable for the control:

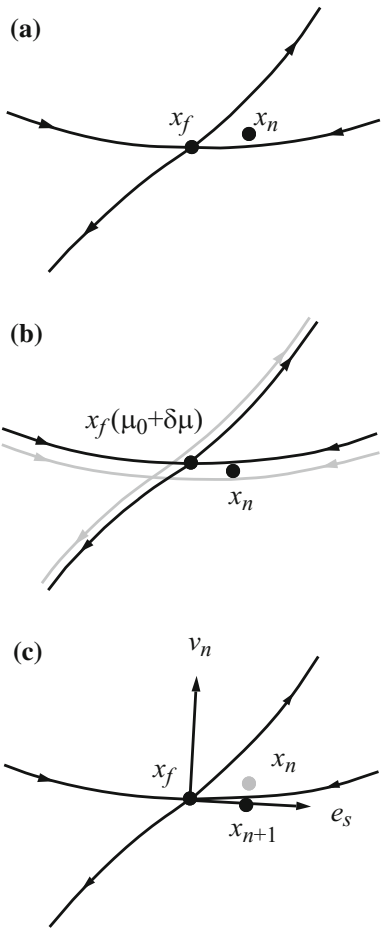

Fig. A.9 OGY control algorithm. **a** Initial state, **b** application of a small perturbation to the parameter, and **c** controlled state

$$\mu_n = -\frac{\lambda_u \mathbf{v}_n \cdot \boldsymbol{\xi}_n}{\mathbf{v}_n \cdot \mathbf{a}} \tag{A.27}$$

When the state of the system is close enough to the point $\mathbf{x}_f$ and the signal given by (A.27) is applied to the system, the state falls down to the fixed point $\mathbf{x}_f$. Figure A.9 schematically shows the OGY control algorithm. In Fig. A.9a, the initial state $\mathbf{x}_n$ is close enough to the fixed point $\mathbf{x}_f$. A small perturbation is applied to the control parameter according to (A.27) as shown in Fig. A.9b. Then, the next state is shifted onto the stable orbit in Fig. A.9c and, finally, the state is attracted to the fixed point. The model here is for a low-dimensional system, but the procedure is also applied to high-dimensional chaotic systems. For a continuous system, it must be approximated to a discrete form in order to apply the OGY algorithm. Further, we must in advance know all the parameter values of the system to perform the control.

Therefore, the method has a limitation for application to real nonlinear systems. For this reason, various control algorithms have been proposed without losing the essence of the OGY algorithm.

Continuous Control

We here describe the continuous chaos control proposed by Pyragas (1993) as an alternative method of chaos control for practical use. The system configuration is shown in Fig. 9.1. The control signal is the difference between the present and time delayed outputs. The delay time introduced is almost equal to the response time of the system (but may not be exactly equal to the response time). Namely, the delay τ corresponds to the typical frequency of the chaotic oscillation. When we can obtain exactly the mathematical description of the system, we can calculate the delay time from the equations. Otherwise, the typical frequency of chaotic oscillations in the experiment would give a good estimate for the delay time. In the continuous control, the system under a certain chaotic oscillation is synchronized to a periodic state by feeding back the difference signal.

Using one of the variables, $y(t)$, in a chaotic system and writing the other variables as a vector representation, $\mathbf{x}(t)$, the equations for the system are given by

$$\frac{\mathrm{d}y}{\mathrm{d}t} = f(y, \mathbf{x}) \tag{A.28}$$

$$\frac{\mathrm{d}\mathbf{x}}{\mathrm{d}t} = g(y, \mathbf{x}) \tag{A.29}$$

where f and g are the nonlinear functions. The feedback signal in the continuous control is proportional to the difference of the present output $y(t)$ and the delayed output $y(t - \tau)$ defined by

$$u(t) = K\{y(t - \tau) - y(t)\} \tag{A.30}$$

For the control, (A.28) is modified as

$$\frac{\mathrm{d}y}{\mathrm{d}t} = f(y, \mathbf{x}) + u(t) \tag{A.31}$$

where K is the strength of the feedback and the effective control is performed by changing this value.

The control signal in (A.30) becomes zero after the success of the control, i.e., $u(t - \tau) = u(t)$, and the output shows periodic oscillation with a fundamental period of τ. The target of the periodic orbit to be controlled must be close to the initial state of the chaotic system and the delay time must be accurately estimated to some degree in advance either theoretically or experimentally. One cannot tell to which state the system is attracted among the possible orbits, when the system includes several unstable periodic orbits close to the initial state. The continuous control does not require the calculation of the Poincaré map such as in the OGY method

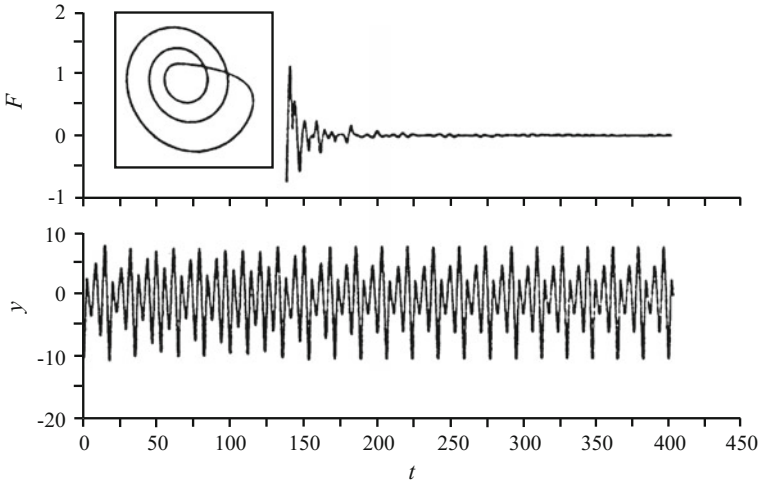

Fig. A.10 Continuous chaos control for Rössler system. The chaotic oscillation is controlled to a period-3 state at the parameter values of $a = 0.2$, $b = 0.2$, $c = 5.7$, $\tau = 17.5$, and $K = 0.2$. *Upper trace* curve F corresponds to the moment of switching on the perturbation and the *inset* is the x-y phase portrait after the control. *Lower trace* output y [after Pyragas (1992); © 1992 Elsevier]

and it is robust for noises. The continuous control is an extension of the OGY method for continuous differential systems. The control is easily realized for practical engineering systems, when the response time is not so fast to implement by using electronic circuits.

We show an example of the continuous control for the Rössler system shown in Fig. A.10. The equations of the system are given as

$$\frac{\mathrm{d}x}{\mathrm{d}t} = -y - z \tag{A.32}$$

$$\frac{\mathrm{d}y}{\mathrm{d}t} = x + ay + u(t) \tag{A.33}$$

$$\frac{\mathrm{d}z}{\mathrm{d}t} = bx - cz + xz \tag{A.34}$$

$u(t)$ in (A.30) is the control term. In the figure, the quasi-periodic or weak chaotic state is controlled to period-3 oscillation (Pyragas 1992). As can be easily seen from the figure, the control signal diminishes after the success of the control.

Another example of the method of chaos control is the occasional proportional feedback (OPF). The OPF control is discussed in Sect. 9.2.2. The control in the OPF method is also a periodic perturbation to the system and the system with chaotic state is attracted to an unstable periodic orbit near the initial state. A small periodic control signal is produced by processing from the system's output in a

digital electronic circuit with an appropriate synchronous reference. Different from the continuous control, the feedback control circuit in the OPF system continually outputs the control signal even after the success of the control. However, the control signal is usually small enough not to disturb the original chaotic attractor and does not change the dynamics of the system.

A.4 Chaos Synchronization

Synchronization between two nonlinear chaotic systems was mathematically studied by Fujisaka and Yamada early in 1983. Synchronization between two nonlinear chaotic systems is not self-evident and was first demonstrated in a Rössler system by Pecora and Carroll (1990). Before the proposal of the method of chaos synchronization by Pecora and Carroll, chaos synchronization had been frequently observed in real nonlinear systems. For example, pendulum clocks mounted on the same wooden beam, all the pendulums swing in the synchronous way without one's noticing it as early as 1600s (Huygens 1986). After the proposal of the method of chaos synchronization, it has been demonstrated in various nonlinear systems including lasers. We prepare almost the same two nonlinear systems with the same parameter values. A fraction of the output from one of the chaotic systems (chaotic transmitter) is sent to the other system (chaotic receiver). Then, the receiver output synchronizes with the transmitter signal under appropriate parameter conditions. The mathematical basis for chaos synchronization is given for discrete and differential systems; however, the mathematical explanation for chaos synchronization in delay differential systems is not easy and the proof has not been given yet. However, numerical and experimental demonstrations of chaos synchronization in discrete, differential, and delay differential systems have been reported.

We explain the general idea of chaos synchronization using a simple differential model. Consider a chaotic system with a set of vector variables $\mathbf{u}$ and $\mathbf{v}$. We divide the transmitter system into two subsystems and describe the nonlinearities for the respective subsystems as $f(\mathbf{u}, \mathbf{v})$ and $g(\mathbf{u}, \mathbf{v})$. Then, the transmitter system is characterized as

$$\frac{\mathrm{d}\mathbf{u}}{\mathrm{d}t} = f(\mathbf{u}, \mathbf{v}) \tag{A.35}$$

$$\frac{\mathrm{d}\mathbf{v}}{\mathrm{d}t} = g(\mathbf{u}, \mathbf{v}) \tag{A.36}$$

The subsystems are mutually coupled and the outputs of $\mathbf{u}$ and $\mathbf{v}$ are assumed to be chaotic. We prepare the receiver system for chaos synchronization. The receiver system consists of only one of the subsystems and it has the same form as (A.35). Namely, the receiver is written as

$$\frac{d\mathbf{w}}{dt} = f(\mathbf{w}, \mathbf{v}) \tag{A.35}$$

Without signal transmission from the transmitter, variable **v** is treated as a certain constant vector. The subsystem is described by the nonlinear function, however the output **w** may be either a chaotic or a stable oscillation when the receiver receives no transmitted signal. Even if the output is chaotic, the output **w** would never show the same chaotic oscillations as the output **u** in the transmitter since chaos has strict sensitivity for initial conditions. However, the output **w** shows completely the same chaotic oscillation as the transmitter output **u** when a fraction of the transmitter output is sent to the receiver under appropriate conditions. In a mathematical sense, there is a condition for having a negative value of the maximum conditional Lyapunov exponent for the difference in the outputs **u** and **w**.

Take an example of a Lorenz system for the demonstration of chaos synchronization. The differential equations with the variables x, y, and z, and the transmitter system is divided into two subsystems as
subsystem 1

$$\left.\begin{aligned} \frac{dy}{dt} &= -xz + rx - y \\ \frac{dz}{dt} &= xy - bz \end{aligned}\right\} \tag{A.38}$$

subsystem 2

$$\frac{dx}{dt} = -\sigma(x - y) \tag{A.39}$$

The receiver system is assumed as a copy of subsystem 1 of the transmitter and it is given as

$$\left.\begin{aligned} \frac{dy'}{dt} &= -xz' + rx - y' \\ \frac{dz'}{dt} &= xy' - bz' \end{aligned}\right\} \tag{A.40}$$

As already noted, the variable x in the receiver is treated as a constant without the transmission of a signal from the transmitter. The outputs x, y, and z of the transmitter are chaotic at the parameter values of $\sigma = 16$, $b = 4$, and $r = 45.92$. On the other hand, it is proved that the maximum Lypunov exponents of the outputs y' and z' of the receiver are negative. Therefore, the receiver exhibits stable outputs without receiving any chaotic signal from the transmitter.

Figure A.11 shows the transients for the chaos synchronization in a Lorenz system. The output z' from the receiver is pulled into the transmitter output z due to the presence of the transmission signal and shows a chaotic oscillation. For a sufficiently elapsed time, the two outputs show the same chaotic oscillation as

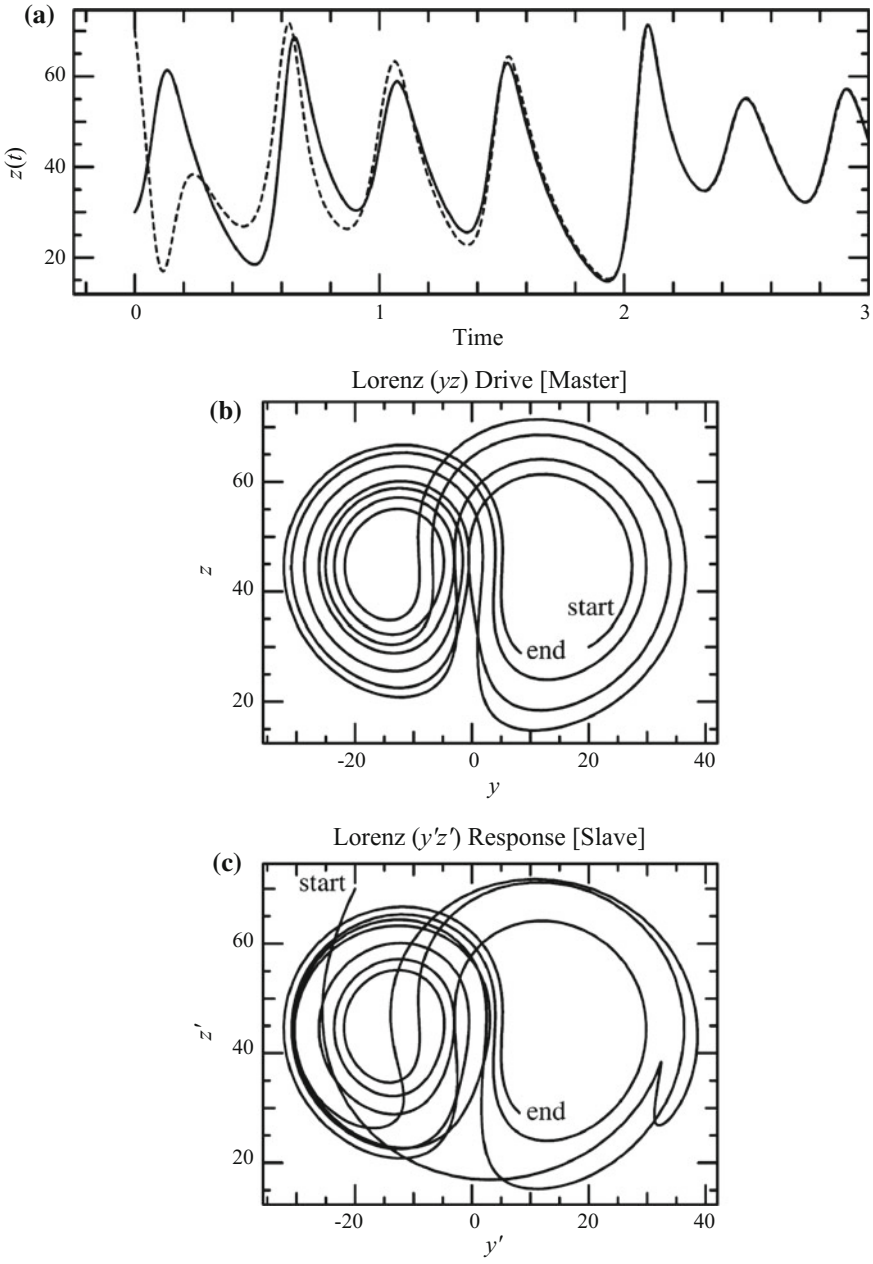

Fig. A.11 Transients of chaos synchronization in Lorenz system. The values of the parameters are $\sigma = 16$, $b = 4$, and $r = 45.92$. **a** Time series of outputs z (*solid curve*) and z' (*broken gray line*). **b** Trajectory at y-z plane, and **c** trajectory at y'-z' plane. The start point is the time at which the receiver receives the transmitted signal

shown in Fig. A.11a. Figure A.11b, c shows the plots of the trajectories for the y-z and y'-z' planes, respectively. The starting points are the time when the transmitted signal is received at the receiver. For the elapse of time, the distance between the two trajectories is reduced and the trajectories finally overlap each other. Thus, chaos synchronization is achieved. Chaos synchronization is only attained under certain conditions. We must take care when choosing a set of subsystems and parameter conditions for successful chaos synchronization. To make suitable subsystems for chaos synchronization, the receiver system must be coincident with the transmitter system when one or more of the transmitter outputs are sent to the receiver. In this instance of the Lorenz system, the receiver conforms the transmitter system with transmission of signal x.

In laser systems, however, the method is not straightforwardly applicable, since we cannot divide the dynamics of laser variables into subsystems. As an alternative technique, two same sets of laser systems are prepared as a transmitter and a receiver and a small portion of the laser output in the transmitter laser is sent to the receiver. Successful chaos synchronization in semiconductor laser systems is achieved under appropriate conditions of the system parameters and the signal transmission as discussed in Chap. 12.

References

H.D.I. Abarbanel, *Analysis of Observed Chaotic Data* (Springer, New York, 1996)

H. Fujisaka, T. Yamada, Stability theory of synchronized motion in coupled-oscillator systems. Prog. Theor. Phy. **69**, 32–47 (1983)

H. Haken, Analogy between higher instabilities in fluids and lasers. Phys. Lett. A **53**, 77–78 (1975)

C. Huygens, *Christiaan Huygens' the Pendulum Clock, or, Geometrical Demonstrations Concerning the Motion of Pendula as Applied to Clocks* (Iowa State Press, 1986)

T.Y. Li, J.A. Yorke, Period three implies chaos. Am. Math. Mon. **82**, 985–992 (1975)

E.N. Lorenz, Deterministic non-periodic flow. J. Atmos. Sci. **20**, 130–148 (1963)

E. Ott, C. Grebogi, J.A. Yorke, Controlling chaos. Phys. Rev. Lett. **64**, 1196–1199 (1990)

A.E. Motter, D.K. Campbell, Chaos at fifty. Phys. Today **66**, 27–33 (2013)

L.M. Pecora, T.L. Carroll, Synchronization in chaotic systems. Phys. Rev. Lett. **64**, 821–824 (1990)

H. Poincaré, *The Foundation of Science: Science and Method* (The Science Press, Lancaster, 1913)

K. Pyragas, Continuous control of chaos by self-controlling feedback. Phys. Lett. A **170**, 421–428 (1992)

K. Pyragas, Predictable chaos in slightly perturbed unpredictable chaotic systems. Phys. Lett. A **181**, 203–210 (1993)
U. Ueda, R.H. Abraham, H.B. Stewart, *The Road to Chaos* (*1. Some Problems in the Theory of Nonlinear Oscillations*) (Aerial Press, 1992)
B. van der Pol, On relaxation-oscillations. Philos. Mag. **7**, 978–992 (1926)

Index

A
Absolute position measurement, 428
Accuracy
  of chaos synchronization, 520
  of synchronization, 543
Achronal chaos synchronization, 564
Achronal state, 472, 498
Achronal synchronization, 561, 573, 574, 581, 582
Active feedback interferometer, 449
Active interferometers, 9
Active layer, 72
Additional enhancement factor, 76
Additive active phase-tracking method, 426
Additive modulation, 534, 535
Adler equation, 340
Adler-type frequency pulling, 194
Air gap, 621
Allan variance, 397
α parameter, 42, 216, 339
Amplified spontaneous emission, 598
Amplitude anisotropy, 288
Amplitude-phase coupling, 177
Amplitude reflectivity, 84
AM sideband, 552
Analog encryption, 512
Analogue-to-digital converter (ADC), 605
Angle measurement, 430
Angular momentum numbers of electron, 286
Angular oscillation frequency, 17
Anticipating chaos synchronization, 465, 478, 489, 563
Anti-mode, 91, 145, 154, 374
Anti-phase
  correlation, 501
  dynamics, 169
  oscillation, 170, 296, 302, 305, 306
  synchronization, 500
  synchronous oscillations, 169
Approximation, 588
Archaic term trans-information, 600
AR-coated semiconductor laser, 386
Ar-ion lasers, 30
ARROW VCSELs, 402
Artificial neural networks, 586
Astigma, 71
Atmospheric model, 631
Atomic detuning, 20
Attractor, 120, 153, 364, 372, 375, 454, 633
Attractor ruins, 153
Auger capture coefficient, 335
Auger coefficient, 45
Auger process, 333
Autocorrelation, 446
Autocorrelation function, 600, 611
Autonomous system, 636
Averaged near-field patterns, 323
Averaged optical frequency, 189
Average mutual information, 547

B
Bad-cavity condition, 25, 26
Band-filling effects, 264
Bandwidth, 552
  of chaos, 614
Bandwidth-enhanced, 255, 342
  chaos synchronization, 480
  chaotic laser, 612
Beam quality factor, 316, 406, 413
Beam shaping, 406, 412
Beat frequency, 211
Bifurcation, 95, 546
  cascade, 382
  diagrams, 121, 123, 138, 160, 168, 184, 243, 248, 268, 341, 368, 382, 444, 451, 495, 630
  scenarios, 154
Birefringence, 287

© Springer International Publishing AG 2017

J. Ohtsubo, *Semiconductor Lasers*, Springer Series in Optical Sciences 111,
DOI 10.1007/978-3-319-56138-7

Birefringence (*cont.*)
frequency splitting, 311
splitting, 299
Bistability, 137, 157, 274
Bistable state, 190, 420
1-bit ADC, 612
1-bit delay Mach–Zehnder interferometer, 623
Bit error rate (BER), 527, 543, 553, 554
Bit rate, 218, 538, 554
Bloch equations, 15
Boltzmann constant, 48
Bottleneck of electronic signal processing, 615
Bragg reflector, 300
Bragg wavelength, 79
Broad-area semiconductor lasers, 6, 311, 390, 403, 411, 412, 487
Broad stripe width, 312
Buried hetero-structure, 71
Bursts of synchronization, 549
Butterfly attractor, 22
Butterworth electronic filter, 523

C
Capacity dimension, 639
Capacity of information, 614
Carrier
capture rate, 335
density, 37, 50, 435
diffusion, 284, 312
hole-burning, 79, 489
hole-burning effect, 313
lifetime, 44, 45, 276, 543
non-uniformity, 409
recombination, 45
relaxation rate, 201
scattering rates, 333
Carrier–carrier scattering coefficient, 335
Carrier-phonon
interaction, 333
scattering coefficient, 335
Catastrophic optical damage (COD), 312, 326
Cavity
anisotropies, 287
decay rate, 201
loss, 80
Q factor, 213
CC-OTDR, 445
Chain connections, 567
Channeled spectrum, 245
Channel noise, 543
Chaos, 2, 19, 119, 627, 639
based secure communications, 512
communications, 10
control, 6, 9, 364, 399, 452, 642
generators, 618
injected laser, 612
islands, 231
keys, 512
maps, 199
masking, 513
modulation, 513
pass-filtering, 520, 529
pass-filtering effect, 500, 538
synchronization, 6, 9, 460, 512, 627, 647
targeting, 382
transmittance, 529
Chaos shift keying (CSK), 513, 516, 527, 542, 549
Chaotic
associative memory, 452
attractor, 120, 405, 473, 527, 546, 627
bifurcation, 94, 121, 138, 161, 197, 280
bifurcation diagrams, 338
bursts, 527
carrier, 514, 520, 547, 548
carrier enhancement, 221
carrier frequency, 205, 220, 532
communications, 7
dimension, 620, 633
evolutions, 325
itinerary, 146, 147
lasers, 606
lidar, 445
oscillation, 94, 120
pulses, 228
pulsing states, 255
receiver, 647
routes, 231
scenario, 125
sea, 364, 642
secure communications, 220
signatures, 609, 621
state, 120
time-series prediction task, 592
trajectories, 489
transmittance, 531
transmitter, 647
Characteristic equation, 52, 92, 187, 233, 370
Chirp to power ratio, 218
Chromatic dispersion, 554
Circular dichroism, 287
Circularly polarized light, 288
Class A lasers, 30, 339, 343, 346, 351, 353, 354
Class B lasers, 3, 28, 34, 46
Class C lasers, 21, 26
Classification of signals, 592
Closed-loop system, 467, 476, 496, 547

Cluster synchronization, 580
CMA, 513, 514, 520, 529, 542, 550, 552
CMO, 513, 514, 525, 533, 535, 542
CO_2 lasers, 3, 29
Code division multiple access (CDMA), 512
Coefficient
  for carrier diffusion, 285
  of gain saturation, 43
  of spontaneous emissions, 44
Coexistence of Chaotic Attractors, 201
Coexistence states, 194, 202, 251, 302, 404
Coherence collapse, 85, 117, 134, 138, 151, 377, 604
Coherence collapse states, 430
Coherence length, 87, 105, 127, 425
Coherent in-phase arrays, 408
Coherent rate-equation model, 350
Combined systems, 583
Commensurate ratio, 611
Common coupling medium, 577
Common drive chaotic system, 540
Communications, key for, 545
Competitions of linear modes, 132
Complete chaos synchronization, 464, 469, 472, 485, 492, 495, 514, 546, 562
Complete synchronization, 488, 576
Complex electric permittivity, 41
Complex refractive index, 42
Complex refractivity, 41
Complex susceptibility, 41, 47
Composite reflectivity, 387
Composite video signal, 551
Conditional Lyapunov exponent, 461, 494, 495, 543
Conduction band, 48
Conductivity, 41
Confinement factor, 36, 46, 285, 315, 333
Confocal Fabry-Perot interferometer, 393
Confocal microscope, 438
Connections, 589
Connections in the Internets, 567
Connection weights, 586, 587
Consistency, 507, 560, 572, 575, 586, 588, 590
Constructive interference, 129
Continuous control method, 365, 367, 645
Continuous systems, 631
Control of LFFs, 380
Control signal, 370, 453
Convective flow, 631
Conversion coefficient, 124, 335
Conversion efficiency, 69, 84, 234, 295, 412, 450
Correlation coefficient, 480, 521, 544
Correlation dimension, 639
Correlation function, 640
Correlation plot, 472, 480, 504
Coupled map lattice (CML), 330
Coupled
  mode theory, 101
  nonlinear networks, 560
  semiconductor lasers, 585
  synaptic neurons, 560
  wave equations, 80
Coupling
  coefficient, 101
  ratio, 330
  strength, 80
C parameter, 85, 89, 150, 421
Critical feedback coefficient, 135
Cross
  correlation, 447
  polarization modes, 172
  gain saturation, 266
  saturation coefficient, 193
Crowd synchrony, 460, 560, 576
Current-voltage (I-V) characteristic, 434
Cutoff frequency, 205, 211, 480

D

Damping
  factor, 55, 213
  oscillations, 19
  rate, 336
Data-transmission rate, 543
3 dB bandwidth, 234
3-dB cutoff frequency, 350
Death by delay, 502, 503
Deconvolution, 148
Degeneration of spin states, 286
Degree of security, 516, 547
Delay
  differential equation, 87, 633
  differential system, 464, 365, 495, 585
  hyper-chaotic systems, 599
  optoelectronic hybrid feedback, 552
  synchronization, 500, 538, 568, 569, 573, 581
  time, 633
  time signature, 581
Depletion of carriers, 272, 285
Desynchronization, 543
Desynchronization bursts, 544
Desynchronized bit error rate (DBER), 544
Deterministic chaos, 141, 599
Deterministic equations, 19, 627
Devil's staircase, 238
DFB laser, 79
Dichroism, 172

Diehard test, 609
Difference of spin states, 289
Differential
  equations, 627, 633
  gain, 78
  relaxation rate, 201
  systems, 465
Differentiated signals, 614
Diffraction
  angle, 318
  coefficient, 313, 316
  grating, 402
  limited profile, 406
  loss, 85
  of light, 297, 312, 316
Differential phase-shift quantum key distribution (DPS-QKD), 622
Diffusion
  coefficient, 57, 314
  constant, 272
  effect, 314
  length, 314
Digital Chbyshev Type I filter, 544
Digital encoding, 512
Digital versatile disks, 270
Dimension, 546
Dimensionless equations, 46
Diodes, 434
Discrete difference equations, 629
Discrete-sequence optical CDMA, 547
Discrete system, 629
Displacement measurement, 426
Dissipative system, 25, 633
Distributed Bragg reflector, 283
Distributed feedback (DFB) lasers, 33
Divergence angle, 410
Divergent spherical wave, 73
Doppler beat, 441
Doppler frequency, 444
Doppler shift, 441
Dot density, 339
Double external mirrors, 372
Drive-response nonlinear systems, 575
Drive-response system, 506, 540, 572, 578
Driving
  force, 500, 539, 565, 570, 575, 579, 583
  laser, 566, 582
  system, 505
Duffing model, 631
Duffing's equations, 636
Dye lasers, 30
Dynamical system modeling, 592
Dynamic targeting, 382

E
Eavesdropper, 538
Effective
  chirping parameter, 219
  mass, 49, 333
  propagation constant, 72
  reflectivity, 95, 98
  refractive index, 37
Eigen-function, 284, 351
Eigen-value equation, 285
Einstein coefficient, 333
Einstein relation, 44
Electric permittivity, 16
Electron
  and hole capture rates, 333
  and hole escape rates, 333
  hole recombination, 34
  lifetime, 348
  spin, 288
  spin states, 286
Embedding space, 639
Energy band, 333
Enhancement factor, 75
Enhancement of modulation bandwidth, 204, 353
Entropy sources, 598
EO Mach–Zehnder interferometer, 552
EO modulator, 244, 257, 520, 526
Equation for carrier density, 44
Equilibrium points, 636
Erbium-doped fiber amplifier (EDFA), 552
Error of chaos synchronization, 474
Etched microstructure, 411
Exclusive-OR (XOR) operation, 606
Exited states, 333
Exponential scaling law, 603
External
  cavity frequency, 115
  cavity length, 421
  cavity mode, 174, 380
  injection ratio, 186
  modes, 91, 145, 154
  quantum efficiency, 345
Extra degree of freedom, 4, 184, 332
Eye opening, 218
Eye pattern, 217, 535

F
Fabry–Perot (FP)
  filter, 108
  lasers, 16, 77
  resonator, 16, 35, 172, 244, 393, 396
Fading memory, 589, 590
False signal, 447

Faraday rotator, 106
Far-field pattern (FFP), 313, 318, 406
Far-infrared lasers, 26
Far-infrared NH_3 laser, 592
Fast random number generations, 612
Feedback
  coefficient, 87, 98, 105
  gain, 235, 365
  induced noises, 278, 379
  interferometer, 448
  phase, 431
Fiber Bragg grating, 100, 156, 390
Fiber Bragg grating optical feedback, 100
Fiber lasers, 3, 29
Field, 16
Fifth-order Butterworth filter, 538
Filamentation, 298, 313, 330, 403, 412, 487
Filamentation effects, 312
Filament fluctuations, 487
Filament synchronization, 487
Filtered feedback, 107, 449
Filtered optical feedback, 163, 172
Finesses, 395
Finite difference time domain (FDTD) method, 315
Finite response phase-conjugate feedback, 162
Finite-response phase-conjugate mirror, 104
Finite response time, 542
First laser threshold, 22
Five-variable model, 334, 336
Fixed point, 364, 644
Fixed state, 120
Flared broad-area lasers, 10
FM feedback noise, 397
Food chains, 567
Forward error correction methods, 622
Four chain-coupled semiconductor lasers, 572
Fourier spectrum, 442
Four-level laser, 350
Four-level model, 287
Four mutually coupled ring lasers, 574
Fourth-order Runge-Kutta algorithm, 88
Four unidirectionally coupled lasers, 573
Four-wave mixing, 102, 391
Fractal dimension, 639
Fractal structure, 636
Free plasma effects, 47
Free-space broadcasting, 541
Frequency
  chirping, 68, 204
  detuning, 98, 161, 169, 184, 199, 207, 479, 485, 500
  difference, 288
  filter, 244
  injection current modulation, 270
  jitter, 389, 393
  locked pulsations, 280
  locked pulsing states, 231
  locked state, 237, 282
  oscillations, 173, 176
  pulling, 194
  pulling effect, 466
  selective filter, 172
  selective optical feedback, 100, 401
  shift, 210, 215
Fringe
  analysis, 420
  counting, 425, 441
  pattern, 420
Full-bit ADC, 612

G

Gain, 35, 38, 43, 96
  absorption section, 620
  at transparency, 43
  bandwidth, 264
  clamping, 347
  coefficient, 54, 291, 335
  defect, 193, 201
  difference, 96, 169, 170
  guided structure, 70, 316
  guide laser, 322
  profile, 47, 264, 266
  recovery time, 351
  reduction, 95
  saturation, 55, 192, 235, 314
  saturation factor, 253
  switching, 228
  to-loss ratio, 287
Gap energy, 49
Gauss-Hermite function, 74
Gaussian, 605
  mode, 73
  random process, 59
  random variables, 59
GCD rule, 584
Generalized chaos synchronization, 469, 471, 485, 488, 546, 563
Generalized synchronization, 464, 552
Generation of random bits, 606
Graphical solution for resonance frequency, 216
Grating mirror feedback, 156
Grating optical feedback, 97, 388, 408
Greatest common divisor, 584
Ground state, 333
Group velocity of light, 40

H
Hamiltonian, 17
Hardware based secure communications, 512
Harmonic oscillations, 452
Helmholtz equation, 72, 313
He–Ne lasers, 3, 26, 30
Heterodyne detection, 441
High-dimensional
  attractor, 599
  chaos, 365, 602
  spaces, 512
  systems, 633, 644
  phase space, 202
  states, 589
Higher
  gain region, 148
  harmonics, 94
  harmonic synchronization, 248
High frequency modulation, 379
Histogram, 605
Hodgkin-Huxley model, 560, 568
Hole-burning, 73, 351
  of carriers, 294, 297, 316
Holographic grating, 393
Homodyne detection techniques, 598
Hopf bifurcation, 24, 122, 189, 203, 341
Hopf bifurcation boundary, 199, 208
Hopfield model, 586
Hub-star coupled systems, 575
Hub-star network, 577
Huygens' pendulum clocks, 460
Hybrid system, 257
Hyper-plane, 589, 635
Hysteresis, 125, 137, 157, 190, 216, 251, 274, 295, 422, 577

I
Imaginary nodes, 586, 589
Imbalance interferometer, 450
Incoherent
  chaos synchronization, 481
  coupling, 534
Incoherent feedback, 105
  optical feedback, 164, 170
  optical feedback systems, 528
  rate equations, 265
Incommensurate ratio, 611
Incommensurate time offset, 613
Index-guided structure, 70
Index-guide laser, 322
Indium phosphide photonic integrated circuit, 599
Infinite dimensional system, 546
Inhomogeneous broadening, 412
Injection
  coefficient, 186
  current density, 44
  current modulation, 5, 65, 248, 280, 380, 497
  locking, 169, 463
  locking condition, 186
  locking effect, 478
  map, 189, 308
  ratio, 199
In-line amplifier, 525
In-phase optical feedback, 115
Instantaneous linewidth, 395
Intensity
  absorption coefficient, 41
  coupling coefficient, 278
  modulation, 67
  reflectivity, 84
Inter-band optical transitions, 34
Interference, 192, 207, 210
Interferogram, 438
Interferometric measurements, 420
Intermediate filter, 178
Intermittent
  chaotic bifurcations, 630
  instability, 144
  oscillations, 24, 325
  route, 141
  state, 259
Internal quantum efficiency, 44
Inter-subband optical transitions, 344
Intrinsic
  chaotic dynamics, 520
  laser noises, 569
  noises, 561
  noises of nonlinear elements, 584
Inverse
  LFFs, 326
  period-doubling bifurcation, 369
  route of chaotic bifurcations, 197
Isochronal solution, 472, 498
Isochronal synchronization, 561
Isolator, 353
Isomer signals, 454

J
Japanese attractor, 2
Jitter, 433
Johnson noise, 540

K
Kerr effect, 313, 523
Kerr media, 102
Kink, 275, 326

Kramers–Kronig relations, 175
K-space, 346
K vector, 48

L
Lagger laser, 500, 539
Langevin force, 57
Langevin noise, 19, 55, 116, 499, 540
Lang-Kobayashi equation, 87
Laser
  arrays, 407
  interferometers, 420
  model, 15
  neurons, 585
  nodes, 584
  oscillation conditions, 35
  oscillation frequency, 36
  threshold, 19
Lateral modes, 316
Leader-laggard dynamics, 537
Leader-lagger configurations, 498
Leader laser, 500, 539, 568
Learning process, 586, 587
Least-significant-bits, 605
Left circular polarization, 287
LFF oscillations, 501
L-I characteristic, 124, 167, 235, 273, 295, 302, 316, 411
LIDAR, 445
Limit-cycle, 636
  bifurcation, 203
  oscillators, 503
Linear
  classifier, 589
  gain, 43
  mode, 93, 94, 371, 380
Linearly polarized modes, 293
Linear phase anisotropy, 287
Linear stability analysis, 8, 22, 24, 51, 60, 92, 159, 185, 206, 212, 232, 250, 366, 370
Linewidth, 42, 65, 85, 96, 99, 148, 158, 387, 392, 395
  broadening, 117
  enhancement factor, 4, 41, 42, 134, 346, 386, 431, 440
  narrowing, 386, 395, 408
  narrowing factor, 387
  reduction, 117
  reduction factor, 99
Littman external cavity, 402
Littrow configuration, 389
Local gain, 284
Local signal scrambler, 541
Locking states, 354
Logical XOR operation, 608
Logistic map, 629
Long external cavity, 145
Long external optical feedback, 105
Longitudinal
  mode, 36, 264, 316
  optical phonon, 344
  relaxation coefficient, 351
Loop gain, 234
LO phonon, 344
Lorentzian, 63, 173, 397
  filter, 175
  frequency filter, 108
  spectrum, 47
Lorentz spectrum, 108
Lorenz, 1
  chaos, 514, 627
  equations, 20, 631
  system, 88, 460, 634, 648
Lorenz–Haken equations, 2, 20
Loss difference, 170
Low-dimensional
  attractor, 546
  chaos, 546
  dissipative systems, 478
  input, 589
  system, 644
Low-frequency fluctuations (LFFs), 91, 122, 140, 302, 326, 375, 499, 569
Low-pass Fabry–Perot filter, 523
LSBs, 605
Lyapunov
  exponent, 628, 640
  dimension, 641

M
Machine learning, 586
Macroscopic generation rate, 315
Magnetic permeability, 16
Magnetic quantum numbers, 287
Many coupled nonlinear elements, 460
Many mutual-coupling semiconductor lasers, 498
Map of oscillation modes, 295
Markov process, 56
Mask function, 590
Master laser, 184
Master–slave configurations, 463
Maximum
  chaotic oscillation, 221
  conditional Lyapunov exponent, 648
  data transmission rate, 480
  enhanced modulation frequency, 213
  gain, 47

Maximum (*cont.*)
gain mode, 36, 91, 145
gain mode condition, 382
Lyapunov exponent, 138
Maxwell–Bloch equations, 18, 20, 320, 350
Maxwell equation, 16
Mean-square error, 588
Mellin transform, 443
Michelson interferometer, 128, 445
Micro-cavity semiconductor lasers, 10
Microscopic model, 333
Microscopic polarization function, 315
Minimum
fluctuation, 397
linewidth, 397
Modal gain, 78, 284
Mode
analysis, 73, 367
competitions, 267
frequency, 36
for laser oscillations, 89
gain coefficient, 267
hopping, 115
hops, 91, 125
jumps, 126
partition noise, 267
separation, 37, 283
switching, 193, 270
transition, 132
Modified C parameter, 394
Modulation
amplitude, 69
bandwidth, 204, 354
characteristics, 65
coefficients, 519
efficiency, 65, 343
response, 67, 207, 217, 219, 342
Modulation transfer function (MTF), 439
Moment, 17
Momentary frequency, 189, 341
Multi-bit samplings, 612
Multi-layer neural network architectures, 577
Multi-longitudinal modes, 77
Multimode, 316, 323
instability, 259
lasers, 8, 264
Multiple
dynamical elements, 577
external cavity modes, 259
reflection effects, 87
transmitter–receiver systems, 461
Multiplicative modulation, 534
Multi-quantum well (MQW) lasers, 33, 77
Multi-section lasers, 618
Multistability, 137, 194, 201
Multistable states, 422, 451
Multi-stripe laser arrays, 330
Multi-wave mixing, 194
Mutual
chaotic communications, 537
coupling, 461
coupling system, 467, 470, 536
information, 600
optical injections, 470
optoelectronic coupling, 502
Mutually coupled
chain lasers, 567, 580
chain neurons, 568
hub-star lasers, 577
nonlinear elements, 561
semiconductor lasers, 498, 564
VCSELs, 500

N
Narrow filter, 178
Narrow-stripe edge-emitting semiconductor lasers, 33
N-coupled mutual ring lasers, 582
N-coupled unidirectional ring semiconductor laser networks, 580
Near-field
images, 293
polarized patterns, 298
Near-field pattern (NFP), 303, 318, 328, 403, 410
Negative feedback, 228, 502
Negative optoelectronic feedback, 237, 396
Network connections, 585
Network topology, 580
Neuron networks, 577, 580
Ne–Xe lasers, 26
NH_3lasers, 3, 26
NIST tests, 608
Nitride quantum-well gain medium, 312
Nodes, 562
Node states, 590
Noise, 376, 546
compression, 218
Spectrum, 60
suppression, 378, 398
Non-degenerate four-wave mixing, 162
Nondeterministic random number generations, 598
Nonlinear
carrier relaxation rate, 201
chaotic networks, 562
dispersion effect, 523
node, 560

phase coupling, 350
saturation coefficient, 267
Schrödinger equation, 523, 617
system, 627
Non-locking regions, 189
Non-radiative carrier–carrier scattering rates, 333
Nonradiative carrier recombination rate, 45
Non-return-to-zero (NRZ), 606
NRZ signal, 521
Number of synchronization clusters, 584
Number state, 48

O
Occasional proportional feedback (OPF) method, 365, 646
Occupation probability density, 334
Off-line processing, 613
Offset frequency detunings, 309
OGY
algorithm, 364, 642
method, 364, 454, 642
ON/OFF CSK, 529, 549
ON/OFF modulation, 542
One-drive and two-response configuration, 624
One-to-one system, 460
Onset of chaos, 134, 353
Open communication channel, 623
Open-loop system, 467, 477, 496, 547
OPF control, 369, 453
Optical
chaos control, 372
clock pulses, 616
dipole matrix element, 315
feedback, 4, 8, 83, 113, 119, 268, 324, 338, 352, 376, 487, 518, 542, 549, 562
feedback loop, 569, 575, 589
feedback noises, 270
fiber, 523
filp-flop, 616
frequency, 37, 449
gain, 47
injection, 8, 307, 327, 339, 406, 447, 474, 490, 542, 562
injection locking, 4, 183
injection map, 354
loss, 42
path difference, 245
phase, 136, 319, 488, 534
remote sensing, 445
secure communications, 205
spectrum, 117
switches, 308
XOR gate, 616
Optic axis, 294
Optoelectronic feedback, 5, 8, 227, 396, 450, 494, 502, 534, 542
Orthogonal optical injection, 310
Orthogonal-polarization feedback, 106
Oscillation linewidth, 353
OTDR, 445
Out-of-phase optical feedback, 115
Over-damped relaxation oscillations, 351

P
Packaged photodiode, 433
Parabolic profile, 74
Parallel-polarization optical feedback, 167
Parameter mismatches, 466, 470, 475, 492, 496, 544, 547, 554
Partition noises, 267
Passive waveguide, 619
Pattern recognition, 592
Peak side-lobe level (PSL), 446
Pendulum clocks, 576, 627
Period-doubling
bifurcation, 122, 131, 420, 630
bifurcation cascade, 154
cascade, 248
cascade route to chaos, 246
route to chaos, 255, 280
Periodic
death islands, 503
orbit, 633
oscillation, 93, 114
solutions, 366, 636
stability conditions, 159
stability enhancement, 128, 132
windows, 130
one oscillations, 353
Period-1 oscillation, 94, 120
Period-2 oscillation, 120
Period-3 oscillation, 197
Period-1 states, 420
Phase
condition, 36, 98
diffusion quantum random number generation, 599
diagram, 161, 162, 165, 199, 341, 375
for stable locking, 188
locking, 103, 163
locking state, 189
map, 489, 634
mismatch, 101
modulation, 68
noise, 62, 395, 598
noise spectrum, 64
portraits, 203, 238, 240, 634

Phase (*cont.*)
section, 620, 621
sensitivity, 136, 152, 326, 408
shift, 103, 531
space, 90, 120, 146, 153, 188, 214, 310, 354, 633, 634
synchronization, 576, 579
Phase-conjugate mirror feedback, 101, 159
Phase-conjugate optical feedback, 390
Phase-space tomography, 146
Phonon scattering time, 348
Photoconduction effect, 434
Photonic
integrated circuits, 618
neurons, 585
structure, 409
VCSELs, 409
Photon
lifetime, 40, 543
noises, 543
number, 45
spin, 288
Photorefractive mirrors, 102
Photorefractive phase-conjugate feedback, 164
Physical random bit generator, 622
Physical random number generators, 598, 606
Planck constant, 17
p–n junction, 34
Poincaré, 1, 627
map, 364, 628, 634, 636, 645
section, 240, 242
Poisson random processes, 57
Polarization
equation, 18
instability, 296
of matter, 16, 46
mode, 344
mode competition, 306
switching, 286, 289, 308
Polarization-rotated mutual coupling systems, 499
Polarization-rotated optical feedback, 106, 167, 305, 482
Polarization selective optical feedback, 303
Population inversion, 18
Positive feedback, 228
Positive optoelectronic feedback, 240
Post-processing techniques, 599, 614
Potential model, 115, 564
Power
conversion efficiency, 311
dropout, 141
drops, 138
law, 398, 577
mode coupling factor, 394
recovery, 141
spectrum, 57, 63, 530
Predation
effect, 297
error, 593
rate, 593
Private key generation rates, 538
Probability functions, 48
Propagation constant, 41, 73, 284
Pseudo-random bit-sequences, 521
Pseudorandom code-modulated CW lidar, 445
Pseudo-random number generators, 598
Public optical communication links, 552
Pulsation oscillation, 165, 229, 249, 340
Pulse
jitter, 280
oscillations, 105, 273
package dynamics, 305
package oscillation, 307
packages, 326
repetition rate, 237
states, 228
width, 237
Pumping parameter, 46
P-value, 608

Q
Q factor, 396
QKD, 622
Q switching effect, 166
Quality factor, 25
Quantum bit error rate, 624
Quantum-cascade semiconductor lasers, 9, 344, 438
Quantum computing, 512
Quantum-confined Stark effect, 312
Quantum dots, 333
Quantum-dot semiconductor laser, 9, 331
Quantum-dot structure, 412
Quantum key distribution, 622
Quantum secure communications, 622
Quantum state, 17
Quantum-well structure, 78
Quasi-Fermi level, 48, 123, 434
Quasi-period doubling bifurcation, 24, 630
Quasi-periodic bifurcation, 122
Quasi-periodic oscillations, 94, 117
Quasi-periodic solutions, 636

R
Ramp
modulation, 428
signal, 428

Random lasers, 10
Random number generations, 7, 10, 598
Range resolution, 446
Rate equation, 7, 18, 88, 103, 105, 107, 185, 192, 251, 266, 273, 278, 284, 288, 291, 300, 313, 329, 333, 348, 351, 394, 449, 468, 470, 483, 487, 491, 494, 518, 533, 534, 603
Rate equation for the field, 39
Recombination coefficient for spontaneous radiation, 45
Recurrent neural network, 586, 587
Red-shift, 210, 347
Reduced model, 334
Reduction of gain, 99
Refractive index, 16, 36, 37, 84
Refractive index at the threshold, 37
Regenerative amplification, 194
Regenerative amplifier, 305
Regular pulse package envelope frequency, 154
Regular pulse package oscillations, 152
Regular pulsing states, 274
Relative intensity noise, 61, 118, 267, 377, 398
Relaxation oscillation, 26, 52, 338, 353
Relaxation oscillation frequency, 23, 53, 54, 220, 305, 548
Relaxation time, 19, 34
Repellor, 203
Repetition rate, 228
Reservoir, 586
Reservoir computing, 7, 10, 586, 587, 592
Residual inaccuracy, 425
Resonance angular frequency, 235
Resonance frequency, 213
Resonant optical feedback, 393
Resonator frequencies, 36
Response function, 100, 108
Response gain, 531
Response ratio, 531
Response systems, 505
Response time, 104, 234, 372, 450, 590
Resynchronization time, 538, 547
Retardation time, 245
Return map, 149
Rf gain, 209
Right circular polarization, 287
RIN, 61
Ring
  connections, 567
  laser, 2
  resonator, 15
Ripples, 230
RLC oscillator, 214
Rössler system, 465, 478, 646, 647
Rotating-wave approximation, 19
Round-trip time, 37, 87, 129, 441
Route to chaos, 24, 138, 339
Rubidium atomic vapor, 393
Rulle–Takens–Newhouse three-frequency, 242

S

Saddle node, 189, 643
  bifurcation, 191, 203, 340
  boundary, 199
  instabilities, 141, 142
Saddle point, 203
Santa Fe time-series competition, 592
Saturable absorbing layers (SALs), 271
Saturation effect, 234, 235
Saturation intensity, 20
Sawtooth-like wave, 431, 433
Sawtooth-like waveform, 425
Scalar wave propagation, 72
Scattering times for electrons, 334
Schawlow-Townes equation, 65
Schawlow-Townes linewidth, 395
Schrödinger equation, 17
Second laser threshold, 23
Second-order dispersion parameter, 523
Secret data transmissions, key for, 538
Secure chaos key generation, 512
Secure chaotic communications, 545
Secure data transmissions, 512
Secure key exchange cryptosystem, 538
Security, 545, 546
Selection rules, 344
Self-assembled method, 331
Self-focusing effects, 316
Self-mixing Doppler velocimetry, 441
Self-mixing effect, 346, 353, 420
Self-mixing interferometers, 9
Self-mixing interferometry, 7, 344
Self-mixing vibrometer, 427
Self-modulations, 304
Self-pulsating semiconductor, 398
Self-pulsating semiconductor laser, 8, 270, 497
Self-pulsation laser, 379
Self-pumped phase-conjugate configuration, 393
Self-saturation effect, 193
Self-sustained pulsation oscillations, 272
Self-sustained pulsations, 240
Semi-classical quantum theory, 17
Semi-classical theory, 47
Semiconductor laser, 3, 29, 33, 119
Semiconductor laser arrays, 329
Semiconductor optical amplifier, 620

Sensitivity for initial condition, 630
Sensitivity to initial condition, 1
Separation, 589
Shifted cavity resonance, 211
Short external cavity, 89, 145, 150
Short optical feedback, 305, 326
Short-term memory, 589
Shot noise, 56, 540
Side-mode excitation, 199
Side modes, 192
Side mode suppression, 265, 389
Side mode suppression ratio (MSR), 265, 391, 410
Shifted key generation rate, 624
Sigmoid function, 586
Signal-to-noise ratio (SNR), 397, 424, 542, 543, 552
Single mode, 87
Single-mode fiber transmission, 554
Sinusoidal modulation, 68
  control, 370
  method, 366, 378
Six-valued mask, 593
Skew, 612
Skewed amplitude distributions, 607
Skewed waveforms, 604
Slab-waveguide model, 72
Slave laser, 184
Sliding fast Fourier transform, 148
Slope efficiency, 143, 235, 303
Slowly varying envelope approximation, 17
Slow response phase-conjugate feedback, 162
Small signal analysis, 219
Small-signal transfer function, 134
Solid-state lasers, 3, 29
Solitary
  condition, 87
  laser mode, 148
  mode, 91
Space–time correlation functions, 322
Spatial filament oscillation, 312
Spatial filter, 403
Spatial hole-burning, 266, 298
Spatial hole-burning effects, 293
Spatially filtered optical feedback, 403
Spatial mode, 284, 313
Spatial mode competitions, 300
Spatial-mode expansion model, 284
Spatio-temporal dynamics, 297, 318
Spatio-temporal instability, 72
Spatio-temporal size of filaments, 323
Speckle modulation, 441
Spectral
  density, 61
  hole-burning, 266
  linewidth, 62, 118, 163
Spectrally resolved near-field pattern, 316
Spiking oscillations, 585
Spin, 49
Spin degeneracy, 333
Spin-flip
  model, 286
  relaxation, 289
  relaxation processes, 287
Spin mixing, 290
Spin relaxation time, 287
Spoken digit/speaker recognition, 594
Spontaneous emission, 43, 55, 56, 75, 235
  coefficient, 253, 266
  factor, 348
  noises, 576
Spontaneous quantum noises, 598
Square root scaling, 154
Square-wave generation, 304
Square-wave oscillations, 170, 172
Stability condition, 22, 93, 159
Stable and unstable map, 474
Stable injection locking, 184
Stable islands, 642
Stacked arrays, 407
Star coupled systems, 580
Static grating, 163
Statistical potential model, 499
Statistical tests, 608
Steady-state, 22
  analysis, 296, 348
  condition, 36, 149, 187
  frequency, 103
  occupation probabilities, 336
  oscillation, 405
  solution, 51, 88, 103, 145, 266, 319, 374, 387, 487, 636
Step response, 353
Stepwise time recovery, 149
Strange attractor, 121, 633
Strength of astigmatism, 76
Stress-induced anisotropy, 312
Stripe width, 72, 316
Strong chaotic oscillations, 602
Strong optical feedback, 97, 106, 386
Subbands, 344
Subcritical bifurcations, 203
Sub-group synchronization, 579
Sublattice synchronization, 572, 582
Subsystem, 462, 514, 539, 647
Supercritical bifurcations, 203
Supercritical Hopf bifurcations, 154
Super-lattice structures, 344

Suppression
of correlation peaks, 604
of frequency chirping, 218
of laser noises, 204
Susceptibility, 315
Sustained pulsations, 164
Switching current, 292
Symmetrical systems, 499
Symmetry breaking, 500, 561, 564
Synaptic neurons, 498, 567, 585
Synchronization, 560
bit error rate, 544
bursts, 549
error, 475, 492, 527, 543
recovery time, 527, 549
Synchronous oscillation, 378
Synchronous signal, 369, 453

T
Tapered cavity, 320
Tasks, 592
TEM_{00} mode, 316
Temporal instability, 258
Thermal laser noises, 598
Thermal lens effect, 409
Thermal lensing, 404
Thermo-electric cooling, 620
Thickness of the active layer, 44
Three chain-coupled semiconductor lasers, 567
Three coupled equations, 88
Three mutually coupled ring lasers, 571
Three-node networks, 566
Three-variable model, 341, 342
Threshold current, 348
Threshold difference, 288
Threshold gain, 36, 79
Threshold reduction, 124, 402
THz biomedical imaging technique, 441
THz light, 344
$TiBaO_3$crystal, 102
Time-delay signatures, 600, 607
Time-differentiated chaotic signals, 605
Time lag, 464
Time of flight, 445
Time series prediction, 592
Time signatures, 599
Topological configurations, 583
Topology of nonlinear networks, 573
Torus, 639
Torus bifurcation, 177, 199
Total BER, 544
Total carrier density, 289
Total loss, 35
Training, 587
Trajectory, 153, 214, 479, 632, 634
Transcendental equation, 174
Transfer function, 134, 529
Transient responses, 590
Transient states, 589
Transient time, 527
Transition
of chaos, 602
probabilities, 48
time, 549
to synchronization, 577
Transmission gain, 531
Transmission rates, 531
Transparency, 42, 288, 291
Transverse-electric (TE) mode, 71, 106, 167, 312
Transverse-magnetic (TM) mode, 71, 106, 167, 312, 344
Transverse-mode oscillations, 297
Transverse relaxation coefficient, 351
Traveling wave amplifier model, 75
Triode, 631
True random number sequence, 604
Truly random bit streams, 614
Tunable semiconductor laser, 244
Turn-on delay, 338
Two chaotic systems, 460
Two-cluster synchronization, 572
Two-frequency quasi-periodic pulsing state, 231
Two-gain model, 291
Two-level atom, 17, 44, 193
Two-level model, 346
Two-torus, 638
Twyman-Green interferometer, 449
Type-II intermittency, 141
Type II pulse packages, 307
Type I pulse packages, 307

U
Ueda attractor, 2
Undamped relaxation oscillations, 178
Unidirectional coupling, 461
Unidirectionally coupled chain lasers, 567
Unidirectionally coupled lasers, 580
Unidirectionally coupled ring lasers, 569
Unidirectionally coupled semiconductor lasers, 563
Unidirectional ring configuration, 603
Uniformity of p-values, 608
Unlocking oscillations, 184
Unlocking regions, 310
Unstable periodic orbits (UPO), 141, 364, 374, 454, 642, 645

Unstable periodic solutions, 371
Unstable pole, 134
Unstable saddle node, 399
Unstable saddle node points, 364, 371
Ununiformity of signals, 614

V
Valence band, 48
Van der Pol/Duffing oscillator, 2
Van der Pol equations, 636
Van der Pol oscillator, 238, 631
Variable optical attenuator, 620
VCSEL arrays, 408, 438
Velocity measurement, 441
Vertical-cavity surface-emitting lasers (VCSELs), 5, 8, 282, 400, 435
Vertical-external-cavity surface-emitting lasers (VECSELs), 402
Vibration measurement, 426
Video data transmission, 550
Virtual nodes, 590
Volume holographic grating, 156, 390
Von Neumann architecture, 586

W
Wave front, 73
Wavefront distortion, 316
Waveguide models, 70
Wavelength filter, 244
Wavelength separation, 264
Wavenumber, 17, 38
Weak chaos, 566
Weak chaotic state, 603
Weak index guide (WIG), 271
Wetting layer, 333
Whispering-gallery-mode, 396
White Gaussian noise, 543
White noise, 446
Wide filter, 178

X
Xe laser, 3, 27
XOR operation, 606, 613

Z
Zero-lag synchronization, 561, 567, 569, 574, 578, 580, 582, 584, 587